Remote Sensing of Vegetation Leaf Area

Knyazikhin and Myneni (Eds.)
Boston University

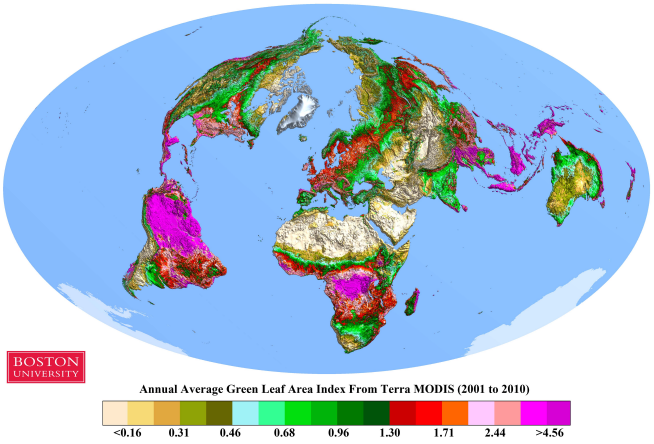

$$
\begin{cases}
U(z,\underline{\Omega}) + \dfrac{1}{|\mu(\underline{\Omega})|}\displaystyle\int_0^z d\xi\, K(z,\xi,\underline{\Omega})\sigma(\underline{\Omega})U(\xi,\underline{\Omega}) \\
= \dfrac{1}{|\mu(\underline{\Omega})|}\displaystyle\int_0^z d\xi \int_{4\pi} d\underline{\Omega}'\, K(z,\xi,\underline{\Omega})\sigma_s(\underline{\Omega}' \to \underline{\Omega})\, U(\xi,\underline{\Omega}') + U(0,\underline{\Omega}), \quad \mu < 0, \\
U(z,\underline{\Omega}) + \dfrac{1}{|\mu(\underline{\Omega})|}\displaystyle\int_z^H d\xi\, K(z,\xi,\underline{\Omega})\sigma(\underline{\Omega})U(\xi,\underline{\Omega}) \\
= \dfrac{1}{|\mu(\underline{\Omega})|}\displaystyle\int_z^H d\xi \int_{4\pi} d\underline{\Omega}'\, K(z,\xi,\underline{\Omega})\sigma_s(\underline{\Omega}' \to \underline{\Omega})U(\xi,\underline{\Omega}') + U(H,\underline{\Omega}), \quad \mu > 0.
\end{cases}
$$

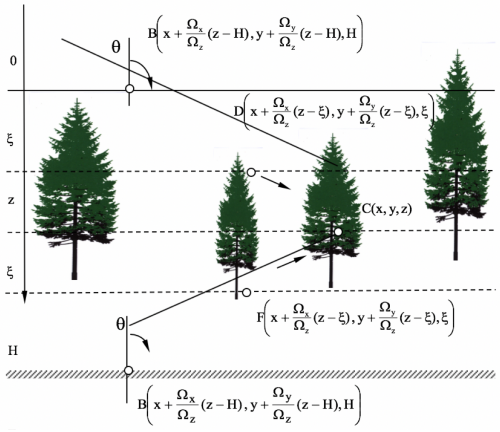

Contents

Chapter 1

The Radiation Field and the Radiative Transfer Equation

Knyazikhin et al.

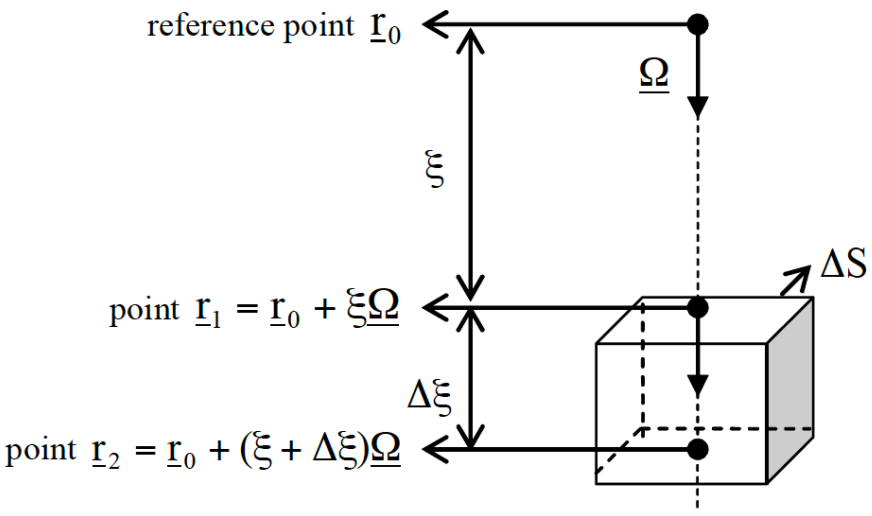

Chapter 1

The Radiation Field and the Radiative Transfer Equation

1. The Radiation Field

Photons: The energy in the radiation field is assumed carried by point mass-less neutral particles called photons. The energy of a photon E (in Joules) is $\hbar\nu$, where $\hbar = 6.626176 \cdot 10^{-34}$ J s (Joules seconds) is Planck's constant and ν is photon frequency (in s^{-1}). Frequency is related to wavelength λ (in meters) as $\nu = c/\lambda$ where $c = 2.99792458 \cdot 10^{8}$ m s^{-1} is speed of light. Photons travel in straight lines between collisions and are regarded as a point particles, with position described in Cartesian coordinates by the vector $\underline{r} = (x, y, z)$ and direction of travel by the unit vector $\underline{\Omega} = (\Omega_x, \Omega_y, \Omega_z)$, $\| \underline{\Omega} \| = 1$ (Fig. 1). Here and throughout the book the symbol $\| \underline{r} \|$ is used to denote the length of the vector $\underline{r}$, i.e., $\| \underline{r} \|^2 = x^2 + y^2 + z^2$. We will also use a polar coordinate system to specify the unit vector $\underline{\Omega}$. Cartesian coordinates of $\underline{\Omega}$ can be expressed via the polar angle θ and the azimuthal angle φ as $\Omega_x = \sin\theta\cos\varphi$, $\Omega_y = \sin\theta \sin\varphi$, $\Omega_z = \cos\theta$ (Fig. 1).

The description of photon distribution requires the consideration of photons traveling in directions confined to a solid angle. A solid angle is a part of space bounded by the line segment from a point (the vertex) to all points of a closed curve. A cone is an example of the solid angle which is bounded by lines from a fixed point to all points on a given circle. The solid angle represents the visual angle under which all points of the given curve can be seen from the vertex.

A measure, or "size", of a solid angle is the area of that part of the unit sphere with center at vertex that is cut off by the solid angle. Units of the solid angle are expressed in steradian (sr). For a unit sphere whose area is 4π, its solid angle is 4π sr. In the polar coordinate system, the differential solid angle $d\underline{\Omega}$ cuts an area consisting of points with polar and azimuthal angles from intervals $[\theta, \theta + d\theta]$ and $[\varphi, \varphi + d\varphi]$.

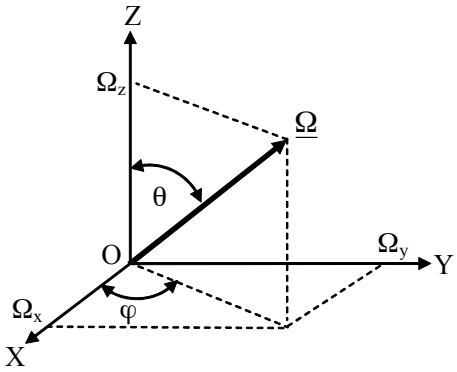

Figure 1. Representation of the unit vector $\underline{\Omega} \equiv (\Omega_x, \Omega_y, \Omega_z)$, $\| \Omega \|^2 = \Omega_x^2 + \Omega_y^2 + \Omega_z^2 = 1$, in Cartesian and polar coordinate systems. Here Ω_x, Ω_y and Ω_z are Cartesian coordinates of $\underline{\Omega}$; θ and φ are the corresponding polar and azimuthal angles in a polar coordinate system.

Particle Distribution Function: Let $f(\underline{r}, \nu, \underline{\Omega}, t)$ denote the density distribution function such that the number of photons dn at time t in the volume element $d\underline{r}$ (in m^3) about the point $\underline{r}$, with *frequency* in a frequency interval ν to $\nu + d\nu$ (in s), and traveling along a direction $\underline{\Omega}$ within solid angle $d\underline{\Omega}$ (in sr, see Problem 3) is

$$dn = f \, d\underline{r} \, d\nu \, d\underline{\Omega}. \tag{1}$$

In the *frequency domain*, the particle distribution function $f(\underline{r}, \nu, \underline{\Omega}, t)$ has units of photon number per m^3 per frequency interval per steradian (m^{-3} s sr^{-1}). In the above definition, one can use the *wavelength* interval λ to $\lambda + d\lambda$ (in m) instead of its frequency counterpart to define the particle distribution function. In the *wavelength domain*, therefore, the particle distribution function has units of photon number per m^3 per m per steradian (m^{-4} sr^{-1}).

Specific Intensity: Many radiometric devices used in remote sensing respond to radiant energy. It is convenient, therefore, to express the particle distribution in terms of energy that photons transport. Consider a volume element $d\underline{r} = d\sigma_\Omega dz$ with the base $d\sigma_\Omega$ (in m^2) perpendicular to a direction $\underline{\Omega}$ and the height dz (in m). The number of photons in this volume traveling along the direction $\underline{\Omega}$ is determined by the number of photons which cross $d\sigma_\Omega$ in the time interval t to t+dz/c where c is speed of light since the distance traversed by a photon within the interval dt = dz/c does not exceed dz. Equation (1) can be rewritten as $dn = f \, d\sigma_\Omega \, c \, dt \, d\nu \, d\underline{\Omega}$. Since the energy of one photon is $\hbar\nu$, the amount, dE, of radiant energy (in J) in a time interval dt and in the frequency interval ν to $\nu + d\nu$, which crosses a surface element $d\sigma_\Omega$ perpendicular to $\underline{\Omega}$ within a solid angle $d\underline{\Omega}$ is given by

$$dE = \hbar\nu \, dn = c\hbar\nu \, f(\underline{r}, \nu, \underline{\Omega}, t) d\sigma_\Omega dt \, d\nu \, d\underline{\Omega}. \tag{2}$$

The distribution of energy that photons transport is given by *specific intensity* (or *radiance*) defined as

$$I(\underline{r}, \nu, \underline{\Omega}, t) = c\hbar\nu f(\underline{r}, \nu, \underline{\Omega}, t). \tag{3a}$$

Its units are J $m^{-2} sr^{-1}$ in the frequency domain and J s^{-1} m^{-3} sr^{-1}=W m^{-3} sr^{-1} in the wavelength domain. Here W (1 watt = Js^{-1}) is the unit of radiant power.

Some radiometric devices count photons impinging on a detection area for a certain time interval. It is also convenient to express the photon distribution in terms of number of photons crossing a surface of unit area, per unit time per unit frequency per unit steradian. This quantity, intensity of photons (in number $s^{-1}m^{-3}sr^{-1}$), is simply the ratio between "radiant" intensity and the energy of one photon $\hbar\nu$ and can be expressed via the particle density distribution function as

$$I(\underline{r}, \nu, \underline{\Omega}, t) = c f(\underline{r}, \nu, \underline{\Omega}, t). \tag{3b}$$

We will use *intensity* as the basic radiaometric quantity throughout this book, allowing for both possibilities in its definition. If the specific intensity is independent of $\underline{\Omega}$ at a point, it is said to be *isotropic* at that point. If the intensity is independent of both $\underline{r}$ and $\underline{\Omega}$, the radiation field is said to be *homogeneous* and *isotropic*. It should be emphasized that the particle distribution function f describes photons *at time* t while the specific intensity refers to radiant energy (number of photons) passing a unit area in *the time interval* t to t+dt.

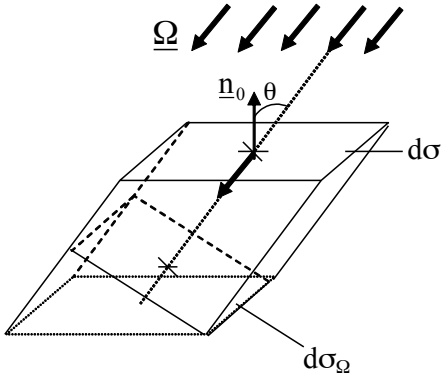

Figure 2. A beam of photons incident on the area dσ at an angle θ to the normal $\underline{n}_0$. Here $d\sigma_\Omega$ is the projection of the area dσ onto a plane perpendicular to a direction $\underline{\Omega}$ of photon travel. Its area can be expressed as $d\sigma_\Omega = d\sigma\cos\theta$. Note that $\cos\theta = |\underline{\Omega} \bullet \underline{n}_0|$ where $\underline{\Omega} \bullet \underline{n}_0$ is the scalar product of two unit vectors $\underline{\Omega}$ and $\underline{n}_0$.

Figure 2 shows an example where a photon beam of intensity I is incident on an area $d\sigma$ at an angle θ to the normal $\underline{n}_0$ to $d\sigma$. It is clear that the number of photon crossing the area $d\sigma$ coincides with the number of photons crossing its projected area $d\sigma_\Omega$. Thus, the amount of radiant energy (number of photons) dE in a time interval dt, in the frequency interval ν to $\nu + d\nu$, which crosses a surface element $d\sigma$ in directions confined to a differential solid angle $d\underline{\Omega}$, which is oriented at an angle θ to the normal $\underline{n}_0$ of $d\sigma$ can be expressed as

$$dE = I(\underline{r}, \nu, \underline{\Omega}, t)\cos\theta\, d\nu\, d\underline{\Omega}\, d\sigma\, dt. \tag{4}$$

Radiative flux density: Equation (4) gives the energy in the frequency interval ν to $\nu + d\nu$ which flows across an element area of $d\sigma$ in a direction which is inclined at an angle θ to its outward normal $\underline{n}_0$ and confined to an element of solid angle $d\underline{\Omega}$. The net flow in all direction is given by

$$F_\nu(\underline{r}) = \int_{4\pi} I(\underline{r}, \nu, \underline{\Omega}, t) \, | \, \underline{n}_0 \bullet \underline{\Omega} \, | \, d\underline{\Omega}, \tag{5}$$

where the integration is performed over the unit sphere 4π of directions. The quantity F_ν is called the *net monochromatic flux density* at $\underline{r}$ and defines the rate of flow of radiant energy across $d\sigma$ of unit area and per unit frequency interval. Its units is J m^{-2} in the frequency domain and W m^{-3} in the wavelength domain.

The net flux can in turn be represented as a sum of two hemispherical fluxes with respect to an arbitrary surface element $d\sigma$ as $F_\nu(\underline{r}) = F_\nu^+(\underline{r}) - F_\nu^-(\underline{r})$. Here $F_\nu^\pm$ are the monochromatic flux densities at different sides of $d\sigma$, or the *monochromatic irradiances*,

$$F_\nu^\pm(\underline{r}) = \int_{\mp \underline{n}_0 \bullet \underline{\Omega} > 0} I(\underline{r}, \nu, \underline{\Omega}, t) \, | \, \underline{n}_0 \bullet \underline{\Omega} \, | \, d\underline{\Omega} \, . \tag{6}$$

The *total hemispherical flux density*, in Wm^{-2}, or irradiance, for all frequencies (wavelengths) can be obtained by integrating the monochromatic irradiance over the entire electromagnetic spectrum

$$F^\pm(\underline{r}) = \int_0^\infty F_\nu^\pm(\underline{r}) d\nu \, . \tag{7}$$

The integral of the irradiance over an area A is the total flux, in W, or *radiant power*,

$$F^\pm = \int_A F^\pm(\underline{r}) d\sigma \, . \tag{8}$$

For homogeneous and isotropic radiation, intensity $I(\underline{r}, \nu, \underline{\Omega}, t) = i(\nu, t)$ is independent of angular and spatial variables, the above quantities are

$$F_\nu^\pm(\underline{r}) = \pi i(\nu, t), \quad F^\pm(\underline{r}) = \pi \int_0^\infty i(\nu, t) d\nu, \quad F^\pm = \pi A \int_0^\infty i(\nu, t) d\nu \, . \tag{9}$$

Normalization of the above quantities by the energy of one photon $\hbar\nu$ results in corresponding fluxes for photons.

2. Interaction of Radiation with Matter

Absorption: The *absorption coefficient* σ_a (in m^{-1}) is defined such that the probability of a photon being absorbed while traveling a distance ds is $\sigma_a(\underline{r}, \nu, \underline{\Omega}, t)ds$. An absorption event signifies true loss of a photon from the count.

Scattering: The *scattering coefficient* σ'_s (in m^{-1}) is defined in analogy to the absorption coefficient,

$$\text{Probability of scattering} = \sigma'_s(\underline{r}, \nu, \underline{\Omega}, t)\, ds.$$

Unlike absorption, a scattering event serves to change the direction and/or frequency of the incident photon. Thus, it is convenient to define a *differential scattering coefficient* σ_s (in m^{-1} sr^{-1}) as,

$$\text{Probability of scattering} = \sigma_s(\underline{r}, \nu' \rightarrow \nu, \underline{\Omega}' \rightarrow \underline{\Omega}, t)\, ds\, d\underline{\Omega}.$$

The change in photon frequency as a result of a scattering event is generally not relevant in optical remote sensing of vegetation. It is important to note that photon scattering in vegetation media depends on the coordinates of $\underline{\Omega}'$ and $\underline{\Omega}$ in general. The scattering coefficients σ'_s and σ_s are related as

$$\sigma'_s(\underline{r}, \nu, \underline{\Omega}, t) = \int_0^\infty d\nu'' \int_{4\pi} d\underline{\Omega}''\, \sigma_s(\underline{r}, \nu \rightarrow \nu'', \underline{\Omega} \rightarrow \underline{\Omega}'', t). \tag{10}$$

In some cases, the differential scattering coefficient is decomposed into the product

$$\sigma_s(\underline{r}, \nu' \rightarrow \nu, \underline{\Omega}' \rightarrow \underline{\Omega}, t) = \sigma'_s(\underline{r}, \nu', \underline{\Omega}', t)\, K(\underline{r}, \nu' \rightarrow \nu, \underline{\Omega}' \rightarrow \underline{\Omega}, t), \tag{11}$$

such that, the kernel K, termed a s*cattering phase function*, has the interpretation of a probability density function,

$$\int_0^\infty d\nu \int_{4\pi} d\underline{\Omega}\, K(\underline{r}, \nu' \rightarrow \nu, \underline{\Omega}' \rightarrow \underline{\Omega}, t) = 1. \tag{12}$$

In the case of coherent scattering, there is no frequency change upon scattering and

$$K(\underline{r}, \nu' \rightarrow \nu, \underline{\Omega}' \rightarrow \underline{\Omega}, t) = K(\underline{r}, \underline{\Omega}' \rightarrow \underline{\Omega}, t)\, \delta(\nu' - \nu), \tag{13a}$$

where δ is the Dirac delta function. In the case of isotropic scattering,

$$K(\underline{r}, \nu' \rightarrow \nu, \underline{\Omega}' \rightarrow \underline{\Omega}, t) = \frac{1}{4\pi} K(\underline{r}, \nu' \rightarrow \nu, t). \tag{13b}$$

Therefore, the simplest scattering kernel corresponds to isotropic coherent scattering, namely,

$$K(\underline{r}, \nu' \to \nu, \underline{\Omega}' \to \underline{\Omega}, t) = \frac{1}{4\pi}\,\delta(\nu' - \nu). \tag{13c}$$

Extinction: The *extinction* or the *total interaction coefficient* σ (in m^{-1}) is simply the sum $\sigma_a + \sigma_s'$. Therefore, $\sigma(\underline{r}, \nu, \underline{\Omega}, t)\,ds$ is the probability that a photon would disappear from the beam while traveling a distance ds in the medium (note that it can reappear at a different frequency and/or direction.) The quantity $1/\sigma$ denotes *photon mean free path*, that is, the average distance a photon will travel in the medium before suffering a collision. The dependence on the direction of photon travel is noteworthy and is especially important in the case of vegetation media.

Single Scattering Albedo: The probability of scattering given that a collision has occurred is given by the *single scattering albedo*, $\omega = \sigma_s'/\sigma$ (dimensionless). In the case of conservative scattering, $\omega = 1$. The case $\omega = 0$ corresponds to pure absorption.

Emission: Photons can be introduced into the medium through external and/or internal sources. In the frequency domain, the number of photons emitted by volume dr at r in the direction $\underline{\Omega}$ about the differential solid angle $d\underline{\Omega}$ at frequency ν in the interval ν to $\nu + d\nu$ between t and t+dt is $q(\underline{r}, \nu, \underline{\Omega}, t)d\underline{r}d\nu\, d\underline{\Omega}\, dt$.

It should be noted that we neglect photon to photon interaction in the above definitions. This means that the photon density is low, that is, low enough such that the overlap in the tails of wavepackets of two photons is negligibly small. This is especially required in the case of source photons emitted at the same location. We also assume that collisions and emission processes occur instantaneously. This imposes a limit on the time resolution over which the above definitions are applicable.

3. The Equation of Transfer

Consider the change dN in time Δt of the number of photons which are located in a volume element $d\underline{r} = \Delta\underline{S}\,\Delta\xi$ about the point $\underline{r}$ (Fig. 3). Here the base $\Delta\underline{S}$ of the volume dr is perpendicular to the direction $\underline{\Omega}$ of photon travel and the height $\Delta\xi = c\Delta t$ where c is speed of light. The number of photons in this volume traveling along the direction $\underline{\Omega}$ is determined by the number of photons which cross ΔS in the time interval t to t+dz/c. It follows from Eq. (3b) that this count is given by

$$\frac{1}{c}\,I(\underline{r}_1, \nu, \underline{\Omega}, t)\,\Delta\underline{S}\,\Delta\xi\,\Delta\nu\,\Delta\underline{\Omega}.$$

The number of photons leaving the volume $d\underline{r}$ through its lower surface ΔS in the direction $\underline{\Omega}$ in the time interval t to t+dz/c can be expressed as

$$\frac{1}{c} I(\underline{r}_2 + c\Delta t\underline{\Omega}, \nu, \underline{\Omega}, t + \Delta t)\, \Delta\underline{S}\, \Delta\xi\, \Delta\nu\, \Delta\underline{\Omega}.$$

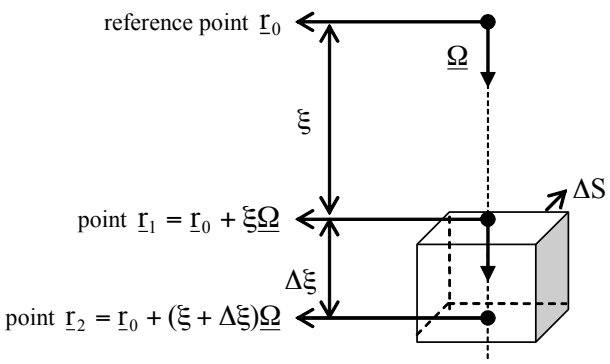

Figure 3. A volume element $d\underline{r} = \Delta\underline{S}\,\Delta\xi$ with the base $\Delta\underline{S}$ perpendicular to a direction $\underline{\Omega}$ and the height $\Delta\xi = c\Delta t$. Points $\underline{r}_1$ and $\underline{r}_2$ on the upper and lower boundaries of the volume element can be represented as $\underline{r}_1 = \underline{r}_0 + \xi\underline{\Omega}$ and $\underline{r}_2 = \underline{r}_0 + (\xi + \Delta\xi)\underline{\Omega}$, respectively. Here ξ and $\xi + \Delta\xi$ are distances between these points and a point $\underline{r}_B$ on the boundary δV along a direction opposite to $\underline{\Omega}$.

The change in time Δt of the number of photons in $d\underline{r}$ is

$$dN = \frac{1}{c}\Delta I\, \Delta\underline{S}\, \Delta\xi\, \Delta\nu\, \Delta\underline{\Omega},$$

where

$$\Delta I = I(\underline{r} + c\Delta t\underline{\Omega}, \nu, \underline{\Omega}, t + \Delta t) - I(\underline{r}, \nu, \underline{\Omega}, t). \tag{14}$$

In the increment (14), the spatial variable $\underline{r}$ depends on t. Using the chain rule for function of several variables, one gets

$$\Delta I = \frac{\partial I}{\partial t}\Delta t + \frac{\partial I}{\partial x}\frac{dx}{dt}\Delta t + \frac{\partial I}{\partial y}\frac{dy}{dt}\Delta t + \frac{\partial I}{\partial z}\frac{dz}{dt}\Delta t,$$

where x, y and z are Cartesian coordinates of points $\underline{r} + ct\underline{\Omega}$, $0 \le t \le \xi/c$. Thus,

$$dN = \left(\frac{1}{c}\frac{\partial I}{\partial t} + \Omega_x\frac{\partial I}{\partial x} + \Omega_y\frac{\partial I}{\partial y} + \Omega_z\frac{\partial I}{\partial z}\right)\Delta t\, \Delta\underline{S}\, \Delta\xi\, \Delta\nu\, \Delta\underline{\Omega},$$

where Ω_x, Ω_y, and Ω_z are Cartesian coordinates of the unit vector $\underline{\Omega}$. The first term, $\partial I/\partial t$, in parentheses is the time rate of change of the number of photons. The other terms represent a derivative $\underline{\Omega} \bullet \nabla I$ at $\underline{r}$ along the direction $\underline{\Omega}$ which shows the net rate of photons streaming out of the volume element along the direction $\underline{\Omega}$. Thus,

$$dN = \underbrace{\frac{1}{c}\frac{\partial I}{\partial t}\Delta t\,\Delta\underline{S}\,\Delta\xi\,\Delta\nu\,\Delta\underline{\Omega}}_{\text{temporal rate of change}} + \underbrace{(\underline{\Omega}\bullet\nabla I)\,\Delta t\,\Delta\underline{S}\,\Delta\xi\,\Delta\nu\,\Delta\underline{\Omega}}_{\text{streaming}}. \tag{15}$$

Here ∇ is the vector operator, called "nabla." Given a scalar function f, vector ∇f has the form

$$\nabla I = \left(\frac{\partial I}{\partial x}, \frac{\partial I}{\partial y}, \frac{\partial I}{\partial z}\right).$$

The change described by Eq. (15) is due to four processes – absorption, outscattering, inscattering and emission, and these are described below.

Absorption: A fraction of photons in the volume element $d\underline{r}$ will be absorbed while traveling a distance $\Delta\xi = c\,\Delta t$ along the direction $\underline{\Omega}$. This fraction is determined by the probability $\sigma_a\Delta\xi$. Thus, the number of absorbed photons is

$$\begin{aligned}\text{absorption} &= \underbrace{\frac{1}{c}I(\underline{r},\nu,\underline{\Omega},t)\,\Delta\underline{S}\,\Delta\xi\,\Delta\nu\,\Delta\underline{\Omega}}_{\text{number of photons}}\ \underbrace{\sigma_a(\underline{r},\nu,\underline{\Omega},t)\Delta\xi}_{\substack{\text{probabiliy of absorption}\\ \text{while traveling }\Delta\xi=c\Delta t}}\\ &= \sigma_a(\underline{r},\nu,\underline{\Omega},t)\,I(\underline{r},\nu,\underline{\Omega},t)\,\Delta\underline{S}\,\Delta t\,\Delta\xi\,\Delta\nu\,\Delta\underline{\Omega}.\end{aligned} \tag{16}$$

Outscattering: Another fraction of photons in the volume element $\underline{r}$ traveling in the direction $\underline{\Omega}$ will change their direction and/or frequency as a result of interaction with matter. The number of photons "lost" due to *outscattering* from ν, $\underline{\Omega}$ to all other frequencies and directions while traveling a distance $\Delta\xi = c\,\Delta t$ is given by

$$\begin{aligned}\text{outscattering} &= c\,\Delta t\,\Delta\underline{S}\,\Delta\xi\,\Delta\nu\,\Delta\underline{\Omega}\int_0^\infty d\nu'\int_{4\pi}d\underline{\Omega}'\,\sigma_s(\underline{r},\nu\to\nu',\underline{\Omega}\to\underline{\Omega}',t)\,\frac{1}{c}I(\underline{r},\nu,\underline{\Omega},t)\\ &= \sigma_s'(\underline{r},\nu,\underline{\Omega},t)\,I(\underline{r},\nu,\underline{\Omega},t)\Delta t\,\Delta\underline{S}\,\Delta\xi\,\Delta\nu\,\Delta\underline{\Omega}.\end{aligned} \tag{17}$$

Inscattering: Similarly, the number of photons gained due to *inscattering* to ν, $\underline{\Omega}$ from all other frequencies and directions can be evaluated as

$$\text{inscattering} = \Delta t\,\Delta\underline{S}\,\Delta\xi\,\Delta\nu\,\Delta\underline{\Omega}\int_0^\infty d\nu'\int_{4\pi}d\underline{\Omega}'\,\sigma_s(\underline{r},\nu'\to\nu,\underline{\Omega}'\to\underline{\Omega},t)\,I(\underline{r},\nu',\underline{\Omega},t). \tag{18}$$

The rate of the production of photons in the volume element is simply

$$\text{emission} = c\,q(\underline{r},\nu,\underline{\Omega},t)\,\Delta t\,\Delta\underline{S}\,\Delta\xi\,\Delta\nu\,\Delta\underline{\Omega}. \tag{19}$$

Transfer Equation: The equation of transfer is essentially a statement of photon number conservation at $\underline{r}$ by equating the sum of the four terms, Eqs. (16) to (19), with appropriate signs to designate a loss or gain, to the overall rate of change given by Eq. (15):

$$dN = - \text{absorption} - \text{outscattering} + \text{inscattering} + \text{emission},$$

or, after dividing all terms by $c\Delta t\Delta S\Delta\xi\Delta\nu\Delta\underline{\Omega}$ and accounting for the definition of the extinction coefficient $\sigma = \sigma_a + \sigma_s'$, one gets

$$\frac{1}{c}\frac{\partial I}{\partial t} + (\underline{\Omega} \bullet \nabla I) + \sigma(\underline{r}, \nu, \underline{\Omega}, t)\, I(\underline{r}, \nu, \underline{\Omega}, t)$$

$$= \int_0^\infty d\nu' \int_{4\pi} d\underline{\Omega}'\, \sigma_s(\underline{r}, \nu' \rightarrow \nu, \underline{\Omega}' \rightarrow \underline{\Omega}, t)\, I(\underline{r}, \nu', \underline{\Omega}', t) + q(\underline{r}, \nu, \underline{\Omega}, t). \qquad (20)$$

Sometimes, the second and the third terms on the left hand side of Eq. (20) are grouped together; the term $[\underline{\Omega} \bullet \nabla + \sigma]$ then denotes the *streaming-collision* operator. An equation for the particle density distribution function can be obtained by normalizing Eq. (20) by $c\hbar\nu$ if I is the radiant intensity or by c if I represents intensity of photons (see Eqs. (3a) and (3b)).

It should be noted that this equation gives the expected or mean value of the photon distribution. Fluctuations about the mean are not considered. The derived equation also assumes unpolarized light. Four parameters are required to specify the state of polarization of a beam of light, and accordingly, a proper description of photon transport including polarization effects involves four coupled equations of transfer. Assuming the light to be unpolarized by the medium, these equations can be averaged to derive a single equation of transfer and this involves some error. Finally, the radiative transfer equation (20) does not describe behavior resulting from interference of waves. Therefore, the equation is valid only when the distance between scatterers is large compared to the wave packets.

4. Initial and Boundary Conditions

In many practical cases, one is interested in the photon distribution in a restricted region of space. It is necessary to specify a domain V in which the radiative transfer process is studied and a surface δV that bounds V. Equation (20) is usually formulated for a domain V whose composition and shape depends on a specific problem under consideration. In solving the radiative transfer equation, it is necessary to specify both the photon distribution in V at some initial time $t = 0$ (initial condition) and the photon distribution incident on V at all times (boundary condition). The initial condition is given by

$$I(\underline{r}, \nu, \underline{\Omega}, 0) = I_0(\underline{r}, \nu, \underline{\Omega}), \quad \underline{r} \in V. \qquad (21)$$

The boundary condition specifies the radiation entering the domain V through points on the boundary δV,

$$I(\underline{r}_B, \nu, \underline{\Omega}, t) = B(\underline{r}_B, \nu, \underline{\Omega}, t), \quad \underline{r}_B \in \delta V, \quad \underline{n}(\underline{r}_B) \bullet \underline{\Omega} < 0. \tag{22}$$

Here B is the *intensity* of photons incident on the domain V at point $\underline{r}_B$ on the surface δV; $\underline{n}(\underline{r}_B)$ is an outward normal vector at this point (Fig. 4). The radiative transfer problem is thus completely specified by the equation of transfer [Eq. (20)], the initial condition [Eq. (21)] and the boundary condition [Eq. (22)].

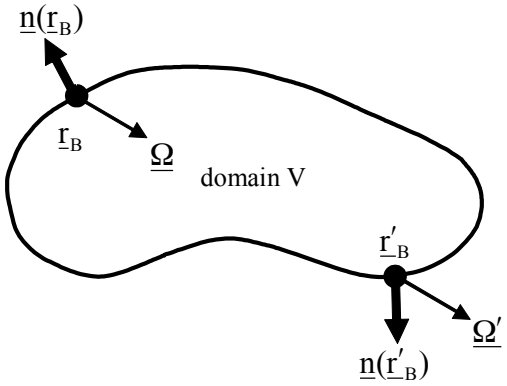

Figure 4. Directions $\underline{\Omega}$ ($\underline{\Omega}'$) along which incident photons can enter (exit) the domain V through the point $\underline{r}_B$ ($\underline{r}'_B$) on the boundary δV satisfies the inequality $\underline{n}(\underline{r}_B) \bullet \underline{\Omega} < 0$ ($\underline{n}(\underline{r}'_B) \bullet \underline{\Omega}' > 0$). Here $\underline{n}(\underline{r}_B)$($\underline{n}(\underline{r}'_B)$) is the outward normal at $\underline{r}_B$ ($\underline{r}'_B$).

The incoming radiation B can result from sources on the boundary δV and photons from V incident on the boundary that the boundary reflects back to the domain V. In the case of the boundary coherent scattering, the incoming radiation B can be written as

$$B(\underline{r}_B, \nu, \underline{\Omega}, t) = \frac{1}{\pi} \int_{\delta V} d\underline{r}'_B \int_{\underline{\Omega}' \bullet \underline{n}(\underline{r}_B) > 0} \rho_B(\underline{r}'_B, \underline{\Omega}'; \underline{r}_B, \Omega) \, | \, \underline{n}(\underline{r}'_B) \bullet \underline{\Omega}' \, | \, I(\underline{r}'_B, \nu, \underline{\Omega}', t) \, d\underline{\Omega}'$$

$$+ q_B(\underline{r}_B, \underline{\Omega}, t), \quad \underline{n}(\underline{r}_B) \bullet \underline{\Omega} < 0. \tag{23}$$

Here $\rho_B(\underline{r}'_B, \underline{\Omega}'; \underline{r}'_B, \underline{\Omega})$ is the *boundary scattering function*; that is, the probability density that a photon having escaped from the domain V through the point $\underline{r}'_B \in \delta V$ in the direction $\underline{\Omega}'$ will come back to V through the point $\underline{r}_B \in \delta V$ in the direction $\underline{\Omega}$. It should be emphasized that in general the boundary condition depends on the solution I of the radiative transfer problem. The case of *vacuum boundary condition* refers to $\rho_B = 0$ and $q_B = 0$.

5. Stationary Radiative Transfer Problem

If the extinction and differential scattering coefficients, emission and the boundary condition do not change with time, $\partial I / \partial t = 0$, the radiative transfer problem becomes a stationary radiative transfer problem. In the case of coherent scattering, the *boundary value problem for radiative transfer equation* in the *wavelength domain* has the form

$$\underline{\Omega} \bullet \nabla I_\lambda(\underline{r},\underline{\Omega}) + \sigma_\lambda(\underline{r},\underline{\Omega})\, I_\lambda(\underline{r},\underline{\Omega}) = \int_{4\pi} d\underline{\Omega}'\, \sigma_{s,\lambda}(\underline{r},\underline{\Omega}' \to \underline{\Omega})\, I_\lambda(\underline{r},\underline{\Omega}') + q_\lambda(\underline{r},\underline{\Omega}), \tag{24a}$$

$$I_\lambda(\underline{r}_B,\underline{\Omega}) = B_\lambda(\underline{r}_B,\underline{\Omega}), \quad \underline{r}_B \in \delta V, \quad \underline{n}(\underline{r}_B) \bullet \underline{\Omega} < 0. \tag{24b}$$

Here $I_\lambda(\underline{r},\underline{\Omega})$ is the monochromatic specific intensity which depend on wavelength λ, location r and direction $\underline{\Omega}$. Note that the wavelength λ is a parameter of the radiative transfer problem. We have emphasized this feature in notations by moving the wavelength from the argument list to subscript. In our analyses of the boundary value problem, therefore, we will often suppress this parameter in notations. The stationary radiative transfer equation is the basic tool used in optical remote sensing. This equation, notations and the convention regarding the wavelength dependence introduced here will be used in the rest of this book.

6. Green's Function and the Reciprocity Principle

Consider a medium V bounded by a non-reflecting ($\rho_B = 0$) and non-emitting ($q_B = 0$) boundary δV. The *volume Green's function*, $G_V(\underline{r},\underline{\Omega};\underline{r}',\underline{\Omega}')$, is the radiative response of V at a point $\underline{r}$, in direction $\underline{\Omega}$, to a monodirectional point source located at a given point $\underline{r}'$, continuously emitting photons in a given direction $\underline{\Omega}'$. The *volume Green* function satisfies the stationary radiative transfer equation [Eq. (24a)] with a delta function source term $q(\underline{r},\underline{\Omega}) = \delta(\underline{\Omega} - \underline{\Omega}')\,\delta_V(\underline{r} - \underline{r}')$ located at $\underline{r}'$ and with zero incoming radiation (B=0), that is,

$$\underline{\Omega} \bullet \nabla G_V(\underline{r},\underline{\Omega};\underline{r}',\underline{\Omega}') + \sigma(\underline{r},\underline{\Omega})\, G_V(\underline{r},\underline{\Omega};\underline{r}',\underline{\Omega}')$$

$$= \int_{4\pi} \sigma_s(\underline{r},\underline{\Omega}'' \to \underline{\Omega}) G_V(\underline{r},\underline{\Omega}'';\underline{r}',\underline{\Omega}')\, d\underline{\Omega}'' + \delta(\underline{\Omega} - \underline{\Omega}')\delta_V(\underline{r} - \underline{r}'), \tag{25a}$$

$$G_V(\underline{r}_B,\underline{\Omega};\underline{r}',\underline{\Omega}') = 0, \quad \underline{r}_B \in \delta V, \quad \underline{\Omega} \bullet \underline{n}(\underline{r}_B) < 0. \tag{25b}$$

Here $\delta(\underline{\Omega} - \underline{\Omega}')$, in sr^{-1}, and $\delta_V(\underline{r} - \underline{r}')$, in m^{-3}, are Dirac delta functions. Note that $\delta(\underline{\Omega} - \underline{\Omega}')\delta_V(\underline{r} - \underline{r}')$ is a *volume source* normalized by its power. The volume Green function, therefore, is expressed in $m^{-2}sr^{-1}$. It should be also noted that the point $\underline{r}'$ and the direction $\underline{\Omega}'$ of the monodirectional source are parameters in the radiative transfer equation; that is, the determination of the complete Green function requires the solution of Eq. (25) for every point $\underline{r}'$ from V and the direction $\underline{\Omega}'$.

The *surface Green's function*, $G_S(\underline{r},\underline{\Omega};\underline{r}'_B,\underline{\Omega}')$, is the solution to the transport equation with the source $q(\underline{r},\underline{\Omega}) = 0$ and the boundary condition

$$G_S(\underline{r},\underline{\Omega};\underline{r}'_B,\underline{\Omega}') = \delta(\underline{\Omega} - \underline{\Omega}')\delta_S(\underline{r}_B,\underline{r}'_B), \quad \underline{r}'_B \in \delta V, \quad \underline{n}(\underline{r}'_B) \bullet \underline{\Omega}' < 0. \tag{26}$$

Here $\delta_S(\underline{r}_B, \underline{r}'_B)$ is a two-dimensional delta function (in m^{-2}). Because the volume sources can be located on the boundary, the volume and surface Green functions are related [Case and Zweifel, 1970]

$$G_S(\underline{r}, \underline{\Omega}; \underline{r}'_B, \underline{\Omega}') = |\, \underline{n}(\underline{r}'_B) \bullet \underline{\Omega}' \,| \, G_V(\underline{r}, \underline{\Omega}; \underline{r}'_B, \underline{\Omega}'). \tag{27}$$

In terms of these two Green's functions, we may write the general solution to the transport equation with arbitrary source $q(\underline{r}, \underline{\Omega})$ and boundary conditions with sources q_B on the non-reflecting boundary δV ($\rho_B = 0$) as

$$I(\underline{r}, \underline{\Omega}) = \int_V d\underline{r}' \int_{4\pi} G_V(\underline{r}, \underline{\Omega}; \underline{r}', \underline{\Omega}') q(\underline{r}', \underline{\Omega}') \, d\underline{\Omega}' + \int_{\delta V} dS \int_{\underline{n}(\underline{r}'_B) \bullet \Omega' < 0} d\underline{\Omega}' \, G_S(\underline{r}, \underline{\Omega}; \underline{r}'_B, \underline{\Omega}') \, q_B(\underline{r}'_B, \underline{\Omega}'). \tag{28}$$

The first term in Eq. (28) is the solution of the radiative transfer equation with the internal source $q(\underline{r}, \underline{\Omega})$ and no incoming radiance. The second term describes the 3D radiation field in V generated by sources q_B distributed over the non-reflecting boundary δV.

Let the differential scattering coefficient satisfies the symmetry property $\sigma_s(\underline{r}, \underline{\Omega}' \rightarrow \underline{\Omega}) = \sigma_s(\underline{r}, -\underline{\Omega} \rightarrow -\underline{\Omega}')$. Under this condition, the volume Green's function possesses the following symmetry property

$$G_V(\underline{r}, \underline{\Omega}; \underline{r}', \underline{\Omega}') = G_V(\underline{r}', -\underline{\Omega}'; \underline{r}, -\underline{\Omega}). \tag{29}$$

This equality expresses the fundamental reciprocity theorem for the stationary radiative transfer equation: *the intensity* $I(\underline{r}, \underline{\Omega})$ *at* $\underline{r}$ *in the direction* $\underline{\Omega}$ *due to a point source at* $\underline{r}'$ *emitting in direction* $\underline{\Omega}'$ *is the same as the intensity* $I(\underline{r}', -\underline{\Omega}')$ *at* $\underline{r}'$ *in the direction* $-\underline{\Omega}'$ *due to a point source at* $\underline{r}$ *emitting in direction* $-\underline{\Omega}$.

The Green function concept was originally developed in neutron transport theory [Bell and Glasstone, 1970]. It has enabled the reformulation of the radiative transfer problems in terms of some "basic" sub-problems and to express the solution of the transport equation with arbitrary sources and boundary conditions as a superposition of the solutions of the basic sub-problems. We will demonstrate this technique later with a relevant example for radiative transfer in the canopy-surface-atmosphere system.

7. Operator Notations.

We introduce the *streaming-collision*, L, and *scattering*, S, operators as

$$LI = \underline{\Omega} \bullet \nabla I(\underline{r},\underline{\Omega}) + \sigma(\underline{r},\underline{\Omega})I(\underline{r},\underline{\Omega}), \quad SI = \int_{4\pi} \sigma_s(\underline{r},\underline{\Omega}' \to \underline{\Omega})I(\underline{r},\underline{\Omega}')d\underline{\Omega}'. \tag{30}$$

We will use the notation $I^{\pm}(\underline{r}_B,\underline{\Omega})$ to denote the intensity of radiation exiting (sign "+") or entering (sign "–") the domain V through the point $\underline{r}_B$, i.e., $I^{\pm}(\underline{r}_B,\underline{\Omega})$ gives values of the intensity at points $\underline{r}_B$ on the boundary δV in directions satisfying the inequality $\underline{n}(\underline{r}_B) \bullet \underline{\Omega} > 0$. To describe reflective properties of the boundary δV, a scattering operator defined on the boundary δV for the intensity I^+ of medium leaving radiation is introduced as

$$\mathcal{R}I^+ = \frac{1}{\pi}\int_{\delta V} d\underline{r}'_B \int_{\underline{n}(\underline{r}'_B)\bullet\underline{\Omega}'>0} \rho_B(\underline{r}'_B,\underline{\Omega}';\underline{r}_B,\underline{\Omega}) \,|\, \underline{n}(\underline{r}'_B) \bullet \underline{\Omega}' \,|\, I^+(\underline{r}'_B,\underline{\Omega}')\, d\underline{\Omega}'. \tag{31}$$

In terms of these notations, the boundary value problem Eq. (24) for the three-dimensional stationary radiative transfer equation can be expressed as

$$LI = SI + q, \quad I^- = \mathcal{R}I^+ + q_B. \tag{32}$$

The boundary value problem is said to be the *standard problem* if $\mathcal{R} = 0$ and $q_B = 0$. To emphasize this in notations, we will use symbol L_0 to denote the streaming-collision operator corresponding to the standard problem.

The boundary value problem for a domain with non-reflecting boundary can always be reduced to a standard problem. Indeed, the solution to the boundary value problem $LI = SI + q$, $I^- = q_B$ can be represented as the sum of two components, $I = Q + I_{dif}$. The first term describes intensity of radiation generated by *uncollided photons*; that is, photons from the boundary source q_B that have not undergone interactions within the domain V. It satisfies the equation $LQ = 0$ and the boundary condition $Q^- = q_B$. The second term, I_{dif}, describes a *collided*, or *diffuse*, radiation field; that is, radiation field generated by photons scattered one or more times. It satisfies the standard problem $L_0 I_{dif} = SI_{dif} + q'$ with the volume source $q' = q + SQ$. The uncollided component Q acts as a source term for scattering process and thus the term SQ gives intensity of photons from the uncollided field Q just after their first scattering event.

In mathematical literature, the standard problem is often formulated in functional spaces. The theory of functional analysis [Riesz and B. Sz.-Nagy 1990; Kantorovich and Akilov, 1964; Krein, 1972] requires the specification of two sets. The first – the domain D of the operator L_0 – identifies "possible candidates" for the solution. The second space – the range H of the operator L_0 – specifies mathematical properties of "acceptable" volume sources. Vladimirov [1963] provides a full mathematical description of the standard problem for the following family of functional spaces. The range H_p, $0 < p \le \infty$, consists of functions $q(\underline{r},\underline{\Omega})$ for which the norm $\|q\|_p$ exists, i.e.,

$$\| q \|_p = \int_{4\pi} d\underline{\Omega} \int_V d\underline{r}\, \sigma(\underline{r},\underline{\Omega}) \, | q(\underline{r},\underline{\Omega}) |^p < \infty,$$
$$0 < p < \infty,$$
$$\| q \|_\infty = \sup_{\underline{r}\in V, \underline{\Omega}\in 4\pi} \text{vrai} \, | q(\underline{r},\underline{\Omega}) | < \infty. \qquad (33)$$

The set D_p, $0 < p \le \infty$, includes all functions (1) which satisfy the zero boundary condition ($I^-=0$) and (2) whose transformations $L_0 I$ and SI exist and are elements of the space H_p. The standard problem is formulated as follows: given q from H_p find an element I from D_p for which $L_0 I = SI + q$. "Visually," this formulation is similar to problems in linear algebra, i.e., where L_0 and S are matrixes, I and q are vectors, and the norm Eq. [33] is the length of the vector. Vladimirov [1963] showed that such an interpretation of the standard problem, with some caveats, is valid and many results from matrix theory can be applied to the radiative transfer equation. This level of abstraction helps to derive many practically important properties of the radiation field whose direct derivation is either very difficult or impossible. We will demonstrate this technique with a relevant example for canopy spectral response to incident solar radiation.

8. The Equation of Transfer in Integral Form

The standard problem can be transformed to two types of *integral equations*. The first one is obtained by inverting the streaming-collision operator L_0, i.e., $I = L_0^{-1}SI + L_0^{-1}q$. The second equation is formulated for a source function J defined as $J = SI + q$. It follows from Eq. (30) with $\mathcal{R} = 0$ and $q_B = 0$ that the intensity I and source function J are related as $I = L_0^{-1}J$. Substituting this equation into the definition of J results in an operator equation of the form $J = SL_0^{-1}J + q$.

Both integral equations require the specification of the inverse operator L_0^{-1} which acts either on SI or J. Let u represents either SI or J. The function $v = L_0^{-1}u$ satisfies the equation

$$\underline{\Omega} \bullet \nabla \, v(\underline{r},\underline{\Omega}) + \sigma(\underline{r},\underline{\Omega}) \, v(\underline{r},\underline{\Omega}) = u(\underline{r},\underline{\Omega}), \qquad (34)$$

with the zero boundary condition, i.e., $u(\underline{r}_B,\underline{\Omega}) = 0$, $\underline{n}(\underline{r}_B) \bullet \underline{\Omega} < 0$. For a straight line $\underline{r}_B + \eta\underline{\Omega}$, $-\infty < \eta < \infty$, along an incoming direction $\underline{\Omega}$, $\underline{n}(\underline{r}_B) \bullet \underline{\Omega} < 0$, this equation takes the following form

$$\frac{dv(\underline{r}_B + \xi\underline{\Omega},\underline{\Omega})}{d\xi} + \sigma(\underline{r}_B + \xi\underline{\Omega},\underline{\Omega}) \, v(\underline{r}_B + \xi\underline{\Omega},\underline{\Omega}) = u(\underline{r}_B + \xi\underline{\Omega},\underline{\Omega}), \quad v(\underline{r}_B,\underline{\Omega}) = 0. \qquad (35)$$

This is an ordinary differential with respect to ξ. Its solution is

$$v(\underline{r}_B + \xi\underline{\Omega}, \underline{\Omega}) = \int_{4\pi}\int_{0}^{\xi} \exp\left(-\int_{\xi'}^{\xi} d\xi'' \, \sigma(\underline{r}_B + \xi''\underline{\Omega}', \underline{\Omega}') \right) u(\underline{r}_B + \xi'\underline{\Omega}', \underline{\Omega}') \, \delta(\underline{\Omega} - \underline{\Omega}') d\underline{\Omega}' d\xi' . \qquad (36)$$

Note that we have artificially expressed the solution of the ordinary integral equation as an integral over $d\xi'\underline{\Omega}'$. The presence of the delta function $\delta(\underline{\Omega} - \underline{\Omega}')$ in Eq. (36), however, makes this integral equivalent to an integral over the line $\underline{r}_B + \eta\underline{\Omega}$ along the direction $\underline{\Omega}$ which is directly obtainable from Eq. (35). Let $\underline{r}$ and $\underline{r}' = \underline{r} - \xi'\underline{\Omega}'$, $\xi' \geq 0$, be two points on the line $\underline{r}_B + \eta\underline{\Omega}'$. We make use of the relationship $d\underline{r}' = \xi'^2 d\xi' d\underline{\Omega}'$ to convert the volume element $\xi'^2 d\xi' d\Omega'$ expressed in polar coordinates with the origin at $\underline{r}$ into the volume element $d\underline{r}'$ in Cartesian coordinates. Noting that $\| \underline{r} - \underline{r}' \| = \xi'$, one can express the unit vector $\underline{\Omega}'$ as $\underline{\Omega}' = (\underline{r} - \underline{r}') / \| \underline{r} - \underline{r}' \|$. In Cartesian coordinates, the function $v = L_0^{-1} u$ can be rewritten as

$$L_0^{-1} u = v(\underline{r}, \underline{\Omega}) = \int_V \frac{\exp\left[-\tau(\underline{r}, \underline{r}', \underline{\Omega}) \right]}{\| \underline{r} - \underline{r}' \|^2} u(\underline{r}', \underline{\Omega}) \, \delta\left(\underline{\Omega} - \frac{\underline{r} - \underline{r}'}{\| \underline{r} - \underline{r}' \|} \right) d\underline{r}' \qquad (37)$$

Here $\tau(\underline{r}, \underline{r}', \underline{\Omega})$ is the optical distance between points $\underline{r}$ and $\underline{r}'$ on a straight line along the direction $\underline{\Omega}$, i.e.,

$$\tau(\underline{r}, \underline{r}', \underline{\Omega}) = \int_0^{\|\underline{r} - \underline{r}'\|} d\xi'' \, \sigma(\underline{r} - \xi''\underline{\Omega}, \underline{\Omega}). \qquad (38)$$

The δ-function in Eq. (37) indicates that the points $\underline{r}$ and $\underline{r}'$ lie on a line along the direction $\underline{\Omega}$. Equation (37) specifies the operator L_0^{-1} which sets in correspondence to a volume source u the three dimensional distribution $v(\underline{r}, \underline{\Omega})$ of photons from the source u that arrive at point r along the direction $\underline{\Omega}$ without suffering a collision.

Substituting $u = SI$ into Eq. (37) one obtains the following integral equation

$$I(\underline{r}, \underline{\Omega}) = \int_{4\pi}\int_{V} \mathcal{K}_I(\underline{r}', \underline{\Omega}' \rightarrow \underline{r}, \underline{\Omega}) I(\underline{r}', \underline{\Omega}') d\underline{r}' d\underline{\Omega}' + Q(\underline{r}, \underline{\Omega}) . \qquad (39)$$

Here

$$\mathcal{K}_I(r', \underline{\Omega}' \rightarrow \underline{r}, \underline{\Omega}) = \frac{\exp\left[-\tau(\underline{r}, \underline{r}', \underline{\Omega}) \right]}{\| \underline{r} - \underline{r}' \|^2} \sigma_s(\underline{r}', \Omega' \rightarrow \underline{\Omega}) \, \delta\left(\underline{\Omega} - \frac{\underline{r} - \underline{r}'}{\| \underline{r} - \underline{r}' \|} \right), \qquad (40)$$

and the source $Q = L_0^{-1} q$ is calculated using Eq. (37). The kernel $\mathcal{K}_I$ is the transition density, i.e., $\mathcal{K}_I d\underline{r}' d\underline{\Omega}'$ is the probability that photons which have undergone interactions at r′ in the direction $\underline{\Omega}'$ will have their next interaction at $\underline{r}$ along the direction $\underline{\Omega}$.

Multiplying Eq. (37) by the differential scattering coefficient $\sigma_s(\underline{r}, \underline{\Omega}' \to \underline{\Omega})$ and integrating over all scattering directions $\underline{\Omega}'$ one obtains a kernel $\mathcal{K}_S$ of the integral operator SL_0^{-1}:

$$\mathcal{K}_S(\underline{r}', \underline{\Omega}' \to \underline{r}, \underline{\Omega}) = \frac{\exp\left[-\tau(\underline{r}, \underline{r}', \underline{\Omega}')\right]}{\| \underline{r} - \underline{r}' \|^2} \sigma_s(\underline{r}, \underline{\Omega}' \to \underline{\Omega}) \delta\left(\underline{\Omega}' - \frac{\underline{r} - \underline{r}'}{\| \underline{r} - \underline{r}' \|}\right). \tag{41}$$

Thus, the source function J satisfies the following integral equation

$$J(\underline{r}, \Omega) = \int\!\!\int_{4\pi V} \mathcal{K}_S(\underline{r}', \underline{\Omega}' \to \underline{r}, \underline{\Omega}) J(\underline{r}', \underline{\Omega}') d\underline{r}' d\underline{\Omega}' + q(\underline{r}, \underline{\Omega}). \tag{42}$$

The intensity I can be expressed via J as $I = L_0^{-1} J$ where the operator L_0^{-1} transforms the function in accordance with Eq. (37). In many cases the solution of the integral equation (42) for the source function is a simpler task than Eq. (40) for the intensity since the integration over $\underline{\Omega}'$ can help to get rid of the angular variable. For example, in the case of isotopic source q, scattering ($\sigma_s = 1/4\pi$) and extinction (i.e., σ does not depend on $\underline{\Omega}$), the solution J becomes a function of the spatial variable while the corresponding intensity $I = L_0^{-1} J$ depends on both spatial and angular variables. The integral equation (42) is especially useful in the study of radiative transfer problems with simple forms of anisotropy. The integral equation for the intensity serves as a theoretical basis for many Monte Carlo models for radiative transfer process in various media.

9. Eigenvalues and Eigenvectors of the Radiative Transfer Equation

An *eigenvalue* of the radiative transfer equation is a number γ such that there exists a function $e(\underline{r}, \underline{\Omega})$ which satisfies

$$\gamma L_0 e = Se. \tag{43}$$

Since the eigenvalue and *eigenvector* problem is formulated for zero boundary conditions (e=0), γ and $e(\underline{r}, \underline{\Omega})$ are independent on the incoming radiation. Under some general conditions [Vladimirov, 1963], the set of eigenvalues γ_k, k=0,1,2, … and eigenvectors $e_k(\underline{r}, \underline{\Omega})$, k=0,1,2, is a discrete set. The eigenvectors are mutually orthogonal, that is,

$$\int\!\!\int_{V\,4\pi} \sigma(\underline{r}, \underline{\Omega}) e_k(\underline{r}, \underline{\Omega}) e_l(\underline{r}, \underline{\Omega}) d\underline{\Omega}\, d\underline{r} = \delta_{k,l}, \tag{44}$$

where $\delta_{k,l}$ is the Kroneker symbol. The solution of the standard problem can be expanded in eigenvectors. The expansion in eigenvectors has mainly a theoretical value because the problem of finding these vectors is much more complicated than finding the solution of the transport equation. However, this approach can be useful to estimate integrals of the solution. Note that Eq. (43) is equivalent to finding of non-trivial solutions to the integral equation $\gamma e_k = L_0^{-1} S e_k$.

The discreteness of the eigenvalue set makes the radiative transfer problem similar to problems in linear algebra, i.e., the intensity can be represented as an infinite vector which satisfies an infinity number of linear algebraic equations given by a matrix determined by $L_0^{-1}S$.

The *transport equation* has a unique positive eigenvalue which corresponds to a unique positive [normalized in the sense of Eq. (44)] eigenvector. This eigenvalue is greater than the absolute magnitudes of the remaining eigenvalues. This means that only one eigenvector, say e_0, takes on positive values for any $\underline{r} \in V$ and $\underline{\Omega}$. This positive couplet of eigenvector and eigenvalue plays an important role in transport theory, for example, in neutron transport theory. The positive eigenvalue alone determines if the fissile assembly will function as a reactor, or as an explosive, or will melt. In vegetation canopy radiative transfer, the positive eigenvalue determines canopy absorption properties. The positive couplet, γ_0 and e_0, can be iterated based on the following property of the operator $T = L_0^{-1}S$

$$\gamma_0 = \lim_{m\to\infty} \gamma_{0,m},$$
$$e_0(\underline{r},\underline{\Omega}) = \lim_{m\to\infty} e_{0,m}(\underline{r},\underline{\Omega}). \tag{45}$$

Here

$$\gamma_{0,m+1} = \frac{\| T^{m+1} q \|_p}{\| T^m q \|_p},$$
$$e_{0,m}(\underline{r},\underline{\Omega}) = \frac{T^m q}{\| T^m q \|_p}, \tag{46}$$

where $\|...\|_p$ is the norm defined by Eq. (33) and q is a source from the functional space H_p. The limits given by Eqs. (45) and (46) do not depend on p (i.e., on functional space H_p in which the problem was formulated) and the source $q \in H_p$ needed to initialize the sequences of $\gamma_{0,m}$ and $e_{0,m}$. If $p = 1$, value of $\gamma_{0,m+1}$ gives the probability that a photon from the source q scattered *m* times will be scattered again. The corresponding function $e_{0,m}(\underline{r},\underline{\Omega})$ is the probability density that a photon scattered *m* times will arrive at $\underline{r}$ along the direction $\underline{\Omega}$ without suffering a collision. These interpretations directly follow from the integral form Eq. (39) of the operator $T = L_0^{-1}S$ and the definition of the total interaction coefficient σ. Note that $\gamma_{0,m}$ and $e_{0,m}$ are related as

$$Te_{0,m} = \gamma_{0,m+1} e_{0,m+1}.$$

There is another formulation of the eigenvalues and eigenvectors in linear transport theory [Case and Zweifel, 1967]. Their approach is similar to that used in the theory of ordinary differential equations, i.e., solutions of the homogeneous problem ($q = 0$) are represented as the product of an exponential function of spatial variable and corresponding eigenfunction which depends on

angular variable. Unlike the definition given by Eq. (33), the Case and Zweifel formulation results in both discrete and continuum of eigenvalues. The eigenfunctions corresponding to the continuum of the eigenvectors are Schwartz distributions, i.e., not functions in the usual sense. This approach allows for analytical solutions to the radiative transfer equation for a number of special cases and, therefore, provides in-depth understanding of the physics of radiative transfer process. For details of this approach, the reader is referred to Case and Zweifel [1967] and Bell and Glasstone [1970]. In this book, we follow the definition of the eigenvalue/eigenvector problem given by Eq. (43).

10. The Law of Energy Conservation

The stationary radiative transfer equation (24a) expresses the l*aw of energy conservation* for each spatial point r within V and for each direction $\underline{\Omega}$. The boundary condition (24b) describes energy exchange between V and the surrounding medium. Here we derive an expression of the energy conservation law for the domain V bounded by a surface δV, i.e., we perform integration of Eq. (24a) over V and the unit sphere 4π of directions,

$$\int_{4\pi\times V} \underline{\Omega} \bullet \nabla I \, d\underline{\Omega}\, d\underline{r} + \int_{4\pi\times V} [\sigma(\underline{r},\underline{\Omega}) - \sigma_s'(\underline{r},\underline{\Omega})] I(\underline{r},\underline{\Omega})\, d\underline{\Omega}\, d\underline{r} = \int_{4\pi\times V} q(\underline{r},\underline{\Omega})\, d\underline{\Omega}\, d\underline{r}. \tag{47}$$

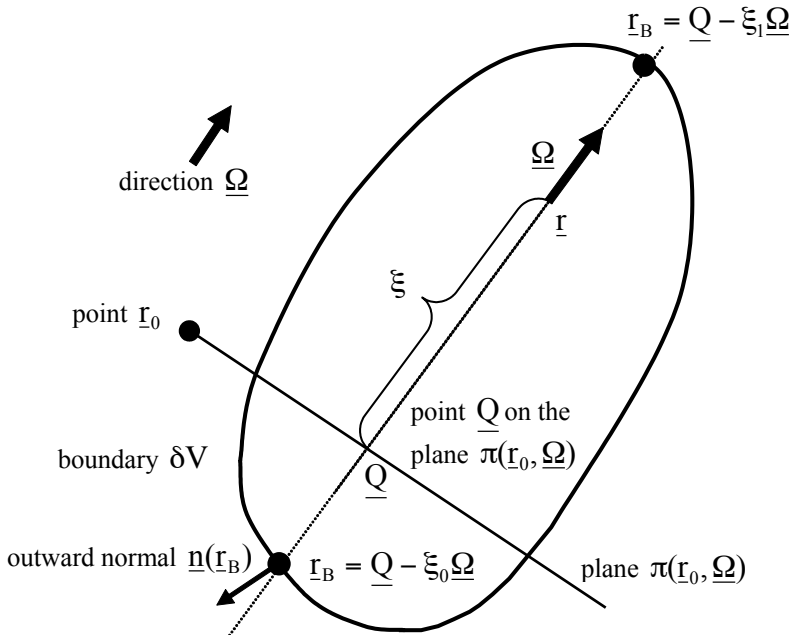

Figure 5. Representation of spatial points within a volume V bounded by the surface δV. Here $\pi(\underline{r}_0, \underline{\Omega})$ is a plane perpendicular to the direction $\underline{\Omega}$ and passing through a fixed point $\underline{r}_0$; ξ_1 and ξ_0 are distances between the point $\underline{Q}$ on the plane $\pi(\underline{r}_0, \underline{\Omega})$ and the boundary δV along the directions $\underline{\Omega}$ and $-\underline{\Omega}$, respectively; $\underline{r}_B$ denotes points on the boundary δV and $\underline{n}(\underline{r}_B)$ is the outward normal to δV at this point.

For a fixed direction $\underline{\Omega}$, let $\pi(\underline{r}_0, \underline{\Omega})$ be a plane perpendicular to $\underline{\Omega}$ and passing through a fixed point $\underline{r}_0$ (Fig. 5). Let $\underline{Q}$ be a variable point on the plane $\pi(\underline{r}_0, \underline{\Omega})$. Thus, the spatial point $\underline{r}$ within V can be represented as $\underline{r} = \underline{Q} + \xi\underline{\Omega}$. A volume element $d\underline{r}$ about $\underline{r}$ is $d\underline{r} = d\underline{Q}\, d\xi$, where $d\underline{Q}$ is a surface element on the plane $\pi(\underline{r}_0, \underline{\Omega})$ around the point $\underline{Q}$. It should be emphasized that

the surface element $d\underline{Q}$ is perpendicular to the direction $\underline{\Omega}$. If one uses another elementary surface $d\underline{Q}'$ around the point $\underline{Q}$ which is perpendicular to a direction $\underline{\Omega}'$, the volume element $d\underline{r}$ is

$$d\underline{r} = \left|\underline{\Omega} \bullet \underline{\Omega}'\right| d\underline{Q}' d\xi. \tag{48}$$

Let ξ_1 and ξ_0 be distances between the point $\underline{Q}$ and the boundary δV along the directions $\underline{\Omega}$ and $-\underline{\Omega}$, respectively. For the first term in Eq. (47), we have

$$\int_{4\pi\times V} \underline{\Omega} \bullet \nabla I \, d\underline{\Omega}\, d\underline{r} = \int_{4\pi} d\underline{\Omega} \int_{\pi(\underline{r}_0,\underline{Q})} d\underline{Q} \int_{-\xi_0}^{\xi_1} \frac{dI(\underline{Q}+\xi\underline{\Omega},\underline{\Omega})}{d\xi}$$

$$= \int_{4\pi} d\underline{\Omega} \int_{\pi(\underline{r}_0,\underline{Q})} d\underline{Q} \left[I(\underline{Q}+\xi_1\underline{\Omega},\underline{\Omega}) - I(\underline{Q}-\xi_0\underline{\Omega},\underline{\Omega}) \right]$$

$$= \int_{4\pi} d\underline{\Omega} \int_{\pi(\underline{r}_0,\underline{Q})} d\underline{Q}\, I(\underline{Q}+\xi_1\underline{\Omega},\underline{\Omega}) - \int_{4\pi} d\underline{\Omega} \int_{\pi(\underline{r}_0,\underline{Q})} d\underline{Q}\, I(\underline{Q}-\xi_0\underline{\Omega},\underline{\Omega})$$

$$= \int_{\delta V} d\underline{r}_B \underbrace{\int_{\underline{n}(\underline{r}_B)\bullet\underline{\Omega}>0} d\underline{\Omega} \left|\underline{n}(\underline{r}_B)\bullet\underline{\Omega}\right| I(\underline{r}_B,\underline{\Omega})}_{\substack{\text{flux density of radiation leaving the medium} \\ \text{at } \underline{r}_B \text{ on the boundary}}} - \int_{\delta V} d\underline{r}_B \underbrace{\int_{\underline{n}(\underline{r}_B)\bullet\underline{\Omega}<0} d\underline{\Omega} \left|\underline{n}(\underline{r}_B)\bullet\underline{\Omega}\right| I(\underline{r}_B,\underline{\Omega})}_{\substack{\text{flux density of radiation entering the medium} \\ \text{through the point } \underline{r}_B \text{ on the boundary}}}$$

$$= \underbrace{\int_{\delta V} F^+(\underline{r}_B)\, d\underline{r}_B}_{\substack{\text{energy of incoming} \\ \text{radiation}}} - \underbrace{\int_{\delta V} F^-(\underline{r}_B)\, d\underline{r}_B}_{\substack{\text{energy of outgoing} \\ \text{radiation}}} = E^+(\delta V) - E^-(\delta V). \tag{49}$$

In the second term of Eq. (47), the difference between σ and σ_s' is the absorption coefficient. This term, therefore, gives the amount of radiant energy at a wavelength λ absorbed by the domain V (in W m^{-1}). We use the symbol $E_a(V)$ to denote this variable. Finally, the right hand integral of Eq. (47) is the total amount of energy emitted by sources located within the volume V. We denote this quantity by q(V). Thus, the law of energy conservation for a given volume V bounded by a surface δV can be expressed as

$$E^+(\delta V) + E_a(V) = E^-(\delta V) + q(V), \tag{50}$$

that is, the amount of radiant energy reflected, $E^+(\delta V)$, and absorbed, $E_a(V)$, by the volume V is equal to the amount of energy, $E^-(\delta V)$, incident on the boundary δV and energy, q(V), emitted by the internal sources of the volume V.

11. Uniqueness Theorems

Here we formulate conditions under which the boundary value problem for the stationary radiative transfer problem has a unique solution. The radiative transfer problem is formulated for a domain V bounded by a reflecting surface δV. Photon interactins with the boundary are specified by Eq. (23).

The following parameters characterize optical properties of scatters and the entire medium as well as the interactions between the medium and the boundary.

The *maximum boundary reflectance*, $\rho_0(\delta V)$, quantifies the magnitude of boundary reflectance and is defined as

$$\rho_0(\delta V) = \sup_{\substack{\underline{r}'_B \in \delta V \\ \underline{n}(\underline{r}'_B)\bullet\underline{\Omega}'>0}} \frac{1}{\pi}\int_{\delta V} d\underline{r}_B \int_{\underline{n}(\underline{r}_B)\bullet\underline{\Omega}<0} \rho_B(\underline{r}'_B,\underline{\Omega}';\underline{r}_B,\underline{\Omega})\,|\,\underline{n}(\underline{r}_B)\bullet\underline{\Omega}\,|\,d\underline{\Omega}. \tag{51}$$

The *maximum optical path* is the maximum value of the optical distance between two points in the domain V [Eq. (38)]

$$\tau_0(V) = \sup_{\substack{\underline{r},\underline{r}'\in V \\ \underline{\Omega}\in 4\pi}} \tau(\underline{r},\underline{r}',\underline{\Omega}). \tag{52}$$

The *maximum single scattering albedo* is the maximum value of the single scattering albedo

$$\varpi_0(V) = \sup_{\underline{r}\in V,\,\underline{\Omega}\in 4\pi} \frac{\sigma'_s(\underline{r},\Omega)}{\sigma(\underline{r},\Omega)}. \tag{53}$$

The following theorem is a special case of Germogenova's maximum principle [Germogenova, 1986] which is proved here under the assumption of symmetry properties for the differential scattering coefficient, $\sigma_s(\underline{r},\underline{\Omega}'\to\underline{\Omega}) = \sigma_s(\underline{r},\underline{\Omega}\to\underline{\Omega}')$ and the boundary scattering function, $\rho_B(\underline{r}'_B,\underline{\Omega}';\underline{r}_B,\underline{\Omega}) = \rho_B(\underline{r}_B,-\underline{\Omega};\underline{r}'_B,-\underline{\Omega}')$. This restriction will be relaxed (cf. next section).

Theorem 1
Let $I(\underline{r},\underline{\Omega})$ *satisfies Eq. (24a) in the domain V and* $\varpi_0(V)\le 1$, $\tau_0(V)<\infty$ *and* $q=0$. *The following inequality holds true*

$$|\,I(\underline{r},\underline{\Omega})\,| \le \sup_{\underline{r}_B\in\delta V;\,\underline{\Omega}\bullet\underline{n}(\underline{r}_B)<0} \left|\,I(\underline{r}_B,\underline{\Omega})\right|, \tag{54}$$

for all $\underline{r}\in V+\delta V$ *and all directions.*

This theorem states that the intensity of radiation within V cannot exceed a maximum value of the intensity of radiation penetrating into V through the boundary δV. This theorem also

presupposes that the incoming radiation field B is given by a bounded function. It means that this theorem cannot be applied if B contains a singular component, e.g., Dirac delta function. It is also assumed that the total interaction coefficient σ and the differential scattering coefficient σ_S are positive functions.

Proof

□ Let $\bar{I} = \sup_{\underline{r}\in V+\delta V;\,\underline{\Omega}\in 4\pi} |\, I(\underline{r},\underline{\Omega})\,|$ where "supremum" is taken over all spatial points from V+δV and over all directions. We have

$$\begin{aligned}
\underline{\Omega}\bullet\nabla I(\underline{r},\underline{\Omega}) &= -\sigma(\underline{r},\underline{\Omega})\, I(\underline{r},\underline{\Omega}) + \int_{4\pi} d\underline{\Omega}'\, \sigma_s(\underline{r},\underline{\Omega}'\to\underline{\Omega})\, I(\underline{r},\underline{\Omega}) \\
&\le -\sigma(\underline{r},\underline{\Omega})\, I(\underline{r},\underline{\Omega}) + \int_{4\pi} d\underline{\Omega}'\, \sigma_s(\underline{r},\underline{\Omega}'\to\underline{\Omega}) \sup_{\underline{r}\in V;\,\underline{\Omega}'\in 4\pi} \left\{ I(\underline{r},\underline{\Omega}') \right\} \\
&= -\sigma(\underline{r},\underline{\Omega})\, I(\underline{r},\underline{\Omega}) + \bar{I}\,\frac{\sigma_s'(\underline{r},\underline{\Omega})}{\sigma(\underline{r},\underline{\Omega})}\,\sigma(\underline{r},\underline{\Omega}) \\
&\le [\varpi_0(V)\bar{I} - I(\underline{r},\underline{\Omega})]\sigma(\underline{r},\underline{\Omega}) \\
&\le [\bar{I} - I(\underline{r},\underline{\Omega})]\sigma(\underline{r},\underline{\Omega}). \qquad (55)
\end{aligned}$$

Note that the symmetry of the differential scattering coefficient was used to relate its integral over incident directions $\underline{\Omega}'$ to the scattering coefficient σ_s' (Section 2). Comparing the first and last term in (55), one obtains

$$[\bar{I} - I(\underline{r},\underline{\Omega})]\sigma(\underline{r},\underline{\Omega}) + \underline{\Omega}\bullet\nabla[\bar{I} - I(\underline{r},\underline{\Omega})] \ge 0. \qquad (56)$$

Multiplying this equation by $\exp\left[-\tau(\underline{r},\underline{r}-\xi\underline{\Omega},\underline{\Omega})\right]$ yields

$$-\frac{d}{d\xi}\left\{\left[\bar{I} - I(\underline{r}-\xi\underline{\Omega},\underline{\Omega})\right]\exp\left(-\tau(\underline{r},\underline{r}-\xi\underline{\Omega},\underline{\Omega})\right)\right\} \ge 0.$$

Integrating the above over the interval [0,ξ] results in

$$\left[\bar{I} - I(\underline{r}-\xi\,\underline{\Omega},\underline{\Omega})\right]\exp\left[-\tau(\underline{r},\underline{r}-\xi\underline{\Omega},\underline{\Omega})\right] \le \bar{I} - I(\underline{r},\underline{\Omega}). \qquad (57)$$

Let us assume that the solution $I(\underline{r},\underline{\Omega})$ reaches its maximum at a point $\underline{r}_0$ within V and in a direction $\underline{\Omega}_0$, i.e., $\bar{I} = I(\underline{r}_0,\underline{\Omega}_0)$. Let ξ_B be the distance between the point $\underline{r}_0$ and the boundary δV along the direction $(-\underline{\Omega}_0)$. It follows from (55) and $\tau_0(V) < \infty$ that

$$0 \le [\bar{I} - I(\underline{r}_0 - \xi_B\underline{\Omega}_0,\underline{\Omega}_0)]\exp\left(-\tau(\underline{r}_0,\underline{r}_0-\xi_B\underline{\Omega}_0,\underline{\Omega}_0)\right) \le \bar{I} - I(\underline{r}_0,\underline{\Omega}_0) = 0,$$

which holds true if and only if $\bar{I} = I(\underline{r}_0\text{-}\xi_B\underline{\Omega}_0,\underline{\Omega}_0)$. It means that the maximum of the solution $I(\underline{r},\underline{\Omega})$ taken over all internal points and over all directions cannot exceed the intensity of

radiation entering the canopy in the direction $\underline{\Omega}_0$ through the point $\underline{r}_0$ on the boundary δV. This completes the proof.■

The inequality given by Eq. (57) for a more general case was originally derived by Germogenova [1986]. This results provides a theoretical justification to many existing radiation models. Based on Theorem 1, the following uniqueness theorem can be easily proved under the assumption of a symmetrical differential scattering coefficient σ_s and boundary bidirectional reflectance factor ρ.

Uniqueness Theorem
Let $\varpi \le 1$, $\rho_0 < 1$ *and* $\tau_0(V) < \infty$. *The radiative regime within a given volume V of space bounded by a reflecting surface* δV *is uniquely determined by sources within V and the boundary conditions given by Eq. (23).*

Proof
□ Let $I_1(\underline{r},\underline{\Omega})$ and $I_2(\underline{r},\underline{\Omega})$ be two solutions of the transport equation (22) with boundary condition given by Eq. (23). The function $\psi(\underline{r},\underline{\Omega}) = I_1(\underline{r},\underline{\Omega}) - I_2(\underline{r},\underline{\Omega})$ satisfies Eq. (24a) with $q = 0$ and the boundary condition given by Eq. (23) with q_B=0. It follows from Theorem 1 and the symmetry $\rho_B(\underline{r}'_B,\underline{\Omega}';\underline{r}_B,\underline{\Omega}) = \rho_B(\underline{r}_B,-\underline{\Omega};\underline{r}'_B,-\underline{\Omega}')$ that the following inequality

$$
\begin{aligned}
|\psi(\underline{r},\underline{\Omega})| &\le \sup_{\substack{\underline{r}_B\in\delta V \\ \underline{\Omega}\bullet\underline{n}(\underline{r}_B)<0}} \left|B(\underline{r}_B,\underline{\Omega})\right| \\
&= \sup_{\substack{\underline{r}_B\in\delta V \\ \underline{\Omega}\bullet n(r_B)<0}} \left| \frac{1}{\pi}\int_{\delta V} d\underline{r}'_B \int_{\Omega'\bullet\underline{n}(r_B)>0} \rho_B(\underline{r}'_B,\underline{\Omega}';\underline{r}_B,\underline{\Omega})\,|\,\underline{n}(\underline{r}'_B)\bullet\underline{\Omega}'\,|\,\psi(\underline{r}'_B,\underline{\Omega}')\,d\underline{\Omega}' \right| \\
&\le \rho_0(\delta V) \sup_{\substack{\underline{r}_B\in\delta V \\ \underline{n}(\underline{r}_B)\bullet\underline{\Omega}<0}} |\psi(\underline{r}_B,\underline{\Omega})|, \qquad (58)
\end{aligned}
$$

is valid for all spatial points $\underline{r}\in V+\delta V$ and directions $\underline{\Omega}\in 4\pi$. Therefore,

$$
\sup_{\substack{\underline{r}_B\in\delta V \\ \underline{n}(\underline{r}_B)\bullet\underline{\Omega}<0}} |\psi(\underline{r}_B,\underline{\Omega})| \le \rho_0(V) \sup_{\substack{\underline{r}_B\in\delta V \\ \underline{n}(\underline{r}_B)\bullet\underline{\Omega}<0}} |\psi(\underline{r}_B,\underline{\Omega})|. \qquad (59)
$$

Since $\rho_0(V) < 1$, the inequality given by Eq. (59) holds true if and only if $|\psi(\underline{r},\underline{\Omega})| = 0$, i.e., $I_1(\underline{r},\underline{\Omega}) = I_2(\underline{r},\underline{\Omega})$. The uniqueness theorem is thus proved.■

12. General Case of Asymmetry

Theorem 1 and consequently the uniqueness theorem were proved under the assumption of certain symmetry in the differential scattering coefficient and the boundary bidirectional

reflectance factor. This assumption was required to derive the inequalities given by Eqs. (55) and (58). To extend the validity of the uniqueness theorem to the general case, consider the adjoint formulation of the transport equation [Bell and Glasstone, 1970; Germogenova, 1986],

$$-\underline{\Omega} \bullet \nabla I^*(\underline{r},\underline{\Omega}) + \sigma(\underline{r},\underline{\Omega})\, I^*(\underline{r},\underline{\Omega}) = \int_{4\pi} \sigma_s(\underline{r},\underline{\Omega} \to \underline{\Omega}')\, I^*(\underline{r},\underline{\Omega}')\, d\underline{\Omega}', \tag{60}$$

$$I^*(\underline{r}_B,\underline{\Omega}) = B^*(\underline{r}_B,\underline{\Omega}), \quad \underline{r}_B \in \delta V, \quad \underline{n}(\underline{r}_B) \bullet \underline{\Omega} > 0, \tag{61}$$

where

$$B^*(\underline{r}_B,\underline{\Omega}) = \frac{1}{\pi} \int_{\delta V} d\underline{r}'_B \int_{\underline{n}(\underline{r}_B)\bullet\underline{\Omega}'<0} \rho_B(\underline{r}_B,\underline{\Omega};\underline{r}'_B,\underline{\Omega}')\, |\, \underline{n}(\underline{r}'_B) \bullet \underline{\Omega}'\, |\, I^*(\underline{r}'_B,\underline{\Omega}')\, d\underline{\Omega}' + q^*(r_B,\Omega), \quad \underline{n}(\underline{r}_B) \bullet \underline{\Omega} > 0. \tag{62}$$

The following differences should be noted between the standard formulation given by Eqs. (24) and (23) and its adjoint counterpart given by Eqs. (60)-(61): (a) the gradient operator $\underline{\Omega} \bullet \nabla$ has the opposite sign; (b) the incident $\underline{\Omega}'$ and scattering $\underline{\Omega}$ directions have been interchanged, i.e., $\underline{\Omega}' \to \underline{\Omega}$ in (23) and (24) becomes $\underline{\Omega} \to \underline{\Omega}'$ in Eqs. (60) and (62); and (c) the boundary condition (61) is formulated in terms of exiting photons, i.e., $\underline{n}(\underline{r}_B) \bullet \underline{\Omega} > 0$.

Physically, the adjoint radiative transfer problem describes the time-reversed photon flow. This gives us the hint that adjoint sources q^* describe the position of detectors while the adjoint transport equation describes the flow backward in time toward. Adjoint equations and their solutions play an important role in radiative transfer theory. Adjoint functions are, in a very real sense, orthogonal to the solutions of the radiative transfer equation [Bell and Glasstone, 1970; Germogenova, 1986]. For this and other reasons, they are widely used in perturbation theory and variational calculations relating to the behavior of 3D optical media. The properties of the solutions of the adjoint RTE are also used in the development of effective Monte Carlo calculations [Marchuk et al., 1980].

Consider the function $I_0^*(\underline{r},\underline{\Omega}) = I^*(\underline{r},-\underline{\Omega})$. It satisfies the standard boundary value problem for the standard transport equation, i.e.,

$$\underline{\Omega} \bullet \nabla I_0^*(\underline{r},\underline{\Omega}) + \sigma(\underline{r},-\underline{\Omega}) I_0^*(\underline{r},\underline{\Omega}) = \int_{4\pi} \sigma_s(\underline{r},-\underline{\Omega} \to -\underline{\Omega}') I_0^*(\underline{r},\underline{\Omega}')\, d\underline{\Omega}', \tag{63}$$

$$I_0^*(\underline{r}_B,\underline{\Omega}) = B^*(\underline{r}_B,-\underline{\Omega}), \quad \underline{r}_B \in \delta V, \quad \underline{n}(\underline{r}_B) \bullet \underline{\Omega} < 0. \tag{64}$$

The uniqueness theorem can be applied to Eqs. (63)-(64) with the maximum boundary albedo, single scattering albedo and optical depth calculated using $\rho_B(\underline{r}_B,-\underline{\Omega};\underline{r}'_B,-\underline{\Omega}')$, $\sigma(\underline{r},-\underline{\Omega})$ and

$\sigma_s(\underline{r},-\underline{\Omega} \rightarrow -\underline{\Omega}')$. According to the Fredholm alternative [Bronshtein and Semendyaev, 1985, p. 783], a linear operator equation and its adjoint counterpart have a unique solution simultaneously. Therefore, we can use the adjoint transport equation to find the conditions under which it has a unique solution. The same conditions guarantee the uniqueness of the transport equation. Thus, the requirement for symmetry in the differential scattering coefficient and the boundary bidirectional reflectance factor can be relaxed.

Problem Sets

- **Problem 1**. The frequency of red light is $\nu = 4.3 \times 10^{14}$ oscillations per second. What is a wavelength λ of red light?
- **Problem 2**. How are particle distribution functions in frequency and wavelength domains related?
- **Problem 3**. Let the differential solid angle $d\underline{\Omega}$ cuts an area consisting of points with polar and azimuthal angles from intervals $[\theta, \theta + d\theta]$ and $[\varphi, \varphi + d\varphi]$. Show that $d\underline{\Omega} = \sin\theta \, d\theta \, d\varphi$.
- **Problem 4**. How are the intensities in frequency and wavelength domains related?
- **Problem 5**. Some instruments (e.q., the LICOR quantum sensor) register broadband (i.e., integrated over a certain spectral interval) fluxes in mol m^{-2} s^{-1}. Therefore, it is often convenient to use the intensity $J(\underline{r}, \nu, \underline{\Omega}, t)$ expressed in mol m^{-3} s^{-1} sr^{-1} instead of $I(\underline{r}, \nu, \underline{\Omega}, t)$ in J m^{-2} sr^{-1}. How are intensities J, I and the particle distribution function f related?
- **Problem 6**. Let x, y and z be Cartesian coordinates of the point $\underline{r}_1$. Find Cartesian coordinates of the point $\underline{r}_2 = \underline{r}_1 + c\Delta t \underline{\Omega}$.
- **Problem 7**. Location $\underline{r}_1(t)$ of a photon at time t traveling along a direction $\underline{\Omega}$ can be expressed as $\underline{r}_1(t) = \underline{r}_B + ct\underline{\Omega}$ where $ct = \xi$ is the distance traversed by a photon in time interval t. Let x_B, y_B and z_B be Cartesian coordinates of the point $\underline{r}_B$. Find Cartesian coordinates of points $\underline{r}_1(t)$ and $\underline{r}_2(t) = \underline{r}_1 + \Delta\xi \underline{\Omega}$ and their derivatives with respect to t.
- **Problem 8**. Show that if the extinction coefficient σ does not depend neither on spatial nor angular variables, $\tau(\underline{r}_1, \underline{r}_2, \underline{\Omega}) = \sigma \| \underline{r}_1 - \underline{r}_2 \|$.
- **Problem 9**. Using Eq. (37) show that the volume Green's function for purely absorbing media (i.e., S=0) is given by

$$G_V(\underline{r}', \underline{\Omega}'; \underline{r}, \underline{\Omega}) = \frac{\exp\left[-\tau(\underline{r}, \underline{r}', \underline{\Omega}')\right]}{\| \underline{r} - \underline{r}' \|^2} \delta(\underline{\Omega}' \rightarrow \underline{\Omega}) \delta\left(\underline{\Omega} - \frac{\underline{r} - \underline{r}'}{\| \underline{r} - \underline{r}' \|}\right).$$

- **Problem 10**. Let the total interaction coefficient σ be independent of the spatial and angular variables. Derive integral equations for the intensity and source function for isotropically scattering media with isotropic sources.
- **Problem 11**. Derive integral equations for the intensity and source function in plane geometry, i.e., a medium in which the total interaction coefficient, differential scattering coefficient and volume source are functions of the horizontal coordinate z.

- **Problem 12**. Let the total interaction coefficient σ be independent of the spatial and angular variables. Derive integral equations for the intensity and source function for a sphere with isotropic scattering and spherically symmetric volume sources. The volume source is said to by spherically symmetric if it depends on $\|\underline{r}\|$ and $\underline{\Omega} \bullet \underline{r} / \|\underline{r}\|$.
- **Problem 13**. Show that $Te_{0,m} = \gamma_{0,m+1} e_{0,m+1}$, where $\gamma_{0,m+1}$ and $e_{0,m}$ are eigenvalues and eigenvectors of transport equation, $\gamma L_0 e = Se$, and $T = L_0^{-1} S$ (cf. Section 9).
- **Problem 14**. Let δV be a reflecting boundary, i.e., a fraction of the medium leaving radiation can be reflected back into V. Assume that the boundary reflects as a Lambertian surface. The radiation I^- penetrating into V through δV is

$$I(\underline{r}_B, \underline{\Omega}) = \frac{\rho}{\pi} \int\limits_{\underline{n}(\underline{r}_b) \bullet \underline{\Omega}' > 0} I(\underline{r}_B, \underline{\Omega}') \left| \underline{n}(\underline{r}_B) \bullet \underline{\Omega}' \right| d\underline{\Omega}' + q(\underline{r}_B, \underline{\Omega}), \quad \underline{n}(\underline{r}_B) \bullet \underline{\Omega} < 0 \ .$$

  Show that $(1-\rho)E^+(\delta V) + E_a(V) = E_q^-(\delta V)$, where

$$E_q^-(\delta V) = \int\limits_{\delta V} d\underline{r}_B \int\limits_{\underline{n}(\underline{r}_B) \bullet \underline{\Omega} < 0} d\underline{\Omega} \left| \underline{n}(\underline{r}_B) \bullet \underline{\Omega} \right| q(\underline{r}_B, \underline{\Omega}) .$$

- **Problem 15**. Let V be the parallelepiped and δV_t, δV_b and δV_l are its top, bottom and lateral surfaces. Show that

$$E^+(\delta V) = E^+(\delta V_b) + E^+(\delta V_t) + E^+(\delta V_l),$$
$$E^-(\delta V) = E^-(\delta V_b) + E^-(\delta V_t) + E^-(\delta V_l).$$

- **Problem 16**. Let V be the parallelepiped and δV_t, δV_b and δV_l are its top, bottom and lateral surfaces. Write the energy conservation law in terms of canopy transmission, t, reflection, r, and horizontal energy flow, h, defined as

$$r = \int\limits_{\underline{n}(\underline{r}_t) \bullet \underline{\Omega} > 0} I(\underline{r}_t, \underline{\Omega}') \left| \underline{n}(\underline{r}_t) \bullet \underline{\Omega}' \right| d\underline{\Omega}',$$

$$t = \int\limits_{\underline{n}(\underline{r}_b) \bullet \underline{\Omega} > 0} I(\underline{r}_b, \underline{\Omega}') \left| \underline{n}(\underline{r}_b) \bullet \underline{\Omega}' \right| d\underline{\Omega}',$$

$$h = \int\limits_{\underline{n}(\underline{r}_l) \bullet \underline{\Omega} > 0} I(\underline{r}_l, \underline{\Omega}') \left| \underline{n}(\underline{r}_l) \bullet \underline{\Omega}' \right| d\underline{\Omega}'.$$

- **Problem 17**. Prove the uniqueness theorem without assuming symmetrical differential scattering coefficient and boundary bidirectional reflectance factor.
- **Problem 18**. Prove that for the horizontally homogeneous media, solution of the transport problem depends on vertical coordinate only.

References

Bronstein, I. N., and K.A. Semendyayev (1985). *Handbook of Mathematics*, Springer-Verlag, Berlin.

Germogenova, T.A. (1986). *The Local Properties of the Solution of the Transport Equation*, Nauka, Moscow (in Russian).

Marchuk, G., G. Mikhailov, M. Nazaraliev, R. Darbinjan, B. Kargin, and B. Elepov (1980) *The Monte Carlo Methods in Atmospheric Optics*, Springer-Verlag, NewYork.

Vladimirov, V.S. (1963). Mathematical problems in the one-velocity theory of particle transport, *Tech. Rep. AECL-1661*, At. Energy of Can. Ltd., Chalk River, Ontario.

Further Readings

Davis, A. and Y. Knyazikhin, *A Primer in Three-Dimensional Radiative Transfer*, in A. Davis and A. Marshak [eds.] (2006) "3D Radiative Transfer in the Cloudy Atmospheres," Springer-Verlag, Berlin Heidelberg.

Bell, G. I., and S. Glasstone (1970) *Nuclear Reactor Theory*, Van Nostrand Reinholt, New York.

Case, K. M., and P.F. Zweifel (1967) *Linear Transport Theory*, Addison-Wesley Publishing Company, Reading, Mass.

Riesz, F., and B. Sz.-Nagy (1990). *Functional Analysis*, Dover Publication, Inc., New York.

Kantoirovich, L.V., and G.P. Akilov (1964). *Functional Analysis in Normed Spaces*, the Macmillan Company, New York.

Krein, S.G. (ed.) (1972). *Functional Analysis*, Groningen, Wolters-Noordhoff.

Chapter 2

Interaction Coefficients for a Leaf Canopy

Myneni et al.

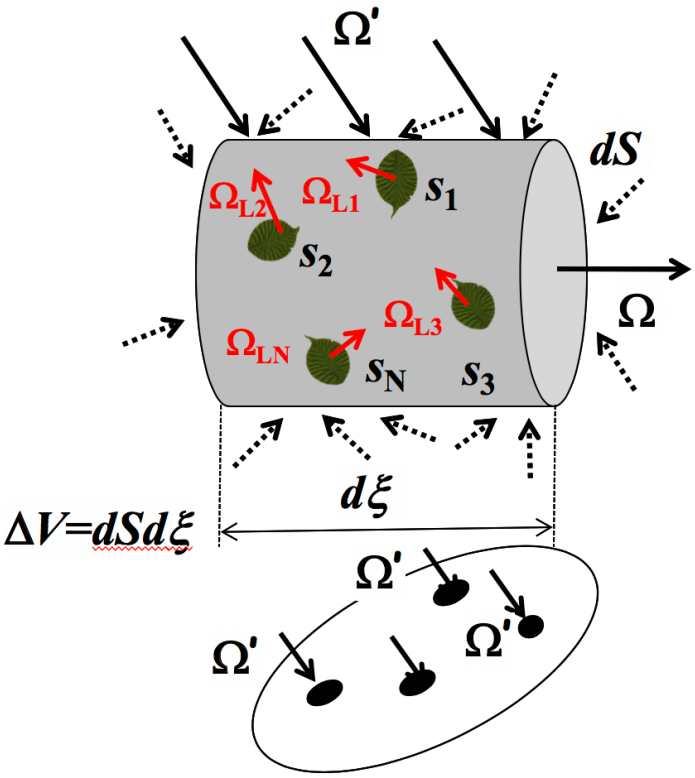

Chapter 2

Interaction Coefficients for a Leaf Canopy

1. Vegetation Canopy Structure

Turbid Medium Approximation: The vegetation canopy is idealized as a medium filled densely with small planar elements of negligible thickness and area, i.e., a turbid medium. All organs other than green leaves are ignored for the time being. Two important structural attributes – leaf area density and leaf normal orientation distribution – are first defined in order to quantify vegetation-photon interactions.

Leaf Area Density Distribution: The one-sided green leaf area per unit volume in the vegetation canopy is defined as the leaf area density distribution $u_L(\underline{r})$ (m^{-1}). The quantity,

$$L(x,y) = \int_0^{z_H} dz\, u_L(x,y,z), \tag{1}$$

is called the leaf area index, one-sided green leaf area per unit ground area at (x,y). Here Z_H is depth of the vegetation canopy. The vertical distribution of $\bar{u}_L(z)$,

$$\bar{u}_L(z) = \frac{1}{X_S Y_S} \int_0^{X_S} dx \int_0^{Y_S} dy\, u_L(x,y,z),$$

where X_S and Y_S are horizontal dimensions of a stand, shows the profile of leaf area distribution along the vertical. The variables L and $\bar{u}_L(z)$ are key parameters of climate, hydrology, bio-geochemistry and ecology models as they govern the exchange of energy, mass and momentum between the land surface and the atmospheric planetary boundary layer.

Direct measurements of L and $\bar{u}_L(z)$ are labor-intensive and expensive. The modeling of $u_L(\underline{r})$ is a challenge as it requires computer simulation of vegetation canopies based on tedious field

measurements (Fig. 1). Hence the interest in remote sensing of these variables from space-based measurements of reflected solar radiation and lidar backscatter returns (Fig. 2).

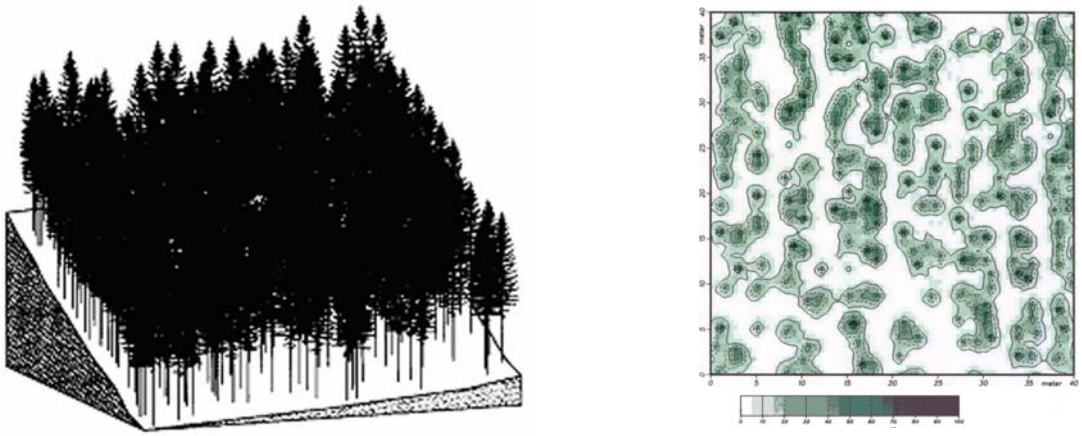

Figure 1. Computer simulated Norway spruce stand about 50 km near Goettingen, Germany, in the Harz mountains. The stand is about 45 years old and situated on the south slope. A 40×40 m^2 section of the stand with 297 trees was sampled for reconstruction. The stem diameters varied from 6 to 28 m and the tallest trees were about 12.5 m in height. The trees were divided into five groups with respect to stem diameter. A model of a Norway spruce based on fractal theory was used to build a representative of each group [Knyazikhin et al., 1996]. Given the distribution of tree stems in the stand, the diameter of each tree, the entire sample site was generated (left panel). The right panel shows the spatial distribution of leaf area index L(x,y) at spatial resolution of 50 cm^2, i.e., distribution of the mean leaf area index L(x,y) taken over each of 50 by 50 cm ground cells.

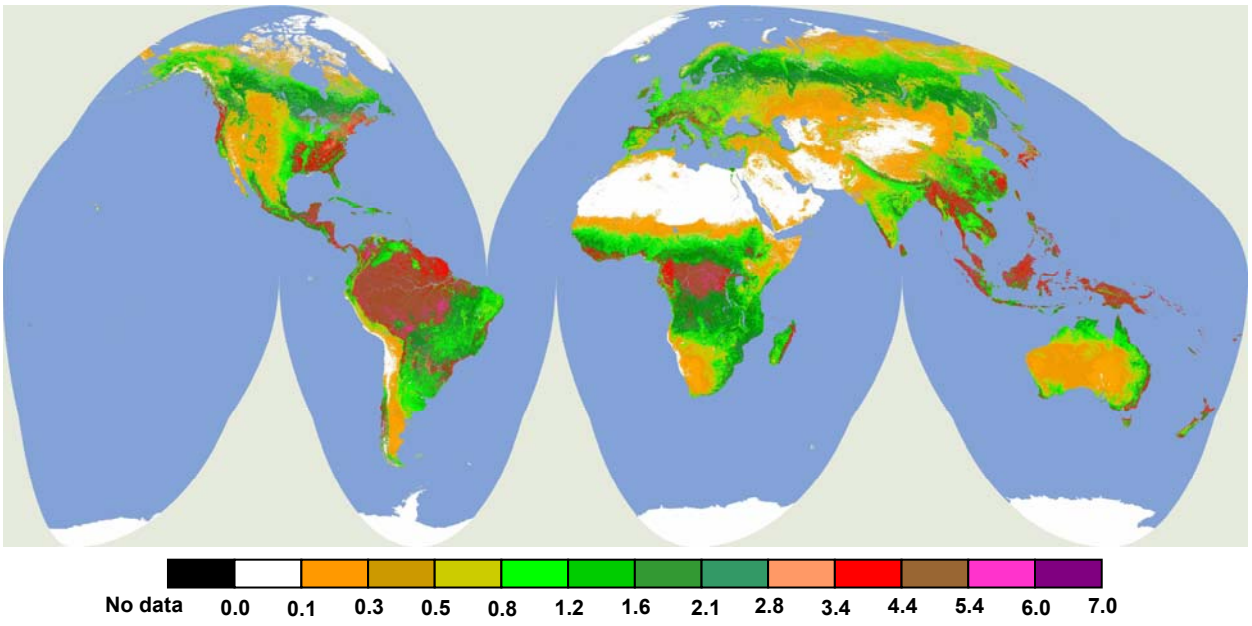

Figure 2. Global distribution of annual average vegetation green leaf area index L(x,y) at 1 km resolution derived from MODIS measurements of surface reflectances [Knyazikhin et al., 1998]. Data from a four year period, July 2000 to June 2004, were used to produce this image. This MODIS product has been developed from an algorithm based on radiative transfer theory developed in this book.

Needle Area Density Distribution: For non-flat leaves such as conifer needles, the counterpart to one-sided leaf area is the hemi-surface or half-of-total leaf (needle) area. In coniferous canopies, thus, the hemi-surface needle area is used in expressing the leaf area density (u_L) and leaf area index (LAI).

Leaf Normal Orientation Distribution: Let

$$\underline{\Omega}_L \equiv (\theta_L, \varphi_L) \equiv (\mu_L, \varphi_L), \quad \mu_L \in (0,1), \quad \varphi_L \in (0,2\pi)$$

be the normal to the upper face of a leaf element. If this normal is in the lower hemisphere, the lower face may be treated as the upper face, i.e., the definition of the upper face of a leaf element is the face the normal to which is in the upper hemisphere. Hence, the space of leaf normal orientation is always 2π steradians. Further, let $(1/2\pi)\, g_L(\underline{\Omega}_L)$ be the probability density function of leaf normal orientation,

$$\frac{1}{2\pi} \int_{2\pi+} d\underline{\Omega}_L \; g_L(\underline{\Omega}_L) = 1. \tag{2}$$

If μ_L and φ_L are assumed independent, then

$$\frac{1}{2\pi}\, g_L(\underline{\Omega}_L) = \bar{g}_L(\mu_L)\, \frac{1}{2\pi}\, h_L(\varphi_L), \tag{3}$$

where $\bar{g}_L(\mu_L)$ and $(1/2\pi)\, h_L(\varphi_L)$ are the probability density functions of leaf normal inclination and azimuth, respectively, and

$$\int_0^1 d\mu_L \, \bar{g}_L(\mu_L) = 1, \quad \frac{1}{2\pi} \int_0^{2\pi} d\varphi_L h_L(\varphi_L) = 1.$$

The functions $g_L(\underline{\Omega}_L)$, $\bar{g}_L(\mu_L)$ and $h_L(\varphi_L)$ will depend on the location $\underline{r}$ in the vegetation canopy but this has been suppressed for clarity.

The simplest model of leaf normal orientation distribution is constant leaf normal inclination and uniform distribution of azimuths,

$$\frac{1}{2\pi}\, g_L(\underline{\Omega}_L) = \frac{1}{2\pi} \delta(\mu_L - \mu_L^*). \tag{4}$$

The following example model distribution functions for leaf normal inclination are widely used [Bunnik, 1978]: (1) planophile – mostly horizontal leaves, (2) erectophile – mostly erect leaves, (3) plagiophile – mostly leaves at 45 degrees, (4) extremophile – mostly horizontal and vertical leaves, (5) uniform – all inclinations equally probable, and (6) spherical – leaf normals distributed as on a sphere. These distributions can be expressed as,

Planophile: $\bar{g}_L(\theta_L)\sin\theta_L = \frac{2}{\pi}(1+\cos 2\theta_L)$, (5a)

Erectophile: $\bar{g}_L(\theta_L)\sin\theta_L = \frac{2}{\pi}(1-\cos 2\theta_L)$, (5b)

Plagiophile: $\bar{g}_L(\theta_L)\sin\theta_L = \frac{2}{\pi}(1-\cos 4\theta_L)$, (5c)

Extremophile: $\bar{g}_L(\theta_L)\sin\theta_L = \frac{2}{\pi}(1+\cos 4\theta_L)$, (5d)

Uniform: $\bar{g}_L(\theta_L)\sin\theta_L = \frac{2}{\pi}$, (5e)

Spherical: $\bar{g}_L(\theta_L)\sin\theta_L = \sin\theta_L$, (5f)

and are plotted in Fig. 3.

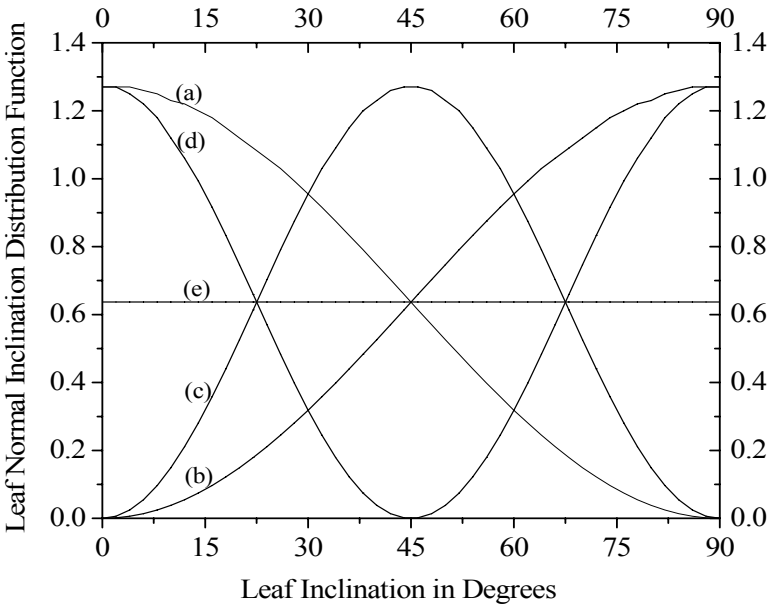

Figure 3. The $\bar{g}(\theta_L)\sin\theta_L$ for (a) planophile (mostly horizontall leaves), (b) erectorphile (mostly vertical leaves), (c) pla-giophile (leaves inclined mostly at about 45^0), (d) extremephile (mostly horizontal and vertical leaves) and (e) uniform (all inclina-tions equally probable) distributions.

Certain plants, such as soybeans and sunflowers, exhibit heliotropism, where the leaf azimuths have a preferred orientation with respect to the solar azimuth. A simple model for h_L in such canopies is [Verstraete, 1987],

$$\frac{1}{2\pi}h_L(\varphi_L,\varphi) = \frac{1}{\pi}\cos^2(\varphi-\varphi_L-\eta), \tag{6}$$

where η is the difference between the azimuth of the maximum of the distribution function h_L and the azimuth of the incident photon φ. In the case of diaheliotropic distributions, which tend to maximize the projected leaf area to the incident stream $\eta = 0$. On the other hand, paraheliotropic distributions tens to minimize the leaf area projected to the incident stream, $\eta = 0.5\pi$. A more general model for the leaf normal orientations is the beta distribution, the

parameters of which can be obtained from fits to field measurements of the leaf normal orientation [Goel and Strebel, 1984].

Needle and shoot orientation: The orientation of three-dimensional and non-cylindrical conifer needles however cannot be defined by one vector alone (as the leaf normal in case of flat leaves) but an additional vector is needed. These two vectors can be defined, for example, as the main axis of a needle and a normal to this axis (Oker-Blom and Kellomäki 1982). The needle axis defines the needle inclination for which the same characterizations as for planar leaves (e.g. a planophile or an erectophile needle inclination distribution) can be used. Whenever the needles are not cylindrical, the rotation angle, defined by the normal to the needle axis, must in addition be specified. We define the spherical needle orientation so that the needle main axis has no preferred direction in space and, for any fixed direction of the needle axis, the rotation angle is uniformly distributed.

Conifer needles are typically tightly grouped into annual shoots, which (for reasons that will become clear later) are often used as the basic foliage elements in modeling radiative transfer in coniferous canopies. To define shoot orientation, the same approach as defined above can be used (Stenberg 1996). For example, the main shoot axis has equal probability of pointing in any direction in the case of spherical shoot orientation distribution.

The shoot inclination in many conifer species changes with depth in the canopy so that it becomes more horizontal deeper down in the canopy. In shade-tolerant species, especially, this change is accompanied by changes in the shoot structure so that, for example, shade shoots are flatter than 'sun shoots' (Fig. 4).

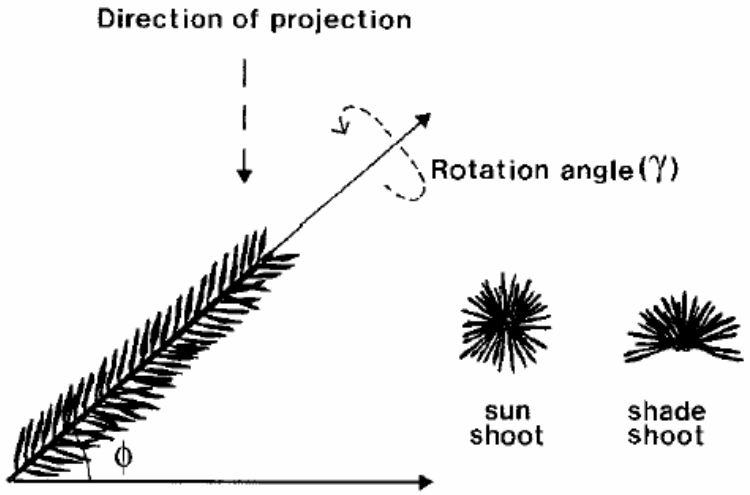

Figure 4. Determination of shoot orientation and illustration of 'sun shoot' and 'shade shoot' geometry.

2. Vegetation Canopy Optics

A photon incident on a leaf element can either be absorbed or scattered depending on its frequency. If the scattered photon emerges from the same side of the leaf as the incident photon, the event is termed reflection. Likewise, if the scattered photon exits the leaf from the opposite

side, the event is termed transmission. Scattering of solar radiation by green leaves does not involve frequency shifting interactions, but is dependent on the wavelength.

A photon incident on a leaf element can either be specularly reflected from the surface depending on its roughness or emerge diffused from interactions in the leaf interior. Some leaves can be quite smooth from a coat of wax-like material, while other leaves can have hairs making the surface rough. Light reflected from the leaf surface can be polarized as well. Specularly reflected photons contain no information about the constitution of the leaf material as this is a surface phenomenon. Photons that do not suffer surface reflection enter the interior of the leaf, where they are either absorbed or refracted because of the many refractive index discontinuities between the cell walls and intervening air cavities. Photons that are not absorbed in the interior of the leaf emerge on both sides, generally diffused in all directions.

Leaf Optics: The interaction of the electromagnetic radiation with plant leaves (reflection, transmission, absorption) depends on the chemical and physical characteristics of these leaves. The absorption is essentially a function of changes in the spin and angular momentum of electrons, transitions between orbital states of electrons in particular atoms (visible: chlorophylls 'a' and 'b', carotenoids, brown pigments, and other accessory pigments) and vibrational-rotational modes within the polyatomic molecules (near infrared and middle infrared: water). The refractive index discontinueties within the leaf ($n \approx 1.40$ for hydrated cell walls, $n \approx 1.33$ for water at 1 μm, and $n = 1$ for air) induce scattering.

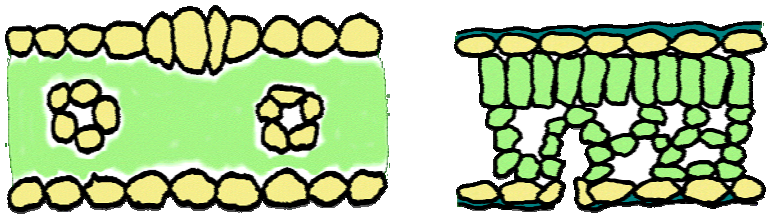

Figure 5. Schematic representation of Monocot (left) and Dicot (right) leaves. Leaf surface (epidermis) is shown in yellow, internal cells (mesophyll) are in green, and mist air space is in white.

Allen et al. (1969) has developed one early model of the leaf optical properties, called 'plate model'. The model considers a compact plant leaf as a single semi-transparent plate with plane parallel surfaces, illuminated by partially isotropic light. The expression for the total reflectance of the plate was derived by summing the amplitudes of successive reflections and refractions. However, plant leaves are not compact but present a wide range of anatomical structures which depend on the species (Fig. 5), which significantly limits the applicability of the 'plate model'. Jacquemoud and Baret (1990) have implemented the 'PROSPECT' model, one of the most popular 'generalized plate model' today. In this model a leaf is represented by a pile of N homogeneous layers separated by N-1 air spaces. The model considers surface layer and remaining N-1 internal layers separately to account for the fact that only surface layer may be exposed to non-isotropic radiation, while internal layers interact with the scattered radiation only. The process of refraction in the system of 1 and N-1 layers of the PROSPECT model is shown in Fig. 6a. An example of simulated leaf transmittance as a function of the spread of incidence angle of the incoming beam is shown in Fig. 6b.

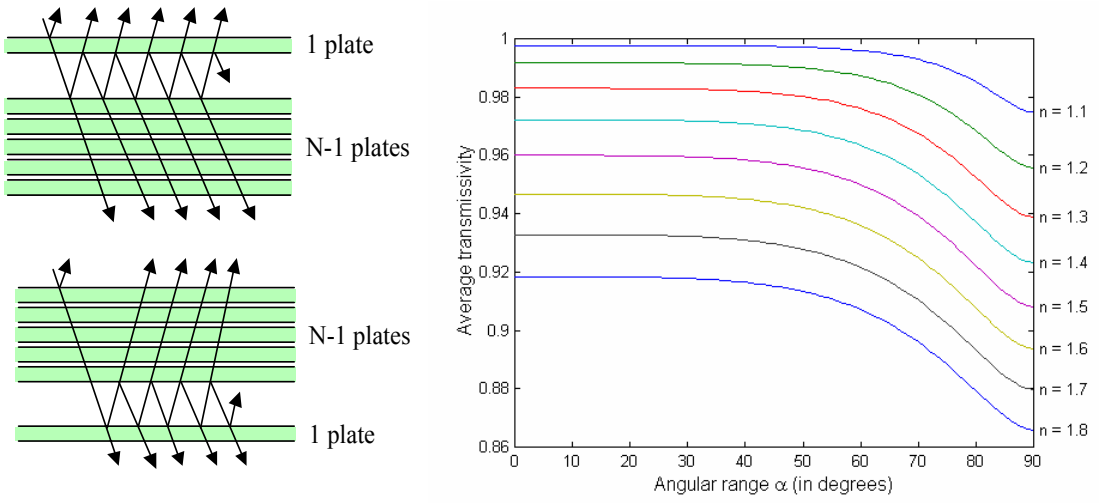

Figure 6. Modeling of leaf optics with the PROPSPECT model. The left panel shows the model representation of the leaf as a pile of N plates (1 surface plate and N-1 internal plates). The right panel shows the PROSPECT model simulations of leaf transmittance as a function of the spread of incidence angle of the incoming beam. Here $\alpha = 0$ corresponds to a monodirectional beam, while $\alpha = 90$ corresponds to a hemispherical flux.

Overall, the 'PROSPECT' model simulates the hemispherical reflectance and transmittance of various plant leaves (monocots, dicots or senescent leaves) over the solar spectrum (from 400 nm to 2500 nm). Scattering is described by a spectral refractive index (n) and a structure parameter, specifying the average number of air/cell wall interfaces within mesophyll (N). Absorption is modeled using pigment concentration (C_{a+b}, $\mu g\ cm^{-2}$), water content (C_w, cm or $g\ cm^{-2}$), and the corresponding specific spectral absorption coefficients (K_{a+b} and K_w). The internal parameters of the model (n, K_{a+b} and K_w) were estimated with field measurements (LOPEX data base for leaves, needles, stems, etc.) The remaining three key parameters (N, C_{a+b}, C_w) constitute the model's input to be adjusted for particular leaves types.

Leaf Scattering Phase Function: The angular distribution of radiant energy scattered by a leaf element is specified by the leaf element scattering phase function. Consider an elemental leaf area $d\sigma_L$ on which monochromatic radiation of intensity I is incident along $\underline{\Omega}'$. The amount of radiant energy flowing through the leaf area $d\sigma_L$ along $\underline{\Omega}'$ confined to the solid angle $d\underline{\Omega}'$ in a time interval dt is

$$dE' = I(\underline{\Omega}') \left| \underline{\Omega}_L \bullet \underline{\Omega}' \right| d\sigma_L d\underline{\Omega}' dt.$$

The wavelength dependence is assumed and will not be explicitly denoted in what follows. One part of dE' is absorbed and the rest is scattered in all directions. Consider the direction $\underline{\Omega}$ about the solid angle $d\underline{\Omega}$ into which some part of the incident energy is scattered dE upon interaction with the leaf element. The leaf scattering phase function γ_L which introduces the appropriate stream is

$$\gamma_L(\underline{\Omega}' \to \underline{\Omega}, \underline{\Omega}_L)d\underline{\Omega} = \frac{dE}{dE'}.$$

The leaf albedo, $\omega_L(\underline{\Omega}', \underline{\Omega}_L)$, is the fraction of incident energy scattered by the leaf, i.e.,

$$\omega_L(\underline{\Omega}', \underline{\Omega}_L) = \frac{\int_{4\pi} dE d\underline{\Omega}}{dE'} = \int_0^{2\pi} d\varphi \int_{-1}^{1} d\mu\, \gamma_L(\underline{\Omega}' \to \underline{\Omega}, \underline{\Omega}_L).$$

Radiant energy may be incident on the upper or the lower faces of the leaf element (–or +) and the scattering event may be either reflection or transmission. Integration of the leaf scattering phase function over the appropriate solid angles gives the leaf hemispherical reflectance $\rho_L^{\mp}$ and transmittance $\tau_L^{\mp}$ coefficients:

$$\rho_L^-(\underline{\Omega}', \underline{\Omega}_L) = \int_{(\underline{\Omega} \bullet \underline{\Omega}_L) > 0} \gamma_L(\underline{\Omega}' \to \underline{\Omega}, \underline{\Omega}_L)\, d\underline{\Omega}, \quad (\underline{\Omega}' \bullet \underline{\Omega}_L) < 0, \tag{7a}$$

$$\tau_L^-(\underline{\Omega}', \underline{\Omega}_L) = \int_{(\underline{\Omega} \bullet \underline{\Omega}_L) < 0} \gamma_L(\underline{\Omega}' \to \underline{\Omega}, \underline{\Omega}_L)\, d\underline{\Omega}, \quad (\underline{\Omega}' \bullet \underline{\Omega}_L) < 0, \tag{7b}$$

$$\rho_L^+(\underline{\Omega}', \underline{\Omega}_L) = \int_{(\underline{\Omega} \bullet \underline{\Omega}_L) < 0} \gamma_L(\underline{\Omega}' \to \underline{\Omega}, \underline{\Omega}_L)\, d\underline{\Omega}, \quad (\underline{\Omega}' \bullet \underline{\Omega}_L) > 0, \tag{7c}$$

$$\tau_L^+(\underline{\Omega}', \underline{\Omega}_L) = \int_{(\underline{\Omega} \bullet \underline{\Omega}_L) > 0} \gamma_L(\underline{\Omega}' \to \underline{\Omega}, \underline{\Omega}_L)\, d\underline{\Omega}, \quad (\underline{\Omega}' \bullet \underline{\Omega}_L) < 0. \tag{7d}$$

The leaf albedo $\omega_L(\underline{\Omega}', \underline{\Omega}_L)$ is simply the sum of ρ_L and τ_L; for example,

$$\omega_L(\underline{\Omega}', \underline{\Omega}_L) = \begin{cases} \rho_L^-(\underline{\Omega}', \underline{\Omega}_L) + \tau_L^-(\underline{\Omega}', \underline{\Omega}_L), & \text{if } (\underline{\Omega} \bullet \underline{\Omega}_L) < 0; \\ \rho_L^+(\underline{\Omega}', \underline{\Omega}_L) + \tau_L^+(\underline{\Omega}', \underline{\Omega}_L), & \text{if } (\underline{\Omega} \bullet \underline{\Omega}_L) > 0; \end{cases} \tag{8}$$

and in general depends on the incident photon direction $\underline{\Omega}'$ and the leaf normal orientation $\underline{\Omega}_L$. Typical spectra of a green leaf reflectance ρ_L and transmittance τ_L are shown in Fig. 7. The diffuse and specular leaf scattering phase functions are discussed below.

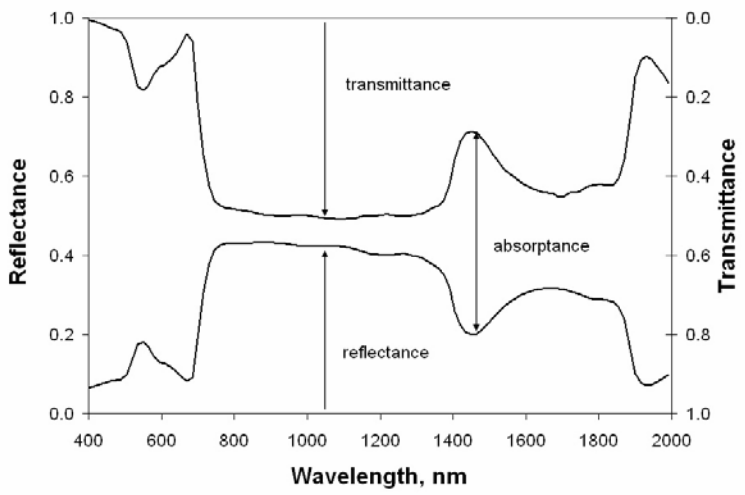

Figure 7. Typical reflectance (left axis) and transmittance (left axis) spectra of an individual plant leaf from 400 to 2000 nm for normal incidence. Note the following features – strong absorption at blue and red, moderate scattering at green, very strong scattering at near-infrared wavelengths and water absorption peaks in the mid-infra red. The dramatic increase in scattering from red (about 700 nm) to near-infrared (800-1100 nm) is often the basis for remote sensing of green vegetation.

Diffuse Leaf Scattering Phase Function: A simple but realistic model for diffuse leaf scattering phase function was proposed by Ross [1981] and others, and is extensively used in remote sensing works. In this model, a fraction $\rho_{L,d}$ of incident energy is assumed reflected in a cosine distribution (i.e., Lambertian) about the leaf normal. Similarly, another fraction $\tau_{L,d}$ is assumed transmitted in a cosine distribution on the opposite side of the leaf. In this model, transmission and reflection do not depend on whether radiant energy is incident on the upper or the lower side of the leaf element. This bi-Lambertian model can be written as

$$\gamma_{L,d}(\underline{\Omega}' \to \underline{\Omega}, \underline{\Omega}_L) = \begin{cases} \frac{1}{\pi}\rho_{L,d}\left|\underline{\Omega} \bullet \underline{\Omega}_L\right|, & (\underline{\Omega} \bullet \underline{\Omega}_L)(\underline{\Omega}' \bullet \underline{\Omega}_L) < 0, \\ \frac{1}{\pi}\tau_{L,d}\left|\underline{\Omega} \bullet \underline{\Omega}_L\right|, & (\underline{\Omega} \bullet \underline{\Omega}_L)(\underline{\Omega}' \bullet \underline{\Omega}_L) > 0. \end{cases} \tag{9}$$

Specular Leaf Scattering Phase Function*:* Specular reflection from the leaf surface depends on the angle of incidence α' (the angle between the leaf normal $\underline{\Omega}_L$ and the incident photon direction $\underline{\Omega}$, the wax coat refractive index n and the roughness of the leaf surface κ. The index of refraction n is a weak function of wavelength and a standard value of about 0.9 is used in most studies (which is why specularly reflected light from smooth leaves looks white). A simple model for specular leaf scattering phase function $\gamma_{L,S}$ is

$$\gamma_{L,S}(\underline{\Omega}' \to \underline{\Omega}, \underline{\Omega}_L) = F_r(n, \alpha')\, K(\kappa, \alpha')\, \delta_2(\underline{\Omega} \bullet \underline{\Omega}^*). \tag{10}$$

Here, F_r is the Fresnel reflectance averaged over the polarization states,

$$F(n, \alpha') = \frac{1}{2}\left[\frac{\sin^2(\alpha' - \theta_s)}{\sin^2(\alpha' + \theta_s)} + \frac{\tan^2(\alpha' - \theta_s)}{\tan^2(\alpha' + \theta_s)}\right],$$

where $\sin\theta_s = (\sin\alpha')/n$. The function K defines the correction factor for Fresnel reflection ($0 \le K \le 1$), and the argument $\kappa \approx 0.1$ to 0.3 characterizes the roughness of the surface. A simple model for leaf surface roughness is

$$K(k,\alpha') = \exp\left[-\kappa \tan(|\alpha'|)\right].$$

The function δ_2 is a surface delta function,

$$\delta_2(\underline{\Omega},\underline{\Omega}^*) = 0, \qquad \underline{\Omega} \neq \underline{\Omega}^*, \quad \int_{4\pi} d\underline{\Omega}\, q(\underline{\Omega})\,\delta_2(\underline{\Omega}\bullet\underline{\Omega}^*) = q(\underline{\Omega}^*). \tag{11}$$

The vector $\underline{\Omega}^* = \underline{\Omega}^*(\underline{\Omega},\underline{\Omega}_L)$ defines the direction of specular reflection. The leaf albedo for specular reflection is therefore,

$$\int_{4\pi} d\underline{\Omega}\, \gamma_{L,s}(\underline{\Omega}' \to \underline{\Omega},\underline{\Omega}_L) = \omega_{L,s}(\alpha',n,\kappa) = K(\kappa,\alpha')\, F_r(n,\alpha'). \tag{12}$$

3. Total Interaction Coefficient

The probability that a photon while traveling a distance $d\xi$ in the medium will interact with the elements of the host medium is given by $\sigma(\underline{r},\underline{\Omega})d\xi$ where $\sigma(\underline{r},\underline{\Omega})$ is the total interaction coefficient (m^{-1}). This probability can be derived as follows.

Consider an elementary volume $dSd\xi$ at r in the medium and which contains a sufficient number of small planar leaf elements of negligible thickness. The probability that photons in the incident radiation will collide with leaf elements in this volume is given by the ratio of the total shadow area of leaves on a plane perpendicular to the direction of photon travel $\underline{\Omega}$ to the area dS,

$$\sigma(\underline{r},\underline{\Omega})d\xi \equiv \frac{\text{total shadow area on a plane perpendicular to } \underline{\Omega}}{dS}$$

$$= \frac{s_1\,|\underline{\Omega}_{L1}\bullet\underline{\Omega}| + s_2\,|\underline{\Omega}_{L2}\bullet\underline{\Omega}| + \ldots + s_N\,|\underline{\Omega}_{LN}\bullet\underline{\Omega}|}{dS}$$

where s_i is the area of leaf element of orientation $\underline{\Omega}_{Li}$. If the leaf elements are sufficiently small and numerous, their shadows do not overlap and, the ratio of the area of all leaf elements $\bar{s}_i$ of orientation $\underline{\Omega}_{Li}$ to the total leaf area S_o in the elementary volume is equivalent to the number or the probability of leaf elements of orientation $\underline{\Omega}_{Li}$, that is,

$$\bar{s}_i(\underline{\Omega}_{Li})/S_o = (1/2\pi)g_L(\underline{r},\underline{\Omega}_{Li})d\underline{\Omega}_{Li}.$$

Thus,

$$\sigma(\underline{r},\underline{\Omega})d\xi = \frac{S_o}{dS}\left[\frac{1}{2\pi}g_L(\underline{r},\underline{\Omega}_{L1})d\underline{\Omega}_{L1}\,|\,\underline{\Omega}_{L1}\bullet\underline{\Omega}\,| + \frac{1}{2\pi}g_L(\underline{r},\underline{\Omega}_{L2})d\underline{\Omega}_{L2}\,|\,\underline{\Omega}_{L2}\bullet\underline{\Omega}\,| + ...\right]$$

$$= \frac{S_o}{dS}\frac{1}{2\pi}\int_{2\pi+} d\underline{\Omega}_L g_L(\underline{r},\underline{\Omega}_L)\,|\,\underline{\Omega}_L\bullet\underline{\Omega}\,|$$

$$= \frac{S_o}{dS}G(\underline{r},\underline{\Omega}_L).$$

Therefore,

$$\sigma(\underline{r},\underline{\Omega}) = u_L(\underline{r})G(\underline{r},\underline{\Omega}), \tag{13}$$

because $(S_o/dSd\xi)$ is the leaf area per unit volume or the leaf area density $u_L(\underline{r})$. The function $G(\underline{r},\underline{\Omega})$ is the geometry factor, first proposed by Ross [1981], and may be defined as the projection of unit leaf area at r onto a plane perpendicular to the direction of photon travel $\underline{\Omega}$. The geometry factor G satisfies the following condition:

$$\frac{1}{2\pi}\int_{2\pi+} d\underline{\Omega}\, G(\underline{r},\underline{\Omega}) = \frac{1}{2}. \tag{14}$$

Example G–functions for model leaf normal orientations are shown in Fig. 8.

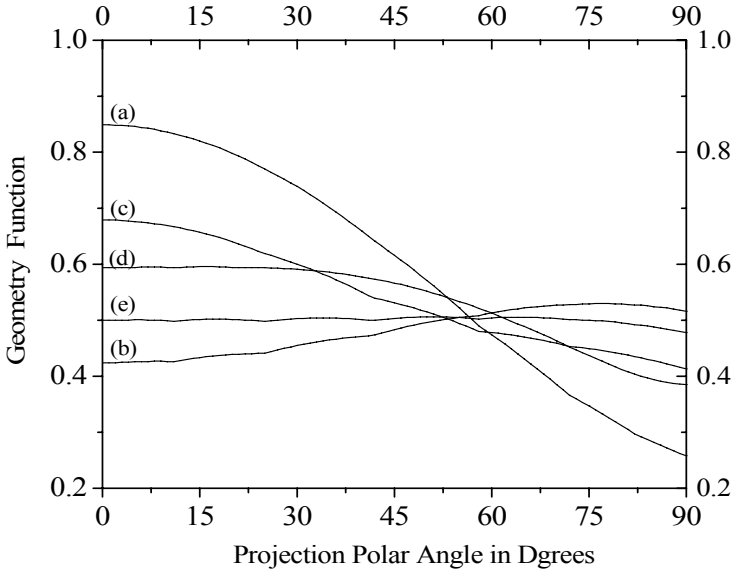

Figure 8. The G-function with projection zenith angle θ for (a) planophile, (b) erectophile, (c) plagiophile, (d) extremophile and (e) spherical leaf normal distribution functions. A distribution with mostly horizontal leaves (planophile) has a higher probability of intcercepting photons incident from directions close to the vertical and vice-versa. The G-function for uniform orientation is equal to one-half. Variations seen in the figure are due to numerical errors.

It is important to note that the geometry factor is an explicit function of the direction of photon travel Ω in the general case of non-uniformly distributed leaf normals. This imbues directional dependence to the interaction coefficients in the case of vegetation canopies, that is, the vegetation canopy radiation transport is non-rotationally invariant. The transport problem reduce to the classical rotationally invariant form only in the case of spherically distributed leaf normals (G = 0.5). Another noteworthy point is the frequency independence of σ, that is, the extinction

probabilities for photons in vegetation media are determined by the structure of the canopy rather than photon frequency or the optics of the canopy.
The total interaction coefficient $\sigma(\underline{r},\underline{\Omega})$ can be estimated from transmission measurements made below the vegetation canopy at wavelengths where leaves strongly absorb the incident radiation. Such measurements can be inverted to solve for the leaf area density distribution $u_L(\underline{r})$ and the leaf normal orientation distribution function $(1/2\pi)g_L(\underline{\Omega}_L)$.

The G-function for needles and shoots: The geometry factor G for needles varies with the cross-sectional needle shape, including forms close to a half circle (Scots pine) or a rhomb (Norway spruce), and cannot be calculated using the simple expressions (sf. Problem Sets, Problem 8). For vertical needles with uniform rotation angle, however, the same value $G = (2/\pi)\sin\theta$ as for vertical leaves is obtained (Oker-Blom and Kellomäki 1982). More importantly, the condition given by Eq. (14) that the mean of G over all possible directions equals 0.5 holds true also for needles, irrespective of their shape as long as they are convex (Lang 1991). Also, the G value of spherically oriented needles equals 0.5 for all directions of the incoming beam.

When using the coniferous shoot as the basic foliage element, the geometry factor G corresponds to the ratio of the shoot's silhouette area on a plane perpendicular to the direction of photon travel to the hemi-surface needle area. Oker-Blom and Smolander (1988) defined it as the silhouette to total area ratio (STAR), where the total (all-sided) needle area was used in the denominator. Because here we use the hemi-surface leaf area as the common basis for both flat leaves and needles, the shoot geometry factor G equals $2\times\mathrm{STAR}$.

The G value of spherically oriented shoots ($2\times\overline{\mathrm{STAR}}$) no longer equals 0.5 but is essentially smaller due to needle overlapping in the shoot (i.e. the shoot is not a convex object). Empirical data for Scots pine and Norway spruce shoots show a range of approximately 0.2 to 0.4 (smaller values in the upper canopy and higher values in lower canopy) and a mean around 0.3 for $2\times\overline{\mathrm{STAR}}$. This corresponds to a 40 % reduction in the G value of shoots as compared to that of single leaves or needles (for which G=0.5)

4. Differential Scattering Coefficient

The probability that a photon while traveling a distance $d\xi$ in the medium will scatter from direction $\underline{\Omega}'$ to direction $\underline{\Omega}$ is given by $\sigma_s(\underline{r},\underline{\Omega}'\rightarrow\underline{\Omega})d\underline{\Omega}\,d\xi$ where σ_s is the differential scattering coefficient (m^{-1} sr^{-1}). This probability can be derived as follows.

Consider an elementary volume $dSd\xi$ at r in the medium and which contains a sufficient number of small planar leaf elements of negligible thickness. The probability that photons incident along $\underline{\Omega}'$ will scatter into a differential solid angle about $\underline{\Omega}$ is given by

$$\sigma_s(\underline{r},\underline{\Omega}'\rightarrow\underline{\Omega})d\underline{\Omega}\,d\xi = \frac{s_1\,|\,\underline{\Omega}_{L1}\bullet\underline{\Omega}'\,|\,\gamma_L(\underline{\Omega}_{L1};\underline{\Omega}'\rightarrow\underline{\Omega})d\underline{\Omega}}{dS}$$

$$+\frac{s_2\,|\,\underline{\Omega}_{L2}\bullet\underline{\Omega}'\,|\,\gamma_L(\underline{\Omega}_{L2};\underline{\Omega}'\rightarrow\underline{\Omega})d\underline{\Omega}}{dS}+\ldots+\frac{s_N\,|\,\underline{\Omega}_{LN}\bullet\underline{\Omega}'\,|\,\gamma_L(\underline{\Omega}_{LN};\underline{\Omega}'\rightarrow\underline{\Omega})d\underline{\Omega}}{dS},$$

where s_i is the area of leaf element of orientation $\underline{\Omega}_{Li}$ and γ_L is the scattering phase function. The point interactions are assumed to be independent and uncorrelated. Implicit in the formulation of the above is the assumption that the leaf elements are sufficiently small and numerous. The ratio of the area of all leaf elements $\bar{s}_i$ of orientation $\underline{\Omega}_{Li}$ to the total leaf area S_o in the elementary volume is therefore equivalent to the number or the probability of leaf elements of orientation $\underline{\Omega}_{Li}$, that is, $\bar{s}_i(\underline{\Omega}_{Li})/S_o = (1/2\pi)g_L(\underline{r},\underline{\Omega}_{Li})d\underline{\Omega}_{Li}$, and,

$$\begin{aligned}\sigma_s(\underline{r},\underline{\Omega}'\rightarrow\underline{\Omega})d\underline{\Omega}\,d\xi &= \frac{S_o}{dS}\Big[\frac{1}{2\pi}g_L(\underline{r},\underline{\Omega}_{L1})d\underline{\Omega}_{L1}\,|\,\underline{\Omega}_{L1}\bullet\underline{\Omega}'\,|\,\gamma_L(\underline{\Omega}_{L1};\underline{\Omega}'\rightarrow\underline{\Omega})d\underline{\Omega}\\ &\qquad+\frac{1}{2\pi}g_L(\underline{r},\underline{\Omega}_{L2})d\underline{\Omega}_{L2}\,|\,\underline{\Omega}_{L2}\bullet\Omega'\,|\,\gamma_L(\underline{\Omega}_{L2};\underline{\Omega}'\rightarrow\underline{\Omega})d\underline{\Omega}+..\Big]\\ &=\frac{S_o}{dS}d\underline{\Omega}\frac{1}{2\pi}\int_{2\pi+}d\underline{\Omega}_L g_L(\underline{r},\underline{\Omega}_L)\,|\,\underline{\Omega}_L\bullet\underline{\Omega}'\,|\,\gamma_L(\underline{\Omega}_L;\underline{\Omega}'\rightarrow\underline{\Omega})\\ &=\frac{S_o}{dS}d\underline{\Omega}\frac{1}{\pi}\Gamma(\underline{r},\underline{\Omega}'\rightarrow\underline{\Omega}).\end{aligned}$$

Thus the differential scattering coefficient may be written as,

$$\sigma_s(\underline{r},\underline{\Omega}'\rightarrow\underline{\Omega})=u_L(\underline{r})\frac{1}{\pi}\Gamma(\underline{r},\underline{\Omega}'\rightarrow\underline{\Omega}),\qquad(15)$$

because $(S_o/dSd\xi)$ is the leaf area per unit volume or the leaf area density $u_L(\underline{r})$. Here $(1/\pi)\Gamma$ is the area scattering phase function first proposed by Ross [1981]. It is important to note that the differential scattering coefficient is non-rotationally invariant, that is, it is an explicit function of the polar coordinates of $\underline{\Omega}'$ and $\underline{\Omega}$. It can be reduced to the rotationally invariant form, $\sigma_s(\underline{r},\underline{\Omega}'\rightarrow\underline{\Omega})=\sigma_s(\underline{r},\underline{\Omega}'\bullet\underline{\Omega})$ in a few limited cases. This property precludes the use of Legendre polynomial expansion and the addition theorem typically used in transport theory for handling the scattering integral.

The scattering phase function combines diffuse scattering from the interior of a leaf and specular reflection from the leaf surface,

$$\Gamma(\underline{r},\underline{\Omega}'\rightarrow\underline{\Omega})=\Gamma_d(\underline{r},\underline{\Omega}'\rightarrow\underline{\Omega})+\Gamma_s(\underline{r},\underline{\Omega}'\rightarrow\underline{\Omega}).$$

The functions Γ_d and Γ_s are discussed below.

Area Scattering Phase Function for Diffuse Scattering: With the bi-Lambertian leaf scattering phase function introduced earlier [Eq. (9)], the diffuse area scattering phase function $\Gamma_d(\underline{r},\underline{\Omega}' \to \underline{\Omega}) = \Gamma_d(\underline{r},\underline{\Omega} \to \underline{\Omega}')$ may be written as,

$$\Gamma_d(\underline{r},\underline{\Omega}' \to \underline{\Omega}) = \rho_{L,d}\Gamma_d^-(\underline{r},\underline{\Omega}' \to \underline{\Omega}) + \tau_{L,d}\Gamma_d^+(\underline{r},\underline{\Omega}' \to \underline{\Omega}), \tag{16}$$

where,

$$\Gamma_d^{\pm}(\underline{\Omega}' \to \underline{\Omega}) = \pm\frac{1}{2\pi}\int_0^1 d\mu_L \int_0^{2\pi} d\varphi_L \; g_L(\mu_L,\varphi_L)\,(\underline{\Omega}\bullet\underline{\Omega}_L)\,(\underline{\Omega}'\bullet\underline{\Omega}_L)\,. \tag{17}$$

The ($\pm$) in the above definition indicates that the φ_L integration is over that portion of the interval $[0,2\pi]$ for which the integrand is either positive (+) or negative (–). The dependence on spatial point r is suppressed for clarity. The bi-Lambertian phase function imbues the area scattering phase function with a useful symmetry property,

$$\Gamma_d(\underline{\Omega}' \to \underline{\Omega}) = \Gamma_d(\underline{\Omega} \to \underline{\Omega}') = \Gamma_d(-\underline{\Omega}' \to -\underline{\Omega}).$$

For the special case of $\rho_{L,d} = \tau_{L,d}$, an additional symmetry holds,

$$\Gamma_d(\underline{\Omega}' \to \underline{\Omega}) = \Gamma_d(-\underline{\Omega}' \to \underline{\Omega}).$$

An expression for the diffuse area scattering phase function can be derived from Eqs. (16) and (17) in canopies with horizontal, vertical and uniformly distributed leaf normals. For horizontal leaves $\mu_L = 1$, one obtains,

$$\Gamma_d(\underline{\Omega}' \to \underline{\Omega}) = \begin{cases} \tau_{L,d}\,\mu\mu', & \mu\mu' > 0, \\ \rho_{L,d}\,|\mu\mu'|, & \mu\mu' < 0. \end{cases} \tag{18}$$

For vertical leaf orientations ($\mu_L = 0$)

$$\Gamma_d(\underline{\Omega}' \to \underline{\Omega}) = \Gamma_1(\beta)\sqrt{1-\mu^2}\,\sqrt{1-\mu'^2}\,, \tag{19}$$

where $\beta \equiv \varphi - \varphi'$; $0 \le \beta \le 2\pi$, and,

$$\Gamma_1(\beta) = \frac{\omega_{L,d}}{2\pi}(\sin\beta - \beta\cos\beta) + \frac{\tau_{L,d}}{2}\cos\beta.$$

In the case of spherically distributed leaf normals, the rotationally invariant scattering phase function is

$$\Gamma_d(\underline{\Omega}' \to \underline{\Omega}) = \frac{\omega_L}{3\pi}(\sin\beta - \beta\cos\beta) + \frac{\tau_L}{\pi}\cos\beta, \tag{20}$$

where $\beta \equiv \arccos(\underline{\Omega}' \bullet \underline{\Omega})$. This form of Γ_d is illustrated in Fig. 9.

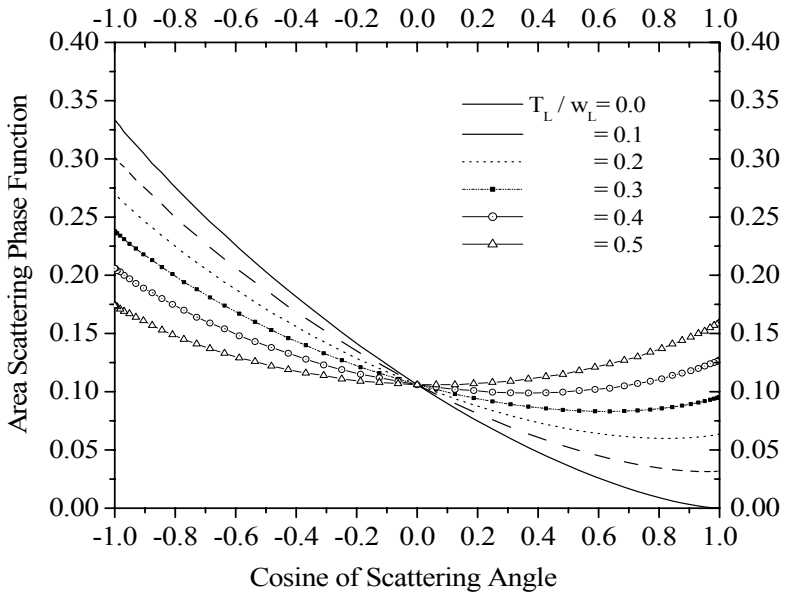

Figure 9. The area scattering phase function $\Gamma(\underline{\Omega}' \to \underline{\Omega})$ for uniformly distributed leaf normals. Each leaf is assumed to scatter according to the bi-Lambertian model. This function is rotationally invariant and in such cases the radiative transfer equation can be solved using standard methods developed in astrophysics and atmospheric physics.

In the general case of distributed leaf normals, the non-rotationally invariant form of the scattering kernel must be solved numerically [Eq. (17)]. Some simplifications are possible in the case of uniform distribution of leaf normal azimuths $h_L = 1$ and the bi-Lambertian leaf scattering phase function. This is achieved by azimuthal averaging of the scattering kernel,

$$\Gamma_d(\mu' \to \mu) = \frac{1}{2\pi}\int_0^{2\pi} d\varphi\, \Gamma_d(\underline{\Omega}' \to \underline{\Omega})$$

$$= \int_0^1 d\mu_L g_L(\mu_L)\left[\tau_{L,d}\Psi^+(\mu,\mu',\mu_L) + \rho_{L,d}\Psi^-(\mu,\mu',\mu_L)\right], \tag{21}$$

where

$$\Psi^{\pm}(\mu,\mu',\mu_L) = (\pm)\frac{1}{4\pi^2}\int_0^{2\pi} d\varphi \int_0^{2\pi} d\varphi_L (\underline{\Omega}' \bullet \underline{\Omega}_L)(\underline{\Omega} \bullet \underline{\Omega}_L). \tag{22}$$

The double integration over φ and φ_L for bi-Lambertian scattering distributions also eliminates φ'. Evaluation of the double integral in Eq. (22) gives [cf. Shultis and Myneni, 1988],

$$\Psi^{\pm}(\mu,\mu',\mu_L) = H(\mu,\mu_L)H(\pm\mu',\mu_L) + H(-\mu,\mu_L)H(\mp\mu',\mu_L), \tag{23}$$

where the H function is,

$$H(\mu,\mu_L)=\begin{cases}\mu\mu_L, & \text{if } (\cot\theta\cot\theta_L)>1,\\ 0, & \text{if } (\cot\theta\cot\theta_L)<-1,\\ \frac{1}{\pi}\left[\mu\mu_L\varphi_t(\mu)+\sqrt{1-\mu^2}\sqrt{1-\mu_L^2}\sin\varphi_t(\mu)\right], & \text{otherwise}\end{cases}$$

and,

$$\sin\varphi_t(\mu)=-\cot\theta\cot\theta_L=\pi-\varphi_t(-\mu).$$

The H function is shown in Fig. 10.

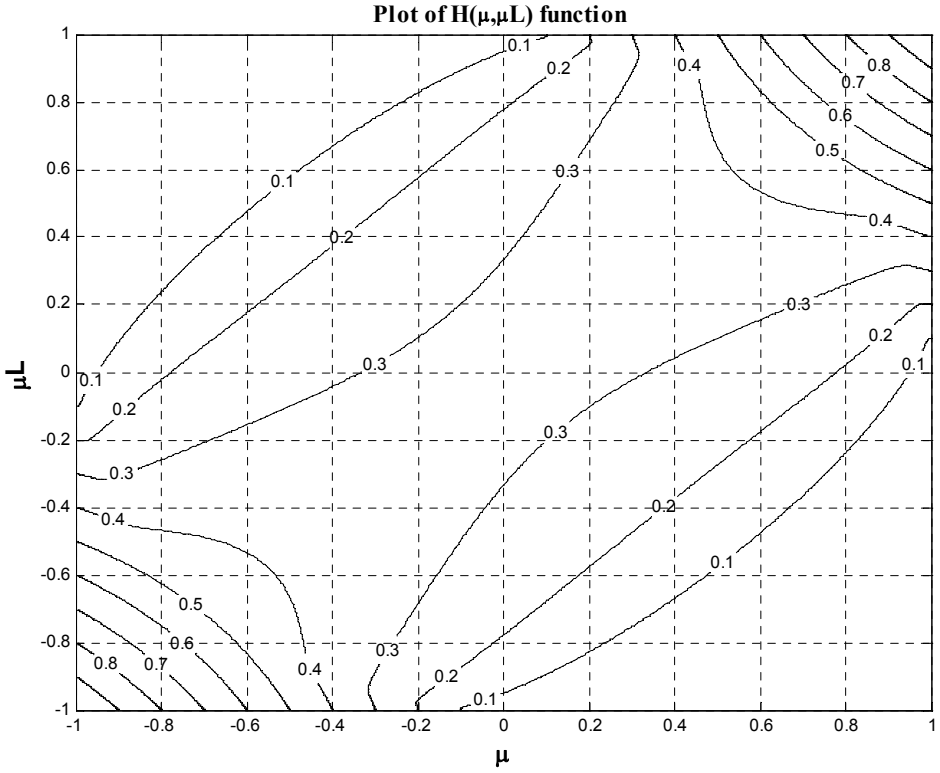

Figure 10. A contour plot of $H(\mu,\mu_L)$ function.

The azimuthally averaged area scattering phase function also possesses symmetry properties, namely,

$$\Gamma_d(\mu'\to\mu)=\Gamma_d(\mu\to\mu')=\Gamma_d(-\mu'\to-\mu).$$

For the special case of $\rho_{L,d}=\tau_{L,d}$, Eqs. (21) reduces to,

$$\Gamma_d(\mu' \to \mu) = \frac{\omega_{L,d}}{2}\int_0^1 d\mu_L g_L(\mu_L)\left[H(\mu,\mu_L) + H(-\mu,\mu_L)\right]\left[H(\mu',\mu_L) + H(-\mu',\mu_L)\right]$$

$$= \frac{\omega_{L,d}}{2}\int_0^1 d\mu_L g_L(\mu_L)\psi(\mu,\mu_L)\psi(\mu',\mu_L), \tag{24}$$

and an additional symmetry occurs, $\Gamma_d(\mu' \to \mu) = \Gamma_d(-\mu' \to -\mu)$. The function ψ in Eq. (24) is given in the Problem 8 of the Problems Sets Section). In the case of horizontal leaf orientation, the area scattering phase function is independent of exit azimuth [Eq. (18)]. However, in the case of vertical leaves, this is not so [Eq. (19)], and integration over φ from 0 to 2π or alternately over β from 0 to π results in,

$$\Gamma_d(\mu' \to \mu) = \frac{2\,\omega_{L,d}}{\pi^2}\sqrt{1-\mu^2}\sqrt{1-\mu'^2}. \tag{25}$$

The scattering coefficient for diffuse bi-Lambertian scattering from the leaf interior σ'_s has the explicit form [cf. Eq. (15), (10)],

$$\sigma'_s(\underline{r},\underline{\Omega}') = u_L(\underline{r})\frac{1}{\pi}\int_{4\pi} d\underline{\Omega}\,\Gamma_d(\underline{\Omega}' \to \underline{\Omega})$$

$$= u_L(\underline{r})\,\omega_{L,d}G(\underline{\Omega}'). \tag{26}$$

The normalized scattering phase function $(1/4\pi)P_d$ is therefore,

$$P_d(\underline{\Omega}' \to \underline{\Omega}) = \frac{4\Gamma_d(\underline{\Omega}' \to \underline{\Omega})}{\omega_{L,d}G(\underline{\Omega}')}, \tag{27}$$

such that,

$$\frac{1}{4\pi}\int_{4\pi} d\underline{\Omega}\,P_d(\underline{\Omega}' \to \underline{\Omega}) = 1.$$

The normalized scattering phase function $P_d(\underline{\Omega}' \to \underline{\Omega})$ for planophile leaf normal inclination distribution and bi-Lambertian leaf scattering distribution is shown in Fig. 11. It is clear that the scattering phase functions in leaf canopies are non-rotationally invariant, that is, they are not unique functions of $(\underline{\Omega}' \bullet \underline{\Omega})$.

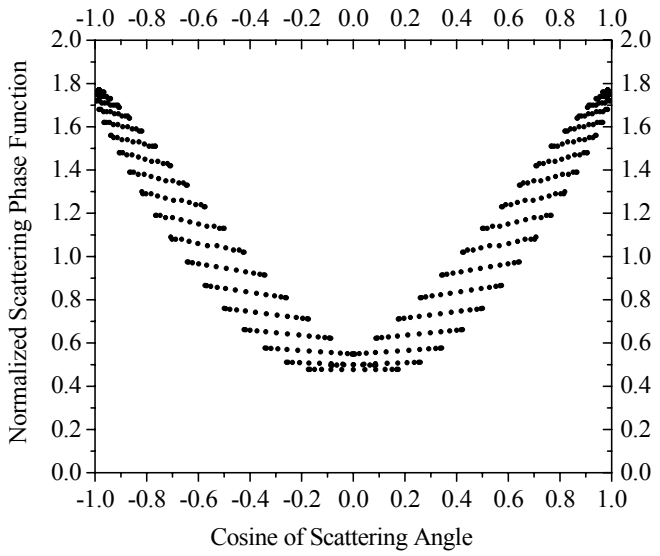

Figure 11. The normalized azimuthally dependent phase function $P(\underline{\Omega}' \rightarrow \underline{\Omega})$ for a planophile canopy [predominantly horizontal leaves]. The leaf transmittance and reflectance are both equal to 0.5, and $\underline{\Omega}'$ is fixed at $\theta' = 170^0$ and $\varphi = 0^0$. Each dot is the value of the phase function for a discrete value of $\Omega_{ij} = (\mu_i, \varphi_j)$ [the nearly horizontal row of dots is for a fixed μ_i and $, \varphi_j$ varies]. These results illustrate that the phase function is non rotationally invariant, i.e., it depends on the coordinates $\underline{\Omega}'$ and $\underline{\Omega}$ and not just on the scattering angle [acos $(\underline{\Omega} \bullet \underline{\Omega}')$].

Area Scattering Phase Function for Specular Reflection: Using the model described earlier [Eq. (10)] for specular reflection from leaf surfaces, the area scattering phase function for specular reflection can be evaluated as (cf. $d\underline{\Omega}_L = d\underline{\Omega}^*/4|\underline{\Omega}' \bullet \underline{\Omega}_L|$),

$$\begin{aligned}
\frac{1}{\pi}\Gamma_s(\underline{\Omega}' \rightarrow \underline{\Omega}) &= \frac{1}{2\pi}\int_{2\pi+} d\underline{\Omega}_L \; g_L(\underline{\Omega}_L)\,|\underline{\Omega}' \bullet \underline{\Omega}_L|\,\gamma_{L,s}(\underline{\Omega}' \rightarrow \underline{\Omega}, \underline{\Omega}_L) \\
&= \frac{1}{8\pi}\int_{4\pi} d\underline{\Omega}^* \; g_L(\underline{\Omega}_L)\,K(\kappa, \alpha')\,F_r(n, \alpha')\,\delta_2(\underline{\Omega} \bullet \underline{\Omega}^*) \\
&= \frac{1}{8\pi} g_L(\underline{\Omega}_L^*)\,K(\kappa, \alpha^*)\,F_r(n, \alpha^*) \qquad (28)
\end{aligned}$$

where $\Omega_L^* = \Omega_L^*(\underline{\Omega}', \underline{\Omega})$ defines leaf normals condusive for specular reflection given the incident and exit photon directions.

The scattering coefficient for specular reflection from the leaf surface σ_s' has the form,

$$\begin{aligned}
\sigma_s'(\underline{r}, \underline{\Omega}') &= u_L(\underline{r})\,\frac{1}{\pi}\int_{4\pi} d\underline{\Omega}\;\Gamma_s(\underline{\Omega}' \rightarrow \underline{\Omega}), \\
&= u_L(\underline{r})\,\frac{1}{2\pi}\int_{2\pi+} d\underline{\Omega}_L \; g_L(\underline{\Omega}_L)\,|\underline{\Omega}' \bullet \underline{\Omega}_L|\,K(\kappa(\alpha')\,F_r(n, \alpha'), \qquad (29) \\
&= u_L(\underline{r})\,\Gamma_s(\underline{\Omega}').
\end{aligned}$$

The normalized scattering phase function is therefore,

$$P_s(\underline{\Omega}' \to \underline{\Omega}) = \frac{4\Gamma_s(\underline{\Omega}' \to \underline{\Omega})}{G_s(\underline{\Omega}')}, \tag{30}$$

such that,

$$\frac{1}{4\pi} \int_{4\pi} d\underline{\Omega}\, P_s(\underline{\Omega}' \to \underline{\Omega}) = 1.$$

Problem Sets

- **Problem 1.** Let $f(\gamma)$, $-1 \le \gamma \le 1$, be a function of one variable; $\underline{\Omega} \equiv (\theta, \varphi)$ and $\underline{\Omega}_L \equiv (\theta_L, \varphi_L)$ are two unit vectors. Show that

$$\int_{2\pi^+} f(\underline{\Omega}_L \bullet \underline{\Omega})\, d\underline{\Omega} = 4\pi\, q(\sin\theta_L).$$

  Here $\underline{\Omega} \bullet \underline{\Omega}_L$ is the scalar product of two vectors, and q(x), $0 \le x \le 1$, is a function of one variable defined as

$$q(x) = \frac{1}{2}\int_x^1 f(\gamma)d\gamma + \frac{1}{2}\int_0^x [\alpha(\gamma, x)f(\gamma) + \beta(\gamma, x)f(-\gamma)]d\gamma,$$

  where $\alpha(\gamma, x) + \beta(\gamma, x) = 1$, and

$$\beta(\gamma, x) = \frac{1}{\pi}\arccos\frac{\gamma\sqrt{1-x^2}}{x\sqrt{1-\gamma^2}}.$$

- **Problem 2.** Letting $f(\gamma) = |\gamma|$, show that

$$\int_{2\pi^+} |\underline{\Omega}_L \bullet \underline{\Omega}|\, d\underline{\Omega} = \pi.$$

- **Problem 3.** Show that the leaf albedo for the bi-Lambertian model is

$$\int_{4\pi} d\underline{\Omega}\, \gamma_{L,d}(\underline{\Omega}' \to \underline{\Omega}, \underline{\Omega}_L) = \rho_{L,d} + \tau_{L,d}.$$

- **Problem 4.** Prove (14).

- **Problem 5.** Show that the geometry factor $G(\underline{r}, \underline{\Omega})$ for spherically distributed leaf normals depends neither $\underline{r}$ nor $\underline{\Omega}$ and is equal to 0.5.

- **Problem 6.** Show that $G = \mu$ for horizontal leaves, and $G = (2/\pi)\sin\theta$ for vertical leaves.

- **Problem 7.** Let the polar angle, θ_L, and azimuth, φ_L, of leaf normals are independent (see Eq. 3). Show that

$$G(\underline{r},\mu) = \int_0^1 d\mu_L \, \overline{g}_L(\underline{r},\mu_L)\,\psi(\mu,\mu_L),$$

where $\mu_L = \cos\theta_L$, $\mu = \cos\theta$, and

$$\psi(\mu,\mu_L) = \frac{1}{2\pi}\int_0^{2\pi} h(\varphi_L)\,|\underline{\Omega}\bullet\underline{\Omega}_L|\,d\varphi_L\ .$$

- **Problem 8.** Show that in canopies where leaf normals are distributed uniformly along the azimuthal coordinate [i.e., $h(\varphi_L) = 1$], $\psi(\mu,\mu_L)$ can be reduced to

$$\psi(\mu,\mu_L) = \begin{cases} |\mu\mu_L|, & \text{if } |\mu\mu_L| \geq |\sin\theta\sin\theta_L|, \\ \mu\mu_L(2\varphi_t/\pi - 1) + (2/\pi)\sqrt{1-\mu^2}\sqrt{1-\mu_L^2}\,\sin\varphi_t, & \text{otherwise,} \end{cases}$$

where the branch angle φ_t is $\arccos(-\cot\theta\times\cot\theta_L)$.

- **Problem 9.** Show that in canopies with constant leaf normal inclination but uniform orientation along the azimuth [cf. Eq. (4)], $G(\mu) = \psi(\mu,\mu_L)$.

- **Problem 10.** Using Eq. (6), derive the $\psi(\mu,\mu_L)$ in the case of heliotropic orientations.

- **Problem 11.** Given the direction of incoming, $\underline{\Omega}$, and reflected, $\underline{\Omega}'$, fluxes at the leaf surface ($\|\underline{\Omega}\| = \|\underline{\Omega}'\| = 1$) show that the direction of leaf normals $\underline{n}_L(\mu_L,\varphi_L)$ in the case of specular reflection is given by

$$\mu_L = \frac{|\mu' - \mu|}{\sqrt{2(1-\underline{\Omega}'\bullet\underline{\Omega})}}$$

$$\tan\varphi_L = \frac{\sqrt{1-\mu'^2}\,\sin\varphi' - \sqrt{1-\mu^2}\,\sin\varphi}{\sqrt{1-\mu'^2}\,\cos\varphi' - \sqrt{1-\mu^2}\,\cos\varphi}$$

References

Allen W.A., H.W. Gausman, A.J. Richardson, and J.R. Thomas (1969). Interaction of isotropic light with a compact leaf. *J. Opt. Soc. Amer.*. **59**, 1376-1379.

Bunnik, N.J.J. (1978). The multispectral reflectance of shortwave radiation by agricultural crops in relation with their morphological and optical properties. Pudoc Publications, Wageningen, The Netherlands.

Goel, N.S. and D.E. Strebel, (1984). Simple Beta distribution representation of leaf orientation in vegetation canopies. *Agron, J*., **76**, 800-802.

Jacquemoud S. and F. Baret F. (1990). PROSPECT: a model of leaf optical properties spectra. *Remote Sens. Environ.,* 34:75-91.

Knyazikhin, Y., J.Kranigk, G. Miessen, O. Panfyorov, N. Vygodskaya, and G. Gravenhorst (1996). Modeling three-dimensional distribution of photosynthetically active radiation in sloping coniferous stands, *Biomass and Bioenergy*. **11**, 2/3: 189-200.

Knyazikhin, Y., J.V., Martonchik, R.B. Myneni, D.J. Diner, and S.W. Running (1998). Synergistic algorithm for estimating vegetation canopy leaf area index and fraction of absorbed photosynthetically active radiation from MODIS and MISR data. *J. Geophys. Res*., **103,** 32257-32275.

Lang, A.R.G. (1991). Application of some of Cauchy's theorems to estimation of surface areas of leaves, needles and branches of plants, and light transmittance. *Agric. For. Meteorol*. **55**,191-212.

Oker-Blom, P. and S. Kellomäki (1982). Effect of angular distribution of foliage on light absorption and photosynthesis in the plant canopy: Theoretical computations. *Agric. For. Meteorol*. **26**, 105-116.

Oker-Blom, P. and H. Smolander (1988). The ratio of shoot silhouette area to total needle area in Scots pine. *Forest Science* **34**, 894-906.

Ross, J. (1981). *The Radiation Regime and Architecture of Plant Stands*. Dr. W. Junk Publishers, Delft, The Netherlands.

Shultis, K.S. and R.B. Myneni (1988). Radiative transfer in vegetation canopies with anisotropic scattering. *J. Quant. Spectroscp. Radiat. Trans*., **39**, 115-129.

Stenberg, P. (1996). Simulations of the effects of shoot structure and orientation on vertical gradients in intercepted light by conifer canopies. *Tree Physiology,* **16**, 99-108.

Vanderbilt, V.C., L. Grant, and S.L. Ustin (1991). Polarization of light by vegetation. In *Photon-Vegetation Interactions: Applications in Optical remote Sensing and Plant Ecology*, R.B. Myneni and J. Ross (eds.), Springer Verlag, Berlin Heildelberg, pp. 191-228.

Verstrate, M.M. (1987). Radiation transfer in plant canopies: transmission of direct solar radiation and the role of leaf orientation. *J. Geophys. Res*., **92,** 10985-10995.

Further Readings

Myneni, R.B., J. Ross, and G. Asrar (1989). A review on the theory of photon transport in leaf canopies. *Agric. For. Meteorol*., **45**, 1-153.

Ross, J. (1981). *The Radiation Regime and Architecture of Plant Stands*. Dr. W. Junk Publishers, Delft, The Netherlands.

Myneni, R.B. and J. Ross (eds.) (1991). *Photon-Vegetation Interactions: Applications in Optical remote Sensing and Plant Ecology*, Springer Verlag, Berlin Heildelberg.

Chapter 2 Derivations by Shabanov et al.

Problem 1. Let $f(\gamma)$, $-1 \le \gamma \le 1$, be a function of one variable, $\underline{\Omega} \equiv (\theta, \varphi)$ and $\underline{\Omega}_L \equiv (\theta_L, \varphi_L)$ are two unit vectors. Show that

$$\int_{2\pi^+} f(\underline{\Omega}_L \bullet \underline{\Omega})\, d\underline{\Omega} = 4\pi\, q(\sin\theta_L)\,.$$

Here $\underline{\Omega} \bullet \underline{\Omega}_L$ is the scalar product of two vectors, and q(x), $0 \le x \le 1$, is a function of one variable defined as

$$q(x) = \frac{1}{2}\int_x^1 f(\gamma)d\gamma + \frac{1}{2}\int_0^x [\alpha(\gamma, x)f(\gamma) + \beta(\gamma, x)f(-\gamma)]d\gamma\,,$$

where $\alpha(\gamma, x) + \beta(\gamma, x) = 1$, and

$$\beta(\gamma, x) = \frac{1}{\pi}\arccos\frac{\gamma\sqrt{1-x^2}}{x\sqrt{1-\gamma^2}}\,.$$

Solution. Let

$$g(\underline{\Omega}_L) \equiv \int_{2\pi^+} f(\underline{\Omega}_L \bullet \underline{\Omega})\, d\underline{\Omega}\,. \tag{1}$$

In the following derivations we assume that $\varphi_L = 0$, that is, vector $\underline{\Omega}_L$ belongs to ZX plane. This assumption does not limit the generality of the derivations as one always can substitute φ with $(\varphi - \varphi_L)$ without changing the domain of the integration (i.e., the upper hemisphere). For convenience of derivations let us transform the original system of coordinates to a new one, where $\underline{\Omega}_L$ is aligned with Z-direction (Fig. 1). This can be accomplished with rotation by angle $-\theta_L$ around the Y-axis as specified with the following linear transform,

$$\underline{R}' \equiv \hat{A}(-\theta_L)\,\underline{R},$$

where

$$\hat{A}(-\theta_L) \equiv \begin{bmatrix} \cos\theta_L & 0 & -\sin\theta_L \\ 0 & 1 & 0 \\ \sin\theta_L & 0 & \cos\theta_L \end{bmatrix}$$

and $\underline{R} = (x, y, z)$ and $\underline{R}' = (x', y', z')$ are vectors in the original and new coordinate system, respectively. Note the minus sign for angle θ_L. This is due to the fact that positive angles are counted *outward from* Z-direction. One example of transformation is for the Z-axis, which is

transformed from $\underline{Z} = (0,0,1)$ in the original system into $\underline{Z'} = (-\sin\theta_L,\ 0,\ \cos\theta_L)$ in the new system.

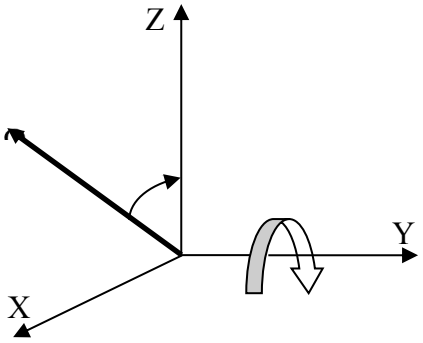

Figure. 1 Coordinate system transform via rotation by angle $-\theta_L$ around the Y-axis.

To determine the integration domain in the new coordinate system, let $\underline{v} = (\sin\theta\cos\varphi,\ \sin\theta\sin\varphi,\ \cos\theta)$ be a unit vector in the new system. The $\underline{v}$ vector falls into the upper hemisphere of the original system if and only if

$$\underline{v} \bullet \underline{z'} \equiv -\sin\theta_L \cdot \sin\theta\cos\varphi + 0 \cdot \sin\theta\sin\varphi + \cos\theta_L \cdot \cos\theta \geq 0.$$

Therefore,

$$\cos\varphi \leq \frac{\cos\theta_L \cos\theta}{\sin\theta_L \sin\theta}. \tag{2}$$

Note that the angular domain of the upper hemisphere in the original coordinate system is $\theta \in [0,\pi]$ and $\varphi \in [0,2\pi]$. This domain is specified differently in the new coordinate system as shown in Fig. 2. Namely, three sectors with respect to θ can be identified: $\theta \in [0, \pi/2 - \theta_L]$ (shown in Red), $\theta \in [\pi/2 - \theta_L, \pi/2 + \theta_L]$ (shown in green), and $\theta \in [\pi/2 + \theta_L, \pi]$ (shown in blue). The corresponding variations of φ can be derived from the algebraic analysis of Eq. (2). The final expression for the angular domain in the new coordinate system is:

$$\begin{cases} \dfrac{\cos\theta_L \cos\theta}{\sin\theta_L \sin\theta} > 1, & \theta \in [0, \dfrac{\pi}{2} - \theta_L), \\ & \varphi \in [0,\ 2\pi]; \\ -1 \leq \dfrac{\cos\theta_L \cos\theta}{\sin\theta_L \sin\theta} \leq 1, & \theta \in [\dfrac{\pi}{2} - \theta_L, \dfrac{\pi}{2} + \theta_L], \\ & \varphi \in [\arccos\dfrac{\cos\theta_L \cos\theta}{\sin\theta_L \sin\theta},\ 2\pi - \arccos\dfrac{\cos\theta_L \cos\theta}{\sin\theta_L \sin\theta}]; \\ \dfrac{\cos\theta_L \cos\theta}{\sin\theta_L \sin\theta} < -1, & \theta \in (\dfrac{\pi}{2} + \theta_L, \pi], \\ & \varphi \in \varnothing. \end{cases} \tag{3}$$

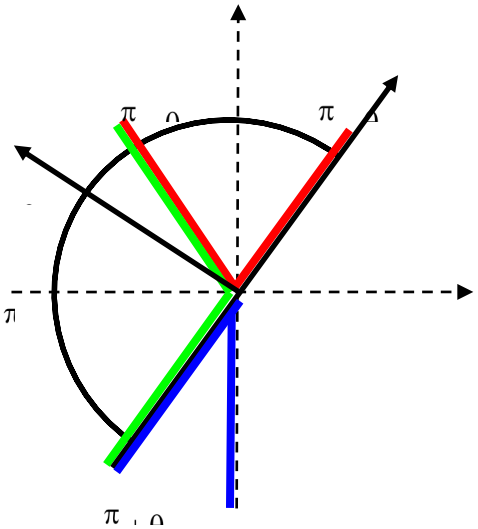

Figure. 2 The upper hemisphere of the original system of coordinates XYZ in a new system of coordinates $X'Y'Z'$. Vector $\underline{\Omega}_L$ is aligned with axis Z' of the new system.

In a view that in the new coordinate system the direction $\underline{\Omega}_L$ coincides with Z', the argument of function $f(\underline{\Omega}_L \bullet \underline{\Omega})$ in Eq. (1) simplifies, i.e., $\underline{\Omega}_L \bullet \underline{\Omega} = \cos\theta$. Therefore,

$$g(\underline{\Omega}_L) \equiv \int_{2\pi^+} f(\underline{\Omega}_L \bullet \underline{\Omega})\, d\underline{\Omega} = \int_{\cos\varphi \le \frac{\cos\theta_L \cos\theta}{\sin\theta_L \sin\theta}} f(\cos\theta)\, d\underline{\Omega}$$

$$= \int_0^{\frac{\pi}{2}-\theta_L} f(\cos\theta)(-d\cos\theta) \int_0^{2\pi} d\varphi + \int_{\frac{\pi}{2}-\theta_L}^{\frac{\pi}{2}+\theta_L} f(\cos\theta)(-d\cos\theta) \int_{\arccos\left(\frac{\cos\theta_L \cos\theta}{\sin\theta_L \sin\theta}\right)}^{2\pi-\arccos\left(\frac{\cos\theta_L \cos\theta}{\sin\theta_L \sin\theta}\right)} d\varphi$$

$$= 2\pi \int_{\theta_L}^{\frac{\pi}{2}} f(\sin\theta)\, d(\sin\theta)$$

$$+ \int_0^{\theta_L} f(\sin\theta) \left[2\pi - 2\arccos\left(\frac{\cos\theta_L \cos\theta}{\sin\theta_L \sin\theta} \right) \right] d(\sin\theta)$$

$$+ \int_0^{\theta_L} f(-\sin\theta) \left[2\arccos\left(\frac{\cos\theta_L \cos\theta}{\sin\theta_L \sin\theta} \right) \right] d(\sin\theta). \qquad (4)$$

Note that in the last step of derivations we substituted θ with $\pi/2 - \theta$, and accounted for the fact that $\cos\theta = \sin(\pi/2 - \theta)$, $\sin\theta = \cos(\pi/2 - \theta)$, and $\arccos(-\psi) = \pi - \arccos(\psi)$. Finally, let $x = \sin(\theta_L)$, $\gamma = \sin(\theta)$, and

$$\beta(\gamma, x) = \frac{1}{\pi} \arccos\left(\frac{\cos\theta_L \sin\theta}{\sin\theta_L \cos\theta} \right) = \frac{1}{\pi} \arccos \frac{\gamma\sqrt{1-x^2}}{x\sqrt{1-\gamma^2}},$$

$$\alpha(\gamma, x) = 1 - \beta(\gamma, x).$$

Substituting the new variables in Eq. (4) and changing the limits of integration according to the variable γ, we finally have

$$g(\underline{\Omega}_L) = 2\pi\int_x^1 f(\gamma)d\gamma + 2\pi\int_0^x [\alpha(\gamma, x)f(\gamma) + \beta(\gamma, x)f(-\gamma)]d\gamma = 4\pi q(x).$$

Problem 2. Letting $f(\gamma) = |\gamma|$, show that

$$\int_{2\pi^+} |\underline{\Omega}_L \bullet \underline{\Omega}| d\underline{\Omega} = \pi.$$

Solution. According to the results of Problem 1

$$\int_{2\pi^+} |\underline{\Omega}_L \bullet \underline{\Omega}| d\underline{\Omega} \equiv \int_{2\pi^+} f(|\gamma|) d\underline{\Omega} = 4\pi \frac{1}{2}\left[\int_x^1 \gamma d\gamma + \int_0^z [\alpha(\gamma, x) + \beta(\gamma, x)]\gamma d\gamma\right].$$

Taking into account that $\alpha(\lambda, x) + \beta(\lambda, x) = 1$ (cf. Problem 1), we have

$$\int_{2\pi^+} |\underline{\Omega}_L \bullet \underline{\Omega}| d\underline{\Omega} = 2\pi\left[\int_x^1 \gamma\, d\gamma + \int_0^z \gamma\, d\gamma\right] = 2\pi\int_0^1 \gamma\, d\gamma = \pi.$$

Problem 3. Show that the leaf albedo for the bi-Lambertian model is

$$\int_{4\pi} d\underline{\Omega}\, \gamma_{L,d}(\underline{\Omega}' \to \underline{\Omega}, \underline{\Omega}_L) = \rho_{L,d} + \tau_{L,d}.$$

Solution. The bi-Lambertian model for diffuse leaf scattering phase function is,

$$\gamma_{L,d}(\underline{\Omega}' \to \underline{\Omega}, \underline{\Omega}_L) = \begin{cases} \frac{1}{\pi}\rho_{L,d}|\underline{\Omega} \bullet \underline{\Omega}_L|, & (\underline{\Omega} \bullet \underline{\Omega}_L)(\Omega' \bullet \underline{\Omega}_L) < 0, \\ \frac{1}{\pi}\tau_{L,d}|\underline{\Omega} \bullet \underline{\Omega}_L|, & (\underline{\Omega} \bullet \underline{\Omega}_L)(\underline{\Omega}' \bullet \underline{\Omega}_L) > 0. \end{cases} \quad (1)$$

Note that the angles $\underline{\Omega}'$ and $\underline{\Omega}_L$ are fixed in the integral of interests and integration over whole sphere can be spitted into two parts, namely,

$$\int_{4\pi} d\underline{\Omega}\, \gamma_{L,d}(\underline{\Omega}' \to \underline{\Omega}, \underline{\Omega}_L)$$

$$= \int\limits_{(\underline{\Omega}\bullet\underline{\Omega}_L)(\underline{\Omega}'\bullet\underline{\Omega}_L)>0} d\underline{\Omega} \quad \gamma_{L,d}(\underline{\Omega}' \to \underline{\Omega}, \underline{\Omega}_L) + \int\limits_{(\underline{\Omega}\bullet\underline{\Omega}_L)(\underline{\Omega}'\bullet\underline{\Omega}_L)<0} d\underline{\Omega} \quad \gamma_{L,d}(\underline{\Omega}' \to \underline{\Omega}, \underline{\Omega}_L). \tag{2}$$

Taking into account Eq. (1), we have

$$\int\limits_{(\underline{\Omega}\bullet\underline{\Omega}_L)(\underline{\Omega}'\bullet\underline{\Omega}_L)>0} d\underline{\Omega} \quad \gamma_{L,d}(\underline{\Omega}' \to \underline{\Omega}, \underline{\Omega}_L) = \frac{1}{\pi}\tau_{L,d} \int\limits_{(\underline{\Omega}\bullet\underline{\Omega}_L)(\underline{\Omega}'\bullet\underline{\Omega}_L)>0} d\underline{\Omega} \quad \left|\underline{\Omega}\bullet\underline{\Omega}_L\right|, \tag{3a}$$

$$\int\limits_{(\underline{\Omega}\bullet\underline{\Omega}_L)(\underline{\Omega}'\bullet\underline{\Omega}_L)<0} d\underline{\Omega} \quad \gamma_{L,d}(\underline{\Omega}' \to \underline{\Omega}, \underline{\Omega}_L) = \frac{1}{\pi}\rho_{L,d} \int\limits_{(\underline{\Omega}\bullet\underline{\Omega}_L)(\underline{\Omega}'\bullet\underline{\Omega}_L)<0} d\underline{\Omega} \quad \left|\underline{\Omega}\bullet\underline{\Omega}_L\right|. \tag{3b}$$

In view that the angles $\underline{\Omega}'$ and $\underline{\Omega}_L$ are fixed, the integrals on the right hand side of Eqs. (3a) and (3b) are identical and equal to the integral over hemisphere ($2\pi^+$ or $2\pi^-$). The last integral was evaluated in the Problem 2, namely,

$$\int\limits_{2\pi^+} d\underline{\Omega} \left|\underline{\Omega}\bullet\underline{\Omega}_L\right| = \pi. \tag{4}$$

Combining Eqs. (2)-(4) we finally have

$$\int\limits_{4\pi} d\underline{\Omega}\, \gamma_{L,d}(\underline{\Omega}' \to \underline{\Omega}, \underline{\Omega}_L) = \frac{1}{\pi}\tau_{L,d}\pi + \frac{1}{\pi}\rho_{L,d}\pi = \tau_{L,d} + \rho_{L,d}.$$

Problem 5. Prove

$$\frac{1}{2\pi}\int\limits_{2\pi^+} d\underline{\Omega}\, G(\underline{r}, \underline{\Omega}) = \frac{1}{2}, \tag{1}$$

Solution. Note,

$$G(\underline{r}, \underline{\Omega}) = \frac{1}{2\pi}\int\limits_{2\pi^+} d\underline{\Omega}_L \; g_L(\underline{\Omega}_L)\left|\underline{\Omega}_L \bullet \underline{\Omega}\right|, \tag{2a}$$

$$\frac{1}{2\pi}\int\limits_{2\pi+} d\underline{\Omega}_L \; g_L(\underline{\Omega}_L) = 1. \tag{2b}$$

Combining Eq. (1)-(2) and result of Problem 2, we have

$$\frac{1}{2\pi}\int\limits_{2\pi^+} d\underline{\Omega}\, G(\underline{r}, \underline{\Omega})$$

$$= \frac{1}{2\pi} \int_{2\pi^+} d\underline{\Omega} \, \frac{1}{2\pi} \int_{2\pi^+} d\underline{\Omega}_L \; g_L(\underline{\Omega}_L) \left| \underline{\Omega}_L \bullet \underline{\Omega} \right|$$

$$= \frac{1}{4\pi^2} \int_{2\pi^+} d\underline{\Omega}_L \; g_L(\underline{\Omega}_L) \int_{2\pi^+} d\underline{\Omega} \left| \underline{\Omega}_L \bullet \underline{\Omega} \right|$$

$$= \frac{1}{4\pi^2} 2\pi \cdot \pi = \frac{1}{2}.$$

Problem 6. Show that the geometry factor $G(\underline{r}, \underline{\Omega})$ for spherically distributed leaf normals depends neither $\underline{r}$ nor $\underline{\Omega}$ and is equal to 0.5.

Solution. Recall,

$$G(\underline{r}, \underline{\Omega}) = \frac{1}{2\pi} \int_{2\pi^+} d\underline{\Omega}_L \; g_L(\underline{\Omega}_L) \left| \underline{\Omega}_L \bullet \underline{\Omega} \right|.$$

Recall also, that for spherically distributed leaf normals $g_L(\underline{\Omega}_L) = 1$. Combining this result with the result of the Problem 2, we have

$$G(\underline{r}, \underline{\Omega}) = \frac{1}{2\pi} \int_{2\pi^+} d\underline{\Omega}_L \left| \underline{\Omega}_L \bullet \underline{\Omega} \right| = \frac{1}{2\pi} \cdot \pi = \frac{1}{2}.$$

Problem 7. Show that $G = \mu$ for horizontal leaves, and $G = (2/\pi)\sin\theta$ for vertical leaves.

Solution. Recall,

$$G(\underline{r}, \underline{\Omega}) = \frac{1}{2\pi} \int_{2\pi^+} d\underline{\Omega}_L \; g_L(\underline{\Omega}_L) \left| \underline{\Omega}_L \bullet \underline{\Omega} \right|.$$

Further, let $\underline{\Omega} = (\sin\theta\cos\varphi, \sin\theta\sin\varphi, \cos\theta)$ and $\underline{\Omega}_L = (\sin\theta_L \cos\varphi_L, \sin\theta_L \sin\varphi_L, \cos\theta_L)$. Therefore,

$$\begin{aligned} \underline{\Omega}_L \bullet \underline{\Omega} &= (\sin\theta_L \cos\varphi_L) \cdot (\sin\theta\cos\varphi) + (\sin\theta_L \sin\varphi_L) \cdot (\sin\theta\sin\varphi) + (\cos\theta_L) \cdot (\cos\theta) \\ &= \sin\theta_L \sin\theta \cdot \cos(\varphi_L - \varphi) + \cos\theta_L \cos\theta. \end{aligned}$$

For *horizontal leaves* the derivations for $G(\underline{r}, \underline{\Omega})$ are as follows. The probability density of leaf normal orientation is

$$g_L(\underline{\Omega}_L) = \frac{\delta(\theta_L - 0)}{\sin\theta_L}.$$

Therefore,

$$G(\underline{r},\underline{\Omega}) = \frac{1}{2\pi}\int_0^{\pi/2} \sin\theta_L d\theta_L \int_0^{2\pi} d\varphi_L\, g_L(\underline{\Omega}_L)\left|\underline{\Omega}_L \bullet \underline{\Omega}\right|$$

$$= \frac{1}{2\pi}\int_0^{\pi/2} d\theta_L \int_0^{2\pi} d\varphi_L \sin\theta_L \frac{\delta(\theta_L - 0)}{\sin\theta_L}\left|\sin\theta_L \sin\theta\cdot\cos(\varphi_L - \varphi) + \cos\theta_L \cos\theta\right|$$

$$= \left|\cos\theta\right| \equiv \mu.$$

Similar derivations can be performed for *vertical leaves*. In this case the probability density of leaf normal orientation is

$$g_L(\underline{\Omega}_L) = \frac{\delta(\theta_L - \pi/2)}{\sin\theta_L}.$$

Therefore,

$$G(\underline{r},\underline{\Omega}) = \frac{1}{2\pi}\int_0^{\pi/2} d\theta_L \int_0^{2\pi} d\varphi_L \sin\theta_L \frac{\delta(\theta_L - \pi/2)}{\sin\theta_L}\left|\sin\theta_L \sin\theta\cdot\cos(\varphi_L - \varphi) + \cos\theta_L \cos\theta\right|$$

$$= \frac{1}{2\pi}\int_0^{2\pi} d\varphi_L \left|1\cdot\sin\theta\cdot\cos(\varphi_L - \varphi) + 0\right| = \frac{2}{\pi}\left|\sin\theta\right|.$$

Problem 8. Let the polar angle, θ_L, and azimuth, φ_L, of leaf normals be independent. Show that

$$G(\underline{r},\mu) = \int_0^1 d\mu_L \bar{g}_L(\underline{r},\mu_L)\psi(\mu,\mu_L),$$

where $\mu_L = \cos\theta_L$, $\mu = \cos\theta$, and

$$\psi(\mu,\mu_L) = \frac{1}{2\pi}\int_0^{2\pi} h_L(\varphi_L)\,|\,\underline{\Omega}\bullet\underline{\Omega}_L\,|\,d\varphi_L\ .$$

Solution. Since the polar angle, θ_L, and azimuth angle, φ_L, of leaf normals are independant, the following representation of the probability density of leaf normal orientation is valid:

$$g_L(\underline{\Omega}_L) = \bar{g}_L(\mu_L)\, h_L(\varphi_L),$$

where $\bar{g}_L(\mu_L)$ and $h_L(\varphi_L)/2\pi$ are the probability density functions of leaf normal inclination and azimuth, respectively. Therefore,

$$\begin{aligned} G(\underline{r},\mu_L) &= \frac{1}{2\pi}\int_{2\pi^+} d\underline{\Omega}_L\; g_L(\underline{r},\underline{\Omega}_L)\left|\underline{\Omega}_L \bullet \underline{\Omega}\right| \\ &= \frac{1}{2\pi}\int_0^1 d\mu_L \int_0^{2\pi} d\varphi_L\, \bar{g}_L(\underline{r},\mu_L)\, h_L(\varphi_L)\left|\underline{\Omega}_L \bullet \underline{\Omega}\right| \\ &= \frac{1}{2\pi}\int_0^1 d\mu_L\, \bar{g}_L(\underline{r},\mu_L)\int_0^{2\pi} d\varphi_L\, h_L(\varphi_L)\left|\underline{\Omega}_L \bullet \underline{\Omega}\right| \\ &= \frac{1}{2\pi}\int_0^1 d\mu_L\, \bar{g}_L(\underline{r},\mu_L)\,\psi(\mu,\mu_L). \end{aligned}$$

Problem 9. Show that in canopies where leaf normals are distributed uniformly along the azimuthal coordinate [i.e., $h_L(\varphi_L) = 1$], $\psi(\mu,\mu_L)$ can be reduced to

$$\psi(\mu,\mu_L) = \begin{cases} |\mu\,\mu_L|, & \text{if } |\mu\,\mu_L| \geq |\sin\theta \sin\theta_L|, \\ \mu\mu_L(2\varphi_t/\pi - 1) + (2/\pi)\sqrt{1-\mu^2}\,\sqrt{1-\mu_L^2}\,\sin\varphi_t, & \text{otherwise,} \end{cases}$$

where the branch angle φ_t is $\arccos(-\cot\theta \times \cot\theta_L)$.

Solution. Recall (cf. Problem 6),

$$\underline{\Omega}_L \bullet \underline{\Omega} = \sin\theta_L \sin\theta \cdot \cos(\varphi_L - \varphi) + \cos\theta_L \cos\theta.$$

Therefore,

$$\begin{aligned} \psi(\mu,\mu_L) &\equiv \frac{1}{2\pi}\int_0^{2\pi} d\varphi_L\, h_L(\varphi_L)\left|\underline{\Omega}_L \bullet \underline{\Omega}\right| \\ &= \frac{1}{2\pi}\int_0^{2\pi} d\varphi_L \left|\sin\theta_L \sin\theta\cos(\varphi_L - \varphi) + \cos\theta_L \cos\theta\right| \\ &= \frac{1}{\pi}\int_0^{\pi} d\varphi_L \left|\sin\theta_L \sin\theta\cos(\varphi_L - \varphi) + \cos\theta_L \cos\theta\right| \end{aligned}$$

$$= \frac{1}{\pi}\int_0^{\pi} d\varphi_L \left| \sin\theta_L \sin\theta \cdot \left(\cos\varphi_L + \mathrm{ctg}\,\theta_L \mathrm{ctg}\,\theta\right)\right| \tag{1}$$

Note that in the above derivations we took into account that $h_L(\varphi_L) = 1$ and also symmetry of function $(a \cdot \cos(\xi) + b)$ in the interval $\xi \in [0, 2\pi]$. In the derivations to follow we need to consider two cases. First, consider the case, when $\left|\mathrm{ctg}\theta_L \mathrm{ctg}\theta\right| \geq 1$. In this case the expression $(\cos\varphi_L + \mathrm{ctg}\,\theta_L \mathrm{ctg}\,\theta)$ in the Eq. (1) does not change the sign over the whole interval of integration, $[0, \pi]$. Therefore,

$$\begin{aligned}
\psi(\mu, \mu_L) &\equiv \frac{1}{\pi}\int_0^{\pi} d\varphi_L \left| \sin\theta_L \sin\theta \cdot \left(\cos\varphi_L + \mathrm{ctg}\,\theta_L \mathrm{ctg}\,\theta\right)\right| \\
&= \frac{1}{\pi}\left|\int_0^{\pi} d\varphi_L \sin\theta_L \sin\theta \cdot \left(\cos\varphi_L + \mathrm{ctg}\theta_L \mathrm{ctg}\theta\right)\right| \\
&= \left|\cos\theta_L \cos\theta\right|. \qquad (2a)
\end{aligned}$$

Now consider the second case, when $\left|\mathrm{ctg}\theta_L \mathrm{ctg}\theta\right| < 1$. Here the value of the expression $(\cos\varphi_L + \mathrm{ctg}\,\theta_L \mathrm{ctg}\,\theta)$ in the Eq. (1) is monotonically decreasing in the interval $\varphi \in [0, \pi]$. The value of $\varphi = \varphi^*$, where the integrand changes the sign is given by

$$\cos\varphi^* + \mathrm{ctg}\,\theta_L \mathrm{ctg}\,\theta = 0 \;\Rightarrow \varphi^* = \arccos\left[-\mathrm{ctg}\,\theta_L \mathrm{ctg}\,\theta\right].$$

Now we can evaluate Eq. (1) by splitting the interval of integration into two parts, where the integrand has the opposite signs,

$$\begin{aligned}
\psi(\mu, \mu_L) &\equiv \frac{1}{\pi}\int_0^{\pi} d\varphi_L \left| \sin\theta_L \sin\theta \cdot \left(\cos\varphi_L + \mathrm{ctg}\,\theta_L \mathrm{ctg}\,\theta\right)\right| \\
&= \frac{1}{\pi}\left|\int_0^{\varphi^*} d\varphi_L \left(\sin\theta_L \sin\theta \cos\varphi_L + \cos\theta_L \cos\theta\right) - \int_{\varphi^*}^{\pi} d\varphi_L \left(\sin\theta_L \sin\theta \cos\varphi_L + \cos\theta_L \mathrm{ctg}\,\theta\right)\right| \\
&= \frac{1}{\pi}\left| 2\sin\theta_L \sin\theta \sin\varphi^* + \cos\theta_L \cos\theta\left(2\varphi^* - \pi\right)\right|. \qquad (2b)
\end{aligned}$$

Combined, the Eq. (2a)-(2b) present the solution to the problem.

Problem 10. Show that in canopies with constant leaf normal inclination but uniform orientation along the azimuth, $G(\mu) = \psi(\mu, \mu_L)$

Solution. For canopies with independent polar angle, θ_L, and azimuth, φ_L, of leaf normals (cf. Problem 7), we have

$$G(\underline{r},\mu) = \int_0^1 d\mu_L \bar{g}_L(\underline{r},\mu_L)\psi(\mu,\mu_L), \tag{1}$$

where $\mu_L = \cos\theta_L$, $\mu = \cos\theta$, and

$$\psi(\mu,\mu_L) = \frac{1}{2\pi}\int_0^{2\pi} h_L(\varphi_L)\,|\,\underline{\Omega}\bullet\underline{\Omega}_L\,|\,d\varphi_L\,. \tag{2}$$

The condition of constant leaf normal inclination and uniform orientation along azimuth implies

$$\bar{g}_L(\underline{r},\mu_L) = \frac{\delta(\theta_L-\theta^*)}{\sin\theta_L} = \delta(\mu_L-\mu^*),$$
$$h_L(\varphi_L) = 1. \tag{3}$$

Combining Eqs. (1)-(3), we have

$$\begin{aligned} G(\underline{r},\mu) &= \int_0^1 d\mu_L \bar{g}_L(\underline{r},\mu_L)\psi(\mu,\mu_L) \\ &= \int_0^1 d\mu_L \delta(\mu_L-\mu^*)\psi(\mu,\mu_L), \\ &= \psi(\mu,\mu^*). \end{aligned}$$

Problem 11. Using Eq. (6), derive the $\psi(\mu,\mu_L)$ in the case of heliotropic orientations.

Solution. Recall (cf. Problem 7),

$$\psi(\mu,\mu_L) \equiv \frac{1}{2\pi}\int_0^{2\pi} h_L(\varphi_L)\,|\,\underline{\Omega}\bullet\underline{\Omega}_L\,|\,d\varphi_L. \tag{1}$$

In the case when the leaf azimuths have a preferred orientation with respect to the solar azimuth orientation (heliotropism) the h_L function may be modeled as follows,

$$\frac{1}{2\pi}h_L(\varphi_L,\varphi) = \frac{1}{\pi}\cos^2(\varphi-\varphi_L-\eta). \tag{2}$$

Recall also (cf. Problem 6),

$$\underline{\Omega}_L \bullet \underline{\Omega} = \sin\theta_L \sin\theta \cdot \cos(\varphi_L - \varphi) + \cos\theta_L \cos\theta. \tag{3}$$

Combining Eq. (1)-(3), we have

$$\begin{aligned}
\psi(\mu,\mu_L) &\equiv \frac{1}{2\pi}\int_0^{2\pi} h_L(\varphi_L)\,|\,\underline{\Omega}\bullet\underline{\Omega}_L\,|\,d\varphi_L \\
&= \frac{1}{\pi}\int_0^{2\pi} d\varphi_L \cos^2(\varphi - \varphi_L - \eta)\,|\sin\theta_L\sin\theta\cos(\varphi-\varphi_L)+\cos\theta_L\cos\theta\,| \\
&= \frac{1}{\pi}\int_0^{2\pi} d\alpha \cos^2(\alpha-\eta)\,|\sin\theta_L\sin\theta\cos\alpha+\cos\theta_L\cos\theta\,| \\
&= \frac{1}{\pi}\int_0^{2\pi} d\alpha \cos^2(\alpha-\eta)\,|\sin\theta_L\sin\theta\cdot(\cos\alpha+\mathrm{ctg}\,\theta_L\mathrm{ctg}\,\theta)\,|,
\end{aligned} \tag{4}$$

where $\alpha = \varphi - \varphi_L$. To evalute the above integral we need to consider two cases (cf. Problem 8). First, consider the case, when $|\mathrm{ctg}\theta_L\,\mathrm{ctg}\theta| \geq 1$. In this case the integrand does not change the sign over whole interval of integration. Therefore,

$$\begin{aligned}
\psi(\mu,\mu_L) &\equiv \frac{1}{\pi}\int_0^{2\pi} d\alpha \cos^2(\alpha-\eta)\,|\sin\theta_L\sin\theta\cos\alpha+\cos\theta_L\cos\theta)\,| \\
&= \frac{1}{\pi}\left|\int_0^{2\pi} d\alpha \cos^2(\alpha-\eta)\left[\sin\theta_L\sin\theta\cos\alpha+\cos\theta_L\cos\theta\right]\right| \\
&= \frac{1}{\pi}\left|\sin\theta_L\sin\theta\int_0^{2\pi} d\alpha\cos^2(\alpha-\eta)\cos\alpha + \cos\theta_L\cos\theta\int_0^{2\pi} d\alpha\cos^2(\alpha-\eta)\right|.
\end{aligned} \tag{5}$$

The evaluation of two definite integrals in Eq. (5) requires derivations of corresponding indefinite integrals, I_1 and I_2:

$$\begin{aligned}
I_1 &\equiv \sin\theta_L\sin\theta\int d\alpha\cos^2(\alpha-\eta)\cos\alpha = \sin\theta_L\sin\theta\int d\alpha\frac{1+\cos(2\alpha-2\eta)}{2}\cos\alpha \\
&= \frac{\sin\theta_L\sin\theta}{2}\left[\sin\alpha+\frac{\sin(\alpha-2\eta)}{2}+\frac{\sin(3\alpha-2\eta)}{6}\right].
\end{aligned} \tag{6a}$$

$$\begin{aligned}
I_2 &\equiv \cos\theta_L\cos\theta\int d\alpha\cos^2(\alpha-\eta) = \cos\theta_L\cos\theta\int d\alpha\frac{1+\cos(2\alpha-2\eta)}{2} \\
&= \frac{\cos\theta_L\cos\theta}{2}\left[\alpha+\frac{\sin(2\alpha-2\eta)}{2}\right].
\end{aligned} \tag{6b}$$

Therefore, the corresponding definite integrals over interval $\alpha \in [0,2\pi]$ are

$$I_1\big|_{\alpha=0}^{\alpha=2\pi} = 0 \text{ and } I_2\big|_{\alpha=0}^{\alpha=2\pi} = \pi\cos\theta_L\cos\theta. \tag{7}$$

Combining Eqs. (5)-(7), we have

$$\psi(\mu,\mu_L) = \left|\cos\theta\cos\theta_L\right| \equiv \mu\,\mu_L\,. \tag{8}$$

Now consider the second case, when $\left|\mathrm{ctg}\theta_L\,\mathrm{ctg}\theta\right| < 1$. In this case the expression under sign of integral in Eq. (4), $(\cos\alpha + \mathrm{ctg}\,\theta_L\,\mathrm{ctg}\,\theta)$, will change sign two times (first at α^* and second at $2\pi - \alpha^*$) over the interval $\alpha \in [0,2\pi]$. The value of α^* is given by

$$(\cos\alpha + \mathrm{ctg}\,\theta_L\,\mathrm{ctg}\,\theta) = 0 \;\Rightarrow \alpha^* = \arccos\left[-\,\mathrm{ctg}\,\theta_L\,\mathrm{ctg}\,\theta\right]. \tag{9}$$

In order to evaluate integral in Eq. (4) we need to consider three intervals, where integrand has constant sign: $\alpha \in [0,\alpha^*]$, $\alpha \in [\alpha^*, 2\pi - \alpha^*]$, and $\alpha \in [2\pi - \alpha^*, 2\pi]$. Therefore,

$$\begin{aligned}
\psi(\mu,\mu_L) &= \frac{1}{\pi}\int_0^{2\pi} d\alpha\,|\,\sin\theta_L\sin\theta\cos^2(\alpha - \eta)\cos\alpha + \cos\theta_L\cos\theta\cos^2(\alpha - \eta)\,| \\
&= \frac{1}{\pi}\left|\left[I_1 + I_2\right]\big|_0^{\alpha^*} - \left[I_1 + I_2\right]\big|_{\alpha^*}^{2\pi-\alpha^*} + \left[I_1 + I_2\right]\big|_{2\pi-\alpha^*}^{2\pi}\right| \\
&= \frac{1}{\pi}\left|\left[I_1 + I_2\right]\big|_0^{2\pi} - 2\cdot\left[I_1 + I_2\right]\Big|_{\alpha^*}^{2\pi-\alpha^*}\right| \qquad (10) \\
&= \frac{1}{\pi}\left|\,I_1\big|_0^{2\pi} - 2\cdot I_1\Big|_{\alpha^*}^{2\pi-\alpha^*} + I_2\big|_0^{2\pi} - 2\cdot I_2\big|_{\alpha^*}^{2\pi-\alpha^*}\right|, \qquad (10)
\end{aligned}$$

where

$$I_1\big|_0^{2\pi} - 2\cdot I_1\Big|_{\alpha^*}^{2\pi-\alpha^*} = \sin\theta\sin\theta_L\cdot\left(\,2\sin\alpha^* + \sin\alpha^*\cos(2\eta) + \frac{1}{3}\sin(3\alpha^*)\cos(2\eta)\right), \tag{11a}$$

$$I_2\big|_0^{2\pi} - 2\cdot I_2\Big|_{\alpha^*}^{2\pi-\alpha^*} = \cos\theta\cos\theta_L\cdot\left(2\alpha^* - \pi + \sin(2\alpha^*)\cos(2\eta)\right). \tag{11b}$$

Combining Eqs. (10)-(11), we have

$$\begin{aligned}
\psi(\mu,\mu_L) = \Bigg|\frac{\sin\theta\sin\theta_L}{\pi}\cdot&\left(\,2\sin\alpha^* + \sin\alpha^*\cos(2\eta) + \frac{1}{3}\sin(3\alpha^*)\cos(2\eta)\right) \\
&+ \frac{\cos\theta\cos\theta_L}{\pi}\cdot\left(2\alpha^* - \pi + \sin(2\alpha^*)\cos(2\eta)\right)\Bigg|, \qquad (12)
\end{aligned}$$

where α^* is given by Eq. (9). Overall, Eqs. (8) and (12) present the complete solution to the problem. Finally, note that in the special case of dia-heliotropic distribution, ($\eta = 0$), the Eq. (12) reduces to

$$\psi(\mu,\mu_L) = \left| \frac{\sin\theta\sin\theta_L}{\pi} \cdot \left(3\sin\alpha^* + \frac{1}{3}\sin(3\alpha^*) \right) + \frac{\cos\theta\cos\theta_L}{\pi} \cdot \left(2\alpha^* - \pi + \sin(2\alpha^*) \right) \right|,$$

and in the case of para-heliotropic distribution ($\eta = \pi/2$), to

$$\psi(\mu,\mu_L) = \left| \frac{\sin\theta\sin\theta_L}{\pi} \cdot \left(2\sin\alpha^* - \frac{1}{3}\sin(3\alpha^*) \right) + \frac{\cos\theta\cos\theta_L}{\pi} \cdot \left(2\alpha^* - \pi - \sin(2\alpha^*) \right) \right|.$$

Problem 12. Calculate area scattering phase function for diffuse radiation, $\Gamma_d(\underline{\Omega}' \to \underline{\Omega})$, in the case of uniform leaf normal distribution, $g_L = 1$.

Solution. Recall,

$$\Gamma_d(\underline{\Omega}' \to \underline{\Omega}) = \rho_{L,d}\Gamma_d^-(\underline{\Omega}' \to \underline{\Omega}) + \tau_{L,d}\Gamma_d^+(\underline{\Omega}' \to \underline{\Omega}), \tag{1a}$$

where,

$$\Gamma_d^{\pm}(\underline{\Omega}' \to \underline{\Omega}) = \pm\frac{1}{2\pi}\int_0^1 d\mu_L \int_0^{2\pi} d\varphi_L \; g_L(\mu_L,\varphi_L)\,(\underline{\Omega}\bullet\underline{\Omega}_L)\,(\underline{\Omega}'\bullet\underline{\Omega}_L). \tag{1b}$$

The ($\pm$) in the above definition indicates that the φ_L integration is over that portion of the interval $[0,2\pi]$ for which the integrand is either positive (+) or negative (–). We need to calculate phase function for the case of uniform leaf normal orientation, $g_L = 1$. In view of the symmetry of the integrand with respect to $\underline{\Omega}_L$, the integral over the upper hemisphere is equal to that over lower hemisphere and,

$$\Gamma_d^{\pm}(\underline{\Omega}' \to \underline{\Omega}) = \pm\frac{1}{2\pi}\int_{2\pi+} d\underline{\Omega}_L\,(\underline{\Omega}\bullet\underline{\Omega}_L)\,(\underline{\Omega}'\bullet\underline{\Omega}_L) = \pm\frac{1}{2}\left\{ \frac{1}{2\pi}\int_{4\pi} d\underline{\Omega}_L\,(\underline{\Omega}\bullet\underline{\Omega}_L)\,(\underline{\Omega}'\bullet\underline{\Omega}_L) \right\}. \tag{1c}$$

The integrand depends on three vectors: $\underline{\Omega}$, $\underline{\Omega}'$, $\underline{\Omega}_L$. In order to simplify integration, let us choose the coordinate system where X-Y plane coincides with the plane of vectors $\underline{\Omega}'$ and $\underline{\Omega}$ ($\mu' = \mu = 0$). Therefore,

$$\begin{aligned} \underline{\Omega} &= (\cos\varphi,\ \sin\varphi,\ 0), \\ \underline{\Omega}' &= (\cos\varphi',\ \sin\varphi',\ 0), \end{aligned} \tag{2}$$

$$\underline{\Omega}_L = (\sin\theta_L \cos\varphi_L,\ \sin\theta_L \sin\varphi_L,\ \cos\theta_L).$$

Taking into account Eq. (2) and performing trigonometric transformations, we have

$$(\underline{\Omega}_L \bullet \underline{\Omega}')(\underline{\Omega}_L \bullet \underline{\Omega}) = \sin^2\theta_L \cos(\varphi_L - \varphi)\cos(\varphi_L - \varphi'). \tag{3}$$

Let $\beta \equiv \varphi' - \varphi$, an angle between $\underline{\Omega}$ and $\underline{\Omega}'$, $\beta = \arccos(\underline{\Omega} \bullet \underline{\Omega}')$. Let $\chi \equiv \varphi_L - \varphi'$, and $d\chi = d\varphi_L$. Therefore,

$$\begin{aligned}\Gamma^{\pm} &= \pm\frac{1}{4\pi}\int_{-1}^{1} d\mu_L (1-\mu^2{}_L)\int_0^{2\pi} d\chi \cos(\chi+\beta)\cos(\chi) \\ &= \pm\frac{1}{4\pi}\int_{-1}^{1} d\mu_L (1-\mu^2{}_L)\int_0^{2\pi} d\chi \frac{1}{2}[\cos(\beta)+\cos(2\chi+\beta)] \\ &= \pm\frac{1}{4\pi}\int_{-1}^{1} d\mu_L (1-\mu^2{}_L)\int_0^{2\pi} dy \frac{1}{2}[\cos(\beta)+\cos(y)]\ . \end{aligned} \tag{4}$$

Note, the integrand in Eq. (4) is changing sign two times over the interval $[0;2\pi]$:

$$\cos(y) = -\cos(\beta) \Rightarrow y = \pi \pm \beta.$$

Namely, the integrand is positive over $[0;\pi-\beta]$, negative over $[\pi-\beta;\pi+\beta]$ and again positive over $[\pi+\beta;\ 2\pi]$. Therefore,

$$\begin{aligned} I^+(\beta) &\equiv \frac{1}{2}\left\{\int_0^{\pi-\beta}[\cos(\beta)+\cos(y)]dy + \int_{\pi+\beta}^{2\pi}[\cos(\beta)+\cos(y)]dy\right\} \\ &= \int_0^{\pi-\beta}[\cos(\beta)+\cos(y)]dy \\ &= (\pi-\beta)\cos(\beta)+\sin(\beta)\ , \end{aligned} \tag{5a}$$

and

$$\begin{aligned} I^-(\beta) &\equiv \frac{1}{2}\int_{\pi-\beta}^{\pi+\beta}[\cos(\beta)+\cos(y)]dy \\ &= \int_{\pi-\beta}^{\pi}[\cos(\beta)+\cos(y)]dy \\ &= \beta\cos(\beta)-\sin(\beta). \end{aligned} \tag{5b}$$

Combining Eq. (4) and (5), we have,

$$\Gamma^{\pm} = \pm\frac{I^{\pm}(\beta)}{4\pi}\int_{-1}^{1} d\mu_L(1-\mu^2{}_L) = \pm\frac{I^{\pm}(\beta)}{3\pi}. \tag{6}$$

Finally, substituting Eq. (6) into Eq. (1), we have

$$\begin{aligned}\Gamma_d(\underline{\Omega}'\to\underline{\Omega}) &= \rho_{L,d}\Gamma_d^-(\underline{\Omega}'\to\underline{\Omega}) + \tau_{L,d}\Gamma_d^+(\underline{\Omega}'\to\underline{\Omega})\\ &= \frac{1}{3\pi}\left\{\rho_{L,d}[-\beta\cos(\beta)+\sin(\beta)] + \tau_{L,d}[(\pi-\beta)\cos(\beta)+\sin(\beta)]\right\}\\ &= \frac{\omega_{L,d}}{3\pi}[\sin(\beta)-\beta\cos(\beta)] + \frac{\tau_{L,d}}{3}\cos(\beta).\end{aligned}$$

Problem 13. Given the direction of incoming, $\underline{\Omega}$, and reflected, $\underline{\Omega}'$, fluxes at the leaf surface ($\|\underline{\Omega}\| = \|\underline{\Omega}'\| = 1$) show that the direction of leaf normals $\underline{n}_L(\mu_L,\varphi_L)$ in the case of specular reflection is given by

$$\mu_L = \frac{|\mu'-\mu|}{\sqrt{2(1-\underline{\Omega}'\bullet\underline{\Omega})}},$$

$$\tan\varphi_L = \frac{\sqrt{1-\mu'^2}\sin\varphi' - \sqrt{1-\mu^2}\sin\varphi}{\sqrt{1-\mu'^2}\cos\varphi' - \sqrt{1-\mu^2}\cos\varphi}.$$

Solution. Consider the geometry of interaction of solar beams with a leaf surface in the case of specular reflection as shown in Fig. (1). Given the incoming, $\underline{\Omega}$, and reflected, $\underline{\Omega}'$, directions, the angle between them is given by $\cos\alpha = \underline{\Omega}\bullet\underline{\Omega}'$. The leaf normal in the case of specular reflection is

$$\underline{n}_L = \frac{\underline{\Omega}-\underline{\Omega}'}{\|\underline{\Omega}-\underline{\Omega}'\|}. \tag{1}$$

The norm $\|\underline{\Omega}-\underline{\Omega}'\|$ can be calculated as follows (cf. Fig. 1(b)):

$$\|\underline{\Omega}-\underline{\Omega}'\| = 2\sin\frac{\alpha}{2} = 2\sqrt{\frac{1-\cos\alpha}{2}} = \sqrt{2(1-\underline{\Omega}\bullet\underline{\Omega}')}. \tag{2}$$

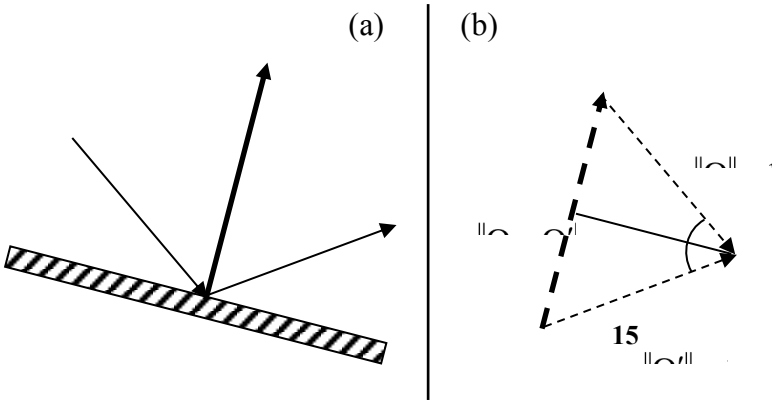

Figure. 1 The geometry of interaction of radiation with leaf. Panel (a) shows direction of leaf surface, leaf normal ($\underline{n}_L$), incoming ($\underline{\Omega}$) and reflected ($\underline{\Omega}'$) beams. Panel (b) is a schematic plot to evaluate the norm of $\|\underline{\Omega}-\underline{\Omega}'\|$.

Let

$$\underline{\Omega} = (\sin\theta\sin\varphi,\ \sin\theta\cos\varphi,\ \cos\theta), \tag{3a}$$

$$\underline{\Omega}' = (\sin\theta'\sin\varphi',\ \sin\theta'\cos\varphi',\ \cos\theta'), \tag{3b}$$

$$\underline{n}_L = (\sin\theta_L\sin\varphi_L,\ \sin\theta_L\cos\varphi_L,\ \cos\theta_L). \tag{3c}$$

Combining Eqs. (1)-(3) we will get formulas for the thee components of vector $\underline{n}_L$, namely,

$$\sin\theta_L\sin\varphi_L = \frac{\sin\theta\sin\varphi - \sin\theta'\sin\varphi'}{\sqrt{2(1-\underline{\Omega}\bullet\underline{\Omega}')}}, \tag{4a}$$

$$\sin\theta_L\cos\varphi_L = \frac{\sin\theta\cos\varphi - \sin\theta'\cos\varphi'}{\sqrt{2(1-\underline{\Omega}\bullet\underline{\Omega}')}}, \tag{4b}$$

$$\cos\theta_L = \frac{\cos\theta - \cos\theta'}{\sqrt{2(1-\underline{\Omega}\bullet\underline{\Omega}')}}. \tag{4c}$$

The Eq. (4c) directly evaluates $\mu_L = \cos\theta_L$. The expression for φ_L can be derived dividing Eq. (4a) by (4b), namely,

$$\tan\varphi_L = \frac{\sin\theta\sin\varphi - \sin\theta'\sin\varphi'}{\sin\theta\cos\varphi - \sin\theta'\cos\varphi'} \equiv \frac{\sqrt{1-\mu^2}\sin\varphi - \sqrt{1-\mu'^2}\sin\varphi'}{\sqrt{1-\mu^2}\cos\varphi - \sqrt{1-\mu'^2}\cos\varphi'}.$$

Chapter 3

Radiative Transfer in Vegetation Canopies

Knyazikhin et al.

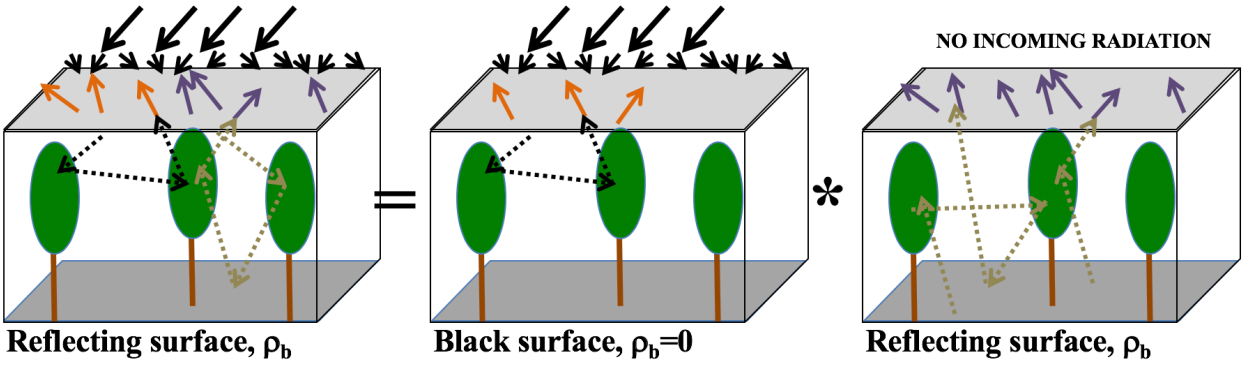

$$\Omega \bullet \nabla I_\lambda + \sigma(r,\Omega) I_\lambda(r,\Omega) = \int_{4\pi} d\Omega' \sigma_{s,\lambda}(r,\Omega' \to \Omega) I_\lambda(r,\Omega')$$

$$I_\lambda(r_t,\Omega) = B_\lambda(r_t,\Omega),\ r_t \in \partial V_t,\ n(r_B) \bullet \Omega < 0$$

$$I(r_b,\Omega) = \frac{1}{\pi} \int_{\Omega' \bullet n(r_B) > 0} \rho_b \,|\, n(r_B') \bullet \Omega' \,|\, I(r_B',\Omega')\, d\Omega'$$

Chapter 3

Radiative Transfer in Vegetation Canopies

1. Radiative Transfer Equation for Vegetation Canopies

Solar radiation scattered from a vegetation canopy and measured by satellite sensors results from interaction of photons traversing through the foliage medium, bounded at the bottom by a radiatively participating surface. Therefore to estimate the canopy radiation regime, three important features must be carefully formulated. They are (1) the architecture of individual plant and the entire canopy; (2) optical properties of vegetation elements (leaves, stems) and soil; the former depends on physiological conditions (water status, pigment concentration); and (3) atmospheric conditions which determine the incident radiation field [Ross, 1981].

We idealize a vegetation canopy as a medium filled with small planar elements of negligible thickness. We ignore all organs other than green leaves. In addition, we neglect the finite size of vegetation canopy elements. Thus, the vegetation canopy is treated as a gas with non-dimensional planar scattering centers, i.e., a turbid medium. In other words, one cuts leaves residing in an elementary volume at a given spatial point r into "dimensionless pieces" and uniformly distributes them within the elementary volume. Three variables, the leaf area density distribution function $u_L(\underline{r})$, the leaf normal distribution, $g_L(\underline{r},\underline{\Omega}_L)$, and the leaf scattering phase function, $\gamma_L(\underline{r},\underline{\Omega}' \to \underline{\Omega},\underline{\Omega}_L)$ (Chapter 3) are used in the theory of radiative transfer in vegetation canopies to convey "information" about the total leaf area, leaf orientations and leaf optical properties in the elementary volume at r before "converting the leaves into the gas."

It should be emphasized that the turbid medium assumption is a mathematical idealization of canopy structure, which ignores finite size of leaves. In reality, finite size scatters can cast shadows. This causes a very sharp peak in reflected radiation about the retro-solar direction. This phenomenon is referred to as the "hot spot" effect. It is clear that point scatters cannot cast shadows and thus the turbid medium concept in its original formulation [Ross, 1981] fails to

predict or duplicate experimental observation of exiting radiation about the retro-illumination direction. Zhang et al. [2002] showed that if the solution to the radiative transfer equation is treated as a Schwartz distribution, then an additional term must be added to the solution of the radiative transfer equation. This term describes the hot spot effect. This result justifies the use of the transport equation as the basis to model canopy radiation regime. Here we will follow classical radiative transfer theory in vegetation canopies proposed by Ross [1981]. For the mathematical theory of Schwartz distributions applicable to the transport equation, the reader is referred to Germogenova [1986], Choulli and Stefanov [1996] and Antyufeev [1996].

In addition to canopy structure and its optics a domain V in which the radiative transfer process is studied should be specified. In remote sensing application, a parallelepiped of horizontal dimensions X_S, Y_S, and height Z_S is usually taken as the domain V. The top δV_t, bottom δV_b, and lateral δV_l surfaces of the parallelepiped form the canopy boundary $\delta V = \delta V_t + \delta V_b + \delta V_l$. The height of a tallest plant in V can be taken as Z_S. The dimension of the upper boundary δV_t coincides with a footprint of the imagery. The function characterizing the radiative field in V is the specific intensity introduced in Chapter 2. Under condition of the absence of polarization, frequency shifting interaction, and emission processes within the canopy, the monochromatic specific intensity $I_\lambda(\underline{r},\underline{\Omega})$ is given by the stationery radiative transfer equation (Chapter 2, Eq. (24)) with $q_\lambda(\underline{r},\underline{\Omega}) = 0$. Substituting vegetation-specific coefficients (Chapter 3, Eqs (13) and (15)) into the transport equation (Chapter 2, Eq. (24)), one obtains the radiative transfer equation for a vegetation canopy occupying the domain V, namely,

$$\underline{\Omega} \bullet \nabla I_\lambda(\underline{r},\underline{\Omega}) + G(\underline{r},\underline{\Omega})u_L(\underline{r})I_\lambda(\underline{r},\underline{\Omega}) = \frac{u_L(\underline{r})}{\pi}\int_{4\pi}\Gamma_\lambda(\underline{r},\underline{\Omega}' \to \underline{\Omega})I_\lambda(\underline{r},\underline{\Omega}')d\underline{\Omega}'. \quad (1)$$

The boundary condition for the radiative transfer problem is given by

$$I_\lambda(\underline{r}_b,\underline{\Omega}) = B_\lambda(\underline{r}_b,\underline{\Omega}), \quad \underline{r}_b \in \delta V, \quad \underline{n}(\underline{r}_b) \bullet \underline{\Omega} < 0. \quad (2)$$

Here $B_\lambda(\underline{r}_b,\underline{\Omega})$ is the intensity of radiation entering the domain V through a point $\underline{r}_B$ on the boundary δV in the direction $\underline{\Omega}$. Directions along which photons can enter the vegetation canopy through the point $\underline{r}_b$ satisfy the inequality $\underline{n}(\underline{r}_b) \bullet \underline{\Omega} < 0$ where $\underline{n}(\underline{r}_b)$ is an outward normal vector at $\underline{r}_b$.

The solution of the boundary value problem, Eqs (1)-(2), i.e., the monochromatic specific intensity $I_\lambda(\underline{r},\underline{\Omega})$, depends on wavelength, λ, location r, and direction $\underline{\Omega}$. Here, the position vector $\underline{r}$ denotes the triplet (x,y,z) with ($0<x<X_S$), ($0<y<Y_S$) and ($0<z<Z_S$) and is expressed in Cartesian coordinates with its origin, O=(0,0,0), at the top of the vegetation canopy and the *Z* axis directed down into the vegetation canopy. The unit vector $\underline{\Omega} \sim (\theta,\varphi)$ has an azimuthal angle φ measured in the (XY) plane from the positive X axis in a counterclockwise fashion and a

polar angle θ with respect to the polar axis that is opposite to the Z axis. In this Chapter we shall omit the sign λ in notations.

2. Vegetated Surfaces Reflectance

Solution of the boundary value problem (Eqs. (1)-(2)) describes the radiative regime in a vegetation canopy and, as a consequence, reflectance properties of the vegetated surface. When describing surface reflectance, standard nomenclature [Nicodemus et al., 1977] dictates that the angular characteristics of the illumination are mentioned first, followed by the angular characteristics of the reflected radiance. In the definitions given below, the prefix hemispherical-directional implies an illumination which is hemispherical in directional extent and a reflected radiance in a single direction. Directional-hemispherical implies that the illumination is single directional and the reflected radiance is integrated over the hemisphere [Martonchik et al., 2000]. The following reflectance quantities are used in remote sensing to describe surface reflective properties.

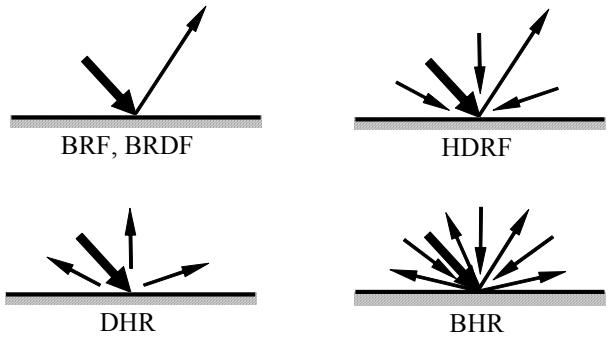

Figure 1. Reflectance nomenclature summary. The broad arrow represents an irradiance from a collima-ted beam. All other arrows represent incident and reflected radiance fields.

The hemispherical-directional reflectance factor (HDRF, dimensionless) for nonisotropic incident radiation is the ratio of the mean radiance leaving the top of the vegetation canopy to radiance reflected from an ideal Lambertian target into the same beam geometry and illuminated under identical atmospheric conditions [Martonchik et al., 2000]; this can be expressed in terms of the solution of Eq. (1)-(2) as

$$R = \frac{\int_0^{X_S}\int_0^{Y_S} I(x,y,0,\underline{\Omega})\,dx\,dy}{\frac{1}{\pi}\int_{2\pi-} |\mu'|\,d\underline{\Omega}' \int_0^{X_S}\int_0^{Y_S} I(x,y,0,\Omega')\,dx\,dy} = \frac{< I(\underline{\Omega}) >_0}{\frac{1}{\pi}\int_{2\pi-} < I(\underline{\Omega}') >_0 d\underline{\Omega}'}, \quad \mu > 0. \tag{3}$$

Here μ and μ' are the cosine of the polar angles of the upward (reflected) $\underline{\Omega}$ and downward (incident) $\underline{\Omega}'$ directions, respectively; the angle brackets $< >_0$ denotes the mean over the upper surface δV_t of the parallelepiped V. The HDRF depends on atmosphere conditions (i.e., the

angular and spectral distribution of the incoming radiation), the surface properties (e.g., vegetation canopy below the boundary δV_t), the area of δV_t, and the direction $\underline{\Omega}$. For the condition of no atmosphere, i.e., the incident solar radiation at the upper canopy boundary δV_t is a parallel beam of light, the HDRF is termed a bidirectional reflectance factor (BRF, dimensionless). The BRF does not depend on atmosphere conditions and characterizes surface reflective properties. Its value varies with the directions, $\underline{\Omega}$ and $\underline{\Omega}'$, of reflected and incident radiation. The bidirectional reflectance distribution function (BRDF) is another reflectance quantity that describes the scattering of a parallel beam of incident radiation from one direction into another direction but, unlike the BRF, its values are expressed relative to the incident flux, i.e., the BRDF is the mean radiance leaving the upper boundary to the incident flux. The BRDF has units of sr^{-1} and is a factor of π smaller than BRF, i.e., $BRDF = \pi^{-1} BRF$.

The bihemispherical reflectance (BHR, dimensionless) for nonisotropic incident radiation is the ratio of the mean irradiance exitance to the incident irradiance [Martonchik et al., 1998], i.e.,

$$A = \frac{\int_{2\pi+} < I(\underline{\Omega}) >_0 |\mu| \, d\underline{\Omega}}{\int_{2\pi-} < I(\underline{\Omega}') >_0 |\mu'| \, d\underline{\Omega}'}. \qquad (4)$$

For the condition of no atmosphere, the BHR becomes directional hemispherical reflectance (DHR, dimensionless). For Lambertian surfaces, HDRF=BRF=BHR=DHR.

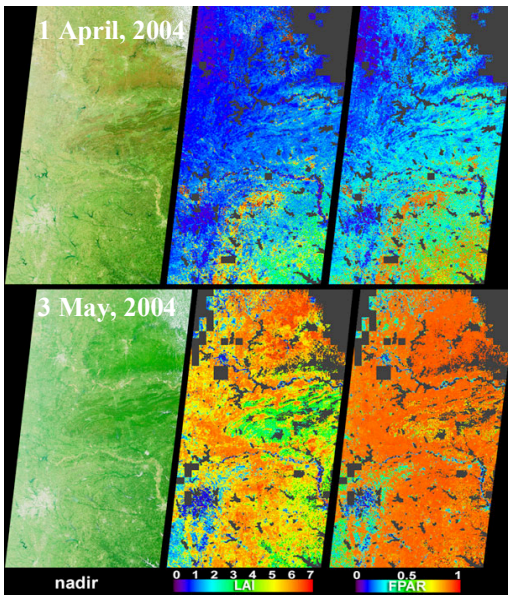

Figure 2. The multiangle imaging spectroradiometer (MISR) onboard the Earth Observing System (EOS) Terra platform provides global imagery at nine discrete viewangles and four visible/near-ibfrared spectral bands. MISR standard products include HDRF, BHR, BRF, DHR, leaf area index (LAI) and fraction of photosynthetically active radiation absorbed by vegetation (FPAR). Vigorous vegetation growth in the Southern United States (Texas, Oklahoma) after heavy rains fell during April and early May, 2004, is quantified in these images and LAI&FPAR product from MISR. The left-hand images are natural-color views from MISR's nadir camera acquired on April 1 (top set) and May 3 (bottom set). The middle and right-hand panels show MISR LAI and FPAR standard products. Data are at 1.1 km spatial resolution, i.e., the dimension of the upper boundary δV_t is 1.1 by 1.1 km.

All the reflectance quantities introduced above can be derived from data acquired by satellite-borne sensors (Fig. 2) which, in turn, are input to various techniques for retrieval of biophysical

parameters from space. In remote sensing, the dimension of the upper boundary δV_t often coincides with a footprint of the imagery. Taking the size of δV_t to zero results in a BRF value defined at a spatial point $\underline{r}_t$. Given the bidirectional reflectance factor, $R_0(\underline{\Omega}', \underline{\Omega})$), and intensity, $I(\underline{r}_t, \underline{\Omega}')$, of radiation incident on a horizontal surface at $\underline{r}_t$, the intensity of reflected radiation, $I(\underline{r}_t, \underline{\Omega})$, can be calculated as

$$I(\underline{r}_t, \underline{\Omega}) = \frac{1}{\pi} \int_{2\pi^-} R_0(\underline{\Omega}', \underline{\Omega}) \, |\mu'| \, I(\underline{r}_t, \underline{\Omega}') \, d\underline{\Omega}' . \tag{5}$$

This equation is used to describe the lower boundary condition for the radiative transfer in the atmosphere.

3. Boundary Conditions

The boundary conditions for a three-dimensional canopy are also three-dimensional. Indeed, the radiation entering the canopy through the top, δV_t, through the bottom, δV_b, and through the lateral, δV_l, surfaces are different. Therefore we consider a very general form of boundary conditions (see Sect. 2.4), namely,

$$I(\underline{r}_b, \underline{\Omega}) = \frac{1}{\pi} \int_{\delta V} d\underline{r}'_b \int_{\underline{\Omega}' \bullet \underline{n}(\underline{r}_b) > 0} \rho_b(\underline{r}'_b, \underline{\Omega}'; \underline{r}_b, \underline{\Omega}) \, |\underline{n}(\underline{r}'_b) \bullet \underline{\Omega}'| \, I(\underline{r}'_b, \underline{\Omega}') \, d\underline{\Omega}'$$
$$+ q(\underline{r}_b, \underline{\Omega}), \quad + n(\underline{r}_b) \bullet \underline{\Omega} < 0. \tag{6}$$

Here $\underline{r}_B$ and $\underline{r}'_B$ are points on the canopy boundary δV; $\underline{n}(\underline{r}_B)$ is the outward normal at the point $\underline{r}_B$; $\rho_B(\underline{r}'_B, \underline{\Omega}'; \underline{r}_B, \underline{\Omega})$ is the boundary scattering function; that is, the probability density that a photon having escaped from the canopy through the point $\underline{r}'_B \in \delta V$ and in the direction $\underline{\Omega}'$ will come back to it through the point $\underline{r}_B \in \delta V$ and in the direction $\underline{\Omega}$; and $q_B(\underline{r}_B, \underline{\Omega})$ is a photon source at the canopy boundary δV. Both ρ_B and q_B are wavelength dependent.

The radiative transfer problem can now be formulated as follows: find the intensity $I(\underline{r}, \underline{\Omega})$ which satisfies the transport equation (Eq. (1)) within the domain V and the condition given by Eq. (6) on the canopy boundary δV. The maximum boundary reflectance, $\rho_0(\delta V)$, canopy optical path, $\tau_0(V)$, and single scattering albedo ϖ_0, (cf. Chapter 2, Section 11) are basic characteristics of boundary reflective properties, canopy structure and leaf optical properties. It follows from the uniqueness theorem that the conditions $\varpi_0 \le 1$, $\rho_0(\delta V) < 1$ and $\tau_0(\delta V) < \infty$ guarantee the existence and uniqueness of the solution to the boundary value problem given by Eq. (3) and (6). Specification of the boundary conditions for the upper, δV_t, lower, δV_b, and lateral, δV_l, surfaces of the parallelepiped are discussed below.

Canopy upper boundary. The upper canopy boundary δV_t is adjacent to the atmosphere. Therefore radiation penetrating into the canopy through the upper boundary δV_t is determined by atmospheric conditions, i.e., the upper canopy boundary is exposed to both direct solar irradiance and diffuse radiation from all points of the sky. The former is caused by photons in the solar parallel beam which arrive at the upper canopy boundary without experiencing a collision. The latter results from photon-atmosphere interactions. Thus, the boundary condition at the upper boundary δV_t can be written as

$$I(\underline{r}_t, \underline{\Omega}) = c_T(\underline{r}_t)\delta(\underline{\Omega} - \underline{\Omega}_0) + d(\underline{r}_t, \underline{\Omega}), \quad \underline{r}_t \in \delta V_t, \quad \mu < 0. \tag{7}$$

Here $c_T(\underline{r}_t, \underline{\Omega})$ and $d(\underline{r}_t, \underline{\Omega})$ are intensities of the solar beam and diffuse radiation at point $\underline{r}_t$ on the boundary δV_t and $\delta(\underline{\Omega} - \underline{\Omega}_0)$ is the Dirac delta function. Both $c_T(\underline{r}_t, \underline{\Omega})$ and $d(\underline{r}_t, \underline{\Omega})$ are wavelength dependent. The direction of the solar beam is given by the unit vector $\underline{\Omega}_0 \sim (\theta_0, \varphi_0)$. Since $\underline{n}(\underline{r}_t) \bullet \underline{\Omega}$ coincides with the cosine of the polar angle θ of the direction $\underline{\Omega}$, the condition $\underline{n}(\underline{r}_t) \bullet \underline{\Omega} < 0$ for incoming directions can be written as $\mu < 0$. In other words, the upper boundary condition is formulated for downward directions. In terms of notations used in Eq. (6), $\rho_B(\underline{r}'_b, \underline{\Omega}'; \underline{r}_b, \underline{\Omega}) = 0$, $q(\underline{r}_b, \underline{\Omega}) = c_T(\underline{r}_b)\delta(\underline{\Omega} - \underline{\Omega}_0) + d(\underline{r}_b, \underline{\Omega})$, for $\underline{r}_b$ on the surface δV_t.

The canopy-radiation regime is sensitive to the partition between the mono-directional and diffuse components of the incoming radiation. The ratio f_{dir} of the mono-directional to the total radiation flux incident on the canopy is used to parameterize the partition; that is,

$$f_{dir}(\underline{r}_t) = \frac{F^{\downarrow}_{dir}(\underline{r}_t)}{F^{\downarrow}_{dir}(\underline{r}_t) + F^{\downarrow}_{diff}(\underline{r}_t)}, \quad \underline{r}_t \in \delta V_t. \tag{8}$$

Here $F^{\downarrow}_{dir}(\underline{r}_t)$ and $F^{\downarrow}_{dif}(\underline{r}_t)$ are monochromatic downward flux densities (irradiances) of mono-directional and diffuse components of the incident radiation, i.e.,

$$F^{\downarrow}_{dir}(\underline{r}_t) = c_T \mid \mu_0 \mid, \quad F^{\downarrow}_{diff}(\underline{r}_t) = \int_{2\pi^-} d(\underline{r}_t, \underline{\Omega}) \left| \underline{\Omega} \bullet \underline{n}(\underline{r}_t) \right| d\underline{\Omega}, \tag{9}$$

where $\mu_0 = \cos\theta_0$. The ratio f_{dir} varies between 0 and 1 and depends on the direction of the mono-directional incident beam, wavelength and atmosphere conditions. This parameter along with the total downward flux $F^{\downarrow}(\underline{r}_t) = F^{\downarrow}_{dir}(\underline{r}_t) + F^{\downarrow}_{dir}(\underline{r}_t)$ can be derived from satellite data [Diner et al., 1999a]. It is conventional, therefore, to parameterize the upper boundary condition in terms of these variables, i.e.,

$$I(\underline{r}_t, \underline{\Omega}) = \left[\frac{f_{dir}}{|\mu_0|} \delta(\underline{\Omega} - \underline{\Omega}_0) + (1 - f_{dir})\, d_0(\underline{r}_t, \underline{\Omega}) \right] F^{\downarrow}(\underline{r}_t), \quad \underline{n}(\underline{r}_t) \bullet \underline{\Omega} < 0, \tag{10}$$

where $d_0(\underline{r}_t, \underline{\Omega}) = d(\underline{r}_t, \underline{\Omega}) / F^{\downarrow}_{dif}$ is the anisotropy factor of the diffuse radiation.

The HDRF and BHR defined in Eqs (3) and (4), respectively, are expressed in terms of solution of the transport equation with the upper boundary condition (Eq. (7)). If $f_{dir} = 0$, the HDRF and BHR become the BRF and DHR, respectively.

In many cases, the anisotropy of diffuse radiation can be assumed wavelength independent. A model of the anisotropy corresponding to clear–sky conditions proposed by Pokrowski [1929]

$$d_0(\underline{r}_t, \underline{\Omega}) = \left[1 - \exp\left(\frac{-0.32}{|\mu|}\right)\right]\frac{1 + \underline{\Omega} \bullet \underline{\Omega}_0}{1 - \underline{\Omega} \bullet \underline{\Omega}_0}, \quad \mu < 0,$$

is an example of the angular distribution of incoming diffuse radiation. In the case of the standard overcast sky ($f_{dir} = 0$), the intensity $d(\underline{r}_t, \underline{\Omega})$ of the incoming diffuse radiation in the photosynthetically active region of solar spectrum, 400–700 nm, can be approximated by

$$d(\underline{r}_t, \underline{\Omega}) = i(\pi)\frac{1 + b|\mu|}{1 + b}, \quad \mu < 0,$$

where 1+b is the ratio between sky brightness in the zenith, $i(\pi)$, and at the horizon, $i(\pi/2)$ and it varies between 2.1 and 2.4 [Monteith and Unsworth, 1990]. Substituting the above equation into $d_0(\underline{r}_t, \underline{\Omega}) = d(\underline{r}_t, \underline{\Omega}) / F^{\downarrow}_{dif}$ and taking into account Eq. (9) one can express $i(\pi)$ and d_0 as

$$i(\pi) = F^{\downarrow}(\underline{r}_t)\frac{1 + b}{\pi(1 + \frac{2}{3}b)}, \quad d_0(\underline{r}_t, \underline{\Omega}) = F^{\downarrow}(\underline{r}_t)\frac{1 + b|\mu|}{\pi(1 + \frac{2}{3}b)}. \tag{11}$$

Canopy lower boundary. At the bottom of the canopy, a fraction of the radiation can be reflected back into the canopy by the ground. In the remote sensing problems, reflective properties of the canopy lower boundary are often approximated as $\rho_B(\underline{r}'_b, \underline{\Omega}'; \underline{r}_b, \underline{\Omega}) = \rho_b(\underline{r}'_b, \underline{\Omega}' \to \underline{\Omega})\delta(\underline{r}'_b - \underline{r}_b)$, $\underline{r}_b,\ \underline{r}'_b \in \delta V_b$ where $\rho_b(\underline{r}'_b, \underline{\Omega}' \to \underline{\Omega})$ is the bidirectional reflectance factor of the canopy ground. The canopy bottom does not emit the radiation at solar wavelengths and thus $q_b(\underline{r}_b, \underline{\Omega}) = 0$. Substituting these equations into Eq. (6) results in

$$I(\underline{r}_b, \underline{\Omega}) = \frac{1}{\pi}\int_{2\pi^-} \rho_b(\underline{r}_b, \underline{\Omega}' \to \underline{\Omega})\left|\underline{n}(\underline{r}_b) \bullet \underline{\Omega}'\right| I(\underline{r}_b, \underline{\Omega}')\, d\underline{\Omega}', \quad \mu > 0. \tag{12}$$

Here $-\underline{n}(\underline{r}_b) \bullet \underline{\Omega}$ coincides with the cosine of the polar angle θ of the direction $\underline{\Omega}$. The condition $\underline{n}(\underline{r}_t) \bullet \underline{\Omega} < 0$ for incoming directions therefore can be written as $\mu > 0$, i.e., the lower boundary condition is formulated for upward directions.

Canopy lateral boundary. The radiation penetrating through the lateral sides of the canopy depends on the neighboring environment. Its influence on the radiation field within the canopy is especially pronounced near the lateral canopy boundary. Therefore inaccuracies in the lateral boundary conditions may cause distortions in the simulated radiation field within the domain V. These features should be taken into account when 3D radiation distribution in a vegetation canopy of a small area is investigated. The problem of photon transport in such canopies arises, for example, in the context of optimal planting and cutting of industrial wood, land surface climatology, and plant physiology.

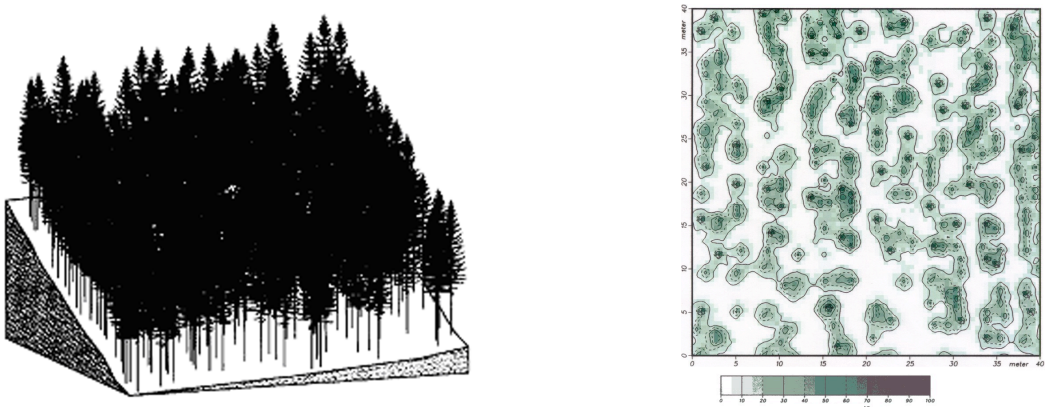

Figure 3. Computer simulated Norway spruce stand about 50 km near Goettingen, Germany, in the Harz mountains. The stand is about 45 years old and situated on the south slope. A 40×40 m^2 section of the stand with 297 trees was sampled for reconstruction. The stem diameters varied from 6 to 28 m and the tallest trees were about 12.5 m in height. The trees were divided into five groups with respect to stem diameter. A model of a Norway spruce based on fractal theory was used to build a representative of each group [Knyazikhin et al., 1996]. Given the distribution of tree stems in the stand, the diameter of each tree, the entire sample site was generated (left panel). The right panel shows the spatial distribution of leaf area index L(x,y) at spatial resolution of 50 cm^2, i.e., distribution of the mean leaf area index L(x,y) taken over each of 50 by 50 cm ground cells.

In order to demonstrate the range of the influence of the neighboring environment we simulate two extreme situations for a small 40 by 40m sample stand bounded from below by a black surface (i.e., ρ_b in Eq. (12) is set to zero). Canopy structure of this stand is shown in Fig. 3. In the first case, we "cut" the forest surrounding the sample plot. The incoming solar radiation can reach the sides of the sample stand without experiencing a collision in this case. The boundary condition (Eq. (6)) with $\rho_b = 0$ and $q(\underline{r}_1, \underline{\Omega}) = c_T(\underline{r}_1)\delta(\underline{\Omega} - \underline{\Omega}_0) + d(\underline{r}_1, \underline{\Omega})$, $\underline{n}(\underline{r}_1) \bullet \underline{\Omega} < 0$, $\underline{r}_L \in \delta V_1$ can be used to describe photons penetrating into the canopy through the lateral surface. In the second case, we "plant" a forest of an extremely high density around the sample stand so that no solar radiation can penetrate into the stand through the lateral boundary δV_1. The lateral boundary condition (Eq. (6)) takes the form $I(\underline{r}_L, \underline{\Omega}) = 0$, $\underline{n}(\underline{r}_1) \bullet \underline{\Omega} < 0$, $\underline{r}_L \in \delta V_1$. The radiative regimes in a real stand usually vary between these extreme situations. For each situation, the boundary value problem (Eqs. (1) and (6)) was solved and a vertical profile of mean downward

radiation flux density was evaluated. Figure 4 demonstrates downward fluxes normalized by the incident flux at noon on both a cloudy and clear sunny day. A downward radiation flux density evaluated by averaging the extinction coefficient $u_L G$ and area scattering phase function Γ over the 40 by 40m area first and then solving the radiative transfer equation is also plotted in this figure. One can see that the radiative regime in the sample stand is more sensitive to the lateral boundary conditions during cloudy days ($f_{dir} = 0$). In both cases, a 3D medium transmits more radiation than those predicted by the 1D transport equation.

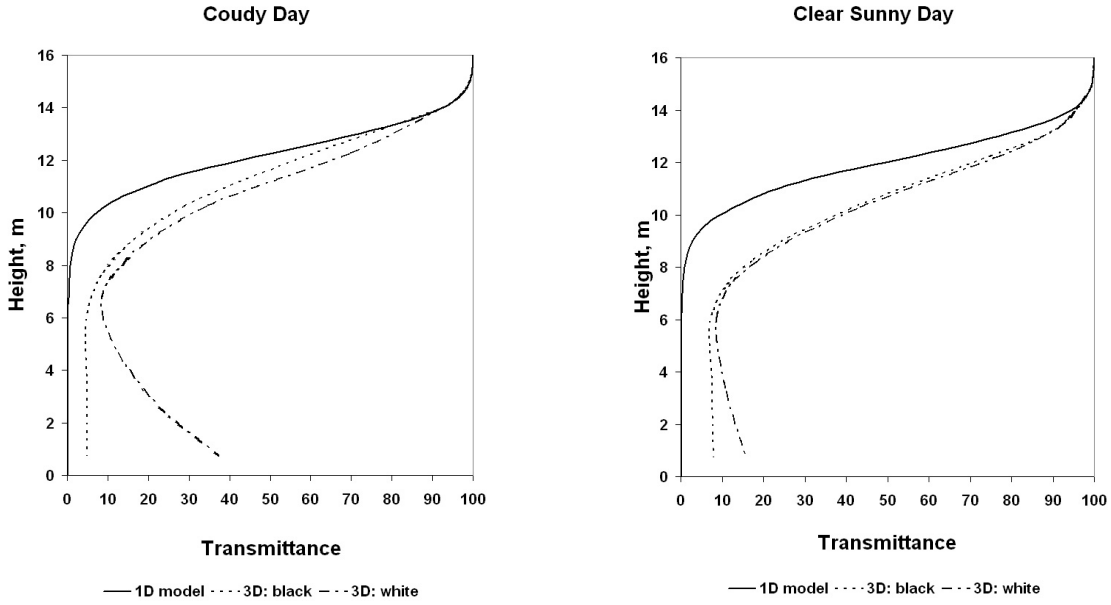

Figure 4. Vertical profile of the downward radiation flux normalized by the incident flux derived from the one-dimensional (1D model) and three-dimensional (3D: black and 3D: white) models on a cloudy day ($f_{dir} = 0$) and on a clear sunny day ($f_{dir} = 1$). Curves 3D: black correspond to a forest stand surrounded by the optically black lateral boundary, and curves 3D: white to an isolated forest stand of the same size and structure (from Knyazikhin et al., [1997]).

The following technique can be used to approximate the lateral boundary condition. One first calculates the radiative field in a vegetation canopy by solving a one-dimensional transport equation using average characteristics of canopy structure and optics over a given stand. Its solution, i.e. the vertical profile of the horizontally averaged radiation intensity, is then taken as the radiation penetrating through the lateral canopy boundary which, to some degree, accounts for photon interactions with both the stand and its neighboring environment. The size of an area impacted by such an approximation of the lateral boundary condition as a function of the adjoining vegetation and atmospheric conditions was studied by Kranigk [1996]. In particular, it has been shown that the "impacted area" consists of points being less than about 5m apart from the lateral boundary of a forest. Thus, the lateral boundary conditions can be expressed as

$$I(\underline{r}_l, \underline{\Omega}) = c_l(z)\delta(\underline{\Omega} - \underline{\Omega}_0) + i_l(z, \underline{\Omega}), \quad r_l = (x_l, y_l, z) \in \delta V_l, \quad \underline{n}(\underline{r}_l) \bullet \underline{\Omega} < 0 . \tag{13}$$

Here $c_1(z)\delta(\underline{\Omega}-\underline{\Omega}_0)$ and i_1 are wavelength dependent mean intensities of the direct and diffuse radiation at depth z predicted with the 1D radiative transfer equation. In terms of notations used in Eq. (6), $\rho_B(\underline{r}'_b,\underline{\Omega}';\underline{r}_b,\underline{\Omega})=0$, $q(\underline{r}_b,\underline{\Omega})=c_T(z_1)\delta(\underline{\Omega}-\underline{\Omega}_0)+i_1(z_1,\underline{\Omega})$ if $\underline{r}_b$ belongs to δV_1. The lateral side effects, however, decrease with distance from this boundary toward the center of the domain. It has been shown that these lateral effects can be neglected when the radiation regime is analyzed in a rather extended canopy. A "zero" boundary condition for the lateral surface can then be used to simulate canopy radiation regime [Knyazikhin et al., 1997].

4. Decomposition of the Boundary Value Problem for Radiative Transfer Equation

The Green's function concept allows us to express the solution to the transport equation with arbitrary sources and boundary conditions as a superposition of the solutions of some basic subproblems. In this section we demonstrate this technique with an example for canopy-surface system. It will be shown that the three-dimensional radiative transfer problem with a reflecting boundary can be expressed as a superposition of the solutions of two radiative transfer sub-problems with purely absorbing boundaries ($\rho_0(\delta V)=0$). The first one is formulated for a vegetation canopy illuminated from above by the incident radiation and bounded from below by an absorbing surface. We term this sub-problem a "black soil problem." The second sub-problem, called "S problem," describes the radiative transfer in the same vegetation canopy which is illuminated from the bottom by anisotropic sources and bounded from above by a non-reflecting surface. Such a decomposition underlies the retrieval technique for operational producing global leaf area index from data provided by two instruments, the moderate resolution imaging spectroradiometer (MODIS) and multiangle imaging spectroradiometer (MISR), during the Earth Observing System (EOS) Terra mission ([Knyazikhin et al., 1998a,b], [Myneni et al., 2002]). The Green's function formalism described in Section 6 of Chapter 2 and operator notations introduced in Section 7 of Chapter 2 are required to follow this section.

Black Soil Problem. Consider the boundary value problem for the 3D radiative transfer equation in vegetation canopy $LI=SI+q$, $I^-=\mathcal{R}I^++q_B$ with the boundary scattering operator $\mathcal{R}$ and source q_B introduced in the previous section. We neglect lateral effects by assuming the zero boundary condition for the lateral surface δV_t. We represent a solution of the boundary value problem as the sum of two components, $I(\underline{r},\underline{\Omega})=I_{bs}(\underline{r},\underline{\Omega})+I_{rest}(\underline{r},\underline{\Omega})$. The first term describes intensity of radiation in the vegetation canopy bounded from below by a *non-reflecting surface* and satisfies

$$
\begin{aligned}
&LI_{bs}=SI_{bs},\\
&I^-_{bs}(\underline{r}_t,\underline{\Omega})=c_T\delta(\underline{\Omega}-\underline{\Omega}_0)+d(z_t,\underline{\Omega}),\\
&I^-_{bs}(\underline{r}_1,\underline{\Omega})=0,
\end{aligned}
$$

$$I^-_{bs}(\underline{r}_b, \underline{\Omega}) = 0. \tag{14a}$$

This is our first basic problem – the black soil problem.

Canopy-Surface Interaction. The function I_{rest} satisfies the radiative transfer equation

$$LI_{rest} = SI_{rest}$$

and the boundary conditions expressed as

$$\begin{aligned} &I^-_{rest}(\underline{r}_t, \underline{\Omega}) = 0, \\ &I^-_{rest}(\underline{r}_l, \underline{\Omega}) = 0, \\ &I^-_{rest}(\underline{r}_b, \underline{\Omega}) = \mathcal{R}\, I^+. \end{aligned} \tag{14b}$$

This boundary value problem describes radiation field due to the interaction between the underlying surface and the vegetation canopy. Unlike the black soil problem, I_{rest} depends on the solution of the "complete transport problem," i.e., $I = I_{bs} + I_{rest}$. And, therefore, requires further transformations to decompose it sub-problems with $\rho_0(\delta V) = 0$.

The lower boundary conditions can be rewritten as

$$I^-_{rest}(\underline{r}_b, \underline{\Omega}) = \frac{\mathcal{R}\, I^+}{T}\, T\,. \tag{15}$$

Here T is downward radiation flux density at the canopy bottom, i.e.,

$$T(\underline{r}_b) = \int\limits_{\underline{n}(\underline{r}_b)\bullet\underline{\Omega}'>0} I(\underline{r}_b, \underline{\Omega}')\left|\underline{\Omega}' \bullet \underline{n}(\underline{r}_b)\right| d\underline{\Omega}', \quad \underline{r}_b \in \delta V_b\,. \tag{16}$$

Note that the ratio $\mathcal{R}I^+ / T$ is a factor of π smaller than ground HDRF. A cosine-weighted integral of the ratio is the ground BHR

$$\rho_{eff}(\underline{r}_b) = \frac{\pi^{-1} \int\limits_{\underline{n}(\underline{r}_b)\bullet\underline{\Omega}'>0} d\underline{\Omega}' \left|\underline{n}(\underline{r}_b) \bullet \underline{\Omega}'\right| I(\underline{r}_b, \underline{\Omega}') \int\limits_{\underline{n}(\underline{r}_b)\bullet\underline{\Omega}<0} \rho_b(\underline{r}_b, \underline{\Omega}' \to \underline{\Omega}) \left|\underline{\Omega} \bullet \underline{n}(\underline{r}_b)\right| d\underline{\Omega}}{\int\limits_{n(\underline{r}_b)\bullet\Omega>0} \left|\underline{\Omega} \bullet \underline{n}(\underline{r}_b)\right| I(\underline{r}_b, \underline{\Omega}') d\underline{\Omega}'}. \tag{17}$$

Here ρ_b is the BRF of the canopy ground (see Eq. (12)). It is clear that the ground BHR depends on ground reflective properties, vegetation canopy and radiation incident on the canopy upper boundary. For horizontally inhomogeneous vegetation canopies, the downward radiation flux T

can vary significantly. However, it does not necessarily involve large variation in the BHR. As it follows from Eq. (17), its range of variation is given by

$$\inf_{\underline{n}(\underline{r}_b)\bullet\underline{\Omega}'>0}\frac{1}{\pi}\int_{\underline{n}(\underline{r}_b)\bullet\underline{\Omega}<0}\rho_b(\underline{r}_b\underline{\Omega}'\to\underline{\Omega})\left|\underline{\Omega}\bullet\underline{n}(\underline{r}_b)\right|d\underline{\Omega}$$
$$\le\rho_{eff}(\underline{r}_b)$$
$$\le\sup_{\underline{n}(\underline{r}_b)\bullet\underline{\Omega}'>0}\frac{1}{\pi}\int_{\underline{n}(\underline{r}_b)\bullet\underline{\Omega}<0}\rho_b(\underline{r}_b\underline{\Omega}'\to\underline{\Omega})\left|\underline{\Omega}\bullet\underline{n}(\underline{r}_b)\right|d\underline{\Omega} \tag{18}$$

If

$$\int_{\underline{n}(\underline{r}_B)\bullet\underline{\Omega}<0}\rho_b(\underline{r}_b,\underline{\Omega}'\to\underline{\Omega})\left|\underline{n}(\underline{r}_b)\bullet\underline{\Omega}\right|\,d\underline{\Omega}$$

is independent on $\underline{\Omega}'$, the ground BHR becomes independent from I^+ and the ground BHR coincides with the ground DHR. Here we neglect the dependence of the ground BHR on the intensity of downward radiation at the canopy bottom within range given by the inequality, Eq. (18).

An effective ground anisotropy is another parameter used to characterize the canopy–ground interaction. This parameter, $d_b(\underline{r}_b,\underline{\Omega})$, is defined as

$$d_b(\underline{r}_b,\underline{\Omega})=\frac{RI^+}{\rho_{eff}T}=\frac{1}{\rho_{eff}(\underline{r}_b)}\cdot\frac{\pi^{-1}\int_{2\pi+}\rho_b(\underline{r}_b,\underline{\Omega}'\to\underline{\Omega})\left|\underline{n}(\underline{r}_b)\bullet\underline{\Omega}'\right|I(\underline{r}_b,\underline{\Omega}')\,d\underline{\Omega}'}{\int_{2\pi^-}\left|\underline{\Omega}'\bullet\underline{n}(\underline{r}_b)\right|I(\underline{r}_b,\underline{\Omega}')d\underline{\Omega}'} \tag{19}$$

Its cosine-weighted integral over downward directions is unity. In terms of these notations, the lower boundary conditions, Eq. (15), can be rewritten as

$$I^-_{rest}(\underline{r}_b,\underline{\Omega})=\rho_{eff}(\underline{r}_b)d_b(\underline{r}_b,\underline{\Omega})T(\underline{r}_b)\,. \tag{20}$$

We neglect variations in ρ_b and d_b due to variation in I^+. However, the downward radiation flux density $T(\underline{r}_b)$ is sensitive to both ground reflectance properties and radiation regime within the vegetation canopy. This variable must be carefully specified.

We use Eq. (28) of Chapter 2 to express I_{rest} in terms of the Green's function, namely,

$$I_{rest}(\underline{r},\underline{\Omega})=\int_{\delta V_b}d\underline{r}'_b\int_{\underline{n}(\underline{r}'_b)\bullet\underline{\Omega}'<0}d\underline{\Omega}'G_S(\underline{r},\underline{\Omega};\underline{r}'_b,\underline{\Omega}')\rho_{eff}(\underline{r}'_b)d_b(\underline{r}'_b,\underline{\Omega}')T(\underline{r}'_b)\,. \tag{21}$$

Substituting this equation into $I(\underline{r},\underline{\Omega})=I_{bs}(\underline{r},\underline{\Omega})+I_{rest}(\underline{r},\underline{\Omega})$ results in

$$I(\underline{r},\underline{\Omega}) = I_{bs}(\underline{r},\underline{\Omega}) + \int_{\delta V_b} d\underline{r}'_b\, \rho_{eff}(\underline{r}'_b) T(\underline{r}'_b) J_S(\underline{r},\underline{\Omega};\underline{r}'_b), \tag{22a}$$

where

$$J_S(\underline{r},\underline{\Omega},\underline{r}'_b) = \int_{\underline{n}(\underline{r}'_b)\bullet\underline{\Omega}'<0} d\underline{\Omega}'\, G_S(\underline{r},\underline{\Omega};\underline{r}'_b,\underline{\Omega}')\, d_b(\underline{r}'_b,\underline{\Omega}'). \tag{22b}$$

is the intensity of radiation field at r generated by a point anisotropic source $d_b(\underline{r}'_b,\underline{\Omega}')\delta(\underline{r}_b - \underline{r}'_b)$ located at $\underline{r}'_b$. Substituting Eq. (22) into Eq. (16) one obtains an integral equation for T

$$T(\underline{r}_b) = T_{bs}(\underline{r}_b) + \int_{\delta V_b} G_d(\underline{r}_b,\underline{r}'_b)\rho_{eff}(\underline{r}'_b) T(\underline{r}'_b)\, d\underline{r}'_b. \tag{23}$$

Here T_{bs} is the downward radiation flux density at the lower boundary for the case of a black surface underneath the vegetation canopy, i.e.,

$$T_{bs}(\underline{r}_b) = \int_{\underline{n}(\underline{r}_b)\bullet\underline{\Omega}'>0} I_{bs}(\underline{r}_b,\underline{\Omega}')\left|\underline{\Omega}'\bullet\underline{n}(\underline{r}_b)\right| d\underline{\Omega}'. \tag{24}$$

The kernel G_d is the downward radiation flux density at $\underline{r}_d$ due to the point anisotropic source $d_b(\underline{r}_b,\underline{\Omega}')\delta(\underline{r}_b - \underline{r}'_b)$,

$$G_d(\underline{r}_b,\underline{r}'_b) = \int_{\underline{n}(\underline{r}_b)\bullet\underline{\Omega}>0} d\underline{\Omega}\left|\underline{\Omega}\bullet\underline{n}(\underline{r}_b)\right| \int_{\underline{n}(\underline{r}'_b)\bullet\underline{\Omega}'<0} G_S(\underline{r}_b,\underline{\Omega};\underline{r}'_b,\underline{\Omega}')\, d_b(\underline{r}'_b,\underline{\Omega}') d\underline{\Omega}'. \tag{25}$$

Note that

$$I_S(\underline{r},\underline{\Omega}) = \int_{\delta V_b} d\underline{r}'_b \int_{\underline{n}(\underline{r}'_b)\bullet\underline{\Omega}'<0} G_S(\underline{r},\underline{\Omega};\underline{r}'_b,\underline{\Omega}')\, d_b(\underline{r}'_b,\underline{\Omega}') d\underline{\Omega}'. \tag{26}$$

is the intensity of radiation field in vegetation canopy generated by the isotropic homogeneous sources d_b located at the canopy bottom. It satisfies the equation $LI_S = SI_S$ and boundary condition $I_S^-(\underline{r}_t,\underline{\Omega}) = 0$, $I_S^-(\underline{r}_1,\underline{\Omega}) = 0$, $I^-(\underline{r}_b,\underline{\Omega}) = d_b(\underline{r}_b,\underline{\Omega})$. This is our second "basic problem" – the "S problem." It follows from this property that

$$\int_{\delta V_b} G_d(\underline{r}_b,\underline{r}'_b)\, d\underline{r}'_b = \int_{\underline{n}(\underline{r}_b)\bullet\underline{\Omega}>0} I_S(\underline{r}_b,\underline{\Omega})\left|\underline{\Omega}\bullet\underline{n}(\underline{r}_b)\right| d\underline{\Omega}. \tag{27}$$

Thus integration of G_d over the lower boundary results in downward flux at $\underline{r}_b \in \delta$ which accounts for contribution from all anisotropic sources at the canopy bottom.

Equations (22) and (23) are basic equations which describe canopy-ground interaction. They are parameterized in terms of ground reflectance properties (the ground BHR and effective ground anisotropy) which are independent on the vegetation canopy; the radiation field in the vegetation canopy bounded at the bottom by a black surface (black soil problem) and radiation field in the vegetation canopy generated by anisotropic heterogeneous source d_b located at the surface underneath the canopy (S problem).

Decomposition Equations. Given $G_d(\underline{r}_b, \underline{r}'_b)$ one can resolve the integral equation (23) and substitute it into Eq. (21). As a results one obtains a solution to the three-dimensional radiative transfer problem with the reflecting lower boundary δV_t. The integral equation (23) allows for an analytical solution in the case of a horizontally homogeneous vegetation canopy bounded from below by a homogeneous Lambertian surface (i.e., the ground BRF is constant with respect to angular variable and points on the canopy bottom). The radiation fluxes T, T_{bs} become independent of horizontal coordinates x and y. The ground BHR is independent of on the intensity of downward radiation at the canopy bottom and coincides with the ground BRF, i.e., $\rho_{eff} = \rho_b$. The effective ground anisotropy is also independent on $I^+(\underline{r}_b, \underline{\Omega})$ and equal to $1/\pi$. The solution of Eq. (23) is then

$$T = \frac{T_{BS}}{1 - \rho_b R_S}, \tag{28}$$

where

$$R_S = \int_{\delta V_b} G_d(\underline{r}_b, \underline{r}'_b)\, d\underline{r}'_b$$

is the downward flux density at $\underline{r}_b \in \delta V_b$ generated by isotropic sources $1/\pi$ distributed over the lower boundary and is given by Eq. (27). This variable is independent of points on the canopy bottom and varies between 0 and 1. Substituting Eq. (26) into Eq. (22) and accounting for Eq. (28) one gets the following decomposition of the boundary value problem into solutions of the black soil and S problems

$$I(z, \underline{\Omega}) = I_{bs}(z, \underline{\Omega}) + \frac{\rho_b T_{BS}}{1 - \rho_b R_S} I_S(z, \underline{\Omega}). \tag{29}$$

In the case of horizontally inhomogeneous medium, however, Eq. (23) needs to be solved in order to decompose the solution of the boundary value problem. The following approximation to I_{rest} can be performed. Consider the ratio

$$R_S(\underline{r}_b) = \frac{\int_{\delta V_b} G_d(\underline{r}_b, \underline{r}'_b)\rho_{eff}(\underline{r}'_b)T(\underline{r}'_b)\,d\underline{r}'_b}{\rho_{eff}(\underline{r}_b)T(\underline{r}_b)}, \quad (30)$$

which is the BHR calculated for the vegetation canopy illuminated by anisotropic sources $\rho_{eff}(\underline{r}'_b)T(\underline{r}'_b)d_b(\underline{r}'_b, \underline{\Omega}')$ from below. We term the ratio, Eq. (30) a "bottom-of-canopy reflectance". For horizontally inhomogeneous vegetation canopies, the downward radiation flux T can vary significantly. However, it does not necessarily involve large variation in R_S. A theoretical explanation of this result can be found in the linear operator analysis [Krein, 1967] and, specifically, in its applications to radiative transfer theory ([Knyazikhin, 1991]; [Kaufmann et al., 2000]; [Zhang et al., 2002]; [Lyapustin and Knyazikhin, 2002]). One of the theorems of the operator theory states that for a continuous positive linear operator B, minimum, m_n, and maximum, M_n, values of the function $\eta_n = \sqrt[n]{B^n u}$ converge to the maximum eigenvalue, $\rho(B)$, of the operator B from below and above for any arbitrarily chosen positive function u, i.e., $m_n \le \rho(B) \le M_n$ and $M_n - m_n$ tends to zero as n tends to infinity. For example, for the problem of atmospheric radiative transfer over common land–surface types, including vegetation, soil sand, and snow, the proximity of m_n and M_n to a high accuracy holds at $n \ge 2$ [Lyapustin and Knyazikhin, 2002]. Here the numerator in Eq. (30) can be treated as a positive integral operator B with a kernel $G_d(\underline{r}_b, \underline{r}'_b)$. For n=1, the ratio (30) varies within an interval $[m_1, M_1]$ around the maximum eigenvalue which is independent of $\rho_{eff}T$. We will demonstrate the eigenvalue technique with an example for canopy spectral response to the incident radiation in next section. Here we assume that an acceptable accuracy takes place at n=1 and we replace $R_S(\underline{r}_b)$ with the maximum eigenvalue $\overline{R}_S$ of an integral operator with the kernel $G_d(\underline{r}_b, \underline{r}'_b)$.

Equation (23) can be rewritten as

$$T(\underline{r}_b) = T_{bs}(\underline{r}_b) + \overline{R}_S \rho_{eff}(\underline{r}_b)T(\underline{r}_b). \quad (31)$$

Solving this equation for T and substituting it into Eq. (21) one gets

$$I(\underline{r}, \underline{\Omega}) = I_{bs}(\underline{r}, \underline{\Omega}) + \int_{\delta V_b} \frac{\rho_{eff}(\underline{r}'_b)T_{bs}(\underline{r}'_b)}{1 - \overline{R}_S \rho_{eff}(\underline{r}'_b)} J_S(\underline{r}, \underline{\Omega}, \underline{r}'_b)d\underline{r}'_b, \quad (32)$$

where $J_S(\underline{r}, \underline{\Omega}, \underline{r}'_b)$ is given by Eq. (22b). Further simplification can be done by either replacing $J_S(\underline{r}, \underline{\Omega}, \underline{r}'_b)$ or the ratio in the integral term of Eq. (32) with a mean value over the canopy bottom. In the former case we have

$$I(\underline{r}, \underline{\Omega}) = I_{bs}(\underline{r}, \underline{\Omega}) + \frac{\overline{\rho}_{eff}\overline{T}_{bs}}{1 - \overline{R}_S \overline{\rho}_{eff}} I_S(\underline{r}, \underline{\Omega}). \quad (33)$$

where I_S is the solution of the S problem and given by Eq. (26); $\overline{\rho}_{eff}$ and $\overline{T}_{bs}$ are mean values of the ground BHR and downward flux density for the black soil problem over the lower boundary δV_b, respectively. Thus we have parameterized the solution of the transport problem in terms of the ground BHR and solutions of the "black-soil problem," I_{bs}, and "*S* problem," I_s. The solution of the "black-soil problem" depends on Sun-view geometry, canopy architecture, and spectral properties of the leaves. The "*S* problem" depends on spectral properties of the leaves and canopy structure only. Substituting Eq. (33) into definitions of the surface HDRF, BHR, BRF, BRDF, and DHR, one obtains the following decompositions of these reflectance quantities

$$R = R_{bs}(\underline{r},\underline{\Omega}) + \frac{\overline{\rho}_{eff} t_{bs}}{1 - \overline{R}_S \overline{\rho}_{eff}} T_S(\underline{\Omega}), \tag{34}$$

$$A = A_{bs} + \frac{\overline{\rho}_{eff} t_{bs}}{1 - \overline{R}_S \overline{\rho}_{eff}} t_S. \tag{35}$$

Here R_{bs} and A_{bs} are HDRF and BHR calculated for a vegetation canopy bounded from below by a black surface; t_{bs} is the canopy transmittance defined as the ratio of the mean downward flux $< T_{bs} >_b$ at the canopy lower boundary to mean incident irradiance $< F^{\downarrow}_{dir} + F^{\downarrow}_{dif} >_0$ where the angle brackets denotes the mean over the upper (subscript "t") or lower boundary (subscript "b") of the parallelepiperd V. If the ratio f_{dir} of the mono-directional to the total incident radiation flux is unity, the HDRF and BHR become BRF and DHR, respectively. The transmittance quantity $T_s(\underline{\Omega})$ is the ratio of the mean radiance, $< I_s >_0$, leaving the top of the vegetation canopy to mean radiance reflected from an ideal Lambertian surface into the same beam geometry and illuminated by anisotropic sources located at the canopy bottom, i.e.,

$$T_S(\underline{\Omega}) = \frac{< I_S(\underline{\Omega}) >_0}{\frac{1}{\pi} \int\limits_{\underline{n}(\underline{r}_b)\bullet\underline{\Omega}<0} < d_b(\underline{\Omega}') >_b | \underline{n}(\underline{r}_b) \bullet \underline{\Omega}' | \, d\underline{\Omega}'}. \tag{36}$$

Finally, t_s is the transmittance of the vegetation canopy illuminated from below by anisotropic sources, i.e., the ratio of the mean irradiance exitance to the mean irradiance of the radiation incident on the canopy from below,

$$t_S(\underline{\Omega}) = \frac{\int\limits_{\underline{n}(\underline{r}_b)\bullet\underline{\Omega}'>0} < I_S(\underline{\Omega}) >_0 | \underline{n}(\underline{r}_b) \bullet \underline{\Omega}' | \, d\underline{\Omega}'}{\frac{1}{\pi} \int\limits_{\underline{n}(\underline{r}_b)\bullet\underline{\Omega}<0} < d_b(\underline{\Omega}') >_b | \underline{n}(\underline{r}_b) \bullet \underline{\Omega}' | \, d\underline{\Omega}'} = \frac{1}{\pi} \int\limits_{\underline{n}(\underline{r}_b)\bullet\underline{\Omega}'>0} T_S(\underline{\Omega}') | \underline{n}(\underline{r}_b) \bullet \underline{\Omega}' | \, d\underline{\Omega}'. \tag{37}$$

Thus, the three-dimensional radiation field can be expressed in terms of ground reflectance properties which are independent on the medium; the radiation field in the medium bounded at the bottom by a black surface (black soil problem); and the radiation field in the medium

generated by anisotropic heterogeneous sources located at the surface underneath the medium (S problem). Solutions to the black soil and S problems are surface independent parameters since no multiple interaction of radiation between the medium and underlying surface is possible and, therefore, have intrinsic canopy information. This decomposition of underlay the retrieval technique for operational producing global leaf area index from data provided by the MODIS and MISR instruments.

Problem Sets

- **Problem 1**. Show that HDRF=BRF=BHR=DHR for Lambertian surfaces.
- **Problem 2**. Show the validity of Eq. (5).
- **Problem 3**. Derive the BRF and DHR for a mirror.
- **Problem 4**. Let a vegetation canopy located in the parallelepiped V is isotropically illuminated from above and bounded from below and lateral sides by a black surface, i.e., $B(\underline{r}_B,\underline{\Omega}) = 1/\pi$ if $\underline{r}_B \in \delta V_t$ and $B(\underline{r}_B,\underline{\Omega}) = 0$, otherwise. Prove that the BHR is less than 1. Use Theorem I.1.
- **Problem 5**. Prove that the BHR is an increasing function with respect to single scattering albedo. Do not use the assumptions of the Problem 4. Use Theorem I.1.
- **Problem 6**. Derive Eq. (11). Explain why Eq. (11) is not used in remote sensing of vegetation.
- **Problem 7**. Show that $\rho_{B,V}$ for the boundary conditions (Eqs (7), (10) and (13)) is given by

$$\rho_{B,V} = \sup_{\underline{r}' \in \delta V_t; \underline{\Omega}' \bullet \underline{n}(\underline{r}') > 0} \frac{1}{\pi} \int_{\underline{\Omega}' \bullet \underline{n}(\underline{r}') < 0} \rho_b(\underline{r}', \underline{\Omega}' \to \underline{\Omega}) \left| \underline{\Omega} \bullet \underline{n}(\underline{r}') \right| d\underline{\Omega}.$$

  This is albedo of the surface underneath the canopy.
- **Problem 8**. Show that $\rho_{eff}(\underline{r}_b) \le \rho_0(\delta V)$.
- **Problem 9**. Demonstrate the validity of Eq. (19).
- **Problem 10**. Find the effective ground reflectance for the case of Lambertian surface underneath the canopy.
- **Problem 11**. Show that

$$\int_{2\pi^-} d_b(\underline{r}_b, \underline{\Omega}) \left| \underline{\Omega} \bullet \underline{n}(\underline{r}_b) \right| d\underline{\Omega} = 1.$$

- **Problem 12**. Find the effective ground anisotropy for the case of Lambertian surface underneath the canopy.
- **Problem 13**. Show that the function

$$I_d(\underline{r}, \underline{\Omega}) = \int_{\delta V_b} d\underline{r}'_b \int_{\underline{n}(\underline{r}'_b) \bullet \underline{\Omega}' < 0} G_S(\underline{r}, \underline{\Omega}; \underline{r}'_b, \underline{\Omega}') \, d_b(\underline{r}'_b, \underline{\Omega}') d\underline{\Omega}'$$

  is the intensity of radiation field in vegetation canopy generated by the anisotropic heterogeneous source db located at the canopy bottom. It follows from this property that

$$\int_{\delta V_b} G_d(\underline{r}_b, \underline{r}'_b) \, d\underline{r}'_b = \int_{\underline{n}(\underline{r}_b) \bullet \underline{\Omega} > 0} I_d(\underline{r}_b, \underline{\Omega}) \left| \underline{\Omega} \bullet \underline{n}(\underline{r}_b) \right| d\underline{\Omega}$$

- **Problem 14**. Show that for a horizontally homogeneous vegetation canopy bounded from below by a homogeneous Lambertian surface the downward flux density,

$$R_S = \int_{\delta V_b} G_d(\underline{r}_b, \underline{r}'_b)\, d\underline{r}'_b$$

  does not depend on r_b and varies between 0 and 1.
- **Problem 15**. Show that for a horizontally homogeneous vegetation canopy bounded from below by a homogeneous Lambertian surface Eq. (26) does not depend on horizontal variables x and y.

References

Bell, G. I., and S. Glasstone (1970). *Nuclear Reactor Theory*, Van Nostrand Reinholt, New York.

Case, K. M., and P.F. Zweifel (1967). *Linear Transport Theory*, Addison-Wesley Publishing Company, Reading, Massachusetts.

Diner, D.J., J.V.Martonchik, C. Borel, S.A.W. Gerstl, H.R. Gordon, Y. Knyazikhin, R. Myneni, B. Pinty, and M.M. Verstraete (1998) MISR: Level 2 surface retrieval algorithm theoretical basis, *JPL Internal Doc. D-11401, Rev. C*, Calif. Inst. of Technol., Jet Propul. Lab., Pasadena.

Germogenova, T.A. (1986). *The Local Properties of the Solution of the Transport Equation* Nauka, Moscow (in Russian).

Knyazikhin, Y., G. Miessen, O. Panfyorov, and G. Gravenhorst (1997). Small-Scale Study of Three-Dimensional Distribution of Photosynthetically Active Radiation in a Forest, *Agric. For. Meteorol*., **88**, 215-239.

Kranigk, J. (1996). *Ein Model für den Strahlungstransport in Fichtenbeständen*, Cuvillier, Göttingen, Germany.

Krein, S.G (ed.) (1972). *Functional Analysis*, Groningen, Wolters-Noordhoff.

Martonchik, J.V., C.J. Bruegge, and A.H. Strahler (2000). A review of reflectance nomenclature used in remote sensing, *Remote Sens. Rev.*, **19,** 9-20.

Monteith, J.L. and M.H. Unsworth (1990). *Principles of Environmental Physics*. E.Arnold, London.

Nicodemus, F.E., J.C. Richmond, I.J. Hsia, I.W. Ginsberg, and T. Limperis (1997). Geometrical consideration and nomenclature for reflectance, NBS Monograph, 160, National Bureau of Standards, US Department of Commerce, Washington, D.C

Pokrowski, G.I. (1929). Über die Helligkeitsverteilung am Himmel. *Physikal. Zeitschr*., **30**, 697-700.

Richards, P. I. (1959). *Manual of Mathematical Physics*. A Pergamon Press Book, New York.

Ross, J. (1981). *The Radiation Regime and Architecture of Plant Stands*. Dr. W. Junk Publishers, Delft, The Netherlands.

Shabanov, N.V., Y. Knyazikhin, F. Baret, and R.B. Myneni (2000). Stochastic modeling of radiation regime in discontinuous vegetation canopy, *Remote Sens. Environ*, **74**, 125-144.

Vladimirov, V.S. (1963). Mathematical problems in the one-velocity theory of particle transport, *Tech. Rep. AECL-1661*, At. Energy of Can. Ltd., Chalk River, Ontario.

Further Readings

Davis, A. and Y. Knyazikhin, *A Primer in Three-Dimensional Radiative Transfer*, in A. Davis and A. Marshak (eds.) (2006). "Three-dimensional Radiative Transfer in the Cloudy Atmosphere," Springer Verlag (in print).

Bell, G. I., and S. Glasstone (1970). *Nuclear Reactor Theory*. Van Nostrand Reinholt, New York.

Case, K. M., and P.F. Zweifel, (1967). *Linear Transport Theory*, Addison-Wesley Publishing Company, Reading, Mass.

Chapter 4

Numerical Solution of the Radiative Transfer Equation

Myneni et al.

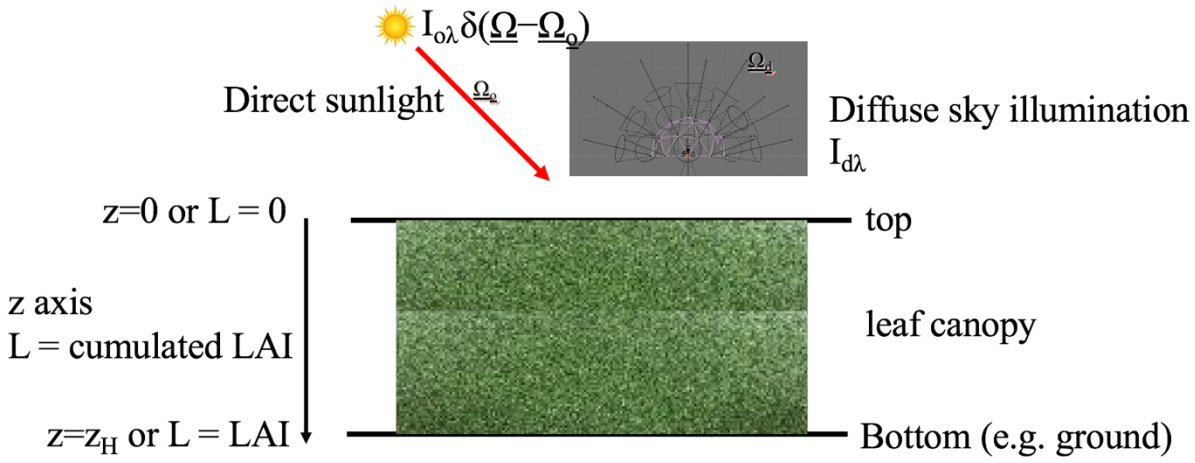

Chapter 4

Numerical Solution of the Radiative Transfer Equation

1. Transport Problem for Vegetation Canopies in One Spatial Dimension

We consider the one-dimensional radiative transfer equation for a leaf canopy confined between depths $z = 0$ at the top and $z = z_H$ at the bottom, that is the vertical ordinate is directed downwards. All directions are measured with respect to –z axis such that $\mu > 0$ for upward traveling directions. The canopy is assumed bounded at the bottom by a reflecting and absorbing ground and illuminated at the top by a mono-directional beam source (direct solar radiation) of intensity I_o along $\underline{\Omega}_o$ and a diffuse source (skylight) of intensity I_d, at wavelength λ. The appropriate transfer equation is

$$-\mu \frac{\partial}{\partial z} I_\lambda(z,\underline{\Omega}) + \sigma(z,\underline{\Omega}) I_\lambda(z,\underline{\Omega}) = \int_{4\pi} d\underline{\Omega}'\, \sigma_{s\lambda}(z,\underline{\Omega}' \to \underline{\Omega})\, I_\lambda(z,\underline{\Omega}') \tag{1}$$

and the boundary conditions are

$$I_\lambda(z=0,\underline{\Omega}) = I_{o\lambda}\delta(\underline{\Omega}-\underline{\Omega}_o) + I_{d\lambda}(\underline{\Omega}), \quad \mu < 0, \tag{2a}$$

$$I_\lambda(z=z_H,\underline{\Omega}) = \frac{1}{\pi}\int_{2\pi^-} d\underline{\Omega}'\, \rho_{s\lambda}(\underline{\Omega}' \to \underline{\Omega})\,|\mu'|\, I_\lambda(z=z_H,\underline{\Omega}'), \quad \mu > 0. \tag{2b}$$

In the above, σ is the wavelength-independent total interaction cross section or the extinction coefficient, $\sigma_{s\lambda}$ is the wavelength-dependent differential scattering cross section and $\rho_{s\lambda}$ is the wavelength-dependent bi-directional reflectance function of the ground, or understory, beneath

the vegetation canopy. The specific intensity I is thus wavelength dependent. However, for ease of expression, this dependence will be not explicitly shown for the reminder of this chapter. It is convenient to express the incident field as (cf. Chapter 4)

$$I_o(\underline{\Omega}) = \frac{f_{dir}}{|\mu_o|}\delta(\underline{\Omega} - \underline{\Omega}_o)F_{in}(z=0),$$
$$I_d(\underline{\Omega}) = (1 - f_{dir})d_o(z=0,\underline{\Omega})F_{in}(z=0)$$

where f_{dir} is the fraction of total incident flux density at the top of the canopy, $F_{in}(z=0)$, is the total irradiance of the incident solar radiation at the top of canopy and d_o is the anisotropy of the diffuse source.

If the leaf normal orientation distribution function g_L is assumed independent of depth z in the canopy, the two cross sections in Eq. (1) can be written as (cf. Chapter 3)

$$\sigma(z,\underline{\Omega}') = u_L(z)G(\underline{\Omega}'), \tag{3a}$$
$$\sigma_S(z,\underline{\Omega}' \to \underline{\Omega}) = u_L(z)\frac{1}{\pi}\Gamma(\underline{\Omega}' \to \underline{\Omega}), \tag{3b}$$

where u_L is the leaf area density distribution, G is the geometry factor

$$G(\underline{\Omega}') = \frac{1}{2\pi}\int_{2\pi^+} d\underline{\Omega}_L g_L(\underline{\Omega}_L)|\underline{\Omega}_L \bullet \underline{\Omega}'|$$

and Γ is the area scattering phase function

$$\frac{1}{\pi}\Gamma(\underline{\Omega}' \to \underline{\Omega}) = \frac{1}{2\pi}\int_{2\pi^+} d\underline{\Omega}_L g_L(\underline{\Omega}_L)|\underline{\Omega}_L \bullet \underline{\Omega}'|\gamma_L(\underline{\Omega}_L;\underline{\Omega}' \to \underline{\Omega})$$

with γ_L being the leaf scattering phase function. The vertical coordinate z can be changed to cumulative leaf area index L by dividing Eq. (1) with u_L. The vegetation canopy is now contained between L = 0 at the top and L = L_H at the bottom, where L_H is the leaf area index of the canopy. The transport problem in one spatial dimension for a vegetation canopy illuminated at the top with unit flux density $[F_{in}(L=0)=1]$ and isotropic skylight is thus,

$$-\mu\frac{\partial}{\partial L}I(L,\underline{\Omega}) + G(L,\underline{\Omega})I(L,\underline{\Omega}) = \frac{1}{\pi}\int_{4\pi} d\underline{\Omega}'\Gamma(\underline{\Omega}' \to \underline{\Omega})I(L,\underline{\Omega}'), \tag{4a}$$
$$I(L=0,\underline{\Omega}) = \frac{f_{dir}}{|\mu_o|}\delta(\underline{\Omega} - \underline{\Omega}_o) + \frac{(1-f_{dir})}{\pi}, \quad \mu < 0, \tag{4b}$$
$$I(L=L_H,\underline{\Omega}) = \frac{1}{\pi}\int_{2\pi^-} d\underline{\Omega}'\rho_s(\underline{\Omega}' \to \underline{\Omega})|\mu'|I(L=L_H,\underline{\Omega}'), \quad \mu > 0. \tag{4c}$$

2. Separation of Uncollided and Collided Intensities

It is convenient for numerical purposes and also to gain insight on the transport physics to separate the uncollided radiation field from the collided field, that is,

$$I(L,\underline{\Omega}) = I^0(L,\underline{\Omega}) + I^C(L,\underline{\Omega}) \tag{5}$$

where I^0 is the specific intensity of uncollided photons and I^C is the specific intensity of photons which experienced collisions with elements of the host medium. By introducing Eq. (5) in Eq. (4), the transport problem can be split into equations for the uncollided intensity,

$$-\mu \frac{\partial}{\partial L} I^0(L,\underline{\Omega}) + G(\underline{\Omega})\, I^0(L,\underline{\Omega}) = 0\,, \tag{6a}$$

$$I^0(L=0,\underline{\Omega}) = \frac{f_{dir}}{|\mu_o|}\delta(\underline{\Omega}-\underline{\Omega}_o) + \frac{(1-f_{dir})}{\pi}, \quad \mu<0, \tag{6b}$$

$$I^0(L=L_H,\underline{\Omega}) = \frac{1}{\pi}\int_{2\pi^-} d\Omega'\, \rho_s(\underline{\Omega}\rightarrow\underline{\Omega})\,|\mu'|\, I^0(L=L_H,\underline{\Omega}'), \quad \mu>0, \tag{6c}$$

and collided intensity,

$$-\mu \frac{\partial}{\partial L} I^C(L,\underline{\Omega}) + G(\underline{\Omega})\, I^C(L,\underline{\Omega}) = Q(L,\underline{\Omega}) + S(L,\underline{\Omega}), \tag{7a}$$

$$I^C(L=0,\underline{\Omega}) = 0, \quad \mu<0\,, \tag{7b}$$

$$I^C(L=L_H,\underline{\Omega}) = \frac{1}{\pi}\int_{2\pi^-} d\underline{\Omega}'\, \rho_s(\underline{\Omega}'\rightarrow\underline{\Omega})\,|\mu'|\, I^C(L=L_H,\underline{\Omega}'), \quad \mu>0, \tag{7c}$$

In the above, Q is the *first collision source*

$$Q(L,\underline{\Omega}) \equiv \frac{1}{\pi}\int_{4\pi} d\underline{\Omega}'\,\Gamma(\underline{\Omega}'\rightarrow\underline{\Omega})\, I^0(L,\underline{\Omega}') \tag{8a}$$

and S is the *distributed source*

$$S(L,\underline{\Omega}) = \frac{1}{\pi}\int_{4\pi} d\underline{\Omega}'\,\Gamma(\underline{\Omega}'\rightarrow\underline{\Omega})\, I^C(L,\underline{\Omega}')\,. \tag{8b}$$

3. Uncollided Problem

The solution to the uncollided problem [Eq. (6)] is,

$$I^0(L,\underline{\Omega}) = I^0(L=0,\underline{\Omega})\, P[\underline{\Omega},(L-0)], \quad \mu<0, \tag{9a}$$

$$I^0(L,\underline{\Omega}) = I^0(L = L_H,\underline{\Omega})\, P[\underline{\Omega},(L_H - L)], \quad \mu > 0 \tag{9b}$$

where

$$P[\underline{\Omega},(L2 - L1)] = \exp\left[-\frac{1}{|\mu|} G(\underline{\Omega})(L2 - L1)\right] \tag{9c}$$

denotes the probability of photons not experiencing collisions while traveling along $\underline{\Omega}$ between depth L1 and L2 (L2>L1). The downward uncollided intensity at the top of the canopy $I^0(L = 0,\underline{\Omega})$ in Eq. (9a) is given by the boundary condition, Eq. (6b). The upward intensity at the ground $I^0(L = L_H,\underline{\Omega})$ in Eq. (9b) can be evaluated as [cf. Eq. (6c)]

$$I^0(L = L_H,\underline{\Omega}) = \frac{1}{\pi}\int_{2\pi^-} d\underline{\Omega}'\, \rho_s(\underline{\Omega} \to \underline{\Omega})\,|\mu'|\, I^0(L = 0,\underline{\Omega})\, P[\underline{\Omega}',(L_H - 0)], \quad \mu > 0. \tag{10}$$

If the ground reflectance is wavelength-independent, then the normalized uncollided radiation field is also wavelength-independent because the extinction coefficient is wavelength independent in vegetation canopies.

4. First Collision Problem

The collided problem specified by Eq. (7) is difficult to solve because of the distributed source term [Eq. (8b)]. Analytical solutions are possible only in the case of simple scattering kernels. As noted previously, the scattering phase function Γ is generally not rotationally-invariant, and this precludes the use of many standard techniques developed in transport theory. If scattering in the medium is weak, a single-scattering approximation may suffice. The corresponding transport problem

$$-\mu \frac{\partial}{\partial L} I^1(L,\underline{\Omega}) + G(\Omega)\, I^1(L,\underline{\Omega}) = Q(L,\underline{\Omega}), \tag{11a}$$

$$I^1(L = 0,\underline{\Omega}) = 0, \quad \mu < 0, \tag{11b}$$

$$I^1(L = L_H,\underline{\Omega}) = \frac{1}{\pi}\int_{2\pi^-} d\underline{\Omega}'\, \rho_s(\underline{\Omega}' \to \underline{\Omega})\,|\mu'|\, I^1(L = L_H,\underline{\Omega}'), \quad \mu > 0 \tag{11c}$$

can be solved for the single-scattered intensity, I^1, that is, radiation intensity of photons scattered once, with just the first collision source term,

$$I^1(L,\underline{\Omega}) = \frac{1}{|\mu|}\int_0^L dL' Q(L',\underline{\Omega})\, P[\underline{\Omega},(L - L')], \quad \mu < 0, \tag{12a}$$

$$I^1(L,\underline{\Omega}) = \frac{1}{|\mu|}\int_L^{L_H} dL' Q(L',\underline{\Omega})\, P[\underline{\Omega},(L'-L)] + I^1(L = L_H,\underline{\Omega}) P(\underline{\Omega}, L_H - L), \quad \mu > 0, \tag{12b}$$

where $I^1(L = L_H, \Omega)$ is given by Eq. (10).

5. Successive Orders of Scattering Approximation

The specific intensity of photons that experienced two collisions in the medium I^2 can be solved with knowledge of first scattered intensity I^1 as follows,

$$I^2(L,\underline{\Omega}) = \frac{1}{|\mu|}\int_0^{L} dL' S_1(L',\underline{\Omega})\, P[\underline{\Omega},(L - L')], \quad \mu < 0, \tag{13a}$$

$$I^2(L,\underline{\Omega}) = \frac{1}{|\mu|}\int_L^{L_H} dL' S_1(L',\underline{\Omega})\, P[\underline{\Omega},(L'-L)] + I^2(L = L_H,\underline{\Omega}) P(\underline{\Omega}, L_H - L), \quad \mu > 0, \tag{13b}$$

where the distributed source term evaluated with first scattered intensity is

$$S_1(L,\underline{\Omega}) = \frac{1}{\pi}\int_{4\pi} d\underline{\Omega}'\, \Gamma(\underline{\Omega}' \to \underline{\Omega})\, I^1(L,\underline{\Omega}'). \tag{14}$$

The foregoing may be generalized for n-th order of scattering as

$$I^n(L,\underline{\Omega}) = \frac{1}{|\mu|}\int_0^{L} dL' S_{n-1}(L',\underline{\Omega})\, P[\underline{\Omega},(L - L')], \quad \mu < 0, \tag{15a}$$

$$I^n(L,\underline{\Omega}) = \frac{1}{|\mu|}\int_L^{L_H} dL' S_{n-1}(L',\underline{\Omega})\, P[\underline{\Omega},(L'-L)] + I^n(L = L_H,\underline{\Omega}) P(\underline{\Omega}, L_H - L), \quad \mu > 0. \tag{15b}$$

The total intensity I and sources S can be evaluated as

$$I(L,\underline{\Omega}) = I^0(L,\underline{\Omega}) + \sum_{n=1}^{\infty} I^n(L,\underline{\Omega}), \tag{16a}$$

$$S(L,\underline{\Omega}) = \sum_{n=1}^{\infty} S_n(L,\underline{\Omega}).. \tag{16b}$$

In practice, the summation in Eq. (16) is limited to N-orders of scattering. Figure 1 shows convergence of

$$\varepsilon_n = S - \sum_{k=1}^{n} S_k,$$

at the top L=0, and the bottom, $L = L_H$, of the canopy. One can see that $\log \varepsilon_n$ follows a straight line if n exceeds a certain number, indicating that $\varepsilon_n \approx c\lambda^n$. Absolute value of the slope λ is the value of the convergence which depends on the re-collision probability, p, single scattering albedo, ϖ_0 and the maximum boundary reflectance, $\rho_0(\delta V)$. For the black soil problem (cf. Chapter 4), $\lambda = \varpi_0 \rho_0$. Thus the number of iterations needed to achieve a desired accuracy ε is inversely proportional to the rate of convergence, i.e. $n = \left| \ln \varepsilon / c \right| / \lambda$, and depends on canopy structure (p), leaf optics (ϖ_0)and boundary reflective properties ($\rho_0(\delta V)$). In general, λ is an increasing function of these variables and thus the higher p, ϖ_0, and $\rho_0(\delta V)$ are, the slower convergence is [Knjazikhin, 1990]. This method has been applied to model vegetation reflection by Myneni et al. [1987].

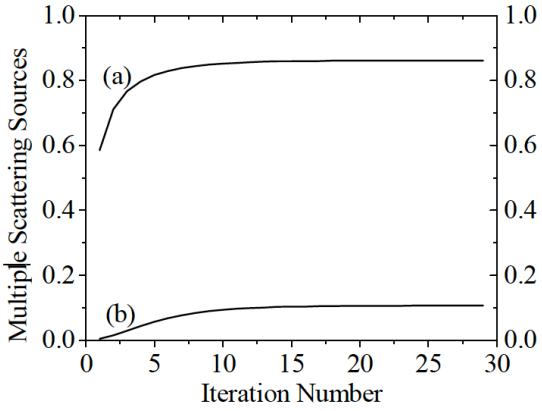

Figure 1. Convergence of the scattering sources S at the top of the canopy (a) and at the bottom of the canopy (b) during the numeric iteration process. The total Leaf Area Index (LAI) of the canopy is 5.0. The canopy is illuminated by diffuse incidence and by direct incidence from the direction (θ=150°, φ=0 °). The direct radiation accounts for 70% of the total incoming flux (F_{dir}=0.7). The leaf norm distribution of the canopy is planophile (mostly horizontal leaves). At the NIR wavelength ,the leaf reflectance ρ_{nir} is 0.475, and the leaf transmittance τ_{nir} is 0.45. The soil reflectance (ρ_{soil}) is 0.2. The threshold for error is considered 1e-05.

6. Gauss-Seidel Iteration Procedure for the Collided Problem

Consider the collided problem specified by Eq. (7). Discretize the angular variable $\underline{\Omega}$ into a finite number of directions, Ω_j, j = 1, 2, …, M, with the weights denoted by w_j. Similarly, discretize the spatial variable L, that is, divide L_H into N layers, each of thickness ΔL. We use the notation L_i and L_{i+1} to denote successive layers. The collided radiation at L_{i+2} and L_i in downward directions can be written as

$$I^C(L_{i+2},\Omega_j) = I^C(L_i,\Omega_j)*P(\Omega_j,2\Delta L) + 1/|\mu_j| * \int_{Li}^{Li+2} dL' \, J(L',\Omega_j)P[\Omega_j,(L_{i+2}-L')], \quad u < 0 \,, \; (17)$$

where J = Q + S is the source term, that is, the sum of first collision and distributed sources. If ΔL is small, then the following approximation is valid

$$\frac{1}{|\mu_j|}\int_{L_i}^{L_{i+2}} dL'\, J(L',\Omega_j)P[\Omega_j,(L_{i+2}-L')]$$

$$= \frac{1}{|\mu_j|}\int_{L_i}^{L_{i+2}} dL'\, J(L',\Omega_j)\, P[\Omega_j,(L'-L_i)]$$

$$\equiv J(L_{i+1},\Omega_j)\left[\frac{1}{G(\Omega_j)}\right]\left\{1-\exp\left[-\frac{1}{|\mu_j|}G(\Omega_j)2\Delta L\right]\right\} \qquad (18)$$

where the source in the intervening layer is evaluated as

$$J(L_{i+1},\Omega_j) = \frac{1}{\pi}\sum_{k=1}^{M} w_k\, \Gamma(\Omega_k \rightarrow \Omega_j)\, I^C(L_{i+1},\Omega_k) + Q(L_{i+1},\Omega_j)\,. \qquad (19)$$

A similar approximation and equation can be derived for upward directions (u > 0).

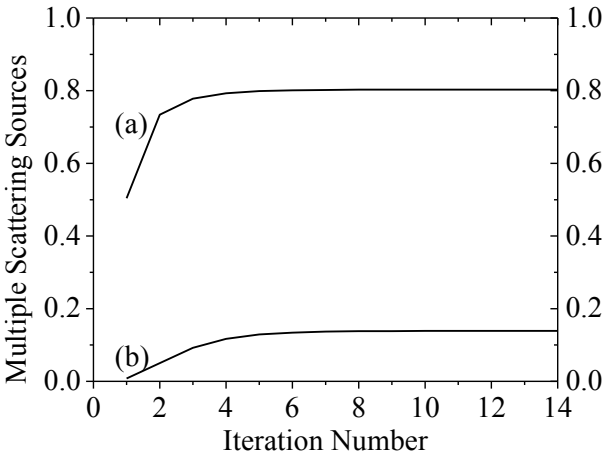

Figure 2. Convergence of multiple scattering sources (S) at the top of the canopy (a) and at the bottom of the canopy (b) during the iteration process. The total Leaf Area Index (LAI) of the canopy is 5. The canopy is illuminated by diffuse radiation and by direct solar radiation along the direction (θ=150^o, φ=0^o). Direct radiation accounts for 70% of the total incoming flux (F_{dir}=0.7). The leaf normal distribution of the canopy is planophile (mostly horizontal leaves). At NIR wavelengths, leaf reflectance (ρ_{nir}) is 0.475, leaf transmittance (τ_{nir}) is 0.45, and soil reflectance (ρ_{soil}) is 0.2.

The resulting system of linear algebraic equations can be solved iteratively for the unknowns $I^C(L_i,\Omega_j)$, i = 1, 2,…, N, j = 1, 2,…, M, using the Gauss-Seidel iteration procedure. The downward and upward intensities are computed from layer to layer for every iteration step. For instance, in the n-th iteration, the values of the downward intensities in layer i+2 are computed from the downward intensities of layer i and i+1 of the same iteration step and from the upward intensities of layer i+1 of the previous iteration step n-1. The convergence of the source with iteration count is shown in Fig. 2.

The advantages of this method are that the internal radiation field is readily available without additional labor and it is possible to account for vertical in-homogeneities in canopy structure and optics. The main limitation is that the iteration becomes tedious in optically deep canopies at

strongly scattering wavelengths. This method has been used to model vegetation reflectance by Knyazikhin and Marshak [1991], and Liang and Strahler [1993].

7. Discrete Ordinates Method for the Collided Problem

We now consider numerical solution of the transport problem for the collided intensity in one spatial dimension using the discrete ordinates method as developed in neutron transport theory. In this method, photons are restricted to travel in a finite number of discrete directions, usually the quadrature directions, such that the angular integrals are evaluated with high precision. The spatial derivatives may be approximated by a finite difference scheme, to result in a set of equations which can be used to solve for the collided radiation field by iterating on the distributed source. This method has been used by Shultis and Myneni [1988] to model the radiation regime in vegetation canopies.

We consider the transport problem for the collided intensity [Eq. (7)]. The angular dependence of the transport equation is approximated by discretizing the angular variables μ and φ into a set of [N x M] discrete directions. The source terms are evaluated by numerical quadrature where $[\mu_i, \varphi_j]$ are the quadrature ordinates and the set of corresponding weights are $[w_i, \hat{w}_j]$. The transport equation for the collided intensity [Eq. (7)] can be written as

$$-\mu_i \frac{\partial}{\partial L} I^C(L,\Omega_{i,j}) + G(\Omega_{i,j})\, I^C(L,\Omega_{i,j}) = Q(L,\Omega_{i,j}) + S(L,\Omega_{i,j}) \tag{20}$$

where the first collision and distributed sources are:

$$Q(L,\Omega_{i,j}) = \frac{1}{\pi}\sum_{n=1}^{N} w_n \sum_{m=1}^{M} \hat{w}_m \Gamma(\Omega_{n,m} \to \Omega_{i,j})\, I^o(L,\Omega_{n,m}), \tag{21a}$$

$$S(L,\Omega_{i,j}) = \frac{1}{\pi}\sum_{n=1}^{N} w_n \sum_{m=1}^{M} \hat{w}_m \Gamma(\Omega_{n,m} \to \Omega_{i,j})\, I^C(L,\Omega_{n,m}). \tag{21b}$$

The vegetation canopy contained between $L = 0$ and $L = L_H$ is divided into K layers of equal thickness ΔL. The spatial derivative in Eq. (20) is approximated as

$$\frac{\partial}{\partial L} I^C(L_{k+0.5},\Omega_{i,j}) = \frac{[I^C(L_{k+1},\Omega_{i,j}) - I^C(L_k,\Omega_{i,j})]}{\Delta L}, \tag{22}$$

where k+0.5 is the center of the layer between the edges k and k+1. The discretized version of transport equation thus reads as

$$-\mu_i \frac{[I^C(L_{k+1},\Omega_{i,j}) - I^C(L_k,\Omega_{i,j})]}{\Delta L} + G(\Omega_{i,j})\, I^C(L_{k+0.5},\Omega_{i,j}) =$$

$$= Q(L_{k+0.5}, \Omega_{i,j}) + S(L_{k+0.5}, \Omega_{i,j}), \tag{23}$$

with k = 1, 2,…, K, i = 1, 2,…, N and j = 1, 2,…, M. To reduce the number of unknowns, a relation between cell-edge and cell-center collided intensities is required. Typically the following is used,

$$I^C(L_{k+0.5}, \Omega_{i,j}) \approx (1-\alpha) I^C(L_k, \Omega_{i,j}) + \alpha \times I^C(L_{k+1}, \Omega_{i,j}), \quad \mu < 0, \tag{24a}$$

$$I^C(L_{k+0.5}, \Omega_{i,j}) \approx (1-\alpha) I^C(L_{k+1}, \Omega_{i,j}) + \alpha \times I^C(L_k, \Omega_{i,j}), \quad \mu > 0 \tag{24b}$$

and if $\alpha = 0.5$, the cell-center intensity is the arithmetic average of the cell-edge intensities.

Equation (23) can be solved for $I^C(L_{k+1}, \Omega_{i.i})$ in terms of $I^c(L_k, \Omega_{i.i})$ in view of Eqs.(24) as

$$I^C(L_{k+1}, \Omega_{i,j}) = a_{i,j}\, I^C(L_k, \Omega_{i,j}) - b_{i,j}\, J(L_{k+0.5}, \Omega_{i,j}), \quad \mu < 0, \tag{25}$$

and for $I^C(L_k, \Omega_{i.i})$ in terms of $I^C(L_{k+1}, \Omega_{i.i})$ as

$$I^C(L_k, \Omega_{i,j}) = c_{i,j}\, I^C(L_{k+1}, \Omega_{i,j}) + d_{i,j}\, J(L_{k+0.5}, \Omega_{i,j}), \quad \mu > 0. \tag{26}$$

In the above,

$$a_{i,j} = \frac{1 + [1-\alpha] f_{i,j}}{[1 - \alpha f_{i,j}]}, \tag{27a}$$

$$b_{i,j} = \frac{f_{i,j}}{G(\Omega_{i,j})[1 - \alpha f_{i,j}]}, \tag{27b}$$

$$c_{i,j} = \frac{1 - [1-\alpha] f_{i,j}}{[1 + \alpha f_{i,j}]}, \tag{27c}$$

$$d_{i,j} = \frac{f_{i,j}}{G(\Omega_{i,j})[1 + \alpha f_{i,j}]}, \tag{27d}$$

$$f_{i,j} = \frac{G(\Omega_{i,j})\Delta L}{\mu_i}, \tag{27e}$$

$$J(L_{k+0.5}, \Omega_{i,j}) = Q(L_{k+0.5}, \Omega_{i,j}) + S(L_{k+0.5}, \Omega_{i,j}). \tag{27f}$$

These equations are of the standard form except for the angular dependence of the coefficients $a_{i,j}$ through $d_{i,j}$ because of the geometry factor G. The set of Eqs. (25) and (26) can be used to solve for collided intensity as follows. While sweeping downwards in the phase space, Eq. (25) is used to step successively down in the mesh. At the bottom, the boundary condition is handled as

$$I^C(L_{K+1}, \Omega_{i,j}) = \frac{1}{\pi} \sum_{n=1}^{N/2} w_n \sum_{m=1}^{M} \hat{w}_m\, \rho_s(\Omega_{n,m} \rightarrow \Omega_{i,j}) \left|\mu_n\right| I^C(L_{K+1}, \Omega_{n,m}). \tag{28}$$

Note that i = (N/2)+1,…, N in the above. Now, Eq. (26) is used to sweep through the grid in upward directions. The distributed source is upgraded [Eq. (21b)] using the relations between cell-edge and cell-center intensities [Eqs. (24)]. This procedure is repeated until the cell-edge intensities in successive iterations do not differ by more than a preset threshold value – the convergence of the source with iteration is shown in Fig. 3.

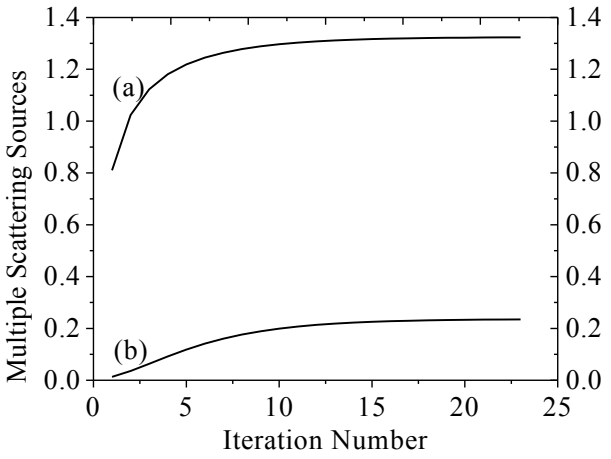

Figure 3. Convergence of multiple scattering sources (S) at the top of the canopy (a) and at the bottom of the canopy (b) during the iteration process. The total Leaf Area Index (LAI) of the canopy is 5. The canopy is illu-minated by diffuse radiation, and by direct solar radia-tion along the direction (θ=150^o, φ=0 ^{o}). Direct radia-tion accounts for 70% of the total incoming flux (f_{dir}=0.7). The leaf normal distribution of the canopy is planophile (mostly horizontal leaves). At NIR wavelengths, leaf reflectance (ρ_{nir}) is 0.475, leaf trans-mittance (τ_{nir}) is 0.45, and soil reflectance (ρ_{soil}) is 0.2.

Numerical results illustrating how vegetation canopy reflectance (and transmittance) changes with respect to leaf area index and sun-view inclination angles are shown in Fig. 4.

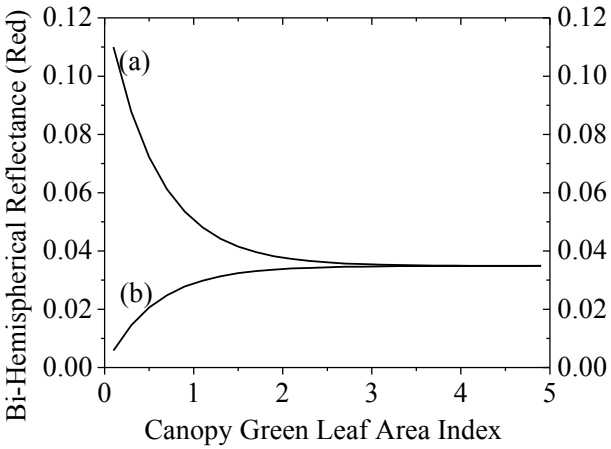

Bi-Hemispherical Reflectance (BHR) at red wavelengths (~ 0.7μm) as a function of canopy green leaf area index (LAI). Ground reflectance (ρ_{soil}) for the two different soil types is (a) 0.125 (typical soil reflectance); and (b) 0 (black soil). The other problem parameters are as in the standard problem described in the figure caption.

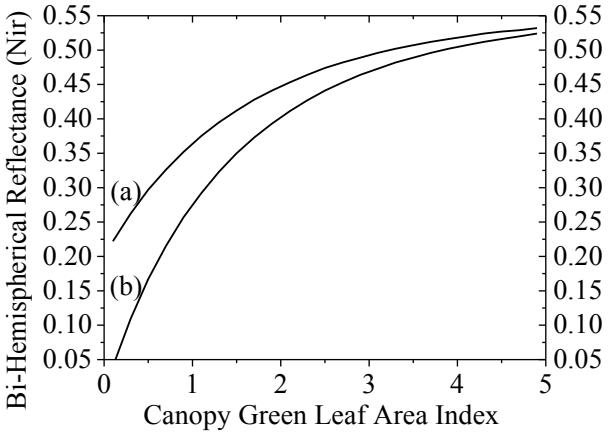

Bi-Hemispherical Reflectance (BHR) at NIR wavelengths (~0.9μm) as a function of canopy green leaf area index (LAI). Ground reflectance (ρ_{soil}) for the two different soil types is: (a) 0.2 (typical soil reflectance); and (b) 0 (black soil). The other problem parameters are as in the standard problem described in the figure caption.

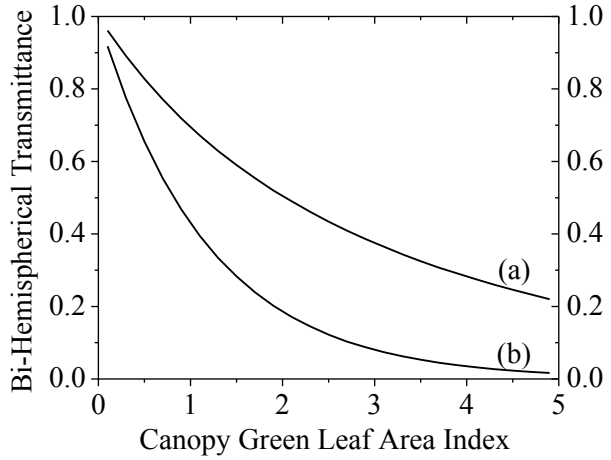

Bi-Hemispherical Transmittance (BHT) at red (~0.7μm) and NIR (~0.9μm) wavelengths as a function of canopy green leaf area index (LAI). The other problem parameters are as in the standard problem described in the figure caption.

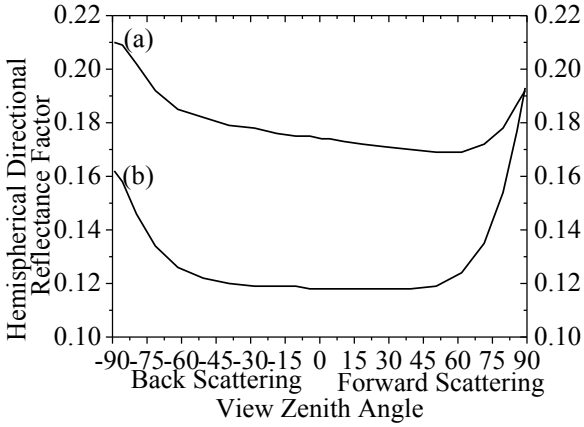

Hemispherical Directional Reflectance Factor (HDRF) in the solar principal plane. For back scattering, $\varphi_{view} = \varphi_0 + \pi$, and for forward scattering, $\varphi_{view} = \varphi_0$. The total Leaf Area Index (LAI) of the canopy is 3.0, and the soil reflectance is 0.2. Optical parameters of the canopy for the two lines are: (a) leaf reflectance is 0.7, and leaf transmittance is 0.225; (b) leaf reflectance is 0.225, and leaf transmittance is 0.7. The other problem parameters are as in the standard problem described in the figure caption.

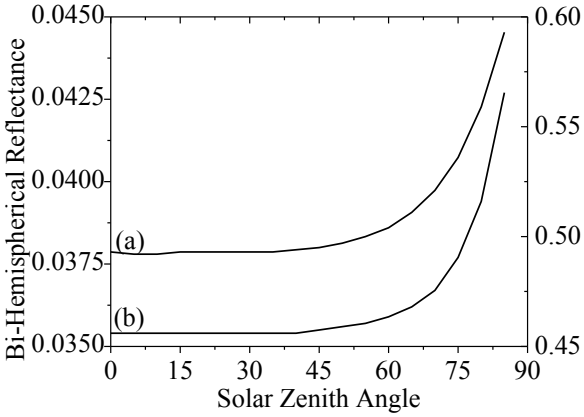

Bi-Hemispherical Reflectance (BHR) at NIR (right axis) and RED (left axis) wavelengths as a function of solar zenith angle. The total Leaf Area Index (LAI) of the canopy is 3.0. The other problem parameters are as in the standard problem described in the figure caption.

Figure 4. The illumination conditions for these cases are as follows – the canopy is illuminated by diffuse solar radiation and direct solar radiation along the direction ($\theta=150^o$, $\varphi=0^o$). Direct solar radiation accounts for 70% of the total incoming flux ($F_{dir}=0.7$). The leaf normal distribution is planophile (mostly horizontal leaves). At NIR wavelengths (a), leaf reflectance (ρ_{nir}) is 0.475 and leaf transmittance (τ_{nir}) is 0.45. At red wavelengths (b), (ρ_{red}) is 0.075, and (τ_{red}) is 0.035.

8. Two-Stream Approximations

In cases where the angular distribution of the radiation field is of less interest, the transport equation can be angle-integrated to derive the appropriate equations for radiation fluxes. One example is the case where one is interested in the evaluation of hemispherical reflectances, BHR or DHR. The resulting differential equations can be solved analytically in some cases. Methods based on flux approximations have been widely used to model vegetation canopy radiation regime because of their simplicity and the possibility of analytical solutions, ([Allen and Richardson, 1968]; [Suits, 1972]; [Dickinson, 1983]; [Verhoef, 1984]; [Sellers, 1985]; amongst others).

Consider the transport problem stated by Eq. (1) and (2). The downward flux density F^d is defined as

$$F^d(L) = \int_{2\pi^-} d\underline{\Omega}\,|\mu|\,I(L,\underline{\Omega}).$$

Integrating Eq. (1) over all downward directions, but with change of vertical coordinate z to cumulative leaf area index L,

$$\begin{aligned}\frac{\partial}{\partial L}F^d(L) + F^d(L)\frac{\int_{2\pi-} d\underline{\Omega}\,G(\underline{\Omega})\,I(L,\underline{\Omega})}{F^d(L)} \\ = F^u(L)\frac{\int_{2\pi-} d\underline{\Omega}\int_{2\pi+} d\underline{\Omega}'\,\frac{1}{\pi}\,\Gamma(\underline{\Omega}'\to\underline{\Omega})\,I(L,\underline{\Omega}')}{F^u(L)} \\ + F^d(L)\frac{\int_{2\pi-} d\underline{\Omega}\int_{2\pi-} d\underline{\Omega}'\,\frac{1}{\pi}\,\Gamma(\underline{\Omega}'\to\underline{\Omega})\,I(L,\underline{\Omega}')}{F^d(L)},\end{aligned} \tag{29}$$

and simplifying results in a differential equation for the downward flux density

$$\frac{\partial}{\partial L}F^d(L) + K_1^d\,F^d(L) = K_2^d\,F^u(L) + K_3^d\,F^d(L). \tag{30}$$

Similarly, a differential equation for the upwards flux density can be derived

$$-\frac{\partial}{\partial L}F^u(L) + K_1^u\,F^u(L) = K_2^u\,F^u(L) + K_3^d\,F^d(L). \tag{31}$$

The initial values for Eqs. (30) and (31) are

$$F^d(L=0) = f_{dir}\,|\mu_0|\,I_0 + (1-f_{dir})\int_{2\pi-} d\underline{\Omega}_d\,|\mu_d|\,I_d(\underline{\Omega}_d), \tag{32}$$

$$F^u(L=L_H) = r_s F^d(L=L_H) \tag{33}$$

where r_s is the hemispherical reflectance of the ground underneath the canopy. While these initial value problems seem simple enough, it is not easy to rigorously derive expressions for the coefficients K in the general case of distributed leaf normals and anisotropic scattering kernels. However, approximate expressions generally surface in many practical instances.

We consider the simple case of a horizontally homogeneous leaf canopy consisting of horizontal leaves. The geometry factor $G(\underline{\Omega}) = |\mu|$ and the area scattering phase function is simply

$$\Gamma(\underline{\Omega}' \to \underline{\Omega}) = \begin{cases} \tau_L \mu\mu', & \mu\mu' > 0, \\ \rho_L |\mu\mu'|, & \mu\mu' < 0. \end{cases}$$

Specular reflection from leaf surfaces is ignored in this formulation. In the above ρ_L and τ_L are the leaf hemispherical reflectance and transmittance. The coefficients for this canopy are, $K_1^d = 1$, $K_2^d = \rho_L$, $K_3^d = \tau_L$, $K_1^u = 1$, $K_2^u = \tau_L$ and $K_3^u = \rho_L$. The differential equations (30) and (31) can be rewritten as

$$\frac{\partial}{\partial L} F^d(L) = \rho_L F^u(L) + (\tau_L - 1) F^d(L), \tag{34a}$$

$$-\frac{\partial}{\partial L} F^u(L) = \rho_L F^d(L) + (\tau_L - 1) F^u(L). \tag{34b}$$

That is, the changes in the downward flux density are given by the sum of backscattered upward flux density (the gain term) and the fraction of downward flux density that is not forward scattered (the loss term). Similarly, the changes in the upward flux density are given by the sum of backscattered downward flux density (the gain term) and the fraction of upward flux density that is not forward scattered (the loss term). The transport equations can be solved with the initial values [Eqs. (32) and (33)] to obtain downward and upward radiation flux density in the medium.

If the leaves are spherically distributed, the geometry factor $G(\underline{\Omega}) = 0.5$ and the area scattering phase function is given by

$$\Gamma(\underline{\Omega}' \to \underline{\Omega}) = \frac{w_L}{3\pi}(\sin\beta - \beta\cos\beta) + \frac{\tau_L}{\pi}\cos\beta,$$

where $\beta = \arccos(\underline{\Omega}' \bullet \underline{\Omega})$, again on the assumption of negligible specular reflection from leaf surfaces. Analytical expressions for the coefficients K and solution of the corresponding transport equations for downward and upwards fluxes are straightforward, although tedious.

9. The Hot-Spot Effect

The hot spot results from considerations of the relative sizes of scatterers in the canopy (leaves, branches, twigs, etc.) in relation to the wavelength of the radiation. Shadowing is ubiquitous and mutual shadowing of scatterers is predominant. The reflected radiation field tends to peak about the retro-illumination direction under such cases - this is termed the hot spot effect in vegetation remote sensing (Fig. 5). The shape and magnitude of the hot spot depends on the structure of the medium and is especially pronounced at shorter wavelengths where scattering is weak because the shadows are darker. The hot spot phenomenon is observational evidence of the limitations of theoretical developments that ignore scatterer size and resulting directional correlations in the

interaction cross sections. Inclusion of such considerations in the transport equation is feasible but complicated [Myneni et al., 1991]. Here we present a simple methodology for inclusion of the hot spot phenomenon in the transport equation. A model of the hot spot effect in the limit of single scattering can be found in Kuusk [1985].

The hot spot effect can be included in the transport equation through the use of a modified total interaction cross section $\tilde{\sigma}$ (cf. Marshak [1989]),

$$\tilde{\sigma}(L,\underline{\Omega},\underline{\Omega}') = \begin{cases} \sigma(L,\underline{\Omega})\,\{1-\exp[-\kappa D(\underline{\Omega}\bullet\underline{\Omega}')]\}, & (\underline{\Omega}\bullet\underline{\Omega}')<0, \\ \sigma(L,\underline{\Omega}), & (\underline{\Omega}\bullet\underline{\Omega}')>0, \end{cases} \tag{35}$$

where κ is a parameter related to the ratio of vegetation height to characteristic leaf dimension. Its values were estimated to be between 1 and 8 from experimental data. The distance D is given by

$$D(\underline{\Omega},\underline{\Omega}') = \sqrt{\frac{1}{\mu'^2}+\frac{1}{\mu^2}+\frac{2(\underline{\Omega}\bullet\underline{\Omega}')}{|\mu'\mu|}}\ .$$

This particular model for the modified total interaction cross section has two desirable features, namely, that for $\underline{\Omega} = -\underline{\Omega}'$, $\tilde{\sigma}$ vanishes to result in the hot spot, and for large scattering angles, it approaches the standard cross section σ. Note that $\tilde{\sigma}$ is always positive.

Figure 5. The hot spot effect of a vegetation canopy.

Consider the one-dimensional leaf canopy transport problem. Let the total radiation intensity be represented as $I = I^0+I^1+I^m$, that is, as the sum of uncollided, first collision and multiple collision intensities. Further, assume for ease of presentation that the incident diffuse skylight $I_d=0$, that is, $f_{dir}=1$. The transport problems for I^0 and I^1, specified by Eqs. (6) and (11), are modified using $\tilde{\sigma}$ instead of σ, or equivalently, instead of $\tilde{G}$ instead of G [cf. Eq. (3a)]. The solutions for the

downward intensities I^0 and I^1 given by Eqs. (9a) and (12a) remain unchanged since $\tilde{G} = G$ for $(\underline{\Omega} \bullet \underline{\Omega}') > 0$. The upward uncollided and first collided radiation intensities are, however, modified because of the modified cross section. They read

$$I^0(L,\underline{\Omega}) = I^0(L = L_H,\underline{\Omega})\,P[\underline{\Omega},\underline{\Omega}_o,(L_H - L)], \quad \mu > 0, \tag{36a}$$

$$I^1(L,\underline{\Omega}) = \frac{1}{|\mu|}\int_L^{L_H} dL'\,Q(L',\underline{\Omega})\,P[\underline{\Omega},\underline{\Omega}_o,(L' - L)], \quad \mu > 0 \tag{36b}$$

where

$$P[\underline{\Omega},\underline{\Omega}_o,(L2 - L1)] = \exp\left[-\frac{1}{|\mu|}\tilde{G}(\underline{\Omega},\underline{\Omega}_o)(L2 - L1)\right] \tag{37}$$

denotes the probability of photons not experiencing collisions while traveling along Ω_o from the top of the canopy (L = 0) to depth L2 and along $\underline{\Omega}$ from L2 and L1 (L2 > L1). This is the required bi-directional gap probability for implementing the hot spot effect.

The multiple collision transport problem is similar to the collided intensity transport problem specified by Eqs. (7) except that the first collision source Q in Eq. (7a) is replaced by the second collision source,

$$Q(L,\underline{\Omega}) = \frac{1}{\pi}\int_{4\pi} d\underline{\Omega}'\,\Gamma(\underline{\Omega}' \to \underline{\Omega})\,I^1(L,\underline{\Omega}').$$

The above formulation allows simulation of the hot spot effect with transport equations. This is accomplished in an *ad hoc* manner by utilizing a modified interaction cross section for the uncollided and first collided intensities arising from incident solar radiation and using the standard cross section for multiply collided transport problem. The uncollided and collided intensities due to incident diffuse skylight can also be solved the standard way utilizing the unmodified cross section.

While the above formalism allows inclusion of the hot spot effect, it does result in a system that violates the energy conservation principle, because the transport problem for the collided intensity is, strictly speaking,

$$-\mu\frac{\partial}{\partial L}I^C(L,\underline{\Omega}) + G(L,\underline{\Omega})I^C(L,\underline{\Omega}) = Q(L,\underline{\Omega}) + S(L,\underline{\Omega}) + [G(\underline{\Omega}) - \tilde{G}(\underline{\Omega},\underline{\Omega}_o)]I^C(L,\underline{\Omega}),$$

$$I^C(L = 0,\underline{\Omega}) = 0, \quad \mu < 0,$$

$$I^1(L = L_H,\underline{\Omega}) = \frac{1}{\pi}\int_{2\pi^-} d\underline{\Omega}'\,\rho_s(\underline{\Omega}' \to \underline{\Omega})\,|\mu'|\,I^C(L = L_H,\underline{\Omega}'), \quad \mu > 0.$$

This is equivalent to a transport equation for the total intensity I [Eqs. (1)] with an additional fictitious internal source, $[G(\underline{\Omega}) - \widetilde{G}(\underline{\Omega},\underline{\Omega}_o)]\cdot I^C(L,\underline{\Omega})$, which results in violation of the energy conservation principle. This has implications for the inverse problems where this principle is used as a constraint.

10. Discrete Ordinates Method in Three Spatial Dimensions

We consider a spatially heterogeneous leaf canopy contained between $0 < z < Z_s$, $0 < x < X_s$, $0 < y < Y_s$, where X_s, Y_s, and Z_s denote the dimensions of the stand. The canopy is assumed homogeneously illuminated on the top and lateral faces by a mono-directional beam source (direct solar radiation) of intensity I_o along $\underline{\Omega}_o$ and a diffuse source (skylight) of intensity I_d. The ground below the canopy is assumed to reflect and absorb the radiation field non-homogeneously. The radiation intensity in the governing transport equation,

$$-\mu\frac{\partial}{\partial z}I(\underline{r},\underline{\Omega}) + \eta\frac{\partial}{\partial y}I(\underline{r},\underline{\Omega}) + \xi\frac{\partial}{\partial y}I(\underline{r},\underline{\Omega}) + \sigma(\underline{r},\underline{\Omega})I(\underline{r},\underline{\Omega}) = \int_{4\pi} d\underline{\Omega}'\,\sigma_s(\underline{r},\underline{\Omega}'\to\underline{\Omega})\,I(\underline{r},\underline{\Omega}'),$$

is separated into uncollided (I^0) and collided (I^C) fields. In the above, $\underline{r} \equiv (x,y,z)$, and μ, η and ξ are the direction cosines with respect to the z, y and x dimensions.

The uncollided problem is given by the transport equation

$$-\mu\frac{\partial}{\partial z}I^0(\underline{r},\underline{\Omega}) + \eta\frac{\partial}{\partial y}I^0(\underline{r},\underline{\Omega}) + \xi\frac{\partial}{\partial y}I^0(\underline{r},\underline{\Omega}) + \sigma(\underline{r},\underline{\Omega})I^0(\underline{r},\underline{\Omega}) = 0, \tag{38a}$$

and the boundary conditions

$$I^0(x,y,z=0,\underline{\Omega}) = I_o\delta(\underline{\Omega}-\underline{\Omega}_o) + I_d(\underline{\Omega}), \quad \mu < 0, \tag{38b}$$

$$I^0(x=0,y,z,\underline{\Omega}) = I_o\delta(\underline{\Omega}-\underline{\Omega}_o) + I_d(\underline{\Omega}), \quad \xi > 0 \text{ and } \mu < 0, \tag{38c}$$

$$I^0(x=X_s,y,z,\underline{\Omega}) = I_o\delta(\underline{\Omega}-\underline{\Omega}_o) + I_d(\underline{\Omega}), \quad \xi < 0 \text{ and } \mu < 0, \tag{38d}$$

$$I^0(x,y=0,z,\underline{\Omega}) = I_o\delta(\underline{\Omega}-\underline{\Omega}_o) + I_d(\underline{\Omega}), \quad \eta > 0 \text{ and } \mu < 0, \tag{38e}$$

$$I^0(x,y=Y_s,z,\underline{\Omega}) = I_o\delta(\underline{\Omega}-\underline{\Omega}_o) + I_d(\underline{\Omega}), \quad \eta < 0 \text{ and } \mu < 0, \tag{38f}$$

$$I^0(x,y,z=Z_s,\underline{\Omega}) = \frac{1}{\pi}\int_{2\pi^-} d\underline{\Omega}'\,\rho_s(x,y,\underline{\Omega}'\to\underline{\Omega})\,|\mu'|\,I^0(x,y,z=Z_s,\underline{\Omega}'), \quad \mu > 0. \tag{38g}$$

In the above, ρ_s is the wavelength-dependent bi-directional reflectance function of the ground below the canopy. The solution to the uncollided problem is

$$I^0(\underline{r},\underline{\Omega}) = I^0(\underline{r}_B,\underline{\Omega})\,P[\underline{\Omega},|\underline{r}-\underline{r}_B|], \quad \mu < 0, \tag{39a}$$

$$I^0(\underline{r},\underline{\Omega}) = I^0(\underline{r}_H,\underline{\Omega})\, P[\underline{\Omega},|\underline{r}-\underline{r}_H|], \quad \mu > 0 \tag{39b}$$

where r_B is a point on the top or the lateral faces of the canopy and r_H is a point on the ground below the canopy. The quantity

$$P[\underline{\Omega},|\underline{r}_2 - \underline{r}_1|] = \exp\left[- \int_0^{|\underline{r}_2-\underline{r}_1|} ds\, \sigma(\underline{r}_1 + s\underline{\Omega},\underline{\Omega}) \right] \tag{40}$$

denotes the probability of photons not experiencing collisions while traveling along $\underline{\Omega}$ between the points $\underline{r}_1$ and $\underline{r}_2$.

The collided problem is given by the transport equation

$$-\mu \frac{\partial}{\partial z} I^C(\underline{r},\underline{\Omega}) + \eta \frac{\partial}{\partial y} I^C(\underline{r},\underline{\Omega}) + \xi \frac{\partial}{\partial y} I^C(\underline{r},\underline{\Omega}) + \sigma(\underline{r},\underline{\Omega})\, I^C(\underline{r},\underline{\Omega}) = S(\underline{r},\underline{\Omega}) + Q(\underline{r},\underline{\Omega}), \tag{41a}$$

where the distributed source S and first collision source Q are

$$S(\underline{r},\underline{\Omega}) = \int_{4\pi} d\underline{\Omega}' \sigma_s(\underline{r};\underline{\Omega}' \to \underline{\Omega})\, I^C(\underline{r},\underline{\Omega}'),$$
$$Q(\underline{r},\underline{\Omega}) = \int_{4\pi} d\underline{\Omega}'\, \sigma_s(\underline{r};\underline{\Omega}' \to \underline{\Omega})\, I^0(\underline{r},\underline{\Omega}').$$

The boundary conditions for the collided intensity are,

$$I^C(x,y,z=0,\underline{\Omega}) = 0, \quad \mu < 0, \tag{41b}$$
$$I^C(x=0,y,z,\underline{\Omega}) = 0, \quad \xi > 0, \tag{41c}$$
$$I^C(x=X_s,y,z,\underline{\Omega}) = 0, \quad \xi < 0, \tag{41d}$$
$$I^C(x,y=0,z,\underline{\Omega}) = 0, \quad \eta > 0, \tag{41e}$$
$$I^C(x,y=Y_s,z,\underline{\Omega}) = 0, \quad \eta < 0, \tag{41f}$$
$$I^C(x,y,z=Z_s,\underline{\Omega}) = \frac{1}{\pi} \int_{2\pi^-} d\underline{\Omega}' \rho_s(x,y,\underline{\Omega}' \to \underline{\Omega})\, |\mu'|\, I^C(x,y,z=Z_s,\underline{\Omega}'), \quad \mu > 0. \tag{41g}$$

Thus, the medium is considered non-re-entrant from the top and lateral faces as far as the collided radiation intensity is considered.

The vegetation canopy is divided into cells bounded by $x_{1/2}, x_{3/2}, \ldots, x_{K+1/2}$ (of width Δx), $y_{1/2}, y_{3/2}, \ldots, y_{J+1/2}$ (of width Δy), and $z_{1/2}, z_{3/2}, \ldots, z_{I+1/2}$ (of width Δz). The cross sections σ and σ_s are assumed to be piece-wise constant and can take new values only at the

cell-boundaries. Within the cell volume V_{ijk}, bounded by $(x_{k-1/2} < x < x_{k+1/2})$, $(y_{i-1/2} < y < y_{i+1/2})$ and $(z_{i-1/2} < z < z_{i+1/2})$, the cross sections are denoted as σ_{iik} and σ_{siik}.

Introducing the first-order finite-difference approximation for the spatial derivatives in the angle-discretized transport equation for the collided intensity and integrating over the cell volume, yields

$$
\begin{aligned}
-\mu_n \int_j dy \int_k dx\, [I_n(x,y,z_{i+1/2}) - I_n(x,y,z_{i-1/2})] \\
+ \eta_n \int_i dz \int_k dx\, [I_n(x,y_{j+1/2},z) - I_n(x,y_{j-1/2},z)] \\
+ \xi_n \int_i dz \int_j dy\, [I_n(x_{k+1/2},y,z) - I_n(x_{k-1/2},y,z)] \\
+ \sigma_{nijk} \int_i dz \int_j dy \int_k dx\, I_n(x,y,z) \\
= \int_i dz \int_j dy \int_k dx\, J_n(x,y,z), \qquad (42)
\end{aligned}
$$

where J is the total source (S+Q) and, $\int dx$ denotes integration from $x_{k-1/2}$ to $x_{k+1/2}$, and so on. The subscript n denotes the discrete direction of photon travel. Dividing Eq. (42) by the cell volume V_{iik} results in

$$
\begin{aligned}
-\frac{\mu_n}{\Delta z}[I_{njk}(z_{i+1/2}) - I_{njk}(z_{i-1/2})] + \frac{\eta_n}{\Delta y}[I_{nik}(y_{j+1/2}) - I_{nik}(y_{j-1/2})] \\
+ \frac{\xi_n}{\Delta x}[I_{nij}(x_{k+1/2}) - I_{nij}(x_{k-1/2})] + \sigma_{nijk} I_{nijk} = J_{nijk}. \qquad (43)
\end{aligned}
$$

In the above, the average radiation intensities over the cell surfaces are

$$I_{njk}(z_{i\pm1/2}) = \frac{1}{\Delta x \Delta y} \int_k dx \int_j dy\, I_n(x,y,z_{i\pm1/2}), \qquad (44a)$$

$$I_{nik}(y_{j\pm1/2}) = \frac{1}{\Delta x \Delta z} \int_k dx \int_i dz\, I_n(x,y_{j\pm1/2},z), \qquad (44b)$$

$$I_{nij}(x_{k\pm1/2}) = \frac{1}{\Delta z \Delta y} \int_i dz \int_j dy\, I_n(x_{k\pm1/2},y,z). \qquad (44c)$$

Similarly, the averages over the cell volume of the specific intensity and the total source are

$$I_{nijk} = \frac{1}{\Delta x \Delta y \Delta z} \int_k dx \int_j dy \int_i dz\, I_n(x,y,z), \qquad (45a)$$

$$J_{nijk} = \frac{1}{\Delta x \Delta y \Delta z} \int_k dx \int_j dy \int_i dz\, J_n(x,y,z). \tag{45b}$$

Equation (43) is exact but not closed. To solve for the cell-center angular intensities I_{nijk} and the flows across the three surfaces through which photons can leave the cell volume, three additional relations are required (note that the flows across the three surfaces through which photons enter the cell are known either from the boundary conditions or from previous calculations). The following simple relations can be used for this purpose

$$I_{nijk} \approx 0.5[I_{njk}(z_{i+1/2}) + I_{njk}(z_{i-1/2})], \tag{46a}$$

$$I_{nijk} \approx 0.5[I_{nik}(y_{j+1/2}) + I_{nik}(y_{i-1/2})], \tag{46b}$$

$$I_{nijk} \approx 0.5[I_{nij}(x_{k+1/2}) + I_{nij}(x_{k-1/2})]. \tag{46c}$$

These relations are simple but can lead to negative intensities, in which case remedies must be implemented in the algorithm. The simplest solution is set the offending intensity to zero and proceed with the calculation.

In this manner, the angular and spatial dependence of the transport equation is discretized while insuring that the condition of positivity, symmetry and balance are satisfied. In each octant, the incoming and outgoing flows are identified depending on the sign of the direction cosines in order not to violate the principle of directional evaluation, that is, sweeping in the phase-space along the direction of photon flow only. Using Eqs. (46), the exiting flows can be eliminated to solve for the cell center intensity. A generic equation for the cell center intensity can be written as

$$I_{nijk} = \frac{J_{nijk} + \frac{2\mu_n}{\Delta z} I_{njk}(z_{i\pm1/2}) + \frac{2\eta_n}{\Delta y} I_{nik}(y_{j\pm1/2}) + \frac{2\xi_n}{\Delta x} I_{nij}(x_{k\pm1/2})}{\sigma_{nijk} + \frac{2\mu_n}{\Delta z} + \frac{2\eta_n}{\Delta y} + \frac{2\xi_n}{\Delta x}}. \tag{47}$$

The three flows in the numerator represent the incoming flows across the three faces of the cell and are specific to an octant. The cell center intensity evaluated with Eq. (47) is then used in the relations given in Eqs. (46) to evaluate the three outgoing flows. For example, in octant 1, μ_n, η_n and ξ_n are positive. The three incoming flows are $I_{njk}(z_{i-1/2})$, $I_{nik}(y_{i-1/2})$ and $I_{nij}(x_{k-1/2})$. The outgoing flows to be evaluated are $I_{njk}(z_{i+1/2})$, $I_{nik}(y_{i+1/2})$ and $I_{nij}(x_{k+1/2})$. This phase-space sweeping along the direction of photon travel is embedded in an iteration on the distributed source with appropriate convergence criteria built in. Details on the implementation and acceleration techniques for the iterative procedure can be found in Myneni et al. [1990].

Problem Sets

- **Problem 1.** Derive the one-angle form of the vegetation transport problem.
- **Problem 2**. Derive the one-angle form of the collided and uncollided transport problems.
- **Problem 3**. Derive the analytical solution of the one-angle uncollided transport problem.
- **Problem 4**. Solve the two-stream differential equations for upward F^u and downward F^d fluxes in a vegetation canopy of horizontal leaves

$$\frac{\partial}{\partial L} F^d(L) = \rho_L F^u(L) + (\tau_L - 1) F^d(L),$$

$$\frac{\partial}{\partial L} F^u(L) = \rho_L F^d(L) + (\tau_L - 1) F^u(L),$$

with the boundary conditions

$$F^d(L = 0) = F_0^d,$$

$$F^u(L = L_H) = r_S F^d(L = L_H).$$

- **Problem 5**. Show the limiting form of F^u for the case of a very dense canopy.

References

Allen, W.A. and A.J. Richardson (1968). Interaction of light with a plant canopy. *J. Opt. Soc. Amer*., **58**, 1023-1028.

Dickinson, R.E. (1983). Land surface processes and climate - surface albedos and energy balance. *Advances in Geophysics*, 305-353.

Knyazikhin, Y. (1990). On the solvability of plane-parallel problems in the theory of radiation transport. *USSR Computer Math. And Math Phys.*, **30**, 557-569. (in Russian translated into English in 1991, pp. 145-154).

Knyazikhin, Y. and A. Marshak (1991). Fundamental equations of radiative transfer in leaf canopies and iterative methods for their solution. In *Photon-Vegetation Interactions: Applications in Plant Physiology and Optical Remote Sensing*, R.B. Myneni and J. Ross (eds.), Springer-Verlag, Berlin Heidelberg, pp. 9-44.

Kuusk, A. (1985). The hot spot effect of a uniform vegetation cover. *Sov. J. Remote Sens*., **3**, 645-658.

Liang, S. and A.H. Strahler (1993). The calculation of the radiance distribution of the coupled atmosphere canopy. *IEEE Trans. Geosci. Remote Sens*., **31,** 491-502.

Marshak, A.L. (1989). Consideration of the effect of hot spot for the transport equation in plant canopies. *J. Quant. Spectroscp. Radiat. Transfer*, **42**, 615-630.

Myneni, R.B., G. Asrar, and E.T. Kanemasu (1987). Light scattering in plant canopies: The method of Successive Orders of Scattering Approximations [SOSA]. *Agric. For. Meteorol*., **39**, 1-12.

Myneni, R.B., G. Asrar, and S.A.W. Gerstl (1990). Radiative transfer in three dimensional leaf canopies. *Transport Theory and Statistical Physics*, **19**, 205-250.

Myneni, R.B., A.L. Marshak, and Y. Knyazikhin (1991). Transport theory for leaf canopies with finite dimensional scattering centers. *J. Quant. Spectroscp. Radiat. Transfer*, **46**, 259-280.

Sellers, P.J. (1985). Canopy reflectance, photosynthesis and transpiration. *Int. J. Remote Sens*., **6**, 1335-1372.

Shultis, J.K. and R.B. Myneni (1988). Radiative transfer in vegetation canopies with anisotropic scattering. *J. Quant. Spectroscp. Radiat. Transfer,* **39**, 115-129.

Suits, G.H. (1972). The calculation of the directional reflectance of a vegetative canopy. *Remote Sens. Environ*., **2**, 117-125.

Verhoef, W. (1984). Earth observation modeling based on layer scattering matrices. National Aerospace Laboratory Report (NLR MP 84015 U), The Netherlands.

Chapter 4 Derivations by Shabanov et al.

Problem 1. Derive the one-angle form of the vegetation transport problem.

Solution. The 1D radiative transfer equation for vegetation canopies is

$$-\mu\frac{\partial}{\partial z}I(z,\underline{\Omega})+u_L(z)G(z,\underline{\Omega})I(z,\underline{\Omega})=\frac{u_L(z)}{\pi}\int_{4\pi}d\underline{\Omega}'\,\Gamma(z,\underline{\Omega}'\to\underline{\Omega})I(z,\underline{\Omega}'). \tag{1}$$

The vertical coordinate z can be changed to cumulative leaf area index L by dividing Eq. (1) with $u_L(z)$, the leaf area density distribution ($L\equiv u_L(z)\cdot z$),

$$-\mu\frac{\partial}{\partial L}I(L,\underline{\Omega})+G(L,\underline{\Omega})I(L,\underline{\Omega})=\frac{1}{\pi}\int_{4\pi}d\underline{\Omega}'\,\Gamma(L,\underline{\Omega}'\to\underline{\Omega})I(L,\underline{\Omega}'). \tag{2}$$

In the following derivations we will assume that the geometry factor and the area scattering phase function are independent of the azimuth angle and cumulative leaf area index, namely,

$$G(L,\underline{\Omega})=G(\mu), \tag{3a}$$

$$\frac{1}{\pi}\Gamma(L,\underline{\Omega}'\to\underline{\Omega})=\frac{1}{\pi}\Gamma(\mu'\to\mu). \tag{3b}$$

In this case the 1D transport equation can be reduced to a one angle problem by averaging Eq. (2) over azimuth angle, φ. The derivations for the first and second items on the left hand side and the remaining item on the right-hand side of Eq. (2) are shown in Eq. (4a)-(4c) below:

$$\frac{1}{2\pi}\int_0^{2\pi}d\varphi\left[-\mu\frac{\partial}{\partial L}I(L,\underline{\Omega})\right]=-\mu\frac{\partial}{\partial L}\frac{1}{2\pi}\int_0^{2\pi}d\varphi\,I(L,\mu,\varphi)=-\mu\frac{\partial}{\partial L}I(L,\mu), \tag{4a}$$

$$\frac{1}{2\pi}\int_0^{2\pi}d\varphi\left[G(L,\underline{\Omega})I(L,\underline{\Omega})\right]=\frac{1}{2\pi}\int_0^{2\pi}d\varphi\,G(L,\varphi,\mu)I(L,\mu,\varphi)=G(\mu)I(L,\mu), \tag{4b}$$

$$\frac{1}{2\pi}\int_0^{2\pi} d\varphi \left[\int_{4\pi} d\Omega' \, \Gamma(L, \underline{\Omega'} \to \underline{\Omega}) \, I(L, \underline{\Omega'}) \right]$$

$$= \frac{1}{2\pi}\int_0^{2\pi} d\varphi \int_{-1}^{1} d\mu' \int_0^{2\pi} d\varphi' \, \Gamma(L, \mu' \to \mu, \varphi' \to \varphi) \, I(L, \mu', \varphi')$$

$$= 2\pi \int_{-1}^{1} d\mu' \, \Gamma(\mu' \to \mu) \; I(L, \mu'). \tag{4c}$$

In the above we introduced angularly averaged intensity,

$$I(L, \mu) \equiv \frac{1}{2\pi}\int_0^{2\pi} d\varphi \; I(L, \mu, \varphi).$$

Therefore, the one-angle form of 1D RT equation is

$$-\mu \frac{\partial}{\partial L} I(L, \mu) + G(\mu) \, I(L, \mu) = 2\int_{-1}^{1} d\mu' \, \Gamma(\mu' \to \mu) \, I(L, \mu'). \tag{5}$$

The corresponding boundary conditions are

$$I(L = 0, \mu) = I_o \delta(\mu - \mu_o) + I_d(\mu), \quad \mu < 0, \tag{6a}$$

$$I(L = L_H, \mu) = 2\int_{-1}^{0} d\mu' |\mu'| \rho_s(\mu' \to \mu) I(L = L_H, \mu'), \quad \mu > 0, \tag{6b}$$

where

$$I_o(\mu) = \frac{f_{dir}}{|\mu_o|} F_{in}(L = 0) \equiv f_{dir} S_o, \quad S_o \equiv \frac{F_{in}(L = 0)}{|\mu_o|},$$

$$I_d(\mu) = (1 - f_{dir}) d_o(L = 0, \mu) F_{in}(L = 0) \equiv (1 - f_{dir}) S_d, \quad S_d \equiv d_o(L = 0, \mu) F_{in}(L = 0).$$

Problem 2. Derive the one-angle form of the collided and uncollided transport problems.

Solution. The total intensity, I, can be separated into uncollided, I^0, and collided, I^C, components, namely,

$$I(L,\mu) = I^0(L,\mu) + I^C(L,\mu). \tag{1}$$

Substituting Eq. (1), into the one angle transport problem (cf. Problem 1, Eqs. (5)-(6)), one can split the total problem into the uncollided problem,

$$-\mu \frac{\partial}{\partial L} I^0(L,\mu) + G(\mu) I^0(L,\mu) = 0, \tag{2a}$$

$$I^0(L=0,\mu) = f_{dir} S_o \delta(\mu - \mu_o) + (1 - f_{dir}) S_d, \quad \mu < 0, \tag{2b}$$

$$I^0(L=L_H,\mu) = 2\int_{-1}^{0} d\mu' |\mu'| \rho_s(\mu' \to \mu) I^0(L=L_H,\mu'), \quad \mu > 0. \tag{2c}$$

and the collided problem,

$$-\mu \frac{\partial}{\partial L} I^C(L,\mu) + G(\mu) I^C(L,\mu) = 2\int_{-1}^{1} d\mu' \Gamma(L,\mu' \to \mu)\left[I^0(L,\mu') + I^C(L,\mu')\right]. \tag{3a}$$

$$I^C(L=0,\mu) = 0, \quad \mu < 0, \tag{3b}$$

$$I^C(L=L_H,\mu) = 2\int_{-1}^{0} d\mu' |\mu'| \rho_s(\mu' \to \mu) I^C(L=L_H,\mu'), \quad \mu > 0. \tag{3c}$$

Problem 3. Derive the analytical solution of the one-angle uncollided transport problem.

Solution. The one-angle transport equation for the uncollided radiation is (cf. Problem 2, Eq. (2a))

$$\frac{\partial}{\partial L} I^0(L,\mu) = \frac{G(\mu)}{\mu} I^0(L,\mu) \tag{1}$$

The solution of this equations is

$$I^0(L,\mu) = A(\mu) \cdot \exp\left(\frac{G(\mu)}{\mu} L \right),$$

where coefficient $A(\mu)$ is determined from boundary conditions (cf. Problem 2, Eq. (2b) for $\mu < 0,$ and (2c) for $\mu > 0$).

If $\mu < 0$ (downwelling radiation),

$$I^0(L,\mu) = \left[f_{dir} S_o \delta(\mu - \mu_o) + (1 - f_{dir}) S_d \right] \cdot \exp\left(\frac{G(\mu)}{\mu} L \right). \tag{2a}$$

If $\mu > 0$ (upwelling radiation),

$$\begin{aligned} I^0(L,\mu) &= 2 \int_{-1}^{0} d\mu' |\mu'| \rho_s(\mu' \to \mu) \left[f_{dir} S_o \delta(\mu' - \mu_o) + (1 - f_{dir}) S_d \right] \exp\left(\frac{G(\mu')}{\mu'} (L - L_H) \right) \\ &= \left[f_{dir} S_o 2|\mu_o| \rho_s(\mu_o \to \mu) \cdot \exp\left(- \frac{G(\mu_o)}{\mu_o} L_H \right) \right. \\ &\quad \left. + (1 - f_{dir}) S_d 2 \int_{-1}^{0} d\mu' |\mu'| \rho_s(\mu' \to \mu) \exp\left(- \frac{G(\mu')}{\mu'} L_H \right) \right] \cdot \exp\left(\frac{G(\mu)}{\mu} (L - L_H) \right). \end{aligned} \tag{2b}$$

Note, in the case of dense canopies

$$I^0(L,\mu)\big|_{L_H \to \infty} \to 0.$$

Problem 4. Solve the two-stream differential equations for upward F^u and downward F^d fluxes in a vegetation canopy of horizontal leaves

$$\frac{\partial}{\partial L}F^d(L) = \rho_L F^u(L) + (\tau_L - 1)F^d(L),$$

$$-\frac{\partial}{\partial L}F^u(L) = \rho_L F^d(L) + (\tau_L - 1)F^u(L),$$

with the boundary conditions

$$F^d(L = 0) = F_0^d,$$

$$F^u(L = L_H) = r_S F^d(L = L_H).$$

Solution. The two-stream equations in this problem correspond to a homogeneous system of linear differential equations, which can be solved using matrix method. The original system can be rewritten in a matrix form as follows

$$\underline{y}'(L) = \hat{A}\underline{y}(L), \tag{1a}$$

where

$$\underline{y}(L) \equiv \begin{bmatrix} F^d(L) \\ F^u(L) \end{bmatrix}, \quad \underline{y}'(L) \equiv \begin{bmatrix} \frac{\partial}{\partial L}F^d(L) \\ \frac{\partial}{\partial L}F^u(L) \end{bmatrix}, \quad \hat{A} \equiv \begin{bmatrix} (\tau_L - 1) & \rho_L \\ -\rho_L & -(\tau_L - 1) \end{bmatrix}. \tag{1b}$$

If matrix $\hat{A}$ has n=2 independent eigenvectors $\underline{v}_1$ and $\underline{v}_2$ corresponding to eigenvalues λ_1 and λ_2, then the general solution of Eqs. (1a)-(1b) is

$$\underline{y}(L) = C_1 \exp(\lambda_1 L)\underline{v}_1(L) + C_2 \exp(\lambda_2 L)\underline{v}_2(L). \tag{2}$$

The eigenvalues of matrix $\hat{A}$ can be found as follows:

$$\det(\hat{A} - \lambda\hat{I}) = 0$$

$$\Rightarrow -(\tau_L - 1 - \lambda)(\tau_L - 1 + \lambda) + \rho_L^2 = 0$$

$$\Rightarrow \lambda_{1,2} = \pm\lambda \equiv \pm\sqrt{(1-\tau_L)^2 - \rho_L^2}. \tag{3a}$$

The corresponding eigenvectors are

$$\underline{v}_{1,2}(L) \equiv \begin{bmatrix} -1 \\ (\tau_L - 1 \pm \lambda)/\rho_L \end{bmatrix}. \tag{3b}$$

Substituting Eq. (3a)-3(b) into Eq. (2) and taking into account definition in given in Eq. (1b), we have

$$\begin{cases} F^d(L) = -C_1 \exp(\lambda L) - C_2 \exp(-\lambda L), \\ F^u(L) = C_1 A \exp(\lambda L) + C_2 B \exp(-\lambda L), \end{cases} \tag{4a}$$

where

$$A = \frac{\tau_L - 1 - \lambda}{\rho_L}, \quad B = \frac{\tau_L - 1 + \lambda}{\rho_L}. \tag{4b}$$

Combining Eq. (4a)-(4b) with original boundary conditions, one solves for C_1 and C_2. Therefore, the solution of the two-stream model is

$$F^d(L) = F_0^d \frac{(A + r_S)\exp(-\lambda L) - (B + r_S)\exp(-\lambda[2L_H - L])}{(A + r_S) - (B + r_S)\exp(-2\lambda L_H)},$$

$$F^u(L) = F_0^d \frac{-(A + r_S)B\exp(-\lambda L) + (B + r_S)A\exp(-\lambda[2L_H - L])}{(A + r_S) - (B + r_S)\exp(-2\lambda L_H)},$$

where coefficients, λ, A, and B are given by Eq. (3a) and (4b).

Problem 5. Show the limiting form of F^u for the case of a very dense canopy.

Solution. Recall (cf. Problem 4),

$$F^u(L) = F_0^d \frac{-(A + r_S)B\exp(-\lambda L) + (B + r_S)A\exp(-\lambda[2L_H - L])}{(A + r_s) - (B + r_s)\exp(-2\lambda L_H)},$$

where

$$A = \frac{\tau_L - 1 - \lambda}{\rho_L}, \quad B = \frac{\tau_L - 1 + \lambda}{\rho_L}, \quad \lambda = \sqrt{(1 - \tau_L)^2 - \rho_L^2}.$$

Therefore, in the case of dense canopies

$$F^u(L)\Big|_{L_H \to \infty} \to F_0^d \frac{1 - \tau - \sqrt{(1 - \tau_L)^2 + \rho_L^2}}{\rho_L} \exp(-L\sqrt{(1 - \tau_L)^2 + \rho_L^2}).$$

The ES_n Quadrature Scheme by Shabanov et al.

The accuracy of numerical solution of the transport equation with method of discrete ordinates highly depends on selection of quadrature, or method of discretization (cf. Chapter 6). The S_n quadratures were developed by Dr. Carlson to optimize discretization of transport equation in the angular domain [Bass et al., 1986]. The major advantage of the S_n quadratures is a more homogeneous, compared to other quadratures, distribution of nodes over the surface of sphere, which allows in some cases to achieve the required accuracy of numerical calculations with less number of nodes per octant [Bass et al., 1986]. Below we detail one simple and efficient version, called the ES_n quadratures.

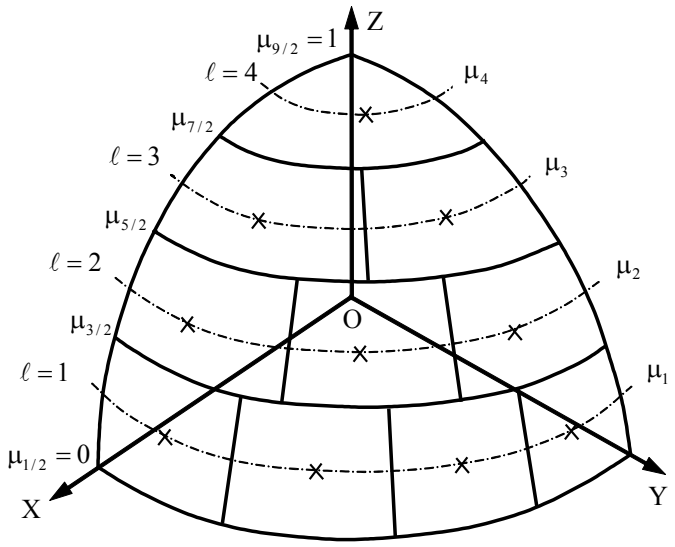

Figure 1. The nodes of ES_n -quadratures for n=8.

The construction the ES_n quadrature, n=2,4,6…, is illustrated for the first octant $\varphi \in [0, \pi/2]$, $\mu \in [0,1]$. The octant is divided into $n(n+2)/8$ parts of equal area, $w_0 = 4\pi/[n(n+2)]$ using latitudes, defined as $\mu = \mu_{\ell+1/2}$, $\ell = 0, 1, ..., n/2$ and longitudes, defined as $\varphi = \varphi_{\ell,\, m+1/2}$, $m = 0, 1, ..., n/2 - \ell + 1$ (Fig. 1). The $\ell-$th layer over μ consists of $n/2 - \ell + 1$ parts of equal area w_0. The total area of the $\ell-$th layer is $\pi w_\ell / 2$, where w_ℓ is the layer width:

$$w_\ell = \frac{4[n-2\ell-2)]}{n(n+2)} = \mu_{\ell+1/2} - \mu_{\ell-1/2}. \tag{1}$$

The coordinates of the boundary $\mu_{\ell\pm1/2}$ and center, $\bar{\mu}_\ell$ of the layer are

$$\mu_{\ell\pm1/2} = 1 - \frac{[n-2\ell+2][n-2(\ell-\pm1)]}{n(n+2)},$$

$$\bar{\mu}_\ell = 1 - \frac{[n-2\ell+2]^2}{n(n+2)}. \tag{2}$$

The nodes of the quadratures are

$$\mu_\ell = \bar{\mu}_\ell + f\cdot\mu_{\ell-\frac{1}{2}}, \quad \ell = 0,1,...,\frac{n}{2}, \tag{3}$$

$$\varphi_{\ell,m} = \frac{\pi}{2}\left[\frac{2m-1}{n-2\ell+2}\cdot A_n + \frac{1}{2}\cdot(1-A_n)\right], \quad m = 1, 2,...,\frac{n}{2}-\ell+1. \tag{4}$$

Here m is the sector number in the $\ell-$th layer. Parameters f and A_n are tuning parameters, the value of which are selected to achieve exact evaluation of the following integrals:

$$\int_0^{2\pi} d\varphi \int_{-1}^{1} \mu^k d\mu, \quad k = 0, 1, 2.$$

Namely,

$$\sum_{\ell=1}^{n/2} w_\ell \mu_\ell^2 = \frac{1}{3}, \quad \sum_{\ell=1}^{n/2}\sum_{m=1}^{n/2-\ell} w_0\,\xi_{\ell,m} = \frac{\pi}{2}\sum_{\ell=1}^{n/2} w_\ell \mu_\ell.$$

In the above, μ_ℓ, ξ_ℓ and η_ℓ are Cartesian coordinates of unit vector $\underline{\Omega}(\theta,\varphi)$

$$\mu_\ell = \cos\theta_\ell, \quad \xi_{\ell,m} = \sqrt{1-\mu_\ell}\cos\varphi_{\ell,m}, \quad \eta_{\ell,m} = \sqrt{1-\mu_\ell}\sin\varphi_{\ell,m}.$$

For the ES_n quadratures the following equalities are valid:

$$w_0 \sum_{\ell,m} \xi_{\ell,m}^2 = w_0 \sum_{\ell,m} \eta_{\ell,m}^2 = w_0 \sum_{\ell,m} \mu_{\ell,m}^2 = \frac{\pi}{6}.$$

The quadratures for the remaining 7 octants are derived using symmetry conditions: $\mu \to -\mu$, $\varphi \to -\varphi$, $\pi/2 - \varphi \to \pi/2 + \varphi$. Note, however, the ES_n quadratures do not posses full symmetry with respect to rotation about coordinate axis X-Y-Z by 90^0, as opposed to the general case of S_n quadratures. Finally, in the case of plane-parallel and spherical geometries the 1-D ES_n quadratures can be used, where weights and nodes over interval [0,1] are specified by Eqs (2) and (3) only.

References

Bass, L., A.M. Voloshenko, A.M., and T.A. Germogenova (1986). *Methods of Discrete Ordinates in Radiation Transport Problems*, Institute of Applied Mathematics, Moscow, (in Russian).

Chapter 5

Stochastic Radiative Transfer

Shabanov et al.

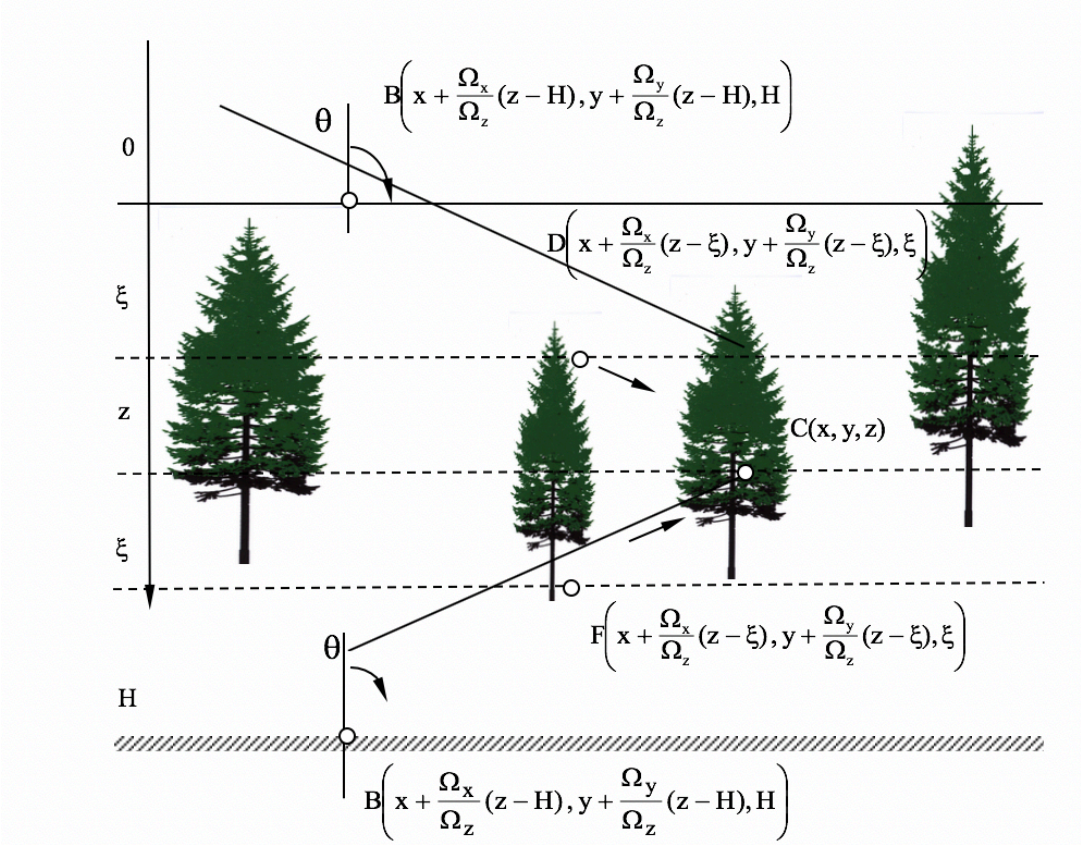

Chapter 5

Stochastic Radiative Transfer

1. Introduction

One key problem of modeling photon transport in vegetation canopies is to account for the three-dimension (3D) canopy structure, which determines the spatial distribution of canopy intercepted solar radiation, or 3D radiation effects [Borel, Gerstl & Powers, 1991; Castel et al., 2001; Jupp et al., 1988, 1989; Knjazikhin et al., 1998a; Li & Strahler, 1992; Myneni & Williams, 1994; Nilson, 1991]. If canopy is short and evenly distributed over the surface (i.e. grass) the *turbid medium* approach is sufficient to represent a canopy structure and the standard 1D Radiative Transfer (RT) equation can be used [Myneni et al., 1997, Ross, 1981]. In contrast, other vegetation biomes, including needle leaf forests, shrublands and savannah, exhibit significant spatial heterogeneity and the full 3D RT modeling is required here [Davis & Knyazikhin, 2005; Myneni, 1991, Myneni et al., 1997]. However, from practical perspective, the use of the 3D RT equation is limited: it requires significant computing resources and, most importantly, numerous input

parameters, which are not always available. The approximations are required which are as physically realistic as 3D model and as analytically and operationally compact as 1D model.

Nilson [1991], later Li and Strahler [1992] introduced the *Geometric-Optical* (GO) approach to evaluate radiation reflected by heterogeneous forest stands. The approach utilizes the notion of Bidirectional Gap Probability (probability to observe radiation reflected by vegetation along the direction $\underline{\Omega}$, if it was illuminated by solar radiation along $\underline{\Omega}_0$) and is based on calculation of mutual shadowing by geometrical figures which represent individual trees. The approach provides the physical explanation for the hot-spot effect (the peak in reflected radiation in the retro-illumination direction, due to absence of shadows in this direction). The approach is valid at VIS part of solar spectrum, where one can restrict the study of radiation interaction to that scattered once from the boundary. In the NIR (and larger) wavelengths leaf absorptance is weak, scattering dominates and GO model is not accurate. In order to enable GO model to describe multiple scattering, the original model was enhanced with RT capabilities, resulting in *hybrid Geometric Optical-Radiative Transfer* (GORT) model [Li, Strahler and Woodcock, 1995]. However, combination of models, based on different approaches raised a new problem to preserve energy conservation law.

The alternative to the GO/GORT approach for heterogeneous canopies is to use RT approach in its stochastic formulation. The theory of radiative transfer in stochastic media aims at deriving a closed system of equations which contains the ensemble-average radiation intensity directly as one of its unknown. Specifically, the ensemble of the 3D random realizations of vegetation canopy structure is rendered for a satellite pixel: in each realization, the elementary volume is occupied by vegetation element or gap. The average over ensemble radiation field over pixel corresponds to the mean radiation intensity, measured by remote sensor. The calculation of the average radiation field faces two options. First option is to average canopy physical properties over the ensemble of realizations and substitute them in corresponding 1D RT equation. However, this option is still equivalent to the turbid medium approach. The second option is to average over ensemble the 3D RT equation formulated for particular realization of canopy structure over satellite pixel. This second option is called *stochastic* RT equation. While the averaging procedure results in a 1D RT equation, it is not equivalent to turbid medium case. The

stochastic 1D RT equation incorporates 3D radiation effects through correlation of vegetation structure as captured by pair-correlation function.

Radiative transfer in stochastic media has been a highly active research field in recent years [Pomraning, 1991, 1995, 1996; Byrne, 2005]. The first significant attempt to apply stochastic approach to radiative transfer in vegetation was made by Menzhulin and Anisimoiv [1991]. However, the first closed system of stochastic RT equations for mean radiation intensity was derived in application to broken clouds by Vainikko [1973a-b] and further developed by Titov and others [Titov, 1990; Zuev & Titov, 1996; Kasianov, 2003].

In this Chapter we develop the stochastic RT (SRT) approach for discontinuous vegetation canopy by adopting Vainikko equations for broken clouds [1973a-b]. This Chapter is organized as follows. In Section 2 we briefly review 3D RT parameterization. In Section 3 we detail derivation of the SRT equations from 3D RT equation. In Section 4 we develop Boolean model of the air-correlation function, key parameter of the SRT, and discuss its basic properties. Section 5 presents numerical scheme of solution of SRT. The ability of the SRT model to reproduce 3D radiation effects reported in literature is discussed in Section 6. Evaluation of the SRT model with field measurements is presented in Section 7. Finally, Section 8 summarizes key results.

2. 3-D RT Model Parameterization

Consider a discontinuous vegetation canopy of height H in a coordinate system with vertical axis z directed downward (Fig. 1). The spatial structure of such canopy can be characterized by the *indicator function* of canopy, $\chi(\underline{r})$ defined for each elementary volume $d\underline{r}$ at spatial location, $\underline{r}$, as follows:

$$\chi(\underline{r}) = \begin{cases} 1, & \text{if } \underline{r} \in \text{vegetation}, \\ 0, & \text{otherwise}. \end{cases} \tag{1}$$

Density of canopy is defined by the Leaf Area Index (LAI) - one-sided green leaf area per unit

ground area [m^2/m^2], namely,

$$LAI = \frac{1}{S}\int_V dV d_L \chi(\underline{r}) = d_L \int_0^H d\xi \frac{1}{S}\int_s dx dy \chi(x, y, \xi) = d_L \int_0^H d\xi\, p(\xi) \tag{2}$$

where d_L is one-sided foliage area volume density [m^2/m^3], which is assumed to be constant through the space. The integration is performed over a volume of canopy, V, with a footprint, S. The integration of the indicator function over area S results in probability of finding vegetation at particular height ξ (cf. Section 3).

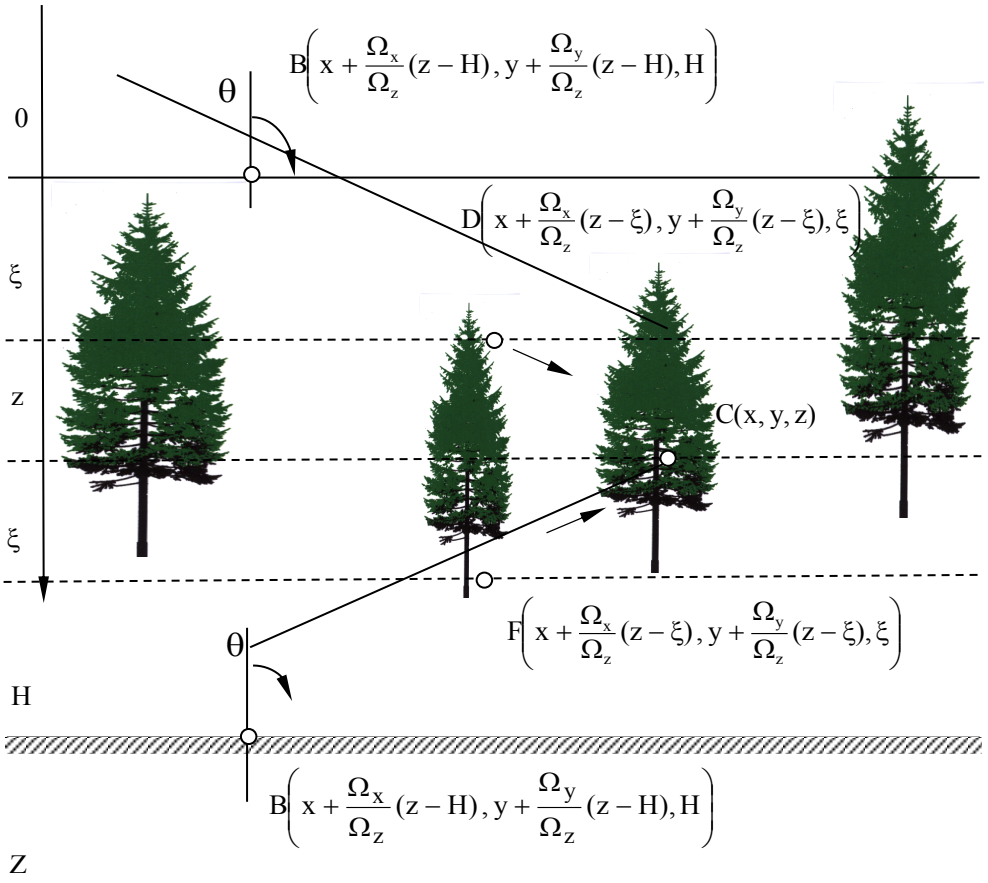

Figure 1. Schematic plot of discontinuous vegetation canopies (needle leaf forests stand) in a coordinate system. The vertical axis, Z, is directed down. Canopy height is H. The angular direction, θ, is measured relative to the upward direction.

The interaction of radiation with canopy leaves is characterized by spatially varying extinction coefficient $\sigma(\underline{r},\underline{\Omega})$ and differential scattering coefficient, $\sigma_S(\underline{r},\underline{\Omega}' \to \underline{\Omega})$, (Chapter 3),

$$\sigma(\underline{r},\underline{\Omega}) = \sigma(\underline{\Omega})\,\chi(\underline{r}) = d_L\,\chi(\underline{r})\,G(\underline{\Omega}), \tag{3}$$

$$\sigma_S(\underline{r},\underline{\Omega}' \to \underline{\Omega}) = \sigma_S(\underline{\Omega}' \to \underline{\Omega})\,\chi(\underline{r}) = \frac{d_L\chi(\underline{r})}{\pi}\,\Gamma(\underline{\Omega}' \to \underline{\Omega}), \tag{4}$$

where $G(\underline{\Omega})$ is the mean projection of leaf normals in the direction $\underline{\Omega}$ and $\Gamma(\underline{\Omega}' \to \underline{\Omega})$ is the area scattering phase function (Chapter 3). The above parameters depend on the probability density of leaf normal orientation, $g_L(\underline{r},\underline{\Omega}_L)$, ($\underline{\Omega}_L$ is a leaf normal direction) and the spectral leaf albedo, $\omega(\underline{r},\lambda)$ (λ is a wavelength). Given the set of structural and optical parameters, the radiation regime in a vegetation canopy is described by the following 3D transport equation for radiation intensity, $I(\underline{r},\underline{\Omega})$:

$$\underline{\Omega}\nabla\, I(\underline{r},\underline{\Omega}) + \sigma(\underline{r},\underline{\Omega})\, I(\underline{r},\underline{\Omega}) = \int_{4\pi} d\underline{\Omega}'\,\sigma_S(\underline{r},\underline{\Omega}' \to \underline{\Omega})\, I(\underline{r},\underline{\Omega}'). \tag{5}$$

The unique solution of the Eq. (5) is specified by the following boundary conditions,

$$\begin{cases} I(z=0,\underline{\Omega}) = \dfrac{f_{dir}(\underline{\Omega}_0)}{\left|\mu(\vec{\Omega}_0)\right|}\,\delta(\underline{\Omega}-\underline{\Omega}_0) + (1-f_{dir})\,d(\underline{\Omega},\underline{\Omega}_0),\ \mu<0, \\ I(z=H,\underline{\Omega}) = \dfrac{\rho_{soil}}{\pi}\displaystyle\int_{2\pi^-} d\underline{\Omega}'\, I(z=H,\underline{\Omega}')\left|\mu(\underline{\Omega}')\right|,\ \mu>0, \end{cases} \tag{6}$$

where the first equation specifies incoming direct, $\delta(\underline{\Omega}-\underline{\Omega}_0)$, and diffuse, $d(\underline{\Omega},\underline{\Omega}_0)$, radiation at the top of canopy, and f_{dir} denotes the ratio of direct to total incoming solar flux. The second equation specifies boundary condition at the canopy bottom, soil surface, which is assumed to be a Lambertian surface with hemispherical reflectance, ρ_{soil}. Note the angular integration notations: integration over the total sphere (4π), lower hemisphere ($2\pi^-$), and upper hemisphere ($2\pi^+$). To simplify numerical solution of the complete RT problem (Eqs. (5) and (6)), two sub-

problems with simplified boundary conditions are formulated: 1) the BS-problem: the original illumination condition at the top of the canopy and the soil reflectance is set to 0; 2) the S-problem: there is no input energy from above, but isotropic (Lambertian) sources of energy are uniformly distributed on the canopy bottom. The solution of the complete problem can be approximated by the solutions of the S- and BS- problems as follows,

$$I(\underline{r},\underline{\Omega}) \approx I_{BS}(\underline{r},\underline{\Omega}) + \frac{\rho_{soil}}{1-\rho_{soil}R_S} T_{BS}\, I_S(\underline{r},\underline{\Omega}), \tag{7a}$$

$$R \approx R_{BS} + \frac{\rho_{soil}}{1-\rho_{soil}R_S} T_{BS}T_S, \tag{7b}$$

$$A \approx A_{BS} + \frac{\rho_{soil}}{1-\rho_{soil}R_S} T_{BS}A_S, \tag{7c}$$

$$T \approx T_{BS} + \frac{\rho_{soil}}{1-\rho_{soil}R_S} T_{BS}R_S. \tag{7d}$$

In the equations above, I, I_{BS}, I_S denote radiation intensities, R, R_{BS}, R_S are canopy albedos, A, A_{BS}, A_S are canopy absorptances, T, T_{BS}, T_S are canopy transmittances for the complete, BS- and S- problems, respectively. The above quantities comply with the energy conservation law,

$$R + A + (1-\rho_{soil})T = 1, \tag{8a}$$

$$R_k + A_k + T_k = 1, \tag{8b}$$

where Eq. (8a) refers to the total problem and Eq. (8b) to two sub-problems (k=S or BS).

3. The Stochastic RT Equations

Vegetation canopy as a stochastic medium: We adopt a stochastic view of the landscape and its spatial structure proposed by Jupp et al. [1998]. We describe the 3D canopy structure with the indicator function $\chi(\underline{r})$ (Eq. (1)). Since the vegetation canopy is treated as a stochastic medium, the indicator function is a stochastic function of space. It provides the most general description of

the canopy structure that accounts for both its *macroscale* (e.g., dimensions of trees and their spatial distribution) and *microscale* (e.g., the clumping of leaves into tree crown) properties.

Given a realization of the canopy structure, $\chi(\underline{r})$, the corresponding realization of the canopy radiation field is described by the deterministic 3D transport equation (Eqs. (5)-(6)). The averaging of this 3D equation over horizontal plane (cf. next sub-section) results in 1D stochastic RT (SRT) equation for mean intensity. The mathematical formulation of the SRT equation requires two types of averages: (1) $U(z,\underline{\Omega})$, *mean intensity over the portion of the horizontal plane at depth z, occupied by vegetation*; (2) $\bar{I}(z,\underline{\Omega})$, *mean intensity over the total space of the horizontal plane* at depth z,

$$U(z,\underline{\Omega}) \equiv \lim_{R\to\infty} \frac{1}{S_R \cap T_z} \iint_{S_R \cap T_z} dxdy\ \chi(x,y,z) I(x,y,z,\underline{\Omega}), \tag{9}$$

$$\bar{I}(z,\underline{\Omega}) \equiv \lim_{R\to\infty} \frac{1}{S_R} \iint_{S_R} dxdy\ I(x,y,z,\underline{\Omega}). \tag{10}$$

In the above, S_R denotes the area of a circle of radius R; T_z denotes the area of the horizontal plane at depth z, occupied by vegetation. Note, that the mathematical expression, infinite limit on R, may be approximated in practice by the size of finite satellite pixel. Thus, the average intensity, $\bar{I}(z,\underline{\Omega})$, corresponds to satellite measurements over pixel.

The averaging procedure (cf. next sub-section) results in the parameterization of the resulting transfer equation in terms of two stochastic moments of a vegetation structure. The first stochastic moment is the *probability*, p, of finding vegetation at canopy depth z,

$$p(z) \equiv \lim_{R\to\infty} \frac{1}{S_R} \iint_{S_R \cap T_z} dxdy\chi(z,x,y) \equiv \lim_{R\to\infty} \frac{S_R \cap T_z}{S_R}. \tag{11}$$

The second moment is the *pair-correlation function*, q, between vegetation at canopy depth z and at depth ξ along the direction $\underline{\Omega}$,

$$q(z,\xi,\underline{\Omega}) \equiv \lim_{R\to\infty} \frac{S_R \cap T_z \cap T_\xi\left[\frac{\Omega_x}{\Omega_z}(z-\xi), \frac{\Omega_y}{\Omega_z}(z-\xi)\right]}{S_R}. \tag{12}$$

In the above, Ω_x, Ω_y, and Ω_z are projections of a unit direction vector, $\underline{\Omega}$, on the x, y, and z axes, respectively; argument for T_ξ denotes a shift of the origin of plane ξ relative to plane z along x and y directions, required to evaluate correlation between the planes in direction $\underline{\Omega}$ (Fig. 1). In essence, pair-correlation function can be evaluated by taking cross-sections of canopy at depth z and ξ, collapsing cross-sections along direction $\underline{\Omega}$ and measuring the portion of area where both cross-sections indicate vegetation. Using the first and second moments of a vegetation structure, the *conditional pair-correlation* of vegetation structure, K, can be evaluated as

$$K(z,\xi,\underline{\Omega}) \equiv \frac{q(z,\xi,\underline{\Omega})}{p(z)}. \tag{13}$$

Derivation of the Stochastic RT Equations: We follow the procedure of Vainikko [1973a] to derive SRT equations. We start by integrating the 3D RT equation (Eq. 5) from the upper (lower) boundary to some internal point $\underline{r}(z,y,z)$ along the direction $\underline{\Omega}$ (cf. Fig. 1). The resulting equation is,

$$\begin{cases} I(x,y,z,\underline{\Omega}) + \dfrac{1}{|\mu(\underline{\Omega})|}\displaystyle\int_0^z d\xi\, \sigma(...,\underline{\Omega}) I(...,\underline{\Omega}) \\ = \dfrac{1}{|\mu(\underline{\Omega})|}\displaystyle\int_0^z d\xi \int_{4\pi} d\underline{\Omega}'\, \sigma_S(..., \underline{\Omega}' \to \underline{\Omega}) I(..., \underline{\Omega}') + I(x,y,0,\underline{\Omega}), \quad \mu < 0, \\ I(x,y,z,\underline{\Omega}) + \dfrac{1}{|\mu(\underline{\Omega})|}\displaystyle\int_z^H d\xi\, \sigma(..., \underline{\Omega}) I(...,\underline{\Omega}) \\ = \dfrac{1}{|\mu(\underline{\Omega})|}\displaystyle\int_z^H d\xi \int_{4\pi} d\underline{\Omega}'\, \sigma_S(..., \underline{\Omega}' \to \underline{\Omega}) I(..., \underline{\Omega}') + I(x,y,H,\underline{\Omega}), \quad \mu > 0, \end{cases} \tag{14}$$

where the following short-cut notation was used:

$$(...) = \left(x + \frac{\Omega_x}{\Omega_z}(z-\xi),\ y + \frac{\Omega_y}{\Omega_z}(z-\xi),\ \xi \right). \tag{15}$$

At the next step, Eq. (14) is averaged over the total space of the horizontal plane z. The key problem at this step is to evaluate the integral terms, which involve $\sigma(...,\underline{\Omega})I(...,\underline{\Omega})$ and $\sigma_S(...,\underline{\Omega}' \to \underline{\Omega})I(...,\underline{\Omega}')$. Due to presence of the indicator function in the definition of σ and σ_S (cf. Eqs. (3-4)) the above integrals over the total space of the horizontal plane ξ are reduced to the integrals over the portion of the plane ξ, occupied by vegetation, T_ξ. The integral terms of interest can be evaluated by shifting the origin of T_ξ, in the x-y plane by the vector

$$\left(\frac{\Omega_x}{\Omega_z}(z-\xi), \frac{\Omega_y}{\Omega_z}(z-\xi) \right),$$

followed by integration over vegetation (Eq. (9)):

$$\begin{aligned}
&\frac{1}{S_R}\iint_{S_R} dxdy\ \sigma(...,\underline{\Omega})I(...,\underline{\Omega}) = \\
&= \frac{1}{S_R} \iint_{S_R \cap T_\xi[\frac{\Omega_x}{\Omega_z}(z-\xi), \frac{\Omega_y}{\Omega_z}(z-\xi)]} dxdy\ \sigma(...,\underline{\Omega})I(...,\underline{\Omega}) \\
&= \frac{1}{S_R} \iint_{S'_R \cap T_\xi} dx'dy'\ \sigma(x',y',\xi',\underline{\Omega})I(x',y',\xi',\underline{\Omega}) \\
&= \frac{S_R \cap T_\xi}{S_R} \cdot \frac{1}{S_R \cap T_\xi} \iint_{S'_R \cap T_\xi} dx'dy'\ \sigma(\underline{\Omega})I(x',y',\xi',\underline{\Omega}) \\
&= p(\xi)\sigma(\underline{\Omega})U(\xi,\underline{\Omega})
\end{aligned} \tag{16}$$

Taking into account the derivations above, the equation for mean intensity over total space of horizontal plane at depth z, $\bar{I}(z,\underline{\Omega})$, is

$$
\begin{cases}
\bar{I}(z,\underline{\Omega}) + \dfrac{1}{|\mu(\underline{\Omega})|}\displaystyle\int_0^z d\xi\; p(\xi)\,\sigma(\underline{\Omega})U(\xi,\underline{\Omega}) \\
= \dfrac{1}{|\mu(\underline{\Omega})|}\displaystyle\int_0^z d\xi \int_{4\pi} d\underline{\Omega}'\; p(\xi)\,\sigma_S(\underline{\Omega}' \to \underline{\Omega})U(\xi,\underline{\Omega}') + \bar{I}(0,\underline{\Omega}), \quad \mu < 0, \\
\bar{I}(z,\underline{\Omega}) + \dfrac{1}{|\mu(\underline{\Omega})|}\displaystyle\int_z^H d\xi\; p(\xi)\,\sigma(\underline{\Omega})U(\xi,\underline{\Omega}) \\
= \dfrac{1}{|\mu(\underline{\Omega})|}\displaystyle\int_z^H d\xi \int_{4\pi} d\underline{\Omega}'\; p(\xi)\sigma_S(\underline{\Omega}' \to \underline{\Omega})U(\xi,\underline{\Omega}') + \bar{I}(H,\underline{\Omega}), \quad \mu > 0.
\end{cases}
\tag{17}
$$

In the above, $\bar{I}(0,\underline{\Omega})$ and $\bar{I}(H,\underline{\Omega})$ denote mean radiation intensities over whole horizontal plane at the canopy boundaries; in the typical case of the uniform boundary conditions they are equal to the corresponding 3D values, $I(z = 0,\underline{\Omega})$ and $I(z = H,\underline{\Omega})$ (cf. Eq. (6)).

According to Eq. (17), $\bar{I}(z,\underline{\Omega})$, depends on $U(z,\underline{\Omega})$. The equations for $U(z,\underline{\Omega})$ can be derived by averaging Eq. (14) over the portion of a horizontal plane, occupied by vegetation. The terms under the sign of integral in this case can be evaluated with the above described technique (Eq. (16)), taking into account Eqs. (9), (11), and (12), as follows,

$$
\begin{aligned}
&\frac{1}{S_R \cap T_z}\iint_{S_R \cap T_z} dxdy\;\sigma(...,\underline{\Omega})\,I(...,\underline{\Omega}) \\
&= \frac{1}{S_R \cap T_z}\iint_{S_R \cap T_z \cap T_\xi\left[\frac{\Omega_x}{\Omega_z}(z-\xi),\frac{\Omega_y}{\Omega_z}(z-\xi)\right]} dxdy\;\sigma(...,\underline{\Omega})\,I(...,\underline{\Omega}) \\
&= \frac{1}{S_R \cap T_z}\iint_{S'_R \cap T'_z \cap T_\xi} dx'dy'\;\sigma(x',y',\xi',\underline{\Omega})I(x',y',\xi',\underline{\Omega}) \\
&= \frac{S'_R \cap T'_z \cap T_\xi}{S_R \cap T_z}\frac{1}{S'_R \cap T'_z \cap T_\xi}\iint_{S'_R \cap T'_z \cap T_\zeta} dx'dy'\;\sigma(\underline{\Omega})\,I(x',y',\xi,\underline{\Omega}) \\
&= \frac{q(z,\xi,\underline{\Omega})}{p(z)}\sigma(\underline{\Omega})U(\xi,\underline{\Omega}) \\
&\equiv K(z,\xi,\underline{\Omega})\,\sigma(\underline{\Omega})U(\xi,\underline{\Omega}).
\end{aligned}
\tag{18}
$$

In the above derivations we assumed that the subset $T_z \cap T_\xi$ contains the same percentage of vegetation as the total set T_z. This assumption is similar to one, introduced by Vainikko [1973a] in the derivation of the original version of stochastic equations for atmosphere. This assumption is called "*local chaotisity and global order*" and is required to close system of stochastic equations using only first two moments of structure. Given Eqs. (18) and (14), we can formulate equation for $U(z,\underline{\Omega})$ as follows,

$$\begin{cases} U(z,\underline{\Omega}) + \dfrac{1}{|\mu(\underline{\Omega})|}\displaystyle\int_0^z d\xi\, K(z,\xi,\underline{\Omega})\,\sigma(\underline{\Omega})U(\xi,\underline{\Omega}) \\ = \dfrac{1}{|\mu(\underline{\Omega})|}\displaystyle\int_0^z d\xi \int_{4\pi} d\underline{\Omega}'\, K(z,\xi,\underline{\Omega})\,\sigma_S(\underline{\Omega}' \to \underline{\Omega})\,U(\xi,\underline{\Omega}') + U(0,\underline{\Omega}), \quad \mu < 0, \\ U(z,\underline{\Omega}) + \dfrac{1}{|\mu(\underline{\Omega})|}\displaystyle\int_z^H d\xi\, K(z,\xi,\underline{\Omega})\,\sigma(\underline{\Omega})U(\xi,\underline{\Omega}) \\ = \dfrac{1}{|\mu(\underline{\Omega})|}\displaystyle\int_z^H d\xi \int_{4\pi} d\underline{\Omega}'\, K(z,\xi,\underline{\Omega})\,\sigma_S(\underline{\Omega}' \to \underline{\Omega})U(\xi,\underline{\Omega}') + U(H,\underline{\Omega}), \quad \mu > 0. \end{cases} \tag{19}$$

In the above, $U(0,\underline{\Omega})$ and $U(H,\underline{\Omega})$ denote mean radiation intensities over the portion of horizontal plane occupied by vegetation at the canopy boundaries; in the typical case of the uniform boundary conditions they are equal to corresponding 3D values, $I(z=0,\underline{\Omega})$ and $I(z=H,\underline{\Omega})$ (cf. Eq. (6)).

Radiation over Gaps: The complementary variable, mean radiation intensity over gaps, $V(z,\underline{\Omega})$, is not a part of the closed system of stochastic equations (Eqs. (17) and (19)), but it could be useful in applications. It is defined as follows

$$V(z,\underline{\Omega}) \equiv \lim_{R\to\infty} \frac{1}{S_R \cap [S_R - T_z]} \iint_{S_R} dxdy\,[1-\chi(x,y,z)]\,I(x,y,z,\underline{\Omega}), \tag{20}$$

The relationship between $\bar{I}(z,\underline{\Omega})$, $U(z,\underline{\Omega})$ and $V(z,\underline{\Omega})$ is as follows

$$\bar{I}(z,\underline{\Omega}) = \frac{1}{S_R}\iint_{S_R} dxdy\ I(x,y,z,\underline{\Omega})$$

$$= \frac{1}{S_R}\iint_{S_R\cap T_z} dxdy\ \chi(x,y,z)\, I(x,y,z,\underline{\Omega}) + \frac{1}{S_R}\iint_{S_R\cap[S_R-T_z]} dxdy[1-\chi(x,y,z)]\, I(x,y,z,\underline{\Omega})$$

$$= \frac{S_R\cap T_z}{S_R}\frac{1}{S_R\cap T_z}\iint_{S_R\cap T_z} dxdy\ \chi(x,y,z)\, I(x,y,z,\underline{\Omega})$$

$$+ \frac{S_R\cap[S_R-T_z]}{S_R}\frac{1}{S_R\cap[S_R-T_z]}\iint_{S_R\cap[S_R-T_z]} dxdy\,[1-\chi(x,y,z)]\, I(x,y,z,\underline{\Omega})$$

$$= p(z)U(z,\underline{\Omega}) - [1-p(z)]V(z,\underline{\Omega}). \qquad (21)$$

Separation of Direct and Diffuse Radiation Components: The average intensity over vegetation, $U(z,\underline{\Omega})$, can be decomposed into the direct and diffuse components, according to the pattern of incoming solar radiation, Eq. (6), namely

$$U(z,\underline{\Omega}) = \frac{f_{dir}(\underline{\Omega}_0)}{|\mu(\underline{\Omega}_0)|}U_\delta(z)\delta(\underline{\Omega}-\underline{\Omega}_0) + U_d(z,\underline{\Omega}). \qquad (22)$$

Substituting this decomposition into Eq. (19) and collecting terms, which contain the Dirac's delta function, $\delta(\underline{\Omega}-\underline{\Omega}_0)$, we will get equation for the direct component of $U(z,\underline{\Omega})$,

$$U_\delta(z) + \frac{1}{|\mu(\underline{\Omega}_0)|}\int_0^z d\xi\ K(z,\xi,\underline{\Omega}_0)\,\sigma(\underline{\Omega}_0)U_\delta(\xi) = 1, \qquad (23)$$

The remaining terms constitute equation for the diffuse component of $U(z,\underline{\Omega})$,

$$\begin{cases} U_d(z,\underline{\Omega}) + \dfrac{1}{|\mu(\underline{\Omega})|}\displaystyle\int_0^z d\xi\ K(z,\xi,\underline{\Omega})\sigma(\underline{\Omega})U_d(\xi,\underline{\Omega}) \\ = \dfrac{1}{|\mu(\underline{\Omega})|}\displaystyle\int_0^z d\xi\ K(z,\xi,\underline{\Omega})S(\xi,\underline{\Omega}) + U_0(z,\underline{\Omega},\underline{\Omega}_0), \quad \mu < 0, \\ U_d(z,\underline{\Omega}) + \dfrac{1}{|\mu(\underline{\Omega})|}\displaystyle\int_z^H d\xi\ K(z,\xi,\underline{\Omega})\sigma(\underline{\Omega})U_d(\xi,\underline{\Omega}) \\ = \dfrac{1}{|\mu(\underline{\Omega})|}\displaystyle\int_z^H d\xi\ K(z,\xi,\underline{\Omega})S(\xi,\underline{\Omega}) + U_H(z,\underline{\Omega},\underline{\Omega}_0), \quad \mu > 0, \end{cases} \tag{24a}$$

where,

$$S(\xi,\underline{\Omega}) = \int_{4\pi} d\underline{\Omega}'\ \sigma_S(\underline{\Omega}' \to \underline{\Omega})U_d(\xi,\underline{\Omega}'), \tag{24b}$$

$$U_0(z,\underline{\Omega},\underline{\Omega}_0) = \frac{f_{dir}(\underline{\Omega}_0)}{|\mu(\underline{\Omega})\mu(\underline{\Omega}_0)|}\int_0^z d\xi\ K(z,\xi,\underline{\Omega})\sigma_S(\underline{\Omega}_0 \to \underline{\Omega})U_\delta(\xi) + [1 - f_{dir}(\underline{\Omega}_0)]d(\underline{\Omega},\underline{\Omega}_0), \tag{24c}$$

$$U_H(z,\underline{\Omega},\underline{\Omega}_0) = \frac{f_{dir}(\underline{\Omega}_0)}{|\mu(\underline{\Omega})\mu(\underline{\Omega}_0)|}\int_z^H d\xi\ K(z,\xi,\underline{\Omega})\sigma_S(\underline{\Omega}_0 \to \underline{\Omega})U_\delta(\xi) + U(H,\underline{\Omega}). \tag{24d}$$

The average intensity over total space of a horizontal plane, $\bar{I}(z,\underline{\Omega})$, can be decomposed similarly to $U(z,\underline{\Omega})$, namely

$$\bar{I}(z,\vec{\Omega}) = \frac{f_{dir}(\underline{\Omega}_0)}{|\mu(\underline{\Omega}_0)|}\bar{I}_\delta(z)\,\delta(\underline{\Omega} - \underline{\Omega}_0) + \bar{I}_d(z,\underline{\Omega}). \tag{25}$$

where $\bar{I}_\delta(z)$ and $\bar{I}_d(z,\underline{\Omega})$ satisfy

$$\bar{I}_\delta(z) = 1 - \frac{1}{|\mu(\underline{\Omega}_0)|}\int_0^z d\xi\ p(\xi)\sigma(\underline{\Omega}_0)U_\delta(\xi), \tag{26}$$

$$
\begin{cases}
\bar{I}_d(z,\underline{\Omega}) = -\dfrac{1}{|\mu(\underline{\Omega})|}\displaystyle\int_0^z d\xi\ p(\xi)\sigma(\underline{\Omega})U_d(\xi,\underline{\Omega}) \\
+\dfrac{1}{|\mu(\underline{\Omega})|}\displaystyle\int_0^z d\xi\ p(\xi)S(\xi,\underline{\Omega}) + U_0(z,\underline{\Omega},\underline{\Omega}_0), \quad \mu < 0, \\
\bar{I}_d(z,\underline{\Omega}) = -\dfrac{1}{|\mu(\underline{\Omega})|}\displaystyle\int_z^H d\xi\ p(\xi)\sigma(\underline{\Omega})U_d(\xi,\underline{\Omega}) \\
+\dfrac{1}{|\mu(\underline{\Omega})|}\displaystyle\int_z^H d\xi\ p(\xi)S(\xi,\underline{\Omega}) + U_H(z,\underline{\Omega},\underline{\Omega}_0), \quad \mu > 0,
\end{cases}
\tag{27}
$$

and, $S(\xi,\underline{\Omega})$, $U_0(z,\underline{\Omega},\underline{\Omega}_0)$ and $U_H(z,\underline{\Omega},\underline{\Omega}_0)$ are defined by Eq. (24).

Energy Balance: The standard procedure to trace the energy input and output to/from the system is to integrate the equation for the mean intensity [Eq. (17)] over canopy space and over all directions. The resulting canopy reflectance and transmittance are expressed, similar to 1D case, through the mean intensity over total space, $\bar{I}(z,\underline{\Omega})$, as follows

$$
R(\lambda) = \int_{2\pi^+} d\underline{\Omega}\,\bar{I}(0,\underline{\Omega})\left|\mu(\underline{\Omega})\right|, \quad T(\lambda) = \int_{2\pi^-} d\underline{\Omega}\,\bar{I}(H,\underline{\Omega})\left|\mu(\underline{\Omega})\right|, \tag{28a}
$$

where R and T correspond to reflectance to reflectance and transmittance of the total problem (similar expressions exist for BS and S problem). However, in contrast to canopy reflectance and transmittance, canopy absorptance is expressed through mean intensity over vegetation, $U(z,\underline{\Omega})$. This can be shown as follows,

$$
\begin{aligned}
A(\lambda) &\equiv \frac{1}{\pi R^2}\int_V d\underline{r}\int_{4\pi} d\underline{\Omega}[1-\omega(\lambda)]\,\sigma(\underline{\Omega})\,\chi(\underline{r})I(\underline{r},\underline{\Omega}) \\
&= [1-\omega(\lambda)]\int_0^H dz\int_{4\pi} d\underline{\Omega}\,\sigma(\underline{\Omega})\frac{1}{\pi R^2}\int_{\pi R^2} dx\,dy\,\chi(\underline{r})\ I(\underline{r},\underline{\Omega}) \\
&= [1-\omega(\lambda)]\int_0^H dz\int_{4\pi} d\underline{\Omega}\ \sigma(\underline{\Omega})p(z)U(z,\underline{\Omega}).
\end{aligned}
\tag{28b}
$$

Hot-Spot Effect: As of time of writing the major shortcoming of SRT approach is that it does not describe the hot spot effect, just as standard 1D RT equation. While SRT implements the 3D RT effects (cf. Section 5), the reason why it is not describe the hot-spot effect is unknown presently. Thus, the standard approach to implement the hot spot is used, that is to modify the extinction coefficient, $\sigma(\underline{\Omega})$. An important feature of the radiation regime in vegetation canopies is the hot-spot effect, which is the peak in reflected radiance distribution along the retro-illumination direction. The standard theory describes the hot-spot by modifying the extinction coefficient $\sigma(\underline{\Omega})$ namely [Marshak, 1989],

$$\sigma(\underline{\Omega},\underline{\Omega}_0) = \sigma(\underline{\Omega})h(\underline{\Omega},\underline{\Omega}_0),$$

$$h(\underline{\Omega},\underline{\Omega}_0) = \begin{cases} 1 - \sqrt{\dfrac{G(\underline{\Omega}_0)\left|\mu(\underline{\Omega})\right|}{G(\underline{\Omega})\left|\mu(\underline{\Omega}_0)\right|}}\exp\{-\Delta(\underline{\Omega},\underline{\Omega}_0)k\}, & \text{if } (\underline{\Omega}\cdot\underline{\Omega}_0) < 0\,, \\ 1, & \text{if } (\underline{\Omega}\cdot\underline{\Omega}_0) > 0\,, \end{cases}$$

$$\Delta(\underline{\Omega},\underline{\Omega}_0) = \sqrt{\frac{1}{\mu^2(\underline{\Omega}_0)} + \frac{1}{\mu^2(\underline{\Omega})} + \frac{2(\underline{\Omega}\cdot\underline{\Omega}_0)}{\left|\mu(\underline{\Omega})\,\mu(\underline{\Omega}_0)\right|}}. \tag{29}$$

In the above, k is an empirical parameter, related to the ratio of vegetation height to characteristic leaf dimension, estimated to be between 1 and 8 based [Stewart, 1990].

4. Pair-Correlation Function

Basic Properties of Pair-Correlation Function: In the case of turbid medium three is no correlation between phytoelements and conditional pair-correlation function, K, simplifies:

$$K(z,\xi,\underline{\Omega}) = \frac{q(z,\xi,\underline{\Omega})}{p(z)} \equiv \frac{p(z)\cdot p(\xi)}{p(z)} = p(\xi). \tag{30}$$

In this case Eq. (17) and (19) are identical. Combining this result with Eq. (21) we have

$$\bar{I}(z,\underline{\Omega}) = U(z,\underline{\Omega}) = V(z,\underline{\Omega}). \tag{31}$$

Thus, the stochastic equations are reduced to 1D RT equation in the case of turbid medium, where gaps are mixed with vegetation at the level of elementary volume, resulting in lack of distinction between mean intensities over gaps and vegetation. Note that in this case 1D RT equation is formulated with the extinction coefficient $\sigma(z,\underline{\Omega}) = [p(z)\,LAI]\cdot G(\underline{\Omega})$ and the differential scattering coefficient $\sigma_s(\underline{\Omega}' \to \underline{\Omega}) = [p(z)\,LAI]\cdot \pi^{-1}\Gamma(\underline{\Omega}' \to \underline{\Omega})$. Thus, solution to the stochastic RT depends on the product $p(z)\,LAI$ but not on absolute values of $p(z)$ and LAI in this case.

Note the other special property of the pair-correlation function. In the general case of correlation of vegetation structure, the following symmetry property holds true:

$$q(z,\xi,\underline{\Omega}) = q(\xi,z,-\underline{\Omega}). \tag{32}$$

This property directly follows from the definition of the pair-correlation function, Eq. (12).

Boolean Models of Pair-Correlation Function: We follow the theory of *stochastic geometry* [Stoyan, Kendall and Mecke, 1995] to derive analytical expressions for the pair-correlation function in the general case of vegetation structure with correlation. To apply the theory of stochastic geometry to our case we need to reformulate *stochastic 3D model of canopy structure* in terms of *Boolean 2D model of random sets* [Strahler & Jupp, 1990].

Following the concepts of the theory of stochastic geometry, we model the spatial distribution of vegetation species as a stationary *Poisson point process*: a) total number of trees in the bounded study area follows Poisson distribution with intensity (stem density) d; b) spatial distribution of trees is random. We further assume that all trees are identical vertical solids (volume obtained by rotating a curve, r (z), about the vertical axis z).

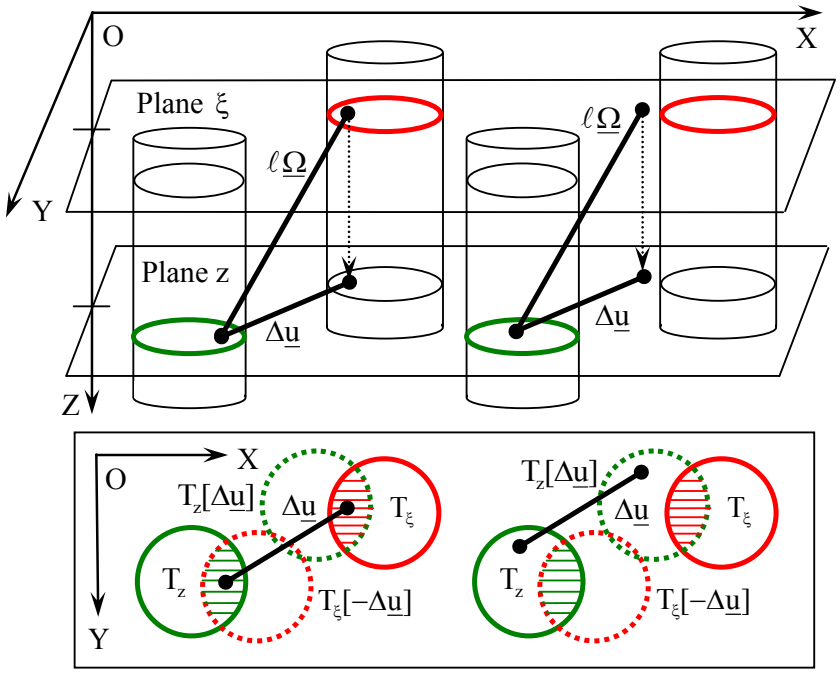

Figure 2. Reducing formulation of pair-correlation function from 3D space (top plot) to 2D Boolean random sets (bottom plot). Cylinders (circles) corresponds to 3D trees (2D projection of trees), while dipole corresponds correlation. If endpoints of 3D dipole, $\ell\underline{\Omega}$, indicate correlation in 3D space, than the 2D projection of dipole, $\Delta\underline{u}$, also indicates correlation (plots at the left) and vice versa (plots at the right).

Now, consider evaluation of the pair-correlation function, $q(z,\xi,\underline{\Omega})$ for the established model of 3D canopy structure (Fig. 2). For simplicity of visualization we represented trees as identical cylinders. Let us define a 3D correlation dipole as a vector $\ell\underline{\Omega}$,

$$\ell\underline{\Omega} \equiv \left(\frac{\Omega_x}{\Omega_z}(z-\xi), \frac{\Omega_y}{\Omega_z}(z-\xi), (z-\xi)\right), \quad \left\|\ell\underline{\Omega}\right\| = \ell = \left|\frac{(z-\xi)}{\cos(\underline{\Omega})}\right|, \tag{33a}$$

whose endpoints belong to planes z and ξ. The projection of 3D dipole $\ell\underline{\Omega}$ on a horizontal plane results in a 2D dipole, $\Delta\underline{u}$,

$$\Delta\underline{u} \equiv \left(\frac{\Omega_x}{\Omega_z}(z-\xi), \frac{\Omega_y}{\Omega_z}(z-\xi)\right), \quad \left\|\Delta\underline{u}\right\| = \Delta = \left|(z-\xi)\tan(\Omega)\right|. \tag{33b}$$

According to definition of $q(z,\xi,\underline{\Omega})$ (Eq. (12)), correlation of vegetation elements between two horizontal planes, z and ξ along the direction $\underline{\Omega}$ in 3D space corresponds to the probability of event when one endpoint of dipole $\ell\underline{\Omega}$ belong to vegetation at plane z (T_z subset), and the other to vegetation at plane ξ (T_ξ subset) ξ (Fig. 2, top portion). To achieve this, the location of one endpoint of dipole is restricted to $T_z \cap T_\xi[-\Delta\underline{u}]$ at the plane z, while the location of the another is simultaneously restricted to $T_z[\Delta\underline{u}] \cap T_\xi$ at the plane ξ. Here argument $\Delta\underline{u}$ corresponds to a shift of subset. Now, we can project 3D stochastic geometry on 2D space, resulting in a union of T_z and T_ξ, $T_z \cup T_\xi$, which is a Boolean random set. Comparing top and bottom portion of Fig. 2, one can see that the location of 3D and 2D dipoles are restricted in the same way to achieve correlation. Comparing such that set of trees will become Boolean random set of trees projection (trees and correlation dipole) on 2D space, one can see that the location of 2D dipole is restricted in the same way as in 3D case. Thus we reduced estimation of pair-correlation function in 3D space to the subject of study stochastic geometry, evaluation of covariance of two points in 2D space of Boolean random sets. Formally,

$$q(z,\xi,\Delta\underline{u}) \equiv \lim_{R\to\infty} \frac{S_R \cap T_z \cap T_\xi[-\Delta\underline{u}]}{S_R} = \Pr\left[\underline{r}_z,\ \underline{r}_z + \Delta\underline{u} \in T_z \cup T_\xi\right]. \qquad (34)$$

In words, the pair-correlation function is equal to covariance of two points ($\underline{r}_z$ and $\underline{r}_z + \Delta\underline{u}$) separated by distance Δ along direction $\underline{u}$ in 2D space of canopy given by union of T_z and T_ξ. In view of azimuthal symmetry of typical landscapes, covariance depends only on absolute value of horizontal distance of correlation, Δ, not direction, $\underline{u}$, that is, $q(z,\xi,\Delta\underline{u}) = q(z,\xi,\Delta)$. Below we briefly describe pair-correlation functions for three models Boolean random sets: the Poisson germ-grain, Matérn cluster and Matérn hard-core processes (cf. Fig. 3).

- *Poisson germ-grain model*: In the above formulation of the stochastic model, the points of the Poisson process are germs of the model while the crown cross sections are the primary grains. The primary grains are represented by discs of the radius $r(z)$ and $r(\xi)$. Following

derivations of Stoyan, Kendall and Mecke [1995] on p. 68, the covariance function (34) takes the following form

$$q(z,\xi,\Delta) = p(z) + p(\xi) - 1 + [1 - p(z)][1 - p(\xi)]\exp\{d\theta(z,\xi,\Delta)\}, \tag{35a}$$

$$p(z) = 1 - \exp\{-d\pi r^2(z)\}. \tag{35b}$$

Here $p(z)$ is defined by Eq. (11) and, for $r(\xi) \geq r(z)$,

$$\theta(z,\xi,\Delta) = \begin{cases} \pi r^2(z), & \text{if } r(\xi) - r(z) > \Delta, \\ 0, & \text{if } r(\xi) + r(z) \leq \Delta, \\ \alpha r^2(z) + \beta r^2(\xi) - \Delta r(\xi)\sin\alpha, & \text{otherwise}, \end{cases} \tag{35c}$$

$$\alpha = \arccos\left(\frac{r^2(\xi) - r^2(z) + \lambda^2}{2\lambda r(\xi)}\right), \quad \beta = \arccos\left(\frac{r^2(z) - r^2(\xi) + \lambda^2}{2\lambda r(z)}\right). \tag{35d}$$

For $r(\xi) < r(z)$, $\theta(z,\xi,\Delta) = \theta(\xi,z,\Delta)$.

For cylindrical in shape trees, $p(z) = g$, $r(\xi) = r(z) = D_B/2$, $\alpha = \beta = \arccos(\Delta/D_B)$. It follows from Eqs. (35) that the pair correlation function depends on the horizontal distance Δ normalized by the crown base diameter D_B, i.e.,

$$q(\lambda) = 2g - 1 + (1-g)^{2-\kappa(\Delta,D_B)}. \tag{36a}$$

The coefficient $k(\Delta, D_B)$ is an area occupied by the intersection of two circles of the radius D_B shifted by a distance Δ normalized by the circle area $\pi D_B^2/4$, i.e.,

$$k(\Delta, D_B) = 2\pi^{-1}\left[\arccos\frac{\Delta}{D_B} - \frac{\Delta}{D_B}\sqrt{1 - \left(\frac{\Delta}{D_B}\right)^2}\right]\mathcal{H}(D_B - \Delta), \tag{36b}$$

where $\mathcal{H}(s)$ is the Heaviside step function. The derivative at the origin $\lambda = 0$ is

$$\left.\frac{dq(\Delta)}{d\Delta}\right|_{\Delta=0} = \frac{4(1-g)\ln(1-g)}{\pi D_B}. \tag{37}$$

- *Matérn cluster process*: Cluster point processes are derived from the stationary Poisson point process of intensity d by replacing each point with a representative cluster C_0 of points. The representative cluster is a point process. The number of points in C_0 has a Poisson distribution with the positive parameter $\overline{m}$. The points of C_0 are independently and uniformly scattered in the circle of the diameter $D_0 = 2r_0$. On each of these points a geometrical figure (clump) is placed. The union of all of these figures is the stochastic cluster model of random sets on the horizontal plane. For clumps represented by circles with the diameter $D_c = 2r_c$, the pair-correlation function can be factorized into probabilities of finding two points in the clusters and finding clumps at these points, i.e.,

$$q(\Delta) = \left[2g_c - 1 + (1-g_c)^{2-\kappa(\Delta, D_C)}\right]\left[2g_0 - 1 + (1-g_0)^{2-\kappa(\Delta, D_0)}\right], \tag{38a}$$

$$g_c = 1 - \exp(-\overline{m}\pi r_c^2), \quad g_0 = 1 - \exp(-d\pi r_0^2). \tag{38b}$$

The probability, $p(z)$, of finding a foliated point at depth *z* is given by $p(z) = g_c\, g_0$.

- *Matérn hard-core model*: Tree crowns in the above classes of models may mutually intersect forming complex patterns. The hard-core models describe patterns produced by the locations of centers of non-overlapping circles of a given radius. Consider the Matérn hard-core point process [Stoyan, Kendall & Mecke, 1995] which is derived from a stationary Poisson point process of intensity d by deleting points satisfying some definite rules. Consider a vegetation canopy consisting of cylindrical trees. Let $\eta = \pi D_B^2$, where D_B is the crown base diameter. The intensity,

d_{HC}, and the second order product density, $\rho^2(\Delta)$, of the Matérn hard-core point process are given by [Stoyan, Kendall & Mecke, 1995]

$$d_{HC} = \frac{1-\exp(-d\eta)}{\eta}, \tag{39a}$$

$$\rho^{(2)}(\Delta) = \frac{2\Gamma(\Delta)[1-\exp(-d\eta)] - 2\eta[1-\exp(-d\Gamma(\Delta))]}{\nu\Gamma(\Delta)[\Gamma(\Delta)-\eta]}\mathcal{H}(\Delta - D_B), \tag{39b}$$

$$\Gamma(\Delta) = \eta\left[2 - k(\Delta, 2D_B)\right]. \tag{39c}$$

The second moment $\rho^2(\Delta)$ can be interpreted as the probability density that two tree centers are separated by the distance Δ. Since the trees crowns are assumed to be not overlapping, the ground cover is $g = d_{HC}\pi D_B^2 = d_{HC}\eta/4$. The pair-correlation function is the sum of probabilities of finding foliated points in the same crown and in different crowns, i.e.,

$$q(\Delta) = gk(\Delta, D_B) + \int_{\substack{\|\underline{v}\|\le D_B \\ \|\underline{v}'\|\le D_B}} d\underline{v}d\underline{v}'\rho^{(2)}(\|\underline{v} - \underline{v}' + \Delta\underline{u}\|), \tag{39d}$$

where $\underline{u} = (0,1)$ is the unit vector on the plane z=0 and $\|\cdot\|$ is the Euclidean distance. Note the second order product density, $\rho^2(\Delta)$, does not depend on $\underline{u}$.

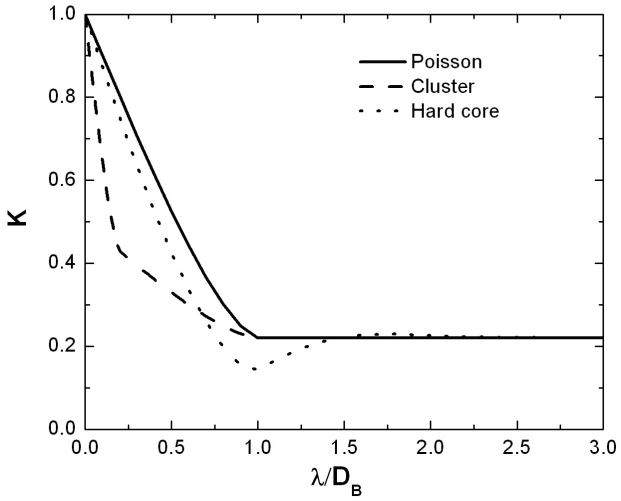

Figure 3. Conditional pair-correlation functions of the Poisson germ-grain, Matérn cluster and Matérn hard-core processes. Cluster, D_0, and clump, D_c, sizes in the Matérn cluster process are set to D_B and $0.2 \cdot D_B$, respectively. The probability, p(z), of finding a foliated point at depth z is 0.22 in all examples.

Pair-Correlation Function and Landscape Properties: It appears that several well known and cdocumented in literature properties of landscape are captured by the pair-correlation function, $q(z,\xi,\Delta)$ or (and) the conditional pair-correlation function, $K(z,\xi,\Delta) \equiv q(z,\xi,\Delta)/p(z)$ (Eqs. (12) and (13)).

First, consider shape of dependence of conditional pair-correlation function, $K(z,\xi,\Delta)$, on correlation distance (cf. Fig. 3). If two points are separated by a short horizontal distance, than $K(z,\xi,\Delta) \to 1$, as $\Delta \to 0$ This property expresses the effect of clumping of foliage elements; that is, detecting a leaf makes it more likely that another leaf will be detected nearby. As correlation distance increases, $K(z,\xi,\Delta)$ reaches its minimum at particular value of distance, which characterizes the crown horizontal size at height z. As horizontal distance increases further, the correlation function tends to increase from its minimum to a constant value, and then levels off. This constant value is the probability, $p(\xi)$, of finding a foliated point at depth ξ (Eq. (30)). Beyond the distance at which correlation function saturates, there is no relation between foliated points.

Second, consider derivative of pair-correlation function, $q(z,\xi,\Delta)$ with respect to correlation distance. Here we rely on the fact that the notion of $q(z,\xi,\Delta)$ is similar to the notion of *semivariance* in the theory of digital image processing, and its spatial derivative at small distances is attributed to the variability of canopy structure at the finest scale [Chen et al., 1993;

Jupp et al., 1989; Roujean, 1999a]. As example, consider $dq/d\Delta$ for $\Delta \to 0$ for the Poisson germ-grain model of a forest consisting of identical cylindrical trees (Eq. (37)). If the derivative is close to zero (e.g., the horizontal tree dimension D_B is large or the ground cover is close to 1), then vegetation canopy is considered to be a "smooth medium", whereas if derivative is high, then the canopy structure is "rough." Inclusion of the within crown leaf spatial correlation will result in a finer scale of the canopy structure variability and value of $|dq/d\Delta|$ at $\Delta \to 0$ will consequently be higher (curve "Cluster" in Fig. 3).

Finally, it is worth to point to several additional properties of the pair-correlation function, $q(z,\xi,\Delta)$. The extreme case when $\Delta \to 0$ is realized in two situations: a) when $\xi \to z$ and b) for vertical directions, when $\theta \to 0^0 (180^0)$. In the first case, $q(z,\xi,\Delta) = p(z)$. The second case is more complex. If trees are represented as vertical solids with height dependent radius, r(h) $q(z,\xi,\Delta) = \min\{p(z), p(\xi)\}$. The general case of complex landscape architecture requires calculation according to definition of $q(z,\xi,\Delta)$ (Eq. 12). Nevertheless, under some reasonable simplifying assumptions pair-correlation function conveys information about mean vertical structure when $\Delta \to 0$. At larger distances, between one and two tree diameter ad depth z, $D(z)$, the pair correlation function provides determines the probability of finding two trees placed Δ apart. In between these extremes, the-pair correlation function describes variation in the canopy structure along different directions, e.g., the distribution of phytoelements that shade leaves at depth ξ along a given direction $\underline{\Omega}$. Overall, the pair-correlation function provides a quantitative description of the canopy structure at all scales of landscape.

5. Numerical Scheme of Solution of the Stochastic RT Equations

According to Eqs. (17) and (19), the solution for the mean intensity over whole horizontal plane, $\bar{I}(z,\underline{\Omega})$, is simply an integration of the mean intensity over vegetation, $U(z,\underline{\Omega})$. Therefore, below we focus on the numerical scheme of solution for the direct and diffuse components of $U(z,\underline{\Omega})$: $U_\delta(z)$ (Eq. (23)) and $U_d(z,\underline{\Omega})$ (Eq. (24)) and. The solution for the direct component

requires solution of the parametric Volterra equation. Solution for the diffuse component is based on the Successive Orders of Scattering Approximations (SOSA) iterative method [Myneni et al., 1987]; at each step of iterations we also need to solve the parametric Volterra equations. First, we outline SOSA method in application to stochastic equations. The n-th approximation to the solution for the diffuse component is:

$$U_d^n(z,\underline{\Omega}) = J_1(z,\underline{\Omega}) + J_2(z,\underline{\Omega}) + ... + J_n(z,\underline{\Omega}).$$

The functions $J_k(z,\underline{\Omega}), k = 1,2,...,n$ are the solutions of the system of two independent equations (Volterra equations), derived from Eq. (24):

$$J_k(z,\underline{\Omega}) + \frac{\sigma(\underline{\Omega})}{|\mu(\underline{\Omega})|}\int_0^z d\xi\, K(z,\xi,\underline{\Omega})\, J_k(\xi,\underline{\Omega}) = R_{k-1}(z,\underline{\Omega}), \quad \mu < 0, \tag{40a}$$

$$J_k(z,\underline{\Omega}) + \frac{\sigma(\underline{\Omega})}{|\mu(\underline{\Omega})|}\int_z^H d\xi\, K(z,\xi,\underline{\Omega})\, J_k(\xi,\underline{\Omega}) = R_{k-1}(z,\underline{\Omega}), \quad \mu > 0. \tag{40b}$$

The right-hand side of Eq. (40) for n=0 is:

$$R_0(z,\underline{\Omega}) = \frac{f_{dir}(\lambda,\underline{\Omega}_0)\,\sigma_S(\underline{\Omega}_0 \to \underline{\Omega})}{|\mu(\underline{\Omega})\,\mu(\underline{\Omega}_0)|}\int_0^z d\xi\, K(z,\xi,\underline{\Omega}) U_\delta(\xi,\underline{\Omega}) + \left[1 - f_{dir}(\lambda,\underline{\Omega}_0)\right] d(\underline{\Omega},\underline{\Omega}_0), \quad \mu < 0,$$

$$R_0(z,\underline{\Omega}) = \frac{f_{dir}(\lambda)\,\sigma_S(\underline{\Omega}_0 \to \underline{\Omega})}{|\mu(\underline{\Omega})\mu(\underline{\Omega}_0)|}\int_z^H d\xi\, K(z,\xi,\underline{\Omega})\, U_\delta(\xi,\underline{\Omega}) + I_H(\underline{\Omega},\underline{\Omega}_0), \quad \mu > 0,$$

If n>0, the right-hand side of Eq (40) is:

$$R_k(z,\underline{\Omega}) = \frac{1}{|\mu(\underline{\Omega})|}\int_0^z d\underline{\Omega} K(z,\xi,\underline{\Omega})\, S_k(\xi,\underline{\Omega}), \quad \mu < 0, \quad \text{when } k \ge 1,$$

$$R_k(z,\underline{\Omega}) = \frac{1}{|\mu(\underline{\Omega})|}\int_z^H d\underline{\Omega}\, K(z,\xi,\underline{\Omega})\, S_k(\xi,\underline{\Omega}), \quad \mu > 0, \quad \text{when } k \ge 1,$$

where the source function $S_k(z,\underline{\Omega})$ is,

$$S_k(z,\underline{\Omega}) = \int_{4\pi} d\Omega' \sigma_S(\underline{\Omega}' \to \underline{\Omega})\, J_k(z,\underline{\Omega}').$$

The algorithm to solve the system of equations for $U(z,\underline{\Omega})$ is as follows: (1) Find $U_\delta(z,\underline{\Omega})$ from the corresponding Volterra equation [Eq. (23)]; (2) Evaluate $R_0(z,\underline{\Omega})$; (3) Solve the Volterra equations [Eq. (40)] with $R_0(z,\underline{\Omega})$ and find $J_1(z,\underline{\Omega})$; (4) Evaluate $S_1(z,\underline{\Omega}) = \int_{4\pi} \sigma_S(\underline{\Omega}' \to \underline{\Omega})\, J_1(z,\underline{\Omega}')\, d\underline{\Omega}'$ with $J_1(z,\underline{\Omega})$; (5) Evaluate $R_1(z,\underline{\Omega})$; (6) Calculate $J_2(z,\underline{\Omega})$; (7) Repeat the following until $\| J_n(z,\underline{\Omega}) \| \le \varepsilon$: (a) Evaluate $S_k(z,\underline{\Omega})$; (b) Calculate $R_k(z,\underline{\Omega})$; (c) Calculate $J_{k+1}(z,\underline{\Omega})$.

The scheme of solution for $U_\delta(z)$ and $U_d(z,\underline{\Omega})$ according to Eqs. (23) and (40) requires the corresponding scheme for the Volterra equation of the following general form:

$$U(z,\underline{\Omega}) + \frac{\sigma(\underline{\Omega})}{|\mu(\underline{\Omega})|} \int_0^z d\xi\, K(z,\xi,\underline{\Omega})\, U(\xi,\underline{\Omega}) = F(z,\underline{\Omega}) \tag{41a}$$

Here $\underline{\Omega}$ is a parameter of the equation. The corresponding discrete scheme is

$$U(k,\underline{\Omega}) + \frac{\sigma(\underline{\Omega})}{|\mu(\underline{\Omega})|} \sum_{j=1}^{j=k} W_{k,j}\, K(k,j,\underline{\Omega})\, U(j,\underline{\Omega}) = F(k,\underline{\Omega}), \tag{41b}$$

where $W_{k,j}$ is the weight, which depends on the numerical scheme used for approximating the integral. Then,

$$U(1,\underline{\Omega}) = F(1,\underline{\Omega}), \text{ when } k=1,$$

and when $k \in [2, N_z + 1]$,

$$U(k,\underline{\Omega}) + \frac{\sigma(\underline{\Omega})}{|\mu(\underline{\Omega})|} W_{k,k}\, K(k,k,\underline{\Omega}) U(k,\vec{\Omega}) = F(k,\underline{\Omega}) - \frac{\sigma(\underline{\Omega})}{|\mu(\underline{\Omega})|} \sum_{j=1}^{j=k-1} W_{k,j}\, K(k,j,\underline{\Omega})\; U(j,\underline{\Omega}),$$

$$\Rightarrow \quad U(k,\underline{\Omega}) = \frac{F(k,\underline{\Omega}) - \dfrac{\sigma(\underline{\Omega})}{|\mu(\underline{\Omega})|} \displaystyle\sum_{j=1}^{j=k-1} W_{k,j}\, K(k,j,\underline{\Omega})\, U(j,\underline{\Omega})}{1 + \dfrac{\sigma(\underline{\Omega})}{|\mu(\underline{\Omega})|} W_{k,k}\, K(k,k,\underline{\Omega})}. \tag{42}$$

For angular descretization the ES_n quadratures are optimal to achieve the target accuracy with the minimum amount of nodes [Bass, Voloshenko & Germogenova, 1986; Appendix B]. Generally, about 30 iterations are sufficient to obtain relative accuracy of 10^{-3}. The physical interpretation of the method of successive orders is as follows: the function $J_k(z,\underline{\Omega})$ is the mean intensity of photons scattered k times. The rate of convergence of this method, ρ_c has been defined by Vladimirov [1963], Marchuk and Lebedev [1971] as

$$\| I - I_n \| \le \text{const} \cdot \rho_c^{\,n} \equiv \text{const} \cdot \left(\left(1 - \exp(-k_0 \cdot H)\right) \cdot \eta \right)^n, \tag{43a}$$

where k_0 is a certain coefficient and effective single scattering albedo η

$$\eta = \sup_{0<z<H} \sup_{\Omega \in 4\pi} \frac{\sigma_S(\underline{\Omega}_0 \to \underline{\Omega})}{\sigma(z,\underline{\Omega})}. \tag{43b}$$

From Eq. (43) it follows that SOSA converges faster in the case of small optical depth of the layer or in case of small η. If $\eta \approx 1$ and the optical depth is large, the method becomes tedious.

6. Analysis of 3D Radiation Effects

The pair-correlation function naturally arises from averaging the 3D canopy radiation field and, therefore, determines its mean characteristics (Section 3). The aim of this section is to illustrate

that the foliage spatial correlation is primary responsible for the 3D effects of the 3D canopy structure on canopy reflective and absorptive properties.

The Poisson germ-grain model of the forest with equal cylindrical in shape trees (Section 4) is used to generate the pair-correlation function simulate the 3D canopy structure. The crown height is H, the crown base diameter is D_B. Non-dimensional scattering centres (leaves) are uniformly distributed and spatially uncorrelated within tree crowns. The probability, p(z), of finding a foliated point at depth *z* (Eq. 11) is constant in this case and coincides with the ground cover *g*, i.e., p(z) = g. The pair-correlation function is given by Eq. (36). The amount of leaf area in the tree crown is parameterized in terms of the plant LAI defined as $L_0 = d_L H$. The canopy LAI is gL_0. Leaf hemispherical reflectance and transmittance are assumed to have the same value and set to 0.07 at Red and 0.38 at the NIR wavelength. Soil reflectance is variable in our calculations. The vegetation canopy is illuminated by a parallel beam of unit intensity. The solar zenith angle set to 30^0.

In addition to simulations in the 3D mode, the stochastic equations were implemented in the 1D mode by utilizing the pair-correlation for turbid medium ($q(z,\xi,\Delta) = p(z) = g = 1$), with other parameters being identical between two modes. Note that in the case when g=1, plant and canopy LAIs coincide (L_0 = LAI). Also, recall that $\bar{I}(z,\underline{\Omega}) = U(z,\underline{\Omega})$ for turbid medium (Eqs. (30)-(31)). The difference in the mean intensities of the 3D and 1D vegetation canopies are utilized to quantify the impact of canopy structure on the canopy radiation regime.

Vertical profiles of radiation fluxes: The upward, $F^{\uparrow}(z)$, and downward, $F^{\downarrow}(z)$, radiation fluxes are derived by integrating mean stochastic intensities over upper and lower hemispheres, that is,

.

$$F_{\Psi}^{\uparrow}(z) \equiv \int_{2\pi^{+}} d\underline{\Omega}\,|\mu(\underline{\Omega})|\Psi(z,\underline{\Omega}) \ , \quad F_{\Psi}^{\downarrow}(z) \equiv \int_{2\pi^{-}} d\underline{\Omega}\,|\mu(\underline{\Omega})|\Psi(z,\underline{\Omega}), \tag{44}$$

where Ψ stands for $\bar{I}$ (mean intensity over total space), U (mean intensity over vegetation) and

V (mean intensity over gaps). The relationship between $F_I^{\downarrow\uparrow}(z)$, $F_U^{\downarrow\uparrow}(z)$ and $F_V^{\downarrow\uparrow}(z)$ can be established by integrating Eq. (21) over upper and lower hemispheres and substation definitions given by Eq. (44):

$$F_I^{\downarrow\uparrow}(z) - F_U^{\downarrow\uparrow}(z) = (1 - p(z))[F_V^{\downarrow\uparrow}(z) - F_U^{\downarrow\uparrow}(z)]. \quad (45)$$

Note, that in the special case of 1D RT model (turbid medium) there is no distinction between mean intensities over vegetation and gaps (Eq. (30)-(31)), which results in $F_U^{\downarrow\uparrow}(z) = F_V^{\downarrow\uparrow}(z) = F_I^{\downarrow\uparrow}(z) \equiv F_{1D}^{\downarrow\uparrow}(z)$.

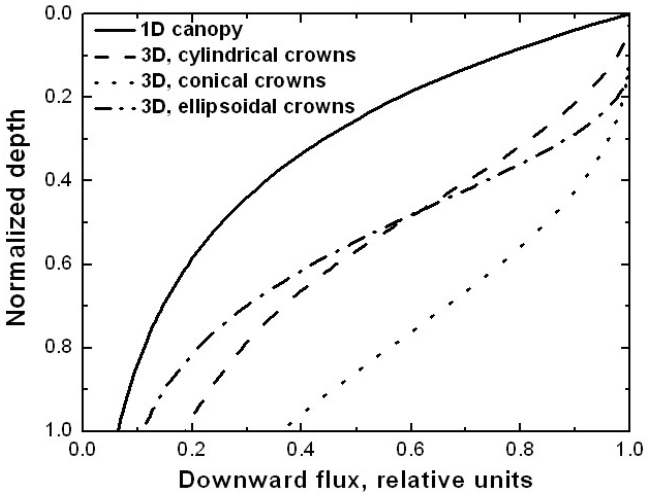

Figure 4. Vertical profiles of mean downward radiation flux densities over between crown space at red wavelength. Calculations are performed for vegetation canopies consisting of cylindrical (dashed line), conical (dotted line) and ellipsoidal (dashed-dotted line) in shape trees. A 1D vegetation canopy is also shown for comparison (solid line). Canopy LAI and ground cover are 4.2 and 0.85, respectively. Soil reflectance is zero.

One key test to verify if RT model capable to simulate 3D radiation effects is to look for the *sigmoidal* shape of the vertical profiles of the between crown downward fluxes, documented by several theoretical and empirical studies [Larsen and Kershaw, 1996; Ni et al., 1997; Roujean, 1999b]. It has been shown that the clumping of phytoelements into tree crown is primarily responsible for this 3D effect [Roujean, 1999b]. Figure 4 shows mean vertical profiles of downward fluxes, averaged over the between crown space, $F_V^{\downarrow}(z)$. Calculations are performed for vegetation canopies consisting of cylindrical, conical and ellipsoidal in shape trees. Equations (35) are used to specify corresponding pair-correlation functions and probabilities, p(z), of finding a foliated point at depth z. In these examples, the ground cover, $g = \max p(z)$, and

canopy leaf area index are fixed and equal to 0.85 and 4.2, respectively. Maximum radius of the crown horizontal cross-sections is set to 0.25H where the crown (canopy) height H is 1 (in relative units). One can see that in contrast to 1D model, the stochastic model captures the sigmoidal shape of the vertical profiles of radiations fluxes and the shape is the simulations are sensitive to the crown geometry.

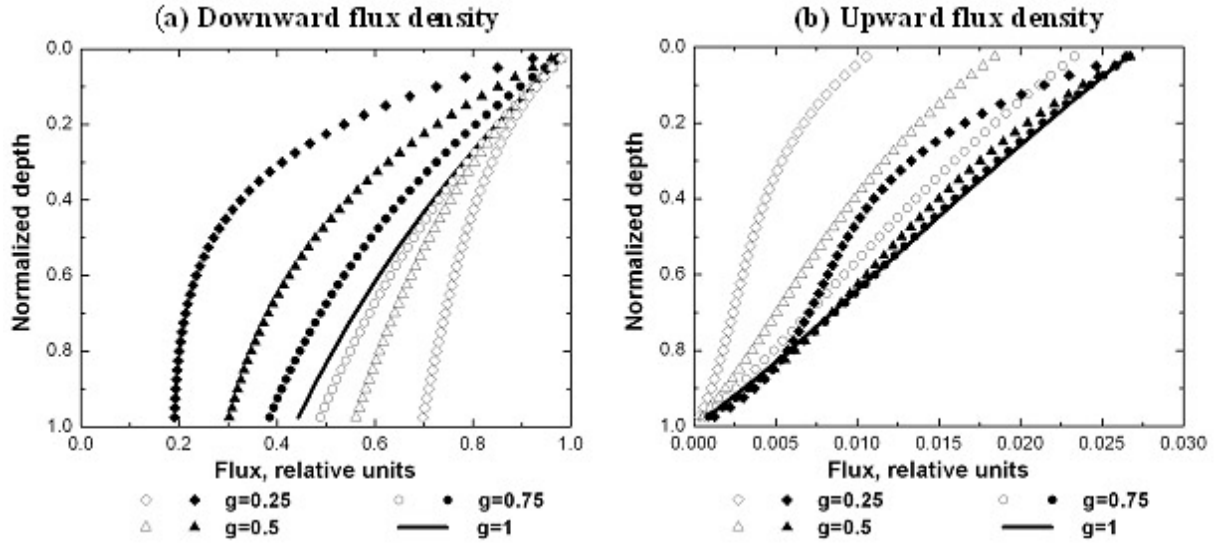

Figure 5. Vertical profiles of mean downward (Panel a) upward (Panel b) radiation flux densities at red wavelength for four values of the ground cover *g*. Ground reflectance is zero. Canopy LAI is fixed and set to 1.5. Plant LAI varies with the ground cover as 1.5/g. The case g=1 (solid lines) corresponds to the 1D vegetation canopy. Solid and hollow symbols represent mean flux densities over crown horizontal cross sections and over the entire horizontal plane, respectively. The dimensionless horizontal axis shows values of z/H_c where H_c is the crown height.

Next, consider vertical profiles of mean downward and upward radiation flux densities accumulated over crown horizontal cross sections ($F_U^{\downarrow}$ and $F_U^{\uparrow}$), and over the total space of horizontal plane ($F_I^{\downarrow}$ and $F_I^{\uparrow}$) as simulated by stochastic model (Fig. 5). For comparison purposes we also present here upward and downward fluxes simulated by 1D model, $F_{1D}^{\downarrow\uparrow}(z)$. First, note that the attenuation of the within crown fluxes is stronger in the case of stochastic model compared to 1D approach, i.e., $F_U^{\downarrow\uparrow}(z) \le F_{1D}^{\downarrow\uparrow}(z)$ (Fig. 5). In this example, LAI=gL_0, a decrease in the ground cover, g, enhances the within crown photon interactions due to an

increase in the plant leaf area index L_0 (Fig. 5). Second, note that the tree crowns transmit less radiation compared to horizontally averaged values, i.e., $F_U^{\downarrow}(z) < F_I^{\downarrow}(z)$ (Fig. 5a). It follows from this inequality and Eq. (45) that $F_V^{\downarrow}(z) > F_U^{\downarrow}(z)$ and thus gaps between trees are primarily responsible for the propagation of radiant energy in downward directions. In contrast, upward fluxes have the opposite tendency, i.e., $F_U^{\uparrow}(z) > F_I^{\uparrow}(z)$ (Fig. 5b). For a vegetation canopy bounded from below by a non-reflecting surface, the scattering from leaves determines the upward radiation field. With a fixed amount of the total leaf area, the upward radiation field is an increasing function with respect to the ground cover since an increase in the ground cover involves a decrease in gaps between trees which do not "participate" in the scattering process. Third, note that the reflectance of an individual tree crown, $F_U^{\uparrow}(0)$, is close to the reflectance of the 1D canopy, $F_{1D}^{\uparrow}(0)$. The mean canopy reflectance, $F_I^{\uparrow}(0)$, results from both scattering occurred in tree crowns and "zero scattering" in the between crown space. This lowers the overall canopy reflectance. The 1D approach ignores the gap effect and mean upward radiation flux densities are consequently overestimated.

Energy conservation law: Many ecosystem productivity models and global models of climate, hydrology and ecology need an accurate information on how solar energy is distributed between vegetation canopies and the ground. Using the NCAR Community Climate Model, Buermann et al. [2001] reported that a more realistic partitioning of the incoming solar radiation between the canopy and the underlying ground results in improved model predictions of near-surface climate. The vegetation structure determines the partitioning of the incoming radiation between canopy absorptance, transmittance and reflectance. Here we illustrate the impact of 3D canopy structure on the shortwave energy balance.

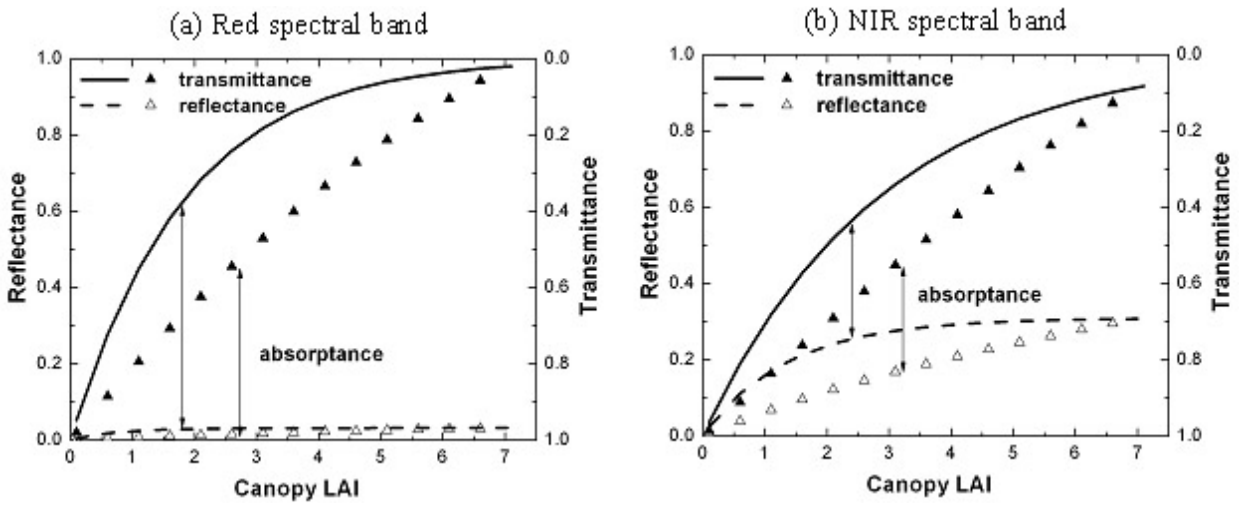

Figure 6. Mean canopy reflectance $F_I^{\uparrow}(0)$ (vertical axis on the left side) and transmittance $F_I^{\downarrow}(1)$ (vertical axis on the right side) at red (Panel a) and near-infrared (Panel b) wavelengths as a function of the canopy LAI. Solid and dashed lines represent the 1D canopy while symbols show its 3D counterpart. Ground reflectance is zero. The canopy absorptance is $1-F_I^{\uparrow}(0)-F_I^{\downarrow}(1)$ (arrows). Plant leaf area index L_0 is fixed and set to 7. Ground cover varies with the canopy LAI as $g = LAI/L_0 = LAI/7$.

Figure 6 shows mean canopy reflectance, $F_I^{\uparrow}(0)$, and transmittance, $F_I^{\downarrow}(1)$. For a vegetation canopy bounded from below by a non reflecting surface, the canopy absorptance is $1 - F_I^{\uparrow}(0) - F_I^{\downarrow}(1)$ as shown in Fig. 8. The 1D approach underestimates canopy transmittance and overestimates canopy reflectance at both Red and NIR wavelengths. As one can see from Fig. 8, these two opposite tendencies do not compensate each other, resulting in an overestimation of canopy absorptance.

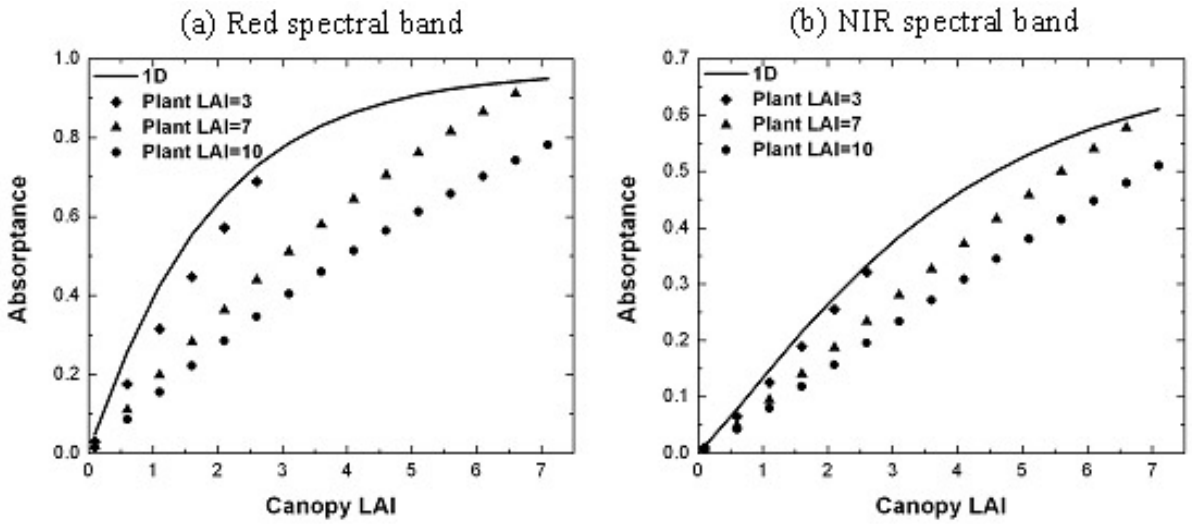

Figure 7. Mean canopy absorptance at red (Panel a) and near infrared (Panel b) wavelengths as a function of canopy LAI for three values of the plant leaf area index L_0. Solid line and symbols represent 1D and 3D vegetation canopies, respectively. Ground cover, g, varies with the canopy LAI as $g = LAI/L_0$. Other parameters are as in Fig. 6

The results given in Fig. 7 show that at a given canopy LAI, canopy absorptance can differ depending upon ground cover and plant LAI. This is not surprising result because a given amount of leaf area can be distributed in different ways in a canopy, for instance, as canopies of dense trees (high plant LAI) with low ground cover or as canopies of sparse trees (low plant LAI) with high ground cover. Although the canopy LAI is the same in both cases, between and within crown radiation regimes are different. Gaps between trees enhance the canopy transmittance at the expense of the canopy absorptance and reflectance. An increase in ground cover involves a decrease in gaps between tree crowns which contribute neither to canopy absorptance nor canopy reflectance. This process enhances canopy reflective (Fig. 6) and absorptive (Fig. 7) properties. It should also be noted that variation in canopy reflectance, absorptance and transmittance with the canopy LAI occurs at a lower rate compared to the 1D model prediction (Figs.6-7). Ignoring the within and between crown radiation regimes can lead to overestimation of the saturation domain, i.e., a range of canopy reflectance values which are insensitive to variation in canopy structure.

Effect of background reflectance: A vegetated surface scatters shortwave radiation into an angular reflectance pattern, or Bidirectional Reflectance Factor (BRF), whose magnitude and shape are governed by the composition, density, optical properties and geometric structure of the vegetation canopy and its underlying surface. By definition, the BRF($\underline{\Omega},\underline{\Omega}_0$) is the surface leaving radiance in direction $\underline{\Omega}$ divided by radiance from a Lambertian reflector illuminated from a single direction, $\underline{\Omega}_0$ [Martonchik et al., 2000]. This parameter has been operationally produced from NASA MODIS and MISR remote sensing measurements [Schaaf et al., 2002; Bothwell at al., 2002].

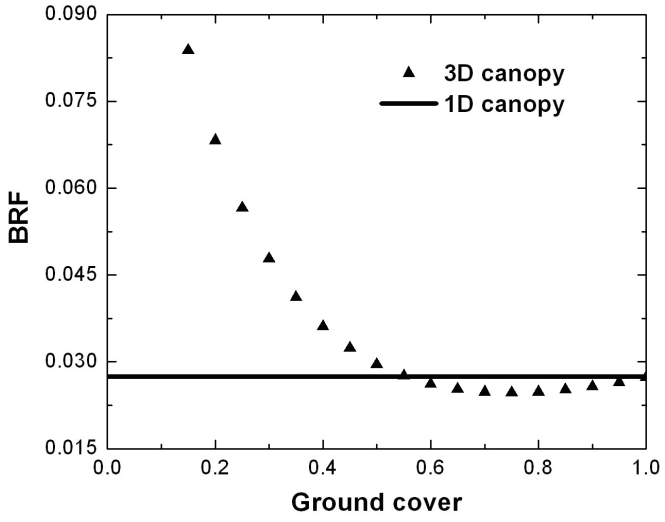

Figure 8. Bidirectional Reflectance Factor (BRF) at red wavelength in nadir view direction as a function of ground cover. Solid line and symbols represent 1D and 3D vegetation canopies, respectively. Canopy LAI is fixed and set to 7. Plant leaf area index varies with ground cover, g, as $7/g$. Surface albedo is 0.18. The solar zenith angle is 30^0. Other parameters are as in Fig. 6.

Figure 8 shows the BRF at red wavelength in the nadir view direction for a vegetation canopy bounded from below by a reflecting surface. For sparse vegetation canopies, photons reflected from the sunlit area of the underlying surface can escape the 3D canopy in the nadir direction without experiencing a collision. This 3D effect results in increased canopy brightness at low ground cover. The BRF exhibits a non monotonic variation with the ground cover. At small-to-moderate values of ground cover, BRF decreases with increasing ground cover due to decrease in the sunlit area which, in turn, reduces the impact of the between crown radiation on the BRF in the nadir direction. However, at sufficiently large ground cover values, the contribution of the underlying surface vanishes and, as in the case of a vegetation canopy with a non–reflecting surface (Figs. 4 and 5b), the BRF becomes an increasing function with respect to the ground

cover. As discussed earlier, the 3D effects make BRF values lower compared to those predicted by 1D model. If the leaf spatial correlation is ignored, i.e., $q(z,\xi,\underline{\Omega}) = g^2$, the BRF becomes independent of the ground cover. Thus ignoring the leaf spatial correlation can result in an underestimation of the contribution of canopy background to the canopy leaving radiation for sparse and intermediately dense vegetations and an overestimation of the canopy BRF for dense vegetations. Accounting for 3D effects of underlying vegetation background is especially important in operational algorithms for retrieval of biophysical vegetation biophysical parameters from remote sensing observations over sparse vegetation (savannah, needle leaf forest, etc.)

Canopy structure and NDVI: The measured spectral reflectance data are often transformed into vegetation indices. More than a dozen such indices are reported in the literature and shown to correlate well with vegetation amount [Tucker, 1979], the fraction of absorbed photosynthetically active radiation (FPAR) [Asrar et al., 1984], unstressed vegetation conductance and photosynthetic capacity [Sellers et al., 1992], and seasonal atmospheric carbon dioxide variations [Tucker et al., 1986]. Here we illustrate the impact of 3D canopy structure on relationships between canopy absorption, LAI and the normalized difference vegetation index.

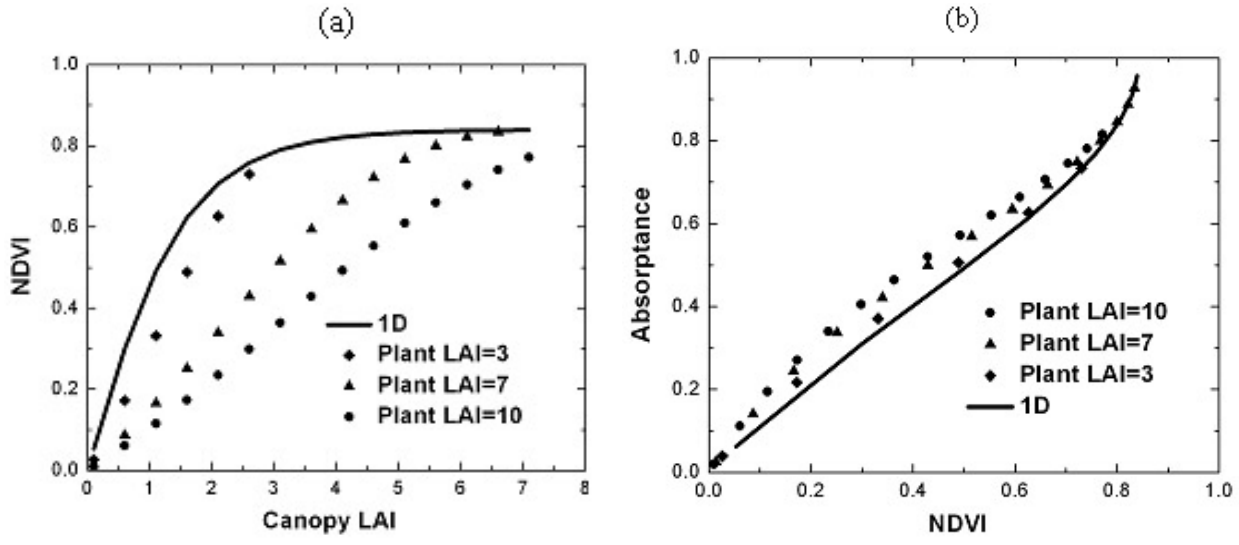

Figure 9. NDVI versus canopy LAI (Panel a) and NDVI versus canopy absorptance (Panel b) canopy absorption at red wavelength for three values of plant leaf area index L_0. Solid line and symbols represent 1D and 3D vegetation canopies, respectively. Ground cover varies with the canopy LAI as $g = LAI/L_0$.

Surface albedo is 0.18 at red and near infrared wavelengths. Other parameters are as in Fig. 7.

The normalized difference vegetation index, NDVI, is defined as the ratio between the difference and the sum of bidirectional reflectance factors at NIR and Red wavelength,

$$\mathrm{NDVI}(\underline{\Omega},\underline{\Omega}_0) = \frac{\mathrm{BRF}_{\mathrm{NIR}}(\underline{\Omega},\underline{\Omega}_0) - \mathrm{BRF}_{\mathrm{RED}}(\underline{\Omega},\underline{\Omega}_0)}{\mathrm{BRF}_{\mathrm{NIR}}(\underline{\Omega},\underline{\Omega}_0) + \mathrm{BRF}_{\mathrm{RED}}(\underline{\Omega},\underline{\Omega}_0)}\,. \tag{46}$$

This parameter has been operationally produced from NASA MODIS remote sensing measurements [Huete et al., 2002]. Here we consider the NDVI at the nadir view direction.

The relationships between NDVI and canopy LAI are shown in Fig. 9a. The results are similar to those shown in Fig. 7a, i.e., at a given canopy LAI, canopy absorptance and NDVI can differ depending upon ground cover and plant LAI. Different radiation regimes in tree crowns and gaps between them are primarily responsible for this effect. Values of canopy absorptance versus corresponding NDVI values are plotted in Fig. 9b. One can see that the impact of 3D canopy structure on the absorptance-NDVI relationship is minimal. This effect is consistent with the results documented in Asrar et al. [1992], i.e., spatial heterogeneity in vegetation canopies does not affect the relationship between NDVI and fraction of absorbed photosynthetically active radiation (FPAR). The relationship is also insensitive to rather large changes in solar zenith angle [Asrar et al., 1992, Kaufmann et al., 2000]. It should be noted, however, that the NDVI-FPAR relationship is sensitive to the background. Theoretical analyses of these regularities are established in [Myneni et al., 1995; Knyazikhin et al., 1998b; Kaufmann et al., 2000].

7. Model Evaluation with Field Measurements

The internal as well as emergent radiation fields simulated by SRT model were evaluated by comparison to the following sources: (i) RT simulations by 1-D and 3-D RT models [Shultis and Myneni, 1988; Shabanov et al., 2000]; (ii) Monte Carlo simulations of computer generated maize canopy [Espana et al., 1998, Shabanov et al., 2000]; (iii) CIMEL sunphotometer and ground vegetation measurements over shrublands during Jornada PROVE experiment in New Mexico

[Privette et al., 2000, Shabanov et al., 2000]; (iv) SLICER lidar and ground vegetation measurements over several needle leaf forest sites in central Canada and eastern Maryland [Kotchenova et al., 2003]; (v) PARABOLA radiometer and ground vegetation measurements at BOREAS needle leaf forest sites in Canada [Huang et al., 2007]. The last exercise is detailed below.

A field campaign was performed in 1994 as a part of the Boreal Ecosystem-Atmosphere Study (BOREAS) experiment at two sites in the Southern Study Area (SSA), central Saskatchewan, Canada [Deering, Eck & Banerjee, 1999]. The BOREAS designated names for these sites are SSA Old Jack Pine (53.916^{0}N, 104.69^{0}W) and SSA Old Aspen (53.63^{0}N, 106.20^{0}W). A field data set includes forest age, stem density, overstory and understory LAIs [Deering, Eck & Banerjee, 1999], tree height, crown height and horizontal crown radius [Chen, 1996; Hardy et al., 1998], optical properties of leaves, needles and understory [Middleton and Sullivan, 2000; Miller et al., 1997]. The characteristics of each site are summarized in Table 1. Their detailed description can be found in [Deering, Eck & Banerjee, 1999].

Variable	SSAOJP site	SSAOA site
Stand age, years	68	60
Stem density, stems/ha	2700	1200
LAI	2.2	2.3
Understory LAI	0	3.23
Tree height, m	12.7	16.2
Crown length, m	7	10.76
Horizontal Crown radius, m	1.2	2.12
Leaf/needle reflectance, Red/ NIR	0.100/ 0.62	0.065/ 0.36
Leaf/needle transmittance, Red/ NIR	0.028/ 0.31	0.135/ 0.60
Understory reflectance, Red/ NIR	0.150/ 0.29	0.090/ 0.40

Table 1. Characteristics of the SSA Old Jack Pine (SSAOJP) and SSA Old Aspen (SSAOA) sites used for model parameterization.

The BRF measurements were made with the PARABOLA instrument [Deering and Leone, 1986]. The instrument performs radiance measurements in three narrow spectral bands (650-670 nm, 810-840 nm, and 1620-1690 nm) for almost the complete sky- and ground-looking hemispheres in 15^0 instantaneous field of view [Deering, Eck & Banerjee, 1999]. The instrument

was suspended from a tram system mounted at about 13-14m above canopy between two towers spaced about 70 m apart. Total of 11 measurements were taken along the tram at each solar zenith angle. The data were processed to obtain mean BRF over sampling points in 15^0 angular increments in view zenith angle and 30^0 angular increments of view azimuth with one of the bins being centered on the solar principal plane [Deering, Eck & Banerjee, 1999].

The parameters of the SRT model were selected as follows. The Poisson germ-grain model of the forest with identical cylindrical trees (cf. Section 4) was selected to construct the pair-correlation function. The ground cover was estimated with Eq. (35b) where the steam density d and the crown radius $r(z) = D_B/2$ are given in Table 1. Its value is 0.71 for the SSAOJP and 0.82 for the SSAOA site. Given ground cover, the pair-correlation function was calculated using Eq. (36a). The plant leaf area index, L_0=LAI/g, and the leaf area volume density, $d_L=L_0/H_c$ are L_0=3.12, d_L=0.46 for SSAOJP and L_0=2.82, d_L=0.26 for SSAOA. Here H_c and LAI are the crown height and the canopy LAI (Table 1). The optical properties of canopy elementary volume, were calculated based on commonly adopted RT approach, where shoot (not individual needle) represents the basic structural element [Stenberg, 1996; Smolander & Stenberg, 2005]. The measured albedo of individual needles was scaled to shoot level (Table 1) using theory of canopy spectral invariants [Oker-Blom & Smolander, 1988, Smolander & Stenberg, 2005; Chapter 3].

Table 2. Root Mean Square Error in predicting nadir BRF at Red (650-670 nm) and NIR (810-840) spectral bands for SSA Old Jack Pine (SSOJP) and SSA Old Aspen (SSAOA) sites.

	Red spectral band		**NIR spectral band**	
	SSAOJP	**SSAOA**	**SSAOJP**	**SSAOA**
3D canopy	0.0021	0.0013	0.021	0.013
1D canopy	0.0061	0.0024	0.053	0.016

Measured and modeled BRFs at red and NIR wavelengths in the nadir direction as a function of the solar zenith angle for the SSAOJP and SSAOA sites are shown in Fig. 10. The BRFs simulated using the 3D model of canopy structure show very good agreement with measurements (Table 2). If one simplifies the canopy structure into a 1D medium by setting the conditional pair correlation function to its saturated value, ground cover g, the disagreement

increases by a factor of about 2.7 for the SSAOJP and 1.5 for SSAOA site (Table 2). In both cases, the 1D approach overestimates the observations. This result is consistent with simulations shown in Fig. 9. The effect of ignoring the leaf spatial correlation is more pronounced at lower ground covers, as expected.

A statistical model given by Eq. (29) was used to simulate the hot spot effect (a sharp peak in reflected radiation about the retro-solar direction). The model requires the specification of a coefficient related to the ratio of vegetation height to the smallest element in the scene. The ratio of tree height to the tree diameter (the finest scale in our simulations) is used. Figure 10 show measured and predicted BRFs and their correlation for the SSAOJP and SSAOA sites. In these examples, the simulations compare well with the field data.

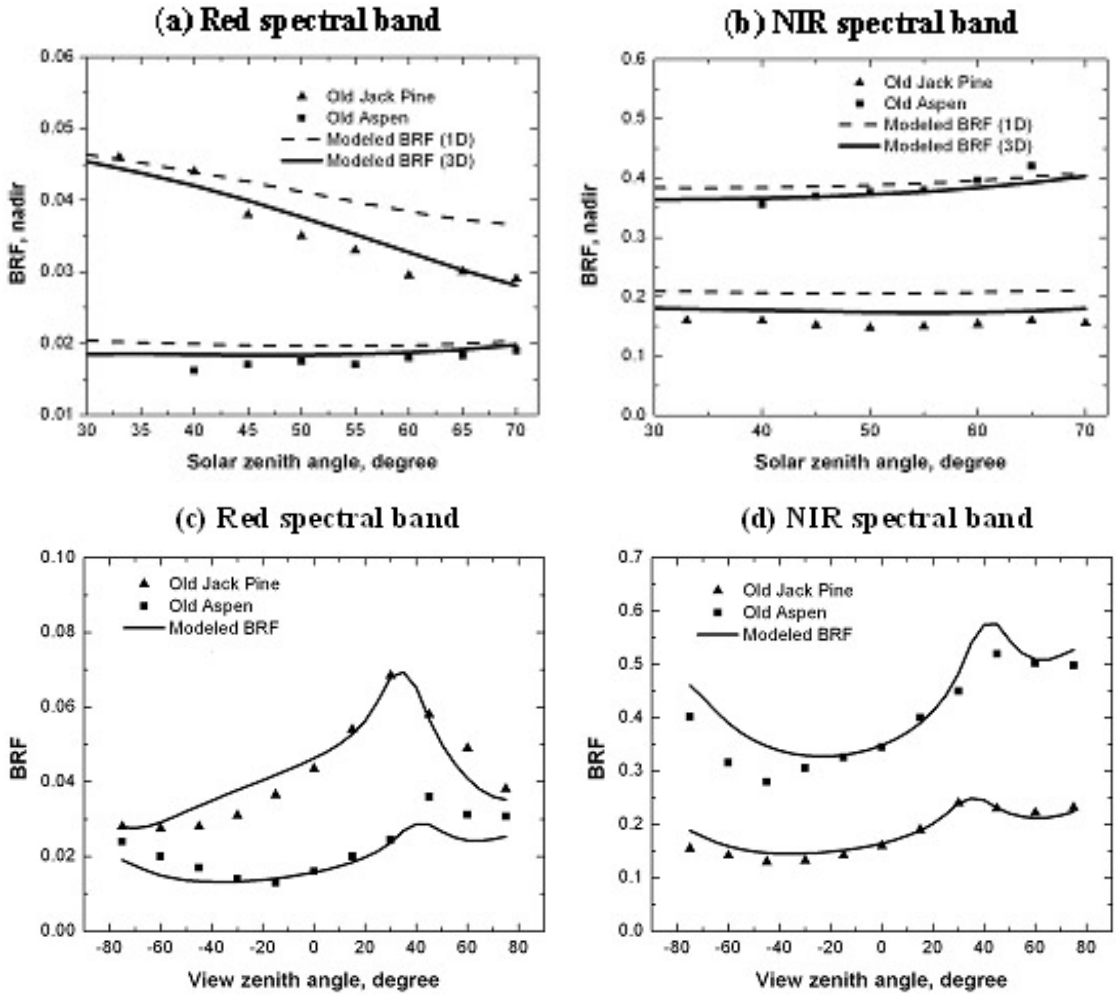

Figure 10. Bidirectional Reflectance Factor at red (Panel a) and NIR (Panel b) wavelengths in the nadir

direction as a function of the solar zenith angle for the SSAOJP and SSAOA sites. Symbols represent measured BRFs. Solid and dashed lines show simulated BRF using 3D and 1D models of canopy structure, respectively. Bidirectional Reflectance Factor in the solar principal plane at red (Panel c) and NIR (Panel d) wavelengths for the SSAOJP and SSAOA sites. The solar zenith angles are 34^0 for SSAOJP and 40^0 for SSAOA. Solid line and symbols represent predicted values and PARABOLA measurements. The RMSE values at red and near infrared spectral bands are 0.0042 and 0.014 for the SSAOJP, 0.0043 and 0.042 for the SSAOA sites.

8. Summary

This chapter introduces the Stochastic Radiative Transfer (SRT) model a powerful RT tool to develop to study biophysical properties of 3D canopy from space measurements. The unique features of the SRT model are: (*i*) its solution coincides exactly with what satellite-borne sensors measure; that is, the mean intensity emanating from the smallest area to be resolved, from a pixel; (*ii*) it accounts for 3D effects through a small set of well defined measurable parameters; and (*iii*) it is as simple as the conventional 1D radiative transfer equation. The 3D canopy structure is accounted in the SRT model with two stochastic moments: (a) probability of finding phytoelements at horizontal plane; and (b) correlation of phytoelements at two horizontal planes. The analysis of the SRT equations indicates that if only the first moment of vegetation structure is used (the case of no correlation), than the SRT model reduces to the 1D turbid medium RT model. Thus, the pair-correlation function is primary responsible for 3D radiation effects. The analytical models of the pair-correlation function, based on theory of Boolean random sets, were in this study. Comparison of 1D and 3D simulations indicates that ignoring the canopy structure can result in an underestimation of the canopy transmittance at the expense of overestimation of the canopy absorptance and reflectance. Transmittance, reflectance and absorptance of the 3D vegetation canopy vary with canopy LAI at a slower rate than 1D model can possible predict. Ignoring this fact in interpretation of satellite data can lead to overestimation of the saturation domain, i.e., a range of canopy reflectance values which are insensitive to variation in canopy structure. The stochastic radiative transfer equations reproduce the effect of sunlit areas of the underlying surface on the canopy leaving radiation. They adequately account for impact of canopy structure on relationships between NDVI, LAI and canopy absorptance. The SRT model was extensively validated with field measurements including comparison with PARABOLA

measurements from two coniferous and broadleaf forest stands in BOREAS Southern Study Areas. The performance was found to be satisfactory. At this point, the major shortcoming of the SRT approach is unability to simulate the hot-spot effect, which was implemented in the present version of the SRT model using the standard ad-hook method of modifying the extinction coefficient.

References

Asrar, G., Fuchs, M., Kanemasu, E.T., & Hatfield, J.L. (1984). Estimating absorbed photosynthetic radiation and leaf area index from spectral reflectance in wheat. *Agronomy Journal*, *76*, 300-306.

Asrar, G., Myneni, R.B., & Choudhury, B.J. (1992). Spatial heterogeneity in vegetation canopies and remote sensing of absorbed photosynthetically active radiation: A model study. *Remote Sensing of Environment, 41*, 85–103.

Bass, L., Voloshenko, A.M., and Germogenova, T.A. (1986), *Methods of Discrete Ordinates in Radiation Transport Problems*, Institute of Applied Mathematics, Moscow, pp. 21-23, (in Russian).

Borel, C.C., Gerstl, S.A.W., Powers, B.J. (1991), The radiosity method in optical remote sensing of structured 3-D surfaces. *Remote Sens. Environ*. 36: 13-44.

Bothwell, G.W., Hansen, E.G., Vargo, R.E., & Miller, K.C. (2002). The Multi-angle Imaging SpectroRadiometer science data system, its products, tools, and performance. *IEEE Transactions on Geoscience and Remote Sensing*, *40*, 1467- 1476.

Buermann, W., Dong, J., Zeng, X., Myneni, R. B., & Dickinson, R. E. (2001). Evaluation of the utility of satellite based vegetation leaf area index data for climate simulations. *Journal of Climate 14(17)*, 3536-3550.

Byrne, N. (2005). Three-dimensional radiative transfer in stochastic media. In: A. Marshak and A. B. Davis [Eds.], "*Three Dimensional Radiative Transfer in the Cloudy Atmosphere*," Springer-Verlag, pp. 385-424.

Castel, T., Beaudoin, A., Floury, N., Le Toan, T., Caraglio, Y., and Barczi, J. F. (2001). Deriving forest canopy parameters for backscatter models using the AMAP architectural plant model. *IEEE Transactions on Geoscience and Remote Sensing*, *39(3)*, 571–583.

Chen, J. M. (1996). Optically-based methods for measuring seasonable variation of leaf area index in boreal conifer stands. *Agricultural and Forest Meteorology*, *80*, 135–163.

Chen, R., Jupp, D.L.B., & Woodcock, C.E. (1993). Nonlinear estimation of scene parameters from digital images using zero-hit run-length statistics. *IEEE Transactions on Geoscience and Remote Sensing*, *31(3)*, 735–746.

Davis, A.B., & Knyazikhin, Y. (2005). A Primer in Three-Dimensional Radiative Transfer. In: A. Marshak and A.B. Davis [Eds.]. "*Three Dimensional Radiative Transfer in the Cloudy Atmosphere*," Springer-Verlag, 153-242.

Deering, D.W., & Leone, P. (1986). A sphere scanning radiometer for rapid directional measurements of sky and ground radiance. *Remote Sensing of Environment*, 19, 1-24.

Deering, D.W., Eck, T. F., & Banerjee, B. (1999). Characterization of the reflectance anisotropy of three boreal forest canopies in spring-summer. *Remote Sensing of Environment*, 67, 205-229.

Espana, M., Baret, F., Chelle, M., Aries, F., Andrieu, B. (1998), A dynamic model of maize 3D architecture: application to the parameterisation of the clumpiness of the canopy. *Agronomie* 18(10): 609-626.

Hardy J.P., R.E. Davis, R. Jordan, W. Ni, & C. Woodcock (1998). Snow ablation modeling in a mature aspen stand of the boreal forest. *Hydrological Processes, 12*, 1763-1778.

Huang, D., Knyazikhin, Y., Wang, W., Deering, W., Stenberg, P., Shabanov., N.V., Tan, B., Myneni, R.B. (2007), Stochastic transport theory for investigating the three-dimensional canopy structure from space measurements. Remote Sensing of Environment, accepted November 2006.

Huete, A., Didan, K., Miura, T., Rodriguez, E.P., Gao, X., and Ferreira, L.G. (2002). Overview of the radiometric and biophysical performance of the MODIS vegetation indices. *Remote Sensing of Environment*, *83*, 195-213.

Jupp, D.L., Strahler, A.H., & Woodcock, C.E. (1988). Autocorrelation and regularization in digital images I. Basic theory. *IEEE Transactions on Geoscience and Remote Sensing*, *26(4)*, 463–473.

Jupp, D.L., Strahler, A.H., & Woodcock, C.E. (1989). Autocorrelation and regularization in digital images II. Simple image models. *IEEE Transactions on Geoscience and Remote Sensing*, *27(3)*, 247–258.

Kasianov E. Stochastic radiative transfer in multilayer broken clouds. Part I: Markovian approach. *Journal of Quantitative Spectroscopy & Radiative Transfer* 2003; 77 (4): 373-393

Kaufmann, R. K., Zhou, L., Knyazikhin, Y., Shabanov, N. V., Myneni, R. B. & Tucker, C. J. (2000). Effect of orbital drift and sensor changes on the time series of AVHRR vegetation index data. *IEEE Transactions on Geoscience and Remote Sensing*, *38(6)*, 2584-2597.

Knyazikhin, Y., Kranigk, J., Myneni, R.B., Panfyorov, O., & Gravenhorst, G. (1998a). Influence of small-scale structure on radiative transfer and photosynthesis in vegetation cover. *Journal of Geophysical Research*, *103*, DD6, 6133-6144.

Knyazikhin, Y., Martonchik, J.V., Diner, D.J., Myneni, R.B., Verstraete, M., Pinty B., Gobron, N. (1998b), Estimation of vegetation canopy leaf area index and fraction of absorbed photosynthetically active radiation from atmosphere-corrected MISR data. *EOS-AM1 special issue of J. Geophys. Res.* 103(D24): 32,239-32,257.

Knyazikhin, Y., Marshak, A., & Myneni, R.B. (2005). Three-Dimensional Radiative Transfer in Vegetation Canopies and Cloud-Vegetation Interaction, In: A. Marshak and A.B. Davis [Eds.]. "*Three Dimensional Radiative Transfer in the Cloudy Atmosphere*," Springer-Verlag, pp. 617-652.

Kotchenova, S.Y., Shabanov, N.V., Knyazikhin, Y., Davis, A.B., Dubayah R., & Myneni, R.B. (2003). Modeling lidar with time-dependent stochastic radiative transfer theory for remote estimation of forest structure. *Journal of Geophysical Research*, 108, Art. No. 4484, 17539-17549.

Larsen, D.R., & Kersaw, Jr., J.A. (1996). Influence of canopy structure assumptions on prediction from Beer's law. A comparision of deterministic and stochastic simulations. *Agricultural and Forest Meteorology*, 81, 61-77.

Li, X, Strahler, A.H. (1992), Geometric-optical bidirectional reflectance modeling of discrete crown vegetation canopy: effect of crown shape and mutual shadowing. *IEEE Trans. Geosci. Remote Sens.* 30(2): 276-292.

Li, X., Strahler, A. H., Woodcock, C.E. (1995), A hybrid Geometric optical-radiative transfer approach for modeling albedo and directional reflectance of discontinuous canopies. *IEEE Trans. Geosci. Remote Sens.* 33(2): 466-480.

Marchuk, G.L., Lebedew, V.I. (1971), *The numerical methods in neutron transport theory*, Atomizdat Publ., Moscow, (in Russian).

Martonchik, J.V., Bruegge, C.J., & Strahler, A. (2000). A review of reflectance nomenclature used in remote sensing. *Remote Sensing Reviews*, *19*, 9-20.

Marshak, A. (1989), Effect of the hot spot on the transport equation in plant canopies. *J. Quant. Spectrosc. Radiat. Transf.* 42: 615-630.

Menzhulin, G. V., Anisimov, O. A., (1991) In *Photon-vegetation interactions. Applications in optical remote sensing and plant ecology* (Myneni, R. B., Ross, J. Ed.), Springer-Verlag, Berlin-Heidelberg., Chap. 4.

Middleton, E., & Sullivan, J. (2000). BOREAS TE-10 Leaf Optical Properties for SSA Species. Data set. Available on-line [http://www.daac.ornl.gov] from Oak Ridge National Laboratory Distributed Active Archive Center, Oak Ridge, Tennessee, U.S.A.

Miller, J. R., White, H. P., Chen, J. M., Peddle, D. R., McDermid, G., Foumier, R. A., Shepherd, P., Rubinstein, I., Freemantle, J., Soffer, R., & LeDrew, E. (1997). Seasonal change in understory reflectance of boreal forests and influence on canopy vegetation indices. *Journal of Geophysical Research*, 102 (D24). 29, 729–736.

Myneni, R.B., Asrar, G. and Kanemasu, E.T. (1987). Light scattering in plant canopies: The method of Successive Orders of Scattering Approximations [SOSA]. *Agric. For. Meteorol*. 39:1-12.

Myneni, R.B. (1991). Modeling radiative transfer and photosynthesis in three-dimensional vegetation canopies. *Agricultural and Forest Meteorology*, 55, 323– 344.

Myneni, R.B., Williams, D.L. (1994). On the Relationship between FAPAR and NDVI. *Remote Sensing of Environment,* 49(3), 200-211.

Myneni, R.B., Hall, F.G., Sellers, P.J., & Marshak, A.L. (1995). The interpretation of spectral vegetation indexes. *IEEE Transactions on Geoscience and Remote Sensing*, *33*, 481-486.

Myneni, R. B., Nemani, R. R., Running S. W. (1997), Estimation of global leaf area index and absorbed PAR using radiative transfer models. *IEEE Trans. Geosci. Remote Sens.* 35(6): 1380-1393.

Ni, W., Li, X., Woodcock, C.E., Roujean, J.L., & Davis, R.E. (1997). Transmission of solar radiation in boreal conifer forests: Measurements and models. *Journal of Geophysical Research*, 102 (D24), 29,555-29,566.

Nilson, T. (1991), In *Photon-vegetation interactions. Applications in optical remote sensing and plant ecology* (Myneni, R. B., Ross, J. Ed.), Springer-Verlag, Berlin-Heidelberg., Chap. 6.

Oker-Blom, P., & Smolander, H. (1988). The ratio of shoot silhouette area to total needle area in Scots pine. *Forest Science 34,* 894-906.

Pomraning, G.C. (1991). *Linear kinetic theory and particle transport in stochastic mixtures*. World Scientific, New Jersey, pp. 235.

Pomraning, G.C., Su, B. (1995), A new higher order closure for stochastic transport equations, proc. *International Conference on Mathematics and Computations, reactor Physics, and Environmental Analyses, American nuclear Society Topical Meeting, Portland, OR*, pp. 537-545

Pomraning, G.C. (1996). Transport theory in discrete stochastic mixtures. *Advances in Nuclear Science and Technology*, *24*, 47–93.

Privette, J.L., Asner, G.P., Conel., J., Nuemmrich, K.F., Olson, R., Rango, A., Rahman, A.F., Thome, K., Walter-Shea, E.A. (2000), The EOS prototype validation excersise (PROVE) at Jornada: Overview and lesson learned. Emote Sensing of Environment, 74(1): 1-12.

Ranson, K. J., Sun, G., Weishampel, J. F., & Knox, R. G. (1997). Forest biomass from combined ecosystem and radar backscatter modeling. *Remote Sensing of Environment*, *59*, 118–133.

Ross, J. (1981). *The Radiation Regime and Architecture of Plant Stands*. Norwell, MA: Dr. W. Junk, pp. 391.

Roujean, J.L. (1999a). Two-Story Equations of Transmission of Solar Energy (TESTSE) in open boreal conifer tree stands. *Journal of Geophysical Research*, 104 (D22), 27,869-27,879.

Roujean, J.L. (1999b). Measurements of PAR transmittance within boreal forest stands during BOREAS. *Agricultural and Forest Meteorology*, *93*, 1-6.

Schaaf, C. B., Gao, F., Strahler, A. H., Lucht, W., Li, X., Tsang, T., Strugnell, N. C., Zhang, X., Jin, Y., Muller, J.-P., Lewis, P., Barnsley, M., Hobson, P., Disney, M., Roberts, G., Dunderdale, M., Doll, C., d'Entremont, R., Hu, B., Liang S., and Privette, J. L. (2002).

First Operational BRDF, Albedo and Nadir Reflectance Products from MODIS. *Remote Sensing of Environment, 83*, 135-148.

Sellers, P.J., Randall, D.A., Betts, A.K., Hall, F.G., Berry, J.A., Collatz, G.J., Denning, A.S., Mooney, H.A., Nobre, C.A., Sato, N., Field, C.B., & Henderson-sellers, A. (1992). Modeling the exchanges of energy, water, and carbon between continents and the atmosphere. *Science*, *275*, 502-509.

Shabanov, N, V., Knyazikhin, Y., Baret, F., & Myneni, R. B. (2000). Stochastic modeling of radiation regime in discontinuous vegetation canopies. *Remote Sensing of Environment*, *74(1)*, 125-144.

Shultis, J.K., Myneni, R.B. (1988), Radiative transfer in vegetation canopies with an isotropic scattering. *J. Quant. Spectrosc. Radiat. Transf.* 39:115-129.

Smolander, S., & Stenberg, P. (2005). Simple parameterizations of the radiation budget of uniform broadleaved and coniferous canopies. *Remote Sensing of Environment, 94*, 355–363.

Stenberg, P. (1996). Simulations of the effect of shoot structure and orientation on vertical gradients in intercepted light by conifer canopies. *Tree Physiology, 16*, 99-108.

Stewart, R. (1990), Modeling radiant energy transfer in vegetation canopies, M.S. Thesis, Kansas State University, Manhattan, Kansas, 66506.

Stoyan, D., Kendall, S. W., & Mecke, J. (1995). *Stochastic Geometry and its Application*. John Wiley & Sons, New York, pp. 436.

Strahler, A.H., & Jupp, D.L.B. (1990). Modeling bidirectional reflectance of forests and woodlands using Boolean models and geometric optics. *Remote Sensing of Enviroment*, *34*, 153–160.

Titov, G.A. (1990). Statistical description of radiation transfer in clouds. *Journal of the Atmospheric Sciences*, *47*, 24–38.

Tucker, C.J. (1979). Red and photographic infrared linear combination for monitoring vegetation. *Remote Sensing of Environment*, *8*, 127-150.

Tucker, C.J., Fung, Y., Keeling, C.D., & Gammon, R.H. (1986). Relationship between atmospheric CO_2 variations and a satellite-derived vegetation index. *Nature*, *319*, 195-199.

Vainikko, G.M. (1973a), The equation of mean radiance in broken cloudiness. *Trudy MGK SSSR, Meteorological investigations* 21: 28-37, (in Russian).

Vainikko, G.M. (1973b), Transfer approach to the mean intensity of radiation in noncontinuous clouds. *Trudy MGK SSSR, Meteorological investigations* 21: 38-57, (in Russian).

Vladimirov, V.S. (1963), *Mathematical problems in the one-velocity theory of particle transport*, Tech. Rep. AECL-1661, At. Energy of can. Ltd., Chalk River, Ontario.

Zuev, V.E., Titov, G.A. (1996), *Atmospheric optics and climate.* The series 'Contemporary problems of atmospheric optics', Vol.9, Spector, Institute of Atm. Optics RAS, (in Russian).

Chapter 6

Stochastic Radiative Transfer in Species Mixtures & Time Dependent SRT

Shabanov et al.

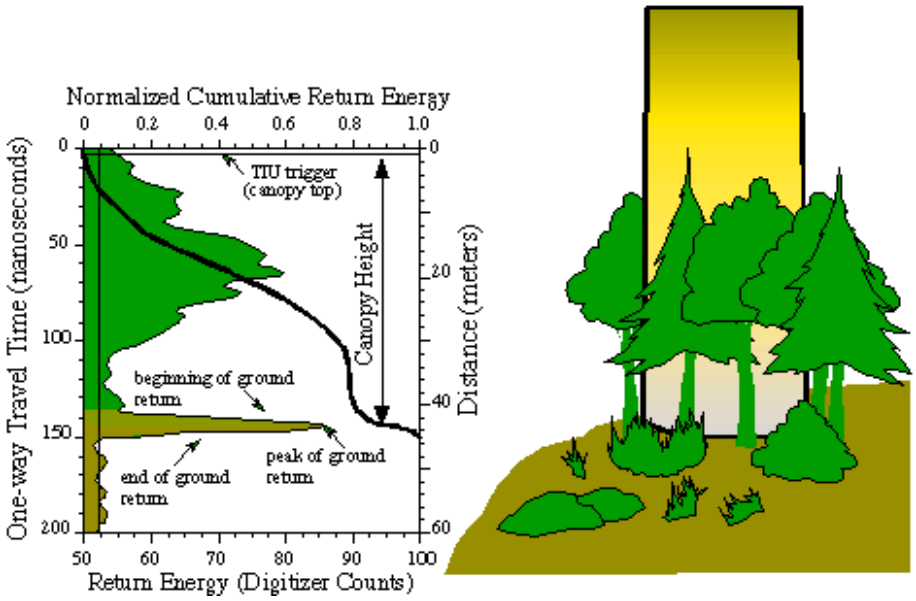

Chapter 6

Stochastic Radiative Transfer in Species Mixtures & Time Dependent SRT

1. Introduction

Chapter 7 introduced the basic principles of the stochastic RT approach, which describes stationary radiation regime in single species discontinuous vegetation canopies. While this is 1D approach, it captures 3D radiation effects. The model parameterization is convenient for operational remote sensing applications. However, the stochastic model allows further enhancements to suite the needs of specialized applications to characterization of 3D canopy structure. Two such applications are detailed in this Chapter: remote sensing of mixtures of vegetation species and lidar remote sensing of vertical vegetation structure.

2. Stochastic Radiative Transfer in a Mixture of Species

2.1. Remote Sensing of Mixtures

The problem of remote sensing of mixture of vegetation species is known as a scaling issue, that is, given biophysical parameters and radiation field over pure species at sub-pixel scale one needs to estimate those parameters at the scale of a mixed pixel (Fig.1). Multiple approaches were developed to address the scaling issue, which can be grouped into two basic categories:

empirical/statistical and physically-based. The approaches from the first category are widely used for sub-pixel land cover characterization: linear mixture models [DeFries et al., 1999], neural networks [Carpenter et al., 1999], Gaussian mixture discriminant analysis [Ju et al., 2003], decision trees [McIver & Friedl, 2002] and others. The key idea of the above methods is to model satellite measured radiation over a mixed pixel as a weighted sum of the radiation fields over pure land cover classes. Linear and non-linear models were implemented to retrieve the unknown weights, corresponding to the proportion of pure land cover classes in the mixed pixel. The linear mixture approach was implemented operationally to generate global vegetation continuous fields product from NASA's MODerate resolution Imaging Spectroradiometer (MODIS) measurements [WWW1; DeFries et al., 1999]. It was noted, however, that species in a mixture may exhibit significant degree of radiative interaction, which may bias retrievals especially in the case of linear models [Borel & Gerstl, 1994].

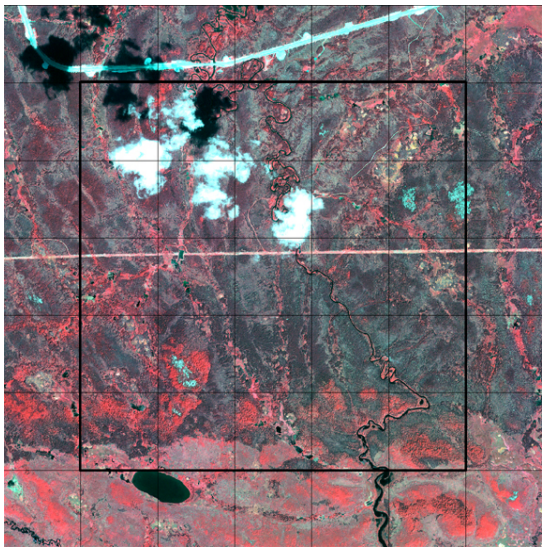

Figure 1. Natural species mixture at NOBS (Northern Old Black Spruce) boreal forest site in northern Manitoba, Canada (55° 52' 46.632" N, 98° 28' 50.916" W). Panel a): 4-m resolution IKONOS false-color image over NOBS site for July 23, 2000. Panel b) 30-m resolution Land cover map over the same area for year 2000. (Images credit: BigFoot team).

In contrast to the empirical methods, physically-based approaches describe in details the physical processes of interaction of radiation with canopy at the level of elementary volume of vegetation. Optical properties of a mixture in such volume are represented as weighted average of optical properties of pure species. The RT equation is used to model the radiation field with effective optical properties of mixed canopy. The above modeling principles were implemented, for instance, in the scaling scheme of the radiation block of the Common Land Model (CLM) [WWW2, Tian et al., 2004] and the MODIS Leaf Area Index (LAI) algorithm [WWW3, Tian et al., 2002]. The major limitation of the above schemes is that they are based on the turbid medium mixture approximation, where canopy is represented as a mixed gas of vegetation species and

gaps. With the turbid medium approach, one major feature of the natural vegetation is missing-spatial structure of a mixture, which may substantially affect radiation regime. Additional closely related theoretical work based on RT equation is the linear kinetic theory of stochastic mixture in cloudy atmospheres, developed by Pomraning [1991].

Below we detail application of the stochastic approach to model radiation regime in a mixture of discontinuous vegetation canopies. The stationary Stochastic RT (SRT) equation for single species (Chapter 7) was extended into the Stochastic Mixture RT (SMRT) equation for multiple species. In general, natural heterogeneity of vegetation (3D canopy structure) has two major components: discontinuity of vegetation; and mixture of species. The stochastic model for single species (Chapter 7) deals only with the first component of heterogeneity, discontinuity of vegetation, while the stochastic mixture model provides complete solution to the problem. The possibility of extending the original stochastic model to the mixture model already can be seen in the fact that single species discontinuous canopy can be treated as a mixture- a mixture of vegetation and gaps. The presentation is organized as follows. We start with the 3D RT equation and required parameterization of structure and optics of mixed canopy. Next, we formulate the SMRT equations and the model of stochastic moments of mixed canopy structure. Next, we perform an analytical and numerical analysis of the 3D radiation effects simulated by the SMRT model.

2.2. Model Formulation

3D RT Equation: Consider a heterogeneous vegetation canopy (a mixture of N different vegetation species and gaps as shown in Fig. 2), eliminated form above by solar radiation (both direct and diffuse components). The radiation regime in this system is described by the stationary 3D transport equation for radiation intensity, $I(\underline{r},\underline{\Omega})$, at spatial location $\underline{r}$ and direction $\underline{\Omega}$:

$$\underline{\Omega}\nabla I(\underline{r},\underline{\Omega}) + \sigma(\underline{r},\underline{\Omega})\, I(\underline{r},\underline{\Omega}) = \int_{4\pi} d\underline{\Omega}'\, \sigma_S(\underline{r},\underline{\Omega}' \to \underline{\Omega})\, I(\underline{r},\underline{\Omega}'), \tag{1}$$

where $\sigma(\underline{r},\underline{\Omega})$ is the extinction coefficient, and $\sigma_S(\underline{r},\underline{\Omega}' \to \underline{\Omega})$ is the differential scattering coefficient, detailed later in this Section. The unique solution of the Eq. (1) is specified by boundary conditions,

$$\begin{cases} I(z=0,\underline{\Omega}) = \dfrac{f_{dir}(\underline{\Omega}_0)}{|\mu(\underline{\Omega}_0)|}\,\delta(\underline{\Omega}-\underline{\Omega}_0) + [1-f_{dir}(\underline{\Omega}_0)]\,d(\underline{\Omega},\underline{\Omega}_0),\ \mu<0, \\ I(z=H,\underline{\Omega}) = \dfrac{\rho_{soil}}{\pi}\displaystyle\int_{2\pi^-} d\underline{\Omega}'\, I(z=H,\underline{\Omega}')\,|\mu(\underline{\Omega}')|,\ \mu>0, \end{cases} \tag{2}$$

where the first equation specifies incoming direct, $\delta(\underline{\Omega} - \underline{\Omega}_0)$, and diffuse, $d(\underline{\Omega}, \underline{\Omega}_0)$, radiation at the top of canopy ($\underline{\Omega}_0$ is the direction of solar beam), and $f_{dir}(\underline{\Omega}_0)$ denotes the ratio of direct to total incoming solar flux. The second equation specifies boundary condition at the canopy bottom, soil surface, which is assumed to be a Lambertian surface with hemispherical reflectance, ρ_{soil}.

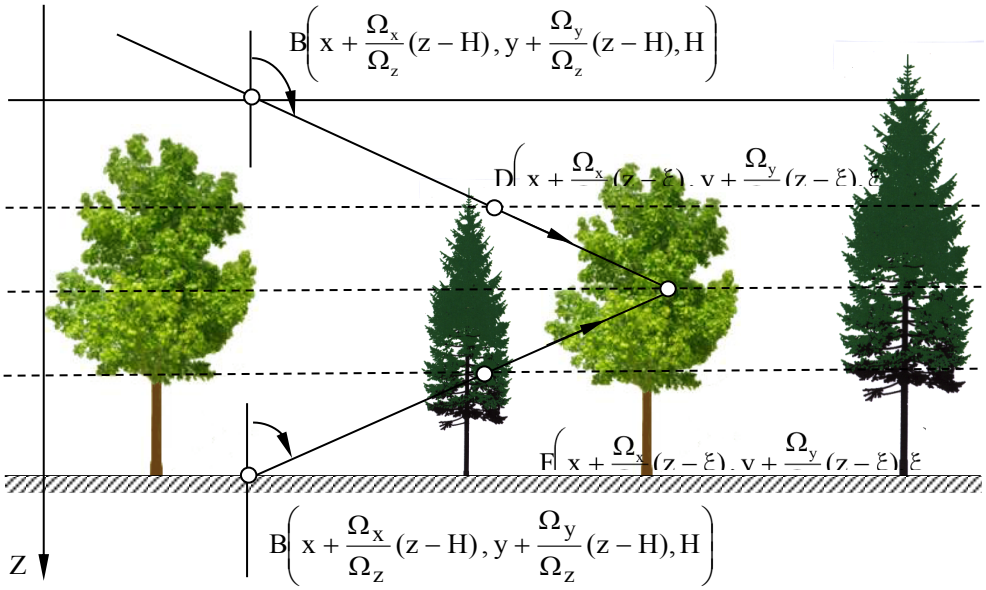

Figure 2. Schematic plot of mixture of discontinuous vegetation canopies (broadleaf and needle leaf species) in a coordinate system. The vertical axis, Z, is directed down. Canopy height is H. The angular direction, θ, is measured relative to the upward direction.

The spatial structure of heterogeneous mixed canopy can be characterized by the indicator function of a canopy, $\chi(\underline{r})$, defined for each spatial location, $\underline{r}$, as follows:

$$\chi(\underline{r}) = \sum_j \chi^{(j)}(\underline{r}), \tag{3a}$$

where $\chi^{(j)}(\underline{r})$ is an indicator function of the individual species 'j':

$$\chi^{(j)}(\underline{r}) = \begin{cases} 1, & \text{if } \underline{r} \in \text{species "j"}, \; j = 1, N, \\ 0, & \text{otherwise.} \end{cases} \tag{3b}$$

The equations above specify overall architecture of vegetation canopy as cumulative contribution of individual species in a mixture. The indicator function is assumed to be a random variable. We further assume that a particular spatial location is occupied only by a single species, i.e.,

$$\chi^{(i)}(\underline{r}) \cdot \chi^{(j)}(\underline{r}) = 0, \; i \neq j. \tag{3c}$$

Density of canopy is defined by the Leaf Area Index (LAI) – one-sided green leaf area per unit ground area [m^2/m^2]. In the case of mixture of species,

$$LAI = \frac{1}{S}\int_V d\underline{r}\; d_L(\underline{r}) = \sum_j \frac{1}{S}\int_V d\underline{r}\; d_L^{(j)}\,\chi^{(j)}(\underline{r}) = \sum_j LAI^{(j)}, \tag{4}$$

where $d_L^{(j)}$ and $LAI^{(j)}$ are one-sided foliage area volume density [m^2/m^3] and LAI of species 'j', respectively, and the integration is performed over a volume of canopy, V, with a footprint, S. Given the indicator function, we can define spatially varying extinction coefficient, $\sigma(\underline{r},\underline{\Omega})$, and differential scattering coefficient, $\sigma_S(\underline{r},\underline{\Omega}' \to \underline{\Omega})$, as follows

$$\sigma(\underline{r},\underline{\Omega}) = \sum_j \sigma^{(j)}(\underline{\Omega})\,\chi^{(j)}(\underline{r}) = \sum_j d_L^{(j)}\,\chi^{(j)}(\underline{r})\; G^{(j)}(\underline{\Omega}), \tag{5}$$

$$\sigma_S(\underline{r},\underline{\Omega}' \to \underline{\Omega}) = \sum_j \sigma_S^{(j)}(\underline{\Omega}' \to \underline{\Omega})\,\chi^{(j)}(\underline{r}) = \sum_j \frac{d_L^{(j)}\,\chi^{(j)}(\underline{r})}{\pi}\,\Gamma^{(j)}(\underline{\Omega}' \to \underline{\Omega}), \tag{6}$$

where $G^{(j)}(\underline{\Omega})$ is the mean projection of leaf normals in the direction $\underline{\Omega}$ and $\Gamma^{(j)}(\underline{\Omega}' \to \underline{\Omega})$ is the area scattering phase function for species 'j' [Ross, 1981]. The above parameters depend on the probability density of species leaf normal orientation, $g_L^{(j)}(\underline{r},\underline{\Omega}_L)$, ($\underline{\Omega}_L$ is a leaf normal direction) and species spectral leaf albedo, $\omega^{(j)}(\lambda)$ (λ is a wavelength) [Ross, 1981]. Finally, note that in the case of singe species, canopy indicator function is equivalent to a single species indicator function, and thus mixture model reduces to a model for single heterogeneous species, detailed in Chapter 7.

Stochastic Mixture RT Equations: The mathematical formulation of the stochastic mixture RT equation requires two types of averages: (1) $U^{(i)}(z,\underline{\Omega})$, mean intensity over the portion of the horizontal plane at depth z, occupied by species 'i'; (2) $\bar{I}(z,\underline{\Omega})$, mean intensity over the total space of the horizontal plane at depth z,

$$U^{(i)}(z,\underline{\Omega}) = \lim_{R\to\infty} \frac{1}{S_R \cap T_z^{(i)}} \iint_{S_R \cap T_z^{(i)}} dxdy\; \chi^{(i)}(x,y,z)\, I(x,y,z,\underline{\Omega}), \tag{7}$$

$$\bar{I}(z,\underline{\Omega}) = \lim_{R\to\infty} \frac{1}{S_R} \iint_{S_R} dxdy\; I(x,y,z,\underline{\Omega}). \tag{8}$$

In the above, S_R denotes the area of a circle of radius R; $T_z^{(i)}$ denotes the area of the horizontal plane at depth z, occupied by species 'i'.

Two stochastic moments characterize structure of the mixed canopy. The first stochastic moment is the probability, p, of finding species "i" at canopy depth z,

$$p^{(i)}(z) = \lim_{R\to\infty} \frac{1}{S_R} \iint_{S_R \cap T_z^{(i)}} dxdy\chi^{(i)}(z,x,y) \equiv \lim_{R\to\infty} \frac{S_R \cap T_z^{(i)}}{S_R}. \quad (9)$$

The second moment is the pair-correlation function, q, between species 'i' at canopy depth z and species 'j' at depth ξ along the direction $\underline{\Omega}$,

$$q^{(i,j)}(z,\xi,\underline{\Omega}) = \lim_{R\to\infty} \frac{S_R \cap T_z^{(i)} \cap T_\xi^{(j)}\left[\frac{\Omega_x}{\Omega_z}(z-\xi), \frac{\Omega_y}{\Omega_z}(z-\xi)\right]}{S_R}. \quad (10)$$

In the above, Ω_x, Ω_y, and Ω_z are projections of a unit direction vector, $\underline{\Omega}$, on the x, y, and z axes, respectively. Argument for $T_\xi^{(j)}$ denotes a shift of the origin of plane ξ relative to plane z along x and y directions, required to evaluate correlation between the planes in direction $\underline{\Omega}$ (cf. Fig. 2). Using the first and second moments of a vegetation structure, the conditional pair-correlation of species, $K^{(i,j)}$, can be evaluated as

$$K^{(i,j)}(z,\xi,\underline{\Omega}) = \frac{q^{(i,j)}(z,\xi,\underline{\Omega})}{p^{(i)}(z)}. \quad (11)$$

The procedure to derive the stochastic RT equations for multiple species from 3D RT equation is similar to one for single species (Chapter 7). The main difference is that integration over space occupied by vegetation should be split into sum of integration over individual species. We skip derivations here and provide only final equations (cf. Shabanov et al. [2007] for details). The system of equation for mean intensity over total space, $\bar{I}(z,\underline{\Omega})$, is

$$\begin{cases} \bar{I}(z,\underline{\Omega}) + \frac{1}{|\mu(\underline{\Omega})|}\sum_j \int_0^z d\xi\, p^{(j)}(\xi)\sigma^{(j)}(\underline{\Omega})U^{(j)}(\xi,\underline{\Omega}) = \\ = \frac{1}{|\mu(\underline{\Omega})|}\sum_j \int_0^z d\xi \int_{4\pi} d\underline{\Omega}'\, p^{(j)}(\xi)\sigma_S^{(j)}(\underline{\Omega}'\to\underline{\Omega})U^{(j)}(\xi,\underline{\Omega}') + \bar{I}(0,\underline{\Omega}), \quad \mu<0, \\ \bar{I}(z,\underline{\Omega}) + \frac{1}{|\mu(\underline{\Omega})|}\sum_j \int_z^H d\xi\, p^{(j)}(\xi)\sigma^{(j)}(\underline{\Omega})U^{(j)}(\xi,\underline{\Omega}) = \\ = \frac{1}{|\mu(\underline{\Omega})|}\sum_j \int_z^H d\xi \int_{4\pi} d\underline{\Omega}'\, p^{(j)}(\xi)\sigma_S^{(j)}(\underline{\Omega}'\to\underline{\Omega})U^{(j)}(\xi,\underline{\Omega}') + \bar{I}(H,\underline{\Omega}), \quad \mu>0. \end{cases} \quad (12)$$

The system of equation for mean intensity over individual species $U^{(i)}(z,\underline{\Omega})$, i=[1,N], is

$$
\begin{cases}
U^{(i)}(z,\underline{\Omega}) + \dfrac{1}{|\mu(\underline{\Omega})|}\sum\limits_j \int\limits_0^z d\xi\ K^{(i,j)}(z,\xi,\underline{\Omega})\,\sigma^{(j)}(\underline{\Omega})\,U^{(j)}(\xi,\underline{\Omega}) = \\
= \dfrac{1}{|\mu(\underline{\Omega})|}\sum\limits_j \int\limits_0^z d\xi \int\limits_{4\pi} d\underline{\Omega}'\ K^{(i,j)}(z,\xi,\underline{\Omega})\,\sigma_S^{(j)}(\underline{\Omega}' \to \underline{\Omega})U^{(j)}(\xi,\underline{\Omega}') + U^{(i)}(0,\underline{\Omega}), \quad \mu < 0, \\
U^{(i)}(z,\underline{\Omega}) + \dfrac{1}{|\mu(\underline{\Omega})|}\sum\limits_j \int\limits_z^H d\xi\ K^{(i,j)}(z,\xi,\underline{\Omega})\,\sigma^{(j)}(\underline{\Omega})U^{(j)}(\xi,\vec{\Omega}) = \\
= \dfrac{1}{|\mu(\underline{\Omega})|}\sum\limits_j \int\limits_z^H d\xi \int\limits_{4\pi} d\underline{\Omega}'\ K^{(i,j)}(z,\xi,\underline{\Omega})\,\sigma_S^{(j)}(\underline{\Omega}' \to \underline{\Omega})U^{(j)}(\xi,\underline{\Omega}') + U^{(i)}(H,\underline{\Omega}), \quad \mu > 0.
\end{cases}
\tag{13}
$$

In the Eq. (12) (Eq. (13)), $\bar{I}(0,\underline{\Omega})$ and $\bar{I}(H,\underline{\Omega})$ ($U^{(i)}(0,\underline{\Omega})$ and $U^{(i)}(H,\underline{\Omega})$) denote mean radiation intensities over whole horizontal plane (individual species) at the canopy boundaries; in the typical case of the uniform boundary conditions they are equal to the corresponding 3D values, $I(z=0,\underline{\Omega})$ and $I(z=H,\underline{\Omega})$ (cf. Eq. (2)). According to Eq. (12), $\bar{I}(z,\underline{\Omega})$, depends on $U^{(i)}(z,\underline{\Omega})$, i=[1,N]. Note that, in contrast to a single equation for single species (Chapter 7), the Eq. (13) for N species corresponds to systems of N equations. This accounts for the fact of species radiative coupling.

Separation of Direct and Diffuse Radiation: The mean intensity over species, $U^{(i)}(z,\vec{\Omega})$, can be decomposed into the direct, $U_\delta^{(i)}(z)$, and diffuse, $U_d^{(i)}(z,\underline{\Omega})$, components, according to the pattern of incoming solar radiation, Eq. (2), namely,

$$
U^{(i)}(z,\underline{\Omega}) = \frac{f_{dir}(\underline{\Omega}_0)}{|\mu(\underline{\Omega}_0)|}\,U_\delta^{(i)}(z)\delta(\underline{\Omega}-\underline{\Omega}_0) + U_d^{(i)}(z,\underline{\Omega}).
$$

Substituting this decomposition into Eq. (13) and collecting terms, which contain the Dirac's delta function, $\delta(\underline{\Omega}-\underline{\Omega}_0)$, we will get system of N equations for the direct component, $U_\delta^{(i)}(z)$:

$$
U_\delta^{(i)}(z) + \frac{1}{|\mu(\underline{\Omega}_0)|}\sum_j \int_0^z d\xi\ K^{(i,j)}(z,\xi,\underline{\Omega}_0)\,\sigma^{(j)}(\underline{\Omega}_0)\,U_\delta^{(j)}(\xi) = 1, \tag{14}
$$

and the system of N equations for the diffuse component, $U_d^{(i)}(z,\underline{\Omega})$:

$$
\begin{cases}
U_d^{(i)}(z,\underline{\Omega}) + \dfrac{1}{|\mu(\underline{\Omega})|}\sum\limits_j \int\limits_0^z d\xi\ K^{(i,j)}(z,\xi,\underline{\Omega})\,\sigma^{(j)}(\underline{\Omega})\,U_d^{(j)}(\xi,\underline{\Omega}) = \\
= \dfrac{1}{|\mu(\underline{\Omega})|}\sum\limits_j \int\limits_0^z d\xi\ K^{(i,j)}(z,\xi,\underline{\Omega})\,S^{(j)}(\xi,\underline{\Omega}) + U_0^{(i)}(z,\underline{\Omega},\underline{\Omega}_0), \quad \mu < 0, \\
U_d^{(i)}(z,\underline{\Omega}) + \dfrac{1}{|\mu(\underline{\Omega})|}\sum\limits_j \int\limits_z^H d\xi\ K^{(i,j)}(z,\xi,\underline{\Omega})\,\sigma^{(j)}(\vec{\Omega})\,U_d^{(j)}(\xi,\underline{\Omega}) = \\
= \dfrac{1}{|\mu(\underline{\Omega})|}\sum\limits_j \int\limits_z^H d\xi\ K^{(i,j)}(z,\xi,\underline{\Omega})\,S^{(j)}(\xi,\underline{\Omega}) + U_H^{(i)}(z,\underline{\Omega},\underline{\Omega}_0), \quad \mu > 0,
\end{cases}
\tag{15a}
$$

where,

$$S^{(j)}(\xi,\underline{\Omega}) = \int_{4\pi} d\underline{\Omega}'\, \sigma_S^{(j)}(\underline{\Omega}' \to \underline{\Omega})\, U_d^{(j)}(\xi,\underline{\Omega}'), \tag{15b}$$

$$U_0^{(i)}(z,\underline{\Omega},\underline{\Omega}_0) = \frac{f_{dir}(\underline{\Omega}_0)}{|\mu(\underline{\Omega})\,\mu(\underline{\Omega}_0)|} \sum_j \int_0^z d\xi\; K^{(i,j)}(z,\xi,\underline{\Omega})\, \sigma_S^{(j)}(\underline{\Omega}_0 \to \underline{\Omega})\, U_\delta^{(j)}(\xi) + \\ + [1 - f_{dir}(\underline{\Omega}_0)]\, d(\underline{\Omega},\underline{\Omega}_0), \tag{15c}$$

$$U_H^{(i)}(z,\underline{\Omega},\underline{\Omega}_0) = \frac{f_{dir}(\underline{\Omega}_0)}{|\mu(\underline{\Omega})\,\mu(\underline{\Omega}_0)|} \sum_j \int_z^H d\xi\; K^{(i,j)}(z,\xi,\underline{\Omega})\, \sigma_S^{(j)}(\underline{\Omega}_0 \to \underline{\Omega}) U_\delta^{(j)}(\xi) + U^{(i)}(H,\underline{\Omega}). \tag{15d}$$

The mean intensity over the total space of the horizontal plane, $\bar{I}(z,\underline{\Omega})$, can be decomposed into direct, $\bar{I}_\delta(z)$, and diffuse, $\bar{I}_d(z,\underline{\Omega})$, components similarly:

$$\bar{I}_\delta(z) = 1 - \frac{1}{|\mu(\underline{\Omega}_0)|} \sum_j \int_0^z d\xi\; p^{(j)}(\xi)\sigma^{(j)}(\underline{\Omega}_0) U_\delta^{(j)}(\xi), \tag{16}$$

and

$$\begin{cases} \bar{I}_d(z,\underline{\Omega}) = -\dfrac{1}{|\mu(\underline{\Omega})|} \sum_j \int_0^z d\xi\; p^{(j)}(\xi)\sigma^{(j)}(\underline{\Omega}) U_d^{(j)}(\xi,\underline{\Omega}) + \\ + \dfrac{1}{|\mu(\underline{\Omega})|} \sum_j \int_0^z d\xi\; p^{(j)}(\xi) S^{(j)}(\xi,\underline{\Omega}) + U_0^{(i)}(z,\underline{\Omega},\underline{\Omega}_0), \quad \mu < 0, \\ \bar{I}_d(z,\underline{\Omega}) = -\dfrac{1}{|\mu(\underline{\Omega})|} \sum_j \int_z^H d\xi\; p^{(j)}(\xi)\sigma^{(j)}(\underline{\Omega}) U_d^{(j)}(\xi,\underline{\Omega}) + \\ + \dfrac{1}{|\mu(\underline{\Omega})|} \sum_j \int_z^H d\xi\; p^{(j)}(\xi) S^{(j)}(\xi,\underline{\Omega}) + U_H^{(i)}(z,\underline{\Omega},\underline{\Omega}_0), \quad \mu > 0, \end{cases} \tag{17}$$

where, $S^{(j)}(\xi,\underline{\Omega})$, $U_0^{(i)}(z,\underline{\Omega},\underline{\Omega}_0)$ and $U_H^{(i)}(z,\underline{\Omega},\underline{\Omega}_0)$ are defined by Eqs. (15b-d).

Absorptance: The terms of the energy conservation law (canopy albedo, absorptance and transmittance) and mean intensities ($\bar{I}(z,\underline{\Omega})$ and $U^{(i)}(z,\underline{\Omega})$), derived according to the stochastic approach, follow the general rules for the BS- and S- problems (Chapter 7). The equation for absorptance has special features as it explicitly accounts for the contribution of different species, characterized by different optical properties. Taking into account the definition of absorptance (cf. Chapter 7), and Eqs. (7) and (9), the absorptance of the multi-species vegetation canopy is

$$A \equiv \frac{1}{S_R} \iint_{V x 4\pi} d\underline{r} d\underline{\Omega}\; (1 - \omega(\underline{r}))\, \sigma(\underline{r},\underline{\Omega})\, I(\underline{r},\underline{\Omega}) \\ = \frac{1}{S_R} \int_0^H dz \int_{4\pi} d\underline{\Omega} \int_{\pi R^2} dxdy \sum_j \chi^{(j)}(\underline{r})\,(1 - \omega^{(j)})\, \sigma^{(j)}(\underline{\Omega})\, I(\underline{r},\underline{\Omega})$$

$$= \sum_j (1-\omega^{(j)}) \int_0^H dz \int_{4\pi} d\underline{\Omega}\, \frac{S_R \cap T_z^{(j)}}{S_R} \cdot \frac{1}{S_R \cap T_z^{(j)}} \int_{S_R} dxdy \chi^{(j)}(\underline{r}) \sigma^{(j)}(\underline{\Omega})\, I(\underline{r},\underline{\Omega})$$

$$= \sum_j (1-\omega^{(j)}) \int_0^H dz \int_{4\pi} d\underline{\Omega}\, p^{(j)}(z) \sigma^{(j)}(\underline{\Omega})\, U^{(j)}(z,\underline{\Omega}). \qquad (18)$$

Taking into account Eq. (18), we evaluate absorptance of the mixture as a linear sum of absorptances of individual species for BS- and S- problems,

$$A \approx \sum_j A_{BS}^{(j)} + \frac{\rho_{soil}}{1-\rho_{soil} R_S} T_{BS} A_S^{(j)} \ . \qquad (19)$$

Conditional Pair-correlation Function of Mixture of Species: The critical parameters of the SMRT equations are two stochastic moments of a canopy structure: the probability of finding species, $p^{(i)}$ (Eq. (9)), and the conditional pair-correlation of species, $K^{(i,j)}$ (Eq. (11)). The following three classes of canopy structure can be identified: a) non-ordered/chaotic mixture of species and gaps or turbid medium; b) ordered mixture of species without gaps; c) ordered mixture of species with gaps. The canopy structure (order/chaoticity) is controlled by the conditional pair-correlation of species, $K^{(i,j)}$, while amount of gaps is controlled by the probability of finding species $p^{(i)}$. In the general case, $K^{(i,j)}$ satisfies the following symmetry condition:

$$p^{(i)}(z) \cdot K^{(i,j)}(z,\xi,\underline{\Omega}) \equiv S_R \cap T_z^{(i)} \cdot \frac{S_R \cap T_z^{(i)} \cap T_\xi^{(j)}}{S_R \cap T_z^{(i)}}$$

$$= S_R \cap T_\xi^{(j)} \cdot \frac{S_R \cap T_\xi^{(j)} \cap T_z^{(i)}}{S_R \cap T_\xi^{(j)}}$$

$$\equiv p^{(j)}(\xi) \cdot K^{(j,i)}(\xi,z,-\underline{\Omega}). \qquad (20)$$

The additional properties of $K^{(i,j)}$ in the special cases of canopy structure are as follows. In the case of turbid medium there is no correlation between phytoelements of different species, and therefore, $K^{(i,j)}$ simplifies:

$$K^{(i,j)}(z,\xi,\underline{\Omega}) = \frac{q^{(i,j)}(z,\xi,\underline{\Omega})}{p^{(i)}(z)} = \frac{p^{(i)}(z)\, p^{(j)}(\xi)}{p^{(i)}(z)} = p^{(j)}(\xi). \qquad (21)$$

In the case of ordered species without gaps, $K^{(i,j)}$ satisfies the following two constraints:

$$\sum_j K^{(i,j)}(z,\xi,\underline{\Omega}) \equiv \sum_j \frac{S_R \cap T_z^{(i)} \cap T_\xi^{(j)}}{S_R \cap T_z^{(i)}} = 1, \qquad (22)$$

$$\sum_i p^{(i)}(z)\cdot K^{(i,j)}(z,\xi,\underline{\Omega}) \equiv \sum_i \frac{S_R \cap T_z^{(i)}}{S_R}\cdot\frac{S_R \cap T_z^{(i)} \cap T_\xi^{(j)}}{S_R \cap T_z^{(i)}} = p^{(j)}(\xi), \tag{23}$$

if and only if,

$$\sum_j p^{(j)}(z) \equiv \sum_j \frac{S_R \cap T_z^{(j)}}{S_R} = 1\,.$$

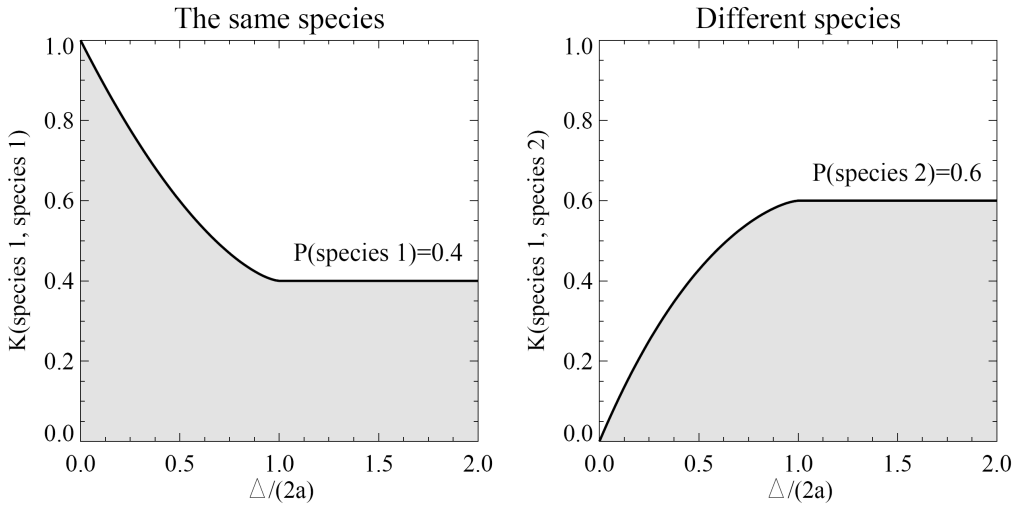

Figure 3. The conditional pair-correlation function, $K^{(i,j)}$, of the SMRT model as function of horizontal distance of correlation, Δ, normalized by three diameter, 2a. The parameters are as follows: two species with probabilities $p^{(1)}$=0.4 and $p^{(2)}$=0.6; ; tree radius a=0.15; canopy height H=1.

Finally, consider the case of ordered mixture of species with gaps. The conditional pair-correlation function was derived according to the theory of stochastic geometry [Stoyan, Kendall and Mecke, 1995]. The derivations in the case of mixture of species [Shabanov et al., 2007] extend those for single species [Huang et al., 2007]. The derivations are based on the following assumptions about 3D stochastic canopy structure: a) tree species are modeled as identical cylinders; b) distribution of the tree centers follows stationary Poisson point process [Stoyan, Kendall and Mecke, 1995]. Under the above assumptions, the conditional pair-correlation function is as follows:

$$K^{(i,j)}(\Delta) = \begin{cases} [2p^{(i)} - 1 + (1-p^{(i)})^{2-\Xi(\Delta)/\pi a^2}]/\,p^{(i)}, & i = j, \\ 1-(1-p^{(i)})^{1-\Xi(\Delta)/\pi a^2}, & i \neq j, \end{cases} \tag{24a}$$

where

$$\Xi(\Delta) = 2a^2\left[\arccos\left(\frac{\Delta}{2a}\right) - \frac{\Delta}{2a}\sqrt{1-\left(\frac{\Delta}{2a}\right)^2}\right]\Theta(2a-\Delta). \qquad (24b)$$

In the above equations, parameter "a" denotes a tree radius, $p^{(i)}$ is the canopy depth independent probability of finding species, $\Theta(x)$ is the Heaviside step function, and Δ is the horizontal distance of correlation,

$$\Delta = \left|(z-\xi)\tan(\underline{\Omega})\right|. \qquad (24c)$$

The conditional pair-correlation function for two species is shown in Fig. 3 In the case of the same species, correlation decreases as distance increases. This corresponds to increasing probability of one of the points being out of the same crown as distance increases. In the case of different species, correlation increases as distance increases. This corresponds to increasing probability of two points to be located in different crowns of different species with increasing distance. In the case of short distances, within-species correlation is 1, while between-species correlation is 0. In the case of large distances, correlation between any species is vanishing and $K^{(i,j)}$ converges to $p^{(i)}$. Both limiting cases are intuitively expected and captured by the proposed model.

Numerical Scheme: The scheme for the stochastic mixture RT equations is an extension of one for single species (Chapter 7, Section 5): single system of linear equations for singles species is expanded into N systems of linear equations for N species. The key steps to solve mixture equations are identical to those for single species. The mean intensity over whole horizontal plane, $\bar{I}(z,\underline{\Omega})$, is just a linear combination of integrals of mean intensities over individual species, $U^{(i)}(z,\underline{\Omega})$, i=[1,N] (Eq. (12)). The scheme to solve for $U^{(i)}(z,\underline{\Omega})$ involves two steps: 1) solve Eq. (14) for direct intensities, $U_\delta^{(i)}(z,\underline{\Omega}_0)$; 2) solve Eq. (15) for diffuse intensities, $U_d^{(i)}(z,\underline{\Omega})$. Evaluation of the direct components, $U_\delta^{(i)}(z,\underline{\Omega}_0)$, requires solution of the system of N parametric Volterra equations. Evaluation of the diffuse components, $U_d^{(i)}(z,\underline{\Omega})$, is based on SOSA method (Chapter 7, Section 5), at each step of iterations one needs to solve system of N parametric Volterra equations. Thus, the key difference in numerical solution of the singe species and mixture equations is that instead of single Volterra equation one needs to solve system of N such equations. The approach to solve the system of parametric Volterra equations is illustrated below with the following equation in the general form

$$Q^{(i)}(z,\underline{\Omega}) + \frac{1}{|\mu(\underline{\Omega})|}\sum_j \int_0^z d\xi\, K^{(i,j)}(z,\xi,\underline{\Omega})\,\sigma^{(j)}(\underline{\Omega})\,Q^{(j)}(\xi,\underline{\Omega}) = F^{(i)}(z,\underline{\Omega}), \quad i=[1,N]. \qquad (25a)$$

Note that Eq. (25a) represents system of N equations, $\underline{\Omega}$ is a parameter of the parametric Volterra equation, and $Q^{(i)}(z,\underline{\Omega})$ is unknown intensity of species i. The discrete form of Eq. (25a) is as follows:

$$Q^{(i)}(k,\underline{\Omega}) + \frac{1}{|\mu(\underline{\Omega})|}\sum_{j}\sum_{\ell=1}^{k} K^{(i,j)}(k,\ell,\underline{\Omega})\,\sigma^{(j)}(\underline{\Omega})\,Q^{(j)}(\ell,\underline{\Omega}) = F^{(i)}(k,\underline{\Omega}). \tag{25b}$$

For the purpose of the following derivations, let us rewrite the above equation as follows,

$$Q^{(i)}(k,\underline{\Omega}) + \frac{1}{|\mu(\underline{\Omega})|}\sum_{j} K^{(i,j)}(k,k,\underline{\Omega})\,\sigma^{(j)}(\underline{\Omega})\,Q^{(j)}(k,\underline{\Omega}) =$$
$$= F^{(i)}(k,\underline{\Omega}) - \frac{1}{|\mu(\underline{\Omega})|}\sum_{j}\sum_{\ell=1}^{k-1} K^{(i,j)}(k,\ell,\underline{\Omega})\,\sigma^{(j)}(\underline{\Omega})\,Q^{(j)}(\ell,\underline{\Omega}). \tag{26}$$

Equation (26) is a system of N linear equations, which can be presented in the following matrix format,

$$\widehat{\mathbf{A}}(k,\underline{\Omega}) \times \mathbf{Q}(k,\underline{\Omega}) = \mathbf{W}(k,\underline{\Omega}), \tag{27a}$$

where $\widehat{\mathbf{A}}(k,\underline{\Omega})$ is an N x N matrix, and $\mathbf{Q}(k,\underline{\Omega})$ and $\mathbf{W}(k,\underline{\Omega})$ are N-elements vectors

$$\widehat{\mathbf{A}}^{(i,j)}(k,\underline{\Omega}) = \begin{cases} 1 + \dfrac{\sigma^{(i)}(\underline{\Omega})}{|\mu(\underline{\Omega})|} K^{(i,i)}(k,k,\underline{\Omega}), & \text{if } i = j, \\ \dfrac{\sigma^{(j)}(\underline{\Omega})}{|\mu(\underline{\Omega})|} K^{(i,j)}(k,k,\underline{\Omega}), & \text{if } i \neq j, \end{cases} \tag{27b}$$

$$\mathbf{W}^{(i)}(k,\underline{\Omega}) = F^{(i)}(k,\underline{\Omega}) - \frac{1}{|\mu(\underline{\Omega})|}\sum_{j}\sum_{\ell=1}^{k-1} K^{(i,j)}(k,\ell,\underline{\Omega})\,\sigma^{(j)}(\underline{\Omega})\,Q^{(j)}(\ell,\underline{\Omega}), \tag{27c}$$

$$\mathbf{Q}^{(i)}(k,\underline{\Omega}) = Q^{(i)}(k,\underline{\Omega}). \tag{27d}$$

The solution of Eq. (27) is derived sequentially starting with k=1. At each step $\widehat{\mathbf{A}}(k,\underline{\Omega})$ is a known matrix, vector $\mathbf{W}(k,\underline{\Omega})$ can be calculated from the previous step. The solution, $\mathbf{Q}(k,\underline{\Omega}) = \widehat{\mathbf{A}}^{-1}(k,\underline{\Omega}) \times \mathbf{W}(k,\underline{\Omega})$, can be derived by Gauss-Jordan, LU-decomposition or similar techniques for solving linear system of equations [Press et al., 1986]. The complete step-by-step numerical scheme is given in Shabanov et al. [2007].

2.3. Analytical Analysis

The analytical analysis of the SMRT equations is performed for the three classes of canopy structure (cf. Section 2.2): a) non-ordered mixture of species and gaps (turbid medium); b) ordered mixture of species without gaps; c) ordered mixture of species with gaps.

Turbid Medium: In the case of non-ordered mixture of vegetation species and gaps (turbid medium) $K^{(i,j)}$ is reduced to $p^{(j)}$ (cf. Eq. (21)). In this case Eq. (13) is equivalent to Eq. (12) and $\bar{I}(z,\underline{\Omega}) = U^{(i)}(z,\underline{\Omega})$ for i=1,N, which implies no variation of the radiation fluxes between

different species. Lack of between species variation of fluxes is a consequence of the lack of spatial gradient of structure in a turbid medium: the same proportion of different species occupies each spatial location at particular canopy depth. Thus, in the case of turbid medium, Eq. (12) and (13) correspond to single equation, where species-dependent optical properties are combined in *effective* optical properties of a mixture as a whole,

$$X^{(eff)}(z) = \sum_j p^{(j)}(z) \cdot X^{(j)}(z), \tag{28}$$

where X corresponds to σ and σ_S, and any expressions including its components or derivatives, such as d_L or $(1-\omega)\cdot\sigma$, etc. As mentioned before (cf. Section 2.1), approach of effective optical properties was already implemented in the scaling scheme of the radiation block of the Command Land Model and the MODIS LAI algorithm. Such approach is valid only for non-ordered canopy (turbid medium) and may lead to a bias in evaluation of the radiation field of a natural structured mixture (cf. discussion later in this Section).

To conclude, consider one important implication of the general rule of Eq. (28) with respect to gaps. In the simplest case of the turbid medium of single species with gaps, the impact of gaps on RT equations is reduced to rescaling of LAI (cf. Eq. (4)-(6)):

$$d_L^{(eff)} = p^{(1)} \cdot d_L^{(1)}, \quad \sigma^{(eff)} = \sigma^{(1)}(d_L^{(eff)}), \quad \sigma_S^{(eff)} = \sigma_S^{(1)}(d_L^{(eff)}).$$

However, in the more complex case of the turbid medium of multiple species with gaps (d_L, σ, and σ_S depend on species), the above simple rescaling rule is not applicable, and effective parameters should be used:

$$d_L^{(eff)} = \sum_j p^{(j)} \cdot d_L^{(j)}, \quad \sigma^{(eff)} = \sum_j p^{(j)} \cdot \sigma^{(j)}(d_L^{(j)}), \quad \sigma_S^{(eff)} = \sum_j p^{(j)} \cdot \sigma_S^{(j)}(d_L^{(j)}).$$

Ordered Mixture without Gaps: Next, consider the special case of ordered mixture of vegetation species with no gaps between them. This case is not equivalent to a turbid medium, because spatial heterogeneity is characterized not only by ordered composition of vegetation clumps and gaps, but also by ordered composition of different species ($K^{(i,j)} \neq p^{(j)}$). In this special case some constraints for the SMRT equations can be derived. In the following derivations we assume

$$\sum_j p^{(j)}(z) = 1. \tag{29}$$

For simplicity we perform derivations for the direct component of radiation over species, $U_\delta^{(i)}(z)$. Multiplying Eq. (14) by $p^{(i)}(z)$ and performing summation over index "i", we have

$$\sum_i p^{(i)}(z)U_\delta^{(i)}(z) + \frac{1}{|\mu(\underline{\Omega}_0)|}\sum_i\sum_j \int_0^z d\xi\, p^{(i)}(z)K^{(i,j)}(z,\xi,\underline{\Omega}_0)\sigma^{(j)}(\underline{\Omega}_0)U_\delta^{(j)}(\xi) = \sum_i p^{(i)}(z) \qquad (30)$$

Taking into account Eqs. (23) and (29), Eq. (30) can be reduced to

$$\sum_j p^{(j)}(z)\, U_\delta^{(j)}(z) + \frac{1}{|\mu(\underline{\Omega}_0)|}\sum_j \int_0^z d\xi\, p^{(j)}(\xi)\,\sigma^{(j)}(\underline{\Omega}_0)\, U_\delta^{(j)}(\xi) = 1\,. \qquad (31)$$

Note, that Eq. (31) does not uniquely specify the solution, rather it provides a general constrain for a family of solutions with different $K^{(i,j)}$. Comparing Eqs. (31) and (16), we have

$$\bar{I}_\delta(z) = \sum_j p^{(j)}(z)U_\delta^{(j)}(z)\,. \qquad (32a)$$

Applying the above derivation technique to Eqs. (15) and (17), we will derive similar equation for total intensity (both direct and diffuse components), namely,

$$\bar{I}(z,\underline{\Omega}) = \sum_j p^{(j)}(z)U^{(j)}(z,\underline{\Omega})\,. \qquad (32b)$$

The above equation can be easily satisfied in the special case of the turbid medium model, as radiation over individual species is the same. However this equation is applicable to a more general case of ordered mixture of species with species-dependant fluxes (cf. further discussion in this Section and Section 2.4).

Radiation over Gaps: Next, consider the general case of ordered species with gaps. In the framework of the SMRT model, gaps can be treated as a special type of vegetation species with $\sigma = \sigma_s = 0$ and $d_L = 0$. The equation for the mean intensity over gaps, $U^{(gap)}(z,\underline{\Omega})$, can be derived as follows. Consider system of N+1 species, i.e., N vegetation species and 1 "species" of gaps, such that

$$\sum_j p^{(j)}(z) + p^{(gap)}(z) = 1\,. \qquad (33)$$

According to Eq. (32b), formulated for the above N+1 species,

$$\bar{I}(z,\underline{\Omega}) = p^{(gap)}U^{(gap)}(z,\underline{\Omega}) + \sum_j p^{(j)}(z)U^{(j)}(z,\underline{\Omega})\,. \qquad (34)$$

Combining Eqs. (33) and (34), we will derive expression for $U^{(gap)}(z,\underline{\Omega})$, namely

$$U^{(gap)}(z,\underline{\Omega}) = \frac{1}{1-\sum_j p^{(j)}(z)}\left[\bar{I}(z,\underline{\Omega}) - \sum_j p^{(j)}(z)U^{(j)}(z,\underline{\Omega})\right]. \quad (35)$$

Note, that in the case of the turbid medium, Eq. (35) is reduced to

$$U^{(gap)}(z,\underline{\Omega}) = \bar{I}(z,\underline{\Omega}) = U^{(j)}(z,\underline{\Omega}). \quad (36)$$

The derived equations for the mean radiation over gaps have important implications for LAI retrievals from field measurements of radiation by a range of commercial optical instruments, including LAI-2000, AccuPAR, TRAC, etc. [Breda, 2003]. Measurements are performed over gaps and retrievals are performed according to the turbid medium model, which does not differentiate between fluxes over gaps and vegetation species (Eq. (36)). In reality, radiation fluxes over individual vegetation species and gaps may show substantial variation. To achieve better accuracy, retrieval technique of the standard optical instruments needs to be reformulated in terms of the stochastic equations.

Uncollided Radiation: Next, consider the SMRT equations in the limiting case of uncollided radiation. This case can serve as an approximation for VIS wavelengths, where absorption is large and scattering is limited. In the following we will compare derivations for turbid medium and ordered medium, to further clarify impact of canopy structure on radiation regime. To simplify derivations and get analytical expression we assume that incoming radiation is purely direct (SZA=0^0) and probabilities of species do not depend on canopy depths, i.e., $p^{(i)}(z) \equiv p^{(i)}$. First, consider the turbid medium case. Recall, that in this case $K^{(i,j)} = p^{(i)}$ (cf. Eq. (21)) and system of Eq. (14) for direct radiation, $U_\delta^{(i)}$, reduces to a single equation:

$$U_\delta(z) + \sum_j p^{(j)}\,\sigma^{(j)} \int_0^z d\xi\; U_\delta(\xi) = 1. \quad (37)$$

The solution of the above equation is

$$U_\delta(z) \equiv I_\delta(z) \equiv T(z) = \exp\left(-\sum_j p^{(j)}\,\sigma^{(j)} z\right), \quad (38)$$

where T(z) denotes canopy transmittance at depth z. The canopy absorptance can also be analytically evaluated (cf. Eq. (18) for $\omega^{(j)} = 0$, j=1,N) as follows,

$$A = \sum_j p^{(j)}\;\sigma^{(j)} \int_0^H d\xi\; U_\delta(\xi) = 1 - \exp\left(-\sum_j p^{(j)}\,\sigma^{(j)}\;H\right). \quad (39)$$

Next, consider the case of ordered species composition. In the following derivation we will use the conditional pair-correlation, as defined by Eqs. (24a-b). According to these equations and the specified assumptions, $K^{(i,j)}=1$, if i=j, and $K^{(i,j)}=0$, if $i \neq j$. In this case Eq. (14) reduces from a system of equations to a set of independent equations for individual species, namely

$$U_{\delta}^{(i)}(z) + \sigma^{(i)} \int_0^z d\xi \, U_{\delta}^{(i)}(\xi) = 1, \quad i=[1,N]. \tag{40}$$

The solution of each equation above depends on parameters of individual species, not whole mixture,

$$U_{\delta}^{(i)}(z) = \exp(-\sigma^{(i)} z). \tag{41}$$

Equation (16) for mean intensity in this case is reduces to

$$\bar{I}_{\delta}(z) \equiv T(z) = 1 - \sum_j p^{(j)} \sigma^{(j)} \int_0^z d\xi \, U_{\delta}^{(j)}(\xi) = 1 - \sum_j p^{(j)} [1 - \exp(-\sigma^{(j)} z)]. \tag{42}$$

The canopy absorptance is calculated as follows,

$$A = \sum_j p^{(j)} \sigma^{(j)} \int_0^H d\xi \, U_{\delta}^{(j)}(\xi) = \sum_j p^{(j)} [1 - \exp(-\sigma^{(j)} H)]. \tag{43}$$

Figure 4. Sunlit areas at the canopy bottom is a 3D effect, arising due to radiation streaming through the gaps without interaction with canopy (Image credit: D. Ahl, University of Wosconsin).

Compare canopy transmittance for the turbid (Eq. (38)) and ordered (Eq. (42) medium. As LAI (or canopy depth, H) is increasing, the canopy transmittance converges to 0 in the case of the turbid medium, and to a gap probability in the case of the ordered medium. The ordered medium case provides a realistic description of the radiation regime, as it accounts for radiation streaming

through gaps without interaction with vegetation, such that portion of the sunlit area at the ground is equal to the gap probability (Fig. 4). Next, compare absorptance for the turbid (Eq. (39)) and ordered (Eq. (43)) medium. As LAI increases the canopy absorptance converges to 1 in the case of turbid medium and to cumulative probability of all species in the case of the ordered medium. Again, the case of ordered medium provides a more realistic description of the radiation regime, as only the portion of photons, traveling through leaves can be absorbed. Finally, comparison of the structure of equations for absorptance and transmittance indicates that in the case of turbid medium species interact significantly, while in the case of structured medium they are radiatively decoupled. Overestimation of species radiative coupling in the turbid medium model take place because this model neglects spatial clumping of species.

Linear Mixing Assumption: Multiple land algorithms utilized for estimation of land cover mixture from coarse resolution satellite data rely on the empirical model of linear mixture of species [DeFries et al., 1999]. Under this assumption canopy spectral reflectance of a mixed pixel is expressed as a linear combination of canopy spectral reflectances of pure species. The linear mixture model ignores species radiative coupling. This coupling in a natural canopy is caused by multiple scattering, that is, after interaction with phytoelements of the first species, photon is scattered into another species.

The SMRT model can be reduced to the linear mixture model, and allows analysis of empirical assumptions of the latter. Indeed, according to Eq. (34), mean radiation over mixed pixel, $\bar{I}(z,\underline{\Omega})$, is equal to a weighted average of the radiation fields over pure species, $U^{(i)}(z,\underline{\Omega})$, and gaps, $U^{(gap)}(z,\underline{\Omega})$. However, $U^{(i)}(z,\underline{\Omega})$ are coupled though system of Eq. (13). In order to derive the linear mixture model from the SMRT model one needs to break the coupling, that is, set to 0 the conditional pair-correlation function for different species, $K^{(i,j)}=0$, when $i \neq j$. This assumption apparently violates the basic geometry constraints on $K^{(i,j)}$ (i.e., Eqs. (22)-(23) in the case of no gaps), and intuitively one may expect that non-physical decoupling may result in the violation of energy conservation law. However this is not true. To demonstrate this, consider system of Eq. (12), where $U^{(i)}(z,\underline{\Omega})$ are derived from Eq. (13), formulated for single species 'i' (more precisely, mixture of species 'i' and gaps). Equation (12) can be rewritten in a short form as

$$\begin{cases} \bar{I}^{(total)}(z) - \bar{I}^{(total)}(0) = \sum_j \Psi^{(j)}(z), & \mu < 0, \\ \bar{I}^{(total)}(z) - \bar{I}^{(total)}(H) = \sum_j \Psi^{(j)}(z), & \mu > 0, \end{cases} \tag{44}$$

where $\Psi^{(j)}(z)$ corresponds to the terms under the sign of sum over species in Eq. (12), $\bar{I}^{(total)}(z)$ is the mean intensity over whole mixture at height z, and $\bar{I}^{(total)}(0)$ ($\bar{I}^{(total)}(H)$) corresponds to boundary value at the canopy top (bottom). The $\Psi^{(j)}(z)$ functions are available from Eq. (12), formulated for single species 'j':

$$\begin{cases} \bar{I}^{(j)}(z) - \bar{I}^{(j)}(0) = \Psi^{(j)}(z), & \mu < 0, \\ \bar{I}^{(j)}(z) - \bar{I}^{(j)}(H) = \Psi^{(j)}(z), & \mu > 0. \end{cases} \tag{45}$$

Combining Eqs. (44) and (45) we have

$$\begin{cases} \bar{I}^{(total)}(z) = \sum_j [\bar{I}^{(j)}(z) - \bar{I}^{(j)}(0)] + \bar{I}^{(total)}(0), & \mu < 0, \\ \bar{I}^{(total)}(z) = \sum_j [\bar{I}^{(j)}(z) - \bar{I}^{(j)}(H)] + \bar{I}^{(total)}(H), & \mu > 0. \end{cases} \tag{46}$$

Next, we integrate Eq. (46) over lower and upper hemispheres to evaluate reflectances, R, and transmittances, T, and substitute the results into the energy conservation law (Chapter 7),

$$\begin{aligned} & R + A + (1-\rho)T = \\ & = \sum_j [R^{(j)} - R^{(j)}(H)] + R^{(total)}(H) + \sum_j A^{(j)} + (1-\rho)\sum_j [T^{(j)} - T^{(j)}(0)] + (1-\rho)T^{(total)}(0) = \\ & = \sum_j [R^{(j)} + A^{(j)} + (1-\rho)T^{(j)}] - \sum_j [R^{(j)}(H) + (1-\rho)T^{(j)}(0)] + R^{(total)}(H) + (1-\rho)T^{(total)}(0) \\ & = n - \sum_j [R^{(j)}(H) + (1-\rho)T^{(j)}(0)] + R^{(total)}(H) + (1-\rho)T^{(total)}(0). \end{aligned} \tag{47}$$

In the last transformation we utilized the fact that the energy conservation law is valid for the single-species problem, that is,

$$R^{(j)} + A^{(j)} + (1-\rho)T^{(j)} = 1.$$

Therefore, for the special case of the BS-problem (cf. Chapter 7), we have

$$F^{(j)}(0) = F^{(total)}(0) = 1, \quad F^{(j)}(H) = F^{(total)}(H) = 0, \quad \rho = 0, \quad \Rightarrow \quad R + A + (1-\rho)T = 1,$$

and for the S-problem (cf. Chapter 7),

$$F^{(j)}(0) = F^{(total)}(0) = 0, \quad F^{(j)}(H) = F^{(total)}(H) = 1, \quad \rho = 0, \quad \Rightarrow \quad R + A + (1-\rho)T = 1.$$

Finally, from the validity of the energy conservation law for BS- and S- problems it follows the validity of this law for the total problem (cf. Chapter 7). Therefore, while radiative decoupling of vegetation species is physically meaningless, it is still a mathematically valid exercise and may describe RT processes in some other medium.

To summarize, the results of this and previous sections indicate that the linear mixture model ignores, while turbid medium overestimates species radiative coupling compared to a realistic

description of the SMRT model. The effect of radiation coupling will be further studied numerically in the next section.

2.4. Numerical Analysis

In the following we numerically investigate features of the SMRT model by comparison to the turbid medium (TM) model. Both cases were implemented with the same set of stochastic equations and input parameters, except the conditional pair-correlation function: Eq. (24) was used to implement the SMRT model, and Eq. (21) for the TM model.

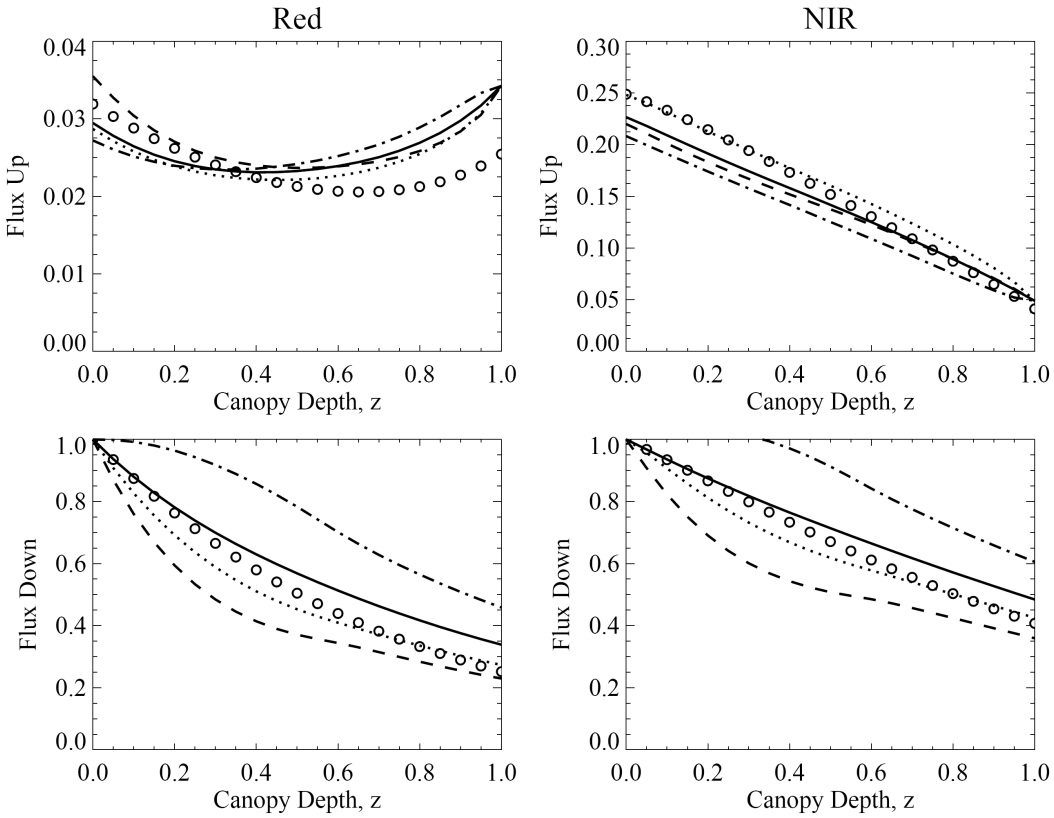

Figure 5. Comparison of vertical profiles of up and down radiation fluxes as simulated by the TM and SMRT models for mixture of two species and gaps. The SMRT model captures spatial variation of fluxes between species 1 (dashed line), species 2 (dotted line), and gaps (dash-dot line) and also evaluates average flux over whole mixture (solid line). The TM model estimates only average flux over whole mixture (hollow dots). The models parameters are as follows: $p^{(1)}= 0.40$, $p^{(2)}=0.20$; $d_L{}^{(1)}= 4$, $d_L{}^{(2)}= 6$; $\omega^{(1)}(\mathrm{Red})=0.12$, $\omega^{(2)}(\mathrm{Red})= 0.20$, $\omega^{(1)}(\mathrm{NIR}) =0.90$, $\omega^{(2)}(\mathrm{NIR})= 0.60$; $\rho_{soil}(\mathrm{Red})= \rho_{soil}(\mathrm{NIR})=0.10$; direct incoming flux, SZA=15^0.

To understand the overall merits of the SMRT model, consider radiation fluxes as function of canopy depth, as shown in Fig. 5. The SMRT model differentiates between radiation fluxes over

individual species, gaps, and whole mixture (corresponding to mean intensities $U^{(i)}$, $U^{(gap)}$ and $\bar{I}$), while the TM model provides no distinction between the above fluxes (cf. Section 2.3). According to the SMRT model, variation of the fluxes between individual vegetation species is relatively smaller compared to difference in fluxes between vegetation and gaps. Also note, that limitations of the TM model result in a bias (both overestimation and underestimation) in estimation of mean fluxes over whole mixture compared to the SMRT simulations (compare fluxes over whole mixture). Detailed analysis of the impact of various parameters on the SMRT and TM models simulations is presented with six case studies below (Figs. 6-11).

First, consider impact of Solar Zenith Angle (SZA) on canopy albedo, absorptance and transmittance as function of LAI, as simulated with the SMRT and TM models at Red and NIR wavelengths (Fig. 6). The simulations were performed with SZA of 0^0 and 60^0. Two vegetation species with gaps were used: $p^{(1)}=0.2$, $p^{(2)}=0.3$, $p^{(gap)}=0.5$. The complete set of parameters is presented in the figure caption. In the case of SZA=0^0, the SMRT model predicts lower albedo, substantially lower absorptance and substantially higher transmittance compared to the TM model. However, in the case of SZA=60^0 both models demonstrate quite similar results. The key physical explanation for the difference between the SMRT and TM simulations at SZA=0^0 is that the SMRT model accounts for radiation streaming through gaps without interaction with vegetation (Fig. 4). This explains results for absorptance and transmittance. Albedo is lower in the case of the SMRT compared to the TM model, because in the former case a dark soil is better exposed through gaps in a relatively bright vegetation (compare ρ_{soil} and ω). Next, note that the numerical simulations for absorptance and transmittance at Red wavelength closely follow analytical expressions, derived for uncollided radiation for SZA=0^0 (cf. Section 2.3). For instance, in the case of high LAI, transmittance from the SMRT model approaches $1-(p^{(1)}+ p^{(2)})$ (Eq. (42)), while transmittance from the TM model converges to 0 (Eq. (38)). Next, we explain results for SZA=60^0. In this case the effect of radiation streaming is negligible: even if photon enters canopy through a gap, it will be intercepted by a lateral surface of a tree foliage. Mathematically, the reasoning is as follows: as angle is increasing, effective distance between vegetation elements, Δ, is increasing (cf. Eq. (24)), which results in convergence of the conditional pair-correlation function for ordered species to one for non-ordered species (Fig 3).

Second, consider the impact of soil reflectance on the radiation quantities (Fig. 7). Set of parameters for this case study was similar to the previous one, except SZA is fixed and equal to 0^0, while two soil albedos (0 and 1) were used. Note the special feature of the canopy albedo for high LAI: in the case of the TM model, albedo converges to a single value, independently from soil albedo, while such convergence does not exist in the case of the SMRT model. This is another effect, associated with radiation streaming through gaps. Next, consider results for absorptance. Canopy absorptance is increasing with increasing soil albedo, and such effect is more pronounced for the SMRT model. The physical explanation for this is that some portion of the total radiation can stream through the gaps to the canopy bottom without being absorbed. If

soil is bright, this radiation is bounced back and receives a second chance to be absorbed by a canopy. However, if soil is dark, this mechanism is vanishing. Finally, consider results for transmittance. In the case of Red wavelength, soil albedo has virtually no effects on transmittance both for the TM and SMRT models. In the case of NIR wavelength, higher soil reflectance results in a higher transmittance and this effect is enhanced in the SMRT simulations due to radiation streaming through gaps.

Third, consider the impact of species composition on a radiation regime (Fig. 8). Here we used two species with optical properties roughly corresponding to broadleaf (species 1) and needle leaf (species 2) forests, which have substantial contrast both at Red and NIR wavelengths. The probability of each species ($p^{(1)}$ and $p^{(2)}$) was varying from 0 up to 0.6, under restriction, that total probability of all species is constant through the simulations, i.e., $p^{(1)}+ p^{(2)}=0.6$=fixed. Thus, radiation regime was evaluated for all possible combinations of two species under significant amount of gaps, $p^{(gap)} =0.4$=fixed. Results indicate that both the TM and SMRT models simulate continuous, fairly large variation of canopy albedo, absorptance and transmittance with respect to species composition. However, the TM model introduces a significant bias in the estimation of the above parameters due to ignoring canopy structure. Finally, note that variations of canopy albedo, absorptance and transmittance with respect to species compositions are quite close to linear at Red wavelength, but demonstrate fairly large deviation from linearity at NIR wavelength. Note that linearity for absorptance with respect to species composition can be seen in Eqs. (39) and (43) in the case of high LAI.

Fourth, consider the role of gaps in a radiation regime (Fig. 9). Simulations were performed for two species under constrain that the probabilities of both species are equal and its sum is varying between 0 (only gaps) and 1 (only vegetation). The SMRT model is not equivalent to the TM model even in the limiting case of no gaps (cf. Section 2.3). Results for canopy albedo are as follows. Albedo at Red wavelength is decreasing as gaps are replaced with vegetation, because albedo of leaves was selected to be comparable to soil albedo, however, when more leaves are introduced, they trap radiation, scattered within canopy, more efficiently. Also, canopy albedo for the TM and SMRT models are approximately equal at Red wavelength. However, at NIR wavelength albedo is increasing with decreasing amount of gaps, and the TM model predicts higher albedo compared to the SMRT model. The physical reason for this is that at NIR wavelength leaves are brighter then soil, and therefore, increasing amount of leaves will increase albedo. Additionally, vegetation gas of the TM model efficiently covers soil, compared to discontinuous canopy with gaps in the SMRT model, which results in further enhancement of albedo in the TM model compared to the SMRT model. Next, the simulations indicate that overestimation of absorptance by the TM model compared to the SMRT model is directly proportional to the gap fraction/clumping of species. Finally, results for canopy transmittance indicate that as amount of gaps is decreasing, transmittance, evaluated by the SMRT model converges to one for the TM model.

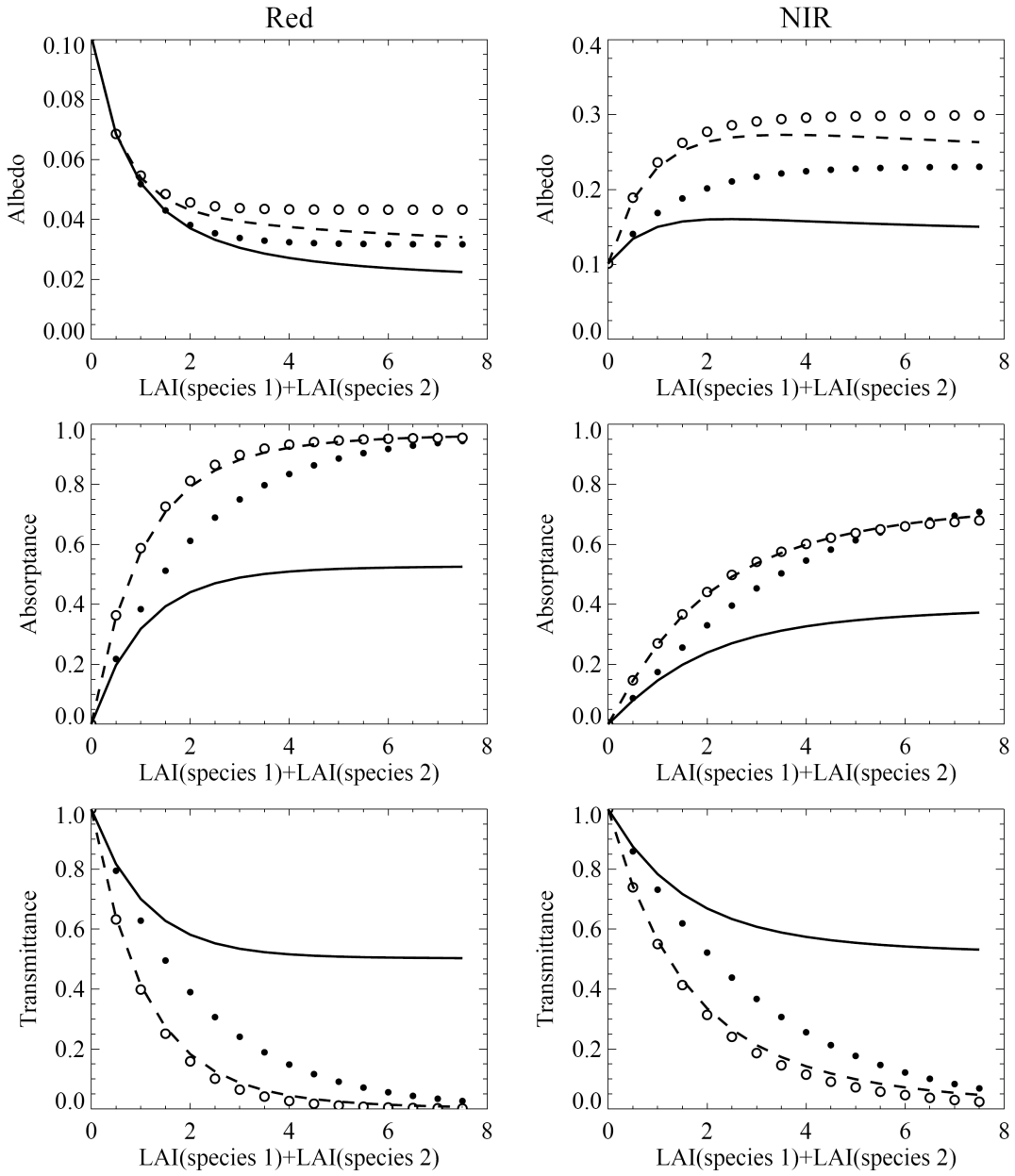

Figure 6. Impact of SZA on canopy albedo, absorptance and transmittance, as evaluated with the TM (dots) and SMRT (lines) models. Runs for direct incoming flux with SZA=0^0 and =60^0 are marked with solid style and style with holes, respectively. The other parameters are as follows: $p^{(1)}$= 0.20, $p^{(2)}$=0.30; $d_L{}^{(1)}$= $d_L{}^{(2)}$= [0.0-16.0]; $\omega^{(1)}(\mathrm{Red})$=0.12, $\omega^{(2)}(\mathrm{Red})$=0.20, $\omega^{(1)}(\mathrm{NIR})$ =0.90, $\omega^{(2)}(\mathrm{NIR})$= 0.60; $\rho_{soil}(\mathrm{Red}) = \rho_{soil}(\mathrm{NIR})$=0.10.

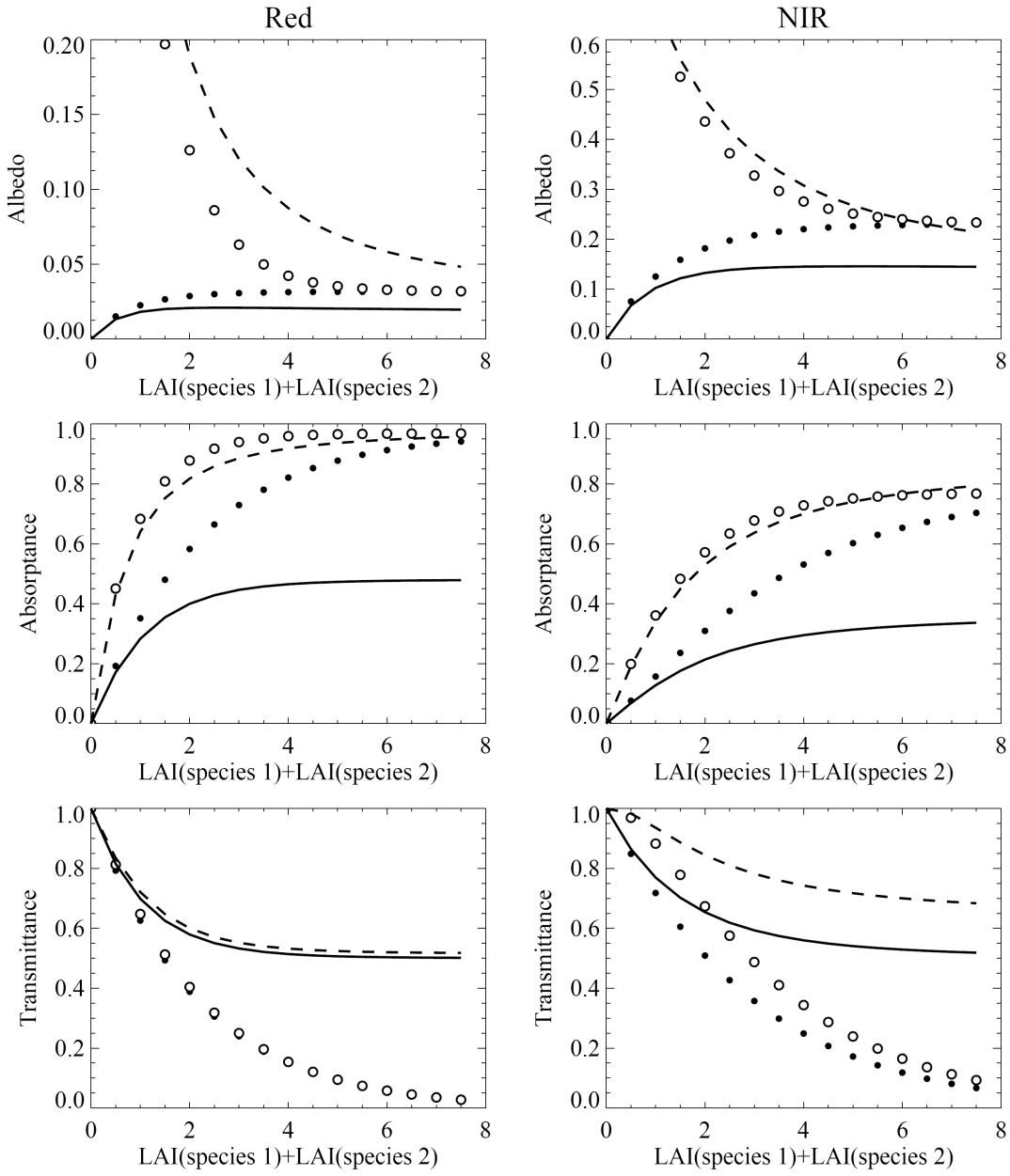

Figure 7. Impact of soil reflectance on canopy albedo, absorptance and transmittance, as evaluated with the TM (dots) and SMRT (lines) models. Runs with soil reflectance $\rho_{soil}(\mathrm{Red}) = \rho_{soil}(\mathrm{NIR}) = 0.0$ and =1.0 are marked with solid style and style with holes, respectively. The other parameters are as follows: $p^{(1)}=0.20$, $p^{(2)}=0.30$; $d_L{}^{(1)} = d_L{}^{(2)} = [0.0\text{-}16.0]$; $\omega^{(1)}(\mathrm{Red})=0.12$, $\omega^{(2)}(\mathrm{Red})=0.20$, $\omega^{(1)}(\mathrm{NIR}) = 0.90$, $\omega^{(2)}(\mathrm{NIR}) = 0.60$; direct incoming flux, SZA=0^0

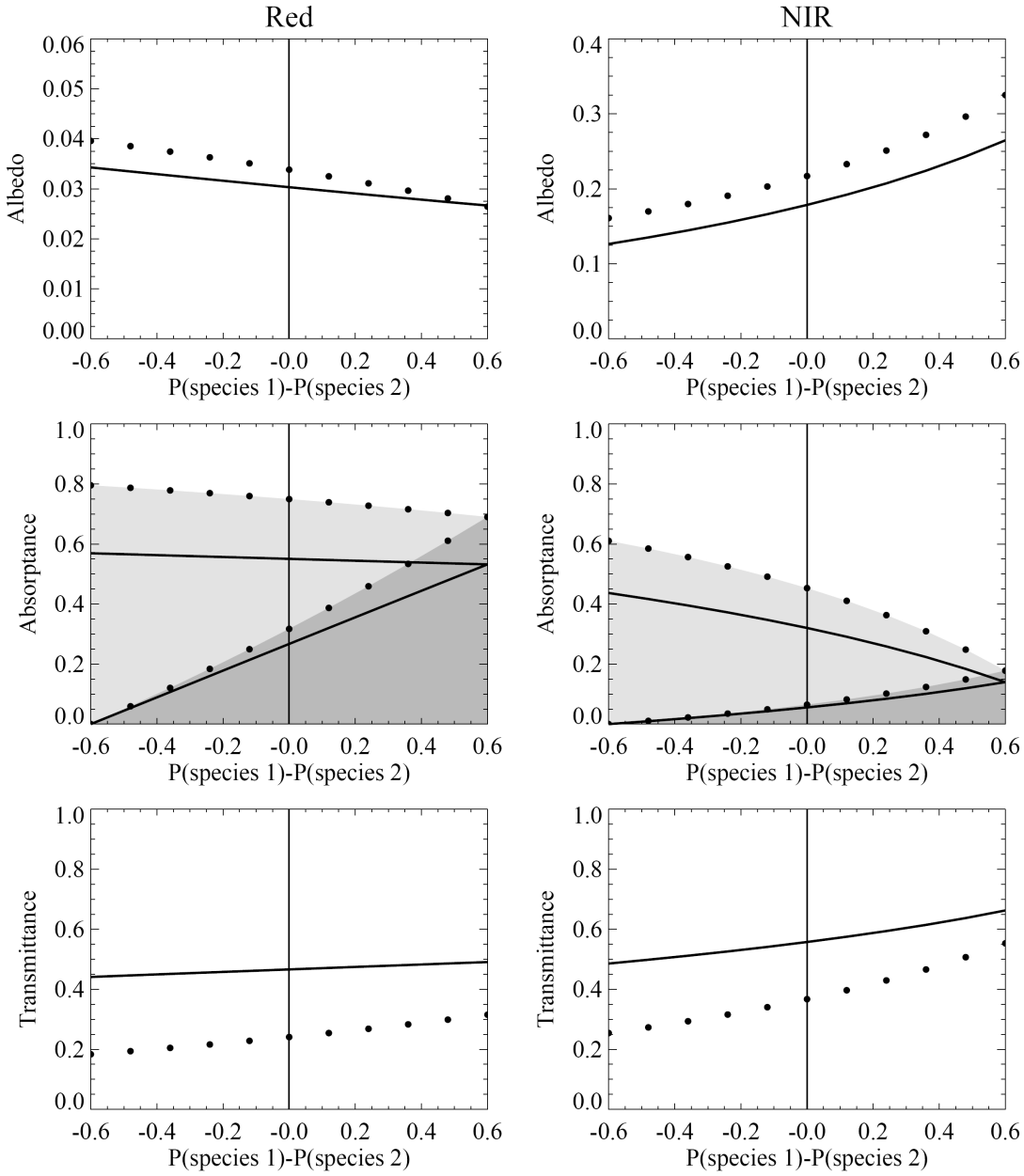

Figure 8. Impact of species composition on canopy albedo, absorptance and transmittance, as evaluated with the TM (dots) and SMRT (lines) models for the case of mixture of two species. The models parameters are as follows: $p^{(1)}+p^{(2)}=0.60$; $d_L{}^{(1)}=4.0$, $d_L{}^{(2)}=6.0$; $\omega^{(1)}(\mathrm{Red})=0.12$, $\omega^{(2)}(\mathrm{Red})=0.20$, $\omega^{(1)}(\mathrm{NIR})=0.90$, $\omega^{(2)}(\mathrm{NIR})=0.60$; $\rho_{soil}(\mathrm{Red})=\rho_{soil}(\mathrm{NIR})=0.10$; direct incoming flux, SZA=0^0. Shaded areas highlight absorptance of individual species in the case of the TM model simulations.

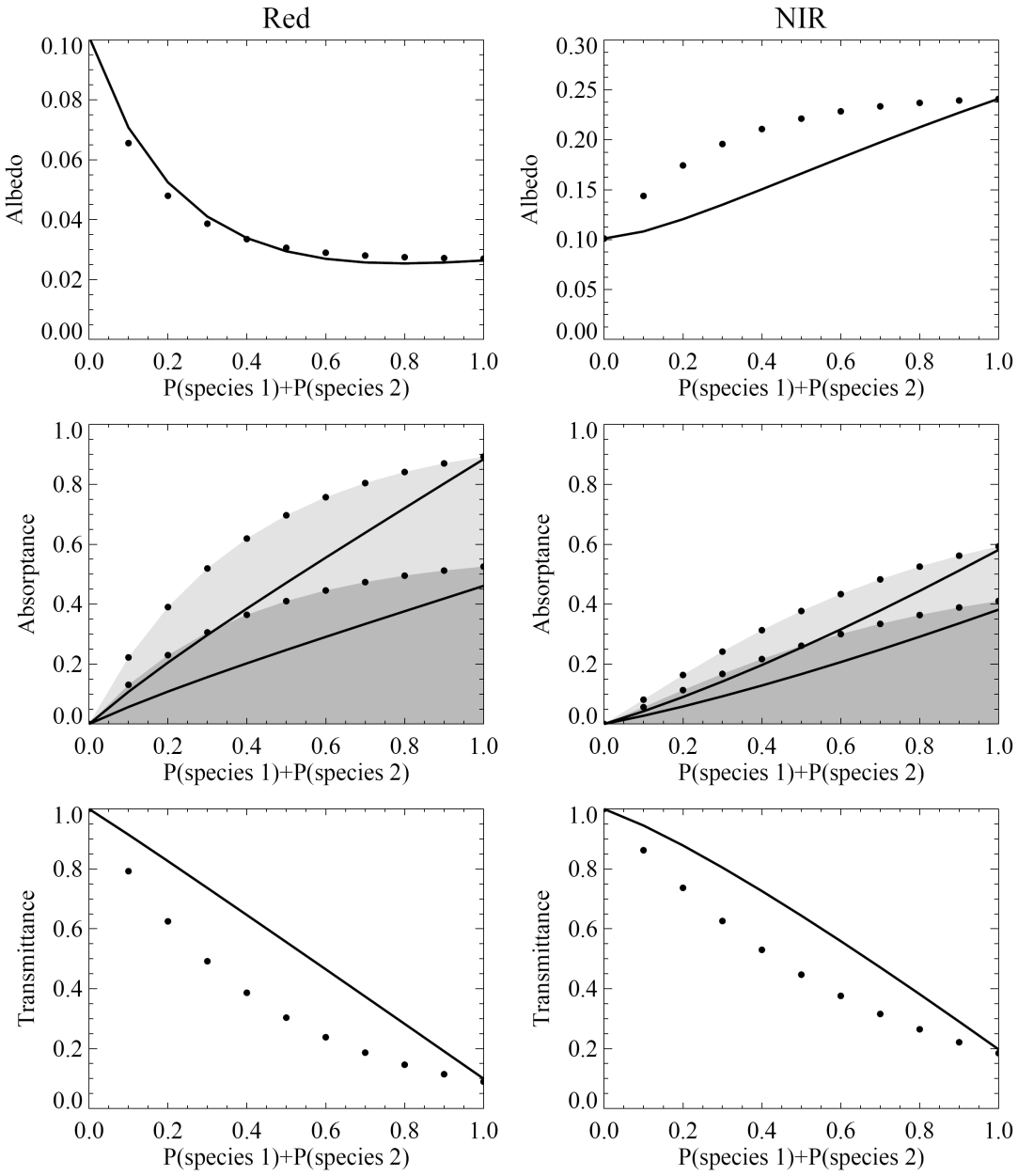

Figure 9. Impact of gaps on canopy albedo, absorptance and transmittance, as evaluated with the TM (dots) and SMRT (lines) models for the case of mixture of two species. The models parameters are as follows: $p^{(1)}=p^{(2)}=[0.0\text{-}0.5]$; $d_L{}^{(1)}=4.0$, $d_L{}^{(2)}=6.0$; $\omega^{(1)}(\mathrm{Red})=0.12$, $\omega^{(2)}(\mathrm{Red})=0.16$, $\omega^{(1)}(\mathrm{NIR})=0.80$, $\omega^{(2)}(\mathrm{NIR})=0.70$; $\rho_{soil}(\mathrm{Red})=\rho_{soil}(\mathrm{NIR})=0.10$; direct incoming flux (SZA=0^0). Shaded areas highlight absorptance of individual species in the case of the TM model simulations.

In the fifth case study we probed deeper special case of mixture of species without gaps (Fig. 10). Intuitively, in the case of no gaps, ordered mixture of species is quite close to non-ordered mixture (turbid medium). In this simulation we addressed two questions: a) When ordered mixture of species is important? b) Why gaps significantly perturb radiation field of ordered mixture of species? As mentioned earlier, key feature of vegetation structure, which differentiates between ordered and non-ordered cases is a presence of spatial gradient of optical properties of a medium (such as leaf albedo, density of LAI, etc). If the medium is ordered, the spatial gradient of the optical properties should be significant enough to modify the radiation regime of the SMRT simulations with respect to the TM simulations. Optical properties of gaps constitute especially large contrast to ones of any vegetation species. This explains special role of gaps in the SMRT simulations. The variation of the optical properties of vegetation species is as follows: leaf albedo may vary by factor of 2 in majority of cases, while variation in the foliage area volume density may be arbitrary large. Our test runs (not presented here) indicate no significant difference between the SMRT and TM simulations as function of variations of leaf albedo for typical vegetation canopies. Simulations for two species with varying foliage area volume density ($d_L^{(1)}$ and $d_L^{(2)}$) indicate significant bias in the estimation of absorptance by the TM model with respect to the SMRT model when $d_L^{(2)}/d_L^{(1)}=0$, no difference when $d_L^{(2)}/d_L^{(1)}=1$, and increasing bias with respect to increasing contrast in the foliage area volume density of species (Fig. 10). Note that the TM model introduces bias not only to total absorptance but also to the partitioning of total canopy absorptance between species.

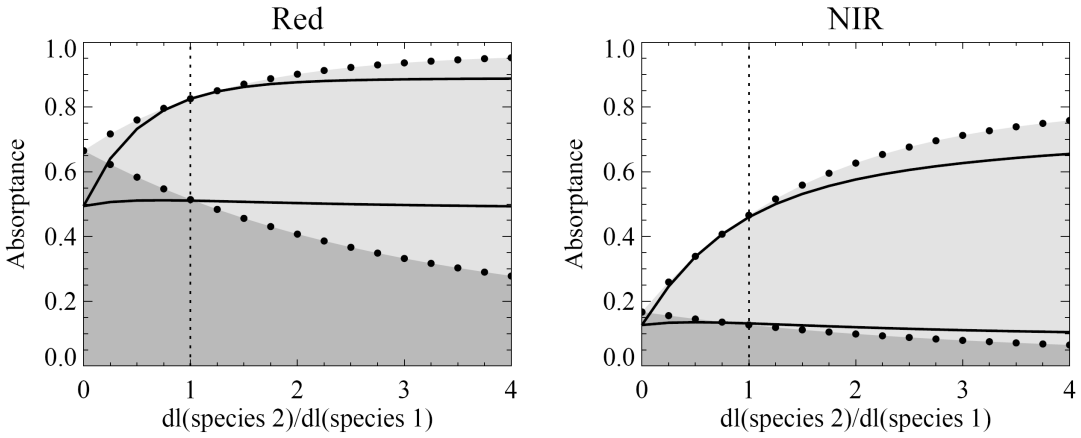

Figure 10. Impact of species LAI density on partitioning of total absorptance between individual species, as evaluated with the TM (dots) and SMRT (lines) models for the case of mixture of two species. The models parameters are as follows: $p^{(1)}=0.4$, $p^{(2)}= 0.6$; $d_L^{(1)}=4.0$, $d_L^{(2)}= [0.0\text{-}16.0]$; $\omega^{(1)}(\mathrm{Red}) =0.12$, $\omega^{(2)}(\mathrm{Red}) =0.20$, $\omega^{(1)}(\mathrm{NIR})=0.90$, $\omega^{(2)}(\mathrm{NIR})= 0.60$; $\rho_{soil}(\mathrm{Red})= \rho_{soil}(\mathrm{NIR})=0.10$; direct incoming flux, SZA=0^0. Shaded areas highlight absorptance of individual species in the case of the TM model simulations

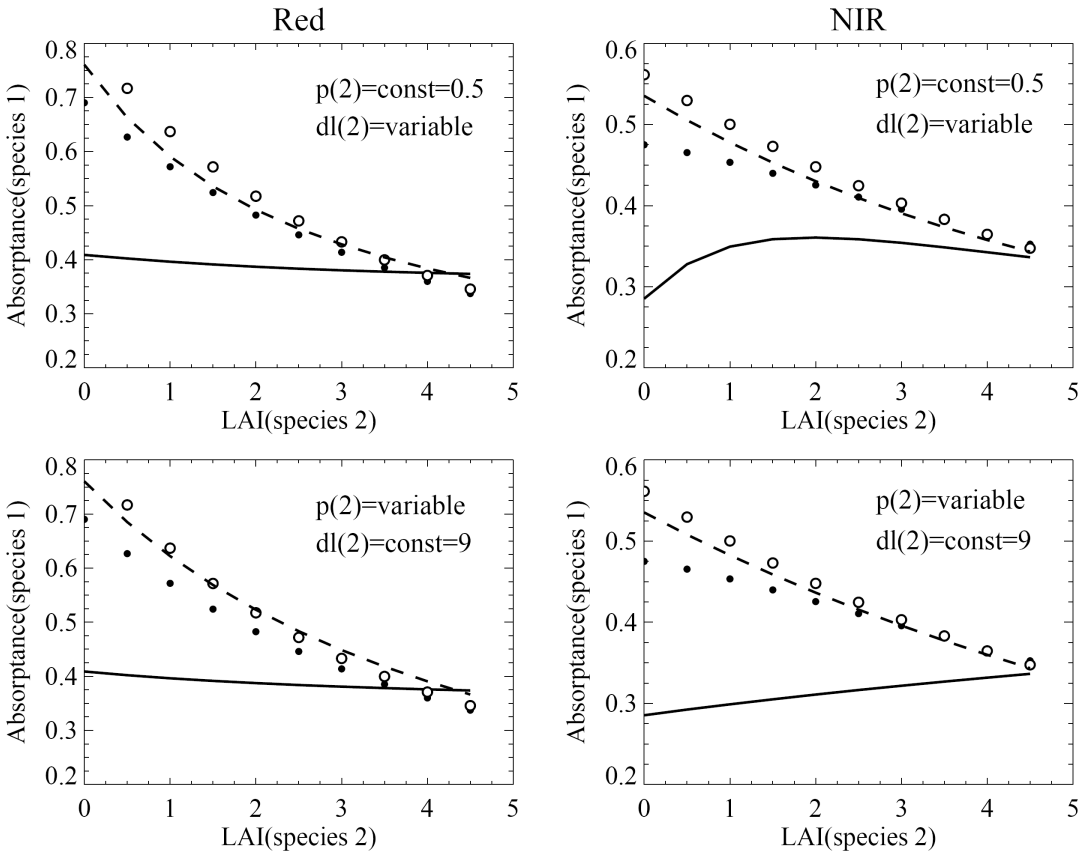

Figure 11. Impact of species interaction on canopy absorptance, as evaluated with the TM (dots) and SMRT (lines) models. Runs for direct (SZA=0^0), and diffuse incoming fluxes are marked with solid style and style with holes, respectively. The other parameters are as follows: $p^{(1)}$=0.4, $p^{(2)}$= 0.5 or variable; $d_L{}^{(1)}$=6.0, $d_L{}^{(2)}$=9.0 or variable; $\omega^{(1)}(\mathrm{Red})$= 0.12, $\omega^{(2)}(\mathrm{Red})$=0.16, $\omega^{(1)}(\mathrm{NIR})$ =0.60, $\omega^{(2)}(\mathrm{NIR})$= 0.80; $\rho_{soil}(\mathrm{Red})$= $\rho_{soil}(\mathrm{NIR})$=0.10.

Next, consider the sixth case study, demonstrating the effect of species radiative interaction (Fig. 11). Here we evaluated the impact of LAI changes of species 2 on the absorptance of species 1. The LAI of species 2 was constructed according to two scenarios: a) keep $p^{(2)}$ constant and vary $d_L{}^{(2)}$ (top two panels for Red and NIR wavelengths); b) keep $d_L{}^{(2)}$ constant and vary $p^{(2)}$ (lower panels). We also used two illumination conditions: purely direct incoming flux, SZA=0^0; and purely diffuse incoming flux. The results indicate, that absorptance of species 1 decreases by factor of two both at Red and NIR wavelengths as LAI of species 2 is changing from 0 to 4 in the case of the TM model under direct illumination. In contrast, the SMRT model predicts no significant variations in the absorptance of species 1 at Red wavelength, and increase by about 15% in the case of NIR wavelength under direct illumination. In the case of diffuse illumination the SMRT and TM models predict similar interaction of species- decrease of the absorptance of the first species as LAI of the second is increasing. This last result of this case study match the results of the first case study: under diffuse illumination or low SZA, the simulations by both

models converge. Overall, this last case study demonstrates that natural mixture of discontinuous species exhibit less radiative coupling compared to the turbid medium approximation.

The final comment is on the overall performance of the SMRT model. The SMRT code is computationally compact- CPU requirements are similar to those for the solution of 1D RT code [Shabanov et al., 2000]. Computational errors increase with increasing LAI, SZA, which is typical for majority of the RT models. Additional errors, specific to the SMRT, can be accumulated under the condition of large number of species with highly varying optical properties. Presently the performance of the model was not evaluated with respect to field measurements, this should be done in the future utilizing the required set of structured parameters and radiation measurements of sufficiently high accuracy. Nevertheless, confidence in the SMRT model performance should be drawn from the fact, that the mixture model extends the one for single species, which was extensively evaluated with field measurements and was utilized in multiple applications in the past [Huang et al., 2007; Kotchenova et al., 2003; Shabanov et al., 2000, 2005].

2.5. Summary

The application of the stochastic approach for remote sensing of vegetation mixtures was introduced. The Stochastic Mixture RT (SMRT) model describes radiation regime in a heterogeneous vegetation canopy with spatially varying optical properties. The SMRT model provides a general solution of the mixture problem, which includes, as special cases, the major approximate solutions, including the linear mixture and turbid medium mixture RT models. The SMRT model solves for the radiation quantities, direct input to remote sensing/climate applications: mean fluxes over mixture and over individual species. The canopy structure is parameterized in the SMRT model in terms of two stochastic moments: the probability of finding species and the conditional pair-correlation of species. The second moment is responsible for the 3D radiation effects, namely, radiation streaming through gaps without interaction with vegetation and variation of the radiation fluxes between different species. If the within- and between- species correlation is vanishing, the SMRT model reduces to the turbid medium RT model. Namely, this situation is realized in the SMRT simulations under direct illumination with low SZA or diffuse illumination. If the between- (but not within-) species correlation is set to zero, the SMRT model reduces to the linear mixture model. The analysis of the SMRT simulations indicates that the variation of radiation fluxes between different species is proportional to the variation of optical properties of species (leaf albedo, density of foliage, etc.) Gaps introduce significant disturbance to the radiation regime in the mixed canopy as their optical properties constitute a major contrast to those of any vegetation species. Set of accurate field measurements on canopy structure and radiation is required to further assess performance of the SMRT model and to improve modeling of the pair-correlation function.

3. Time-dependent Stochastic Radiative Transfer

3.1. Lidar Remote Sensing

Active remote sensing complements and enhances passive remote sensing measurements of the 3D canopy structure. In general, signals recorded by passive sensors, operating at visible and mid-infrared wavelength, undergo influence of a range of physical factors, including atmospheric contamination, background scattering and effect of view-illumination geometry. Thus passive remote sensing measurements have to be corrected before attempting retrievals of the canopy structure. Some of the above problems can be eliminated (however new challenges arises) with the use of major types of active remote sensing instruments, including active Synthetic Aperture Radar (SAR) systems, and small and large footprint laser altimeters. Like passive optical systems, SAR polarimetry systems map well the horizontal organization of vegetation, however fail to provide direct information on its vertical distribution. In the case of the small footprint lidars, the small-diameter beams frequently miss the top of vegetation in sparse canopies, while in dense canopies, it is difficult to determine whether a particular shot has penetrated through the canopy and reached the ground. A new class of instruments, large footprint waveformrecording laser altimeters (lidars), has demonstrated a potential to significantly improve remote estimates of *vertical forest structure* [Drake et al., 2002a-b; Lefsky et al., 1999a-b, 2002]. The group of existing large footprints lidars includes two air-borne instruments, the formerly utilized Scanning Lidar Imager of Canopies by Echo Recovery (SLICER) and current instrument, Laser Vegetation Imaging Spectrometer (LVIS), and the space-borne Geoscience Laser Altimeter System (GLAS), onboard the ICESat satellite. Another space-borne instrument, Vegetation Canopy Lidar (VCL), is under development presently.

SLICER transmits short-duration pulses (4 ns pulse width at the half of the amplitude) with a beam divergence of approximately 2 mrad at frequency of 80 Hz. It operates in NIR wavelengths (1064 nm). The energy transmitted per pulse is about 0.7 mJ. The SLICER footprint distribution pattern on the ground is a swath consisting of five contiguous footprint lines along the direction of flight. Each footprint is approximately 9 m in diameter. The diameter of the area covered by the telescope field-of-view (FOV) is five times as much as the laser footprint diameter. The telescope FOV is aligned to seize five contiguous cross-track footprints [Harding et al., 2000; Lefsky et al., 1999a].

LVIS is an advanced version of SLICER. It emits Gaussian-shaped pulses with 10 ns pulse-width at repetition rates of up to 500 Hz in the NIR wavelengths (1064 nm). The energy transmitted per pulse is about 5 mJ. The LVIS telescope FOV significantly exceeds that for SLICER, 7^0 versus 2^0, which allows it to operate in a number of different modes. Footprint sizes from 1 to 80 m are possible, determined by the altitude of the airplane and the focal length of a diverging lens in the output path. The distance between adjacent footprints can be changed both

along and across track. A standard sampling pattern consists of parallel 1-km wide swaths generated using 30-40 25-m wide footprints separated by 10-20 m along and across track [Blair & Hofton, 1999].

GLAS instrument onboard the ICESat platform provides continuous global measurements along the 183-day repeat tracks with a maximum cross-track separation of 15 km at the equator. Pulses are emitted at rate of 40 Hz with pulse width of 5 ns in NIR (1064 nm). Large, non-contiguous GLAS footprints with the diameter of ~ 70 m are not optimized for retrieval of vegetation structural parameters. The primary goal of the ICESat mission is to measure ice, ocean and land elevation and cloud structure. Nevertheless, as the GLAS waveforms have high vertical resolution (of 15 cm) and good signal-to-noise ratio, some vegetation structural parameters are possible to retrieve where the ground and canopy echoes can be decomposed [Zwally et al., 2002].

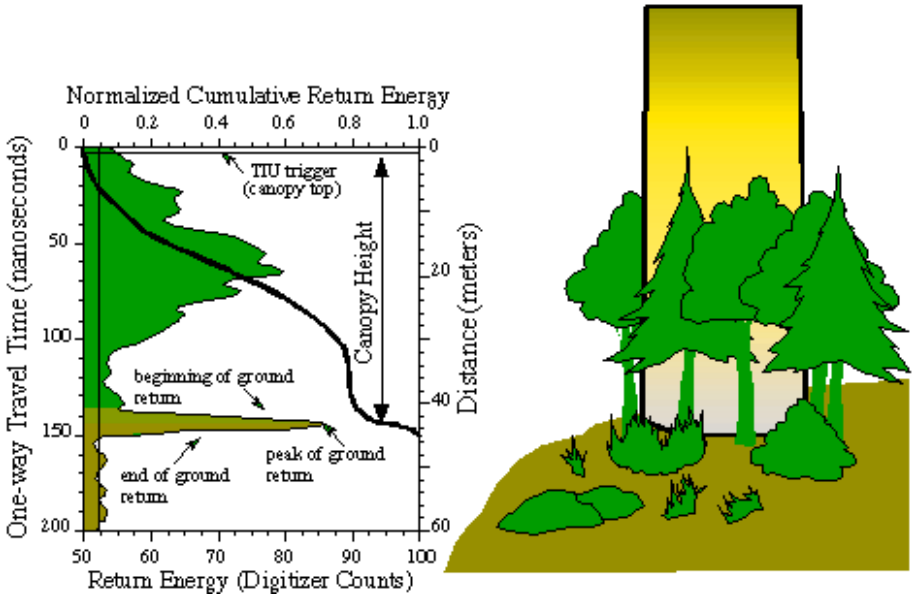

Figure 12. Schematic plot of lidar waveform measurements with the SLICER instrument. (Graphycs credit: Dr. Harding, NASA GSFC).

Lidar instruments operate according to the following general scheme. A short-duration laser pulse is sent from the zenith to nadir, and then the amplitude of reflected energy is recorded as a function of time. The obtained distribution of intercepted surfaces with height is referred to as *lidar waveform* (Fig. 12). The first significant return above a noise threshold is used to estimate the top of the canopy, the midpoint of the last return represents the reflection from the ground, and canopy height is calculated as the distance between these two returns [Harding et al., 2001]. The amplitude of the recorded waveform measures the strength of the return. For surfaces with similar reflective properties and geometry within a footprint, the larger amplitude indicates more canopy material.

Current applications of the large-footprint lidars fall into three main categories: remote sensing of the ground topography, measurement of the three-dimensional canopy structure, and

estimation of forest structural attributes [Lefsky et al., 2002; Dubayah et al., 2000]. Canopy height and ground elevation are the only parameters that are measured by the lidars directly. Other structural attributes biomass and *canopy height profiles* (*CHP*s), or the distribution of canopy material with height requires apriory knowledge and modeling.

The current algorithm for retrieval of CHPs from lidar-recorded signals [Lefsky et al., 1999a; Harding et al., 2001] suffers from two significant drawbacks. The algorithm was developed following the main principles of MacArthur & Horn [1969] for estimation of foliage height profiles (FHPs) in broadleaf forests. It is based on the simplifying assumptions that (1) the horizontal distribution of leaves is uniform and (2) only single scattered photons contribute to the return signal. The assumption of uniform horizontal distribution ignores foliage clumping. However, due to foliage clumping more radiation is allowed to penetrate deeper into the canopy without being intercepted by foliage [Ni-Meister et al., 2001]. Additionally, a lidar pulse at NIR wavelengths is weakly absorbed and the returned waveform is affected by multiple scattering, especially in the case of dense forests [Govaerts, 1996]. One of the effects of multiple scattering in dense canopies is related to a significant enhancement of the lower part of the signal. The main reason for this effect is that the path of multiply scattered photons is longer than the straight line path between the instrument and the target and, thus, those photons appear delayed, compared to single-scattered photons. The significance of the effect of multiple scattering in lidar measurements is currently under debate presently [Blair & Hofton, 1999; Sun & Ranson, 2000].

Below we detail application of the stochastic approach for modeling of propagation of lidar signal in heterogeneous vegetation canopies. The stationary Stochastic RT equation for single species (Chapter 7) was extended to the Time-dependent Stochastic RT (TSRT) equation. The stochastic description of the process arises naturally due to the fact that large footprint lidars measure mean pulse intensity over the extended area of their footprints. Additionally, the stochastic equations allows to account for multiple scattering, realistic representation of forest structure including clumping and gaps, and simulation of off-nadir and multi-angular observations. The presentation is organized as follows. Starting form 3D Time-dependant RT equation we formulate the time-dependant stochastic equations. Next, the sensitivity study of the simulated non-stationary radiation regime is performed. Next, simulated waveforms are evaluated with respect to SLICER measurements over coniferous and mixed-deciduous stands and the impact of multiple scattering is assessed.

3.2. Model Formulation

3D RT Equation: Consider a single species heterogeneous vegetation canopy. A lidar beam illuminates a vertical vegetation stand of the diameter of the laser footprint. Due to the small divergence angle, photons can be assumed incident parallel on the top of the stand. The radiation

regime inside the canopy is strongly time-dependent due to the short duration of a lidar pulse. The propagation of photons through vegetation is described by the time-dependent 3D transport equation for radiation intensity, $I(t,\underline{r},\underline{\Omega})$, at time t, spatial location $\underline{r}$ and direction $\underline{\Omega}$:

$$\frac{1}{c}\frac{\partial I(t,\underline{r},\underline{\Omega})}{\partial t}+\underline{\Omega}\nabla I(t,\underline{r},\underline{\Omega})+\sigma(\underline{r},\underline{\Omega})\,I(t,\underline{r},\underline{\Omega})=\int_{4\pi}d\underline{\Omega}'\sigma_S(\underline{r},\underline{\Omega}'\to\underline{\Omega})\,I(t,\underline{r},\underline{\Omega}'), \tag{48}$$

where; $\sigma(\underline{r},\underline{\Omega})$ is the extinction coefficient, and $\sigma_S(\underline{r},\underline{\Omega}'\to\underline{\Omega})$ is the differential scattering coefficient [Ross, 1981]. Both coefficients are formulated in the same way as for stationary RT for singe heterogeneous species: $\sigma(\underline{r},\underline{\Omega})=\chi(\underline{r})\sigma(\underline{\Omega})$ and $\sigma_S(\underline{r},\underline{\Omega}'\to\underline{\Omega})=\chi(\underline{r})\sigma_S(\underline{\Omega}'\to\underline{\Omega})$ where $\sigma(\underline{\Omega})$ and $\sigma_S(\underline{\Omega}'\to\underline{\Omega})$ are coefficients for vegetated portion space, and $\chi(\underline{r})$ is a canopy indicator function (cf. Chapter 7). The unique solution of Eq. (48) is specified by *boundary and initial conditions*:

$$\begin{cases} I(t,\underline{r}_{xy},0,\underline{\Omega})=\begin{cases}0, & \underline{r}_{xy}\notin S_f,\quad \mu(\underline{\Omega}_0)<0,\\ f(t)\,\delta(\underline{\Omega}-\underline{\Omega}_0), & \underline{r}_{xy}\in S_f,\quad \mu(\underline{\Omega}_0)<0,\end{cases}\\ I(0,\underline{r},\underline{\Omega})=0, \quad 0<z<H,\\ I(t,\underline{r}_{xy},H,\underline{\Omega})=\dfrac{\rho_{soil}}{\pi}\displaystyle\int_{2\pi^-}d\underline{\Omega}'\,I(t,\underline{r}_{xy},H,\underline{\Omega}')\left|\mu(\underline{\Omega}')\right|, \quad \mu(\underline{\Omega})>0, \end{cases} \tag{49}$$

where $\underline{\Omega}_0$ is the direction of incoming radiation; $f(t)$ is a function characterizing pulse intensity; S_f is a footprint area; and $\rho_{soil}(\lambda)$ is the hemispherical reflectance of ground which is assumed to be a Lambertian surface.

Stochastic RT Equations: A procedure to derive Time-dependant Stochastic RT (TSRT) equations from time-dependant 3D equation is similar to one for stationary 3D equation for single species (Chapter 7). Following this procedure we derive equations for the mean intensities over total space, $\bar{I}(t,z,\underline{\Omega})$, and over vegetated areas, $U(t,z,\underline{\Omega})$. The system of equation for $\bar{I}(t,z,\underline{\Omega})$ is,

$$\begin{cases} \bar{I}(t,z,\underline{\Omega})+\dfrac{1}{|\mu(\underline{\Omega})|}\displaystyle\int_0^z\sigma(\underline{\Omega})p(\xi)U(t,\xi,\underline{\Omega})\,d\xi+\dfrac{1}{|\mu(\underline{\Omega})|}\dfrac{1}{c}\dfrac{\partial}{\partial t}\int_0^z\bar{I}(t,\xi,\underline{\Omega})d\xi\\ =\dfrac{1}{|\mu(\underline{\Omega})|}\displaystyle\int_0^z d\xi\,p(\xi)\int_{4\pi}\sigma_S(\underline{\Omega}'\to\underline{\Omega})U(t,\xi,\underline{\Omega}')\,d\vec{\Omega}'+\bar{I}(t,0,\underline{\Omega}), \quad \mu(\underline{\Omega})<0,\\ \bar{I}(t,z,\underline{\Omega})+\dfrac{1}{\mu(\underline{\Omega})}\displaystyle\int_z^H\sigma(\underline{\Omega})p(\xi)U(t,\xi,\underline{\Omega})\,d\xi+\dfrac{1}{\mu(\underline{\Omega})}\dfrac{1}{c}\dfrac{\partial}{\partial t}\int_z^H\bar{I}(t,\xi,\underline{\Omega})d\xi\\ =\dfrac{1}{\mu(\underline{\Omega})}\displaystyle\int_z^H d\xi p(\xi)\int_{4\pi}\sigma_S(\underline{\Omega}'\to\underline{\Omega})U(t,\xi,\underline{\Omega}')\,d\underline{\Omega}'+\bar{I}(t,H,\underline{\Omega}), \quad \mu(\underline{\Omega})>0. \end{cases} \tag{50}$$

The system of equations for $U(t,z,\underline{\Omega})$ is,

$$
\begin{cases}
U(t,z,\underline{\Omega}) + \dfrac{1}{|\mu(\underline{\Omega})|}\int\limits_0^z \sigma(\underline{\Omega})\,K(z,\xi,\underline{\Omega})\,U(t,\xi,\underline{\Omega})\,d\xi + \dfrac{1}{|\mu(\underline{\Omega})|}\dfrac{1}{c}\dfrac{\partial}{\partial t}\int\limits_0^z U(t,\xi,\underline{\Omega})d\xi \\
= \dfrac{1}{|\mu(\underline{\Omega})|}\int\limits_0^z d\xi\, K(z,\xi,\underline{\Omega})\int\limits_{4\pi}\sigma_S(\underline{\Omega}'\to\underline{\Omega})U(t,\xi,\underline{\Omega}')\,d\underline{\Omega}' + \bar{I}(t,0,\underline{\Omega}), \quad \mu(\underline{\Omega}) < 0, \\
U(t,z,\underline{\Omega}) + \dfrac{1}{\mu(\underline{\Omega})}\int\limits_z^H \sigma(\underline{\Omega})K(z,\xi,\underline{\Omega})U(t,\xi,\underline{\Omega})\,d\xi + \dfrac{1}{\mu(\underline{\Omega})}\dfrac{1}{c}\dfrac{\partial}{\partial t}\int\limits_z^H U(t,\xi,\underline{\Omega})\,d\xi \\
= \dfrac{1}{\mu(\underline{\Omega})}\int\limits_z^H d\xi K(z,\xi,\underline{\Omega})\int\limits_{4\pi}\sigma_S(\underline{\Omega}'\to\underline{\Omega})U(t,\xi,\underline{\Omega}')\,d\underline{\Omega}' + \bar{I}(t,H,\underline{\Omega}), \quad \mu(\underline{\Omega}) > 0.
\end{cases}
\tag{51}
$$

The averaging procedure leads to a parameterization of the TSRT equations in terms of the probability of finding vegetation elements at height z, p(z), and the conditional pair-correlation function of vegetation elements at two layers z and in direction in direction $\underline{\Omega}$, $K(z,\xi,\underline{\Omega})$ (cf. Chapter 7). Note that the boundary source terms in Eq. (51) are the same as in Eq. (50). The equality, $U(t,0,\underline{\Omega}) = \bar{I}(t,0,\underline{\Omega})$, follows from the assumption of a uniform horizontal distribution of incident laser energy. The equality $U(t,H,\underline{\Omega}) = \bar{I}(t,H,\underline{\Omega})$ follows from the assumption of homogeneity of the ground surface.

Two important issues related to Eqs. (50)-(51) need to be discussed. First, the integration is performed over the area approximately equal to the laser footprint area with 8.4 – 9.0 m in diameter for the coniferous sites and 10.4 – 11.0 m for the deciduous sites. As this area is relatively large, radiation fluxes through the lateral boundaries can be neglected and the concept of mean intensity is appropriate. Second, the spatial distribution of laser energy across the footprint has a circular, Gaussian distribution [Harding et al., 2000]. We approximate the Gaussian distribution with a uniform distribution in order to satisfy the requirements of a stochastic approach. The total amount of energy within the footprint area remains the same. It should be noted, in general, the use of the Gaussian and uniform distributions of incident energy would lead to different forms of the return. Within the chosen approach, however, a layer within vegetation is treated as a horizontal surface with averaged parameters characterizing its reflection and transmission properties. Thus, the model is sensitive only to the total amount of radiation incident at each layer and the Gaussian distribution can be replaced with the uniform distribution.

Separation of Direct and Diffuse Radiation: The procedure to derive equations for direct and diffuse components of mean radiation intensity over total space, $I(t,z,\underline{\Omega})$, and over vegetation, $U(t,z,\underline{\Omega})$, in the case of time-dependant equations is identical to that for stationary equations (cf. Chapter 7). We express the solution of Eq. (51) for $U(t,z,\underline{\Omega})$ as the sum of direct and diffuse components, that is,

$$
U(t,z,\underline{\Omega}) = U_\delta(t,z)\,\delta(\underline{\Omega}-\underline{\Omega}_0) + U_d(t,z,\underline{\Omega})\,. \tag{52}
$$

Substituting Eq. (52) into Eq. (51) and separating the terms with $\delta(\underline{\Omega}-\underline{\Omega}_0)$ results in an equation for the direct component,

$$U_\delta(t,z)+\frac{\sigma(\underline{\Omega}_0)}{|\mu(\underline{\Omega}_0)|}\int_0^z K(z,\xi,\underline{\Omega}_0)U_\delta(t,\xi)d\xi+\frac{1}{|\mu(\underline{\Omega}_0)|}\frac{1}{c}\frac{\partial}{\partial t}\int_0^z U_\delta(t,\xi)d\xi=f(t), \tag{53a}$$

where $f(t)$ characterizes the intensity of incoming radiation (cf. Eq. (49)). The diffuse component, $U_d(t,z,\underline{\Omega})$, satisfies the following equations:

$$\begin{cases} U_d(t,z,\underline{\Omega})+\dfrac{\sigma(\underline{\Omega})}{|\mu(\underline{\Omega})|}\displaystyle\int_0^z K(z,\xi,\underline{\Omega})U_d(t,\xi,\underline{\Omega})d\xi+\dfrac{1}{|\mu(\underline{\Omega})|}\dfrac{1}{c}\dfrac{\partial}{\partial t}\int_0^z U_d(t,\xi,\underline{\Omega})d\xi \\ =\dfrac{1}{|\mu(\underline{\Omega})|}\displaystyle\int_0^z K(z,\xi,\underline{\Omega})S(t,\xi,\underline{\Omega})d\xi \\ +\dfrac{\sigma_S(\underline{\Omega}_0\to\underline{\Omega})}{|\mu(\underline{\Omega})|}\displaystyle\int_0^z K(z,\xi,\underline{\Omega})U_\delta(t,\xi)d\xi, \quad \mu(\underline{\Omega})<0, \\ U_d(t,z,\underline{\Omega})+\dfrac{\sigma(\underline{\Omega})}{\mu(\underline{\Omega})}\displaystyle\int_z^H K(z,\xi,\underline{\Omega})U_d(t,\xi,\underline{\Omega})d\xi+\dfrac{1}{\mu(\underline{\Omega})}\dfrac{1}{c}\dfrac{\partial}{\partial t}\int_z^H U_d(t,\xi,\underline{\Omega})d\xi \\ =\dfrac{1}{\mu(\underline{\Omega})}\displaystyle\int_z^H K(z,\xi,\underline{\Omega})S(t,\xi,\underline{\Omega})d\xi+\dfrac{\sigma_S(\underline{\Omega}_0\to\underline{\Omega})}{\mu(\underline{\Omega})}\int_z^H K(z,\xi,\underline{\Omega})U_\delta(t,\xi)d\xi \\ +\bar{I}(t,H,\underline{\Omega}), \quad \mu(\underline{\Omega})>0, \end{cases} \tag{53b}$$

where

$$S(t,\xi,\underline{\Omega})=\int_{4\pi}\sigma_S(\underline{\Omega}'\to\underline{\Omega})U_d(t,\xi,\underline{\Omega}')d\underline{\Omega}'. \tag{53c}$$

The mean intensity over the total space of the horizontal plane, $\bar{I}(t,z,\underline{\Omega})$, can be decomposed into direct, $\bar{I}_\delta(t,z)$, and diffuse, $\bar{I}_d(t,z,\underline{\Omega})$, components similarly:

$$\bar{I}_\delta(t,z)+\frac{\sigma(\underline{\Omega}_0)}{|\mu(\underline{\Omega}_0)|}\int_0^z p(\xi)U_\delta(t,\xi)d\xi+\frac{1}{|\mu(\underline{\Omega}_0)|}\frac{1}{c}\frac{\partial}{\partial t}\int_0^z \bar{I}_\delta(t,\xi)d\xi=f(t). \tag{54a}$$

and,

$$
\begin{cases}
\bar{I}_d(t,z,\underline{\Omega}) + \dfrac{\sigma(\underline{\Omega})}{|\mu(\underline{\Omega})|}\int_0^z p(\xi)U_d(t,\xi,\underline{\Omega})d\xi + \dfrac{1}{|\mu(\underline{\Omega})|}\dfrac{1}{c}\dfrac{\partial}{\partial t}\int_0^z \bar{I}_d(t,\xi,\underline{\Omega})d\xi \\
= \dfrac{1}{|\mu(\underline{\Omega})|}\int_0^z p(\xi)S(t,\xi,\underline{\Omega})d\xi + \dfrac{\sigma_S(\underline{\Omega}_0 \to \underline{\Omega})}{|\mu(\vec{\Omega})|}\int_0^z p(\xi)U_\delta(t,\xi)d\xi, \quad \mu(\underline{\Omega}) < 0, \\
\bar{I}_d(t,z,\underline{\Omega}) + \dfrac{\sigma(\underline{\Omega})}{\mu(\underline{\Omega})}\int_z^H p(\xi)U_d(t,\xi,\underline{\Omega})d\xi + \dfrac{1}{\mu(\underline{\Omega})}\dfrac{1}{c}\dfrac{\partial}{\partial t}\int_z^H \bar{I}_d(t,\xi,\underline{\Omega})d\xi \\
= \dfrac{1}{\mu(\underline{\Omega})}\int_z^H p(\xi)S(t,\xi,\underline{\Omega})d\xi + \dfrac{\sigma_S(\underline{\Omega}_0 \to \underline{\Omega})}{\mu(\underline{\Omega})}\int_z^H p(\xi)U_\delta(t,\xi)d\xi \\
+ I(t,H,\underline{\Omega}), \quad \mu(\underline{\Omega}) > 0.
\end{cases}
\tag{54b}
$$

where, $S^{(j)}(t,\xi,\underline{\Omega})$ is defined by Eq. (53c).

Numerical Scheme: The numerical scheme of solutions of the time-dependant stochastic RT is an extension of the corresponding scheme for the stationary stochastic RT equation for single species (Chapter 7). The key steps are the same. The mean intensity over whole horizontal plane, $\bar{I}(t,z,\underline{\Omega})$, is derived based on mean intensity over vegetation, $U(t,z,\underline{\Omega})$ (Eq. (50)). The scheme to solve for $U(t,z,\underline{\Omega})$ involves two steps: 1) solve Eq. (53a) for direct intensity, $U_\delta(t,z,\underline{\Omega}_0)$; 2) solve Eq. (53b) for diffuse intensity, $U_d(t,z,\underline{\Omega})$. To solve for direct intensity, Eq. (53a) is integrated over time step, $[t_{i-1},t_i]$, and the obtained integrals are approximated with a trapezoidal quadrature scheme. Next, terms that depend on t_{i-1} are grouped, (to be referenced below as $F_\delta(t_{i-1},z,\underline{\Omega}_0)$), and an integral equation for U_δ is formulate with the remaining terms at time t_i,

$$
U_\delta(t_i,z) + \frac{\sigma(\underline{\Omega}_0)}{|\mu(\underline{\Omega}_0)|}\int_0^z K'(z,\xi,\underline{\Omega}_0)U_\delta(t_i,\xi)d\xi = f(t_i,\lambda) + F_\delta(t_{i-1},z,\underline{\Omega}_0), \tag{55a}
$$

where

$$
K'(z,\xi,\underline{\Omega}_0) \equiv K(z,\xi,\underline{\Omega}_0) + (cW_t\sigma(\underline{\Omega}_0))^{-1}, \tag{55b}
$$

$$
F_\delta(t_{i-1},z,\underline{\Omega}_0) \equiv f(t_{i-1},\lambda) - U_\delta(t_{i-1},z) - \frac{\sigma(\underline{\Omega}_0)}{|\mu(\underline{\Omega}_0)|}\int_0^z K''(z,\xi,\underline{\Omega}_0)U_\delta(t_{i-1},\xi)d\xi, \tag{55c}
$$

$$
K''(z,\xi,\underline{\Omega}_0) \equiv K(z,\xi,\underline{\Omega}_0) - (cW_t\sigma(\underline{\Omega}_0))^{-1}. \tag{55d}
$$

Here $W_t = 0.5\cdot\Delta t$ is the weight that depends on the numerical scheme used to approximate the integrals over the interval $[t_{i-1},t_i]$. Note that at each time step t_i, the solution of Eq. (55a), U_δ, depends on U_δ at the previous time step, t_{i-1}. Intensity U_δ at t=0 is given by initial conditions (Eq. (49)). At each following time step, Eq. (55a) is solved numerically according to scheme of solution of Volterra integral equation, detailed in Chapter 7 (Eq. (42)).

Next, diffuse intensity, $U_d(t,z,\underline{\Omega})$, is evaluated. Implementing the above described time-integration procedure with respect to Eq. (54), we get

$$\begin{cases} U_d(t_i,z,\underline{\Omega}) + \dfrac{\sigma(\underline{\Omega})}{|\mu(\underline{\Omega})|}\int_0^z K'(z,\xi,\underline{\Omega})U_d(t_i,\xi,\underline{\Omega})d\xi = \dfrac{1}{|\mu(\underline{\Omega})|}\int_0^z K(z,\xi,\underline{\Omega})S(t_i,\xi,\underline{\Omega})d\xi \\ + \dfrac{\sigma_S(\underline{\Omega}_0 \to \underline{\Omega})}{|\mu(\underline{\Omega})|}\int_0^z K(z,\xi,\underline{\Omega})U_\delta(t_i,\xi)d\xi + F_d(t_{i-1},z,\underline{\Omega}), \quad \mu(\underline{\Omega}) < 0, \\ U_d(t_i,z,\underline{\Omega}) + \dfrac{\sigma(\underline{\Omega})}{\mu(\underline{\Omega})}\int_z^H K'(z,\xi,\underline{\Omega})U_d(t_i,\xi,\underline{\Omega})d\xi = \dfrac{1}{\mu(\underline{\Omega})}\int_z^H K(z,\xi,\underline{\Omega})S(t_i,\xi,\underline{\Omega})d\xi \\ + \dfrac{\sigma_S(\underline{\Omega}_0 \to \underline{\Omega})}{\mu(\underline{\Omega})}\int_z^H K(z,\xi,\underline{\Omega})U_\delta(t_i,\xi)d\xi + F_d(t_{i-1},z,\underline{\Omega}) + I_d(t_i,H,\underline{\Omega}), \quad \mu(\underline{\Omega}) > 0. \end{cases} \tag{56}$$

Here $F_d(t_{i-1},z,\underline{\Omega})$ includes, similar to $F_\delta(t_{i-1},z,\underline{\Omega}_0)$, all the terms of integration of Eq. (53b) which depends on t_{i-1}. The solution U_d at time t_i depends on U_d at previous time step, t_{i-1}. At each time step the right hand side of Eq. (55a) is evaluated from know $U_\delta(t_i)$ at this time step and $U_d(t_{i-1})$ at previous time step. Equation (55a) is solved at each time step, t_i, with method of successive orders of scattering approximations (SOSA, Chapter 7, Eq. (40)).

The descretization of the equations for the mean intensity over a whole horizontal plane (Eq. (54), direct and diffuse components) are similar to those for mean intensity over vegetation (cf. Eq. (55)). Namely, the discreate equation for the direct component is

$$\bar{I}_\delta(t_i,z) + \frac{1}{cW_t|\mu(\underline{\Omega}_0)|}\int_0^z \bar{I}_\delta(t_i,\xi)d\xi = -\frac{\sigma(\underline{\Omega}_0)}{|\mu(\underline{\Omega}_0)|}\int_0^z p(\xi)U_\delta(t_i,\xi)d\xi + f(t_i) + G_\delta(t_{i-1},z,\underline{\Omega}_0). \tag{57}$$

The discreate equation for diffuse component is

$$\begin{cases} \bar{I}_d(t_i,z,\underline{\Omega}) + \dfrac{1}{cW_t|\mu(\underline{\Omega})|}\int_0^z \bar{I}_d(t_i,\xi,\underline{\Omega})d\xi = G_d(t_{i-1},z,\underline{\Omega}) \\ + \dfrac{1}{|\mu(\underline{\Omega})|}\int_0^z \left[\begin{array}{l} -\sigma(\underline{\Omega})U_d(t_i,\xi,\underline{\Omega}) + \sigma_S(\underline{\Omega}_0 \to \underline{\Omega})U_\delta(t_i,\xi) \\ + S(t_i,\xi,\underline{\Omega}) \end{array}\right] p(\xi)d\xi, \quad \mu(\underline{\Omega}) < 0, \\ \bar{I}_d(t_i,z,\underline{\Omega}) + \dfrac{1}{cW_t\mu(\underline{\Omega})}\int_z^H \bar{I}_d(t_i,\xi,\underline{\Omega})d\xi = G_d(t_{i-1},z,\underline{\Omega}) \\ + \dfrac{1}{\mu(\underline{\Omega})}\int_z^H \left[\begin{array}{l} -\sigma(\underline{\Omega})U_d(t_i,\xi,\underline{\Omega}) + \sigma_S(\underline{\Omega}_0 \to \underline{\Omega})U_\delta(t_i,\xi) \\ + S(t_i,\xi,\underline{\Omega}) \end{array}\right] p(\xi)d\xi, \quad \mu(\underline{\Omega}) > 0. \end{cases} \tag{58}$$

Functions $G_\delta(t_{i-1}, z, \underline{\Omega}_0)$ and $G_d(t_{i-1}, z, \underline{\Omega})$ are derived similarly to $F_\delta(t_{i-1}, z, \underline{\Omega}_0)$ and $F_d(t_{i-1}, z, \underline{\Omega})$. As Eq. (57) and (58) are structurally similar to Eqs. (55) and (56), the scheme of solution are also similar. Note, that in order to solve for $\bar{I}_\delta$ and $\bar{I}_d$, one needs to know U_δ and U_d.

3.3. Model Evaluation with Field Measurements

Field Measurements: A SLICER instrument measurements over four coniferous forests and mixed-deciduous sites in North America were selected to evaluate performance of the TSRT model. Ground measurements of vegetation parameters are available from multiple field campaigns performed at those sites. The characteristics of forests stands at each site are summarized in Table 1 and brief description of measurements is given below.

Table 1. Characteristics of the four sites used for model parameterization. SOJP and SOBS are southern old jack pine and black spruce stands measured during the BOREAS field campaign in 1996. The SERC sites are mixed deciduous forest stands at the Smithsonian Environmental Research Center (SERC), with the overstory predominantly comprised of tulip poplar.

Site	Age, years	Density, stems/ha	Tree height H, m	Crown length L, m	Leaf refl.	Leaf transm.	LAI	Ground refl.	Clump. Index
SOJP	60-75	1600-4000	16.5-18.5	11.0-12.3	0.53	0.32	2.61	0.330	0.5
SOBS	0-155	3700-5800	10.0-11.0	6.7-7.3	0.41	0.32	4.00	0.303	0.5
SERC (interm)	41	840	31.5-33.0	21.0-22.0	0.45	0.45	5.16	0.225	0.7
SERC (mature)	99	1187	32.0-36.5	21.3-24.3	0.45	0.45	5.26	0.225	0.7

The first two sites, southern old jack pine (*Pinus banksiana*), (SOJP, $53^0$55' N, $104^0$42' W), and southern old black spruce (*Picea mariana*), (SOBS, $53^0$59' N, $105^0$07' W), are located in the BOREAS southern study area in Saskatchewan, Canada. These sites were the subjects of intensive field campaigns carried out in 1994 as part of BOREAS field activities. A field data on forest age, stem density, tree structural parameters (height, LAI, crown length, foliage area volume density), and optical properties of leaves and ground, were collected [Chen et al., 1997; Middleton et al., 1997; Ni-Meister, 2001]. SLICER measurements over the BOREAS southern area, including SOJP and SOBS, sites were taken on July 29, 1996. We neglect change in the stands biophysical parameters during the two-year period between the field and SLICER measurements.

The other two sites are closed-canopy stands located in a mixed deciduous forest at the Smithsonian Environmental Research Center (SERC, $38^0$53' N, $76^0$33' W), about 10 km south-

southeast of Annapolis, MD, on the western shore of Chesapeake Bay [Harding et al., 2001]. The stands belong to the tulip poplar association, a mixed-deciduous forest with the overstory predominantly comprised of tulip poplar (*Liriodendron tulipifera*). The other species include sweet gum, oak, hickory, and American beech. The stands represent distinct stages in canopy development. The intermediate stand is a broad unimodal canopy consisting of 14 different species. The mature stand has a bimodal vertical leaf area structure and consists of 19 species. The gap fraction is relatively small: 0.05 for the intermediate stand and 0.02 for the mature stand. SLICER data for these sites were collected on September 7, 1995. Ground measurements were taken within two weeks after that [Harding et al., 2001]. The trees were fully leaved at this time. Canopy structural parameters (forest age, stem density, tree heights and LAI) are listed in [Harding et al., 2001]; crown lengths are assumed to be two third of tree heights [Oliver & Larson, 1990]; leaf optical properties are taken from [Parker et al., 2001]. The ground surface is dominantly comprised of leaf-litter with some bare soil and rare live foliage. The reflectance of the ground is assumed to be half that of the canopy.

Selection of Model Parameters: The stochastic model parameters were selected based on values given in Table 1 for each site. Below two additional modeling issues are discussed: 1) representation of lidar signal; 2) representation of stochastic canopy structure. SLICER lidar pulses are characterized by a curved "Raleigh" shape and a width of 4 ns [Harding et al., 2000]. The vertical resolution of recorded waveforms is 0.112 m. We smoothed SLICER signals to obtain the resolution of 0.336 m. The amount of transmitted energy per pulse is 0.7 mJ. The canopy is divided into n layers of thickness, $\Delta z = 0.336\,\mathrm{m}$. The observation time is divided into m intervals, $[t_{i-1}, t_i]$, $\Delta t = t_i - t_{i-1} = \Delta z / c$ (c is the speed of light). The simulated Raleigh pulse is divided into k narrow pulses of duration, Δt. At each moment, t_i, i=[0;m], the intensity of incoming radiation is equal to the pulse amplitude at that moment.

The canopy structure was modeled as follows. The first moment of canopy structure, probability to find vegetation elements at height z, $p(z)$, was implemented based on the assumption of hemi-ellipsoid crown shapes and field-measured values of LAI:

$$p(z) = p_0\left[1 - \frac{(z-L)^2}{L^2}\right], \tag{59}$$

where $p_0 \equiv 3\,\mathrm{LAI}/(2\,L\,u_L)$, was derived according to definition (Chapter 7, Eq. (2)). Small variation of p-values (within 10%) was applied to each layer to provide a more realistic representation of canopy structure. The second moment of canopy structure, the conditional pair-correlation function, $K(z, \xi, \underline{\Omega})$, was implemented according to turbid medium approximations, adjusted for canopy clumping, namely,

$$K(z,\xi,\underline{\Omega}) = \beta \frac{p(z)\,p(\xi)}{p(z)} = \beta\, p(\xi). \qquad (60)$$

Here β is the clumping index [Chen et al., 1997]: $\beta=1$ for uniformly distributed foliage (turbid medium); $\beta>1$ if leaves are regularly distributed (i.e leaves are all laid side by side); $\beta<1$ if leaves are clumped. Canopy clumping is ad-hook parameter, commonly used to adjust extinction coefficient [Chen et al., 1997]. In fact, Eq. (60) is equivalent to Chen et al. [1997] as $K(z,\xi,\underline{\Omega})$ is coupled with extinction coefficient in the stochastic equations (cf. Eq. (51)). Physical meaning of the Eq. (60) is as follows: clumping reduces the probability of finding vegetated elements in two layers simultaneously moving along a given direction.

Sensitivity Study: The following problems were analyzed: 1) the behavior of the model as function of the laser pulse duration; 2) the sensitivity of the model to the number of iterations. The model parameters used in this study correspond to BOREAS SOBS site (cf. Table 1). With respect to the first problem, note that, if a constant photon flux is incident on the top of vegetation over an extended period of time, the solution of the time-dependent stochastic RT equation converges to the solution of the stationary equation (Chapter 7). Figure 13 illustrates the convergence of the upward diffuse radiation flux at the top of canopy evaluated with the time-dependent model to that of stationary model. It requires about 60 ns to reach the stationary limit in this particular case. During this time, photons travel a distance of 20 m, which is approximately equal to 2H. Figure 13 also demonstrates that the use of a steady-state radiative transfer in optical remote sensing is valid. Namely, the time for radiation to propagate through the system (tens of ns) is short compared to variations in illumination conditions (typically, tens of minutes) or canopy geometry (seconds). The ability of the model to describe non-stationary and stationary radiation regimes makes it valuable for interpretation of both active and passive remote sensing data.

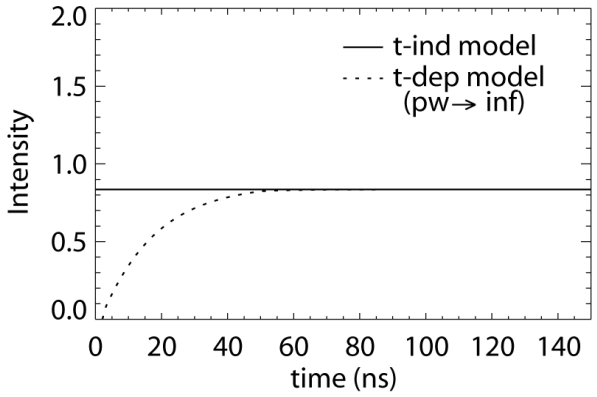

Figure 13. Upward diffuse radiation at the top of canopy as a function of time. The solid line represents the simulations by the stationarry model. The dotted line corresponds to simulations by the time-dependent model with increasing pulse width (pw $\rightarrow$ inf).

Second, the contribution of photons scattered n times to the radiation regime at a given moment of time is evaluated. The integral

$$E_n(t) = \int_0^L dz \int_{4\pi} d\underline{\Omega}\, J_n(t, z, \underline{\Omega}) \tag{61}$$

is taken as a measure of the number of photons, scattered n times within the vegetation canopy at moment t. Here $J_n(t_i, z, \underline{\Omega})$ is the intensity of photons scattered n times. Figure 14 shows the ratios

$$-\ln\frac{E_n(t)}{E_1(t)} \text{ and } -\ln\frac{E_{n+1}(t)}{E_n(t)}$$

as functions of the scattering order, n, for different instants of time, t. The former shows the proportion of multiply-scattered to single-scattered photons, while the latter is the rate at which multiply scattered photons contribute to the radiation field. One can see that the contribution of high-order scattering decreases rapidly for $t \le 17\text{ns}$. For a sufficiently large n, all curves can be asymptotically replaced by the following curves:

$$-\ln\frac{E_n(t)}{E_1(t)} = -n\ln\rho(t) - \ln c(t)\,, \tag{62}$$

where $-\ln\rho(t)$ is the slope ratio, and $-\ln c(t)$ is a function, characterizing the shift of the plotted curves with time. Note that for the cases with large values of time, the ratio $-\ln[E_n(t)/E_1(t)]$ first decreases for small n. It describes the situation when $E_n(t) > E_1(t)$. In the stationary case, the maximum number of photons scattered n times would not change with time due to stationary input of radiation into the canopy. In the time-dependant case, photon flux enters the canopy during a small period of time equal to the laser pulse duration. With time, some fraction of photons scattered only once leaves the canopy and number of multiple-scattered photons exceeds the number of single-scattered photons inside the canopy.

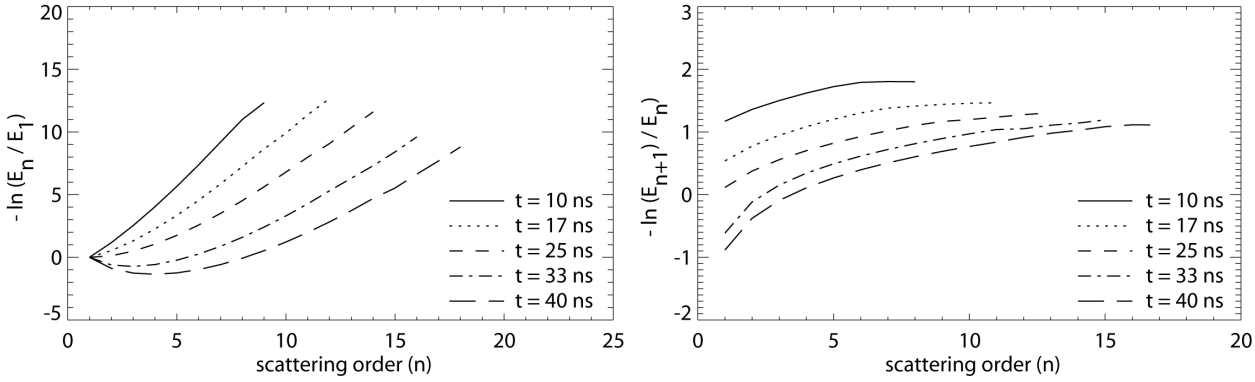

Figure 14. Contribution of photons scattered n times at different time moments (t = 10, 17, 25, 33, 40 ns). The laser pulse is assumed to be incident at the top of canopy at time t = 0. Function E_i is a measure of n umber of photons scattered I times.

It follows from Eq. (62) that, for a sufficiently large n, E_n can be approximated by

$$E_n(t) = (\rho(t))^n c(t). \tag{63}$$

Here $(\rho(t))^n$ can be interpreted as the probability for a photon to be scattered n times and $c(t)$ as a function characterizing the dependence on time. The rate of convergence of the SOSA method is defined as

$$E - E_n = E_{n+1} + E_{n+2} + ... = c(t)(\rho(t))^{n+1}(1 + \rho(t) + ...) = c(t)\frac{(\rho(t))^{n+1}}{1-\rho(t)}. \tag{64}$$

Thus the contribution of multiply scattered photons to the radiation field at a given instant of time is proportional to $(\rho(t))^n/(1-\rho(t))$. The higher the probability of scattering events, the higher the contribution of multiply scattered photons to the radiation field. In this example, about $n = 10$ iterations are required to obtain a relative accuracy of 10^{-3}.

Simulations of Lidar Waveforms: For each of the sites, six SLICER waveforms were extracted. The selection was made among data from the three interior footprints; waveforms corresponding to the two outer footprint positions were discarded as anomalous due to misalignment between the scan pattern and the outer edges of the instruments receiver field-of-view [Lefsky et al., 1999a].

The selected signals were normalized by the maximum return signal in each waveform. It is the ground return for SOBS and SOJP and the maximum canopy return for the SERC sites. The digitizer bin units were converted into distance, with one digitizer bin corresponding to 0.1112 m. A smoothing procedure was applied to the signals: three adjacent bins were summed and the averaged value was taken. The ground return was identified as the last discrete return above the mean background noise level. The maximum value of the ground return was assigned a height of zero. Tree height is the distance between the maximum ground return and the first canopy return. As the plotted SLICER signals reveal different heights for the same forest stand, the tree heights and crown sizes used in model simulations were defined for each signal individually.

Figures 15 and 16 summarize the results for SOBS/SOJP and SERC sites respectively. For convenience, each waveform is accompanied by the site name and a number. The gap fraction is high in the coniferous stands (SOJP and SOBS) and the return from the ground is pronounced most. The unimodal shapes of the SLICER waveforms over those sites imply the absence of secondary forest understory. The third SOBS plot reveals some understory, seen as a small wide spike near the maximum return. For the first SOBS plot, the amplitude of the SLICER signal is greater than that in the simulations. Differences in foliage density affect the strength of the SLICER signals, while the model simulations assume a constant value. The agreement between

the SLICER signals and model simulations is better for the signals with a slow decay of the waveform. The SOBS SLICER signals shown in Fig. 15 were collected over the region where ground measurements described in Chen et al. [1997] were made. For the SOJP site, none of the SLICER tracks coincides with the location of Chen et al.'s measurements. Two SLICER tracks cross the area of another field campaign described in [Sun & Ranson, 2000]. The data from these tracks are used here. For the SERC forest stands, the SLICER data sets include regions where ground measurements were taken. Several subpeaks of canopy return, and small or even undistinguishable ground returns are typical for the waveforms collected over both mature and intermediate stands. The signals with identifiable ground returns were chosen to calculate tree heights. Only relatively unimodal waveform profiles are represented in Fig. 16, for the model does not include multi-layer vegetation structure. Some small understory, in the second and third mature and intermediate plots, is acceptable. The majority of radiation is intercepted in the upper layer of the canopy in view of high foliage density in these stands.

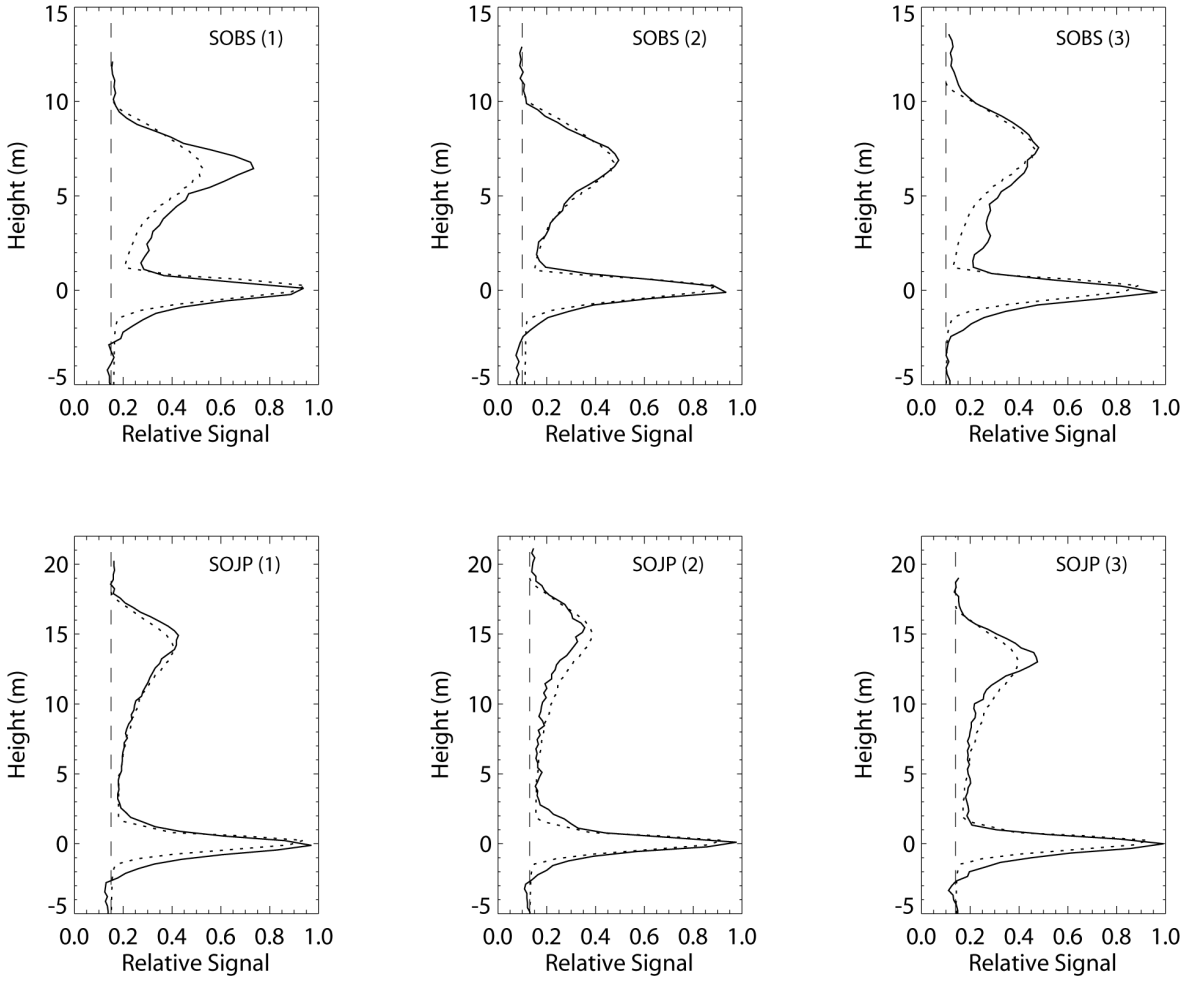

Figure 15. Comparison of model simulations (dotted curves) and corresponding SLICER measurements (solid curves) for BOREAS SOBS and SOJP sites. The noise level is shown as a vertical dashed line.

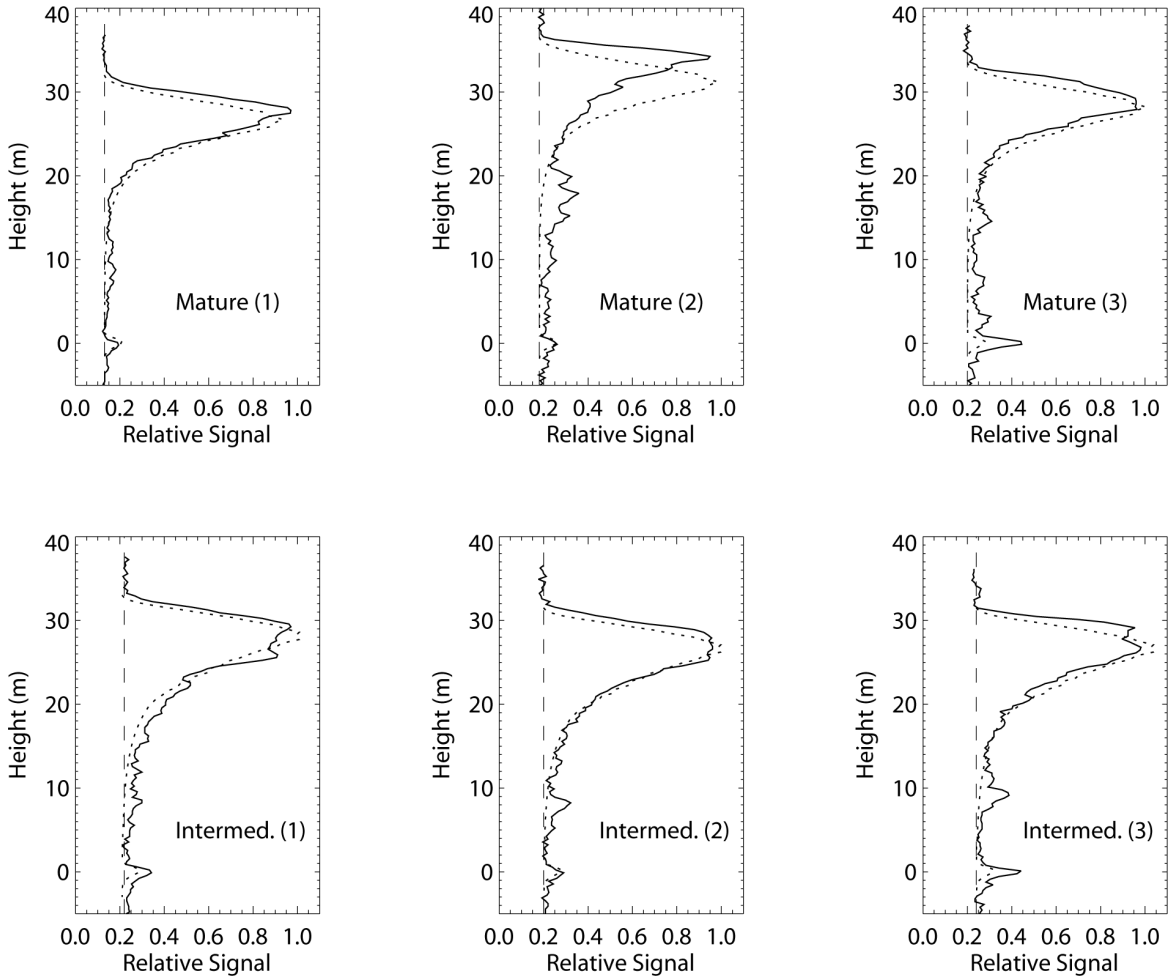

Figure 16. Comparison of model simulations (dotted curves) and corresponding SLICER measurements (solid curves) for SERC mature and intermediate forest stands. The noise level is shown as a vertical dashed line.

3.4. Effect of Multiple Scattering

The simulated returns generated from single and multiple scattering are next compared to evaluate the contribution of multiply scattered photons. From the plots shown in Fig. 15 and 16, those that agreed best with SLICER data were chosen for this investigation; one plot for each forest stand. These are SOBS (2), SOJP (1), Mature (3), and Intermediate (1). The model-simulated signals in the single scattering approximation were added to each plot. The results are shown in Fig. 17.

The inclusion of multiple scattering magnifies the signal and enhances significantly the lower part of the waveform. In general, multiply scattered photons carry information on canopy

structural parameters, namely, foliage density and gap fraction. When a photon path in the canopy is limited to a single interaction, the total travel time is the round trip time between the sensor and the interaction point: $t_{total} = t_{ps}$. If a photon has interacted several times before leaving the canopy in the direction of the sensor, the total travel time is increased to $t_{total} = t_{ps} + t_{pm}$, where t_{pm} is the extra time due to multiple scattering. This extra time depends on two variables: the number of interactions and the mean distance of photon travel between two interactions (photon mean free path). The photon mean free path is inversely proportional to the extinction coefficient $\sigma(\underline{r}, \underline{\Omega})$, which is directly related to canopy structure. A vegetation canopy with high density will generate more multiple scattering but with relatively short free paths. Conversely, in sparse canopies, the contribution of multiple scattering will be relatively lower but with longer paths.

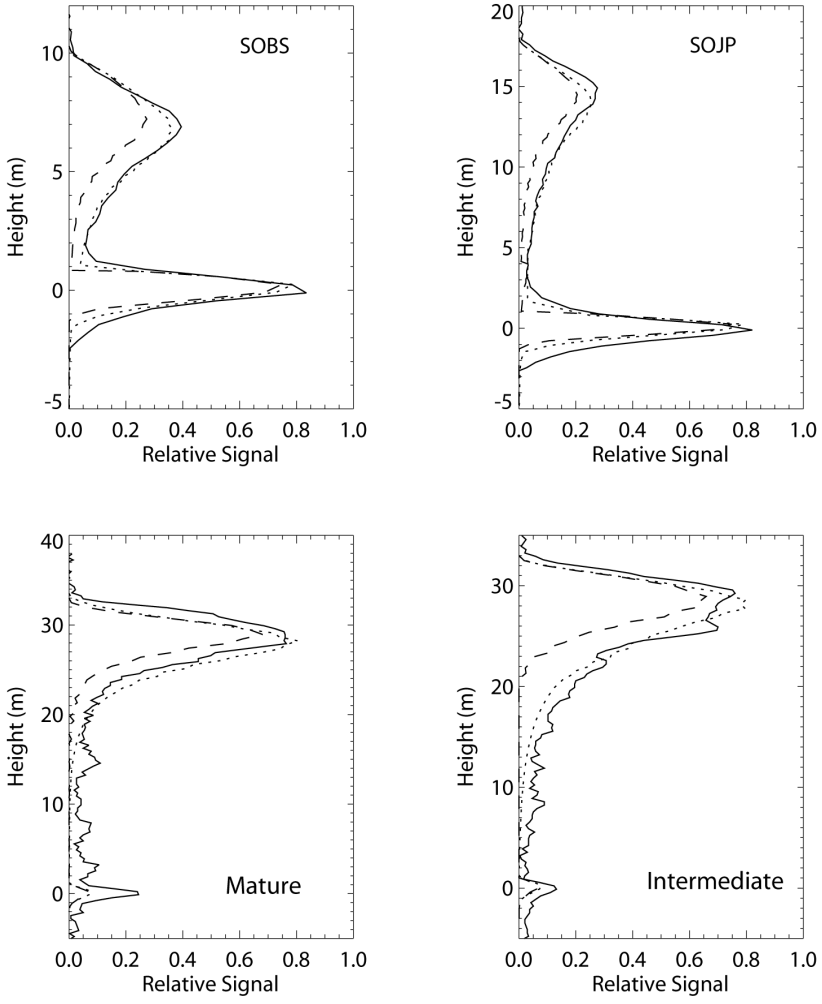

Figure 17. SLICER waveforms and model simulations with and without multiple scattering for four different sites. The solid curves represent the SLICER signals. The single scattering simulations are shown with dashed curves, while the dotted curves represent multiple scattering simulations. Noise is subtracted.

In case of sparse canopies, single-scattering approximation models are expected to provide good approximation of lidar recorded signals. A hybrid geometric optical and radiative transfer model (GORT) was tested with data from four BOREAS sites: SOBS, SOJP, NOBS (northern old black spruce), and NOJP (northern old jack pine) [Ni-Meister et al., 2001]. Selected SLICER

waveforms were normalized by the maximum signal (ground return). The model provided good agreement between the measured and simulated waveforms, but the relative amplitude of vegetation return was low: less than 0.15 for the SOBS site and less than 0.1 for the others. This indicates that the density of measured vegetation was relatively low and the effects of multiple scattering were probably insignificant. For the study presented here, the lower boundary of relative amplitude was 0.3 for SOJP and 0.4 for SOBS.

The waveform shapes change dramatically in a set of measurements for the same site. It depends on the density of vegetation and the number of trees within the footprint. As a result, some waveforms may show effects of multiple scattering, while the others may not. The effect of multiple scattering also depends on the amplitude and duration of a laser pulse. The model shows that this effect is more significant in the simulations with longer pulse widths. An increase of the amplitude makes it more detectable.

3.5. Summary

The application of the stochastic approach for the large footprint lidar remote sensing of heterogeneous vegetation was introduced. The Time-dependant Stochastic RT (TSRT) model describes non-stationary radiation regime of lidar measurements (the stream of photons, emitted by lidar, enters vegetation canopy, propagate through vegetation bounded by soil via mechanism of single and multiple scattering and exit canopy back to lidar receiver). Sensitivity study indicates that as the duration of lidar pulse exceed the time required for photon to travel the distance twice of canopy height, the solution of the TSRT model converges to one of the stationary stochastic equation. Also, contribution of the multiple-scattered photon with respect to single-scattered photons was quantified (how it changes with time and how it depends on the order of scattering). The simulated lidar waveforms were evaluated with respect to SLICER lidar measurements and ancillary ground measurements of vegetation biophysical parameters over four coniferous and mixed-deciduous stands. The inclusion in the TSRT simulations of multiple scattering magnifies the signal and enhances significantly the lower part of the waveform. In general, multiply- scattered photons carry information on canopy structural parameters, namely, foliage density and gap fraction. A vegetation canopy with high density will generate more multiple scattering but with relatively short free paths. Conversely, in sparse canopies, the contribution of multiple scattering will be relatively lower but with longer paths. In case of sparse canopies, single-scattering approximation models are expected to provide good approximation of lidar recorded signals. The effect of multiple scattering also depends on the amplitude and duration of a laser pulse. This effect is more significant in the simulations with longer pulse widths. Further modeling efforts are required to improve representation of the conditional pair-correlation function (inclusion of stem density, canopy roughness, canopy layering, leaf distribution) in order to better capture relationship between canopy structure and lidar waveforms.

References

Blair, J.B., and M.A. Hofton (1999). Modeling laser altimeter return waveforms over complex vegetation using high-resolution elevation data. *Geophys. Res. Lett.*, **26**, 2509-2512.

Borel, C., and S. Gerstl (1994). Nonlinear spectral mixing models for vegetative and soil surfaces. *Remote Sens. of Environ*., **47**, 403-416.

Breda, N.J.J. (2003). Ground-based measurements of Leaf Area Index: a review of methods, instruments and current controversies. *J. Exp. Botany*, **64**(**392**), 2403-2417.

Carpenter, G.A., S. Gopal, S. Macomber, S. Martens, and C.E.Woodcock (1999). A neural network method for mixture estimation for vegetation mapping. *Remote Sens. Environ.*, **70**, 135-152.

Chen, J.M., P.M. Rich, S.T. Gower, J.M. Norman, and S. Plummer (1997). Leaf area index of boreal forests: Theory, techniques, and measurements. *J. Geophys. Res.*, **102** (**D24**), 29429-29443.

DeFries, R.S., J.R.G Townshend, M.C. Hansen (1999). Continuous fields of vegetation characteristics at the global scale 1-km resolution. *J. Geophys. Res.-Atmosphere*, **104**(**D14**), 16911-16923.

Drake, J.B., R. Dubayah, D.B. Clark, R.G. Knox, J.B. Blair, M.A. Hofton, R.L. Chazdon, J.F. Weishampel, and S. Prince (2002a). Estimation of tropical forest structural characteristics using large-footprint lidar. *Remote Sens. Environ.,* **79**, 305-319.

Drake, J.B., R. Dubayah, R.G. Knox, D.B. Clark, and J.B. Blair (2002b). Sensitivity of large-footprint lidar to canopy structure and biomass in a neotropical forest. *Remote Sens. Environ.*, **81**, 378-392.

Dubayah, R., R. Knox, M. Hofton, J.B. Blair, and J. Drake (2000). *Land surface characterization using lidar remote sensing, in Spatial Information for Land Use Management*, Hill, M., and Aspinall, R. (Eds.), Gordon and Breach, Newark, NJ.

Ju J., E.D. Kolaczyk, and S. Gopal (2003). Gaussian mixture discriminant analysis and sub-pixel land cover characterization in remote sensing. Remote Sens. Environ. **84**, 550-560.

Govaerts, Y. M. (1996). *A model of light scattering in three-dimensional plant canopies: a Monte Carlo ray tracing approach*, Space Applications Institute, JRC, European Commission.

Harding, D.J., J.B. Blair, D.L. Rabine, and K.L. Still (2000). *SLICER airborne laser altimeter characterization of canopy structure and sub-canopy topography for the BOREAS northern and southern study regions: Instrument and data product description*, in *Technical report series on the Boreal Ecosystem-Atmospheric Study (BOREAS)*, Hall F.G., and Nickeson, J. (Eds.) Washington, DC: NASA/TM-2000-209891.

Harding, D.J., M.A. Lefsky, G.G. Parker, and J.B. Blair (2001). Laser altimeter canopy height profiles. Methods and validation for closed-canopy, broadleaf forests. *Remote Sens. Environ.*, **76**, 283-297.

Huang D., Y. Knyazikhin, W. Yang, W. Wang, J. Privette, D. Deering, N. Shabanov, and R.B. Myneni (2007). Stochastic transport theory for investigating the three-dimensional canopy structure from space measurements. *Remote Sens. Environ. in press*.

Kotchenova, S.Y., N.V. Shabanov, Y. Knyazikhin, A. Davis, R. Dubayah, and R.B. Myneni (2003). Modeling lidar waveforms with time-dependent stochastic radiative transfer theory for remote estimates of forest structure. *J. Geophys. Res.- Atmospheres*, **108**(**D15**), 4484, doi:10.1029/2002JD003288.

Lefsky, M.A., D.J. Harding, W.B. Cohen, G.G. Parker, and H.H. Shugart (1999a). Surface lidar remote sensing of basal area and biomass in deciduous forests of eastern Maryland, USA, *Remote Sens. Environ.*, **67**, 83-98.

Lefsky, M.A., W.B. Cohen, S.A. Acker, G.G. Parker, T.A. Spies, and D. Harding (1999b). Lidar remote sensing of the canopy structure and biophysical properties of Douglas-fir western hemlock forests. *Remote Sens. Environ.,*, **70**, 339-361.

Lefsky, M.A., W.B. Cohen, G.G. Parker, and D.J. Harding (2002). Lidar remote sensing for ecosystem studies. *Bioscience*, **52**(**1**), 19-30.

MacArthur, R.H., and H.C. Horn (1969). Foliage profiles by vertical measurements. *Ecology*, **50**, 802-804.

McIver D.K, and M.A. Friedl (2002). Using prior probabilities in decision-tree classification of remotely sensed data. R*emote Sens. Environ*., **81**, 253-261.

Middleton, E.M., S.S. Chan, R.J. Rusin, and S.K. Mitchell (1997). Optical properties of black spruce and jack pine needles at BOREAS sites in Saskatchewan, Canada. *Canadian J. Remote Sens.*, **23**(**2**), 108-119.

Ni-Meister, W., D.L.B. Jupp, and R. Dubayah (2001). Modeling lidar waveforms in heterogeneous and discrete canopies, *IEEE Trans. Geosci. Remote Sens.*, **39**(**9**), 1943-1958.

Oliver, C.D., and B.C. Larson (1990). *Forest stand dynamics*, McGraw-Hill, Inc., New-York.

Parker, G.G., M.A. Lefsky, and D.J. Harding, (2001). Light transmittance in forest canopies determined using airborne laser altimetry and in-canopy quantum measurements", *Remote Sens. Environ.*, **73**, 298-310.

Pomraning, G.C. (1991). *Linear kinetic theory and particle transport in stochastic mixtures. Series on advances in mathematics for applied sciences*.-Vol. 7. Singapore: World Scientific.

Press, W.H., B.P. Flannery, S.A. Teukolsky, and W.T. Vetterling. (1986). *Numerical recipes: the art of scientific computing.* p.19-38, Cambridge University Press.

Ross ,J. (1981). *The radiation regime and architecture of plant stands*. Hague: Dr. W. Junk Publishers, 1981.

Shabanov, N.V., Y. Knyazikhin, F. Baret, and R.B. Myneni (2000). Stochastic modeling of radiation regime in discontinuous vegetation canopies. *Remote Sens. Environ*., **74**(**1**), 125-144.

Shabanov, N.V., D. Huang, W. Yang, B. Tan, Y. Knyazikhin, R.B. Myneni, D.E. Ahl, S.T. Gower, A. Huete, L.E. Aragao, and Y.E. Shimabukuro (2005). Analysis and optimization of the MODIS LAI and algorithm retrievals over broadleaf forests. *IEEE Trans. Geosci. Remote Sens.*, **43**(**8**), 1855-1865.

Shabanov, N.V., D. Huang, R.E. Dickinson, Y. Knyazikhin, and R.B. Myneni (2007). Stochastic radiative transfer model for mixture of discontinuous vegetation canopies. *J. Quant. Spectroscopy and Radiative Transf.*; in press.

Stoyan, D., W.S. Kendall, and J. Mecke (1995). *Stochastic geometry and its applications*. p.67-69, Wiley Series in Probability and Statistics, Second Ed., John Wiley & Sons.

Sun, G., and K.J. Ranson (2000). Modeling lidar returns from forest canopies, *IEEE Trans. Geosci. Remote Sens.*, **38**(**6**), 2617-2626.

Tian Y, Y. Wang, Y. Zhang, Y. Knyazikhin, J. Bogaert, and R.B. Myneni (2002). Radiative transfer based scaling of LAI/FPAR retrievals from reflectance data of different resolutions. *Remote Sens. Environ.*; **84**, 143-159.

Tian. Y, R.E. Dickinson, L. Zhou, X. Zeng, Y. Dai, R.B. Myneni, Y. Knyazikhin, X. Zhang, M. Friedl, H. Yu, W. Wu, and M. Shaikh (2004). Comparison of seasonal and spatial variations of LAI/FPAR from MODIS and Common Land Model. *J. Geophys. Res.-Atmosphere*, **109**(**D1**), D01103, 10.1029/2003JD003777.

Zwally, H.J., B. Schutz, W. Abdalati, J. Abshire, C. Bentley, A. Brenner, J. Bufton, J. Dezio, D. Hancock, D. Harding, T. Herring, B. Minster, K. Quinn, S. Palm, J. Spinhirne, and R. Thomas (2002). ICESat's laser measurements of polar ice, atmosphere, ocean and land. *J. Geodynamics*, **34**, 405-445.

Chapter 7

Canopy Spectral Invariants: Shabanov et al.

(Re)View: Stenberg et al.

(Re)View: Wang et al.

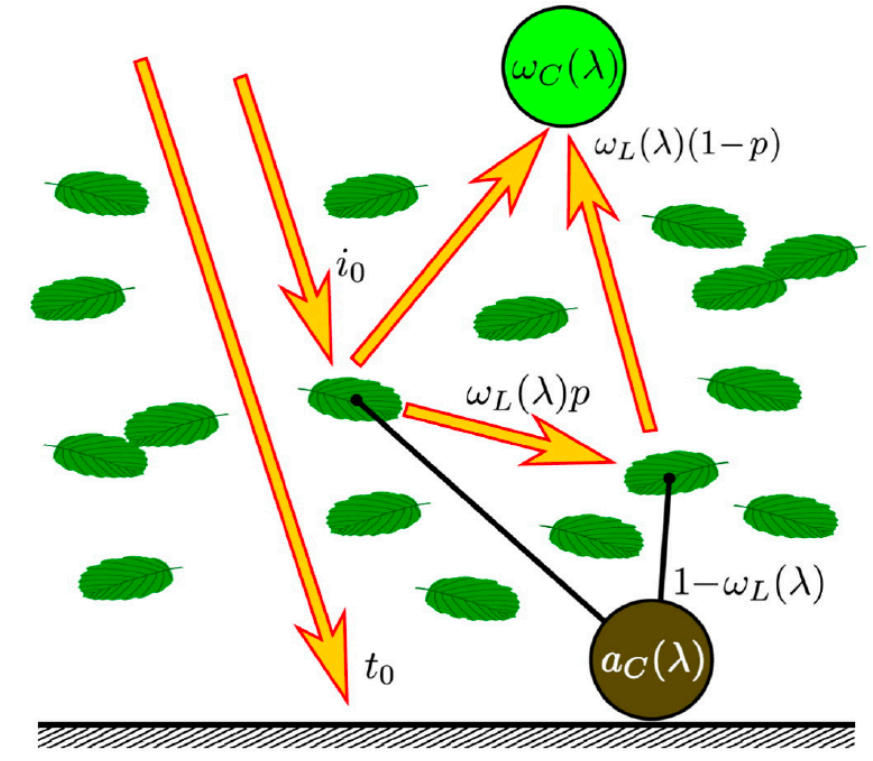

Chapter 7

Canopy Spectral Invariants

1. Introduction

The *shortwave radiation budget* describes how the fraction of radiation absorbed by or scattered out from the canopy to the underlying background or back to space are related to the structural and optical properties of canopy and background. Operational remote sensing or climate applications of the model of shortwave radiation budget naturally require that such model should build upon a canopy representation with only a small set of basic parameters which govern the radiation budget with sufficient accuracy.

The interaction of solar radiation with the vegetation canopy is fully described by the three-dimensional (3D) RT equation. The scale of the elementary volume of the equation (scale of leaves, branches, twigs, etc.) is large compared to the wavelength of solar radiation, and, according to principles of physics, the photon free path between two successive interactions is independent of the wavelength. Namely, while the scattering and absorption processes are different at different wavelengths, the interaction probabilities for photons in vegetation media (interaction cross-section or extinction coefficient) are determined by the structure of the canopy rather than photon wavelength or the optics of the canopy.

This feature of the RT equation allowed formulation of the concept of canopy *spectral invariants*. This concept states that simple algebraic combinations of leaf and canopy spectral transmittance and reflectance become wavelength independent and determine a small set of canopy structure specific variables. The set of structural variables includes *canopy interceptance*, *recollision* and *escape probabilities*. These variables specify the spectral response of a vegetation canopy to the incident solar radiation and allow for a simple and accurate parameterization of the partitioning of the incoming radiation into canopy transmission, reflection and absorption at any wavelength in the solar spectrum. In addition to the spectral invariance property, these variables poses fundamental scaling property, allowing to scale RT parameters over full range of landscape scales from leaf internals, through leaf, shoots, crowns to whole canopy. Thus, the spectral invariant approach provides a compact alternative to the full 3D RT equation for operational remote sensing or climate applications.

This chapter is organized as follows. We start by introducing basic physical principles of the spectral invariants and supporting field measurements. Next, we present rigorous mathematical formulation of the spectral invariants based on the method Successive Orders of Scattering approximations (SOSA) or Neumann series and eigenvalue/eigenvector theory of functional analysis. Finally, we discuss the scaling properties of spectral invariants and illustrate this fundamental feature with two case studies: (a) scaling from needles to shoots in the needle leaf canopies and (b) scaling form leaf internals to leaf.

2. Physical Principles of Spectral Invariants

Radiation Fluxes at Leaf and Canopy Scale: The 3D RT equation can be interpreted as the link between leaf and canopy scale radiation fluxes (Chapter 3 and 4). At the *leaf scale* the radiation fluxes are described in terms of spectral leaf transmittance and reflectance. The *leaf transmittance* (reflectance) is the portion of radiation flux density incident on the leaf surface that the leaf transmits (reflects) (Chapter 3). The leaf albedo, $\omega(\lambda)$, is the sum of the leaf reflectance, $\rho_L(\lambda)$, and transmittance, $\tau_L(\lambda)$,

$$\omega(\lambda) = \rho_L(\lambda) + \tau_L(\lambda). \quad (1)$$

The fluxes at the *canopy scale* are described in terms of spectral canopy interceptance, absorptance, reflectance and transmittance. The canopy *interceptance (absorptance)* is the ratio of the mean flux density intercepted (absorbed) by canopy leaves to the downward radiation flux density above the canopy. Similarly, *canopy transmittance* (*reflectance*) is the ratio of the mean downward radiation flux density at the canopy bottom (mean upward radiation flux density at the canopy top) to the downward radiation flux density above the canopy. According to RT theory (Chapter 3), the canopy interceptance, $i(\lambda)$, absorptance, $a(\lambda)$, reflectance, $r(\lambda)$, and transmittance, $t(\lambda)$, are defined as follows:

$$i(\lambda) \equiv \int_V d\underline{r} \int_{4\pi} d\underline{\Omega}\, \sigma(\underline{r},\underline{\Omega})\, I(\lambda,\underline{r},\underline{\Omega}), \tag{2a}$$

$$a(\lambda) \equiv \int_V d\underline{r} \int_{4\pi} d\underline{\Omega}\, \sigma_a(\underline{r},\underline{\Omega})\, I(\lambda,\underline{r},\underline{\Omega}), \tag{2b}$$

$$r(\lambda) \equiv \int_{2\pi+} d\underline{\Omega}\, \mu(\underline{\Omega}) I(\lambda,\underline{r}=0,\underline{\Omega}), \tag{2c}$$

$$t(\lambda) \equiv \int_{2\pi-} d\underline{\Omega}\, \mu(\underline{\Omega}) I(\lambda,\underline{r}=H,\underline{\Omega}). \tag{2d}$$

In the above, $I(\lambda,\underline{r},\underline{\Omega})$ is the radiation intensity at wavelength λ, spatial location $\underline{r}$, and in direction $\underline{\Omega}$, $\sigma(\underline{r},\underline{\Omega})$ is the interaction cross-section, and $\sigma_a(\underline{r},\underline{\Omega})$ is the absorption cross-section. The interaction cross-section is treated as wavelength independent considering the size of the scattering elements (leaves, branches, twigs, etc.) relative to the wavelength of solar radiation [Ross, 1981]. The interaction cross-section, $\sigma(\underline{r},\underline{\Omega})$, consist of absorption, $\sigma_a(\underline{r},\underline{\Omega})$ and scattering, $\sigma'_s(\underline{r},\underline{\Omega})$, cross-sections (cf. Chapter 3):

$$\sigma(\underline{r},\underline{\Omega}) = \sigma_a(\underline{r},\underline{\Omega}) + \sigma'_s(\underline{r},\underline{\Omega}), \tag{3a}$$

where

$$\sigma_a(\underline{r},\underline{\Omega}) = [1-\omega(\lambda)]\sigma(\underline{r},\underline{\Omega}), \tag{3b}$$

$$\sigma_s'(\underline{r},\underline{\Omega}) \equiv \int_{4\pi} d\underline{\Omega}'\,\sigma_s(\underline{r},\underline{\Omega}\rightarrow\underline{\Omega}') = \omega(\lambda)\sigma(\underline{r},\underline{\Omega}). \tag{3c}$$

In the above $\sigma_s(\underline{r},\underline{\Omega}\rightarrow\underline{\Omega}')$ is the differential scattering cross-section. Thus, combining Eqs. (2) and (3) we have,

$$a(\lambda) = [1-\omega(\lambda)]\,i(\lambda). \tag{4}$$

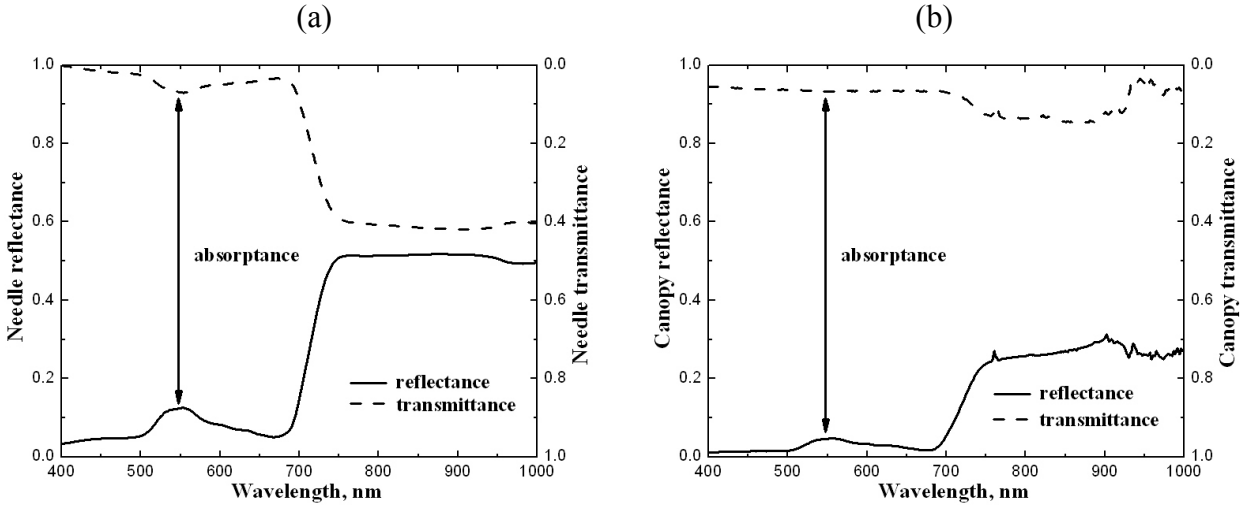

Figure 1. Needle (Panel a) and canopy (Panel b) spectral reflectance (vertical axis on the left side) and transmittance (vertical axis on the right side) for a Norway spruce (*Picea abies (L.) Karst*) stand at Flakaliden site in Sweden. Arrows show needle and canopy absorptance. The effective LAI at the site was 4.37. The needle transmittance, τ_L, and albedo, ω, follow the regression line $\tau_L = 0.47\omega - 0.02$.

The canopy absorptance, reflectance and transmittance are the three components of the shortwave energy conservation law which describes canopy spectral response to incident solar radiation at the *canopy scale*. If reflectance of the ground below the vegetation is zero (black soil, cf. Chapter 4), the portion of radiation absorbed, $a(\lambda)$, transmitted, $t(\lambda)$, or reflected, $r(\lambda)$, by the canopy totals to unity, i.e.,

$$t(\lambda) + r(\lambda) + a(\lambda) = 1. \quad (5)$$

The key reference data set for this Chapter will be field data collected in Flakaliden site in Sweden [Huang et al., 2007]. Other ancillary sources will be mentioned as appropriate. Canopy spectral transmittance and reflectance, soil and understorey reflectance spectra, needle optical properties, shoot structure and LAI were collected in six 50x50 m plots composed of Norway spruce (*Picea abies* (L.) Karst) located at Flakaliden research area ($64^0 14'$N, $19^0 46'$E), operated by the Swedish University of Agricultural Studies. The spectral measurements of canopy and needles were taken by ASD Field spec Pro handheld spectroradiometer. Needle spectral reflectances and transmittances of an average needle were obtained by averaging 50 measured spectra with highest weight given to the 2-year-old needles (80%) and equal weights to the current (10%) and 1-year (10%) needles. Figure 1 shows needle and canopy transmittance, reflectance and absorptance spectra at the Flakaliden site.

Mechanism of Scattering: Consider the following basic scheme of the relationship between leaf and canopy scales radiation fluxes. We assume that canopy is illuminated from the top by monodirectional unit flux. Canopy bottom is assumed to be absolutely absorbing, such that photons hit background will not re-enter, but exit canopy. The incident unit flux undergo multiple interactions with phytoelements and ultimately is partitioned into absorbed, $a(\lambda)$, transmitted, $t(\lambda)$, and reflected, $r(\lambda)$, portions. To analyze multiple scattering, we separate the radiation flux incident on vegetation canopy into two components (Fig. 2): directly intercepted by leaves and available for future interaction events (*zero-order interceptance*, i_0), and directly transited to the canopy bottom without hitting a leaf (*zero-order transmittance*, t_0):

$$1 = i_0 + t_0. \quad (6a)$$

The intercepted photons, i_0, will participate in the multiple scattering and ultimately will be either absorbed, $a(\lambda)$, or scattered outside of canopy, $s(\lambda)$:

$$i_0 = a(\lambda) + s(\lambda). \quad (6b)$$

Thus,

$$1 = a(\lambda) + s(\lambda) + t_0 . \qquad (6c)$$

Note, i_0 and t_0 are zero-order scattering quantities, while $a(\lambda)$ and $s(\lambda)$ are total quantities, accumulated over multiple events of scattering. While $a(\lambda)$ and $s(\lambda)$ are wavelength dependent, i_0 and t_0 don't depend on wavelength, that is, they are function of overall canopy structure/architecture and illumination geometry, but not leaf optical properties.

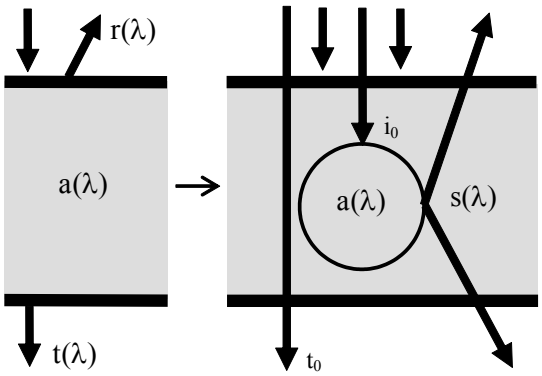

Figure 2. Partitioning of the incoming flux between canopy absorptance, $a(\lambda)$, transmittance, $t(\lambda)$, and reflectance, $r(\lambda)$, (left panel) as the result of the scattering process (right panel). The incoming flux is intercepted by canopy, (zero-order intrerceptance, i_0) or directly transmitted through canopy (zero-order transmittance, t_0). The intersepted flux participates in multiple scattering and is further subdivided between absorptance, $a(\lambda)$, and scattering out of canopy, $s(\lambda)$.

The scheme of multiple scattering is as follows. At each individual event of interaction in the sequence of multiple scattering, the $\omega(\lambda)$ portion of intercepted photons is scattered and $1 - \omega(\lambda)$ portion is absorbed (Fig. 3). In turn, the scattered portion, $\omega(\lambda)$, can be further subdivided into two parts: with probability p (*recollision probability*) photon will further participate in multiple scattering and will hit new leaf again, while with the probability 1-p the photon will be removed from canopy. Thus, the three components of the radiation budget for the singe photon-phytoelement interaction event are (Fig. 3):

[Absorbed] + [Re-scattered] + [Scattered out of canopy] =

$$= \left[1-\omega(\lambda)\right] + \left[p\omega(\lambda)\right] + \left[(1-p)\omega(\lambda)\right] \equiv 1. \qquad (7)$$

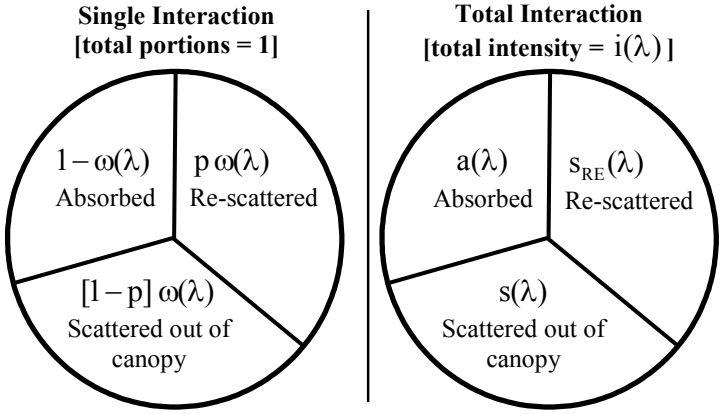

Figure 3. Partitioning of energy between absorbed, scattered out of canopy and rescattered within canopy portions is preserved through the individual scattering events (left panel). This leads to the same proportions for the total radiation regime (right panel).

Consider the sequence of scattering events generating the total observed radiation regime as detailed in Fig. 4. Part of the incoming intensity in the amount of t_0 is directly transmitted to the canopy bottom and will not participate in the process of multiple scattering. The remaining part of the incoming radiation, i_0, will be intercepted by canopy and become the source of the first interaction event resulting in the first-order absorptance, $a_1 = [1-\omega(\lambda)]\cdot i_0$, scattering out of canopy, $s_1 = [1-p]\omega(\lambda)\cdot i_0$ and re-scattering, $s_{RE,1} = \omega(\lambda)p\cdot i_0$, all are in proportions as shown in Fig. 3. The re-scattered portion will serve as a source for the second-order interaction events, and so on. Referring to Fig. 4, the canopy total *interceptance,* $i(\lambda)$, absorptance, $a(\lambda)$, scattering, $s(\lambda)$, and rescattering, $s_{RE}(\lambda)$ are calculated as the sum of contributions of individual scattering events:

$$i(\lambda) \equiv i_0 + i_1(\lambda) + i_2(\lambda) + ... = i_0 \sum_{k=0}^{\infty} \left[\omega(\lambda)p\right]^k = \frac{1}{1-p\omega(\lambda)} \cdot i_0 \equiv n_{eff}(\lambda)\cdot i_0, \qquad (8a)$$

$$a(\lambda) = i_0[1-\omega(\lambda)] \sum_{k=0}^{\infty} \left[\omega(\lambda)p\right]^k = \frac{1-\omega(\lambda)}{1-p\omega(\lambda)} \cdot i_0, \qquad (8b)$$

$$s(\lambda) = i_0[1-p]\omega(\lambda) \sum_{k=0}^{\infty} \left[\omega(\lambda)p\right]^k = \frac{[1-p]\omega(\lambda)}{1-p\omega(\lambda)} \cdot i_0, \qquad (8c)$$

$$s_{RE}(\lambda) = i_0 p\omega(\lambda)\sum_{k=0}^{\infty}\left[\omega(\lambda)p\right]^k = \frac{p\omega(\lambda)}{1-p\omega(\lambda)}\cdot i_0. \qquad (8d)$$

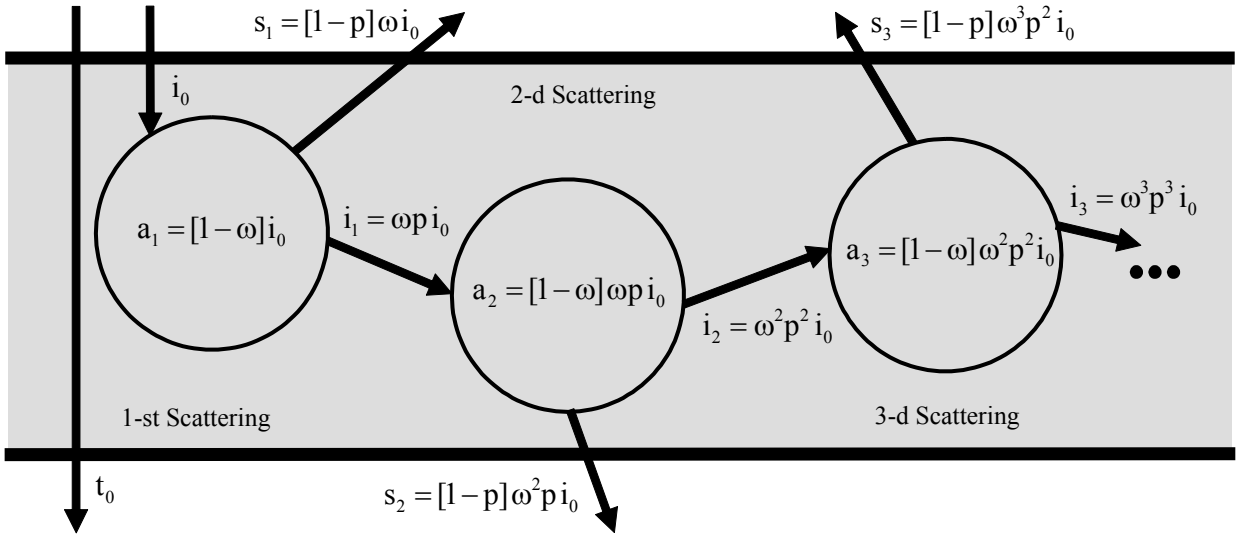

Figure 4. Quantitative presentation of the scattering scheme shown in Fig. 2. The sequence of cicles represents sequence of scattering events. The energy budget for each individual scattering event (intercepted, absorbed, scattered out of canopy and rescattered within the canopy portions) is according to Fig.3.

Refer to Fig. 5, which explains the meaning of the effective number of photon-phytoelement interactions, n_{eff}, appearing in Eq. (8a). According to the definition, the total intercepted by phytoelements radiation is the infinite sum of the amounts of intercepted radiation of decreasing intensity, corresponding to infinite series of photon-phytoelement interactions [Eq. (8a)] Alternatively, the contribution of infinite series can be represented by finite number of photon-phytoelement interactions, n_{eff}, assuming each has constant interceptance of i_0. Also note the following notations. Sometimes, the normalized versions of absorptance and scattering are used in the literature: *canopy absorption (scattering) coefficient*, $a(\lambda)/i_0$ ($s(\lambda)/i_0$), is the portion of intercepted photons that canopy absorb (escape canopy in upward and downward directions).

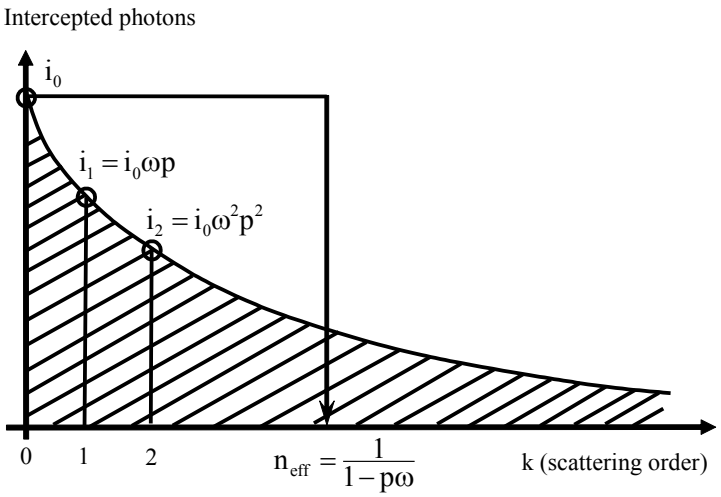

Figure 5. Derivation of the effective number of scattering events, n_{eff}. The total canopy interceptance is accumulated with the infinte number of scattering events, k, with declining interceptance, i_k. Effectively this can be represented as the contribution of finite number, n_{eff}, of interactions with constant interceptance, i_0. The numer n_{eff} is derived from the condition that area of rectange $n_{eff} \times i_0$ is equal to the area under curve i_k.

Refer to Eq. (8) and Figs. 3 and 6, and note the following properties of interceptance, absorptance, scattering out of canopy and rescattering. First, the series for interceptance, $i(\lambda)$, are unique in terms that the first term (zero-order interceptance) does not depends on wavelength. Second, the relationship between interceptance, absorptance, scattering out of canopy and rescattering is

$$\begin{cases} i(\lambda) = i_0 + s_{RE}(\lambda), \\ i_0 = a(\lambda) + s(\lambda). \end{cases} \Rightarrow \quad i(\lambda) = a(\lambda) + s(\lambda) + s_{RE}(\lambda). \tag{9}$$

Thus, the total canopy interceptance, $i(\lambda)$, consist of fixed component (absorptance and scattering out of canopy) and transit component (rescattering). The transit component is volatile, energy transferred from one scattering to another will ultimately be either absorbed or scattered out of canopy. Third, the relationship between energy fluxes at leaf and canopy are established with the following ratios:

$$\frac{i(\lambda)}{a(\lambda)} = \frac{1}{1-\omega(\lambda)}, \quad \frac{s(\lambda)}{a(\lambda)} = \frac{[1-p]\omega(\lambda)}{1-\omega(\lambda)}, \quad \frac{s_{RE}(\lambda)}{a(\lambda)} = \frac{p\,\omega(\lambda)}{1-\omega(\lambda)}. \tag{10}$$

The physical meaning of ratios in Eq. (10) is as follows [cf. Fig. 3]. In view that at each individual photon-phytoelement interaction the intercepted energy is distributed between absorptance, scattering out of canopy and rescattering in the constant proportion, independent on scattering order, this same proportion will be preserved at the whole canopy scale. For instance, the scattering out of canopy constitute $[1-p]\omega(\lambda)$ portion, while absorptance constitutes $1-\omega$ portion, and this holds true both at phytoelement and canopy scales.

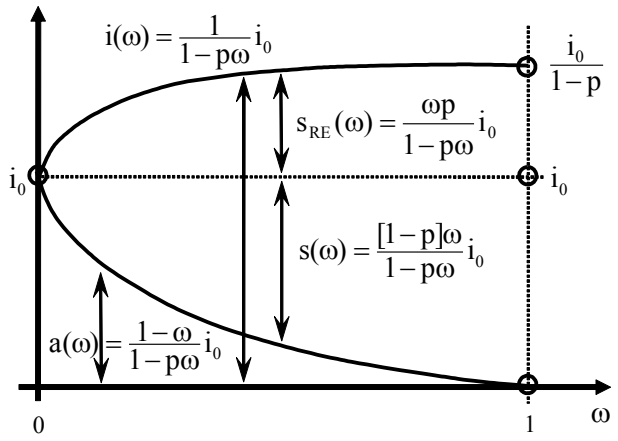

Figure 6. Functional dependance of canopy inteceptance, $i(\omega)$, absorptance, $a(\omega)$, scattering out of canopy, $s(\omega)$, and rescattering within canopy, $s_{RE}(\omega)$, on single scattering albedo, ω. Here, i_0 is the zero-order canopy interceptance and p is the recollision probability.

Next, consider functional dependence of interceptance, absorptance, and two scattering quantities on single scattering albedo, ω [cf. Fig. 6]. Note, zero-order quantities and the same quantities at $\omega = 0$ convey a distinct meaning and should not be used interchangeably. In the case of interceptance, i_0 and $i(\omega = 0)$ coincide, but the definition of i_0 does not require ω equal zero, as it is constant for all values of ω. In contrast, in the case of absorptance, a_0 and $a(\omega = 0)$ are different, and a_0 depends on ω. As ω increases, total interceptance increases starting from i_0 due to contribution of multiple scattering. In contrast, total absorptance is highest for black leaves ($\omega = 0$) and decreases with ω, because multiple scattering removes energy out of canopy. The two scattering quantities (scattering out of canopy and rescattering) are equal to zero at $\omega = 0$, but increase with increasing ω. The overall functional dependence and specific limits of all above quantities are shown in Fig. 6. Finally, note the consistency between series of scattering formulation [Eq. (10)] and RT equation [Eq. (4)].

Canopy Spectral Invariant for Interceptance: Consider total canopy interceptance at two independent wavelengths, $i(\lambda_1) = i_0/[1 - p\omega(\lambda_1)]$ and $i(\lambda_2) = i_0/[1 - p\omega(\lambda_2)]$ for $\lambda_1 \neq \lambda_2$ [cf. Eq. (8a)]. The system of the above two equations can be solved for the recollision probability:

$$p = \frac{i(\lambda_1) - i(\lambda_2)}{i(\lambda_1)\omega(\lambda_1) - i(\lambda_2)\omega(\lambda_2)}. \tag{11}$$

This equation expresses the principle of spectral invariance with respect to canopy interceptance. Recall [cf. Eqs. (7) and (9)] the total canopy interceptance, $i(\lambda)$, is partitioned between total canopy absorptance, $a(\lambda) = [1 - \omega(\lambda)]i(\lambda)$, and total canopy scattering, $s(\lambda) + s_{RE}(\lambda) = \omega(\lambda)i(\lambda)$. The principle of spectral invariance states that the ratio between difference in the amount of intercepted photons, $i(\lambda_1) - i(\lambda_2)$, and those of scattered photons, $\omega(\lambda_1)i(\lambda_1) - \omega(\lambda_2)i(\lambda_2)$, is spectrally invariant with respect to any wavelength λ_1 and λ_2, and is equal to the recollision probability. Figure 7 shows amount of photons intercepted, $i(\lambda)$, and scattered, $\omega(\lambda)i(\lambda)$, by canopy as function of wavelengths derived from measurements at Flakaliden site. Also shown is the frequency of values of the recollision probability, p, corresponding to all combinations of λ and λ_0. The sharp peak of the distribution suggests that the recollision probability, p, is invariant with respect to the wavelength with sufficiently high accuracy. The minor spread of the distribution is due to measurements errors and ignoring surface contribution.

(a) (b)

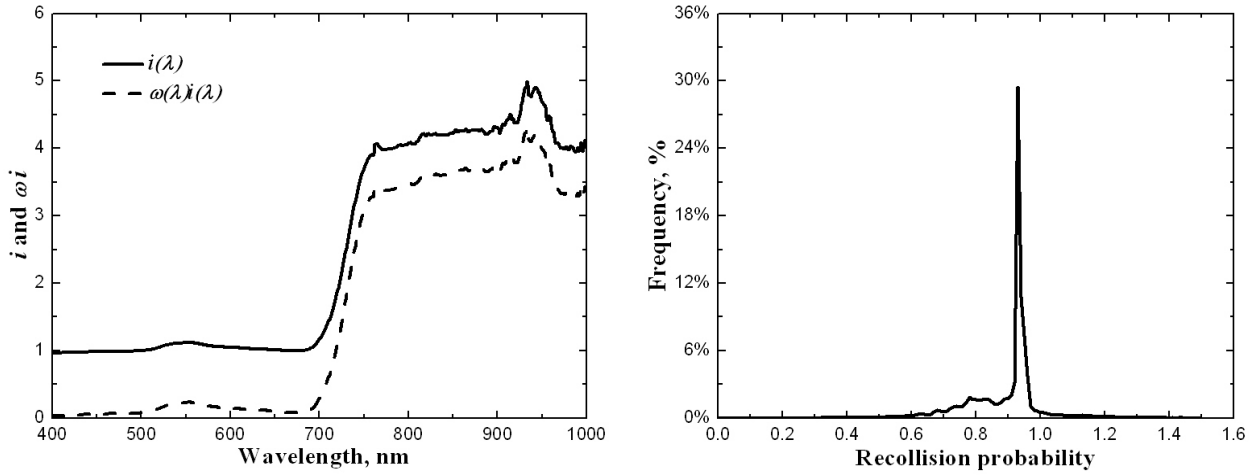

Figure 7. Retrieval of the recollision probability, p, from Flakaliden field data (Fig. 1). Panel (a) shows total canopy interceptance, $i(\lambda)$ (solid line), and total canopy scattering, $s(\lambda) + s_{RE}(\lambda) = \omega(\lambda) i(\lambda)$ (dashed line). Panel (b) shows frequency of values of the recollision probability derived according to Eq. (11).

The Equation (11) can be rearranged to a different form, which we use to derive p and i_0 ($= i(\omega = 0)$) from field data, namely,

$$\frac{1}{i(\lambda)} = \frac{1}{i_0} - \frac{p}{i_0}\omega(\lambda) .$$

If the reciprocal of the total canopy interceptance calculated from measured canopy absorption and needle albedo is plotted versus measured needle albedo, a linear relationship is obtained (Fig. 8). The recollision probability, p, and canopy interceptance, i_0, can be inferred from the slope and intercept.

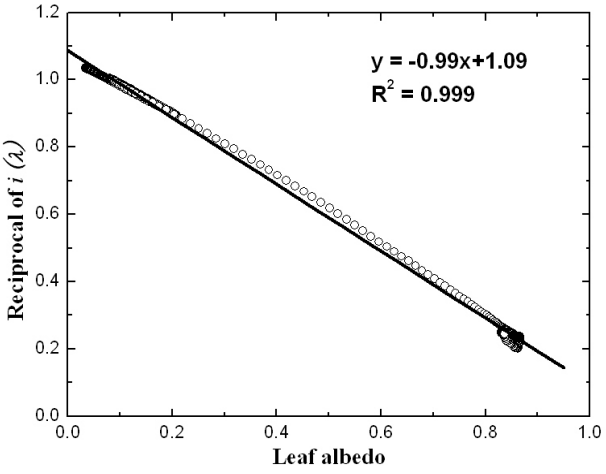

Figure 8. Reciprocal of $i(\lambda)$ and (b) $\omega(\lambda)/[i(\lambda) - i_0]$ versus leaf albedo $\omega(\lambda)$ derived from Flakaliden field data (Fig. 1). The recollision probability, p=0.91, and canopy interceptance, i_0=0.92, are derived from the slope and intercept of the line.

The key properties of the recollision probability are as follows. The recollision probability establishes the link between leaf and canopy scales, and thus it is a scaling parameter in RT theory for vegetation. This parameter accounts for the effect of the canopy structure on RT regime across range of scales. The parameter is wavelength independent. Monte Carlo simulations [Smolander and Stenberg, 2005] suggest that the recollision probability is minimally

sensitive to rather large changes in the direction of the incident beam. However, other numerical simulations [Lewis and Disney, 2007] indicate that the recollision probability depends on scattering order and LAI (Fig. 9). Thus, one should discriminate between the *actual recollision probability*, p_{actual}, which is function of scattering order, its *asymptotic value*, p_{inf}, a plateau, reached under condition of infinite scattering, and *effective value*, p_{efff}, evaluated over scattering events.

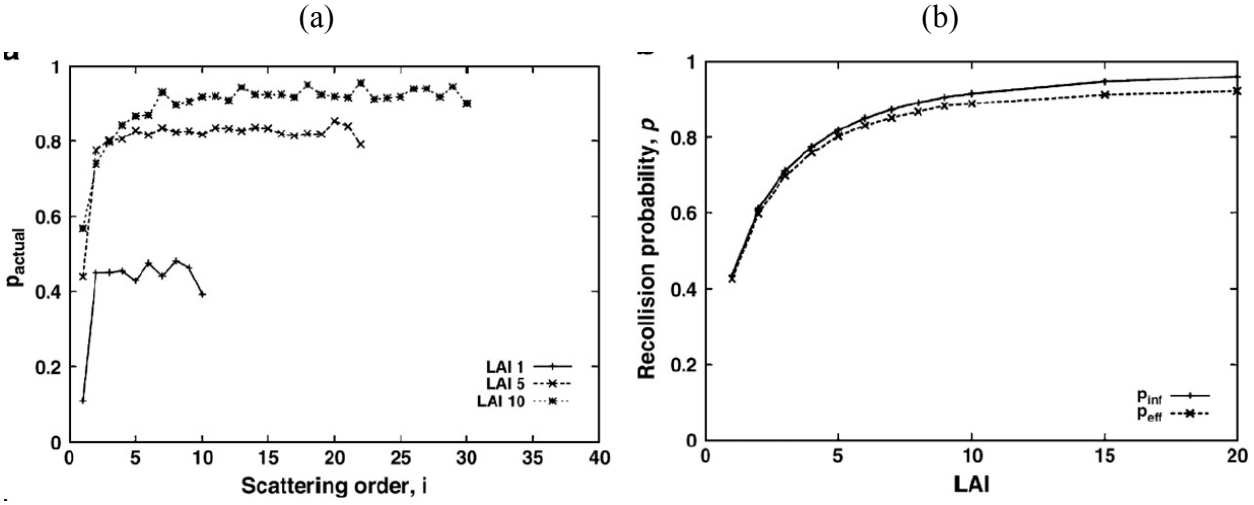

Figure 9. Recollision probability, p_{actual}, as a function of scattering order calculated for canopies with LAI 1, 5, 10. Infinite scattering order recollision probability (p_{inf}) and effective recollision probability (p_{efff}) as a function of LAI. Monte-Carlo simulations are performed for canopies composed of randomly located non-overlapping disks with a spherical leaf angle distribution (from Lewis and Disney, [2007]).

Canopy Spectral Invariant for Reflectance and Transmittance: The total canopy scattering consist of rescattering between phytoelements, $s_{RE}(\lambda)$, and scattering out of canopy, $s(\lambda)$. The rescattering term, $s_{RE}(\lambda)$, is characterized by recollision probability, p. The scattering out of canopy term, $s(\lambda)$, can be subdivided further into upward and downward components to derive reflectance and transmittance. The probability that scattered photon will escape the vegetation canopy through the upper (or lower) boundary is called *escape probabilities* ρ and τ, respectively. At each individual event of photon-phytoelement interaction, all possible outcomes of scattering are limited to photon escaping canopy in upward, or downward direction, or colliding another phytoelement, thus,

$$\rho + \tau + p = 1. \tag{12}$$

As in the case of recollision probability, p, the escape probabilities, ρ and τ, depend, in general, on scattering order, but reach constant value (plateau) after several iterations. The number of interaction events before this plateau is reached depends on the canopy structure and the needle transmittance-albedo ratio. Monte Carlo simulations suggest that the recollision and escape probabilities saturate after two-three photon-canopy interactions for low to moderate LAI canopies [Lewis and Disney, 2007]. This result underlies the approximation to the canopy reflectance, $r(\lambda)$, proposed by Disney and Lewis [2005],

$$r(\lambda) = \omega(\lambda)R_1 + \frac{\omega(\lambda)^2 R_2}{1 - p_r\omega(\lambda)}, \tag{13a}$$

where coefficients R_1, R_2 and p_r are determined by fitting Eq. (13a) to measured reflectance spectrum. Under assumption that the recollision, p, and escape probability, τ, remains constant in successive interactions,

$$R_1 \to \rho i_0, \quad R_2 \to \rho p i_0, \quad p_r \to p. \tag{13b}$$

The first term evaluates the portion of photons from the intercepted flux, i_0 that escape the vegetation canopy in upward directions as a result of one interaction with phytoelements. The second term accounts for photons that have undergone two and more interactions. Violation of the above condition results in a transformation of ρi_0, $\rho p i_0$, and p to some effective values R_1, R_2 and p_r as the result of the fitting procedure. The difference between actual and effective values of the escape probabilities depends on its speed of convergence as the number of interactions increases. A detailed analysis of this effect will be presented in Section 3. A simplified expression, $R_2 = p_r R_1$, can also be used, with a reduction in accuracy of the approximation [Disney and Lewis, 2005].

Figure 10 shows correlation between measured and evaluated according to Eq. (13) canopy reflectance over Flakaliden site. Overall close agreement supports the approximation of Disney and Lewis. In this example the selected values for R_1 and p_r give the best fit to the measured reflectance spectrum. These coefficients can also be evaluated from the slope and intercept of the regression line, derived from values of the needle albedo, $\omega(\lambda)$, and the reciprocal of $r(\lambda)/\omega(\lambda)$ at wavelengths [700 - 750 nm]. At those wavelengths values of $\omega(\lambda)$ are uniformly distributed in the interval [0.1, 0.9] and the canopy reflectance exhibits a strong correlation with $\omega(\lambda)$. These features allow reducing the impact of ground reflectance and measurement uncertainties on the specification of R_1 and p_r from the regression line.

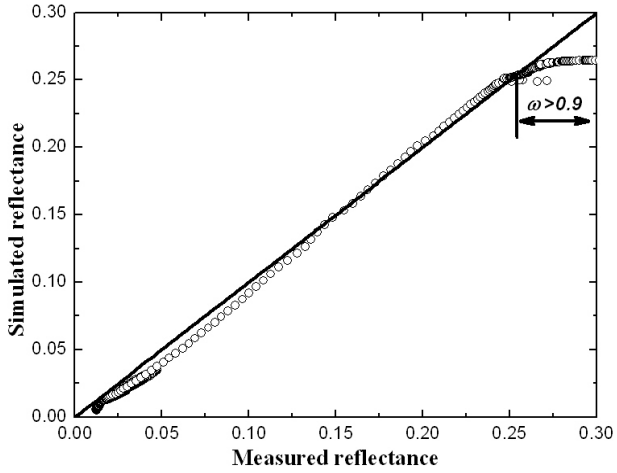

Figure 10. Correlation between measured canopy reflectance and canopy reflectance evaluated using Eq. (13) with $R_1 = 0.15$, $p_r = 0.59$, and $R_2 = p_r R_1 = 0.09$ for the spectral interval $400 \le \lambda \le 900$ nm. The arrow indicates a range of reflectance values corresponding to $\omega \ge 0.9$. Field data are from Flakaliden site (Fig. 1).

Analogous to Eq. (13) for canopy reflectance, a similar relationship can be established between canopy transmittance and phytoelements albedo, namely

$$t(\lambda) = t_0 + \frac{T_1\,\omega(\lambda)}{1 - p_t\omega(\lambda)}, \qquad (14a)$$

where the values of coefficients t_0, T_1 and p_t are chosen by fitting Eq. (14a) to the measured spectrum of canopy transmittance. Analogous to Eq. (13b), the coefficients T_1 and p_t are effective values and under assumption that the recollision, p, and escape probability, τ, remains constant in successive interactions,

$$T_1 \to \tau i_0, \quad p_t \to p. \tag{14b}$$

Under the above assumption, the value of t_0 converges to zero-order transmittance [cf. Eq. (6)]. Figure 11 shows correlation between measured and evaluated according to Eq. (14) canopy transmittance over Flakaliden site. A theoretical analysis of this approximation will be presented in Section 3. It should be noted that canopy transmittance is sensitive to the needle transmittance to albedo ratio $\tau_L(\lambda)/\omega(\lambda)$ [Panferov et al., 2001]. This may imbue wavelength dependence to the escape probabilities for low order photon scattering.

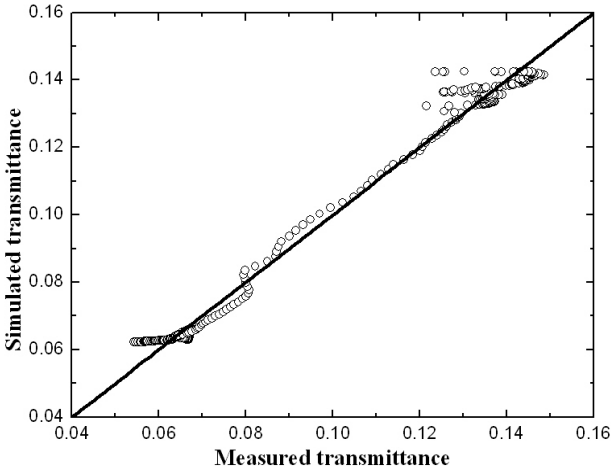

Figure 11. Correlation between measured canopy transmittance and canopy transmittance simulated using Eq. (14) with $t_0 = 0.06$, $T_1 = 0.017$ and $p_t = 0.94$. Energy conservations for i_0 and t_0 is preserved with good accuracy, i.e., $i_0 + t_0 = 0.92+0.06=0.98$. Field data are from Flakaliden site (Fig. 1).

Impact of Soil Reflectance: The total canopy transmittance, $t(\lambda)$, reflectance, $r(\lambda)$, and absorptance, $a(\lambda)$, for the general RT problem of canopy above soil background can be represented by contribution of black-soil and soil sub-problems as follows (cf. Chapter 4):

$$t(\lambda) = \frac{t_{BS}(\lambda)}{1-\rho_{soil}(\lambda)r_S(\lambda)} = t_{BS}(\lambda) + t(\lambda)\rho_{soil}(\lambda)r_S(\lambda), \tag{42a}$$

$$r(\lambda) = r_{BS}(\lambda) + t(\lambda)\rho_{soil}(\lambda)t_S(\lambda), \tag{42b}$$

$$a(\lambda) = a_{BS}(\lambda) + t(\lambda)\rho_{soil}(\lambda)a_S(\lambda). \tag{42c}$$

Here, ρ_{soil} is the hemispherical reflectance of the canopy ground. Variables r_{BS} and r_S; t_{BS} and t_S; a_{BS} and a_S denote canopy reflectance, transmittance, and absorptance calculated for a vegetation canopy (1) illuminated from above by the incident radiation and bounded from below by a non reflecting surface (subscript "BS", for black soil); and (2) illuminated from the bottom by normalized isotropic sources and bounded from above by a non-reflecting boundary (subscript "S"). These variables are related via the energy conservation law, i.e.,

$$a_i(\lambda) + r_i(\lambda) + t_i(\lambda) = 1, \quad \text{i=BS or S-problem.}$$

The canopy spectral invariants are formulated for r_{BS}, t_{BS} and a_{BS}. The measured spectral transmittance, t, and reflectance, r, are taken as estimates of r_{BS}, t_{BS}. The absorptance a_{BS} is approximated using Eq. (5). It follows from Eq. (42) that the relative errors, Δ_a, Δ_t and Δ_r, and in a_{BS}, t_{BS}, and r_{BS} due to the neglecting of surface reflection can be estimated in terms of measured t, r and ρ_{soil} as:

$$\Delta_a \equiv \frac{a_{BS} - a}{a} = \frac{t}{1 - t - r}\rho_{ssoil}(1 - t_S - r_S) \le \frac{t}{1 - t - r}\rho_{soil}, \tag{43a}$$

$$\Delta_t \equiv \frac{t - t_{BS}}{t} = \rho_{soil}\, r_S \le \rho_{soil}, \tag{43b}$$

$$\Delta_r \equiv \frac{r - r_{BS}}{r} = \frac{t}{r}\rho_{soil}\, t_S \le \frac{t}{r}\rho_{soil}, \tag{43c}$$

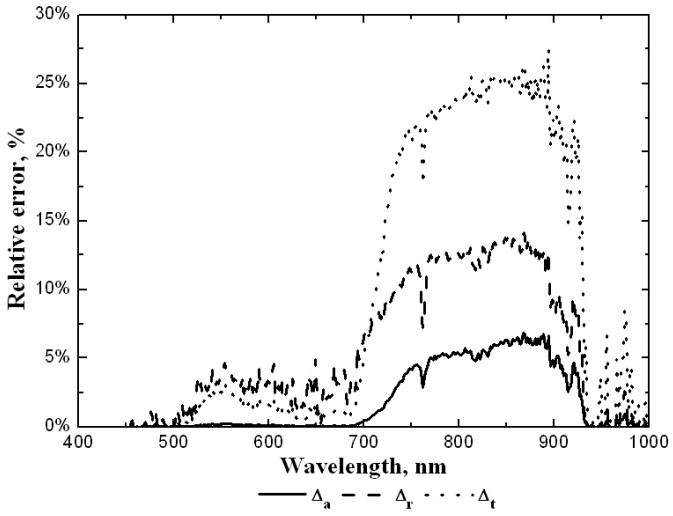

Figure 12. Upper limits of the relative errors Δ_t, Δ_r, and Δ_a in the estimates of t_{BS}, r_{BS} and a_{BS}, arising due to the effect of non-black soil reflectance. Reference field data are from Flakaliden site in Sweden (Fig. 1).

Thus, neglecting contribution of soil, results in overestimation of reflectance and transmittances and underestimation of absorptances. Figure 12 shows upper limits of the relative errors Δ_t, Δ_r,and Δ_a.as a function of the wavelength for Flakaliden data. It follows from the above analysis that measured canopy absorptance approximates a_{BS} with an accuracy of about 5%. Deviations of measured canopy transmittance and reflectance from t_{BS} and r_{BS} in the interval $400 \le \lambda \le 700$ nm do not exceed 5%, however they increase substantially in the interval $700 \le \lambda \le 900$ nm.

Major Assumptions for Spectral Invariants: We summarize key assumptions of the theory of spectral invariants along three categories. (1) Boundary conditions assumptions: a vegetation canopy is illuminated from above by a wavelength independent parallel beam and bounded from below by a non-reflecting (black) surface. The last assumption is required to avoid re-entrance of photons exiting through background. (2) Phytoelements scattering properties assumptions: the interaction cross-section, $\sigma(\underline{r},\underline{\Omega})$, is treated as wavelength independent considering the size of the scattering elements (leaves, branches, twigs, etc.) relative to the wavelength of solar radiation. (3) Effective values assumptions: the recollision and escape probabilities (p, ρ, τ) are generally dependant on the scattering order, but tend to reach plateau and could be replaced with corresponding effective values. The uncertainties of retrievals of interceptance (or absorptance) are relatively low, as those variables depend on recollision probability only, while

uncertainties for transmittance and reflectance are higher as those variables depend both on recollision and escape probabilities.

3. RT Theory of Spectral Invariants

Successive Orders of Scattering Approximation: Below we formulate the rigorous mathematical basis underlying the principle of spectral invariance, introduced in the previous section. We adopt functional analysis formulation of the transport equation (Vladimirov [1963], Marchuk et al [1980]). Let V and δV be the domain where radiative transfer occurs and its boundary, respectively. The domain V can be a shoot, tree crown, tree stand, etc. Let L and S_λ be the *streaming-collision* and *scattering* linear operators (Chapter 2),

$$LI_\lambda \equiv \underline{\Omega}\nabla I_\lambda(\underline{r},\underline{\Omega}) + \sigma(\underline{r},\underline{\Omega})I_\lambda(\underline{r},\underline{\Omega}), \tag{15a}$$

$$S_\lambda I_\lambda \equiv \int_{4\pi} \sigma_{s,\lambda}(\underline{r},\underline{\Omega}' \to \underline{\Omega})I_\lambda(\underline{r},\underline{\Omega}')d\underline{\Omega}', \tag{15b}$$

where $I_\lambda(\underline{r},\underline{\Omega})$ is the radiation intensity at wavelength λ, spatial location $\underline{r}$ and direction $\underline{\Omega}$; σ and σ_S are extinction and differential scattering coefficients, respectively. In the following we assume that single scattering albedo, $\omega(\lambda)$, does not depend on $\underline{r}$ and $\underline{\Omega}$. The 3D radiative transfer equation (Chapter 4) can be formulated in operator notations as follows

$$LI_\lambda = S_\lambda I_\lambda. \tag{16a}$$

The boundary conditions include canopy top to be illuminated from above by unit beam in direction $\underline{\Omega}_0$ and canopy bottom to be absolutely absorbing,

$$I_\lambda(\underline{r}_{top},\Omega) = \delta(\Omega - \Omega_0), \quad \underline{r}_{top} \in \delta V, \quad \mu(\underline{\Omega}) < 0, \tag{16b}$$

$$I_\lambda(\underline{r}_{bottom},\underline{\Omega}) = 0, \quad \underline{r}_{bottom} \in \delta V, \quad \mu(\underline{\Omega}) > 0. \tag{16c}$$

We solve Eq. (16) with method of successive order of scattering approximations (SOSA). The total radiation intensity is represented as the sum of uncollided, Q_0, and collided, components (cf. Chapter 2),

$$I_\lambda = Q_0(\underline{r},\underline{\Omega}) + I_\lambda^{dif}(\underline{r},\underline{\Omega}). \tag{17}$$

By definition, Q_0 is the radiation intensity of photons in the incident flux that will arrive at $\underline{r}$ along direction $\underline{\Omega}$ without suffering a collision. This is a wavelength independent parameter. Q_0 satisfies the equation

$$LQ_0 = 0, \tag{18}$$

and the original boundary conditions, Eq. (16b-c). $I_\lambda^{dif}(\underline{r},\underline{\Omega})$ is the collided (or diffuse) radiation intensity, that is, radiation generated by photons scattered one or more times. This is a wavelength dependant parameter. Combining Eqs. (16)-(18) one can verify that $I_\lambda^{dif}(\underline{r},\underline{\Omega})$ satisfies the following equation,

$$LI_\lambda^{dif} = SQ_0 + SI_\lambda^{dif}, \tag{19}$$

and zero boundary conditions at the top and bottom of canopy. Finally, by combining Eq. (17) and (19), the Eq. (16a) can be rewritten in the form of the following integral radiative transfer equation,

$$I_\lambda = Q_0 + TI_\lambda, \tag{20}$$

where operator $T \equiv L^{-1}S$. The SOSA method states that the solution of Eq. (20) is given by

$$I_\lambda = \sum_{m=0}^{\infty} Q_m, \quad \text{where } Q_m = TQ_{m-1} = T^m Q_0, \ m = [1,\infty]. \tag{21}$$

One can verify the validity of solution given by Eq. (21) by substituting it in Eq. (20) and taking into account properties of operator T. The physical meaning of Eq. (21) is as follows. Q_m is the radiation intensity of photons, scattered m times. The uncollided photons with intensity Q_0, serve as the source for the photons scattered one time with intensity Q_1, which in turn serve as a source of photons scattered two times, and so on (cf. Fig. 4). In Monte Carlo simulations, operator T corresponds to a procedure, which inputs Q_0, simulates the scattering event, calculates the photon free path and outputs the distribution, Q_1, of photons just before their next interaction with phytoelements; the procedure is repeated with the source of photons evaluated as output at the previous step.

Spectral Invariant for Canopy Interceptance: Let $\|f\|$ be the norm of 3D radiation field $f(\underline{r},\underline{\Omega})$ in the domain $V \times 4\pi$, according to notations of functional analysis [Vladimirov, 1963; and Marchuk et al., 1980],

$$\| f \| = \int_V d\underline{r} \int_{4\pi} d\underline{\Omega}\, \sigma(\underline{r},\underline{\Omega}) \, | f(\underline{r},\underline{\Omega}) | , \tag{22}$$

In terms of these notations, the total canopy interceptance, $i(\lambda)$, and m-order canopy interceptance, i_m, are $\|I_\lambda\|$ and $\|Q_m\|$, respectively [cf. Eqs. (2a) and (8a)]. The distribution of probability, $e_m(\underline{r},\underline{\Omega})$, that a photon scattered m times will arrive at $\underline{r}$ along the direction $\underline{\Omega}$ without suffering a collision can be expressed as the radiation intensity of the photons, scattered m times, normalized by its norm

$$e_m(\underline{r},\underline{\Omega}) \equiv \frac{Q_m(\underline{r},\underline{\Omega})}{\| Q_m \|}, \quad \| e_m \| = 1. \tag{23}$$

The normalization is required, as $Q_m(\underline{r},\underline{\Omega})$ is the radiation intensity, whose norm, interceptance, i_m, decreases with order of scattering m (cf. Fig. 5), while $e_m(\underline{r},\underline{\Omega})$ is the distribution of probability, whose norm is required to be unity.

The recollision probability can be expressed in terms of $\|Q_m\|$. The recollision probability, p_m, at the step m of scattering is the ratio of radiation intensity rescattered inside of canopy to the total intensity of scattering (i.e., rescattered inside of canopy and escaped canopy) [cf. Figs. 3-4 and Eq. (7)]. The radiation intensity scattered m-1 times is Q_{m-1}, therefore, $\|Q_{m-1}\|$ will be intercepted and $\omega\|Q_{m-1}\|$ will be available for the total scattering at the current step m of scattering. The total radiation available for scattering originates the radiation intensity Q_m at current step m of scattering. The rescattered intensity at the current step m is equal to the intercepted intensity at the next step m+1, $\|Q_m\|$. Therefore,

$$p_m = \frac{\| Q_m \|}{\omega \| Q_{m-1} \|}. \tag{24}$$

For convenience of the following derivations we will use $\gamma_m \equiv p_m \omega$. Taking into account Eqs. (21), (23) and (24), the distributions $e_{m-1}(\underline{r},\underline{\Omega})$ and $e_m(\underline{r},\underline{\Omega})$ between successive orders of scattering m-1 and m are related as

$$Te_{m-1}(\underline{r},\underline{\Omega}) = T\frac{Q_{m-1}(\underline{r},\underline{\Omega})}{\|Q_{m-1}\|} = \frac{\|Q_m\|}{\|Q_{m-1}\|} \times \frac{Q_m(\underline{r},\underline{\Omega})}{\|Q_m\|} = \gamma_m e_m(\underline{r},\underline{\Omega}). \tag{25}$$

The above equation explicitly states the nature of operator T: it converts the probability distribution of photons from previous to the next order of scattering and evaluates recollision probability.

The set $(\gamma_m,\ e_m(\underline{r},\underline{\Omega}))$, $m = [0,\infty]$, derived from operator T according to SOSA method poses one fundamental property established in *eigenvalues/eigenvectors theory* of functional analysis

[Vladimirov, 1963]. An eigenvalue of the radiative transfer equation is a number χ such that there exist a function $\psi(\underline{r},\underline{\Omega})$ that satisfies the equation

$$T\psi(\underline{r},\underline{\Omega}) = \chi\,\psi(\underline{r},\underline{\Omega}) \tag{26}$$

and zero boundary conditions. Under some general conditions [Vladimirov, 1963], the set of eigenvalues and eigenvectors $(\chi_m, \psi_m(\underline{r},\underline{\Omega}))$ is a discrete set. Since the eigenvalue and eigenvector problem is formulated for zero boundary conditions, χ and $\psi(\underline{r},\underline{\Omega})$ are independent on the incoming radiation. The radiative transfer equation has a *unique positive eigenvalue*, χ^*, that corresponds to a *unique positive eigenvector*, ψ^* [Vladimirov, 1963],

$$T\psi^*(\underline{r},\underline{\Omega}) = \chi^*\psi^*(\underline{r},\underline{\Omega}), \quad \| \psi^* \| = 1.$$

It should be emphasized that set $(\chi_m, \psi_m(\underline{r},\underline{\Omega}))$, derived according to eigenvalue problem [Eq. (26)] is different from $(\gamma_m, e_m(\underline{r},\underline{\Omega}))$, derived according SOSA method [Eq. (25)]. In general, $(\gamma_m,\ e_m(\underline{r},\underline{\Omega}))$ vary with the scattering order m. However, they tend to converge to plateaus as the number of interactions increases according to numerical results [Lewis and Disney, 1998]. Further, according to general principles of functional analysis [Riesz and Sz.-Nagy, 1990; Vladimirov, 1963] the set $(\gamma_m, e_m(\underline{r},\underline{\Omega}))$ converges to the unique positive eigenvector/eigenvalue of operator T, as number of scattering increases,

$$\lim_{m\to\infty} \gamma_m = \chi^*, \quad \lim_{m\to\infty} e_m(\underline{r},\underline{\Omega}) = \psi^*(\underline{r},\underline{\Omega}). \tag{27}$$

Assuming negligible variation in γ_m and $e_m(\underline{r},\underline{\Omega})$ for the scattering order m and higher and accounting for Eqs. (21) and (23), the radiation field, $I_\lambda(\underline{r},\underline{\Omega})$, can be approximated as follows

$$I_\lambda(\underline{r},\underline{\Omega}) = \sum_{k=0}^{\infty} \| Q_k \| e_k = \sum_{k=0}^{m} \| Q_k \| e_k + \sum_{k=m+1}^{\infty} \| Q_k \| e_k$$

$$= \sum_{k=0}^{m} \| Q_k \| e_k + \sum_{\ell=0}^{\infty} \gamma_{m+1}^{\ell} \| Q_{m+1} \| e_{m+1} + \delta_m$$

$$= \sum_{k=0}^{m} \| Q_k \| e_k + \| Q_m \| \frac{\gamma_{m+1}}{1-\gamma_{m+1}} e_{m+1} + \delta_m$$

$$\equiv I_{\lambda,m}(\underline{r},\underline{\Omega}) + \delta_m . \qquad (28)$$

That is, radiation field, $I_\lambda(\underline{r},\underline{\Omega})$, is approximated with $I_{\lambda,m}(\underline{r},\underline{\Omega})$, for which the contribution of the first m scattering orders is calculated exactly and contribution of higher order scattering is approximated assuming that γ_k and $e_k(\underline{r},\underline{\Omega})$ are constant with respect to k for $k \geq m+1$. The error of this approximation is δ_m.

Following the above approach, we examine the accuracy of the approximation of the canopy interceptance as a function of the scattering order m. It follows form Eq. (28) that the m-th approximation, $i_m(\lambda)$, to $i(\lambda)$ is

$$i_m(\lambda) \equiv \left\| I_{\lambda,m}(\underline{r},\underline{\Omega}) \right\| = \sum_{k=0}^{m} \| Q_k \| + \| Q_m \| \frac{\gamma_{m+1}}{1-\gamma_{m+1}} = i_0 \left(\sum_{k=0}^{m} \theta_k + \frac{\theta_{m+1}}{1-\gamma_{m+1}} \right). \qquad (29)$$

Here $i_0 \equiv \| Q_0 \|$ is the zero-order canopy interceptance; $\theta_0 = 1$, and

$$\theta_k \equiv \frac{\| Q_k \|}{\| Q_0 \|} = \frac{\| Q_k \|}{\| Q_{k-1} \|} \times \frac{\| Q_{k-1} \|}{\| Q_{k-2} \|} \times \ldots \times \frac{\| Q_1 \|}{\| Q_0 \|} = \gamma_1 \gamma_2 \ldots \gamma_k , \quad k \geq 1. \qquad (30)$$

The error, $\delta i_m(\lambda)$, in the m-th approximation is given by [Huang et al., 2007]

$$| \delta i_m | = \left| i(\lambda) - i_m(\lambda) \right| \leq \varepsilon_{\gamma,m+1} \frac{\theta_{m+1}}{1-\gamma_{m+1}} s_{m+1} i_0 , \qquad (31)$$

where

$$\varepsilon_{\gamma,m+1} = \max_{k \geq 1} \frac{| \gamma_{m+1+k} - \gamma_{m+1} |}{\gamma_{m+1+k}}, \quad s_{m+1} = \sum_{k=1}^{\infty} \frac{\theta_{m+1+k}}{\theta_{m+1}} . \qquad (32)$$

Note that $\lim_{m\to\infty} \sqrt[m]{\theta_m} = \gamma_\infty$. If m is large enough, i.e. $\sqrt[m+1]{\theta_{m+1}} \approx \gamma_\infty$, the ratio $\theta_{m+1+k} / \theta_{m+1}$ can be approximated by γ_∞^k. Substituting this relationship into Eq. (32) one obtains $s_m \approx \gamma_\infty /(1-\gamma_\infty)$.

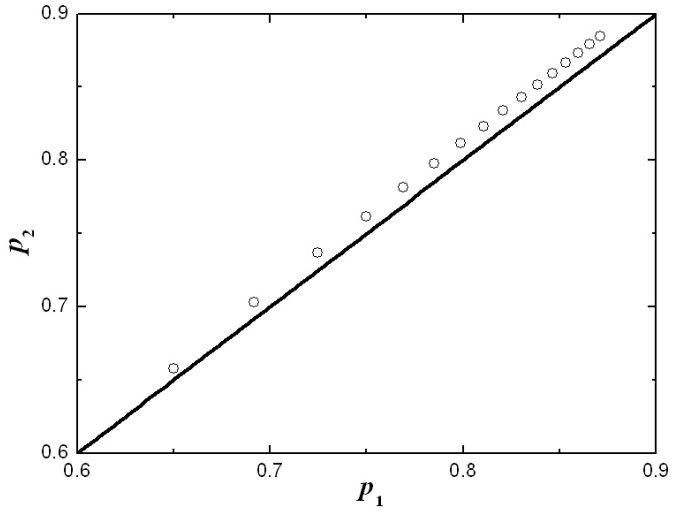

Figure 13. Correlation between first and second scattering order recollision probabilities (p_1 and p_2) for a range of LAI. The RT simulations were performed with the stochastic RT model for a canopy modeled with identical cylindrical "trees" uniformly distributed over black background. Crown height=1, ground cover=variable and plant LAI=10, SZA=30^0.

Two factors determine the accuracy of the m-th approximation of canopy interceptance. The first is the difference between successive approximations γ_{m+1} and γ_{m+1+k}; that is, the smaller this difference, the more accurate the approximation is. The second factor is the contribution of photons scattered m+1 or more times to the canopy radiation field. Their contribution is given by $\theta_{m+1} /(1-\gamma_{m+1}) \approx \gamma_\infty^{m+1} /(1-\gamma_\infty)$ which depends on the recollision probability, p_∞, and the single scattering albedo, ω; that is, the higher $\gamma_\infty = p_\infty \omega$ is, the higher order of approximation is needed to estimate the canopy interceptance. This is illustrated in Fig. 13. The variations in the recollision probability as function of scattering order reaches its maximum at high values of p (here the recollision probabilities for the first and second order of scattering were compared). The spectral invariant can not be derived if $p_\infty \omega = 1$ since the Neumann series (24) do not converge in this case.

Spectral Invariants for the Canopy Transmittance and Reflectance: Let the domain V be a layer $0 \le z \le H$. The surfaces S, $z = 0$ and $z = H$ constitute its upper and lower boundaries, respectively. Let $\|f\|_r$ and $\|f\|_t$ be norms of 3D radiation field $f(\underline{r}, \underline{\Omega})$ in the domain $S \times 2\pi$,

$$\| f \|_r = \int_{z=0} d\underline{r} \int_{2\pi^+} d\underline{\Omega} f(r,\underline{\Omega}) |\mu|,$$

$$\| f \|_t = \int_{z=H} d\underline{r} \int_{2\pi^-} d\underline{\Omega} f(r,\underline{\Omega}) |\mu|, \tag{33}$$

where the first integral is taken over the top boundary and in upward direction, while second is taken over lower boundary in downward directions. In terms of notations of Eq. (33), the canopy reflectance, $r(\lambda)$, and transmittance, $t(\lambda)$, are given by $\|I_\lambda\|_r$ and $\|I_\lambda\|_t$. Recall, according to notations of Eq. (22) canopy interceptance, $i(\lambda)$, is given by $\|I_\lambda\|$. The relationship between reflectance, transmittance and interceptance for some order of scattering m can be derived as follows. Recall, $Q_m = TQ_{m-1}$ [cf. Eq. (21)], or, in terms of operators L and S [cf. Eq. (15)], $LQ_m = SQ_{m-1}$. Integrating the last equation over the domain $V \times 4\pi$, we have:

$$\int_{4\pi} d\underline{\Omega} \int_V dV \Omega \nabla Q_m(\underline{r},\underline{\Omega}) + \int_{4\pi} d\underline{\Omega} \int_V dV \sigma(\underline{\Omega}) Q_m(\underline{r},\underline{\Omega}) = \int_{4\pi} d\underline{\Omega} \int_V dV \int_{4\pi} d\underline{\Omega}' \sigma_S(\underline{\Omega}' \to \underline{\Omega}) Q_{m-1}(\underline{r},\underline{\Omega}'),$$

$$\Rightarrow \quad \int_{4\pi} d\underline{\Omega} \int_S d\underline{S}\underline{\Omega} Q_m(\underline{r},\underline{\Omega}) + \int_{4\pi} d\underline{\Omega} \int_V dV \sigma(\underline{\Omega}) Q_m(\underline{r},\underline{\Omega}) = \omega \int_{4\pi} d\underline{\Omega} \int_V dV \sigma(\underline{\Omega}) Q_{m-1}(\underline{r},\underline{\Omega}'),$$

$$\Rightarrow \quad \|Q_m\|_r + \|Q_m\|_t + \|Q_m\| = \omega \|Q_{m-1}\|. \tag{34}$$

In the above derivations we accounted for definition of norms [Eqs. (22) and (33)], relationship between extinction coefficient, $\sigma(\underline{\Omega})$, and differential scattering coefficient, $\sigma_S(\underline{\Omega}' \to \underline{\Omega})$, [Eq. (3)] and Gauss theorem for converting volume integral to the surface integral for some scalar function. Normalizing Eq. (34) by $\omega\|Q_{m-1}\|$ we finally have

$$\rho_m + \tau_m + p_m = 1, \tag{35a}$$

where ρ_m and τ_m are escape probabilities for reflectance transmittance and p_m is the recollision probability for the m-th order of scattering,

$$\rho_m \equiv \frac{\| Q_m \|_r}{\omega \| Q_{m-1} \|}, \quad \tau_m \equiv \frac{\| Q_m \|_t}{\omega \| Q_{m-1} \|}, \quad p_m \equiv \frac{\|Q_m\|}{\omega \|Q_{m-1}\|}. \tag{35b}$$

The physical interpretation of Eqs. (34) and (35) follows those given for Eq. (24). The recollision probability, p_m (escape probability in upward, ρ_m, and downward, τ_m, directions) at the step m of scattering is the ratio of radiation intensity rescattered inside of canopy (escaped canopy in upward and downward directions) to the total intensity of scattering. The total intensity available for scattering at the current step m of scattering is $\omega\|Q_{m-1}\|$. This total intensity is distributed between rescattered intensity at current step m, $\|Q_m\|$, escaped canopy in upward directions, $\|Q_m\|_r$, and escaped canopy in downward direction, $\|Q_m\|_t$. This explains Eq. (34). The ratio of above quantities according to definition of recollision and escape probabilities explains Eq. (35b). The escape and recollision probabilities correspond to portions of all possible events of scattering (escaped upward, downward or rescattered), which explains Eq. (35a). Note also, the escape probabilities vary with the scattering order, but, as in the case of recollision probabilities, they reach plateaus (ρ_∞ and τ_∞) as the number of interactions increases.

It follows from Eq. (28) that the m-th approximation, $r_m(\lambda)$ and $t_m(\lambda)$, to the canopy reflectance and transmittance are

$$r_m(\lambda) \equiv \| I_{\lambda,m} \|_r = \left[\sum_{k=1}^{m} \rho_k \theta_{k-1} + \frac{\theta_m \rho_{m+1}}{1-\gamma_{m+1}} \right] \omega i_0 , \tag{36a}$$

$$t_m(\lambda) \equiv \| I_{\lambda,m} \|_t = t_0 + \left[\sum_{k=1}^{m} \tau_k \theta_{k-1} + \frac{\theta_m \tau_{m+1}}{1-\gamma_{m+1}} \right] \omega i_0 . \tag{36b}$$

Here i_0 and t_0 are zero-order canopy interceptance and transmittance, respectively [cf. Eq. (6)]; and θ_k is defined by Eq. (30). Errors in the m-th approximation of canopy reflectance and transmittance are given by [Huang et al., 2007]

$$\left|\delta r_m\right| = \left| r(\lambda) - r_m(\lambda)\right| \le (\varepsilon_{r,m+1} + \varepsilon_{\gamma,m+1}) \frac{\theta_m \rho_{m+1}}{1-\gamma_{m+1}} s_{r,m} \omega i_0 , \tag{37a}$$

$$\left|\delta t_m\right| = \left| t(\lambda) - t_m(\lambda)\right| \le (\varepsilon_{t,m+1} + \varepsilon_{\gamma,m+1}) \frac{\theta_m \tau_{m+1}}{1-\gamma_{m+1}} s_{t,m} \omega i_0 . \tag{37b}$$

Here $\varepsilon_{\gamma,m}$ is defined by Eq. (32) and

$$\varepsilon_{\kappa,m+1} = \max_{k\ge 1} \frac{\left| \kappa_{m+1+k} - \kappa_{m+k} \right|}{\kappa_{m+k}}, \quad s_{\kappa,m} = \sum_{k=1}^{\infty} \frac{\theta_{m+k}}{\theta_m} \frac{\kappa_{m+k}}{\kappa_{m+1}} , \tag{37c}$$

where κ and κ_m represent either canopy reflectance ($\kappa = r$, $\kappa_m = \rho_m$) or canopy transmittance ($\kappa = t$, $\kappa_m = \tau_m$).

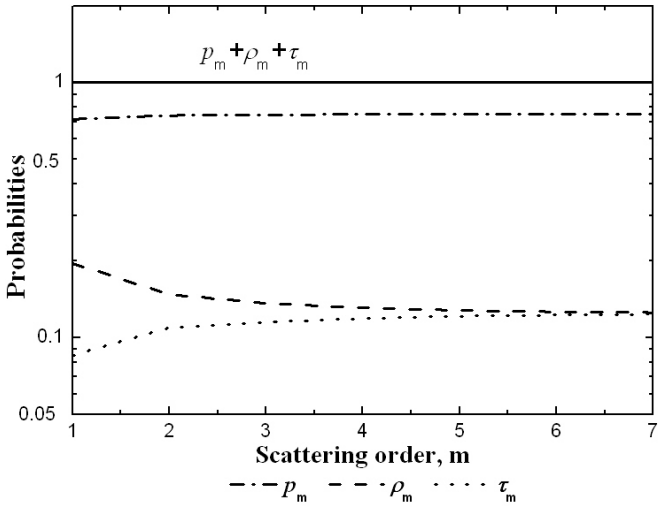

Figure 14. Recollision probability, p_m, and escape probabilities, τ_m and ρ_m, as a function of the scattering order m. Their limits are p_∞=0.75, τ_∞=0.125 and ρ_∞=0.125. The relative difference $\varepsilon_{\gamma,m+1}$ in the recollision probability is 3% for m=0 and 0.8% for m=1. Parameters of the RT simulations are the same as for Fig. 12, except ground cover=0.16.

In addition to two factors that determine the accuracy in the m-th approximation of the canopy interceptance [cf. Eq. (31)], δr_m and δt_m also depend on the convergence of two successive approximations κ_{m+k} and κ_{m+k+1} to ρ_∞ or τ_∞. Thus, the errors in the m-th approximations to the canopy reflectance and transmittance result from the errors in the recollision and escape probabilities, and from a contribution of photon multiple scattering to the canopy radiation regime. The m-th approximation to the canopy reflectance and transmittance, therefore, is less accurate compared to that to the canopy interceptance. This is illustrated in Fig. 14. In this example, the relative difference $|\gamma_{m+1+k} - \gamma_{m+1}|/\gamma_{m+1+k}$ is 3% for $m = 0$ and becomes negligible for $m \geq 1$. The zero and first order approximations provide accurate spectral invariant relationships for the canopy interceptance. The corresponding differences in the escape probabilities do not exceed 4% for $m \geq 2$, indicating that two scattering orders are required to evaluate spectral invariants for canopy transmittance and reflectance with accuracy comparable to that given by zero approximation to the canopy interceptance.

Spectral Invariant for Canopy BRF: The m-th approximation, $BRF \equiv I_{\lambda,m}(z = 0, \underline{\Omega})$, $\mu(\underline{\Omega}) > 0$ to the canopy bidirectional reflectance factor (BRF), is given by Eq. (28). Its error, $|\delta BRF_m| \equiv |\delta I_m(z = 0, \underline{\Omega})|$ is given by [Huang et al., 2007]

$$| \delta BRF_m | \leq i_0 \frac{\theta_{m+1}}{1-\gamma_{m+1}} S_{BRF,m+1} \times$$
$$\times \left[\max_{k \geq 1, \Omega \in 2\pi^+} \frac{| e_{m+1+k}(z = 0, \underline{\Omega}) - e_{m+k}(z = 0, \underline{\Omega}) |}{e_{m+k}(z = 0, \underline{\Omega})} + \max_{k \geq 1} \frac{| \gamma_{m+k+1} - \gamma_{m+1} |}{\gamma_{m+k+1}} \right], \qquad (38)$$

where

$$S_{BRF,m+1}(z = 0, \underline{\Omega}) = \sum_{k=1}^{\infty} \frac{\theta_{m+1+k}}{\theta_{m+1}} e_{m+k}(z = 0, \underline{\Omega}).$$

If m is large enough, i.e., $\sqrt[m+1]{\theta_{m+1}} \approx \gamma_\infty$ and $e_{m+1} \approx e_\infty$, the term $S_{BRF,m+1}$ can be approximated as $S_{BRF,m+1} \approx e_\infty \gamma_\infty / (1-\gamma_\infty)$. Its values, therefore, are mainly determined by the contribution of photons scattered m+1 and more times to the canopy radiation regime.

According to Eq. (38), the accuracy in the m-th approximation to the canopy BRF depends on the convergence of γ_{m+k} and e_{m+k} to the eigenvalue, γ_∞, and corresponding eigenvector, e_∞, of the operator T. Convergence of the former is illustrated in Fig. 15. This figure shows variations in $\max_{\Omega \in 2\pi+}\{e_{m+1}(\underline{r},\underline{\Omega})/e_m(\underline{r},\underline{\Omega})\}$ and $\min_{\Omega \in 2\pi+}\{e_{m+1}(\underline{r},\underline{\Omega})/e_m(\underline{r},\underline{\Omega})\}$ with the scattering order m. In this example, the difference $e_{m+1+k} - e_{m+k}$ is negligible for $m \geq 4$, indicating that the forth approximation provides an accurate spectral invariant relationship for the canopy BRF. Variation in the probability e_m with the scattering order m should be accounted to evaluate the contribution of low order scattered photons.

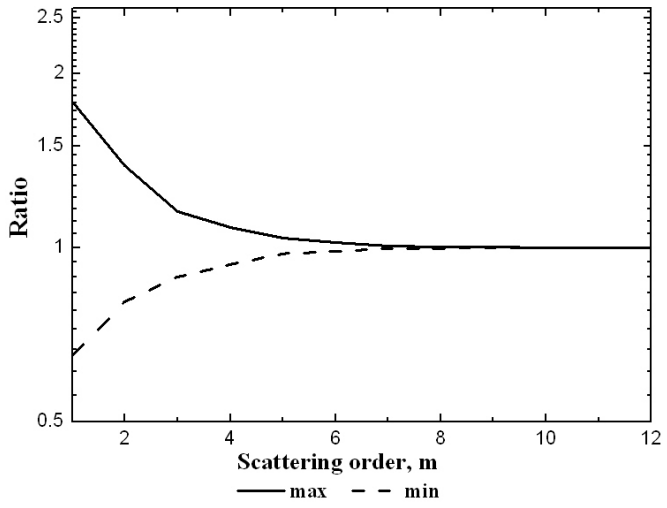

Figure 15. Convergence of e_m to the positive eigenvector, e_∞, of the operator T. The upper boundary of variations of the ratio e_{m+1}/e_m, $\max_{\Omega \in 2\pi}\{e_{m+1}/e_m\}$ (solid line) and corresponding lower boundary $\min_{\Omega \in 2\pi}\{e_{m+1}/e_m\}$ (dashed line) are shown with respect to the scattering order m. For $m \geq 5$, their values fall in the interval between 0.98 and 1.04. Parameters of the RT simulations are the same as for Fig. 13.

Inverse Linear Approximation to the Canopy Reflectance and Transmittance: The empirical and theoretical analysis indicates that the zero-order approximation provides an accurate spectral invariant relationship for the canopy interceptance; however more iterations are required to achieve comparable accuracy for the canopy transmittance and reflectance. The empirical analysis also suggests that zero-order approximation may result in a good accuracy in

case of reflectance and transmittance, if the recollision probability is replaced with its effective values.

In the following we derive effective recollision probabilities for canopy reflectance and transmittance in the zero-order approximation from the first-order approximation. According to Eqs. (36a), (37a) and (30), the first-order approximation (m=1) to the canopy spectral reflectance is

$$r(\lambda) = r_1(\lambda) + \delta r_1 = \left[\rho_1 + \frac{\omega p_1 \rho_2}{1 - p_2 \omega} + \frac{\omega p_1 \rho_2}{1 - p_2 \omega} S_{r,1} \right] \omega i_0 = \frac{1 - p_2 \omega \Delta_{r,1}}{1 - p_2 \omega} \omega \rho_1 i_0 . \qquad (39a)$$

Here $S_{r,1}$ [cf. Eq. (37c)] and $\Delta_{r,1}$ characterize the accuracy of the first approximation,

$$\Delta_{r,1} = 1 - \frac{\rho_2}{\rho_1} \frac{p_1}{p_2} [1 + S_{r,1}], . \quad S_{r,1} = \sum_{k=1}^{\infty} \frac{\theta_{k+1}}{\theta_1} \frac{\rho_{k+1}}{\rho_2} \left(\frac{\rho_{k+2} - \rho_{k+1}}{\rho_{k+1}} + \frac{\gamma_{k+1} - \gamma_2}{\gamma_{k+1}} \right). \qquad (39b)$$

Note, according to zero-order approximation [cf. Eq. (14a)] the reciprocal of the canopy spectral reflectance normalized by the leaf albedo, ω, varies linearly with ω. Based on this observation, we replace the relationship between the reciprocal of $r/(\omega i_0 \rho_1)$ and the leaf albedo ω given by first-order approximation [Eq. (39a)] with its zero-order form, given by a linear regression, $Y = \alpha_r - \beta_r p_2 \omega$. The coefficients R_1, R_2 and p_r in the zero-order approximation (14a), can be specified from the slope β_r and intercept α_r, namely

$$r(\lambda) = \omega(\lambda) R_1 + \frac{\omega(\lambda)^2 R_2}{1 - p_r \omega(\lambda)}, \quad R_1 = \frac{i_0 \rho_1}{\alpha_r}, \quad p_r = p_2 \frac{\beta_r}{\alpha_r}, \qquad (40a)$$

$$\alpha_r = 1 - 2 p_2 \int_0^1 \frac{1 - \Delta_{r,1}}{1 - p_2 \Delta_{r,1} \omega} \omega(2 - 3\omega) d\omega, \quad \beta_r = 6 \int_0^1 \frac{1 - \Delta_{r,1}}{1 - p_2 \Delta_{r,1} \omega} \omega(2\omega - 1) d\omega . \qquad (40b)$$

Similarly, the canopy transmittance is

$$t(\lambda) - t_0 = \frac{T_1\omega}{1 - p_t\omega}, \quad T_1 = \frac{i_0\tau_1}{\alpha_t}, \quad p_t = p_2\frac{\beta_t}{\alpha_t}. \tag{41}$$

Here α_t and β_t are given by Eq. (40b) but for $\Delta_{t,1}$ and $S_{t,1}$ which are calculated with τ_1, τ_2. We term this approach an *inverse linear approximation*. Note that if the escape probabilities do not vary with the scattering order ($\Delta_{r,1} = \Delta_{t,1} = 0$), the slope $\beta_r = \beta_t = p_2$ and intercept $\alpha_r = \alpha_t = 1$, and the inverse linear approximation coincides with the zero-order approximation. If variations in the escape probabilities become negligible for $m \geq 2$, ($\varepsilon_{\kappa,2} \approx 0, \kappa = r, t$), the effective probabilities p_r and p_t are functions of p_1, p_2, ρ_1, ρ_2 and, p_1, p_2, τ_1, τ_2 respectively.

Figure 16 demonstrates the energy conservation [Eq. (35a)] for $m = 1$. The escape probabilities are calculated from Eqs. (40) and (41) as R_1/i_0 and T_1/i_0. It follows from Fig. 15 that the impact of the regression coefficients α_r and α_t on the escape probabilities is minimal; that is, deviation of $R_1/i_0 + T_1/i_0 + p_1$ from unity does not exceed 5%. This is not surprising because values of $(1 - \Delta_{\kappa,1})/(1 - \Delta_{\kappa,1}p_2\omega)$ in Eq. (40b) for α_r ($\kappa = r$) and α_t ($\kappa = t$) are multiplied by the function $\omega(2 - 3\omega)$, integral of which is zero. The effective values of the recollision probabilities, p_r and p_t, however, depend on β_r and β_t.

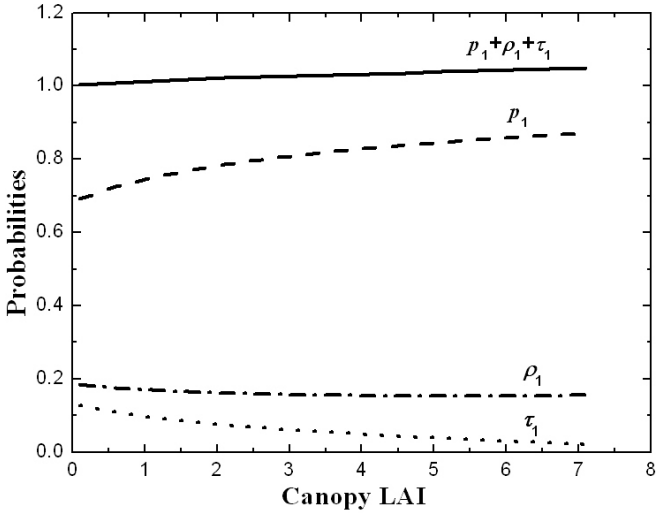

Figure 16. Energy conservation relationship $\rho_1 + \tau_1 + p_1 = 1$ as function of LAI. The escape probabilities ρ_1 and τ_1 were calculated as the ratios of coefficients R_1 and T_1 in the inverse linear approximations to i_0, i.e., $\rho_1 = R_1/i_0$ and $\tau_1 = T_1/i_0$. The deviation of $\rho_1 + \tau_1 + p_1$ from unity does not exceed 5%. Parameters of the RT simulations are the same as for Fig. 13.

Since eigenvalues and eigenvectors of the operator T are independent from the incident radiation, the limits p_∞, ρ_∞ and τ_∞ of the recollision and escape probabilities do not vary with the incident beam. Smolander and Stenberg [2005] showed that the first and higher orders of approximations to the recollision probability are insensitive to rather large changes in the solar zenith angle. Although the first approximations to the escape probabilities exhibit a higher sensitivity (Fig. 17) to the solar zenith angle, their sum, $\rho_1 + \tau_1 = 1 - p_1$, remains almost constant. This is consistent with the above theoretical results, suggesting that the canopy interaction coefficient requires less iterations to reach a plateau compared to the canopy reflectance and transmittance. The sensitivity of the effective recollision probabilities to the solar zenith angle is much smaller compared to the canopy interceptance.

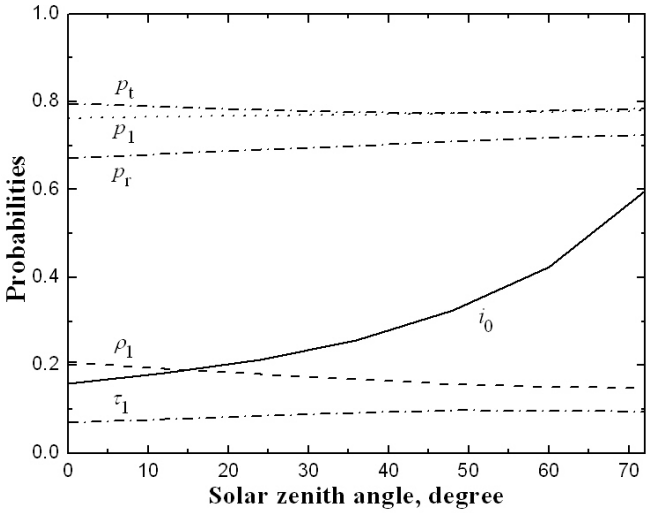

Figure 17. Recollision probability, p_1, its effective values, p_r and p_t, escape probabilities, ρ_1 and τ_1, and the canopy interceptance, i_0, as functions of SZA. Equation (40) was used to specify ρ_1 and τ_1. Parameters of the RT simulations are the same as for Fig. 13.

Figure 18 shows relative errors in the inverse linear approximation and the m-th approximations, m = 1, 2 and 3, to the canopy reflectance as a function of ω and LAI. The error decreases with the scattering order. For a fixed m, it increases with ω and LAI. This is consistent with the theoretical results stating that the convergence depends on the maximum eigenvalue $\gamma_\infty = p_\infty \omega$; that is, the higher its value is , the higher order of approximation is needed to estimate the canopy reflectance. In this example, the third and inverse linear approximations have the same accuracy level, i.e., they are accurate to within 5% if $\omega \le 0.9$. The relative error in the canopy transmittance (not shown here) exhibits similar behavior.

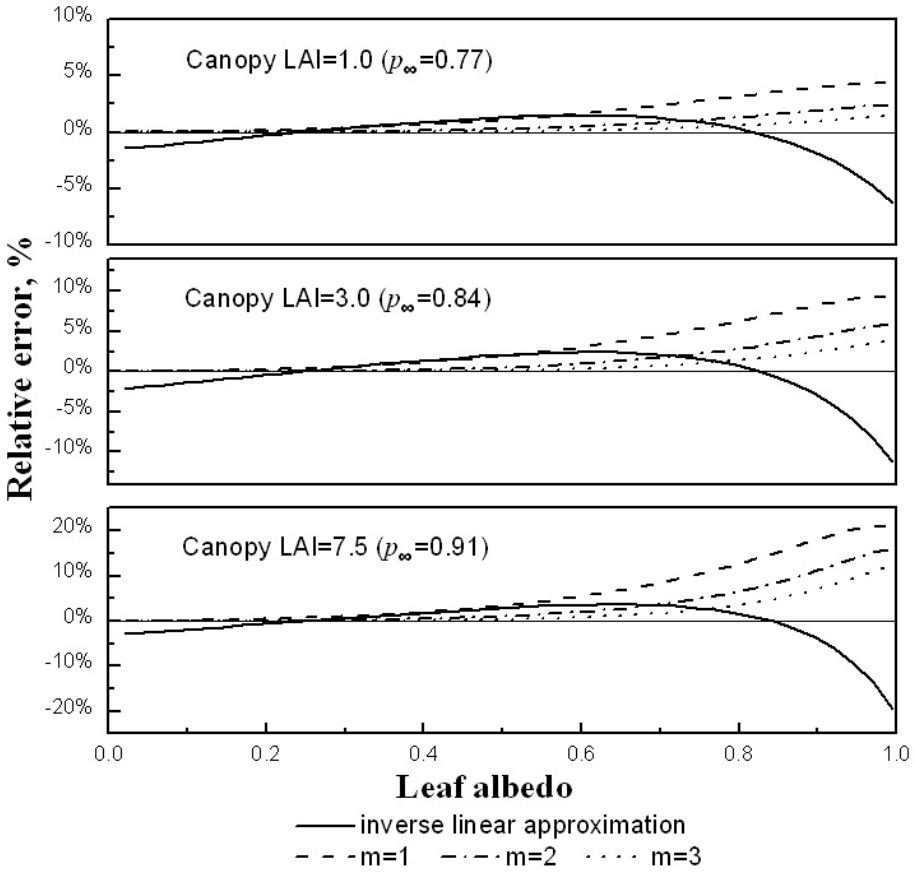

Figure 18. Relative error in the canopy reflectance as a function of ω and LAI. Parameters of the RT simulations are the same as for Fig. 13.

4. Scaling Properties of Spectral Invariants

The scaling effect, or scale dependence of RT parameters, arises due to phenomena of spatial heterogeneity (discontinuity) of canopy optical properties. For instance, single scattering albedo, $\omega(\lambda, V)$, is a function of the scale (volume, V) where it is defined. Consider sequence of *nested scales* represented by corresponding volumes: needle leaf tree stand (V_0), tree crowns (V_1), needle leaf shoots (V_2), and needles (V_3) (Fig. 19). Select a couple of scattering albedos, $\omega(\lambda, V_1)$ and $\omega(\lambda, V_2)$, which quantify the scattering properties at the scale of tree crown of volume V_1 and constituent objects (shoots) of volume V_2. By definition, single scattering of volume V_1 is the ratio of energy scattered by that volume to the amount of the energy intercepted

by the same volume. According to Eq. (8b) the tree crown single scattering albedo, $\omega(\lambda, V_1)$, can be expressed as

$$\omega(\lambda, V_1) \equiv \frac{s(\lambda, V_1)}{i_0(V_1)} = \omega(\lambda, V_2) \frac{1 - p(V_2 \to V_1)}{1 - \omega(\lambda, V_2)\, p(V_2 \to V_1)}. \qquad (44a)$$

Here $i_0(V_1)$ and $s(V_1)$ are the portion of photons intercepted and scattered by the volume V_1, and $p(V_2 \to V_1)$ is the recollision probability defined as the probability that a photon scattered by a volume V_2 (shoot) resided in the volume V_1 (tree crown) will hit again another volume V_2 (another shoot) in V_1. Its value is determined by the distribution of volumes V_2 (e.g., shoots) within V_1 (crowns). Thus, Eq. (44a) can be interpreted as one that provides a link between vegetation RT properties at different scales.

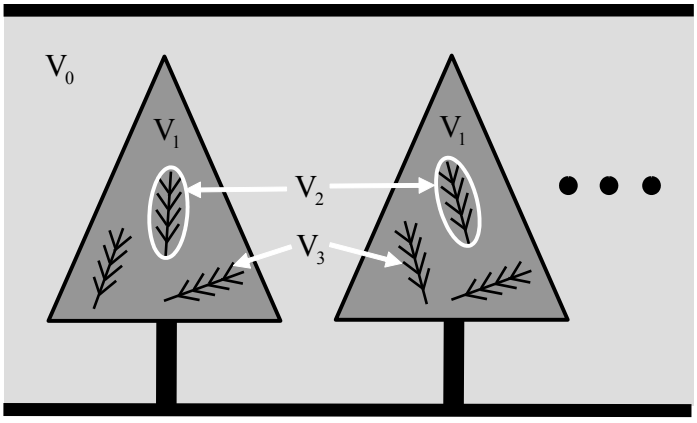

Figure 19. Schematic plot of nesting of scales. Tree stand occupies volume V_0, which consist of individual trees crowns of volume V_1, which, in turn, consist of shoots of volume V_2, which in turn consist of needles of volume V_3. The tree volumes are nested: $V_0 \supset V_1 \supset V_2 \supset V_3$.

Both $\omega(\lambda, V_1)$ and $p(V_2 \to V_1)$ vary with the scale V_1. However since the left-hand side of Eq. (44a) does not depend on V_2, the algebraic expression on the right-hand side of this equation should also be independent on the scale of V_2. Based on this property, variation in the leaf single scattering albedo and the recollision probability with the scale V can be specified as follows. Let us rewrite Eq. (44a) for needles (V_3) and shoot (V_2),

$$\omega(\lambda, V_2) = \omega(\lambda, V_3)\frac{1 - p(V_3 \to V_2)}{1 - \omega(\lambda, V_3)p(V_3 \to V_2)}. \quad (44b)$$

Substituting $\omega(\lambda, V_2)$ from Eq. (44b) into Eq. (44a) preserves the structure of Eq. (44a):

$$\omega(\lambda, V_1) = \omega(\lambda, V_3)\frac{1 - p(V_3 \to V_1)}{1 - \omega(\lambda, V_3)\, p(V_3 \to V_1)}, \quad (44c)$$

where

$$p(V_3 \to V_1) = p(V_3 \to V_2) + \left[1 - p(V_3 \to V_2)\right]p(V_2 \to V_1). \quad (45)$$

One can see that the probability $p(V_3 \to V_1)$ that a photon scattered by a volume V_3 (e.g., needles) will interact within volume V_1 (e.g., crown) again follows the *Bayes' formula*. Accordingly, Eq. (45) is called *nesting of scales*. The single scattering albedo and p-parameter exhibit the following scaling properties. Referring to Fig. 19 and taking into account Eqs. (44)-(45), provided $\omega, p \le 1$, one can derive that,

$$\omega(\lambda, V_2) \le \omega(\lambda, V_3) \text{ and } p(V_3 \to V_1) \ge p(V_2 \to V_1), \text{ if } V_3 \subset V_2;$$

$$p(V_3 \to V_1) \ge p(V_3 \to V_2), \text{ if } V_2 \subset V_1. \quad (46)$$

Consider the second property shown in Eq. (46), which conveys a fundamental law. It implies that the recollision probability increases with increasing complexity of canopy architecture (cf. Fig. 20). Namely, according to its definition, p=0 for the "Big Leaf" model, as there are no multiple scattering. As we add more hierarchical levels of structure, if photon reached particular structure elements it get trapped on structural sublevels, which increases probability of rescattering and thus value of p-parameter. The recollision probability, therefore, is a scaling parameter that accounts for a cumulative effect of the landscape's multi-level hierarchy.

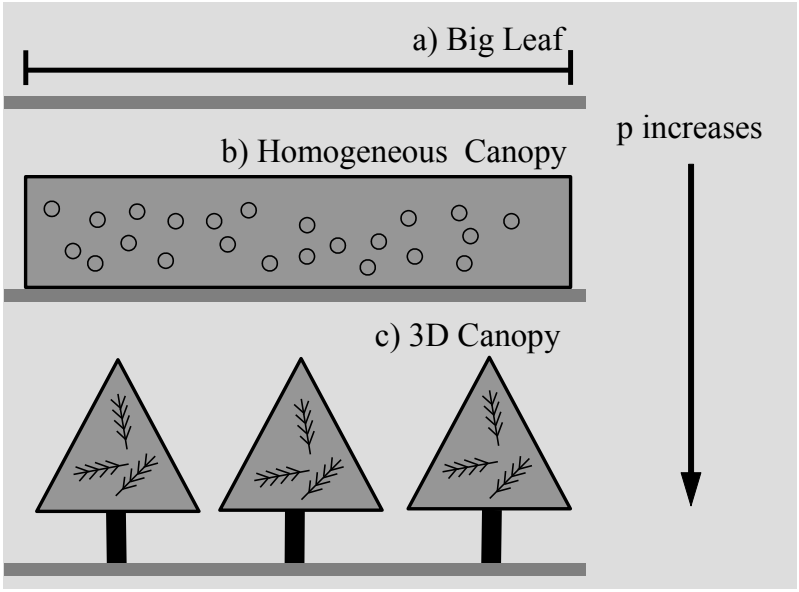

Figure 20. Recolision probability, p, as function of canopy structural hierarchy: (a) "Big Leaf" Canopy; (b) Turbid Medium; (c) 3D Canopy with nested scales of structure.

Case Study - Scaling from Needles to Shoots: The scaling properties of the p-parameter were first demonstrated by Smolander and Stenberg [2003; 2005] in the application for coniferous canopies. The 3D structure of the coniferous canopies exhibits foliage clumping at multiple scales, including clumping of needles into shoots and clumping of shoots into tree crowns; both give rise to the scaling effect. In particular, small-scale clumping of needles into shoots results in mutual shading and multiple scattering of light between needles of a shoot (Fig. 21), which ultimately leads to the known RT effect of coniferous canopies to appear darker than broadleaved canopies.

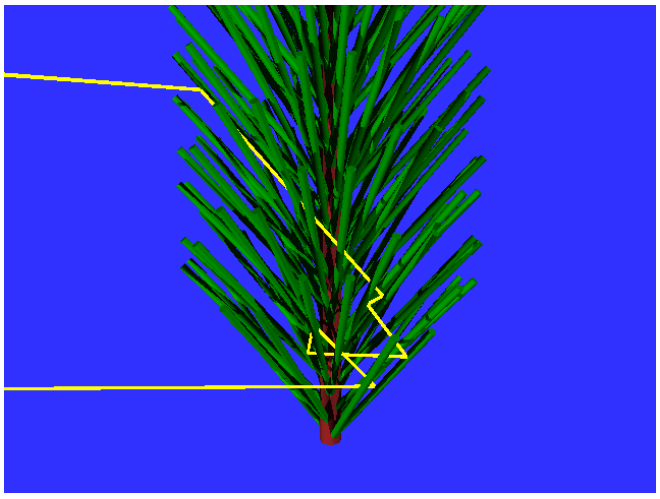

Figure 21. Scattering of photons on individual needles within shoot. The scattering is associated with loss of energy and thus shoot albedo is lower than albedo of individual needles (from Smolander and Stenberg, 2003].

The canopy clumping is described in the RT approach with spatially varying foliage volume density. However, the scale of variation of foliage density is limited by the size of canopy elementary volume. The elementary volume must be large enough to contain sufficient number of statistically independent foliage elements for the foliage volume density to be defined. Therefore, the approach is typically implemented at the large (landscape) scale, identifies individual tree crowns and space between them and defines the elementary volume to contain multiple leafs or needle shoots. The small-scale clumping of needles into shoots requires complex statistical description of distribution of needles. To overcome this problem, shot itself is typically used as the basic structural element in place of leaf for broadleaved canopies. The deviation of optical properties of elementary volume from those of individual needles, caused by shoot structure, is typically accounted for in the RT equation by adjusting extinction coefficient with empirically estimated clumping index (cf. Chapter 2). This *ad hook* approach is deficient in describing physical process of light scattering inside of a shoot, as it ignores wavelength dependence of the process and artificially couples shoot structure and needle optics.

Smolander and Stenberg [2003; 2005] developed p-parameter based RT framework to describe the effect of the small-scale clumping of needles into shoots to explain the difference in RT regimes in broadleaved and coniferous canopies. This study was focused only on small-scale clumping and large scale clumping was ignored. To support the theory, ray tracing simulations were performed for the model of canopy structure satisfying minimal requirements needed to meet the objectives of the study: a) realistic 3D model of shoots to represent small-scale structure; b) simple homogeneous turbid medium model for Poisson canopy to represent macroscopic structure. Foliage elements (shoots or leaves) were randomly distributed and spherically oriented (G-function and phase-function for spherically oriented leaves, cf. Chapter 3). Needle reflectances and transmittance were assumed to be similar to those of leaves, thus the difference between the two canopies reflectances caused solely by shoot structure. Geometrical model of Scots Pine (*Pinus Sylvestris L.*) shots was implemented referencing field measurements [Stenberg et al., 2002]. Three types of canopies were simulated: 1) *flat leaves*, 2) *shoots*, 3) *shoot-like leaves*, composed of leaves with the same G function and similar scattering properties

as shoots. Simulations were performed to generate reflectance of these canopies, assumed to be bounded below by black soil.

Recall (Chapter 3), shoot scale scattering in the needle leaf canopies is parameterized in terms shoot silhouette to total area ratio (STAR). Spherically averaged STAR is typically utilized,

$$\overline{\mathrm{STAR}} = \frac{1}{\mathrm{TNA}} \frac{1}{4\pi} \int_{4\pi} \mathrm{SSA}(\underline{\Omega}) \mathrm{d}\underline{\Omega}, \tag{47}$$

where $\underline{\mathrm{SSA}(\Omega)}$ is the shoot silhouette area in direction $\underline{\Omega}$ and TNA denotes the total needle area of the shoot. The $\overline{\mathrm{STAR}}$ parameter is analogous to G-function for leaves (cf. Chapter 3). In the case of spherically oriented scattering elements, the following holds:

$$\mathrm{G} = \begin{cases} 0.5, & \text{for leaves,} \\ 2\,\overline{\mathrm{STAR}}, & \text{for shoots.} \end{cases}$$

Note, the $\overline{\mathrm{STAR}}$ parameter is related to shoot structural parameter, $\mathrm{p}(\mathrm{L} \to \mathrm{Sh})$, which can be shown as follows. It follows from Cauchy's theorem for of convex, non self-shadowing objects that the ratio of silhouette to total area is ¼,. In contrast, needle leaf canopy shoot is a self-shadowing object due to self-shadowing of needles, and this ratio, the $\overline{\mathrm{STAR}}$ parameter, is smaller. Therefore, $(1/4 - \overline{\mathrm{STAR}}) \div 1/4 \equiv 1 - 4\,\overline{\mathrm{STAR}}$ quantifies the degree of self-shadowing, or the portion energy trapped inside of object due to self-shadowing. From another side, shoot structural parameter, $\mathrm{p}(\mathrm{L} \to \mathrm{Sh})$, is defined as the probability that a photon scattered by needle of the shoot will interact again with another needle of the same shoot. Comparing the above two definitions, we infer that

$$\mathrm{p}(\mathrm{L} \to \mathrm{Sh}) \approx 1 - 4\,\overline{\mathrm{STAR}}\,. \tag{48}$$

Note the following features of Eq. (48). First, the reason for the lack of exact equality is that $1 - 4\,\overline{\mathrm{STAR}}$ is defined as the mean over points on the surface, while $\mathrm{p}(\mathrm{L} \to \mathrm{Sh})$ is defined as

spatially averaged over points of interaction. Second, in contrast to $\overline{\mathrm{STAR}}$, $p(L \to Sh)$ is not just a function of shoot geometry but has some dependency on needle optical properties since they affect the directional distribution of scattered photons. Third, $p(L \to Sh)$ is defined based on the assumption that the probability of interactions stays constant with successive interactions. Equation (48) was verified with ray-tracing simulations for nine pine shoots and results are presented in Fig. 22.

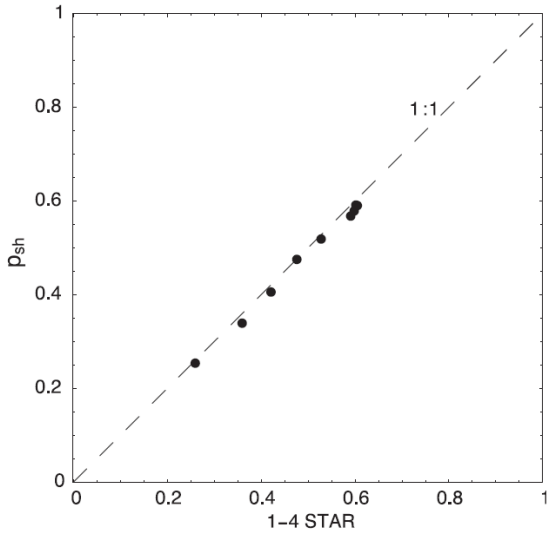

Figure 22. Relationship between p_{sh} and 1-4 $\overline{\mathrm{STAR}}$ for nine pine shoots. Shoot structural data from Stenberg et al. [2001] is used (from Smolander and Stenberg, [2003]).

In the shoot canopies shoot albedo varies with the direction of incoming beam (cf. results of simulations below). Average (over directions) shoot albedo, $\omega_{sh}(\lambda)$, is defined as fraction of scattered photons to photons intercepted by the shoot in an isotropic radiation field. Given $\mathrm{SSA}(\underline{\Omega})$ and $\omega_{sh}(\underline{\Omega})$, shoot silhouette area and shoot scattering coefficient in direction $\underline{\Omega}$, and taking into account that the number of intercepted photons is proportional to $\mathrm{SSA}(\underline{\Omega})$,

$$\omega_{sh}(\lambda) \equiv \frac{1}{4\pi\overline{\mathrm{SSA}}} \int_{4\pi} \omega_{sh}(\underline{\Omega})\mathrm{SSA}(\underline{\Omega})\mathrm{d}\underline{\Omega}\,. \tag{49}$$

The interaction of photon with the shoot occurred with probability $\mathrm{SSA}(\underline{\Omega})/S$, and thus the total fraction of intercepted photons N_i/N was proportional to $\overline{\mathrm{SSA}}$. The shoot albedo is equal to the fraction of photons escaped canopy to intercepted photons, N_e/N_i.

The shoot scattering phase-function and shoot albedo were generated with the 3D ray tracing. At each individual photon-needle interaction, a photon was scattered according to inform distribution with probability $\omega_L(\lambda)$, and absorbed with probability $1-\omega_L(\lambda)$, respectively,. Needle (or leaf) transmittance, $\tau_L(\lambda)$, and reflectance, $\rho_L(\lambda)$, were chosen as follows: $\rho_L(\lambda) = \tau_L(\lambda) = 0.5 \cdot \omega_L(\lambda)$; $\omega_L(\mathrm{Red})=0.1$, and $\omega_L(\mathrm{NIR})=0.9$. According to simulations for the NIR wavelength ($\omega_L(\mathrm{NIR}) = 0.9$), the shoot albedo was $\omega_{sh}(\mathrm{NIR}) = 0.81$, with reflectance $\rho_{sh}(\mathrm{NIR}) = 0.47$ and transmittance $\tau_{sh}(\mathrm{NIR}) = 0.34$. For the Red wavelength ($\omega_L(\mathrm{Red}) = 0.1$), the shoot albedo was $\omega_{sh}(\mathrm{Red}) = 0.059$, with $\rho_{sh}(\mathrm{Red}) = 0.034$ and $\tau_{sh}(\mathrm{Red}) = 0.025$. According to simulations, shoot albedo depends on shoot structural parameter, $p(\mathrm{L} \rightarrow \mathrm{Sh})$, and needle albedo, $\omega_L(\lambda)$, but is not sensitive to the ratio of needle transmittance to reflectance, $\tau_L(\lambda)/\rho_L(\lambda)$. Namely, ratio $\tau_L(\lambda)/\rho_L(\lambda)$ controls the shape of scattering phase function (forward vs. backward scattering), but does not change total needle albedo, and consequently has minor impact on canopy reflectance.

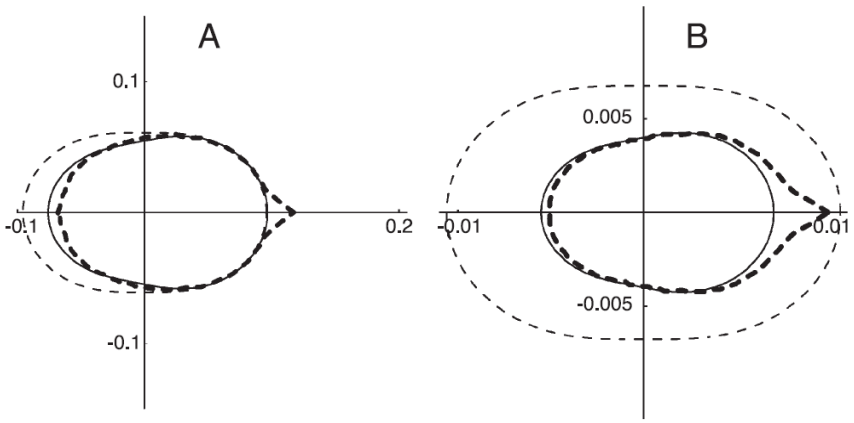

Figure 23. Cross-sectional views of scattering phase functions for (A) leaf with $\rho_L = 0.45$, $\tau_L = 0.45$ (thin dashed line), shoot (thick dashed line) with values $\rho_L = 0.45$ and $\tau_L = 0.45$ for its needles, and leaf with $\rho_L = 0.47$ and $\tau_L = 0.34$ (thin line), (B) leaf with $\rho_L = 0.05$, $\tau_L = 0.05$ (thin dashed line), shoot (thick dashed line) with values $\rho_L = 0.05$ and $\tau_L = 0.05$ for its needles, and leaf with $\rho_L = 0.034$ and $\tau_L = 0.025$ (thin line). The radiation is assumed to come from the direction of positive x-axis and to meet the object in origin (from Smolander and Stenberg, [2003]).

The scattering phase function of the spherically oriented shoots can be closely approximated by the scattering phase function of the shoot-like leaf, for which transmittance $\tau_L(\lambda)$ was 42% of $\omega_L(\lambda)$ at both wavelengths. Thus, the shoot scattering phase functions had more weight in the backscattering directions than the corresponding leaf scattering phase functions. Figure 23 shows the scattering phase function for the three types of foliage elements (flat leaves, shoots and shoot-like leaves). Note also the within-shoot hot spot effect in the backscattering direction in the shoot scattering phase-function, which can not be described by the bi-Lambertian distribution for flat leaves. However hot-spot effect can not be included for the shoot-like leaves. Overall, the effect of needle clumping and mutual shadowing in a shoot (compared to flat Lambertian leaf) is to decrease the radiation interception efficiency (G-function) and the shoot albedo, and to change the shape of the scattering phase function to weight it more towards the backscattering directions.

The relationship between shoot albedo, $\omega_{sh}(\lambda)$, and needle albedo, $\omega_L(\lambda)$, can be established as follows (cf. Section 2). At each interaction of photon and needle, photon is absorbed with probability $\omega_L(\lambda)$ and scattered with probability $1-\omega_L(\lambda)$ and can interact with shoot again. Assuming that the probability that scattered photon will interact with shoot again remains constant in successive interactions ($p(L \to Sh) = const$), shoot absorptance is obtained with infinite series,

$$A_{sh}(\lambda) \equiv [1-\omega_L(\lambda)] + [1-\omega_L(\lambda)]p(L \to Sh)\omega_L(\lambda) + [1-\omega_L(\lambda)]p^2(L \to Sh)\omega_L^2(\lambda) + ...$$
$$= \frac{1-\omega_L(\lambda)}{1-p(L \to Sh)\omega_L(\lambda)}.$$

Taking into account that $A_{sh}(\lambda) \equiv 1-\omega_{sh}(\lambda)$ the relationship between $\omega_{sh}(\lambda)$ and $\omega_L(\lambda)$ can be established,

$$\omega_{sh}(\lambda) = \omega_L(\lambda)\frac{1-p(L \to Sh)}{1-p(L \to Sh)\,\omega_L(\lambda)}. \qquad (50a)$$

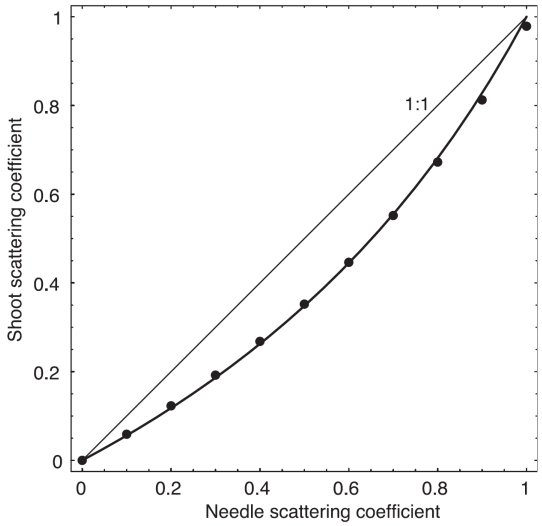

Figure 24. Predicted and simulated shoot albedo, $\omega_{sh}(\lambda)$, for different needle albedos, $\omega_L(\lambda)$ (from Smolander and Stenberg, [2003]).

Thus, if $p(L \to Sh)$ and needle albedo are known, the shoot albedo for any given wavelength can be calculated. Note, in case of $p(L \to Sh)=0$, corresponding to no within-shoot shading, than $\omega_{sh}(\lambda) = \omega_L(\lambda)$. At fixed $p(L \to Sh)$ the ratio $\omega_{sh}(\lambda) / \omega_L(\lambda)$ increases with $\omega_L(\lambda)$, i.e., the decrease in the shoot scattering from mutual shading is relatively less at wavelengths with high needle scattering. Equation (50a) was verified with ray-tracing simulations and results are presented in Fig. 24. The value of $p(L \to Sh)$ calculated according to ray tracing simulations (directly counting photons interactions) was 0.474, while $p(L \to Sh)$ estimated by fitting Eq. (50a) to the data points in Fig. 24 by the least squares method yields an estimate of 0.467 (1.5% difference). The difference is due to approximations in estimation of $p(L \to Sh)$, as it was assumed constant with respect to scattering order. In the simulations, the density of photons where scattering occurs varies with the scattering order, and it is not possible to analytically define the weight on the area over which $p(L \to Sh)$ is averaged.

Equation (50a) demonstrates effect of scaling between needles and shoot. Similar equation can be formulated for scaling at one level higher in the hierarchy, i.e. between shoot and canopy scales,

$$\omega_C(\lambda) = \omega_{sh}(\lambda) \frac{1 - p(Sh \to C)}{1 - p(Sh \to C)\, \omega_L(\lambda)}, \qquad (50b)$$

where $\omega_C(\lambda)$ is the canopy albedo, and $p(Sh \to C)$ is the recollision probability that photon scattered by shoot will interact again with another shoot with the canopy. Combining Eqs (50a) and (50b) we have:

$$\omega_C(\lambda) = \omega_L(\lambda)\frac{1 - p(L \to C)}{1 - p(L \to C)\,\omega_L(\lambda)}, \tag{51a}$$

where

$$p(L \to C) = p(L \to Sh) + [1 - p(L \to Sh)]p(Sh \to C). \tag{51b}$$

In words, the scattering between needles inside of whole canopy ($p(L \to C)$) can be decomposed into scattering between individual needles inside of a shoot ($p(L \to Sh)$) and scattering between shots inside of whole canopy ($p(Sh \to C)$). The relationship between $p(L \to C)$ and $p(Sh \to C)$ was verified with ray-tracing simulations for a range of LAI and results are shown in Fig. 23. In this simulations $\overline{STAR}$=0.133, $p(L \to Sh) = 1 - 4\overline{STAR}$=0.47 for *Pinus sylvestris* L. The parameter $p(Sh \to C)$ as function of LAI was well approximated by the relationship,

$$p(Sh \to C) = p(Sh \to C)_{max}[1 - \exp(-kLAI^b)], \tag{52}$$

where $p(Sh \to C)_{max}$=0.88, k=0.7, and b=0.75. In turn, $p(L \to C)$ was well predicted by the decomposition formula (Eq. 51), evaluated using $p(Sh \to C)$ and $p(L \to Sh)$. Note that there is a systematic offset between $p(L \to C)$ and $p(Sh \to C)$ due to between-needles scattering inside shoot ($p(L \to Sh)$). Simulations as function of direction (zenith angle) of incoming photons demonstrated low sensitivity of $p(Sh \to C)$ to zenith angles variations in spite the fact that zenith angle controls the distribution of the points of the first interaction of photons within canopy. Namely, for zenith angles < 50^0, the variation in $p(Sh \to C)$ was less than 1.2%.

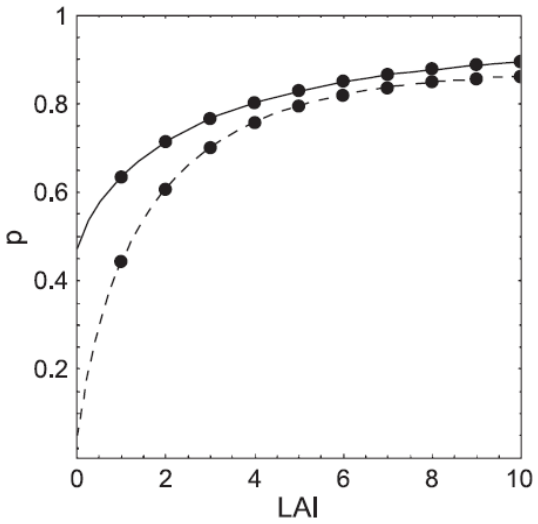

Figure 25. Recollision probabilities $p(Sh \to C)$ and $p(L \to Sh)$ as a function of LAI. Dots denote the p values derived from ray-tracing simulations. The dashed curve depicts $p(Sh \to C)$ according to fitting equation (Eq. (52)). The solid curve depicts $p(L \to C)$ according to the decomposition formula (Eq. (51)) (from Smolander and Stenberg, [2005]).

Finally consider Fig. 26 which compares ray-tracing simulated canopy BRF at Red and NIR wavelengths for the three canopy types (shoot, leaf and shoot-like leaf) bounded by a black surface. Clumping of needles into shoots produces a wavelength dependent reduction in canopy reflectance of need leaf canopy compared to that of broadleaf canopy with similar LAI. The reason for this effect is that the mutual shading of needle in a shoot leads to reduction of G-function and canopy interceptance for needle leaf compared to broadleaf canopies. Notice that the reflectance of the needle leaf canopy was well approximated by the shoot-like leaf canopy. Thus, integrating small-scale shoot structure in large-scale canopy RT models provides means to account for the observed difference between radiation regimes in coniferous and broadleaved canopies. Taking into account crown mutual shading will, presumably, further enhance this effect.

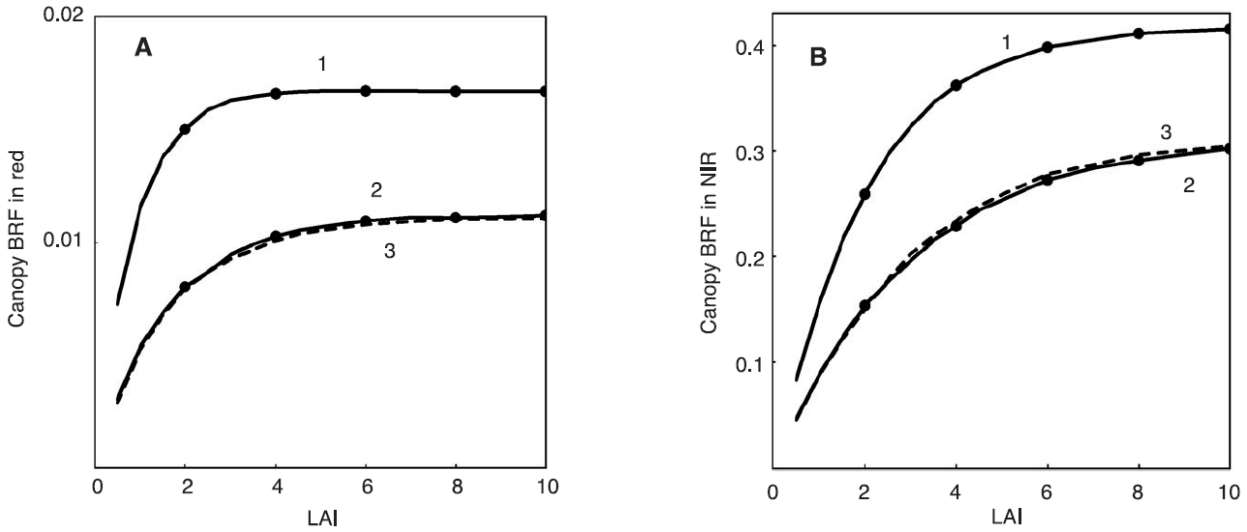

Figure 26. Predicted Canopy bidirectional reflectance factor (BRF) at Red and NIR wavelengths as a function of LAI for canopies bounded underneath by black soil. Curve (1) is for leaf canopy, curve (2) for shoot canopy and the dashed curve (3) for shoot-like leaf canopy. The black dots denote LAI values of 2, 4, 6, 8 and 10. The solar zenith angle is 45^0 and the view zenith angle is 0^0 (from Smolander and Stenberg, [2003]).

Case Study- Scaling from Leafs to Leaf Internals: Lewis and Disney [2007] further investigated the hypothesis that the scaling equations are applicable (in a consistent manner) across full range of scales from within leaf to canopy level scattering. The study utilized the PROSPECT leaf scattering model (Chapter 3). PROSPECT is a solar spectrum plate model of radiative transfer within a leaf. Leaf albedo, $\omega_L(\lambda)$, is calculated as function of leaf cell- air interface *refractive index* (n), the number of leaf layers, N and *absorption coefficient*, $A(\lambda)$. The absorption coefficient is a linear function of the concentration C_i [units of mass/unit LAI] of m biochemical constituents,

$$A(\lambda) = \sum_{i=1,m} C_i k_i(\lambda), \tag{53}$$

where $k_i(\lambda)$ is the *specific absorption coefficient* of the i-th constituent, a function of wavelength λ. Figure 27 shows $k_i(\lambda)$ as a function of wavelength for chlorophyll, water and dry leaf matter.

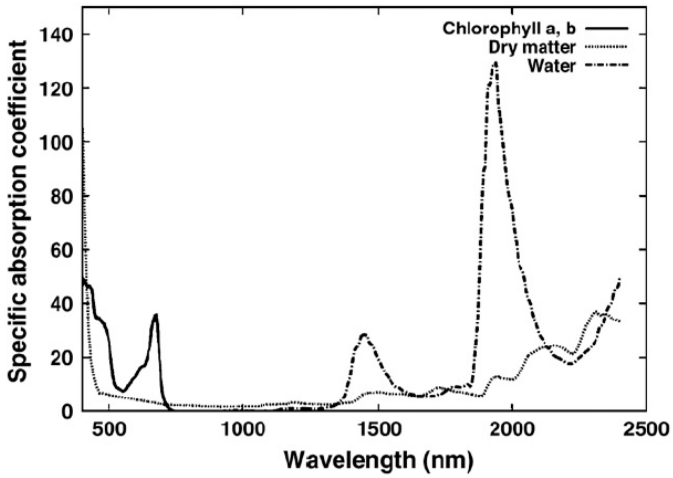

Figure 27. Specific absorption coefficients for chlorophyll, dry matter and water according to the PROSPECT model (from Disney and Lewis, [2007]).

The PROSPECT model identifies two components of leaf albedo, which corresponds to scattering (1) by leaf surface and (2) by leaf internals. Let $\omega_\infty(\lambda)$ be albedo of scattering from leaf surface, where the subscript accounts for the fact that scattering form leaf surface is equivalent to scattering from infinite leaf internals. Albedo $\omega_\infty(\lambda)$ is a function of a refractive index, which can be approximated by a quadratic $\omega_\infty(\lambda)$=-0.0492-0.00618n+0.04836n^2 (RMSE=2.37x10^{-3}, r^2=0.998). Let $\omega'_L(\lambda)$ be adjusted leaf albedo, which quantifies total scattering on leaf internals only and excludes scattering on leaf surface,

$$\omega'_L(\lambda) \equiv \frac{\omega_L(\lambda) - \omega_\infty(\lambda)}{1 - \omega_\infty(\lambda)}. \tag{54}$$

Note that denominator in Eq. (54) is introduced to ensure the standard range of variation of albedo, [0-1]. Lewis and Disney [2007] hypothesized that the general scaling relationship (cf. Eq. (44a)) should hold between adjusted leaf albedo, $\omega'_L(\lambda)$, and albedo of leaf internals, $\omega_{LI}(\lambda)$,

$$\omega'_{L}(\lambda) = \omega_{LI}(\lambda)\frac{1 - p(LI \to L)}{1 - \omega_{LI}(\lambda)\, p(LI \to L)}, \tag{55}$$

where albedo of leaf internals can be expressed as

$$\omega_{LI}(\lambda) \equiv \exp[-a(\lambda)\, A(\lambda)], \tag{56}$$

where, in turn, absorption coefficient, $A(\lambda)$, is given by Eq. (53) and coefficient $a(\lambda)$ is a function of refractive index, which can be approximated by quadratic, $a=1.3168-0.02294n + 0.01299n^2$ (RMSE= 5.06×10^{-5}, $r^2=0.9999$). Term $p(LI \to L)$ is the *equivalent recollision probability* for leaf internals, analogous to the *effective recollision probability*, $p(L \to Sh)$, defined by Smolander and Stenberg [2003] for the needles scattering inside a shoot . The leaf internals recollision probability extends set of similar terms, $p(L \to Sh)$ and $p(L \to C)$, recollision probabilities for shoot and canopy introduced by Smolander and Stenberg [2003]. The dependence of $p(LI \to L)$ on the refractive index, n, can be represented with quadratic, $p(LI \to L) = -1.2523+2.2307n-0.6094n^2$ (RMSE=8.95×10^{-4}, $r^2=0.9999$). The dependence of $\omega_{\infty}(\lambda)$, a, and $p(LI \to L)$ on refractive index is summarized in Fig. 28.

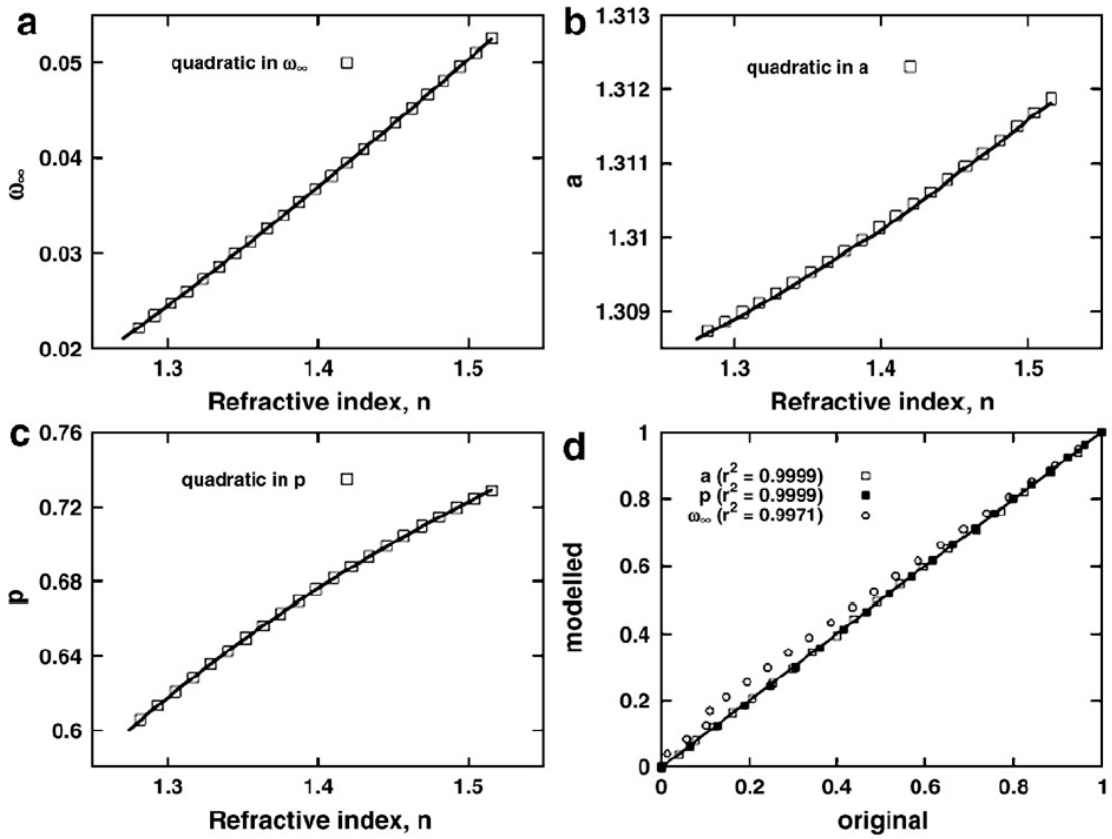

Figure 28. Variation of ω_∞ (Panel a), a (Panel b); and p_{leaf} (Panel c) with refractive index n as predicted with in PROSPECT (solid line) and quadratic approximation (symbols). Panel (d) shows scatter in each case against 1:1 line (from Lewis and Disney, [2007]).

While $p(LI \to L)$ varies significantly between 0.60 and 0.73 over the refractive index range across the solar spectrum (Fig. 28c), it appears that the assumption $p(LI \to L)$=const has negligible impact on simulated spectra of leaf albedo. Lewis and Disney [2007] set n=1.39, which corresponds to mid-range of solar spectrum and simultaneously minimizes errors in simulations of $\omega_L(\lambda)$. In this case according to quadratic approximation, $p(LI \to L)$=0.6708 and $\omega_\infty(\lambda)$=0.03566 and error in $\omega_L(\lambda)$ (difference between PROSPECT and approximation) is 0.010. Figure 29 compares $\omega_L(\lambda)$ retrievals based on spectral invariants approximation (Eq. (55)) and PROSPECT model for a range of concentrations of absorbing constituents. Two cases of spectral invariant model were tested: (1) variable and (2) fixed refractive index. In the first case r^2>0.9997, RMSE<0.0042, max error<0.013 and in the second case r^2>0.995, RMSE<0.016,

max error<0.049. Overall, spectral invariant approximation even in the case of fixed refractive index delivers very accurate estimate of leaf albedo spectra.

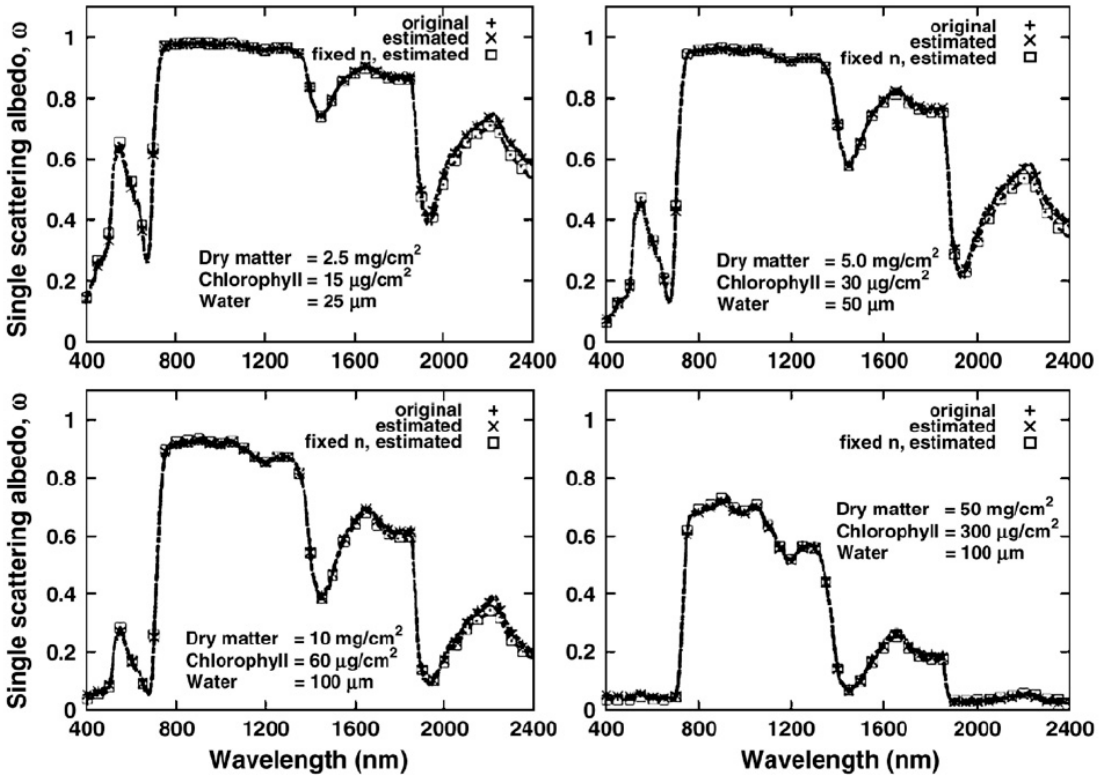

Figure 29. Accuracy of modeling of leaf spectra with spectral invariants approximation. Results shown for PROSPECT model ('original'); spectral invariant approximations with varying refractive index ('estimated'); and spectral invariant approximation with fixed refractive index ('fixed n, estimated') (from Lewis and Disney, [2007]).

The scaling approach, implemented by Smolander and Stenberg [2005] for "Canopy → Shoot → Leaf" scaling, was further extended by Lewis and Disney [2007] to incorporate one additional level down the hierarchy, Leaf Internals → Leaf. Combining Eqs. (51) and (55) and neglecting $\omega_\infty(\lambda)$ (Fig. 28), one can derive scaling relationship "Canopy → Shoot → Leaf → Leaf Internals" as follows,

$$\omega_C(\lambda) = \omega_{LI}(\lambda)\frac{1-p(LI \to C)}{1-\omega_{LI}(\lambda)\,p(LI \to C)}, \qquad (57a)$$

where $\omega_C(\lambda)$ is the canopy single scattering albedo, $\omega_{LI}(\lambda)$ is the single scattering albedo of leaf internals [Eq. (56)]. The recollision probability from leaf internals to canopy scales, $p(LI \to C)$, is given by the following *nesting* rule:

$$p(LI \to C) = p(LI \to L) + \left[1 - p(LI \to L)\right]$$

$$\times \left\langle p(L \to Sh) \quad + [1 - p(L \to Sh)]\, p(Sh \to C) \right\rangle . \qquad (57b)$$

Specifically, note the nesting of "leaf to shoot scattering" term (term in angular brackets, cf. Eq. (51b)) inside of "leaf internals to canopy scattering equation", which confirms the *Bayes' formula*. Overall, the scaling approach [Eq. (57)] is a powerful theoretical implementation of the shortwave radiation block in terms of few key parameters (canopy albedo, leaf biochemistry, and structural information). Nevertheless, practical implementation of the approach with multi-spectral remote sensing measurements may encounter challenges. P-parameter is an effective value, it can not be directly measured; rather it should be inferred from radiometric measurements, assuming knowledge of leaf biochemistry or leaf albedo. Leaf albedo can vary significantly over the canopy volume. For instance, coniferous forests exhibit vertical gradients of leaf biochemistry due to variations in needle and stand age, density of plants, etc. Therefore there is an internal difficulty in defining a (weighted) mean needle scattering spectra for use in the scaling applications to derive structural parameters. Further, there is a relatively strong coupling between leaf biochemistry and canopy structural parameters. Namely, the same spectra of leaf albedo can be derived from different combinations of structural information and leaf biochemistry [Lewis and Disney, 2007]. Consequently, the absolute concentration (per unit leaf area) of any biochemical constituents can not be derived from hyperspectral observations of total scattering.

References

Disney, M., P. Lewis, T. Quaife, and C. Nichol (2005). A spectral invariant approach to modeling canopy and leaf scattering. *Proc. The 9th International Symposium on Physical*

Measurements and Signatures in Remote Sensing (ISPMSRS), 17-19 October 2005, Beijing, China, Part 1, 318-320.

Huang, D., Y. Knyazikhin, R.E. Dikinson, M. Rautiainen, P. Stenberg, M. Disney, P. Lewis, A. Cescatti, Y. Tian, W. Verhoef, J.V. Martonchik, R.B. Myneni (2007). Canopy spectral invariants for remote sensing and model applications. *Remote Sens. Environ.,* **105**, 106-122.

Knyazikhin, Y., J.V. Martonchik, R.B. Myneni, D.J. Diner, S.W. and Running (1998). Synergistic algorithm for estimating vegetation canopy leaf area index and fraction of absorbed photosynthetically active radiation from MODIS and MISR data. *J. Geophys. Res*., **103**, 32257–32274.

Lewis, P., and M. Disney (2007). Spectral invariants and scattering across multiple scales from within-leaf to canopy. *Remote Sens. Environ.,* **xx**, xx-xx..

Marchuk, G.I., G.A. Mikhailov, M.A. Nazaraliev, R.A. Darbinjan, B.A. Kargin, and B.A. Elepov (1980). *The Monte Carlo Methods in Atmospheric Optics*, 208 pp., Springer-Verlag, New York.

Panferov, O., Y. Knyazikhin, R.B. Myneni, J. Szarzynski, S. Engwald, K.G. Schnitzler, and G. Gravenhorst (2001). The role of canopy structure in the spectral variation of transmission and absorption of solar radiation in vegetation canopies. *IEEE Trans. on Geosci. and Remote Sens.,* **39**, 241–253.

Riesz, F., and B. Sz.-Nagy (1990). *Functional Analysis*, Dover Publication, Inc., New York, 504 pp.

Ross, J. (1981). *The Radiation Regime and Architecture of Plant Stands*, Norwell, MA: Dr. W. Junk, pp. 391.

Smolander, S., and P. Stenberg (2003). A method to account for shoot scale clumping in coniferous canopy reflectance models. *Remote Sens. Environ.,* **88,** 363–373.

Smolander, S., and P. Stenberg (2005). Simple parameterizations of the radiation budget of uniform broadleaved and coniferous canopies. *Remote Sens. Environ.,* **94,** 355–363.

Vladimirov, V.S. (1963). Mathematical problems in the one-velocity theory of particle transport. *Tech. Rep. AECL-1661*, At. Energy of Can. Ltd., Chalk River, Ontario, 302 pp.

Remote Sensing of Environment 183 (2016) 98–108

Contents lists available at ScienceDirect

Remote Sensing of Environment

journal homepage: www.elsevier.com/locate/rse

Review

Photon recollision probability in modelling the radiation regime of canopies — A review

P. Stenberg [a,*], M. Mõttus [b], M. Rautiainen [c,d]

[a] University of Helsinki, Department of Forest Sciences, PO Box 27, FI-00014 Helsinki, Finland
[b] University of Helsinki, Department of Geosciences and Geography, PO Box 68, FI-00014, Finland
[c] Aalto University, School of Engineering, Department of Built Environment, PO Box 15800, FI-00076, Finland
[d] Aalto University, School of Electrical Engineering, Department of Radio Science and Engineering, PO BOX 13000, FI-00076, Finland

ARTICLE INFO

Article history:
Received 15 January 2016
Received in revised form 6 May 2016
Accepted 22 May 2016
Available online xxxx

Keywords:
Spectral invariants
Photon recollision probability
Radiative transfer
Conifer
DASF
PARAS model
Albedo
fPAR

ABSTRACT

Nearly two decades ago, the idea of the 'spectral invariants theory' was put forth as a new tool to model the shortwave radiation absorbed or scattered by vegetation. The theory states that the amount of radiation absorbed by a canopy should to a great accuracy depend only on the wavelength and a wavelength-independent parameter describing canopy structure. The revolutionary idea behind this theory was that it would be possible to approximate vegetation canopy absorptance, transmittance and reflectance based on only the optical properties of foliage elements and the spectrally invariant parameter(s). This paper explains how this so-called spectral invariant is related to photon recollision probability and to canopy structural variables. Other spectral invariants were later introduced to quantify the directionality of canopy scattering. Moreover, the paper reviews the advances in the theoretical development of the photon recollision probability (p) concept and demonstrates some of its applications in global and local monitoring of vegetation using remote sensing data.

Contents

* Corresponding author.
E-mail address: pauline.stenberg@helsinki.fi (P. Stenberg).

http://dx.doi.org/10.1016/j.rse.2016.05.013
0034-4257/

1. Introduction

Physically-based remote sensing of vegetation relies upon accurate models of the canopy shortwave radiation budget, which quantitatively describe how the fractions of solar radiation absorbed, transmitted and reflected by the canopy are related to the optical and structural properties of the canopy and background. Optical properties comprise the scattering and absorption spectra of the vegetation elements, which vary with the wavelength, whereas the structural canopy descriptors are independent of wavelength, or *spectrally invariant*. The variable focused on in this review — the *photon recollision probability*, is not one of the input parameters to the classical three-dimensional radiative transfer (RT) equation for vegetation (Ross, 1981), but is closely related to the solution of this equation (Knyazikhin, Martonchik, Myneni, Diner, & Running, 1998).

The concept of recollision probability can be pictured by thinking of the radiative transfer as a stochastic process: When a photon interacts with an element in the canopy, the probability that it will be absorbed or scattered varies with the wavelength. However, once the photon has been scattered, the probability that it will collide with the canopy again depends only on the location of the scattering event and the direction it was scattered into. This recollision probability is a geometric quantity which, in geometric optics approximation, does not depend on the wavelength. One may define a canopy averaged mean photon recollision probability, which was shown to link together the optical properties at canopy and leaf level by a set of simple algebraic relationships (Smolander & Stenberg, 2005). The existence of a spectrally invariant '*p*-parameter' satisfying similar relationships was, however, first discovered and theoretically established by Knyazikhin et al. (1998). Only a clear interpretation of this parameter was still lacking at the time. The fact that the somewhat heuristic 'photon recollision probability'-approach was found to be coherent with physically-based radiative transfer started a new era in the application of the 'spectral invariants theory': the single parameter representing canopy structure had now been defined and thus could also be quantified.

Knyazikhin et al. (1998) put forth the idea of the 'spectral invariants theory' when developing the theoretical grounds of the MODIS algorithm for retrieval of the leaf area index (LAI) and the fraction of photosynthetically active radiation (fPAR). They proposed a revolutionary idea that it would be possible to approximate vegetation canopy absorptance, transmittance and reflectance using only the optical properties of foliage elements and one spectrally invariant parameter for each approximated canopy characteristic. The theory states that, knowing the leaf albedo (1-absorptance), canopy absorptance at any wavelength can be estimated with high accuracy from canopy absorptance at a reference wavelength. This property laid the foundation for the synergistic look-up-table (LUT) based algorithm developed by Knyazikhin et al. (1998), which has been successfully implemented in the retrieval of global leaf area index (LAI) from canopy reflectance data measured by the MODIS instrument.

This approach was contrary to many other lines of development where more complexity was favored in canopy radiation models. A couple of years later, several independent research lines in Boston University, University of Helsinki and University College London were investigating the spectral invariants theory and its applications. This paper reviews the advances in the theoretical concepts behind the spectral invariants and shows examples of various applications of the concept in global and local monitoring of vegetation using remote sensing data.

2. *p*-Theory

2.1. The concept of recollision probability

Knyazikhin et al. (1998) proposed that the unique positive eigenvalue of the radiative transfer equation can be expressed as the product of the leaf albedo and a wavelength independent parameter, and the name '*p*-theory' originates from the symbol they used for this canopy structural parameter. Empirical evidence for the spectral invariant behavior of the *p* parameter was provided later by Panferov et al. (2001) and Wang et al. (2003) based on the measured spectral reflectance and transmittance data of forest canopies. However, a clear interpretation of how *p* is related to the canopy structure, allowing it to be estimated from canopy structural measurements, was still missing. A step towards this goal was taken by Smolander and Stenberg (2005), who defined *p* as a conditional probability — the recollision probability, and in their simulation study derived tight relationships between *p* and LAI in model canopies. It was shown that, in addition to LAI, *p* is linked to the clumping of foliage.

Smolander and Stenberg (2005) were thus first to introduce the term recollision probability for *p*, which they defined as the probability by which a photon scattered from a phytoelement (leaf or needle) in a vegetation canopy will interact within the canopy again. The escape probability $(1 - p)$ correspondingly is the probability by which a scattered photon will escape the canopy. These probabilities are defined conditional to the photon having survived an interaction inside the canopy. The fraction of photons that enter the vegetation from above and are intercepted by elements in the canopy is called the *canopy interceptance* (i_0). The zero order (or *uncollided*) transmittance (t_0) in turn is the fraction of photons that are transmitted directly through gaps in the canopy: $t_0 = 1 - i_0$. In a canopy bounded underneath by a non-reflecting ('black') surface (Fig. 1), the transmitted photons will not interact within the canopy again. Under this condition, and assuming further that the *p* remains constant in successive interactions, canopy absorptance (a) at a specific wavelength (λ) is obtained as the sum of a geometric series:

$$a(\lambda) = i_0\left[(1-\omega_L(\lambda)) + \omega_L(\lambda)p(1-\omega_L(\lambda)) + \omega_L(\lambda)^2p^2(1-\omega_L(\lambda)) + \ldots\right] = i_0\frac{1-\omega_L(\lambda)}{1-p\omega_L(\lambda)}. \quad (1)$$

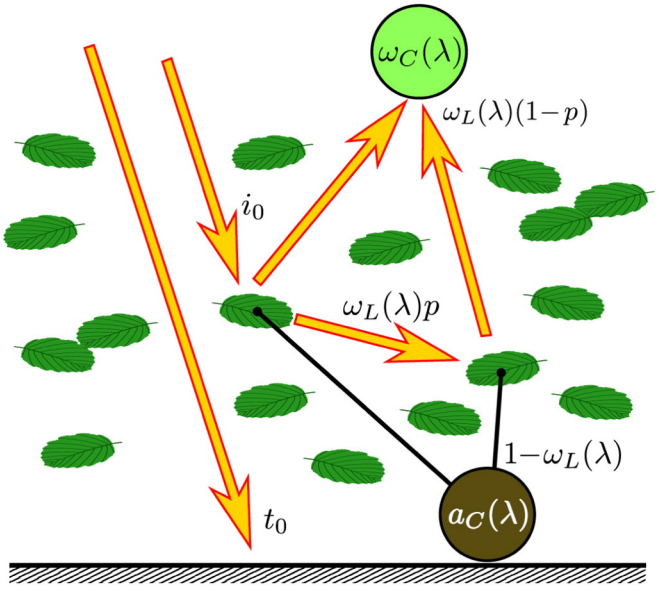

Fig. 1. Photons entering a canopy bounded below by black soil are first intercepted by leaves (i_0) or directly transmitted to and absorbed by the ground (t_0). The intercepted part is eventually absorbed (α_C) or scattered out from the canopy (ω_C) after one or multiple interaction and recollision events.

In Eq. (1), ω_L denotes the leaf scattering coefficient (single scattering albedo) and the common ratio ($p\omega_L$) of the series corresponds to the joint probability of recollision and a new scattering event.

Canopy scattering (s) under the black soil assumption is similarly obtained as:

$$s(\lambda) = i_0 \frac{\omega_L(\lambda) - p\omega_L(\lambda)}{1 - p\omega_L(\lambda)}. \quad (2)$$

Canopy absorptance and scattering sum up to the canopy interceptance: $a(\lambda) + s(\lambda) = i_0$. These wavelength dependent components normalized by i_0 thus define the *canopy spectral absorption and scattering coefficients*, α_C and ω_C:

$$\alpha_C(\lambda) = \frac{a(\lambda)}{i_0} = \frac{1 - \omega_L(\lambda)}{1 - p\omega_L(\lambda)} \quad (3)$$

and

$$\omega_C(\lambda) = \frac{s(\lambda)}{i_0} = \frac{\omega_L(\lambda) - p\omega_L(\lambda)}{1 - p\omega_L(\lambda)}. \quad (4)$$

We note that the derivation of Eqs. (1)–(4) rely on the assumptions of black soil and a constant p. Canopy absorption by Eq. (1) represents the solution to the so called 'black soil problem' (Knyazikhin et al. 1998; Wang et al. 2003), which in the case of a dark soil (background) and/or a dense canopy may be a good approximation. Whenever this is not true, another component, the solution to the 'soil problem', must be added. Similarly, the fact that p in reality is not constant must be carefully considered. The degree to which these issues limit the applicability of the recollision probability concept, and how to overcome the problems, will be addressed in subsequent sections.

2.2. Links to the radiative transfer equation

The link between the photon recollision probability p and the unique positive eigenvalue γ_0 of the radiative transfer equation is described by Huang et al. (2007) and Knyazikhin, Schull, Liang, Myneni, and Samanta (2011). In the successive orders of scattering approach, canopy scattering is calculated as the sum of contributions by different scattering orders, i.e. photons scattered 1, 2, …, n times before exiting the canopy. In this approach, we may define the operator $\mathbf{T}$ such that the radiation field I_λ of order $i + 1$ equals:

$$I_\lambda(i+1) = \mathbf{T} I_\lambda(i), \quad i = 1, 2, \ldots. \quad (5)$$

The largest (and the only positive) eigenvalue of operator $\mathbf{T}$, γ_0, is a linear function of the leaf albedo $\omega_L(\lambda)$: $\gamma_0 = p_{\text{inf}}\omega_L(\lambda)$. The spectrally invariant parameter p_{inf} is the limiting recollision probability as the order of scattering reaches infinity ($i \to \infty$).

Knyazikhin et al. (1998) used the largest eigenvalue of operator $\mathbf{T}$ to demonstrate the existence of the spectral invariants for canopy absorptance, although without introducing the concept of photon recollision probability. They derived the spectral invariant relationship for the norm $||I_\lambda||_1$ of the solution to the radiative transfer equation, or the product of the monochromatic radiance I_λ and the interaction cross-section σ integrated over the canopy volume and all directions. $||I_\lambda||_1$ is the mean spectral irradiance on all sides of a leaf and is thus a key component of the energy conservation law. For vegetation bounded underneath by a black surface and irradiated with unit irradiance, it corresponds to the mean number of photon interactions with phytoelements at wavelength λ in the canopy, and is called the interaction coefficient, i.e. $i(\lambda) = ||I_\lambda||_1$. The interaction coefficient multiplied by the leaf absorptance gives canopy absorptance: $a(\lambda) = i(\lambda)[1 - \omega_L(\lambda)]$. Knyazikhin et al. (1998) showed that, if the interaction cross-section (σ) does not depend on wavelength, then for the first eigenvector $e_0(\lambda)$ of Eq. (5), the norms $||I_\lambda e_0||_1$ at two arbitrary wavelengths, λ and λ_0, are linked together as:

$$||I_\lambda e_0||_1 = \frac{1 - \gamma_0(\lambda_0)}{1 - \gamma_0(\lambda)} ||I_{\lambda_0} e_0||_1 = \frac{1 - p_{inf}\omega_L(\lambda_0)}{1 - p_{inf}\omega_L(\lambda)} ||I_{\lambda_0} e_0||_1. \quad (6)$$

Next, based on the demonstrated proximity between the spectral dependencies of $e_0 I_{\lambda 1}$ and $I_{\lambda 1}$, Knyazikhin et al. (1998) derived the relationship for $i(\lambda) = ||I_\lambda||_1$:

$$i(\lambda) \approx \frac{1 - p\omega_L(\lambda_0)}{1 - p\omega_L(\lambda)} i(\lambda_0). \quad (7)$$

The recollision probability p is an approximation to p_{inf}. The goodness of this approximation depends on two factors: the contributions of the different scattering orders on total scattering, and how fast (in terms of scattering orders) the recollision probability approaches the diffuse limit p_{inf}. The speed of convergence depends, in turn, on the recollision probability and the leaf albedo: the higher the value of $p_{\text{inf}}\omega_L$, the slower the convergence. A detailed analysis of the accuracy of the approximation is given by Huang et al. (2007).

The conditions under which the spectral invariant relationships can be derived from the three-dimensional radiative transfer (RT) equation for vegetation are described in detail by Knyazikhin et al. (1998, 2011) and Huang et al. (2007). Some of the central assumptions and concepts are briefly summarized here. First of all, the interaction cross-section σ can be considered wavelength independent due to the large size of scattering elements relative to the wavelength of solar radiation (Ross, 1981). Another assumption used in the derivation is that the single scattering albedo (ω) inside the canopy volume does not depend on the location inside the canopy and the direction (Ω), and that it coincides with the leaf single scattering albedo (ω_L), i.e. the canopy consists of leaves only. The ratio $p = \gamma_0/\omega_L(\lambda)$ is then wavelength independent.

Substituting $i(\lambda) = a(\lambda) / [1 - \omega_L(\lambda)]$ in Eq. (7), the corresponding equation for canopy absorptance takes the form:

$$a(\lambda) = \frac{1 - p\omega_L(\lambda_0)}{1 - p\omega_L(\lambda)} \frac{1 - \omega_L(\lambda)}{1 - \omega_L(\lambda_0)} a(\lambda_0). \quad (8)$$

Evaluating Eq. (8) at $\omega_L(\lambda_0) = 0$ and $a(\lambda_0) = i_0$ gives

$$a(\lambda) = i_0 \frac{1 - \omega_L(\lambda)}{1 - p\omega_L(\lambda)} \quad (9)$$

which is seen to be identical to Eq. (1).

Similar relationships as Eq. (7) for the canopy interaction coefficient (i) can be formulated for canopy diffuse transmittance (t) and reflectance (r) (Smolander & Stenberg, 2005). Empirical evidence for the spectrally invariant behavior of the corresponding parameters (p, p_t and p_r) was derived from forest spectral reflectance and transmittance measurements by Panferov et al. (2001). It was found that specific combinations of the canopy spectral reflectance values r calculated as

$$\xi_r(\lambda_0, \lambda_1) = \frac{r(\lambda_0) - r(\lambda_1)}{\omega_L(\lambda_0) r(\lambda_0) - \omega_L(\lambda_1) r(\lambda_1)} \quad (10)$$

were concentrated around a certain canopy-specific value p_r, the mathematical expectation of ξ_r. Eq. (10) can be easily rearranged so that the dependence of the canopy reflectance r on the leaf albedo ω_L becomes similar to that of the canopy scattering ω_C in Eq. (4). An equation similar to Eq. (10) can be written for the transmittance t and the spectral invariant p_t.

The empirically-derived invariants p_r and p_t are approximate combinations of the spectrally invariant factors of the eigenvalues γ_i. More recently, Mõttus and Stenberg (2008) proposed a different

parameterization of canopy spectral reflectance using the reflectance ratio $r_C(\lambda)/\omega_C(\lambda)$ parameterized as:

$$\frac{r_C}{\omega_C} = \frac{1}{2} + \frac{q}{2}\frac{1-p\omega_L}{(1-p)\omega_L}. \quad (11)$$

The parameter q in Eq. (11) can be shown to be an approximation of the ratio of the two largest eigenvalues of $\mathbf{T}$, $q = \gamma_1/\gamma_0$ (Mõttus, 2010).

2.3. Scaling of p from leaf (needle) to canopy

The recollision probability can be defined at different hierarchical levels of the canopy and links the scattering properties at any two consecutive levels. For example, in their first simulation study with application of the p-theory, Smolander and Stenberg (2003) derived Eq. (4) at shoot level to model the effect of clumping of needles into shoots on the shoot scattering coefficient (ω_{sh}):

$$\omega_{sh}(\lambda) = \frac{\omega_L(\lambda) - p_{sh}\omega_L(\lambda)}{1 - p_{sh}\omega_L(\lambda)} \quad (12)$$

In Eq. (12), the 'shoot structural parameter' p_{sh} is the recollision probability within the shoot: it is the conditional probability that a photon which has survived an interaction within a shoot will interact again with a needle from the same shoot.

More generally, Eq. (4) can obviously be used at any level of the structural hierarchy to link the scattering coefficient of a unit (ω_{unit}) to that of its elements ($\omega_{element}$). Furthermore, letting $n(\lambda)$ denote the average number of interactions within the unit (shoot, canopy) for photons of wavelength λ, the ratio of these coefficients can be expressed as:

$$\frac{\omega_{unit}(\lambda)}{\omega_{element}(\lambda)} = n(\lambda)(1 - p_{unit}). \quad (13)$$

Eq. (13) states that the scattering coefficient of any unit normalized by that of its elements equals the (wavelength dependent) number of interactions multiplied by the spectrally invariant probability of escape ($1 - p$).

The total canopy *recollision and escape probabilities* in turn can be decomposed as

$$p(canopy) = p_1 + (1-p_1)p_2 + \ldots + (1-p_1)\ldots(1-p_{n-1})p_n \quad (14)$$

and

$$1 - p(canopy) = (1-p_1)(1-p_2)\ldots(1-p_n) \quad (15)$$

where n is the number of levels and p_i is the probability that a photon leaving a "clump" at the hierarchical level $i - 1$ will collide with a clump at level i (Fig. 2). The albedos at any two consecutive levels are linked by the equation (see Eq. (4)):

$$\omega_{i+1}(\lambda) = \frac{\omega_i(\lambda) - p_i\omega_i(\lambda)}{1 - p_i\omega_i(\lambda)}. \quad (16)$$

The goodness of the scaling depends on how well the p-theory approximates the radiation field inside the vegetation canopy. Theoretically, this is linked to the speed of convergence of the recollision probability with scattering order to its limiting value. As discussed in the following sections, in structurally complex extremely dense canopies, the connection between the photon recollision probability p and the eigenvalue γ_0 is lost, although the approximating equation (Eq. (9)) can still be used to describe total canopy absorption.

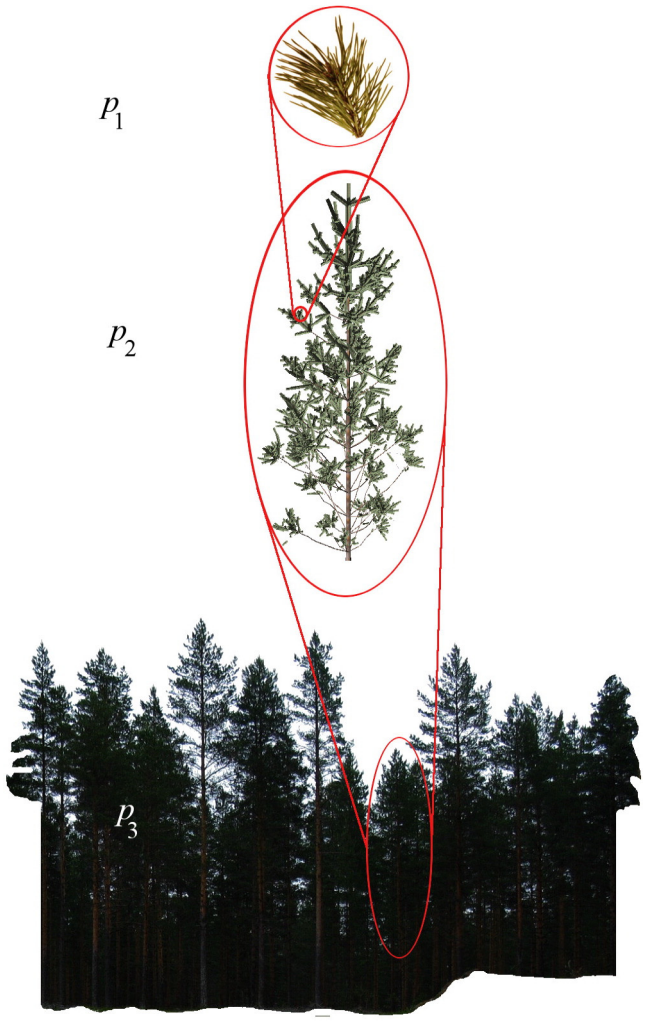

Fig. 2. In the forest depicted here, p_1 would be the recollision probability within a shoot, p_2 the recollision probability of a shoot-leaving photon within the crown, and p_3 the recollision probability of a crown-leaving photon with another, different crown.

2.4. Link between p and STAR

Smolander and Stenberg (2003) calculated the mean probability of escape ($1 - p_{sh}$) within modelled Scots pine shoots using Monte Carlo ray tracing (see Section 3.2.). They found that, to a very close approximation, $1 - p_{sh} = 4\text{STAR}$, where STAR is the spherically averaged silhouette to total needle area ratio of a shoot (Oker-Blom & Smolander, 1988) and 4STAR is analogous to the shoot shading factor β (Stenberg, 1996). As shown by Smolander and Stenberg (2003), 4STAR can be interpreted as the mean probability that a photon emitted from a random point on the needle surface of the shoot will not hit another needle of the shoot. Assuming Lambertian reflectance, it follows that the only difference between the escape probability and 4STAR comes from the spatial averaging: if the points of interaction were uniformly distributed over the total needle area of the shoot then the two quantities would coincide.

Based on the same assumption at canopy level, i.e. that the points of interaction are uniformly distributed over the total canopy leaf (needle) surface area, Stenberg (2007) later derived a simple analytical expression for the relationship between the total escape probability $1 - p$,

the leaf area index (LAI) and the canopy interceptance in diffuse (isotropic) radiation (i_D) (Eq. (A1) in Appendix A):

$$1-p=\frac{i_D}{\mathrm{LAI}}. \tag{17}$$

In deriving Eq. (17), Stenberg (2007) first defined the escape probability (P_{esc}) of a single photon scattered from a point r on a leaf (or needle) assumed to scatter as a Lambertian surface, i.e. reradiating photons following a cosine distribution around the direction Ω_r of the leaf normal, as:

$$P_{esc}(r)=\frac{1}{\pi}\int_{2\pi(\Omega_r)}\chi(r,\Omega)\cos(\Omega,\Omega_r)\mathrm{d}\Omega. \tag{18}$$

In Eq. (18), the function χ is defined such that it takes the value 1 if there is a free line of sight through the canopy from r to the direction Ω, and 0 otherwise, and integration is performed over the hemisphere $2\pi(\Omega_r)$ facing the leaf surface at r. The mean escape probability, $1-p$ (Eq. (17)), was then defined as P_{esc} averaged over (all the points r on) the total leaf (needle) surface area of the canopy, which was shown to equal the ratio of canopy diffuse interceptance (i_D) to the hemisurface LAI. In complete analogy to the shoot level p, the canopy level p (Eq. (17)) can be interpreted as the mean probability that a photon emitted from a random point on a Lambertian leaf (or needle) surface of the canopy will not hit another leaf of the canopy.

At a fixed LAI, the ratio i_D/LAI is smaller (and p larger) the more aggregated is the distribution of leaves in the canopy, or the smaller is the *canopy clumping index*. The clumping index (Γ), as defined by Eqs. (A2)–(A3) in the Appendix A, furthermore provides the link between the true LAI and the *effective leaf area index* (L_e) as $L_e = \Gamma\mathrm{LAI}$ (Eq. (A4) in Appendix A). Using these definitions, Eq. (17) can be written in the form

$$1-p=\Gamma\frac{i_D}{L_e}. \tag{19}$$

Rautiainen, Mõttus, and Stenberg (2009) studied the relationship between p, LAI and L_e based on empirical data (provided by measurements with the LAI-2000 Plant Canopy Analyzer) from five coniferous dominated test sites in Finland, containing in total 1032 pure or mixed plots with Norway spruce, Scots pine, Silver birch and Downy birch. They observed a tight relationship between i_D and L_e (Fig. 3), as could be expected based on their definitions (Eqs. (A1) and (A4)). This means that, at a fixed L_e, the ratio i_D/L_e has a near constant value and the escape probability (Eq. (19)) becomes proportional to the clumping index Γ.

2.5. Empirical proof of the p-theory

The first empirical proof of the p-theory was obtained in a joint laboratory experiment carried out by the University of Helsinki and University of Zurich in spring 2011 (Rautiainen et al., 2012). The aim of the experiment was to test if it was possible to upscale needle albedo to shoot albedo using only one parameter describing the shoots, i.e. the spherically averaged shoot silhouette to total needle area ratio (STAR). In other words, to test empirically the validity of Eq. (16).

First, using a spectroradiometer attached to the LAGOS goniometer located in the Remote Sensing Laboratories (University of Zurich), the upper and lower hemispherical bidirectional reflectance distribution functions (BRDF) for the study shoots were measured. The measured data were further processed to shoot spectral albedos. Simultaneously, the reflectance and transmittance values of single needles were measured. After the spectral measurements, the structure of the studied Scots pine shoots, including needle dimensions and shoot silhouette to total area ratios (STAR), were carefully measured in order to calculate the STAR values for the shoots.

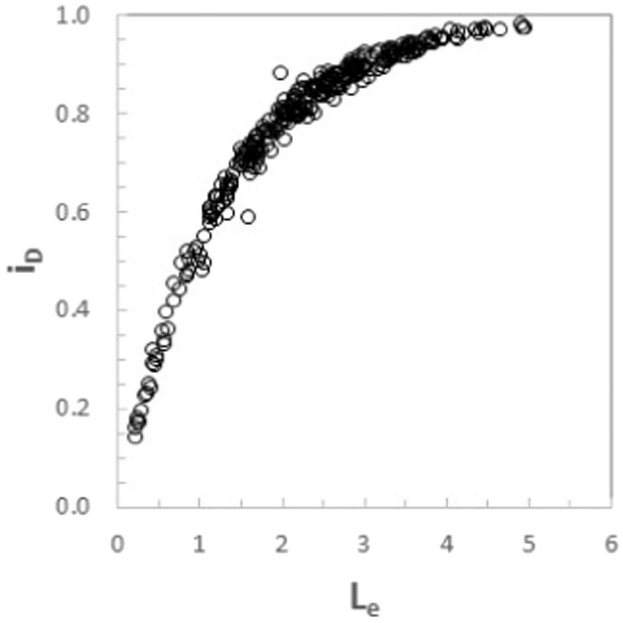

Fig. 3. The relationship between effective LAI (L_e) and canopy diffuse interceptance (i_D) can be easily measured with, for example, LAI-2000 Plant Canopy Analyzer or obtained from hemispherical photographs. This figure is based on 307 forest stands measured in Hyytiälä, Finland in 2013 (Majasalmi, Rautiainen, Stenberg and Manninen, 2015).

The empirical results confirmed the theory: STAR (which is linearly related to p) could indeed be used to scale between needle and shoot spectral albedos at these two hierarchical levels (Fig. 4). In an empirical follow-up study, Mõttus and Rautiainen (2013) also showed that common spectral vegetation indices, such as the normalized difference vegetation indices (NDVI) or photochemical reflectance index (PRI),

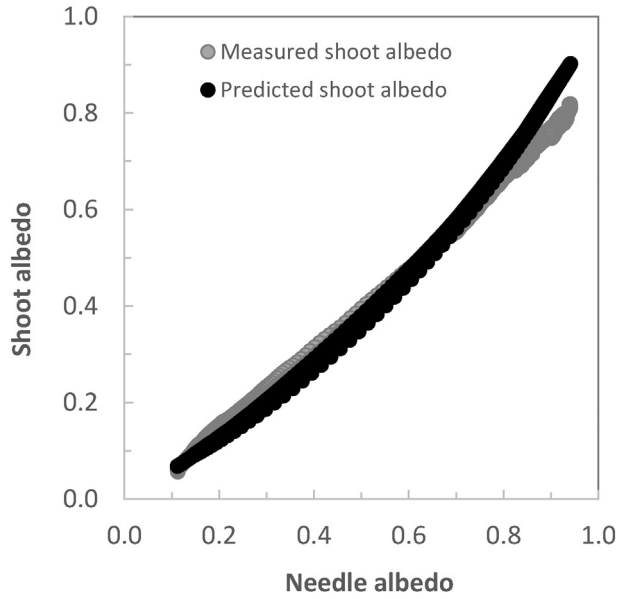

Fig. 4. The relationship between needle and shoot spectral albedos (400–1800 nm) averaged for ten Scots pine shoots. The needle albedos were measured, and the shoot albedos were both measured and predicted by STAR (which is linearly related to p) (see Section 2.4 and Eq. (16)).
The measurements and data are described in detail by Rautiainen et al. (2012).

can be scaled between needle and shoot levels using p. What still remains empirically unexplored, due to technical challenges in the measurement set-ups, is whether the same method could be used to scale between shoot and crown levels.

3. Simulation studies

3.1. Ray tracing to track collision and escape events

Tracking of individual photons inside a vegetation canopy, and thus directly determining the escape and recollision probabilities, is not possible. The closest alternative to measurement is Monte Carlo modelling using physically realistic representations of canopies. Such models sample the radiation field inside and above the canopy by tracing single photons drawn randomly from the incident radiation field. For the models used in the studies of photon recollision probability, a detailed 3D description of the canopy had been given as model input. As the photons are traced in the canopy, the fractions of photons which are scattered out after each scattering provide the recollision probabilities $p(1)$, $p(2)$, …, $p(i)$, …, where i is the scattering order. The recollision probability p is calculated as the average $p(i)$ weighted by the contribution of each order to the total canopy scattering.

The first simulation results were reported for a fractal-based three-dimensional barley canopy already in 1998 (Lewis & Disney, 1998). The geometric expansion (Eq. (1)) was found to be a useful way of representing canopy scattering as the rate of decay (i.e. photon recollision probability in modern terms) was found to be nearly constant for scattering orders of two and above. A more detailed simulation study in a canopy with randomly located, non-overlapping circular leaves with a spherical leaf angle distribution confirmed the monotonic increase of $p(i)$ with the scattering order i. The value of i after which $p(i)$ remained almost constant approximately equaled LAI (Lewis & Disney, 2007). Nevertheless, assuming a constant p for $i > 1$ gives reasonable accuracy for modelling total canopy scattering. The modelling exercises in these relatively simple canopies confirmed the quick convergence of $p(i)$ to p_{inf} mentioned above (Fig. 5).

Disney, Lewis, Quaife, and Nichol (2005) proposed an approximation of canopy reflectance where $p(1)$ is calculated separately from the recollision probability for $i > 1$, $p(i>1)$. Total canopy scattering now becomes

$$\omega_C(\lambda) = a\omega_L(\lambda) + \frac{b\omega_L^2(\lambda)}{1-p(i>1)\omega_L(\lambda)} \quad (20)$$

where a and b are the geometric (spectrally invariant) parts of the first- and multiple-order scattering, respectively. Disney et al. (2005) also suggest a simpler, but less accurate approximation assuming $b = a^2$. Later, the second-order recollision probability has been found to be a good substitute for the average p (Mõttus, 2007) or even the diffuse limit p_{inf} (Huang et al., 2007; Lewis & Disney, 2007). The first-order recollision probability, on the other hand, is markedly smaller than both p and p_{inf}.

Disney et al. (2005) validated the suitability of Eq. (20) for approximating the reflectance of five Sitka spruce stands of various ages. The stand-level reflectance, assumed proportional to ω_C was measured with a helicopter-mounted spectroradiometer in the visible and near infrared spectral regions. Needle spectral albedo was sampled with a contact probe. Eq. (20) was found to fit the data extremely well ($R^2 > 0.997$) even assuming $b = a^2$.

The situation was found to be more complicated for highly structured needleleaf forest canopies (Disney & Lewis, 2007). In some dense and complex pine canopies, $p(i)$ did not reach the diffuse limit even at $i = 100$. The authors also noted a marked impact of non-green material, i.e. tree trunks, on the distribution of exiting photons with scattering order. While the p-theory (Eq. (4)) was still a good approximation of the relationship between needle and canopy scattering, the fitted p-value became decoupled from its physical interpretation.

3.2. Deriving relationships between p and canopy structure

Smolander and Stenberg (2005) calculated the average p values (p_{LC} and p_{CC}) for two model canopies of varying LAI: a 'leaf canopy' (LC) and a coniferous 'shoot canopy' (CC), which were composed of randomly distributed single leaves or coniferous shoots, respectively. In both canopies, values of p were estimated in two different ways, which turned out to be in close to perfect agreement. First, p was obtained by fitting

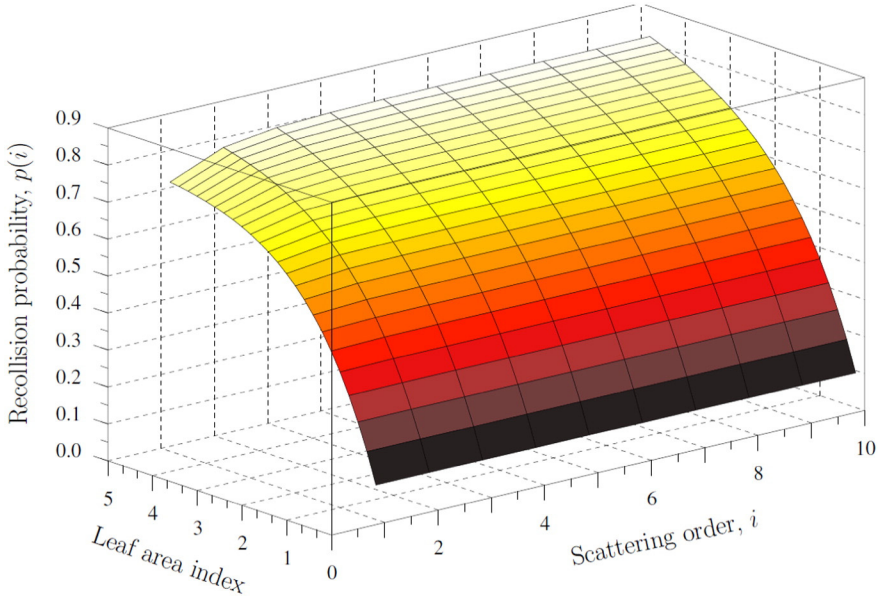

Fig. 5. Variation in p with scattering order for different values of LAI.
From Mõttus (2007).

Eq. (4) to simulated canopy scattering (ω_C) at different wavelengths (values of leaf albedo, ω_L). Secondly, p was calculated using the above described single photon ray tracing method with $\omega_L = 1$.

From simulations performed assuming a solar zenith angle (SZA) of 45°, a tight relationship of the form $p = a(1 - \exp(-b\mathrm{LAI}))$ was found between p_{LC} and LAI for the leaf canopy. The dependence between p of the coniferous shoot canopy (p_{cc}) and LAI, in turn, was accurately predicted from the shoot level p value (p_{sh}) and p_{LC} of the leaf canopy with similar effective LAI (L_e) by the decomposition formula (see Eq. (14)):

$$p_{CC} = p_{sh} + (1-p_{sh})p_{LC}(L_e). \tag{21}$$

The effect on p_{LC} of different incidence angles of the incoming photons was studied separately. It was found that p_{LC} was practically insensitive to the solar zenith angle in the range commonly used in satellite remote sensing (less than 1.2% at solar zenith angles <50°). Finally, simulated values of the ratio of upward to total scattering (r_C/ω_C) at different wavelengths showed an increase with LAI and a slight decrease with increasing ω_L (as would be predicted by Eq. (11)). At similar values of LAI, the ratio r_C/ω_C was larger for the leaf canopy than for the shoot canopy.

Later, Stenberg (2007) applied Eq. (17) to estimate p of the same model canopies ('leaf canopy' and 'shoot canopy') as in Smolander and Stenberg (2005) and found very good agreement between the analytically derived and the Monte Carlo simulated values of p. The fit was the best at low to moderate values of LAI and, at similar LAI, was better for the shoot canopy than for the leaf canopy. This can be explained by that the assumption behind Eq. (17), that the points of interaction are evenly distributed over the total leaf (needle) area, is closer to the truth the more 'transparent' is the canopy, i.e. the smaller is the effective LAI (L_e).

Mõttus, Stenberg, and Rautiainen (2007) derived the relationships between p and LAI for forest stands of more complicated structures using simulations by the Kuusk–Nilson FRT model (Kuusk & Nilson, 2000) and assessed the effect on canopy structure on p by comparing the results to those obtained for 'structureless' (homogeneous) canopies of the same LAI by a two-stream model. Simulations by both models produced tight relationships between LAI and p but, as expected, for a fixed LAI p was larger when canopy structure was accounted for. More generally, results from the study confirmed that the concept of recollision probability is coherent with physically based canopy reflectance models.

The concept of spectral invariants was tested on multiple scales from within leaf to a horizontally homogeneous canopy by Lewis and Disney (2007). They demonstrated that the p-theory can very accurately approximate the leaf scattering computed with the widely-used PROSPECT model (Jacquemoud et al., 1996). Inside the leaf, the role of ω is taken by the exponent of the product of pigment concentration and its spectral absorption coefficient. The "within-leaf recollision probability" p_{leaf} (note that at within-leaf scale, no physical connection has been established between the collision events and p_{leaf}) was found to vary with the refractive index of the leaf wax layer between 0.60 and 0.73. For a wide range of leaf properties, the p-theory approximated PROSPECT with $R^2 > 0.9997$ and RMSE < 0.0042. Using the (de)composition formula, leaf- and canopy level p-values can be combined thus linking canopy spectral reflectance to the pigment concentration with a single parameter. Based on their results, Lewis and Disney (2007) concluded that "without knowledge of either p, or the leaf biochemical constituents, independent retrieval of either from total scattering measurements is not possible."

In a simulation study, Stenberg and Manninen (2015) used the approach proposed by Disney et al. (2005) to separate the first order and multiple order recollision probabilities and calculated canopy scattering by Eq. (20), where parameters a and b were derived as: $a = 1 - p(1)$ and $b = p(1)(1 - p)$. For the modelled canopies, the first order $p(1)$ was calculated analytically and the multiple order mean p was calculated using Eq. (17). Results confirmed that $p(1)$ indeed differs more from the mean p the denser is the canopy but that the difference decreases with clumping. In dense but clumped canopies, thus, the difference between $p(1)$ and mean p had only minor effect on total canopy scattering (ω_C). However, the reflectance ratio (r_C/ω_C) was found to decrease with clumping because it reduces the relative contribution of first order scattering (with higher reflectance ratio) to the total scattering.

4. Use of *p* in modelling canopy reflectance and radiation regime

4.1. Canopy BRF using PARAS model

A family of models, called 'PARAS', where canopy structure is parameterized purely based on the recollision probability, has been developed to simulate different components of the canopy radiation budget, e.g., canopy reflectance (BRF, albedo) and absorption (fPAR). The first version of the PARAS model was formulated for the canopy BRF by Rautiainen and Stenberg (2005) as:

$$\mathrm{BRF} = cgf(\theta_1)\rho_G cgf(\theta_2) + f(\theta_1,\theta_2)i_0(\theta_2)\frac{\omega_L - p\omega_L}{1 - p\omega_L}. \tag{22}$$

Here, the assumption of 'black soil' was relaxed so that the contribution from photons arriving through gaps in the illumination direction (θ_2), reflected at the ground (ρ_G), and escaping through gaps in the view direction (θ_1) was added to the canopy-only reflectance. Multiple scattering between canopy and soil was not accounted for. The second term on the right hand of Eq. (22) is simply canopy scattering for the black soil problem (Eq. (2)) weighted by the function f, which describes the directional distribution of escaped photons normalized so that integrated over all view directions (Ω_1) it yields unity:

$$\frac{1}{\pi}\int_{4\pi} f(\theta_1,\theta_2)|\cos\theta_1|\mathrm{d}\Omega_1 = 1. \tag{23}$$

Integration over the upper hemisphere, in turn, gives the total upwards (or backwards) scattered fraction of the radiation intercepted by the canopy:

$$\frac{1}{\pi}\int_{2\pi^+} f(\theta_1,\theta_2)|\cos\theta_1|\mathrm{d}\Omega_1 = Q. \tag{24}$$

The incoming direction of radiation (θ_2) has an impact on the canopy interceptance (i_0), but its possible influence on p (through its effect on where the first interactions occur) is not explicitly taken into account in the model formulation. Originally, the value of p for input to the model (Eq. (22)) was calculated using the relationships between p and LAI for leaf and shoot canopies derived by Smolander and Stenberg (2005) in their simulation study. (Recall that in that study the dependence of p on the solar zenith angle was found to be insignificant.) In later applications of the PARAS models, Eq. (17) has generally been used to produce the input value of p. Note that using Eq. (17) for the estimation of p requires that the LAI is measured (or estimated) independent of the canopy diffuse interceptance (i_D), or alternatively, using some known or assumed value of the clumping index (Γ). Also, although the variation in f with view angle is represented in the model formulation, it has (so far) not been a subject of study in the applications. If the canopy reflectance is assumed to be Lambertian (i.e. f is constant), then it follows from Eq. (23) that $f(\theta_1,\theta_2) = Q$ for all view

directions. While the PARAS BRF model does not rely upon such a (false) assumption, in the first model applications the value of f for a nadir view ($\theta_1 = 0$) was approximated using simulated data on Q ($= r_C/\omega_C$) by Smolander and Stenberg (2005). The first analytical approach to separate canopy scattering into reflectance and transmittance, i.e. to estimate Q (Eq. (11)), was presented by Mõttus and Stenberg (2008). They also derived values of Q by simulation for a set of (measured) forest stands of varying LAI, and these simulation based dependencies of Q on LAI have later been used in the PARAS BRF model. Note that the reflectance ratio as predicted by Eq. (11) is not strictly spectrally invariant.

The model (Eq. (22)) was applied to show improved agreement between modelled and measured BRF for coniferous stands when within-shoot scattering accounted for (in calculating the p) (Rautiainen & Stenberg, 2005), and later Rautiainen et al. (2007) successfully applied the model to subarctic forests to demonstrate the role of understory vegetation in forming stand reflectance. Stenberg, Rautiainen, Manninen, Voipio, and Mõttus (2008) used the model to investigate which spectral vegetation indices would perform well in mapping LAI of boreal forests. More recently, the PARAS model has also been used to estimate chlorophyll content of spruce needles from CHRIS PROBA data (Yanez-Rausell et al., 2015).

4.2. Canopy albedo and absorption using PARAS model

Manninen and Stenberg (2009) extended the original PARAS model to include multiple scattering between canopy and ground with the motivation to make it applicable also in the case of a highly reflective background such as snow. They used it to simulate the effect of snow covered forest floor on the black- and white-sky albedos. Two components were thus added to the right hand side of Eq. (22): 1) photons first scattered downwards from the canopy, then reflected from the forest floor and transmitted without interaction through the canopy upwards, and 2) photons reflected from the forest floor and scattered upwards through the canopy. In addition, hemispherical integration over all view angles (for black-sky albedo) or integration over both incident and view angles (for white-sky albedo) was performed to convert BRF to black sky and white sky albedo, respectively. Simulation results showed that for snow covered forest floors the added multiple scattered component increased the total canopy albedo in NIR by up to 0.2 units. In summer conditions, on the other hand, the contribution to the albedo from the added components was negligible in the red band and not larger than about 0.05 in NIR. Evaluation of the albedo model against measured forest albedo data from the Arctic Research Centre of the Finnish Meteorological Institute (FMI-ARC) in Sodankylä (northern Finland) showed that it successfully simulated the main features of measured albedo values.

The PARAS albedo model developed later by Stenberg, Lukeš, Rautiainen, and Manninen (2013) is a simplified version of the Manninen and Stenberg (2009) model, but provides separately the three different components of the total radiation budget. The total canopy spectral absorption (A_C) and ground absorption (A_G) are defined as the fractions of the incoming photons at a specific wavelength which will finally be absorbed by the canopy or be transmitted to and absorbed by the ground. The spectral *albedo* (R_C), or the fraction of the incoming photons that escapes the canopy upwards, is then obtained as:

$$R_C(\lambda) = 1 - A_C(\lambda) - A_G(\lambda). \tag{25}$$

In the model two simplifying assumptions were made allowing A_C and A_G to be derived with help of geometric series. First, it was assumed that the fractions of backward scattering (Q) and forward scattering ($1 - Q$) do not depend on whether the canopy is irradiated from above or below. Secondly, the ground reflectance (ρ_G) was assumed to be purely Lambertian. (The first assumption was used also in the simulations by Manninen and Stenberg (2009), but the snow albedo was modelled as combination of completely forward/backward and Lambertian scattering.) The equations for canopy (A_c) and ground spectral absorption (A_G) are:

$$A_C(\lambda) = i_0\alpha_C(\lambda) + \frac{[t_0 + i_0(1-Q)\omega_C(\lambda)]\rho_G(\lambda)i_D\alpha_C(\lambda)}{1 - Q\omega_C(\lambda)i_D\rho_G(\lambda)} \tag{26}$$

and

$$A_G(\lambda) = [t_0 + i_0(1-Q)\omega_C(\lambda)](1-\rho_G(\lambda)) + \frac{[t_0 + i_0(1-Q)\omega_C(\lambda)]\rho_G(\lambda)i_D Q\omega_C(\lambda)(1-\rho_G(\lambda))}{1 - Q\omega_C(\lambda)i_D\rho_G(\lambda)}. \tag{27}$$

Derivation of the model actually followed the same principle as presented in Knyazikhin et al. (1998) and further outlined in Wang et al. (2003) so that, in Eqs. (26) and (27), the first term represents the solution to the 'black soil problem', and the second term is the additional contribution due to interactions between the canopy and underlying surface. Note that Eqs. (26) and (27) above are formulated for radiation incident from a specific angle (e.g. the sun zenith angle), at which t_0 and i_0 correspond to the uncollided transmittance and the interceptance, respectively, but they can easily be applied also to diffuse radiation by integrating over the respective distribution of sky radiation.

The model by Stenberg et al. (2013) was used to produce the black-sky albedos of 644 boreal forest stands in Finland composed of Scots pine, Norway spruce and Silver birch. Results were compared to those simulated using the detailed reflectance and transmittance model (FRT) by Kuusk and Nilson (2000) with input from an extensive forest inventory database and locally measured spectral data on leaf and needle albedos, and ground (understory) reflectance. Results showed that the albedos of the stands simulated by PARAS and FRT had approximately the same range and strong positive correlation. Inclusion of branch area index (BAI) in calculating the p value (by adding the BAI to LAI in Eq. (17)) further improved the agreement, so that the overall root mean square error (RMSE) between the PARAS and FRT simulated albedos was 0.011, and the ranges of albedo values were almost identical. It was concluded that although complex 3D models using detailed input on the structure of stands may be required to realistically describe the angular variation in reflectance (BRDF) for a forest, the spectrally invariant parameters are an efficient means to couple forest canopy structure and albedo.

The model was also adapted for calculating the fraction of absorbed photosynthetically active radiation (fPAR) (canopy spectral absorptance by Eq. (26) integrated over PAR wavelengths) of a forest by Majasalmi et al. (2014) and Majasalmi, Rautiainen and Stenberg (2015). First, the simulated fPAR values were validated against measurements in differently structured boreal coniferous and broadleaved stands, which was followed by simulations of diurnal and seasonal fPAR dynamics. Overall, the model performed well in fPAR calculations: the RMSE between the simulated and measured fPAR values ranged from 0.03 to 0.06, depending on the time of the day and sky conditions. As ground reference measurements of fPAR are tedious and slow, a physically-based model could be used to produce the in situ estimates of fPAR for validating satellite-based products for a larger area. For boreal forests, Majasalmi, Rautiainen, Stenberg and Manninen (2015) explored the potential of using this fPAR model to produce the ground reference values for the validation of MODIS (MOD15A2) and GEOV1 fPAR (g2_BIOPAR_FAPAR) products. Application of the model also allowed separating the contributions of understory and tree layer fPAR, and analysing their role in the performance of the satellite-based products. Thus, Majasalmi, Rautiainen, Stenberg and Manninen (2015) were able to report, for example, that the MODIS fPAR represented the fPAR of the tree canopy layer whereas the GEOV1 fPAR product was more similar to the total fPAR of both the understory and tree layers. Similarly for agricultural areas, Fan, Liu, and Xiru (2014) also applied a photon recollision based model to generate fPAR values comparable to

satellite products (MOD15A2). These studies on forest albedo, fPAR and satellite product validation are examples of how the *p*-theory can be used as a tool to estimate canopy radiation budget in different types of vegetation canopies. A strength of the *p*-theory based model approach is its simple parameterization, as described in the following section.

4.3. Measurements of PARAS model input parameters

A key property of any canopy radiation model is that the input parameters have a physical interpretation and can be measured in the field or in a laboratory. The PARAS family of models is based on a small, measurable set of input parameters describing the structure and optical properties of forest elements. Canopy structure is mainly parameterized through the recollision probability p which, knowing the clumping index (Γ), can be calculated by Eq. (17) or (19) using the effective LAI (L_e) and canopy diffuse interceptance (i_D) obtained from measurements with, for example, the LAI-2000 Plant Canopy Instrument (Li-Cor Inc.) or a camera with a hemispherical lens (Fig. 6A). The clumping index is not a directly measurable parameter, but the shoot level clumping can be estimated by STAR (Fig. 6B). In addition to p, the structural input data required by the model are canopy gap fractions to estimate bidirectional gap probabilities of the forest floor (or understory layer). These canopy gap fractions can also be obtained from LAI-2000 data or hemispherical photographs of the canopies. Besides the abovementioned canopy structural variables, the model requires spectral data on the foliage elements and forest floor. The spectral albedos of leaves or needles can be measured in laboratory (or field conditions) (e.g. Lukeš, Stenberg, Rautiainen, Mõttus, & Vanhatalo, 2013), and the BRF or BRDF of forest floor vegetation in the field (e.g. Peltoniemi et al., 2005; Rautiainen et al., 2011). The PARAS models do not require expert guesses for input parameters as they can be measured (Fig. 6).

5. Applications in monitoring vegetation

Operational monitoring of vegetation, such as producing LAI maps for extensive areas, requires an algorithm which is based on a simple set of input parameters. Therefore, the concept of spectral invariants (or photon recollision probability) has originally been applied in LAI/

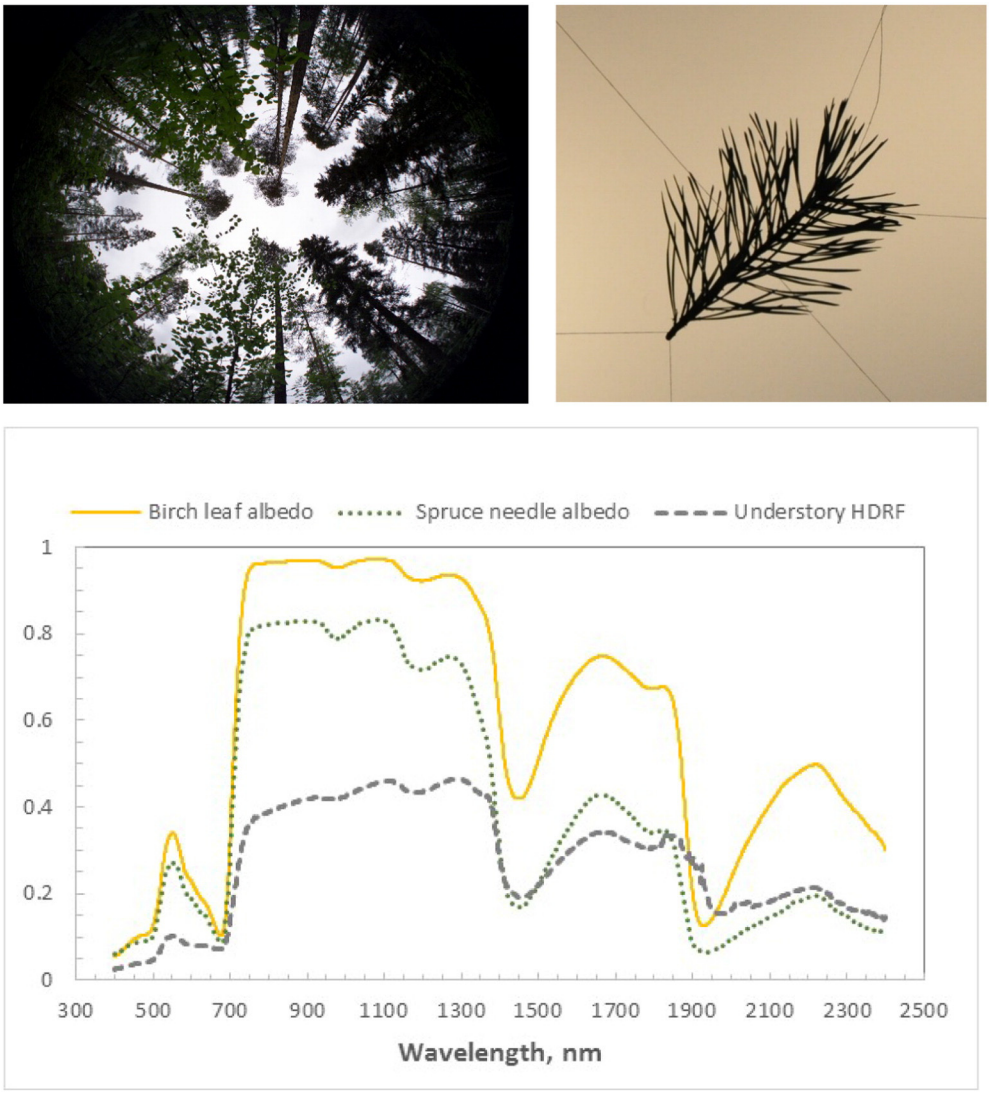

Fig. 6. Measurements of input variables needed for the PARAS models. A. Data on canopy gap fractions and diffuse interceptance, and leaf area index which are needed to calculate p (see Eq. (17)) and the contribution of understory (see Eq. (22)) can directly be obtained from LAI-2000 Plant Canopy Analyzer output files or hemispherical photographs. B. STAR values of coniferous shoots can be measured using photographic methods. STAR is linearly related to p (see Section 2.4). C. Data on the spectral properties of tree leaves and needles, and understory vegetation are also needed as input and can be measured with spectroradiometers. These examples are based on data measured in Hyytiälä, Finland.

fPAR retrieval algorithms utilizing MODIS (Knyazikhin et al., 1998; Shabanov et al., 2003) and Landsat or SPOT (Ganguly et al., 2008a,b, 2012; Heiskanen, Rautiainen, Korhonen, Mõttus, & Stenberg, 2011) data. In addition to LAI and fPAR, spectral invariants have been linked to other variables describing canopy structure. For example, Schull et al. (2007) showed that the spectral invariants theory can be applied to retrieve height of canopies from airborne multiangular remote sensing data. Furthermore, Schull et al. (2011) showed that, if leaf single scattering albedo is known, p (and related information on canopy structure) can be retrieved from hyperspectral remote sensing data using a simple linear regression method. Lukeš, Rautiainen, Stenberg, and Malenovský (2011) evaluated independently Schull's methods for retrieving the recollision probability and escape factor from multiangular CHRIS PROBA data for a spruce site. They were able to reproduce Schull et al.'s (2007) findings using completely different data sets from another biome, and concluded e.g. that in coniferous canopies the spectral invariants theory performs well in the near infrared spectral range.

The most recent development in the spectral invariants theory has been the introduction of the directional area scattering factor (DASF, Knyazikhin et al., 2012), formulated as an extension to the work by Schull et al. (2007, 2011). DASF is an estimate of the fraction of leaf area in a canopy that is visible from outside the canopy in a given direction. Formally, it is defined as the canopy BRF if the foliage does not absorb radiation ($\omega_L = 1$). For a canopy bounded underneath by black soil, DASF is identical to the product of i_0 and f (Eq. (22)), and the ratio of BRF to DASF equals the canopy scattering coefficient (ω_C). For dense canopies ($i_0 \sim 1$), furthermore, DASF approximately coincides with the function f which describes the proportion of photons scattered from a canopy into a particular direction (the view direction). In other words, DASF varies with view direction and is a function of geometric properties of the tree canopy (e.g. foliage grouping, crown shape, spatial distribution of trees). For closed canopies (i.e. canopies where the influence of forest floor is negligible), DASF can be directly estimated from air or satellite borne BRF data in the spectral range between 710 nm and 790 nm (Knyazikhin et al., 2012).

By now, the concept of DASF has been shown useful in mapping vegetation structure in both forest and agricultural vegetation. In a study based on reflectance data from CHRIS PROBA, Latorre-Carmona et al. (2014) reported that the DASF is directly related to crop type. Vanhatalo, Rautiainen, and Stenberg (2014), on the other hand, reported that DASF shows good potential in monitoring the broadleaf fraction of boreal forests when using hyperspectral satellite data (e.g. EO-1 Hyperion images). Furthermore, Stenberg and Manninen (2015) suggested that this might be linked to different degrees of clumping in broadleaved vs coniferous stands based on their result that, for a nadir view, DASF increases with the clumping index. The validity of the applications described above is, however, confined to dense canopies due to the underlying assumption of a vegetation bounded underneath by a non-reflecting black surface as shown in an empirical study by Vanhatalo et al. (2014). Alternatively, methods for removing the impact of background (e.g. forest floor) on total forest (or other vegetation canopy) reflectance need to be applied in sparse canopies.

Currently, the team led by Prof. Yuri Knyazikhin (Boston University) applies DASF in the development of new algorithms for retrieving global data records of fraction of photosynthetically active radiation absorbed by green leaves, leaf area and its sunlit fraction from Deep Space Climate Observatory (DSCOVR, launched in 2015) data. Future applications can also be expected to arise from the applications of spectral invariants in describing the radiation budget of vegetation in global radiation balance or climate models.

Acknowledgments

This study was partly funded by the Academy of Finland (grants 266152, 286390).

Appendix A

Canopy diffuse interceptance, or the interceptance of *isotropic* radiation, is obtained as:

$$i_D = 2\int_0^{\frac{\pi}{2}} [1 - t_0(\theta)] \cos\theta \sin\theta d\theta. \quad (A1)$$

The uncollided transmittance (or gap probability), t_0, can be expressed by the Beer's law equation as a function LAI, the mean projection of unit foliage area (G) and a clumping index (Γ) as (Nilson, 1971):

$$t_0(\theta) = \exp[-\Gamma(\theta) G(\theta) \mathrm{LAI} / \cos\theta]. \quad (A2)$$

Eq. (A2) with $\Gamma(\theta) = 1$ (for all θ) applies to a Poisson canopy composed of randomly distributed leaves and the clumping index consequently is defined as the parameter needed to correct for deviations in the relationship between t_0 and LAI caused by a non-random leaf dispersion.

As $\Gamma(\theta)$ varies with the direction, the total hemispherical clumping index Γ is defined as:

$$\Gamma = 2\int_0^{\pi/2} \Gamma(\theta) G(\theta) \sin\theta d\theta. \quad (A3)$$

With the clumping index defined by Eq. (A3), the effective leaf area index (L_e) now becomes equal to the product of and the true leaf area index:

$$L_e = -2\int_0^{\frac{\pi}{2}} \ln[t_0(\theta)] \cos\theta \sin\theta d\theta = 2\int_0^{\frac{\pi}{2}} \Gamma(\theta) G(\theta) L \sin\theta d\theta = \Gamma L. \quad (A4)$$

References

Disney, M., & Lewis, P. (2007). Spectral invariant behaviour of a complex 3D forest canopy. In M. Schaepman, S. Liang, N. Groot, & M. Kneubühler (Eds.), *Proc. 10th international symposium on physical measurements and signatures in remote sensing (ISPMSRS'07). The international archives of the ISPRS, Vol. XXXVI.* (pp. 102–107).

Disney, M., Lewis, P. T., Quaife, T., & Nichol, C. (2005). A spectral invariant approach to modelling canopy and leaf scattering. *Proc. 9th international symposium on physical measurements and signatures in remote sensing, Beijing, China, 17–19 Oct 2005* (pp. 318–320).

Fan, W., Liu, Y., & Xiru, X. (2014). A new FAPAR analytical model based on the law of energy conservation: A case study in China. *IEEE Journal of Selected Topics in Applied Earth Observations and Remote Sensing, 7*(9), 3945–3955.

Ganguly, S., Nemani, R., Zhang, G., Hashimoto, H., Milesi, C., Michaelis, A., ... Myneni, R. (2012). Generating global Leaf Area Index from Landsat: Algorithm formulation and demonstration. *Remote Sensing of Environment, 122*, 185–202.

Ganguly, S., Schull, M., Samanta, A., Shabanov, N., Milesi, C., Nemani, R., ... Myneni, R. (2008a). Generating vegetation leaf area index earth system data record from multiple sensors. Part 1: Theory. *Remote Sensing of Environment, 112*(12), 4333–4343.

Ganguly, S., Schull, M., Samanta, A., Shabanov, N., Milesi, C., Nemani, R., ... Myneni, R. (2008b). Generating vegetation leaf area index Earth system data record from multiple sensors. Part 2: Implementation, analysis and validation. *Remote Sensing of Environment, 112*(12), 4318–4332.

Heiskanen, J., Rautiainen, M., Korhonen, L., Mõttus, M., & Stenberg, P. (2011). Retrieval of boreal forest LAI using a forest reflectance model and empirical regressions. *International Journal of Applied Earth Observation and Geoinformation, 13*, 595–606.

Huang, D., Knyazikhin, Y., Dickinson, R. E., Rautiainen, M., Stenberg, P., Disney, M., ... Myneni, R. B. (2007). Canopy spectral invariants for remote sensing and model applications. *Remote Sensing of Environment, 106*, 106–122.

Jacquemoud, S., Ustin, S. L., Verdebout, J., Schmuck, G., Andreoli, G., & Hosgood, B. (1996). Estimating leaf biochemistry using the PROSPECT leaf optical properties model. *Remote Sensing of Environment, 56*, 194–202.

Knyazikhin, J., Martonchik, J. V., Myneni, R. B., Diner, D. J., & Running, S. W. (1998). Synergistic algorithm for estimating vegetation canopy leaf area index and fraction of absorbed photosynthetically active radiation from MODIS and MISR data. *Journal of Geophysical Research, 103*(D24), 32,257–32,275.

Knyazikhin, Y., Schull, M. A., Liang, X., Myneni, R. B., & Samanta, A. (2011). Canopy spectral invariants. Part 1: A new concept in remote sensing. *Journal of Quantitative Spectroscopy & Radiative Transfer, 112*, 727–735.

Knyazikhin, Y., Schull, M. A., Stenberg, P., Mõttus, M., Rautiainen, M., Yang, Y., ... Myneni, R. B. (2012). Hyperspectral remote sensing of foliar nitrogen content. *PNAS*. http://dx.doi.org/10.1073/pnas.1210196109.

Kuusk, A., & Nilson, T. (2000). A directional multispectral forest reflectance model. *Remote Sensing of Environment*, *72*, 244–252.
Latorre-Carmona, et al. (2014). On hyperspectral remote sensing of leaf biophysical constituents: Decoupling vegetation structure and leaf optics using CHRIS-PROBA data over crops in barrax. *IEEE Geoscience and Remote Sensing Letters*, *11*(9), 1579–1583.
Lewis, P., & Disney, M. (1998). *The Botanical Plant Modelling System (BPMS): A case study of multiple scattering in a barley canopy. Proc. geoscience and remote sensing symposium (IGARSS '98), Vol. 3.* (pp. 1481–1483), 1481–1483.
Lewis, P., & Disney, M. (2007). Spectral invariants and scattering across multiple scales from within-leaf to canopy. *Remote Sensing of Environment*, *109*, 196–206.
Lukeš, P., Rautiainen, M., Stenberg, P., & Malenovský, Z. (2011). Empirical test of the spectral invariants theory using imaging spectroscopy data from a coniferous forest. *International Journal of Applied Earth Observation and Geoinformation*, *13*, 668–675.
Lukeš, P., Stenberg, P., Rautiainen, M., Mõttus, M., & Vanhatalo, K. (2013). Optical properties of leaves and needles for boreal tree species in Europe. *Remote Sensing Letters*, *4*(7), 667–676.
Majasalmi, T., Rautiainen, M., & Stenberg, P. (2015a). Corrigendum to "modeled and measured fPAR in a boreal forest: Validation and application of a new model". *Agricultural and Forest Meteorology*, *204*, 46–47.
Majasalmi, T., Rautiainen, M., Stenberg, P., & Manninen, T. (2015b). Validation of MODIS and GEOV1 fPAR products in a boreal forest site in Finland. *Remote Sensing*, *7*(2), 1359–1379.
Majasalmi, T., Rautiainen, M., & Stenberg, P. (2014). Modeled and measured fPAR in a boreal forest: Validation and application of a new model. *Agricultural and Forest Meteorology*, *189*, 118–124.
Manninen, T., & Stenberg, P. (2009). Simulation of the effect of snow covered forest floor on the total forest albedo. *Agricultural and Forest Meteorology*, *149*, 303–319.
Mõttus, M. (2007). Photon recollision probability in discrete crown canopies. *Remote Sensing of Environment*, *110*, 176–185.
Mõttus, M. (2010). The physics of spectral invariants. *Proceedings of the 2nd Workshop on Hyperspectral Image and Signal Processing: Evolution in Remote Sensing (WHISPERS), Reykjavik, Iceland, June 14–16, 2010*. http://dx.doi.org/10.1109/WHISPERS.2010.5594910 (4 pp.).
Mõttus, M., & Rautiainen, M. (2013). Scaling PRI between coniferous canopy structures. *IEEE Journal of Selected Topics in Applied Earth Observations and Remote Sensing*, *6*(2), 708–714.
Mõttus, M., & Stenberg, P. (2008). A simple parameterization of canopy reflectance using photon recollision probability. *Remote Sensing of Environment*, *112*, 1545–1551.
Mõttus, M., Stenberg, P., & Rautiainen, M. (2007). Photon recollision probability in heterogeneous forest canopies: Compatibility with a hybrid GO model. *Journal of Geophysical Research — Atmospheres*, *112*, D103104. http://dx.doi.org/10.1029/2006JD007445.
Nilson, T. (1971). A theoretical analysis of the frequency of gaps in plant stands. *Agricultural Meteorology*, *8*, 25–38.
Oker-Blom, P., & Smolander, H. (1988). The ratio of shoot silhouette area to total needle area in Scots pine. *Forest Science*, *34*, 894–906.
Panferov, O., Knyazikhin, Y., Myneni, R. B., Szarzynski, J. E., Schnitzler, K. G., & Gravenhorst, G. (2001). The role of canopy structure in the spectral variation of transmission and absorption of solar radiation in vegetation canopies. *IEEE Transactions on Geoscience and Remote Sensing*, *39*, 241–253.
Peltoniemi, J. I., Kaasalainen, S., Näränen, J., Rautiainen, M., Stenberg, P., Smolander, H., ... Voipio, P. (2005). BRDF measurement of understorey vegetation in pine forests: Dwarf shrubs, lichen and moss. *Remote Sensing of Environment*, *94*, 343–354.
Rautiainen, M., & Stenberg, P. (2005). Application of photon recollision probability in coniferous canopy reflectance simulations. *Remote Sensing of Environment*, *96*, 98–107.
Rautiainen, M., Mõttus, M., Heiskanen, J., Akujärvi, A., Majasalmi, T., & Stenberg, P. (2011). Seasonal reflectance dynamics of common understory types in a Northern European boreal forest. *Remote Sensing of Environment*, *115*, 3020–3028.
Rautiainen, M., Mõttus, M., & Stenberg, P. (2009). On the relationship of canopy LAI and photon recollision probability in boreal forests. *Remote Sensing of Environment*, *113*, 458–461.
Rautiainen, M., Mõttus, M., Yanez-Rausell, L., Homolova, L., Malenovsky, Z., & Schaepman, M. E. (2012). A note on upscaling coniferous needle spectra to shoot spectral albedo. *Remote Sensing of Environment*, *117*, 469–474.
Rautiainen, M., Suomalainen, J., Mõttus, M., Stenberg, P., Voipio, P., Peltoniemi, J., & Manninen, T. (2007). Coupling forest canopy and understory reflectance in the Arctic latitudes of Finland. *Remote Sensing of Environment*, *110*, 332–343.
Ross, J. (1981). *The radiation regime and architecture of plant stands.* The Hague: Dr. W. Junk Publishers (391 pp.).
Schull, M. A., Ganguly, S., Samanta, A., Huang, D., Shabanov, N. V., Jenkins, J. P., ... Knyazikhin, Y. (2007). Physical interpretation of the correlation between multi-angle spectral data and canopy height. *Geophysical Research Letters*, *34*(18), L18405.
Schull, M. A., Knyazikhin, Y., Xu, L., Samanta, A., Carmona, P. L., Lepine, L., ... Myneni, R. B. (2011). Canopy spectral invariants. Part 2: Application to classification of forest types from hyperspectral data. *Journal of Quantitative Spectroscopy & Radiative Transfer*, *112*, 727–735.
Shabanov, et al. (2003). Effect of foliage spatial heterogeneity in the MODIS LAI and FPAR algorithm over broadleaf forests. *Remote Sensing of Environment*, *85*(4), 410–423.
Smolander, S., & Stenberg, P. (2003). A method to account for shoot scale clumping in coniferous canopy reflectance models. *Remote Sensing of Environment*, *88*, 363–373.
Smolander, S., & Stenberg, P. (2005). Simple parameterizations of the radiation budget of uniform broadleaved and coniferous canopies. *Remote Sensing of Environment*, *94*, 355–363.
Stenberg, P. (1996). Correcting LAI-2000 estimates for the clumping of needles in shoots of conifers. *Agricultural and Forest Meteorology*, *79*, 1–8.
Stenberg, P. (2007). Simple analytical formula for calculating average photon recollision probability in vegetation canopies. *Remote Sensing of Environment*, *109*, 221–224.
Stenberg, P., & Manninen, T. (2015). Effect of clumping on canopy scattering and its directional properties: A model simulation using spectral invariants. *International Journal of Remote Sensing*. http://dx.doi.org/10.1080/01431161.2015.1049383.
Stenberg, P., Lukeš, P., Rautiainen, M., & Manninen, T. (2013). A new approach for simulating forest albedo based on spectral invariants. *Remote Sensing of Environment*, *137*, 12–16.
Stenberg, P., Rautiainen, M., Manninen, T., Voipio, P., & Mõttus, M. (2008). Boreal forest leaf area index from optical satellite images: Model simulations and empirical analyses using data from central Finland. *Boreal Environment Research*, *13*, 433–443.
Vanhatalo, K. M., Rautiainen, M., & Stenberg, P. (2014). Monitoring the broadleaf fraction and canopy cover of boreal forests using spectral invariants. *Journal of Quantitative Spectroscopy and Radiative Transfer*. http://dx.doi.org/10.1016/j.jqsrt.2013.09.011.
Wang, Y., Buermann, W., Stenberg, P., Smolander, H., Häme, T., Tian, Y., ... Myneni, R. B. (2003). A new parameterization of canopy spectral response to incident solar radiation: Case study with hyperspectral data from pine dominant forest. *Remote Sensing of Environment*, *85*(3), 304–315.
Yanez-Rausell, L., Malenovsky, Z., Rautiainen, M., Clevers, J., Lukeš, P., Hanuš, J., & Schaepman, M. (2015). Estimation of spruce needle-leaf chlorophyll content based on DART and PARAS canopy reflectance models. *Journal of Selected Topics in Applied Earth Observations and Remote Sensing*. http://dx.doi.org/10.1109/JSTARS.2015.2400418.

remote sensing

MDPI

Review

An Interplay between Photons, Canopy Structure, and Recollision Probability: A Review of the Spectral Invariants Theory of 3D Canopy Radiative Transfer Processes

Weile Wang [1,2,*], Ramakrishna Nemani [1], Hirofumi Hashimoto [1,2], Sangram Ganguly [1,3], Dong Huang [4], Yuri Knyazikhin [5], Ranga Myneni [5] and Govindasamy Bala [6]

1 NASA Ames Research Center, Moffett Field, CA 94035, USA; rama.nemani@nasa.gov (R.N.); hirofumi.hashimoto@gmail.com (H.H.); sangram.ganguly@gmail.com (S.G.)
2 School of Natural Sciences, California State University Monterey Bay, Seaside, CA 93955, USA
3 Bay Area Environmental Research Institute, Moffett Field, CA 94035, USA
4 NASA Goddard Space Flight Center, Greenbelt, MD 20771, USA; hdtown@gmail.com
5 Department of Earth and Environment, Boston University, Boston, MA 02215, USA; jknjazi@bu.edu (Y.K.); rmyneni@bu.edu (R.M.)
6 Center for Atmospheric and Oceanic Sciences, Indian Institute of Science, Bangalore 560012, India; bala.gov@gmail.com
* Correspondence: weile.wang@nasa.gov; Tel.: +1-650-604-3916

Received: 1 October 2018; Accepted: 12 November 2018; Published: 14 November 2018

Abstract: Earth observations collected by remote sensors provide unique information to our ever-growing knowledge of the terrestrial biosphere. Yet, retrieving information from remote sensing data requires sophisticated processing and demands a better understanding of the underlying physics. This paper reviews research efforts that lead to the developments of the stochastic radiative transfer equation (RTE) and the spectral invariants theory. The former simplifies the characteristics of canopy structures with a pair-correlation function so that the 3D information can be succinctly packed into a 1D equation. The latter indicates that the interactions between photons and canopy elements converge to certain invariant patterns quantifiable by a few wavelength independent parameters, which satisfy the law of energy conservation. By revealing the connections between plant structural characteristics and photon recollision probability, these developments significantly advance our understanding of the transportation of radiation within vegetation canopies. They enable a novel physically-based algorithm to simulate the "hot-spot" phenomenon of canopy bidirectional reflectance while conserving energy, a challenge known to the classic radiative transfer models. Therefore, these theoretical developments have a far-reaching influence in optical remote sensing of the biosphere.

Keywords: vegetation remote sensing; stochastic radiative transfer equation; spectral invariants theory

1. Introduction

The past a few decades have seen rapid development in scientific research and applications that monitor and/or simulate terrestrial ecosystems with the help of remote sensing data [1]. Thanks to advances in technology, we have sensors that operate across a broad spectral range, at high spatial, temporal, and spectral resolutions, and with passive or active modes. For instance, on sun-synchronous orbits the classic MODIS (Moderate Resolution Imaging Spectroradiometer) and SUOMI NPP (National Polar-Orbiting Partnership) VIIRS (Visible Infrared Imaging Radiometer Suite) are now joined by

Landsat 8/OLI (Operational Land Imager) [2,3], Copernicus Sentinel-2 [4], and JPSS (Joint Polar Satellite System) VIIRS [5]. On geostationary orbits we now have advanced multi-band imagers on Himawari-8/9 [6], GOES-16/17 [7,8], FengYun-4 [9] and the forthcoming sensors from Korea Meteorological Administration and European Organization for the Exploitation of Meteorological Satellites (EUMETSAT). On the International Space Station there is ECOSTRESS (Ecosystem Spaceborne Thermal Radiometer Experiment on Space Station), which will be soon joined by GEDI (Global Ecosystem Dynamics Investigation) [10]. A plethora of remote sensing products have been derived that reflect various characteristics of the terrestrial biosphere, including vegetation spectral indices, land cover types, canopy structural parameters, and many others. As remote sensing data uniquely provide consistent coverage over large spatial scales, it is rare nowadays that a global change study does not use such information.

Remote sensing data are not uncertainty-free but come with caveats. In optical remote sensing, for example, photons that reach the sensor have gone through complicated interactions with the atmosphere-vegetation-soil medium [11]. A series of processing must be conducted to calibrate and correct the top-of-atmosphere signals before information about the surface can be extracted from them. As remote sensors cannot directly measure the surface biophysical characteristics of interest, models are used to transform the measurements into estimates of the desirable vegetation canopy variables (e.g., Leaf Area Index), a process methodologically called "inversion." The inverse problems encountered in remote sensing are often under-determined and "ill-posed" [12], thus *a priori* information, additional constraints on potential solution space, and regularization techniques are often applied to make the problem solvable [13–17]. Given these challenges, a better understanding of the methodological backgrounds of remote sensing products can be beneficial for users of these datasets.

Interactions between photons and the atmosphere-vegetation-soil medium are succinctly quantified by the radiative transfer equation (RTE) and the associated boundary conditions [18]. The theory of radiative transfer was originally developed to study the scattering and absorption of sunlight in the atmosphere and later to simulate the transport of neutrons in nuclear reactors [19]. The theory was applied to model the radiation regime in vegetation canopy in the second half of the last century [20–22]. A range of models have been developed to describe the radiation regime in vegetation canopies as well as their interactions with the atmosphere and the soil. Some of the representative models, for instance, include Raytran [23], DART (Discrete Anisotropic Radiative Transfer) [24,25], SAIL (Scattering by Arbitrary Inclined Leaves) [26–28], PROSPECT [29], GORT (Geometric Optical-Radiative Transfer) [30,31], and PARAS [32]. A recent review of the canopy radiative transfer models can be found in Reference [18].

Compared with turbid media or nuclear reactors, vegetation canopy has its own structural and optical characteristics. On one hand, leaves have finite sizes and therefore cast shadows [33], which violates the assumptions of Beer's law [34,35]. For instance, the mutual shadowing effects of the canopy elements are mainly responsive for a sharp peak of the canopy reflectance in the retro-illumination direction. This phenomenon is often called the "hot-spot" effect, which is difficult to simulate with the classic RTE [33,36]. On the other side, the sizes of leaves (and twigs, branches, etc.) are often much larger than the spectral wavelengths considered in optical remote sensing. The total extinction coefficient (or cross-section) of photons in vegetation canopies is thus determined by the structural distribution of the leaves (and other phytoelements) rather than the wavelengths of photons [37]. Such characteristics of the vegetation medium present both challenges and opportunities to research efforts on the radiative transfer theory in vegetation canopies.

This paper intends to contribute a review of the theoretical advancements in modeling radiative transfer processes in 3D vegetation canopies. It particularly focuses on the developments of the stochastic radiative equation and the spectral invariant theory, which have been widely applied in retrieving vegetation structural information from remote sensors like MODIS and MISR (Multi-Angle Imaging Spectroradiometer) to the recent EPIC (Earth Polychromatic Imaging Camera) on the DSCOVR (Deep Space Climate Observatory) platform and the latest geostationary sensors like AHI (Advanced

Himawari Imager; on Himawari-8/9) and ABI (Advanced Baseline Imager; on GOES-16/17). However, a detailed account of such theoretical progresses is somewhat scarce in recent review papers [38–45] or textbooks [46] on remote sensing sciences and applications, which becomes a main motivation for this paper.

A question may rise: Why should we care so much about the theoretical properties of the radiative transfer processes in a time of big data, artificial intelligence and machine learning? It is true that in general the RTE has to be solved numerically [47]. In many applications we rely on statistical or empirical methods to solve the problem at hand [43]. Artificial intelligence and machine learning tools have also been introduced into remote sensing applications since their early stages and are gaining increasing popularity with rapid developments in the technology [48]. However, as mentioned earlier, the task of remote sensing is essentially ill-posed. The solution to the inverse problem often is not unique [43] and may not even be physical [35]. For instance, though the spectroscopy of a single leaf may be accurately measured in a laboratory, those measured for a forest stand by remote sensors convolute signals from the phytoelements (e.g., leaves, twigs, branches, trunks), the land surface, the atmosphere in between, as well as the interactions among them [22]. It is far from straightforward to establish a robust quantitative link between satellite measurements and leaf-level biogeochemical or biogeophysical traits. Without a clear understanding of the underlying processes, we may misinterpret empirically identified correlations from the data [49]. Furthermore, physically-based radiative transfer models (RTM) usually assume many parameters, which make them difficult to invert in practice [43]. The success of an RTM in remote sensing applications thus requires a balance between the simplicity of the model formulation and the fidelity of physics it preserves. Such a task can only be achieved with a deep understanding of the radiative transfer processes. As we will discuss later, the stochastic RTE and the spectral invariant theory represent elegant advancements with this modeling aspect regarded.

The rest of the paper is organized as follows. We begin by introducing the radiative transfer equation formulated for 3D vegetation canopies. We then focus on four particular topics in the main text, including the decomposition of RTE into the black-soil ("BS") and the soil ("S") problems, the development of the stochastic RTE that efficiently packs 3D canopy features into a 1D form, the spectral invariants theory that links the solutions of the RTE at different wavelengths by a few key canopy structural parameters, and the latest effort to address the "hot-spot" problem in vegetation remote sensing. We conclude the paper with a brief summary of the key ideas reviewed in these topics.

We would like to emphasize that, although the concepts of the spectral invariants and stochastic canopy geometrical properties may appear abstract, they have concrete physical interpretations and are measurable from ground and remote observations. Additionally, the basic ideas behind these theoretical developments are actually simple. Their derivations repeatedly make use of the ideas of decomposition and superposition, convergence and invariants, and the law of energy conservation. Therefore, we invite the readers to pay more attention to these ideas rather than the mathematical details of the theory, if the latter appears to be a bit complicated at the first look.

2. Radiative Transfer Equation for Vegetation Canopy

The classic RTE theory assumes that the radiative transfer properties of a vegetation canopy are largely determined by how the leaves are distributed in space, how they are oriented, and the fashions in which photons interact with the leaves [11,22,37,50]. These three aspects are mathematically described by the leaf area density distribution function $u_L(x)$, the leaf normal distribution function $g_L(x, \Omega_L)/2\pi$, and the leaf element scattering phase function $\gamma_L(\lambda, x, \Omega \to \Omega\prime, \Omega_L)$, respectively (Figure 1). Here, Ω_L represents the direction of the leaf normal, Ω is the incident direction, and $\Omega\prime$ is the direction in which photons are scattered into. Note that the scattering phase function γ_L explicitly depends on both Ω and $\Omega\prime$ but not only the scattering angle $\cos^{-1}\left(\Omega \cdot \Omega^{-1}\right)$, which is a key difference between vegetation canopies and gaseous media [37].

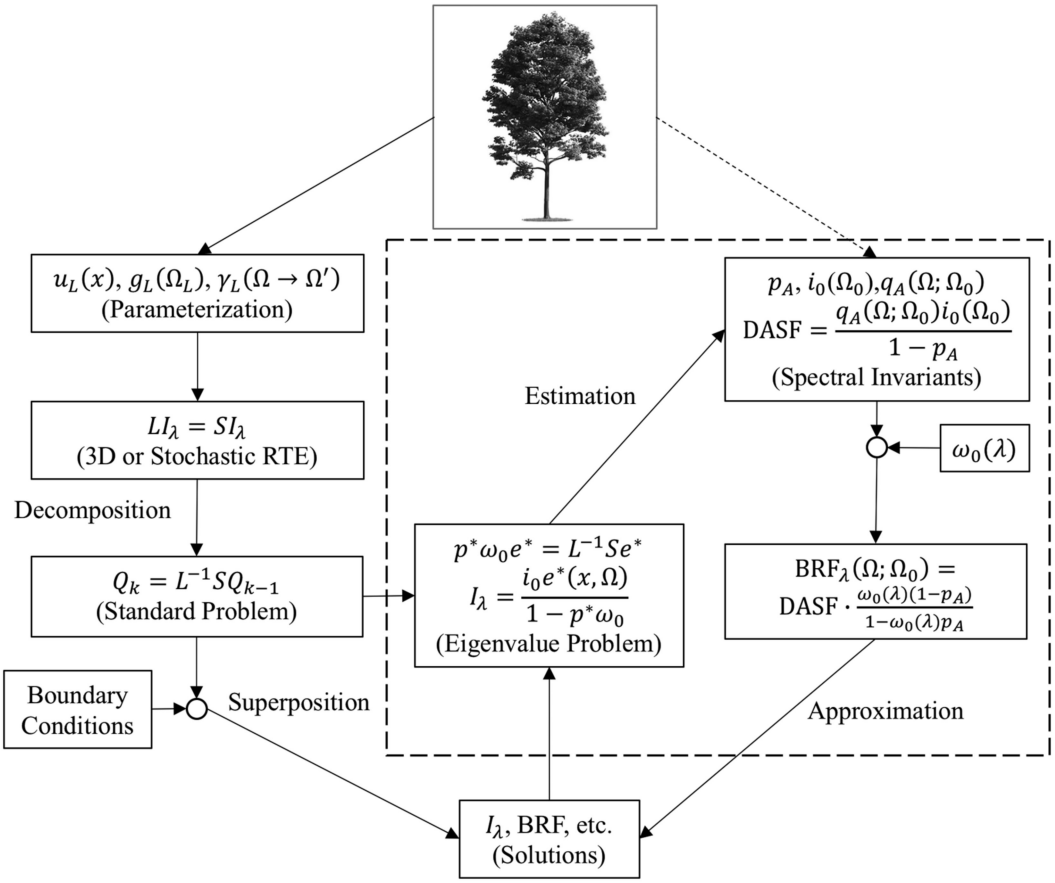

Figure 1. Schematic diagram of the Radiative Transfer Equation (RTE) and the Spectral Invariants theory. The left side of the flowchart (outside the dashed box) describes the successive-order scattering approximation (SOSA) scheme to solve the RTE. The right side of the diagram (inside the dashed box) indicates the logic flow of the spectral invariants theory. The symmetric arrangement of the diagram is to emphasizes that the canopy spectral invariants provide an equivalent set of parameters (other than the traditional ones) to succinctly characterize the canopy structural properties.

From these functions we can derive a few key parameters to be used in RTE, including the single scattering albedo $\omega_0(\lambda)$, the total extinction cross-section $\sigma(\Omega)$, and the differential scattering cross-section $\sigma_S(\Omega \to \Omega\prime)$. Here we have assumed that ω_0 is a variable of only spectral wavelength and that $\sigma(\Omega)$ and $\sigma_S(\Omega \to \Omega\prime)$ do not depend on locations (x) or spectral wavelengths (x). The detailed definitions of these variables and their relationships are given in the Appendix A. Note that although the single scattering albedo is generally understood as the averaged leaf albedo, its definition actually depends on the spatial scales of the elementary scatters considered in the equation [51]. As will be discussed later, this parameter is related to the canopy scattering coefficients by the associated scaling rules [45].

Denoting $I_\lambda(x,\Omega)$ as the monochromatic radiation intensity (radiance), we use the operator notations [52] to describe the radiative transfer processes in vegetation canopies (for readers who are not familiar with linear differential/integral operators, you may think them as matrices with infinite dimensions). In particular, the streaming-collision operator (L) describes the spatial/directional change of the radiation intensity and the extinction of radiance due to collisions between photons and phytoelements (Reference [52]; the same for Equations (2)–(5)),

$$LI_\lambda \equiv \Omega \cdot \nabla I_\lambda(x,\Omega) + \sigma(x,\Omega) I_\lambda(x,\Omega) \quad (1)$$

The scattering operator (S_λ) describes the addition of radiance by photons scattered in from other directions,

$$S_\lambda I_\lambda \equiv \int_{4\pi} \omega_0(\lambda)\sigma_S(x, \Omega\prime \to \Omega) I_\lambda(x, \Omega\prime) d\Omega\prime \tag{2}$$

The steady state RTE is thus

$$LI_\lambda = S_\lambda I_\lambda, \tag{3}$$

with the boundary conditions specified by

$$I_\lambda(x_T, \Omega) = \delta(\Omega - \Omega_0), n_T \cdot \Omega < 0 \tag{4}$$

and

$$I_\lambda(x_B, \Omega) = \frac{1}{\pi} \int_{n_B \cdot \Omega\prime > 0} \rho_\lambda(x_B, \Omega\prime \to \Omega) I_\lambda(x_B, \Omega\prime) |n_B \cdot \Omega\prime| d\Omega\prime, n_B \cdot \Omega < 0 \tag{5}$$

where x_T and $x_B \in \partial V$, n_T and n_B and the outward normal of the boundary, ρ_λ is the bidirectional reflectance factor (BRF) of the lower boundary (i.e., soil surface). In remote sensing applications the influence of lateral boundaries is considered small and thus neglected [35,37]. For simplicity we also only consider the direct solar illumination but neglect the diffuse radiation. This corresponds to the case where the influences of path radiances are removed through atmospheric corrections.

The RTE of Equation (3) describes photon-canopy interactions in three spatial dimensions (i.e., x) and two directional dimensions (Ω and $\Omega\prime$). As the phase function γ_L is not rotational invariant, we cannot decompose the solution in spherical harmonics to simplify the calculation [37]. Direct numerical schemes to solve the equation thus have to perform 5-dimensional integration at every iteration, which is complicated and prone to numerical errors. Therefore, we seek to simplify the problem based on its mathematical/physical properties, which is discussed in the following sections.

3. Black-Soil and Soil Problems

A key property of the RTE is its linearity with regard to I_λ, which allows the problem to be decomposed into a set of sub-problems that are easier to solve. The classic MODIS algorithm [35] decomposes the RTE problem according to its boundary conditions. The easiest boundary condition is represented by the black-soil ("BS") problem, which is formulated for a vegetation canopy illuminated from above by a mono-directional sun beam and otherwise bounded by purely absorbing (i.e., "black") surface from below. In contrast, the soil ("S") problem is formulated for the same canopy but illuminated from below by anisotropic sources and bounded by absorbing surfaces everywhere else. Such a decomposition scheme separates the influence of illumination conditions from those of soils. The two sub-problems are solved independently but their solutions can be flexibly superposed to render the full solution of the original problem (Figure 1).

To solve the black-soil problem, we further decompose the radiation field into the un-collided component, Q_0,

$$Q_0(x_T, \Omega) = \delta(\Omega - \Omega_0),\ n_T \cdot \Omega < 0 \tag{6}$$

and the collided (or diffuse) components, I_{dif}, which satisfies the so-called standard problem with zero boundary conditions where no photon entering the canopy from above or below [53],

$$L_0 I_{dif} = S_\lambda I_{dif} + S_\lambda Q_0. \tag{7}$$

As L is an ordinary differential operator, the solution of Q_0 can be relatively easily obtained. By introducing the integral operator $T = L_0^{-1} S_\lambda$, we write the diffuse component, I_{dif}, symbolically as

$$I_{dif} = T I_{dif} + T Q_0. \tag{8}$$

We should explain the physical meaning of the T operator later in Section 5. For now, note that we can solve for I_{dif} as

$$I_{dif} = \frac{TQ_0}{E - T}, \tag{9}$$

where "E" is the identity operator (i.e., $EI_{dif} = I_{dif}$). Adding Q_0 to both sides, we obtain the solution of the black-soil problem as

$$\begin{aligned} I_{bs} = I_{dif} + Q_0 = \tfrac{Q_0}{E-T} \\ = \left(E + T + T^2 + \cdots + T^k + \cdots\right) Q_0. \end{aligned} \tag{10}$$

The last line of Equation (10) is the expansion of the operator $(E - T)^{-1}$ in Neumann series, which is analogous to geometrical series of numbers. Physically it indicates that I_{BS} is the superposition of photons that are un-collided, once-collided, twice-collided, and so on. The condition that the series converge is provided by the law of energy conservation because the system is dissipative. This superposition scheme, generally referred to as "successive-order scattering approximation" (SOSA; Reference [54]), also bridges the black-soil problem solution to a few key concepts in the radiative transfer theory in vegetation canopies.

The soil ("S") problem is formulated as follows:

$$\begin{aligned} LI_s = S_\lambda I_s, \\ I_s(x_B, \Omega) = d_B(x_B, \Omega), n_B \cdot \Omega < 0, \end{aligned} \tag{11}$$

where $d_B(x_B, \Omega)$ is an anisotropic source normalized to have its hemispherical integral (i.e., irradiance) to be unit. Note that the soil problem also assumes purely absorbing boundaries and the only difference is that the canopy is illuminated from below by a diffuse source. It can be solved with the same approach as the black-soil problem.

We now explain how to use the solutions of the black-soil and the soil problems to model interactions between the canopy and the underlying soil surface. First, the anisotropic source in the S-problem is initialized by radiation that passes through the canopy and reflected by the soil surface. If the spatial distribution pattern of the downward radiation (as which is regulated by the structure of the canopy) does not change significantly, we may assume that the anisotropy is determined by the soil surface but independent on the incoming radiation field [35].

Let the spatial mean effective ground bi-hemispherical reflectance (BHR) of the soil surface to be ρ_{eff} and the mean radiation flux (irradiance) from the downward radiance generated by the black-soil problem to be F_{bs}. As the system is linear, the radiation field that generated by the first interaction of the canopy and the soil surface is (approximately) $\rho_{eff} F_{bs} I_s$. A part of the photons will be scattered back by the canopy to interact with the soil surface again. Denote the mean BHR of the canopy illuminated by the anisotropic source $d_B(x_B, \Omega)$ to be $\overline{R}_s$, and the radiation field generated by the second interaction between the canopy and the soil surface is thus $\left(\rho_{eff}\right)^2 R_s F_{bs} I_s$. As this process iterates, we arrive at the total radiation generated by the interactions between the canopy and the soil surface

$$I_{rest}(x, \Omega) = \frac{\rho_{eff} F_{bs}}{1 - \rho_{eff} R_s} I_s(x, \Omega) \tag{12}$$

and the solution to the full RTE problem is therefore

$$I_\lambda(x, \Omega) = I_{bs}(x, \Omega) + \frac{\rho_{eff} F_{bs}}{1 - \rho_{eff} R_s} I_s(x, \Omega). \tag{13}$$

The above derivation of Equation (13) is slightly different from Reference [35] but shares the same the idea. Ultimately, these decomposition schemes can be derived from the concept of Green's function of the RTE [53]. The assumption about the constancy of canopy BHR (R_s) and the anisotropy $d_B(x_B, \Omega)$ is reasonable. This is because the diffused radiation field within the canopy tend to converge toward certain spatial distributions that are independent on external illumination conditions (see below).

4. Stochastic Radiative Transfer Equation

In remote sensing applications we are generally more interested in the statistical mean of the radiation fields than individual solutions [35]. An apparent way to achieve this goal is to generate an ensemble of representative canopy realizations, solve the RTE for them separately, and then calculate the mean in the end. However, this approach costs time and computation resources. Alternatively, we can also calculate the statistical mean canopy first before solving for the RTE. The second approach is the main idea behind the development of the Stochastic RTE, which turns out to be more efficient in addressing the question [55]. As the ensemble mean is usually equivalent to the average of the 3D radiation field over the horizontal space (i.e., the ergodicity assumption), the central task of Stochastic RTE is the same as to efficiently pack a 3D radiative regime into a 1D form.

To illustrate, recall that $\Omega \cdot \nabla I(x, \Omega)$ is a directional derivative, i.e.,

$$\Omega \cdot \nabla I(x, \Omega) = \frac{\mathrm{d}I(x_B + \xi\Omega, \Omega)}{\mathrm{d}\xi} = \frac{\mathrm{d}I(x_B + (z - z_B)/\mu\Omega, \Omega)}{1/\mu \mathrm{d}z}. \tag{14}$$

Integrating the RTE over the vertical dimension from the top ($z = 0$) or the bottom ($z = 1$) of the canopy leads to

$$\begin{aligned} &I(x, \Omega) + \tfrac{1}{\mu} \textstyle\int_Z u_L(x')\sigma(\Omega)I(x', \Omega)dz' \\ &= \tfrac{1}{\mu} \textstyle\int_Z \omega_0 u_L(x')dz' \int\limits_{4\pi} \sigma_s(\Omega\prime \to \Omega)I(x', \Omega\prime)d\Omega\prime + I(x_B, \Omega) \end{aligned} \tag{15}$$

where $x' = x + (z' - z)/\mu\Omega$ and Z represents appropriate integration intervals. The subscript "B" denotes general boundaries, which may be "top" or "bottom" according to the direction of the integration [55]. Let $\langle \cdot \rangle$ denote the horizontal average. Apply the operator to both sides of the equation and we obtain,

$$\begin{aligned} &I(x, \Omega) + \tfrac{1}{\mu} \textstyle\int_Z \sigma(\Omega)\langle u_L(x')I(x', \Omega)\rangle dz' \\ &= \tfrac{1}{\mu} \textstyle\int_Z \omega_0 dz' \int\limits_{4\pi} \sigma_s(\Omega\prime \to \Omega)\langle u_L(x')I(x', \Omega\prime)\rangle d\Omega\prime + I(x_B, \Omega) \end{aligned} \tag{16}$$

where $I(x, \Omega) = \langle I(x, \Omega)\rangle$. Therefore, the original RTE becomes a 1D equation with regard to the vertical ("z") dimension.

Note that in Equation (16) $I(x, \Omega)$ is the mean radiation intensity (at the vertical level z) averaged over the whole horizontal domain while the "second-moment" variable $\langle u_L(x)I(x, \Omega)\rangle$ is the mean intensity averaged only at locations where a leaf element presents. These two variables are generally different from each other except for special cases. In order to evaluate $\langle u_L(x)I(x, \Omega\rangle)$, we multiply both sides of the RTE by $u_L(x)$ and integrate over the horizontal scale to get

$$\begin{aligned} &\langle u_L(x)I(x, \Omega)\rangle + \tfrac{1}{\mu}\sigma(\Omega) \textstyle\int_Z \langle u_L(x)u_L(x')I(x', \Omega)\rangle dz' \\ &= \tfrac{1}{\mu} \textstyle\int_Z \omega_0 dz' \int\limits_{4\pi} \sigma_s(\Omega\prime \to \Omega)\langle u_L(x)u_L(x')I(x', \Omega\prime)\rangle d\Omega\prime + \langle u_L(x_B)I(x, \Omega)\rangle \end{aligned} \tag{17}$$

Now another new (the "third-moment") variable, $\langle u_L(x)u_L(r')I(r', \Omega\prime)\rangle$, appears in the equation! The procedure can go on and on, but every time we try to solve for a lower-moment variable, we end up introducing a new higher-order unknown into the equation. The process is conceptually analogous

to the "Reynolds Averaging" technique in fluid dynamics. A parameterization scheme thus must be introduced to "close" the Stochastic RTE [56].

The scheme adopted in the current literature is derived based on the binary-medium assumption, under which the leaf density function $u_L(x)$ is represented by an indicator function $\chi(x)$ that specifies the presence ($\chi = 1$) or absence ($\chi = 0$) of a unit leaf element (d_L), i.e., $u_L(x) = d_L\chi(x)$. Note that for a random variable like $\chi(x)$ its spatial averaging ($\langle\cdot\rangle$) is essentially the same as its spatial expectation. As $\chi(x) = \chi(x)^2$, by the standard formula of statistical covariance of two variables, we see that

$$\begin{aligned}&\langle\chi(x)\chi(x')I(x',\Omega\prime)\rangle = \langle\chi(x)\chi(x')^2I(x',\Omega\prime)\rangle\\&= \langle\chi(x)\chi(x')\rangle\langle\chi(x')I(x',\Omega\prime)\rangle + \mathrm{cov}(\chi(x)\chi(x'),\chi(x')I(x',\Omega\prime)).\end{aligned} \tag{18}$$

The first term in Equation (18) represents the "global mean" of $\chi(x)\chi(x')$ and $\chi(x')I(x',\Omega\prime)$, respectively, whose meaning will be explained below. The second (the covariance) term represents their "local chaotisity", which is assumed negligible [57]. We thus arrive at

$$\langle\chi(x)\chi(x')I(x',\Omega\prime)\rangle \approx \langle\chi(x)\chi(x')\rangle\langle\chi(x')I(x',\Omega\prime)\rangle. \tag{19}$$

By the common notation of the literature [55,58], we define

$$\begin{aligned}p_c(z) &= \langle\chi(x)\rangle,\\ q_c(z,z',\Omega) &= \langle\chi(x)\chi(x')\rangle,\\ K(z,z',\Omega) &= q_c(z,z,\Omega)/p_c(z),\\ U(z,\Omega) &= \langle\chi(x)I(x,\Omega)\rangle/p_c(z),\end{aligned} \tag{20}$$

where $p_c(z)$ is the probability of finding leaf elements at locations z. $q_c(z,z',\Omega)$ and $K(z,z',\Omega)$ are the joint and the conditional probability (or pair correlation functions) of finding leaf elements at locations z and z' along the direction Ω simultaneously. $U(z,\Omega)$ is the mean radiation intensity averaged over vegetation occupied horizontal space (i.e., with gaps excluded). The stochastic RTE is then fully specified as [55,58]

$$\begin{aligned}&I(z,\Omega) + \tfrac{1}{\mu}\textstyle\int_Z \sigma(\Omega)p_c(z')U(z',\Omega)dz'\\&= \tfrac{1}{\mu}\textstyle\int_Z \omega_0 dz' \int\limits_{4\pi} p_c(z')U(z',\Omega\prime)\sigma_s(\Omega\prime\to\Omega)d\Omega\prime + I(z_B,\Omega)\end{aligned} \tag{21}$$

and

$$\begin{aligned}&U(z,\Omega) + \tfrac{1}{\mu}\sigma(\Omega)\textstyle\int_Z K(z,z',\Omega)U(z',\Omega)dz'\\&= \tfrac{1}{\mu}\textstyle\int_Z \omega_0 dz' \int\limits_{4\pi} \sigma_s(\Omega\prime\to\Omega)K(z,z',\Omega\prime)U(z',\Omega\prime)d\Omega\prime + U(x_B,\Omega)\end{aligned} \tag{22}$$

with corresponding boundary conditions adapted for $I(x_B,\Omega)$ and $U(x_B,\Omega)$, respectively. In general, we must evaluate $U(z,\Omega)$ first by Equation (22) before solving Equation (21) for $I(z,\Omega)$. Note that because $K(z,z',\Omega\prime)$ is a function of both z' and z, Equation (22) is a Volterra integral equation.

The stochastic RTE was initially developed to solve the mean radiation intensity in the medium of broken clouds [57,59,60]. It was first applied to the vegetation canopy by Reference [61]. The current form of the Stochastic RTE in vegetation canopy was introduced in Reference [55], who also detailed a SOSA procedure to solve the Volterra integral equation.

The most important feature of the Stochastic RTE is the incorporation of the pair correlation function $K(z,\ z',\Omega\prime)$. The function succinctly characterizes the structural and the spatial distribution properties such as heterogeneity and anisotropy of the 3D canopies. It encompasses information presented by traditional metrics like forest gap fractions and clumping indices. Indeed, the introduction of $K(z,\ z',\ \Omega\prime)$ allows the 1D RTE to resolve the differences between $U(x_B,\Omega)$ and $I(x_B,\Omega)$, which can be used to retrieve canopy gap fractions [62]. The first set of realistic pair-correlation functions was derived by Reference [58] using stochastic geometry models [63]. The approach is to idealize individual

tree crowns as regular geometrical objects (e.g., spheres, cylinders, cones, etc.) and assume their locations follow certain spatial patterns (e.g., Poisson's distribution). The pair-correlation functions then can be computed analytically or statistically. Reference [58] presents detailed examples of the pair correlation functions for different crown shapes and canopy distribution patterns. As a special case, when the leaf elements are spatially not correlated, $K(z,\ z',\Omega\prime)$ reduces to $p_c(z)$, Equation (22) reduces to a classic 1D RTE, and $U(z,\Omega)$ becomes the same as $I(z,\Omega)$. Reference [58] also systematically compared the simulation results of the stochastic RTE with those of the classic 1D RTE as well as field measurements, showing that the Stochastic RTE is able to capture the 3D radiation effects previously reported in the literature and therefore the pair-correlation function provides a "most natural and physically meaningful" [58] measure to 3D canopy structural properties over a range of scales.

There are a couple of more facts about the Stochastic RTE that need attention. First, the pair correlation function is not a merely theoretical concept but can be evaluated from observations for real-world applications. With the development of terrestrial lidar scanning (TLS) instruments, now we can measure the 3D structure of forest stands with relative ease and the pair correlation function of the canopy can be accurately computed with such measurements. The function can also be estimated from high-resolution satellite imageries and air-/space-born lidar data over larger spatial scales. Second, as the pair correlation function encapsulates purely the structural or geometrical characteristics of the canopy, it has a close connection with the school of geometrical optical (GO) models in remote sensing [30,31,64,65]. Indeed, the stochastic geometry models used in deriving the theoretical pair correlation functions in Reference [58] are essentially the same as those used in References [64,65]. However, the two schools are different in the specific approaches to use the canopy geometric information. In GO models, the information is used to derive "kernels" of the bidirectional reflectance distribution function (BRDF), which allow the model to fit with observations in a semi-empirical fashion. In contrast, the Stochastic RTE tries to preserve the law of energy conservation and rigorously follows the radiative transfer formulation. As a cost, the Stochastic RTE inherits the limitations of the 3D RTE and cannot resolve, at least to certain spatial scales, the "hot-spot" effects of the canopy radiation regime [33]. We shall return to this topic in Section 6.

5. Canopy Spectral Invariants

The preceding sections have described the traditional algorithms to solve the RTE at a specific wavelength (λ). In remote sensing applications we often need to obtain solutions at many wavelengths to sample the (multiple or hyperspectral) bandwidth of the sensors. Do we have to iterate the process for $I_\lambda(x,\Omega)$ at every wavelength? This question is the main concern of the spectral invariant theory (Figure 1).

The idea underlying the spectral invariant theory is simple: The single albedo $\omega_0(\lambda)$ is the only parameter in the RTE of Equation (1) that depends on wavelengths, while all the other parameters are determined by the structures of the canopy [52]. Therefore, we seek a formula to separate the influence of $\omega_0(\lambda)$ on the solutions of $I_\lambda(x,\Omega)$ at different wavelengths. There are multiple ways in the literature [35,52,66] to derive the spectral invariants theory. Below we follow the SOSA approach described in Reference [66], which represents the most general case and is the easiest to understand. We will use the black-soil problem as the example, though the same methods can be applied to the "S" problem as well [67].

Recall that the black-soil problem can be decomposed to successively collided problems, each of which satisfies the Law of Energy Conservation. For instance, integrating the first-collision problem over the spatial domain and the solid angles eventually leads to (Appendix A)

$$\int_{\delta V} \mathrm{d}x_B \int_{\Omega\cdot\mathrm{n}(x_B)>0} Q_1|\Omega\cdot\mathrm{n}(x_B)|\mathrm{d}\Omega + \int_{4\pi\times V} \sigma Q_1 \mathrm{d}\Omega\mathrm{d}x = \omega_0 \int_{4\pi\times V} \sigma Q_0 \mathrm{d}\Omega\mathrm{d}x \tag{23}$$

or, by the norm notation [66],

$$\| Q_1 \|_\rho + \| Q_1 \| = \omega_0 \| Q_0 \|, \tag{24}$$

where "$\| \cdot \|$" and "$\| \cdot \|_\rho$" indicate the intercepted and the escaped (either being reflected or transmitted) radiation energy, respectively. Equation (24) simply indicates that the portion (i.e., ω_0) of photons scattered from the first collision will either escape through the boundary or collide with the canopy again.

Note that the stream-collision operator (L or L_0) depends only on canopy structural parameters, and the un-collided radiation field Q_0 and the initial interceptance $\| Q_0 \|$ are therefore wavelength independent. The first-collided radiation field Q_1 (and thus $\| Q_1 \|$) is regulated by $\omega_0(\lambda)$, but the ratios

$$\begin{aligned} p_1 &= \frac{\|Q_1\|}{\omega_0 \|Q_0\|} \\ q_1 &= \frac{\|Q_1\|_r}{\omega_0 \|Q_0\|} \end{aligned} \tag{25}$$

are also wavelength independent. Physically p_1 represents the recollision probability that the scattered photons will re-collide with the canopy again and q_1 denotes the probability that the photos will escape the canopy. Clearly $p_1 + q_1 = 1$, satisfying the conservation of energy.

Following the same idea, we normalize the radiation fields as

$$e_k(x, \Omega) = \frac{Q_k(x, \Omega)}{\| Q_k \|}, k = 1, 2, \ldots \tag{26}$$

It is easy to see that $\| e_k(x, \Omega) \| = 1$ and they satisfy the standard RTE

$$p_k \omega_0 e_k = T e_{k-1}. \tag{27}$$

Equations (26) and (27) have clear physical interpretations: $e_k(x, \Omega)$ represents the probability density function that a photon scattered k times will arrive at x along the direction Ω. Therefore, the operator T transforms the probability distribution of photons between successive orders of scattering and evaluates their recollision probability [66]. Note that the factor ω_0 is separated from $e_k(x, \Omega)$ so that the normalized radiation fields are indeed wavelength-independent.

Based on the above definitions we can re-write the solution of the black-soil problem as:

$$I_\lambda(x, \Omega) = \| Q_0 \| \left(\sum_{k=0}^{\infty} T^k \right) \frac{Q_0}{\| Q_0 \|} = i_0 \sum_{k=0}^{\infty} \theta_k^k \omega_0^k e_k(x, \Omega) \tag{28}$$

where $i_0 = \| Q_0 \|, \theta_k = \sqrt{p_0 p_1 p_2 \cdots p_k k}$, and $p_0 = 1$. Note that i_0, θ_k, and $e_k(x, \Omega)$ are all wavelength independent.

In Equation (28) if the θ_k's and the e_k's change little (i.e., invariant) over the order of scattering, the equation can be significantly simplified. Fortunately, this is exactly what the spectral invariants theory suggests: Based on a fundamental property established for the eigenvalues/eigenvectors of the linear RTE operator T [68], the theory indicates that the RTE has a unique dominant eigenvalue γ^* (or $p^* \omega_0$) that corresponds to a positive (and physically feasible) eigenvector $e^*(x, \Omega)$, such that

$$p^* \omega_0 e^*(x, \Omega) = T e^*(x, \Omega). \tag{29}$$

Therefore, if $e_0 = e^*(x, \Omega)$, we will subsequently have $e_k = e^*(x, \Omega)$ and $\theta_k = p^*$, so that

$$I_\lambda = \frac{i_0 e^*(x, \Omega)}{1 - \gamma^*} = \frac{i_0 e^*(x, \Omega)}{1 - p^* \omega_0(\lambda)}. \tag{30}$$

Although the set ($p_k \omega_0$, e_k) derived by the SOSA method are generally different from the ideal eigenvalue-eigenvector pair ($p^* \omega_0$, e^*), analyses show that they converge rapidly so that we only

need a couple of (p_k, e_k) pairs to accurately represent the full solution of Equation (28). For instance, Reference [66] uses a zero-order approximation to satisfactorily estimate the recollision probability p^* and the initial interceptance i_0 from field measured $i(\lambda)$ and $\omega_0(\lambda)$. A detailed analysis of the SOSA approximation can be found in Reference [66] and earlier studies [69–72]. Consistent results are also supported by simulations from Monte Carlo Ray Tracing (MCRT) models [73–75]. The key message is that once we have estimated a few parameters and functions (p_k, e_k, and i_0), the solution $I_\lambda(x, \Omega)$ can be easily obtained with the knowledge of ω_0 at any other wavelength (Figure 1).

The interpretation of the parameter p^* as the recollision probability of photons by Reference [76] represents an important contribution to the spectral invariants theory. It helps us develop a physical intuition to the mathematical concept of the leading eigenvalue of the RTE and associate it with measurable structural properties of vegetation canopies. Once established, the interpretation sees immediate applications in scaling relevant canopy properties across different canopy hierarchies [32,74,76]. For instance, suppose p^*_{sh} and p^*_{cr} are the recollision probabilities of shoots and crowns, the overall p^* parameter for the two-level canopy, resulting from a finite-state Markov process [67], naturally follows

$$p^* = p^*_{sh} + (1 - p^*_{sh})p^*_{cr}. \tag{31}$$

Similarly, the apparent single scattering albedos of two levels of canopy structures (e.g., shoots and crowns) are related by

$$\omega_{cr} = \frac{\omega_{sh}(1 - p^*_{sh})}{1 - p^*_{sh}\omega_{sh}}. \tag{32}$$

It can be easily verified that the canopy scattering albedo W can be represented by either ω_{cr} or ω_{sh} [76]:

$$W = \frac{\omega_{cr}(1 - p^*_{cr})}{1 - p^*_{cr}\omega_{cr}} = \frac{\omega_{sh}(1 - p^*)}{1 - p^*\omega_{sh}}. \tag{33}$$

Therefore, the single albedo of a higher level structure (e.g., ω_{cr}) totally encapsulates the scattering properties of the lower level structures (e.g., ω_{sh}). The overall scattering coefficients of the crown (or the canopy) will not change if we replace the shoots (needles) with broadleaves of the same (apparent) single albedo. This property suggests that we can use the same set of simulation results (i.e., Look-Up Tables) to retrieve effective structural parameters for both clumped and non-clumped canopies. Additionally, the scaling rules of the recollision coefficients and the scattering coefficients are often associated with changes in spatial scales. They can be used to generate consistent products from satellite sensors operating at different spatial resolutions [77,78]. A detailed review of the physical interpretation of the p^* parameter, its links with measurements, and the scaling rules can be found in a recent review by Reference [45].

In practice, the recollision probability (p^*) of a vegetation canopy can be estimated from field measurements of canopy reflectance, absorptance, transmittance, and single-scattering albedo [66,72]. In remote sensing applications, the common measurements of the surface after atmospheric corrections are the bidirectional reflectance factor (BRF). Therefore, it is desirable to derive a relationship between BRFs and the spectral invariant parameters. Note that under the assumption that the irradiance of the incoming solar radiation is unity, the BRF is just the averaged top-of-canopy radiance (Equation (28) or Equation (30) for the ideal case) multiplied by a constant factor (π). The desired relationship is thus [52]

$$\mathrm{BRF}_\lambda(\Omega; \Omega_0) = \frac{\pi p_A \langle e(x_B, \Omega)\rangle_{x_B} i_0}{1 - p_A} \cdot \frac{\omega_0(\lambda)(1 - p_A)}{1 - \omega_0(\lambda)p_A}, \tag{34}$$

where $\langle\cdot\rangle_{x_B}$ denotes spatial average over the canopy boundary x_B, and p_A denotes the effective recollision probability. In Equation (34) we have neglected the un-collided component of the radiance, as it does not contribute to the reflectance.

In Equation (34) the first term on the right side combines the recollision probability (p_A), the interceptance (i_0), and canopy escape probability ($q_A = \pi p_A \langle e(x_B, \Omega) \rangle_{x_B}$), all being spectral invariant. We define this term the Directional Area Scattering Factor (DASF) [52,79],

$$\mathrm{DASF}(\Omega; \Omega_0) = \frac{q_A(\Omega; \Omega_0) i_0(\Omega_0)}{1 - p_A}, \tag{35}$$

which can be understood as the BRF for a purely reflective canopy (e.g., $\omega_0 = 1$). The second term on the right side of Equation (34) is just the canopy scattering coefficient W in Equation (33). Therefore, BRF is succinctly represented by the product of DASF and the canopy single scattering albedo W.

An important feature of DASF is that it is measurable from both field observations and satellite remote sensing data. When $\omega_0(\lambda)$ is known, DASF can be easily estimated from ground measurements of spectral BRF using the inverse linear regression method [66]. In remote sensing applications where $\omega_0(\lambda)$ is difficult to obtain, Reference [49] developed an algorithm to retrieve DASF from BRF between 710 nm and 790 mm with an intrinsic leaf scattering spectrum $\varpi_0(\lambda)$, where $\varpi_0(\lambda)$ is computed with theoretical models. A key component of the algorithm is to use the scaling rule of Equation (33) to estimate $\omega_0(\lambda)$ from $\varpi_0(\lambda)$ with a within-leaf recollision probability p_L, an intermediate variable that is later cancelled from the calculation. The algorithm is recently used in Reference [80] to derive a global DASF map from the GOME-2 (Global Ozone Monitoring Experiment-2) data.

Of the above spectral invariant parameters, only p^* is an intrinsic property of the canopy while the others (i_0, p_A, q_A and DASF) are influenced by the external illumination conditions. The values of these parameters generally change with the direction of the incident beam (Ω_0). Indeed, the directional illumination has an important effect on the angular signature of canopy BRF (and DASF), which we review in the next section.

6. The "Hot-Spot" Problem

In optical remote sensing, the term "hot spot" refers to the phenomenon that the canopy reflectance has a sharp peak in the retro-illumination direction. The main physical mechanism of the phenomenon is the mutual shadowing of the canopy elements. This is because shadows are invisible from the backscattering direction but become increasingly visible when the view and the illumination angles deviate away from each other [33,36].

It is known that the classic RTE has difficulties simulating the hot-spot effects. This is because the stream-collision operator, which follows the Beer's law, is essentially formulated for gaseous media where the spatial distribution of the scatters is statistically independent at all spatial scales [34]. On the contrary, leaves have finite sizes and their spatial distributions are intrinsically correlated at a certain level. To illustrate the difference between the two cases, we consider a conceptual experiment that a purely absorptive ($\omega_0 = 0$) canopy bounded below by a perfect mirror ($\rho_\lambda = 1$) that is positioned to reflect the nadir incident photons back along the same paths they come from (i.e., the retro-illumination direction). Let the optical depth of the canopy be σ and the intensity of the radiation beam be 1. Under the gaseous media assumption, the intensity of the reflected radiation beam at the top of the canopy will be $\exp(-2\sigma)$, attenuated by the same fashion on the incident and the return paths. For finite-sized leaves, the intensity of the reflected radiation will be $\exp(-\sigma)$, for all the photons that reach the lower surface (i.e., mirror) are guaranteed a free path to travel through the canopy on the way back.

The above example suggests that, due to the effects of mutual shadowing, the canopy extinction cross section in the backscattering direction $\sigma(x, -\Omega_0)$ appears to be smaller than those of other directions. Therefore, previous efforts to model the hot-spot phenomenon focused on developing a function $H(x, \Omega, \Omega_0)$ to regulate the cross section $\sigma(x, \Omega)$, especially for the first collision component [33,81–83]. However, the incorporation of $H(x, \Omega, \Omega_0)$ in the RTE is equivalent to the introduction of an additional source term in the equation. As a result, the solution no longer satisfies the law of energy conservation [35].

Recently, Reference [79] developed a new algorithm that uses the spectral invariant theory to model the spectral BRF of vegetation canopies in the hot-spot region. A key idea of the algorithm is to decompose the canopy into sun-lit and sun-shaded leaf area, where the former is referred to as the "stochastic reflecting boundary" and the latter as the "interior" of the canopy. Photons escaping from the sun-shaded leaf area must have gone through multiple scattering. Thus, their escape probability approximately converges to a certain value, $q_{iso}(\Omega)$. Photons reflected from the sun-lit leaf area that is visible from the direction Ω can escape with a unit probability. Thus, their conditional escape probability, $q_{lit}(\Omega;\Omega_0)$, is expected to be higher than $q_{iso}(\Omega)$. Therefore, we need to evaluate their contribution to the canopy directional escape probability $q_A(\Omega;\Omega_0)$ separately. Let $h(\Omega_0,\Omega)$ represent the correlation between the sun-lit and the visible leaf areas. The probability $q_A(\Omega;\Omega_0)$ is therefore composed of two components that is weighted by $h(\Omega_0,\Omega)$ as

$$q_A(\Omega;\Omega_0) = [1 - h(\Omega_0;\Omega)]q_{iso}(\Omega) + h(\Omega_0;\Omega)q_{lit}(\Omega_0;\Omega). \tag{36}$$

Similarly, we can decompose DASF and BRF by contributions from the interior leaves and the stochastic boundary separately [79].

In the above equation $q_{lit}(\Omega_0;\Omega)$ can be evaluated from canopy structural properties and q_{iso} can be estimated with the classic RTE [79]. Therefore, if the correlation function h is known, we can estimate q_A. Conversely, if q_A is known, we can estimate the correlation function h as [79]

$$h(\Omega;\Omega_0) = \frac{q_A(\Omega;\Omega_0) - q_{iso}(\Omega)}{q_{lit}(\Omega;\Omega_0) - q_{iso}(\Omega)}. \tag{37}$$

The current algorithm of Reference [79] uses the latter approach to evaluate correlation coefficient $h(\Omega_0;\Omega)$ with a stochastic RTE (Section 3) that is modified to incorporate an additional hot-spot parameter c_{HS} [36]. The stochastic RTE needs to run twice, with an actual c_{HS} and with a zero value, respectively, in order to evaluate $q_A(\Omega;\Omega_0)$ and $q_{iso}(\Omega)$ [79].

The algorithm of Reference [79] has two main benefits. First, some of the intermediate results are easy to verify with field measurements. For instance, the visible fraction of leaf area (VFLA) can be estimated with below canopy measurements of transmittance $t_0(\Omega)$ as [79]

$$VFLA(\Omega) = \frac{1 - t_0(\Omega)}{|\ln(t_0(\Omega))|} = \frac{i_0(\Omega)}{|\ln(t_0(\Omega))|}, \tag{38}$$

and the canopy DASF under isotropic illumination conditions (an approximation for the interior canopy component) can be estimated as [79]

$$\frac{q_{iso}(\Omega)i_0(\Omega_0)}{1 - p_{iso}} \approx \frac{i_0(\Omega)i_0(\Omega_0)}{2{\cdot}i_{dif}}, \tag{39}$$

where i_{dif} is the canopy interceptance under the isotropic sky radiation [84]. These relationships provide a set of convenient tools to validate the solutions.

Second and more importantly, the spectral invariants relationships do not necessarily depend on the formulation of the classic RTE but are supported by both observations and the simulation results of MCRT models, whose formulation does not require Beer's law at all [85]. Therefore, the spectral invariants relationships may conserve energy and capture the hot-spot phenomenon at the same time. Reference [79] illustrates this potential with a simple stochastic Monte Carlo model. Though the algorithm is still subjected to further examinations and refinements in the future, it introduces a new and promising perspective to address the old challenge.

7. Summary

This paper reviews developments of the radiative transfer theory in optical remote sensing of terrestrial vegetation, including the decomposition of the black-soil (BS) and the soil (S) problems, the development of the stochastic RTE, the theory of spectral invariants, and the latest effort to address the "hot-spot" challenge. The first three topics are centered around the idea as how to simplify the solutions of the RTE under different boundary conditions (e.g., soil reflective properties), over full 3-dimensional spatial domains, and with regard to radiation at different wavelengths. The last topic is intended to highlight the advantage of the spectral invariants theory in remote sensing applications.

As the RTE is linear as regard to I_λ, a fundamental strategy to solve the equation is decomposition and superposition. The separation of the black-soil and the soil problems, the expansion of Neumann's series, and the method of successive orders of scattering approximation discussed in Section 3 are all demonstrations of this strategy. The concept of invariants, the convergence of the radiation field to a certain distribution that does not change (except for the magnitude) over subsequent scattering, is also a natural result that follows the line of thinking. The existence of such a unique intrinsic solution is backed by the mathematical theories of eigenvalues/eigenvectors of the RTE and the physical law of energy conservation.

Another important thread of developments in the Stochastic RTE and the spectral invariants theory is to efficiently represent the canopy structural or geometrical information in the equation. The stochastic RTE introduces a pair-correlation function $K(z,\ z', \Omega)$, which describes the probability of simultaneously finding leaves at two locations $(z,\ z')$ along the direction Ω. It characterizes the heterogeneity and anisotropy characteristics of the canopies and regulate the corresponding cross sections (σ and σ_s). Therefore, the function provides a natural and physically meaningful measure of 3D canopy structural properties over a range of scales.

The spectral invariants theory further simplifies the representation of canopy structural characteristics to a single wavelength-independent parameter p^*, which defines the recollision probability that a scattered photon will interact with the canopy again. Once p^* (and the corresponding escape probability function) is estimated, we can accurately approximate the solution (radiance or BRF) of the RTE at any other wavelength with the knowledge of $\omega_0(\lambda)$, which imbues the wavelength-dependent influence on the radiation field. As p^* represents recollision probability, it can be used to scale canopy properties (e.g., scattering coefficients) across various canopy hierarchies or spatial scales.

Although the pair-correlation function $K(z,\ z', \Omega)$, the photon recollision probability p^*, and the other spectral invariants functions/parameters such as DASF appear to be "abstract," they all can be estimated from field measurements or remote sensing data. For instance, the pair-correlation function can be derived from high-resolution satellite images and lidar data. The recollision probability of a vegetation canopy can be determined from field measurements of canopy reflectance, absorptance, transmittance, and single-scattering albedo with simple linear correlations. DASF can also be retrieved directly from ground measurements or hyperspectral remote sensing data between 710 nm and 790 mm for dense vegetation in a similar fashion. These concepts, backed by rigorous mathematical analysis and physical principles, thus represent our current best understanding of the empirical relationships identified from observations.

The spectral invariants theory also provides a promising approach to solve the "hot-spot" problem known to the classic RTE models. This challenge has its roots in the formulation of the equation based on the turbid medium assumption and Beer's law. On the contrary, leaves are finite sized and their spatial correlations cannot be neglected. Previous efforts to address this problem usually introduce a semi-empirical factor to regulate the extinction cross section in the equation, which however violate the law of energy conservation. A new algorithm was recently developed to address the challenge based on the spectral invariants theory. The algorithm decomposes the canopy into a reflective boundary and interior points and models the escape probability (and DASF) for the two components separately. The directional escape probability from the reflective boundary is assumed to be unity, a feature that

cannot be simulated by the classic RTE. As such, the new approach does not depend on the Beer's law formulation in the RTE but satisfies the law of energy conservation. This example further demonstrates the spectral invariants theory as a powerful tool in optical remote sensing applications.

Funding: W.W., R.N., H.H., and S.G. are supported by the National Aeronautics and Space Administration (NASA) under grants to NASA Earth Exchange (NEX). Y.K. is supported by NASA under grant NNX15AR03G.

Acknowledgments: The authors are grateful to four anonymous reviewers, whose constructive comments have helped significantly improve the quality of the paper. We are also thankful to Yujie Wang of NASA Goddard Space Flight Center and Bin Yang of Hunan University, China for insightful discussions on the spectral invariants theory.

Conflicts of Interest: The authors declare no conflict of interest.

Nomenclature

$\gamma_L(\lambda, x, \Omega \to \Omega\prime, \Omega_L)$	Leaf element scattering phase function
θ_k	Geometric mean of photon recollision probabilities, i.e., $\sqrt{p_0 p_1 \cdots p_k k}$
λ	Wavelength
μ	Cosine of zenith angle of direction Ω
$\sigma(x, \Omega)$	Total extinction coefficient (or cross section)
$\sigma_S(\lambda, x, \Omega \to \Omega\prime)$	Differential scattering coefficient (or cross section)
$\omega_0(\lambda)$	Single scattering albedo
Ω_L	Leaf normal direction vector
Ω, $\Omega\prime$	Incident and scattered radiation direction vectors, respectively
$g_L(x, \Omega_L)$	Leaf normal distribution function
$i_0(\Omega_0)$	Canopy interceptance
p^*, p_A	Theoretical and effective photon recollision probability, respectively
$q(\Omega; \Omega_0)$	Photon escape probability density function
$u_L(x)$	Leaf area density distribution function
BRF	Bidirectional reflectance factor
DASF	Directional area scattering factor
E	Identity operator
$I_\lambda(x, \Omega)$	Monochromatic radiation intensity (radiance)
$K(z, z', \Omega)$	Conditional pair correlation functions of finding leaf elements at locations z and z' along Ω simultaniously
L	Streaming-collision operator
Q_k	The k-th collided component of radiation field
S_λ	Scattering operator
T	Integral operator defined as $L_0^{-1} S_\lambda$
$U(z, \Omega)$	Horizontal mean radiation intensity averaged over vegetated area
$\langle \cdot \rangle$	Horizontal average operator
$\| \cdot \|$, $\| \cdot \|_\rho$	Integral norm operator that indicates the intercepted and the escaped radiation energy, respectively.

Appendix

Appendix A.1 Definitions of the Canopy Structural Parameters

The leaf albedo is mathematically defined as

$$\omega_L(\lambda, x, \Omega, \Omega_L) = \int_{4\pi} \gamma_L(\lambda, x, \Omega \to \Omega\prime, \Omega_L) d\Omega \tag{A1}$$

the total extinction coefficient (or cross-section) is

$$\sigma(x, \Omega) = \frac{u_L(x)}{2\pi} \int_{2\pi+} g_L(x, \Omega_L) |\Omega \cdot \Omega_L| d\Omega_L \tag{A2}$$

and the differential scattering cross-section is

$$\sigma_S(\lambda, x, \Omega \to \Omega\prime) = \frac{u_L(x)}{2\pi} \int\limits_{2\pi+} g_L(x, \Omega_L)|\Omega{\cdot}\Omega_L|\gamma_L(\lambda, x, \Omega \to \Omega\prime, \Omega_L)d\Omega_L \tag{A3}$$

As photons scattered from one direction provide sources for radiation in other directions, the two cross-section terms are closely related by

$$\int\limits_{4\pi} \sigma_S(\lambda, x, \Omega \to \Omega\prime)d\Omega\prime = \omega_0(\lambda, x, \Omega)\sigma(x, \Omega) \tag{A4}$$

where $\omega_0(\lambda, x, \Omega)$ is the single scattering albedo, which is usually defined as an average to the leaf albedo

$$\omega_0(\lambda, x, \Omega) = \frac{\int_{2\pi+} g_L(x, \Omega_L)|\Omega{\cdot}\Omega_L|\omega_L(\lambda, x, \Omega, \Omega_L)d\Omega_L}{\int_{2\pi+} g_L(x, \Omega_L)|\Omega{\cdot}\Omega_L|d\Omega_L} \tag{A5}$$

For simplicity, in the paper we further made the following assumptions

$$\begin{array}{c} \omega_0(\lambda, x, \Omega) = \omega_0(\lambda), \\ \sigma(x, \Omega) = u_L(x)\sigma(\Omega), \\ \sigma_S(\lambda, x, \Omega \to \Omega\prime) = \omega_0(\lambda)u_L(x)\sigma_S(\Omega \to \Omega\prime). \end{array} \tag{A6}$$

Note that ω_0 is only a variable of spectral wavelength while $\sigma(\Omega)$ and $\sigma_S(\Omega \to \Omega\prime)$ are spatially and spectrally independent.

Appendix A.2 Derivation of Equation (23)

Integrating the first-collision problem over the spatial domain and the solid angles leads to

$$\int\limits_{4\pi\times V} L_0 Q_1 \mathrm{d}\Omega\mathrm{d}x = \int\limits_{4\pi\times V} SQ_0 \mathrm{d}\Omega\mathrm{d}x \tag{A7}$$

By Stokes' Theorem,

$$\int\limits_{4\pi\times V} \Omega{\cdot}\nabla Q_1 \mathrm{d}\Omega\mathrm{d}x = \int\limits_{\delta V} \mathrm{d}x_B \int\limits_{4\pi} Q_1|\Omega{\cdot}\mathrm{n}(x_B)|\mathrm{d}\Omega \tag{A8}$$

where δV represents the boundary of the domain. As the incoming radiation (i.e., $\Omega{\cdot}\mathrm{n}(x_B) < 0$) in the standard problem is zero, Equation (A7) thus becomes

$$\int\limits_{\delta V} \mathrm{d}x_B \int\limits_{\Omega{\cdot}\mathrm{n}(x_B)>0} Q_1|\Omega{\cdot}\mathrm{n}(x_B)|\mathrm{d}\Omega + \int\limits_{4\pi\times V} \sigma Q_1 \mathrm{d}\Omega\mathrm{d}x = \int\limits_{4\pi\times V} SQ_0 \mathrm{d}\Omega\mathrm{d}x \tag{A9}$$

By the definition of the scattering operator (Equation (2)), we have

$$\begin{array}{l} \int\limits_{4\pi\times V} SQ_0 \mathrm{d}\Omega\mathrm{d}x = \int\limits_{4\pi\times V} \int\limits_{4\pi} \omega_0(\lambda)\sigma_S(x, \Omega\prime \to \Omega)Q_0(x, \Omega\prime)d\Omega\prime\, \mathrm{d}\Omega\mathrm{d}x \\ = \int\limits_{4\pi\times V} \int\limits_{4\pi} \omega_0(\lambda)\sigma_S(x, \Omega\prime \to \Omega)Q_0(x, \Omega\prime)\mathrm{d}\Omega\, \mathrm{d}\Omega\prime\, \mathrm{d}x \\ = \omega_0(\lambda) \int\limits_{4\pi\times V} \sigma Q_0\, \mathrm{d}\Omega\prime\, \mathrm{d}x \end{array} \tag{A10}$$

In the last step of Equation (A10) we used the relationship from Equation (A4). As the integration is performed over all solid angles (i.e., 4π), we can safely exchange $\Omega\prime$ with Ω and thus obtain Equation (23) in the main text.

Appendix A.3 Energy Conservation between p_A and q_A

Integrating the effective directional escape probability density function over all the out-scattering directions Ω, we have

$$\frac{1}{\pi}\int_{4\pi} q_A(\Omega;\Omega_0)|\mu|\mathrm{d}\Omega = (1-p_A)\sum_{k=1}^{\infty}\left(\frac{1}{\pi}\int_{4\pi} q_k(\Omega;\Omega_0)|\mu|\mathrm{d}\Omega\right)\theta_{k-1}^{k-1} \tag{A11}$$

By Equations (25) and (35),

$$\frac{1}{\pi}\int_{4\pi} q_k(\Omega;\Omega_0)|\mu|\mathrm{d}\Omega = q_k = 1-p_k \tag{A12}$$

where q_k on the right-hand-side of the equation is the k-th escape probability. Substituting it into Equation (A11), we have

$$\begin{aligned}&\tfrac{1}{\pi}\textstyle\int_{4\pi} q_A(\Omega;\Omega_0)|\mu|\mathrm{d}\Omega = (1-p_A)\sum_{k=1}^{\infty}(1-p_k)\theta_{k-1}^{k-1}\\ &= (1-p_A)\textstyle\sum_{k=1}^{\infty}\left(\theta_{k-1}^{k-1}-\theta_k^k\right)\\ &= 1-p_A\end{aligned} \tag{A13}$$

In the last step of Equation (A13) we used the fact that $\theta_0 = p_0 = 1$ (Equation (28)).

References

1. National Research Council (NRC). *Earth Observations from Space: The First 50 Years of Scientific Achievements*; The National Academies Press: Washington, DC, USA, 2008; p. 142.
2. Roy, D.P.; Wulder, M.A.; Loveland, T.R.; Woodcock, C.E.; Allen, R.G.; Anderson, M.C.; Helder, D.; Irons, J.R.; Johnson, D.M.; Kennedy, R.; et al. Landsat-8: Science and product vision for terrestrial global change research. *Remote Sens. Environ.* **2014**, *145*, 154–172. [CrossRef]
3. Loveland, T.R.; Irons, J.R. Landsat 8: The plans, the reality, and the legacy. *Remote Sens. Environ.* **2016**, *185*, 1–6. [CrossRef]
4. Drusch, M.; Del Bello, U.; Carlier, S.; Colin, O.; Fernandez, V.; Gascon, F.; Hoersch, B.; Isola, C.; Laberinti, P.; Martimort, P.; et al. Sentinel-2: ESA's optical high-resolution mission for GMES operational services. *Remote Sens. Environ.* **2012**, *120*, 25–36. [CrossRef]
5. Goldberg, M.D.; Kilcoyne, H.; Cikanek, H.; Mehta, A. Joint Polar Satellite System: The United States next generation civilian polar-orbiting environmental satellite system. *J. Geophys. Res. Atmos.* **2013**, *118*, 13463–13475. [CrossRef]
6. Bessho, K.; Date, K.; Hayashi, M.; Ikeda, A.; Imai, T.; Inoue, H.; Kumagai, Y.; Miyakawa, T.; Murata, H.; Ohno, T.; et al. An Introduction to Himawari-8/9—Japan's New-Generation Geostationary Meteorological Satellites. *J. Meteorol. Soc. Jpn.* **2016**, *94*, 151–183. [CrossRef]
7. Schmit, T.J.; Griffith, P.; Gunshor, M.M.; Daniels, J.M.; Goodman, S.J.; Lebair, W.J. *A Closer Look at the ABI on the GOES-R Series*; BAMS: Boston, MA, USA, 2017.
8. Kalluri, S.; Alcala, C.; Carr, J.; Griffith, P.; Lebair, W.; Lindsey, D.; Race, R.; Wu, X.; Zierk, S. From Photons to Pixels: Processing data from the Advanced Baseline Imager. *Remote Sens.* **2018**, *10*, 177. [CrossRef]
9. Yang, J.; Zhang, Z.; Wei, C.; Lu, F.; Guo, Q. *Introducing the New Generation of Chinese Geostationary Weather Satellites, Fengyun-4*; BAMS: Boston, MA, USA, 2017.
10. Starvros, E.N.; Schimel, D.; Pavlick, R.; Serbin, S.; Swann, A.; Duncanson, L.; Fisher, J.B.; Fassnacht, F.; Ustin, S.; Dubayah, R.; et al. ISS observations offer insights into plant function. *Nat. Ecol. Evol.* **2017**, *1*, 0194. [CrossRef] [PubMed]
11. Myneni, R.B.; Maggion, S.; Iaquinta, J.; Privette, J.L.; Gobron, N.; Pinty, B.; Kimes, D.S.; Verstraete, M.M.; Williams, D.L. Optical remote sensing of vegetation: Modeling, caveats, and algorithms. *Remote Sens. Environ.* **1995**, *51*, 169–188. [CrossRef]
12. Rodgers, C.D. *Inverse Methods for Atmospheric Sounding: Theory and Practice*; World Scientific Publishing Co. Pte. Ltd.: Singapore, 2000; p. 238.
13. Combal, B.; Baret, F.; Weiss, M.; Trubuil, A.; Macé, D.; Pragnére, A. Retrieval of canopy biophysical variables from bidirectional reflectance using prior information to solve the ill-posed inverse problem. *Remote Sens. Environ.* **2002**, *84*, 1–15. [CrossRef]
14. Baret, F.; Buis, S. Estimating Canopy Characteristics from Remote Sensing Observations: Review of Methods and Associated Problems. In *Advances in Land Remote Sensing*; Liang, S., Ed.; Springer: Dordrecht, The Netherlands, 2008.

15. Lauvernet, C.; Baret, F.; Hascoët, L.; Buis, S.; Le Dimet, F.-X. Multitemporal-patch ensemble inversion of coupled surface–atmosphere radiative transfer models for land surface characterization. *Remote Sens. Environ.* **2008**, *112*, 851–861. [CrossRef]
16. Dorigo, W.; Richter, R.; Baret, F.; Bamler, R.; Wagner, W. Enhanced automated canopy characterization from hyperspectral data by a novel two step radiative transfer model inversion approach. *Remote Sens.* **2009**, *1*, 1139–1170. [CrossRef]
17. Atzberger, C.; Richter, K. Spatially constrained inversion of radiative transfer models for improved LAI mapping from future Sentinel-2 imagery. *Remote Sens. Environ.* **2012**, *120*, 208–218. [CrossRef]
18. Kuusk, A. Canopy radiative transfer modeling. In *Comprehensive Remote Sensing: Remote Sensing of Terrestrial Ecosystem*; Liang, S., Ed.; Elsevier: Amsterdam, The Netherlands, 2018; Volume 3.
19. Shore, S.N. Blue sky and hot piles: The evolution of radiative transfer theory from atmosphere to nuclear reactors. *Hist. Math.* **2002**, *29*, 463–489. [CrossRef]
20. Ross, J.; Nilson, T. Concerning the theory of plant cover radiation regime. In *Investigations on Atmospheric Physics*; Inst. Phys. Astron. Acad. Sci. ESSR: Tartu, Estonia, 1963; pp. 42–64. (In Russian)
21. Ross, J.; Nilson, T. Radiation exchange in plant canopies. In *Heat and Mass Transfer in the Biosphere*; de Vries, D.A., Afgan, H.H., Eds.; Scripta: Washington, DC, USA, 1975; pp. 327–336.
22. Ross, J. *The Radiation Regime and Architecture of Plant Stands*; Dr. W. Junk: Norwell, MA, USA, 1981; p. 391.
23. Govaerts, Y.; Verstraete, M. Raytran: A Monte Carlo ray-tracing model to compute light scattering in three-dimensional heterogeneous media. *IEEE Trans. Geosci. Remote Sens.* **1998**, *36*, 493–505. [CrossRef]
24. Gastellu-Etchegorry, J.; Demarez, V.; Pinel, V.; Zagolski, F. Modeling radiative transfer in heterogeneous 3-D vegetation canopies. *Remote Sens. Environ.* **1996**, *58*, 131–156. [CrossRef]
25. Gastellu-Etchegorry, J.; Yin, T.; Lauret, N.; Cajgfinger, T.; Gregoire, T.; Grau, E.; Feret, J.-B.; Lopes, M.; Guilleux, J.; Dedieu, G.; et al. Discrete anisotropic radiative transfer (DART 5) for modeling airborne and satellite spectroradiometer and LIDAR acquisitions of natural and urban landscapes. *Remote Sens.* **2015**, *7*, 1667–1701. [CrossRef]
26. Verhoef, W. Light scattering by leaf layers with application to canopy reflectance modeling: The SAIL model. *Remote Sens. Environ.* **1984**, *16*, 125–141. [CrossRef]
27. Verhoef, W.; Bach, H. Simulation of hyperspectral and directional radiance images using coupled biophysical and atmospheric radiative transfer models. *Remote Sens. Environ.* **2003**, *87*, 23–41. [CrossRef]
28. Verhoef, W.; Bach, H. Coupled soil–leaf-canopy and atmosphere radiative transfer modeling to simulate hyperspectral multi-angular surface reflectance and TOA radiance data. *Remote Sens. Environ.* **2007**, *109*, 166–182. [CrossRef]
29. Jacquemoud, S.; Baret, F. PROSPECT: A model of leaf optical properties spectra. *Remote Sens. Environ.* **1990**, *34*, 75–91. [CrossRef]
30. Li, X.; Strahler, A.; Woodcock, C. A hybrid geometric optical-radiative transfer approach for modeling albedo and directional reflectance of discontinuous canopies. *IEEE Trans. Geosci. Remote Sens.* **1995**, *33*, 466–480.
31. Ni, W.; Li, X.; Woodcock, C.; Caetano, M.; Strahler, A. An analytical hybrid GORT model for bidirectional reflectance over discontinuous plant canopies. *IEEE Trans. Geosci. Remote Sens.* **1999**, *37*, 987–999.
32. Rautiainen, M.; Stenberg, P. Application of photon recollision probability in coniferous canopy reflectance model. *Remote Sens. Environ.* **2005**, *96*, 98–107. [CrossRef]
33. Kuusk, A. The hot spot effect of a uniform vegetative cover. *Sov. J. Remote Sens.* **1985**, *3*, 645–658.
34. Knyazikhin, Y.; Kranigk, J.; Myneni, R.B.; Panfyorov, O.; Gravenhorst, G. Influence of a small-scale structure on radiative transfer and photosynthesis in vegetation canopies. *J. Geophys. Res.* **1998**, *103*, 6133–6144. [CrossRef]
35. Knyazikhin, Y.; Martonchik, J.V.; Myneni, R.B.; Diner, D.J.; Running, S.W. Synergistic algorithm for estimating vegetation canopy leaf area index and fraction of absorbed photosynthetically active radiation from MODIS and MISR data. *J. Geophys. Res.* **1998**, *103*, 32257–32274. [CrossRef]
36. Kuusk, A. The hot spot effect in plant canopy reflectance. In *Photon-Vegetation Interactions: Applications in Optical Remote Sensing and Plant Ecology*; Myneni, R.B., Ross, J., Eds.; Springer: Berlin, Germany, 1991; pp. 139–159.
37. Knyazikhin, Y.; Marshak, A.; Myneni, R.B. Three-dimensional radiative transfer in vegetation canopies and cloud–vegetation interaction. In *Three-Dimensional Radiative Transfer in the Cloudy Atmosphere*; Marshak, A., Davis, A.B., Eds.; Springer: Berlin, Germany, 2005; pp. 617–652.

38. Bergen, K.M.; Goetz, S.J.; Dubayah, R.O.; Henebry, G.M.; Hunsaker, C.T.; Imhoff, M.L.; Nelson, R.F.; Parker, G.G.; Radeloff, V.C. Remote sensing of vegetation 3-D structure for biodiversity and habitat: Review and implications for lidar and radar spaceborne missions. *J. Geophys. Res.* **2009**, *114*. [CrossRef]
39. Meroni, M.; Rossini, M.; Guanter, L.; Alonso, L.; Rascher, U.; Bolombo, R.; Moreno, J. Remote sensing of solar-induced chlorophyll fluorescence: Review of methods and applications. *Remote Sens. Environ.* **2009**, *113*, 2037–2051. [CrossRef]
40. Koch, B. Status and future of laser scanning, synthetic aperture radar and hyperspectral remote sensing data for forest biomass assessment. *ISPRS J. Photogramm. Remote Sens.* **2010**, *65*, 581–590. [CrossRef]
41. Hansen, M.; Loveland, T.R. A review of large area monitoring of land cover change using Landsat data. *Remote Sens. Environ.* **2012**, *122*, 66–74. [CrossRef]
42. Wulder, M.A.; White, J.C.; Nelson, R.F.; Næsset, E.; Ørka, H.O.; Coops, N.C.; Hilker, T.; Bater, C.W.; Gobakken, T. Lidar sampling for large-area forest characterization: A review. *Remote Sens. Environ.* **2012**, *121*, 196–209. [CrossRef]
43. Verrelst, J.; Camps-Valls, G.; Muñoz-Marí, J.; Rivera, J.P.; Veroustraete, F.; Clevers, J.G.P.W.; Moreno, J. Optical remote sensing and the retrieval of terrestrial vegetation bio-geophysical properties—A review. *ISPRS J. Photogramm. Remote Sens.* **2015**, *108*, 273–290. [CrossRef]
44. Schimel, D.; Pavlick, R.; Fisher, J.B.; Asner, G.P.; Saatchi, S.; Townsend, P.; Miller, C.; Frankenberg, C.; Hibbard, K.; Cox, P. Observing terrestrial ecosystems and the carbon cycle from space. *Glob. Chang. Biol.* **2015**, *21*, 1762–1776. [CrossRef] [PubMed]
45. Stenberg, P.; Mõttus, M.; Rautiainen, M. Photon recollision probability in modelling the radiation regime of canopies—A review. *Remote Sens. Environ.* **2016**, *183*, 98–108. [CrossRef]
46. Liang, S. (Ed.) *Comprehensive Remote Sensing*; Elsevier: Amsterdam, The Netherlands, 2018; p. 3134.
47. Evans, K.F.; Marshak, A. Numerical Methods. In *Three-Dimensional Radiative Transfer in the Cloudy Atmosphere*; Marshak, A., Davis, A.B., Eds.; Springer: Berlin, Germany, 2005; pp. 243–281.
48. Camps-Valls, G.; Bioucas-Dias, J.; Crawford, M. A special issue on advances in machine learning for remote sensing and geosciences (from the guest editors). *IEEE Geosci. Remote Sens. Mag.* **2016**, *4*, 5–7. [CrossRef]
49. Knyazikhin, Y.; Schull, M.A.; Stenberg, P.; Mõttus, M.; Rautiainen, M.; Yang, Y.; Marshak, A.; Carmona, P.L.; Kaufmann, R.K.; Lewis, P.; et al. Hyperspectral remote sensing of foliar nitrogen content. *PNAS* **2013**, *110*, E185–E192. [CrossRef] [PubMed]
50. Nilson, T.; Kuusk, A. A reflectance model for the homogeneous plant canopy and its inversion. *Remote Sens. Environ.* **1989**, *27*, 157–167. [CrossRef]
51. Tian, Y.; Wang, Y.; Zhang, Y.; Knyazikhin, Y.; Bogaert, J.; Myneni, R.B. Radiative transfer based scaling of LAI retrievals from reflectance data of different resolutions. *Remote Sens. Environ.* **2002**, *84*, 143–159. [CrossRef]
52. Knyazikhin, Y.; Schull, M.A.; Xu, L.; Myneni, R.B.; Samanta, A. Canopy spectral invariants. Part 1: A new concept in remote sensing. *J. Quant. Spectrosc. Radiat. Transf.* **2011**, *112*, 727–735. [CrossRef]
53. Davis, A.B.; Knyazikhin, Y. A primer in three-dimensional radiative transfer. In *Three-Dimensional Radiative Transfer in the Cloudy Atmosphere*; Marshak, A., Davis, A.B., Eds.; Springer: Berlin, Germany, 2005; pp. 153–242.
54. Myneni, R.B.; Asrar, G.; Kanemasu, E.T. Light scattering in plant canopies: The method of Successive Orders of Scattering Approximations [SOSA]. *Agric. For. Meteorol.* **1987**, *39*, 1–12. [CrossRef]
55. Shabanov, N.V.; Knyazikhin, Y.; Baret, F.; Myneni, R.B. Stochastic modeling of radiation regime in discontinuous vegetation canopies. *Remote Sens. Environ.* **2000**, *74*, 125–144. [CrossRef]
56. Huang, D.; Liu, Y. A novel approach for introducing cloud spatial structure into cloud radiative transfer parameterizations. *Environ. Res. Lett.* **2014**, *9*, 124022. [CrossRef]
57. Vainikko, G.M. The equation of mean radiance in broken cloudiness. *Trudy MGK SSR Meteorol. Investig.* **1973**, *21*, 28–37. (In Russian)
58. Huang, D.; Knyazikhin, Y.; Wang, W.; Deering, D.W.; Stenberg, P.; Shabanov, N.; Tan, B.; Myneni, R.B. Stochastic transport theory for investigating the three-dimensional canopy structure from space measurements. *Remote Sens. Environ.* **2008**, *112*, 35–50. [CrossRef]
59. Titov, G.A. Statistical description of radiation transfer in clouds. *J. Atmos. Sci.* **1990**, *47*, 24–38. [CrossRef]
60. Zuev, V.E.; Titov, G.A. *Atmospheric Optics and Climate*; The Series "Contemporary Problems of Atmospheric Optics"; Spector, Institute of Atmospheric Optics RAS: Tomsk, Russia, 1996; Volume 9. (In Russian)

61. Menzhulin, G.V.; Anisimov, O.A. Principles of Statistical Phytoactinometry. In *Photon-Vegetation Interactions: Applications in Optical Remote Sensing and Plant Ecology*; Myneni, R.B., Ross, J., Eds.; Springer: Berlin, Germany, 1991; pp. 111–138.
62. Shabanov, N.; Gastellu-Etchegorry, J.-P. The stochastic Beer–Lambert–Bouguer law for discontinuous vegetation canopies. *J. Quant. Spectrosc. Radiat. Transf.* **2018**, *214*, 18–32. [CrossRef]
63. Stoyan, D.; Kendall, S.W.; Mecke, J. *Stochastic Geometry and Its Applications*; John Wiley & Sons: New York, NY, USA, 1995.
64. Li, X.; Strahler, A. Geometrical–optical modelling of a conifer forest canopy. *IEEE Trans. Geosci. Remote Sens.* **1985**, *23*, 705–721. [CrossRef]
65. Li, X.; Strahler, A.H. Geometrical–optical bidirectional reflectance modelling of a conifer forest canopy. *IEEE Trans. Geosci. Remote Sens.* **1986**, *24*, 906–919. [CrossRef]
66. Huang, D.; Knyazikhin, Y.; Dickinson, R.E.; Rautiainen, M.; Stenberg, P.; Disney, M.; Lewis, P.; Cescatti, A.; Tian, Y.; Verhoef, W.; et al. Canopy spectral invariants for remote sensing and model applications. *Remote Sens. Environ.* **2007**, *106*, 106–122. [CrossRef]
67. Silván-Cárdenas, J.L.; Corona-Romero, N. Radiation budget of vegetation canopies with reflective surface: A generalization using the Markovian approach. *Remote Sens. Environ.* **2017**, *189*, 118–131. [CrossRef]
68. Vladimirov, V.S. *Mathematical Problems in the One-Velocity Theory of Particle Transport*; Tech. Rep. AECL-1661; At. Energy of Can. Ltd.: Chalk River, ON, Canada, 1963; 302p.
69. Panferov, O.; Knyazikhin, Y.; Myneni, R.B.; Szarzynski, J.; Engwald, S.; Schnitzler, K.G.; Gravenhorst, G. The role of canopy structure in the spectral variation of transmission and absorption of solar radiation in vegetation canopies. *IEEE Trans. Geosci. Remote Sens.* **2001**, *39*, 241–253. [CrossRef]
70. Zhang, Y.; Tian, Y.; Myneni, R.B.; Knyazikhin, Y.; Woodcock, C.E. Assessing the information content of multiangle satellite data for mapping biomes: I. Statistical analysis. *Remote Sens. Environ.* **2002**, *80*, 418–434. [CrossRef]
71. Zhang, Y.; Shabanov, N.; Knyazikhin, Y.; Myneni, R.B. Assessing the information content of multiangle satellite data for mapping biomes: II. Theories. *Remote Sens. Environ.* **2002**, *80*, 435–446. [CrossRef]
72. Wang, Y.; Buermann, W.; Stenberg, P.; Smolander, H.; Häme, T.; Tian, Y.; Hu, J.; Knyazikhin, Y.; Myneni, R.B. A new parameterization of canopy spectral response to incident solar radiation: Case study with hyperspectral data from pine dominant forest. *Remote Sens. Environ.* **2003**, *85*, 304–315. [CrossRef]
73. Disney, M.; Lewis, P.; Quaife, T.; Nichol, C. A spectral invariant approach to modeling canopy and leaf scattering. In Proceedings of the 9th International Symposium on Physical Measurements and Signatures in Remote Sensing (ISPMSRS), Beijing, China, 17–19 October 2005; pp. 318–320.
74. Lewis, P.; Disney, M. Spectral invariants and scattering across multiple scales from within-leaf to canopy. *Remote Sens. Environ.* **2007**, *109*, 196–206. [CrossRef]
75. Lewis, P.; Disney, M. On canopy spectral invariants and hyperspectral ray tracing. In Proceedings of the 2nd Workshop on Hyperspectral Image Processing: Evolution in Remote Sensing (WHISPERS), Reykjavik, Iceland, 14–16 June 2010; pp. 1–4. [CrossRef]
76. Smolander, S.; Stenberg, P. Simple parameterizations of the radiation budget of uniform broadleaved and coniferous canopies. *Remote Sens. Environ.* **2005**, *94*, 355–363. [CrossRef]
77. Ganguly, S.; Schull, M.; Samanta, A.; Shabanov, N.; Milesi, C.; Nemani, R.; Knyazikhin, Y.; Mynenia, R.B. Generating vegetation leaf area index earth system data record from multiple sensors. Part 1: Theory. *Remote Sens. Environ.* **2008**, *112*, 4333–4343. [CrossRef]
78. Ganguly, S.; Schull, M.; Samanta, A.; Shabanov, N.; Milesi, C.; Nemani, R.; Knyazikhin, Y.; Mynenia, R.B. Generating vegetation leaf area index Earth system data record from multiple sensors. Part 2: Implementation, analysis and validation. *Remote Sens. Environ.* **2008**, *112*, 4318–4332. [CrossRef]
79. Yang, B.; Knyazikhin, Y.; Mõttus, M.; Rautiainen, M.; Stenberg, P.; Yan, L.; Chen, C.; Yan, K.; Choi, S.; Park, T.; et al. Estimation of leaf area index and its sunlit portion from DSCOVR EPIC data: Theoretical basis. *Remote Sens. Environ.* **2017**, *198*, 69–84. [CrossRef] [PubMed]
80. Köhler, P.; Guanter, L.; Kobayashi, H.; Walther, S.; Yang, W. Assessing the potential of sun-induced fluorescence and the canopy scattering coefficient to track large-scale vegetation dynamics in Amazon forests. *Remote Sens. Environ.* **2018**, *204*, 769–785. [CrossRef]
81. Marshak, A. The effect of the hot spot on the transport equation in plant canopies. *J. Quant. Spectrosc. Radiat. Transf.* **1989**, *42*, 615–630. [CrossRef]

82. Verstraete, M.M.; Pinty, B.; Dickinson, R.E. A physical model of the bidirectional reflectance of vegetation canopies 1. Theory. *J. Geophys. Res.* **1990**, *95*, 11755–11765. [CrossRef]
83. Pinty, B.; Verstraete, M.M. Modeling the scattering of light by homogeneous vegetation in optical remote sensing. *J. Atmos. Sci.* **1998**, *55*, 137–150. [CrossRef]
84. Stenberg, P. Simple analytical formula for calculating average photon recollision probability in vegetation canopies. *Remote Sens. Environ.* **2007**, *109*, 221–224. [CrossRef]
85. Disney, M.I.; Lewis, P.; North, P.R.J. Monte Carlo ray tracing in optical canopy reflectance modelling. *Remote Sens. Rev.* **2000**, *18*, 163–196. [CrossRef]

Chapter 8

Inverse Problem of Leaf Area Estimation

Yang et al.

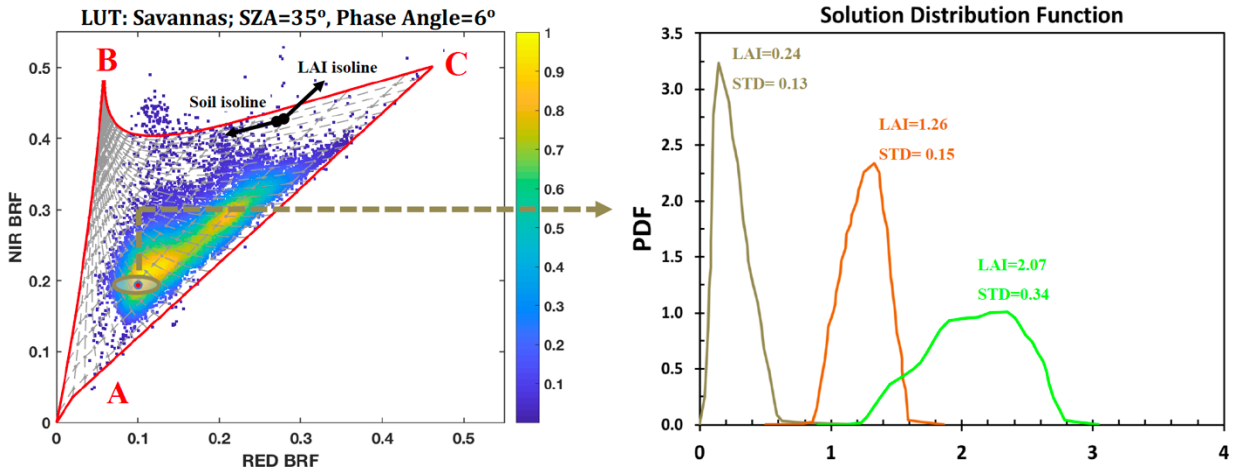

Remote Sensing of Environment 198 (2017) 69–84

Contents lists available at ScienceDirect

Remote Sensing of Environment

journal homepage: www.elsevier.com/locate/rse

Estimation of leaf area index and its sunlit portion from DSCOVR EPIC data: Theoretical basis

Bin Yang [a,b], Yuri Knyazikhin [a,*], Matti Mõttus [c], Miina Rautiainen [d,e], Pauline Stenberg [f], Lei Yan [b], Chi Chen [a], Kai Yan [a,g], Sungho Choi [a], Taejin Park [a], Ranga B. Myneni [a]

[a] Department of Earth and Environment, Boston University, Boston, MA 02215, USA
[b] Beijing Key Laboratory of Spatial Information Integration and 3S Application, School of Earth and Space Sciences, Peking University, Beijing 100871, China
[c] VTT Technical Research Centre of Finland, PO Box 1000, FI-02044 VTT, Finland
[d] Aalto University, School of Engineering, Department of Built Environment, P.O. Box 14100, FI-00076 Aalto, Finland
[e] Aalto University, School of Electrical Engineering, Department of Electronics and Nanoengineering, P.O. Box 13000, FI-00076 Aalto, Finland
[f] Department of Forest Sciences, University of Helsinki, P.O. Box 27, FI-00014, Finland
[g] School of Geography, Beijing Normal University, Beijing 100875, China

ARTICLE INFO

Article history:
Received 16 August 2016
Received in revised form 11 May 2017
Accepted 24 May 2017
Available online xxxx

Keywords:
DSCOVR mission
Sunlit leaf area index
Spectral invariants
Hot spot
Operational algorithm
Radiative transfer

ABSTRACT

This paper presents the theoretical basis of the algorithm designed for the generation of leaf area index and diurnal course of its sunlit portion from NASA's Earth Polychromatic Imaging Camera (EPIC) onboard NOAA's Deep Space Climate Observatory (DSCOVR). The Look-up-Table (LUT) approach implemented in the MODIS operational LAI/FPAR algorithm is adopted. The LUT, which is the heart of the approach, has been significantly modified. First, its parameterization incorporates the canopy hot spot phenomenon and recent advances in the theory of canopy spectral invariants. This allows more accurate decoupling of the structural and radiometric components of the measured Bidirectional Reflectance Factor (BRF), improves scaling properties of the LUT and consequently simplifies adjustments of the algorithm for data spatial resolution and spectral band compositions. Second, the stochastic radiative transfer equations are used to generate the LUT for all biome types. The equations naturally account for radiative effects of the three-dimensional canopy structure on the BRF and allow for an accurate discrimination between sunlit and shaded leaf areas. Third, the LUT entries are measurable, i.e., they can be independently derived from both below canopy measurements of the transmitted and above canopy measurements of reflected radiation fields. This feature makes possible direct validation of the LUT, facilitates identification of its deficiencies and development of refinements. Analyses of field data on canopy structure and leaf optics collected at 18 sites in the Hyytiälä forest in southern boreal zone in Finland and hyperspectral images acquired by the EO-1 Hyperion sensor support the theoretical basis.

1. Introduction

The NASA's Earth Polychromatic Imaging Camera (EPIC) onboard NOAA's Deep Space Climate Observatory (DSCOVR) mission was launched on February 11, 2015 to the Sun-Earth Lagrangian L1 point where it began to collect radiance data of the entire sunlit Earth every 65 to 110 min in June 2015. It provides imageries in near backscattering directions with the scattering angle between 168° and 176° at ten ultraviolet to near infrared (NIR) narrow spectral bands centered at 317.5 (band width 1.0) nm, 325.0 (2.0) nm, 340.0 (3.0) nm, 388.0 (3.0) nm, 433.0 (3.0) nm, 551.0 (3.0) nm, 680.0 (3.0) nm, 687.8 (0.8) nm, 764.0 (1.0) nm and 779.5 (2.0) nm (https://epic.gsfc.nasa.gov/epic). The reflectance of vegetation reaches its maximum in the backscattering direction. This phenomenon is known as the hot spot effect (Gerstl, 1999 Knyazikhin and Marshak, 1991 Kuusk, 1991 Qin et al., 1996 Ross and Marshak, 1988). It has been widely recognized that the hot spot region represents the most information-rich directions in the directional distribution of canopy reflected radiation (Gerstl, 1999 Goel et al., 1997 Qin et al., 2002 Ross and Marshak, 1988). The uniqueness of the DSCOVR EPIC observing strategy is its ability to provide frequent observations of every region of the Earth in near hot spot directions that the existing Low-Earth-Orbiting and Geostationary satellites do not have. The EPIC level 1 data and accompanying documentation are available from the NASA Langley Atmospheric Science Data Center (https://eosweb.larc.nasa.gov/project/dscovr/dscovr_table).

The EPIC team is responsible for development and validation of algorithms for producing a series of products which include vegetation green Leaf Area Index (LAI) and its sunlit portion at 10 km spatial

* Corresponding author at: Earth and Environment, Boston University, 675 Commonwealth Avenue, Boston, MA 02215, USA.
E-mail address: jknjazi@bu.edu (Y. Knyazikhin).

http://dx.doi.org/10.1016/j.rse.2017.05.033
0034-4257/

resolution. Whereas LAI is a standard product of many satellite missions (Garrigues et al., 2008 Yan et al., 2016b), the Sunlit Leaf Area Index (SLAI) is a new satellite-derived parameter. Sunlit and shaded leaves exhibit different radiative response to incident Photosynthetically Active Radiation (400–700 nm) (Mercado et al., 2009 Stenberg, 1998), which in turn triggers various physiological and physical processes required for the functioning of plants. Leaf area and its sunlit portion are key state parameters in most ecosystem productivity models (Bonan et al., 2003 Chen et al., 2012 Dai et al., 2004 He et al., 2013 Mercado et al., 2009 Norman, 1982) and carbon/nitrogen cycle (Chen et al., 2003 Doughty and Goulden, 2008 Wang et al., 2001). Our objective is to develop an algorithm for the retrieval of leaf area index and diurnal course of sunlit leaf area index from EPIC Bidirectional Reflectance Factor (BRF) of vegetated land.

LAI and SLAI are defined as the total hemi-surface (Chen and Black, 1992) and sunlit leaf areas per unit ground area. We adapt the retrieval approach implemented in the MODIS operational LAI/FPAR algorithm to retrieve these parameters (Knyazikhin et al., 1998a Knyazikhin et al., 1998b). The algorithm compares measured spectral BRF with those evaluated from model-based entries stored in a look-up-table (LUT). All canopy structural variables and ground reflectance for which modeled and measured BRFs agree within uncertainties in the observed and modeled canopy reflectances are considered as acceptable solutions. The mean value of a structural variable of interest (LAI, SLAI) and its dispersion are taken as the solution of the inverse problem and its retrieval uncertainty. In addition to the measured BRFs, the observation and model uncertainties are also inputs to the retrieval technique (Wang et al., 2001). The former come largely from the correction of the in-orbit data for atmospheric and other environmental effects whereas the latter are determined by the range of natural variation in biophysical parameters not accounted for by the LUT.

A biome classification map is another important ancillary data layer used as input to the algorithm. The global classification of canopy structural types utilized in the Collection 6 MODIS LAI/FPAR algorithm is adopted (Yan et al., 2016a). Global vegetation is stratified into eight canopy architectural types, or biomes. The eight biomes are grasses and cereal crops, shrubs, broadleaf crops, savannas, evergreen broadleaf forests, deciduous broadleaf forests, evergreen needle leaf forests and deciduous needle leaf forests. The biome map reduces the number of unknowns in the inverse technique through the use of simplifying assumptions. The LUT is generated for each biome type. The 8-biome map is provided by the MODIS Global Land Cover Type product (https://lpdaac.usgs.gov/dataset_discovery/modis/modis_products_table).

Thus, the EPIC algorithm inputs BRFs at red (680.0 nm) and NIR (779.5 nm) spectral bands, their uncertainties, canopy structural type, and outputs mean LAI, SLAI and their dispersions. The LUT is a key element of the retrieval technique that determines its performance. Our primary objective is to develop a new LUT that incorporates recent advances in the theory of canopy spectral invariants, accounts for the uniqueness of the EPIC observation geometry and allows for the integration of retrieving SLAI into the operational MODIS LAI algorithm. Our goal is not only to incorporate spectral invariants into the retrieval technique but also resolve known issues in the theory. The hot spot phenomenon is one of them. A special emphasis therefore is given to its integration into the spectral invariant technique.

Whereas protocols for validation of satellite derived LAI are well advanced (Garrigues et al., 2008), there are neither ground truth SLAI data nor methods for obtaining such data from field measurements. Our secondary objective therefore is to outline approaches to ground measurements that would allow us not only to validate satellite derived SLAI but also help product developers to identify deficiencies in the operational algorithm and develop refinements.

This paper is organized as follows. A parameterization of the process of photon-canopy interactions in terms of spectrally invariant parameters and how they are linked to variables measurable in the field are discussed in Section 2 and Appendices A–C. Study area, field data on canopy structure, leaf and ground spectral reflectance as well as hyperspectral images needed to validate the LUT are described in Section 3. The stochastic radiative transfer equations are used to generate the LUT entries. Its initialization and analyses of its ability to provide relationships between BRF and canopy structural variables are demonstrated in Sections 4, 5 and Appendix D. The differences between the MODIS and EPIC LUTs are discussed in Section 6. Finally, Section 7 summarizes the results.

2. Theoretical basis

We introduce a directional variable, Visible Fraction of Leaf Area, VFLA(Ω) defined as the fraction of the total hemi-surface leaf area that is visible from outside the canopy along the direction $-\Omega$. Visible Leaf Area Index, VLAI(Ω), in the direction Ω is the product of LAI and VFLA. Their values give the Sunlit Fraction of Leaf Area (SFLA) and Sunlit Leaf Area Index (SLAI) in the hot spot direction, i.e., when the direction Ω coincides with the direction to the sun. Understanding the relationship between canopy BRF, VFLA and VLAI is our main focus.

The fraction of photons incident on the canopy that are intercepted by phytoelemets is called the canopy interceptance (Stenberg et al., 2016). The canopy directional uncollided transmittance is the fraction of photons that are transmitted directly through gaps in the canopy. These variables depend on canopy structure and vary with the solar direction. We use the symbols $i_0(\Omega)$ and $t_0(\Omega)$ to signify the interceptance of, and directional uncollided transmittance through, the vegetation illuminated from above by a monodirectional beam in the direction $-\Omega$. Clearly, $i_0(\Omega)+t_0(\Omega)=1$. Note that $t_0(\Omega)$ can be estimated from field measurements of canopy transmitted radiation using, e.g., a directional gap fraction sensor LAI-2000 PCA (Rautiainen and Stenberg, 2015). The VFLA(Ω), $i_0(\Omega)$ and $t_0(\Omega)$ do not depend on wavelength.

The intercepted photons initiate the process of photon-canopy multiple interactions. We will use the concept of recollision probability to describe this process (Huang et al., 2007 Knyazikhin et al., 2011 Stenberg, 2007 Stenberg et al., 2016 Wang et al., 2003). This variable is the probability that a photon scattered by a phytoelement in the canopy will interact within the canopy again. The scattered photons can escape the vegetation through gaps between phytoelements. This event is quantified by the escape probability. Fig. 1 illustrates these definitions. The solid arrows depict photons incident on both sides of leaf surfaces from different directions. Their total number is N. A fraction of these photons will be scattered and hit leaves again (dashed arrows). The

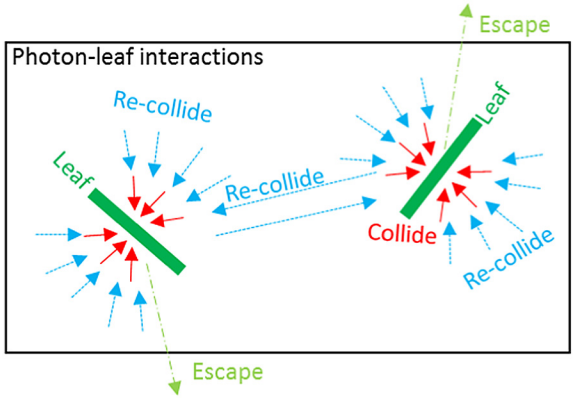

Fig. 1. Recollision and escape probabilities. Solid arrows depict photons incident on leaf surfaces from different directions. A fraction of these photons will be scattered and hit leaves again (dashed arrows). The scattering event is quantified by the wavelength dependent leaf albedo, ω_λ, defined as the fraction of radiation incident on a leaf that is reflected or transmitted. Given total numbers, N and N', of photons incident on leaf surfaces before ("solid arrows") and after one interaction ("dashed arrows") with leaves, the recollision probability is just $p=N'/(\omega N)$. The directional escape probability is the probability by which a scattered photon will escape the vegetation in a given direction Ω ("dash-dot arrows").

scattering event is quantified by the wavelength dependent leaf albedo, ω_λ, defined as the fraction of radiation incident on the leaf that is reflected, or transmitted. Let N' be the total number of scattered photons that hit leaves ("dashed arrows" in Fig. 1). Given N, N' and ω_λ, the recollision probability is $p = N'/(\omega_\lambda N)$. With the probability $(1-p)$ the scattered photons will escape the vegetation. Their angular distribution is given by the directional escape probability density, $\rho(\Omega)$, defined as $\rho(\Omega)|\mu|\,d\Omega = \pi M(\Omega)d\Omega/(\omega_\lambda N)$. Here $M(\Omega)d\Omega$ is the number of scattered photons exiting the canopy in the direction Ω ("dash-dot arrows"); $\mu = \cos\theta$ and θ is the polar angle of Ω. Spherical integration of $\pi^{-1}\rho(\Omega)|\mu|$ results in $(1-p)$. Note that whereas the leaf albedo depends on wavelength, the recollision and escape probabilities are determined by the structure of the canopy rather than photon frequency or the optics of the canopy (Knyazikhin et al., 2011). Our goal is to parameterize the process of photon-canopy interactions in terms of spectrally invariant parameters that include VFLA, canopy interceptance, recollision and escape probabilities.

2.1. A simple canopy radiative regime, VFLA and spectral invariants

It follows from the above definitions that the recollision and escape probabilities depend on radiation field in the vegetation canopy, i.e., on the magnitude and angular distribution of radiation incident on leaf surfaces. We start our analyses with the simplest case where non-absorbing leaves ($\omega_\lambda = 1$) in a vegetation canopy are illuminated by spatially independent isotropic radiation. Here we use a simple stochastic model of canopy structure to evaluate the spectrally invariant parameters. In this model the vegetation canopy is treated as a stationary Poisson germ-grain stochastic process (Fig. 2 and Appendix A). For each realization of the canopy structure we count (a) scattered photons that recollide or (b) exit the canopy in a given direction Ω, and (c) leaf area (number of segments, Fig. 2b) from which scattered photons can exit the canopy through gaps along the direction Ω. From this statistics, canopy interceptance, $i_0(\Omega)$, visible fraction of leaf area, VFLA(Ω), recollision, p_{iso}, and directional escape, $\rho_{iso}(\Omega)$, probabilities are estimated (Appendix A). We use the subscript "*iso*" to designate the special case when leaves are subjected to isotropic radiation. In Sections 2.3–2.4 we will analyze this technique in the case of more realistic heterogeneous canopies under varying within-canopy radiation field.

In our simple model, the directional uncollided transmittance follows Beer's exponential transmission law, i.e., $t_0(\Omega) = \exp(-\tau(\Omega))$ where $\tau(\Omega) = G(\Omega)LAI/|\mu|$ represents the mean optical path in the direction Ω and $G(\Omega)$ is the geometry factor defined as the mean projection of unit leaf area onto a plane perpendicular to the direction Ω (Ross, 1981 Stenberg, 2006). The visible leaf area index can be estimated as $\mathrm{VLAI} = i_0(\Omega)|\mu|/G(\Omega)$ (Wilson, 1967). It follows from these relationships that the visible fraction of leaf area is the ratio between canopy interceptance and the mean optical path, which can be expressed in terms of the canopy directional uncollided transmittance as

$$\mathrm{VFLA}(\Omega) = \frac{1 - t_0(\Omega)}{|\ln(t_0(\Omega))|}. \quad (1)$$

Fig. 3a shows VFLA vs. LAI curve derived from the stochastic simulations of canopy structure can be accurately approximated by Eq. (1) in the case of spherically oriented leaves. Fig. 3b shows that this is true for other types of leaf orientation.

Eq. (1) is expressed in terms of the directional uncollided transmittance, a variable that can be estimated from field measurements of canopy transmitted radiation (Rautiainen and Stenberg, 2015). In real canopy the mean optical path depends on foliage clumping. For example, if we replace discs in the stochastic model with coniferous shoots the mean optical path becomes $\tau(\Omega) = G(\Omega)fLAI/|\mu|$. The clumping factor f converts area of needles on the shoot to the shoot silhouette area, which actually is the visible fraction of needle areas of the shoot. The VFLA calculated using Eq. (1) should be multiplied by the clumping factor, f, to obtain its true value. In the general case Eq. (1) therefore results in the effective VFLA, i.e., visible leaf area, VLAI, normalized by the effective leaf area, $f \cdot LAI$. The visible leaf area index is then $VLAI = VFLA \cdot f \cdot LAI$. It follows from this simple relationship that VLAI is independent of the clumping factor in the sense that its specification does not depend on whether true values, $(VFLA \cdot f)$ and LAI, or their effective counterparts, $VFLA$ and $(f \cdot LAI)$, are used. This property provides a simple approach to derive VLAI from field data. Indeed, both the effective VFLA and effective LAI can be estimated from measured directional uncollided transmittance. The former is calculated using Eq. (1) whereas the latter using the standard technique based on Miller (1967) equation.

In our simple model, the directional escape probability density is related to canopy interceptance as

$$\rho_{iso}(\Omega) = 0.5\frac{i_0(\Omega)}{LAI}. \quad (2)$$

Spherical integration of $\pi^{-1}\rho_{iso}(\Omega)|\mu|$ results in the following relationships

$$\frac{1}{\pi}\int_{4\pi} \rho_{iso}(\Omega)|\mu|d\Omega = 1 - p_{iso} = \frac{i_{dif}}{\mathrm{LAI}}. \quad (3)$$

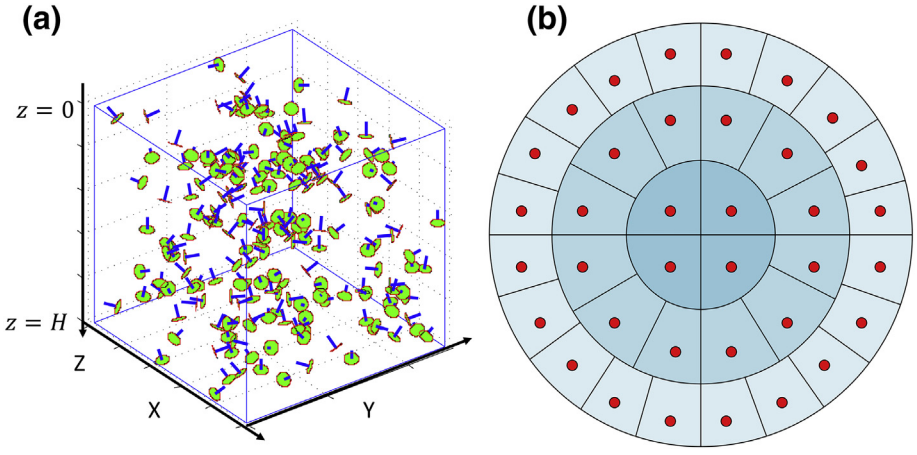

Fig. 2. Stochastic model of canopy structure. Points are scattered in a volume V according to a stationary Poisson point process of intensity d (panel a). On each of these points a disc of radius r (panel b) is placed. Their random orientation is generated with a leaf normal distribution function. The discs represent bi-Lambertian leaves, i.e., the incident photons are reflected from, or transmitted though, the disc in a cosine distribution about its upward normal. The disc is divided into n equal areas, which represent smallest resolvable scale. Panel (a) shows a realization of canopy structure with 207 leaves, each containing $n = 36$ equal areas. The leaf radius to canopy height ratio, r/H, and mean leaf area volume density, u_L, are 0.03 and 0.5, respectively. Leaf normals are shown as blue bars. More details are in Appendix A.

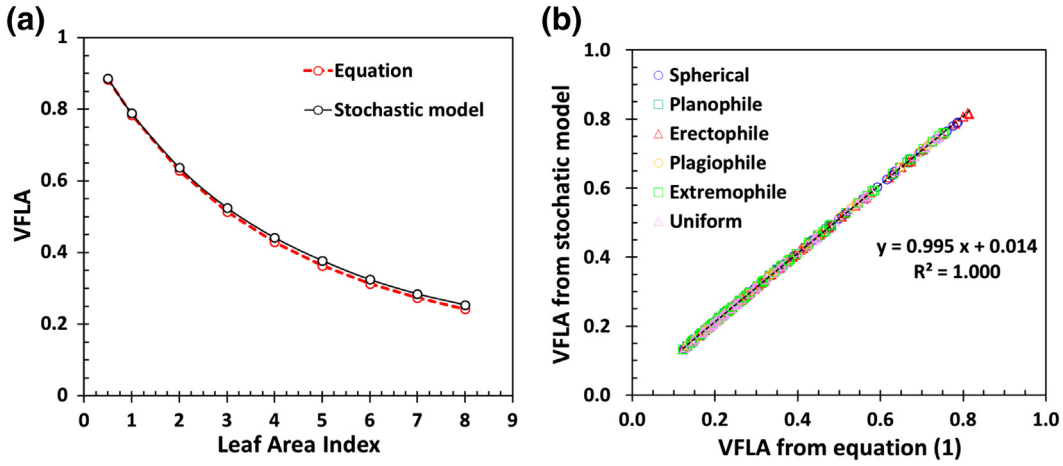

Fig. 3. Visible Fraction of Leaf Area (VFLA). Panel a: VFLA for spherically oriented leaves as a function of Leaf Area Index (LAI) for a zenith angle of 9.44° estimated directly from the stochastic model (legend "Stochastic model") and calculated with Eq. (1) (legend "Equation"). Panel b: Correlation between VFLA estimated from the stochastic model (vertical axis) and Eq. (1) (horizontal axis) for LAI and zenith angle ranges from 1 to 8, and from 0° to 60°, respectively. The scatter plot includes spherical, planophile, erectophile, plagiophile, extremophile and uniform leaves (Appendix A). The VFLAs from the stochastic model were estimated as described in Appendix A.

Here i_{dif} is the interceptance of the vegetation canopy illuminated by the isotropic sky radiation. This relationship was originally documented in Stenberg (2007). It follows from Eqs. (2) and (3) that

$$\frac{\rho_{iso}(\Omega)}{1-p_{iso}} = 0.5\frac{i_0(\Omega)}{i_{dif}}. \quad (4)$$

The left hand side of this equation is the fraction of photons exiting the canopy in the direction Ω relative to the total number of canopy leaving photons. Air- and satellite-borne sensors measure the canopy reflected radiation and thus the fraction of exiting photons can potentially be estimated from satellite data. On the other hand, it can also be derived from canopy directional uncollided transmittance. Eq. (4) therefore provides an important link between satellite and ground-based measurements.

Thus the VFLA, fraction of canopy leaving photons, recollision and escape probabilities for our simple model are expressed in terms of structural variables, $i_0(\Omega)$ and i_{dif}, which in turn can be estimated from below canopy measurements of the canopy directional uncollided transmittance using, e.g., the LAI-2000 plant analyzer (Rautiainen et al., 2009 Rautiainen and Stenberg, 2015 Stenberg, 2007). The VLAI and consequently SLAI can be estimated from VFLA without knowledge of foliage clumping and leaf normal orientation. Theoretically the VFLA could be derived from measurements of the above canopy radiation using Eqs. (1)–(4) if leaves were illuminated by a spatially homogeneous isotropic radiation. This of course is not the case in reality. The question then arises if there is a relationship between this simple case and real canopy reflectance. This will be discussed in Sections 2.3–2.4, which generalize the results to 3D heterogeneous canopy structure including clumping.

2.2. Stochastic reflecting boundary

The BRF of the vegetation reaches its maximum in the backscattering direction. This is so-called hot spot effect. The EPIC sensor therefore sees the brightest portion of the canopy reflected radiation. To account for the hot spot phenomenon in the spectral invariants we introduce a stochastic reflecting canopy boundary as points on leaf surfaces from which incident photons can enter the vegetation canopy. For a vegetation canopy illuminated by a monodirectional solar beam, the sunlit leaves form the boundary, which depends on the direction, $-\Omega_0$, of the incident beam and the distribution of sunlit leaves within the canopy space. Since the sunlit leaves can occur, with a certain probability, anywhere in the canopy, the boundary is subjected to both the direct solar beam and within-canopy diffuse radiation. The boundary scatters the intercepted photons, which in turn can exit or enter the canopy. The direct incident beam causes leaf shadowing. At strongly absorbing wavelength such as the blue or red spectral intervals a fraction of photons scattered by the boundary that enter the canopy will be absorbed with a high probability. This makes the diffuse radiation negligible. The canopy reflected radiation is mainly determined by the canopy boundary in this case. At weakly absorbing wavelength, e.g., the near infrared spectral region, the diffuse radiation is strong, which in turn tends to weaken the shadows and consequently makes the sunlit and shaded leaves less contrasting (Kuusk, 1991 Nilson, 1991).

The canopy boundary is an important structural parameter that impacts canopy reflective properties. To characterize its stochastic properties we use a Bi-directional Sunlit Fraction of Leaf Area, BSFLA(Ω&Ω_0), defined as a fraction of leaf area that is simultaneously visible from outside the canopy along directions, $-\Omega$ and $-\Omega_0$. Fig. 4a shows BSFLA for our simple stochastic model. We also plot VFLA(Ω), VFLA(Ω)VFLA(Ω_0) (Fig. 4a) and the correlation coefficient of VFLA(Ω) and VFLA(Ω_0) given by Eq. (A2) (Fig. 4b). There are two important features noteworthy in relation between the leaf areas. First, the events of seeing gaps from leaf surfaces in two directions are not independent (Fig. 4b and Eq. (A2) in Appendix A). This is effect of finite sizes of the foliage (Kuusk, 1991 Nilson, 1991), which in turn causes the canopy hot spot effect, i.e. a sharp increase in canopy reflected radiation when scattering direction Ω approaches the direction to the sun Ω_0 (Kuusk, 1991 Nilson, 1991 Qin et al., 1996 Ross and Marshak, 1988). Second, with the increase in the angle between Ω_0 and Ω, the correlation decreases from its maximum to zero, and then levels off (Fig. 4b). Its width decreases with a decrease of leaf sizes and vanishes for infinitesimal scatters. Beyond a point at which the correlation saturates, the events become uncorrelated.

The fraction of leaf surface areas "visible" outside the canopy along the direction $-\Omega$ can be expressed as VFLA(Ω) $=[1-h_{iso}(\Omega;\Omega_0)]$VFLA($\Omega$) $+h_{iso}(\Omega;\Omega_0)$VFLA($\Omega$). The summands represent fractions of shaded and sunlit leaf areas (Appendix A), and h_{iso} is the correlation coefficient of VFLA(Ω) and SFLA (Fig. 4b). The probability that photons scattered by shaded leaves will exit the vegetation in the direction Ω is $[1-h_{iso}(\Omega;\Omega_0)]\rho_{iso}(\Omega)$ (Appendix A). Some of the photons scattered by the boundary will escape vegetation canopy with unit probability. Their fraction is given by $j_{iso}(\Omega;\Omega_0)h(\Omega;\Omega_0)$ where j_{iso} is the anisotropy of the boundary reflected radiation, which is determined by the area scattering phase function and geometry factor (Appendix A).

Thus, the escape probability density, $\rho_{b,iso}(\Omega;\Omega_0)$, for our simple model with the stochastic boundary in the direction Ω_0 is a weighted

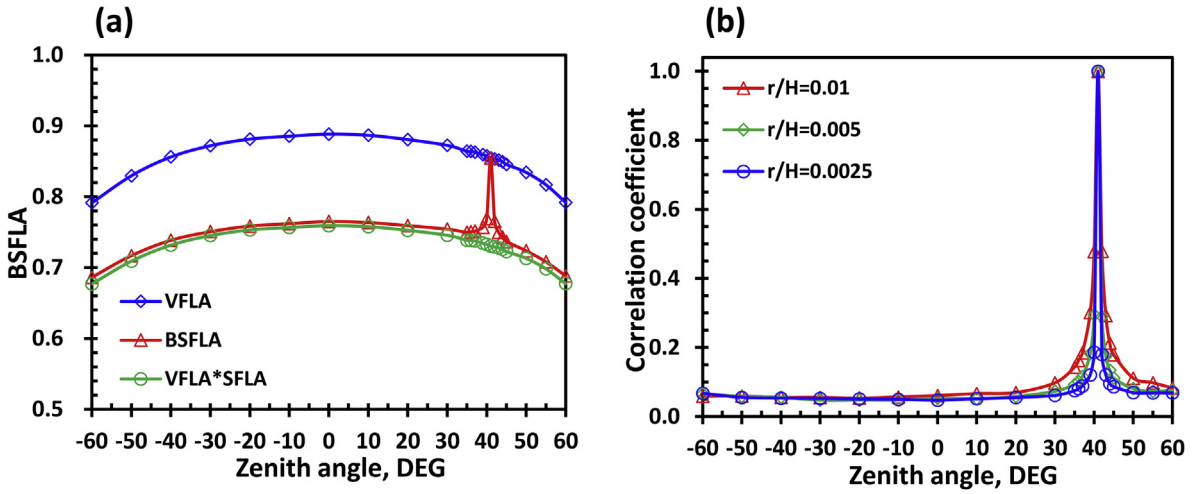

Fig. 4. Bi-directional Sunlit Fraction of Leaf Area, BSFLA($\Omega\&\Omega_0$), derived from the stochastic model of canopy structure (Fig. 2). Panel a: BSFLA($\Omega\&\Omega_0$) as a function of zenith angle θ of the direction Ω (legend "BSFLA"). Zenith angle of Ω_0 is 41°. Also shown are VFLA(Ω) (legend "VFLA") and VFLA(Ω)VFLA(Ω_0) (legend "VFLA*SFLA"). Here $r/H=0.005$; $d=6366$; $u_L=\pi^2 d=0.5$. Panel b: Correlation coefficient of VFLA(Ω) and SFLA = VFLA(Ω_0) as a function of θ for relative leaf sizes $r/H=0.01$, 0.005 and 0.0025. Its definition is given in Appendix A.

sum of the escape probabilities for shaded and sunlit leaves, i.e., $\rho_{b,iso}(\Omega;\Omega_0)=[1-h_{iso}(\Omega;\Omega_0)]\rho_{iso}(\Omega)+h_{iso}(\Omega;\Omega_0)j_{iso}(\Omega;\Omega_0)$. Spherical integration of $\pi^{-1}\rho_{b,iso}(\Omega)|\mu|$ results in $(1-p_{b,iso})$ where $p_{b,iso}$ is the recollision probability. Some of the boundary scattered photons will escape the vegetation with unit probability. This lowers the probability for photons to recollide (i.e., $p_{b,iso}\le p_{iso}$) and consequently enhances the likelihood of photons escaping the vegetation (i.e., $\rho_{b,iso}(\Omega;\Omega_0)\ge\rho_{iso}(\Omega)$). Our next step is to demonstrate validity of these relationships in the general case of 3D heterogeneous canopy.

2.3. Generalization to 3D heterogeneous vegetation canopies

The goal of this section is to generalize our results presented in Sections 2.1 and 2.2. This will be done based on analyses of the stochastic radiative transfer equations (SRTE) (Appendix B). These equations accurately account for the canopy structure over a wide range of scale through the use of the pair-correlation function (Huang et al., 2008). Here we focus on the 3D vegetation canopy bounded from below by a non-reflecting surface. A physically based technique to account for contributions from reflecting canopy background will be detailed in Section 5 as part of our validation efforts.

Let the 3D vegetation canopy bounded from below by a non-reflecting surface be subjected to a monodirectional beam in the direction $-\Omega_0$. We represent the directions to the Sun, Ω_0, and sensor, Ω, by cosines of the sun, $\mu_0=\cos\theta_0$, and sensor, $\mu=\cos\theta$, polar angles, and their associated azimuths. The sunlit leaves in the direction Ω_0 form the canopy boundary. The incoming photons scattered by the boundary will interact with both shaded leaves and the boundary. The singly scattered photons that have not exited the canopy undergo the second interaction, resulting in a radiation field generated by photons scattered two times. A fraction of these photons in turn will recollide and give rise to a radiation field generated by photons scattered three times, etc. Let $I_m(z,\Omega)$ and F_m be the horizontal average radiance of radiation field generated by photons scattered m times and associated mean irradiance on leaf sides (Eq. (B2) in Appendix B.1), respectively. By definition (Fig. 1), the escape and recollision probabilities are $\rho_m(\Omega;\Omega_0)=\pi I_m(z_b,\Omega)/(\omega_\lambda F_{m-1})$ and $p_m=F_m/(\omega_\lambda F_{m-1})$. Here $z_b=0$ represents the upper horizonal surface above the canopy in the case of upward directions, and a surface beneath the canopy, $z_b=H$, for downward directions. Here symbols Ω and $-\Omega$ designate upward and downward directions. We start our analyses assuming that the foliage does not absorb radiation i.e., $\omega_\lambda=1$.

The Directional Area Scattering Function (DASF) is defined as the BRF of a vegetation canopy with non-absorbing leaves ($\omega_\lambda=1$) and bounded underneath by a non-reflecting surface (Knyazikhin et al., 2013). It can be expanded in successive order of scattering, or in Neumann series (Huang et al., 2007),

$$\begin{aligned}&\mathrm{DASF}(\Omega;\Omega_0)\mu_0\\&=\left[\rho_1(\Omega;\Omega_0)+\rho_2(\Omega;\Omega_0)\theta_1+\ldots+\rho_{m+1}(\Omega;\Omega_0)\theta_m^m+\cdots\right]i_0(\Omega_0),\end{aligned}\quad(5)$$

where $\theta_m=\sqrt[m]{p_1p_2\ldots p_m}$. The escape probability corresponding to the mth scattering order can be represented as

$$\rho_m(\Omega;\Omega_0)=[1-h_m(\Omega;\Omega_0)]\rho_{0m}(\Omega)+j_{iso}(\Omega;\Omega_0)h_m(\Omega;\Omega_0).\quad(6)$$

Here ρ_m and ρ_{0m} are escape probability densities for canopies with and without the stochastic boundary, respectively, and h_m is the correlation coefficient calculated as detailed in Appendix B.2. Integration of $\pi^{-1}\rho_m|\mu|$ over the unit sphere results in $1-p_m$ (Huang et al., 2007). The aim of this subsection is to understand relationships between ρ_{iso}, p_{iso}, ρ_m and p_m. Here we closely follow the theory documented in Huang et al. (2007). All calculations were performed using the stochastic radiative transfer equations.

Fig. 5 shows the escape, $\rho_m(\Omega;\Omega_0)$, and recollision, p_m, probabilities as functions of m. For view directions outside of the hot spot region, i.e., $h_m(\Omega;\Omega_0)\sim0$ and $\rho_m(\Omega;\Omega_0)\sim\rho_{0m}(\Omega)$, the escape probabilities for up- and downward directions vary with the number of successive scattering and reach plateaus from above and below after about 7–8 iterations (Fig. 5a). The semi-sum, $\overline{\rho}_m(\Omega;\Omega_0)=0.5[\rho_m(\Omega;\Omega_0)+\rho_m(-\Omega;\Omega_0)]$, saturates faster, after two to three scattering events in this example. The corresponding recollision probability p_m is related to $\overline{\rho}_m$ via Eq. (3) and thus it converges at the same or a faster rate. The limits $\overline{\rho}_m$ and p_m approximate $\rho_{b,iso}(\Omega)$ and $p_{b,iso}$. In the hot spot direction (Fig. 5b), i.e., when $\Omega\sim\Omega_0$ (and $h_m(\Omega;\Omega_0)\sim1$), the escape probability $\rho_m(\Omega;\Omega_0)$ is almost independent of the scattering order and approximates $j_{iso}(\Omega;\Omega_0)h_m(\Omega;\Omega_0)$, suggesting a negligible variation of h_m with m.

Fig. 6a shows an important feature of radiation fields corresponding to scattering orders at which the escape probability density saturates: $I_8(z,\Omega;\Omega_0)$ is proportional to $I_7(z,\Omega;\Omega_0)$, i.e., $I_8(z,\Omega;\Omega_0)=p_8I_7(z,\Omega;\Omega_0)$. It means that the radiative field generated by photons scattered 7 times is reduced by a factor p_8 as result of one interaction. The coefficient of proportionality is the recollision probability, i.e., $p_8=F_8/F_7$ (Huang et al., 2007). It follows from these relationships that $I_8(z,\Omega;\Omega_0)/F_8=I_7(z,\Omega;\Omega_0)/F_7$. This example illustrates a fundamental property of the 3D radiative transfer equation, i.e., the sequences $p_m=F_m/F_{m-1}$ and $e_m(z,\Omega;\Omega_0)=I_m(z,\Omega;\Omega_0)/F_m$, $m=1,2,\cdots$, converge to the unique

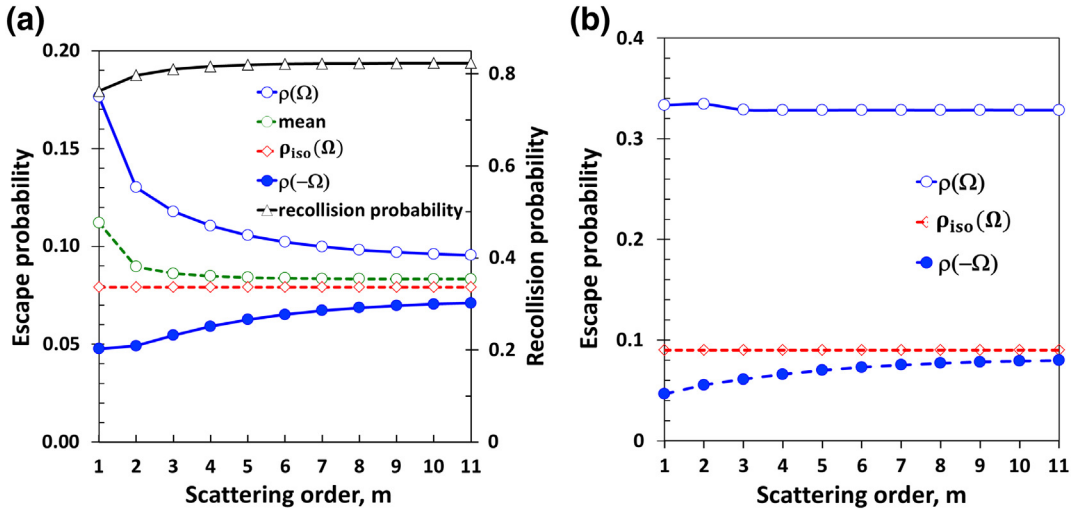

Fig. 5. Panel a: Directional escape probability densities in up-, $\rho_m(\Omega)$, and downward, $\rho_m(-\Omega)$, directions, their mean, $0.5[\rho_m(\Omega)+\rho_m(-\Omega)]$ (left axis), and recollision probability, p_m (right axis) for 11 scattering orders. Here solar zenith angle (SZA) and view zenith angle (VZA) are 41° and 49.1°, respectively. Panel b: Directional escape probabilities in up-, $\rho_m(\Omega)$, and downward, $\rho_m(-\Omega)$, directions for SZA = VZA = 49.1° and 11 scattering orders. $\rho_{iso}(\Omega)$ is shown on both plots. The stochastic radiative transfer equations were used to derive these variables. LAI = 5, ground cover was 0.8.

positive eigenvalue p_∞ of the radiative transfer equation, corresponding to the unique positive (normalized to unity) eigenvector $e_\infty(z,\Omega;\Omega_0)$ (Huang et al., 2007 Vladimirov, 1963). For a sufficiently large number of scattering events, the radiance $I_m(z,\Omega;\Omega_0)$ and, consequently, the escape probability density can be accurately approximated as $I_m(z,\Omega;\Omega_0)=p_\infty^m e_\infty(z,\Omega;\Omega_0)$ and $\rho_m(\Omega;\Omega_0)=p_\infty e_\infty(z_b,\Omega;\Omega_0)$. In this example e_m reaches its limit after 6–7 iterations, i.e., $I_m(z,\Omega;\Omega_0)=p_\infty^m e_7(z,\Omega;\Omega_0)$, and because p_m saturates after two to three scattering events (Fig. 5a), $p_\infty \approx \sqrt{p_1 p_2} \approx p_{iso}$. In general case the rate of convergence depends on p_∞: the higher its value, the slower the convergence (Huang et al., 2007).

Fig. 6b illustrates Eq. (6) for $m=7$. The boundary lowers the probability for photons to recollide and consequently enhances the likelihood of photons escaping the vegetation. This is seen in Fig. 6b: $\rho_m(\Omega;\Omega_0)$ differs from $\rho_{0m}(\Omega)$ by factor $(1-h_7)$ and therefore $\rho_m(\Omega;\Omega_0)\geq\rho_{0m}(\Omega)$. This yields an opposite inequality for the recollision probabilities. The escape probability densities $\rho_{0m}(\Omega)$ and $\rho_{0m}(-\Omega)$ converge to their limits almost symmetrically from above and below for all directions. Their semi-sum therefore approximates $\rho_{iso}(\Omega)$ for all directions, too. This is because the sensitivity of the term $\rho_{0m}(\Omega)$ to Ω_0 diminishes with the scattering order m. Its limit becomes independent on the direction of the incident beam in the case of canopies without stochastic boundary.

Solutions of the radiative transfer equation describe photons just before their interactions with scattering centers. In vegetation canopies it is radiance incident on the leaf surface. Distribution of photons just after their interactions is treated as distribution of sources on leaf surfaces, which is given by the source function (Eq. (B3) in Appendix B.1). Fig. 7a shows vertical profiles of the horizontal and angular averages of source functions, S_m, generated by the normalized radiance $e_m(z,\Omega)$ incident on leaf surfaces. Spherical integration of $e_m(z,\Omega)$ (as defined by Eq. (B3) in Appendix B.1) significantly lowers the angular variation in the source function (Davis and Knyazikhin, 2005 Knyazikhin et al., 2011). In this example the coefficient of angular variation of the source function (std/mean) is below 1.7% (Fig. 7b).

Thus, the scattering properties of the vegetation canopy are calculated as the sum of contributions from photons of different scattering orders (Eq. (5)). For sufficiently large m, the within canopy radiation regime is generated by spatially varying almost isotropic sources on leaf surfaces (Fig. 7). This feature makes the radiative regime similar

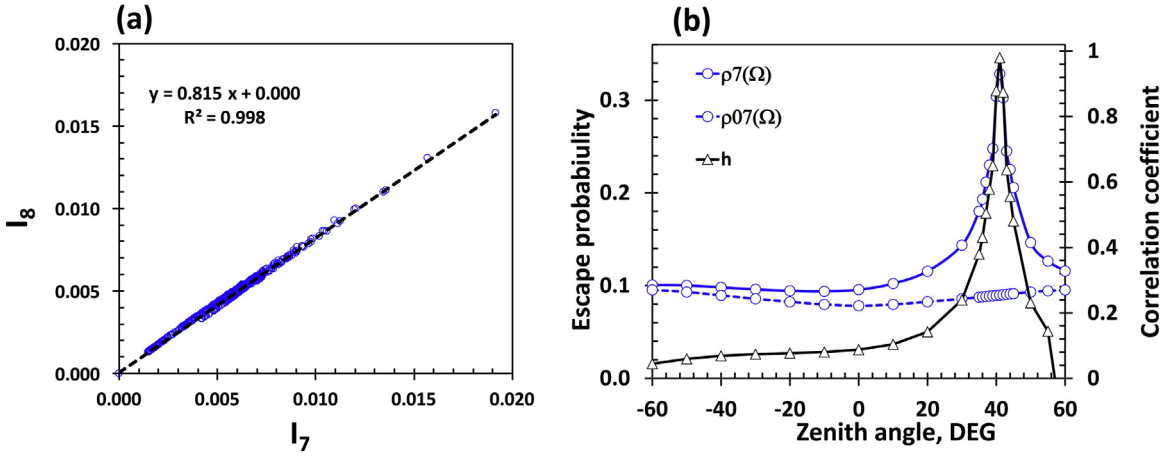

Fig. 6. Panel a: Relationship between $I_8(z,\Omega;\Omega_0)$ and $I_7(z,\Omega;\Omega_0)$ for $z=0,0.2,0.4,\cdots,1$ (in relative units) and 217 upward directions. Panel b: Escape probabilities $\rho_7(\Omega;\Omega_0)$, $\rho_{07}(\Omega)$ (vertical axis on the left side) and the correlation coefficient h_7 (vertical axis on the right side) in the principal plane as functions of view zenith angle of Ω. The probabilities are related as $\rho_7(\Omega;\Omega_0)=(1-h_7)\rho_{07}(\Omega)+h_7 j_{iso}(\Omega;\Omega_0)$ where the correlation coefficient h_7 was calculated as described in Appendix B.2. The stochastic radiative transfer equations with inputs as in Fig. 5 were used to derive these variables.

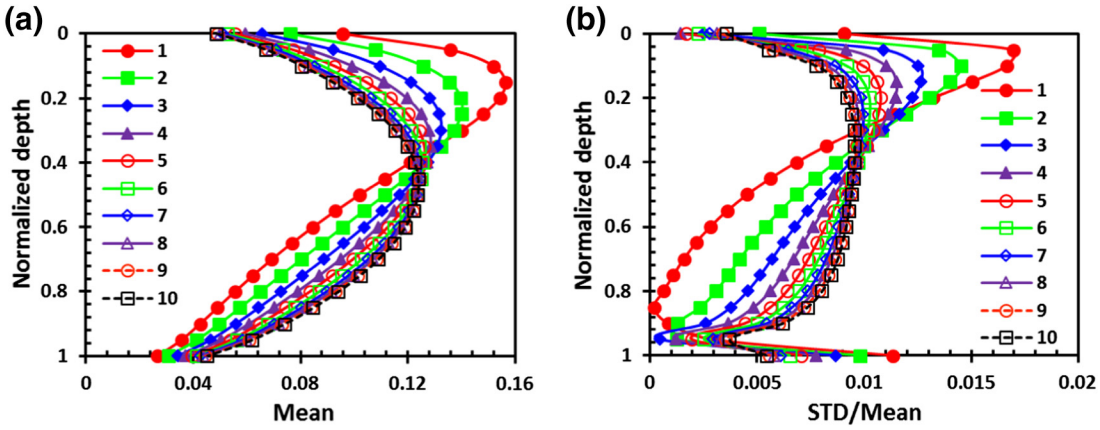

Fig. 7. Vertical profiles of horizontal and angular averages of source functions (panel a) and coefficient of variation (std/mean, panel b) due to radiative filed $e_m(z,\Omega)$ for 10 scattering orders. The dimensionless vertical axes show values of z/H where H is the canopy height. The stochastic radiative transfer equations with inputs as in Fig. 5 were used. The source function is defined by Eq. (B3).

to our simple model where the leaf-scattered radiation generates perfectly isotropic sources. Spatial variation of sources does not impact the recollision and escape probabilities. This is not true for low scattering orders. Our next step is to understand their impact on the average escape and recollision probabilities.

2.4. DASF and BRF

Based on Eq. (5) we define the average escape probability density as

$$\rho_A(\Omega;\Omega_0)=\sum_{m=1}^{\infty}\rho_m(\Omega;\Omega_0)w_{m-1}. \tag{7}$$

The weight $w_m=\theta_m^m/\sum_{k=0}^{\infty}\theta_k^k$, with θ_0 set to 1, accounts for the contribution of the mth scattering order. Because spherical integration of $\pi^{-1}\rho_m(\Omega)|\mu|$ results in $1-p_m$ for each m (Huang et al., 2007), the average escape probability also follows this relationship, i.e.,

$$\frac{1}{\pi}\int_{4\pi}\rho_A(\Omega;\Omega_0)|\mu|d\Omega=1-\sum_{m=1}^{\infty}p_m w_{m-1}=1-p_A, \tag{8}$$

where p_A is the average recollision probability (Stenberg, 2007 Stenberg et al., 2016). Note that the weight w_m can be expressed as $w_m=\theta_m^m(1-p_A)$. In terms of these notations the DASF takes the following form,

$$\mathrm{DASF}(\Omega;\Omega_0)=\frac{\rho_A(\Omega;\Omega_0)i_0(\Omega_0)}{1-p_A}. \tag{9}$$

The escape and recollision probabilities were introduced as conditional probabilities, i.e., they refer to photons that "survive" the scattering event (Fig. 1). The joint probabilities of recollision, escape and scattering events are $\omega_\lambda\rho_A$ and $\omega_\lambda p_A$. The BRF therefore becomes,

$$\mathrm{BRF}_\lambda(\Omega;\Omega_0)=\frac{\omega_\lambda\rho_A(\Omega;\Omega_0)i_0(\Omega_0)}{1-\omega_\lambda p_A}=\mathrm{DASF}\cdot W_\lambda(p_A), \tag{10}$$

where

$$W_\lambda(p_A)=\omega_\lambda\frac{1-p_A}{1-\omega_\lambda p_A}, \tag{11}$$

is the canopy scattering coefficient (Knyazikhin et al., 2013 Lewis and Disney, 2007 Smolander and Stenberg, 2005 Stenberg et al., 2016). Eq. (10) is the solution of the stochastic radiative transfer equations for the mean radiance formulated for a vegetation canopy bounded from below by a non-reflecting surface. We point out some features that are useful for developing inverse remote sensing techniques and their validation.

First, for vegetation canopies with a dark background or for sufficiently dense vegetation where the impact of the canopy background is negligible, the DASF and the scattering coefficient can be directly retrieved from the BRF spectrum without the use of canopy reflectance models, prior knowledge, or ancillary information regarding the leaf optical properties using a simple algorithm documented in Knyazikhin et al. (2013). The DASF, which is stored in the LUT, can be directly assessed using hyperspectral reflectance data acquired over dense canopies. We also use this algorithm to obtain the average escape and recollision probabilities from solutions of the stochastic radiative transfer equations (Appendix C).

Second, the decomposition Eq. (6) is also valid for the average escape probability density, i.e., ρ_A is a weighted sum of the averaged escape probability densities for shaded, $\rho_{0A}(\Omega)$, and sunlit, $j_{iso}(\Omega;\Omega_0)$, leaves. The DASF therefore can be represented as

$$\begin{aligned}\mathrm{DASF}(\Omega;\Omega_0)\mu_0&=[1-h(\Omega;\Omega_0)]\frac{\rho_{0A}(\Omega)i_0(\Omega_0)}{1-p_A}+h(\Omega;\Omega_0)\frac{j_{iso}(\Omega;\Omega_0)i_0(\Omega_0)}{1-p_A}\\&=[1-h(\Omega;\Omega_0)]\mathrm{DASF}_0(\Omega;\Omega_0)\mu_0+h(\Omega;\Omega_0)\mathrm{DASF}_b(\Omega;\Omega_0)\mu_0.\end{aligned} \tag{12}$$

Fig. 8a shows the average probabilities $\rho_A(\Omega;\Omega_0)$, $\rho_{0A}(\Omega;\Omega_0)$, and the correlation coefficient h. Our analyses suggest that the correlation coefficient varies insignificantly with scattering order (Fig. 5b). Fig. 8b reinforces this feature: the correlation coefficient derived from full solutions of the stochastic radiative transfer equations compares well with its 7th order approximation. This property has a simple physical interpretation. Indeed, photons scattered by the boundary toward the sun will escape vegetation with unit probability. Their amount depends on the boundary area, which in turn is determined by the canopy structure rather than within-canopy radiation regime.

Finally, the semi-sum $\overline{\rho}_{0m}(\Omega)$ and geometric mean θ_m of recollision probabilities converge to $\rho_{iso}(\Omega)$ and p_{iso} very fast (Fig. 5a). Approximating $\overline{\rho}_{0m}(\Omega)$ and θ_m in Eq. (7) by their limiting values, one obtains an approximation of the average semi-sum, i.e., $\overline{\rho}_{0A}(\Omega)(1-p_{iso})/(1-p_A)\approx\rho_{iso}(\Omega)$. For view directions outside of the hot spot region therefore the following relationship takes place,

$$\frac{\rho_{iso}(\Omega)}{1-p_{iso}}i_0(\Omega_0)\approx\frac{\overline{\rho}_A(\Omega)}{1-p_A}i_0(\Omega_0). \tag{13}$$

The left hand side of this equation is the Directional Area Scattering Factor, DASF_{iso}, in the case when leaves are subjected to isotropic radiation. This variable can be estimated from below canopy measurements

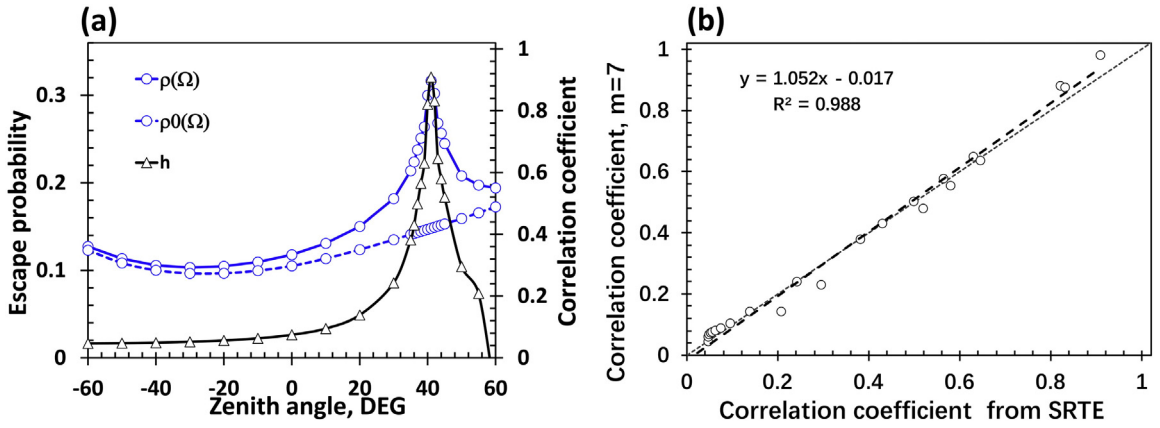

Fig. 8. Panel a: Average escape probabilities $\rho_A(\Omega;\Omega_0)$, $\rho_{0A}(\Omega)$ (vertical axis on the left side) and the correlation coefficient h (vertical axis on the right side) as functions of view zenith angle of Ω. Panel b: Comparison of the correlation coefficients derived from the SRTE (horizontal axis) and radiative field generated by photons scattered 7 times (vertical axis).

of the canopy directional uncollided transmittance using Eq. (4). Eqs. (1)–(4) therefore provide a basis for validation of the radiative transfer approach and assessments of retrieval techniques based on this approach.

Thus the BRF of a vegetation canopy bounded from below by a non-reflecting surface is expressed as a solution of the stochastic radiative transfer equations parameterized in terms of the measurable spectrally invariant parameters. This underlies our theoretical basis for developing LUT for the use with the DSCOVR EPIC data.

3. Study area and data used

3.1. Site description

This research is focused on Hyytiälä forest (Fig. 9) in the southern boreal zone in central Finland (61°50′N, 24°17′E). Dominant tree species are Norway spruce (*Picea abies*), Scots pine (*Pinus sylvestris*) and Silver birch (*Betula pendula*). Understory vegetation is classified as xeric, sub-xeric, mesic or herb-rich vegetation based on the species richness and abundance. The understory typically consists of two layers: the ground layer, which is mainly composed of mosses and lichens, and the upper layer, which is composed of, for example, dwarf shrubs and grasses. The growing season typically begins in early May and senescence in late August. Eighteen study sites representing different species and understory compositions were chosen for our analyses (Table 1). A detailed description of the study sites can be found in Heiskanen et al. (2013).

3.2. Field data

Data used in our research were sampled during peak growing season (June–July) on 18 locations (Fig. 9) in 2010 and 2012 (Lukeš et al., 2013 Rautiainen and Lukeš, 2015 Rautiainen et al., 2011).

The effective leaf area index and canopy directional uncollided transmittances were estimated from LAI-2000 Plant Canopy Analyzer data collected on selected locations between June 22 and July 4, 2010 when foliage had reached its maximum size. The measurements were taken shortly after (before) sunset (sunrise), or during overcast days, when forest was illuminated only by diffuse light. The sampling scheme was a cross with 12 measurement points: two perpendicular 6-point transects with 4-meter intervals between the measurement points. The forest measurements were made without view restrictors. The understory was excluded from the field of view since the measurements were taken at a height of 0.7 m. In addition to LAI-2000 measurements, stand basal area (BA), fractions of pine, spruce and birch trees (based on basal area), mean stem diameter at breast height (DBH), mean crown lengths and understory type for all 18 plots were measured (Table 1). The stand density was calculated as $BA/[\pi\cdot(0.5DBH)^2]$ (in stem/m^2). Angular profiles of canopy directional uncollided transmittances and effective LAI are shown in Fig. 10a. A detailed description of the measurements is documented in Heiskanen et al. (2012)and Rautiainen and Lukeš (2015).

Nadir hemispherical-conical reflectance factors (HCRF) of the understory in the spectral region from 325 nm to 1075 nm at spectral resolution of approximately 3 nm at 700 nm were measured between June

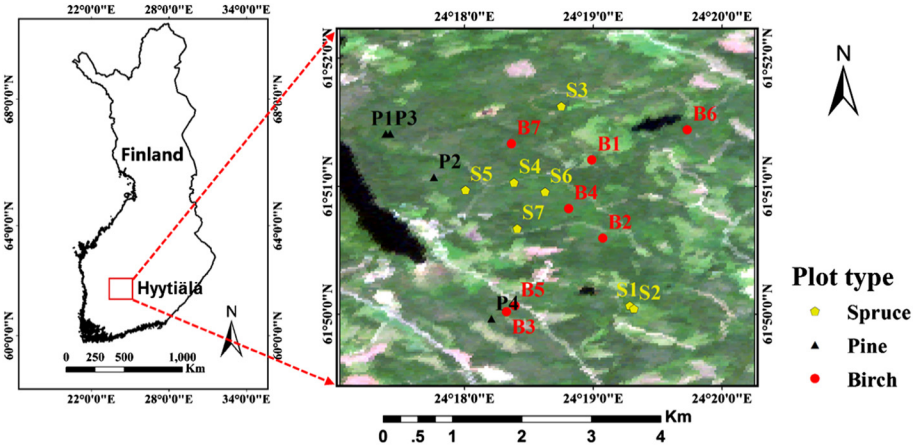

Fig. 9. Hyytiälä forest and distribution of study sites. The true color composite image is from Hyperion hyperspectral cube acquired on July 3, 2010.

Table 1
Species compositions, mean stem diameter at breast height (DBH), mean crown length, mean stand basal area (BA) and understory type for 18 plots in Hyytiälä forest. The Silver birch dominated site B7 and Norway spruce dominated site S4 are also treated as mixed forests.

Site ID	Scots pine, %	Norway spruce, %	Silver birch, %	DBH, cm	Crown length, m	BA, m^2/ha	Understory
B1	0	12.1	87.9	16.3	9.5	10.7	Mesic
B2	0	0	100.0	12.2	10.6	10.7	Herb-rich
B3	0	0	100.0	12.3	7.9	21.0	Mesic
B4	0	2.7	97.3	12.0	5.8	20.6	Herb-rich
B5	0	11.1	88.9	8.9	4.9	27.0	Herb-rich
B6	0	8.1	91.9	14.2	5.8	20.9	Mesic
B7	0	48.2	51.8	24.3	10.1	27.2	Mesic
P1	99.6	0.4	0	17.7	6.6	20.4	Mesic
P2	83.8	14.7	1.5	25.1	3.3	20.5	Sub-xeric
P3	95.2	1.5	3.2	20.0	8.6	24.3	Mesic
P4	65.4	26.9	7.7	24.3	6.2	26.0	Sub-xeric
S1	22.6	70.7	6.7	17.8	11	24.9	Mesic
S2	4.0	89.0	7.0	18.9	9.7	20.9	Mesic
S3	0.7	99.3	0	8.8	6.9	10.0	Mesic
S4	8.1	51.0	40.9	14.2	8.1	22.2	Mesic
S5	0	76.1	23.9	18.7	11.1	27.5	Mesic
S6	0	99.0	1.0	14.4	7.3	31.7	Mesic
S7	9.1	76.9	13.9	17.3	10.5	29.1	Xeric

29 and July 6, 2010 under diffuse light conditions using a FieldSpec UV/VNIR Spectroradiometer without fore-optics (i.e. the field-of-view was 25°). Forty measurement points were made for each understory type at intervals of 0.7 m on a 28 m long permanent transect. The ground area sampled at each point was approximately a circle with radius of 25 cm (Rautiainen et al., 2011). Spectra of understory HCRFs are shown in Fig. 10(b). Note that we follow standard reflectance nomenclature used in remote sensing (Martonchik et al., 2000 Schaepman-Strub et al., 2006)

Directional-hemispherical reflectance (DHRF) and transmittance (DHTF) of abaxial and adaxial sides of Norway spruce, Scots pine and Silver birch needles and leaves from the Hyytiälä forests were measured under laboratory conditions using ASD RTS-3ZC integrating sphere and ASD FieldSpec 3 PRO spectroradiometer in the spectral interval from 350 to 2500 nm with a spectral resolution of 3 nm at 700 nm and 10 nm at 1400 and 2100 nm between June 11 and 28, 2012 (Lukeš et al., 2013). Leaf albedo was calculated as sum of DHRF and DHTF. To measure conifer needle optical properties, the needles were secured in a special holder developed by Malenovský et al. (2006) at distances equal to or smaller than their thickness. The needle samples were scanned using a desktop document scanner, from which between-needle gap fractions were estimated using Otsu's automatic threshold method (Otsu, 1975). The gap fraction was used to correct DHRF and DHTF of conifer needles. A detailed description of this data set and measurement technique are documented in Lukeš et al. (2013). Mean spectra of leaf albedos used in our research are shown in Fig. 10(c). Maximum values of standard deviations were 0.029 (birch), 0.038 (pine) and 0.047 (spruce). The data are publicly available through the SPECCHIO database (Hueni et al., 2009).

3.3. Hyperion data

We used hyperspectral data from EO-1 Hyperion image (L1B product) acquired over the Hyytiälä forest on July 3, 2010. Hyperion is a narrowband imaging spectrometer that registers radiance in 242 spectral bands from 356 to 2577 nm, with about 10 nm bandwidth. Data spatial resolution is 30 m. The swath width is 7.7 km, and data are typically collected in 7.5 km by 100 km images (Pearlman et al., 2003). The striping, missing lines and spectral smile were removed from images or corrected using spectral moment matching (Sun et al., 2008), local destriping (Goodenough et al., 2003), interpolation and the pre-launch calibration measurements, respectively. The atmospheric correction was performed with the Fast Line-of-sight Atmospheric Analysis of Spectral Hypercubes (FLAASH) algorithm (Matthew et al., 2000). This technique results in an approximation of surface BRF. A detailed description of the processing of Hyperion images acquired over our study area can be found in Heiskanen et al. (2013) and Rautiainen and Lukeš (2015). The solar and view zenith angles were 41° and 13.8°; the relative azimuthal angle (RAA) of the Hyperion sensor was 62.73°. BRF spectra of pure Silver birch (B3), Scots pine (P1), Norway spruce (S3) and mixed (B7) plots are shown in Fig. 10(c). In our analyses, a plot was defined "pure" when at least 90% of the trees (by stem count) belonged to the given tree species.

4. Initialization of the stochastic radiative transfer equations

Structural variables that the stochastic radiative transfer equations admit include the conditional pair-correlation function, $K(z,\xi,\Omega)$, the fraction, $a(z)$, covered by tree crowns at depth z, and extinction coefficient, $\sigma(\Omega)$ (Appendix B.1). Our goal is to derive these variables from field data. We use analytical equations for K and a developed for mean tree crown idealized as a vertical solid, i.e., volume obtained by rotating a curve about the vertical axis (Huang et al., 2008). Under this assumption the conditional pair-correlation function and fraction $a(z)$ are explicit functions of the aspect ratio (crown length to crown diameter ratio) and stand density (Schull et al., 2011).

Specification of the extinction coefficient, $\sigma(\Omega)=u_L G(\Omega)$, requires effective leaf area volume density u_L (in m^2/m^3) and geometry factor $G(\Omega)$. The latter is determined by the type of leaf orientation (Ross, 1981 Stenberg, 2006). We use the inclination index of foliage area to parameterize the geometry factor (Ross, 1981). This index characterizes the deviation of leaf orientation from the spherical distribution and allows us to approximate the extinction coefficient for leaf and needle canopies as $\sigma(\Omega)=0.5\beta u_L$, where the weight β varies between 0 and 2. In the framework of the stochastic approach the effective leaf area volume density is related to the effective leaf area index, LAI, mean crown length, H_c, and stand density, d, as (Schull et al., 2011)

$$\mathrm{LAI}=u_L\int_0^{H_c}\{1-\exp[-d\pi r^2(z)]\}dz \tag{14}$$

Here $r(z)$ is the mean radius of the crown horizontal cross section at depth z, which in turn depends on the crown shape and aspect ratio (Schull et al., 2011).

Thus, data on stand density, d, mean crown length, H_c, leaf orientation, β, leaf area volume density, u_L, and crown aspect ratio, A, are needed to specify the coefficients that appear in the stochastic radiative transfer equations. The Norway spruce, Scots pine (Rautiainen et al., 2008) and Silver birch stands were idealized as forests consisting of ellipsoidal in shape trees. The stand density was calculated from the BA and DBH data as described in Section 3. The leaf area volume density can be estimated from Eq. (14) if the aspect ratio, crown length and effective LAI are known.

The site specific crown aspect ratio, A, and parameter β were estimated by selecting the most probable pair (A,β) for which angular profiles of canopy directional uncollided transmittance predicted by the stochastic radiative transfer equations (Eqs. (B1a) and (B1b) in Appendix B.1), agree with their measured counterparts (Fig. 10a) to within measurement uncertainties as follows. First, we expressed the effective leaf area volume density as a function of aspect ratio using Eq. (14) and measured effective LAI, stand density and mean crown length. Second, for each pair (A,β) we solved the stochastic radiative transfer equations for the directional uncollided transmittance (Appendix B.1) to obtain the angular profile of the directional uncollided transmittance as a function of the aspect ratio and leaf orientation. Next, we generated a set of acceptable solutions, which contained pairs (A,β) for which the RMSE between the modeled and measured profiles was below measurement uncertainty, which was

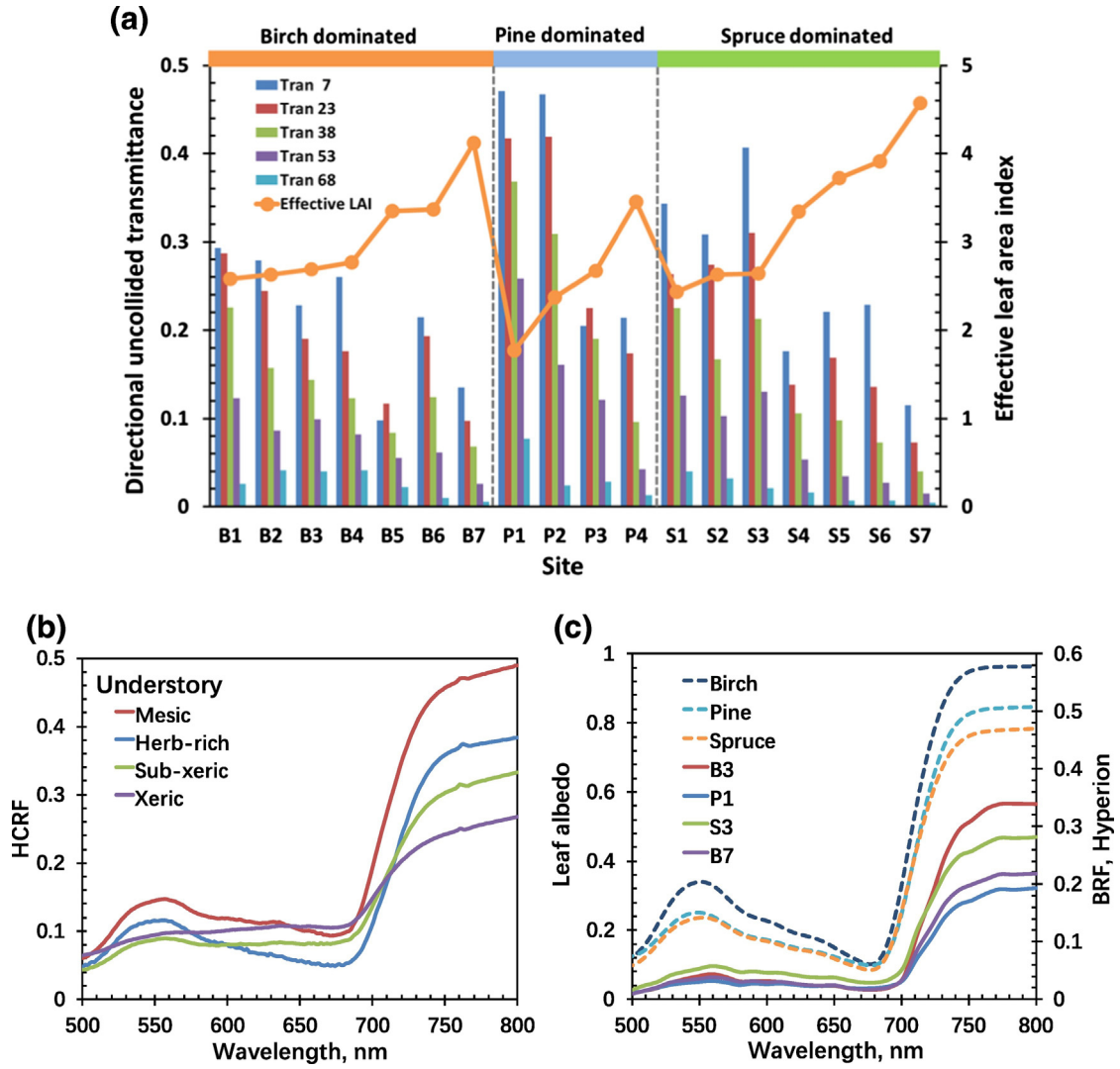

Fig. 10. Panel a: Angular profile of canopy directional uncollided transmittance (vertical axis on the left side) and effective leaf area index (vertical axis on the right side) for 18 locations (Table 1). Canopy directional uncollided transmittances are centered at five zenith angles: 7°, 23°, 38°, 53°, and 68° (legends "Tran 7" through "Tran 68"). Panel b: HCRF spectra of four understory types: herb-rich, mesic, sub-seric and xeric. Panel c: Leaf spectral albedo of Scots pine, Norway spruce needles, and Silver birch leaf (dashed lines, vertical axis on the left side). BRF spectra of pure Silver birch (B3), Scots pine (P1), Norway spruce (S3) and mixed (B7) plots (solid lines, vertical axis on the right side).

set to 0.025. Finally, we selected most probable pair (A,β) from histograms of the acceptable A and β values. This algorithm estimates mean within-crown extinction coefficient by correcting mean optical paths for crown geometry effects.

The above procedure was applied to each of 18 sites. Comparisons between simulated and predicted angular profiles suggest that the stochastic radiative transfer equations with the site specific structural parameters provide accurate estimates of the canopy directional uncollided transmittance (Fig. 11).

We used Eq. (13) to assess the ability of the stochastic radiative transfer equations to predict diffuse canopy radiation regime. The left hand side of this equation can be estimated from data on canopy directional uncollided transmittance, $t_0(\Omega)$ (Fig. 10a), which sums with the interceptance $i_0(\Omega)$ to unity, i.e., $i_0(\Omega) = 1 - t_0(\Omega)$, and the diffuse interceptance, i_{dif}, which is directly obtainable from the LAI-2000 Plant Canopy Analyzer readings (Rautiainen et al., 2009 Stenberg, 2007). It follows from Eq. (4) and (13) that $DASF_{iso} = 0.5(1 - t_0(\Omega))(1 - t_0(\Omega_0))/i_{dif}$. The right hand side of Eq. (13) can be estimated from solutions of the diffuse stochastic radiative transfer equations for vegetation canopy with non-reflecting leaves and bounded underneath by a non-reflecting surface (Section 2.4). Fig. 12 illustrates that the $DASF_{iso}$ predicted by the diffuse stochastic radiative transfer equations

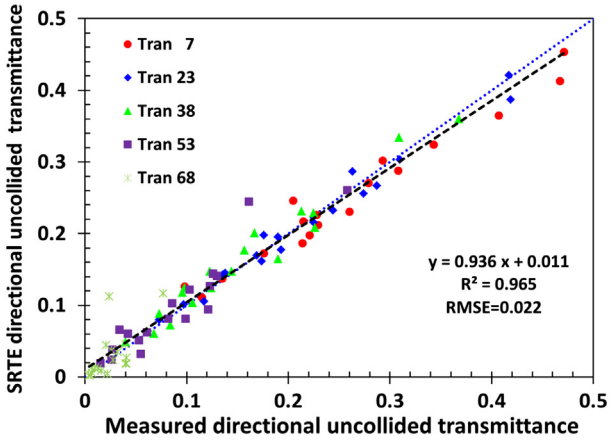

Fig. 11. Correlation between measured directional uncollided transmittances (horizontal axis) and predicted by the stochastic radiative transfer equations (vertical axis) for five zenith angles, 7°, 23°, 38°, 53° and 68° (legends "Tran 7" through "Tran 68") over 18 study plots.

with site specific structural parameters agree well with its measured counterpart.

Thus, we derived site specific wavelength independent extinction coefficients, conditional pair-correlation functions and vertical profiles of fraction covered by tree crowns, i.e., canopy structural variables that the stochastic radiative transfer equations require as input. These parameters are used in all our radiative transfer calculations.

5. Canopy-ground multiple interactions

The theoretical framework for the canopy BRF and DASF presented in Section 2 was developed under the assumption that the vegetation canopy is bounded from below by a non-reflecting surface. A radiative-transfer-based technique developed for the MODIS LAI/FPAR operational algorithm (Knyazikhin et al., 1998a) is adapted here to account for ground contributions.

The BRF of the vegetation canopy with a reflective ground can be represented as a sum of two components: the BRF calculated for the vegetation canopy with a non-reflecting underlying surface (termed as the "black soil" problem) and the contribution due to photon multiple interactions with canopy and ground, i.e.,

$$\mathrm{BRF}_\lambda(\Omega;\Omega_0) = \mathrm{BRF}_{BS,\lambda}(\Omega;\Omega_0) + \frac{r_\lambda}{1-r_\lambda \cdot R_{S,\lambda}} T_{BS,\lambda}(\Omega_0) I_{S,\lambda}(\Omega). \quad (15)$$

Here $T_{BS,\lambda}$ represents the total directional transmittance (uncollided and diffuse) for the black soil problem, and r_λ is the effective ground reflectance. The terms $I_{S,\lambda}(\Omega)$ and $R_{S,\lambda}$ are solutions of so-called "S problem," i.e, they represent canopy leaving radiance and downward reflectance if our canopy were illuminated from below by isotropic sources uniformly distributed over the canopy ground. Because $I_{S,\lambda}(\Omega)$ and $R_{S,\lambda}$ are solutions of the radiative transfer equation with non-reflecting ground, the spectral invariant approach presented in Section 2 is applicable to these terms. The BRF of the vegetated canopy with a reflective ground therefore can be expressed in terms of the wavelength dependent effective ground reflectance and leaf albedo, and spectrally invariant canopy interceptance, recollision and escape probabilities.

Results presented in Section 4 suggest that the stochastic radiative transfer equations can predict the canopy DASF, which a purely structural variable. Its estimation does not require information about leaf scattering properties. Specification of the basic structural element and its scattering coefficient is needed to estimate the canopy spectral BRF. In coniferous canopies, for example, clumped shoot structure causes multiple scattering within a shoot. The stochastic radiative transfer equations are not applicable at the needle scale because fluctuations of the number of needles in a shoot do not follow Poisson statistics. In radiative transfer models for conifers the shoot can be taken as the basic structural element (Smolander and Stenberg, 2003 Smolander and Stenberg, 2005). Its scattering coefficient, $\omega_{s,\lambda}$, is related to the needle albedo, $\omega_{0\lambda}$ as (Smolander and Stenberg, 2003 Smolander and Stenberg, 2005)

$$\omega_{s,\lambda} = \omega_{0\lambda} \frac{k_0}{1-p_0\omega_{0\lambda}}, \quad (16)$$

where the wavelength independent coefficients k_0 and p_0 depend on needle surface properties and their arrangement at a finer scale, i.e., within the shoot. The coefficients sum to unity if impact of needle surface properties can be neglected (Knyazikhin et al., 2013 Latorre-Carmona et al., 2014 Yang et al., 2016). The basic structural element can be associated e.g. with leaf, shoot, branch or tree crown. In all cases the relationship between their scattering coefficients and the leaf or needle albedo follows Eq. (16) where k_0 and p_0 account for the foliage distribution at a finer hierarchical level.

Solutions of the radiative transfer equation for the black soil and S problems have the form of Eq. (10). The canopy scattering coefficient, W_λ, is calculated using Eq. (11) with ω_λ representing the scattering coefficient of the basic structural element. The basic structural element specifies the recollision probability that appears in the canopy scattering coefficient W_λ. The DASF contains the ratio between the escape probability density and its spherical integral (see Eq. (9)). This makes this variable independent of the choice of the basic structural element (Eqs. (7) and (8) in Schull et al., 2011). The scaling properties of the scattering coefficient, recollision and escape probabilities underlie a technique to adjust retrieval algorithms for the sensor spatial resolution and spectral band composition (Ganguly et al., 2008b): the structural parameters can be pre-calculated at a fixed base scale (e.g., tree crown); the spectral BRF can be adjusted for the sensor resolution by transforming the measured leaf or needle albedo to the scattering coefficient of the basic structural element using Eq. (16) (Ganguly et al., 2008b).

In our case the tree crown is taken as the base scale. Leaves or needles are distributed within the crown in a certain fashion. We illustrate the technique outlined above to achieve consistency between the canopy scattering coefficient, within crown foliage arrangement and the spectral BRF at the Hyperion spatial resolution using data from the spectral interval between 710 and 790 nm. In this spectral interval albedo of any green leaf is related to a fixed spectrum via Eq. (16) (Knyazikhin et al., 2013 Latorre-Carmona et al., 2014 Schull et al., 2011 Yang et al., 2016) and thus two wavelength independent parameters, k_0 and p_0, suffice to specify the canopy scattering coefficient. The following algorithm was implemented. First, the spectrally invariant parameters were pre-calculated for the black soil and S problems using the stochastic radiative transfer equations with input collected at our sites. Note that the solution $I_{S,\lambda}(\Omega)$ of the S problem also have the form of Eq. (10) with the difference that spectrally invariant parameters p_A, ρ_A and i_0 are calculated assuming that our canopy is isotropically illuminated from below. Second, for each pair (k_s, p_0) the spectral BRF was calculated using scattering coefficient, $\omega_{s,\lambda}(k_s, p_0)$, obtained by transforming measured leaf albedo with Eq.(16), pre-computed structural parameters, and measured understory reflectance r_λ. Finally, we selected values of k_s and p_0 that minimized the RMSE between Hyperion and simulated BRF in the spectral interval between 710 nm and 790 nm. Fig. 13 illustrates proximity of the Hyperion and simulated BRF spectra for our 18 study plots.

To summarize, the spectral invariant approach is applicable in the general case of canopy reflective ground. The use of spectral invariants to parameterize the canopy spectral BRF makes the stochastic radiative transfer equations scalable, i.e., its solutions calculated at a fixed base scale can be adjusted for the sensor resolution and spectral band composition by changing the leaf or needle albedo with the spectrally invariant parameters unaltered.

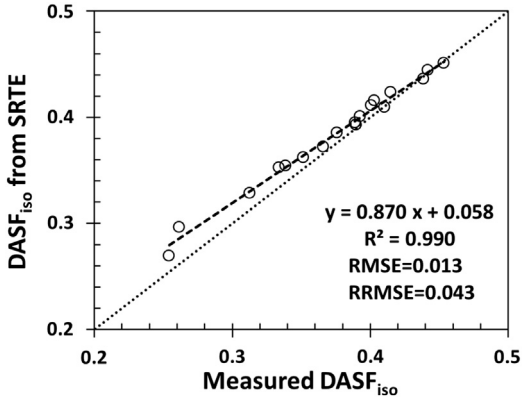

Fig. 12. Correlation between DASF_{iso} derived from field measurements (horizontal axis) and predicted by the stochastic radiative transfer equations (vertical axis) for the Hyperion sun-sensor geometry: SZA = 41°, VZA = 13.8° and RAA = 62.73°.

6. Discussion

We adapted retrieval approach implemented in the MODIS operational LAI/FPAR algorithm (Knyazikhin et al., 1998a Knyazikhin et al., 1998b). The algorithm compares measured spectral BRF with those evaluated from model-based entries stored in the LUT. All canopy structural variables and ground reflectance for which modeled and measured BRFs agree within uncertainties in the observed and modeled canopy reflectances are considered as acceptable solutions. The mean value of a structural variable of interest (e.g., LAI, VFLA and SLAI = LAI·VFLA) and its dispersion are taken as the solution of the inverse problem and its retrieval uncertainty. In addition to the measured BRFs, biome type and uncertainties in model and observations are also inputs to the algorithm (Wang et al., 2001). The LUT is a key element of the retrieval technique that determines its performance. Here we discuss differences between MODIS and EPIC LUTs.

Both LUTs are based on the representation of the modeled BRF via solutions of the black soil and S problems (Section 5), which are stored in the LUT. The EPIC LUT contains pre-calculated values of DASF, escape and recollision probabilities for the black soil and S problems, which correspond to various combinations of the sun-sensor geometry and canopy structural organization. The BRF for the black soil problem and solution of the S problem, $I_{S,\lambda}$, are calculated using Eq. (10). The spectral leaf albedo that appears in this equation becomes a biome-dependent configurable parameter that accounts for the sensor resolution and spectral band composition. Its specification is a part of the algorithm calibration and is based on analyses of the measured and simulated BRFs over validation sites representing various biome types as outlined in Section 5. Given sun-sensor geometry and biome type, the spectral BRF is modeled using Eq. (15), pre-calculated structural variables and spectral patterns of the effective ground reflectance (which are also stored in the LUT).

Note that Eq. (10) not only provides a highly accurate approximation of solutions of the radiative transfer equations for vegetation canopies with non-reflecting ground, but also follows scaling relationships between the basic structural element, its scattering spectrum and spectral BRF. This feature underlies the scale-dependent formulation of the radiative transfer process in vegetation canopies. The spectrally invariant relationships for canopy transmittance, absorptance and reflectance used in various process oriented models (Stenberg et al., 2016) are special cases of Eq. (15) that naturally follow from its hemispherical integrations (Huang et al., 2007).

The MODIS LUT stores the ratio between BRF and directional hemispherical reflectance (DHR) at a fixed wavelength for the black soil and S problems as a function of the sun-sensor geometry and canopy structure (Knyazikhin et al., 1998a Knyazikhin et al., 1998b). The spectral DHR is expressed via spectral canopy transmittance and absorptance, which in turn are calculated using spectrally invariant relationships for the canopy transmittance and absorptance. The BRF is assembled using Eq. (15), pre-calculated ratio, spectral DHR and patterns of the effective ground reflectance. The biome dependent spectral leaf albedo is also configurable parameter that controls consistency between the basic structural element and canopy spectral transmittance and absorptance at the sensor spatial resolution. The scaling properties however are not fully realized in the MODIS LUT because the spectrally invariant relationships are utilized only for the special cases of canopy reflectance and transmittance. This results in higher model uncertainties due to adjustments of the LUT for the sensor characteristics compared to the EPIC LUT.

Another important distinction between the EPIC and MODIS LUTs is that the former accounts for the stochastic boundary whereas the latter assumes infinitesimal scatters. The MODIS LUT based algorithm does not perform retrievals if the view direction falls within the hot spot region. Recall that DASF for the vegetation canopy with the stochastic boundary is a weighted sum of $DASF_0$ calculated assuming infinitesimal scatters and $DASF_b$ of the stochastic boundary (Eq. (12)). The EPIC LUT incorporates this decomposition, i.e., it contains $DASF_0$, $DASF_b$ and the correlation coefficient h. The correlation coefficient depends on a model used to simulate the hot spot effect. This feature allows for integration of various hot spot models into the retrieval technique without recalculating $DASF_0$ and $DASF_b$.

The parameterization of the LUT in terms of structural variables obtainable from both space and ground measurements is the key advantage of the EPIC LUT over its MODIS counterpart. For example, for vegetation canopies with a dark background or for sufficiently dense vegetation where the impact of the canopy background is negligible, the DASF can be directly retrieved from the BRF spectrum in the 710 to 790 nm interval without the use of canopy reflectance models, prior knowledge, or ancillary information regarding the leaf optical properties using a simple algorithm documented in Knyazikhin et al. (2013). The DASF can be compared with LUT entries. In general case the removal of the ground contribution to BRF should precede retrieval of DASF. Eq. (15), which is incorporated in the LUT, provides physical basis for removing ground influences from measured spectral BRF. The field and hyperspectral data therefore can be used to assess the EPIC LUT, to diagnose its deficiencies and to develop refinements. We illustrate this feature using field data and hyperspectral images.

First, we used the pre-calculated site specific spectral invariants for the black soil and S problems (Section 4), measured ground reflectance and the sensor adjusted leaf albedo to evaluate the term in Eq. (15) that accounts for ground contributions. This term was subtracted from the Hyperion BRF to estimate $BRF_{BS,\lambda}(\Omega;\Omega_0)$. We applied the algorithm reported in Knyazikhin et al. (2013) to $BRF_{BS,\lambda}$ to derive Hyperion $DASF(\Omega;\Omega_0)$ (Appendix D) over our study sites. The view direction of

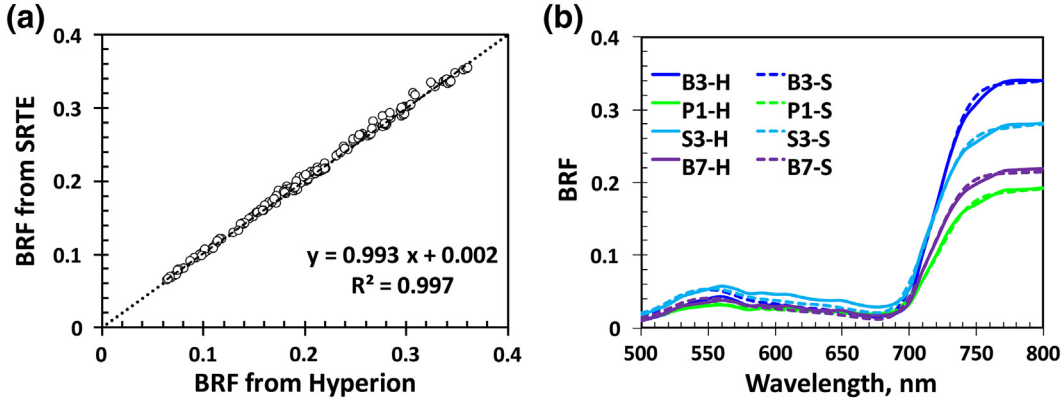

Fig. 13. Panel a: Correlation between Hyperion $BRF_{H,\lambda}(\Omega)$ and SRTE-estimated $BRF_{\lambda}(\Omega)$ in the 710- to 790 nm spectral interval for 18 study plots. Panel b: Simulated (dashed lines) and Hyperion (solid lines) BRF spectra of pure Silver birch (B3), Scots pine (P1), Norway spruce (S3) and mixed (B7) forests. The RMSE (and R^2) for the 500 to 700 nm interval are 0.007 (0.845), 0.003 (0.831), 0.005 (0.778) and 0.004 (0.807), respectively. The remaining sites showed similar behavior.

the Hyperion sensor was outside of the hot spot region (i.e., $h(\Omega;\Omega_0)\approx 0$) and thus the retrieved DASF provides an estimate of $DASF_0$ in the direction to the sensor.

Next, we calculated DASF in the direction $-\Omega$ using the stochastic radiative transfer equations and site specific canopy structural parameters. The simulated and Hyperion DASFs were then used to evaluate $DASF_{iso}$ as the semi-sum of their values for up- and downward directions. The correlation between $DASF_{iso}$ derived from Hyperion images and field data shown in Fig. 14 suggests that the modeled DASF is accurate for our broad- and needle leaf dominant forest sites at the Hyperion resolution and LAI range between 2 and 5.

Finally, we estimated $i_0(\Omega)$ from Eq. (4) as $i_0(\Omega) = 2DASF_{iso} i_{dif}/i_0(\Omega_0)$ with the ratio $i_{dif}/i_0(\Omega_0)$ calculated using the stochastic radiative transfer equations and site specific canopy structural parameters. The canopy interceptance in the direction Ω was then converted to VFLA(Ω) with Eq. (1). The VFLA(Ω) can also be directly estimated from below canopy measurements of the canopy directional uncollided transmittance. The correlation between VFLA derived from field measurements and Hyperion image shown in Fig. 15 suggests the LUT developed for our sites provides an accurate relationship between canopy BRF and VFLA at the Hyperion resolution and consequently supports our theoretical basis.

7. Concluding remarks

This paper presents the theoretical basis of the algorithm designed for the generation of leaf area index and its sunlit fraction from NASA's EPIC instrument onboard NOAA's DSCOVR spacecraft. The algorithm ingests spectral surface BRF data, canopy architectural type (or biome), model and observation uncertainties. The technique used in the MODIS LAI/FPAR operational algorithm is adapted to select most probable values of LAI, SFLA, SLAI = SFLA·LAI and their uncertainties. The use of spectral invariants in the parameterization of the MODIS LUT imbued scale dependency to the algorithm, which is among key requirements to generate long-term records of biophysical parameters from remote sensing measurements of multiple sensors (Ganguly et al., 2008a Ganguly et al., 2008b). The theoretical basis of the MODIS LUT however has not been revised since 1998 when the first spectrally invariant parameter, maximum eigenvalue of the radiative transfer equation, was originally introduced (Knyazikhin et al., 1998a Knyazikhin et al., 1998b). The purpose of our study has been to modify the LUT through incorporations of the canopy hot spot phenomenon and recent advances in the theory of canopy spectral invariants (Stenberg et al., 2016) and to integrate the retrieval of the VFLA into the MODIS algorithm. The modifications improve decoupling of the structural and radiometric components of the BRF and algorithm scaling properties,

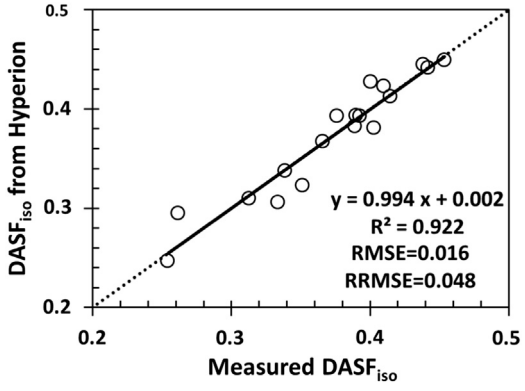

Fig. 14. Correlation between $DASF_{iso}$ derived from field measurements (horizontal axis) and Hyperion image (vertical axis) for 18 study sites. Here SZA = 41°, VZA = 13.8° and RAA = 62.73°.

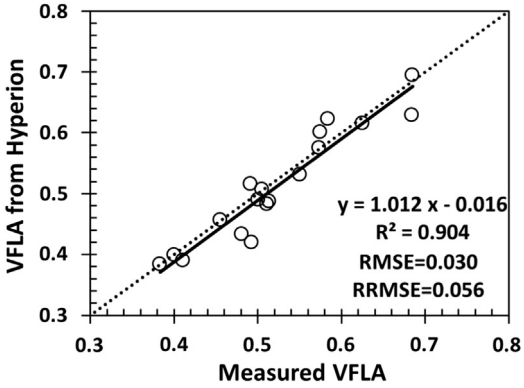

Fig. 15. Correlation between VFLA derived from field measurements (horizontal axis) and Hyperion image (vertical axis) for 18 study sites. Here SZA = 41°, VZA = 13.8° and RAA = 62.73°.

which are important prerequisites for achieving consistency and complementarity between DSCOVR EPIC and existing satellite derived land surface biophysical parameters. The stochastic radiative transfer equations are used to generate the EPIC LUT for all biome types. The equations naturally account for the effects of the three-dimensional canopy structure on the BRF and therefore an accurate discrimination between sunlit and shaded leaf areas is expected. The entries of the EPIC LUT are measurable, i.e., they can be independently derived from both below canopy measurements of the transmitted and above canopy measurements of reflected radiation fields. This is the key advantage of the EPIC LUT over its MODIS counterpart because this feature makes possible direct validation of the LUT, facilitates identification of its deficiencies and development of refinements. Analyses of field data and hyperspectral images suggest that the EPIC LUT accurately follows regularities expected from the theory.

Acknowledgment

This research was funded by the NASA DSCOVR project under grant NNX15AB11G. B. Yang and L. Yan were supported in part by the National Natural Science Foundation of China No. 41371492, Doctoral Program No. 20130001110046 and Chinese Scholarship Council No. 201406010058. M. Mõttus and M. Rautiainen were supported by the Academy of Finland under grants 266152 and 13286390, respectively.

Appendix A. Stochastic model of canopy structure and radiation regime

We use the Boolean model of random set to simulate 3D canopy structure (Stoyan et al., 1995). The following stationary Poisson germ-grain stochastic process of intensity d (in number per volume) is implemented. A random number $k = dV$ of leaves within a volume $V = HS$ is selected using the Poisson distribution $P(k) = (\bar{k})^k \exp(-\bar{k})/k!$ where $\bar{k}$ is the mean value of the random variable k. Random locations of k leaves in V are generated with a uniform distribution function. On each of these points a disc of radius r (Fig. 2b) is placed. Their random orientation is generated with a leaf normal distribution function $g_L(\Omega_L)$. The volume V with k randomly oriented leaves (Fig. 2a) is a realization of the canopy structure. The leaf area volume density of the canopy realization is $\pi r^2 k/V$. Its ensemble average value results in $u_L = \pi r^2 d$. In the terminology the points of the Poisson process are the germs while the discs represent the grains (Stoyan et al., 1995).

The discs simulate bi-Lambertian leaves, i.e., the incident photons are reflected from, or transmitted though, the disc in a cosine distribution about its normal. Its scattering properties are parameterized in terms of leaf transmittance, τ_L, and reflectance, r_L. Their sum is the leaf albedo, $\omega = \tau_L + r_L$. The leaf normal distribution function for spherically oriented leaves is $g_L(\Omega_L) = 1$. For non-spherically oriented leaf normal

$\Omega_L=(\theta_L,\varphi_L)$, a trigonometrical representation of $g_L(\Omega_L)$ is used (Bunnik, 1978), i.e.,

$$g_L(\Omega_L)=\frac{2}{\pi}\left(\frac{1+a\ \cos b\theta_L}{\sin\theta_L}\right). \tag{A1}$$

This model includes planophile ($a=1,b=2$), erectophile ($a=-1,b=2$), plagiophile ($a=-1,b=4$), extremophile ($a=1,b=4$) and uniform ($a=0$) leaves.

Each disc is divided into n equal sub-areas $s_0=\pi r^2/n$, which represents smallest resolvable scale (Fig. 2b). The bi-Lambertian scattering is simulated for each sub-area s_0. The disc radius is expressed relative to the canopy height H, i.e., $r/H=\alpha$. We define the indicator function $\chi(\mathbf{x},\Omega)$ of gaps such that it is 1 if there is a free line of sight through the canopy from the point $\mathbf{x}$ on a sub-area s_0 in the direction Ω, and 0 otherwise (Stenberg, 2007). Since the canopy structure is treated as a stochastic process, the gap distribution $\chi(\mathbf{x},\Omega)$ is a stochastic function of space. Its ensemble average value describes gap density per unit solid angle per unit leaf area.

For each realization of canopy structure and a set of N_Ω directions distributed on a unit sphere, we count photons that recollide, $N'=\sum_{\mathbf{x},\Omega}[1-\chi(\mathbf{x},\Omega)]|\Omega\cdot\Omega_L(\mathbf{x})|$ and exit the canopy through gaps along the direction Ω, $M(\Omega)=\sum_{\mathbf{x}}\ \chi(\mathbf{x},\Omega)|\Omega\cdot\Omega_L(\mathbf{x})|$. Realizations of the total leaf semi-surface area, A_T, their visible, $A_V(\Omega)$, shaded, $A_{sh}(\Omega\neg\Omega_0)$, and bi-directional sunlit, $B(\Omega\&\Omega_0)$, areas were estimated as $A_T=s_0kn$, $A_V(\Omega)=s_0\sum_{\mathbf{x}}\ \chi(\mathbf{x},\Omega)$, $A_{sh}(\Omega\neg\Omega_0)=s_0\sum_{\mathbf{x}}\chi(\mathbf{x},\Omega)(1-\chi(\mathbf{x},\Omega_0))$, and $B(\Omega\&\Omega_0)=s_0\sum_{\mathbf{x}}\chi(\mathbf{x},\Omega)\chi(\mathbf{x},\Omega_0)$. Ensemble average values of these random variables were assigned to the recollision, $p_{iso}=\langle N'\rangle/\langle A_T\rangle$ and escape $2\rho_{iso}(\Omega)=\langle M(\Omega)\rangle/\langle A_T\rangle$ probabilities, $\mathrm{VFLA}(\Omega)=\langle A_V(\Omega)\rangle/\langle A_T\rangle$, $\mathrm{VFLA}_{sh}(\Omega\neg\Omega_0)=\langle A_{sh}(\Omega)\rangle/\langle A_T\rangle$, $\mathrm{BSFLA}(\Omega\&\Omega_0)=\langle B(\Omega\&\Omega_0)\rangle/\langle A_T\rangle$, and $i_0(\Omega)=\langle M(\Omega)\rangle/(S\mu)$. Here $\langle\cdot\rangle$ designates ensemble averaging, i.e., over all realizations of canopy structure in V. The correlation coefficient of $\mathrm{VFLA}(\Omega)$ and $\mathrm{SFLA}=\mathrm{VFLA}(\Omega_0)$ was calculated as

$$h_{iso}(\Omega;\Omega_0)=\frac{\mathrm{BSFLA}(\Omega\&\Omega_0)-\mathrm{VFLA}(\Omega)\mathrm{VFLA}(\Omega_0)}{\sqrt{\left[\mathrm{VFLA}(\Omega)-\mathrm{VFLA}^2(\Omega)\right]\left[\mathrm{VFLA}(\Omega_0)-\mathrm{VFLA}^2(\Omega_0)\right]}} \tag{A2}$$

From simulations, the joint probability $\mathrm{VFLA}_{sh}(\Omega\neg\Omega_0)$ was found to be equal to $[1-h_{iso}(\Omega;\Omega_0)]\mathrm{VFLA}(\Omega)(1-\mathrm{VFLA}(\Omega_0))$, as expected. We introduce a fraction of shaded leaves visible outside the canopy along a given direction $-\Omega$ as the conditional probability of seeing a shaded leaf under the condition that the leaf area does not belong to the canopy boundary, i.e $\mathrm{VFLA}_{sh}(\Omega;\Omega_0)=\mathrm{VFLA}_{sh}(\Omega\neg\Omega_0)/(1-\mathrm{VFLA}(\Omega_0))=(1-h(\Omega;\Omega_0))\mathrm{VFLA}(\Omega)$.

The joint probability that a photon scattered by the boundary and escape the vegetation was calculated as $\langle\sum_r\chi(\mathbf{x},\Omega)\chi(\mathbf{x},\Omega_0)|\Omega\cdot\Omega_L(\mathbf{x})||-\Omega_0\cdot\Omega_L(\mathbf{x})|\rangle/\langle A_T\rangle$. From simulations, this probability was found to be equal to $\mathrm{BSFLA}(\Omega\&\Omega_0)\Gamma(\Omega_0\to\Omega)/G(\Omega_0)$, as expected, where G and Γ are the geometry factor and area scattering phase function, respectively (Ross, 1981). The conditional probability density by which a photon scattered by the boundary will escape the vegetation in the direction Ω is $j_{iso}(\Omega;\Omega_0)=\Gamma(\Omega_0\to\Omega)/G(\Omega_0)$. It describes number of canopy leaving photons per unit sunlit area (i.e., per unit boundary area). The escape probability, $\rho_{b,iso}(\Omega;\Omega_0)$, for the stochastic model with the boundary in the direction Ω_0 can therefore be represented as $\rho_{b,iso}(\Omega;-\Omega_0)=(1-h_{iso}(\Omega;\Omega_0))\rho_{iso}(\Omega)+j_{iso}(\Omega;\Omega_0)h_{iso}(\Omega;\Omega_0)$. Solving this equation for h_{iso} one obtains

$$h_{iso}(\Omega;\Omega_0)=\frac{\rho_{b,iso}(\Omega;\Omega_0)-\rho_{iso}(\Omega)}{j_{iso}(\Omega;\Omega_0)-\rho_{iso}(\Omega)} \tag{A3}$$

We use this equation to evaluate the correlation coefficient from solutions of the stochastic radiative transfer equations as detailed in Appendix B.2.

Appendix B. Stochastic radiative transfer equations

B.1. Ensemble average intensity and its second moment

Let a stochastic canopy resided in the layer $0\le z\le H$ be subjected to a monodirectioanl beam in the direction $\Omega_0=(\theta_0,\varphi_0)$ of intensity L_0. Vertical profiles of the horizontal average intensity, $I(z,\Omega)$, and its second moment, the mean intensity incident on the leaf surface, $U(z,\Omega)$, at depth z satisfy a system of stochastic equations (Huang et al., 2008). The vertical profiles, $L_0I_0(z)\delta(\Omega-\Omega_0)$ and $L_0U_0(z)\delta(\Omega-\Omega_0)$, of the uncollided (direct) intensities in the direction Ω_0 are solutions of the following equations,

$$I_0(z)+\frac{\sigma(\Omega_0)}{\mu_0}\int_0^z a(\xi)U_0(\xi)d\xi=1, \tag{B1a}$$

$$U_0(z)+\frac{\sigma(\Omega_0)}{\mu_0}\int_0^z K(z,\xi,\Omega_0)U_0(\xi)d\xi=1. \tag{B1b}$$

Here $\mu_0=\cos\theta_0$; $\sigma(\Omega)$ denotes the extinction coefficient; $a(\xi)$ is the probability of finding a foliated point at depth ξ, and $K(z,\xi,\Omega)$ represents the conditional pair-correlation function, i.e., $a(z)K(z,\xi,\Omega)$ is the probability of finding simultaneously foliated points at depths z and ξ along a given direction Ω (Huang et al., 2008 Vainikko, 1973). The conditional pair-correlation function describes spatial correlation between phytoelements, e.g., clumping of leaves into branches, branches into crowns, etc. If leaves are not spatially correlated ($K=a(\xi)$), Eqs. (B1a) and (B1b) coincide and their solutions are the Beer-Lambert law. Equations for diffuse components and various models of a and K can be found in Huang et al. (2008).

Solution of Eqs. (B1a) and (B1b) at the canopy bottom, $z=H$, is the canopy directional uncollided transmittance in the direction Ω_0. This variable can be estimated from measurements of downward fluxes below and above the canopy using the LAI-2000 plant analyzer (Rautiainen et al., 2009 Rautiainen and Stenberg, 2015 Stenberg, 2007). The canopy interceptance is then $i_0(\Omega_0)=1-I_0(H)$.

The mean irradiance on leaf sides, F, and source function, S, are given by

$$F=\int_0^H\int_{4\pi}\sigma(\Omega)a(z)U(z,\Omega)dzd\Omega, \tag{B2}$$

$$S(z,\Omega)=\frac{1}{\pi}\int_{4\pi}P(\Omega'\to\Omega)\sigma(\Omega')U(z,\Omega')d\Omega' \tag{B3}$$

where $P(\Omega'\to\Omega)=\Gamma(\Omega'\to\Omega)/G(\Omega')$. We use the stochastic radiative transfer equations to simulate BRF of vegetated surface. The method of successive orders of scattering approximation was used to numerically solve the system for the diffuse components as well as to estimate terms in Neumann series (Eq. (5)).

B.2. Correlation coefficient

The radiative transfer equation is formulated for interior points in the domain in which the radiative transfer process occurs. The shaded leaves represent the interior points. To exclude the stochastic boundary from the domain the leaf area volume density is represented as $u_L[1-c_{HS}(\Omega;\Omega_0)]$ where c_{HS} is a hot spot parameter that accounts for the statistical dependency of seeing gaps in the direction Ω from the sunlit areas of leaves. We followed (Kuusk, 1991) techniques to evaluate this parameter. The escape probability density, $\rho(\Omega;\Omega_0)$, derived from solutions of the boundary value problem for the radiative transfer equation accounts for both photons scattered by shaded and sunlit leaf areas. If

c_{HS} is set to zero the corresponding escape probability density, $\rho_0(\Omega)$, quantifies the escape event due to photon interactions with shaded leaves. In this case the equation acts in much the same way as we estimate the probabilities in Section 2.1, i.e., it assumes that there are no points on leaf surfaces from which photons can escape the vegetation with unit probability. The correlation coefficient h can be estimated from Eq. (A3) in which $\rho(\Omega;\Omega_0)$ and $\rho_0(\Omega)$ are used in place of $\rho_{b,iso}(\Omega;\Omega_0)$ and $\rho_{iso}(\Omega)$. Its specification requires to solve the stochastic equations two times, first with an actual c_{HS} to get $\rho_b(\Omega;\Omega_0)$, and then with c_{HS} set to zero in order to obtain $\rho_0(\Omega)$.

Appendix C. Estimation of average escape and recollision probabilities

It follows from Eq. (10) that the ratio $BRF_\lambda(\Omega;\Omega_0)/\omega_\lambda$ is linearly related to $BRF_\lambda(\Omega;\Omega_0)$ where slope and intercept give p_A and $\rho_A(\Omega;\Omega_0)i_0(\Omega_0)$. We use this obvious property to specify the average recollision and escape probabilities as follows: solve stochastic radiative transfer equations for several values of leaf albedo first and then specify slope and intercept from the $BRF_\lambda(\Omega;\Omega_0)/\omega_\lambda$ vs. $BRF_\lambda(\Omega;\Omega_0)$ linear relationship. The slope is the average recollision probability. The average escape probability is the ratio between the intercept and $i_0(\Omega_0)$. The escape probability can be decomposed into contributions from shaded and sunlit leaves as described in Sect. B2.

Appendix D. Retrieving DASF from hyperspectral BRF

The algorithm for the estimation of DASF from the BRF spectrum in the 710 to 790 nm interval uses the transformed reference leaf albedo $\varpi_{0\lambda}$, which is related to the sensor-adjusted leaf albedo, $\omega_{s,\lambda}$, as (Knyazikhin et al., 2013)

$$\omega_{s,\lambda} = \frac{1-p_L}{1-\varpi_{0\lambda}p_L}\,\varpi_{0\lambda}i_L, \tag{D1}$$

where p_L is the wavelength independent within-leaf recollision probability, and i_L represents the fraction of radiation scattered at the surface of leaves. The latter is a wavelength-independent function of leaf surface properties. The algorithm results in the following estimate of the DASF (Knyazikhin et al., 2013),

$$\mathrm{DASF}(\Omega;\Omega_0) = \frac{\rho_A(\Omega;\Omega_0)i_0(\Omega_0)}{1-p_Ai_L}\,i_L, \tag{D2}$$

where $i_0(\Omega_0)$, $\rho_A(\Omega;\Omega_0)$ and p_A are the canopy interceptance, average escape and recollision probabilities. The retrieved DASF should be normalized by $(1-p_A)i_L/(1-p_Ai_L)$ to obtain its LUT counterpart. Site specific values of i_L can be found from measured spectra of leaf albedo (Latorre-Carmona et al., 2014 Schull et al., 2011 Vanhatalo et al., 2014). We followed the methodology documented in Schull et al. (2011).

References

Bonan, G.B., Levis, S., Sitch, S., Vertenstein, M., Oleson, K.W., 2003. A dynamic global vegetation model for use with climate models: concepts and description of simulated vegetation dynamics. Glob. Chang. Biol. 9, 1543–1566.

Bunnik, N.J.J., 1978. The Multispectral Reflectance of Shortwave Radiation by Agricultural Crops in Relation With Their Morphological and Optical Properties.

Chen, J.M., Black, T., 1992. Defining leaf area index for non-flat leaves. Plant Cell Environ. 15, 421–429.

Chen, J.M., Liu, J., Leblanc, S.G., Lacaze, R., Roujean, J.-L., 2003. Multi-angular optical remote sensing for assessing vegetation structure and carbon absorption. Remote Sens. Environ. 84, 516–525.

Chen, J.M., Mo, G., Pisek, J., Liu, J., Deng, F., Ishizawa, M., Chan, D., 2012. Effects of foliage clumping on the estimation of global terrestrial gross primary productivity. Glob. Biogeochem. Cycles 26.

Dai, Y., Dickinson, R.E., Wang, Y.-P., 2004. A two-big-leaf model for canopy temperature, photosynthesis, and stomatal conductance. J. Clim. 17, 2281–2299.

Davis, A.B., Knyazikhin, Y., 2005. A primer in 3D radiative transfer. 3D Radiative Transfer in Cloudy Atmospheres. Springer, pp. 153–242.

Doughty, C.E., Goulden, M.L., 2008. Seasonal patterns of tropical forest leaf area index and CO_2 exchange. J. Geophys. Res. Biogeosci. 2005–2012, 113.

Ganguly, S., Samanta, A., Schull, M.A., Shabanov, N.V., Milesi, C., Nemani, R.R., Knyazikhin, Y., Myneni, R.B., 2008a. Generating vegetation leaf area index Earth system data record from multiple sensors. Part 2: implementation, analysis and validation. Remote Sens. Environ. 112, 4318–4332.

Ganguly, S., Schull, M.A., Samanta, A., Shabanov, N.V., Milesi, C., Nemani, R.R., Knyazikhin, Y., Myneni, R.B., 2008b. Generating vegetation leaf area index earth system data record from multiple sensors. Part 1: theory. Remote Sens. Environ. 112, 4333–4343.

Garrigues, S., Lacaze, R., Baret, F., Morisette, J.T., Weiss, M., Nickeson, J.E., Fernandes, R., Plummer, S., Shabanov, N.V., Myneni, R.B., 2008. Validation and intercomparison of global Leaf Area Index products derived from remote sensing data. J. Geophys. Res. Biogeosci. 113 (G02028), 58–70.

Gerstl, S.A.W., 1999. Building a global hotspot ecology with Triana data. Remote Sens. Earth Sci. Ocean Sea Ice Applic. 3868, 184–194.

Goel, N.S., Qin, W.H., Wang, B.Q., 1997. On the estimation of leaf size and crown geometry for tree canopies from hotspot observations. J. Geophys. Res.-Atmos. 102, 29543–29554.

Goodenough, D.G., Dyk, A., Niemann, K.O., Pearlman, J.S., Hao, C., Tian, H., Murdoch, M., West, C., 2003. Processing hyperion and ALI for forest classification. IEEE Trans. Geosci. Remote Sens. 41, 1321–1331.

He, M., Ju, W., Zhou, Y., Chen, J., He, H., Wang, S., Wang, H., Guan, D., Yan, J., Li, Y., 2013. Development of a two-leaf light use efficiency model for improving the calculation of terrestrial gross primary productivity. Agric. For. Meteorol. 173, 28–39.

Heiskanen, J., Rautiainen, M., Stenberg, P., Mõttus, M., Vesanto, V.-H., Korhonen, L., Majasalmi, T., 2012. Seasonal variation in MODIS LAI for a boreal forest area in Finland. Remote Sens. Environ. 126, 104–115.

Heiskanen, J., Rautiainen, M., Stenberg, P., Mõttus, M., Vesanto, V.-H., 2013. Sensitivity of narrowband vegetation indices to boreal forest LAI, reflectance seasonality and species composition. ISPRS J. Photogramm. Remote Sens. 78, 1–14.

Huang, D., Knyazikhin, Y., Dickinson, R.E., Rautiainen, M., Stenberg, P., Disney, M., Lewis, P., Cescatti, A., Tian, Y., Verhoef, W., 2007. Canopy spectral invariants for remote sensing and model applications. Remote Sens. Environ. 106, 106–122.

Huang, D., Knyazikhin, Y., Wang, W., Deering, D.W., Stenberg, P., Shabanov, N., Tan, B., Myneni, R.B., 2008. Stochastic transport theory for investigating the three-dimensional canopy structure from space measurements. Remote Sens. Environ. 112, 35–50.

Hueni, A., Nieke, J., Schopfer, J., Kneubühler, M., Itten, K.I., 2009. The spectral database SPECCHIO for improved long-term usability and data sharing. Comput. Geosci. 35, 557–565.

Knyazikhin, Y., Marshak, A., 1991. Fundamental equations of radiative transfer in leaf canopies and iterative methods for their solution. In: Myneni, R.B., Ross, J. (Eds.), Photon-Vegetation Interactions: Applications in Plant Physiology and Optical Remote Sensing. Springer-Verlag, Berlin Heidelberg, pp. 9–43.

Knyazikhin, Y., Martonchik, J., Myneni, R., Diner, D., Running, S., 1998a. Synergistic algorithm for estimating vegetation canopy leaf area index and fraction of absorbed photosynthetically active radiation from MODIS and MISR data. J. Geophys. Res. Atmos. 103, 32257–32275 (1984–2012).

Knyazikhin, Y., Martonchik, J.V., Diner, D.J., Myneni, R.B., Verstraete, M., Pinty, B., Gobron, N., 1998b. Estimation of vegetation canopy leaf area index and fraction of absorbed photosynthetically active radiation from atmosphere-corrected MISR data. J. Geophys. Res.-Atmos. 103, 32239–32256.

Knyazikhin, Y., Schull, M.A., Xu, L.A., Myneni, R.B., Samanta, A., 2011. Canopy spectral invariants. Part 1: a new concept in remote sensing of vegetation. J. Quant. Spectrosc. Radiat. Transf. 112, 727–735.

Knyazikhin, Y., Schull, M.A., Stenberg, P., Mottus, M., Rautiainen, M., Yang, Y., Marshak, A., Carmona, P.L., Kaufmann, R.K., Lewis, P., Disney, M.I., Vanderbilt, V., Davis, A.B., Baret, F., Jacquemoud, S., Lyapustin, A., Myneni, R.B., 2013. Hyperspectral remote sensing of foliar nitrogen content. Proc. Natl. Acad. Sci. U. S. A. 110, E185–E192.

Kuusk, A., 1991. The hot spot effect in plant canopy reflectance. Photon-Vegetation Interactions. Springer, pp. 139–159.

Latorre-Carmona, P., Knyazikhin, Y., Alonso, L., Moreno, J.F., Pla, F., Yan, Y., 2014. On hyperspectral remote sensing of leaf biophysical constituents: decoupling vegetation structure and leaf optics using CHRIS–PROBA data over crops in Barrax. IEEE Geosci. Remote Sens. Lett. 11, 1579–1583.

Lewis, P., Disney, M., 2007. Spectral invariants and scattering across multiple scales from within-leaf to canopy. Remote Sens. Environ. 109, 196–206.

Lukeš, P., Stenberg, P., Rautiainen, M., Mõttus, M., Vanhatalo, K.M., 2013. Optical properties of leaves and needles for boreal tree species in Europe. Remote Sens. Lett. 4, 667–676.

Malenovský, Z., Albrechtová, J., Lhotáková, Z., Zurita-Milla, R., Clevers, J.G.P.W., Schaepman, M.E., Cudlín, P., 2006. Applicability of the PROSPECT model for Norway spruce needles. Int. J. Remote Sens. 27, 5315–5340.

Martonchik, J.V., Bruegge, C.J., Strahler, A.H., 2000. A review of reflectance nomenclature used in remote sensing. Remote Sens. Rev. 19, 9–20.

Matthew, M.W., Adler-Golden, S.M., Berk, A., Richtsmeier, S.C., Levine, R.Y., Bernstein, L.S., Acharya, P.K., Anderson, G.P., Felde, G.W., Hoke, M.L., Ratkowski, A.J., Burke, H.-h.K., Kaiser, R.D., Miller, D.P., 2000. Status of Atmospheric Correction Using a MODTRAN4-based Algorithm. pp. 199–207.

Mercado, L.M., Bellouin, N., Sitch, S., Boucher, O., Huntingford, C., Wild, M., Cox, P.M., 2009. Impact of changes in diffuse radiation on the global land carbon sink. Nature 458, 1014–1017.

Miller, J., 1967. A formula for average foliage density. Aust. J. Bot. 15, 141–144.

Nilson, T., 1991. Approximate analytical methods for calculating the reflection functions of leaf canopies in remote sensing applications. Photon-Vegetation Interactions. Springer, pp. 161–190.

Norman, J.M., 1982. Simulation of microclimates. Biometeorology in Integrated Pest Management, pp. 65–99.
Otsu, N., 1975. A threshold selection method from gray-level histograms. Automatica 11, 23–27.
Pearlman, J.S., Barry, P.S., Segal, C.C., Shepanski, J., Beiso, D., Carman, S.L., 2003. Hyperion, a space-based imaging spectrometer. IEEE Trans. Geosci. Remote Sens. 41, 1160–1173.
Qin, W., Goel, N.S., Wang, B., 1996. The hotspot effect in heterogeneous vegetation canopies and performances of various hotspot models. Remote Sens. Rev. 14, 283–332.
Qin, W.H., Gerstl, S.A.W., Deering, D.W., Goel, N.S., 2002. Characterizing leaf geometry for grass and crop canopies from hotspot observations: a simulation study. Remote Sens. Environ. 80, 100–113.
Rautiainen, M., Lukeš, P., 2015. Spectral contribution of understory to forest reflectance in a boreal site: an analysis of EO-1 Hyperion data. Remote Sens. Environ. 171, 98–104.
Rautiainen, M., Stenberg, P., 2015. On the angular dependency of canopy gap fractions in pine, spruce and birch stands. Agric. For. Meteorol. 206, 1–3.
Rautiainen, M., Mõttus, M., Stenberg, P., Ervasti, S., 2008. Crown envelope shape measurements and models. Silva Fenn. 42, 19–23.
Rautiainen, M., Mõttus, M., Stenberg, P., 2009. On the relationship of canopy LAI and photon recollision probability in boreal forests. Remote Sens. Environ. 113, 458–461.
Rautiainen, M., Mõttus, M., Heiskanen, J., Akujärvi, A., Majasalmi, T., Stenberg, P., 2011. Seasonal reflectance dynamics of common understory types in a northern European boreal forest. Remote Sens. Environ. 115, 3020–3028.
Ross, J., 1981. The Radiation Regime and Architecture of Plant Stands. Dr W. Junk Publishers.
Ross, J.K., Marshak, A.L., 1988. Calculation of canopy bidirectional reflectance using the Monte-Carlo method. Remote Sens. Environ. 24, 213–225.
Schaepman-Strub, G., Schaepman, M.E., Painter, T.H., Dangel, S., Martonchik, J.V., 2006. Reflectance quantities in optical remote sensing-definitions and case studies. Remote Sens. Environ. 103, 27–42.
Schull, M.A., Knyazikhin, Y., Xu, L., Samanta, A., Carmona, P.L., Lepine, L., Jenkins, J.P., Ganguly, S., Myneni, R.B., 2011. Canopy spectral invariants, part 2: application to classification of forest types from hyperspectral data. J. Quant. Spectrosc. Radiat. Transf. 112, 736–750.
Smolander, S., Stenberg, P., 2003. A method to account for shoot scale clumping in coniferous canopy reflectance models. Remote Sens. Environ. 88, 363–373.
Smolander, S., Stenberg, P., 2005. Simple parameterizations of the radiation budget of uniform broadleaved and coniferous canopies. Remote Sens. Environ. 94, 355–363.
Stenberg, P., 1998. Implications of shoot structure on the rate of photosynthesis at different levels in a coniferous canopy using a model incorporating grouping and penumbra. Funct. Ecol. 12, 82–91.
Stenberg, P., 2006. A note on the G-function for needle leaf canopies. Agric. For. Meteorol. 136, 76–79.
Stenberg, P., 2007. Simple analytical formula for calculating average photon recollision probability in vegetation canopies. Remote Sens. Environ. 109, 221–224.
Stenberg, P., Mõttus, M., Rautiainen, M., 2016. Photon recollision probability in modelling the radiation regime of canopies — a review. Remote Sens. Environ. 183, 98–108.
Stoyan, D., Kendall, S.W., Mecke, J., 1995. Stochastic Geometry and Its Applications. John Wiley & Sons, New York.
Sun, L., Neville, R., Staenz, K., White, H.P., 2008. Automatic destriping of hyperion imagery based on spectral moment matching. Can. J. Remote. Sens. 34, S68–S81.
Vainikko, G.M., 1973. Transfer approach to the mean intensity of radiation in non-continuous clouds. Trudy MGK SSSR. Meteorol. Invest. 21, 28–37.
Vanhatalo, K.M., Rautiainen, M., Stenberg, P., 2014. Monitoring the broadleaf fraction and canopy cover of boreal forests using spectral invariants. J. Quant. Spectrosc. Radiat. Transf. 133, 482–488.
Vladimirov, V., 1963. Mathematical Problems in the One-Velocity Theory of Particle Transport. Atomic Energy of Canada Limited Chalk River, Ontario.
Wang, S., Grant, R., Verseghy, D., Black, T., 2001. Modelling plant carbon and nitrogen dynamics of a boreal aspen forest in CLASS—the Canadian Land Surface Scheme. Ecol. Model. 142, 135–154.
Wang, Y.J., Buermann, W., Stenberg, P., Smolander, H., Hame, T., Tian, Y.H., Hu, J.N., Knyazikhin, Y., Myneni, R.B., 2003. A new parameterization of canopy spectral response to incident solar radiation: case study with hyperspectral data from pine dominant forest. Remote Sens. Environ. 85, 304–315.
Wilson, J.W., 1967. Stand structure and light penetration. III. Sunlit foliage area. J. Appl. Ecol. 4, 159–165.
Yan, K., Park, T., Yan, G., Chen, C., Yang, B., Liu, Z., Nemani, R., Knyazikhin, Y., Myneni, R., 2016a. Evaluation of MODIS LAI/FPAR product collection 6. Part 1: consistency and Improvements. Remote Sens. 8, 359.
Yan, K., Park, T., Yan, G., Liu, Z., Yang, B., Chen, C., Nemani, R., Knyazikhin, Y., Myneni, R., 2016b. Evaluation of MODIS LAI/FPAR product collection 6. Part 2: validation and intercomparison. Remote Sens. 8, 460.
Yang, B., Knyazikhin, Y., Lin, Y., Yan, K., Chen, C., Park, T., Choi, S., Mõttus, M., Rautiainen, M., Myneni, R., Yan, L., 2016. Analyses of impact of needle surface properties on estimation of needle absorption spectrum: case study with coniferous needle and shoot samples. Remote Sens. 8, 563.

Chapter 9

Evaluation of Satellite Leaf Area Products

Yan et al.

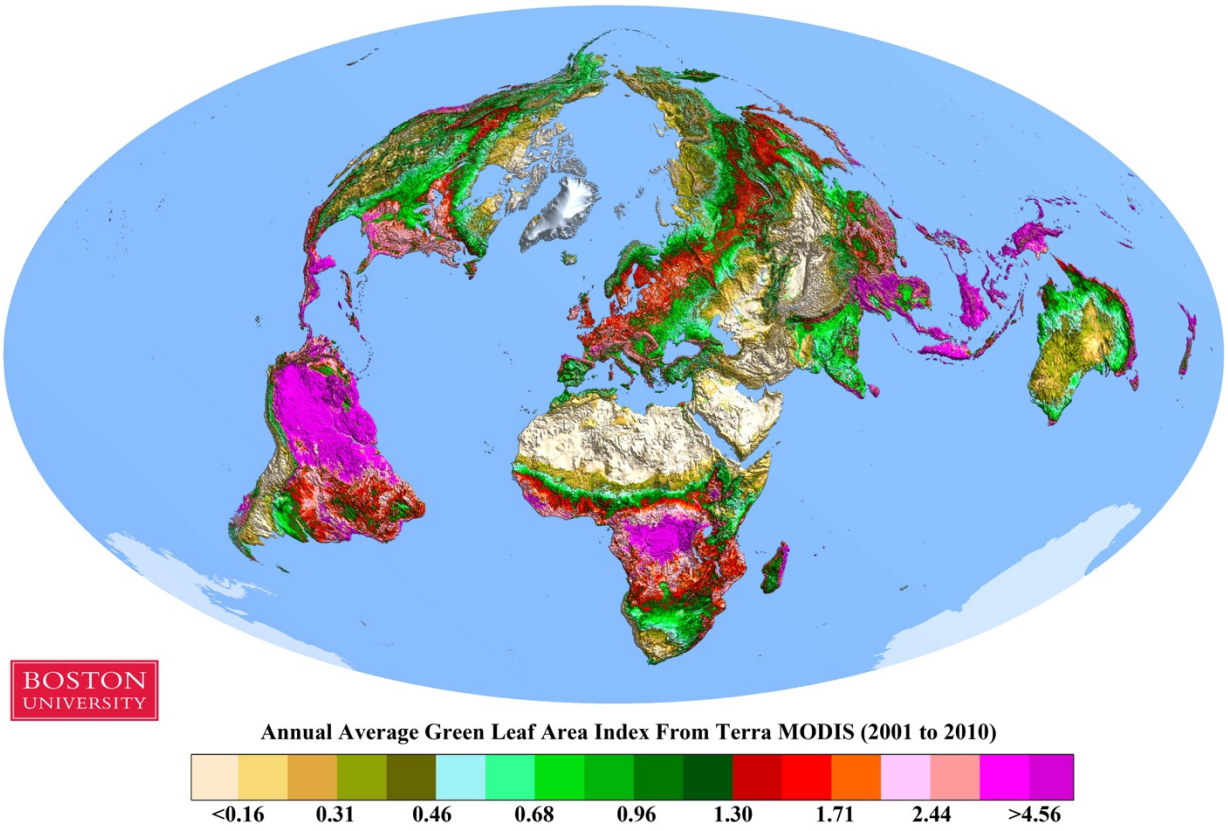

remote sensing

MDPI

Article

Evaluation of MODIS LAI/FPAR Product Collection 6. Part 1: Consistency and Improvements

Kai Yan [1,2,*], Taejin Park [2,*], Guangjian Yan [1], Chi Chen [2], Bin Yang [2,3], Zhao Liu [2], Ramakrishna R. Nemani [4], Yuri Knyazikhin [2] and Ranga B. Myneni [2]

1 School of Geography, State Key Laboratory of Remote Sensing Science, Beijing Normal University, Beijing 100875, China; gjyan@bnu.edu.cn

2 Department of Earth and Environment, Boston University, Boston, MA 02215, USA; chenchi@bu.edu (C.C.); ybjason@bu.edu (B.Y.); liuzhaofairy@gmail.com (Z.L.); jknjazi@bu.edu (Y.K.); ranga.myneni@gmail.com (R.B.M.)

3 Beijing Key Lab of Spatial Information Integration & Its Applications, Institute of RS & GIS, Peking University, Beijing 100871, China

4 NASA Ames Research Center, Moffett Field, CA 94035, USA; rama.nemani@nasa.gov

* Correspondence: kaiyan.earthscience@gmail.com (K.Y.); taejin1392@gmail.com (T.P.); Tel.: +86-186-1001-1902 (K.Y.); +1-617-893-1988 (T.P.)

Academic Editors: Sangram Ganguly, Compton Tucker, Clement Atzberger and Prasad S. Thenkabail
Received: 7 March 2016; Accepted: 20 April 2016; Published: 26 April 2016

Abstract: As the latest version of Moderate Resolution Imaging Spectroradiometer (MODIS) Leaf Area Index (LAI) and Fraction of Photosynthetically Active Radiation (FPAR) products, Collection 6 (C6) has been distributed since August 2015. This collection is evaluated in this two-part series with the goal of assessing product accuracy, uncertainty and consistency with the previous version. In this first paper, we compare C6 (MOD15A2H) with Collection 5 (C5) to check for consistency and discuss the scale effects associated with changing spatial resolution between the two collections and benefits from improvements to algorithm inputs. Compared with C5, C6 benefits from two improved inputs: (1) L2G–lite surface reflectance at 500 m resolution in place of reflectance at 1 km resolution; and (2) new multi-year land-cover product at 500 m resolution in place of the 1 km static land-cover product. Global and seasonal comparison between C5 and C6 indicates good continuity and consistency for all biome types. Moreover, inter-annual LAI anomalies at the regional scale from C5 and C6 agree well. The proportion of main radiative transfer algorithm retrievals in C6 increased slightly in most biome types, notably including a 17% improvement in evergreen broadleaf forests. With same biome input, the mean RMSE of LAI and FPAR between C5 and C6 at global scale are 0.29 and 0.091, respectively, but biome type disagreement worsens the consistency (LAI: 0.39, FPAR: 0.102). By quantifying the impact of input changes, we find that the improvements of both land-cover and reflectance products improve LAI/FPAR products. Moreover, we find that spatial scale effects due to a resolution change from 1 km to 500 m do not cause any significant differences.

Keywords: Leaf Area Index (LAI); Fraction of Photo-synthetically Active Radiation (FPAR); MODIS; Collection 6; evaluation; consistency

1. Introduction

The launch of NASA's Terra and Aqua satellites began a new era in remote sensing of Earth's atmosphere, oceans and land surface. On board these platforms, the MODerate resolution Imaging Spectroradiometer (MODIS) instrument successfully started production and distribution of a variety of products of Earth system parameters [1]. Among these parameters, Leaf Area Index (LAI) and Fraction of Photosynthetically Active Radiation (0.4–0.7 μm) absorbed by vegetation (FPAR) play an important

role in most global models of climate, hydrology, biogeochemistry, and ecosystem productivity by characterizing vegetation canopy structure and energy absorption capacity [2,3].

To take full advantage of MODIS's multi-angular and multi-spectral observation ability, a physical algorithm based on Radiative Transfer (RT) was developed for generating MODIS LAI/FPAR products (MOD15) [4,5]. The MODIS science team aims to provide users with better products by updating product cohorts that are called collections. Since the launch of Terra in December 1999, MODIS land data records have been reprocessed four times. Having stage one validation status, Collection 3 (C3) is the first release of MODIS LAI/FPAR products and covered the period of November 2000 to December 2002. The product accuracy of this version has been estimated using ground measurements obtained from some field campaigns [6]. Collection 4 (C4) covered the period from February 2000 to December 2006 and benefited from the improved inputs and updated look-up-tables (LUTs) [7]. Aimed at reducing the impact of environmental conditions and temporal compositing period, Collection 5 (C5) combined Terra- and Aqua-MODIS sensor data and generated four LAI/FPAR products from February 2000 to present [8]. In addition, C5 used a static 8-biome land-cover map instead of previous 6-biome one. Algorithm refinements were carried out over all biomes but with a major focus on woody vegetation for which a new stochastic RT model was utilized [9].

Collection 6 (C6) represents the latest version and contains the entire time series from February 2000 to the present. This version has been released and distributed free of charge to the public since August 2015 and is expected to benefit from improvements to upstream inputs of the LAI/FPAR algorithm. Before being released, LAI and FPAR products should go through three procedures—algorithm development, product analysis, and validation [8]. Since C6 inherits the same algorithm from C5, we focus on the last two steps and document them in this two-paper series. Product analysis includes assessment of algorithm performance, version consistency and product uncertainty caused by errors in input data [6–8,10]. A check of the consistency between different versions of products is a good way to make sure that there are no theoretical or artificial errors (bugs) in computing code. Moreover, products users should be aware of the improvements in a new version. In this paper, we compare C6 with C5 to check for consistency in terms of spatial distribution, seasonal variations, inter-annual anomalies and spatial coverage. The impact on algorithm retrievals due to changes in inputs is also investigated. Product validation includes direct validation using field measurements, indirect validation using other related parameters such as climatic variables, and inter-comparison with other existing products [11–14]. This part is described in the second paper.

This paper is organized as follows. Section 2 briefly reviews the MODIS LAI/FPAR algorithm and documents improvements seen in C6. Section 3 details the consistency between C6 and C5 along four fronts. Section 4 demonstrates the benefits from improved land-cover and reflectance products that are inputs to the algorithm. A simulation experiment about scale effects is also presented in this section. Concluding remarks are presented in Section 5.

2. MODIS LAI/FPAR Products

2.1. Algorithm Theoretical Description

The operational MODIS LAI/FPAR algorithm consists of a main algorithm that is based on the three-dimensional radiative transfer (3D RT) equation. By describing the photon transfer process, this algorithm links surface spectral bi-directional reflectance factors (BRFs) to both structural and spectral parameters of the vegetation canopy and soil [15,16]. Given atmosphere-corrected BRFs and their uncertainties, the algorithm finds candidates of LAI and FPAR by comparing observed and modeled BRFs that are stored in biome type specific LUTs. All canopy/soil patterns for which observed and modeled BRFs differ within biome-specified thresholds of uncertainties (e.g., 30% and 15% for red and near-infrared bands, respectively, for forest biomes) are considered candidate solutions and the mean values of LAI and FPAR from these solutions are reported as outputs. The law of energy conservation and the theory of spectral invariance are two important features of this main algorithm. The detailed

theoretical basis of the algorithm and implementation aspects are documented in references [1,5,17]. The main algorithm may fail to localize a solution if uncertainties of input BRFs are larger than threshold values or due to deficiencies of the RT model that result in incorrect simulated BRFs. In such case, a back-up empirical method based on relations between the Normalized Difference Vegetation Index (NDVI) and LAI/FPAR [4,18] is utilized to output LAI/FPAR with relatively poor quality—this is called the backup algorithm.

2.2. Algorithm Inputs

Theoretically, the MODIS algorithm can make use of multiple atmosphere-corrected BRFs and their uncertainties. Currently, the MODIS algorithm only utilizes daily surface reflectance at red (648 nm) and near-infrared (858 nm) bands because of high uncertainties in other bands [19]. The uncertainty of input BRFs from the calibration and atmospheric correction process will propagate into the products even if the science algorithm is sound. As critical information, reflectance uncertainties as well as model uncertainties are incorporated to set the threshold of difference between observed and modeled BRFs [5]. Another important input is the biome map, in which global vegetation is classified into eight biomes with different canopy and soil patterns (Figure S1). The eight biomes are: (B1) grasses and cereal crops; (B2) shrubs; (B3) broadleaf crops; (B4) savannas; (B5) evergreen broadleaf forests; (B6) deciduous broadleaf forests; (B7) evergreen needleleaf forests and (B8) deciduous needleleaf forests. With simplifying assumptions and standard constants (e.g., vegetation and soil optical properties) which are assumed to vary with biome and soil types only, using a biome map as prior-knowledge can reduce the number of unknowns of the "ill-posed" inverse problem [1,20].

2.3. Temporal Compositing and Quality Control

Figure 1 shows the flow of MODIS LAI/FPAR C6 production. The algorithm ingests MODIS daily red and near-infrared (NIR) BRFs and a biome map to generate daily LAI/FPAR retrievals without pre-quality-control on inputs. A temporal compositing approach is used to select the best retrievals and generate 8-day or 4-day products from daily retrievals. The compositing algorithm is a two-step scheme: (1) the retrievals are selected according to algorithm path: main algorithm retrievals have the highest priority, and if none are available, back-up algorithm retrievals are selected; (2) the LAI value is selected based on maximum FPAR value [8]. Compositing reduces the impact of day-to-day artificial variations in surface reflectance that are due to cloud and residual atmospheric effects and it is effective in removing contaminated retrievals. As well as LAI/FPAR values, MODIS products store the corresponding quality control (QC) data layers and the users are advised to consult the quality flags when using these products [7]. The key indicator of the quality of retrievals is the algorithm path, which distinguishes the following five categories: (1) main algorithm without saturation; (2) main algorithm with saturation; (3) back-up algorithm due to bad geometry; (4) back-up algorithm due to other problems; and (5) not produced. In addition to algorithm path, the QC layer provides information about presence of clouds, aerosols, and snow, inherited from input reflectance products.

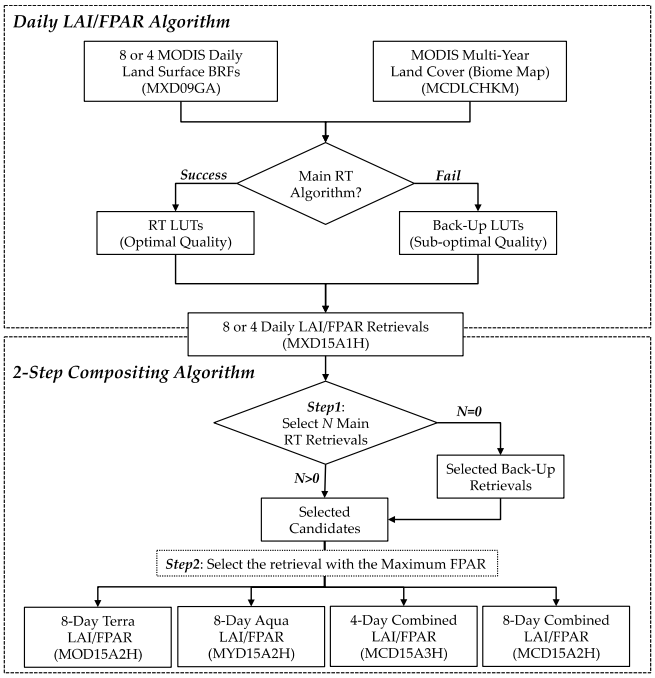

Figure 1. Algorithm flow of MODIS LAI/FPAR Collection 6 production. Four different global products with different compositing (8-day or 4-day) periods and sensor platform combinations (Terra and/or Aqua) are available.

2.4. Improvements of Collection 6

MODIS LAI/FPAR C6 uses the same science algorithm and LUTs as C5. However, this new version can still benefit from improved inputs as discussed below. As the only two inputs, the intermediate data at 1 km resolution of surface reflectances and biome map are replaced by their 500 m version, thus enabling the C6 LAI/FPAR products to have half-kilometer spatial resolution. The significance of this upgrade is two-fold. First, downstream land surface models can benefit from this finer resolution LAI/FPAR products. Second, the LAI/FPAR algorithm uses biome type classification to reduce unknown parameters and each pixel is assumed to belong to only one biome type with some pre-set structural and optical parameters. This assumption is more likely to be satisfied at finer resolutions because of the higher heterogeneity in coarse pixels [21]. Moreover, the smaller pixel ground coverage can reduce the scale gap between remote sensing pixels and ground point measurements, which will reduce uncertainties and human labor during the process of products validation using ground measurements [6,22].

The new version of publicly available MODIS daily surface reflectances (MOD09GA C6) is used to replace the previous intermediate dataset (MODAGAGG) which was generated by aggregating four MOD09GA C5 pixels [23]. This makes it possible for the community to test their own LAI/FPAR algorithms and compare with MODIS products. Improved aerosol retrieval and correction algorithm are employed in the generation of MOD09GA C6 dataset. Moreover, BRDF database is used to better constrain the thresholds used in the snow/cloud detection algorithm. MODIS land-cover product C5 (as input for LAI/FPAR C6) is also reported to be significantly improved through algorithm refinement and input data revise. Comparison of C5 land-cover with C4 (as input for LAI/FPAR C5) showed substantial differences. Cross-validation accuracy assessment indicates an overall accuracy of 75% in C5 land-cover product [24]. In addition, C6 LAI/FPAR replaced the static land-cover input with new multi-year land-cover maps generated with three years of C5 land-cover data. Compared with the previous static land-cover, this new biome type source has a three-year temporal resolution and thus can capture the dynamic changes of biome types. According to previous experience [1,7], C6 LAI/FPAR products can benefit from the improved upstream reflectance and land-cover products [25].

3. Consistency between C5 and C6 LAI/FPAR Products

Good consistency between different product versions creates confidence in LAI/FPAR data sets in both product producers and users, while poor consistency such as large differences diverts attention away from both of them. In this paper, we study the consistency between C5 and C6 along four fronts as discussed below. Note that, except for Sections 3.1 and 3.4 we only focus on the retrievals from the main algorithm.

3.1. Global Distribution

The spatial distribution of LAI and FPAR over the globe during two 8-day composite periods in January and July in the year 2003 are shown in Figure 2a,d and Figure S2. For both LAI and FPAR, there is no visually distinguishable difference between C5 and the new C6. The products from two collections exhibit similar spatial patterns. FPAR shows a similar distribution pattern to LAI, which can be explained by radiative transfer theory [1]. The LAI patterns closely coincide with the biome type distribution (Figure S1)—high LAI over forests and low LAI over herbaceous vegetation. As expected, tropical evergreen forests (e.g., amazon rain forests) have high LAI values (up to 7); somewhat less green are the middle latitude broadleaf forests (e.g., eastern United States). Except bare land and deserts, regions covered by grasses and shrubs generally have low LAI values. The globe looks greener in boreal summer time because of ample illumination conditions over the northern hemisphere, which has greater land surface.

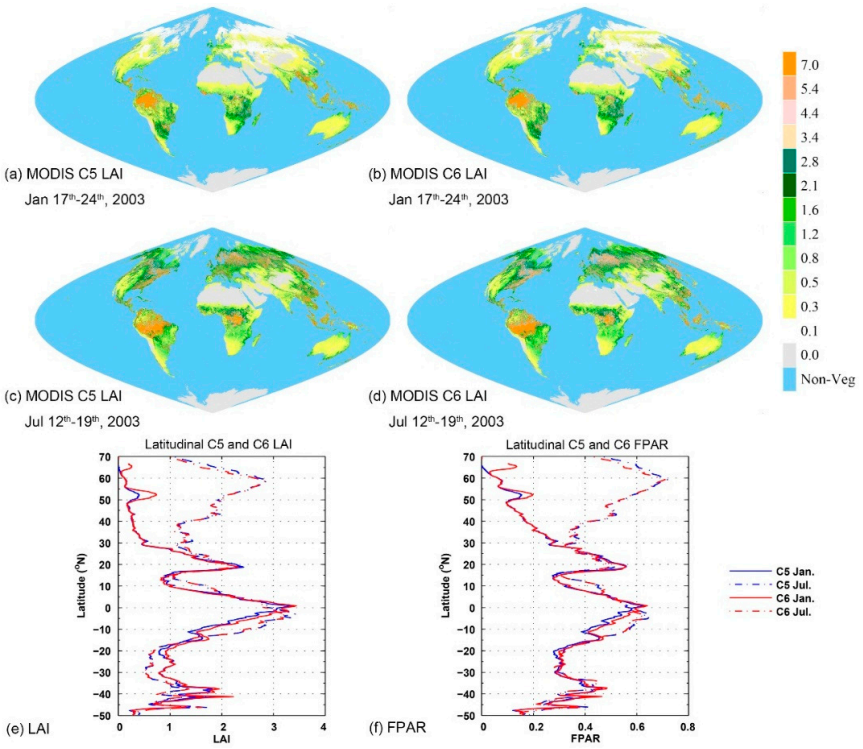

Figure 2. Global distribution of LAI/FPAR from January (17–24 January) and July (12–19 July) of 2003. Panel (**a**–**d**) are color-coded maps of MODIS C6 and C5 LAI. Figure S2 shows FPAR. Area-equal sinusoidal projection is used here; panels (**e**,**f**) show the latitudinal distribution of global LAI and FPAR, respectively. The latitude interval is 0.1°. In these plots, MODIS C6 and C5 use red and blue lines, respectively. Solid and dashed lines depict January and July, respectively.

Figure 2e,f compare the zonal mean LAI and FPAR values from C5 and C6 in January and July. For both LAI and FPAR, the profiles derived from C6 and C5 products match well at most latitude bands

and show consistent latitudinal distribution of LAI and FPAR values. There are two obvious peaks in the tropics (23°N–23°S) which can be explained by the dense vegetation coverage in the three tropical rainforests (South America, Africa and Southeast Asia). As illumination is ample, there is no obvious seasonal difference in these latitude bands. In the higher latitudes, the northern hemisphere shows clear seasonal difference than the southern hemisphere. This is because the dominant biome types in the southern hemisphere are savannas, shrubs and grasses that have smaller seasonal variations than the forests that dominate the northern hemisphere [26] (see Figure S1). We also notice that C5 underestimates C6 in the bands 50°N–55°N and 63°N–70°N. This is caused by changes in input biome type and will be further discussed in Section 4.1.

3.2. Spatial Coverage of Main Algorithm

As a key indicator of the quality of retrievals, the algorithm path of each pixel is stored in the LAI/FPAR products. By comparing the retrieval rate of different algorithm paths at global scale, we can evaluate the overall quality of the products from C5 and C6. The main algorithm outputs retrievals at high precision in the case of low LAI and at moderate precision when LAI is high and surface reflectance has low sensitivity to LAI. In the case of main algorithm failure, low-precision retrievals are obtained from the empirical back-up algorithm. Figure 3a compares the biome-specific yearly and globally averaged retrieval rate of different algorithm paths. C6 and C5 show similar patterns for all biomes except biome 5 (evergreen broadleaf forests) and biome 7 (evergreen needleleaf forest). C6 shows 17% and 7% higher main algorithm retrieval rates than C5 for biomes 5 and 7, respectively. This improvement is due to an updated biome map, which will be discussed in Section 4.1. As the main algorithm has better performance than the backup algorithm, the success rate of the main algorithm (Retrieval Index, RI) can be seen as a quality indicator. The RI of all biome types except biomes 5 and 7 is higher than 90%. Biomes 1 to 4 have the highest RI (more than 95%). The retrieval rate of main algorithm without saturation is lowest in the case of evergreen broadleaf forests because of reflectance saturation in dense canopies. This means the reflectances do not contain sufficient information to localize a LAI value. The other three forest types also show a large proportion of retrievals under saturation. Because evergreen needleleaf forests are located in the high latitude regions where the solar zenith angles are low in winter season, biome 7 shows obvious backup algorithm retrievals that are due to poor sun-sensor geometry. Nevertheless, C6 shows slightly higher RI than C5.

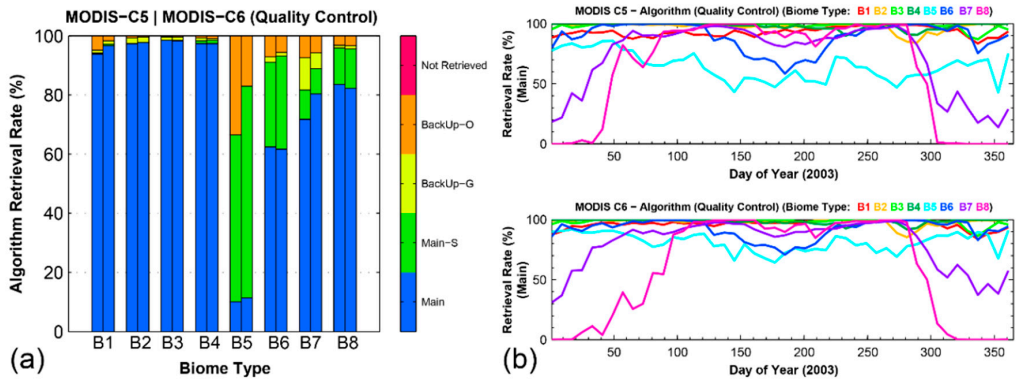

Figure 3. Comparison of global retrieval rate of different algorithm paths (retrieval index) for eight biome types. (**a**) Yearly and globally averaged (in 2003) retrieval rate of different algorithm paths. Possible algorithm paths are (i) Main (Main algorithm without saturation); (ii) Main-S (Main algorithm with saturation); (iii) BackUp-G (Backup algorithm because of bad sun-sensor geometry); (iv) BackUp-O (Backup algorithm because of other reasons) and (v) Not Retrieved (not executed because BRF data are not available). For each biome, the left bar is for C5 and right one is for C6; (**b**) Annual variation of main algorithm spatial coverage in 2003 (upper plot is for C5 and lower plot is for C6). This statistic is done after quality control using cloud and aerosol flags.

The seasonal variations of RI in C5 and C6 for all eight biomes in 2003 shown in Figure 3b indicate that the annual cycles of C6 and C5 are quite consistent. As in Figure 3a, the RI of biome 5 has been improved from C5 to C6. A strong seasonality is seen in needleleaf forests (biomes 7 and 8) with RI varying from about 90% during the boreal summer to less than 30% during the boreal winter. The RI of deciduous needleleaf forests can even be zero in the boreal winter season. The decrease of RI in the boreal winter results from unsuitable illumination conditions, extreme solar zenith angles, and snow or cloud contamination. The fact that almost all needleleaf forests appear only in the northern hemisphere makes the seasonal variation more obvious.

3.3. Seasonal LAI/FPAR Variations

Seasonal variations in C5 and C6 LAI/FPAR retrievals are shown in Figure 4 and Figure S3. These lines show globally averaged biome-specific LAI/FPAR values as a function of Julian day in 2003. This analysis only uses retrievals derived by the main algorithm. We note that C5 and C6 products show good consistency of LAI/FPAR seasonal variations. All biome types except for evergreen broadleaf forests and savannas show seasonality at different levels. The retrievals over deciduous forests demonstrate expected obvious seasonality in both LAI and FPAR. LAI of deciduous broadleaf forests (deciduous needleleaf forests) drops from around 5 (3) in boreal summer to around 0.5 (<0.5) in boreal winter. With ample illumination in tropics and subtropics, evergreen broadleaf forests have LAI values of about 5 through the year with negligible seasonal variations. By checking the seasonal variations of the algorithm path (see Figure S4), we find that the missing part in case of deciduous needleleaf forests is due to unavailable retrievals from main algorithm because of bad sun-sensor geometry (solar zenith angle larger than 52.5° or view zenith angle larger than 67.5°). Seasonal variations of algorithm path can also explain these erratic artifacts in LAI/FPAR variations (e.g., the sudden drop at DOY 10 to 20 and the peak around DOY 200 for deciduous needleleaf forests in Figure 4a).

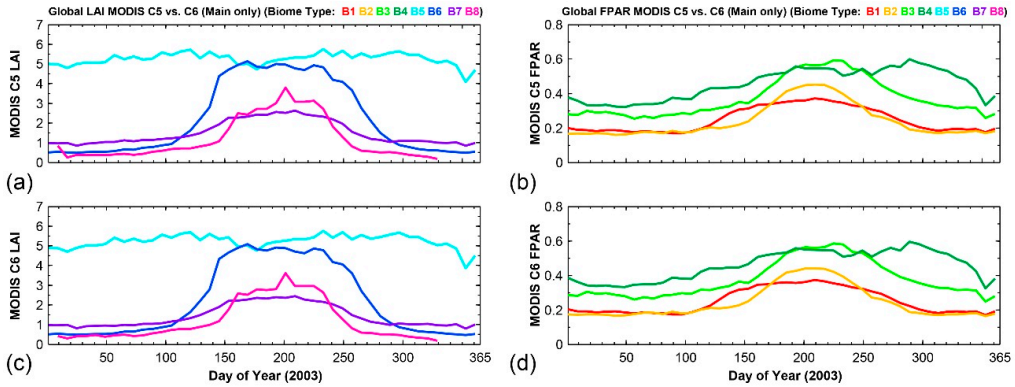

Figure 4. Seasonal variations of globally averaged MODIS (**a**) LAI C5; (**b**) FPAR C5; (**c**) LAI C6; and (**d**) FPAR C6 in 2003. Left panels show seasonal LAI trajectories over four different forest types (evergreen broadleaf forest (B5), deciduous broadleaf forest (B6), evergreen needle leaf forest (B7) and deciduous needle leaf forest (B8)). FPAR panels (right) show other four non-forest biome types (grasses/cereal crops (B1), shrubs (B2), broadleaf crops (B3) and savannas (B4)). LAI of non-forest biome types and FPAR of forest types are shown in Figure S3 for the sake of clarity.

3.4. Inter-Annual LAI Anomalies

In this section, we check the consistency of 13 years (2002–2014) of LAI anomalies from C5 and C6. The importance of this work is two-fold. First, an LAI anomaly represents the difference between LAI values of a specific year and the multi-year mean LAI value, from which we can deduce potential annual variations in carbon, water and energy balances. Second, using independent geographic variables to explain the annual variation of LAI is a good way to validate the products indirectly.

The spatial and temporal averages of LAI anomalies from C5 and C6 during the period from 2002 to 2014 (2000 and 2001 were discarded because of missing data) are compared in Figure 5. Panel (a) shows the anomaly of annual averaged LAI in two precipitation-limited regions (Eastern Australia and Northeastern Brazil). For both regions, C5 and C6 LAI anomalies match very well. The correlation coefficients between C5 and C6 in the two regions are 0.972 and 0.975, respectively. The LAI in Northeastern Brazil shows a large decrease in 2012, which can be explained by the severe drought in Northeast Brazil in that year [27]. Panel (b) shows anomaly of growing season (May to September) averaged LAI in two temperature-limited regions (North America and Eurasia). Also for these two regions, C5 and C6 show similar LAI annual variations. We note that the slopes of C6 are slightly higher than C5 in all these plots. This is because the improved sensor calibration of C6 solved the Terra MODIS sensor degradation issue in C5 [28]. A more detailed explanation for these LAI inter-annual variations will be presented in the second part of this two-paper series.

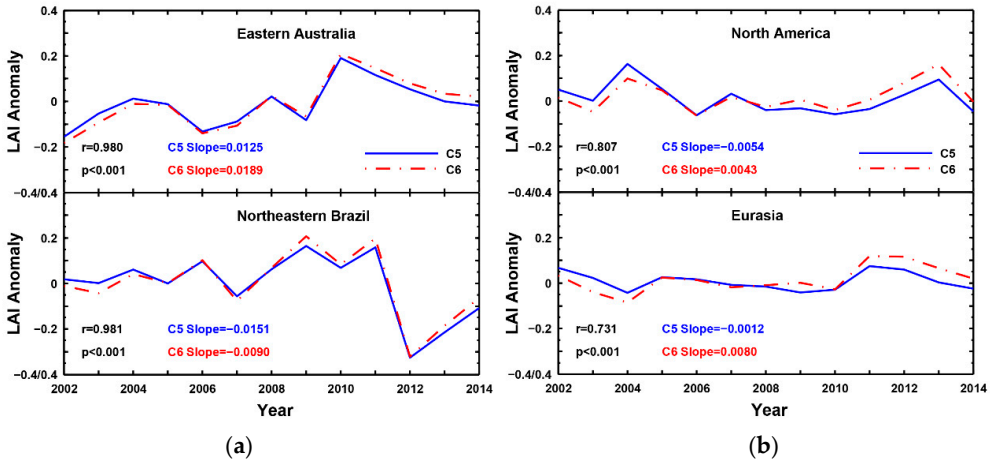

Figure 5. Comparison of anomalies of spatially averaged LAI values from C5 (blue solid lines) and C6 (red dashed lines). Panel (**a**) shows the anomaly of annual averaged LAI in two precipitation-limited regions (Eastern Australia, 20°S–40°S, 145°E–155°E and Northeastern Brazil, 3°S–12°S, 35°W–45°W). Panel (**b**) shows the anomaly of growing season (May to September) averaged LAI in two temperature-limited high latitude (>60°N) regions (North America and Eurasia). Correlation coefficient (r) between the two MODIS collections and its significance (p) are given in each panel. Moreover, slopes are provided as indicators of the trend of inter-annual LAI.

4. Benefits from Improved Input Data

From the above comparisons, we see there are no significant discrepancies between C5 and C6 products in terms of global distribution, seasonal variations, inter-annual LAI anomalies and spatial coverage of high quality retrievals. However, pixel-to-pixel comparison still shows differences between C5 and C6 at the regional scale. As C6 inherits the algorithm and LUTs from C5 directly, the improvements in input data and change of spatial resolution are the only two sources of LAI/FPAR differences between the two versions. Here we investigate and quantify the impact of input changes and the scale effect of the algorithm.

4.1. Benefits from Biome Map Improvement

As an important prior knowledge about the land surface, a biome map is utilized to reduce the number of unknowns in the inverse problem of LAI/FPAR estimation. In the operational algorithm, structurally and spectrally different parameterization in 3D RT is used for each biome type. Specification of biome type for each pixel is thus critically important to choose the correct RT dependent LUT for LAI/FPAR estimation. Errors in biome classification can therefore propagate into LAI/FPAR retrievals. Numerical experiments suggest that a mismatch in biome specific LUT will result in either

a low RI and/or incorrect LAI/FPAR values [1]. Conversely, increased biome accuracy will help to reduce uncertainty in LAI/FPAR products. As LAI/FPAR production requires prior knowledge of surface biome type, the biome input is generally based on an earlier version of land-cover product. This means C4 and C5 land-cover products have been used for C5 and C6 LAI/FPAR production, respectively. Biome input (based on C5 MODIS land-cover product) for C6 LAI/FPAR production is reported to be substantially improved relative to the biome input (based on C4 MODIS land-cover product) for C5 LAI/FPAR production in terms of accuracy, stability across years due to refinements in the land-cover classification algorithm and ancillary datasets used [24].

Figure 6a shows the proportion of pixels derived from each biome type in the C6 biome map for each class in the C5 biome type at the global scale during 2001 to 2003. Some biomes in C6, for example biomes 1, 2, 4, 5 and 8, are relatively consistent with C5 (more than 70% consistency). Around 30% of the pixels labeled as biome 6 and biome 7 in C5 change to other biome types in C6. Compared to other biomes, biome 3 has the largest proportion of differently classified biome cases. Around 50% of biome 3 pixels in C5 are classified into biome 1 in C6. We note that most of the differently classified pixels change to their neighboring biome types, which have similar canopy structural characteristics in RT realization. For instance, most of the "changed" pixels in biome 3 (broadleaf crops) are labeled as biome 1 (grass and cereal crop) in C6. This result agrees with [24].

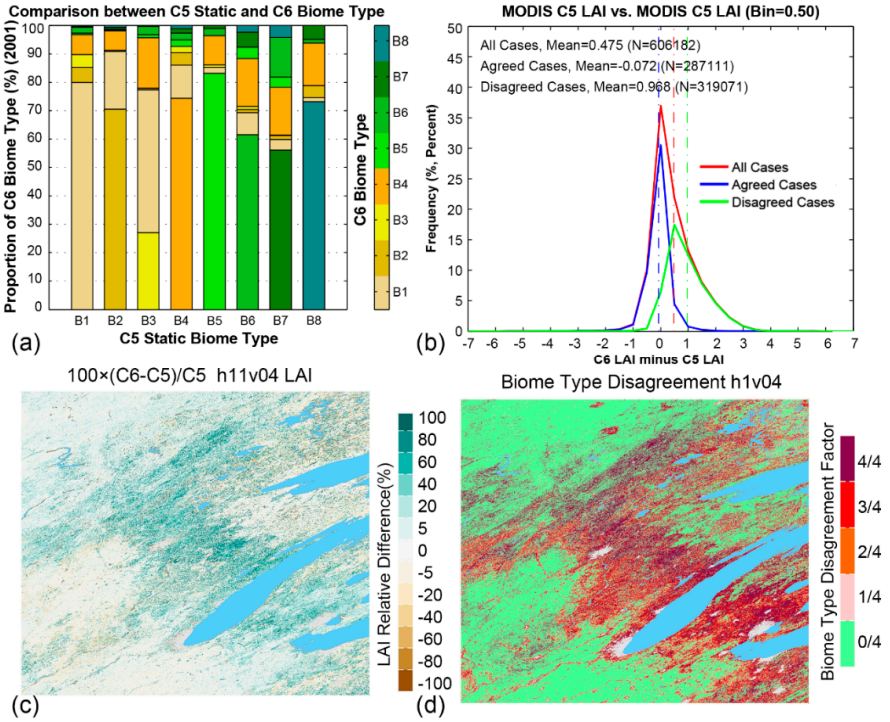

Figure 6. Impact of input biome map change on LAI/FPAR retrievals. (**a**) Areal proportion of globally changed biome type from static C5 to dynamic C6 input biome type (2001–2003). Proportions of C6 biomes are calculated with respect to total area in each C5 biome type; (**b**) Histogram of the difference between C5 and C6 LAI values in tile h11v04 (red box in Figure 7) during 12th–19th July of 2003. The blue line and green line show consistent biome type and changing biome type, respectively; (**c**) Spatial distribution of relative difference in LAI between C5 and C6 in tile h11v04 (dominant biome type is broadleaf crops); (**d**) Spatial distribution of BTDF (biome type disagreement factor) showing how many 500 m C6 pixels in a 1 km C5 pixel are different with the C5 biome type.

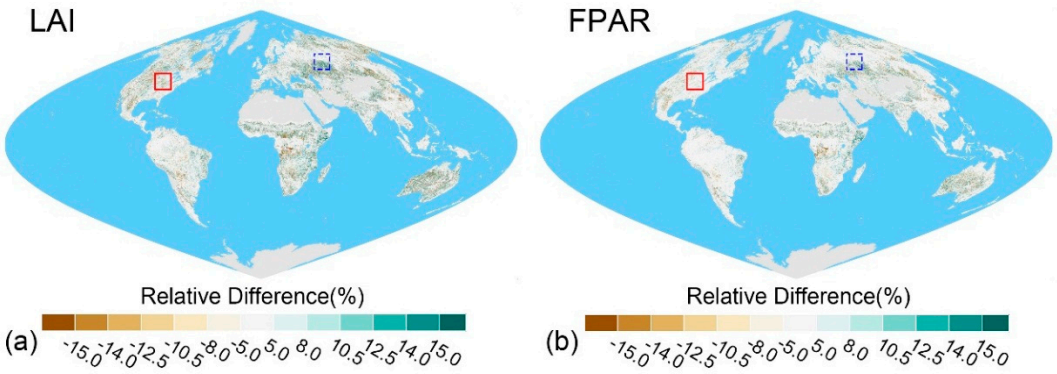

Figure 7. Spatial distribution of relative difference (100 × (C6-C5)/C5) for pixels with the same biome types (BTDF = 0) during 12th July to 19th July in 2003. (**a**) LAI; (**b**) FPAR. Detailed results from two tiles (h11v04 and h22v03) shown as red and blue boxes are given in Figure 8.

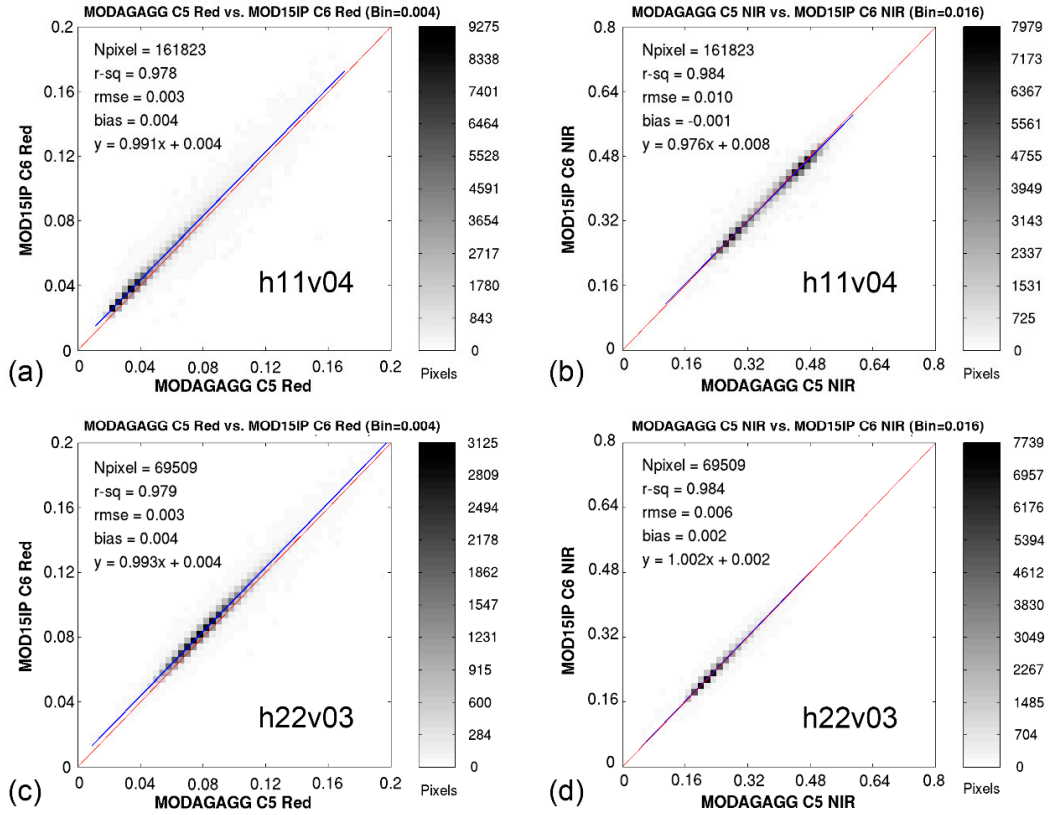

Figure 8. Density scatter plots of land surface reflectance (BRFs) of red band (left panels) and NIR band (right panels) of the two example tiles (**a**) and (**b**) are for tile h11v04; (**c**) and (**d**) are for h22v03 shown as boxes in Figure 7.

To quantify the impact of biome type change on LAI retrievals, we investigate the tile (1200 by 1200 km) h11v04 as an example as 53% of this region shows changes between C5 and C6. We divide all pixels into two categories, pixels with consistent and changed biome types, and compare the LAI differences. Histograms of the difference for these two categories and for all pixels are shown in Figure 6b. The mean difference of all pixels with consistent biome type (about 27% of pixels) is −0.072, which is obviously smaller than that of all pixels with changing biome types (0.968). The mean difference of all pixels in this tile is 0.475. Such biased patterns are depicted in Figure 6c,d.

For further investigation, we define the biome type disagreement factor (BTDF) as the proportion of pixels with changing biome type. As four 500 m C6 pixels compose a 1 km C5 biome type, this factor can be 0, 1/4, 1/2, 3/4 or 1. It can be seen that when there is no biome type change, the relative difference in LAI will be within ±5%. This can be as high as ±100% in pixels with changing biome type. In particular, note that the directionality of observed difference is not uniform across cases of biome change.

The mean value and standard deviation of the difference and RMSE between C5 and C6 LAI are listed in Table 1 (Table S1 shows the same for FPAR). When the biome type disagreement factor is small (0/4 or 1/4), C6 retrievals underestimate C5 for most biome type cases. Interestingly, the discrepancy between C5 and C6 gets larger with increasing biome type disagreement factor. With the same biome input (BTDF = 0/4), the mean RMSE of LAI and FPAR are 0.29 and 0.091, respectively, but biome type disagreement worsened the consistency (LAI: 0.39, FPAR: 0.102). Overall C6 estimates global LAI and FPAR by C5-0.01 and C5-0.004, respectively.

Table 1. Biome specific differences between C5 and C6 LAI at the global scale in 2003. Mean value and standard deviation of the difference and RMSE (values in brackets) between C5 and C6 (C6 minus C5) are listed in the table.

Biome Type	BTDF = 0/4	BTDF = 1/4	BTDF = 2/4	BTDF = 3/4	BTDF = 4/4
Grasses/Cereal crops (B1)	0.00 ± 0.24 (0.24)	−0.01 ± 0.30 (0.30)	0.01 ± 0.33 (0.33)	0.02 ± 0.39 (0.39)	0.08 ± 0.43 (0.44)
Shrubs (B2)	−0.01 ± 0.15 (0.15)	0.02 ± 0.21 (0.21)	0.04 ± 0.24 (0.24)	0.06 ± 0.25 (0.25)	0.05 ± 0.23 (0.24)
Broadleaf crops (B3)	−0.02 ± 0.22 (0.22)	0.11 ± 0.23 (0.25)	0.21 ± 0.28 (0.35)	0.31 ± 0.35 (0.46)	0.42 ± 0.40 (0.57)
Savanna (B4)	0.00 ± 0.26 (0.26)	−0.04 ± 0.30 (0.30)	−0.07 ± 0.36 (0.37)	−0.11 ± 0.42 (0.43)	−0.16 ± 0.40 (0.43)
[1] EBF (B5)	−0.08 ± 0.62 (0.63)	−0.45 ± 0.65 (0.79)	−0.88 ± 0.71 (1.12)	−1.32 ± 0.82 (1.55)	−1.71 ± 1.00 (1.98)
[2] DBF (B6)	−0.09 ± 0.48 (0.49)	−0.01 ± 0.48 (0.48)	0.05 ± 0.52 (0.52)	0.10 ± 0.58 (0.58)	0.03 ± 0.52 (0.52)
[3] ENF (B7)	−0.17 ± 0.51 (0.54)	−0.23 ± 0.50 (0.55)	−0.31 ± 0.54 (0.62)	−0.40 ± 0.60 (0.72)	−0.45 ± 0.73 (0.85)
[4] DNF (B8)	−0.19 ± 0.57 (0.60)	−0.26 ± 0.56 (0.62)	−0.38 ± 0.61 (0.72)	−0.49 ± 0.68 (0.84)	−0.58 ± 0.82 (1.00)
Mean	−0.02 ± 0.29 (0.29)	−0.03 ± 0.33 (0.33)	−0.02 ± 0.40 (0.40)	−0.02 ± 0.50 (0.50)	0.02 ± 0.60 (0.60)
Overall			−0.01 ± 0.39 (0.39)		

[1] Evergreen broadleaf forest; [2] Deciduous broadleaf forest; [3] Evergreen needleleaf forest; [4] Deciduous needleleaf forest.

4.2. Benefits from Surface Reflectance Improvement

To elucidate the impact of changes in input surface reflectance, we only focus on pixels with consistent biome type (BTDF = 0). Between Table 1 and Table S1, we can see that C6 LAI and FPAR values of all biomes, except biomes 1 and 4 for LAI and biome 4 for FPAR, are smaller than C5. Figure 7a,b shows the global distribution of relative difference (100 × (C6-C5)/C5) of LAI and FPAR. h11v04 (red box) and h22v03 (blue box) are two example tiles showing lower and higher C6 LAI estimation cases, respectively. As expected, both LAI and FPAR display similar spatial patterns. By only considering biome input consistent pixels, differences in LAI and FPAR between C5 and C6 vary within ±15%. Possible explanations for this discrepancy are two-fold: surface reflectance input changes and scale effect of the algorithm, further discussed below.

Comparisons of reflectance between C5 and C6 are shown in Figure 8. Panels (a) and (b) are for tile h11v04 (Figure 7) in which C6 underestimates C5. Panels (c) and (d) are for tile h22v03 (Figure 7) in which C6 overestimates C5. In both tiles, NIR (near-infrared) band reflectance shows good consistency between the two versions. However, the red band reflectances in C6 are relatively higher than in C5, especially at the lower range of reflectances. As leaves in the canopy absorb more red photons,

higher red reflectances will lead to lower LAI retrievals. These changes in reflectances resulted from refinements to the atmospheric correction algorithm. The overestimation in C6 over the tile h22v03 could be explained by the scale effects which are discussed below.

4.3. Impact of Scale Effect

With the development of quantitative remote sensing, scale effects, as a common phenomenon, have attracted more and more attention from the community. The term "scale" is widely used in many other fields as with as remote sensing and has different meanings in various disciplines [29]. In this paper, scale effects refer to the discrepancy between two products derived from the same algorithm but at different spatial resolutions. As mentioned above, MODIS LAI/FPAR products improved the spatial resolution from 1 km to 500 m using the same retrieval algorithm, which raises two questions: (1) what is the behavior of the scale effect in LAI/FPAR product and algorithm and (2) is the difference caused by the scale effect negligible? Figure 9 theoretically demonstrates the relationship between the two LAI products (C5 and C6). The discrepancy between LAI1 and LAI2 is caused by both heterogeneity of land surface and nonlinear characteristics of the retrieval models [29]. On the one hand, landscape homogeneity cannot be assumed especially in the case of a coarser spatial resolution footprint. In other words, a MODIS pixel should be considered as a mosaic of different biome types. On the other hand, the radiative transfer-based algorithm is scale-dependent [1]. This is because the pixels are likely to contain an increasing amount of radiative contribution from the background [30]. Thus, the MODIS LAI/FPAR products are scale-dependent and the scale effect could be one of the causal factors introducing a certain level of discrepancy between C5 and C6.

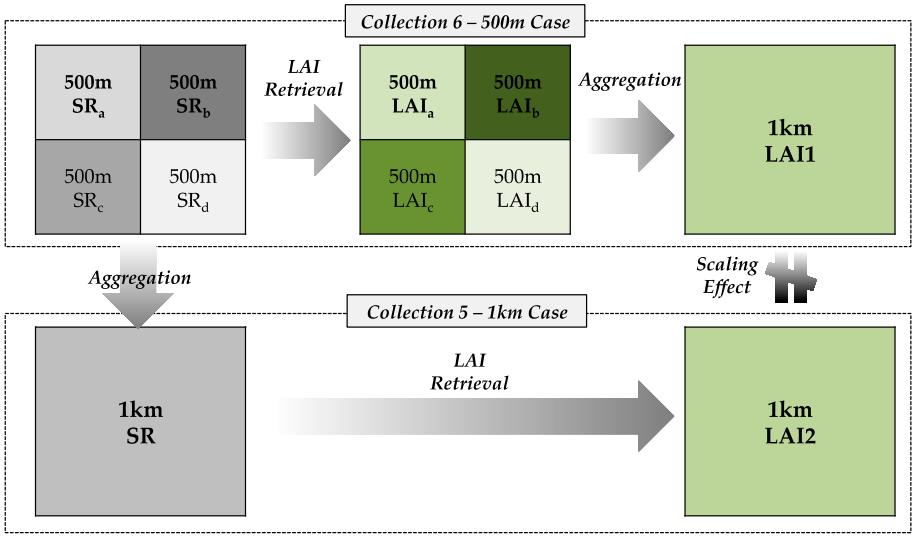

Figure 9. Theoretical description of scale effect.

To understand the discrepancy between C5 and C6 products due to scale effects, we conducted a simulation experiment using biome 6 (deciduous broadleaf forests) as an example. Note that the simulation results will not be similar across biome types due to biome-specific RT parameterizations. Only retrievals from the main RT based algorithm were analyzed. We simulated the heterogeneity in one 1 km (C5) pixel by adding 5% or 15% bias on NIR reflectance (red reflectance is fixed) for four 500 m (C6) pixels. Figure 10 shows the results of this experiment. The LAI values for C5 were selected along the black line in the red-NIR spectral space depicted in Figure 10a. It is clear that the relationship between LAI and reflectance is nonlinear. Moreover, there is a clear division between the saturated and unsaturated parts. This is more obvious in Figure 10b where both LAI and FPAR show an inflection point when saturation appears. Irrespective of saturation, the relationship between LAI and NIR reflectance is roughly a concave function. In this relationship, if reflectance SR2 is the

mean value of SR1 and SR3, the LAI (SR2) is smaller than the mean value of LAI (SR1) and LAI (SR3). Before saturation, the relationship between FPAR and NIR reflectance is almost linear. When saturation appears, the relationship changes to a concave function as well. The short parallel lines at small LAI and FPAR indicate that LAI or FPAR does not vary with NIR reflectance. This is because of sparse distribution of retrievals in the LUT at low LAI values [31].

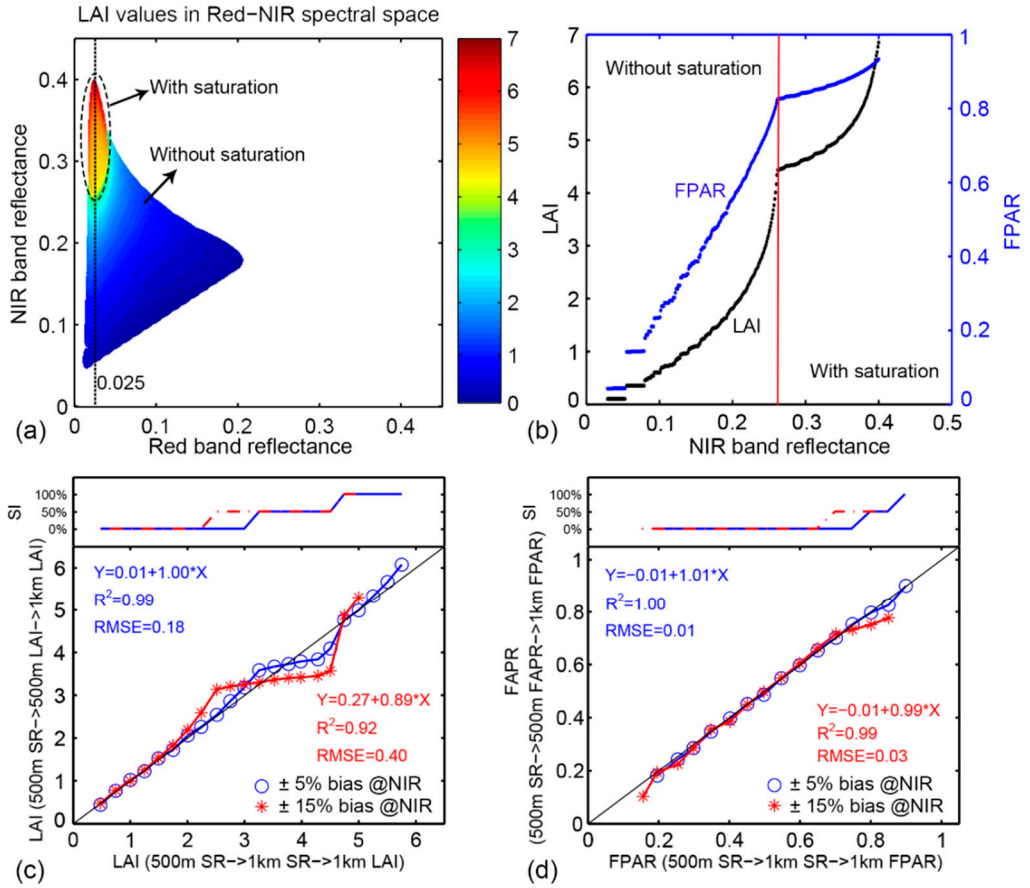

Figure 10. Scale effect of MODIS LAI/FPAR main algorithm. Biome 6 (deciduous broadleaf forests) is used as an example here. The solar zenith angle is fixed at 30° and the view direction is nadir. (**a**) Distribution of LAI values derived from the main RT based algorithm in the Red-NIR spectral space. Equally spaced LAI values along the vertical black line (red = 0.025) are selected as experimental retrievals from C5 (LAIc5). The corresponding reflectances of C5 are REDc5 and NIRc5. Let the red reflectance of all the four C6 pixels (REDc6) be equal to REDc5. To satisfy the energy conservation law, we add a positive bias to NIRc5 to obtain NIRc6_1 for two C6 pixels and add a negative bias to NIRc5 to obtain NIRc6_2 for the two left C6 pixels. Thus, four C6 LAIs can be derived using REDc6 and NIRc6; (**b**) Denotes the variations of LAI (black points) and FPAR (blue points) with NIR reflectance along the black line in (**a**). Retrievals with and without saturation are separated by a red line; (**c**,**d**) demonstrate the discrepancy in LAI and FPAR caused by scale effects, respectively. 5% and 15% bias are shown in blue and red. The saturation index (SI) for different LAI (FPAR) values is also plotted in the figures.

The discrepancy in LAI and FPAR due to scale effects is demonstrated in Figure 10c,d. The x-axis and y-axis can be seen as C5 products and C6 products, respectively. The four retrievals of C6 pixels can be partially and completely derived from unsaturated or saturated algorithmic conditions because of the bias in NIR reflectance. We define the Saturation Index (SI) as the proportion of unsaturated pixels. When SI equals 0% (all retrievals from the unsaturated part), there is no obvious difference between C5 and C6 LAI values at a low range of LAI values. However, C6 LAI tends to be higher than C5 with an increase in LAI. When SI is about 50% (two retrievals from unsaturated and the other

two from saturated part), C6 LAI tends to be smaller than C5. When SI equals 100%, C6 LAI increases again. These changes can be explained by the relationship between LAI and NIR reflectance shown in Figure 10b. As expected, a 15% bias causes a larger scale effect than a 5% bias (RMSE 0.4 *vs.* 0.18). Compared to LAI, FPAR shows less and even negligible scale effects with RMSE 0.01 and 0.03 for 5% and 15% bias. This is because the FPAR-reflectance relationship is almost linear, especially prior to saturation conditions. Because of the regional convex relationship when saturation starts to appear, C6 can be lower than C5.

5. Conclusions

This paper presents version consistency and improvements in the latest MODIS LAI/FPAR C6 product. Compared to previous C5, the most important change in C6 is that the products are being produced at 500 m spatial resolution instead of 1 km. In addition, as discussed here, C6 benefited from improved surface reflectances and biome type inputs. The refined C6 atmospheric correction algorithm generates relatively higher red band reflectances, which results in lower LAI/FPAR values. The new multi-year land-cover product provides biome type input to the algorithm with better accuracy. The differences caused by scale effects are found to be negligible for FPAR and in cases where LAI is low. Scale effects can explain some of the discrepancy between 1 km C5 and 500 m C6 products, especially for cases of high LAI values. In view of these changes in inputs and spatial resolution, a consistency check of C6 products with C5 was performed in terms of global distributions, spatial coverage of high quality retrievals, seasonal variations and inter-annual LAI anomalies. From these analyses, we found no significant discrepancies between C5 and C6 LAI/FPAR products. The proportion of main radiative transfer algorithm retrievals in C6 increases slightly in most biome types, notably including 17% improvement in evergreen broadleaf forests. With the same biome input, the mean RMSEs of LAI and FPAR are 0.29 and 0.091, respectively, but biome type disagreement worsens the consistency (LAI: 0.39, FPAR: 0.102). Overall C6 estimates global LAI and FPAR by C5-0.01 and C5-0.004. Moreover, C5 and C6 shows consistent inter-annual LAI anomalies over two temperature-limited regions and two precipitation-limited regions. These results produce confidence in the new C6 products. Further evaluation of MODIS LAI/FPAR C6 products through validation using field measurements and inter-comparison with other exiting products will be presented in the second part of this series.

Supplementary Materials: The following are available online at www.mdpi.com/2072-4292/8/5/359, Figure S1: Three-year global 500 m eight-biome map used for MODIS LAI/FPAR C6 products from 2001 to 2003; Figure S2: Color-coded maps of MODIS C5 and C6 FPAR for January (17th–24th January) and July (12th–19th July) of 2003; Figure S3: Seasonal variations of globally averaged MODIS LAI and FPAR from C5 and C6 in 2003; Figure S4: Seasonal variations of algorithm path of C5 and C6 in 2003; Table S1: Biome type specific differences between C5 and C6 FPAR for global scale in 2003.

Acknowledgments: Help from MODIS & VIIRS Science team members is gratefully acknowledged. This work is supported by the MODIS program of NASA and partially funded by the National Basic Research Program of China (Grant No. 2013CB733402), the key program of NSFC (Grant No. 41331171) and Chinese Scholarship Council.

Author Contributions: Kai Yan, Yuri Knyazikhin, Ramakrishna R. Nemani and Ranga B. Myneni conceived and designed the experiments; Taejin Park and Kai Yan performed the experiments; Chi Chen, Taejin Park and Bin Yang analyzed the data; Zhao Liu and Guangjian Yan contributed to Sections 3.4 and 4.3 respectively. All authors contributed to the writing of the paper.

Conflicts of Interest: The authors declare no conflict of interest.

Abbreviations

The following abbreviations are used in this manuscript:

MODIS	Moderate Resolution Imaging Spectroradiometer
LAI	Leaf Area Index
FPAR	Fraction of Photosynthetically Active Radiation

C3	Collection 3
C4	Collection 4
C5	Collection 5
C6	Collection 6
RT	Radiative Transfer
LUT	Look-Up-Table
BRF	Bi-directional Reflectance Factors
NDVI	Normalized Difference Vegetation Index
QC	Quality Control
BTDF	Biome Type Disagreement Factor
RI	Retrieval Index
SI	Saturation Index

References

1. Myneni, R.B.; Smith, G.R.; Lotsch, A.; Friedl, M.; Morisette, J.T.; Votava, P.; Running, S.W.; Hoffman, S.; Knyazikhin, Y.; Privette, J.L.; *et al.* Global products of vegetation leaf area and fraction absorbed PAR from year one of MODIS data. *Remote Sens. Environ.* **2002**, *83*, 214–231. [CrossRef]
2. Sellers, P.J.; Dickinson, R.E.; Randall, D.A.; Betts, A.K.; Hall, F.G.; Berry, J.A.; Collatz, G.J.; Denning, A.S.; Mooney, H.A.; Nobre, C.A. Modeling the exchanges of energy, water, and carbon between continents and the atmosphere. *Science* **1997**, *275*, 502–509. [CrossRef] [PubMed]
3. Zhu, Z.; Bi, J.; Pan, Y.; Ganguly, S.; Anav, A.; Xu, L.; Samanta, A.; Piao, S.; Nemani, R.; Myneni, R. Global data sets of vegetation leaf area index (LAI)3g and Fraction of Photosynthetically Active Radiation (FPAR)3g derived from Global Inventory Modeling and Mapping Studies (GIMMS) Normalized Difference Vegetation Index (NDVI3g) for the Period 1981 to 2011. *Remote Sens.* **2013**, *5*, 927–948.
4. Knyazikhin, Y.; Martonchik, J.V.; Myneni, R.B.; Diner, D.J.; Running, S.W. Synergistic algorithm for estimating vegetation canopy leaf area index and fraction of absorbed photosynthetically active radiation from MODIS and MISR data. *J. Geophys. Res. Atmos.* **1998**, *103*, 32257–32275. [CrossRef]
5. Knyazikhin, Y.; Glassy, J.; Privette, J.L.; Tian, Y.; Lotsch, A.; Zhang, Y.; Wang, Y.; Morisette, J.T.; Votava, P.; Myneni, R.B. *MODIS Leaf Area Index (LAI) and Fraction of Photosynthetically Active Radiation Absorbed by Vegetation (FPAR) Product (MOD15) Algorithm Theoretical Basis Document*; Theoretical Basis Document; NASA Goddard Space Flight Center: Greenbelt, MD, USA, 1999; pp. 1–170.
6. Yang, W.; Tan, B.; Huang, D.; Rautiainen, M.; Shabanov, N.V.; Wang, Y.; Privette, J.L.; Huemmrich, K.F.; Fensholt, R.; Sandholt, I.; *et al.* MODIS leaf area index products: From validation to algorithm improvement. *IEEE Trans. Geosci. Remote Sens.* **2006**, *44*, 1885–1898. [CrossRef]
7. Yang, W.; Huang, D.; Tan, B.; Stroeve, J.C.; Shabanov, N.V.; Knyazikhin, Y.; Nemani, R.R.; Myneni, R.B. Analysis of leaf area index and fraction of PAR absorbed by vegetation products from the terra MODIS sensor: 2000–2005. *IEEE Trans. Geosci. Remote Sens.* **2006**, *44*, 1829–1842. [CrossRef]
8. Yang, W.; Shabanov, N.V.; Huang, D.; Wang, W.; Dickinson, R.E.; Nemani, R.R.; Knyazikhin, Y.; Myneni, R.B. Analysis of leaf area index products from combination of MODIS Terra and Aqua data. *Remote Sens. Environ.* **2006**, *104*, 297–312. [CrossRef]
9. Shabanov, N.V.; Knyazikhin, Y.; Baret, F.; Myneni, R.B. Stochastic Modeling of Radiation Regime in Discontinuous Vegetation Canopies. *Remote Sens. Environ.* **2000**, *74*, 125–144. [CrossRef]
10. Buermann, W. Analysis of a multiyear global vegetation leaf area index data set. *J. Geophys. Res.* **2002**, *107*, D22. [CrossRef]
11. Ganguly, S.; Samanta, A.; Schull, M.A.; Shabanov, N.V.; Milesi, C.; Nemani, R.R.; Knyazikhin, Y.; Myneni, R.B. Generating vegetation leaf area index Earth system data record from multiple sensors. Part 2: Implementation, analysis and validation. *Remote Sens. Environ.* **2008**, *112*, 4318–4332. [CrossRef]
12. Fang, H.; Jiang, C.; Li, W.; Wei, S.; Baret, F.; Chen, J.M.; Garcia-Haro, J.; Liang, S.; Liu, R.; Myneni, R.B.; *et al.* Characterization and intercomparison of global moderate resolution leaf area index (LAI) products: Analysis of climatologies and theoretical uncertainties. *J. Geophys. Res. Biogeosci.* **2013**, *118*, 529–548. [CrossRef]
13. Majasalmi, T.; Rautiainen, M.; Stenberg, P.; Manninen, T. Validation of MODIS and GEOV1 fPAR Products in a Boreal Forest Site in Finland. *Remote Sens.* **2015**, *7*, 1359–1379. [CrossRef]

14. Garrigues, S.; Lacaze, R.; Baret, F.; Morisette, J.T.; Weiss, M.; Nickeson, J.E.; Fernandes, R.; Plummer, S.; Shabanov, N.V.; Myneni, R.B.; *et al.* Validation and intercomparison of global Leaf Area Index products derived from remote sensing data. *J. Geophys. Res.* **2008**, *113*. [CrossRef]
15. Ross, J. *The Radiation Regime and Architecture of Plants Stands*; Springer Science & Business Media: Medford, MA, USA, 1981.
16. Myneni, R.B.; Ross, J. *Photon-Vegetation Interactions: Applications in Optical Remote Sensing and Plant Ecology*; Springer Science & Business Media: Medford, MA, USA, 1991.
17. Huang, D.; Knyazikhin, Y.; Dickinson, R.E.; Rautiainen, M.; Stenberg, P.; Disney, M.; Lewis, P.; Cescatti, A.; Tian, Y.; Verhoef, W.; *et al.* Canopy spectral invariants for remote sensing and model applications. *Remote Sens. Environ.* **2007**, *106*, 106–122. [CrossRef]
18. Myneni, R.B.; Williams, D.L. On the relationship between FAPAR and NDVI. *Remote Sens. Environ.* **1994**, *49*, 200–211. [CrossRef]
19. Wang, Y.; Tian, Y.; Zhang, Y.; El-Saleous, N.; Knyazikhin, Y.; Vermote, E.; Myneni, R.B. Investigation of product accuracy as a function of input and model uncertainties: Case study with SeaWiFS and MODIS LAI/FPAR algorithm. *Remote Sens. Environ.* **2001**, *78*, 299–313. [CrossRef]
20. Myneni, R.B.; Ramakrishna, R.; Nemani, R.; Running, S.W. Estimation of global leaf area index and absorbed par using radiative transfer models. *IEEE Trans. Geosci. Remote Sens.* **1997**, *35*, 1380–1393. [CrossRef]
21. Fang, H.; Li, W.; Myneni, R.B. The impact of potential land cover misclassification on MODIS leaf area index (LAI) estimation: A statistical perspective. *Remote Sens.* **2013**, *5*, 830–844. [CrossRef]
22. Garrigues, S.; Shabanov, N.V.; Swanson, K.; Morisette, J.T.; Baret, F.; Myneni, R.B. Intercomparison and sensitivity analysis of Leaf Area Index retrievals from LAI-2000, AccuPAR, and digital hemispherical photography over croplands. *Agric. Forest Meteorol.* **2008**, *148*, 1193–1209. [CrossRef]
23. Vermote, E.F.; Vermeulen, A. Atmospheric Correction Algorithm: Spectral Reflectances (MOD09). Algorithm Theoretical Background Document. Available online: http://dratmos.geog.umd.edu/files/pdf/atbd_mod09.pdf (accessed on 7 March 2016).
24. Friedl, M.A.; Sulla-Menashe, D.; Tan, B.; Schneider, A.; Ramankutty, N.; Sibley, A.; Huang, X. MODIS Collection 5 global land cover: Algorithm refinements and characterization of new datasets. *Remote Sens. Environ.* **2010**, *114*, 168–182. [CrossRef]
25. Wolfe, R.E.; Devadiga, S.; Masuoka, E.J.; Running, S.W.; Vermote, E.; Giglio, L.; Wan, Z.; Riggs, G.A.; Schaaf, C.; Myneni, R.B.; *et al.* Improvements to the MODIS Land Products in Collection Version 6. Available online: http://adsabs.harvard.edu/abs/2013AGUFM.B41D0430W (accessed on 7 March 2016).
26. Masson, V.; Champeaux, J.; Chauvin, F.; Meriguet, C.; Lacaze, R. A global database of land surface parameters at 1-km resolution in meteorological and climate models. *J. Climat.* **2003**, *16*, 1261–1282. [CrossRef]
27. Marengo, J.A.; Alves, L.M.; Soares, W.R.; Rodriguez, D.A.; Camargo, H.; Riveros, M.P.; Pabló, A.D. Two contrasting severe seasonal extremes in tropical South America in 2012: Flood in Amazonia and drought in northeast Brazil. *J. Climat.* **2013**, *26*, 9137–9154. [CrossRef]
28. Wang, D.; Morton, D.; Masek, J.; Wu, A.; Nagol, J.; Xiong, X.; Levy, R.; Vermote, E.; Wolfe, R. Impact of sensor degradation on the MODIS NDVI time series. *Remote Sens. Environ.* **2012**, *119*, 55–61. [CrossRef]
29. Wu, H.; Li, Z. Scale Issues in Remote Sensing: A Review on Analysis, Processing and Modeling. *Sensors* **2009**, *9*, 1768–1793. [CrossRef] [PubMed]
30. Tian, Y.; Wang, Y.; Zhang, Y.; Knyazikhin, Y.; Bogaert, J.; Myneni, R.B. Radiative transfer based scaling of LAI retrievals from reflectance data of different resolutions. *Remote Sens. Environ.* **2003**, *84*, 143–159. [CrossRef]
31. Ganguly, S.; Schull, M.A.; Samanta, A.; Shabanov, N.V.; Milesi, C.; Nemani, R.R.; Knyazikhin, Y.; Myneni, R.B. Generating vegetation leaf area index earth system data record from multiple sensors. Part 1: Theory. *Remote Sens. Environ.* **2008**, *112*, 4333–4343. [CrossRef]

remote sensing

MDPI

Article

Evaluation of MODIS LAI/FPAR Product Collection 6. Part 2: Validation and Intercomparison

Kai Yan [1,2], Taejin Park [2], Guangjian Yan [1,*], Zhao Liu [2], Bin Yang [2,3], Chi Chen [2], Ramakrishna R. Nemani [4], Yuri Knyazikhin [2] and Ranga B. Myneni [2]

1 School of Geography, State Key Laboratory of Remote Sensing Science, Beijing Normal University, Beijing 100875, China; kaiyan.earthscience@gmail.com
2 Department of Earth and Environment, Boston University, Boston, MA 02215, USA; taejin1392@gmail.com (T.P.); liuzhaofairy@gmail.com (Z.L.); ybjason@bu.edu (B.Y.); chenchi@bu.edu (C.C.); jknjazi@bu.edu (Y.K.); ranga.myneni@gmail.com (R.B.M.)
3 Beijing Key Lab of Spatial Information Integration and Its Applications, Institute of RS and GIS, Peking University, Beijing 100871, China
4 The National Aeronautics and Space Administration (NASA) Ames Research Center, Moffett Field, CA 94035, USA; rama.nemani@nasa.gov
* Correspondence: gjyan@bnu.edu.cn; Tel.: +86-010-5880-2085

Academic Editors: Alfredo R. Huete and Prasad S. Thenkabail
Received: 4 April 2016; Accepted: 25 May 2016; Published: 30 May 2016

Abstract: The aim of this paper is to assess the latest version of the MODIS LAI/FPAR product (MOD15A2H), namely Collection 6 (C6). We comprehensively evaluate this product through three approaches: validation with field measurements, intercomparison with other LAI/FPAR products and comparison with climate variables. Comparisons between ground measurements and C6, as well as C5 LAI/FPAR indicate: (1) MODIS LAI is closer to true LAI than effective LAI; (2) the C6 product is considerably better than C5 with RMSE decreasing from 0.80 down to 0.66; (3) both C5 and C6 products overestimate FPAR over sparsely-vegetated areas. Intercomparisons with three existing global LAI/FPAR products (GLASS, CYCLOPES and GEOV1) are carried out at site, continental and global scales. MODIS and GLASS (CYCLOPES and GEOV1) agree better with each other. This is expected because the surface reflectances, from which these products were derived, were obtained from the same instrument. Considering all biome types, the RMSE of LAI (FPAR) derived from any two products ranges between 0.36 (0.05) and 0.56 (0.09). Temporal comparisons over seven sites for the 2001–2004 period indicate that all products properly capture the seasonality in different biomes, except evergreen broadleaf forests, where infrequent observations due to cloud contamination induce unrealistic variations. Thirteen years of C6 LAI, temperature and precipitation time series data are used to assess the degree of correspondence between their variations. The statistically-significant associations between C6 LAI and climate variables indicate that C6 LAI has the potential to provide reliable biophysical information about the land surface when diagnosing climate-driven vegetation responses.

Keywords: Leaf Area Index (LAI); Fraction of Photosynthetically-Active Radiation (FPAR); MODIS; Collection 6; evaluation; validation; intercomparison

1. Introduction

The Leaf Area Index (LAI) and Fraction of Photosynthetically-Active Radiation absorbed by vegetation (FPAR) are two key biophysical variables required by most global models of climate, ecosystem productivity, biogeochemistry, hydrology and ecology [1]. Satellite remote sensing is the most effective way of collecting these variables at a large scale over a long period of time on a regular basis [2]. The MODerate resolution Imaging Spectroradiometer (MODIS) instruments on

board NASA's Terra and Aqua platforms are designed for monitoring the Earth's atmosphere, ocean and land surface and started operational production and distribution of the LAI/FPAR products from 2000. These datasets are widely used as inputs for land surface models and as training data for neural-network-based LAI/FPAR products, such as GLASS and GEOV1 [3,4]. During the past sixteen years, the MODIS science team aimed to provide users with better products by updating product cohorts, which are called collections. Collection 6 (C6) represents the latest such cohort and contains the entire time series from February 2000 to the present. C6 was released and distributed free of charge to the public from August 2015 and is expected to benefit from improvements of the input data [5].

It is critical to understand the accuracy of the product in order to effectively use LAI/FPAR in land surface models [6–11]. There are several schemes to evaluate remote sensing products, including direct validation, intercomparison and other indirect approaches. Many evaluation efforts for previous collections of MODIS LAI/FPAR products can be found in the literature from both the MODIS science team and interested users [9–13]. Special attention has been paid to the accuracy of the estimates, improvements in a new version and consistency with other global products. Collection 5 (C5) products were found to benefit from refinements of algorithm and input data [9]. Intercomparisons with other global products suggested that C5 products are reliable and consistent [8,11]. The main drawbacks of C5 LAI/FPAR were reported to be unrealistically strong temporal variability and systematic overestimation of FPAR over sparsely-vegetated areas [8].

The recently released C6 products have not been validated with ground measurements or compared to existing global products. Thus, it is critical to evaluate the new products, as users are advised to switch to C6. In this context, the primary objectives of this paper are to evaluate the MODIS LAI/FPAR C6 products and to investigate the differences between MODIS products and other global products. This is achieved comprehensively through three approaches: (1) direct validation with ground measurements; (2) intercomparison with GLASS, CYCLOPES and GEOV1 products; and (3) comparison with climate variables.

This paper is organized as follows. Section 2 provides a general description of the datasets used in this study, including global LAI/FPAR products, validation sites and time series of climate variables. Section 3 details three approaches used for validating and intercomparing the LAI/FPAR products. Results and discussion from the various evaluation analyses are documented in Section 4. Concluding remarks are presented in Section 5.

2. Datasets

2.1. Global LAI/FPAR Products

In this section, the main characteristics of the remotely-sensed global LAI/FPAR products under study are described. A brief summary of these characteristics is given in Table 1.

2.1.1. MODIS LAI/FPAR

As described in [2,14], the main algorithm generating the MODIS LAI/FPAR products is based on a three-Dimensional Radiative Transfer (3D RT) model in which atmospherically-corrected reflectances observed by the MODIS instrument and a biome map are used to generate the retrievals. Given daily land surface Bi-directional Reflectance Factors (BRFs) and their uncertainties, the algorithm finds the best LAI and FPAR estimates from biome-specific Look-Up-Tables (LUTs). A back-up empirical method based on the relationships between the Normalized Difference Vegetation Index (NDVI) and LAI/FPAR are utilized to produce estimates with relatively poor quality. LAI and FPAR are produced daily. The LAI value corresponding to the maximum FPAR is selected over the four-day or eight-day compositing period. Vegetation clumping is accounted for at the plant and canopy scales through the model. Therefore, the LAI corresponds to true LAI in all biomes. However, in the case of needle-leaf forest, shoot clumping is not accounted for. The FPAR is defined as the instantaneous black-sky value

at the time of the Terra overpass (10:30 a.m.). MODIS products store the corresponding Quality Control (QC) data layers, and the users are advised to consult the quality flags when using these products.

C6 represents the latest version of MODIS LAI/FPAR [5]. The most important change in C6 is that products are being produced at 500-m spatial resolution instead of 1 km, as in C5. A new version of MODIS surface reflectances (MOD09GA C6) is used to replace the previous used 1-km intermediate dataset (MODAGAGG). C6 also replaces the 1-km static land cover input with new multi-year land cover maps at 500-m resolution. From a consistency check of C6 with C5 [5], there are no significant discrepancies between the two collections in terms of global distributions, seasonal variations, interannual LAI anomalies and the spatial coverage of high quality retrievals. A simulation experiment suggested that the differences caused by scale effects are negligible for FPAR and low in the case of LAI [5]. In this study, we only use data from Terra (MOD) instead of Aqua (MYD) or the combined product (MCD) for three reasons: (1) the earlier overpass time of Terra results in more successful retrievals due to low cloud contamination; (2) the GLASS, CYCLOPES and GEOV1 products have a similar acquisition time s Terra; and (3) the GLASS and GEOV1 products have partly been based on MODIS LAI/FPAR from the Terra-MODIS sensor [15].

Table 1. Global LAI/FPAR products investigated in this study. GSD, LUT, RT, GRNN, ANN, tLAI and eLAI stand for "Ground Sampling Distance", "Look-Up Table", "Radiative Transfer", "General Regression Neural Network", "Artificial Neural Network", "true LAI" and "effective LAI", respectively.

Product	GSD	Frequency	Projection	Sensor	Main Algorithm	LAI Type	Ref.
MODIS C5	1 km	8-day	SIN [4]	MODIS	LUT based on 3D RT	tLAI	[2,14]
MODIS C6	500 m	8-day	SIN	MODIS	LUT based on 3D RT	tLAI	[5]
GLASS [1] V03	1 km	8-day	SIN	MODIS	GRNN trained with CYC * and MOD [5]	tLAI	[3,16]
CYC [2] V3.1	1/112°	10-day	Plate Carrée	VGT	ANN trained with 1D RT	eLAI	[17,18]
GEOV1 [3] V1.3	1/112°	10-day	Plate Carrée	VGT	ANN trained with CYC and MOD	Fused with tLAI and eLAI	[4,8]

[1] MODIS period; [2] CYCLOPES; [3] VGT period; [4] Sinusoidal; [5] clumping-corrected CYCLOPES, "MOD" stands for "MODIS"; * stands for "CYCLOPES".

2.1.2. CYCLOPES LAI/FPAR

The CYCLOPES LAI/FPAR product (http://postel.mediasfrance.org) was produced with data from the SPOT-VGT sensor at 1/112° (about 1 km at the Equator) spatial resolution and a 10-day temporal resolution, in a Plate Carrée projection, for the period 1999–2007 [17,18]. The algorithm used the red, near-infrared and short-wave infrared reflectances, which had been normalized to a standard geometry. LAI and FPAR were estimated using a neural network trained from simulations from a coupled leaf and canopy radiative transfer model (PROSAIL [19]) without using land cover input. Clumping at the plant and canopy scales was not represented in the algorithm, but landscape clumping was represented by considering mixed pixels made of a fraction of pure vegetation and a complement fraction of pure bare soil. Therefore, the LAI corresponds to effective LAI rather than true LAI. The FPAR is defined as the instantaneous black-sky FPAR at 10:00 a.m., referring only to the green elements. The CYCLOPES product was provided with the corresponding error estimate and a quality flag. The early saturation of LAI was reported as the main drawback of the CYCLOPES product [8].

2.1.3. GLASS LAI

The Global Land Surface Satellite (GLASS) LAI dataset was generated and released by Beijing Normal University (http://www.bnu-datacenter.com) [16]. This product has a temporal resolution

of eight days and spans from 1982–2012. From 1982–1999, the product was generated from AVHRR reflectances and provided in a geographic projection at the resolution of 0.05°. From 2000–2012, the product was derived from MODIS land surface reflectance (MOD09A1) and provided in a sinusoidal projection at a resolution of 1 km for the globe. In this study, we only focus on the product during the MODIS period. GLASS LAI was derived from reprocessed MODIS reflectance data using General Regression Neural Networks (GRNNs) [3]. GRNNs were trained by a database that was generated from MODIS and clumping-corrected CYCLOPES LAI products over BELMANIP (Benchmark Land Multisite Analysis and Intercomparison of Products) sites during the period from 2001–2003. MODIS LAI and clumping-corrected CYCLOPES LAI were fused in a weighted linear combination in order to obtain the best LAI estimate as follows:

$$LAI_{fused} = \omega LAI_{mod} + (1-\omega) LAI^{*}_{cyc}, \text{ with} \quad (1)$$

$$\omega = f_{mod}/(f_{mod} + f_{cyc}) \quad (2)$$

where, LAI_{fused} is a combined estimate of LAI, LAI_{mod} is the smoothed and gap-filled MODIS LAI, LAI^{*}_{cyc} is the true LAI converted from the CYCLOPES LAI and ω is the normalized weight for the MODIS LAI. Thus, linear regressions were constructed between MODIS and CYCLOPES for each biome type. The weights for each biome were determined by the deviation of MODIS and CYCLOPES (*i.e.*, f_{mod} and f_{cyc}) from the ground-measured LAIs. A quality control layer was attached to show the processing status, the quality of inputs and contamination by snow, clouds and shadows.

2.1.4. GEOV1 LAI/FPAR

The GEOV1 LAI/FPAR is the first version of the global biophysical products under the Geoland2 project (http://www.copernicus.eu/projects/geoland2). More than 30 years (1981–present) of the global LAI and FPAR were derived from AVHRR, SPOT-VGT and PROBA-V observations during three temporal periods using neural networks. In this study, we use the product during the VGT-derived period (1998–2014). LAI and FPAR during this period were derived at 1/112° spatial resolution with a 10-day step in a Plate Carrée projection (http://land.copernicus.vgt.vito.be) [4,8]. The MODIS and CYCLOPES products were first fused to obtain the best LAI (same for FPAR) estimate as follows:

$$LAI_{fused} = \omega LAI_{mod} + (1-\omega) LAI_{cyc}, \text{ with} \quad (3)$$

$$\omega = \min(1, \frac{1}{4} LAI_{cyc}) \quad (4)$$

where LAI_{fused} is a combined estimate of LAI, LAI_{mod} is the MODIS LAI, LAI_{cyc} is the CYCLOPES LAI and ω is the weight for MODIS LAI. The weight is determined by LAI_{cyc} and a threshold value (LAI_{cyc} = 4), which corresponds to the value when CYCLOPES starts to saturate. Neural networks were trained between the fused LAI and the VGT surface directionally-normalized reflectances over BELMANIP sites without biome type specification. Once trained, these networks were run to provide LAI/FPAR every 10 days within the 30-day composite period from the VGT sensor along with quality flags and quantitative uncertainties. The GEOV1 LAI is the combination of true and effective LAI, because MODIS and CYCLOPES LAI correspond to true and effective LAI, respectively. GEOV1 FPAR corresponds to the instantaneous black-sky value around 10:15 a.m. and is calculated by selecting 70% of the cumulative FPAR distribution of daily values within the compositing period instead of the maximum FPAR, as in the case of MODIS [2].

2.2. Validation Sites and BELMANIP Network

The validation dataset is from a collection of sites for which ground measurements have been collected and processed according to the CEOS/WGCV-LPV guidelines [7,20]. An empirical "transfer function" between high spatial resolution radiometric data and the biophysical measurements was

used to scale local ground measurements up to the 3 km × 3 km area of the site. There are currently 113 such datasets available, corresponding to sites and various dates of measurements.

The BELMANIP network of sites was designed to represent the global variability of vegetation types and climatological conditions [21]. This network was mainly built using sites from existing experimental networks (FLUXNET, AERONET, VALERI, BigFoot, *etc.*) and complemented with additionally sites from the GLC2000 land cover map. The site selection was performed for each band of latitude (10° width) by keeping the same proportion of biome types within the selected sites as within the whole latitude band. Attention was paid so that the sites were homogeneous over a 10 × 10 km^2 area, almost flat and with a minimum proportion of urban area and permanent water bodies. Note that there are no ground measurements for most of these sites, and therefore, this network is always used for intercomparison, rather than direct validation. Representing the latest version, the BELMANIP2.1 currently contains 445 sites and is used in this study.

2.3. Time Series of Climate Variables

This study uses the Time Series (TS) datasets of global surface temperature and precipitation that were produced by the Climatic Research Unit (CRU) at the University of East Anglia [22]. Climate variables were calculated for each 0.5° × 0.5° latitude/longitude grid, monthly, by employing a triangulated linear interpolation method. Through the auspices of the World Meteorological Organization (WMO) in collaboration with the U.S. National Oceanographic and Atmospheric Administration (NOAA), archives provided by more than 4000 meteorological stations were used to cover the world's land areas. At present, the latest time series data (TS 3.23) were generated by the CRU for the period 1901–2014 and publicly available from http://www.cru.uea.ac.uk.

3. Methodology

3.1. Direct Validation with Ground Measurements

3.1.1. Selection of Reliable Ground Measurements

We use the spatially-averaged values over a 3 km × 3 km reference map as the "ground truth" at each validation site, as in previous studies [7,8]. However, several sources of uncertainties reduce the reliability of these measurements. First, optical instruments (e.g., LAI2000) that are generally used for point-scale measurements only provide effective LAI (eLAI), which may result in an underestimation of true LAI (tLAI) [23] up to 70% in coniferous forests [24]. Second, the scale effect in indirect ground measurement can result in obvious uncertainties when the sampling length is not properly selected and this has often been ignored [25]. Third, the up-scaling scheme using an empirical "transfer function" between high spatial resolution reflectances and point-scale biophysical measurements requires a relatively large homogenous area, which may not be satisfied at some sites. Last but not least, uncertainties can arise due to the effects of the point spread function and geo-location errors of the satellite pixel. The overall uncertainty at each site differs with vegetation type, surface homogeneity, equipment used, sampling strategy, *etc.* [26]. However, absolute uncertainties of LAI reference maps corrected for clumping and non-green elements are expected to be smaller than 1 LAI unit in most sites [27]. The uncertainty is expected to be around 0.1 for FPAR [8].

Figure 1 shows the biome type distribution within each 3 km × 3 km validation site based on the MODIS land cover product (500-m resolution, C5). The upper part of the plot denotes the information entropy of the biome type for each site. This serves as an indicator of surface homogeneity. The information entropy is calculated using the proportion of each biome type within a specific site as follows:

$$H = -\sum_{i=1}^{11} (P_i * \log_2 P_i) \quad (5)$$

where H is information entropy and P_i represents the proportion of the area covered by the i-th biome type. The value 11 corresponds to the total number of MODIS land cover types. We screened out some of the 113 sites to improve the overall accuracy of these measurements. This screening was based on four criteria: (1) Presence of 500 m × 500 m pixels labeled as "water" with the 3 km × 3 km site; (2) the information entropy of biome type was greater than 1; (3) the proportion of invalid MODIS pixels (based on QC in Table 2) was larger than 40%; and (4) suspicious LAI/FPAR values (e.g., LAI < 2 for dense forests, Site #42) based on field experience and literature reports [8].

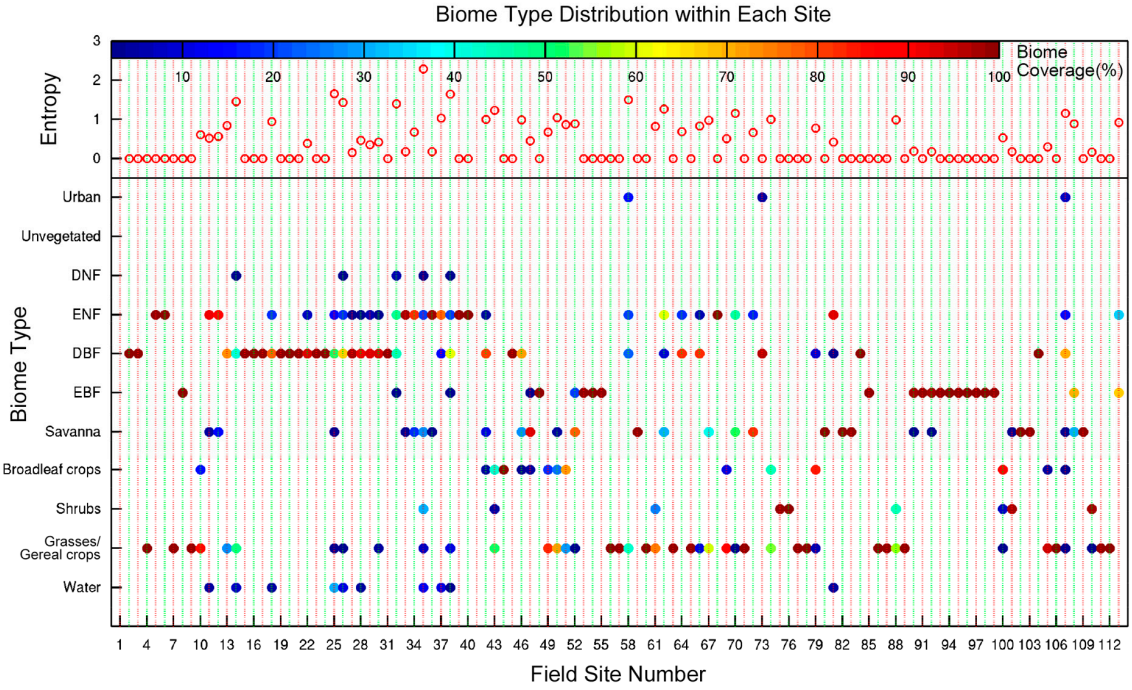

Figure 1. Biome type distribution within each 3 km × 3 km validation site based on the 500-m resolution MODIS C5 land cover product. The bottom part of the plot shows biome types and the corresponding proportion of coverage within each site. EBF, DBF, ENF and DNF stand for "Evergreen Broadleaf Forest", "Deciduous Broadleaf Forest", "Evergreen Needleleaf Forest" and "Deciduous Needleleaf Forest", respectively. The top part of the plot shows the biome type information entropy of each site calculated using Equation (5). Zero means there is only one biome type in the site or the site is a homorganic site. A larger entropy value means larger heterogeneity.

Table 2. Quality control for the four products under study.

Product	Quality Flag	Snow	Cloud	Shadow	Aerosol	Cirrus	Suspect	Overall
MODIS	FparLaiQC	Clear	Clear	-	No	No	-	-
	FparExtraQC	-	Clear	Clear	-	-	-	Good
GLASS	QC	Clear	Clear	Clear	-	-	-	Good
CYCLOPES	SM	Clear	-	-	Pure	-	No	Good
GEOV1	QFLAG	Clear	-	-	Pure	-	No	Good

3.1.2. Validation of MODIS LAI/FPAR Product

We compared both MODIS C5 and C6 products with ground measurements. The spatial and temporal mismatch between the remote sensing product and ground truth is the main issue related to such a comparison [4,18]. A 3 × 3 array of surrounding pixels has been recommended for calculating the mean value to reduce geolocation uncertainties [8]. Considering that reference maps cover a 3 km × 3 km area, which contains about 36 (6 × 6) MODIS C6 pixels and 9 (3 × 3) C5 pixels,

we averaged all of the valid pixels within the reference map. The corresponding 8-day composite, which includes the date of ground measurements was extracted. Thus, the maximum temporal mismatch is about 7 days, which should have minimal impact in most cases. Compared to the overall uncertainties of the LAI reference maps, uncertainties caused by spatial and temporal mismatch may be thus ignored. As suggested by the MODIS product user guide, the QC layers were consulted to exclude retrievals with poor quality caused by snow, clouds or high aerosol content (details in Section 3.2.1). Only retrievals from the main algorithm were used for the validation analyses reported here.

3.2. Intercomparison with Existing Global Products

3.2.1. Quality Control for Products

All of the four products under study provide QC layers, and users are advised to consult the quality flags when using them. Therefore, we performed quality control for each product using the criteria listed in Table 2. In agreement with other studies [6–8,10,18], land pixels contaminated by clouds or marked as "snow", "aerosol", "cirrus" or "suspected" according to the QC information were marked as invalid data. Note that quality control for different products was not identical because of different QC layers. For instance, MODIS and GLASS were masked by cloud, while CYCLOPES and GEOV1 were not. The MODIS biome map was used to exclude bare areas from this analysis. This study used retrievals from both the main and back-up algorithms in order to show the performance of the products instead of algorithms.

3.2.2. Comparison of Spatial Distribution

This study evaluated the four global LAI/FPAR products at the continental and global scale to characterize their performances. These products must be resampled to an identical projection and period to enable pixel-by-pixel comparisons. The four products were first quality controlled as described in Section 3.2.1 and then resampled to the Plate Carrée projection with a quarter degree spatial resolution. The LAI/FPAR values for each $0.25^\circ \times 0.25^\circ$ pixel were computed as the average of all valid native pixels falling within the coarser grid. A no-data value was assigned if more than 30 percent of the native pixels were composed of invalid data (based on QC in Table 2). The datasets with different temporal compositing periods were averaged into a monthly time step. The pixel was assigned with a no-data value if there were no valid data within the whole month.

Pixel-by-pixel absolute differences (MODIS minus other products) between MODIS and the other three LAI products and other two FPAR products were calculated and mapped at the global scale for visual comparison. Histograms of global LAI and FPAR from each product were computed and compared. Two particular months—January and July in 2001—were selected to represent the boreal winter and summer, respectively. In addition, the spatial consistency of LAI over the African continent was investigated. As in [7], we extracted and compared latitudinal LAIs from the four products along the longitudes between 20° E and 25° E.

3.2.3. Comparison at the Site Scale

We compared four LAI products and three FPAR products over 445 BELMANIP2.1 sites. Products were masked by QC flags and aggregated into a monthly time step. LAI and FPAR values from the 60 months of the 2001–2005 period were used to assess the discrepancies between different products through scatterplots. In this exercise, the original projections of the products were kept, and a 1-km (for MODIS and GLASS) or $1/112^\circ$ (for CYCLOPES and GEOV1) spatial resolution was adapted. This is because of two reasons: (1) the high homogeneity of these sites reduces the geolocation uncertainties due to different projection systems, target shift and different point spread functions [21]; and (2) any additional processing including reprojection and resampling would introduce more uncertainties [6].

The MODIS land cover map was used to divide the 445 sites into three broad vegetation classes in terms of canopy structure and leaf shape. The three classes are non-forest (Biomes 1–4), broadleaf

forests (Biomes 5 and 6) and needleleaf forests (Biomes 7 and 8). Regression equations for any two products, as well as the corresponding coefficient of determination (R^2) and root-mean-squared error (RMSE) were computed to assess the consistency.

3.2.4. Temporal Comparison

We evaluated temporal LAI/FPAR profiles of the four products extracted over seven validation sites where some ground measurements were available during the period from 2001–2004. Each site represented one vegetation type in the MODIS classification scheme. There was no validation site that could be used for DNF. Monthly LAI/FPAR estimates were first calculated using the same approach described in Section 3.2.3. Then, the seasonal variations of the four products were compared for both LAI and FPAR with R^2 and RMSE denoting the consistency.

3.3. Comparison with Climate Variables

Using independent geographic variables to explain the interannual variations of LAI/FPAR is a novel approach of indirectly evaluating these products. Due to a lack of long-term data, this evaluation method has not been used for MODIS LAI/FPAR previously. In this study, we applied this approach using thirteen years (2002–2014) of MODIS C6 LAI data. 2000 and 2001 were not included because of the missing data in these two years. The C5 and C6 LAI products were firstly resampled to the Plate Carrée projection and aggregated to a half degree spatial resolution and a monthly time step. QC information was taken into account to exclude retrievals with poor quality. In this manner, the LAI dataset matched the datasets of climate variables both spatially and temporally. Further averaging over some specific regions and over the whole year or some specific months was done to obtain the time series for statistical analyses. An area-weighted approach was used to eliminate geometrical effects. Anomalies of LAI, temperature and precipitation were computed by subtracting the thirteen-year mean from data of specific years. We calculated standardized anomalies (anomalies normalized by their standard deviations) of LAI and surface temperature during the beginning of the growing season (April and May) for four temperature-limited regions within 60°N–90°N. We also calculated standardized anomalies of annual averages of LAI and precipitation for two water-limited regions. In addition, the correlation between annual averaged LAI and annual total precipitation in the tropical latitudes (23° S–23° N) was investigated.

4. Results and Discussion

4.1. Direct Validation

4.1.1. Characteristics of Measurements

As mentioned above, the validation data used in this paper is from a collection of sites all over the world. Therefore, the method of ground measurement (e.g., destructive sampling, LAI-2000, digital hemispherical photos, TRAC, AccuPAR and allometry) may vary from site to site and from date to date. Details of these sites can be found on http://calvalportal.ceos.org/web/olive. Note that effective LAI measured by optical instruments may differ significantly from true LAI, particularly in forests [24]. These indirect measurements that have been corrected for clumping effect are also considered as true LAI in this study. Measurements without clumping correction were discarded in some studies [7,8], but were investigated separately in this study. We also compared the MODIS FPAR with ground measurements, which was seldom done in previous studies. Measurements at the same site, but different dates were considered independently.

Table 3. Biome-specific information of ground measurements after pre-selection. The numbers of ground measurements of tLAI, eLAI and FPAR for each biome are listed. The mean values and standard deviations of both ground measurements and retrievals from the C5 and C6 products are also provided (mean value ± standard deviation).

Biome Type	# of tLAI	Ground tLAI	MODIS C5 LAI	MODIS C6 LAI	# of eLAI	Ground eLAI	MODIS C5 LAI	MODIS C6 LAI	# of FPAR	Ground FPAR	MODIS C5 FPAR	MODIS C6 FPAR
B1 [1]	12	1.37 ± 1.01	1.20 ± 0.80	1.32 ± 0.85	49	0.93 ± 0.94	0.83 ± 0.50	0.94 ± 0.62	36	0.26 ± 0.24	0.32 ± 0.14	0.33 ± 0.16
B2 [2]	2	0.18 ± 0.19	0.21 ± 0.01	0.21 ± 0.01	1	0.03 ± 0.00	0.20 ± 0.00	0.20 ± 0.00	2	0.26 ± 0.34	0.28 ± 0.21	0.31 ± 0.24
B3 [3]	0	N/A	N/A	N/A	3	2.14 ± 0.75	2.09 ± 0.43	2.14 ± 0.55	0	N/A	N/A	N/A
B4 [4]	15	1.61 ± 0.55	1.43 ± 0.69	1.46 ± 0.47	15	1.26 ± 0.36	1.43 ± 0.69	1.46 ± 0.47	4	0.44 ± 0.14	0.56 ± 0.18	0.53 ± 0.15
B5 [5]	2	4.65 ± 0.39	4.44 ± 1.66	4.65 ± 0.39	2	3.27 ± 0.18	4.44 ± 1.66	4.95 ± 1.02	2	0.92 ± 0.04	0.73 ± 0.20	0.79 ± 0.10
B6 [6]	14	3.58 ± 0.40	3.77 ± 0.99	3.79 ± 0.82	7	3.78 ± 1.26	4.74 ± 1.10	4.67 ± 0.59	0	N/A	N/A	N/A
B7 [7]	9	2.69 ± 0.76	2.58 ± 1.08	2.42 ± 0.73	5	1.72 ± 0.48	2.31 ± 0.80	2.60 ± 0.97	1	0.49 ± 0.00	0.53 ± 0.00	0.61 ± 0.00
B8 [8]	0	N/A	N/A	N/A	0	N/N	N/A	N/A	0	N/A	N/A	N/A
Overall	54	2.31 ± 1.26	2.25 ± 1.46	2.28 ± 1.38	82	1.37 ± 1.21	1.49 ± 1.36	1.59 ± 1.35	45	0.31 ± 0.27	0.36 ± 0.18	0.38 ± 0.19

[1] Grasses/cereal crops; [2] shrubs; [3] broadleaf crops; [4] savanna; [5] EBF; [6] DBF; [7] ENF; [8] DNF.

Table 3 shows biome-specific information of ground measurements after pre-selection, as described in Section 3.1.1. The mean values and standard deviations of both ground measurements and retrievals from C5 and C6 products are provided. After pre-selection, there are 54 true LAI, 82 effective LAI and 45 FPAR measurements left for further analyses. Note that there are no valid true LAI and FPAR measurements for broadleaf crops, and there are no FPAR measurements for DBF. We also lack LAI and FPAR measurements for DNF. The absence of a valid ground truth suggests that more field measurements are needed in the future to further refine this assessment. Ground measurements and MODIS estimates indicate the same vegetation density sequence: broadleaf forests > needleleaf forests > savannas > grasses/cereal crops > shrubs. LAI/FPAR values extracted from the C5 and C6 products show good agreement in all vegetation types. The slight overestimation in C6 relative to C5 is due to scale effects and refinements to surface reflectances [5]. C5 shows the most obvious underestimation in savanna, which is in agreement with [28]. This issue has been mitigated by C6 to some extent. We note that MODIS LAI overestimates the ground measurements in DBF, which was also reported by [8]. As expected, effective LAIs are lower than true LAIs for all biomes due to the lack of correction for clumping. MODIS LAI estimates are found to be closer to true LAI rather than effective LAI. The largest difference between measured LAI and C5 is achieved in EBF. However, this difference is corrected in C6. Considering all biomes, measured LAI (2.31) agrees with C6 (2.28) better than with C5 (2.25). Broadleaf forests show large differences between measured effective LAI and MODIS estimates, which is due to the unneglectable clumping effects. MODIS FPAR shows overestimation in all biomes, except for EBF, where radiative signals may saturate.

4.1.2. Comparison with Ground Measurements

Figure 2a,b compares measured LAI with MODIS C5 and C6 LAI, respectively. As expected, MODIS shows better agreement with true LAI than with effective LAI. MODIS retrievals are found to systematically overestimate effective LAI measurements, especially in forests, which agrees with Stenberg *et al.* [29], who suggested that an effective LAI can produce errors of 30%–70%. In comparison with true LAI measurements, C6 performs better than C5 with the RMSE decreasing from 0.8 down to 0.66 and R^2 increasing from 0.70–0.77. Large uncertainties are found in high LAI values, which can be explained by relatively lower algorithm accuracy due to signal saturation. Overall, most of the data are within ± 1 LAI bias, indicating that the total uncertainty of this validation work is less than 1 LAI unit. Note that this uncertainty comes from both MODIS products and other sources, including the uncertainties of reference maps and mismatch in spatial and temporal domains. We also note that the distribution of the measurements is problematic with an over-representation of low values. This is expected to be solved by adding more ground measurements, especially for broadleaf crops and forests, according to the CEOS/WGCV-LPV guidelines.

In comparisons to ground measurements, MODIS FPAR performs relatively poorly compared to LAI (Figure 2c,d). The RMSE of C5 and C6 are 0.16 and 0.15, respectively. The R^2 increases from 0.68–0.74 from C5 to C6. We notice a significant overestimation of MODIS retrievals in both C5 and C6 at low FPAR values. This systematic overestimation of FPAR over sparsely-vegetated areas was reported as a main drawback of the MODIS FPAR product [8]. However, the disagreement in this study may also be due to the fact that understories are usually not taken into account in ground measurements, which will underestimate the true FPAR [15]. Overall, most data are within ± 0.2 bias with all uncertainties included.

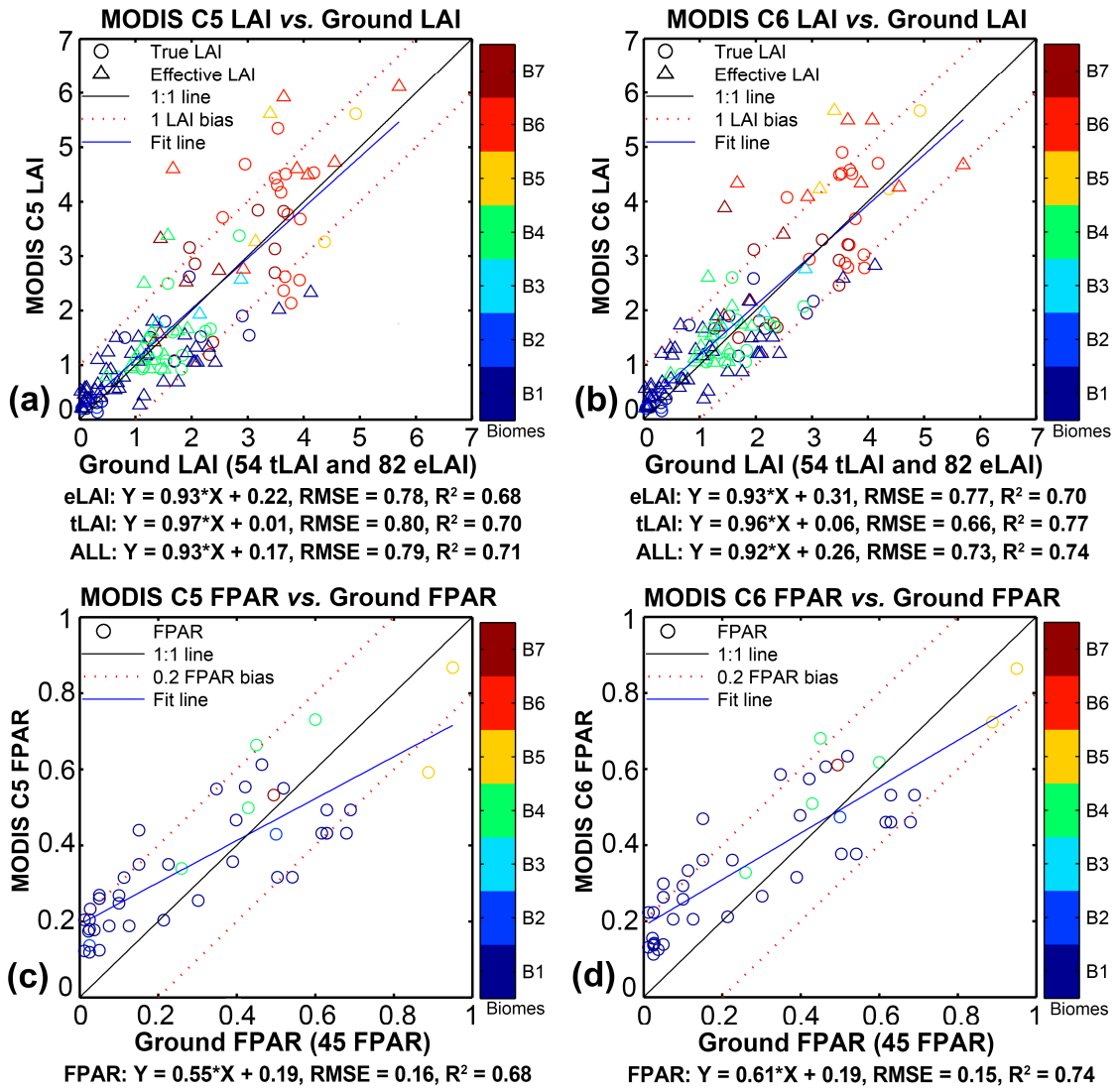

Figure 2. Comparisons between ground measured LAI (**a**,**b**) and FPAR (**c**,**d**) with MODIS C5 (left panels) and C6 (right panels) retrievals. Fifty four true LAI, 82 effective LAI and 45 FPAR measurements are used here. The 3 km × 3 km sites dominated by different biome types are depicted by different colors. Circles (triangles) in (**a**) and (**b**) represent ground LAI measurements corrected (not corrected) for clumping.

4.2. Intercomparison

4.2.1. Global LAI/FPAR Distribution

Figure 3a–c displays the global distribution of absolute LAI differences between MODIS and three other products in July 2001. Figure 3d,e shows the corresponding FPAR. As expected, the four products generally show a continuous LAI/FPAR distribution at the global scale. We notice that CYCLOPES and GEOV1 do not provide LAI or FPAR estimates at high latitudes (>74°) due to the absence of SPOT-VGT observations in these regions. South Asia and Southeast Asia are the largest regions with missing data for MODIS, CYCLOPES and GEOV1. This is caused by the frequent cloudy weather related to the southwest monsoon in these regions [30]. The reason why the GLASS product has valid data is due to gap-filling. MODIS also has missing data over the high latitudes of North America due to cloud contamination or poor atmospheric conditions.

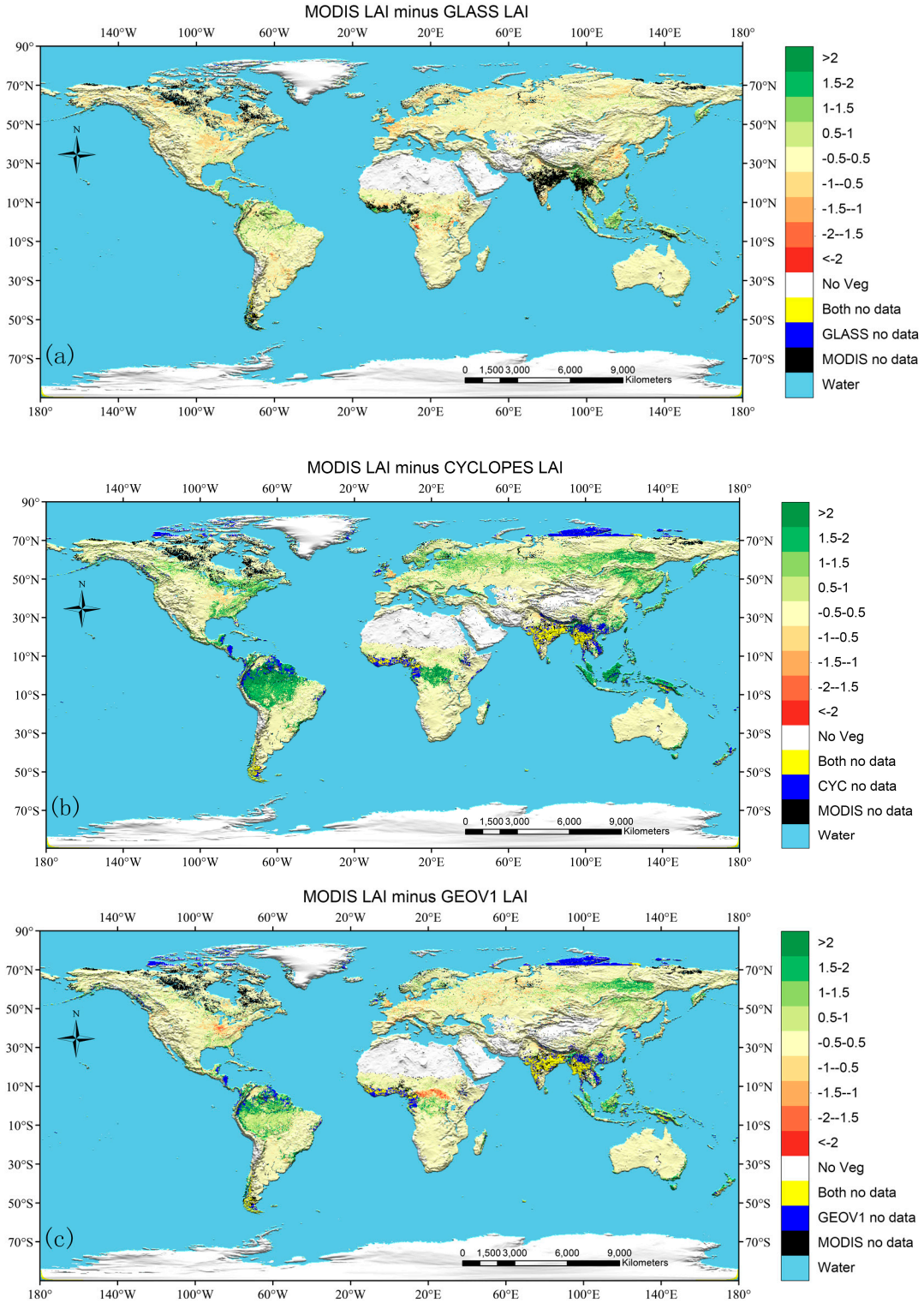

Figure 3. *Cont.*

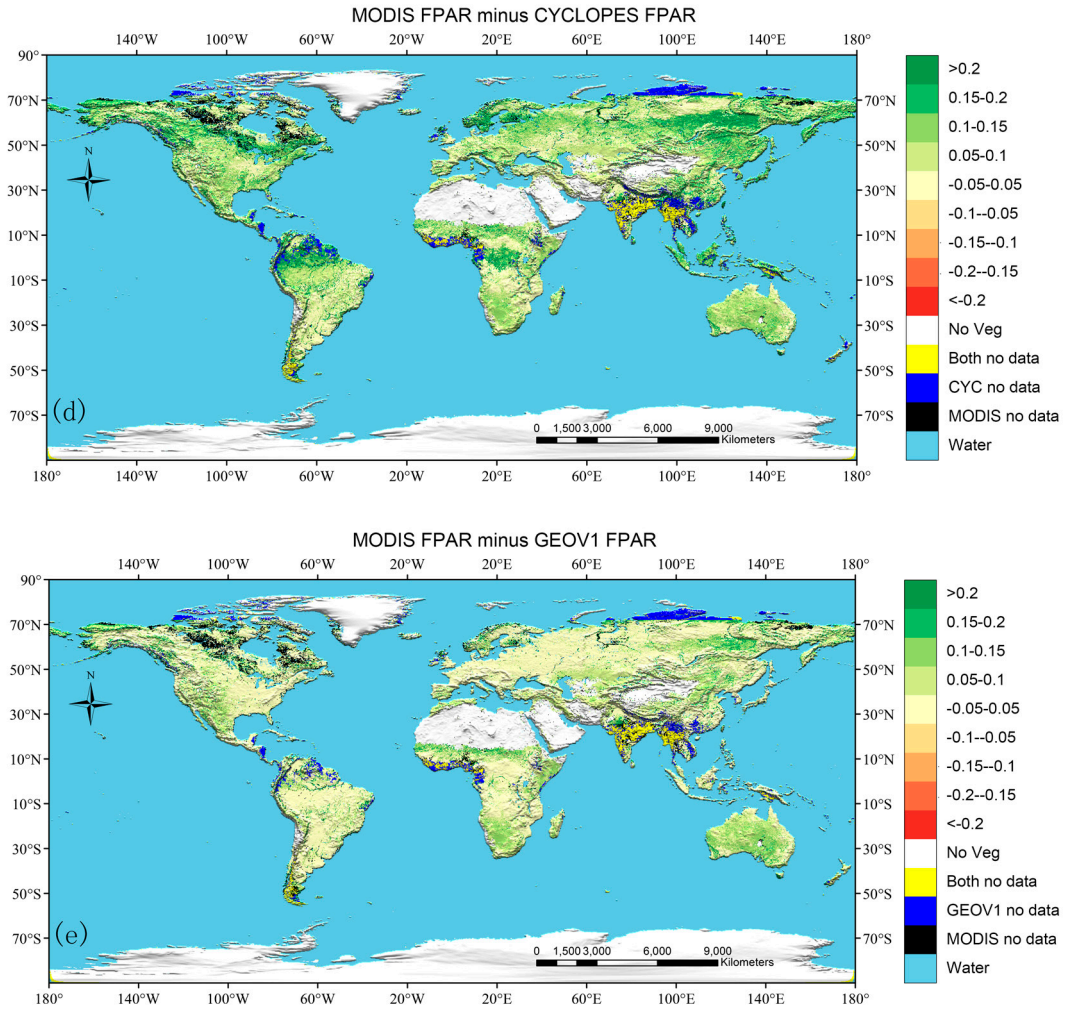

Figure 3. Global distribution of absolute differences between (**a**) MODIS and GLASS LAI; (**b**) MODIS and CYCLOPES LAI; (**c**) MODIS and GEOV1 LAI; (**d**) MODIS and CYCLOPES FPAR; and (**e**) MODIS and GEOV1 FPAR in July 2001. The spatial resolution is 0.25 degrees.

MODIS is found to agree best with GLASS, as expected, with absolute differences within $\pm$0.5 LAI units for most of the land surface (Figure 3a). The reasons are two-fold: (1) the surface reflectance data input to the two algorithms are from the same MODIS instrument; (2) MODIS LAI products are used as one part of the ANN training data for GLASS. Compared to GLASS, most overestimation of MODIS LAI is seen in tropical densely-vegetated regions. From Figure 3b,d, we notice significant underestimation from CYCLOPES, especially in densely-vegetated regions. These discrepancies between MODIS and CYCLOPES can reach to two for LAI and 0.2 for FPAR. This result agrees with previous studies and was found related to premature saturation in the CYCLPOES algorithm [7,8]. This issue was reportedly solved in GEOV1 by using the MODIS product as the training data when LAI is larger than four [4]. Indeed, we find that MODIS agrees better with GEOV1 than CYCLOPES. However, GEOV1 still shows underestimation in some regions, e.g., forests in the Amazon and South Asia. Note that the distributions of discrepancies between MODIS and GEOV1 are not consistent for LAI and FPAR.

In Figure 4a,b, the four products show smooth and consistent LAI distributions at the global scale for both January and July. Differences between global distributions are smaller in January than in July, indicating that most inconsistency occurs during the growing season of northern latitudes. The global mean LAIs calculated from MODIS, GLASS, CYCLOPES and GEOV1 are 1.42, 1.43, 1.02 and 1.15 in January and increase to 2.02, 2.09, 1.53 and 1.81 in July, respectively. Note that the number of valid

overlapping pixels also increases from 96,346 in January to 180,603 in July. This increase is caused by better atmospheric conditions and less cloud or snow contamination in the boreal summer season. Unlike other products, CYCLOPES shows a peak at around LAI = 2.5 and drops rapidly to zero after LAI = 4 in July, which confirms the early saturation issue reported previously. Compared to LAI, FPAR discrepancies are found to be relatively larger (Figure 4c,d). The global mean FPARs calculated from MODIS, CYCLOPES and GEOV1 are 0.4, 0.31 and 0.35 in January and increase to 0.54, 0.43 and 0.5 in July, respectively. The frequency of low LAI and FPAR values is considerably smaller for MODIS than for other products, which is due to the overestimation of the MODIS product in sparsely-vegetated regions [7].

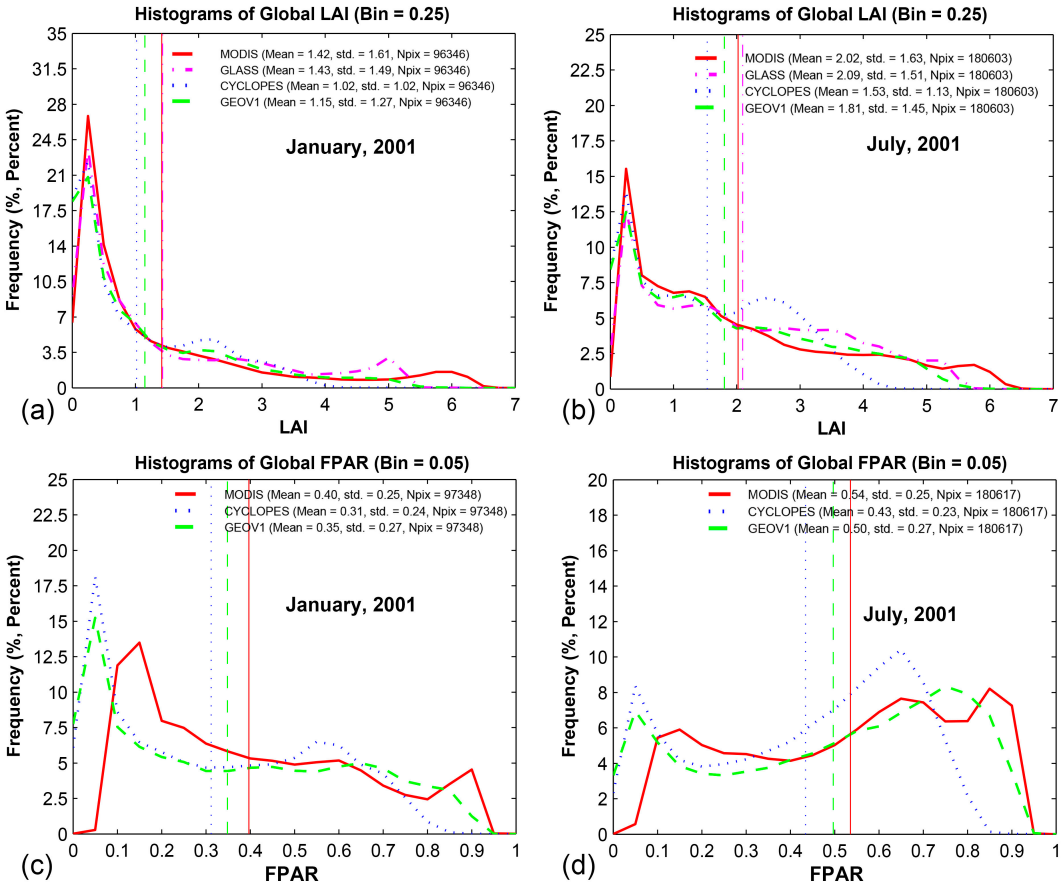

Figure 4. Histograms of global LAI (**a**,**b**) and FPAR values (**c**,**d**) from four products analyzed in this study during the months of January and July of 2001. The frequency is given as the percentage of the total number of global vegetated pixels. Global mean LAI values are depicted by vertical lines. The bins used for LAI and FPAR are 0.25 and 0.05, respectively.

4.2.2. Continental Consistency

The African continent, which is divided by the equator, was selected to assess the spatial consistency among LAIs from the four products at the continental scale. Figure 5a–c indicates that the best spatial agreement is achieved between MODIS and GLASS, with LAI differences ranging within ± 1. A significant underestimation (>2 LAI unit) is found over the central Africa forests in the case of CYCLOPES. This is somewhat alleviated in GEOV1. Missing data are not found in these annual average datasets, except in the case of MODIS near the boundaries of water bodies or barren areas.

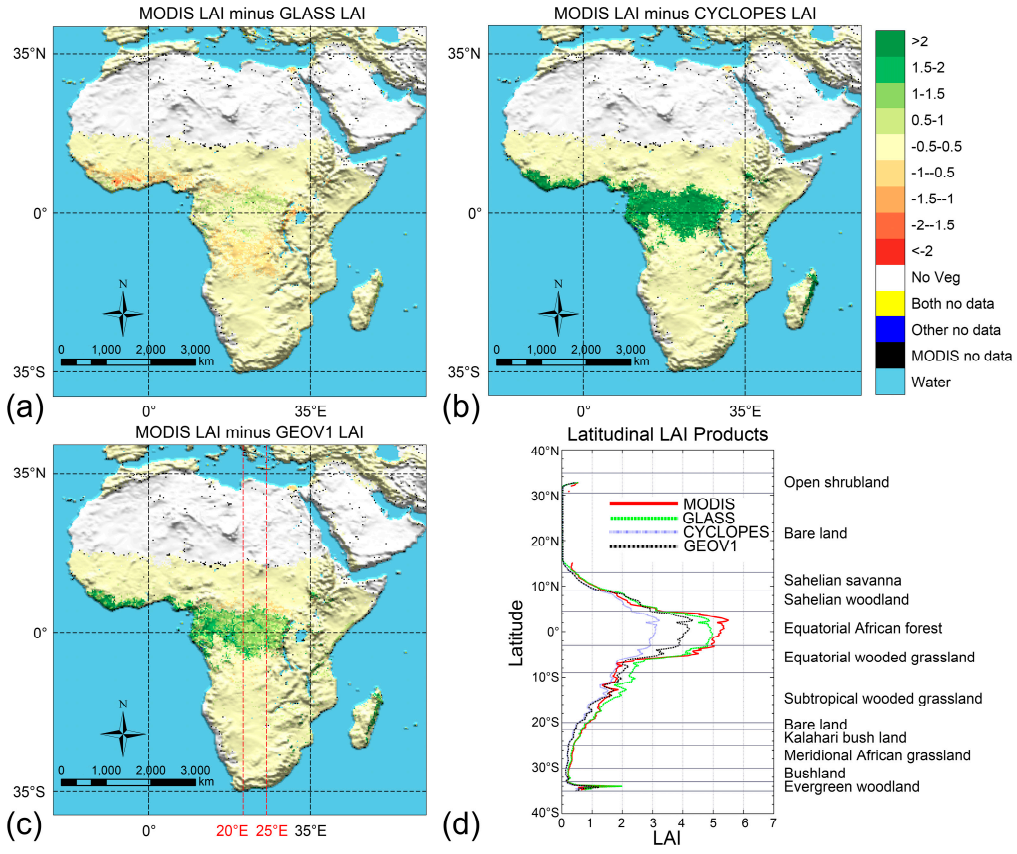

Figure 5. Comparisons of annual averaged LAI from the MODIS, GLASS, CYCLOPES and GEOV1 products over Africa in 2001. (**a**–**c**) Absolute differences between MODIS C6 and GLASS, CYCLOPES and GEOV1; (**d**) LAI from four products along the transect in Africa between 20° E and 25° E.

Figure 5d displays LAIs from MODIS, GLASS, CYCLOPES and GEOV1 along the transect within the longitude bands between 20° E and 25° E. The most obvious inconsistency is seen in equatorial forests, where LAI differences can reach one unit. CYCLOPES underestimates other products in these regions with unrealistically low LAI values. The products agree better over open shrublands and savannas. GEOV1 and CYCLOPES also show good consistency over the subtropical wooded grasslands, while GLASS overestimates them significantly. Two product groups (MODIS-GLASS and GEOV1-CYCLOPES) can be distinguished clearly over the bush lands and meridional African grasslands. This suggests that the input data sources to the algorithms play an important role in affecting the variation and magnitude of LAI/FPAR retrievals.

4.2.3. Comparison over BELMANIP Sites

Density scatter plots of monthly LAI extracted from the four products over BELMANIP2.1 sites during the period from 2001–2005 are shown in Figure 6. Results for three broad vegetation classes (non-forest, broadleaf forests and needleleaf forests) are shown separately in Table 4.

Table 4. Statistics of the intercomparisons among four LAI/FPAR products over BELMANIP sites during 2001–2005. Eight biome types are grouped into three broad categories (1–4: non-forest; 5–6: broadleaf forests; 7–8: needleleaf forests). R^2, RMSE and regression equations are provided.

Biomes		MODIS-GLASS	MODIS-CYCLOPES	MODIS-GEOV1	GLASS-CYCLOPES	GLASS-GEOV1	CYC-GEOV1
LAI	1–4	0.82/0.41/y = 1.03x + 0.10	0.83/0.36/y = 0.94x − 0.01	0.81/0.42/y = 1.05x − 0.03	0.86/0.34/y = 0.85x − 0.03	0.83/0.41/y = 0.94x − 0.06	0.95/0.23/y = 1.09x − 0.01
	5–6	0.82/0.63/y = 0.66x + 1.11	0.72/0.66/y = 0.50x + 0.81	0.79/0.74/y = 0.69x + 0.73	0.77/0.59/y = 0.69x + 0.17	0.80/0.72/y = 1.03x + 0.10	0.89/0.55/y = 1.26x + 0.05
	7–8	0.63/0.62/y = 0.74x + 0.86	0.58/0.59/y = 0.65x + 0.66	0.64/0.61/y = 0.76x + 0.64	0.65/0.57/y = 0.73x + 0.25	0.70/0.60/y = 0.86x + 0.16	0.85/0.43/y = 1.07x + 0.06
	All	0.90/0.53/y = 0.83x + 0.31	0.83/0.53/y = 0.64x + 0.26	0.88/0.56/y = 0.82x + 0.19	0.89/0.44/y = 0.74x + 0.06	0.91/0.50/y = 0.95x − 0.06	0.95/0.36/y = 1.23x − 0.07
FPAR	1–4	N/A	0.89/0.07/y = 1.04x − 0.08	0.88/0.08/y = 1.17x − 0.08	N/A	N/A	0.97/0.04/y = 1.12x + 0.01
	5–6	N/A	0.75/0.08/y = 0.77x + 0.07	0.80/0.08/y = 0.88x + 0.09	N/A	N/A	0.93/0.05/y = 1.06x + 0.06
	7–8	N/A	0.53/0.10/y = 0.75x + 0.09	0.59/0.10/y = 0.82x + 0.12	N/A	N/A	0.82/0.07/y = 0.93x + 0.11
	All	N/A	0.91/0.08/y = 0.95x − 0.05	0.91/0.09/y = 1.08x − 0.05	N/A	N/A	0.97/0.05/y = 1.12x + 0.01

Figure 6a–c shows comparisons over non-forest sites where the best agreements between any two products are observed. LAI values over these sites range from 0–2. Within this range, reflectances are not saturated, and the respective algorithms perform well. Regression lines are close to the 1:1 line with R^2 better than 0.81 and RMSE smaller than 0.42 (LAI) and 0.08 (FPAR) in all cases. This result satisfies the target accuracy (±0.5 LAI unit) expected by the Global Climate Observation System (GCOS) [31]. MODIS seems to underestimate GLASS and GEOV1, but slightly overestimates CYCLOPES. Minimum bias (R^2 = 0.95, RMSE = 0.23) is achieved between CYCLOPES and GEOV1.

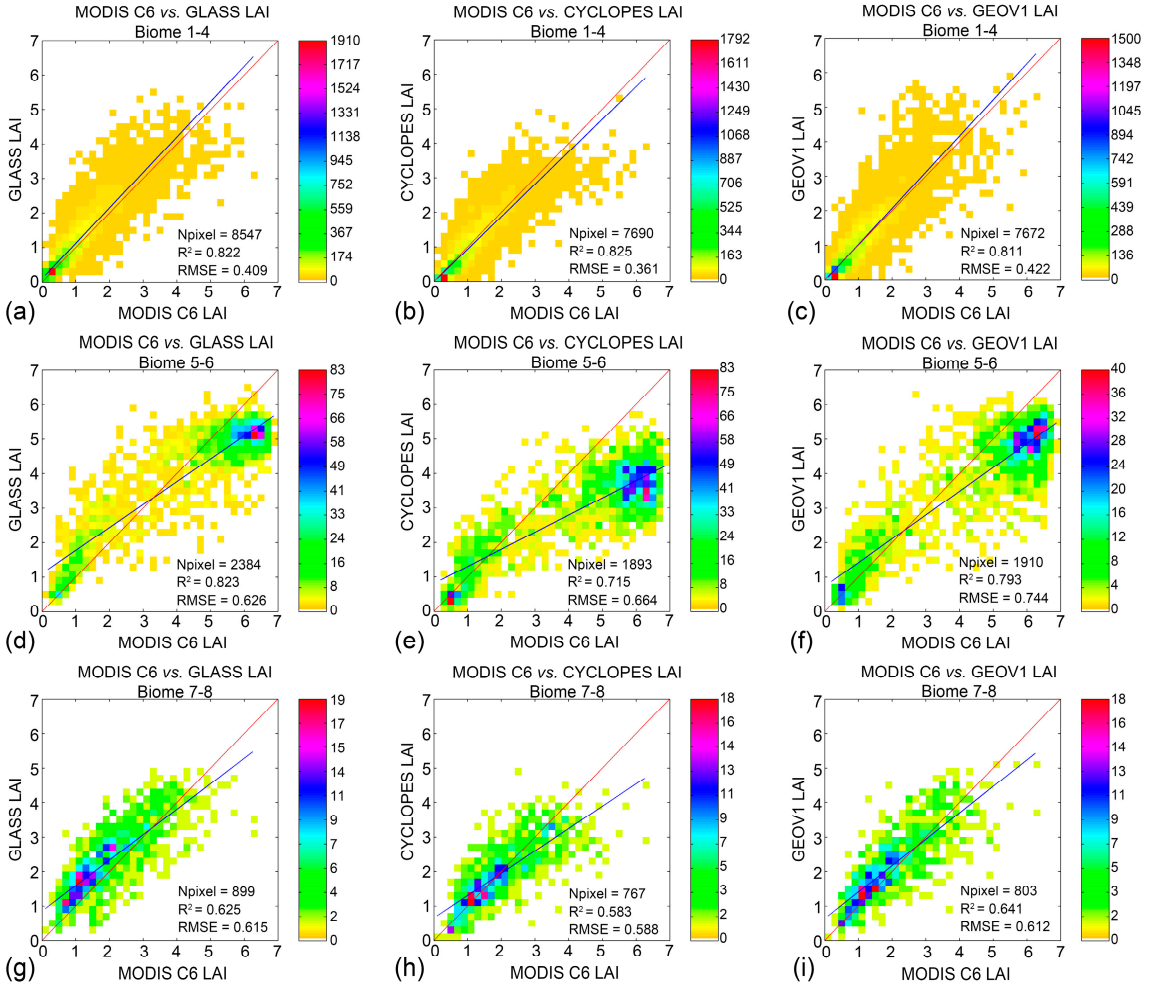

Figure 6. Density scatter plots of monthly MODIS LAI and three other LAI products (left: GLASS; middle: CYCLOPES; right: GEOV1) over BELMANIP sites during the time period from 2001–2005. The plots show a correlation between MODIS and other products for non-forest ((**a**–**c**) Biomes 1–4) in the first row, broadleaf forests ((**d**–**f**) Biomes 5 and 6) in the second row and needle leaf forests ((**g**–**i**) Biomes 7 and 8) in the third row. The red lines and blue lines are the 1:1 lines and regression lines derived from the scatter plots, respectively.

Figure 6d–f shows the case for broadleaf forests where the largest discrepancies are observed. The largest RMSE (0.74) is seen in the MODIS *versus* GEOV1 comparison and the smallest (0.55) between CYCLOPES and GEOV1. The plots show an interesting pattern where the data are in two clusters, which may be due to the monthly temporal resolution in this analysis resulting in missing some parts of the seasonality of deciduous forests. MODIS tends to underestimate in the low-LAI domain and overestimate in the high-LAI domain, relative to other products.

Similar comparisons over needleleaf forests are shown in Figure 6g–i. The total number of observations is less than 900, and this may result in additional uncertainties. CYCLOPES and GEOV1 agree well in terms of R^2 (0.85 for LAI and 0.82 for FPAR) and minimum RMSE (0.43 for LAI and 0.07 for FPAR). The discrepancies between MODIS and other products are similar with R^2 around 0.6. A slight underestimation can be noticed for MODIS at low values, especially compared to GLASS.

When considering all biome types, the RMSE of LAI (FPAR) derived from any two products ranges from 0.36 (0.05)–0.56 (0.09). The sequence from best to worst agreement is: CYCLOPES-GEOV1, GLASS-CYCLOPES, GLASS-GEOV1, MODIS-GLASS, MODIS-CYCLOPES and MODIS-GEOV1.

4.2.4. Temporal Comparison

Temporal Continuity

In the time series of LAI/FPAR products, there would be some gaps (missing data) mainly due to cloud or snow contamination, poor atmospheric conditions or technical problems, which will limit their use in land surface models [7,8]. Here, we define the "annual missing data rate" as the percent of months without valid data during the whole year. It represents the fraction in time of missing data. Note that the quality control applied for different products could be an important factor affecting this criterion.

The four lines in the upper part of Figure 7 represent variations of missing data for MODIS, GLASS, CYCLOPES and GEOV1 through four years (2001–2004). Missing data are also indicated by gaps in the LAI/FPAR time series. The missing data rate ranges from 0%–40% (five months of no data) over the seven sites. Most missing data are in the winter season, which is related to cloudiness, snow and poor atmospheric conditions, especially for high latitude sites. Sites with shrubs, broadleaf crops, savannas and broadleaf forests show low missing data rates (<20%). The four products exhibit different behaviors over different sites, and no clear conclusions can be drawn. GLASS tends to have low missing data, which may be due to a gap-filling procedure in its algorithm. GEOV1 shows a similar missing data rate as CYCLOPES, which may be expected, as both products use the same preprocessed SPOT-VGT data. MODIS shows a moderate missing data rate for most sites, which is not in agreement with some other studies [8]. This may be because our study is based on a normalized monthly temporal step instead of the native temporal resolution of each product. In addition, quality control procedures applied to the different products also affect the number of valid data in the time series.

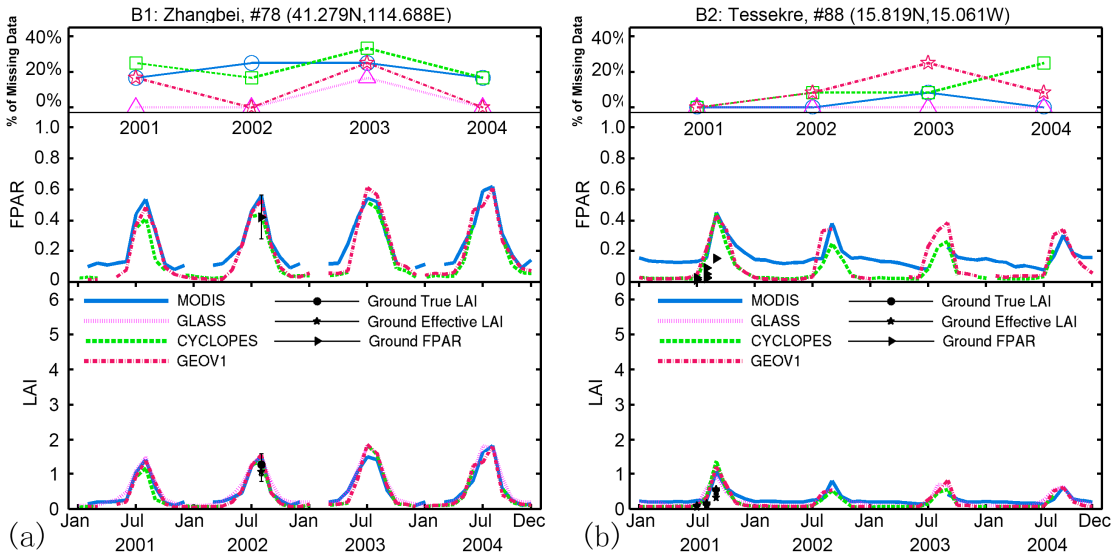

Figure 7. *Cont.*

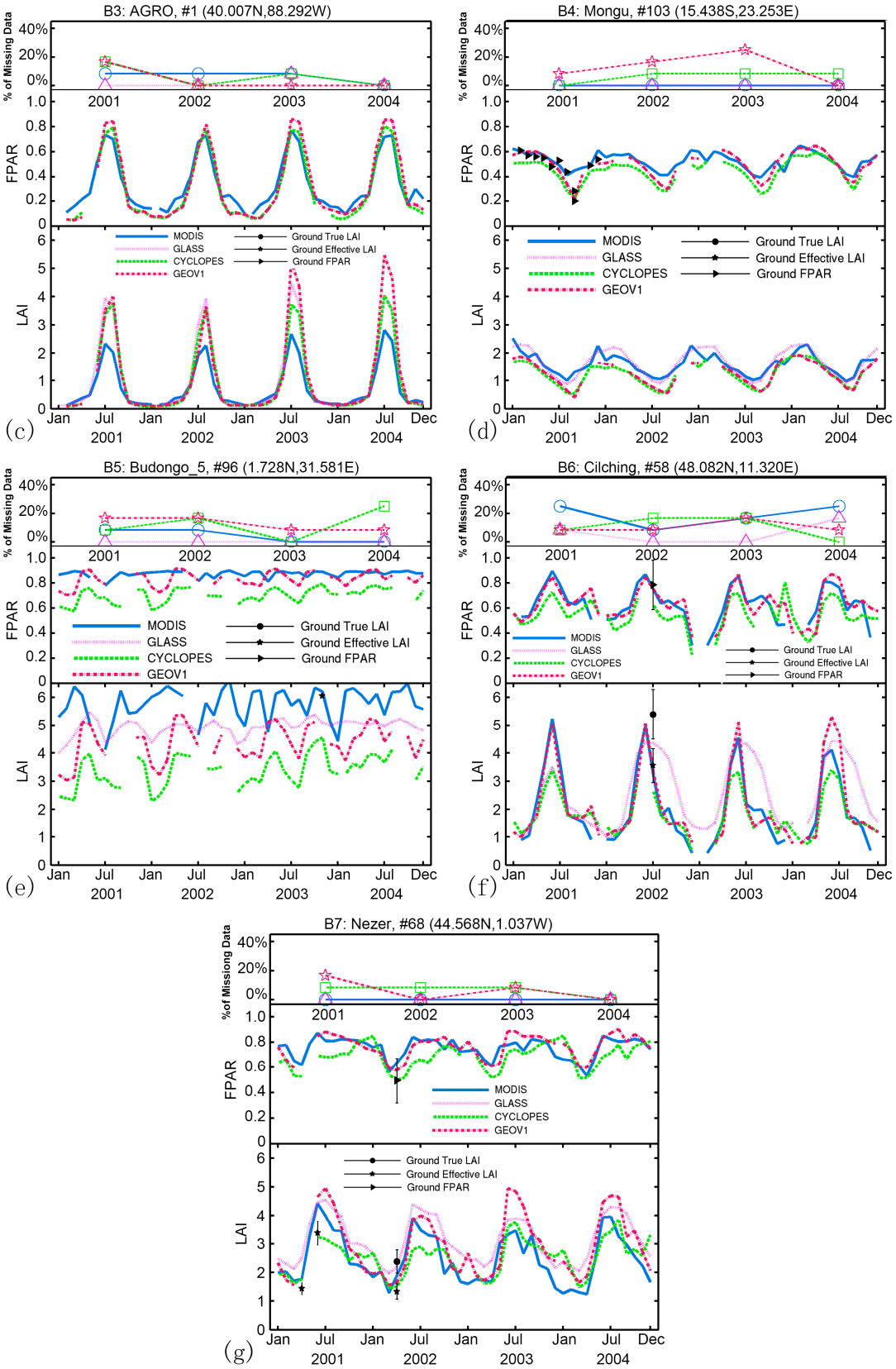

Figure 7. Temporal comparisons of LAI and FPAR among MODIS C6, GLASS, CYCLOPES and GEOV1 products over seven validation sites. Monthly averaged LAI and FAPR values for the time period from 2001–2004 are shown here. Circles, stars and triangles represent ground measurements of true LAI, effective LAI and FPAR, respectively. The four lines plotted at the top represent variations in missing data in each year. (**a**) Grasses; (**b**) shrubs; (**c**) broadleaf crops; (**d**) savanna; (**e**) EBF; (**f**) DBF; and (**g**) ENF.

Temporal Consistency

The consistency of the temporal trajectory of each product over seven validation sites for the period from 2001–2004 is discussed in this section (Figure 7). All available ground measurements are plotted in these figures as a reference. Statistics (R^2 and RMSE) of these temporal comparisons are given in Table 5.

The four products show smooth and consistent annual variations in the case of the Zhangbei grassland site in China, with some gaps in the winter season that may be due to snow contamination (Figure 7a). LAI and FPAR exhibit bell-shaped profiles, with LAI ranging from almost zero in winter to more than one in summer and FPAR ranging from 0–0.5. CYCLOPES displays systematic underestimation, as documented previously [8]. MODIS C6 is still found to systematically overestimate FPAR in sparse canopies, a problem also seen in C5 [15].

All of the products achieve good temporal continuity in shrubs (Figure 7b). LAI and FPAR are relatively low, as rainfall is limited over this site. GLASS, CYCLOPES and GEOV1 agree well, especially at low values of LAI and FPAR. MODIS shows a generally different seasonal profile, which may be realistic [32]. We find that all products overestimate both LAI and FPAR ground measurements.

Figure 7c shows the temporal variations of broadleaf crops over the AGRO site. This site shows similar temporal variations as the Zhangbei site, being about the same latitude, but there are differences in magnitude. LAI and FPAR values can reach four and 0.8, respectively. GLASS, CYCLOPE and GEOV1 agree with each other well, especially in the years 2001 and 2002. However, MODIS shows an underestimation for LAI during the growing season and overestimation of FPAR in the winter season. The LAI difference between MODIS and GEOV1 is larger than two in 2003.

The savanna site shows a different pattern of seasonality as compared to grasses, shrubs and broadleaf crops (Figure 7d). The seasonality is relatively damped with LAI values ranging from 0.5–2. The four products show similar LAI/FAPR variations and agree with ground measurements well. MODIS has no missing data during the four years.

The consistency between the four products is the worst over the EBF site (Figure 7e). This site is in Budongo rainforests where the dry season only spans from December–February and June/July. The field campaign conducted in October/November 2005 reported that LAI varies between 5.19 and 10.47 [33]. However, no clear seasonality is captured by any of the products from LAI or FPAR with high missing data rate. Similar results were reported by other studies [7,8]. This can be explained by the poor quality of satellite products due to cloud contamination and poor atmospheric conditions. The ground measurement in 2003 shows good agreement with MODIS LAI.

Figure 7f shows the case for a DBF site located in the northern high latitude. GEOV1 and MODIS agree best and are the closest to ground measurements for both LAI and FPAR in 2002. As expected, CYCLOPES underestimates all of the other products because of a lack of correction for clumping effects. Compared to others, GLASS shows artifacts related to smoothing and/or gap-filling procedures.

The four products show very similar seasonality over the ENF site (Figure 7g). LAI at this site ranges from 1–5. Thus, saturation effects are prominently seen in CYCLOPES. The MODIS profiles are noisier due to the sensitivity of retrievals to noise in reflectances at high values of LAI [7]. All products generally agree with available ground measurements. We note that CYCLOPES is closer to effective LAI measurements that is smaller than true LAI due to clumping effects.

Table 5 shows the statistical results from temporal comparisons among the four LAI/FPAR products over the seven sites during 2001–2004. R^2 and RMSE are provided as indicators of consistency. The best agreement among four products is seen in the grasses (B1) and broadleaf crops (B3) sites, with R^2 better than 0.9. The agreement between MODIS and other products is least over the EBF (B5) site. Over this site, the RMSE between MODIS and CYCLOPES is 2.56 and 0.19 for LAI and FPAR, respectively. Lager RMSE values over densely-vegetated sites (B4–B7) are observed between CYCLOPES and other products, which is due to premature saturation in the CYCLOPES algorithm [8]. Overall, MODIS agrees best with GLASS, and CYCLOPES agrees best with GEOV1. This is not surprising, as these pairs of products have the same underlying reflectances.

Table 5. Statistics of temporal comparisons among four LAI/FPAR products over seven validation sites during 2001–2004. R^2 and RMSE are provided. Values out of and in blankets are for LAI and FPAR, respectively.

Site and Biome	MODIS-GLASS		MODIS-CYC		MODIS-GEOV1		GLASS-CYC		GLASS-GEOV1		CYCLOPES-GEOV1	
	R^2	RMSE	R^2	RMSE	R^2	RMSE	R^2	RMSE	R^2	RMSE	R^2	RMSE
#78:B1	0.96	0.14	0.91(0.91)	0.17(0.09)	0.94(0.93)	0.15(0.07)	0.95	0.16	0.94	0.17	0.97(0.97)	0.10(0.05)
#88:B2	0.65	0.12	0.61(0.69)	0.20(0.11)	0.76(0.60)	0.16(0.10)	0.82	0.11	0.87	0.10	0.86(0.88)	0.10(0.06)
#1:B3	0.98	0.66	0.96(0.96)	0.62(0.08)	0.93(0.94)	0.95(0.10)	0.98	0.20	0.94	0.39	0.95(0.98)	0.45(0.05)
#103:B4	0.84	0.21	0.75(0.72)	0.42(0.10)	0.79(0.80)	0.40(0.06)	0.89	0.42	0.90	0.38	0.96(0.95)	0.1(0.06)
#96:B5	0.08	1.01	0.01(0.00)	2.56(0.19)	0.00(0.00)	1.70(0.08)	0.53	1.61	0.45	0.76	0.81(0.80)	1.01(0.13)
#58:B6	0.54	1.12	0.89(0.66)	0.57(0.12)	0.86(0.66)	0.56(0.08)	0.50	1.15	0.48	1.12	0.91(0.76)	0.74(0.10)
#68:B7	0.89	0.72	0.45(0.34)	0.69(0.12)	0.74(0.64)	0.68(0.06)	0.57	0.81	0.83	0.53	0.76(0.58)	0.74(0.11)

4.3. Evaluation with Climate Variables

Spatial and temporal variations of biophysical variables can be assessed for consistency with changes observed in meteorological fields. Several studies have focused on the relationship between the temporal variation of LAI and climate variables that govern plant growth in particular regions. From these studies, obvious correlation between LAI and precipitation in tropical regions and temperature in high latitudes regions have been reported [7,11,34,35]. In this section, we discuss the correlation between C6 LAI and temperature in northern latitudes and precipitation in some ENSO (El Niño-Southern Oscillation)-affected regions.

4.3.1. LAI Variation with Surface Temperature

Here, we present interannual variations of C6 LAI and assess their correlation to surface temperature, which can be helpful in verifying the variations in the LAI product. The spatial (60° N–90° N) and temporal (April and May) averages of standardized anomalies of LAI and surface temperature are shown in Figure 8a,b for forests and tundra, respectively. The greening trend in Eurasia was reported to be more obvious than in North America [36]. Therefore, the analysis was done separately for these two continents.

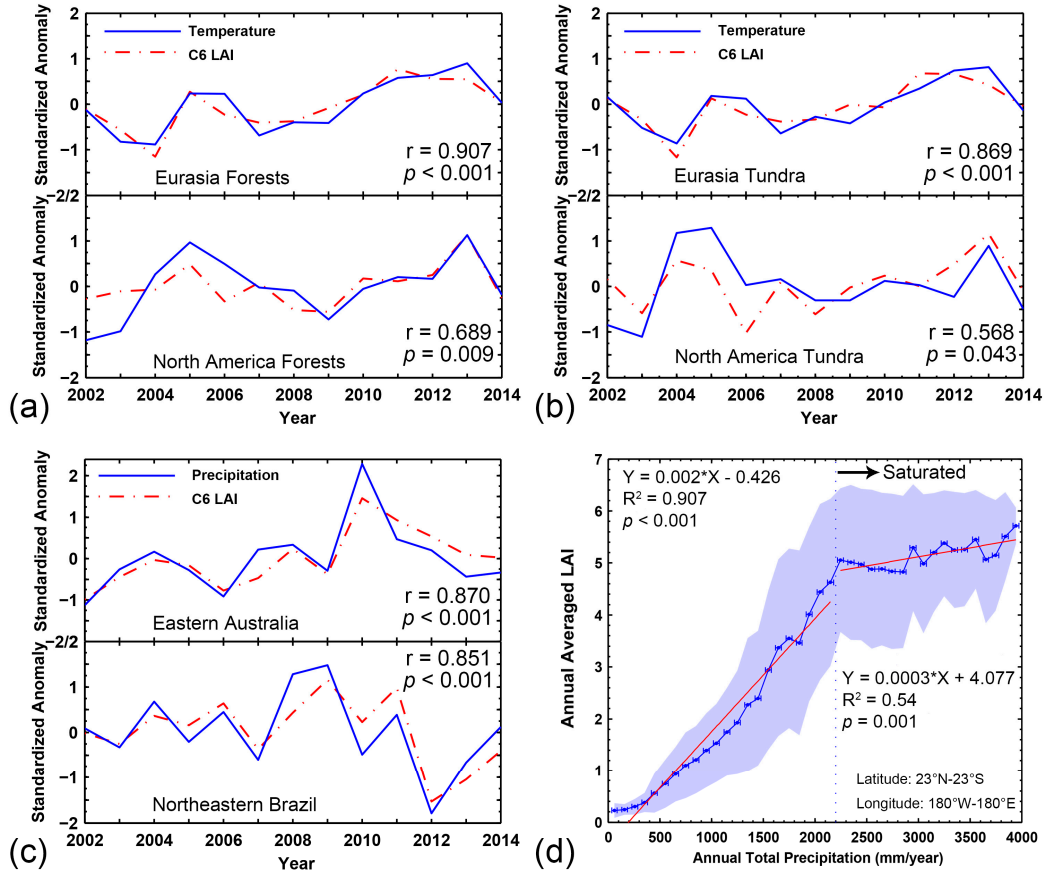

Figure 8. Evaluation of the MODIS LAI C6 product with temperature in the northern latitudes and precipitation in the ENSO-affected regions. (**a**) Temporal variations of the standardized anomalies of the growing season start period (April and May) averages of LAI and temperature for forest pixels in the northern latitudes; (**b**) same as (**a**), but for tundra pixels; (**c**) temporal variations of the standardized anomalies of annual summed LAI and precipitation in eastern Australia (20° S–40° S, 145° E–155° E) and northeastern Brazil (3° S–12° S, 35° W–45° W); (**d**) correlation between annual averaged LAI and annual total precipitation in the tropical latitudes (23° S–23° N). Standard deviations of LAIs and precipitations are denoted by blue shadow and horizontal error bars, respectively.

The anomaly time series of surface temperature and LAI correlate remarkably well, especially in Eurasian forests with a 0.907 correlation coefficient. The linkage is stronger in Eurasia than in North America. This is because North American boreal forests have experienced declining photosynthetic activity due to recent warming-induced drought, wild fires and pest infestations [37]. Our results also indicate that correlations in tundra are considerably weaker than in forests. This could be due to fewer valid data over tundra resulting from poor Sun-sensor geometry and illumination conditions. Nevertheless, we observe a slight warming and greening trend in Eurasian forests (p = 0.033 in a Mann–Kendall trend test [38]). However, no statistically-significant trend is found in tundra or North American forests ($p > 0.1$), which agrees with [11,35].

4.3.2. LAI Variation with Precipitation

The standardized anomalies of thirteen years of LAI and precipitation in two semiarid regions are shown in Figure 8c. Significant coherence between LAI and rainfall anomalies are found in both eastern Australia (r = 0.87, $p < 0.001$) and northeastern Brazil (r = 0.851, $p < 0.001$). We do not find particular directional changes in precipitation or vegetation greenness in these two regions during the period of our study. However, the high precipitation events leading to damaging Australian floods in 2010–2011 [39] are obvious with a peak in both precipitation and LAI variations. Moreover, we notice a severe drought with corresponding vegetation browning occurring in northeastern Brazil in 2012, which has been confirmed in [40].

Figure 8d shows the correlation between annual averaged LAI and annual total precipitation in the tropical latitudes (23° S–23° N). Note that this analysis was not for a specific year, but for the average of thirteen years. The precipitation range (0–4000 mm/year) was divided into 40 intervals. The mean and standard deviation of annual averaged LAI in each of the 40 precipitation bins were first computed for each of the thirteen years and then averaged over the thirteen years. We find a highly significant correlation (R^2 = 0.97, $p < 0.001$) between the two variables when precipitation is less than 2200 mm/year from where this relationship turns to saturated. Large standard deviations of LAI within each precipitation interval indicate the role of other factors in governing plant growth [35].

5. Conclusions

The objective of this paper is to evaluate the newly-released MODIS LAI/FPAR C6 product (MOD15A2H). This is achieved comprehensively through three independent approaches: validation with ground measurements, intercomparison with other satellite products and comparison with climate variables. Fifty four true LAI, 82 effective LAI and 45 FPAR ground measurements with high reliability extracted from 113 sites were used to validate the C6 and C5 LAI/FPAR products. The results showed that MODIS LAI is closer to true LAI, rather than effective LAI, due to the clumping correction in the algorithm. We found that MODIS C6 performed considerably better than C5 in comparisons to true LAI measurements. The RMSE decreased from 0.80 down to 0.66, which is close to the target accuracy ($\pm$0.5) as required by the GCOS. Both C5 and C6 showed an overestimation of FPAR over sparsely-vegetated areas, as noted previously in other studies.

Intercomparisons with three other satellite products (GLASS, CYCLOPES and GEOV1) were carried out at the site, continental and global scales to investigate the differences. The four products showed similar spatial distributions of LAI and FPAR in both January and July. MODIS and GLASS (CYCLOPES and GEOV1) were found to achieve the best agreement, most likely because the surface reflectances used as inputs to the respective algorithms were acquired from the same instrument. CYCLOPES underestimated LAI and FPAR systematically due to the lack of correction for clumping effects and premature saturation. Temporal comparisons for the 2001–2004 period indicated that the products properly captured the seasonality of different biomes, except in EBF, where the poor quality of satellite products resulted in erratic and unrealistic seasonal profiles. The four products showed different performances at different sites in terms of missing data, and no clear conclusion could be drawn.

To further imbue confidence in the LAI product, we assessed correlations between the variations of satellite-derived LAI and station-measured temperature and precipitation data over a thirteen year period. Statistically-significant agreements between these data series indicated that the interannual variations in LAI are not an artifact of remote sensing data or the algorithm.

The research presented here is critical for the further understanding and proper use of C6 LAI/FPAR products in land surface models. Furthermore, the validation and intercomparison approaches presented in this work can be used for the evaluation of similar products in the future.

Acknowledgments: Help from MODIS and VIIRS Science team members is gratefully acknowledged. This work is supported by the MODIS program of NASA and partially funded by the National Basic Research Program of China (Grant No. 2013CB733402) and the key program of NSFC (Grant No. 41331171). Kai Yan gives thanks for the scholarship from the China Scholarship Council.

Author Contributions: Kai Yan, Guangjian Yan, Yuri Knyazikhin, Ramakrishna R. Nemani and Ranga B. Myneni conceived of and designed the experiments. Taejin Park and Kai Yan performed the experiments. Taejin Park and Bin Yang analyzed the data. Zhao Liu and Chi Chen contributed to the Sections 3.3 and 4.3. All authors contributed to the writing of the paper.

Conflicts of Interest: The authors declare no conflict of interest. The founding sponsors had no role in the design of the study; in the collection, analyses or interpretation of the data; in the writing of the manuscript; nor in the decision to publish the results.

Abbreviations

The following abbreviations are used in this manuscript:

MODIS	Moderate Resolution Imaging Spectroradiometer
LAI	Leaf Area Index
FPAR	Fraction of Photosynthetically-Active Radiation
C5	Collection 5
C6	Collection 6
RT	Radiative Transfer
LUT	Look-Up-Table
BRF	Bi-directional Reflectance Factors
NDVI	Normalized Difference Vegetation Index
GSD	Ground Sampling Distance
ANN	Artificial Neural Network
GRNN	General Regression Neural Network
tLAI	True LAI
eLAI	Effective LAI
QC	Quality Control
GLASS	Global Land Surface Satellite
BELMANIP	Benchmark Land Multisite Analysis and Intercomparison of Products
TS	Time Series
CRU	Climatic Research Unit
WMO	World Meteorological Organization
NOAA	National Oceanographic and Atmospheric Administration
NASA	National Aeronautics and Space Administration
EBF	Evergreen Broadleaf Forest
DBF	Deciduous Broadleaf Forest
ENF	Evergreen Needleleaf Forest
DNF	Deciduous Needleleaf Forest
ENSO	El Niño-Southern Oscillation

References

1. Sellers, P.J.; Dickinson, R.E.; Randall, D.A.; Betts, A.K.; Hall, F.G.; Berry, J.A.; Collatz, G.J.; Denning, A.S.; Mooney, H.A.; Nobre, C.A. Modeling the exchanges of energy, water, and carbon between continents and the atmosphere. *Science* **1997**, *275*, 502–509. [CrossRef]
2. Myneni, R.B.; Smith, G.R.; Lotsch, A.; Friedl, M.; Morisette, J.T.; Votava, P.Ô.N.R.; Running, S.W.; Hoffman, S.; Knyazikhin, Y.; Privette, J.L.; *et al.* Global products of vegetation leaf area and fraction absorbed PAR from year one of MODIS data. *Remote Sens. Environ.* **2002**, *83*, 214–231. [CrossRef]

3. Xiao, Z.; Liang, S.; Wang, J.; Chen, P.; Yin, X.; Zhang, L.; Song, J. Use of general regression neural networks for generating the GLASS leaf area index product from time-series MODIS surface reflectance. *IEEE Trans. Geosci. Remote Sens.* **2014**, *52*, 209–223. [CrossRef]
4. Baret, F.; Weiss, M.; Lacaze, R.; Camacho, F.; Makhmara, H.; Pacholcyzk, P.; Smets, B. GEOV1: LAI and FAPAR essential climate variables and FCOVER global time series capitalizing over existing products. Part1: Principles of development and production. *Remote Sens. Environ.* **2013**, *137*, 299–309. [CrossRef]
5. Yan, K.; Park, T.; Yan, G.; Chen, C.; Yang, B.; Liu, Z.; Nemani, R.; Knyazikhin, Y.; Myneni, R. Evaluation of MODIS LAI/FPAR product Collection 6. Part 1: Consistency and improvements. *Remote Sens.* **2016**, *8*, 359. [CrossRef]
6. Fang, H.; Wei, S.; Liang, S. Validation of MODIS and CYCLOPES LAI products using global field measurement data. *Remote Sens. Environ.* **2012**, *119*, 43–54. [CrossRef]
7. Garrigues, S.; Lacaze, R.; Baret, F.; Morisette, J.T.; Weiss, M.; Nickeson, J.E.; Fernandes, R.; Plummer, S.; Shabanov, N.V.; Myneni, R.B.; *et al.* Validation and intercomparison of global Leaf Area Index products derived from remote sensing data. *J. Geophys. Res.* **2008**, *113*. [CrossRef]
8. Camacho, F.; Cernicharo, J.; Lacaze, R.; Baret, F.; Weiss, M. GEOV1: LAI, FAPAR essential climate variables and FCOVER global time series capitalizing over existing products. Part 2: Validation and intercomparison with reference products. *Remote Sens. Environ.* **2013**, *137*, 310–329. [CrossRef]
9. Yang, W.; Tan, B.; Huang, D.; Rautiainen, M.; Shabanov, N.V.; Wang, Y.; Privette, J.L.; Huemmrich, K.F.; Fensholt, R.; Sandholt, I.; *et al.* MODIS leaf area index products: From validation to algorithm improvement. *IEEE Trans. Geosci. Remote Sens.* **2006**, *44*, 1885–1898. [CrossRef]
10. Fang, H.; Jiang, C.; Li, W.; Wei, S.; Baret, F.; Chen, J.M.; Garcia-Haro, J.; Liang, S.; Liu, R.; Myneni, R.B.; *et al.* Characterization and intercomparison of global moderate resolution leaf area index (LAI) products: Analysis of climatologies and theoretical uncertainties. *J. Geophys. Res. Biogeosci.* **2013**, *118*, 529–548. [CrossRef]
11. Ganguly, S.; Samanta, A.; Schull, M.A.; Shabanov, N.V.; Milesi, C.; Nemani, R.R.; Knyazikhin, Y.; Myneni, R.B. Generating vegetation leaf area index Earth system data record from multiple sensors. Part 2: Implementation, analysis and validation. *Remote Sens. Environ.* **2008**, *112*, 4318–4332. [CrossRef]
12. Steinberg, D.C.; Goetz, S.J.; Hyer, E.J. Validation of MODIS F/sub PAR/products in boreal forests of Alaska. *IEEE Trans. Geosci. Remote Sens.* **2006**, *44*, 1818–1828. [CrossRef]
13. Tan, B.; Hu, J.; Zhang, P.; Huang, D.; Shabanov, N.; Weiss, M.; Knyazikhin, Y.; Myneni, R.B. Validation of Moderate Resolution Imaging Spectroradiometer leaf area index product in croplands of Alpilles, France. *J. Geophys. Res. Atmos.* **2005**, *110*. [CrossRef]
14. Knyazikhin, Y.; Glassy, J.; Privette, J.L.; Tian, Y.; Lotsch, A.; Zhang, Y.; Wang, Y.; Morisette, J.T.; Votava, P.; Myneni, R.B. *MODIS Leaf Area Index (LAI) and Fraction of Photosynthetically Active Radiation Absorbed by Vegetation (FPAR) Product (MOD15) Algorithm Theoretical Basis Document*; Theoretical Basis Document; NASA Goddard Space Flight Center: Greenbelt, MD, USA, 1999; p. 20771.
15. Majasalmi, T.; Rautiainen, M.; Stenberg, P.; Manninen, T. Validation of MODIS and GEOV1 fPAR Products in a Boreal Forest Site in Finland. *Remote Sens.* **2015**, *7*, 1359–1379. [CrossRef]
16. Liang, S.; Zhao, X.; Liu, S.; Yuan, W.; Cheng, X.; Xiao, Z.; Zhang, X.; Liu, Q.; Cheng, J.; Tang, H. A long-term Global LAnd Surface Satellite (GLASS) data-set for environmental studies. *Int. J. Digit. Earth* **2013**, *6*, 5–33. [CrossRef]
17. Baret, F.; Hagolle, O.; Geiger, B.; Bicheron, P.; Miras, B.; Huc, M.; Berthelot, B.; Niño, F.; Weiss, M.; Samain, O. LAI, fAPAR and fCover CYCLOPES global products derived from VEGETATION: Part 1: Principles of the algorithm. *Remote Sens. Environ.* **2007**, *110*, 275–286. [CrossRef]
18. Weiss, M.; Baret, F.; Garrigues, S.; Lacaze, R. LAI and fAPAR CYCLOPES global products derived from VEGETATION. Part 2: Validation and comparison with MODIS collection 4 products. *Remote Sens. Environ.* **2007**, *110*, 317–331. [CrossRef]
19. Jacquemoud, S.; Verhoef, W.; Baret, F.; Bacour, C.; Zarco-Tejada, P.J.; Asner, G.P.; François, C.; Ustin, S.L. PROSPECT+ SAIL models: A review of use for vegetation characterization. *Remote Sens. Environ.* **2009**, *113*, S56–S66. [CrossRef]
20. Morisette, J.T.; Baret, F.; Privette, J.L.; Myneni, R.B.; Nickeson, J.E.; Garrigues, S.; Shabanov, N.V.; Weiss, M.; Fernandes, R.; Leblanc, S.G. Validation of global moderate-resolution LAI products: A framework proposed within the CEOS land product validation subgroup. *IEEE Trans. Geosci. Remote Sens.* **2006**, *44*, 1804. [CrossRef]
21. Baret, F.; Morissette, J.T.; Fernandes, R.A.; Champeaux, J.L.; Myneni, R.B.; Chen, J.; Plummer, S.; Weiss, M.; Bacour, C.; Garrigues, S.; *et al.* Evaluation of the representativeness of networks of sites for the global validation and intercomparison of land biophysical products: Proposition of the CEOS-BELMANIP. *IEEE Trans. Geosci. Remote Sens.* **2006**, *44*, 1794–1803. [CrossRef]

22. Harris, I.; Jones, P.D.; Osborn, T.J.; Lister, D.H. Updated high-resolution grids of monthly climatic observations—The CRU TS3. 10 Dataset. *Int. J. Climatol.* **2014**, *34*, 623–642. [CrossRef]
23. Hu, R.; Yan, G.; Mu, X.; Luo, J. Indirect measurement of leaf area index on the basis of path length distribution. *Remote Sens. Environ.* **2014**, *155*, 239–247. [CrossRef]
24. Chen, J.M.; Cihlar, J. Quantifying the effect of canopy architecture on optical measurements of leaf area index using two gap size analysis methods. *IEEE Trans. Geosci. Remote Sens.* **1995**, *33*, 777–787. [CrossRef]
25. Yan, G.; Hu, R.; Wang, Y.; Ren, H.; Song, W.; Qi, J.; Chen, L. Scale Effect in Indirect Measurement of Leaf Area Index. *IEEE Trans. Geosci. Remote Sens* **2016**. [CrossRef]
26. Martínez, B.; García-Haro, F.J.; Camacho-de Coca, F. Derivation of high-resolution leaf area index maps in support of validation activities: Application to the cropland Barrax site. *Agric. For. Meteorol.* **2009**, *149*, 130–145. [CrossRef]
27. Fernandes, R.; Butson, C.; Leblanc, S.; Latifovic, R. Landsat-5 TM and Landsat-7 ETM+ based accuracy assessment of leaf area index products for Canada derived from SPOT-4 VEGETATION data. *Can. J. Remote Sens.* **2003**, *29*, 241–258. [CrossRef]
28. Mayr, M.; Samimi, C. Comparing the dry season *in-situ* Leaf Area Index (LAI) derived from high-resolution rapideye imagery with MODIS LAI in a namibian Savanna. *Remote Sens.* **2015**, *7*, 4834–4857. [CrossRef]
29. Stenberg, P. Correcting LAI-2000 estimates for the clumping of needles in shoots of conifers. *Agric. For. Meteorol.* **1996**, *79*, 1–8. [CrossRef]
30. Rajeevan, M.; Bhate, J.; Kale, J.D.; Lal, B. High resolution daily gridded rainfall data for the Indian region: Analysis of break and active monsoon spells. *Curr Sci. India* **2006**, *91*, 296–306.
31. GCOS. *Systematic Observation Requirements for Satellite-Based Products for Climate: Supplemental Details to the Satellite-Based Component of the "Implementation Plan for the Global Observing System for Climate in Support of the UNFCCC"*; GCOS: Singapore, Singapore, 2006.
32. Elmore, A.J.; Guinn, S.M.; Minsley, B.J.; Richardson, A.D. Landscape controls on the timing of spring, autumn, and growing season length in mid-Atlantic forests. *Glob. Chang. Biol.* **2012**, *18*, 656–674. [CrossRef]
33. Kraus, T.; Schmidt, M.; Dech, S.W.; Samimi, C. The potential of optical high resolution data for the assessment of leaf area index in East African rainforest ecosystems. *Int. J. Remote Sens.* **2009**, *30*, 5039–5059. [CrossRef]
34. Buermann, W. Analysis of a multiyear global vegetation leaf area index data set. *J. Geophys. Res. Atmos.* **2002**, *107*. [CrossRef]
35. Zhu, Z.; Bi, J.; Pan, Y.; Ganguly, S.; Anav, A.; Xu, L.; Samanta, A.; Piao, S.; Nemani, R.; Myneni, R. Global data sets of vegetation Leaf Area Index (LAI)3g and Fraction of Photosynthetically Active Radiation (FPAR)3g derived from Global Inventory Modeling and Mapping Studies (GIMMS) Normalized Difference Vegetation Index (NDVI3g) for the period 1981 to 2011. *Remote Sen.* **2013**, *5*, 927–948.
36. Zhou, L.; Tucker, C.J.; Kaufmann, R.K.; Slayback, D.; Shabanov, N.V.; Myneni, R.B. Variations in northern vegetation activity inferred from satellite data of vegetation index during 1981 to 1999. *J. Geophys. Res. Atmos.* **2001**, *106*, 20069–20083. [CrossRef]
37. Goetz, S.J.; Bunn, A.G.; Fiske, G.J.; Houghton, R.A. Satellite-observed photosynthetic trends across boreal North America associated with climate and fire disturbance. *Proc. Natl. Acad. Sci. USA* **2005**, *102*, 13521–13525. [CrossRef] [PubMed]
38. Yue, S.; Pilon, P.; Cavadias, G. Power of the Mann—Kendall and Spearman's rho tests for detecting monotonic trends in hydrological series. *J. Hydrol.* **2002**, *259*, 254–271. [CrossRef]
39. Boening, C.; Willis, J.K.; Landerer, F.W.; Nerem, R.S.; Fasullo, J. The 2011 La Niña: So strong, the oceans fell. *Geophys. Res. Lett.* **2012**, *39*. [CrossRef]
40. Marengo, J.A.; Alves, L.M.; Soares, W.R.; Rodriguez, D.A.; Camargo, H.; Riveros, M.P.; Pabló, A.D. Two contrasting severe seasonal extremes in tropical South America in 2012: Flood in Amazonia and drought in northeast Brazil. *J. Clim.* **2013**, *26*, 9137–9154. [CrossRef]

Chapter 10

The Greening Earth

Piao et al.

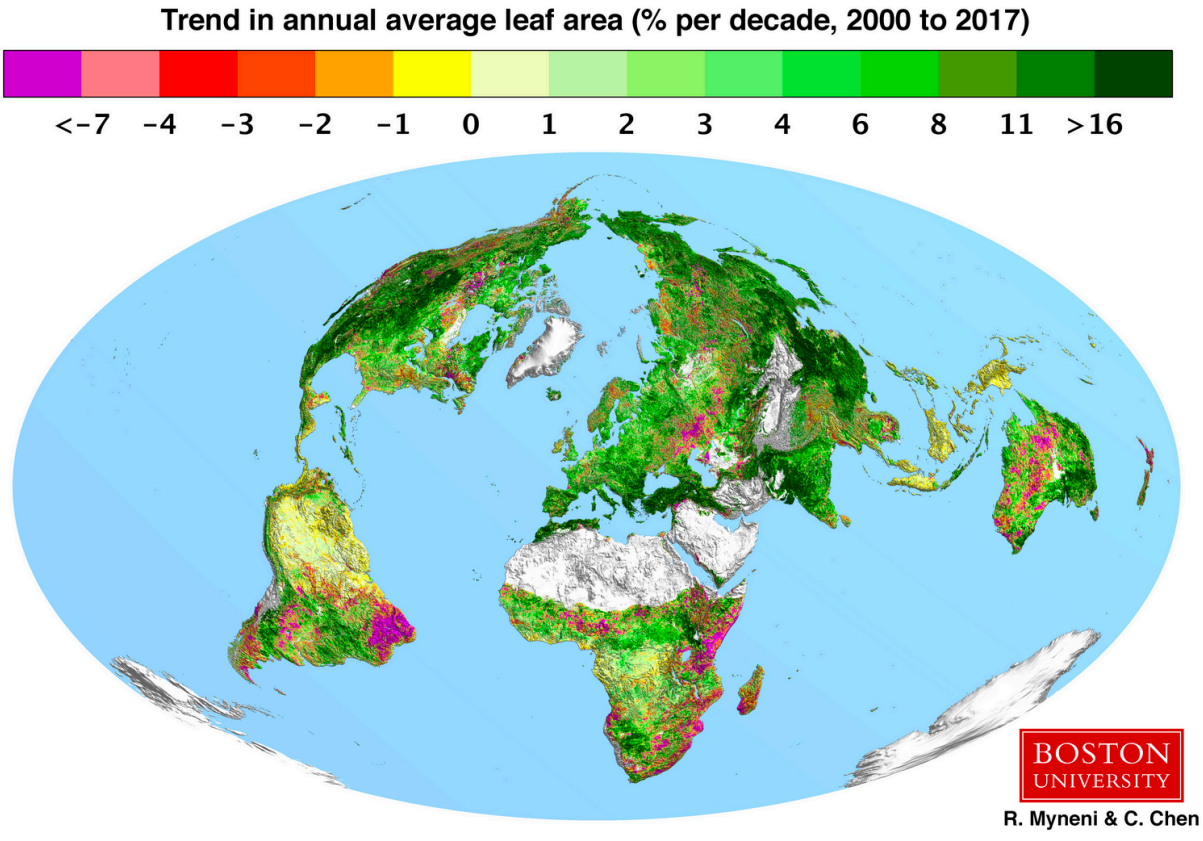

Characteristics, drivers and feedbacks of global greening

Shilong Piao[1,2,3], Xuhui Wang[1], Taejin Park[4], Chi Chen[4], Xu Lian[1], Yue He[1], Jarle W. Bjerke[5], Anping Chen[6], Philippe Ciais[1,7], Hans Tømmervik[5], Ramakrishna R. Nemani[8] and Ranga B. Myneni[4]*

Q1 Abstract | Vegetation greenness has been increasing globally since at least 1981, when satellite technology enabled large-scale vegetation monitoring. The greening phenomenon, together with warming, sea-level rise and sea-ice decline, represents highly credible evidence of anthropogenic climate change. In this Review, we examine the detection of the greening signal, its causes and its consequences. Simulations with vegetation models revealed that CO_2 fertilization was the main driver of greening on the global scale, with climate change, increased nitrogen deposition and land-use change also notable drivers at the regional scale. Modelling indicated that greening could mitigate global warming by increasing the carbon sink on land and altering biogeophysical processes, mainly evaporative cooling. Coupling high temporal and fine spatial resolution remote observations with ground measurements, increasing sampling in the tropics and Arctic, and modelling Earth systems in more detail will further our insights into the greening of Earth.

Afforestation
The conversion of treeless lands to forests through planting trees.

Greening
An increasing trend in vegetation greenness.

Vegetation controls the exchange of carbon, water, momentum and energy between the land and the atmosphere, and provides food, fibre, fuel and other valuable ecosystem services[1,2]. Changes in vegetation structure and function are driven by climatic and environmental changes, and by human activities such as land-use change. Given that increased carbon storage in vegetation, such as through afforestation, could combat climate change[3,4], quantifying vegetation change and its impact on carbon storage and climate has elicited considerable interest from scientists and policymakers.

However, it is not possible to detect vegetation changes at the global scale using ground-based observations due to the heterogeneity of change and the lack of observations that can detect these changes both spatially and temporally. While monitoring the changes in some vegetation properties (for example, stem-size distribution and below-ground biomass) at the global scale remains impossible, satellite-based remote sensing has enabled continuous estimation of a few important metrics, including vegetation greenness, since the 1980s (BOX 1).

In 1986, a pioneering study by Tucker et al.[5] on remotely sensed normalized difference vegetation index (NDVI; a radiometric measure of vegetation greenness) (BOX 1) revealed a close connection between vegetation canopy greenness and photosynthesis activity (as inferred from seasonal variations in atmospheric CO_2 concentration). This index was successfully used to constrain vegetation primary production globally[6]. Using NDVI data from 1981 to 1991, Myneni et al.[7] reported an increasing trend in vegetation greenness in the Northern Hemisphere, which was subsequently observed across the globe[8–13]. This 'vegetation greening' is defined as a statistically significant increase in annual or seasonal vegetation greenness at a location resulting, for instance, from increases in average leaf size, leaf number per plant, plant density, species composition, duration of green-leaf presence due to changes in the growing season and increases in the number of crops grown per year.

There has also been considerable interest in understanding the mechanisms or drivers of greening[11,14]. Lucht et al.[14] and Xu et al.[10] revealed that warming has eased climatic constraints, facilitating increasing vegetation greenness over the high latitudes. Zhu et al.[11] further investigated key drivers of greenness trends and concluded that CO_2 fertilization is a major factor driving vegetation greening at the global scale. Subsequent studies based on fine-resolution and medium-resolution satellite data[13] have shown the critical role of land-surface history, including afforestation and agricultural intensification, in enhancing vegetation greenness. The large spatial scale of vegetation greening and the robustness of its signal have led the Intergovernmental Panel on Climate Change (IPCC) special report on climate change and land[15] to list it, together with global-scale warming, sea-level rise[16] and sea-ice decline[16], as highly credible evidence of the environmental impact of anthropogenic climate change.

Greener vegetation not only results from climate and atmospheric changes but also feeds back to the climate

*e-mail: slpiao@pku.edu.cn

https://doi.org/10.1038/s43017-019-0001-x

Key points

- Long-term satellite records reveal a significant global greening of vegetated areas since the 1980s, which recent data suggest has continued past 2010.
- Pronounced greening is observed in China and India due to afforestation and agricultural intensification.
- Simplified global vegetation models suggest that CO_2 fertilization is the main driver of global vegetation greening.
- Warming is the major cause of greening in boreal and Arctic biomes, but has negative effects on greening in the tropics.
- Greening was found to mitigate global warming through enhanced land carbon uptake and evaporative cooling, but could also lead to decreased albedo that could potentially cause local warming.
- Greening enhances transpiration, a process that reduces soil moisture and runoff locally, but can either amplify or reduce runoff and soil moisture regionally.

Browning
A decreasing trend in vegetation greenness.

through biogeochemical and biogeophysical processes. These feedbacks are often studied with Earth system models (ESMs), in which vegetation is coupled with the atmosphere and the hydrologic cycle[17]. ESM-based studies have demonstrated that greening can accelerate the hydrologic cycle by increasing the amount of water transpired by plants, alter the energy exchange between land and the atmosphere, and affect atmospheric circulation patterns[18,19].

In this Review, we synthesize past and recent efforts to characterize the spatiotemporal patterns of vegetation greening since the 1980s. We discuss how rising atmospheric CO_2 concentration, climate change, land-use change and nitrogen deposition are the key drivers of greenness changes on the global and regional scale. We assess the impacts of vegetation greening on carbon, water and energy balances, and conclude by identifying key challenges and perspectives for future research.

Greenness changes

Global-scale vegetation greening has been demonstrated using nearly four decades of NDVI and leaf area index (LAI) greenness data derived from the Advanced Very-High-Resolution Radiometer (AVHRR) instrument (FIG. 1a,b). While early studies primarily used the NDVI to detect changes in global greenness, recent studies widely use the LAI, since it has clear physical interpretation and is a fundamental variable in almost all land-surface models (BOX 1). An ensemble of LAI datasets has shown that 52% ($P<0.05$) to 59% ($P<0.10$) of global vegetated lands displayed an increasing trend in growing season LAI since the 1980s[11] (FIG. 1a). Although some studies reported a stalling, or even a reversal, of the greening trend since 2000 based on AVHRR[20] and collection 5 (C5) of the Moderate Resolution Imaging Spectroradiometer (MODIS) data[21], this signal might be an artefact of sensor degradation and/or processing[22–24]. For example, using a revised calibration of the MODIS data in the most recent collection 6 (C6) dataset[24], Chen et al.[13] showed that leaf area increased by 5.4 million km^2 over 2000–2017, an area equivalent to the areal extent of the Amazon rainforest[13]. Indeed, 34% of vegetation land exhibited greening ($P<0.10$), whereas only 5% experienced browning ($P<0.10$).

New satellite-based vegetation indices also support the global greening trend observed since 2000 (FIG. 1), including the enhanced vegetation index (EVI) and near-infrared reflectance of terrestrial vegetation (NIRv) (BOX 1). However, while vegetation greenness is increasing at the global scale, the changes vary considerably between regions and seasons.

Regional trends. In the high northern latitudes (>50°N), AVHRR and Landsat records indicate a widespread increase in vegetation greenness since the 1980s[8,12,25] (FIG. 2a–d). Regions with the greatest greening trend include northern Alaska and Canada, the low-Arctic parts of eastern Canada and Siberia, and regions of Scandinavia[12,25,26]. Dendrochronological data and photographic evidence further corroborate these findings[27–30]. In general, the LAI over high northern latitudes will continue to increase by the end of this century[31], based on the results of an ensemble of ESMs (FIG. 2e–h). While only a 3% area of the high latitudes shows browning during 1982–2014 (REF.[25]), there is a growing proportion of Arctic areas exhibiting a browning trend[32]. Such trends first emerged in boreal forests, where a multitude of disturbances (for example, fires, harvesting and insect defoliation) prevail[9,33–37]. The North American boreal forests in particular exhibit browning areas nearly 20 times larger than the Eurasian boreal forests, showing heterogeneous regional greenness change[38].

The northern temperate region (25–50°N) is another vegetation greening hotspot, experiencing faster rates of greening than the high latitudes since 2000 (FIG. 2b,d). Indeed, ~14 million km^2 of the temperate region greened ($P<0.10$), contributing about one-half of the global net leaf area increase over this time period[13]. The increase of vegetation greenness is especially strong in agricultural regions (for example, India[13]) and recently afforested areas (for example, China[13,39]); collectively, China and India alone contribute more than 30% of the total net increase in the global LAI[13].

Tropical regions (25°S–25°N) are also greening (FIG. 2b,d), contributing about a quarter of the net global increase in leaf area since 2000 (REF.[13]). However, the tropics also have areas where significant browning was reported, for example, in the Brazilian Cerrado and Caatinga regions and Congolian forests[13,40]. It is worth noting that substantial uncertainties remain in the tropical vegetation greenness estimations due to the saturation effects of greenness indices in dense vegetation[41] and contamination by clouds and aerosols[42]. These

Author addresses

[1]Sino-French Institute for Earth System Science, College of Urban and Environmental Sciences, Peking University, Beijing, China.
[2]Key Laboratory of Alpine Ecology, Institute of Tibetan Plateau Research, Chinese Academy of Sciences, Beijing, China.
[3]Center for Excellence in Tibetan Earth Science, Chinese Academy of Sciences, Beijing, China.
[4]Department of Earth and Environment, Boston University, Boston, MA, USA.
[5]Norwegian Institute for Nature Research, FRAM – High North Research Centre for Climate and the Environment, Tromsø, Norway.
[6]Department of Biology, Colorado State University, Fort Collins, CO, USA.
[7]Laboratoire des Sciences du Climat et de l'Environnement, CEA CNRS UVSQ, Gif-sur-Yvette, France.
[8]NASA Ames Research Center, Moffett Field, CA, USA.

Box 1 | **Remotely sensed vegetation greenness**

Remotely sensed vegetation greenness generally refers to spectral vegetation indices (VIs) or the leaf area index (LAI). Photosynthetic pigments in plant leaves (mainly chlorophyll and carotenoids) strongly absorb photosynthetically active radiation, which largely overlaps with the visible spectrum (400–700 nm), particularly red wavelengths (620–700 nm). In the near-infrared (NIR) domain (700–1,300 nm), absorbance by leaf constituents is either small or absent; thus, scattering increases the likelihood that photons will exit the leaf. This is the biophysical basis for high leaf-level reflectance in the NIR region. At the canopy scale, structural properties such as LAI and leaf-angle distribution dominate variability in NIR reflectance[176]. This unique spectral signature of vegetation in the red and NIR channels, a characteristic not present in common, non-vegetative features such as soil, snow and water[177,178], has thus been utilized to derive numerical VIs measuring vegetation greenness[176,179,180] (Supplementary Table S1). For example, the normalized difference vegetation index, which is one of the most widely used VIs in assessing vegetation greenness and its changes from local to global scales (Supplementary Table S2), is useful for measuring canopy structural properties, such as leaf area, light interception and biomass[41,181,182]. Satellite sensors, such as the Advanced Very-High-Resolution Radiometer (AVHRR), Moderate Resolution Imaging Spectroradiometer (MODIS), Vegetation, Medium Resolution Imaging Spectrometer (MERIS) and Visible Infrared Imaging Radiometer Suite (VIIRS), have been deployed with varying temporal coverage, providing VI products based on a wide range of spectral-band specifications and data processing (Supplementary Table S3). For example, the AVHRR does not have a blue channel, so this sensor is unable to produce blue-band-based greenness indices like the enhanced vegetation index. These sensor differences make it a non-trivial challenge to produce consistent and continuing long-term greenness products[183].

Compared with VIs, the LAI (the one-sided green leaf area per unit ground area in broadleaf canopies or one-half of the total needle surface area per unit ground area in coniferous canopies[184,185]) is a well-defined physical attribute of vegetation. The LAI is a state variable in all land models and key to quantifying the exchanges of mass, momentum and energy between the surface and the atmosphere. Multiple approaches for retrieving the LAI from remote sensing data have been developed — these can be conceptually categorized as: empirical approaches that are based on relationships between VIs and the LAI[186,187]; machine-learning approaches that train surface reflectance or VIs to given reference LAIs[182,188,189]; and physical approaches that are based on the physics of radiation interaction with elements of a canopy and transport within the vegetative medium[7,184,190,191]. See Supplementary Table S4 for currently available global LAI products.

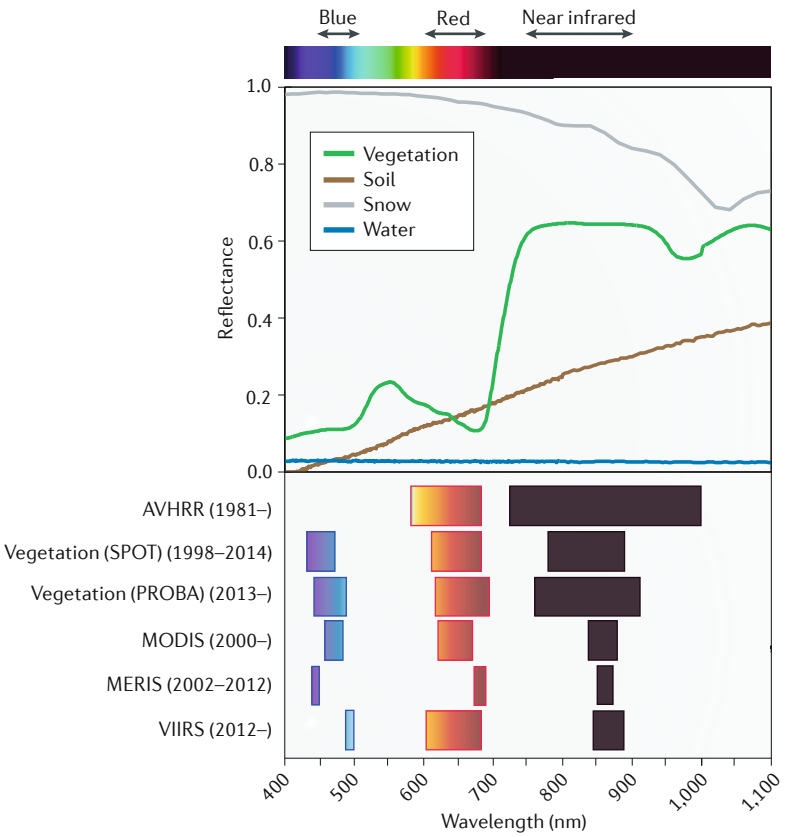

uncertainties partly underlay the disagreement between the MODIS and AVHRR products[13] when measuring tropical greenness and the debate on whether the Amazonian forests have greened or browned in response to droughts[42–44].

The extratropical Southern Hemisphere (>25°S) experienced a general greening trend since the 1980s[13,45], but this is lower than experienced in the temperate and high-latitude Northern Hemisphere[13] (FIG. 2a–d). Regional greening hotspots in southern Brazil and southeast Australia mostly overlap with the intensive cropping areas[13], highlighting the increasing contribution of managed ecosystems to vegetation greening. Note that most of this region is dominated by semi-arid ecosystems[46], where vegetation coverage is generally sparse. Thus, satellite vegetation indices over this region are generally sensitive to change in soil background. For example, browning was detected from the AVHRR dataset since the 2000s[20] (FIG. 2b), but MODIS C6 data (which is better calibrated and can distinguish vegetation from background more accurately) instead showed an overall greening trend particularly since 2002 (REF.[13]; FIG. 2c,d).

Seasonal changes of greenness. In the northern temperate and high latitudes, greenness often shows distinctive seasonal patterns within a calendar year (FIG. 3). Several metrics of land-surface phenology have been developed to depict the seasonal cycle of greenness[47], including the widely used start of the growing season (SOS) and end of the growing season (EOS)[48]. Although phenology dates can vary depending on the greenness product or algorithm used[49–51], significant trends towards both earlier SOS (2–8 days decade^{-1}) and later EOS (1–6 days decade^{-1}) and, thus, longer lengths of the growing season (LOS) (2–10 days decade^{-1}), have been observed in most Northern Hemisphere regions during the past four decades[7,8,25,52–54] (FIG. 3a–c). These trends are corroborated by ground-based observation data in spring and autumn[55–57]. The increase in LOS is driven mainly by an advanced SOS in Eurasia (53–81% of LOS lengthening is due to SOS advance) and delayed EOS in North America (57–96% of LOS lengthening is due to EOS delay), with the more rapid total LOS increase seen in Eurasia[25,58–60].

In addition to longer growing seasons, satellite greenness data also reveal important shifts in the timing and magnitude of the seasonal peak greenness[47,61]. For example, the timing of peak greenness has advanced by 1.2 days decade^{-1} during 1982–2015 (REF.[62]) and 1.7 days decade^{-1} during 2000–2016 (REF.[61]) over the extratropical Northern Hemisphere (FIG. 3a), with the boreal region peak greenness advancing twice as fast as the Arctic tundra and temperate ecosystem peaks[61]. Since the 1980s, the magnitude of the peak greenness has also increased over the extratropical Northern Hemisphere by ~0.1 standardized NDVI anomaly per year[62], with a stronger signal in the pan-Arctic region[63,64].

Phenology changes, including the SOS advancement, EOS delay and peak greenness enhancement, can significantly change the Earth's seasonal landscape. Northern high latitudes, which traditionally have high seasonality

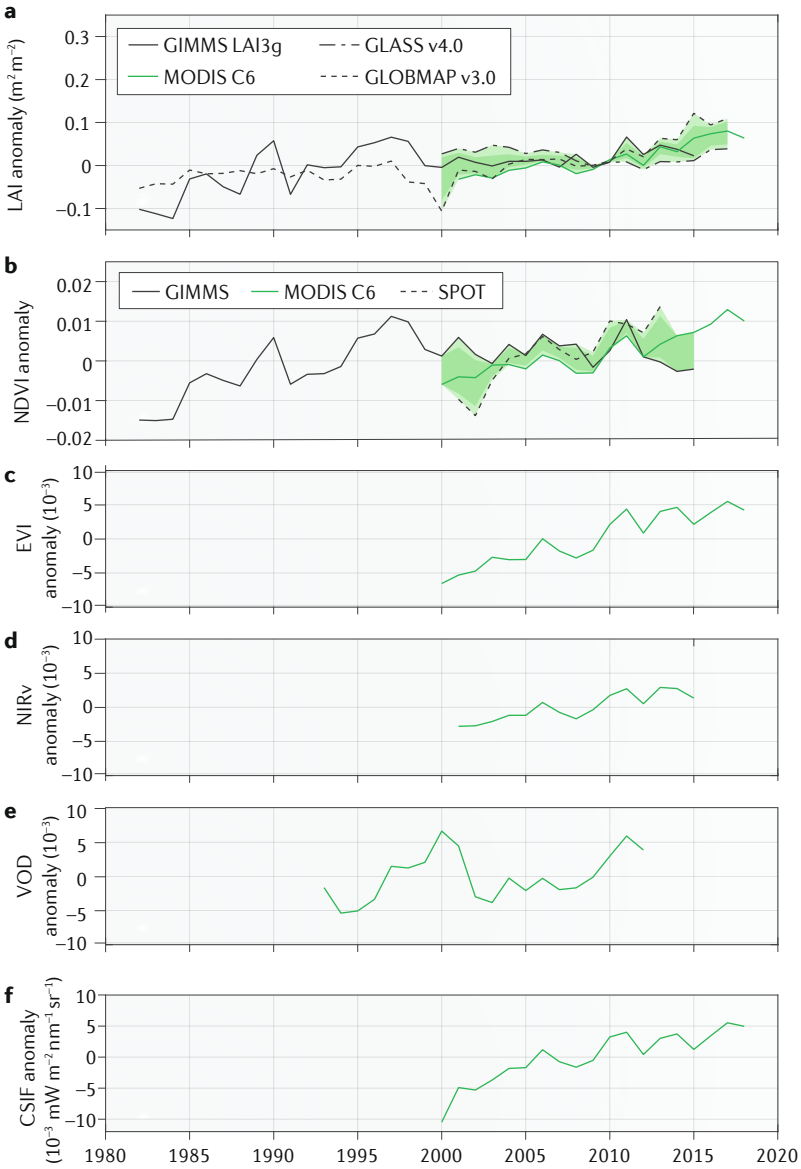

Fig. 1 | **Changes in satellite-derived global vegetation indices, vegetation optical depth and contiguous solar-induced fluorescence. a** | Leaf area index (LAI) from four products: GIMMS[13], GLASS[192], GLOBMAP[23] and Moderate Resolution Imaging Spectroradiometer (MODIS) C6 (REF.[193]). **b** | Normalized difference vegetation index (NDVI) from three products: GIMMS[194], MODIS C6 (REF.[195]) and SPOT[196]. **c** | Enhanced vegetation index (EVI) from MODIS C6 (REF.[195]). **d** | Near-infrared reflectance of terrestrial vegetation (NIRv)[197]. **e** | Vegetation optical depth (VOD)[119]. **f** | Contiguous solar-induced fluorescence (CSIF)[114]. In parts **a** and **b**, the light-green shading denotes the range of LAI and NDVI across different products and the dark-green shading denotes the interquartile range (between the 25th and 75th percentiles). Only measurements during the growing season[11] were considered.

Land-surface phenology
Cyclic phenomena in vegetated land surfaces observed from remote sensing.

Carboxylation
The addition of CO_2 to ribulose-1,5-bisphosphate during photosynthesis.

(that is, short and intense growing seasons), are exhibiting seasonality similar to that of their counterparts 6° to 7° south in the 1980s. In other words, the latitudinal isolines of northern vegetation seasonality have shifted southward since the 1980s. The diminished seasonality of the northern high-latitude vegetation[10] is consistent with changes in the velocity of vegetation greenness (defined as the ratio of temporal greenness change to its spatial gradient)[65], which showed faster northward movement of the SOS (3.6 ± 1.0 km year^{-1}) and the EOS (6.0 ± 1.1 km year^{-1}) than the peak greenness (3.1 ± 1.0 km year^{-1}) during 1982–2011 (REF.[65]).

Fig. 2 | **Spatial patterns of changes in leaf area index.** **a** | Growing season (GS) mean Advanced Very-High-Resolution Radiometer (AVHRR) leaf area index (LAI) trend during 1982–2009. The AVHRR LAI dataset is the average of three different products (GIMMS[13], GLOBMAP[23] and GLASS[192]). **b** | Change in the GS mean AVHRR LAI over four regions during 1982–2009. **c** | GS mean Moderate Resolution Imaging Spectroradiometer (MODIS) LAI during 2000–2018. **d** | Change in the GS mean MODIS LAI over four regions during 2000–2018. MODIS LAI is from collection 6 (REF.[193]). **e** | Relative change in GS mean LAI between 1981–2000 and 2081–2100 under the Representative Concentration Pathway 2.6 (RCP2.6), based on the Coupled Model Intercomparison Project Phase 5 (CMIP5) multi-model ensemble. **f** | Relative change in GS mean CMIP5 LAI between 2018–2100 under RCP2.6, relative to 1981–2000. **g** | Relative change in GS mean LAI between 1981–2000 and 2081–2100 under RCP8.5, based on CMIP5. **h** | Relative change in GS mean CMIP5 LAI between 2018–2100 under RCP8.5, relative to 1981–2000. The number of CMIP5 models used in the calculation of the multi-model mean is 16 and 19, for RCP2.6 and RCP8.5, respectively (Supplementary Table S5). In parts **a**, **c**, **e** and **g**, the white land areas depict barren lands, permanent ice-covered areas, permanent wetlands, built-up areas and water. In parts **b**, **d**, **f** and **h**, blue represents the high-latitude Northern Hemisphere (NH) (50–90°N), green represents the temperate NH (25–50°N), purple represents the tropical zone (25°S–25°N) and yellow represents the extratropical Southern Hemisphere (SH) (90–25°S). The shading shows the ±1 inter-model standard deviation.

Drivers of greening

Several factors are thought to impact vegetation greening, including rising atmospheric CO_2 concentrations, climate change, nitrogen deposition and land-use changes. However, nonlinear impacts and interactions make it challenging to quantify the individual contribution of these factors to the observed greening trend. In this section, we review the contribution of several key drivers of vegetation greening and efforts to quantitatively attribute the observed greening trend to each of these factors.

CO_2 fertilization. As CO_2 is the substrate for photosynthesis, rising atmospheric CO_2 concentration can enhance photosynthesis[66] by accelerating the rate of carboxylation; this process is known as the 'CO_2 fertilization effect'. In addition, increased CO_2 concentrations can also enhance vegetation greenness by partially closing leaf stomata, leading to enhanced water-use efficiency[67], which should relax water limitation to plant growth, particularly over semi-arid regions[45,68,69]. Analysis of the 'Trends and drivers of the regional-scale sources and sinks of carbon dioxide' (TRENDY) ensemble of dynamic global vegetation models (DGVMs)[70] suggests that rising CO_2 is the dominant driver of vegetation greening, accounting for nearly 70% of global LAI trend since the 1980s[11] (FIG. 4). Statistical modelling also supports the important role of rising atmospheric CO_2 concentration in driving vegetation greening[71,72]. Free-air CO_2 enrichment (FACE) experiments show that

1982–2009 (GIMMS, GLOBMAP and GLASS mean)

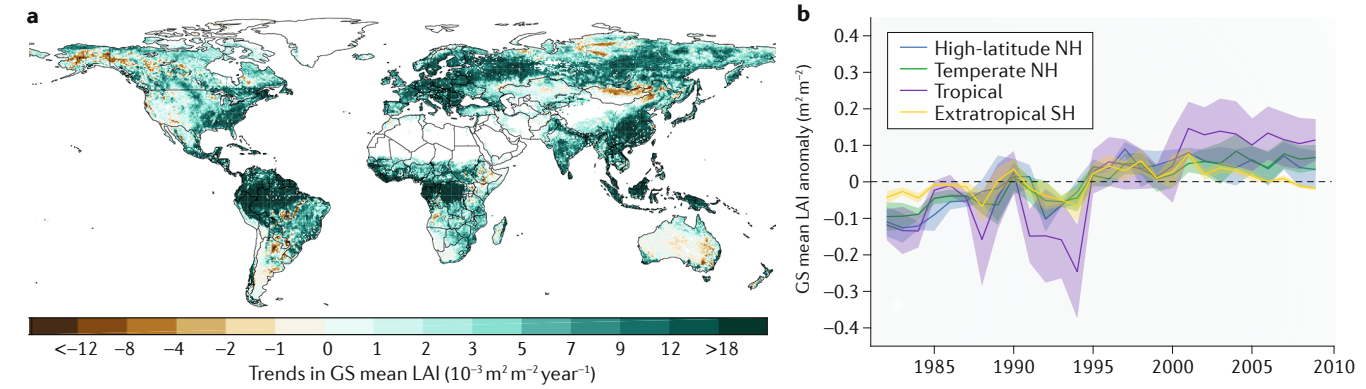

2000–2018 (MODIS)

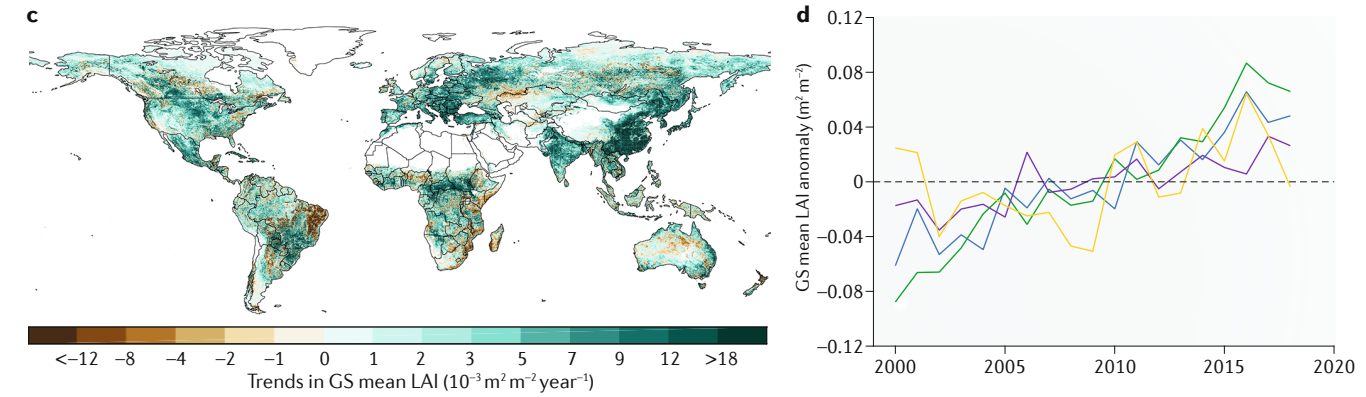

2081–2100 relative to 1981–2000, RCP2.6

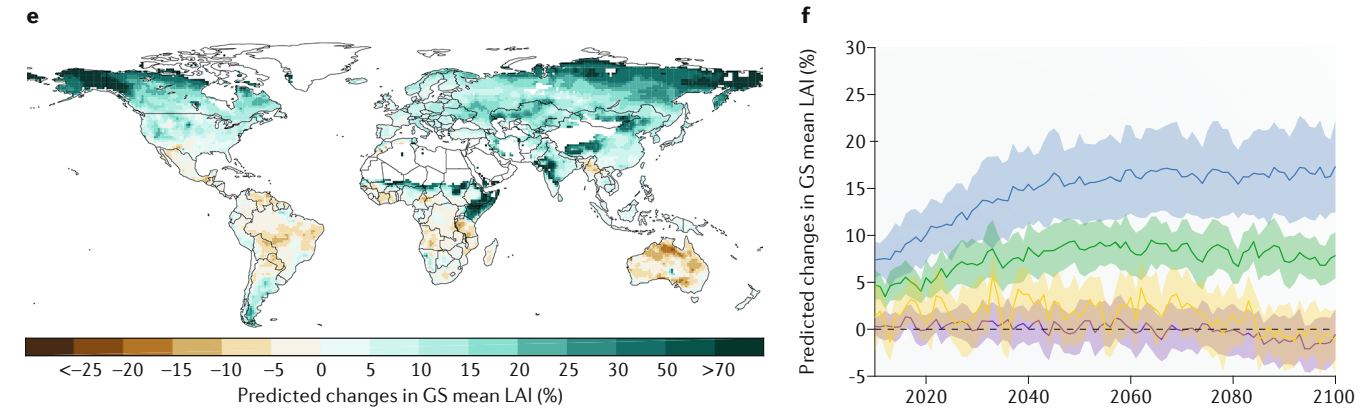

2081–2100 relative to 1981–2000, RCP8.5

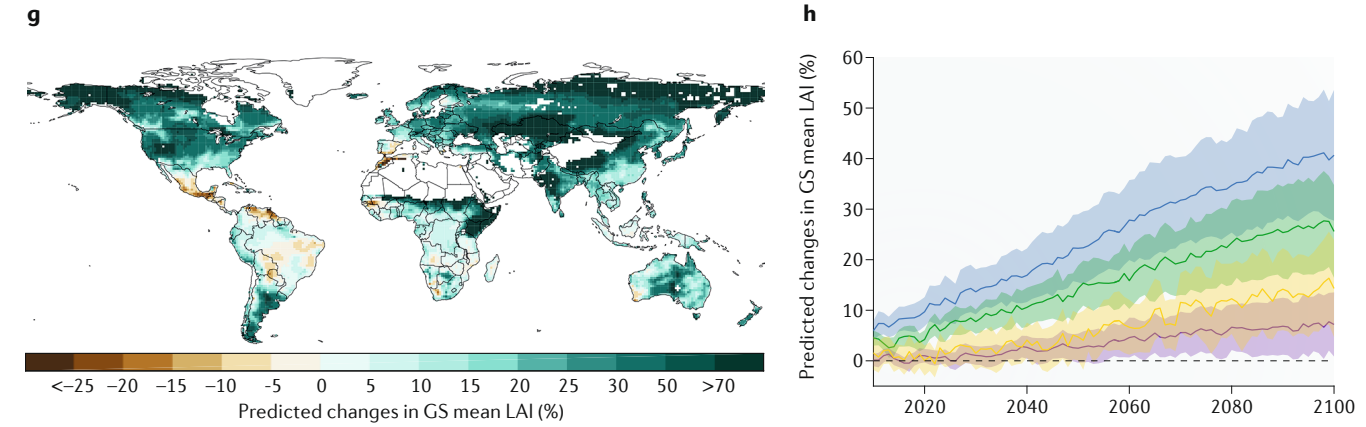

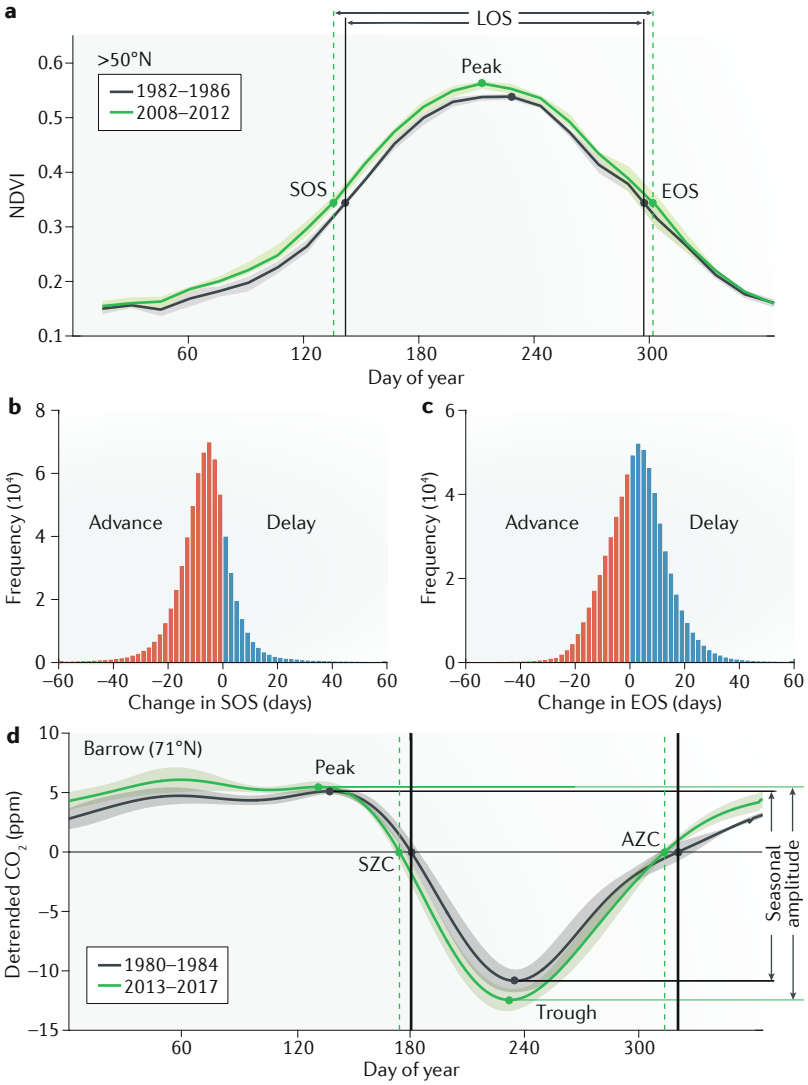

Fig. 3 | **Changes in the seasonality of vegetation greenness and atmospheric CO_2 concentration. a** | Five-year mean seasonal variations of the normalized difference vegetation index (NDVI) over Northern Hemisphere high latitudes (>50°N) during 1982–1986 (black line) and 2008–2012 (green line). Start of the growing season (SOS) and end of the growing season (EOS) are shown as 50% of the maximum NDVI. The length of the growing season (LOS) is the difference between the EOS and the SOS. **b** | Frequency distribution of SOS change in the Northern Hemisphere during 1982–2012. **c** | Frequency distribution of EOS change in the Northern Hemisphere during 1982–2012. **d** | Five-year mean detrended seasonal CO_2 variations at Barrow, AK, USA (71°N) (NOAA ESRL archive: https://www.esrl.noaa.gov/gmd/ccgg/obspack/) during 1980–1984 (black line) and 2013–2017 (green line). Vertical lines mark the spring zero-crossing date (SZC) and autumn zero-crossing date (AZC). Horizontal lines mark the seasonal amplitude as the difference between the maximum and the minimum of detrended seasonal CO_2 variations. Shaded areas show the range of interannual variations in the NDVI in part **a** and the standard deviation of the detrended CO_2 mole fraction (ppm) in part **d** at the day of year. NDVI data are the updated dataset from Tucker et al.[194]. Parts **b** and **c** are adapted with permission from REF.[48], Wiley-VCH.

elevating the CO_2 concentration by ~200 ppm above the ambient conditions significantly enhances vegetation productivity[73] and increases leaf area[74]. Different plant species vary largely in the magnitude of LAI enhancement[75], with the larger effect on forest stands having lower LAI at the ambient conditions[76]. In DGVMs, elevated CO_2 increases vegetation productivity more in tropical ecosystems than in temperate and boreal ecosystems[11,77,78] (FIG. 4b). However, the strength of the CO_2 fertilization effect can be limited by extreme weather events[79,80] and nutrient and water availability[73,81,82]. Indeed, nitrogen and phosphorus have been shown to regulate the global pattern of CO_2 fertilization effects[83]. Since nutrient processes were under-represented in the ESMs used in the IPCC Fifth Assessment Report (AR5), the predictions of continued greening trends through 2100 (REF.[31]) (FIGS 2e–h,5) might overestimate the CO_2 fertilization effects.

Climate change. Although rising atmospheric CO_2 concentration is the main driver of global greening, climate change, such as anthropogenic warming and regional trends in precipitation, is a dominant driver of greenness changes over 28% of the global vegetated area[11]. The global contribution of climate change to increasing greenness is only 8% (FIG. 4a), however, because impacts of climate change on vegetation greenness vary between regions[11]. For example, warming could reduce vegetation growth in the tropics[84], where ambient temperature is close to vegetation optimal temperature[85], but warming significantly increases vegetation greenness in the boreal and Arctic regions[86] by enhancing metabolism[87] and extending the growing season[59,88,89]. DGVM simulations show that the positive effects of climate change, primarily from warmer temperature[14], dominate the greening trend over more than 55% of the northern high latitudes (FIG. 4b) and in the Tibetan Plateau[11]. However, this positive impact of anthropogenic warming on greenness appears to have weakened during the past four decades[90,91], when the correlation coefficient between temperature and greenness decreased by more than 50%[90,91], suggesting a possible saturation of future greening in response to warmer temperature.

In water-limited ecosystems, changes in precipitation — reflecting either decadal climate variability or trends from anthropogenic climate change — were suggested as the main driving factor of greening and browning[45,92]. Precipitation-driven greening is most evident in the African Sahel[93,94] and semi-arid ecosystems of southern Africa and Australia[45,95] (FIG. 4c). Both empirical models and DGVMs indicate that 'the greening Sahel', one of the early examples of vegetation greening detected by satellite measurements[93,94], was primarily driven by increases in precipitation after a severe drought in the early 1980s[96–98]. This causal relationship between precipitation and greenness changes was further supported through analyses of recent microwave satellite measurements and long-term field surveys[99,100].

Land-use change. Like climate change, land-use change exerts a considerable but highly spatially variable influence on greenness changes[11,13] (FIG. 4). Specifically, deforestation dominates the tropics[101,102], while afforestation increases forest area over temperate regions, particularly in China, where the forest area has increased by more than 20% since the 1980s[103]. The TRENDY ensemble of DGVMs[70] indicates that greenness changes over 19% of the northern temperate vegetation (25–50°N) are primarily driven by land-use change[11] (FIG. 4c). However, this might be an underestimate since critical land-use

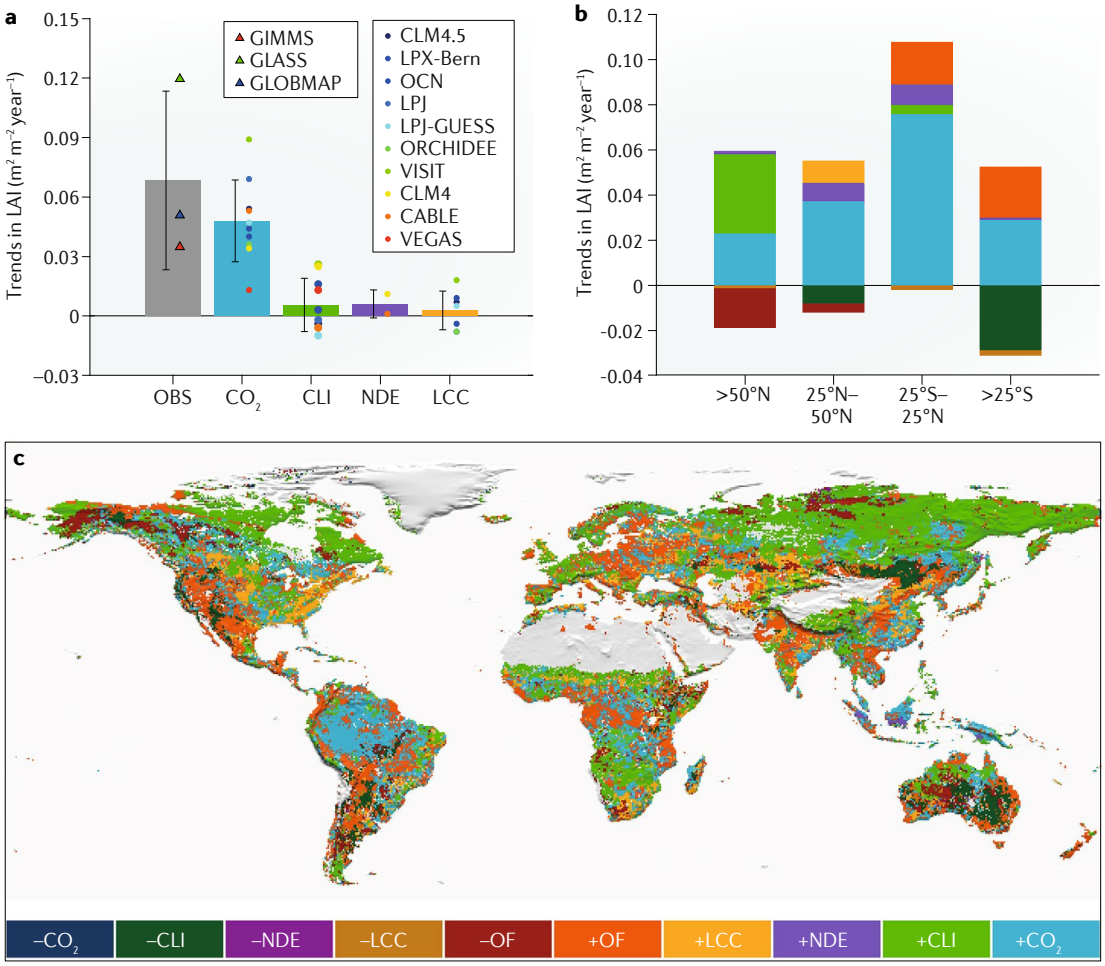

Fig. 4 | **Attribution of trends in growing season mean leaf area index. a** | Trends in the global-averaged leaf area index (LAI) derived from satellite observation (OBS) and attributed respectively to rising CO_2 (CO_2), climate change (CLI), nitrogen deposition (NDE) and land cover change (LCC) during 1982–2009 (REF.[11]). The error bars show the standard deviation of trends derived from satellite data and model simulations. Individual model-estimated contributions of each driver to LAI trends are shown as coloured dots. **b** | Contribution of different drivers to LAI change in latitude bands (>50°N, 25–50°N, 25°S–25°N, >25°S). **c** | Spatial distribution of the dominant driver of growing season mean LAI trend, defined as the driver that contributes the most to the increase (or decrease) in LAI in each vegetated grid cell. Other factors (OF) is defined by the fraction of the observed LAI trends not accounted for by modelled factors. Parts **b** and **c** share the same colour legend, where the '+' prefix indicates a positive effect from the corresponding driver on LAI trends and the '−' prefix indicates a negative effect. Data courtesy of Zhu et al.[11].Part **c** adapted from REF.[11], Springer Nature Limited.

processes[104,105] are under-represented or missing in the current generation of DGVMs. For example, forest-age dynamics are not represented in most DGVMs, even though one-third of the global forests are younger than 20 years old[106], implying that forest regrowth might contribute to global greening in the future. In addition, agricultural intensification with multiple cropping, irrigation and fertilizer usage must contribute considerably to vegetation greening, which is exemplified by the dominance of other unmodelled factors over agricultural lands of India, China and Eastern Europe (FIG. 4c).

Nitrogen deposition. Anthropogenic changes in the amount, rate and distribution of nitrogen deposition can impact greening patterns, since insufficient nitrogen availability can stunt plant growth[107–109], potentially slowing greening or causing browning, but excess nitrogen can enhance plant growth in nitrogen-limited systems[109]. However, the few DGVMs that include the nitrogen cycle do not indicate that nitrogen deposition plays a dominant driving role on the greening at either the global or regional scales (FIG. 4). Modelling studies differ on the contribution of increasing nitrogen deposition to the global LAI increase[11] (9 ± 12%), largely due to the incomplete representation of nitrogen-related processes[110]. A growing number of DGVMs are currently incorporating nitrogen processes[111], though, and future research priorities include better measurement and representation of processes such as plant nitrogen uptake and allocation[110].

Impact of greening on the carbon cycle

Greening increases the amount of photosynthetically active sunlight that is absorbed by vegetation and, thus, enhances productivity[112,113]. There has been substantial evidence showing enhanced vegetation productivity from contiguous solar-induced fluorescence (CSIF;

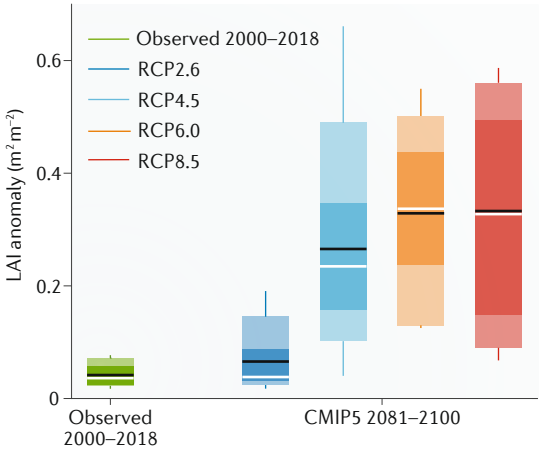

Fig. 5 | **Current and predicted global leaf area index.** Current leaf area index (LAI) anomaly ($m^2\ m^{-2}$) from an average of satellite measurements based on GIMMS[13], GLASS[192], GLOBMAP[23] and Moderate Resolution Imaging Spectroradiometer (MODIS) C6 (REF.[193]). Predicted LAI anomalies from the Coupled Model Intercomparison Project Phase 5 (CMIP5) multi-model (Supplementary Table S5) projections during 2081–2100. The boxes and whiskers indicate the minimum, 10th, 25th, 50th, 75th and 90th percentiles and the maximum LAI of CMIP5 models; the black and white lines indicate the mean and median LAI of CMIP5 models, respectively. LAI anomalies were calculated against the average during 1980–2005. RCP, Representative Concentration Pathway.

FIG. 1f) observations[114], empirical models of vegetation productivity[92,115] and DGVM and ESM simulations[70,116] (FIG. 6). It should be noted, though, that CSIF is not fully independent from MODIS greenness indices, since its derivation relies on both solar-induced fluorescence measurements from Orbiting Carbon Observatory 2 and MODIS reflectance measurements[114].

Enhanced vegetation productivity increases terrestrial carbon storage, slowing down anthropogenic climate warming[117]. For example, about 29% of the anthropogenic CO_2 emissions since the 1980s is offset by the land carbon sink (2.5 ± 1.0 PgC $year^{-1}$)[111]. This vegetation-induced large land carbon sink was also inferred from forest inventories[118] and above-ground biomass estimated from the vegetation optical depth (FIG. 1e), a microwave-based satellite measurement of both woody and leaf biomass[119]. Multiple lines of evidence, including analyses from DGVMs, atmospheric inversion models and the residual land sink (the mass balance residual of anthropogenic CO_2 emissions, atmospheric CO_2 growth rate and ocean CO_2 budget), confirm the increasing magnitude of the global land carbon sink since the 1980s[111] (FIG. 6). An ecosystem model driven by satellite LAI measurements estimated that increased LAI accounts for 36% (0.4 PgC $year^{-1}$) of the land carbon sink enhancement of 1981–2016 (REF.[112]). Recent studies indicate that the trend in the land carbon sink has further accelerated since the late 1990s[120,121]. For example, the rate of update during 1998–2012 was three times that of 1980–1988 (0.17 PgC $year^{-2}$ in comparison with 0.05 PgC $year^{-2}$)[121], attributed to afforestation-induced greening in the temperate Northern Hemisphere[13,121]. These hotspots of afforestation and forest regrowth are in accordance with the greening pattern observed since 2000 by MODIS (FIG. 2c). Recent DGVM studies[122,123] have further confirmed that the carbon sink during the 2000s was partly driven by afforestation and forest regrowth in East Asia and Europe[124]. The extensive greening over croplands, however, has probably contributed less to the carbon sink, because only a minor portion of assimilated carbon by crops remain sequestered due to crop harvest.

The impact of greening on the carbon cycle is also partly responsible for the increasing seasonality of atmospheric CO_2 in the northern high latitudes[125]. The amplitude of the Northern Hemisphere CO_2 seasonal cycle increased by as much as 50% for latitudes north of 45°N[126,127] since the 1960s, indicating enhanced vegetation productivity in northern ecosystems during the carbon-uptake period[128]. The spring zero-crossing date — the time when the detrended seasonal CO_2 variations downcross the zero line in spring — is a phenological indicator of the timing of early season net carbon uptake[125,129]. From 1987 to 2009, the spring zero-crossing date has advanced at high-latitude stations[130] (from −0.5 days $decade^{-1}$ to −1.8 days $decade^{-1}$) (FIG. 3d), a trend that is consistent with the advancing SOS (FIG. 3b). At the end of the net carbon-uptake period, the autumn zero-crossing dates of detrended seasonal CO_2 variations — the time when the detrended seasonal CO_2 variations up-cross the zero line in autumn — have also advanced over 8 of the 10 Northern Hemisphere stations studied[131]. The observed autumn zero-crossing date advancement (FIG. 3d) is in contrast to the delayed EOS (FIG. 3a) in autumn. This divergence in the autumnal CO_2 and greenness trends suggests that, unlike in spring, autumn vegetation greening does not lead to an increased carbon sink because respiration is increasing faster than photosynthesis in autumn[131]. Visual observations (for example, from the Pan European Phenology Project PEP725) and cameras (for example, PhenoCam datasets) are providing an increasing amount of ground-based phenological evidence of this process. In the future, these data can be paired with eddy covariance flux data, to further our mechanistic understanding of the climate-change-induced seasonal change in greenness and carbon balance.

Biogeophysical impacts of greening

Greening has discernable impacts on the hydrologic cycle and climate through modifying surface biogeophysical properties (for example, albedo, evapotranspiration (ET) and surface roughness) on local to regional and global scales[19,132] (FIG. 7). Vegetation's biogeophysical feedbacks to climate are, thus, critical to understanding the potential of ecosystem management, such as afforestation, for climate change mitigation[3,132,133]. In this section, we present the feedbacks of vegetation greening on the hydrologic cycle and land-surface air temperature.

The hydrologic cycle. Vegetation greening modulates water cycling. Land water losses to the atmosphere occur through ET, which includes transpiration (60–90% of the total land ET[134–136]) and evaporation. Greening increases water losses through an extended area of

Evapotranspiration
(ET). The flux of water emitted from the Earth's surface to the atmosphere. It is the sum of evaporation by the soil, wet canopy, open-water surfaces and transpiration by plant stomata.

Transpiration
The loss of water from plants to the atmosphere.

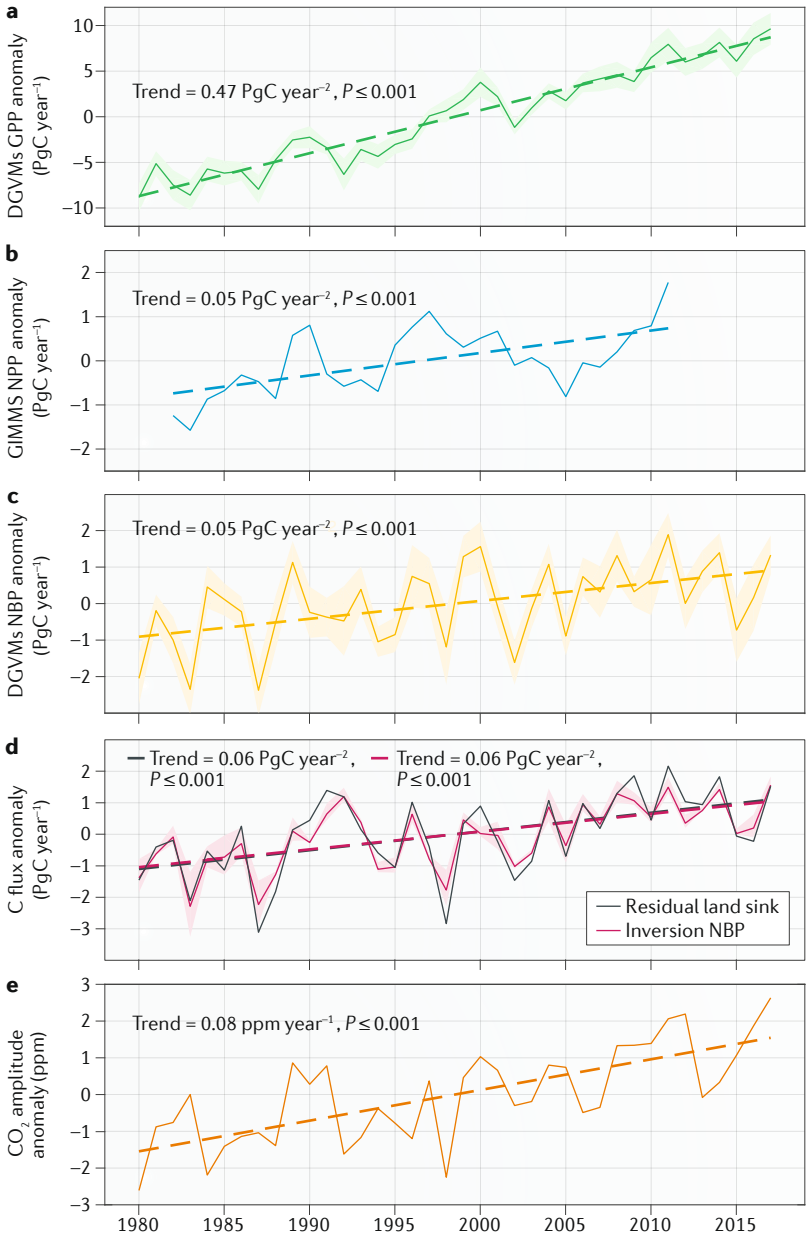

Fig. 6 | **Changes in global carbon fluxes and seasonal CO_2 amplitude.** The graphs depict global gross primary production (GPP) (part **a**), net primary production (NPP) (part **b**), net biome production (NBP) (part **c**), residual land sink (part **d**) and seasonal CO_2 amplitude (part **e**) at Barrow, AK, USA since 1980. The GPP is from the ensemble mean of 16 dynamic global vegetation models (DGVMs)[111]. The NPP is from greenness-based modelling by Smith et al.[198]. The NBP is from the ensemble mean of 16 DGVMs and two atmospheric inversions[111]. Residual land sink is the mass balance residual of anthropogenic CO_2 emissions, the atmospheric CO_2 growth rate and the ocean CO_2 budget[111]. The shaded areas indicate the standard deviation of the GPP, NPP or NBP across models. The dashed lines indicate linear trends.

leaves performing transpiration[137]. A larger foliage area reduces the bare ground surface from which soil evaporation occurs, but increases the re-evaporation of rainfall intercepted by leaves[138], so that greening can cause the net evaporation to either increase or decrease. Various remote-sensing-based ET estimates consistently point to a significant increase in global terrestrial ET over the past four decades, suggesting an intensified water exchange between the land and the atmosphere concurrent with the greening trend[139]. More than half of the global ET increase since the 1980s has been attributed to vegetation greening[138,139] (FIG. 7).

By controlling the changes in ET, vegetation greening also alters the water distribution between regions and water pools (for example, water in soil, rivers and the atmosphere). Assuming that precipitation does not change in response to vegetation greening, a greening-induced ET increase will reduce soil moisture and runoff, which can intensify droughts at the catchment scale[140,141]. In China's Loess Plateau for instance, where intensive afforestation is associated with a pronounced local greening, the river discharge has indeed decreased by a rate of 0.25 km^3 $year^{-2}$ over the past six decades[142]. However, when using ESMs that consider both the greening-induced ET increase and consequent changes in precipitation, simulations forced only with satellite-observed LAI trends do not generate dramatic changes in soil moisture or runoff at continental or global scales[143,144]. This is because greening-induced ET enhancement increases atmospheric water vapour content, which, in turn, promotes downwind precipitation[145,146]. The enhanced precipitation over transpiring regions is particularly evident in moist forests[147] like the Amazon or Congo, which are 'closed' atmospheric systems where 80% of the rainfall originates from upwind ET[145]. Such an efficient atmospheric water recycling mitigates water loss from the soil, sustains inland vegetation and maintains mesic and humid ecosystems.

In addition to intensifying water cycling at the annual scale, vegetation greening also induces seasonal hydrologic changes. There is emerging evidence that spring-greening-enhanced ET leads to a reduction in soil moisture content, which carries over into the following summer and likely suppresses vegetation growth and increases the risk of heatwaves[148,149]. The greening-induced water loss through ET is recycled as land precipitation in subsequent months, benefitting some remote regions through modulating large-scale atmospheric circulation patterns, despite often being insufficient to compensate for evaporative water loss locally[149]. Proposed climate-mitigation strategies, such as afforestation, therefore need to fully consider coupling between vegetation and other components of the Earth system.

Land-surface air temperatures. Greening impacts the exchange of energy between the land and the atmosphere, which ultimately leads to modifications in surface air temperature[150]. Greening increases ET, which cools the surface through evaporative cooling[19,150], but greener canopies have a lower albedo than bare ground and absorb more sunlight, which can result in a larger sensible heat flux. This enhanced sensible heat warms the land surface, an effect called albedo warming[151]. The net effect of greening on surface air temperature in many cases can be viewed as the balance between evaporative cooling and albedo warming[152,153], which was estimated globally to be −0.9 W m^{-2} from evaporative cooling and +0.1 W m^{-2} from albedo warming[19] (FIG. 7c).

Greening can also trigger a series of changes through atmospheric circulation that indirectly affect the surface temperature[154]. For example, the additionally transpired

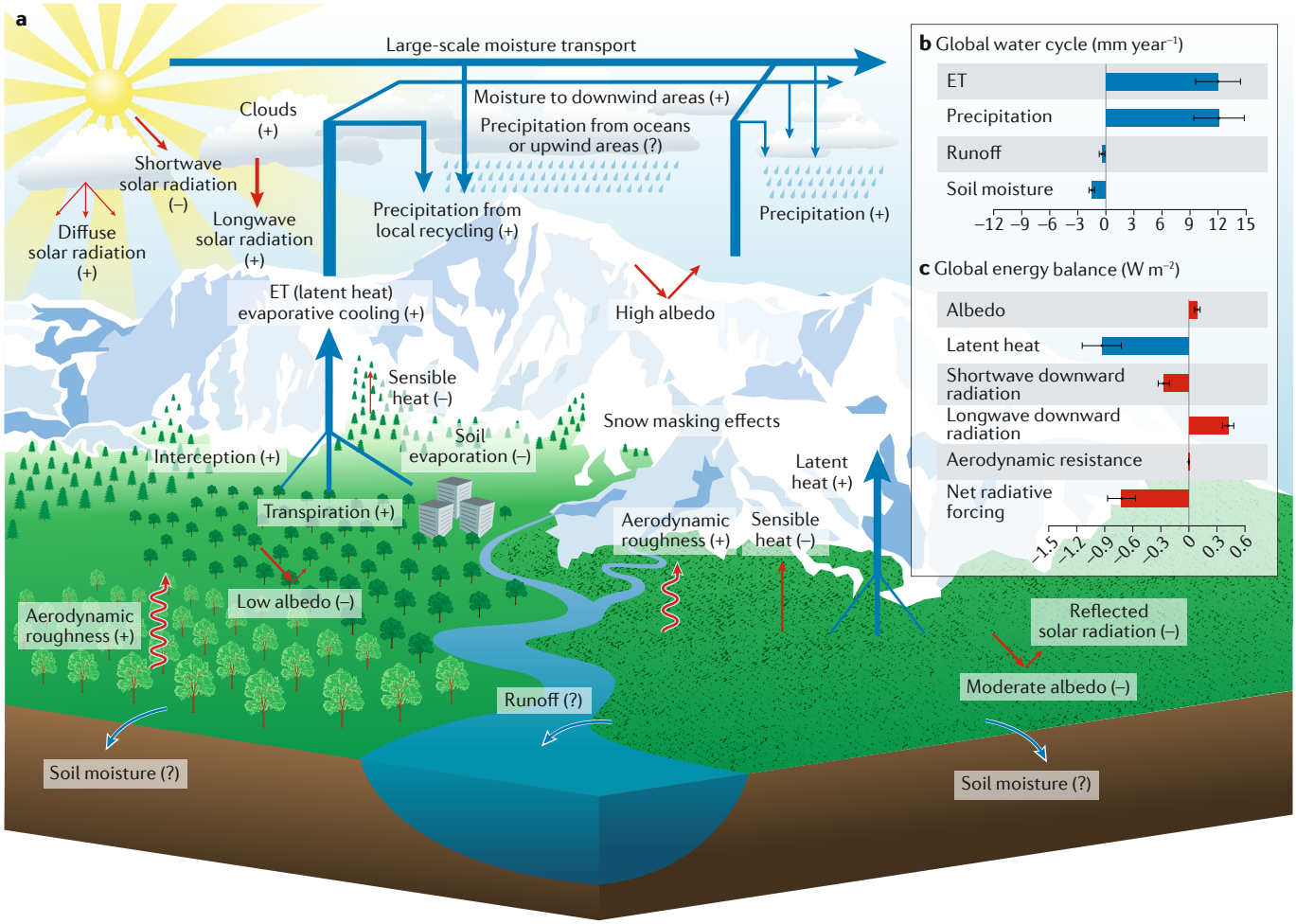

Fig. 7 | **Biogeophysical feedbacks of recent vegetation greening to the climate system. a** | Schematic diagram summarizing land-surface and atmospheric processes through which changes in vegetation greenness feed back into the climate system. For each process or flux, the corresponding symbols '–', '+' and '?' in brackets represent an increasing, decreasing and unknown trend, respectively, in response to vegetation greening, and the colour of arrows represents impacts on water (blue) or energy balance (red, except the latent heat in blue). **b** | Summary of greening-induced changes in major global water cycle fluxes in mm year^{-1} from 1982 to 2011. Data courtesy of Zeng et al.[19]. **c** | Summary of greening-induced changes in global surface energy balance in W m^{-2} from 1982 to 2011. Data courtesy of Zeng et al.[144]. The error bars show the standard error of the estimates. The bar colours are the same as the corresponding fluxes shown in part **a**. ET, evapotranspiration.

water enhances atmospheric water vapour content, which results in more longwave solar radiation entrapment and re-emission in the atmosphere, but reducing the amount of shortwave solar radiation reaching the Earth's surface through increased cloud formation[19,155,156] (FIG. 7). When all the aforementioned impacts of vegetation greening on near-surface air temperature were simulated in coupled ESMs driven by the satellite-based greening since the 1980s, the results suggested a net cooling trend by 12% ± 3% of the concurrent observed warming rate[19].

In warm regions such as the tropics and subtropics, evaporative cooling effects are generally larger than albedo warming effects, leading to a net cooling effect when vegetation greenness increases[19,157,158]. However, the net effect of greening on surface air temperature over the Northern Hemisphere extratropical regions is still subject to debate. Studies based on idealized afforestation and/or deforestation experiments[1,159] or comparisons of the energy budget differences between paired forest and short vegetation sites[132,153] suggested that the albedo warming effect plays a dominant role. These studies, though, assumed complete land cover changes, whereas greening can be gradual. By integrating satellite observations with ESMs, several studies provided an alternative approach that more realistically simulated the effects of vegetation greenness changes and isolated the signal of climate response to greening. These studies found that greening slowed down warming through evaporative cooling in Arctic and boreal regions[19], the Tibetan Plateau[160] and temperate regions like East Asia[161]. Nonetheless, current state-of-the-art modelling efforts are still inconclusive, as some processes are not yet well represented in ESMs, such as snow masking by greener canopies during cold seasons[162–164] and the partitioning of transpiration and evaporation

that is sensitive to vegetation greenness change[136]. Since most ESMs underestimate the ratio of transpiration to ET[136], evaporative cooling by greening could have been underestimated[19,133].

Conclusions

Widespread vegetation greening since the 1980s is one of the most notable characteristics of biosphere change in the Anthropocene. Greening has significantly enhanced the land carbon sink, intensified the hydrologic cycle and cooled the land surface at the global scale. A mechanistic understanding of the underlying drivers shows how anthropogenic forcing has fundamentally altered today's Earth system through a set of feedback loops. Improved knowledge of greenness changes, together with recent progress in observing technology and modelling capacity, has resulted in major advances in understanding global vegetation dynamics. Nonetheless, we still face many challenges ahead.

One key challenge is to continue developing the capacity of remote sensing to measure vegetation structure and functions. Although the vegetation greenness indices described in this Review have proved highly reliable, contemporary satellite greenness products still suffer from limitations, such as inadequate sensitivity to detect changes in dense vegetation, aliasing between snow cover decrease and leaf area increase in cold ecosystems (such as boreal forests), atmospheric contamination, orbital drift and sensor replacements. Compared with the AVHRR, the new moderate-resolution spectral bands and spatial resolutions of 250 m to 1 km of the MODIS sensors on board the Terra (operating since 1999) and Aqua (operating since 2002) satellites have provided global datasets that largely improved the long-term monitoring of vegetation greenness[13]. The current scientific community needs to include Earth observations with higher temporal, richer spectral and finer spatial resolutions to capture various ecosystem functions and processes responding to different parts of the electromagnetic spectrum[165]. We expect the development of next-generation satellite missions and vegetation indices to better fulfil these needs. For example, ongoing efforts on developing hyperspectral remote sensing such as the EnMAP, FLEX, and HyspIRI missions will improve the richness and specificity of spectral information on vegetation structure and functioning.

Another equally important challenge is to validate satellite-based greenness changes with ground observations. Currently, the lack of systematic long-term ground observations covering a large spatial gradient from the high Arctic to the tropics has led to few available ground truths[166] to confirm greenness changes detected through satellite products. Therefore, expanding existing observational networks (such as PhenoCam and FLUXNET) is a high priority. For example, the mismatch between the spatial distribution of vegetation productivity and the density of FLUXNET sites[167] highlights the need to expand the current network from the mid-latitudes to the tropics, where the most photosynthesis takes place. Also, growing crowd-sourced observations by citizen scientists, such as the CrowdCurio phenology observations over the eastern USA[168], can provide valuable data that complement the more expensive professional ground observation networks. These increasing types and amounts of data, together with the rapid development of deep learning[169] and process modelling[11], offer promising tools for improving our understanding of vegetation greening[169].

Considerable uncertainties remain in ESM projections on if and where vegetation greening will occur. Recent studies have identified several processes causing vegetation browning in some regions, including forest diebacks[170], insect[35] and disease outbreaks[171], thermokarst development[172], human mismanagement[36,173], destructive logging[174] and industrial development[175]. These emerging threats could lead to unexpected changes in vegetation greenness relative to our current projections (such as the projections shown in FIGS 2e–h,5), since these processes are under-represented in ESMs. Thus, integrating continued space and ground monitoring and advancing ESM developments is a critical cross-sectoral research priority.

1. Bonan, G. B., Pollard, D. & Thompson, S. L. Effects of boreal forest vegetation on global climate. *Nature* **359**, 716–718 (1992).
2. Haberl, H. et al. Quantifying and mapping the human appropriation of net primary production in earth's terrestrial ecosystems. *Proc. Natl Acad. Sci. USA* **104**, 12942–12947 (2007).
3. Griscom, B. W. et al. Natural climate solutions. *Proc. Natl Acad. Sci. USA* **114**, 11645–11650 (2017).
4. Bastin, J.-F. et al. The global tree restoration potential. *Science* **365**, 76–79 (2019).
5. Tucker, C. J., Fung, I. Y., Keeling, C. D. & Gammon, R. H. Relationship between atmospheric CO_2 variations and a satellite-derived vegetation index. *Nature* **319**, 195–199 (1986).
6. Fung, I. Y., Tucker, C. J. & Prentice, K. C. Application of advanced very high resolution radiometer vegetation index to study atmosphere-biosphere exchange of CO_2. *J. Geophys. Res. Atmos.* **92**, 2999–3015 (1987).
7. Myneni, R. B., Keeling, C. D., Tucker, C. J., Asrar, G. & Nemani, R. R. Increased plant growth in the northern high latitudes from 1981 to 1991. *Nature* **386**, 698–702 (1997).
The first study to reveal large-scale vegetation greening over the Northern Hemisphere.
8. Zhou, L. et al. Variations in northern vegetation activity inferred from satellite data of vegetation index during 1981 to 1999. *J. Geophys. Res. Atmos.* **106**, 20069–20083 (2001).
9. Goetz, S. J., Bunn, A. G., Fiske, G. J. & Houghton, R. A. Satellite-observed photosynthetic trends across boreal North America associated with climate and fire disturbance. *Proc. Natl Acad. Sci. USA* **102**, 13521–13525 (2005).
10. Xu, L. et al. Temperature and vegetation seasonality diminishment over northern lands. *Nat. Clim. Change* **3**, 581–586 (2013).
11. Zhu, Z. et al. Greening of the Earth and its drivers. *Nat. Clim. Change* **6**, 791–795 (2016).
A detailed attribution study of global leaf area index change during the past three decades with ensemble dynamic global vegetation models.
12. Ju, J. & Masek, J. G. The vegetation greenness trend in Canada and US Alaska from 1984–2012 Landsat data. *Remote. Sens. Environ.* **176**, 1–16 (2016).
13. Chen, C. et al. China and India lead in greening of the world through land-use management. *Nat. Sustain.* **2**, 122–129 (2019).
Demonstrated the pattern of global greening since 2000 with the latest MODIS C6 collection data.
14. Lucht, W. et al. Climatic control of the high-latitude vegetation greening trend and Pinatubo effect. *Science.* **296**, 1687–1689 (2002).
15. Arneth, A. et al. IPCC special report on climate change and land. *Intergovernmental Panel on Climate Change (IPCC)* https://www.ipcc.ch/report/srccl/ (2019) (**accessed** October 2019).
16. Abram, N. et al. IPCC special report on the ocean and cryosphere in a changing climate. *Intergovernmental Panel on Climate Change (IPCC)* https://www.ipcc.ch/srocc/home/ (**accessed** October 2019).
17. Eyring, V. et al. Overview of the Coupled Model Intercomparison Project Phase 6 (CMIP6) experimental design and organization. *Geosci. Model. Dev.* **9**, 1937–1958 (2016).
18. Swann, A. L. S., Fung, I. Y. & Chiang, J. C. H. Mid-latitude afforestation shifts general circulation and tropical precipitation. *Proc. Natl Acad. Sci. USA* **109**, 712–716 (2012).
19. Zeng, Z. et al. Climate mitigation from vegetation biophysical feedbacks during the past three decades. *Nat. Clim. Change* **7**, 432–436 (2017).
A quantification of the climatic impacts of vegetation greening through modulating land-atmosphere energy and water exchanges, with an Earth system model forced by satellite-observed leaf area index change during the past three decades.
20. de Jong, R., Verbesselt, J., Schaepman, M. E. & De Bruin, S. Trend changes in global greening and

browning: contribution of short-term trends to longer-term change. *Glob. Change Biol.* **18**, 642–655 (2012).
21. Tian, F. et al. Evaluating temporal consistency of long-term global NDVI datasets for trend analysis. *Remote. Sens. Environ.* **163**, 326–340 (2015).
22. Zhang, Y., Song, C., Band, L. E., Sun, G. & Li, J. Reanalysis of global terrestrial vegetation trends from MODIS products: Browning or greening? *Remote. Sens. Environ.* **191**, 145–155 (2017).
23. Liu, Y., Liu, R. & Chen, J. M. Retrospective retrieval of long-term consistent global leaf area index (1981–2011) from combined AVHRR and MODIS data. *J. Geophys. Res. Biogeosciences* **117**, G04003 (2012).
24. Lyapustin, A. et al. Scientific impact of MODIS C5 calibration degradation and C6+ improvements. *Atmos. Meas. Tech.* **7**, 4353–4365 (2014).
25. Park, T. et al. Changes in growing season duration and productivity of northern vegetation inferred from long-term remote sensing data. *Environ. Res. Lett.* **11**, 084001 (2016).
26. Beck, P. S. A. & Goetz, S. J. Satellite observations of high northern latitude vegetation productivity changes between 1982 and 2008: ecological variability and regional differences. *Environ. Res. Lett.* **6**, 045501 (2011).
27. Sturm, M., Racine, C. & Tape, K. Climate change: increasing shrub abundance in the Arctic. *Nature* **411**, 546–547 (2001).
28. Frost, G. V. & Epstein, H. E. Tall shrub and tree expansion in Siberian tundra ecotones since the 1960s. *Glob. Change Biol.* **20**, 1264–1277 (2014).
29. Myers-Smith, I. H. et al. Climate sensitivity of shrub growth across the tundra biome. *Nat. Clim. Change* **5**, 887–891 (2015).
30. Myers-Smith, I. H. et al. Shrub expansion in tundra ecosystems: dynamics, impacts and research priorities. *Environ. Res. Lett.* **6**, 045509 (2011).
31. Mahowald, N. et al. Projections of leaf area index in earth system models. *Earth Syst. Dyn.* **7**, 211–229 (2016).
32. Bhatt, U. et al. Recent declines in warming and vegetation greening trends over pan-Arctic tundra. *Remote. Sens.* **5**, 4229–4254 (2013).
33. Verbyla, D. The greening and browning of Alaska based on 1982–2003 satellite data. *Glob. Ecol. Biogeogr.* **17**, 547–555 (2008).
34. Senf, C., Pflugmacher, D., Wulder, M. A. & Hostert, P. Characterizing spectral–temporal patterns of defoliator and bark beetle disturbances using Landsat time series. *Remote. Sens. Environ.* **170**, 166–177 (2015).
35. Bjerke, J. W. et al. Understanding the drivers of extensive plant damage in boreal and Arctic ecosystems: Insights from field surveys in the aftermath of damage. *Sci. Total. Environ.* **599**, 1965–1976 (2017).
36. White, J. C., Wulder, M. A., Hermosilla, T., Coops, N. C. & Hobart, G. W. A nationwide annual characterization of 25 years of forest disturbance and recovery for Canada using Landsat time series. *Remote. Sens. Environ.* **194**, 303–321 (2017).
37. Sulla-Menashe, D., Woodcock, C. E. & Friedl, M. A. Canadian boreal forest greening and browning trends: an analysis of biogeographic patterns and the relative roles of disturbance versus climate drivers. *Environ. Res. Lett.* **13**, 014007 (2018).
38. Bi, J., Xu, L., Samanta, A., Zhu, Z. & Myneni, R. Divergent Arctic-boreal vegetation changes between North America and Eurasia over the past 30 years. *Remote. Sens.* **5**, 2093–2112 (2013).
39. Feng, X. et al. Revegetation in China's Loess Plateau is approaching sustainable water resource limits. *Nat. Clim. Change.* **6**, 1019–1022 (2016).
40. Zhou, L. et al. Widespread decline of Congo rainforest greenness in the past decade. *Nature* **509**, 86–90 (2014).
41. Goswami, S., Gamon, J., Vargas, S. & Tweedie, C. Relationships of NDVI, biomass, and leaf area index (LAI) for six key plant species in Barrow, Alaska. *PeerJ PrePrints* **3**, e913v1 (2015).
42. Samanta, A. et al. Amazon forests did not green-up during the 2005 drought. *Geophys. Res. Lett.* **37**, L05401 (2010).
43. Saleska, S. R., Didan, K., Huete, A. R. & Da Rocha, H. R. Amazon forests green-up during 2005 drought. *Science* **318**, 612 (2007).
44. Asner, G. P. & Alencar, A. Drought impacts on the Amazon forest: the remote sensing perspective. *New Phytol.* **187**, 569–578 (2010).
45. Fensholt, R. et al. Greenness in semi-arid areas across the globe 1981–2007—an Earth Observing Satellite based analysis of trends and drivers. *Remote. Sens. Environ.* **121**, 144–158 (2012).
46. Ahlström, A. et al. The dominant role of semi-arid ecosystems in the trend and variability of the land CO_2 sink. *Science* **348**, 895–899 (2015).
47. Buitenwerf, R., Rose, L. & Higgins, S. I. Three decades of multi-dimensional change in global leaf phenology. *Nat. Clim. Change* **5**, 364–368 (2015).
48. Piao, S. et al. Plant phenology and global climate change: current progresses and challenges. *Glob. Change Biol.* **25**, 1922–1940 (2019).
49. White, M. A. et al. Intercomparison, interpretation, and assessment of spring phenology in North America estimated from remote sensing for 1982–2006. *Glob. Change Biol.* **15**, 2335–2359 (2009).
50. Schwartz, M. D. & Hanes, J. M. Intercomparing multiple measures of the onset of spring in eastern North America. *Int. J. Climatol.* **30**, 1614–1626 (2010).
51. Richardson, A. D., Hufkens, K., Milliman, T. & Frolking, S. Intercomparison of phenological transition dates derived from the PhenoCam Dataset V1.0 and MODIS satellite remote sensing. *Sci. Rep.* **8**, 5679 (2018).
52. Jeong, S.-J., Ho, C.-H., Gim, H.-J. & Brown, M. E. Phenology shifts at start vs. end of growing season in temperate vegetation over the Northern Hemisphere for the period 1982–2008. *Glob. Change Biol.* **17**, 2385–2399 (2011).
53. Keenan et al. Net carbon uptake has increased through warming-induced changes in temperate forest phenology. *Nat. Clim. Change* **4**, 598–604 (2014).
54. Garonna, I., de Jong, R. & Schaepman, M. E. Variability and evolution of global land surface phenology over the past three decades (1982–2012). *Glob. Change Biol.* **22**, 1456–1468 (2016).
55. Menzel, A. et al. European phenological response to climate change matches the warming pattern. *Glob. Change Biol.* **12**, 1969–1976 (2006).
56. Cleland, E. E., Chuine, I., Menzel, A., Mooney, H. A. & Schwartz, M. D. Shifting plant phenology in response to global change. *Trends Ecol. Evol.* **22**, 357–365 (2007).
57. Gill, A. L. et al. Changes in autumn senescence in northern hemisphere deciduous trees: a meta-analysis of autumn phenology studies. *Ann. Bot.* **116**, 875–888 (2015).
58. Barichivich, J. et al. Large-scale variations in the vegetation growing season and annual cycle of atmospheric CO_2 at high northern latitudes from 1950 to 2011. *Glob. Change Biol.* **19**, 3167–3183 (2013).
59. Piao, S., Friedlingstein, P., Ciais, P., Viovy, N. & Demarty, J. Growing season extension and its impact on terrestrial carbon cycle in the Northern Hemisphere over the past 2 decades. *Glob. Biogeochem. Cycles* **21**, GB3018 (2007).
60. Julien, Y. & Sobrino, J. A. Global land surface phenology trends from GIMMS database. *Int. J. Remote. Sens.* **30**, 3495–3513 (2009).
61. Park, T. et al. Changes in timing of seasonal peak photosynthetic activity in northern ecosystems. *Glob. Change Biol.* **25**, 2382–2395 (2019).
62. Gonsamo, A., Chen, J. M. & Ooi, Y. W. Peak season plant activity shift towards spring is reflected by increasing carbon uptake by extratropical ecosystems. *Glob. Change Biol.* **24**, 2117–2128 (2018).
63. Bhatt, U. S. et al. Changing seasonality of panarctic tundra vegetation in relationship to climatic variables. *Environ. Res. Lett.* **12**, 055003 (2017).
64. Epstein, H. et al. Tundra greenness. In Arctic Report Card 2018. National Oceanic and Atmospheric Administration (NOAA), 46–52 (2018).
65. Huang, M. et al. Velocity of change in vegetation productivity over northern high latitudes. *Nat. Ecol. Evol.* **1**, 1649–1654 (2017).
66. Farquhar, G. D. & Sharkey, T. D. Stomatal conductance and photosynthesis. *Annu. Rev. Plant. Physiol.* **33**, 317–345 (1982).
67. Keenan, T. F. et al. Increase in forest water-use efficiency as atmospheric carbon dioxide concentrations rise. *Nature* **499**, 324–327 (2013).
68. Donohue, R. J., Roderick, M. L., McVicar, T. R. & Farquhar, G. D. Impact of CO_2 fertilization on maximum foliage cover across the globe's warm, arid environments. *Geophys. Res. Lett.* **40**, 3031–3035 (2013).
69. Ukkola, A. M., Prentice, I. C., Keenan, T. F., van Dijk, A. I. J. M., Viney, N. R., Myneni, R. B. & Bi, J. Reduced streamflow in water-stressed climates consistent with CO_2 effects on vegetation. *Nat. Clim. Change* **6**, 75–78 (2015).
70. Sitch, S. et al. Recent trends and drivers of regional sources and sinks of carbon dioxide. *Biogeosciences* **12**, 653–679 (2015).
71. Ahlbeck, J. R. Comment on "Variations in northern vegetation activity inferred from satellite data of vegetation index during 1981–1999" by L. Zhou et al. *J. Geophys. Res. Atmos.* **107**, ACH–9 (2002).
72. Los, S. O. Analysis of trends in fused AVHRR and MODIS NDVI data for 1982–2006: Indication for a CO_2 fertilization effect in global vegetation. *Glob. Biogeochem. Cycles* **27**, 318–330 (2013).
73. Norby, R. J., Warren, J. M., Iversen, C. M., Medlyn, B. E. & McMurtrie, R. E. CO_2 enhancement of forest productivity constrained by limited nitrogen availability. *Proc. Natl Acad. Sci.USA* **107**, 19368–19373 (2010).
74. Dubey, S. K., Tripathi, S. K. & Pranuthi, G. Effect of elevated CO_2 on wheat crop: Mechanism and impact. *Crit. Rev. Environ. Sci. Technol.* **45**, 2283–2304 (2015).
75. Ainsworth, E. A. & Long, S. P. What have we learned from 15 years of free-air CO_2 enrichment (FACE)? A meta-analytic review of the responses of photosynthesis, canopy properties and plant production to rising CO_2. *New Phytol.* **165**, 351–372 (2005).
76. Norby, R. J. & Zak, D. R. Ecological lessons from free-air CO_2 enrichment (FACE) experiments. *Annu. Rev. Ecol. Evol. Syst.* **42**, 181–203 (2011).
77. Hickler, T. et al. CO_2 fertilization in temperate FACE experiments not representative of boreal and tropical forests. *Glob. Change Biol.* **14**, 1531–1542 (2008).
78. Schimel, D., Stephens, B. B. & Fisher, J. B. Effect of increasing CO_2 on the terrestrial carbon cycle. *Proc. Natl Acad. Sci. USA* **112**, 436–441 (2015).
79. Obermeier, W. A. et al. Reduced CO_2 fertilization effect in temperate C3 grasslands under more extreme weather conditions. *Nat. Clim. Change* **7**, 137–141 (2017).
80. Gray, S. B. et al. Intensifying drought eliminates the expected benefits of elevated carbon dioxide for soybean. *Nat. Plants* **2**, 16132 (2016).
81. Reich, P. B. & Hobbie, S. E. Decade-long soil nitrogen constraint on the CO_2 fertilization of plant biomass. *Nat. Clim. Change* **3**, 278–282 (2013).
82. Reich, P. B., Hobbie, S. E. & Lee, T. D. Plant growth enhancement by elevated CO_2 eliminated by joint water and nitrogen limitation. *Nat. Geosci.* **7**, 920–924 (2014).
83. Terrer, C. et al. Nitrogen and phosphorus constrain the CO_2 fertilization of global plant biomass. *Nat. Clim. Change* **9**, 684–689 (2019).
84. Corlett, R. T. Impacts of warming on tropical lowland rainforests. *Trends Ecol. Evol.* **26**, 606–613 (2011).
85. Huang, M. et al. Air temperature optima of vegetation productivity across global biomes. *Nat. Ecol. Evol.* **3**, 772–779 (2019).
86. Keenan, T. F. & Riley, W. J. Greening of the land surface in the world's cold regions consistent with recent warming. *Nat. Clim. Change* **8**, 825–828 (2018).
87. Braswell, B. H., Schimel, D. S., Linder, E. & Moore, B. III The response of global terrestrial ecosystems to interannual temperature variability. *Science* **278**, 870–873 (1997).
88. Linderholm, H. W. Growing season changes in the last century. *Agric. For. Meteorol.* **137**, 1–14 (2006).
89. Richardson, A. D. et al. Influence of spring and autumn phenological transitions on forest ecosystem productivity. *Philos. Trans. R. Soc. Lond.* **365**, 3227–3246 (2010).
90. Piao, S. et al. Evidence for a weakening relationship between interannual temperature variability and northern vegetation activity. *Nat. Commun.* **5**, 5018 (2014).
Discusses the weakening temperature impacts on northern vegetation greenness since the 1980s.
91. Vickers, H. et al. Changes in greening in the high Arctic: insights from a 30 year AVHRR max NDVI dataset for Svalbard. *Environ. Res. Lett.* **11**, 105004 (2016).
92. Nemani, R. R. et al. Climate-driven increases in global terrestrial net primary production from 1982 to 1999. *Science* **300**, 1560–1563 (2003).
93. Eklundh, L. & Olsson, L. Vegetation index trends for the African Sahel 1982–1999. *Geophys. Res. Lett.* **30**, 1430 (2003).
94. Anyamba, A. & Tucker, C. J. Analysis of Sahelian vegetation dynamics using NOAA-AVHRR NDVI data from 1981–2003. *J. Arid. Environ.* **63**, 596–614 (2005).
95. Donohue, R. J., McVicar, T. R. & Roderick, M. L. Climate-related trends in Australian vegetation cover as inferred from satellite observations, 1981–2006. *Glob. Change Biol.* **15**, 1025–1039 (2009).

96. Herrmann, S. M., Anyamba, A. & Tucker, C. J. Recent trends in vegetation dynamics in the African Sahel and their relationship to climate. *Glob. Environ. Change* **15**, 394–404 (2005).
97. Hickler, T. et al. Precipitation controls Sahel greening trend. *Geophys. Res. Lett.* **32**, L21415 (2005).
98. Huber, S., Fensholt, R. & Rasmussen, K. Water availability as the driver of vegetation dynamics in the African Sahel from 1982 to 2007. *Glob. Planet. Change* **76**, 186–195 (2011).
99. Dardel, C. et al. Re-greening Sahel: 30 years of remote sensing data and field observations (Mali, Niger). *Remote. Sens. Environ.* **140**, 350–364 (2014).
100. Brandt, M. et al. Changes in rainfall distribution promote woody foliage production in the Sahel. *Commun. Biol.* **2**, 133 (2019).
101. Brandt, M. et al. Human population growth offsets climate-driven increase in woody vegetation in sub-Saharan Africa. *Nat. Ecol. Evol.* **1**, 0081 (2017).
102. Curtis, P. G., Slay, C. M., Harris, N. L., Tyukavina, A. & Hansen, M. C. Classifying drivers of global forest loss. *Science* **361**, 1108–1111 (2018).
103. Eighth National Forest Resource Inventory Report (2009–2013) (State Forestry Administration of the People's Republic of China, 2014).
104. Luyssaert, S. et al. Land management and land-cover change have impacts of similar magnitude on surface temperature. *Nat. Clim. Change* **4**, 389–393 (2014).
105. Song, X.-P. et al. Global land change from 1982 to 2016. *Nature* **560**, 639–643 (2018).
106. Poulter, B. et al. The global forest age dataset and its uncertainties (GFADv1.1). *NASA National Aeronautics and Space Administration, PANGAEA* https://doi.org/10.1594/PANGAEA.897392 (2019).
107. Reich, P. B. et al. Nitrogen limitation constrains sustainability of ecosystem response to CO_2. *Nature* **440**, 922–925 (2006).
108. Penuelas, J. et al. Human-induced nitrogen–phosphorus imbalances alter natural and managed ecosystems across the globe. *Nat. Commun.* **4**, 2934 (2013).
109. Greaver, T. L. et al. Key ecological responses to nitrogen are altered by climate change. *Nat. Clim. Change* **6**, 836–843 (2016).
110. Zaehle, S. et al. Evaluation of 11 terrestrial carbon–nitrogen cycle models against observations from two temperate Free-Air CO_2 Enrichment studies. *New Phytol.* **202**, 803–822 (2014).
111. Le Quéré, C. et al. Global carbon budget 2018. *Earth Syst. Sci. Data* **10**, 2141–2194 (2018).
112. Chen, J. M. et al. Vegetation structural change since 1981 significantly enhanced the terrestrial carbon sink. *Nat. Commun.* **10**, 4259 (2019).
113. van Dijk, A. I. J. M., Dolman, A. J. & Schulze, E.-D. Radiation, temperature, and leaf area explain ecosystem carbon fluxes in boreal and temperate European forests. *Glob. Biogeochem. Cycles* **19**, GB2029 (2005).
114. Zhang, Y., Joiner, J., Alemohammad, S. H., Zhou, S. & Gentine, P. A global spatially contiguous solar-induced fluorescence (CSIF) dataset using neural networks. *Biogeosciences* **15**, 5779–5800 (2018).
115. Cheng, L. et al. Recent increases in terrestrial carbon uptake at little cost to the water cycle. *Nat. Commun.* **8**, 110 (2017).
116. Winkler, A. J., Myneni, R. B., Alexandrov, G. A. & Brovkin, V. Earth system models underestimate carbon fixation by plants in the high latitudes. *Nat. Commun.* **10**, 885 (2019).
117. Shevliakova, E. et al. Historical warming reduced due to enhanced land carbon uptake. *Proc. Natl Acad. Sci. USA* **110**, 16730–16735 (2013).
118. Pan, Y. et al. A large and persistent carbon sink in the world's forests. *Science* **333**, 988–993 (2011).
119. Liu, Y. Y. et al. Recent reversal in loss of global terrestrial biomass. *Nat. Clim. Change* **5**, 470–474 (2015).
120. Keenan, T. F. et al. Recent pause in the growth rate of atmospheric CO_2 due to enhanced terrestrial carbon uptake. *Nat. Commun.* **7**, 13428 (2016).
121. Piao, S. et al. Lower land-use emissions responsible for increased net land carbon sink during the slow warming period. *Nat. Geosci.* **11**, 739–743 (2018).
122. Kondo, M. et al. Plant regrowth as a driver of recent enhancement of terrestrial CO_2 uptake. *Geophys. Res. Lett.* **45**, 4820–4830 (2018).
123. Pugh, T. A. M. et al. Role of forest regrowth in global carbon sink dynamics. *Proc. Natl Acad. Sci. USA* **116**, 4382–4387 (2019).
124. Naudts, K. et al. Europe's forest management did not mitigate climate warming. *Science* **351**, 597–600 (2016).
125. Keeling, C. D., Chin, J. F. S. & Whorf, T. P. Increased activity of northern vegetation inferred from atmospheric CO_2 measurements. *Nature* **382**, 146–149 (1996).
126. Graven, H. D. et al. Enhanced seasonal exchange of CO_2 by northern ecosystems since 1960. *Science* **341**, 1085–1089 (2013).
127. Piao, S. et al. On the causes of trends in the seasonal amplitude of atmospheric CO_2. *Glob. Change Biol.* **24**, 608–616 (2018).
128. Forkel, M. et al. Enhanced seasonal CO_2 exchange caused by amplified plant productivity in northern ecosystems. *Science* **351**, 696–699 (2016).
Presents the linkage between increasing photosynthesis of northern vegetation and the enlarging seasonal CO_2 amplitude.
129. Piao, S. et al. Weakening temperature control on the interannual variations of spring carbon uptake across northern lands. *Nat. Clim. Change* **7**, 359–363 (2017).
130. Barichivich, J., Briffa, K. R., Osborn, T. J., Melvin, T. M. & Caesar, J. Thermal growing season and timing of biospheric carbon uptake across the Northern Hemisphere. *Glob. Biogeochem. Cycles* **26**, GB4015 (2012).
131. Piao, S. et al. Net carbon dioxide losses of northern ecosystems in response to autumn warming. *Nature* **451**, 49–52 (2008).
132. Alkama, R. & Cescatti, A. Biophysical climate impacts of recent changes in global forest cover. *Science* **351**, 600–604 (2016).
Presents evidence for feedbacks of forest cover change to land-surface temperature and its regional disparities.
133. Arora, V. K. & Montenegro, A. Small temperature benefits provided by realistic afforestation efforts. *Nat. Geosci.* **4**, 514–518 (2011).
134. Jasechko, S. et al. Terrestrial water fluxes dominated by transpiration. *Nature* **496**, 347–350 (2013).
135. Good, S. P., Noone, D. & Bowen, G. Hydrologic connectivity constrains partitioning of global terrestrial water fluxes. *Science* **349**, 175–177 (2015).
136. Lian, X. et al. Partitioning global land evapotranspiration using CMIP5 models constrained by observations. *Nat. Clim. Change* **8**, 640–646 (2018).
137. Bernacchi, C. J. & VanLoocke, A. Terrestrial ecosystems in a changing environment: a dominant role for water. *Annu. Rev. Plant. Biol.* **66**, 599–622 (2015).
138. Zhang, Y. et al. Multi-decadal trends in global terrestrial evapotranspiration and its components. *Sci. Rep.* **6**, 19124 (2016).
139. Zeng, Z., Peng, L. & Piao, S. Response of terrestrial evapotranspiration to Earth's greening. *Curr. Opin. Environ. Sustain.* **33**, 9–25 (2018).
140. Bosch, J. M. & Hewlett, J. D. A review of catchment experiments to determine the effect of vegetation changes on water yield and evapotranspiration. *J. Hydrol.* **55**, 3–23 (1982).
141. Evaristo, J. & McDonnell, J. J. Global analysis of streamflow response to forest management. *Nature* **570**, 455–461 (2019).
142. Wang, S. et al. Reduced sediment transport in the Yellow River due to anthropogenic changes. *Nat. Geosci.* **9**, 38–41 (2016).
143. Li, Y. et al. Divergent hydrological response to large-scale afforestation and vegetation greening in China. *Sci. Adv.* **4**, eaar4182 (2018).
144. Zeng, Z. et al. Impact of Earth greening on the terrestrial water cycle. *J. Clim.* **31**, 2633–2650 (2018).
145. van der Ent, R. J., Savenije, H. H. G., Schaefli, B. & Steele-Dunne, S. C. Origin and fate of atmospheric moisture over continents. *Water Resour. Res.* **46**, W09525 (2010).
Discusses the importance of land evapotranspiration to sustain downwind precipitation.
146. Teuling, A. J. et al. Observational evidence for cloud cover enhancement over western European forests. *Nat. Commun.* **8**, 14065 (2017).
147. Spracklen, D. V., Arnold, S. R. & Taylor, C. M. Observations of increased tropical rainfall preceded by air passage over forests. *Nature* **489**, 282–285 (2012).
148. Buermann, W. et al. Widespread seasonal compensation effects of spring warming on northern plant productivity. *Nature* **562**, 110–114 (2018).
149. Lian, X. et al. Summer soil drying exacerbated by earlier spring greening of northern vegetation. *Sci. Adv.* (in the press).
150. Bonan, G. B. Forests, climate, and public policy: A 500-year interdisciplinary odyssey. *Annu. Rev. Ecol. Evol. Syst.* **47**, 97–121 (2016).
151. Davin, E. L. & de Noblet-Ducoudré, N. Climatic impact of global-scale deforestation: Radiative versus nonradiative processes. *J. Clim.* **23**, 97–112 (2010).
152. Bonan, G. B. Forests and climate change: forcings, feedbacks, and the climate benefits of forests. *Science* **320**, 1444–1449 (2008).
153. Lee, X. et al. Observed increase in local cooling effect of deforestation at higher latitudes. *Nature* **479**, 384–387 (2011).
154. Winckler, J., Lejeune, Q., Reick, C. H. & Pongratz, J. Nonlocal effects dominate the global mean surface temperature response to the biogeophysical effects of deforestation. *Geophys. Res. Lett.* **46**, 745–755 (2019).
155. Green, J. K. et al. Regionally strong feedbacks between the atmosphere and terrestrial biosphere. *Nat. Geosci.* **10**, 410–414 (2017).
156. Devaraju, N., de Noblet-Ducoudré, N., Quesada, B. & Bala, G. Quantifying the relative importance of direct and indirect biophysical effects of deforestation on surface temperature and teleconnections. *J. Clim.* **31**, 3811–3829 (2018).
157. Bateni, S. M. & Entekhabi, D. Relative efficiency of land surface energy balance components. *Water Resour. Res.* **48**, 4510 (2012).
158. Forzieri, G., Alkama, R., Miralles, D. G. & Cescatti, A. Satellites reveal contrasting responses of regional climate to the widespread greening of Earth. *Science* **356**, 1180–1184 (2017).
159. Betts, R. A. Offset of the potential carbon sink from boreal forestation by decreases in surface albedo. *Nature* **408**, 187–190 (2000).
160. Shen, M. et al. Evaporative cooling over the Tibetan Plateau induced by vegetation growth. *Proc. Natl Acad. Sci. USA* **112**, 9299–9304 (2015).
161. Jeong, S., Ho, C., Kim, K. & Jeong, J. Reduction of spring warming over East Asia associated with vegetation feedback. *Geophys. Res. Lett.* **36**, L18705 (2009).
162. Essery, R. Large-scale simulations of snow albedo masking by forests. *Geophys. Res. Lett.* **40**, 5521–5525 (2013).
163. Thackeray, C. W., Fletcher, C. G. & Derksen, C. The influence of canopy snow parameterizations on snow albedo feedback in boreal forest regions. *J. Geophys. Res. Atmos.* **119**, 9810–9821 (2014).
164. Wang, L. et al. Investigating the spread in surface albedo for snow-covered forests in CMIP5 models. *J. Geophys. Res. Atmos.* **121**, 1104–1119 (2016).
165. National Academies of Sciences, Engineering, and Medicine. Thriving on our changing planet: A decadal strategy for Earth observation from space (National Academies Press, 2018) https://doi.org/10.17226/24938.
166. Metcalfe, D. B. et al. Patchy field sampling biases understanding of climate change impacts across the Arctic. *Nat. Ecol. Evol.* **2**, 1443–1448 (2018).
167. Schimel, D. et al. Observing terrestrial ecosystems and the carbon cycle from space. *Glob. Change Biol.* **21**, 1762–1776 (2015).
168. Park, D. S. et al. Herbarium specimens reveal substantial and unexpected variation in phenological sensitivity across the eastern United States. *Philos. Trans. R. Soc. Lond. B Biol. Sci.* **374**, 20170394 (2018).
169. Reichstein, M. et al. Deep learning and process understanding for data-driven Earth system science. *Nature* **566**, 195–204 (2019).
170. Allen, C. D. et al. A global overview of drought and heat-induced tree mortality reveals emerging climate change risks for forests. *For. Ecol. Manage.* **259**, 660–684 (2010).
171. Sturrock, R. N. et al. Climate change and forest diseases. *Plant. Pathol.* **60**, 133–149 (2011).
172. Raynolds, M. K. & Walker, D. A. Increased wetness confounds Landsat-derived NDVI trends in the central Alaska North Slope region, 1985–2011. *Environ. Res. Lett.* **11**, 085004 (2016).
173. Matasci, G. et al. Three decades of forest structural dynamics over Canada's forested ecosystems using Landsat time-series and lidar plots. *Remote. Sens. Environ.* **216**, 697–714 (2018).
174. Mitchard, E. T. A. The tropical forest carbon cycle and climate change. *Nature* **559**, 527–534 (2018).

175. Esau, I., Miles, V. V., Davy, R., Miles, M. W. & Kurchatova, A. Trends in normalized difference vegetation index (NDVI) associated with urban development in northern West Siberia. *Atmos. Chem. Phys.* **16**, 9563–9577 (2016).
176. Knyazikhin, Y. et al. Hyperspectral remote sensing of foliar nitrogen content. *Proc. Natl Acad. Sci. USA* **110**, E185–E192 (2013).
177. Tucker, C. J. Red and photographic infrared linear combinations for monitoring vegetation. *Remote. Sens. Environ.* **8**, 127–150 (1979).
178. Bannari, A., Morin, D., Bonn, F. & Huete, A. R. A review of vegetation indices. *Remote. Sens. Rev.* **13**, 95–120 (1995).
179. Myneni, R. B., Hall, F. G., Sellers, P. J. & Marshak, A. L. The interpretation of spectral vegetation indexes. *IEEE Trans. Geosci. Remote. Sens.* **33**, 481–486 (1995).
180. Xue, J. & Su, B. Significant remote sensing vegetation indices: A review of developments and applications. *J. Sens.* **2017**, 1353691 (2017).
181. Ganguly, S. et al. Generating vegetation leaf area index Earth system data record from multiple sensors. Part 2: Implementation, analysis and validation. *Remote. Sens. Environ.* **112**, 4318–4332 (2008).
182. Zhu, Z. et al. Global data sets of vegetation leaf area index (LAI) 3g and fraction of photosynthetically active radiation (FPAR) 3g derived from global inventory modeling and mapping studies (GIMMS) normalized difference vegetation index (NDVI3g) for the period 1981 to 2011. *Remote. Sens.* **5**, 927–948 (2013).
183. Pinzon, J. & Tucker, C. A non-stationary 1981–2012 AVHRR NDVI3g time series. *Remote. Sens.* **6**, 6929–6960 (2014).
Discusses some complexities and challenges in detecting greenness change with the longest available NDVI dataset (AVHRR NDVI) since the 1980s.
184. Knyazikhin, Y., Martonchik, J. V., Myneni, R. B., Diner, D. J. & Running, S. W. Synergistic algorithm for estimating vegetation canopy leaf area index and fraction of absorbed photosynthetically active radiation from MODIS and MISR data. *J. Geophys. Res. Atmos.* **103**, 32257–32275 (1998).
185. Chen, J. M. & Black, T. A. Defining leaf area index for non-flat leaves. *Plant. Cell Environ.* **15**, 421–429 (1992).
186. Asrar, G. Q., Fuchs, M., Kanemasu, E. T. & Hatfield, J. L. Estimating absorbed photosynthetic radiation and leaf area index from spectral reflectance in wheat 1. *Agron. J.* **76**, 300–306 (1984).
187. Cohen, W. B., Maiersperger, T. K., Gower, S. T. & Turner, D. P. An improved strategy for regression of biophysical variables and Landsat ETM+ data. *Remote. Sens. Environ.* **84**, 561–571 (2003).
188. Baret, F. et al. GEOV1: LAI and FAPAR essential climate variables and FCOVER global time series capitalizing over existing products. Part1: Principles of development and production. *Remote. Sens. Environ.* **137**, 299–309 (2013).
189. Claverie, M., Matthews, J., Vermote, E. & Justice, C. A 30+ year AVHRR LAI and FAPAR climate data record: Algorithm description and validation. *Remote. Sens.* **8**, 263 (2016).
190. Ross, J. K. & Marshak, A. L. Calculation of canopy bidirectional reflectance using the Monte Carlo method. *Remote. Sens. Environ.* **24**, 213–225 (1988).
191. Yang, B. et al. Estimation of leaf area index and its sunlit portion from DSCOVR EPIC data: Theoretical basis. *Remote. Sens. Environ.* **198**, 69–84 (2017).
192. Xiao, Z. et al. Long-time-series global land surface satellite leaf area index product derived from MODIS and AVHRR surface reflectance. *IEEE Trans. Geosci. Remote. Sens.* **54**, 5301–5318 (2016).
193. Myneni, R., Knyazikhin, Y. & Park, T. MOD15A2H MODIS/terra leaf area index/FPAR 8-day L4 global 500 m SIN grid V006. *NASA EOSDIS L. Process. DAAC* (2015).
194. Tucker, C. J. et al. An extended AVHRR 8-km NDVI dataset compatible with MODIS and SPOT vegetation NDVI data. *Int. J. Remote. Sens.* **26**, 4485–4498 (2005).
195. Huete, A. et al. Overview of the radiometric and biophysical performance of the MODIS vegetation indices. *Remote. Sens. Environ.* **83**, 195–213 (2002).
196. Maisongrande, P., Duchemin, B. & Dedieu, G. VEGETATION/SPOT: an operational mission for the Earth monitoring; presentation of new standard products. *Int. J. Remote. Sens.* **25**, 9–14 (2004).
197. Badgley, G., Field, C. B. & Berry, J. A. Canopy near-infrared reflectance and terrestrial photosynthesis. *Sci. Adv.* **3**, e1602244 (2017).
198. Smith, W. K. et al. Large divergence of satellite and Earth system model estimates of global terrestrial CO_2 fertilization. *Nat. Clim. Change* **6**, 306–310 (2016).

Acknowledgements
This study was supported by the National Natural Science Foundation of China (41861134036) and the Research Council of Norway (grant no. 287402), the National Key R&D Program of China (2017YFA0604702) and the Thousand Youth Talents Plan project in China. The works of C.C., R.B.M. and T.P. were funded by NASA's Earth Science Division. The authors thank Z. Zhu, Y. Li, K. Wang, Y. Deng, M. Gao and X. Li for their help in preparing the manuscript.

Author contributions
S.P., X.W., T.P., C.C., X.L., Y.H., J.W.B., A.C., P.C., H.T. and R.B.M. wrote the first draft of the manuscript. S.P., X.W. and R.B.M. reviewed and edited the manuscript before submission. All authors made substantial contributions to the discussion of content.

Competing interests
The authors declare no competing interests.

Publisher's note
Springer Nature remains neutral with regard to jurisdictional claims in published maps and institutional affiliations.

Reviewer information
Nature Reviews Earth & Environment thanks the three anonymous reviewers, for their contribution to the peer review of this work.

Supplementary information
Supplementary information is available for this paper at https://doi.org/10.1038/s43017-019-0001-x.

RELATED LINKS
PEP725: http://www.pep725.eu
PhenoCam: http://www.phenocam.us
EnMAP: http://www.enmap.org/
FLEX: https://Earth.esa.int/web/guest/missions/esa-future-missions/flex
HyspIRI: https://hyspiri.jpl.nasa.gov/
FLUXNET: https://fluxnet.fluxdata.org/

QUERY FORM

Nature Reviews Earth & Environment	
Manuscript ID	**1**
Author	**Shilong Piao**

AUTHOR:

The following queries have arisen during the editing of your manuscript. Please answer by making the requisite corrections directly in the e.proofing tool rather than marking them up on the PDF. This will ensure that your corrections are incorporated accurately and that your paper is published as quickly as possible.

Query No.	*Nature of Query*
Q1:	in the original manuscript, reference 38 appeared before references 32–38, so this has been adjusted also.
Q2:	Please check your article carefully, coordinate with any co-authors and enter all final edits clearly in the eproof, remembering to save frequently. Once corrections are submitted, we cannot routinely make further changes to the article.
Q3:	Note that the eproof should be amended in only one browser window at any one time; otherwise changes will be overwritten.
Q4:	Author surnames have been highlighted. Please check these carefully and adjust if the first name or surname is marked up incorrectly. Note that changes here will affect indexing of your article in public repositories such as PubMed. Also, carefully check the spelling and numbering of all author names and affiliations, and the corresponding email address(es).
Q5:	You cannot alter accepted Supplementary Information files except for critical changes to scientific content. If you do resupply any files, please also provide a brief (but complete) list of changes. If these are not considered scientific changes, any altered Supplementary files will not be used, only the originally accepted version will be published.

Supplement information for:

Characteristics, drivers and feedbacks of global greening

Shilong Piao[1,2,3*], Xuhui Wang[1], Taejin Park[4], Chi Chen[4], Xu Lian[1], Yue He[1], Jarle W. Bjerke[5], Anping Chen[6], Philippe Ciais[1,7], Hans Tømmervik[5], Ramakrishna R. Nemani[8], Ranga B. Myneni[4]

[1] Sino-French Institute for Earth System Science, College of Urban and Environmental Sciences, Peking University, Beijing 100871, China.

[2] Key Laboratory of Alpine Ecology and Biodiversity, Institute of Tibetan Plateau Research, Chinese Academy of Sciences, Beijing 100085, China.

[3] Center for Excellence in Tibetan Earth Science, Chinese Academy of Sciences, Beijing 100085, China.

[4] Department of Earth and Environment, Boston University, Boston, MA 02215, USA.

[5] Norwegian Institute for Nature Research, FRAM – High North Research Centre for Climate and the Environment, PO Box 6606, Tromsø NO-9296, Norway.

[6] Department of Biology, Colorado State University, Fort Collins, CO 80523, USA.

[7] Laboratoire des Sciences du Climat et de l'Environnement, CEA CNRS UVSQ, Gif-sur-Yvette 91191, France.

[8] NASA Ames Research Center, Moffett Field, CA 94035, USA.

* Correspondence should be addressed to Shilong Piao (slpiao@pku.edu.cn)

Table. S1 | Categorization of vegetation indices based on three derivative forms of surface reflectance with respect to wavelength. Details for the derivative forms can be found in ref. 1.

Type	Vegetation Index
Type 1	NDVI (Normalized Difference Vegetation Index; ref. 2), SR (Simple Ration; ref. 3), SAVI (Soil Adjusted Vegetation Index; ref. 4), TSAVI (Transformed Soil Adjusted Vegetation Index; ref. 5), OSAVI (Optimized Soil Adjusted Vegetation Index; ref. 6), PVI (Perpendicular Vegetation Index; ref. 7), WDVI (Weighted Difference Vegetation Index; ref. 8), GCI (Green Chlorophyll Index, ref. 9), GNDVI (Green Normalized Difference Vegetation Index; ref. 10), GRVI (Green Ratio Vegetation Index; ref. 11), PRI (Photochemical Reflectance Index; ref. 12), DVI (Difference Vegetation Index; ref. 13), NDWI (Normalized Difference Water Index; ref. 14), CCI (Chlorophyll/Carotenoid Index; ref. 15)
Type 2	GEMI (Global Environmental Monitoring Index; ref. 16), Greenness (ref. 17), NLI (Non-Linear Index; ref.18), NIRv (Near-Infrared Reflectance of Vegetation, ref. 19)
Type 3	EVI (Enhanced Vegetation Index, ref. 20), ARVI (Atmospherically Resistant Vegetation Index; ref. 21), SARVI (Soil Adjusted and Atmospherically Resistant Vegetation Index; ref. 21), GARI (Green Atmospherically Resistant Index; ref. 22)

Table. S2 | Summary of satellite global NDVI products.

NDVI Product	Time span	Data input source	Ground Sampling Distance	Frequency	Reference
MODIS[#,*]	2000 (2002) – Present	Terra(Aqua)/MODIS C6 reflectance	250 m, 500 m, 1 km, and 0.05º	16-day & Monthly	Ref. 23
VIIRS[#,*]	2012 - Present	Suomi-NPP/VIIRS reflectance	500 m, 1 km, and 0.05º	16-day & Monthly	Ref. 24
DSCOVR[#]	2015 – Present	DSCOVR/EPIC reflectance	10 km	Hourly & daily	Ref. 25
NDVI3g	1981 - 2018	AVHRR GAC level-1b data	1/12º	Biweekly	Ref. 26
VIP4	1981 - 2016	LTDR3 AVHR09C1 and MOD09CMG data	0.05º	Daily, 7-day, 15-day, monthly	Ref. 27
LTDR5[#]	1981 - Present	AVHRR GAC level-1b data	0.05º	Daily	Ref. 28
CGLS[#] (or GEOV2)	1999 - Present	SPOT/VGT & PROVA-V reflectance	1/112º	10-day	Ref. 29

[#]: The product has been operationally generated, archived, and disseminated.

[*]: EVI (Enhanced Vegetation Index) is also available in this product.

Table. S3 | Comparison of data and processing from AVHRR, MODIS, SPOT-VGT and MERIS sensors.

AVHRR	MODIS	SPOT-VGT	MERIS
Broad red and near-infrared wavelength channels. These are not necessarily chosen to be responsive to changes in vegetation as these are meteorological sensors.	Narrow red and near-infrared wavelength channels designed specifically to respond to vegetation changes [30].	Moderately narrow red and near-infrared wavelength channels designed specifically to respond to vegetation changes[31].	Very narrow red and near-infrared wavelength channels designed specifically to respond to vegetation changes.
No on-board calibration. Sensor calibrated before launch, but loses calibration over time[32].	On-board calibration. Sensor calibrated before launch and during operation regularly. The sensor is also periodically calibrated using the moon[33].	No on-board calibration. Sensor calibrated before launch, but loses calibration over time[31].	Sensor calibrated before launch and during operation regularly. MERIS on-board calibration is based on on-board measurements of sunlight[34].
Multiple sequential sensors with little or no overlap[26]. Each sensor data span is about 3 to 4 years. Inter-sensor data calibration is a major problem.	Two near-simultaneous sensors. The Terra MODIS data stream started in Feb 2000 (Aqua MODIS stream started in May 2002). Overlaps allows inter-sensor calibration.	Two sensors. VEGETATION 1 (VGT1) on board SPOT4, launched in March 1998, and VEGETATION 2 (VGT2) on board SPOT5 launched in May 2002[35]. After February 2003, VGT1 has no longer been used for VI products. Overlaps allows inter-sensor calibration.	One sensor. The ENVISAT MERIS LAI data stream started in July 2002 and ended in March 2012[36]. No official products for NDVI and EVI.

Satellite loses orbit over time. Data is collected over progressively lower and lower sun angles[37]. Variations in data due to sun angle changes are conflated with changes in vegetation.	Both Terra and Aqua platforms maintain precise orbits. Any orbit loss is periodically corrected by pushing the satellites into their designated orbits. Variations in data due to changes in sun-sensor geometry are explicitly considered during LAI retrievals[38,39] .	The signal is stable. Irradiance variations due to sun-earth distance and sun-sensor geometry are explicitly corrected[31].	Orbital information is unknown.
Minimal correction for atmospheric contamination of signals emanating from vegetation. Sensor lacks additional wavelength channels required for accurate cloud screening, correction for daily tropospheric aerosol contamination and periodic stratospheric aerosol contamination (following volcanic eruptions)[40].	Sensor has several channels that are used to accurately screen for clouds, including high cirrus. Atmospheric correction for molecular and tropospheric aerosol contamination is performed accurately with a radiative transfer-based algorithm on a daily basis for each of the seven vegetation channels[41,42].	A simplified physics-based atmospheric correction algorithm (based on the 6S method) is employed for water vapor, ozone, and tropospheric aerosol[31].	Several different radiative transfer-based algorithms are used for atmospheric correction for aerosol optical thickness, columnar water vapor and surface reflectance, as well as for LAI retrieval[36,43].
As no physics-based processing is possible with AVHRR channel data. NDVI and EVI generally corresponds to the data with minimal	The physics-based processing removes atmospheric effects and provides users with at-ground reflectance data for each of the seven	A simplified physics-based processing removes atmospheric effects and provides users with at-ground reflectance data for NDVI	No official products available for NDVI and EVI. Various approaches were proposed based on top of atmosphere reflectance and surface

atmospheric contamination[26,44].	channels, and for NDVI and EVI products[20,42].	and EVI products.	reflectance.
LAI products are derived using black-box approaches such as neural nets. Partial validation with ground measurements[40]. No suitable field data prior to 2000 exist for validation.	The channel reflectance data are used in other physics-based algorithms to derive leaf area estimates[39,45] . The derived products are extensively validated with ground measurements[46]. All the algorithms have been periodically updated and the entire archive is re-processed to produce newer versions of the data products.	LAI products are derived using black-box approaches i.e., neural networks. The product has been extensively validated with ground measurements[47].	The LAI retrieval based on the BEAM MERIS vegetation processor. This algorithm is trained by neural networks with a suite of simulated top-of-atmosphere radiances, using the Scattering by Arbitrarily Inclined Leaves (SAIL), PROSPECT and a simplified method for atmospheric correction[36].
Low spatial resolution (8×8 km^2) and 15-day frequency for the period July 1981 to December 2016[26,40].	Moderate spatial resolution (500×500 m^2), 8-day/16-day frequency for the period Feb 2000 to Dec 2018[20,46,48].	1/112° ×1/112° spatial resolution (1×1 km^2), 10-day frequency for the period 1999-present[47].	1/360° ×1/360° spatial resolution (300×300 m^2), 10-day frequency for the from 2002-2012[36].

Table. S4 | Summary of satellite global LAI products.

LAI Product	Time span	Data input source	Ground Sampling Distance	Frequency	Algorithm	Reference
MODIS[#]	2000 (2002) – Present	Terra(Aqua)/MODIS C6 reflectance	500 m	8-day (4-day for Terra/Aqua combined)	LUT based on 3D RT	Ref. 46,48
VIIRS[#]	2012 – Present	Suomi-NPP/VIIRS reflectance	500 m	8-day	LUT based on 3D RT	Ref. 49
DSCOVR[#]	2015 – Present	DSCOVR/EPIC reflectance	10 km	Hourly & daily	LUT based on 3D RT	Ref. 50
LAI3g	1981 – 2018	GIMMS NDVI3g	1/12º	Biweekly	ANN trained with MODIS LAI	Ref. 40
GLASS	1981 – 2017	NOAA/AVHRR LTDR reflectance & Terra/MODIS C6 reflectance	0.05º (1km available from 2000)	8-day	GRNN trained with CYCLOPES and MODIS LAIs	Ref. 51
TCDR[#]	1981 – Present	NOAA/AVHRR TCDR reflectance	0.05º	Daily	ANN trained with MODIS LAI	Ref. 52
GLOBMAP	1981 – 2017	GIMMS NDVI & Terra/MODIS C6 reflectance	1/13.75º	Biweekly, 1982 – 1999/2 8-day, 2000/3 – 2017	LUT based on RT	Ref. 53

CGLS[#] (or GEOV2)	1999 – Present	SPOT/VGT & PROVA-V reflectance	1/112º	10-day	ANN trained with CYCLOPES and MODIS LAIs	Ref. 29
MERIS	2002-2012	ENVISAT/MERIS reflectance	1/360º	10-day	ANN trained with 1D RT	Ref. 36

[#]: The product has been operationally generated, archived, and disseminated.

Data Archives

MODIS: https://earthdata.nasa.gov/
VIIRS: https://earthdata.nasa.gov/
GLASS: http://globalchange.bnu.edu.cn/research/lai
TCDR: https://www.ncei.noaa.gov/data/avhrr-land-leaf-area-index-and-fapar/access/
LAI3g: http://sites.bu.edu/cliveg/datacodes/
GLOBMAP: http://www.globalmapping.org/
CGLS LAI: https://land.copernicus.eu/global/products/lai
CGLS NDVI: https://land.copernicus.eu/global/products/ndvi
NDVI3g: https://ecocast.arc.nasa.gov/data/pub/gimms/3g.v1/
VIP4: https://vip.arizona.edu/viplab_data_explorer.php
LTDR5: https://ltdr.modaps.eosdis.nasa.gov/cgi-bin/ltdr/ltdrPage.cgi?fileName=products

Table. S5 | CMIP5 models used in this study.

Model abbreviation	historical	RCP2.6	RCP4.5	RCP6.0	RCP8.5
bcc-csm1-1	√	√	√	√	√
Bcc-csm1-1-m	√	√	√	√	√
BNU-ESM	√	√	√		√
CCSM4	√	√	√	√	
CESM1-BGC	√		√		√
CESM1-CAM5	√	√	√	√	√
CanESM2	√	√	√		√
GFDL-CM3	√		√		
GFDL-ESM2G	√	√		√	√
GFDL-ESM2M	√		√	√	√
HadGEM2-CC	√		√		√
HadGEM2-ES	√	√	√	√	√
IPSL-CM5A-LR	√	√	√	√	√
IPSL-CM5A-MR	√	√	√	√	√
MIROC-ESM-CHEM	√	√	√	√	√
MIROC-ESM	√	√	√	√	√
MPI-ESM-LR	√	√	√		√
MPI-ESM-MR	√	√	√		√
NorESM1-ME	√	√	√	√	√
NorESM1-M	√	√	√	√	√
inmcm4	√		√		√

References

1. Myneni, R. B. *et al*. The meaning of spectral vegetation indices. *IEEE Trans*. *Geosc*. *Remote Sens*. **33**, 481-486 (1995).
2. Rouse, J., Haas, R.H., Schell, J.A. & Deering, D.W. Monitoring vegetation systems in the Great Plains with ERTS. *In Proceedings of the 3rd ERTS Symposium, Washington DC, USA, NASA SP-351*, 309-317 (1974).
3. Birth, G. S., & McVey, G. R. Measuring the color of growing turf with a reflectance spectrophotometer 1. *Agron*. *J*. **60**, 640-643 (1968).
4. Huete, A.R. A soil-adjusted vegetation index (SAVI). *Remote Sens*. *Environ*. **25**, 295-309 (1988).
5. Baret, F., Guyot, G. and Major, D.J. TSAVI: a vegetation index which minimizes soil brightness effects on LAI and APAR estimation. *In 12th Canadian Symposium on Remote Sensing Geoscience and Remote Sensing Symposium* **3**, 1355-1358 (1989).
6. Rondeaux, G., Steven, M. & Baret, F. Optimization of soil-adjusted vegetation indices. *Remote Sens*. *Environ*. **55**, 95-107. (1996).
7. Richardson, A.J. & Wiegand, C.L. Distinguishing vegetation from soil background information. *Photogramm*. *Eng*. *Remote Sens*. **43**, 1541-1552 (1977).
8. Clevers, J.G.P.W. Application of a weighted infrared-red vegetation index for estimating leaf area index by correcting for soil moisture. *Remote Sens*. *Environ*. **29**, 25-37 (1989).
9. Gitelson, A.A., Gritz, Y. & Merzlyak, M.N. Relationships between leaf chlorophyll content and spectral reflectance and algorithms for non-destructive chlorophyll

assessment in higher plant leaves. *J*. *Plant Physiol*. **160**, 271-282 (2003).

10. Gitelson, A.A. & Merzlyak, M.N. Remote sensing of chlorophyll concentration in higher plant leaves. *Adv*. *Space Res*. **22**, 689-692 (1998).

11. Sripada, R.P., Heiniger, R.W., White, J.G. & Meijer, A.D. Aerial color infrared photography for determining early in-season nitrogen requirements in corn. *Agron*. *J*. **98**, 968-977 (2006).

12. Gamon, J.A., Penuelas, J. & Field, C.B. A narrow-waveband spectral index that tracks diurnal changes in photosynthetic efficiency. *Remote Sens*. *Environ*. **41**, 35-44 (1992).

13. Tucker, C.J. Red and photographic infrared linear combinations for monitoring vegetation. *Remote Sens*. *Environ*. **8**, 127-150 (1979).

14. McFeeters, S.K. The use of the Normalized Difference Water Index (NDWI) in the delineation of open water features. *Int*. *J*. *Remote Sens*. **17**, 1425-1432 (1996).

15. Gamon, J.A. *et al*. A remotely sensed pigment index reveals photosynthetic phenology in evergreen conifers. *Proc*. *Natl*. *Acad*. *Sci*. *U*.*S*.*A*. **113**, 13087-13092 (2016).

16. Pinty, B. & Verstraete, M.M. GEMI: a non-linear index to monitor global vegetation from satellites. *Vegetatio* **101**, 15-20 (1992).

17. Jackson, R.D. Spectral indices in n-space. *Remote Sens*. *Environ*. **13**, 409-421 (1983).

18. Goel, N.S. & Qin, W. Influences of canopy architecture on relationships between various vegetation indices and LAI and FPAR: A computer simulation. *Remote Sens*. *Rev*. **10**, 309-347 (1994).

19. Badgley, G., Field, C. B. & Berry, J. A. Canopy near-infrared reflectance and terrestrial

photosynthesis. *Sci*. *Adv*. **3**, e1602244 (2017).

20. Huete, A., Didan, K., Miura, T., Rodriguez, E. P., & Gao, X. Overview of the radiometric and biophysical performance of the MODIS vegetation indices. *Remote Sens*. *Environ*. **83**, 195-213 (2002).

21. Kaufman, Y.J. & Tanre, D. Atmospherically resistant vegetation index (ARVI) for EOS-MODIS. *IEEE Trans*. *Geosci*. *Remote Sens*. **30**, 261-270 (1992).

22. Gitelson, A.A., Kaufman, Y.J. & Merzlyak, M.N. Use of a green channel in remote sensing of global vegetation from EOS-MODIS. *Remote Sens*. *Environ*. **58**, 289-298 (1996).

23. Didan, K., Munoz, A.B., Solano, R. & Huete, A., MODIS vegetation index user's guide (MOD13 series). *Vegetation Index and Phenology Lab, The University of Arizona,* 1-38 (2015).

24. Didan, K., Munoz, A.B., Compton, J.T. & Pinzon, J.E. Suomi-VIIRS Vegetation Index Product Suite User Guide & Abridged Algorithm Theoretical Basis Document. *Vegetation Index and Phenology Lab, The University of Arizona*, 1-100 (2017).

25. Knyazikhin, Y., Song, W., Yang, B., Park, T. & Myneni, R.B. DSCOVR EPIC Vegetation Earth System Data Record Science Data Product Guide (2018).

26. Pinzon, E. J. & Tucker, J. C. A Non-Stationary 1981–2012 AVHRR NDVI3g Time Series. *Remote Sens*. **6**, 6929-6960 (2014).

27. Barreto-munoz, A., Didan, K., Miura, T. & Tsend-Ayush, J. December. Version 4 of the Vegetation Index and Phenology Earth Science Data Records. *In AGU Fall Meeting*

Abstracts (2014).

28. Pedelty, J. *et al*. Generating a long-term land data record from the AVHRR and MODIS instruments. *In 2007 IEEE International Geoscience and Remote Sensing Symposium* 1021-1025 (2007).
29. Baret, F., *et al*. GEOV1: LAI and FAPAR essential climate variables and FCOVER global time series capitalizing over existing products. Part1: Principles of development and production. *Remote Sens*. *Environ*. **137**, 299-309 (2013).
30. Justice, C. O., Townshend, J., & Vermote, E. F. An overview of MODIS Land data processing and product status. *Remote Sens*. *Environ*. **83**, 3-15 (2002).
31. Toté, C. *et al*. Evaluation of the SPOT/VEGETATION Collection 3 reprocessed dataset_ Surface reflectances and NDVI. *Remote Sens*. *Environ*. **201**, 219-233 (2017).
32. Staylor, W. F. Degradation rates of the AVHRR visible channel for the NOAA 6, 7, and 9 spacecraft. *J*. *Atmos*. *Oceanic Technol*. **7**, 411-423 (1990).
33. Xiong, X., Wu, A., & Cao, C. On-orbit calibration and inter-comparison of Terra and Aqua MODIS surface temperature spectral bands. *Int*. *J*. *Remote Sens*. **29**, 5347-5359 (2008).
34. Bourg, L., & Delwart, S. MERIS instrument calibration. *In Second MERIS and AATSR Calibration and Geophysical Validation Workshop, Frascati, Italy* 20-24 (2006).
35. Deronde, B. *et al*. 15 years of processing and dissemination of SPOT-VEGETATION products. *Int*. *J*. *Remote Sens*. **35**, 2402-2420 (2014).
36. Tum, M., *et al*. Global gap-free MERIS LAI time series (2002–2012). *Remote Sens*. **8**, 69

(2016).

37. Kaufman, R. K. *et al*. Effect of orbital drift and sensor changes on the time series of AVHRR vegetation index data. *IEEE Trans*. *Geosci*. *Remote Sens*. **38**, 2584-2597 (2000).

38. Knyazikhin, Y. *et al*. Synergistic algorithm for estimating vegetation canopy leaf area index and fraction of absorbed photosynthetically active radiation from MODIS and MISR data. *J*. *Geophys*. *Res*. *D: Atmos*. **103**, 32257-32275 (1998).

39. Myneni, R. B. *et al*. Increased plant growth in the northern high latitudes from 1981 to 1991. *Nature* **386**, 698-702 (1997).

40. Zhu, Z. *et al*. Global Data Sets of Vegetation Leaf Area Index (LAI)3g and Fraction of Photosynthetically Active Radiation (FPAR)3g Derived from Global Inventory Modeling and Mapping Studies (GIMMS) Normalized Difference Vegetation Index (NDVI3g) for the Period 1981 to 2011. *Remote Sens*. **5**, 927-948 (2013).

41. Frey, R. A. *et al*. Cloud Detection with MODIS. Part I: Improvements in the MODIS Cloud Mask for Collection 5. *J*. *Atmos*. *Oceanic Technol*. **25**, 1057-1072 (2008).

42. Vermote, E. F., Saleous, El, N. Z., & Justice, C. O. Atmospheric correction of MODIS data in the visible to middle infrared: first results. *Remote Sens*. *Environ*. **83**, 97-111 (2002).

43. Guanter, L., Gómez-Chova, L., & Moreno, J. Coupled retrieval of aerosol optical thickness, columnar water vapor and surface reflectance maps from ENVISAT/MERIS data over land. *Remote Sens*. *Environ*.**112**, 2898-2913 (2008).

44. Holben, B. N. Characteristics of maximum-value composite images from temporal

158 AVHRR data. *Int*. *J*. *Remote Sens*. **7**, 1417-1434 (1986).
159 45. Knyazikhin, Y. *et al*. Estimation of vegetation canopy leaf area index and fraction of
160 absorbed photosynthetically active radiation from atmosphere-corrected MISR data. *J*.
161 *Geophys*. *Res*. *D: Atmos*. **103**, 32239-32256 (1998).
162 46. Yan, K. *et al*. Evaluation of MODIS LAI/FPAR Product Collection 6. Part 2: Validation
163 and Intercomparison. *Remote Sens*. **8**, 460 (2016).
164 47. Verger, A., Baret, F., & Weiss, M. GEOV2/VGT: near real time estimation of global
165 biophysical variables from VEGETATION-P data. *In MultiTemp 2013: 7th International*
166 *Workshop on the Analysis of Multi-Temporal Remote Sensing Images*, 1-4 (2013).
167 48. Yan, K. *et al*. Evaluation of MODIS LAI/FPAR Product Collection 6. Part 1: Consistency
168 and Improvements. *Remote Sens*. **8**, 359 (2016).
169 49. Yan, K. *et al*. Generating global products of lai and fpar from snpp-viirs data: Theoretical
170 background and implementation. *IEEE Trans*. *Geosci*. *Remote Sens*. **56**, 2119-2137
171 (2018).
172 50. Yang, B., *et al*. Estimation of leaf area index and its sunlit portion from DSCOVR EPIC
173 data: Theoretical basis. *Remote Sens*. *Environ*. **198**, 69-84 (2017).
174 51. Xiao, Z., Liang, S., Wang, T., & Jiang, B. Retrieval of Leaf Area Index (LAI) and
175 Fraction of Absorbed Photosynthetically Active Radiation (FAPAR) from VIIRS
176 Time-Series Data. *Remote Sens*. **8**, 351 (2016).
177 52. Claverie, M., Matthews, J., Vermote, E. & Justice, C. A 30+ year AVHRR LAI and
178 FAPAR climate data record: Algorithm description and validation. *Remote Sens*. **8**, 263

(2016).

53. Liu, Y., Liu, R., & Chen, J. M. Retrospective retrieval of long-term consistent global leaf area index (1981-2011) from combined AVHRR and MODIS data. *J. Geophys. Res. Biogeosci*. **117**, G04003 (2012).

Chapter 11

Seasonality of Amazonian Rainforests

Myneni et al.

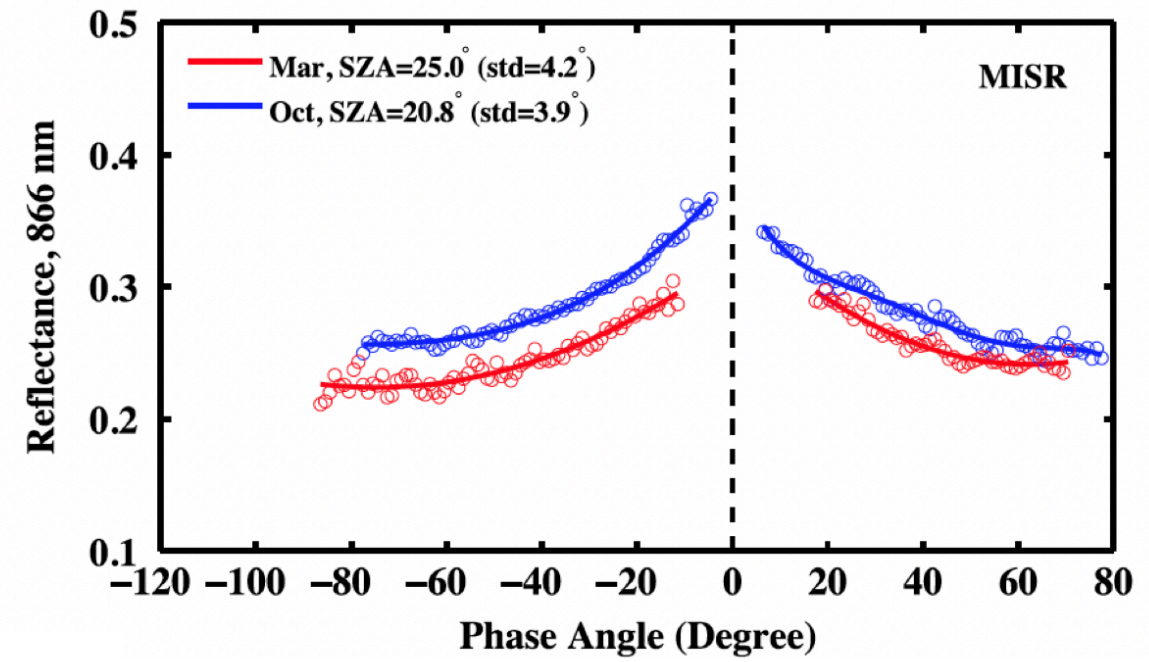

Large seasonal swings in leaf area of Amazon rainforests

Ranga B. Myneni[a], Wenze Yang[a,b], Ramakrishna R. Nemani[c], Alfredo R. Huete[d], Robert E. Dickinson[e,f], Yuri Knyazikhin[a], Kamel Didan[d], Rong Fu[e], Robinson I. Negrón Juárez[e], Sasan S. Saatchi[g], Hirofumi Hashimoto[h], Kazuhito Ichii[i], Nikolay V. Shabanov[a], Bin Tan[a,j], Piyachat Ratana[d], Jeffrey L. Privette[k,l], Jeffrey T. Morisette[m], Eric F. Vermote[k,n], David P. Roy[o], Robert E. Wolfe[p], Mark A. Friedl[a], Steven W. Running[q], Petr Votava[h], Nazmi El-Saleous[r], Sadashiva Devadiga[r], Yin Su[a], and Vincent V. Salomonson[s]

[a]Department of Geography and Environment, Boston University, 675 Commonwealth Avenue, Boston, MA 02215; [c]Ecosystem Science and Technology Branch, National Aeronautics and Space Administration (NASA) Ames Research Center, Mail Stop 242-4, Moffett Field, CA 94035; [d]Department of Soil, Water, and Environmental Science, University of Arizona, Tucson, AZ 85721; [e]School of Earth and Atmospheric Sciences, Georgia Institute of Technology, 311 Ferst Drive, Atlanta, GA 30332; [g]Jet Propulsion Laboratory, California Institute of Technology, 4800 Oak Grove Drive, Pasadena, CA 91109; [h]California State University at Monterey Bay and Ecosystem Science and Technology Branch, NASA Ames Research Center, Mail Stop 242-4, Moffett Field, CA 94035; [i]San Jose State University and Ecosystem Science and Technology Branch, NASA Ames Research Center, Mail Stop 242-4, Moffett Field, CA 94035; [k]Biospheric Sciences Branch, NASA Goddard Space Flight Center, 8600 Greenbelt Road, Mail Code 614.4, Greenbelt, MD 20771; [m]Terrestrial Information Systems Branch, NASA Goddard Space Flight Center, 8600 Greenbelt Road, Mail Code 614.5, Greenbelt, MD 20771; [n]Department of Geography, University of Maryland, College Park, MD 20742; [o]Geographic Information Science Center of Excellence, South Dakota State University, Wecota Hall, Box 506B, Brookings, SD 57007; [p]Raytheon Technology Services Corporation at NASA Goddard Space Flight Center, 8600 Greenbelt Road, Mail Code 614.5, Greenbelt, MD 20771; [q]School of Forestry, University of Montana, Missoula, MT 59812; [r]Science Systems and Applications, Inc., at NASA Goddard Space Flight Center, 8600 Greenbelt Road, Mail Code 614.5, Greenbelt, MD 20771; and [s]Department of Geography and Meteorology, University of Utah, Salt Lake City, UT 84112-0110

Contributed by Robert E. Dickinson, December 22, 2006 (sent for review June 5, 2006)

Despite early speculation to the contrary, all tropical forests studied to date display seasonal variations in the presence of new leaves, flowers, and fruits. Past studies were focused on the timing of phenological events and their cues but not on the accompanying changes in leaf area that regulate vegetation–atmosphere exchanges of energy, momentum, and mass. Here we report, from analysis of 5 years of recent satellite data, seasonal swings in green leaf area of ≈25% in a majority of the Amazon rainforests. This seasonal cycle is timed to the seasonality of solar radiation in a manner that is suggestive of anticipatory and opportunistic patterns of net leaf flushing during the early to mid part of the light-rich dry season and net leaf abscission during the cloudy wet season. These seasonal swings in leaf area may be critical to initiation of the transition from dry to wet season, seasonal carbon balance between photosynthetic gains and respiratory losses, and litterfall nutrient cycling in moist tropical forests.

remote sensing | tropical forests phenology | vegetation climate interaction

The trees of tropical rainforests are known to exhibit a range of phenological behavior, from episodes of ephemeral leaf bursts followed by long quiescent periods to continuous leafing, and from complete intraspecific synchrony to complete asynchrony (1). Several agents (e.g., herbivory, water stress, day length, light intensity, mineral nutrition, and flood pulse) have been identified as proximate cues for leafing and abscission in these communities (1–8). These studies were focused on the timing of phenological events but not on the accompanying changes in leaf area. Leaves selectively absorb solar radiation, emit longwave radiation and volatile organic compounds, and facilitate growth by regulating carbon dioxide influx and water vapor efflux from stomates. Therefore, leaf area dynamics are relevant to studies of climatic, hydrological, and biogeochemical cycles.

The sheer size and diversity of rainforests preclude a synoptic view of leaf area changes from ground sampling. We therefore used data on green leaf area of the Amazon basin ($\approx 7.2 \times 10^6$ km^2) derived from measurements made by the Moderate Resolution Imaging Spectroradiometer (MODIS) onboard the National Aeronautics and Space Administration's (NASA's) Terra satellite [see ref. 9 and supporting information (SI) *Materials and Methods*]. These data were expressed as one-sided green leaf area per unit ground area [leaf area index (LAI)].

Results

Seasonality in LAI Time Series. Leaf area data for the Amazon rainforests exhibit notable seasonality, with an amplitude (peak-to-trough difference) that is 25% of the average annual LAI of 4.7 (Fig. 1*A*). This average amplitude of 1.2 LAI is about twice the error of a single estimate of MODIS LAI, and thus is not an artifact of remote observation or data processing (see *SI Materials and Methods*). The aggregate phenological cycle appears timed to the seasonality of solar radiation in a manner that is suggestive of anticipatory and opportunistic patterns of leaf flushing and abscission. These patterns result in leaf area leading solar radiation during the entire seasonal cycle, with higher leaf area during the shorter dry season when solar radiation loads are high and lower leaf area during the longer wet season when radiation loads decline significantly. This seasonality is roughly consistent with the hypothesis that in moist tropical forests, where rainfall is abundant and herbivore pressures are modest, seasonal increase in solar radiation during the dry season might act as a proximate cue for leaf production (1, 2, 4).

In a community dominated by leaf-exchanging (10) evergreen trees, leaf area can increase if some of the older leaves that are photosynthetically less efficient because of epiphylls and poor stomatal control are exchanged for more numerous new leaves. Leaf area can decrease if the new leaves are less numerous than

Author contributions: R.B.M. and A.R.H. designed research; Y.K., R.I.N.J., H.H., K.I., N.V.S., B.T., P.R., and M.A.F. performed research; R.R.N., R.F., R.I.N.J., S.S.S., H.H., K.I., J.L.P., J.T.M., E.F.V., D.P.R., R.E.W., M.A.F., S.W.R., P.V., N.E.-S., S.D., and V.V.S. contributed new reagents/analytic tools; W.Y., K.D., and Y.S. analyzed data; and R.B.M., A.R.H., R.E.D., R.F., J.L.P., J.T.M., E.F.V., D.P.R., and S.W.R. wrote the paper.

The authors declare no conflict of interest.

Freely available online through the PNAS open access option.

Abbreviations: LAI, leaf area index; MODIS, Moderate Resolution Imaging Spectroradiometer.

[b]Present address: Department of Atmospheric, Oceanic, and Space Sciences, University of Michigan, 2455 Hayward Street, Ann Arbor, MI 48109.

[f]To whom correspondence should be addressed. E-mail: robted@eas.gatech.edu.

[j]Present address: Earth Resources Technology, Inc., 10810 Guilford Road, Suite 105, Annapolis Junction, MD 20701.

[l]Present address: Remote Sensing and Applications Division, National Oceanic and Atmospheric Administration, National Climatic Data Center, 151 Patton Avenue, Asheville, NC 28801.

This article contains supporting information online at www.pnas.org/cgi/content/full/0611338104/DC1.

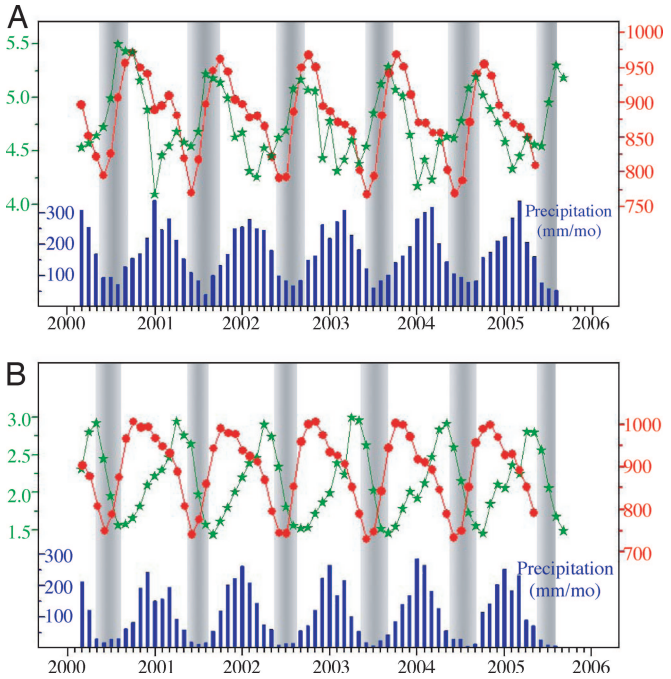

Fig. 1. Time series of monthly LAI from the Terra MODIS instrument (green), monthly maximum of hourly average surface solar radiation from the Terra Clouds and the Earth's Radiant Energy System (CERES) and Geostationary Operational Environmental Satellite 8 (GOES-8) instruments (red), and monthly merged precipitation from the Tropical Rainfall Measuring Mission (TRMM) and other sources (blue). (*A*) Time series based on data averaged over all Amazon rainforest pixels, as identified in the MODIS land cover map (SI Fig. 4*B*), south of the equator. The start of the data record is March 2000 and the end points are September 2005 (LAI), May 2005 (solar radiation), and August 2005 (precipitation). The shaded areas denote dry seasons, defined as months with precipitation <100 mm or less than one-third the precipitation range [0.33·(maximum–minimum) + minimum]. The solar radiation data are for all sky conditions and include direct and diffuse components. (*B*) Same as *A* except that the data are from savanna and grassland pixels adjacent to the Amazon basin in Brazil and south of the equator (SI Fig. 4*B*). The shaded areas denote dry seasons, defined as months with precipitation <50 mm. Information on the data is given in *SI Materials and Methods*.

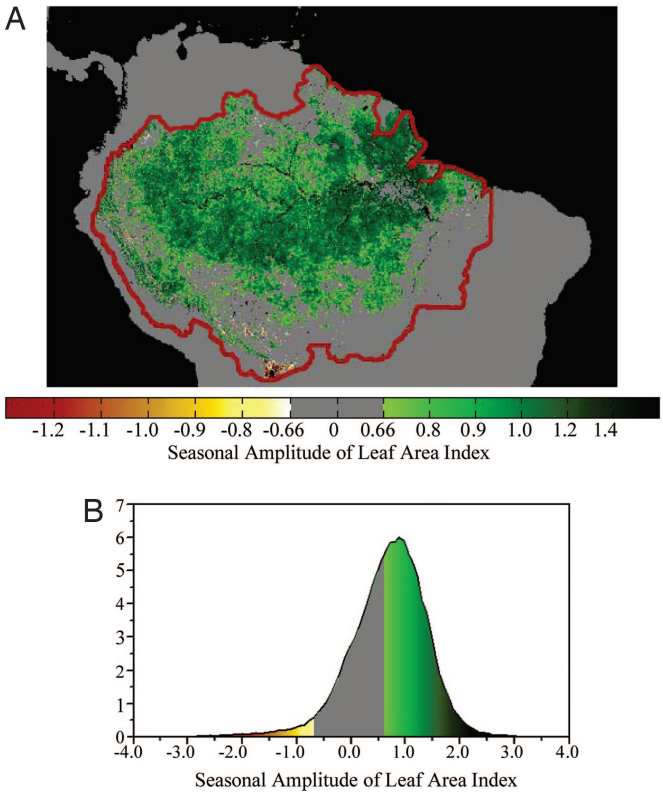

Fig. 2. Seasonal amplitude of LAI. (*A*) Color-coded map of LAI amplitudes greater than 0.66 or less than −0.66; this threshold (|0.66|) is the smallest LAI difference discernable with the MODIS LAI data set (see *SI Materials and Methods*). In regions with dry seasons longer than 3 months, the amplitude is calculated as the difference between the maximum 4-month average LAI in the dry season minus the minimum 4-month average LAI in the wet season. Where the dry season is three or fewer months, the amplitude is calculated as the difference between the dry-season average LAI and the minimum 4-month average LAI in the wet season. The dry and wet seasons are defined based on the precipitation data set at 15′ spatial resolution (see *SI Materials and Methods*). Thus, the seasons vary spatially and interannually. (*B*) Distribution of LAI amplitude for all Amazon rainforest pixels. The color scheme is similar to that in *A*.

the older ones that are dropped. If such exchanges are staggered in time among the individuals over a large area, for example due to asynchrony (7), they can result in a gradually increasing spatially averaged leaf area over a period of several months during the ascending phase of the seasonal cycle, and a gradually decreasing leaf area during the descending phase, while maintaining the evergreen character of the rainforest (Fig. 1*A*). These patterns of net leaf flushing and abscission also generate higher leaf litterfall in the dry season relative to the wet season, as reported in refs. 11–13. Such a leaf strategy will enhance photosynthetic gain during the light-rich dry season (14–19), provided the trees are well hydrated (2), and reduce respiratory burden during the cloudy wet season.

Leaf area changes in the adjacent grasslands and savannas in Brazil are concordant with rainfall data (Fig. 1*B*): higher leaf area in the wet season and lower leaf area in the dry season. This expected behavior imbues confidence in the opposing seasonality of deep-rooted and generally well hydrated (2), but light-limited (2, 4, 17, 18), rainforests inferred from the same LAI data set.

Geographic Details of Leaf Area Changes. The satellite data provide geographic details of leaf area changes in the Amazon (Fig. 2*A*). The region with a distinct seasonality of leaf area spans a broad contiguous swath of land that is anchored to the Amazon River, from its mouth in the east to its westernmost reaches in Peru, in the heart of the basin. This pattern is notable for at least two reasons. First, for its homogeneity; a higher dry-season leaf area relative to the wet season is observed in ≈58% of all rainforest-occupied pixels, whereas only 3% show the opposite change (Fig. 2*B*). Second, the homogeneous region roughly overlies the precipitation gradient (20) in the basin (see *SI Materials and Methods* and SI Fig. 4*C*), suggesting that the amplitude is, to a first approximation, independent of the duration and intensity of the dry season. For example, an amplitude of ≈1 LAI unit is observed in areas with two to five dry months in a year. Ostensibly, these forests maintain high leaf area (19, 21) and remain well hydrated during the dry season in nondrought years (see *SI Materials and Methods* and SI Fig. 5) via their deep root systems (2, 22) and/or through hydraulic redistribution (23, 24), which is also verified through a recent model study (see *SI Materials and Methods*: *Modeling GPP Seasonality of Amazon Rainforests by Constraining Rooting Depths*). Similar changes are not seen in ≈40% of the rainforest pixels, some of which represent transitional and drier rainforests to the south and east.

Correlation Among Changes in Leaf Area, Solar Radiation, and Precipitation. To associate quantitatively the changes in leaf area, solar radiation, and precipitation, we correlated the successive

ENVIRONMENTAL SCIENCES

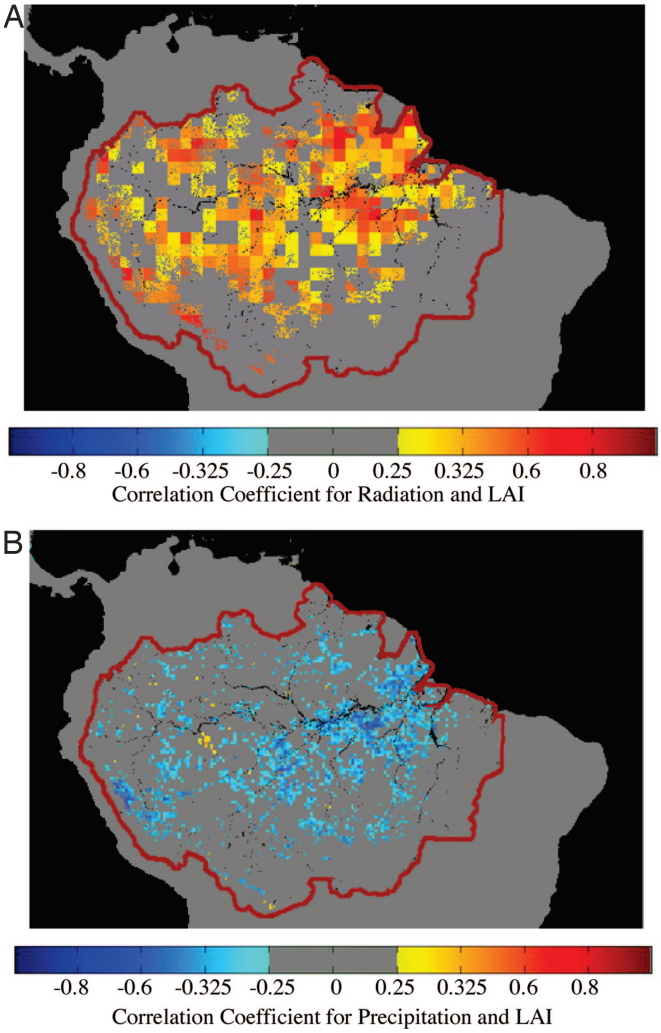

Fig. 3. Correlation coefficients. (*A*) Correlation between first differences of LAI and solar radiation. The first differences of LAI [ΔLAI(*t*)] are calculated as LAI($t + 1$) − LAI(t), where t is months in the timeline March 2000 to May 2005. The number of data points is 62 for each pixel. Correlation coefficients greater than 0.25 or less than −0.25 are shown ($P < 0.05$). The analysis was performed for rainforest pixels with LAI amplitudes greater than 0.66 or less than −0.66; this threshold (|0.66|) is the smallest LAI difference discernable with the MODIS LAI data set (see *SI Materials and Methods*). (*B*) Correlation between first differences of LAI and precipitation.

monthly differences of these variables, first by using the spatially averaged data shown in Fig. 1*A* and second by using pixel-level data. Changes in LAI are both positively correlated with changes in solar radiation ($P < 0.0001$) and negatively correlated with changes in precipitation ($P < 0.0001$), but the correlations between leaf area and radiation changes are larger and, at the pixel level, more numerous (Fig. 3 and SI Fig. 6). The negative correlations between LAI and precipitation are likely an indirect effect of the changes in cloudiness and radiation associated with precipitation changes (17). These results, together with past phenological studies, support the idea of an evolved pattern of endogenously controlled vegetative phenology that is timed to the seasonality of solar radiation (2, 10).

Discussion

The consistency between leaf area, solar radiation, and precipitation data from various satellite instruments is especially noteworthy. However, the strong seasonality in cloud cover and tropospheric aerosol loading may introduce seasonally opposing artifacts in MODIS leaf area. In the Amazon region there is significant cloudiness, which varies greatly between the wet and dry seasons. This seasonality in cloud cover can bias the results if cloud-contaminated retrievals are not screened out from the analysis. To minimize the impact of clouds, we used a coarse-resolution (8 km and monthly) data set that was derived by averaging the best-quality LAI values from the standard 1-km, 8-day MODIS data set (see *SI Materials and Methods*). Although some of the coarse-resolution LAI values were based on fewer high-quality estimates in the wet season, this did not bias the inferred seasonal LAI amplitudes.

The high aerosol content in the dry season, from biomass burning, natural biogenic emissions, and soil dust resuspension (25), can result in artificially low LAI values unless the reflectance data are corrected for aerosol effects. The MODIS processing system was found to correct well for such effects (see *SI Materials and Methods* and SI Fig. 7). The LAI values may have been underestimated by ≈5% from any residual aerosol effects. This effect is small and of opposite timing relative to the observed seasonality. Other possible sources of bias, such as reflectance saturation at high leaf area and changes in the light scattering and absorption properties of leaves due to aging and epiphylls (26), were found to be small and with the wrong timing to significantly alter our estimates of the amplitude of LAI seasonality (see *SI Materials and Methods*).

A robust validation of leaf area seasonality recorded in the MODIS satellite data requires a large number of leaf area measurements. These are presently lacking for the obvious reasons of cost, site accessibility, and the difficulty and questionable accuracy of ground sampling techniques. Nevertheless, the available data and published evidence support early to mid-dry season leaf area enhancement (21, 22), although further testing of this phenomenon is needed. The mechanism by which leaf area increases through the early dry season and decreases through the wet season (cf. Fig. 1) is partially supported by published observations on litterfall seasonality (11–13), but data on accompanying leaf emergence and expansion are lacking.

There is emerging evidence that the rainforest plays a critical role in initiating the onset of the wet season in the Amazon (ref. 27; see also *SI Materials and Methods*). An increase in surface evapotranspiration at the end of the dry season appears to be the primary cause of increased buoyancy of surface air, which consequently increases the probability of atmospheric convection and rainfall. The 25% increase in LAI over nearly 60% of the Amazon rainforest during the dry season reported in this article therefore suggests a potentially important role of vegetation in controlling the initiation of the wet season.

The seasonal dynamics and interplay between canopy photosynthesis and ecosystem respiration will likely be altered by this unexpected seasonality in leaf area (11, 14–19, 28), with attendant consequences for litterfall nutrient cycling (29). However, depending on other environmental and ecological constraints associated with vapor pressure deficits, temperatures, water and nutrient availability, etc., the dry-season increase in leaf area and sunlight may or may not result in enhanced photosynthetic activity. The transitional and seasonally dry forests in the southern Amazon do not show enhanced dry-season greening, which may indicate that these forests could be water-limited. A similar response can be envisioned for the more humid forests in drought years, especially those associated with strong El Niño events. Therefore, it is important to further investigate the significance of these changes in regard to climatic, hydrological, and biogeochemical cycles, and whether such swings in leaf area also exist in the moist forests of Africa and Asia.

Materials and Methods

A continuous record of data on green leaf area from the MODIS onboard NASA's Terra satellite was used to track leaf area changes over the Amazon basin from March 2000 to September 2005. An 8-km monthly LAI data set obtained by averaging the cloud-free main algorithm LAI estimates available in the standard 1-km, 8-day data set was used in this study. Monthly precipitation data at 15′ spatial resolution for the period January 1998 to August 2005, and monthly solar radiation data at 1° spatial resolution for the period March 2000 to May 2005, were also used. A detailed description of these data sets and of the validation of the MODIS LAI data set are given in *SI Materials and Methods* and SI Table 1.

This work was supported by grants from the National Aeronautics and Space Administration. V.V.S. is a Senior Scientist (Emeritus) of NASA Goddard Space Flight Center.

1. van Schaik CP, Terborgh JW, Wright SJ (1993) *Annu Rev Ecol Syst* 24:353–377.
2. Wright SJ (1996) in *Tropical Forest Plant Ecophysiology*, eds Mulkey SS, Chazdon RL, Smith AP (Chapman & Hall, New York), pp 440–460.
3. Morellato PC (2003) in *Phenology: An Integrative Environmental Science*, ed Schwartz MD (Kluwer, Dordrecht, The Netherlands), pp 75–92.
4. Wright SJ, van Schaik CP (1994) *Am Nat* 143:192–199.
5. Borchert R (1994) *Ecology* 75:1437–1449.
6. Schöngart J, Piedade MTF, Ludwigshausen S, Horna V, Worbes M (2002) *J Trop Ecol* 18:581–597.
7. Singh KP, Kushwaha CP (2005) *Curr Sci* 89:964–975.
8. Borchert R, Rivera G, Hagnauer W (2002) *Biotropica* 34:27–39.
9. Salomonson VV, Barnes WL, Maymon PW, Montgomery HE, Ostrow H (1989) *IEEE Trans Geosci Remote Sens* 27:145–153.
10. Borchert R (2000) in *Dormancy in Plants: From Whole Plant Behaviour to Cellular Control*, eds Viemont JD, Crabbe J (CABI, Wallingford, UK), pp 87–107.
11. Goulden ML, Miller SD, da Rocha HR, Menton MC, Freitas HC, Figueira AMS, de Sousa CAD (2004) *Ecol Appl* 14(Suppl):S42–S54.
12. Luizao FJ (1989) *Geo J* 19:407–417.
13. Rodrigues WA, Furch K, Klinge H (2001) *Amazoniana* 16:441–462.
14. Carswell FE (2002) *J Geophys Res* 107:8076.
15. Würth MKR, Peláez-Riedl S, Wright SJ, Körner C (2005) *Oecologia* 143:11–24.
16. Graham EA, Mulkey SS, Kitajima K, Phillips NG, Wright SJ (2003) *Proc Nat Acad Sci USA* 100:572–576.
17. Schuur EAG (2003) *Ecology* 84:1165–1170.
18. Nemani RR, Keeling CD, Hashimoto H, Jolly WM, Piper SC, Tucker CJ, Myneni RB, Running SW (2003) *Science* 300:1560–1563.
19. Huete AR, Didan K, Shimabukuro YE, Ratana P, Saleska S, Yang W, Nemani RR, Myneni RB, Hutyra L, Fitzjarrald D (2006) *Geophys Res Lett* 33:L06405.
20. Sombroek W (2001) *Ambio* 30:388–396.
21. Asner GP, Nepstad DC, Cardinot G, Ray D (2004) *Proc Nat Acad Sci USA* 101:6039–6044.
22. Nepstad DC, de Carvalho CR, Davidson EA, Jipp PH, Lefebvre PA, Negreiros GH, da Silva ED, Stone TA, Trumbore SE, Vieira S (1994) *Nature* 372:666–669.
23. da Rocha HR, Goulden ML, Miller SD, Menton MC, Pinto LDVO, de Freitas HC, Figueira AMES (2004) *Ecol Appl* 14(Suppl):S22–S32.
24. Oliveira RS, Dawson TE, Burgess SSO, Nepstad DC (2005) *Oecologia* 145:354–363.
25. Echalar F, Artaxo P, Martins JV, Yamasoe M, Gerab F, Maenhaut W, Holben B (1998) *J Geophys Res* 103:31849–31864.
26. Roberts DA, Nelson BW, Adams JB, Palmer F (1998) *Trees* 12:315–325.
27. Fu R, Li W (2004) *Theor Appl Climatol* 78:98–110.
28. Seleska SR, Miller SD, Matross DM, Goulden ML, Wofsy SC, da Rocha HR, de Camargo PB, Crill P, Daube BC, de Freitas HC, *et al.* (2003) *Science* 302:1554–1557.
29. Vitousek PM, Sanford RL, Jr, (1986) *Annu Rev Ecol Syst* 17:137–167.

Seasonal changes in leaf area of Amazon forests from leaf flushing and abscission

Arindam Samanta,[1,2] Yuri Knyazikhin,[1] Liang Xu,[1] Robert E. Dickinson,[3] Rong Fu,[3] Marcos H. Costa,[4] Sassan S. Saatchi,[5] Ramakrishna R. Nemani,[6] and Ranga B. Myneni[1]

Received 18 July 2011; revised 23 November 2011; accepted 1 December 2011; published 11 February 2012.

[1] A large increase in near-infrared (NIR) reflectance of Amazon forests during the light-rich dry season and a corresponding decrease during the light-poor wet season has been observed in satellite measurements. This increase has been variously interpreted as seasonal change in leaf area resulting from net leaf flushing in the dry season or net leaf abscission in the wet season, enhanced photosynthetic activity during the dry season from flushing new leaves and as change in leaf scattering and absorption properties between younger and older leaves covered with epiphylls. Reconciling these divergent views using theory and observations is the goal of this article. The observed changes in NIR reflectance of Amazon forests could be due to similar, but small, changes in NIR leaf albedo (reflectance plus transmittance) resulting from the exchange of older leaves for newer ones, but with the total leaf area unchanged. However, this argument ignores accumulating evidence from ground-based reports of higher leaf area in the dry season than the wet season, seasonal changes in litterfall and does not satisfactorily explain why NIR reflectance of these forests decreases in the wet season. More plausibly, the increase in NIR reflectance during the dry season and the decrease during the wet season would result from changes in both leaf area and leaf optical properties. Such change would be consistent with known phenological behavior of tropical forests, ground-based reports of seasonal changes in leaf area, litterfall, leaf optical properties and fluxes of evapotranspiration, and thus, would reconcile the various seemingly divergent views.

Citation: Samanta, A., Y. Knyazikhin, L. Xu, R. E. Dickinson, R. Fu, M. H. Costa, S. S. Saatchi, R. R. Nemani, and R. B. Myneni (2012), Seasonal changes in leaf area of Amazon forests from leaf flushing and abscission, *J. Geophys. Res.*, *117*, G01015, doi:10.1029/2011JG001818.

1. Introduction

[2] The spectral signatures of Amazon forests as measured by passive optical satellite sensors such as the Moderate Resolution Spectroradiometer (MODIS) are characterized by two distinguishing features, strong scattering in the near-infrared (NIR) from internal-leaf cellular structures, and equally strong absorption in the shorter red and blue wavelengths from chlorophyll and other pigments vital to the process of photosynthesis. The NIR reflectance, the fraction of incident solar radiation at NIR wavelengths reflected by a surface, of these forests is an order of magnitude greater than the reflectance at red and blue wavelengths (Figure 1 and Figure S1 in the auxiliary material), and in any given year, increases by about 23% during the dry season and similarly decreases during the following wet season (Figure 1) [also *Asner et al.*, 2004].[1] This large increase in NIR reflectance of Amazon forests during the light-rich dry season has been variously interpreted, but generally characterized as from a greening of the Amazon forests during the dry season [*Huete et al.*, 2006; *Xiao et al.*, 2006; *Brando et al.*, 2010; *Myneni et al.*, 2007]. The objective of this paper is to harmonize these divergent interpretations of dry season greening of Amazon forests.

[3] The MODIS Enhanced Vegetation Index (EVI) is defined by an algebraic manipulation of vegetation reflectances at NIR, red and blue wavelengths [*Huete et al.*, 2002]. It is principally sensitive to NIR reflectance, as one can readily deduce from its formulation (cf. Section 3.3, equation (4)). Not surprisingly, the EVI displays higher values in the late dry season compared to the wet season or early dry season [*Huete et al.*, 2006; *Xiao et al.*, 2006;

[1]Department of Geography and Environment, Boston University, Boston, Massachusetts, USA.
[2]Atmospheric and Environmental Research Inc., Lexington, Massachusetts, USA.
[3]Department of Geological Sciences, University of Texas at Austin, Austin, Texas, USA.
[4]Agricultural and Environmental Engineering, Federal University of Viçosa, Vicosa, Brazil.
[5]Jet Propulsion Laboratory, California Institute of Technology, Pasadena, California, USA.
[6]Biospheric Sciences Branch, NASA AMES Research Center, Moffett Field, California, USA.

0148-0227/12/2011JG001818

[1]Auxiliary materials are available in the HTML. doi:10.1029/2011JG001818.

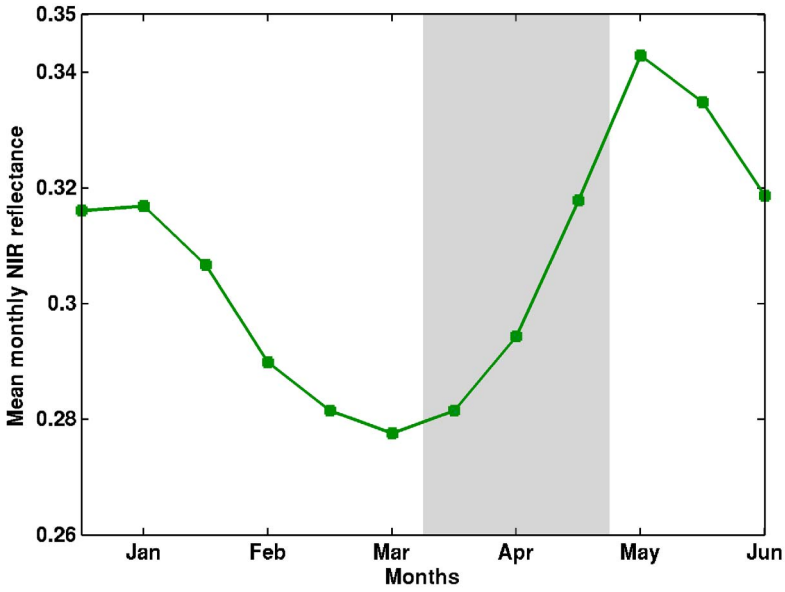

Figure 1. Monthly mean near-infrared (NIR) reflectance over forests, in the Amazon region 0°–20°S and 80°–40°W, with statistically significant green-up from June to October during 2000–2009 (Figure 6a).

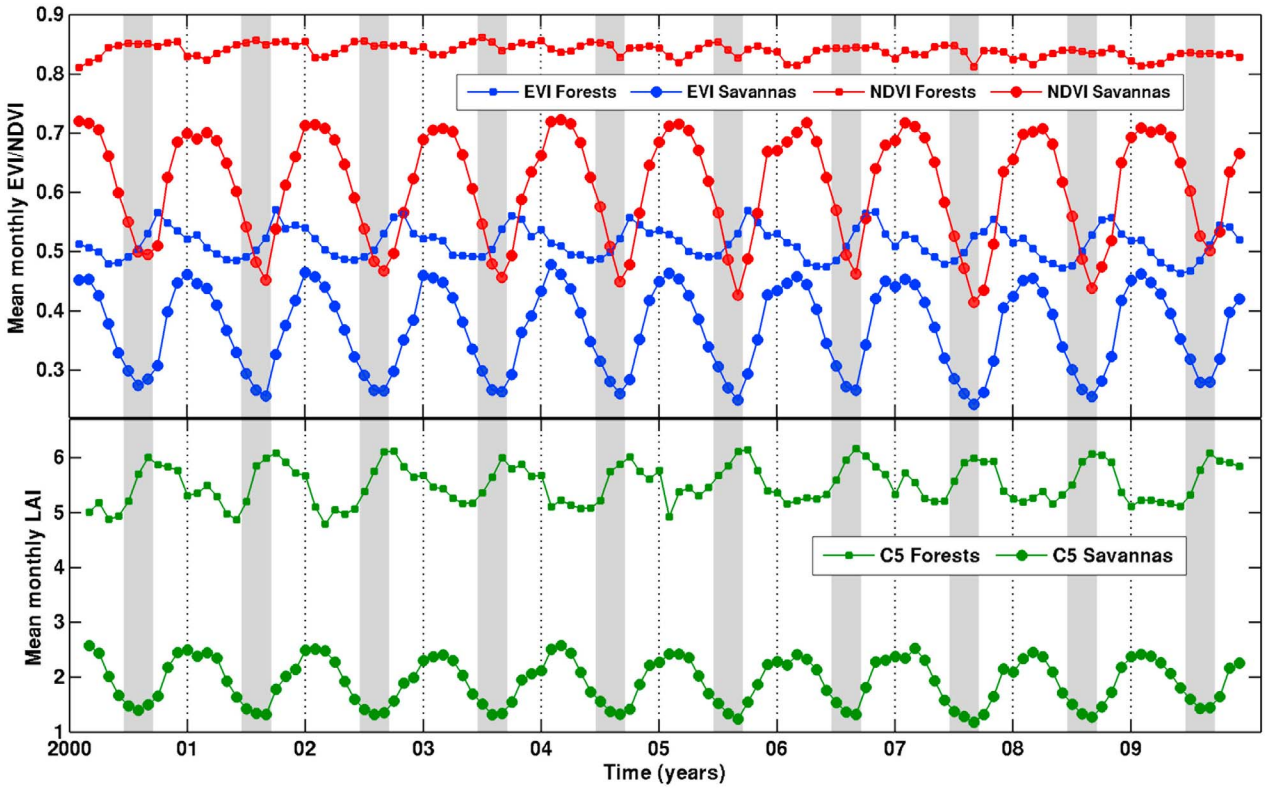

Figure 2. Monthly time series of EVI, NDVI and LAI over forests and savannas in the region 0°–20°S and 80°–40°W. Valid EVI and NDVI values are averaged over all forest pixels showing statistically significant green-up from June to October for EVI (Figure 6a). Similarly, valid LAI values are averaged over all forest pixels showing statistically significant increase in LAI (Figure 6c). Mean EVI, NDVI and LAI for savannas are the mean values over all savanna pixels in the region. The dry season, July to September, is shaded.

Brando et al., 2010] over the Amazon forests (Figure 2). What does an increase in EVI mean? Spatiotemporal changes in EVI are proposed to characterize similar variations in vegetation greenness [*Huete et al.*, 2002]. But, greenness itself is a poorly defined property of vegetation, unlike leaf area, for example. Nevertheless, a corresponding increase in dry season gross primary production (GPP) inferred from flux tower measurements at two experimental sites in Amazon forests [*Huete et al.*, 2006] lends credibility to the idea of enhanced greening, possibly from flushing of new leaves, during the light-rich dry season.

[4] The same seasonal changes in spectral reflectances of Amazon forests have been interpreted as resulting from large seasonal changes in green leaf area, a gradual increase through the dry season and a corresponding decrease through the wet season [*Myneni et al.*, 2007] (Figure 2). Green leaf area per unit ground area, or leaf area index (LAI) for short, is a physical attribute of vegetation, and thus measurable, and can be used to mechanistically quantify the exchange of energy, mass and momentum between the surface and the boundary layer [*Dickinson*, 1983]. The inferred seasonal swings in LAI were hypothesized to result from net leaf flushing in the light-rich dry season and net leaf abscission in the light-poor wet season, a behavior that is consistent with earlier reports of sunlight as the dominant proximate cue for leaf flushing in tropical forests [*Wright and van Schaik*, 1994] and not inconsistent with observations of enhanced GPP [*Huete et al.*, 2006] and carbon uptake [*Carswell et al.*, 2002; *Saleska et al.*, 2003] during the dry season, relative to the wet season, as younger leaves tend to be more photosynthetically vigorous than epiphyll-infested older leaves with poor stomatal control, as long as these light-limited forests [*Nemani et al.*, 2003; *Würth et al.*, 2005; *Graham et al.*, 2003; *Schuur*, 2003] remain well hydrated through deep roots [*Nepstad et al.*, 1994].

[5] The idea that tropical forests flush new leaves in response to various cues, and most prominently to sunlight, is not new [e.g., *Wright and van Schaik*, 1994]. However, the idea that these evergreen forests display large seasonal changes in leaf area is new [*Myneni et al.*, 2007]. It has also been argued by *Myneni et al.* [2007] that a gradually increasing leaf area enhances the evapotranspiratory water vapor flux into the atmosphere during the dry season, which would facilitate convection and increase the probability of rainfall during the late dry season, factors that influence a transition to the wet season [*Li and Fu*, 2004; *Fu and Li*, 2004]. Field-based studies support these ideas through reports of enhanced leaf area: 5.5 to 6.5 [*Carswell et al.*, 2002], 3.32 to 4.25 [*Pinto-Junior et al.*, 2010], 8% increase [*Malhado et al.*, 2009], a small increase [*Negrón Juárez et al.*, 2009] but consistent with work of *Myneni et al.* [2007], and a moderate increase in LAI [*Doughty and Goulden*, 2008]. Besides, higher (on average 30%) evapotranspiration fluxes have been observed during the dry season [*Juárez et al.*, 2007, 2008].

[6] Nevertheless, changes in vegetation canopy spectral reflectances do not necessarily imply changes in LAI. Changes in leaf optical properties from the exchange of older leaves for newer ones during the dry season, without changes in total leaf area, can also result in observed changes in vegetation canopy spectral reflectances. In fact, this has been the argument in one recent study [*Doughty and Goulden*, 2008], which reported disagreement between the seasonal course of MODIS LAI and ground-measured LAI. This is inconsistent with other data from the same forest in the Amazon that shows considerable litterfall in the wet season [*Xiao et al.*, 2005]. A more recent detailed analysis of litterfall data from 81 sites across the forests of tropical South America actually shows a relationship between litterfall and rainfall seasonality, with some evidence of high levels of litterfall during the wet season, in addition to the dry season [*Chave et al.*, 2010]. Nevertheless, a sensitivity analysis with a simple radiative transfer model confirmed [*Doughty and Goulden*, 2008] that changes in canopy reflectances could be explained from changes in leaf optical properties [*Roberts et al.*, 1998] alone. These findings have additional support from another study [*Asner and Alencar*, 2010], which suggested that the higher NIR canopy reflectance during the dry season could be due to enhanced new leaf area at the top of the canopy, with overall canopy leaf area remaining unchanged, presumably through abscission of more numerous older leaves in the bottom reaches of the canopy. Neither of these studies provided valid explanation for the observed decrease in NIR canopy reflectance during the wet season (Figure 1), although aging and epiphylls are invoked by *Doughty and Goulden* [2008] in a manner that is inconsistent with observations of leaf demography [*Reich et al.*, 2004] and phenological behavior (see Introduction by *Myneni et al.* [2007]) in tropical forests.

[7] This brings us to the heart of the debate: are the observed seasonal changes in NIR reflectance of Amazon forests (Figure 1) due to changes in leaf area, or to changes in leaf optical properties, or both? The proposition that changes in forest canopy reflectances are due alone to changes in leaf optical properties, as argued by *Doughty and Goulden* [2008] and *Asner and Alencar* [2010] and recently discussed by *Brando et al.* [2010], does not acknowledge ground-based measurements of seasonal leaf area changes [*Asner et al.*, 2004; *Carswell et al.*, 2002; *Pinto-Junior et al.*, 2010; *Malhado et al.*, 2009; *Negrón Juárez et al.*, 2009; *Doughty and Goulden*, 2008] and litterfall [*Xiao et al.*, 2005; *Chave et al.*, 2010], and emerging evidence regarding the role Amazon forests play in the transition from dry to wet season [*Li and Fu*, 2004; *Fu and Li*, 2004; *Juárez et al.*, 2007, 2008], all of which support the interpretation proposed by *Myneni et al.* [2007]. On the other hand, the argument that only leaf area changes explain changes of forest canopy reflectance ignores the very obvious changes in leaf optical properties between younger and older leaves and between healthy and epiphyll infested leaves. A way to reconcile these divergent views is the goal of this research.

[8] The rest of this paper is organized as follows: data and methods are described in Sections 2 and 3, respectively. Results are presented in Section 4, followed by discussion in Section 5. Finally, conclusions are presented in Section 6.

2. Data

2.1. Satellite Vegetation Data

[9] The latest version of NASA land products, Collection 5 (C5) Enhanced Vegetation Index (EVI), Normalized Difference Vegetation Index (NDVI) and Leaf Area Index (LAI) and landcover data sets are used in this study.

2.1.1. Collection 5 (C5) Vegetation Indices (VI)

[10] These are satellite data based measurements of vegetation greenness produced by NASA using blue (BRF_{BLUE}, 459–479 nanometers (nm)), red (BRF_{RED}, 620–670 nm) and near-infrared (BRF_{NIR}, 842–876 nm) band surface reflectance data, called Bidirectional Reflectance Factor (*BRF*), from the MODIS instrument aboard the Terra and Aqua satellites [*NASA Land Processes Data Active Archive Center* (*LP DAAC*), 2010a; *Huete et al.*, 2002]. VIs consist of NDVI and EVI. NDVI (1) is a radiometric measure of photosynthetically active radiation absorbed by canopy chlorophyll, and therefore, is a good surrogate measure of the physiologically functioning surface greenness level in a region [*Myneni et al.*, 1995]. NDVI has been used in many studies of vegetation dynamics in the Amazon [e.g., *Asner et al.*, 2000; *Dessay et al.*, 2004; *Ferreira and Huete*, 2004]. EVI (2) is also a measure of greenness that generally correlates well with ground measurements of photosynthesis [e.g., *Rahman et al.*, 2005; *Sims et al.*, 2008] and found to be especially useful in high biomass tropical broadleaf forests like the Amazon [*Huete et al.*, 2006]. C5 MODIS Terra VI data were used in this study.

$$NDVI = \frac{BRF_{NIR} - BRF_{RED}}{BRF_{NIR} + BRF_{RED}} \quad (1)$$

$$EVI = 2.5\frac{BRF_{NIR} - BRF_{RED}}{1 + BRF_{NIR} + 6BRF_{RED} - 7.5BRF_{BLUE}} \quad (2)$$

Two kinds of VI data sets were used, 1×1 km^2 and 16-day MOD13A2, and $0.05° \times 0.05°$ and 16-day MOD13C1, for the period February 2000–December 2009. The data set "Vegetation Indices 16-Day L3 Global 1 km" (MOD13A2) contains EVI (NDVI) at 1×1 km^2 spatial resolution and 16-day frequency. This 16-day frequency arises from compositing, i.e., assigning one best-quality EVI (NDVI) value to represent a 16-day period [*Huete et al.*, 2002]. This data set is available in tiles ($10° \times 10°$ at the equator) of Sinusoidal projection; 16 such tiles cover the Amazon region (approximately 10°N–20°S and 80°W–45°W). The data were obtained from the NASA Land Processes Data Active Archive Center (LP DAAC) (https://lpdaac.usgs.gov). The data set "Vegetation Indices 16-Day L3 Global 0.05Deg CMG" (MOD13C1) contains EVI (NDVI) at $0.05° \times 0.05°$ spatial resolution and 16-day frequency. These are "cloud-free spatial composites" of MOD13A2 [*LP DAAC*, 2010b].

2.1.2. Collection 5 (C5) Leaf Area Index (LAI)

[11] LAI is defined as the one-sided green leaf area per unit ground area in broadleaf canopies, and one-half the total surface area per unit ground area in needleleaf canopies (coniferous) [*Myneni et al.*, 2007]. LAI is operationally derived from atmospherically corrected surface reflectance in the red and NIR bands measured by the MODIS sensor onboard NASA's Terra and Aqua satellites [*LP DAAC*, 2010c]. The LAI retrieval algorithm ingests surface reflectances and their uncertainties, and information about land cover as well as sun and view geometry to estimate LAI from "look-up tables" (LUTs) pre-calculated using vegetation canopy radiative transfer model simulations [*Knyazikhin et al.*, 1998]. The C5 algorithm incorporates major improvements including an 8 biome input landcover map and refined LUTs, especially over woody biomes [*Shabanov et al.*, 2005]. The LAI product has been validated globally as well as at sites in the Amazon [*Yang et al.*, 2006; *Aragao et al.*, 2005], and has been used in studies of vegetation dynamics [e.g., *Myneni et al.*, 2007]. C5 MODIS Terra LAI data are used in this study.

[12] The data set "Leaf Area Index – Fraction of Photosynthetically Active Radiation 8-Day L4 Global 1 km" (MOD15A2) contains LAI at 1×1 km^2 spatial resolution and 8-day temporal frequency. This 8-day frequency arises from compositing, i.e., assigning one best-quality LAI value to represent an 8-day period. This data set is available in tiles ($10° \times 10°$ at the equator) of Sinusoidal projection; 16 such tiles cover the Amazon region (approximately 10°N–20°S and 80°W–45°W) [*LP DAAC*, 2010c]. The data were obtained from the NASA LP DAAC (https://lpdaac.usgs.gov) for the period February 2000–December 2009.

2.1.3. Landcover Data

[13] Land cover information was obtained from the "MODIS Terra Land Cover Type Yearly L3 Global 1 km SIN Grid" product (MOD12Q1). This is the official NASA C5 land cover data set [*LP DAAC*, 2009; *Friedl et al.*, 2010]. It consists of five land cover classification schemes at 1×1 km^2 spatial resolution. The International Geosphere Biosphere Programme (IGBP) land cover classification scheme was used to identify forest pixels in the Amazon region.

2.2. Leaf Spectral Data

[14] Leaf albedo (reflectance + transmittance) data in NIR were obtained from two published studies on the effects of age and epiphyll cover on leaf spectra in the Amazon [*Roberts et al.*, 1998; *Toomey et al.*, 2009]. Epiphylls comprise a wide range of organisms-lichens, liverworts, fungi, algae and bacteria-that infest leaf surfaces in humid tropical forests [*Toomey et al.*, 2009]. Epiphylls coat the surface of leaves, which decreases light interception in both the photosynthetically active (PAR, 400–700 nm) and NIR spectral intervals [*Roberts et al.*, 1998; *Toomey et al.*, 2009]. The data are categorized into two classes, age-based and epiphyll-based. The age-based class consists of new and old leaves: new leaves are about 70 days in age (late dry season), fully formed and with minimal infestation while old leaves are a year old (late wet season/early dry season) and moderately infested. Spectra for this class are available for four plants of the Caatinga (low density scrubs, woodlands and woodland forests) dominant *Aldina heterophylla* [*Roberts et al.*, 1998]. The epiphyll-based class comprises clean and colonized leaves; clean leaves refer to mature leaves with no epiphyll infestation while colonized leaves refer to mature leaves that are moderately colonized by epiphyll. Spectra for this category are available for two Caatinga dominants, *Pradosia schomburgkiana* and *Protium heptaphyllam* [*Roberts et al.*, 1998], and three Terra Firme (dense forests) dominants, *Byrsonima* cf *poeppigiana*, *Inga* cf *sertulifera* and *Porouma tomentosa* [*Toomey et al.*, 2009]. The higher leaf albedo of new leaves is due to greater transmittance, while reflectance changes are minimal. The effect of epiphyll infestation is to reduce both reflectance and transmittance; relative decline in

transmittance is greater than reflectance [*Roberts et al.*, 1998; *Toomey et al.*, 2009].

3. Methods

3.1. VI Data Quality

[15] The quality of VI (EVI/NDVI) data in each pixel can be assessed using the accompanying 16-bit quality flags, in both 1×1 km^2 as well as the $0.05° \times 0.05°$ products. Sets of bits, from these 16 bits, are assigned to flags pertaining to clouds and aerosols (details can be found in work by *Samanta et al.* [2010, 2011a, 2011b] and *Xu et al.* [2011]). Each 1×1 km^2 16-day composite VI value is considered valid when (a) VI data is produced—"MODLAND_QA" equals 0 (good quality) or 1 (check other QA), (b) VI Usefulness is between 0 and 11, (c) Clouds are absent—"Adjacent cloud detected" (0), "Mixed Clouds" (0) and "Possible shadow" (0), and (d) Aerosol content is low or average—"Aerosol Quantity" (1 or 2). Note that "MODLAND_QA" checks whether VI is produced or not, and if produced, its quality is good or whether other quality flags should also be checked. Besides, VI Usefulness Indices between 0 to 11 essentially include all VI data. Thus, these two conditions serve as additional checks. Each $0.05° \times 0.05°$ 16-day VI pixel is considered valid when (a) VI data is produced—"MODLAND_QA" equals 0 (good quality) or 1 (check other QA), (b) VI Usefulness is between 0 and 11, (c) Clouds are absent—"Adjacent cloud detected" (0) and "Mixed Clouds" (0), and (d) Aerosol content is low or average—"Aerosol Quantity" (1 or 2). Here, the utility of "MODLAND_QA" and VI Usefulness flags is the same as in the case of 1×1 km^2 VI validity.

3.2. LAI Data Quality

[16] The quality of LAI data in each 1×1 km^2 8-day pixel can be assessed using two accompanying 8-bit quality flags, FparLai_QC and FparExtra_QC (details can be found in work by *Samanta et al.* [2011b]). The validity of LAI was determined through a two-stage process: (1) a 1×1 km^2 8-day LAI pixel was considered valid when (a) data is of good quality—"SCF_QC" equals 0 (main algorithm without saturation) or 1 (main algorithm with saturation), (b) Clouds are absent—"CloudState" (0), "Cirrus" (0), "MODAGAGG_Internal_CloudMask" (0) and "MODAGAGG_Cloud_Shadow" (0). (2) As the 8-day LAI aerosol flag does not distinguish between average and high aerosol loadings nor reports climatology aerosols, valid 8-day values are averaged to 16-day LAI whose validity was further determined using MOD13A2 cloud and aerosol flags: (a) VI data is produced-"MODLAND_QA" equals 0 (good quality) or 1 (check other QA), (b) VI Usefulness is between 0 and 11, (c) Clouds are absent—"Adjacent cloud detected" (0), "Mixed Clouds" (0) and "Possible shadow" (0), and (d) Aerosol content is low or average-"Aerosol Quantity" (1 or 2). Valid 1×1 km^2 16-day values were averaged to obtain monthly LAI. Finally, valid 1×1 km^2 monthly LAI values are aggregated to 8×8 km^2 spatial resolution. This 8×8 km^2 monthly LAI data set spanning February 2000–December 2009 was used in this study.

[17] In order to test the effectiveness of the quality flags, we have analyzed the seasonal time series of surface reflectances and vegetation indices (VI) of both uncorrupted (clean) and corrupted (contaminated) data (Figure S1). Interaction of photons with dense Amazonian forests is characterized by strong scattering in near-infrared (NIR), and equally strong absorption in the shorter red and blue wavelengths. The NIR reflectance of these forests is an order of magnitude greater than the reflectance at red (blue) wavelengths. On the other hand, atmospheric influences scatter more strongly in the shorter red/blue wavelengths. Thus, NIR reflectance is much less affected by atmospheric effects in comparison to red (blue) reflectance, which is shown in Figure S1a. Contaminated red reflectances are artificially higher-almost double in magnitude in comparison to clean values (Figure S1a). The difference between clean and contaminated red reflectance remains steady during the course of the year, which indicates lack of bias due to seasonal changes in atmospheric effects, such as high aerosol loads in the dry season from biomass burning (e.g., as discussed by *Samanta et al.* [2010]). These changes in surface reflectances translate into lower estimates of surface greenness or VIs. NDVI reduces by about 24% and EVI by about 18%, especially during the dry season (Figure S1b). Moreover, *Myneni et al.* [2007] have reported that residual atmospheric effects reduce leaf area index (LAI) estimates by about 5% during the dry season. These results show that seasonal variations in atmosphere-corrupted data are inconsistent with those observed with clean data. Furthermore, any remaining residual atmospheric influences that would reduce seasonal changes in measured greenness are eliminated by ensuring that the observed increase in VIs is greater than the errors in VIs (as mentioned in the caption of Figure 6). Thus, we conclude that the seasonal changes in vegetation greenness reported in the manuscript are not an artifact of residual atmospheric effects in surface reflectances.

3.3. Saturation of NDVI

[18] Photosynthesizing (green) vegetation strongly absorbs in red and blue bands and scatters in the NIR band. NIR reflectance of dense canopies such as Amazonian forests is an order of magnitude higher than red reflectance (Figures 1 and S1). In such situations, the formulation of NDVI (1) renders it relatively insensitive to changes in NIR, which can be shown as follows:

$$\delta NDVI = \frac{2BRF_{RED}}{(BRF_{NIR}+BRF_{RED})^2}\delta BRF_{NIR} - \frac{2BRF_{NIR}}{(BRF_{NIR}+BRF_{RED})^2}\delta BRF_{RED}$$

$$\delta NDVI = \frac{2BRF_{RED}}{(BRF_{NIR}+BRF_{RED})^2}\delta BRF_{NIR}, \delta BRF_{NIR} \gg \delta BRF_{RED}$$

$$\frac{\delta NDVI}{NDVI} = 0.2\frac{\delta BRF_{NIR}}{BRF_{NIR}}, BRF_{NIR} \sim 10BRF_{RED} \quad (3)$$

Similarly, for EVI we can write,

$$\delta EVI = G\frac{(1+C1)BRF_{RED} - C2BRF_{BLUE} + L}{(BRF_{NIR} + C1BRF_{RED} - C2BRF_{BLUE} + 1)^2}\delta BRF_{NIR},$$

$$\delta BRF_{NIR} \gg \delta BRF_{RED}, \delta BRF_{BLUE}$$

$$\frac{\delta EVI}{EVI} = \left(\frac{\delta BRF_{NIR}}{BRF_{NIR}}\right)\left[\frac{1+0.325BRF_{NIR}}{0.9(1+1.225BRF_{NIR})}\right],$$

$$C1 = 6, C2 = 7.5, BRF_{NIR} \sim 10BRF_{RED}, BRF_{RED} \sim 2BRF_{BLUE} \quad (4)$$

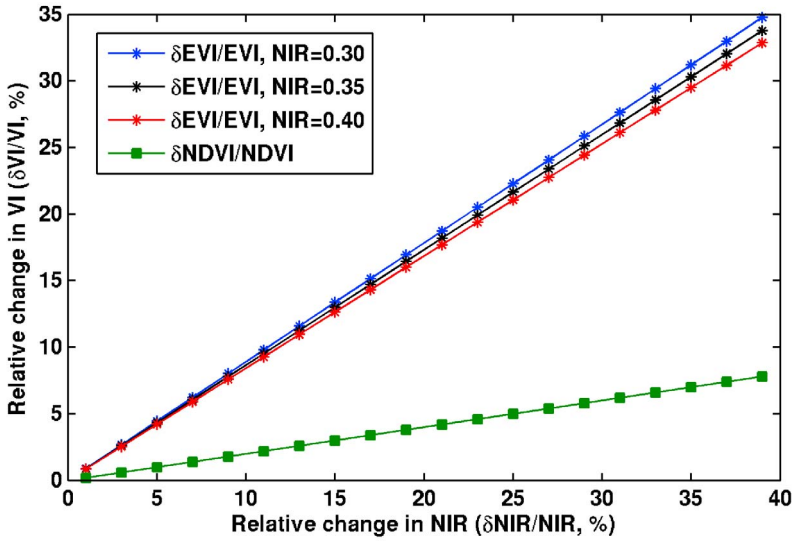

Figure 3. Sensitivity of Enhanced Vegetation Index (EVI) and Normalized Difference Vegetation Index (NDVI) to changes in near-infrared (NIR) reflectance (BRF_{NIR}) for dense vegetation. NIR reflectance is set at 10*red (BRF_{RED}) and 20*blue (BRF_{BLUE}), which is typically observed in dense canopies such as Amazon forests. Note that relative change in NDVI is independent of the magnitude of NIR reflectance.

Equation (4) implies that a given increase in NIR would translate into a five times lesser increase in NDVI (Figure 3). On the other hand, EVI is very sensitive to changes in NIR and does not exhibit the saturation problem (Figure 3).

3.4. Sensitivity of BRF to Variation in LAI and Leaf Optics

[19] The theory of spectral invariants [*Knyazikhin et al.*, 2010] was used to examine the sensitivity of the canopy near-infrared (NIR) *BRF* to LAI and leaf optical properties under saturation conditions. If the impact of canopy background on canopy reflectance is negligible as in the case of dense Amazonian forests, the spectral *BRF* can be approximated as [*Knyazikhin et al.*, 2010; *Schull et al.*, 2010; *Huang et al.*, 2008]:

$$BRF(\lambda,\Omega)=\frac{\rho(\Omega)\omega_\lambda}{1-p\omega_\lambda}i_0=\left[\frac{\rho(\Omega)}{1-p}i_0(\Omega_0)\right]\left[\frac{\omega_\lambda(1-p)}{1-p\omega_\lambda}\right]=K(\Omega,\Omega_0)W_\lambda \tag{5}$$

Here ρ is the directional escape probability, i.e., probability that a photon scattered by a leaf will escape the vegetation medium in a given direction Ω. It also can be interpreted as the probability of seeing a gap in the direction Ω from a leaf surface [*Stenberg*, 2007]. Spherical integration of ρ over all directions gives the total escape probability, $(1-p)$, where p is the recollision probability, i.e., the probability that a photon scattered by a leaf will interact with another leaf in the canopy again. Further, i_0, the probability of initial collision, or canopy interceptance, is the portion of incoming photons that collide with leaves for the first time. It depends on the direction of radiation incident on the vegetation canopy. Finally, ω_λ is the leaf albedo, which is the portion of the radiation incident on the surface of an individual leaf that the leaf transmits or reflects. In the present approach, this is the only variable that is dependent on the wavelength. It allows the parameterization of *BRF* in terms of leaf albedo rather than wavelength. Therefore wavelength dependence will be suppressed in further notations.

[20] Two separate factors are shown in equation (5), each exhibiting a different sensitivity to canopy structure and leaf optics. The wavelength independent ratio $P = \rho/(1 - p)$ gives the portion of gaps as seen from a leaf surface in a given direction Ω. This variable is sensitive to canopy geometrical properties such as spatial distribution of trees, ground cover, crown shape, size, and transparency [*Schull et al.*, 2010]. In the case of Amazon forests, changes in canopy structure over monthly time-scales are assumed negligible. At high LAI values, the canopy interceptance i_0 varies insignificantly with LAI due to the saturation. Under such conditions, the observed variation in NIR *BRF* is much stronger than corresponding variation in $K = Pi_0$, typically 2–3%, and thus changes in canopy structure alone cannot explain the observations (cf. Section 3.4.1).

[21] The second factor is the canopy scattering coefficient, $W_\lambda = \omega_\lambda\ (1 - p)\ /\ (1 - p\omega_\lambda)$ [*Smolander and Stenberg*, 2005], which depends on both canopy structure and leaf optics. It increases with the leaf albedo; the more the leaves scatter, the brighter the canopy is. Variations in LAI, however, trigger an opposite tendency. As the recollision probability increases with LAI [*Knyazikhin et al.*, 1998; *Smolander and Stenberg*, 2005; *Rautiainen et al.*, 2009], an increase in LAI results in more photon-canopy interactions and consequently a higher chance for photon to be absorbed. This mechanism makes the canopy appear darker. The effect of multiple scattering is described by the denominator in the equation for W_λ [*Huang et al.*, 2008], which in turn is fully determined by the product $\kappa = p\omega_\lambda$. An increase in κ not only enhances the effect of multiple scattering but also changes the sensitivity of the *BRF*: the closer its value is to unity, the stronger the response of canopy *BRF* to variations in canopy structure and leaf optics. If variation in K is negligible, changes in *BRF* can be reduced to examining variations in the scattering coefficient.

[22] The vegetation canopy is parameterized in terms of the recollision probability, $0 \le p \le 1$, leaf albedo, $0 \le \omega \le 1$, and the sensitivity parameter, $\kappa = p\omega \le \min(\omega, p)$. Let the sensitivity of *BRF* to canopy structure and leaf optics at time t and $t_1 = t + \Delta t$ be κ and $\kappa_1 = \kappa + \delta\kappa$, $\delta\kappa \ge 0$, respectively. Note that κ and κ_1 do not uniquely specify the recollision probabilities and leaf albedos since various combinations can result in the same values of the sensitivity parameter, which impact canopy reflective properties differently. To characterize the contribution of LAI to a change in the sensitivity parameter from by κ to $\kappa+\delta\kappa$, the following impact function is introduced:

$$k = \frac{\delta p/p}{\delta\kappa/\kappa} = \frac{\delta p/p}{\delta p/p + \delta\omega/\omega} \tag{6}$$

In general, k varies between $-\infty$ and $+\infty$. Values of k greater than 1 imply a decrease in leaf albedo, i.e., $\delta\omega/\omega < 0$. Variations in LAI and leaf optics make the vegetation darker in this case. On the other hand, a decrease in canopy structure, $\delta p/p < 0$, involves a negative value of the parameter k. In this case, changes in p and ω lead to brightening of the vegetated surface. This study will focus on the case when both LAI and leaf albedo increase, i.e., k varies between 0 (no change in LAI) and 1 (no change in leaf albedo). Such variations trigger competing processes: changes in LAI tend to darken the vegetation while variations in the leaf albedo suppress it. It should be emphasized, however, that this mechanism refers to the scattering coefficient W_λ and is applicable to $BRF = KW_\lambda$ (cf. equation (5)) if variations in K are negligible. In general, K increases with LAI and therefore compensates for a decrease in the canopy scattering coefficient. This lowers the darkening effect and even can result in an increase in the canopy *BRF* (cf. Sections 3.4.2 and 3.4.3).

[23] Under saturation conditions (i.e., $\delta BRF/BRF \gg \delta K/K$), the impact function ($k$), sensitivity parameter (κ), leaf albedo at time t (ω), variations $\delta BRF/BRF$, $\delta K/K$ and $\delta\kappa/\kappa$ are related as (cf. Section 3.4.1):

$$k(\omega) = \frac{\omega - \kappa}{\omega}\theta \tag{7}$$

where

$$\theta = \frac{1}{1-\kappa} - \beta, \beta = \frac{\delta BRF/BRF - \delta K/K}{\delta\kappa/\kappa} \tag{7a}$$

Here β characterizes the amplitude of the variability in reflectance. Since the goal of this study is to examine contributions of LAI and leaf albedo to large positive changes in the canopy *BRF* under saturation conditions, i.e., $\delta BRF/BRF \gg \delta K/K$, this analysis is restricted to the case when $\beta > 0$. It should be noted that in general, $\delta K/K$ is proportional to the impact function k (cf. Section 3.4.1). Under saturation conditions, this term can be neglected, and thus, equation (7) quantifies the impact of canopy structure on the *BRF* when both LAI and ω vary.

[24] If $k(\omega) = 1$ ($\delta\kappa/\kappa = \delta p/p$), then $(\omega-\kappa)\theta/\omega = 1$. This relationship holds true if and only if $\beta \le 0$ (cf. Section 3.4.1). It means that LAI alone cannot explain positive changes in canopy *BRF* under the saturation condition.

[25] If $k(\omega) = 0$ ($\delta\kappa/\kappa = \delta\omega/\omega$), then either $\omega = \kappa$ or $\theta = 0$. The former corresponds to an extreme and unrealistic case when $p = 1$. It means that photons cannot escape the vegetation canopy and therefore $BRF = 0$. The latter implies that variations in canopy *BRF* are proportional to $\delta\omega/\omega$, i.e.,

$$\frac{\delta BRF}{BRF} = \frac{1}{1-\kappa}\frac{\delta\omega}{\omega} \tag{8}$$

One can see that the closer the value of the sensitivity parameter is to unity, the stronger the response of the *BRF* to leaf albedo. Changes in leaf optics alone can explain a rather large range of variation in canopy reflectance under the saturation conditions.

[26] If $0 < k(\omega) < 1$ (i.e., $\delta p/p > 0$ and $\delta\omega/\omega > 0$), the contribution of LAI to the *BRF* is given by equation (7). It should be emphasized that this equation refers to the case when both LAI and the leaf albedo are changing. Figure 4 illustrates the LAI versus leaf albedo "competing process" under saturation conditions, which results in the observed *BRF* change by 23% ($\delta BRF/BRF = 0.23$ and $\delta BRF/BRF \gg \delta K/K = 0.01$, cf. Sections 3.4.2 and 3.4.3).

3.4.1. Derivation of Equation (7)

[27] It follows from equation (5) that

$$\frac{\delta BRF}{BRF} = \delta \ln BRF = \frac{\delta K}{K} + \frac{1}{1-p\omega}\left[\frac{\delta\omega}{\omega} - \frac{p(1-\omega)}{1-p}\frac{\delta p}{p}\right] \tag{9}$$

We parameterize the relative variation in *BRF* in terms of the sensitivity parameter, κ, its variation, $\delta\kappa/\kappa$, and the impact function, k, by substituting $p = \kappa/\omega$, $\delta p/p = k\delta\kappa/\kappa$ and $\delta\omega/\omega = (1-k)\delta\kappa/\kappa$ into equation (9). Solving the resulting equation for k yields equation (7).

[28] Case $k(\omega) = 1$: Letting $\delta\omega/\omega = 0$ in equation (9) and taking into account that $p(1-\omega)/(1-p\omega)(1-p)$ decreases with ω, one gets

$$-\frac{\delta p}{1-p} \le \frac{\delta BRF}{BRF} - \frac{\delta K}{K} \le 0 \tag{10}$$

Thus, a positive response of *BRF* to a positive variation in the recollision probability can be achieved if the parameter β defined by equation (7a) is negative.

3.4.2. Assumptions

[29] Since our goal is the qualitative description of the sensitivity of *BRF* to LAI and leaf albedo under the saturation conditions, we use a simple canopy model to specify the relationship between $\delta p/p$, δLAI/LAI and $\delta K/K$. We idealize the vegetation canopy as a spatially homogeneous layer filled with small planar elements of infinitesimally small sizes. All organs other than green leaves are ignored. For such a structurally simple uniform canopy, *Stenberg* [2007] found an analytical formula that relates the recollision probability, p, and canopy interceptance, $i_{0,d}$, under diffuse illumination condition, i.e.,

$$i_{0,d} = (1-p)LAI \tag{11}$$

Analyses of LAI-2000 data suggest the following relationship between $i_{0,d}$ and *LAI* [*Rautiainen et al.*, 2009]

$$i_{0,d} = 1 - \exp(-k_{CAN} \cdot LAI) \tag{12}$$

where the coefficient $k_{CAN} = 0.81$ was found to be almost insensitive to stand age, tree species or growing conditions. Finally, the canopy interceptance, i_0, can be estimated as $i_0 = 1 - \exp(-G \cdot \mathrm{LAI}/\mu_0)$ where G and μ_0 are the geometry

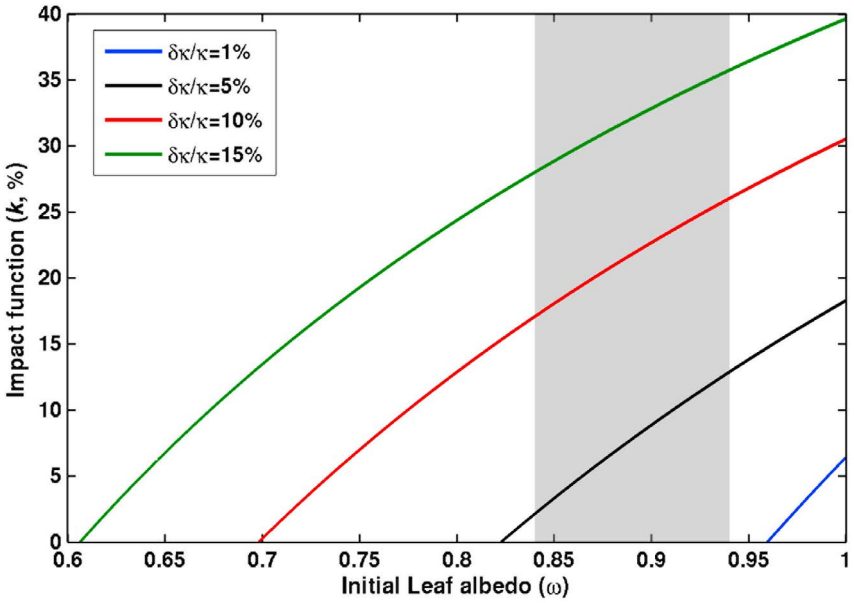

Figure 4. Impact function k (%) for a 23% increase in canopy near-infrared (NIR) bi-directional reflectance factor (*BRF*) and three values of the sensitivity parameter, $\kappa = 0.6$, 0.7, 0.82 and 0.96. The horizontal axis represents the initial value (late wet season/early dry season, June) of the leaf albedo ω, i.e., $\omega p = \kappa$. Each line corresponds to a fixed change in the sensitivity parameter from κ to $\kappa + \delta\kappa/\kappa$ and crosses the horizontal axis at the corresponding sensitivity parameter κ. Vertical axis shows the relative contribution of the recollision probability p to the 23% change in the NIR *BRF*. For example, if $\omega = 0.9$, a value of the recollision probability corresponding to $\kappa = 0.7$ is 0.7/0.9 = 0.78. For this combination of $p = 0.78$ and $\omega = 0.9$, the 23% change in *BRF* is attainable from changes in the recollision probability and leaf albedo by $k(0.9)\delta\kappa/\kappa = 0.23 \times 0.10 = 2.3\%$ (red curve) and $(1-k(0.9))\delta\kappa/\kappa = 0.77 \times 0.10 = 7.7\%$, respectively. The 2.3% change in $p = 0.78$ translates to an 11% increase in LAI of 4.5. The shaded region shows the range of initial NIR leaf albedo values (late wet season/early dry season, and leaves that are old and/or epiphyll infested) from field-based studies in the Amazon (cf. Section 2.2).

factor [*Ross*, 1981] and cosine of the solar zenith angle (SZA), respectively. It follows from this equation and equation (11) that

$$1 - i_0 = \left(1 - i_{0,d}\right)^{\alpha} \tag{13}$$

where $\alpha = G/(k_{CAN}\mu_0)$. For simplicity, the geometry factor G is set to $k_{CAN}\mu_0 = 0.81*\cos(30) = 0.81*0.87 = 0.70$ (mean SZA = 30°, std. = 5°–6° (20%)). The mean SZA for the dry season is about 30° and varies by about 5°–6° during this time, as reported in the MODIS VI data. Therefore, the small changes in SZA are not likely to induce large changes in μ_0, and G. Under the above assumptions, LAI is the only variable that fully describes canopy structure. The recollision probability (p) is an increasing function of LAI.

[30] We neglect angular dependence of the directional escape probability by replacing this term by its hemispherically integrated counterpart, i.e., $\rho(\Omega) = r/\pi$ where r is the probability that a scattered photon will escape the vegetation canopy through its upper boundary. Neglecting radiation transmitted through a very dense canopy, we get $\rho(\Omega) = (1 - p)/\pi$. The relative portion of gaps as seen from a leaf surface, $P = \rho/(1 - p)$, is approximated by a constant and thus $\delta K/K = \delta P/P + \delta i_0/i_0 \approx \delta i_0/i_0$. Note that this approximation is accurate for the uniform canopies with horizontally oriented leaves since such canopies transmit and reflect radiation diffusely and approximate for other canopies.

3.4.3. Properties of the Impact Function

[31] The impact function k requires specification of the parameter θ, which includes the term $\delta BRF/BRF - \delta K/K$ that appears in β. Our structurally simple canopy suggests negligible contribution of $\delta K/K \approx \delta i_0/i_0$ under the saturation conditions. For example, a change in LAI from 5 to 6 results in $\delta i_0/i_0 \approx 1\%$ which is significantly below the observed variation, $\delta BRF/BRF \approx 23\%$, in NIR surface reflectance. Although a more realistic canopy model can result in a different value of the relative variation in K, its use would not change our qualitative results as long as $\delta BRF/BRF \gg \delta K/K$. Figure 5 and the following properties of the impact function provide the necessary justification.

[32] If $\theta \geq 0$, the impact function k has the following properties (Figure 5).

$$\text{A. } \lim_{\omega \to 0+} k(\omega) = -\infty;$$

$$\text{B. } k(\kappa) = 0;$$

$$\text{C. } \lim_{\omega \to \infty} k(\omega) = \theta = \frac{1}{1-\kappa} - \beta;$$

[33] D. *If* $\theta > 1$, the equation $k(\omega) = 1$ has a unique solution given by $\omega^* = \kappa\psi$ where

$$\psi(\beta, \kappa) = \frac{\theta}{\theta - 1} = \frac{1 - \beta(1-\kappa)}{\kappa - \beta(1-\kappa)} = \frac{1}{\kappa} \quad \frac{1 - \beta(1-\kappa)}{1 - \beta\frac{1-\kappa}{\kappa}}$$

The function ψ increases with β and decreases with κ.

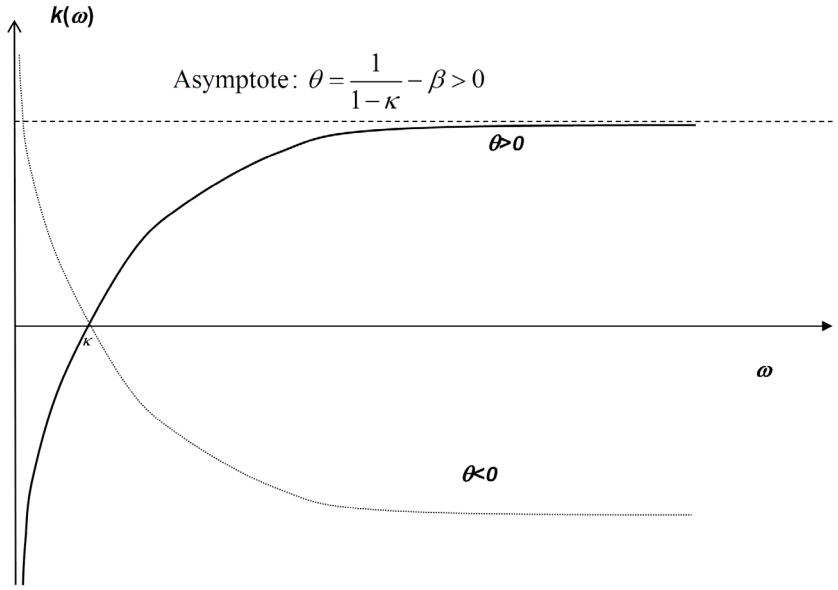

Figure 5. Schematics of properties A–C of the impact function $k(\omega)$. For positive θ, interpretation of $\delta BRF/BRF$ depends on the location of the asymptote relative to unity, i.e., whether $\theta \leq 1$ or $\theta > 1$ (i.e., property D described in Section 3.4.1).

[34] If $\theta \leq 0$, its properties can be formulated in a similar manner (see Figure 5). Let $\theta > 0$, i.e., $\beta < 1/(1 - \kappa)$. As one can see from Figure 5, interpretation of variation in the *BRF* depends on the location of the asymptote and the root of the equation $k(\omega) = 1$ relative to unity. The following cases are possible.

[35] Case 1: $0 < \theta < 1$, i.e., $\beta > \kappa/(1 - \kappa)$. The asymptote is below unity. If $\omega \leq \kappa$, the impact of canopy structure is negative (i.e., LAI should decrease in order to achieve a given variation in *BRF*). If $\omega > \kappa$, both the canopy structure and leaf optics have a positive impact. If θ tends to zero, the impact of canopy structure becomes negligible.

[36] Case 2: $\theta \geq 1$, i.e., $\beta \leq \kappa/(1 - \kappa)$. The asymptote is above unity. The equation $k(\omega) = 1$ has a solution given by $\omega^* = \kappa\psi$. Since ψ increases with β, the solution is above unity if $\beta > 0$; is equal to 1 if $\beta = 0$ and approaches to κ if β tends to $-\infty$. If κ tends to unity, the solution tends to unity, resulting in a jump from $k = 0$ to 1 at $\omega = \kappa$. Thus, if $\omega \leq \kappa$, the impact of canopy structure is negative. If $\kappa < \omega \leq \omega^*$, both structure and leaf optics positively contribute to variation in *BRF*. If $\omega > \omega^*$, the impact of structure is positive and leaf optics is negative.

[37] To summarize, a small variation in the parameter β does not change qualitatively the behavior of the impact function. Under saturation conditions, i.e., $\delta BRF/BRF \gg \delta K/K$, and the term $\delta K/K$ can be neglected.

4. Results

4.1. Comparison of Dry-Season Greening Patterns With Previous Studies

[38] Nearly 48% of Amazon forests (forests south of the Equator) display statistically significant EVI increase of about 16% from June to October in a given year during 2000–2009, which is in contrast to about 22% decline in EVI over the adjoining savannas from June to September (Figures 6a and 2). Approximately opposing changes are observed over these two vegetation types during the wet season (Figure 2). Interestingly, NDVI data do not show any appreciable changes in forests during the dry season (Figure 6b), or during other times of the year (Figure 2). However, the same data display large swings over savannas consisting of decline during the dry season and increase during the wet season, with an amplitude of about 41% (Figure 2). Further, LAI increase of about 0.93 units (18%) is observed over 33% of Amazon forests, while LAI decline of about 1.1 units is observed over adjacent Savannas during the dry season (Figures 6c and 2). These LAI variations are part of a seasonal cycle of opposing timing between forests and savannas (Figure 2). Thus, MODIS EVI and LAI data show large seasonal variations of approximately opposing timing over forests and savannas, with green-up of 16–18% over a third to half of Amazon forests during dry seasons of the decade 2000–2009.

[39] The spatial patterns of dry-season EVI increase seen here (Figure 6a) are consistent with a previous report [*Huete et al.*, 2006], albeit the magnitude of forest green-up is smaller (16% versus 25%) and is similar over a broad region extending across a large gradient in number of dry seasons, from the perpetually wet northwestern parts to the seasonally dry southeastern parts of the Amazon basin. Besides, the elimination of atmosphere-corrupted data (persistent during the dry season [e.g., *Samanta et al.*, 2010]) results in missing patches, especially in eastern Amazonia (Figures 6a and 6b). While the spatial patterns of dry-season enhancement in LAI (Figure 6c) are similar to those in work by *Myneni et al.* [2007], the extent (33% versus 68%) and average magnitude (0.93 versus 1.2) of LAI upswing are smaller than the previous estimate. These changes are attributable to the improved C5 LAI algorithm [*Shabanov et al.*, 2005] and

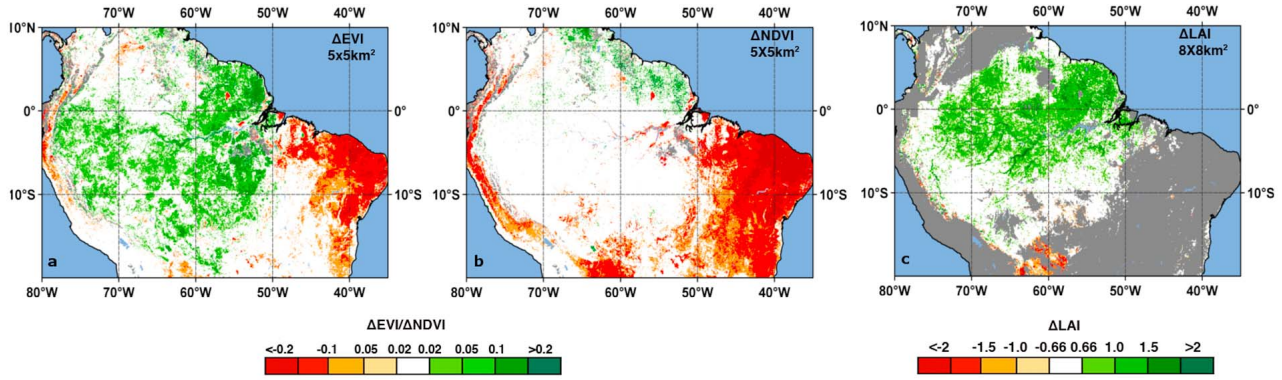

Figure 6. Spatial patterns of dry season greenness changes in the Amazon. (a) Change in Enhanced Vegetation Index (EVI), at 0.05° × 0.05° spatial resolution, from June (EVI_{jun}) to October (EVI_{oct}) expressed as ΔEVI (EVI_{oct} - EVI_{jun}) as in work by *Huete et al.* [2006]. Shown are only statistically significant changes i.e., $|\Delta EVI| >= |0.04*EVI_{jun} + 0.04|$ (2 standard deviation or 95% confidence interval of error in EVI_{jun} [*Vermote and Kotchenova*, 2008]). (b) Same as Figure 6a but for Normalized Difference Vegetation Index (NDVI). (c) Change in Leaf area index (LAI), at 8 × 8 km^2 spatial resolution, greater than 0.66 or less than −0.66. This threshold (|0.66|) is the smallest LAI difference discernable with the MODIS LAI data set. The amplitude, in regions with dry seasons longer than three months, is calculated as the difference between the maximum four-month average LAI in the dry season minus the minimum four-month average LAI in the wet season. Where the dry season is three or fewer months, the amplitude is calculated as the difference between the dry season average LAI and the minimum four-month average LAI in the wet season. The definition of the dry season is the same as in work by *Myneni et al.* [2007]. LAI difference for only forest pixels is shown as by *Myneni et al.* [2007]. Missing data are also shaded white.

with stricter screening of cloud-and aerosol-corrupted data. The patterns of seasonal greenness changes of Amazon forests observed with the latest version (C5) of MODIS greenness data are generally similar to previous reports.

4.2. Plausible Mechanisms of Dry-Season Increase in NIR Reflectance

[40] The cause of dry season increase in NIR BRF of Amazon forests (Figure 1) can be ascertained by assessing its sensitivity to LAI and leaf albedo (see Section 3.4; in this section, the term *BRF* is used instead of the more colloquial term, reflectance, to be technically consistent with the formulation in Section 3.4). This is determined by the sensitivity parameter ($\kappa = p\omega$), which couples vegetation canopy structure p (a function of LAI) and leaf albedo, ω. Positive changes in p and ω lead to an increase in the sensitivity parameter κ, which in turn alters how the *BRF* responds to changes in canopy structure and leaf optics. An increase in canopy *BRF* can be due to changes in (*i*) the sensitivity parameter from κ to $\kappa_1 = \kappa + \delta\kappa$ and (*ii*) canopy structure from p to $p_1 = p + \delta p$ and leaf optics from ω to $\omega_1 = \omega + \delta\omega$ such that $\kappa_1 = p_1\omega_1$ (cf. Section 3.4). The observed dry season increase in NIR *BRF* can be achieved variously, as discussed below.

4.2.1. Increase in LAI and Leaf Albedo Unchanged

[41] In this case, $\delta p/p > 0$ and $\delta\omega/\omega = 0$, i.e., $k = 100\%$ and $\delta\kappa/\kappa = \delta p/p$ (see Section 3.4). Variation in *BRF* does not exceed variation in K (see equation (5)), resulting in a negative value of the parameter β (cf. Section 3.4.1). In other words, adding more leaf area with the same spectral properties as the rest of the canopy will not change the observed canopy reflectance. Thus, the observed change in NIR *BRF* cannot be achieved by only increasing LAI.

4.2.2. Increase in Leaf Albedo and LAI Unchanged

[42] In this case, $\delta p/p = 0$ and $\delta\omega/\omega > 0$, i.e., $k = 0$ and $\delta\kappa/\kappa = \delta\omega/\omega$ (see Section 3.4). The relationship between variation in *BRF* and leaf albedo is given by (equation (8)), which suggests a strong response of the *BRF* to variation in leaf albedo. This response becomes stronger as the sensitivity parameter approaches unity, which is typical of dense vegetation and leaf albedo at NIR wavelengths. For instance, the observed 23% increase in NIR *BRF* can be attained through an increase in ω by $\delta\omega/\omega = 6.9\%$ for $\kappa = 0.7$ and any combination of ω and p such that $\omega p = \kappa = 0.7$. In the case of Amazonian forests, possible combinations could be $\omega = 0.9$ and $p = 0.78$ (which corresponds to LAI = 4.5), or $\omega = 0.88$ and $p = 0.8$ (LAI = 5). Thus, variations in leaf optics alone can explain the observed *BRF* changes, consistent with the arguments by *Doughty and Goulden* [2008], *Asner and Alencar* [2010], and *Brando et al.* [2010].

4.2.3. Increase in Both LAI and Leaf Albedo

[43] In this case, $\delta p/p > 0$ and $\delta\omega/\omega > 0$, i.e., $0 < k < 100\%$ and $\delta\kappa/\kappa = \delta\omega/\omega + \delta p/p$ (see Section 3.4). Changes in leaf optics and LAI that can lead to the observed dry season variation in *BRF* depend on the sensitivity parameter κ and its increment $\delta\kappa$. This is illustrated in Figure 4. For instance, consider a 10% change in the *BRF* sensitivity from $\kappa = 0.7$ (in early dry season, June) to $\kappa_1 = 0.77$ (in late dry season, September/October) ($\delta\kappa/\kappa = 0.10$). This case is described by the red curve in Figure 4. Assuming $\omega = 0.9$ in June (horizontal axis in Figure 4), the impact of canopy structure to *BRF* change is $k(0.9) = 23\%$ (vertical axis in Figure 4). It means that the 23% increase in NIR *BRF* would require an

increase in p of 2.3% ($k(0.9)$, $\delta\kappa/\kappa = 0.23 \times 0.10 = 2.3\%$; $p = \kappa/\omega = 0.78$ in June to $p_1 = 0.80$ in September/October) which translates into an 11% increase in LAI of 4.5. The corresponding increase in leaf albedo is 7.7% [$(1 - k(0.9))\delta\kappa/\kappa = 0.77 \times 0.10$]. In this example, a larger increment of the leaf albedo is required to achieve a given increase in *BRF* compared to the previous case of $\kappa = 0.7$ and unchanged LAI ($\delta\omega/\omega = 6.9\%$). Thus, variation in both leaf optics and LAI can equally well explain the observed *BRF* change, not inconsistent with *Myneni et al.* [2007], who interpreted the increased NIR *BRF* as more leaf area during the dry season and vice versa.

5. Discussion

[44] The dry season NIR reflectance (*BRF*) increase of 0.06 units, or about 23% (Figure 1), translates to a 16% increment in EVI (Figure 2), which is primarily sensitive to NIR (cf. Section 3.3), and this sensitivity increases with the magnitude of NIR reflectance (Figure 3). This change in EVI cannot be unambiguously interpreted because the exact property of the vegetation that this index measures is unknown. Another widely used index, the Normalized Difference Vegetation Index (NDVI), on the other hand, increases by only a small amount (4–5%) for the same increase in NIR reflectance (cf. Section 3.3), because its formulation is such that it dampens NIR reflectance changes and is independent of the magnitude of NIR reflectance (Figure 3). This NDVI change in absolute units is only 0.04, which is insignificant relative to the annual mean NDVI value of about 0.85 (Figure 2); this behavior is known as saturation in dense vegetation canopies, such as the Amazon forests. This rather small increase in NDVI, compared to a much larger increase in EVI, for the same change in canopy spectral reflectances further highlights the limitations of using vegetation indices for remote sensing of vegetation (as in work by *Huete et al.* [2006], *Xiao et al.* [2006], and *Brando et al.* [2010]).

[45] The MODIS LAI algorithm converts surface red and NIR reflectances and their overall uncertainties to most probable values of LAI [*Knyazikhin et al.*, 1998]. Uncertainties in surface reflectances include both observation and model uncertainties [*Wang et al.*, 2001]. The latter account for possible deviations of simulated reflectances from prescribed values in the look-up table due to variations in leaf optical properties. Thus, the algorithm converts surface spectral reflectances into LAI under the assumption that both leaf optical properties and LAI can vary (i.e., the impact function $k(\omega)$ is strictly positive, Section 3.4). Therefore, the algorithm is capable of detecting changes in leaf area. The MODIS algorithm reports approximately 18% increase in LAI (Figure 2) given the observed increase in NIR reflectance (Figure 1) during the dry season and a similar decrease in LAI during the wet season.

[46] New and mature leaves have leaf albedos (leaf reflectance plus transmittance) at NIR wavelengths that are 2–10% higher than those of older leaves due to aging and epiphyll cover [*Roberts et al.*, 1998; *Toomey et al.*, 2009]. The observed changes in NIR reflectance of Amazon forests (Figure 1) could be due to similar, but small, changes in NIR leaf albedos only, from exchanging older with newer leaves, with total leaf area unchanged, as argued by *Doughty and Goulden* [2008] and *Asner and Alencar* [2010] and confirmed by our analysis in Section 4.2.2. However, this ignores accumulating evidence from ground-based studies of higher leaf area in the dry season relative to the wet season, seasonal changes in litterfall and does not satisfactorily explain why NIR reflectance of these forests decreases in the following wet season. A more convincing explanation for the observed increase in NIR reflectance during the dry season and decrease during the wet season is one that invokes changes in both leaf area and leaf optical properties (Section 4.2.3). Such an argument is consistent with known phenological behavior of tropical forests (see the Introduction by *Myneni et al.* [2007]), ground-based reports of changes in leaf area [*Asner et al.*, 2004; *Carswell et al.*, 2002; *Pinto-Junior et al.*, 2010; *Malhado et al.*, 2009; *Negrón Juárez et al.*, 2009; *Doughty and Goulden*, 2008], litterfall [*Xiao et al.*, 2005; *Chave et al.*, 2010], leaf optical properties [*Roberts et al.*, 1998; *Toomey et al.*, 2009] and fluxes of evapotranspiration [*Juárez et al.*, 2007, 2008] and reconciles the various seemingly divergent views.

[47] A different line of reasoning on the cause of the dry season increase in NIR reflectance has been presented in a recent study by *Galvão et al.* [2011] using MODIS and hyperspectral (Hyperion and Hymap) data from a forest-savanna transitional site in Mato Grasso. The authors suggest that the dry season increase in NIR reflectance is caused by decreasing shade fraction resulting from large changes ($\sim$20°) in solar zenith angle (SZA), which in turn drives increase in EVI and MODIS LAI, given no observable changes in field-measured leaf area. While this study has correctly interpreted the increase in EVI arising from its dependence on NIR reflectance, the interpretation is based on correlation between the two rather than a thorough theoretical analysis presented here (cf. Section 3.3, Figure 3). The large SZA changes could be very specific to their study site because we have found significantly smaller changes in average SZA over Amazon forests (5°–6°, cf. Section 3.4.2). The suggestion that MODIS LAI changes are not representative of actual changes in leaf area is without basis because the MODIS LAI algorithm explicitly accounts for changes in SZA [*Knyazikhin et al.*, 1998] so as to preclude spurious LAI changes. Moreover, a large body of literature presents evidence of dry season leaf area increase [*Asner et al.*, 2004; *Carswell et al.*, 2002; *Pinto-Junior et al.*, 2010; *Malhado et al.*, 2009; *Negrón Juárez et al.*, 2009; *Doughty and Goulden*, 2008]. In addition, *Galvão et al.* [2011] did not examine the influence of leaf flush—leaf spectral changes—on NIR reflectance changes, which is presented here. All of these suggest that the results of *Galvão et al.* [2011] could be specific to their field site, as noted by the authors themselves, and may not be relevant to the vast expanse of Amazonian forests, the focus of our study.

[48] We have shown that the observed seasonal changes in NIR reflectance of Amazon forests are unlikely to be caused by changes in leaf area alone, but could, more plausibly, result from changes in both leaf area and leaf optical properties; however, our analysis is restricted to leaf optical property changes owing to leaf aging and epiphyll cover, given the paucity of literature on the sources of leaf optical property changes. The presence of a film of water on leaf surfaces, for instance due to a rainfall event, would tend to decrease greenness estimates because water reflects strongly

in red (blue) relative to NIR, an effect which is similar to the presence of residual atmospheric influences in the surface reflectances (cf. Figure S1). The use of VI error budget [from *Vermote and Kotchenova*, 2008] as an additional constraint on valid greenness increase in the dry season (cf. Figure 6 caption) would eliminate data showing such an effect. Among other possible causes of changes in leaf optical properties are leaf water content changes, dust coatings and coating with soot and carbonaceous particles emanating from biomass burning which is prevalent during the dry season. Thus, there is a need to explore these different mechanisms of leaf optical property variations. Finally, future research should also focus on spatial patterns of the causes (leaf area and leaf optical properties) of seasonal NIR reflectance variations of Amazonian forests.

[49] **Acknowledgment.** This work was supported by the NASA Earth Science Enterprise.

References

Aragao, L., Y. E. Shimabukuro, F. D. B. Espirito-Santo, and M. Williams (2005), Spatial validation of the collection 4 MODIS LAI product in Eastern Amazonia, *IEEE Trans. Geosci. Remote Sens.*, *43*(11), 2526–2534, doi:10.1109/TGRS.2005.856632.

Asner, G. P., and A. Alencar (2010), Drought impacts on the Amazon forest: The remote sensing perspective, *New Phytol.*, *187*(3), 569–578, doi:10.1111/j.1469-8137.2010.03310.x.

Asner, G. P., A. R. Townsend, and B. H. Braswell (2000), Satellite observation of El Niño effects on Amazon forest phenology and productivity, *Geophys. Res. Lett.*, *27*(7), 981–984, doi:10.1029/1999GL011113.

Asner, G. P., D. Nepstad, G. Cardinot, and D. Ray (2004), Drought stress and carbon uptake in an Amazon forest measured with spaceborne imaging spectroscopy, *Proc. Natl. Acad. Sci. U. S. A.*, *101*(16), 6039–6044, doi:10.1073/pnas.0400168101.

Brando, P. M., S. J. Goetz, A. Baccini, D. C. Nepstad, P. S. A. Beck, and M. C. Christman (2010), Seasonal and interannual variability of climate and vegetation indices across the Amazon, *Proc. Natl. Acad. Sci. U. S. A.*, *107*(33), 14,685–14,690, doi:10.1073/pnas.0908741107.

Carswell, F. E., et al. (2002), Seasonality in CO_2 and H_2O flux at an eastern Amazonian rain forest, *J. Geophys. Res.*, *107*(D20), 8076, doi:10.1029/2000JD000284.

Chave, J., et al. (2010), Regional and seasonal patterns of litterfall in tropical South America, *Biogeosciences*, *7*, 43–55, doi:10.5194/bg-7-43-2010.

Dessay, N., H. Laurent, L. A. T. Machado, Y. E. Shimabukuro, G. T. Batista, A. Diedhiou, and J. Ronchail (2004), Comparative study of the 1982–1983 and 1997–1998 El Niño events over different types of vegetation in South America, *Int. J. Remote Sens.*, *25*(20), 4063–4077, doi:10.1080/0143116031000101594.

Dickinson, R. E. (1983), Land surface processes and climate-surface albedos and energy balance, *Adv. Geophys.*, *25*, 305–353, doi:10.1016/S0065-2687(08)60176-4.

Doughty, C. E., and M. L. Goulden (2008), Seasonal patterns of tropical forest leaf area index and CO_2 exchange, *J. Geophys. Res.*, *113*, G00B06, doi:10.1029/2007JG000590.

Ferreira, L. G., and A. R. Huete (2004), Assessing the seasonal dynamics of the Brazilian Cerrado vegetation through the use of spectral vegetation indices, *Int. J. Remote Sens.*, *25*(10), 1837–1860, doi:10.1080/0143116031000101530.

Friedl, M. A., D. Sulla-Menashe, B. Tan, A. Schneider, N. Ramankutty, A. Sibley, and X. M. Huang (2010), MODIS Collection 5 global land cover: Algorithm refinements and characterization of new datasets, *Remote Sens. Environ.*, *114*(1), 168–182, doi:10.1016/j.rse.2009.08.016.

Fu, R., and W. Li (2004), The influence of land-surface on transition from dry to wet season in Amazonia, *Theor. Appl. Climatol.*, *78*, 97–110, doi:10.1007/s00704-004-0046-7.

Galvão, L. S., et al. (2011), On intra-annual EVI variability in the dry season of tropical forest: A case study with MODIS and hyperspectral data, *Remote Sens. Environ.*, *115*, 2350–2359, doi:10.1016/j.rse.2011.04.035.

Graham, E. A., S. S. Mulkey, K. Kitajima, N. G. Phillips, and S. J. Wright (2003), Cloud cover limits productivity in a tropical rain forest tree during La Nina, *Proc. Natl. Acad. Sci. U. S. A.*, *100*, 572–576, doi:10.1073/pnas.0133045100.

Huang, D., Y. Knyazikhin, W. Wang, D. W. Deering, P. Stenberg, N. Shabanov, B. Tan, and R. B. Myneni (2008), Stochastic transport theory for investigating the three-dimensional canopy structure from space measurements, *Remote Sens. Environ.*, *112*(1), 35–50, doi:10.1016/j.rse.2006.05.026.

Huete, A., K. Didan, T. Miura, E. P. Rodriguez, X. Gao, and L. G. Ferreira (2002), Overview of the radiometric and biophysical performance of the MODIS vegetation indices, *Remote Sens. Environ.*, *83*(1–2), 195–213, doi:10.1016/S0034-4257(02)00096-2.

Huete, A. R., K. Didan, Y. E. Shimabukuro, P. Ratana, S. R. Saleska, L. R. Hutyra, W. Z. Yang, R. R. Nemani, and R. Myneni (2006), Amazon rainforests green-up with sunlight in dry season, *Geophys. Res. Lett.*, *33*, L06405, doi:10.1029/2005GL025583.

Juárez, R. I. N., M. G. Hodnett, R. Fu, M. L. Goulden, and C. von Randow (2007), Control of dry season evapotranspiration over Amazonian forest as inferred from observations at a southern Amazon forest site, *J. Clim.*, *20*, 2827–2839, doi:10.1175/JCLI4184.1.

Juárez, R. I. N., et al. (2008), An empirical approach to retrieving monthly evapotranspiration over Amazonia, *Int. J. Remote Sens.*, *29*(24), 7045–7063, doi:10.1080/01431160802226026.

Knyazikhin, Y., J. V. Martonchik, R. B. Myneni, D. J. Diner, and S. W. Running (1998), Synergistic algorithm for estimating vegetation canopy leaf area index and fraction of absorbed photosynthetically active radiation from MODIS and MISR data, *J. Geophys. Res.*, *103*(D24), 32,257–32,275, doi:10.1029/98JD02462.

Knyazikhin, Y., L. Xu, M. A. Schull, R. B. Myneni, and A. Samanta (2010), Canopy spectral invariants. Part 1: A new concept in remote sensing of vegetation, *J. Quant. Spectrosc. Radiat. Transfer*, *112*, 727–735, doi:10.1016/j.jqsrt.2010.06.014.

Li, W., and R. Fu (2004), Transition of the large-scale atmospheric and land surface conditions from the dry to the wet season over Amazonia as diagnosed by the ECMWF Reanalysis, *J. Clim.*, *17*, 2637–2651, doi:10.1175/1520-0442(2004)017<2637:TOTLAA>2.0.CO;2.

Malhado, A. C. M., M. H. Costa, F. Z. de Lima, K. C. Portilho, and D. N. Figueiredo (2009), Seasonal leaf dynamics in an Amazonian tropical forest, *For. Ecol. Manage.*, *258*(7), 1161–1165, doi:10.1016/j.foreco.2009.06.002.

Myneni, R. B., F. G. Hall, P. J. Sellers, and A. L. Marshak (1995), The interpretation of spectral vegetation indexes, *IEEE Trans. Geosci. Remote Sens.*, *33*(2), 481–486, doi:10.1109/36.377948.

Myneni, R. B., et al. (2007), Large seasonal swings in leaf area of Amazon rainforests, *Proc. Natl. Acad. Sci. U. S. A.*, *104*(12), 4820–4823, doi:10.1073/pnas.0611338104.

NASA Land Processes Data Active Archive Center (LP DAAC) (2009), Land Cover Type Yearly L3 Global 1 km SIN Grid (MOD12Q1), https://lpdaac.usgs.gov/lpdaac/products/modis_products_table/land_cover/yearly_l3_global_1km2/mod12q1, USGS EROS Data Cent., Sioux Falls, S. D.

NASA Land Processes Data Active Archive Center (LP DAAC) (2010a), Vegetation Indices 16-Day L3 Global 1 km (MOD13A2), https://lpdaac.usgs.gov/lpdaac/content/view/full/6648, USGS EROS Data Cent., Sioux Falls, S. D.

NASA Land Processes Data Active Archive Center (LP DAAC) (2010b), Vegetation Indices 16-Day L3 Global 0.05deg CMG (MOD13C1), https://lpdaac.usgs.gov/content/view/full/6661, USGS EROS Data Cent., Sioux Falls, S. D.

NASA Land Processes Data Active Archive Center (LP DAAC) (2010c), Leaf Area Index–Fraction of Photosynthetically Active Radiation 8-Day L4 Global 1 km (MOD15A2), https://lpdaac.usgs.gov/lpdaac/products/modis_products_table/leaf_area_index_fraction_of_photosynthetically_active_radiation/8_day_l4_global_1km/mod15a2, USGS EROS Data Cent., Sioux Falls, S. D.

Negrón Juárez, R. I., H. R. da Rocha, A. Figueira, M. L. Goulden, and S. D. Miller (2009), An improved estimate of leaf area index based on the histogram analysis of hemispherical photographs, *Agric. For. Meteorol.*, *149*(6–7), 920–928, doi:10.1016/j.agrformet.2008.11.012.

Nemani, R. R., C. D. Keeling, H. Hashimoto, W. M. Jolly, S. C. Piper, C. J. Tucker, R. B. Myneni, and S. W. Running (2003), Climate-driven increases in global terrestrial net primary production from 1982 to 1999, *Science*, *300*(5625), 1560–1563, doi:10.1126/science.1082750.

Nepstad, D. C., C. R. Decarvalho, E. A. Davidson, P. H. Jipp, P. A. Lefebvre, G. H. Negreiros, E. D. Dasilva, T. A. Stone, S. E. Trumbore, and S. Vieira (1994), The role of deep roots in the hydrological and carbon cycles of Amazonian forests and pastures, *Nature*, *372*(6507), 666–669, doi:10.1038/372666a0.

Pinto-Junior, Q. B., L. Sanches, F. D. Lobo, A. A. Brandao, and J. S. Nogueira (2010), Leaf area index of a tropical semi-deciduous forest of the southern Amazon Basin, *Int. J. Biometeorol.*, *55*, 109–118, doi:10.1007/s00484-010-0317-1.

Rahman, A. F., D. A. Sims, V. D. Cordova, and B. Z. El-Masri (2005), Potential of MODIS EVI and surface temperature for directly estimating

per-pixel ecosystem C fluxes, *Geophys. Res. Lett.*, *32*, L19404, doi:10.1029/2005GL024127.

Rautiainen, M., M. Mottus, and P. Stenberg (2009), On the relationship of canopy LAI and photon recollision probability in boreal forests, *Remote Sens. Environ.*, *113*(2), 458–461, doi:10.1016/j.rse.2008.10.014.

Reich, P. B., C. Uhl, M. B. Walters, L. Prugh, and D. S. Ellsworth (2004), Leaf demography and phenology in Amazonian rain forest: A census of 40,000 leaves of 23 tree species, *Ecol. Monogr.*, *74*(1), 3–23, doi:10.1890/02-4047.

Roberts, D. A., B. W. Nelson, J. B. Adams, and F. Palmer (1998), Spectral changes with leaf aging in Amazon Caatinga, *Trees (Heidelberg, Ger.)*, *12*, 315–325, doi:10.1007/s004680050157.

Ross, J. (Ed.) (1981), *The Radiation Regime and Architecture of Plant Stands*, Dr. W. Junk, Boston, Mass.

Saleska, S. R., et al. (2003), Carbon in Amazon forests: Unexpected seasonal fluxes and disturbance-induced losses, *Science*, *302*(5650), 1554–1557, doi:10.1126/science.1091165.

Samanta, A., S. Ganguly, H. Hashimoto, S. Devadiga, E. Vermote, Y. Knyazikhin, R. R. Nemani, and R. B. Myneni (2010), Amazon forests did not green-up during the 2005 drought, *Geophys. Res. Lett.*, *37*, L05401, doi:10.1029/2009GL042154.

Samanta, A., S. Ganguly, and R. B. Myneni (2011a), MODIS Enhanced Vegetation Index data do not show greening of Amazon forests during the 2005 drought, *New Phytol.*, *189*(1), 11–15, doi:10.1111/j.1469-8137.2010.03516.x.

Samanta, A., M. H. Costa, E. L. Nunes, S. L. Vieira, L. Xu, and R. Myneni (2011b), Comment on "Drought-induced reduction in global terrestrial net primary production from 2000 through 2009", *Science*, *333*(6046), 1093, doi:10.1126/science.1199048.

Schull, M. A., et al. (2010), Canopy spectral invariants, Part 2: Application to classification of forest types from hyperspectral data, *J. Quant. Spectrosc. Radiat. Transfer*, *112*, 736–750, doi:10.1016/j.jqsrt.2010.06.004.

Schuur, E. A. G. (2003), Net primary productivity and global climate revisited: The sensitivity of tropical forest growth to precipitation, *Ecology*, *84*, 1165–1170, doi:10.1890/0012-9658(2003)084[1165:PAGCRT]2.0.CO;2.

Shabanov, N. V., et al. (2005), Analysis and optimization of the MODIS leaf area index algorithm retrievals over broadleaf forests, *IEEE Trans. Geosci. Remote Sens.*, *43*(8), 1855–1865, doi:10.1109/TGRS.2005.852477.

Sims, D. A., et al. (2008), A new model of gross primary productivity for North American ecosystems based solely on the enhanced vegetation index and land surface temperature from MODIS, *Remote Sens. Environ.*, *112*(4), 1633–1646, doi:10.1016/j.rse.2007.08.004.

Smolander, S., and P. Stenberg (2005), Simple parameterizations of the radiation budget of uniform broadleaved and coniferous canopies, *Remote Sens. Environ.*, *94*(3), 355–363, doi:10.1016/j.rse.2004.10.010.

Stenberg, P. (2007), Simple analytical formula for calculating average photon recollision probability in vegetation canopies, *Remote Sens. Environ.*, *109*(2), 221–224, doi:10.1016/j.rse.2006.12.014.

Toomey, M., D. Roberts, and B. Nelson (2009), The influence of epiphylls on remote sensing of humid forests, *Remote Sens. Environ.*, *113*(8), 1787–1798, doi:10.1016/j.rse.2009.04.002.

Vermote, E. F., and S. Kotchenova (2008), Atmospheric correction for the monitoring of land surfaces, *J. Geophys. Res.*, *113*, D23S90, doi:10.1029/2007JD009662.

Wang, Y. J., Y. H. Tian, Y. Zhang, N. El-Saleous, Y. Knyazikhin, E. Vermote, and R. B. Myneni (2001), Investigation of product accuracy as a function of input and model uncertainties: Case study with SeaWiFS and MODIS LAI/FPAR algorithm, *Remote Sens. Environ.*, *78*(3), 299–313, doi:10.1016/S0034-4257(01)00225-5.

Wright, S. J., and C. P. van Schaik (1994), Light and the phenology of tropical trees, *Am. Nat.*, *143*(1), 192–199, doi:10.1086/285600.

Würth, M. K. R., S. Peláez-Riedl, S. J. Wright, and C. Körner (2005), Non-structural carbohydrate pools in a tropical forest, *Oecologia*, *143*, 11–24, doi:10.1007/s00442-004-1773-2.

Xiao, X., et al. (2005), Satellite-based modeling of gross primary production in a seasonally moist tropical evergreen forest, *Remote Sens. Environ.*, *94*, 105–122, doi:10.1016/j.rse.2004.08.015.

Xiao, X. M., S. Hagen, Q. Y. Zhang, M. Keller, and B. Moore (2006), Detecting leaf phenology of seasonally moist tropical forests in South America with multi-temporal MODIS images, *Remote Sens. Environ.*, *103*(4), 465–473, doi:10.1016/j.rse.2006.04.013.

Xu, L., A. Samanta, M. H. Costa, S. Ganguly, R. R. Nemani, and R. B. Myneni (2011), Widespread decline in greenness of Amazonian vegetation due to the 2010 drought, *Geophys. Res. Lett.*, *38*, L07402, doi:10.1029/2011GL046824.

Yang, W., N. V. Shabanov, D. Huang, W. Wang, R. E. Dickinson, R. R. Nemani, Y. Knyazikhin, and R. B. Myneni (2006), Analysis of leaf area index products from combination of MODIS Terra and Aqua data, *Remote Sens. Environ.*, *104*(3), 297–312, doi:10.1016/j.rse.2006.04.016.

M. H. Costa, Federal University of Viçosa, Av. P. H. Rolfs, s/n, Viçosa, MG CEP 36570-000, Brazil.

R. E. Dickinson and R. Fu, Department of Geological Sciences, University of Texas at Austin, Austin, TX 78712, USA.

Y. Knyazikhin, R. B. Myneni, and L. Xu, Department of Geography and Environment, Boston University, Boston, MA 02215, USA.

R. R. Nemani, Biospheric Sciences Branch, NASA AMES Research Center, Moffett Field, CA 94035, USA.

S. S. Saatchi, Jet Propulsion Laboratory, California Institute of Technology, Pasadena, CA 91109, USA.

A. Samanta, Atmospheric and Environmental Research Inc., Lexington, MA 02421, USA. (arindam.sam@gmail.com)

Environmental Research Letters

LETTER

Sunlight mediated seasonality in canopy structure and photosynthetic activity of Amazonian rainforests

Jian Bi[1,20], **Yuri Knyazikhin**[1,20], **Sungho Choi**[1], **Taejin Park**[1], **Jonathan Barichivich**[2], **Philippe Ciais**[3], **Rong Fu**[4], **Sangram Ganguly**[5], **Forrest Hall**[6], **Thomas Hilker**[7], **Alfredo Huete**[8], **Matthew Jones**[9], **John Kimball**[9], **Alexei I Lyapustin**[10], **Matti Mõttus**[11], **Ramakrishna R Nemani**[12], **Shilong Piao**[13,14], **Benjamin Poulter**[15], **Scott R Saleska**[16], **Sassan S Saatchi**[17,18], **Liang Xu**[17], **Liming Zhou**[19] **and Ranga B Myneni**[1]

[1] Department of Earth and Environment, Boston University, Boston, MA 02215, USA
[2] Climatic Research Unit, School of Environmental Sciences, University of East Anglia, Norwich NR4 7TJ, UK
[3] Laboratoire des Sciences du Climat et de l'Environnement, IPSL-LSCE, CEA-CNRS-UVSQ, 91191 Gif sur Yvette Cedex, France
[4] Department of Geological Sciences, The University of Texas at Austin, Austin, TX 78712, USA
[5] Bay Area Environmental Research Institute, NASA Ames Research Center, Moffett Field, CA 94035, USA
[6] Biospheric Sciences Laboratory, NASA Goddard Space Flight Center, Greenbelt, MD 20771, USA
[7] College of Forestry, Oregon State University, Corvallis, OR 97331, USA
[8] Plant Functional Biology and Climate Change Cluster, University of Technology Sydney, New South Wales 2007, Australia
[9] Numerical Terradynamic Simulation Group, The University of Montana, Missoula, MT 59812, USA
[10] Climate and Radiation Laboratory, NASA Goddard Space Flight Center, Greenbelt, MD 20771, USA
[11] Department of Geosciences and Geography, University of Helsinki, FI-00014, Helsinki, Finland
[12] NASA Advanced Supercomputing Division, Ames Research Center, Moffett Field, California 94035, USA
[13] Department of Ecology, Peking University, Beijing 100871, People's Republic of China
[14] Institute of Tibetan Plateau Research, Chinese Academy of Sciences, Beijing 100085, People's Republic of China
[15] Department of Ecology, Montana State University, Bozeman, MT 59717, USA
[16] Department of Ecology and Evolutionary Biology, University of Arizona, Tucson, AZ 85721, USA
[17] Institute of the Environment and Sustainability, University of California, Los Angeles, CA 90095, USA
[18] Radar Science and Engineering section, Jet Propulsion Laboratory, California Institute of Technology, Pasadena, CA 91109, USA
[19] Department of Atmospheric and Environmental Sciences, University at Albany, State University of New York, Albany, New York 12222, USA
[20] These authors contributed equally to this work.

E-mail: jknjazi@bu.edu

OPEN ACCESS

RECEIVED
26 February 2015

REVISED
28 May 2015

ACCEPTED FOR PUBLICATION
1 June 2015

PUBLISHED
16 June 2015

Keywords: Amazonian rainforests, seasonality, remote sensing, MISR, MODIS

Supplementary material for this article is available online

Abstract

Resolving the debate surrounding the nature and controls of seasonal variation in the structure and metabolism of Amazonian rainforests is critical to understanding their response to climate change. *In situ* studies have observed higher photosynthetic and evapotranspiration rates, increased litterfall and leaf flushing during the Sunlight-rich dry season. Satellite data also indicated higher greenness level, a proven surrogate of photosynthetic carbon fixation, and leaf area during the dry season relative to the wet season. Some recent reports suggest that rainforests display no seasonal variations and the previous results were satellite measurement artefacts. Therefore, here we re-examine several years of data from three sensors on two satellites under a range of sun positions and satellite measurement geometries and document robust evidence for a seasonal cycle in structure and greenness of wet equatorial Amazonian rainforests. This seasonal cycle is concordant with independent observations of solar radiation. We attribute alternative conclusions to an incomplete study of the seasonal cycle, i.e. the dry season only, and to prognostications based on a biased radiative transfer model. Consequently, evidence of dry season greening in geometry corrected satellite data was ignored and the absence of evidence for seasonal variation in lidar data due to noisy and saturated signals was misinterpreted as evidence of the absence of changes during the dry season. Our results, grounded in the physics of radiative transfer, buttress previous reports of dry season increases in leaf flushing, litterfall, photosynthesis and evapotranspiration in well-hydrated Amazonian rainforests.

1. Introduction

Understanding the seasonal variation in functioning of rainforests and its controls are requisite for understanding how rainforests will respond to climate change. *In situ* studies report counter-intuitive seasonal variation in wet equatorial Amazonian rainforests —higher photosynthetic and evapotranspiration rates and increased litterfall and leaf flushing during the Sunlight-rich dry season (Saleska *et al* 2003, da Rocha *et al* 2004, Goulden *et al* 2004, Rice *et al* 2004, Hasler and Avissar 2007, Hutyra *et al* 2007, Negrón Juárez *et al* 2009, Costa *et al* 2010, Jones *et al* 2014). Water limitation during the dry season is alleviated in these forests through deep roots and hydraulic redistribution (Nepstad *et al* 1994, Oliveira *et al* 2005). Satellite data, which cover a large area and span a long time period, support findings of *in situ* studies—higher radiometric greenness level and green leaf area during the dry season compared to the wet season (Xiao *et al* 2005, Huete *et al* 2006, Myneni *et al* 2007, Samanta *et al* 2012, Hilker *et al* 2014, Jones *et al* 2014, Maeda *et al* 2014). This convergent view of seasonality, parsed from several studies, shows how sunlight interacts with adaptive mechanisms to result in higher rates of leaf flushing, litterfall, photosynthesis and evapotranspiration in tropical forests if water limitation is absent (Wright and Van Schaik 1994, Restrepo-Coupe *et al* 2013, Borchert *et al* 2015, Guan *et al* 2015).

This community-consensual view was questioned in recent studies (Galvão *et al* 2011, Morton *et al* 2014). The studies claim that the dry season greening inferred from passive remote sensing data resulted from an artificial increase in forest canopy reflectance at near-infrared (NIR) wavelengths caused by variations in sun-satellite sensor geometry. Their analyses of satellite-borne lidar data suggested that these forests exhibited no seasonal variations in canopy structure or leaf area. Relying on model simulations to guide and imbue a physical meaning to the satellite data analysis, the studies conclude that Amazon rainforests maintain consistent structure and greenness during the dry season.

These contradictory results justify a re-examination of the same satellite data with the goal of assessing seasonality in wet equatorial Amazonian rainforests. In addition to data from NASA's Moderate Resolution Imaging Spectroradiometer (MODIS) on the Terra platform and the Geoscience Laser Altimeter System (GLAS) instrument onboard the Ice, Cloud and land Elevation Satellite (ICESat) used in (Morton *et al* 2014), we also include data from the MODIS instrument on Aqua and Multiangle Imaging Spectroradiometer (MISR) on the Terra satellite. The MISR sensor views the Earth's surface with nine cameras simultaneously, as opposed to the two MODIS sensors, which are capable of only one view each. This feature enables the rigorous use of the theory of radiative transfer in vegetation canopies—the fundamental theory that explains from first principles the mechanisms underlying the signals generated by the canopy and measured by a remote sensor (Knyazikhin *et al* 2005).

This study is focused on terra firme rainforests in central Amazonia that are relatively undisturbed by human activities (supplementary data and methods section 1, figure S1). The period June to May is treated as one seasonal cycle as per convention (Huete *et al* 2006, Morton *et al* 2014). It consists of a short dry season, June to October, and a long wet season thereafter (supplementary data and methods section 1). The following analysis of satellite borne sensor data addresses the question at the center of current debate —did previous studies (Xiao *et al* 2005, Huete *et al* 2006, Myneni *et al* 2007, Brando *et al* 2010, Samanta *et al* 2012) misinterpret changes in near-infrared (NIR) reflectance caused by seasonal changes in sun-satellite sensor geometry (figures S2 and S3) as seasonal variations in rainforest canopy structure and greenness (Galvão *et al* 2011, Morton *et al* 2014)?

2. Data and methods

A detailed description of methods and data used is given in the supplementary information available at stacks.iop.org/ERL/10/064014/mmedia. A brief summary is provided here. The study region and the various data analysed in this study are detailed in the supplementary data and methods section 1–2. The sun-sensor geometry relevant to the discussion in this article is presented in the supplementary data and methods section 3. The theory of remote measurements and evaluation of NIR reflectance angular signatures (figure 3) and their interpretation is described in the supplementary data and methods section 4. A critical look at Morton *et al* 2014 analyses of MODIS and GLAS data is presented in the supplementary discussion. Abbreviations and symbols are listed in supplementary table S5.

3. Results and discussioin

3.1. Leaf area index seasonality

The seasonal cycle of green leaf area inferred from satellite data (figure 1(a)) exhibits rising values during the dry season (June to October), high values during the early part of the wet season (November to February) and decreasing values thereafter (March to May). This seasonal variation of about 20% is imposed on a base value of Leaf Area Index (LAI, one-sided green leaf area per unit ground area) of about 5.75, is greater than the uncertainty of the LAI product (0.66 LAI, Yang *et al* 2006) and is observed in nearly 70% of the rainforests in the study domain (figure S4(a)); the rest lacked valid data. Is this seasonal variation real or a misinterpretation of changes in satellite-sensor measurements caused by seasonal changes in sun position

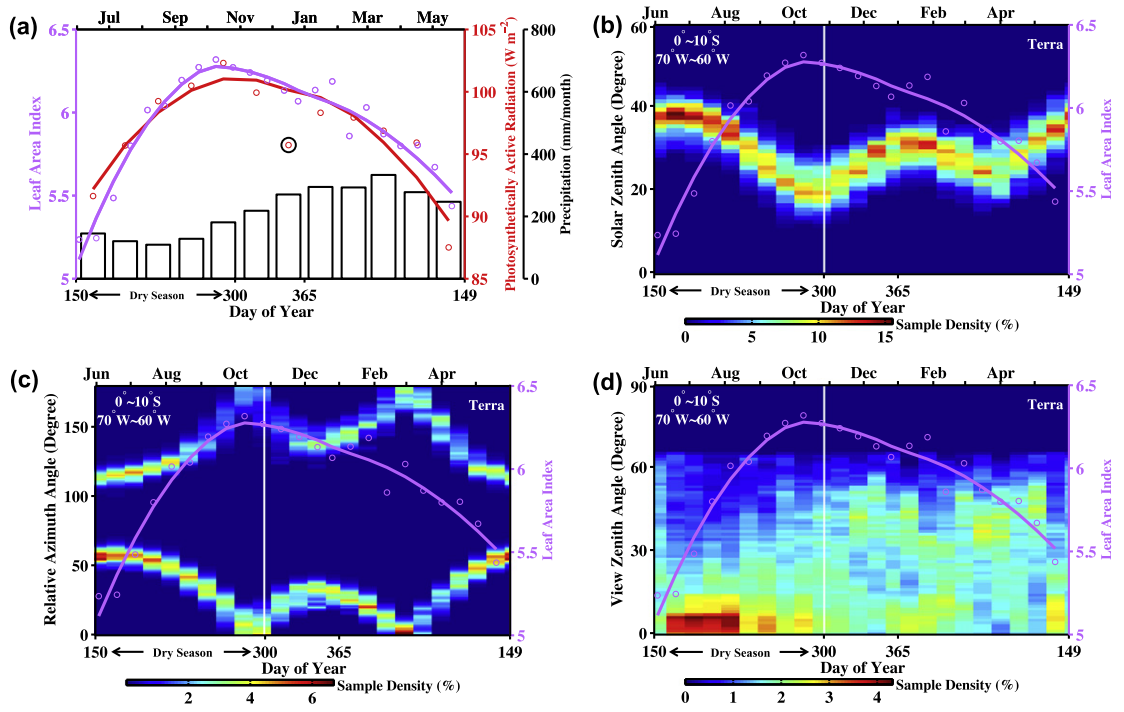

Figure 1. Seasonal variations in green leaf area of central Amazonian rainforests. (a) Seasonal cycles of Terra MODIS leaf area index (LAI), at-surface photosynthetically active radiation (PAR) from CERES, and TRMM precipitation. The PAR polynomial regression curve excludes the circled data point. The seasonal profiles represent average values over pixels that exhibited dry season greening in at least 4 out of 7 seasonal cycles analyzed (63% of all forest pixels). (b)–(d) Seasonal cycle of LAI, as in panel (a), contrasted against seasonal variations in (b) solar zenith angle, (c) sensor view relative azimuth angle and (d) view zenith angle.

in the sky and the manner in which the sensor measures reflected radiation ('sun-sensor geometry')? The answer requires an understanding of how this geometry changes during the seasonal cycle, which is described in the supplementary data and methods section 3.

The seasonal cycle of leaf area in figure 1(a) cannot be an artefact of seasonal changes in sun-sensor geometry because the algorithm with which leaf area is derived explicitly accounts for geometry changes, i.e. the algorithm is capable of differentiating between changes in measurements caused by leaf area changes and those caused by geometry changes (Knyazikhin *et al* 1999, Knyazikhin *et al* 1998). This is also evident from the fact that the seasonal cycle of leaf area does not track the seasonal course of either the Sun position in the sky (figure 1(b)) or the MODIS sensor sampling (figures 1(c) and (d)). Instead, it tracks independently obtained observations of seasonal variation in sunlight (figure 1(a)). This behavior is consistent with the idea that sunlight acts as a proximate cue for leaf production in moist tropical forests if water limitation is absent (Wright and Van Schaik 1994, Borchert *et al* 2015, Guan *et al* 2015). Thus, relatively high sunlight levels from absence of clouds during the dry season cause leaf area to increase, which in turn generates higher rates of photosynthesis (Saleska *et al* 2003, Da Rocha *et al* 2004, Restrepo-Coupe *et al* 2013, Gatti *et al* 2014). But, photosynthesis becomes decoupled from sunlight during the early to middle part of the wet season. This results in increasing rates of photosynthesis, which are possibly sustained by still sufficiently high levels of light and increasing leaf production (Restrepo-Coupe *et al* 2013). All three decrease rapidly thereafter. A bimodal seasonal cycle of LAI reported in one instance could be site-specific (figure 2 in Doughty and Goulden (2008)) as alternate *in situ* evidence does not exist (Restrepo-Coupe *et al* 2013, Xiao *et al* 2005, Asner *et al* 2000, Carswell *et al* 2002, Chave *et al* 2010, Malhado *et al* 2009, Negrón Juárez *et al* 2009).

3.2. Evidence for seasonality after sun-sensor geometry correction

The Enhanced Vegetation Index (EVI) is a proven proxy for the potential photosynthetic carbon fixation by vegetation (Xiao *et al* 2005, Huete *et al* 2006, Brando *et al* 2010). It is calculated from satellite-sensor measurements of reflected solar radiation at three different wavelength bands. These measurements depend on sun-sensor geometry, but this dependency can be eliminated by expressing the measurements in a fixed geometry (Morton *et al* 2014, Lyapustin *et al* 2012). The EVI calculated from MODIS sensor measurements in a fixed geometry, i.e. nadir viewing direction and 45° solar zenith angle, shows a distinct wet season decrease (figure 2(a)) and dry season increase (figure 2(b)). These changes are greater than a highly conservative estimate of the precision in 43% of the pixels during the wet season and 31% of the pixels

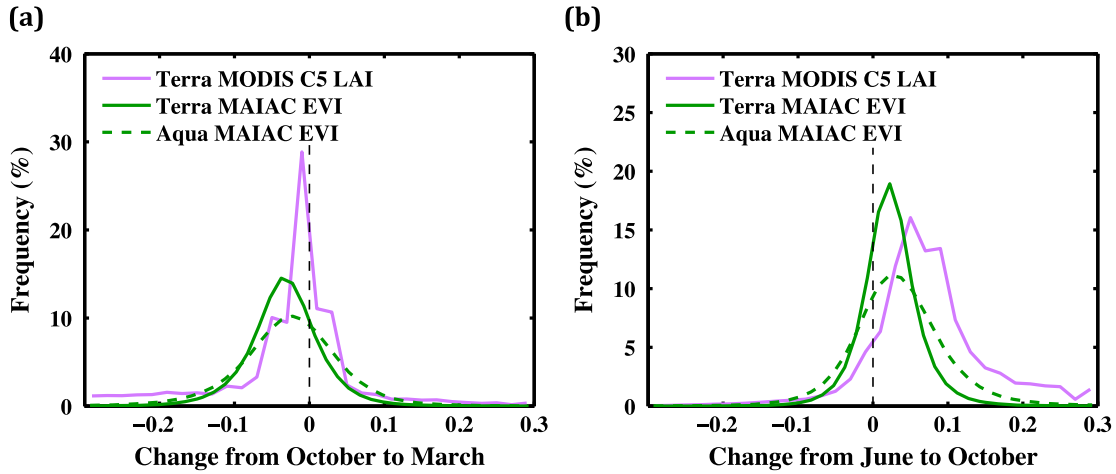

Figure 2. Wet and dry season changes in sun-sensor geometry corrected estimates of leaf area and greenness. Per-pixel changes in MODIS leaf area index (LAI) and MODIS MAIAC enhanced vegetation index (EVI) from (a) October to March and (b) June to October. LAI values are normalized by 10. The changes are calculated as the difference between the values in March and October, and October and June, respectively.

in the dry season. Here, the precision is estimated as the spatial standard deviation of the EVI data in the study domain. Analogous to EVI, pixel level estimates of green leaf area show a strong decrease in the wet season and increase during the dry season. The wet season decrease (figure 2(a)) suggests net leaf abscission, i.e. more older leaves dropped than those newly flushed, and the dry season increase indicates net leaf flushing (figure 2(b)), resulting in a sunlight mediated phenological behavior (Myneni *et al* 2007). The fact that both EVI and LAI show congruent changes during the seasonal cycle even though the Sun-sensor geometry effect is removed from measurements in different ways (Knyazikhin *et al* 1999, Knyazikhin *et al* 1998, Lyapustin *et al* 2012, Hilker *et al* 2014, Maeda *et al* 2014) is particularly noteworthy.

3.3. Evidence for seasonality from multiple sensors and geometries

Now we turn to satellite-sensor measurements of reflected solar radiation at the NIR wavelength band, which are at the heart of the controversy. These measurements are usually expressed as normalized quantities called reflectances (supplementary data and methods section 4.1–4.2). The geometric structure and radiation scattering properties of the rainforest canopy determine the magnitude and angular distribution of reflected radiation. The angular signatures of reflectance are therefore unique and rich sources of diagnostic information about rainforest canopies (Diner *et al* 1999). We first examine NIR angular signatures from the late dry season (October 15 to 30) and the middle part of the wet season (March 5 to 20). The Solar Zenith Angle (SZA) at the time when Terra (10:30 am) and Aqua (1:30 pm) satellites view the central Amazonian forests in March and October is between 20° and 30°. This variation minimally impacts the shape of angular signatures (supplementary data and methods section 4.4). MODIS and MISR sensors sample the rainforests very differently (figures S2(c)–(f); also see figure S1(c)). However, all the sensors record a distinct decrease in reflected NIR radiation in all view directions between October and March with no change in the overall shape of the angular signatures (figures 3(a) and (b)). Such a simple change in magnitude can only result from a change in canopy properties—this conclusion is based on the physics of how solar radiation interacts with foliage in vegetation canopies (supplementary data and methods section 4.3, figures S5(a) and (b)). The EVI, although evaluated from reflectances at NIR, red and blue wavelength bands, is tightly linked to NIR reflectance (Samanta *et al* 2012). Thus, the decrease in sun-sensor geometry corrected EVI (figure 2(a)) is in agreement with directly observed decreases in NIR angular signatures from October to March (figures 3(a) and (b)).

The wet season reduction in greenness is inconsistent with the hypothesis of invariant dry season greenness. Indeed the net loss of leaf area, without a corresponding net gain elsewhere during the seasonal cycle, will result in rainforests without leaves in a few years. If wet Amazonian forests somehow maintain consistent canopy structure and greenness during the dry season, then they must be either aseasonal or the entire seasonal cycle must be confined to the wet season, but this argument lacks empirical support. The question then arises whether variations in angular signatures of forest reflectance during the dry season support this inference?

Therefore, let us now consider NIR reflectances from early (25 June to 10 July) and the late dry season (15 October to 30 October) when both sun position in the sky and sensor sampling vary significantly (figures S2(a)–(d); also see figure S1(c)). MODIS and MISR measurements are made at significantly higher SZA in June (~35°–40°) compared to October (~20°–30°).

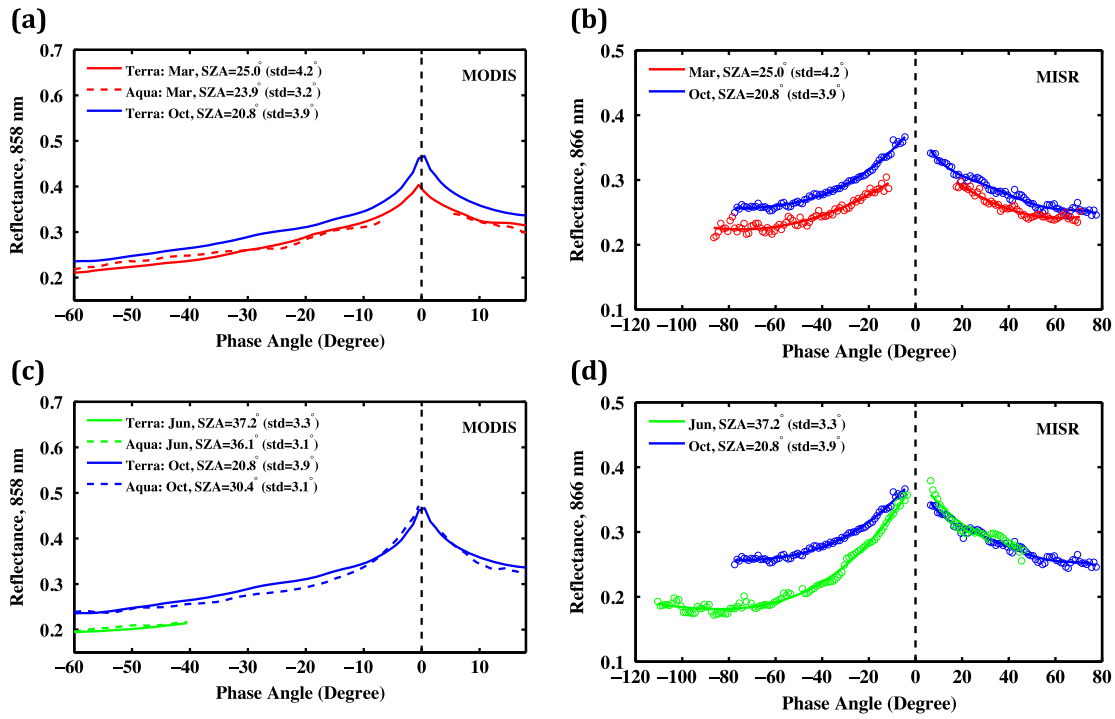

Figure 3. Seasonal changes in angular signatures of near-infrared (NIR) reflectance from three satellite borne sensors. Angular signatures of NIR reflectance in March (5 Mar to 20 Mar), June (25 Jun to 10 Jul) and October (15 Oct to 30 Oct). The Aqua MODIS signature for October is shown in panel (c) for clarity. The phase angle is the angle between the directions to the Sun and sensor (figure S1(c)).

The magnitude and shape of angular signatures are impacted when both canopy properties and SZA vary. However, a higher or equal reflectance at lower SZA relative to reflectance at higher SZA always indicates an increase in leaf area and foliage scattering properties according to the physics of radiation interaction in vegetation (supplementary data and methods section 4.4–4.5, figures S5(c)–(f)). This is observed clearly in MISR data (figure 3(d)) because this sensor views the Earth's surface with nine cameras simultaneously, as opposed to the two MODIS sensors (figure 3(c)), which are capable of only one view each (figure S3). Further, the juxtaposition of the two angular signatures in figure 3(d) is significantly different than that predicted by theory for the case of identical canopies (supplementary data and methods section 4.6). Thus, the NIR angular signatures in figure 3(d) indicate a change in vegetation structure (LAI) and greenness (EVI) during the dry season.

4. Conclusions

Satellite data indicate a distinct sunlight-mediated seasonality in leaf area and photosynthetic carbon fixation over unstressed rainforests in central Amazonia. This seasonal cycle is not an artefact of seasonal changes in sun position in the sky or how the satellite-sensor measures the reflected radiation field. The spatially expansive remote sensing data agree with available *in situ* data. A better understanding of how the rainforests will respond to climate change depends on future ground campaigns as satellite data can complement, but not substitute, field data.

Acknowledgments

This study was supported by NASA Earth Science Division.

Author contributions

J B, Y K, S C and T P performed the analyses. RBM wrote the initial draft. All authors contributed with ideas to the analyses and with writing the article. The authors declare no conflict of interest.

References

Asner G P, Townsend A R and Braswell B H 2000 Satellite observation of El Nino effects on Amazon forest phenology and productivity *Geophys. Res. Lett.* **27** 981–4

Brando P M, Goetz S J, Baccini A, Nepstad D C, Beck P S and Christman M C 2010 Seasonal and interannual variability of climate and vegetation indices across the Amazon *Proc. Natl Acad. Sci. USA* **107** 14685–90

Borchert R, Calle Z, Strahler A H, Baertschi A, Magill R E, Broadhead J S, Kamau J, Njoroge J and Muthuri C 2015 Insolation and photoperiodic control of tree development near the equator *New Phytol.* **205** 7–13

Carswell F *et al* 2002 Seasonality in CO2 and H2O flux at an eastern Amazonian rain forest *J. Geophys. Res. Atmos.* **107** LBA43–1

Chave J *et al* 2010 Regional and seasonal patterns of litterfall in tropical South America *Biogeosciences* **7** 43–55

Costa M H *et al* 2010 Atmospheric versus vegetation controls of Amazonian tropical rain forest evapotranspiration: are the

wet and seasonally dry rain forests any different? *J. Geophys. Res. Biogeosci.* **115** G04021

Da Rocha H R, Goulden M L, Miller S D, Menton M C, Pinto L D, De Freitas H C and Silva Figueira A M E 2004 Seasonality of water and heat fluxes over a tropical forest in eastern Amazonia *Ecol. Appl.* **14** S22–32

Diner D J, Asner G P, Davies R, Knyazikhin Y, Muller J P, Nolin A W, Pinty B, Schaaf C B and Stroeve J 1999 New directions in earth observing: scientific applications of multiangle remote sensing *Bull. Am. Meteorol. Soc.* **80** 2209–28

Doughty C E and Goulden M L 2008 Seasonal patterns of tropical forest leaf area index and CO_2 exchange *J. Geophys. Res. Biogeosci.* **113** G00B06

Galvão L S, Dos Santos J R, Roberts D A, Breunig F M, Toomey M and De Moura Y M 2011 On intra-annual EVI variability in the dry season of tropical forest: a case study with MODIS and hyperspectral data *Remote Sens. Environ.* **115** 2350–9

Gatti L *et al* 2014 Drought sensitivity of Amazonian carbon balance revealed by atmospheric measurements *Nature* **506** 76–80

Goulden M L, Miller S D, Da Rocha H R, Menton M C, De Freitas H C, Silva Figueira A M E and De Sousa C D 2004 Diel and seasonal patterns of tropical forest CO_2 exchange *Ecol. Appl.* **14** S42–54

Guan K *et al* 2015 Photosynthetic seasonality of global tropical forests constrained by hydroclimate *Nature Geosci.* **8** 284–9

Hasler N and Avissar R 2007 What controls evapotranspiration in the Amazon basin? *J. Hydrometeorol.* **8** 380–95

Hilker T *et al* 2014 Vegetation dynamics and rainfall sensitivity of the Amazon *Proc. Natl Acad. Sci. USA* **111** 16041–6

Huete A R *et al* 2006 Amazon rainforests green-up with sunlight in dry season *Geophys. Res. Lett.* **33** L06405

Hutyra L R *et al* 2007 Seasonal controls on the exchange of carbon and water in an Amazonian rain forest *J. Geophys. Res. Biogeosci.* **112** G03008

Jones M O, Kimball J S and Nemani R R 2014 Asynchronous Amazon forest canopy phenology indicates adaptation to both water and light availability *Environ. Res. Lett.* **9** 124021

Knyazikhin Y *et al* 1999 MODIS leaf area index (LAI) and fraction of photosynthetically active radiation absorbed by vegetation (FPAR) product (MOD15) *Algorithm Theoretical Basis Document* (https://lpdaac.usgs.gov/products/modis_products_table/mcd15a2)

Knyazikhin Y, Martonchik J, Myneni R, Diner D and Running S 1998 Synergistic algorithm for estimating vegetation canopy leaf area index and fraction of absorbed photosynthetically active radiation from MODIS and MISR data *J. Geophys. Res. Atmos.* **103** 32257–75

Knyazikhin Y, Marshak A and Myneni R B 2005 Three-dimensional radiative transfer in vegetation canopies and cloud-vegetation interaction *Three Dimensional Radiative Transfer in the Cloudy Atmosphere* ed A Marshak and A B Davis (Berlin, Heidelberg: Springer) pp 617–51

Lyapustin A I *et al* 2012 Multi-angle implementation of atmospheric correction for MODIS (MAIAC): 3. Atmospheric correction *Remote Sens. Environ.* **127** 385–93

Maeda E E, Heiskanen J, Aragão L E O C and Rinne J 2014 Can MODIS EVI monitor ecosystem productivity in the Amazon rainforest? *Geophys. Res. Lett.* **41** 7176–83

Malhado A, Costa M H, de Lima F Z, Portilho K C and Figueiredo D N 2009 Seasonal leaf dynamics in an Amazonian tropical forest *For. Ecol. Manage.* **258** 1161–5

Morton D C *et al* 2014 Amazon forests maintain consistent canopy structure and greenness during the dry season *Nature* **506** 221–4

Myneni R B *et al* 2007 Large seasonal swings in leaf area of Amazon rainforests *Proc. Natl Acad. Sci. USA* **104** 4820–3

Negrón Juárez R I, da Rocha H R, Goulden M L and Miller S D 2009 An improved estimate of leaf area index based on the histogram analysis of hemispherical photographs *Agric. For. Meteorol.* **149** 920–8

Nepstad D C *et al* 1994 The role of deep roots in the hydrological and carbon cycles of Amazonian forests and pastures *Nature* **372** 666–9

Oliveira R S, Dawson T E, Burgess S S and Nepstad D C 2005 Hydraulic redistribution in three Amazonian trees *Oecologia* **145** 354–63

Restrepo-Coupe N *et al* 2013 What drives the seasonality of photosynthesis across the Amazon basin? A cross-site analysis of eddy flux tower measurements from the Brasil flux network *Agric. For. Meteorol.* **182** 128–44

Rice A H *et al* 2004 Carbon balance and vegetation dynamics in an old-growth Amazonian forest *Ecol. Appl.* **14** 55–71

Saleska S R *et al* 2003 Carbon in Amazon forests: unexpected seasonal fluxes and disturbance-induced losses *Science* **302** 1554–7

Samanta A *et al* 2012 Seasonal changes in leaf area of Amazon forests from leaf flushing and abscission *J. Geophys. Res. Biogeosci.* **117** G01015

Wright S J and Van Schaik C P 1994 Light and the phenology of tropical trees *Am. Nat.* **143** 192–9

Xiao X *et al* 2005 Satellite-based modeling of gross primary production in a seasonally moist tropical evergreen forest *Remote Sens. Environ.* **94** 105–22

Yang W *et al* 2006 MODIS leaf area index products: from validation to algorithm improvement *IEEE Trans. Geosci. Remote Sens.* **44** 1885–98

SUPPLEMENTARY INFORMATION

Sunlight mediated seasonality in canopy structure and photosynthetic activity of Amazonian rainforests

Jian Bi, Yuri Knyazikhin, Sungho Choi, Taejin Park, Jonathan Barichivich, Philippe Ciais, Rong Fu, Sangram Ganguly, Forrest Hall, Thomas Hilker, Alfredo Huete, Matthew Jones, John Kimball, Alexei I. Lyapustin, Matti Mõttus, Ramakrishna R. Nemani, Shilong Piao, Benjamin Poulter, Scott R. Saleska, Sassan S. Saatchi, Liang Xu, Liming Zhou, and Ranga B. Myneni

This document provides Supplementary information not provided in the main text of the article "Sunlight Mediated Seasonality in Canopy Structure and Photosynthetic Activity of Amazonian Rainforests." It contains (*i*) Supplementary Data and Methods, which provides an extended description of the data and methods used; (*ii*) Supplementary Discussion related to various issues in previous studies that led to incorrect conclusions; (*iii*) Supplementary References; (*iv*) Supplementary Figures and (*v*) Supplementary Tables.

Supplementary Data and Methods

1. Study region and greening pixels

This study is focused on a 1200×1200 km^2 region in central Amazonia (MODIS tile "h11v09"; 0° to 10°S and 60°W to 70°W; figure S1(a)). About 95% of this region is covered with terra firme rainforests (Nepstad *et al* 1994). The average annual rainfall varies from about 1800 mm in the south to about 3700 mm in the northwest (figure S1(b)). The number of dry months, generally defined as months with rainfall less than 100 mm, varies from about 4 in the south to less than 2 in the northwest. For comparison purposes (Morton *et al* 2014), the dry season is defined as June to October (137 mm/month) and the wet season as November to May (276 mm/month). This is one of two tiles studied by (Morton *et al* 2014). Expanding the area to match that study did not alter our results and conclusions.

Terra MODIS and MISR data analysed in this study consisted of seven seasonal cycles (June to May), while the Aqua MODIS data consisted of four cycles, as in (Morton *et al* 2014). Forest pixels with valid Enhanced Vegetation Index (EVI) data are classified as greening pixels during a seasonal cycle if the average EVI value during the month of October is greater than the average EVI value during the month of June. Here, EVI refers to Terra MODIS Collection 5 EVI data (Section 2.5). The MODIS and MISR analyses in this study are focused on these "greening pixels" because we wish to address this key question: is the dry season greening purely an artefact of variations in sun-sensor geometry (Galvão *et al* 2011, Morton *et al* 2014) or does it reflect actual changes in canopy after accounting for variations in sun-sensor geometry (Xiao *et al* 2005, Huete *et al* 2006, Myneni *et al* 2007, Brando *et al* 2010, Samanta *et al* 2012)? The proportion of greening pixels varies from year to year. It averages ~60% of all rainforest pixels in the case of the Terra MODIS sensor (table S1) due to strict quality filtering. Nearly every rainforest pixel in the study region exhibits dry season greening at least once, if not more, because the data are accumulated, not averaged, over multiple seasonal cycles.

2. Data

2.1. TRMM Precipitation Data: Monthly precipitation data from the Tropical Rainfall Measuring Mission (TRMM) at quarter degree spatial resolution for the period January 1998 to December 2012 (TRMM product 3B43, Version 7) are used in this study (WWW-TRMM).

2.2. CERES Surface PAR Fluxes: Monthly at-surface Photosynthetically Active Radiation (PAR,

400-700 nm; the sum of "Computed PAR Surface Flux Direct – All-sky" and "Computed PAR Surface Flux Diffuse – All-sky") data at 1°×1° spatial resolution from June 2000 to May 2008 are used in this study (WWW-CERES).

2.3. CRU Temperature Data: The latest version of the 0.5° temperature data set produced by the Climatic Research Unit (CRU; University of East Anglia; CRU TS3.21) is used in this study (WWW-CRU).

2.4. MODIS Land Cover: Evergreen broadleaf forests in the study region are identified using the Collection 5 land cover data set "MODIS Land Cover Type Yearly L3 Global 500 m SIN Grid" (MCD12Q1) (WWW-MCD12Q1).

2.5. MODIS NIR Reflectance and EVI: The following Collection 5 EVI data are used in this study: (a) Terra Moderate Resolution Imaging Spectroradiometer (MODIS) EVI data from June 2000 to May 2008 (WWW-MOD13A2) and (b) Aqua MODIS EVI data from June 2003 to May 2008 (WWW-MYD13A2). Data from June 2005 to May 2006 are not used due to the dry season drought in 2005 (Samanta *et al* 2010a). These data sets also include surface reflectance at the near infrared (NIR) spectral band (858 nm) and sun-sensor measurement geometry. The data are at a spatial resolution of 1×1 km^2 and 16-day temporal frequency. The same EVI data were used in previous studies (Galvão *et al* 2011, Morton *et al* 2014). The quality of NIR reflectance and MODIS EVI data in each pixel is assessed using the 16-bit quality flags (Samanta *et al* 2010b, Xu *et al* 2011). The number of pixels with valid EVI data in June, October and March are shown in table S2.

2.6. MODIS MAIAC EVI: EVI data from Terra (June 2000 to May 2008) and Aqua (June 2003 to May 2008) MODIS sensors at 1×1 km^2 spatial resolution and 8-day temporal frequency generated with the Multi-angle Implementation of Atmospheric Correction (MAIAC) algorithm (Lyapustin *et al* 2012) are used in this study (WWW-MAIAC). The MAIAC EVI data are standardized to a fixed sun-sensor geometry (nadir viewing direction, solar zenith angle of 45^o). Thus, the MAIAC EVI data are free of sun-sensor geometry effects.

2.7. MODIS LAI: Collection 5 Leaf Area Index (LAI) data from Terra MODIS for the period June 2000 to May 2008 are used in this study (WWW-MOD15A2). Data from June 2005 to May 2006 are excluded from analyses of LAI seasonal changes (figures 1 and 2) due to the dry season drought in 2005 (Samanta *et al* 2010a). The data are at 1×1 km^2 spatial resolution and 8-day temporal frequency. Valid LAI data in each 1×1 km^2 8-day pixel are identified using quality flags (Samanta *et al* 2011, Poulter and Cramer, 2009).

2.8. MISR Bidirectional Reflectance Factor: Land Surface Data (version 22) from the Terra Multiangle Imaging Spectroradiometer (MISR) for the period June 2000 to May 2008 are used in this study (WWW-ASDC). Data from June 2005 to May 2006 are not used due to the dry season drought in 2005 (Samanta *et al* 2010a). The data are at a spatial resolution of 1.1 × 1.1 km^2 and include Bidirectional Reflectance Factors (BRF) at the nine MISR view angles (nadir, ±26.1°, ±45.6°, ±60.0° and ±70.5°) in four spectral bands (446, 558, 672, and 866 nm). MISR data with LandQA=0 (cloud free, aerosol optical depth below 0.3) are considered valid.

2.9. GLAS Centroid and Apparent Reflectance: Data from the Geoscience Laser Altimeter System (GLAS) instrument onboard the Ice, Cloud and land Elevation Satellite (ICESat) acquired during four periods – May 20 to June 23, 2005 (L3c), May 24 to June 26, 2006 (L3f), October 3 to November 8, 2004 (L3a) and October 2 to November 5, 2007 (L3i) – are used to analyze the sensitivity of the waveform centroid relative height (WCRH) and Apparent Reflectance (AR) to LAI (WWW-GLAS). The same data were used in (Morton *et al* 2014). For comparison purposes, low quality data were filtered as described in (Morton *et al* 2014). Additionally, GLAS footprints over non-forest and/or bare ground were screened by imposing the following conditions: (a) MODIS Land Cover corresponding to GLAS footprints is "Evergreen Broadleaf Forests" and (b) number of GLAS waveform Gaussian peaks exceeds one. GLAS lidar analysis is focused on the region spanning 0° to 10°S and 60°W to 80°W – the spatial extent of the blue and red squares in figure S1(a).

3. Sun-Sensor Geometry

Three angles characterize the sun-sensor geometry of a pixel (figure S1(c)): (a) solar zenith angle (SZA), (b) relative azimuth angle (RAA), and (c) view zenith angle (VZA). All three change

during the year in the case of MODIS. The distribution of these angles for pixels in the study region during each of the twenty-three 16-day compositing periods in a year is shown in figure 1 for Terra MODIS. The geometry for Aqua MODIS is very similar to that of Terra MODIS. The view zenith angles are fixed in the case of MISR. The following discussion of sun-sensor geometry is specific to this study's region (figure S1(a)).

The geometry in terms of SZA and RAA is approximately cyclical with a period of six months (figures 1(b) and (c)). Terra and Aqua MODIS and Terra MISR measurements are made at higher SZA ($\sim 30^o$ to 40^o) about the solstices, June/July and December/January, and at lower SZA ($\sim 20^o$ to 30^o) about the equinoxes, September/October and February/March (figure 1(b)). The progression of Terra and Aqua MODIS RAA during the year shows a similar cyclical behavior (figure 1(c)). The measurements are made closer to the solar azimuthal plane, or the principal plane, (RAA $\sim 0°$ and $180°$), about the equinoxes and approximately $\pm 30°$ to $\pm 45°$ off the orthogonal plane (RAA $\sim 130^o$ and 50^o) about the solstices (figure 1(c) and figure S2). View zenith angle varies between $0°$ (nadir) and $60°$ (figure 1(d)). The RAA of MISR sampling along the spacecraft flight track follows its Terra counterpart, but is shifted by about $90°$ (not shown). Half of Terra and Aqua MODIS observations about the solstices were collected at VZA below $15°$ and $20°$, respectively. Around 50% of the measurements about the equinoxes were made at VZA below $35°$ (Terra) and $20°$ (Aqua). The MISR VZAs are strongly peaked as expected around their nominal values of $0.0°$, $\pm 26.1°$, $\pm 45.6°$, $\pm 60.0°$ and $\pm 70.5°$ (figure S2).

Choosing three 16-day composites, one each in June (Jun 25 to Jul 10), October (Oct 15 to 30) and March (Mar 5 to 20), is sufficient to assess whether the previously reported seasonality in radiometric greenness (Xiao *et al* 2005, Huete *et al* 2006, Brando *et al* 2010) and leaf area (Myneni *et al* 2007, Samanta *et al* 2012) of Amazonian rainforests is an artefact of sun-sensor geometry (Galvão *et al* 2011, Morton *et al* 2014) or not. The three periods correspond to the beginning of the dry season, end of the dry season and mid wet season, respectively. The Terra and Aqua MODIS observations provide pairs of matching RAA (October vs. March), varying RAA (June vs. October), matching SZA (Terra and Aqua in June and March), varying SZA (October from Terra and Aqua) (figure S2). The Terra MISR sensor samples the surface close to the principal plane in June and near the orthogonal plane in October and March. This manner of sampling is opposite to that of MODIS (figure S2). The juxtaposition of MODIS and MISR sampling provides an interesting opportunity for assessing the presence or absence of seasonal variations in these rainforests.

4. Forest Reflectance

4.1. Bidirectional Reflectance Factor (BRF): The reflected radiation field from a vegetation canopy illuminated by a solar beam in a coordinate system with the polar axis pointed to the sun is considered here. The reflected radiance is expressed relative to a surface perpendicular to the solar beam and depends on the phase angle, γ, and azimuth, ψ. The phase angle is the angle between the directions to the sun and sensor (figure S1(c)). The plane ψ is chosen such that the phase angle varies between $-(90° + \theta_0)$ and $+(90° - \theta_0)$ where θ_0 is the sun zenith angle. In this coordinate system the Bidirectional Reflectance Factor, $BRF(\gamma, \psi)$, is the ratio of radiance reflected from the vegetation canopy to the radiance reflected from an ideal Lambertian surface under identical illumination conditions. The Lambertian surface in this instance is perpendicular to the solar beams. For a plane given by ψ and $\psi + 180°$, the BRF is a function of SZA, phase angle and wavelength. Its magnitude and angular shape depends on the composition, density, geometric structure of the reflecting medium, in addition to the foliage optical properties.

4.2. Transformation of MODIS and MISR BRF data: Let $BRF_{xy}(\theta_0, \theta_v, \Delta\varphi)$ be the observed BRF at a location (x, y) on the Earth's surface. The BRF_{xy} is a standard product of MODIS and MISR sensors, which is expressed relative to a horizontal surface. The sun-sensor geometry is represented by the sun, θ_0, and sensor, θ_v, view zenith angles, and the view azimuth φ_v (figure S1(c)). First, we introduce a new coordinate system with the polar axis pointed to the sun. The quantities, $I_{xy} = BRF_{xy} \cos\theta_0$, represent radiances reflected from forests illuminated by a

parallel beam of unit intensity. The radiances are expressed relative to the unit surface perpendicular to the solar beam and depend on the phase angle, γ, and azimuth, ψ, in this system. The phase angle is the angle between directions to the sun and sensor, i.e., $\gamma = \text{acos}[\cos\theta_v \cos\theta_0 + \sin\theta_v \sin\theta_0 \cos\varphi_v]$.

Second, we group I_{xy} with respect to the phase angle (figure S3). This procedure transforms the standard BRF product into BRF expressed in terms of the phase angle, γ, and azimuth, ψ. The azimuth specifies sampling plane of satellite-borne sensors. The MODIS instrument scans the Earth across the Terra and Aqua spacecraft flight track, which is approximately from East to West (figure S3(a)). The MISR instrument measures reflected radiation along the Terra flight track, which is approximately from North to South (figure S3(b)). The sampling planes are fixed for MODIS and MISR instruments. We assign the sign "plus" to γ if the direction to the sensor approaches the direction to sun from East (Terra MODIS), West (Aqua MODIS) or North (Terra MISR), and "minus" otherwise. The phase angle varies between $-(90° + \theta_0)$ and $90° - \theta_0$. The probability density distribution function $p(\theta_0, \gamma)$ of the phase angle is evaluated from the fraction of data in each group.

Finally, the reflected radiances in each group are averaged. This methodology is applied to transform standard BRF products from Terra and Aqua MODIS observations (figure S3(a)). In the case of MISR, the algorithm is applied to each MISR camera to derive camera specific BRF (figure S3(b)) and corresponding probability density functions. The camera specific BRFs for which $|\gamma - \bar{\gamma}| \leq \sigma$ are used in further analyses. Here $\bar{\gamma}$ and σ denote camera specific mean and standard deviation of the phase angle γ.

4.3. Effect of Changing Canopy Properties on BRF: figures S5(a) and (b) illustrate the effect of changing canopy properties on BRF. Here, SZA is held constant. An increase in LAI, with leaf optical properties unchanged, increases the interception of incoming solar radiation by the vegetation canopy, which in turn increases the amount of reflected radiation. This increases the magnitude of BRF at all phase angles, i.e. a non-linear upward shift in the angular signature of the BRF, as shown in figure S5(b). The overall shape of the BRF remains unchanged. This is a well-known fact: the reflectance of dense vegetation, or a vegetation canopy with a dark background, is an increasing function of LAI (e.g. figure 1 in (Huang *et al* 2008)). Changes in leaf optical properties either augment or suppress the LAI effect on the reflectance factor (Samanta *et al* 2012). Thus, changing canopy properties and holding SZA constant changes the magnitude of the BRF but not the overall shape of the signature. This explains the observed BRF changes in figures 3(a) and (b).

4.4. Effect of Changing SZA on BRF: figures S5(c) and (d) illustrate the effect of changing SZA on BRF. Here, canopy properties are held constant. The cumulative contribution of within-canopy sources generated by single- and multiple-scattered photons to canopy-exiting radiation along a given direction increases with photon path length, L, as $\sim(1 - \exp(-\sigma L))$, where L is the distance between sources within the canopy and the upper boundary of the canopy and σ is the extinction coefficient. An increase in SZA results in longer photon path lengths for positive phase angles (figure S5(c)). The opposite is true for negative phase angles. Increasing SZA with constant canopy therefore results in an asymmetric transformation of the BRF signature, that is, enhanced values for positive phase angles and depressed values for negative phase angles (figure S5(d)). It also decreases the range of BRF variation at positive phase angles and a corresponding increase in the range of BRF variation at negative phase angles. Thus, both the shape and magnitude of the BRF signature are changed. The asymmetric transformation also causes the two BRF signatures to intersect, as illustrated in figure S5(d). The phase angle at which the two signatures intersect can be calculated using the principle of directional reciprocity (Section 4.6).

It is important to note that the path L varies with SZA as $\sim 1/\cos(SZA)$. It means that effect of changing SZA on the BRF's angular shape is weak at low SZA. For example, a change in SZA from 20° to 30° involves a change in L from ~1.06 to ~1.15. The impact, however, increases with SZA. This explains why SZA variation has no discernable impact on the angular signatures of reflectances in figures 3(a) and (b).

4.5. Effect of Changing Canopy Properties and SZA on BRF: figures S5(e) and (f) illustrate the effect of changing both canopy properties and SZA on BRF. Changing canopy properties but holding SZA constant changes the magnitude of BRF but retains its overall angular shape (Section 4.3). Changing SZA but holding canopy properties invariant changes the magnitude of BRF differently for positive and negative phase angles, thus changing the shape of the BRF as well (Section 4.4). Changing canopy properties and SZA simultaneously combines these two effects, i.e. the BRF is transformed asymmetrically and shifted in magnitude. For example, decreasing SZA depresses the BRF at positive phase angles and enhances the same at negative phase angles – transformation of the green colored BRF signature to dashed-blue color signature in figure S5(f). Increasing canopy properties, say LAI and/or foliage optical properties, shifts the overall BRF signature up in magnitude – transformation of the dashed-blue color signature to solid-blue color signature in figure S5(f). This explains the BRF signature changes in figures 3(c) and (d). Importantly, it follows from this argumentation that *higher or equal values of BRF at lower SZA relative to BRFs at higher SZA always indicate a change in canopy properties*.

4.6. Proof of Dry Season Changes From the Directional Reciprocity Principle: The optical reciprocity theorem (Davis and Knyazikhin, 2005) provides a proof relevant to our study. It states that switching detector and source and inverting the directions of propagation yield the same result for BRF. It follows from the theorem that the BRFs of a canopy, or two similar canopies, corresponding to different sun positions, say Ω_0 and Ω_1, necessarily intersect at $\gamma_0 = -\text{acos}(\Omega_0 \cdot \Omega_1)$. Indeed, the BRF in direction Ω_1 due to a mono-directional solar beam in direction $-\Omega_0$ is related to the BRF in direction Ω_0 due to a mono-directional solar beam in direction $-\Omega_1$ as $BRF(-\Omega_0, +\gamma) = BRF(-\Omega_1, -\gamma)$. If $BRF(-\Omega_0, \gamma)$ is symmetric at $\gamma_0 = \text{acos}(\Omega_0 \cdot \Omega_1)$ (e.g., as in October), the BRFs should intersect at $\gamma_0 = -\text{acos}(\Omega_0 \cdot \Omega_1)$. Changing canopy properties with illumination conditions unchanged results in an upward or downward shift in the angular signature of the BRF (Section 4.5). This causes the intersection point to deviate from γ_0, indicating a difference in canopy properties. The deviation of the intersection point around $-5.5°$ from $\gamma_0 = -37.1°$ shown in figure 3(d) is significant, indicating *different canopy properties in June and October*.

Supplementary Discussion

Galvão *et al* (2011) and Morton *et al* (2014) claim that previous studies (Xiao *et al* 2005, Huete *et al* 2006, Myneni *et al* 2007, Brando *et al* 2010, Samanta *et al* 2012) misinterpreted changes in near-infrared (NIR) reflectance caused by seasonal changes in sun-satellite sensor geometry as seasonal variations in rainforest canopy structure and greenness. They conclude that Amazonian rainforests maintain consistent structure and greenness during the dry season based on their analysis of satellite borne sensor data (MODIS and Lidar) and model exercises. Here we present a detailed critique of their analysis.

An incomplete analysis of the seasonal cycle, i.e. one that is focused only on the dry season, encourages misleading interpretation of both intra- and inter-annual greenness (EVI or LAI) variations as artefacts of changing sun-sensor geometry. For example, if the sun-sensor geometry artefact argument is valid, then the seasonal course of LAI from December to May should be similar to that from June to November because of a repeat in sun-sensor geometry (figures 1(b) and (c)), but it is not (figure 1(a)). Also, if the change in MODIS sampling from the orthogonal plane in June to the principal plane in October (figures S2(a) and (c)) causes the rainforests to appear greener, then the change in MISR sampling from the principal plane in June to the orthogonal plane in October (figures S2(b) and (d)) should cause the rainforests to appear browner. But, greening is observed as well (figure 3(d)).

Interannually, the attribution of anomalous dry season greening (increase in EVI or LAI) in drought year 2005, *vis a vis* dry seasons of non-drought years, to a higher proportion of brighter backscattering MODIS observations is flawed because it is selectively based on data from the first fortnight of October (ED-figure 9 (Morton *et al* 2014)). A higher fraction of backscattering measurements is not seen in 2005 when the analysis is focused on July to September period

(figure S4(b)) as in the original studies (Samanta *et al* 2010a, Samanta *et al* 2010b, Saleska *et al* 2007). Moreover, if claims of geometric artefacts are true, higher backscatter fraction and greenness should also be seen during the more intense dry season drought in 2010 (Xu *et al* 2011). They are not (figure S4(b)), even in their selective analysis (ED-figure 9 (Morton *et al* 2014)).

Crucially, the misinterpretations in Morton *et al* (2014) stem from reliance on prognostications of an untested radiative transfer model. In a critical test of how well the model simulates variation in sunlit and shaded proportions of the canopy, which is central to arguments about geometric artefacts, the model underestimates measurements by ~45% (figure S4(c)). The model is also unrealistically sensitive to litter reflectance in dense vegetation (table 1 (Morton *et al* 2014)), an indication of incorrect physics and/or modeling of foliage spatial distribution. The failure to test the model is compounded by an unquestioned belief in its validity, else the observed dry season greening in geometry-corrected EVI would not have been ignored (figure 3(b) (Morton *et al* 2014) and ED-figure 7(b) (Morton *et al* 2014)). Various statistical analyses of this geometry-corrected EVI data strongly reject the null hypothesis of no change in forest greenness (Saleska *et al* 2015). Indeed the physics of radiative transfer in dense media (Section 2.9 (Knyazikhin *et al* 1999)) informs that these changes in geometry-corrected EVI (figure 2, figure 3(b) in (Morton *et al* 2014) and ED-figure 7(b) in (Morton *et al* 2014)) correspond to large changes in LAI (figure. 1(a)). Thus, there is no valid statistical or theoretical basis to dismiss dry season increase in geometry-corrected EVI (figure 2(b), figure 3(b) in (Morton *et al* 2014) and ED-figure 7(b) in (Morton *et al* 2014)).

The unorthodox belief that Amazonian rainforests should conform to model predictions affects their interpretation of satellite lidar data also. The conclusion that structure and greenness of rainforests remain invariant does not follow from absence of evidence in lidar data for their model prediction that an increase in LAI from 4.5 to 6.5 should result in an increase in Waveform Centroid Relative Height - the height of median return energy relative to the full waveform extent (WCRH; table 1 in (Morton *et al* 2014)). A prudent interpretation might be that the model prediction does not conform to data. Even if the model is assumed to be capable of accurate predictions, the predicted change in WCRH (0.06) is comparable to the spatial standard deviations of June and October WCRH data (~0.07). This clearly suggests a need for additional analysis.

The lack of insight into what might be reasonably expected from lidar data and saturation of lidar signals in dense vegetation compound the problem of detecting seasonal LAI changes. For example, studies that have investigated the relationship between LAI and lidar waveforms (Castillo *et al* 2012, Tang *et al* 2012, Drake *et al* 2002) show that WCRH saturates in mature and secondary growth tropical forests aged over ~20 years (Tang *et al* 2012, Drake *et al* 2002) because the majority of lidar hits are confined to the upper canopy. This saturation of signals emanating from vegetation is different than sensor saturation (Neuenschwander *et al* 2008) – the latter have been filtered out from all analyses.

The saturation effect can be potentially documented through these three analyses. First, although a range of LAI values are observed in Amazonian rainforests, from about 4 to 6 in June and greater than 6 in October, the two lidar metrics, WCRH and Apparent Reflectance (AR), exhibit no correspondent variations (figure S6). Second, rainforests with low (3.5 to 4.5) and high (greater than 5.5) LAI have the same WCRH and AR (figures S7 (a) and (b)). Third, rainforests with low (<0.5) and high (>0.6) WCRH have the same LAI (figure S7(c)). Likewise, rainforests with low (<0.5) and high (>0.6) AR have identical LAI (figure S7(d)). Inference of saturation from figure S6 and figures S7 (a)–(d) depends on the validity of the MODIS LAI data. To alleviate this concern, we present similar results for deciduous broadleaf forests where a broader range of LAI values are encountered. The curvilinear relationship in deciduous forests, where WCRH increases for LAI values 0 to 3 and saturates thereafter (figures S8(a) and (c)), is as expected, and is similar to other relations between LAI and remote measurements (Knyazikhin *et al* 1999, Huang *et al* 2008).

Unlike WCRH, the AR shows no relationship to LAI (figures S6 (b) and (d), figures S8 (b) and (d)), even in sparsely foliated canopies (LAI less

than 3; figures S8 (b) and (d)). Also, the inverse relationship with WCRH is perplexing (figures S7 (e) and (f)). To ascertain whether these results indicate potential data quality problems, we investigated the relationship between the lidar metrics and key climatic variables that govern plant growth, i.e. water, radiation and temperature (Nemani *et al* 2003). The WCRH data are positively related (p-value < 0.001) to all three climatic variables (table S4). This is as it should be, i.e. tall and dense tree stands with higher WCRH are located in climatically favorable environments of higher annual precipitation, solar radiation and mean temperature (table S4). The AR data, on the other hand, show negative relation with two of the three climatic variables. We therefore conclude that GLAS AR data have quality problems.

Morton *et al* (2014)'s interpretations of AR data are contradictory - on the one hand, their validity is discounted by citing corruption from aerosols due to biomass burning, and on the other hand, their invariance is counted as proof that Amazonian rainforests maintain consistent structure and greenness (figure 2(c) (Morton *et al* 2014)). Why table 1 (Morton *et al* 2014) does not show model predictions of AR seasonal variations, unlike WCRH, is unknown. Given these ambiguities, their analyses of AR data must also be deemed inconclusive.

In addition to the analyses presented in this article, three independent studies have rebutted Galvão *et al* (2011) and Morton *et al* (2014) claims with a multitude of satellite and in situ data (Maeda *et al* 2014, Hilker *et al* 2014, Jones *et al* 2014). Dry season greening in sun-sensor geometry corrected data obtained from Morton et al. is due for publication (Saleska *et al* 2015).

Supplementary References

Brando P M, Goetz S J, Baccini A, Nepstad D C, Beck P S and Christman M C 2010 Seasonal and interannual variability of climate and vegetation indices across the Amazon. *Proc. Natl. Acad. Sci. USA.* **107** 14685–14690

Castillo M, Rivard B, Sánchez-Azofeifa A, Calvo-Alvarado J and Dubayah R 2012 LIDAR remote sensing for secondary Tropical Dry Forest identification. *Remote Sens. Environ.* **121** 132–143

Davis A B and Knyazikhin Y 2005 A primer in 3D radiative transfer. *Three Dimensional Radiative Transfer in the Cloudy Atmosphere*, eds Marshak A, Davis A B (Springer-Verlag, Berlin Heidelberg), pp 153-242

Drake J B, et al. 2002 Estimation of tropical forest structural characteristics using large-footprint lidar. *Remote Sens. Environ.* **79** 305–319

Galvão L S, Dos Santos J R, Roberts D A, Breunig F M, Toomey M and de Moura Y M 2011 On intra-annual EVI variability in the dry season of tropical forest: A case study with MODIS and hyperspectral data. *Remote Sens. Environ.* **115** 2350–2359

Hilker T *et al* 2014 Vegetation dynamics and rainfall sensitivity of the Amazon. *Proc. Natl. Acad. Sci. USA.* **111** 16041–16046

Huang D *et al* 2008 Stochastic transport theory for investigating the three-dimensional canopy structure from space measurements. *Remote Sens. Environ.* **112** 35–50

Huete A R *et al* 2006 Amazon rainforests green-up with sunlight in dry season. *Geophys. Res. Lett.* **33** L06405

Jones M O, Kimball J S and Nemani R R 2014 Asynchronous Amazon forest canopy phenology indicates adaptation to both water and light availability. *Environ. Res. Lett.* **9** 124021

Knyazikhin Y *et al* 1999 *MODIS leaf area index (LAI) and fraction of photosynthetically active radiation absorbed by vegetation (FPAR) product (MOD15) algorithm theoretical basis document*, <https://lpdaac.usgs.gov/products/modis_products_table/mcd15a2>

Lyapustin A I *et al* 2012 Multi-angle implementation of atmospheric correction for MODIS (MAIAC): 3. Atmospheric correction. *Remote Sens. Environ.* **127** 385–393

Maeda E E, Heiskanen J, Aragão L E O C and Rinne J 2014 Can MODIS EVI monitor ecosystem productivity in the Amazon rainforest? *Geophys. Res. Lett.* **41** 7176–7183

Morton D C *et al* 2014 Amazon forests maintain consistent canopy structure and greenness during the dry season. *Nature* **506** 221–224

Myneni R B *et al* 2007 Large seasonal swings in leaf area of Amazon rainforests. *Proc. Natl. Acad. Sci. USA* **104** 4820–4823

Nemani R R *et al* 2003 Climate-driven increases in global terrestrial net primary production from 1982 to 1999. *Science* **300** 1560–1563

Nepstad D C *et al* 1994 The role of deep roots in the hydrological and carbon cycles of Amazonian forests and pastures *Nature* **372** 666–669

Neuenschwander A L, Urban T J, Gutierrez R and Schutz B E 2008 Characterization of ICESat/GLAS waveforms over terrestrial ecosystems: Implications for vegetation mapping. *J. Geophys. Res. Biogeosci.* **113** G02S03

Poulter B and Cramer W 2009 Satellite remote sensing of tropical forest canopies and their seasonal dynamics. *Int. J. Remote Sens.* **30** 6575–6590

Saleska S R *et al* 2015 Dry-season greening of Amazon forests. Brief Communications Arising in *Nature* (in press)

Saleska S R, Didan K, Huete A R and Da Rocha H R 2007 Amazon forests green-up during 2005 drought. *Science* **318** 612–612

Samanta A *et al* 2010a Amazon forests did not green-up during the 2005 drought. *Geophy. Res. Lett.* **37** L05401

Samanta A *et al* 2012 Seasonal changes in leaf area of Amazon forests from leaf flushing and abscission. *J. Geophys. Res. Biogeosci.* **117** G01015

Samanta A, Costa M H, Nunes, E L, Vieira S A, Xu, L and Myneni R B 2011 Comment on "Drought-Induced Reduction in Global Terrestrial Net Primary Production from 2000 Through 2009". *Science* **333** 1093

Samanta A, Ganguly S and Myneni R B 2010b MODIS Enhanced Vegetation Index data do not show greening of Amazon forests during the 2005 drought. *New Phytol.* **189** 11–15

Tang H *et al* 2012 Retrieval of vertical LAI profiles over tropical rain forests using waveform lidar at La Selva, Costa Rica. *Remote Sens. Environ.***124** 242–250

WWW-ASDC. NASA Langley Research Center Atmospheric Science Data Center (ASDC) Home page. Available at https://eosweb.larc.nasa.gov/

WWW-CERES. Atmospheric Science Data Center: The Clouds and the Earth's Radiant Energy System (CERES). Available at https://eosweb.larc.nasa.gov/project/ceres/ceres_table

WWW-CRU. Climatic Research Unit (CRU) Time-Series High-Resolution Gridded Datasets. Available at http://www.cru.uea.ac.uk/cru/data/hrg/

WWW-GLAS. Geoscience Laser Altimeter System (GLAS) lidar waveform data. Available at https://nsidc.org/data/icesat/data-dictionaries-landing-page.html

WWW-MAIAC. MAIAC Amazon Data. *Level 1 and Atmosphere Archive and Distribution System (LAADS)*. Available at ftp://ladsweb.nascom.nasa.gov/MAIAC/

WWW-MCD12Q1. Land Cover Type Yearly L3 Global 500 m SIN Grid (MCD12Q1). *Land Process Distributed Active Archive Center*. Available at https://lpdaac.usgs.gov/products/modis_products_table/mcd12q1

WWW-MOD13A2. Vegetation Indices 16-Day L3 Global 1km (MOD13A2). *Land Process Distributed Active Archive Center*. Available at https://lpdaac.usgs.gov/products/modis_products_table/myd13a12

WWW-MOD15A2. Leaf Area Index - Fraction of Photosynthetically Active Radiation 8-Day L4 Global 1km (MOD15A2). *Land Process Distributed Active Archive Center.* Available at https://lpdaac.usgs.gov/products/modis_products_table/mod15a12

WWW-MYD13A2. Vegetation Indices 16-Day L3 Global 1km (MYD13A2). *Land Process Distributed Active Archive Center*. Available at https://lpdaac.usgs.gov/products/modis_products_table/myd13a12

WWW-TRMM. Tropical Rainfall Measuring Mission (TRMM) data. *Goddard Earth Science Data and Information Center*. Available at http://mirador.gsfc.nasa.gov/

Xiao X *et al* 2005 Satellite-based modeling of gross primary production in a seasonally moist tropical evergreen forest. *Remote. Sens. Environ.* **94** 105–122

Xu L *et al* 2011 Widespread decline in greenness of Amazonian vegetation due to the 2010 drought. *Geophy. Res. Lett.* **38** L07402

Yang W *et al* 2006 MODIS leaf area index products: From validation to algorithm improvement. *IEEE Trans. Geosci. Remote. Sens.* **44** 1885–1898

Supplementary Figures

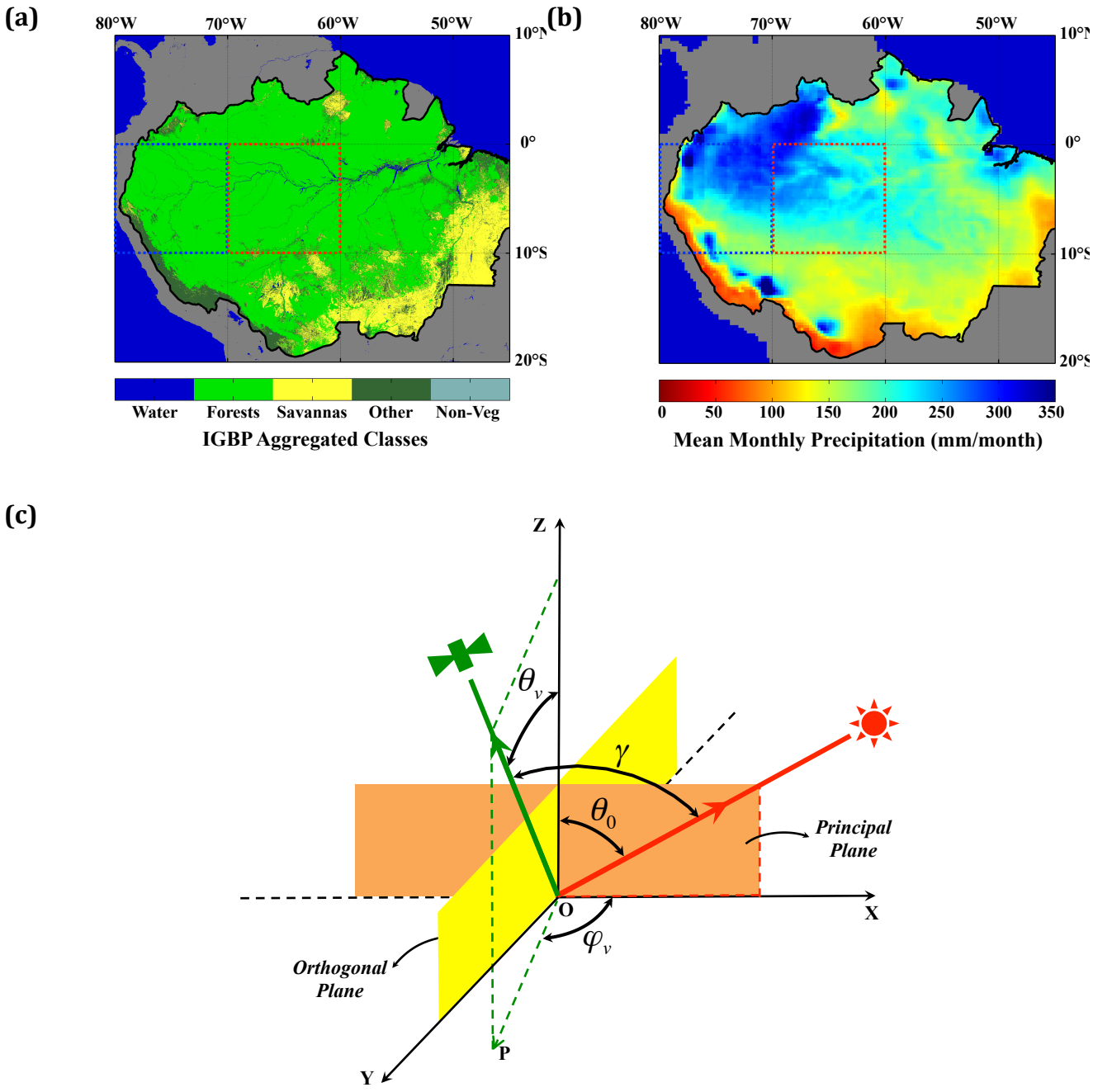

Figure S1. The study domain and sun-sensor geometry. (a) The domain of MODIS and MISR analysis is the red square. The domain of GLAS lidar analysis is both blue and red squares. (b) Monthly mean rainfall from TRMM. (c) Three angles characterize the sun-sensor measurement geometry of a pixel: (1) solar zenith angle, SZA=θ_0 ($0° < \theta_0 \leq 90°$), (2) view zenith angle, VZA=θ_v ($0° \leq \theta_v \leq 90°$) and (3) view azimuth, φ_v ($0° \leq \varphi_v \leq 360°$), measured relative to the principal plane. The angle between the projection, OP, of the direction to the sensor and X axis is the relative azimuth angle (RAA), i.e., RAA=φ_v if $0 \leq \varphi_v < 180°$ and RAA=$360° - \varphi_v$, otherwise. It varies between 0° and 180°. The angle between the directions to the sun and sensor is the phase angle, PA=γ.

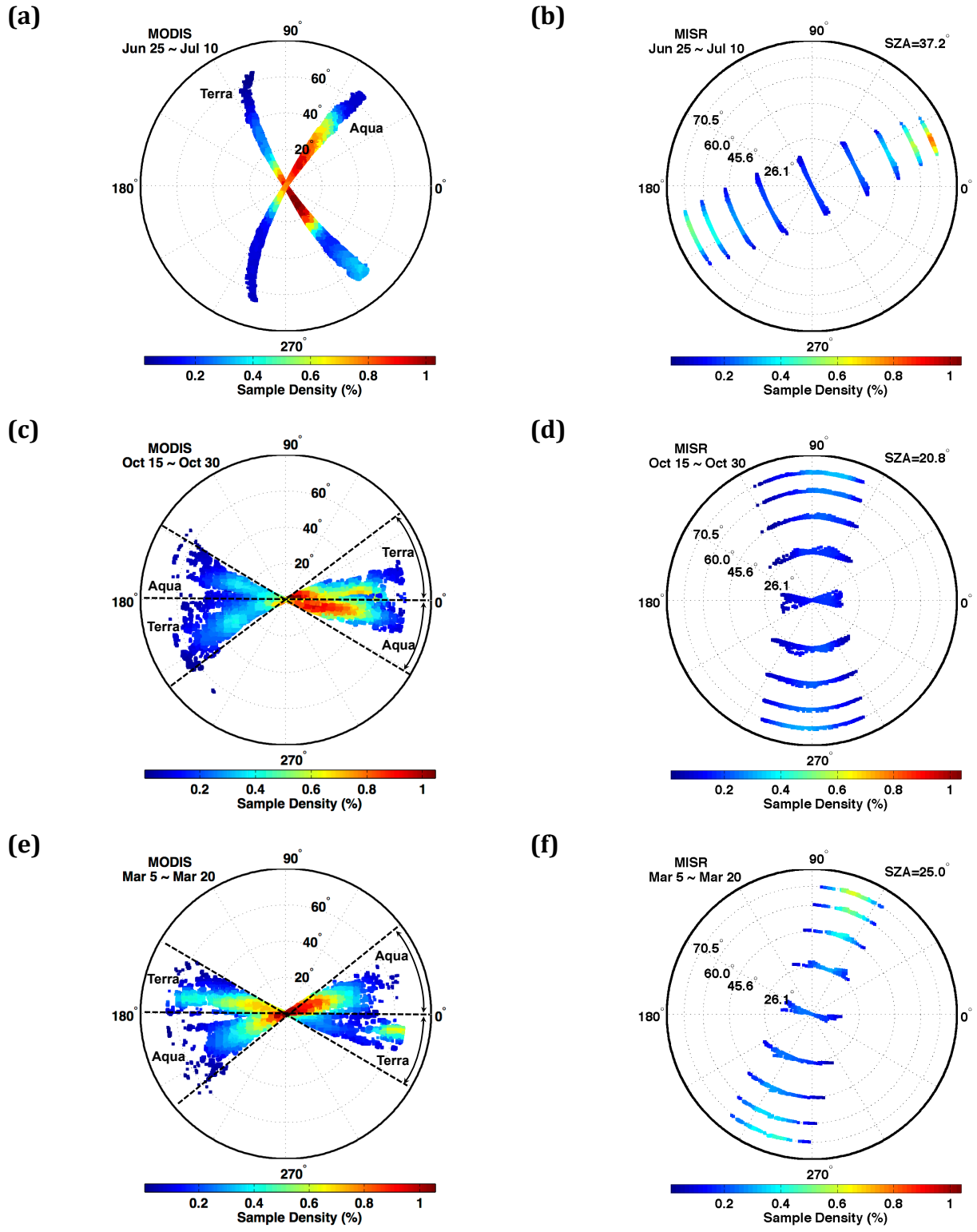

Figure S2. MODIS and MISR sampling geometries. Terra and Aqua MODIS (left panels) and Terra MISR (right panels) sampling geometries during a 16-day compositing period in the months of (a, b) June 2003, (c, d) October 2003, and (e, f) March 2003. The MODIS sensors sample the surface close to the orthogonal plane in June and near the principal plane in October and March. This sampling is opposite to that of MISR sensor.

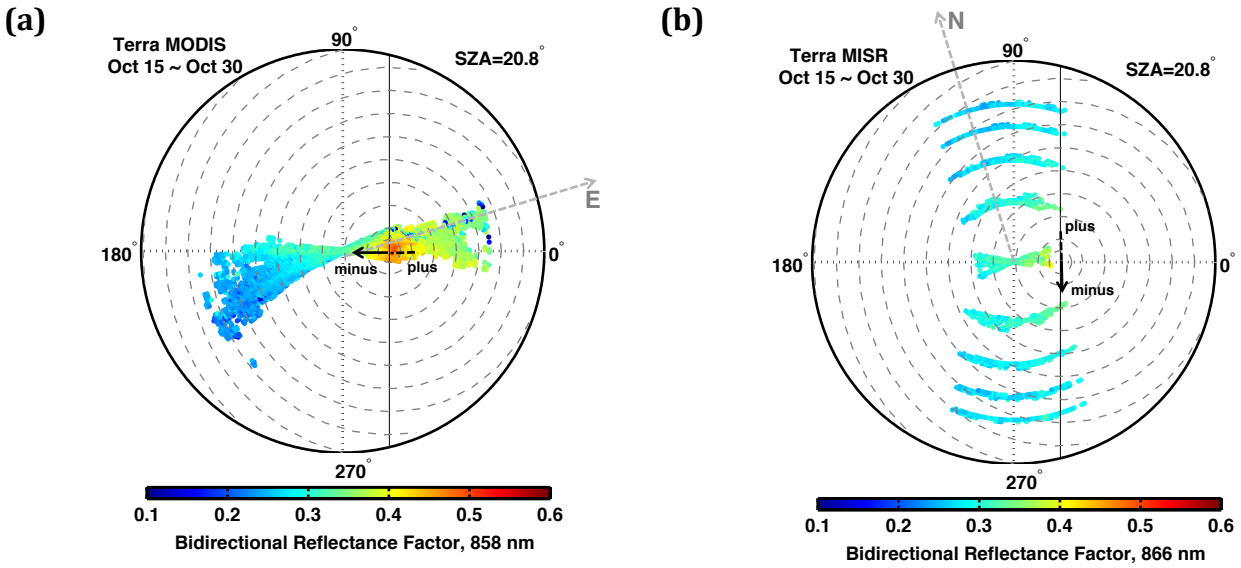

Figure S3. MODIS and MISR reflectances in a modified coordinate system. Terra MODIS (a) and MISR (b) NIR BRFs during a 16-day composite in October 2003. BRF values are expressed in a coordinate system with the polar axis pointed to the Sun. Solid arrows indicate sampling direction that determines the phase angle sign (angle between solar and sensor view directions).

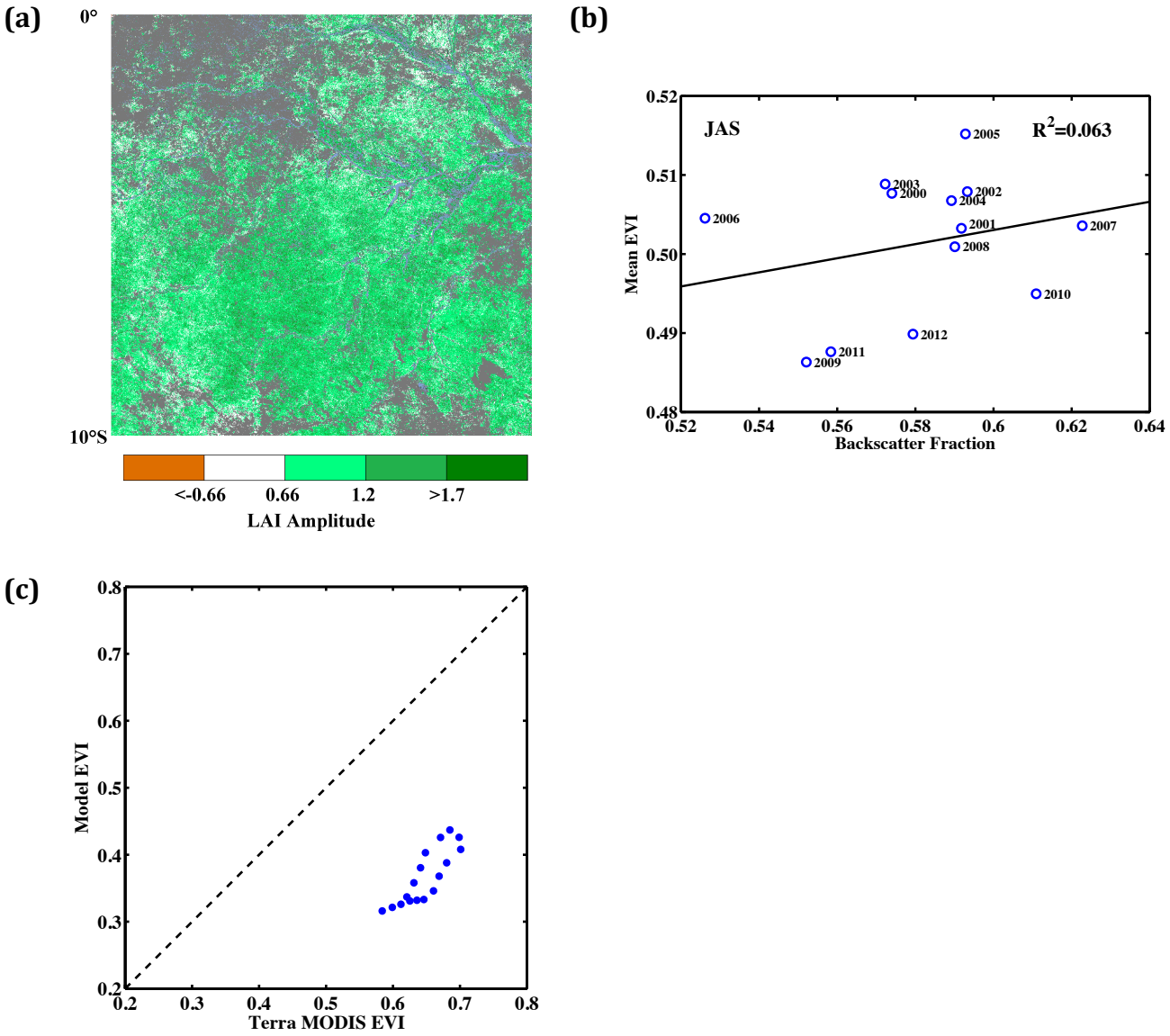

Figure S4. Evidence for seasonality of leaf area and misinterpretation of data following the guidance of an erroneous radiative transfer model (Morton *et al* 2014). (a) Spatial pattern of seasonal Terra MODIS LAI amplitude expressed as the difference between the maximum value during September to November and the minimum value during the following May to June period. White pixels denote locations with LAI amplitudes less than |0.66|, which is the accuracy of MODIS LAI data (Yang *et al* 2006). White and colored pixels together denote pixels that exhibited dry season greening in at least 4 out of 7 seasonal cycles (63% of all forest pixels in the study region). (b) Mean Terra MODIS EVI over rainforests as a function of backscattering fraction evaluated from all 16-day compositing periods in July, August and September (DOY 177 to 272). The backscattering fraction is defined (Morton *et al* 2014) as the fraction of observations with view azimuth less than 90° and greater than 270°. (c) Comparison of model simulated EVI (obtained by digitizing figure 1(c) in Morton *et al* (2014)) with Terra MODIS EVI over Amazonian rainforests. The MODIS EVI is from a 16-day October composite (15th to the 30th) accumulated over 7 seasonal cycles (Section 2.5). The comparison is for phase angles in the range ±10°, that is, ±10° around the hot spot (view zenith angles from 10° to 30° in figure 1(c) of (Morton *et al* 2014)).

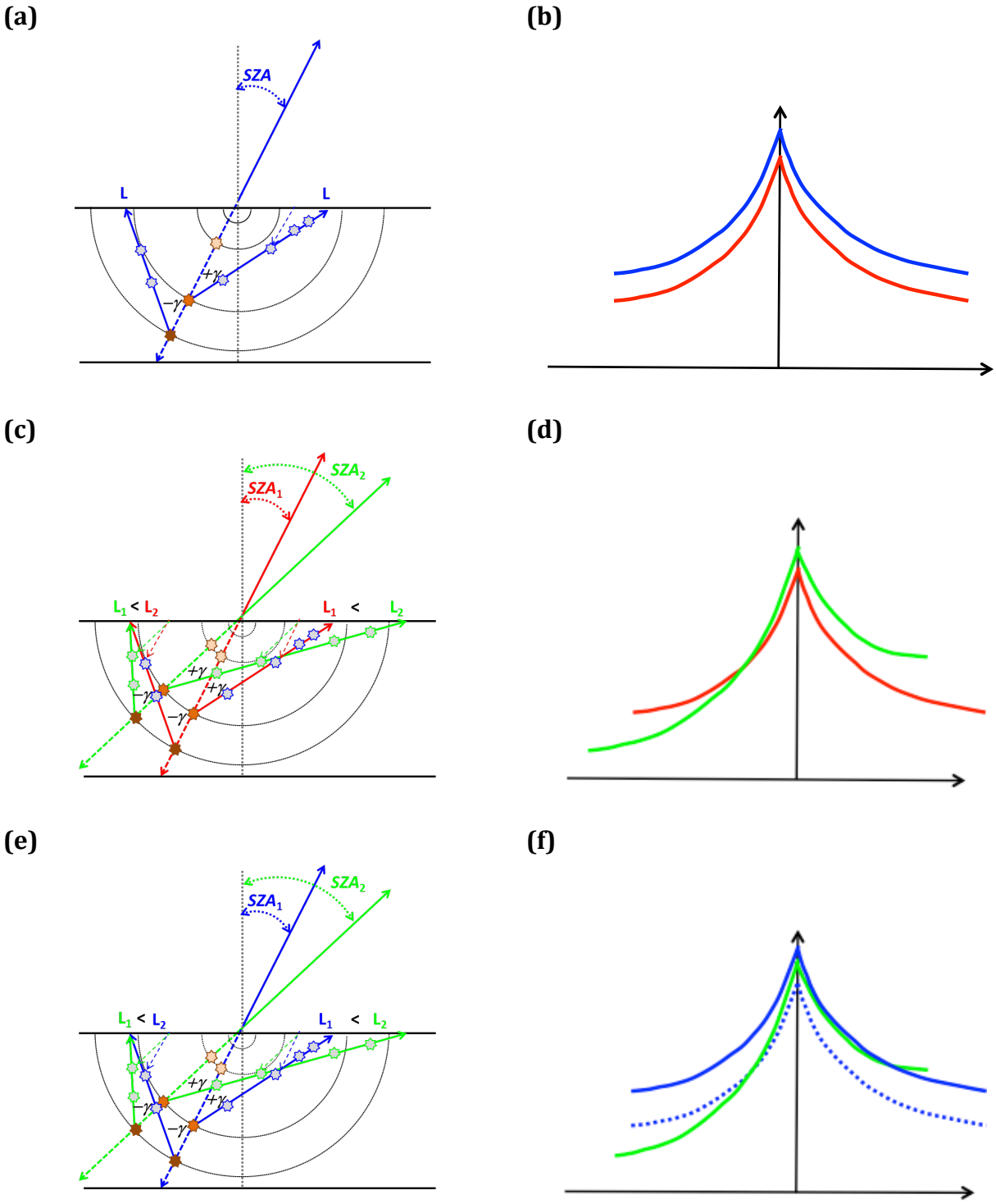

Figure S5. Interpretation of angular signatures of reflectance. Illustration of how the angular signature of Bidirectional Reflectance Factors (BRF) is transformed when (a, b) sun-sensor geometry is held invariant but canopy properties are changed; (c, d) sun-sensor geometry is changed but canopy properties are held invariant; (e, f) both sun-sensor geometry and canopy properties are changed. The dashed arrows depict direction of incident parallel beam of unit intensity.

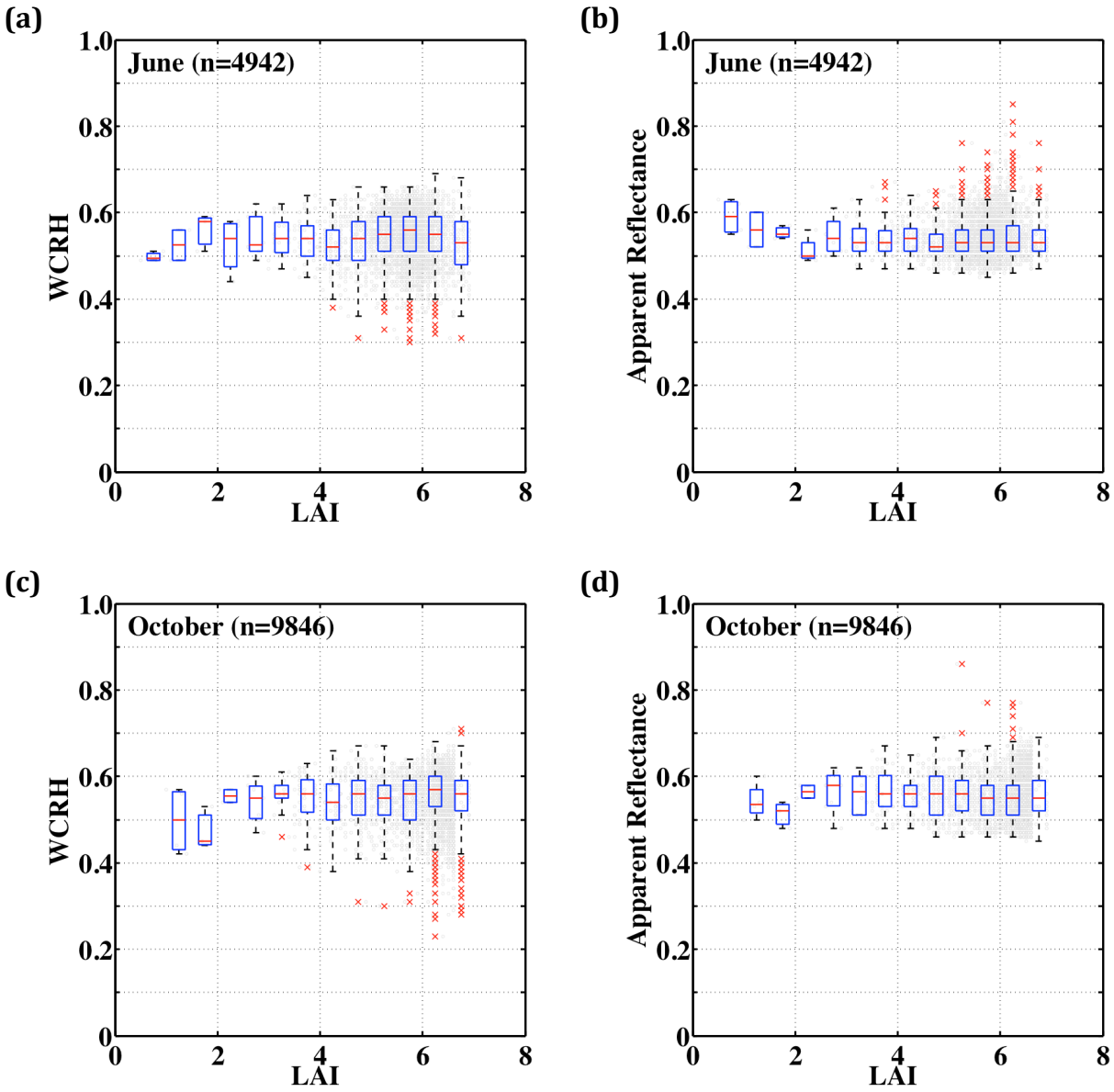

Figure S6. Saturation of GLAS lidar metrics over central Amazonian forests. Distributions of GLAS Waveform Centroid Relative Height (WCRH) and Apparent Reflectance as a function of Terra MODIS LAI in the case of central Amazonian rainforests at the (a, b) beginning and (c, d) end of the dry season. Gray dots and red crosses show distributions of lidar metrics within 0.5 LAI bins. Upper, middle (red line) and lower box edges show the 75%, 50% and 25% percentiles of GLAS metrics. The red crosses are outliers, each representing upper and lower 0.25% of the GLAS lidar observations. June represents data from May-20 to June-23, 2005 and May-24 to June-26, 2006. October represents data from October-3 to November-8, 2004 and October-2 to November-5, 2007. MODIS pixels with valid LAI values and four or more GLAS lidar observations were used (table S3).

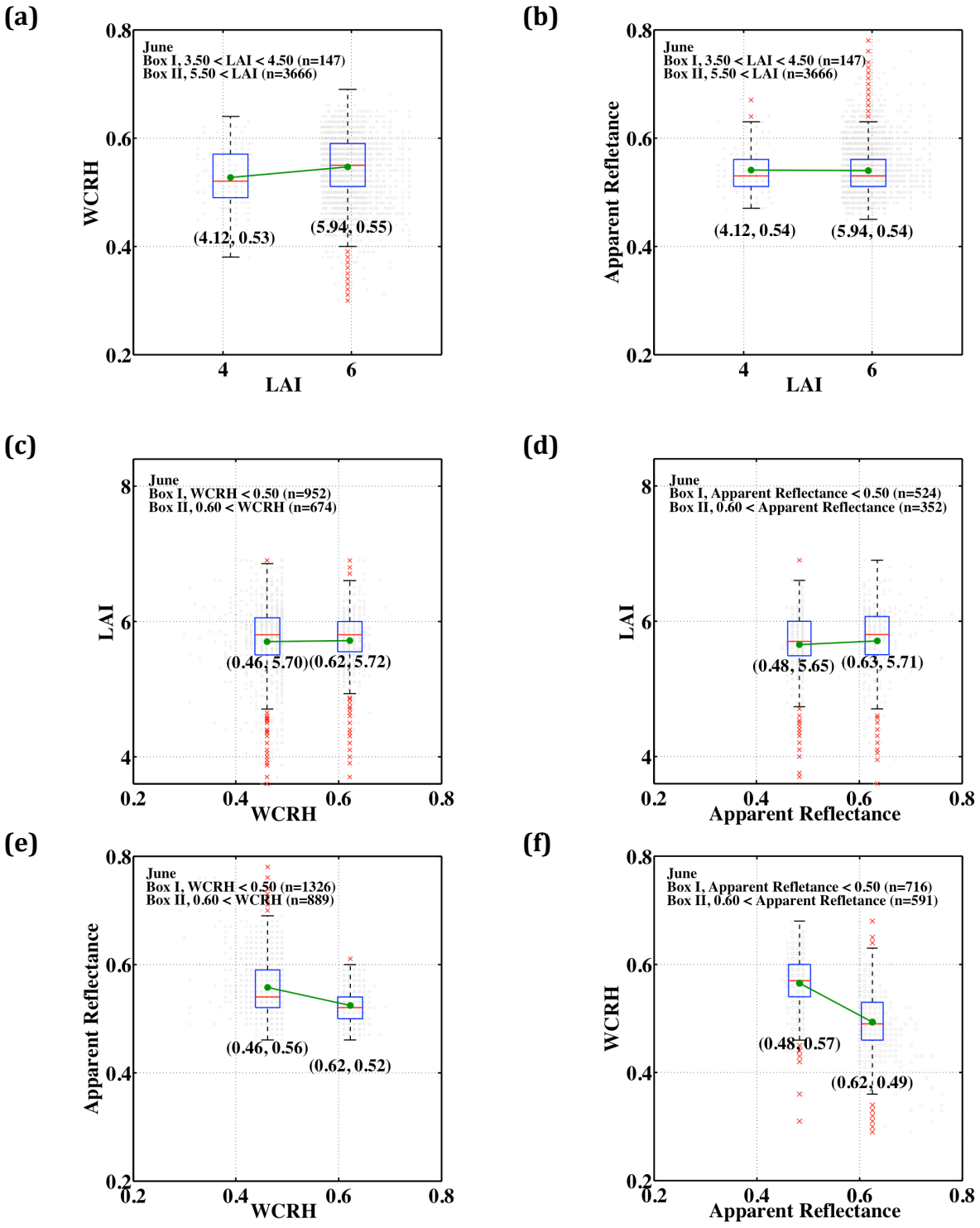

Figure S7. Relationship between GLAS lidar metrics and with LAI. (a, b) Variation in GLAS Waveform Centroid Relative Height (WCRH) and Apparent Reflectance (AR) for pixels with low and high Terra MODIS LAI values. (c, d) Variation in LAI for pixels with low and high values of WCRH and AR. (e, f) Relationship between WCRH and AR. Gray dots and red crosses show the data. Upper, middle (red line) and lower box edges separate the 75%, 50% and 25% percentiles of data used. The red crosses are outliers, each representing upper and lower 0.25% of the data. Similar relations are found for October (not shown).

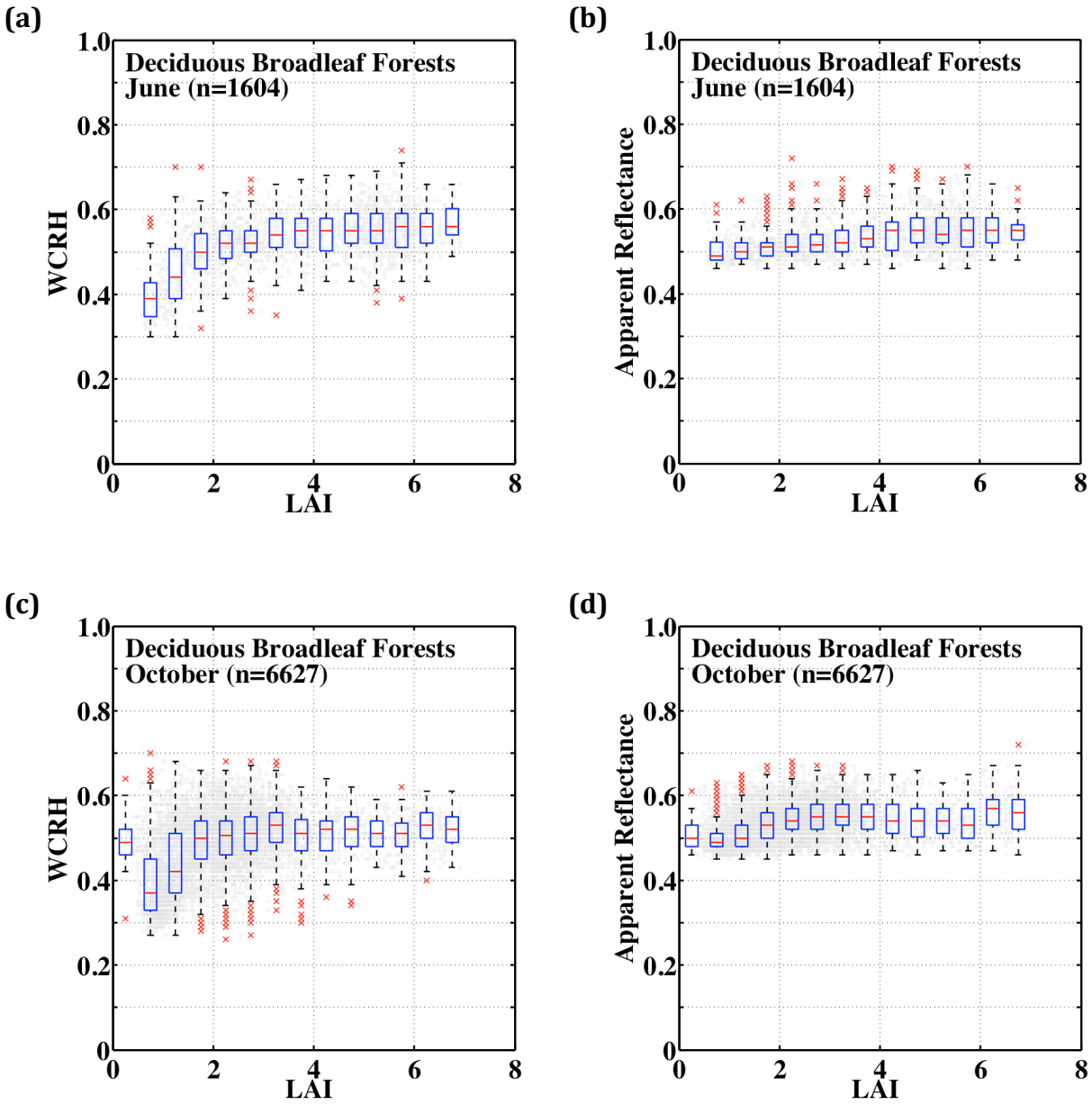

Figure S8. Relationship between GLAS lidar metrics and LAI in deciduous broadleaf forests. Distributions of GLAS Waveform Centroid Relative Height (WCRH) and Apparent Reflectance as a function of Terra MODIS LAI in the case of deciduous (temperate) broadleaf forests in the northern hemisphere in (a, b) June and (c, d) October. Gray dots and red crosses show distributions of lidar metrics within 0.5 LAI bins. Upper, middle (red line) and lower box edges show the 75%, 50% and 25% percentiles of GLAS metrics. The red crosses are outliers, each representing upper and lower 0.25% of the GLAS lidar observations. June represents data from May-20 to June-23, 2005 and May-24 to June-26, 2006. October represents data from October-3 to November-8, 2004 and October-2 to November-5, 2007. MODIS pixels with valid LAI values and four or more GLAS lidar observations were used (table S3).

Supplementary Tables

Table S1. Number of greening pixels (Section 1) from Terra and Aqua MODIS sensors

	Terra		Aqua	
Year	Number of greening pixels	As a % of rainforest pixels	Number of greening pixels	As a % of rainforest pixels
2000	804,550	59.02	N/A	N/A
2001	723,796	53.10	N/A	N/A
2002	990,863	72.69	N/A	N/A
2003	518,857	38.06	238,998	17.53
2004	919,820	67.48	233,140	17.10
2005	N/A	N/A	N/A	N/A
2006	901,602	66.14	227,926	16.72
2007	783,164	57.45	260,370	19.10

Table S2. Number of pixels with valid EVI and BRF data in June, October and March accumulated over a 7-year period (June 2000 to May 2008, excluding June 2005 to May 2006 due to the dry season drought in 2005) from Terra MODIS and MISR sensors. The table also shows the same for the Aqua MODIS sensor, but accumulated over a 4-year period (June 2003 to May 2008 excluding June 2005 to May 2006)

		Fraction of Rainforest Pixels With Valid Data (%)		
Sensor	Number of Valid Data	June	October	March
Terra MODIS	One or more	96.67	94.38	70.92
Aqua MODIS	One or more	33.65	30.32	12.10
Terra MISR	One or more	48.07	25.75	15.33

Table S3. Number of pixels with valid Terra MODIS LAI data and four or more valid GLAS footprints in June and October

	June		October	
Year	Number of valid LAI pixels	Number of corresponding GLAS footprints	Number of valid LAI pixels	Number of corresponding GLAS footprints
		Amazonian Rainforests		
2004	N/A	N/A	3,859	17,293
2005	3,031	13,536	N/A	N/A
2006	1,911	8,607	N/A	N/A
2007	N/A	N/A	5,987	29,858
Total	4,942	22,143	9,846	47,151
		Deciduous Broadleaf Forests		
2004	N/A	N/A	2,419	10,719
2005	955	4,164	N/A	N/A
2006	649	2,761	N/A	N/A
2007	N/A	N/A	4,208	19,650
Total	1,604	6,925	6,627	30,369

Table S4. Regression relationships between climate and GLAS Waveform Centroid Relative Height (WCRH) and Apparent Reflectance (AR). Climate is represented by annual total precipitation from TRMM, photosynthetically active radiation from CERES and mean annual temperature from CRU. Long-term means of climate variables were evaluated from 2001 to 2010 data, but excluding 2005 and 2010 drought years. Each TRMM pixel contains 10 or more GLAS observations; CERES pixel has 160 or more, and CRU pixel has 40 or more

x	y	Slope	Intercept	R^2	p-value
WCRH	Annual Precipitation (mm $year^{-1}$)	4428.3	297.1	0.17	<0.001
WCRH	Photosynthetically Active Radiation (W m^{-2})	21.8	83.6	0.08	<0.001
WCRH	Mean Annual Temperature (°C)	8.3	22.1	0.15	<0.001
AR	Annual Precipitation (mm $year^{-1}$)	-600.4	3011.2	0.00	0.16
AR	Photosynthetically Active Radiation (W m^{-2})	-65.6	130.9	0.26	<0.001
AR	Mean Annual Temperature (°C)	-10.3	32.1	0.10	<0.001

Table S5. List of Abbreviations

AR	Apparent Reflectance
Aqua	NASA scientific research satellite in a Sun-synchronous near polar circular orbit around the Earth; crosses Equator at 1:30pm
BRF	Bidirectional Reflectance Factor
C5	Collection 5
CERES	Clouds and the Earth's Radiant Energy System
CRU	Climatic Research Unit
DOY	Day of Year (designates the beginning of the compositing period)
ED	Extended Data
EVI	Enhanced Vegetation Index
GLAS	Geoscience Laser Altimeter System
ICESat	Ice, Cloud and land Elevation Satellite
JAS	July, August, and September
LAI	Leaf Area Index
LiDAR	Light Detection and Ranging
MAIAC	Multi-angle Implementation of Atmospheric Correction
MISR	Multiangle Imaging Spectroradiometer
MODIS	Moderate-resolution Imaging Spectroradiometer
NASA	National Aeronautics and Space Administration
NIR	Near Infrared
PA	Phase angle
PAR	Photosynthetically Active Radiation
PDF	Probability Density Function
RAA	Relative Azimuth Angle between solar and sensor view directions
SI	Supplementary Information
SZA	Solar Zenith Angle
SOM	Space Oblique Mercator
Terra	NASA scientific research satellite in a Sun-synchronous near polar circular orbit around the Earth; crosses Equator at 10:30am
TRMM	Tropical Rainfall Measuring Mission
VI	Vegetation Index
VZA	View Zenith Angle
WCRH	Waveform Centroid Relative Height

SUPPLEMENTARY INFORMATION

Sunlight mediated seasonality in canopy structure and photosynthetic activity of Amazonian rainforests

Jian Bi, Yuri Knyazikhin, Sungho Choi, Taejin Park, Jonathan Barichivich, Philippe Ciais, Rong Fu, Sangram Ganguly, Forrest Hall, Thomas Hilker, Alfredo Huete, Matthew Jones, John Kimball, Alexei I. Lyapustin, Matti Mõttus, Ramakrishna R. Nemani, Shilong Piao, Benjamin Poulter, Scott R. Saleska, Sassan S. Saatchi, Liang Xu, Liming Zhou, and Ranga B. Myneni

This document provides Supplementary information not provided in the main text of the article "Sunlight Mediated Seasonality in Canopy Structure and Photosynthetic Activity of Amazonian Rainforests." It contains (*i*) Supplementary Data and Methods, which provides an extended description of the data and methods used; (*ii*) Supplementary Discussion related to various issues in previous studies that led to incorrect conclusions; (*iii*) Supplementary References; (*iv*) Supplementary Figures and (*v*) Supplementary Tables.

Supplementary Data and Methods

1. Study region and greening pixels

This study is focused on a 1200×1200 km^2 region in central Amazonia (MODIS tile "h11v09"; 0° to 10°S and 60°W to 70°W; figure S1(a)). About 95% of this region is covered with terra firme rainforests (Nepstad *et al* 1994). The average annual rainfall varies from about 1800 mm in the south to about 3700 mm in the northwest (figure S1(b)). The number of dry months, generally defined as months with rainfall less than 100 mm, varies from about 4 in the south to less than 2 in the northwest. For comparison purposes (Morton *et al* 2014), the dry season is defined as June to October (137 mm/month) and the wet season as November to May (276 mm/month). This is one of two tiles studied by (Morton *et al* 2014). Expanding the area to match that study did not alter our results and conclusions.

Terra MODIS and MISR data analysed in this study consisted of seven seasonal cycles (June to May), while the Aqua MODIS data consisted of four cycles, as in (Morton *et al* 2014). Forest pixels with valid Enhanced Vegetation Index (EVI) data are classified as greening pixels during a seasonal cycle if the average EVI value during the month of October is greater than the average EVI value during the month of June. Here, EVI refers to Terra MODIS Collection 5 EVI data (Section 2.5). The MODIS and MISR analyses in this study are focused on these "greening pixels" because we wish to address this key question: is the dry season greening purely an artefact of variations in sun-sensor geometry (Galvão *et al* 2011, Morton *et al* 2014) or does it reflect actual changes in canopy after accounting for variations in sun-sensor geometry (Xiao *et al* 2005, Huete *et al* 2006, Myneni *et al* 2007, Brando *et al* 2010, Samanta *et al* 2012)? The proportion of greening pixels varies from year to year. It averages ~60% of all rainforest pixels in the case of the Terra MODIS sensor (table S1) due to strict quality filtering. Nearly every rainforest pixel in the study region exhibits dry season greening at least once, if not more, because the data are accumulated, not averaged, over multiple seasonal cycles.

2. Data

2.1. TRMM Precipitation Data: Monthly precipitation data from the Tropical Rainfall Measuring Mission (TRMM) at quarter degree spatial resolution for the period January 1998 to December 2012 (TRMM product 3B43, Version 7) are used in this study (WWW-TRMM).

2.2. CERES Surface PAR Fluxes: Monthly at-surface Photosynthetically Active Radiation (PAR,

400-700 nm; the sum of "Computed PAR Surface Flux Direct – All-sky" and "Computed PAR Surface Flux Diffuse – All-sky") data at 1°×1° spatial resolution from June 2000 to May 2008 are used in this study (WWW-CERES).

2.3. CRU Temperature Data: The latest version of the 0.5° temperature data set produced by the Climatic Research Unit (CRU; University of East Anglia; CRU TS3.21) is used in this study (WWW-CRU).

2.4. MODIS Land Cover: Evergreen broadleaf forests in the study region are identified using the Collection 5 land cover data set "MODIS Land Cover Type Yearly L3 Global 500 m SIN Grid" (MCD12Q1) (WWW-MCD12Q1).

2.5. MODIS NIR Reflectance and EVI: The following Collection 5 EVI data are used in this study: (a) Terra Moderate Resolution Imaging Spectroradiometer (MODIS) EVI data from June 2000 to May 2008 (WWW-MOD13A2) and (b) Aqua MODIS EVI data from June 2003 to May 2008 (WWW-MYD13A2). Data from June 2005 to May 2006 are not used due to the dry season drought in 2005 (Samanta *et al* 2010a). These data sets also include surface reflectance at the near infrared (NIR) spectral band (858 nm) and sun-sensor measurement geometry. The data are at a spatial resolution of 1×1 km^2 and 16-day temporal frequency. The same EVI data were used in previous studies (Galvão *et al* 2011, Morton *et al* 2014). The quality of NIR reflectance and MODIS EVI data in each pixel is assessed using the 16-bit quality flags (Samanta *et al* 2010b, Xu *et al* 2011). The number of pixels with valid EVI data in June, October and March are shown in table S2.

2.6. MODIS MAIAC EVI: EVI data from Terra (June 2000 to May 2008) and Aqua (June 2003 to May 2008) MODIS sensors at 1×1 km^2 spatial resolution and 8-day temporal frequency generated with the Multi-angle Implementation of Atmospheric Correction (MAIAC) algorithm (Lyapustin *et al* 2012) are used in this study (WWW-MAIAC). The MAIAC EVI data are standardized to a fixed sun-sensor geometry (nadir viewing direction, solar zenith angle of 45^o). Thus, the MAIAC EVI data are free of sun-sensor geometry effects.

2.7. MODIS LAI: Collection 5 Leaf Area Index (LAI) data from Terra MODIS for the period June 2000 to May 2008 are used in this study (WWW-MOD15A2). Data from June 2005 to May 2006 are excluded from analyses of LAI seasonal changes (figures 1 and 2) due to the dry season drought in 2005 (Samanta *et al* 2010a). The data are at 1×1 km^2 spatial resolution and 8-day temporal frequency. Valid LAI data in each 1×1 km^2 8-day pixel are identified using quality flags (Samanta *et al* 2011, Poulter and Cramer, 2009).

2.8. MISR Bidirectional Reflectance Factor: Land Surface Data (version 22) from the Terra Multiangle Imaging Spectroradiometer (MISR) for the period June 2000 to May 2008 are used in this study (WWW-ASDC). Data from June 2005 to May 2006 are not used due to the dry season drought in 2005 (Samanta *et al* 2010a). The data are at a spatial resolution of 1.1 × 1.1 km^2 and include Bidirectional Reflectance Factors (BRF) at the nine MISR view angles (nadir, ±26.1°, ±45.6°, ±60.0° and ±70.5°) in four spectral bands (446, 558, 672, and 866 nm). MISR data with LandQA=0 (cloud free, aerosol optical depth below 0.3) are considered valid.

2.9. GLAS Centroid and Apparent Reflectance: Data from the Geoscience Laser Altimeter System (GLAS) instrument onboard the Ice, Cloud and land Elevation Satellite (ICESat) acquired during four periods – May 20 to June 23, 2005 (L3c), May 24 to June 26, 2006 (L3f), October 3 to November 8, 2004 (L3a) and October 2 to November 5, 2007 (L3i) – are used to analyze the sensitivity of the waveform centroid relative height (WCRH) and Apparent Reflectance (AR) to LAI (WWW-GLAS). The same data were used in (Morton *et al* 2014). For comparison purposes, low quality data were filtered as described in (Morton *et al* 2014). Additionally, GLAS footprints over non-forest and/or bare ground were screened by imposing the following conditions: (a) MODIS Land Cover corresponding to GLAS footprints is "Evergreen Broadleaf Forests" and (b) number of GLAS waveform Gaussian peaks exceeds one. GLAS lidar analysis is focused on the region spanning 0° to 10°S and 60°W to 80°W – the spatial extent of the blue and red squares in figure S1(a).

3. Sun-Sensor Geometry

Three angles characterize the sun-sensor geometry of a pixel (figure S1(c)): (a) solar zenith angle (SZA), (b) relative azimuth angle (RAA), and (c) view zenith angle (VZA). All three change

during the year in the case of MODIS. The distribution of these angles for pixels in the study region during each of the twenty-three 16-day compositing periods in a year is shown in figure 1 for Terra MODIS. The geometry for Aqua MODIS is very similar to that of Terra MODIS. The view zenith angles are fixed in the case of MISR. The following discussion of sun-sensor geometry is specific to this study's region (figure S1(a)).

The geometry in terms of SZA and RAA is approximately cyclical with a period of six months (figures 1(b) and (c)). Terra and Aqua MODIS and Terra MISR measurements are made at higher SZA ($\sim 30^o$ to 40^o) about the solstices, June/July and December/January, and at lower SZA ($\sim 20^o$ to 30^o) about the equinoxes, September/October and February/March (figure 1(b)). The progression of Terra and Aqua MODIS RAA during the year shows a similar cyclical behavior (figure 1(c)). The measurements are made closer to the solar azimuthal plane, or the principal plane, (RAA $\sim 0°$ and $180°$), about the equinoxes and approximately $\pm 30°$ to $\pm 45°$ off the orthogonal plane (RAA $\sim 130^o$ and 50^o) about the solstices (figure 1(c) and figure S2). View zenith angle varies between $0°$ (nadir) and $60°$ (figure 1(d)). The RAA of MISR sampling along the spacecraft flight track follows its Terra counterpart, but is shifted by about $90°$ (not shown). Half of Terra and Aqua MODIS observations about the solstices were collected at VZA below $15°$ and $20°$, respectively. Around 50% of the measurements about the equinoxes were made at VZA below $35°$ (Terra) and $20°$ (Aqua). The MISR VZAs are strongly peaked as expected around their nominal values of $0.0°$, $\pm 26.1°$, $\pm 45.6°$, $\pm 60.0°$ and $\pm 70.5°$ (figure S2).

Choosing three 16-day composites, one each in June (Jun 25 to Jul 10), October (Oct 15 to 30) and March (Mar 5 to 20), is sufficient to assess whether the previously reported seasonality in radiometric greenness (Xiao *et al* 2005, Huete *et al* 2006, Brando *et al* 2010) and leaf area (Myneni *et al* 2007, Samanta *et al* 2012) of Amazonian rainforests is an artefact of sun-sensor geometry (Galvão *et al* 2011, Morton *et al* 2014) or not. The three periods correspond to the beginning of the dry season, end of the dry season and mid wet season, respectively. The Terra and Aqua MODIS observations provide pairs of matching RAA (October vs. March), varying RAA (June vs. October), matching SZA (Terra and Aqua in June and March), varying SZA (October from Terra and Aqua) (figure S2). The Terra MISR sensor samples the surface close to the principal plane in June and near the orthogonal plane in October and March. This manner of sampling is opposite to that of MODIS (figure S2). The juxtaposition of MODIS and MISR sampling provides an interesting opportunity for assessing the presence or absence of seasonal variations in these rainforests.

4. Forest Reflectance

4.1. Bidirectional Reflectance Factor (BRF): The reflected radiation field from a vegetation canopy illuminated by a solar beam in a coordinate system with the polar axis pointed to the sun is considered here. The reflected radiance is expressed relative to a surface perpendicular to the solar beam and depends on the phase angle, γ, and azimuth, ψ. The phase angle is the angle between the directions to the sun and sensor (figure S1(c)). The plane ψ is chosen such that the phase angle varies between $-(90° + \theta_0)$ and $+(90° - \theta_0)$ where θ_0 is the sun zenith angle. In this coordinate system the Bidirectional Reflectance Factor, $BRF(\gamma, \psi)$, is the ratio of radiance reflected from the vegetation canopy to the radiance reflected from an ideal Lambertian surface under identical illumination conditions. The Lambertian surface in this instance is perpendicular to the solar beams. For a plane given by ψ and $\psi + 180°$, the BRF is a function of SZA, phase angle and wavelength. Its magnitude and angular shape depends on the composition, density, geometric structure of the reflecting medium, in addition to the foliage optical properties.

4.2. Transformation of MODIS and MISR BRF data: Let $BRF_{xy}(\theta_0, \theta_v, \Delta\varphi)$ be the observed BRF at a location (x, y) on the Earth's surface. The BRF_{xy} is a standard product of MODIS and MISR sensors, which is expressed relative to a horizontal surface. The sun-sensor geometry is represented by the sun, θ_0, and sensor, θ_v, view zenith angles, and the view azimuth φ_v (figure S1(c)). First, we introduce a new coordinate system with the polar axis pointed to the sun. The quantities, $I_{xy} = BRF_{xy} \cos\theta_0$, represent radiances reflected from forests illuminated by a

parallel beam of unit intensity. The radiances are expressed relative to the unit surface perpendicular to the solar beam and depend on the phase angle, γ, and azimuth, ψ, in this system. The phase angle is the angle between directions to the sun and sensor, i.e., $\gamma = \text{acos}[\cos\theta_v \cos\theta_0 + \sin\theta_v \sin\theta_0 \cos\varphi_v]$.

Second, we group I_{xy} with respect to the phase angle (figure S3). This procedure transforms the standard BRF product into BRF expressed in terms of the phase angle, γ, and azimuth, ψ. The azimuth specifies sampling plane of satellite-borne sensors. The MODIS instrument scans the Earth across the Terra and Aqua spacecraft flight track, which is approximately from East to West (figure S3(a)). The MISR instrument measures reflected radiation along the Terra flight track, which is approximately from North to South (figure S3(b)). The sampling planes are fixed for MODIS and MISR instruments. We assign the sign "plus" to γ if the direction to the sensor approaches the direction to sun from East (Terra MODIS), West (Aqua MODIS) or North (Terra MISR), and "minus" otherwise. The phase angle varies between $-(90° + \theta_0)$ and $90° - \theta_0$. The probability density distribution function $p(\theta_0, \gamma)$ of the phase angle is evaluated from the fraction of data in each group.

Finally, the reflected radiances in each group are averaged. This methodology is applied to transform standard BRF products from Terra and Aqua MODIS observations (figure S3(a)). In the case of MISR, the algorithm is applied to each MISR camera to derive camera specific BRF (figure S3(b)) and corresponding probability density functions. The camera specific BRFs for which $|\gamma - \bar{\gamma}| \leq \sigma$ are used in further analyses. Here $\bar{\gamma}$ and σ denote camera specific mean and standard deviation of the phase angle γ.

4.3. Effect of Changing Canopy Properties on BRF: figures S5(a) and (b) illustrate the effect of changing canopy properties on BRF. Here, SZA is held constant. An increase in LAI, with leaf optical properties unchanged, increases the interception of incoming solar radiation by the vegetation canopy, which in turn increases the amount of reflected radiation. This increases the magnitude of BRF at all phase angles, i.e. a non-linear upward shift in the angular signature of the BRF, as shown in figure S5(b). The overall shape of the BRF remains unchanged. This is a well-known fact: the reflectance of dense vegetation, or a vegetation canopy with a dark background, is an increasing function of LAI (e.g. figure 1 in (Huang *et al* 2008)). Changes in leaf optical properties either augment or suppress the LAI effect on the reflectance factor (Samanta *et al* 2012). Thus, changing canopy properties and holding SZA constant changes the magnitude of the BRF but not the overall shape of the signature. This explains the observed BRF changes in figures 3(a) and (b).

4.4. Effect of Changing SZA on BRF: figures S5(c) and (d) illustrate the effect of changing SZA on BRF. Here, canopy properties are held constant. The cumulative contribution of within-canopy sources generated by single- and multiple-scattered photons to canopy-exiting radiation along a given direction increases with photon path length, L, as $\sim(1 - \exp(-\sigma L))$, where L is the distance between sources within the canopy and the upper boundary of the canopy and σ is the extinction coefficient. An increase in SZA results in longer photon path lengths for positive phase angles (figure S5(c)). The opposite is true for negative phase angles. Increasing SZA with constant canopy therefore results in an asymmetric transformation of the BRF signature, that is, enhanced values for positive phase angles and depressed values for negative phase angles (figure S5(d)). It also decreases the range of BRF variation at positive phase angles and a corresponding increase in the range of BRF variation at negative phase angles. Thus, both the shape and magnitude of the BRF signature are changed. The asymmetric transformation also causes the two BRF signatures to intersect, as illustrated in figure S5(d). The phase angle at which the two signatures intersect can be calculated using the principle of directional reciprocity (Section 4.6).

It is important to note that the path L varies with SZA as $\sim 1/\cos(SZA)$. It means that effect of changing SZA on the BRF's angular shape is weak at low SZA. For example, a change in SZA from 20° to 30° involves a change in L from ~1.06 to ~1.15. The impact, however, increases with SZA. This explains why SZA variation has no discernable impact on the angular signatures of reflectances in figures 3(a) and (b).

4.5. Effect of Changing Canopy Properties and SZA on BRF: figures S5(e) and (f) illustrate the effect of changing both canopy properties and SZA on BRF. Changing canopy properties but holding SZA constant changes the magnitude of BRF but retains its overall angular shape (Section 4.3). Changing SZA but holding canopy properties invariant changes the magnitude of BRF differently for positive and negative phase angles, thus changing the shape of the BRF as well (Section 4.4). Changing canopy properties and SZA simultaneously combines these two effects, i.e. the BRF is transformed asymmetrically and shifted in magnitude. For example, decreasing SZA depresses the BRF at positive phase angles and enhances the same at negative phase angles – transformation of the green colored BRF signature to dashed-blue color signature in figure S5(f). Increasing canopy properties, say LAI and/or foliage optical properties, shifts the overall BRF signature up in magnitude – transformation of the dashed-blue color signature to solid-blue color signature in figure S5(f). This explains the BRF signature changes in figures 3(c) and (d). Importantly, it follows from this argumentation that *higher or equal values of BRF at lower SZA relative to BRFs at higher SZA always indicate a change in canopy properties*.

4.6. Proof of Dry Season Changes From the Directional Reciprocity Principle: The optical reciprocity theorem (Davis and Knyazikhin, 2005) provides a proof relevant to our study. It states that switching detector and source and inverting the directions of propagation yield the same result for BRF. It follows from the theorem that the BRFs of a canopy, or two similar canopies, corresponding to different sun positions, say Ω_0 and Ω_1, necessarily intersect at $\gamma_0 = -\text{acos}(\Omega_0 \cdot \Omega_1)$. Indeed, the BRF in direction Ω_1 due to a mono-directional solar beam in direction $-\Omega_0$ is related to the BRF in direction Ω_0 due to a mono-directional solar beam in direction $-\Omega_1$ as $BRF(-\Omega_0, +\gamma) = BRF(-\Omega_1, -\gamma)$. If $BRF(-\Omega_0, \gamma)$ is symmetric at $\gamma_0 = \text{acos}(\Omega_0 \cdot \Omega_1)$ (e.g., as in October), the BRFs should intersect at $\gamma_0 = -\text{acos}(\Omega_0 \cdot \Omega_1)$. Changing canopy properties with illumination conditions unchanged results in an upward or downward shift in the angular signature of the BRF (Section 4.5). This causes the intersection point to deviate from γ_0, indicating a difference in canopy properties. The deviation of the intersection point around $-5.5°$ from $\gamma_0 = -37.1°$ shown in figure 3(d) is significant, indicating *different canopy properties in June and October*.

Supplementary Discussion

Galvão *et al* (2011) and Morton *et al* (2014) claim that previous studies (Xiao *et al* 2005, Huete *et al* 2006, Myneni *et al* 2007, Brando *et al* 2010, Samanta *et al* 2012) misinterpreted changes in near-infrared (NIR) reflectance caused by seasonal changes in sun-satellite sensor geometry as seasonal variations in rainforest canopy structure and greenness. They conclude that Amazonian rainforests maintain consistent structure and greenness during the dry season based on their analysis of satellite borne sensor data (MODIS and Lidar) and model exercises. Here we present a detailed critique of their analysis.

An incomplete analysis of the seasonal cycle, i.e. one that is focused only on the dry season, encourages misleading interpretation of both intra- and inter-annual greenness (EVI or LAI) variations as artefacts of changing sun-sensor geometry. For example, if the sun-sensor geometry artefact argument is valid, then the seasonal course of LAI from December to May should be similar to that from June to November because of a repeat in sun-sensor geometry (figures 1(b) and (c)), but it is not (figure 1(a)). Also, if the change in MODIS sampling from the orthogonal plane in June to the principal plane in October (figures S2(a) and (c)) causes the rainforests to appear greener, then the change in MISR sampling from the principal plane in June to the orthogonal plane in October (figures S2(b) and (d)) should cause the rainforests to appear browner. But, greening is observed as well (figure 3(d)).

Interannually, the attribution of anomalous dry season greening (increase in EVI or LAI) in drought year 2005, *vis a vis* dry seasons of non-drought years, to a higher proportion of brighter backscattering MODIS observations is flawed because it is selectively based on data from the first fortnight of October (ED-figure 9 (Morton *et al* 2014)). A higher fraction of backscattering measurements is not seen in 2005 when the analysis is focused on July to September period

(figure S4(b)) as in the original studies (Samanta *et al* 2010a, Samanta *et al* 2010b, Saleska *et al* 2007). Moreover, if claims of geometric artefacts are true, higher backscatter fraction and greenness should also be seen during the more intense dry season drought in 2010 (Xu *et al* 2011). They are not (figure S4(b)), even in their selective analysis (ED-figure 9 (Morton *et al* 2014)).

Crucially, the misinterpretations in Morton *et al* (2014) stem from reliance on prognostications of an untested radiative transfer model. In a critical test of how well the model simulates variation in sunlit and shaded proportions of the canopy, which is central to arguments about geometric artefacts, the model underestimates measurements by ~45% (figure S4(c)). The model is also unrealistically sensitive to litter reflectance in dense vegetation (table 1 (Morton *et al* 2014)), an indication of incorrect physics and/or modeling of foliage spatial distribution. The failure to test the model is compounded by an unquestioned belief in its validity, else the observed dry season greening in geometry-corrected EVI would not have been ignored (figure 3(b) (Morton *et al* 2014) and ED-figure 7(b) (Morton *et al* 2014)). Various statistical analyses of this geometry-corrected EVI data strongly reject the null hypothesis of no change in forest greenness (Saleska *et al* 2015). Indeed the physics of radiative transfer in dense media (Section 2.9 (Knyazikhin *et al* 1999)) informs that these changes in geometry-corrected EVI (figure 2, figure 3(b) in (Morton *et al* 2014) and ED-figure 7(b) in (Morton *et al* 2014)) correspond to large changes in LAI (figure. 1(a)). Thus, there is no valid statistical or theoretical basis to dismiss dry season increase in geometry-corrected EVI (figure 2(b), figure 3(b) in (Morton *et al* 2014) and ED-figure 7(b) in (Morton *et al* 2014)).

The unorthodox belief that Amazonian rainforests should conform to model predictions affects their interpretation of satellite lidar data also. The conclusion that structure and greenness of rainforests remain invariant does not follow from absence of evidence in lidar data for their model prediction that an increase in LAI from 4.5 to 6.5 should result in an increase in Waveform Centroid Relative Height - the height of median return energy relative to the full waveform extent (WCRH; table 1 in (Morton *et al* 2014)). A prudent interpretation might be that the model prediction does not conform to data. Even if the model is assumed to be capable of accurate predictions, the predicted change in WCRH (0.06) is comparable to the spatial standard deviations of June and October WCRH data (~0.07). This clearly suggests a need for additional analysis.

The lack of insight into what might be reasonably expected from lidar data and saturation of lidar signals in dense vegetation compound the problem of detecting seasonal LAI changes. For example, studies that have investigated the relationship between LAI and lidar waveforms (Castillo *et al* 2012, Tang *et al* 2012, Drake *et al* 2002) show that WCRH saturates in mature and secondary growth tropical forests aged over ~20 years (Tang *et al* 2012, Drake *et al* 2002) because the majority of lidar hits are confined to the upper canopy. This saturation of signals emanating from vegetation is different than sensor saturation (Neuenschwander *et al* 2008) – the latter have been filtered out from all analyses.

The saturation effect can be potentially documented through these three analyses. First, although a range of LAI values are observed in Amazonian rainforests, from about 4 to 6 in June and greater than 6 in October, the two lidar metrics, WCRH and Apparent Reflectance (AR), exhibit no correspondent variations (figure S6). Second, rainforests with low (3.5 to 4.5) and high (greater than 5.5) LAI have the same WCRH and AR (figures S7 (a) and (b)). Third, rainforests with low (<0.5) and high (>0.6) WCRH have the same LAI (figure S7(c)). Likewise, rainforests with low (<0.5) and high (>0.6) AR have identical LAI (figure S7(d)). Inference of saturation from figure S6 and figures S7 (a)–(d) depends on the validity of the MODIS LAI data. To alleviate this concern, we present similar results for deciduous broadleaf forests where a broader range of LAI values are encountered. The curvilinear relationship in deciduous forests, where WCRH increases for LAI values 0 to 3 and saturates thereafter (figures S8(a) and (c)), is as expected, and is similar to other relations between LAI and remote measurements (Knyazikhin *et al* 1999, Huang *et al* 2008).

Unlike WCRH, the AR shows no relationship to LAI (figures S6 (b) and (d), figures S8 (b) and (d)), even in sparsely foliated canopies (LAI less

than 3; figures S8 (b) and (d)). Also, the inverse relationship with WCRH is perplexing (figures S7 (e) and (f)). To ascertain whether these results indicate potential data quality problems, we investigated the relationship between the lidar metrics and key climatic variables that govern plant growth, i.e. water, radiation and temperature (Nemani *et al* 2003). The WCRH data are positively related (p-value < 0.001) to all three climatic variables (table S4). This is as it should be, i.e. tall and dense tree stands with higher WCRH are located in climatically favorable environments of higher annual precipitation, solar radiation and mean temperature (table S4). The AR data, on the other hand, show negative relation with two of the three climatic variables. We therefore conclude that GLAS AR data have quality problems.

Morton *et al* (2014)'s interpretations of AR data are contradictory - on the one hand, their validity is discounted by citing corruption from aerosols due to biomass burning, and on the other hand, their invariance is counted as proof that Amazonian rainforests maintain consistent structure and greenness (figure 2(c) (Morton *et al* 2014)). Why table 1 (Morton *et al* 2014) does not show model predictions of AR seasonal variations, unlike WCRH, is unknown. Given these ambiguities, their analyses of AR data must also be deemed inconclusive.

In addition to the analyses presented in this article, three independent studies have rebutted Galvão *et al* (2011) and Morton *et al* (2014) claims with a multitude of satellite and in situ data (Maeda *et al* 2014, Hilker *et al* 2014, Jones *et al* 2014). Dry season greening in sun-sensor geometry corrected data obtained from Morton et al. is due for publication (Saleska *et al* 2015).

Supplementary References

Brando P M, Goetz S J, Baccini A, Nepstad D C, Beck P S and Christman M C 2010 Seasonal and interannual variability of climate and vegetation indices across the Amazon. *Proc. Natl. Acad. Sci. USA.* **107** 14685–14690

Castillo M, Rivard B, Sánchez-Azofeifa A, Calvo-Alvarado J and Dubayah R 2012 LIDAR remote sensing for secondary Tropical Dry Forest identification. *Remote Sens. Environ.* **121** 132–143

Davis A B and Knyazikhin Y 2005 A primer in 3D radiative transfer. *Three Dimensional Radiative Transfer in the Cloudy Atmosphere*, eds Marshak A, Davis A B (Springer-Verlag, Berlin Heidelberg), pp 153-242

Drake J B, et al. 2002 Estimation of tropical forest structural characteristics using large-footprint lidar. *Remote Sens. Environ.* **79** 305–319

Galvão L S, Dos Santos J R, Roberts D A, Breunig F M, Toomey M and de Moura Y M 2011 On intra-annual EVI variability in the dry season of tropical forest: A case study with MODIS and hyperspectral data. *Remote Sens. Environ.* **115** 2350–2359

Hilker T *et al* 2014 Vegetation dynamics and rainfall sensitivity of the Amazon. *Proc. Natl. Acad. Sci. USA.* **111** 16041–16046

Huang D *et al* 2008 Stochastic transport theory for investigating the three-dimensional canopy structure from space measurements. *Remote Sens. Environ.* **112** 35–50

Huete A R *et al* 2006 Amazon rainforests green-up with sunlight in dry season. *Geophys. Res. Lett.* **33** L06405

Jones M O, Kimball J S and Nemani R R 2014 Asynchronous Amazon forest canopy phenology indicates adaptation to both water and light availability. *Environ. Res. Lett.* **9** 124021

Knyazikhin Y *et al* 1999 *MODIS leaf area index (LAI) and fraction of photosynthetically active radiation absorbed by vegetation (FPAR) product (MOD15) algorithm theoretical basis document*, <https://lpdaac.usgs.gov/products/modis_products_table/mcd15a2>

Lyapustin A I *et al* 2012 Multi-angle implementation of atmospheric correction for MODIS (MAIAC): 3. Atmospheric correction. *Remote Sens. Environ.* **127** 385–393

Maeda E E, Heiskanen J, Aragão L E O C and Rinne J 2014 Can MODIS EVI monitor ecosystem productivity in the Amazon rainforest? *Geophys. Res. Lett.* **41** 7176–7183

Morton D C *et al* 2014 Amazon forests maintain consistent canopy structure and greenness during the dry season. *Nature* **506** 221–224

Myneni R B *et al* 2007 Large seasonal swings in leaf area of Amazon rainforests. *Proc. Natl. Acad. Sci. USA* **104** 4820–4823

Nemani R R *et al* 2003 Climate-driven increases in global terrestrial net primary production from 1982 to 1999. *Science* **300** 1560–1563

Nepstad D C *et al* 1994 The role of deep roots in the hydrological and carbon cycles of Amazonian forests and pastures *Nature* **372** 666–669

Neuenschwander A L, Urban T J, Gutierrez R and Schutz B E 2008 Characterization of ICESat/GLAS waveforms over terrestrial ecosystems: Implications for vegetation mapping. *J. Geophys. Res. Biogeosci.* **113** G02S03

Poulter B and Cramer W 2009 Satellite remote sensing of tropical forest canopies and their seasonal dynamics. *Int. J. Remote Sens.* **30** 6575–6590

Saleska S R *et al* 2015 Dry-season greening of Amazon forests. Brief Communications Arising in *Nature* (in press)

Saleska S R, Didan K, Huete A R and Da Rocha H R 2007 Amazon forests green-up during 2005 drought. *Science* **318** 612–612

Samanta A *et al* 2010a Amazon forests did not green-up during the 2005 drought. *Geophy. Res. Lett.* **37** L05401

Samanta A *et al* 2012 Seasonal changes in leaf area of Amazon forests from leaf flushing and abscission. *J. Geophys. Res. Biogeosci.* **117** G01015

Samanta A, Costa M H, Nunes, E L, Vieira S A, Xu, L and Myneni R B 2011 Comment on "Drought-Induced Reduction in Global Terrestrial Net Primary Production from 2000 Through 2009". *Science* **333** 1093

Samanta A, Ganguly S and Myneni R B 2010b MODIS Enhanced Vegetation Index data do not show greening of Amazon forests during the 2005 drought. *New Phytol.* **189** 11–15

Tang H *et al* 2012 Retrieval of vertical LAI profiles over tropical rain forests using waveform lidar at La Selva, Costa Rica. *Remote Sens. Environ.***124** 242–250

WWW-ASDC. NASA Langley Research Center Atmospheric Science Data Center (ASDC) Home page. Available at https://eosweb.larc.nasa.gov/

WWW-CERES. Atmospheric Science Data Center: The Clouds and the Earth's Radiant Energy System (CERES). Available at https://eosweb.larc.nasa.gov/project/ceres/ceres_table

WWW-CRU. Climatic Research Unit (CRU) Time-Series High-Resolution Gridded Datasets. Available at http://www.cru.uea.ac.uk/cru/data/hrg/

WWW-GLAS. Geoscience Laser Altimeter System (GLAS) lidar waveform data. Available at https://nsidc.org/data/icesat/data-dictionaries-landing-page.html

WWW-MAIAC. MAIAC Amazon Data. *Level 1 and Atmosphere Archive and Distribution System (LAADS)*. Available at ftp://ladsweb.nascom.nasa.gov/MAIAC/

WWW-MCD12Q1. Land Cover Type Yearly L3 Global 500 m SIN Grid (MCD12Q1). *Land Process Distributed Active Archive Center*. Available at https://lpdaac.usgs.gov/products/modis_products_table/mcd12q1

WWW-MOD13A2. Vegetation Indices 16-Day L3 Global 1km (MOD13A2). *Land Process Distributed Active Archive Center*. Available at https://lpdaac.usgs.gov/products/modis_products_table/myd13a12

WWW-MOD15A2. Leaf Area Index - Fraction of Photosynthetically Active Radiation 8-Day L4 Global 1km (MOD15A2). *Land Process Distributed Active Archive Center.* Available at https://lpdaac.usgs.gov/products/modis_products_table/mod15a12

WWW-MYD13A2. Vegetation Indices 16-Day L3 Global 1km (MYD13A2). *Land Process Distributed Active Archive Center*. Available at https://lpdaac.usgs.gov/products/modis_products_table/myd13a12

WWW-TRMM. Tropical Rainfall Measuring Mission (TRMM) data. *Goddard Earth Science Data and Information Center*. Available at http://mirador.gsfc.nasa.gov/

Xiao X *et al* 2005 Satellite-based modeling of gross primary production in a seasonally moist tropical evergreen forest. *Remote. Sens. Environ.* **94** 105–122

Xu L *et al* 2011 Widespread decline in greenness of Amazonian vegetation due to the 2010 drought. *Geophy. Res. Lett.* **38** L07402

Yang W *et al* 2006 MODIS leaf area index products: From validation to algorithm improvement. *IEEE Trans. Geosci. Remote. Sens.* **44** 1885–1898

Supplementary Figures

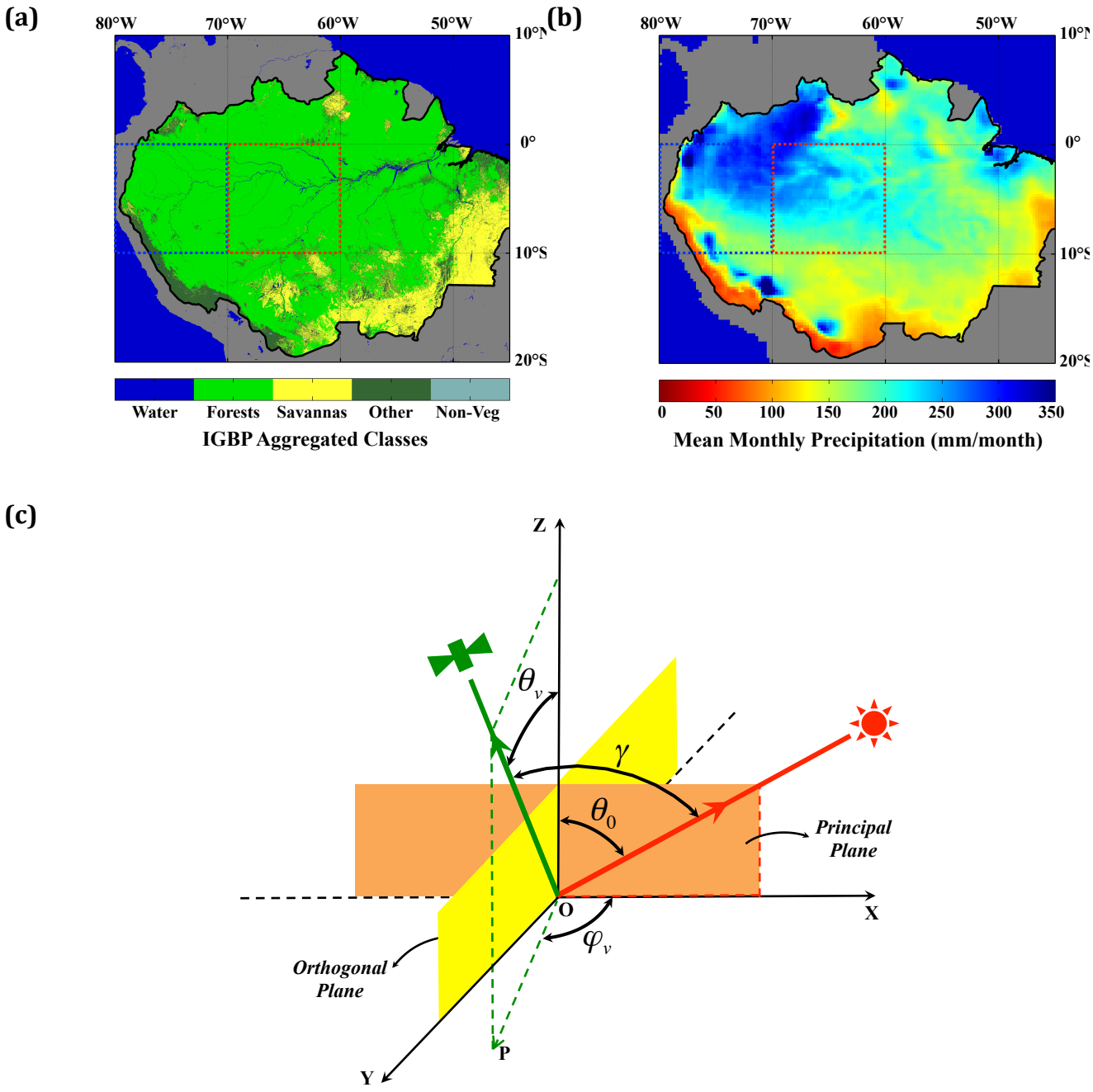

Figure S1. The study domain and sun-sensor geometry. (a) The domain of MODIS and MISR analysis is the red square. The domain of GLAS lidar analysis is both blue and red squares. (b) Monthly mean rainfall from TRMM. (c) Three angles characterize the sun-sensor measurement geometry of a pixel: (1) solar zenith angle, SZA=θ_0 ($0° < \theta_0 \leq 90°$), (2) view zenith angle, VZA=θ_v ($0° \leq \theta_v \leq 90°$) and (3) view azimuth, φ_v ($0° \leq \varphi_v \leq 360°$), measured relative to the principal plane. The angle between the projection, OP, of the direction to the sensor and X axis is the relative azimuth angle (RAA), i.e., RAA=φ_v if $0 \leq \varphi_v < 180°$ and RAA=$360° - \varphi_v$, otherwise. It varies between 0° and 180°. The angle between the directions to the sun and sensor is the phase angle, PA=γ.

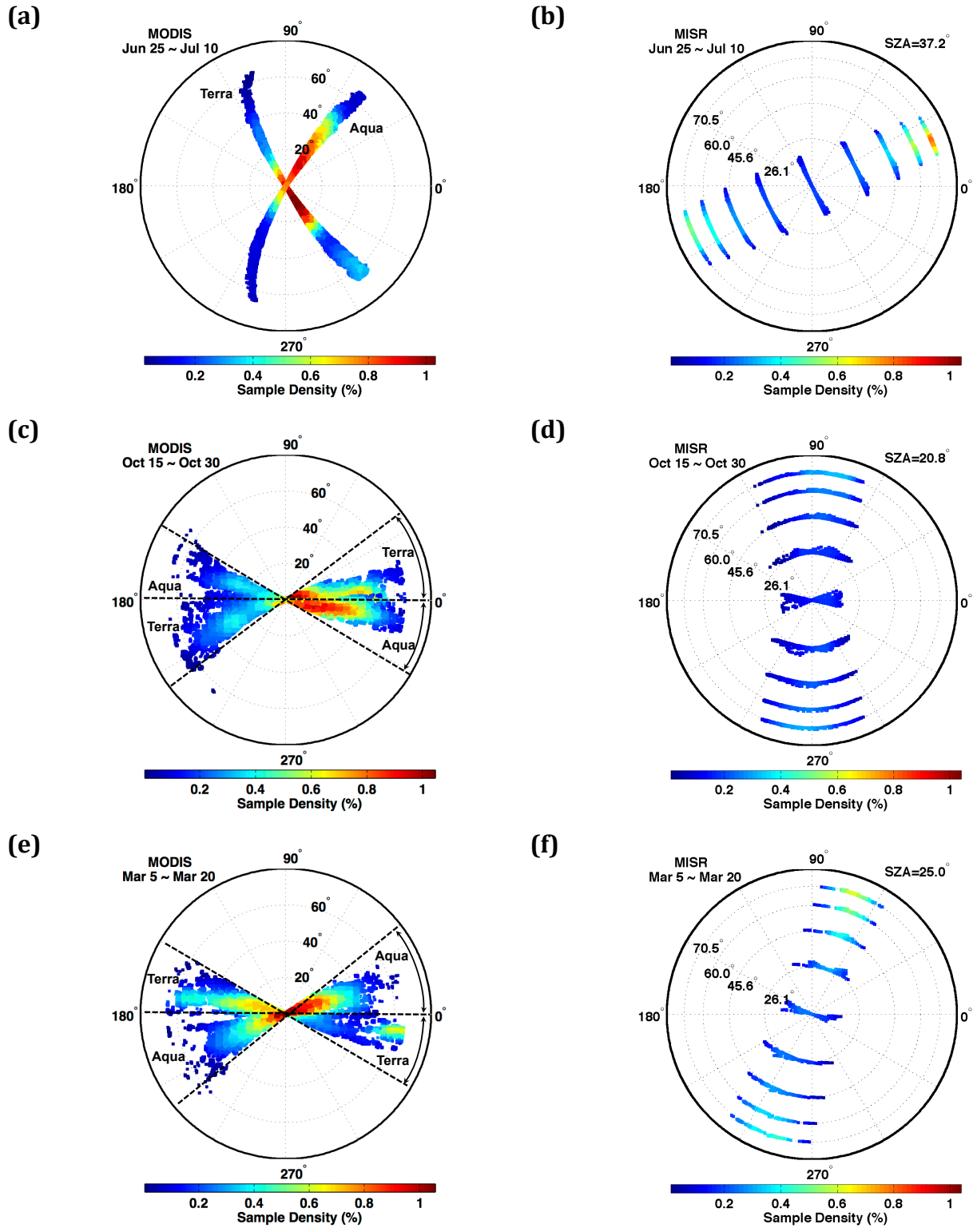

Figure S2. MODIS and MISR sampling geometries. Terra and Aqua MODIS (left panels) and Terra MISR (right panels) sampling geometries during a 16-day compositing period in the months of (a, b) June 2003, (c, d) October 2003, and (e, f) March 2003. The MODIS sensors sample the surface close to the orthogonal plane in June and near the principal plane in October and March. This sampling is opposite to that of MISR sensor.

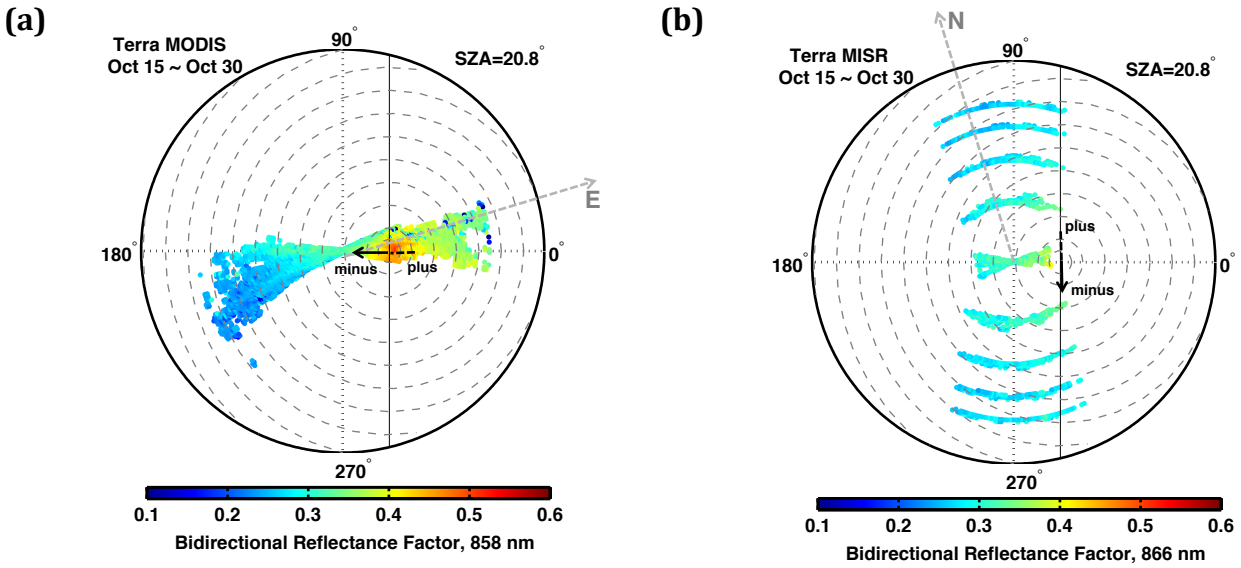

Figure S3. MODIS and MISR reflectances in a modified coordinate system. Terra MODIS (a) and MISR (b) NIR BRFs during a 16-day composite in October 2003. BRF values are expressed in a coordinate system with the polar axis pointed to the Sun. Solid arrows indicate sampling direction that determines the phase angle sign (angle between solar and sensor view directions).

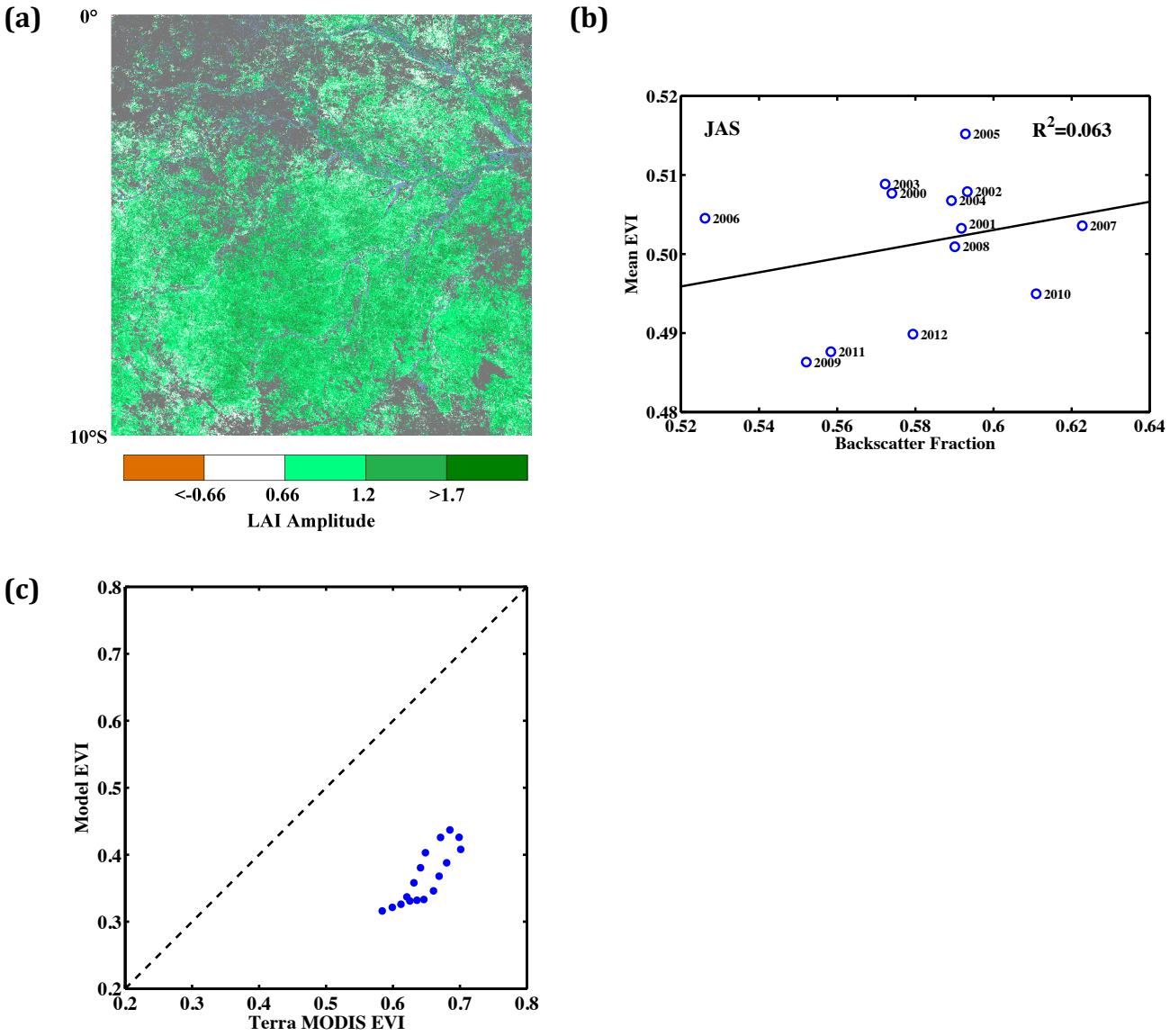

Figure S4. Evidence for seasonality of leaf area and misinterpretation of data following the guidance of an erroneous radiative transfer model (Morton *et al* 2014). (a) Spatial pattern of seasonal Terra MODIS LAI amplitude expressed as the difference between the maximum value during September to November and the minimum value during the following May to June period. White pixels denote locations with LAI amplitudes less than |0.66|, which is the accuracy of MODIS LAI data (Yang *et al* 2006). White and colored pixels together denote pixels that exhibited dry season greening in at least 4 out of 7 seasonal cycles (63% of all forest pixels in the study region). (b) Mean Terra MODIS EVI over rainforests as a function of backscattering fraction evaluated from all 16-day compositing periods in July, August and September (DOY 177 to 272). The backscattering fraction is defined (Morton *et al* 2014) as the fraction of observations with view azimuth less than 90° and greater than 270°. (c) Comparison of model simulated EVI (obtained by digitizing figure 1(c) in Morton *et al* (2014)) with Terra MODIS EVI over Amazonian rainforests. The MODIS EVI is from a 16-day October composite (15th to the 30th) accumulated over 7 seasonal cycles (Section 2.5). The comparison is for phase angles in the range ±10°, that is, ±10° around the hot spot (view zenith angles from 10° to 30° in figure 1(c) of (Morton *et al* 2014)).

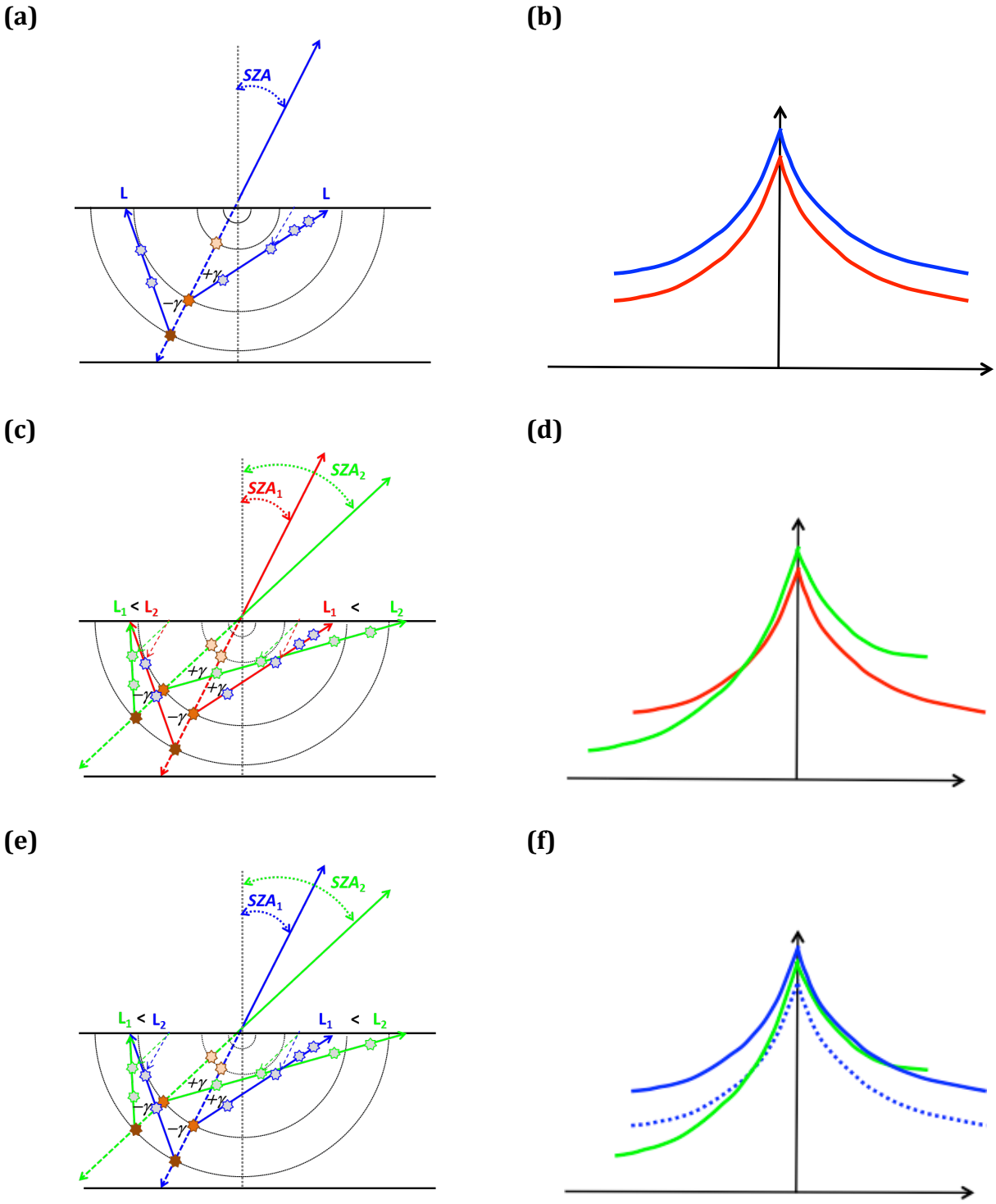

Figure S5. Interpretation of angular signatures of reflectance. Illustration of how the angular signature of Bidirectional Reflectance Factors (BRF) is transformed when (a, b) sun-sensor geometry is held invariant but canopy properties are changed; (c, d) sun-sensor geometry is changed but canopy properties are held invariant; (e, f) both sun-sensor geometry and canopy properties are changed. The dashed arrows depict direction of incident parallel beam of unit intensity.

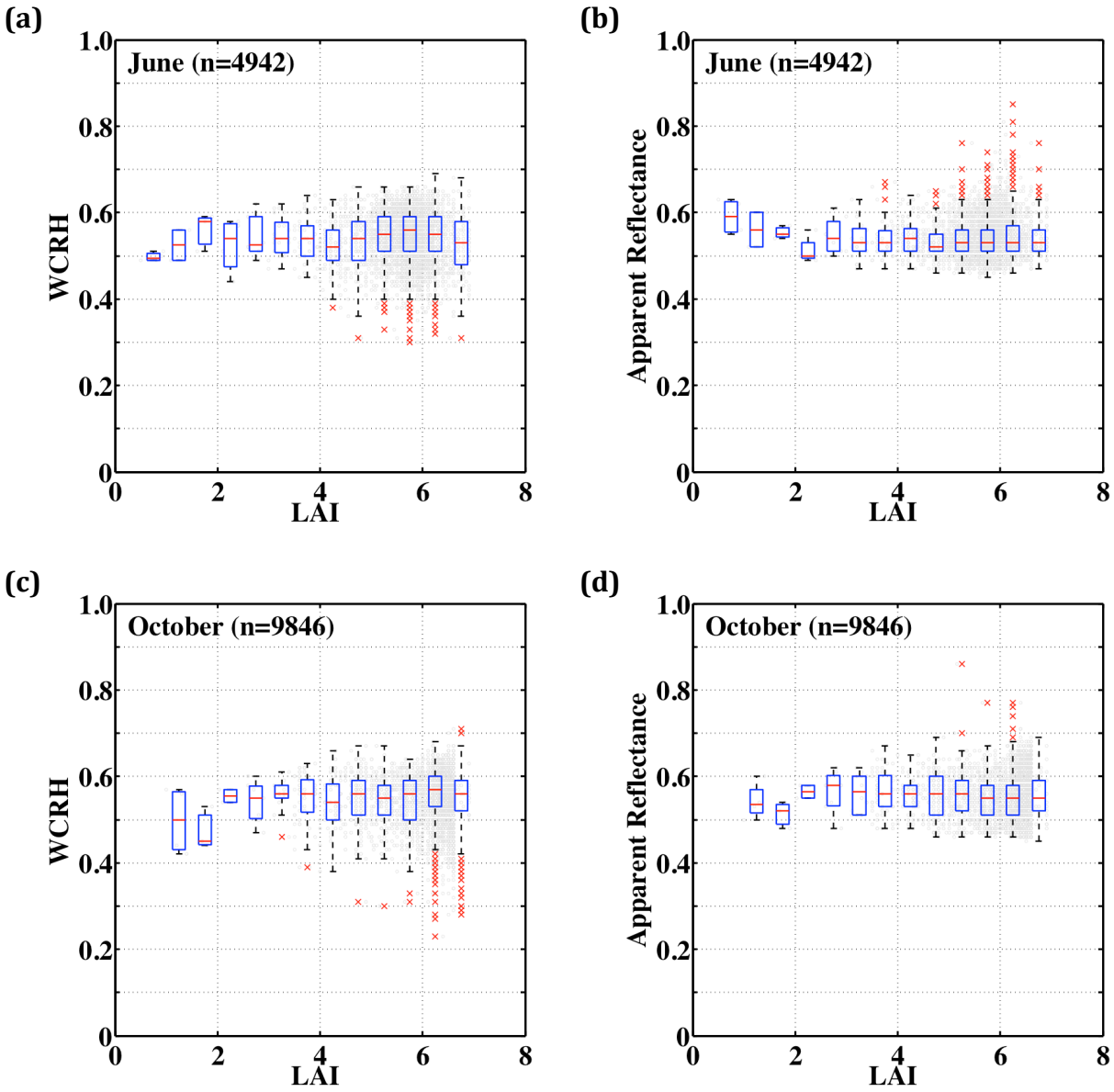

Figure S6. Saturation of GLAS lidar metrics over central Amazonian forests. Distributions of GLAS Waveform Centroid Relative Height (WCRH) and Apparent Reflectance as a function of Terra MODIS LAI in the case of central Amazonian rainforests at the (a, b) beginning and (c, d) end of the dry season. Gray dots and red crosses show distributions of lidar metrics within 0.5 LAI bins. Upper, middle (red line) and lower box edges show the 75%, 50% and 25% percentiles of GLAS metrics. The red crosses are outliers, each representing upper and lower 0.25% of the GLAS lidar observations. June represents data from May-20 to June-23, 2005 and May-24 to June-26, 2006. October represents data from October-3 to November-8, 2004 and October-2 to November-5, 2007. MODIS pixels with valid LAI values and four or more GLAS lidar observations were used (table S3).

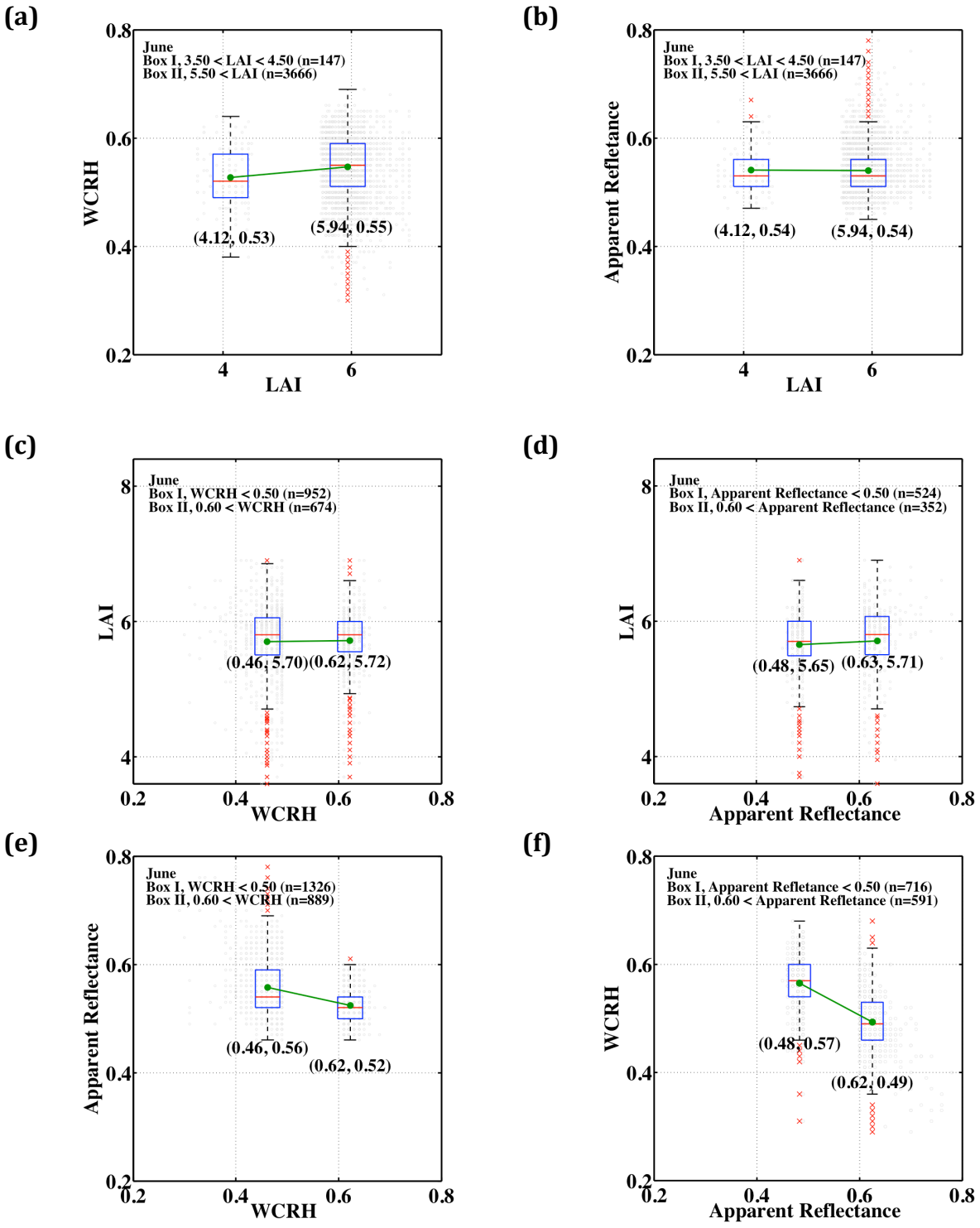

Figure S7. Relationship between GLAS lidar metrics and with LAI. (a, b) Variation in GLAS Waveform Centroid Relative Height (WCRH) and Apparent Reflectance (AR) for pixels with low and high Terra MODIS LAI values. (c, d) Variation in LAI for pixels with low and high values of WCRH and AR. (e, f) Relationship between WCRH and AR. Gray dots and red crosses show the data. Upper, middle (red line) and lower box edges separate the 75%, 50% and 25% percentiles of data used. The red crosses are outliers, each representing upper and lower 0.25% of the data. Similar relations are found for October (not shown).

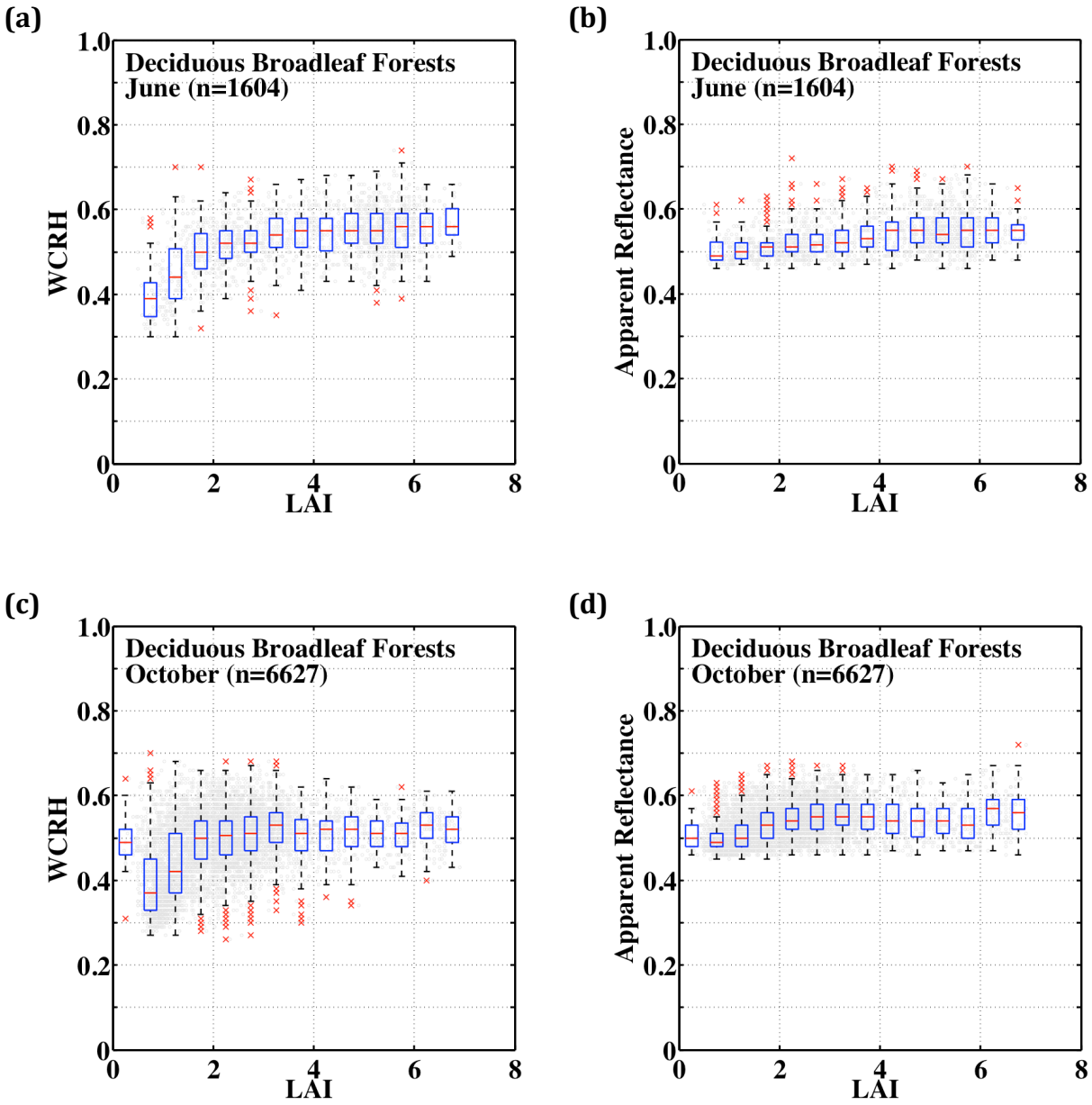

Figure S8. Relationship between GLAS lidar metrics and LAI in deciduous broadleaf forests. Distributions of GLAS Waveform Centroid Relative Height (WCRH) and Apparent Reflectance as a function of Terra MODIS LAI in the case of deciduous (temperate) broadleaf forests in the northern hemisphere in (a, b) June and (c, d) October. Gray dots and red crosses show distributions of lidar metrics within 0.5 LAI bins. Upper, middle (red line) and lower box edges show the 75%, 50% and 25% percentiles of GLAS metrics. The red crosses are outliers, each representing upper and lower 0.25% of the GLAS lidar observations. June represents data from May-20 to June-23, 2005 and May-24 to June-26, 2006. October represents data from October-3 to November-8, 2004 and October-2 to November-5, 2007. MODIS pixels with valid LAI values and four or more GLAS lidar observations were used (table S3).

Supplementary Tables

Table S1. Number of greening pixels (Section 1) from Terra and Aqua MODIS sensors

	Terra		Aqua	
Year	Number of greening pixels	As a % of rainforest pixels	Number of greening pixels	As a % of rainforest pixels
2000	804,550	59.02	N/A	N/A
2001	723,796	53.10	N/A	N/A
2002	990,863	72.69	N/A	N/A
2003	518,857	38.06	238,998	17.53
2004	919,820	67.48	233,140	17.10
2005	N/A	N/A	N/A	N/A
2006	901,602	66.14	227,926	16.72
2007	783,164	57.45	260,370	19.10

Table S2. Number of pixels with valid EVI and BRF data in June, October and March accumulated over a 7-year period (June 2000 to May 2008, excluding June 2005 to May 2006 due to the dry season drought in 2005) from Terra MODIS and MISR sensors. The table also shows the same for the Aqua MODIS sensor, but accumulated over a 4-year period (June 2003 to May 2008 excluding June 2005 to May 2006)

		Fraction of Rainforest Pixels With Valid Data (%)		
Sensor	Number of Valid Data	June	October	March
Terra MODIS	One or more	96.67	94.38	70.92
Aqua MODIS	One or more	33.65	30.32	12.10
Terra MISR	One or more	48.07	25.75	15.33

Table S3. Number of pixels with valid Terra MODIS LAI data and four or more valid GLAS footprints in June and October

	June		October	
Year	Number of valid LAI pixels	Number of corresponding GLAS footprints	Number of valid LAI pixels	Number of corresponding GLAS footprints
		Amazonian Rainforests		
2004	N/A	N/A	3,859	17,293
2005	3,031	13,536	N/A	N/A
2006	1,911	8,607	N/A	N/A
2007	N/A	N/A	5,987	29,858
Total	4,942	22,143	9,846	47,151
		Deciduous Broadleaf Forests		
2004	N/A	N/A	2,419	10,719
2005	955	4,164	N/A	N/A
2006	649	2,761	N/A	N/A
2007	N/A	N/A	4,208	19,650
Total	1,604	6,925	6,627	30,369

Table S4. Regression relationships between climate and GLAS Waveform Centroid Relative Height (WCRH) and Apparent Reflectance (AR). Climate is represented by annual total precipitation from TRMM, photosynthetically active radiation from CERES and mean annual temperature from CRU. Long-term means of climate variables were evaluated from 2001 to 2010 data, but excluding 2005 and 2010 drought years. Each TRMM pixel contains 10 or more GLAS observations; CERES pixel has 160 or more, and CRU pixel has 40 or more

x	y	Slope	Intercept	R^2	p-value
WCRH	Annual Precipitation (mm $year^{-1}$)	4428.3	297.1	0.17	<0.001
WCRH	Photosynthetically Active Radiation (W m^{-2})	21.8	83.6	0.08	<0.001
WCRH	Mean Annual Temperature (°C)	8.3	22.1	0.15	<0.001
AR	Annual Precipitation (mm $year^{-1}$)	-600.4	3011.2	0.00	0.16
AR	Photosynthetically Active Radiation (W m^{-2})	-65.6	130.9	0.26	<0.001
AR	Mean Annual Temperature (°C)	-10.3	32.1	0.10	<0.001

Table S5. List of Abbreviations

AR	Apparent Reflectance
Aqua	NASA scientific research satellite in a Sun-synchronous near polar circular orbit around the Earth; crosses Equator at 1:30pm
BRF	Bidirectional Reflectance Factor
C5	Collection 5
CERES	Clouds and the Earth's Radiant Energy System
CRU	Climatic Research Unit
DOY	Day of Year (designates the beginning of the compositing period)
ED	Extended Data
EVI	Enhanced Vegetation Index
GLAS	Geoscience Laser Altimeter System
ICESat	Ice, Cloud and land Elevation Satellite
JAS	July, August, and September
LAI	Leaf Area Index
LiDAR	Light Detection and Ranging
MAIAC	Multi-angle Implementation of Atmospheric Correction
MISR	Multiangle Imaging Spectroradiometer
MODIS	Moderate-resolution Imaging Spectroradiometer
NASA	National Aeronautics and Space Administration
NIR	Near Infrared
PA	Phase angle
PAR	Photosynthetically Active Radiation
PDF	Probability Density Function
RAA	Relative Azimuth Angle between solar and sensor view directions
SI	Supplementary Information
SZA	Solar Zenith Angle
SOM	Space Oblique Mercator
Terra	NASA scientific research satellite in a Sun-synchronous near polar circular orbit around the Earth; crosses Equator at 10:30am
TRMM	Tropical Rainfall Measuring Mission
VI	Vegetation Index
VZA	View Zenith Angle
WCRH	Waveform Centroid Relative Height